6th International Conference

GEOMATE 2016

Geotechnique, Construction Materials & Environment

EDITORS

Zakaria Hassain
Suksun Horpibulsuk

ISBN: 978-4-9905958-6-9 C3051

November 14 – 16, 2016

SwissOtel Le Concorde, Bangkok, Thailand

GEOMATE 2016 BANGKOK, THAILAND
GEOTECHNIQUE, CONSTRUCTION MATERIALS AND ENVIRONMENT

PROCEEDINGS OF SIXTH INTERNATIONAL CONFERENCE – GEOMATE 2016 GEOTECHNIQUE, CONSTRUCTION MATERIALS AND ENVIRONMENT, BANGKOK, THAILAND 14-16 NOVEMBER, 2016

Geotechnique, Construction Materials and Environment

Edited by

Prof. Zakaria Hossain
Department of Environmental Science and Technology
Graduate School of Bioresources
Mie University, Japan

Prof. Suksun Horpibulsuk
Center of Excellence in Innovation for Sustainable Infrastructure Development
School of Civil Engineering
Suranaree University of Technology, Thailand

THE GEOMATE INTERNATIONAL SOCIETY

Published by:
The GEOMATE International Society
Tsu city, Mie, Japan
E-mail: society@geomate.org
http://www.geomate.org/

ISBN Number: 978-4-9905958-6-9 C3051

Table of Contents

Preface

On behalf of the GEOMATE 2016 Organizing Committee, we would like to welcome you in attending the International Conference on Geotechnique, Construction Materials and Environment held at the Swissotel Le Concorde, Bangkok, Thailand in conjunction with the GEOMATE International Society, Southeast Asian Geotechnical Society (SEAGS), Suranaree University of Technology, Thailand, AOI-Engineering, Useful Plant Spread Society, HOJUN, Cosmo Winds, and Glorious International, Japan

On Friday 11 March 2011, at 14:46 Japan Standard Time, the north east of Japan was struck and severely damaged by a series of powerful earthquakes which also caused a major tsunami. This conference was first dedicated to the tragic victims of the Tohoku-Kanto earthquake and tsunami disasters. The Geomate 2016 conference covers three major themes with 17 specific themes including:

- Advances in Composite Materials
- Computational Mechanics
- Foundation and Retaining Walls
- Slope Stability
- Soil Dynamics
- Soil-Structure Interaction
- Pavement Technology
- Tunnels and Anchors
- Site Investigation and Rehabilitation
- Ecology and Land Development
- Water Resources Planning
- Environmental Management
- Public Health and Rehabilitation
- Earthquake and Tsunami Issues
- Safety and Reliability
- Geo-Hazard Mitigation
- Case History and Practical Experience

This year we have received many paper submissions from different countries all over the world, including Australia, Bank Receipt, Czech Republic, India, Indonesia, Japan, Malaysia, Oman, Philippines, Russia, Switzerland, Tajikistan, Thailand, Tunisia, United Kingdom, United States and Vietnam. The technical papers were selected from the vast number of contributions submitted after a review of the abstracts. The final papers in the proceedings have been peer reviewed rigorously and revised as necessary by the authors. It relies on the solid cooperation of numerous people to organize a conference of this size. Hence, we appreciate everyone who support as well as participate in this joint conferences.

Last but not least, we would like to express our gratitude to all the authors, session chairs, reviewers, participants, institutions and companies for their contribution to GEOMATE 2016. We hope you enjoy the conference and find this experience inspiring and helpful in your professional field. We look forward to seeing you at our upcoming conference next year.

Best regards,

Prof. Dr. Suksun Horpibulsuk, Conference Chairman

Prof. Dr. Md. Zakaria Hossain, Conference Director

Organization

Conference Honorary Chairmen:

Emeritus Professor Dr. Sohji Inoue, Mie University, Japan
Emeritus Professor Dr. Teruo Nakai, Nagoya Institute of Technology, Japan
Emeritus Professor Dr. Fusao Oka, Kyoto University, Japan

Scientific Committees:

Conference Chairman: Dr. Suksun Horpibulsuk, Prof. Suranaree University of Tech., Thailand
Conference Vice Chairmen: Dr. Avirut Chinkulkijniwat, A/Prof. Suranaree Univ of Tech., Thailand
Dr. Jim Shiau, Senior Lecturer, USQ, Australia

Conference Director: Dr. Zakaria Hossain, Prof. Mie University, Japan
Conference General Secretary: Dr. Shinya Inazumi, A/Prof. National Ins. of Tech., Akashi, Japan

Conference Organizing Committee:

Dr. Suksun Horpibulsuk, Prof. Suranaree Uni. of Tech., (Chair)
Dr. Watcharin Gasaluck, Prof. Khon Kaen Uni., (Co-Chair)
Dr. Avirut Chinkulkijniwat, A/Prof. Suranaree Univ of Tech. (VC)
Dr. Jim Shiau, Senior Lecturer, USQ, Australia (VC)
Dr. Sohji Inoue, E/Prof. Mie University, Japan (Co-Chair)
Dr. Toshinori Sakai, Prof. Mie University, Japan (Co-Chair)
Dr. Zakaria Hossain, Prof. Mie University, Japan (Director)
Dr. Shinya Inazumi, A/Prof. National Ins. of Tech., Akashi (GS)

National & International Advisory Committee:

Dr. Sittisak Uparivong, Prof. Khon Kaen University, Thailand
Dr. Jirayut Suebsuk, A/Prof. Rajamangala Uni of Tech., Thailand
Dr. Phacharaporn B., A/Prof., Kasetsart Uni., Thailand
Dr. Dolrerdee Hormdee, A/Prof., Khon Kaen Uni, Thailand
Dr. Vanchai Sata, A/Prof., Khon Kaen University, Thailand
Dr. Chinapat Buachart, A/Prof. Chiang Mai University, Thailand
Dr. Mark Jaksa, Prof., University of Adelaide, Australia
Dr. Fumio Tatsuoka, Prof. Tokyo University of Science, Japan
Dr. Jing-Cai Jiang, Prof. University of Tokushima, Japan
Dr. Toshihiro Morii, Prof. Niigata University, Japan
Dr. Kimitoshi Hayano, Prof. Yokohama National Univ., Japan
Dr. Sai Vanapalli, Prof. University of Ottawa, Canada
Dr. M. Bouassida, Prof. National Sch. of Engg. of Tunis
Dr. L.R. Austriaco, Prof. Angles Univ. Found, Philippines
Dr. A.S.M. Abdul Awal, Prof. Univ. Technology Malaysia
Dr. M. Ibn Ibrahimy, Prof. Int. Islamic Univ., Malaysia
Dr. Bujang B.K. Huat, Prof. Univ. Putra Malaysia
Dr. Nemy Banthia, Prof. UBC, Canada
Dr. Ian Jefferson, Prof. Univ. of Birmingham, UK
Dr. John Bolander, Prof. Univ. of California, USA
Dr. Shamsul Chowdhury, Prof. Roosevelt Univ., USA
Dr. Isabel Pinto, Prof. University of Coimbra, Portugal
Dr. Hj. Ramli Bin Hj. Nazir, A/Prof.. UTM, Malaysia

Dr. Aly Ahmed, A/Prof..Beni-Suef University, Egypt
Dr. Chang-Yu Ou, Prof. National Taiwan Univ. of Sci. &Tech.

International Technical Program Committee:

Prof. Sai Vanapalli, University of Ottawa, Canada
Prof. Alaa Masoud, Tanta University, Egypt
Prof. Aly Ahmed, Beni-Suef University, Egypt
Prof. Aminaton Marto, Universiti Teknologi Malaysia, Malaysia
Prof. Bandari Shankar, Osmania University, India
Prof. Bashir Ahmed Mir, National Institute of Technology, India
Prof. Hamidi Abdul, Aziz, Universiti Sains Malaysia (USM), Malaysia
Prof. Hussein Elarabi, University of Khartoum, Sudan
Prof. M. Shohidullah Miah, International Univ. of Business Agriculture &Tech., Bangladesh
Prof. Michele, Casagrande, Pontifical University Catholic of Rio De Janeiro, Brazil
Prof. Radim Cajka, Technical University of Ostrava, Czech Republic
Prof. Rajaraman Jambunathan, AMET University, India
Prof. Reshma Chandran T., Global Institute of Architecture, India
Prof. Roslan Hashim, University of Malaya, Malaysia
Prof. Seyed Naser Moghaddas Tafreshi, K.N. Toosi University of Technology, Iran
Prof. Valeriy Perminov, Tomsk Polytechnic University, Russia
A/ Prof. Abdoullah Namdar, Sichuan University, China
A/ Prof. Abdul Naser Abdul Ghani, Universiti Sains Malaysia, Malaysia
A/ Prof. Alaeddinne Eljamassi, Islamic University of Gaza, Palestine
A/ Prof. Alina Paranina, Herzen State Pedagogical University of Russia, Russia
A/ Prof. Ashraf Elmoustafa, Ain Shams Univeristy, Egypt
A/ Prof. Bindu C S, Cochin University of Science& Technology, India
A/ Prof. Chee-Ming Chan, Universiti Tun Hussein Onn Malaysia, Malaysia
A/ Prof. Chidanand Naik, Anjuman Instistute of Technology and Management, India
A/ Prof. Dahlia Hafez, Cairo University, Egypt
A/ Prof. Deepa G Nair, Isfahan University of Technology, India
A/ Prof. Dolrerdee Hormdee, Khon Kaen University, Thailand
A/ Prof. Farhad Behnamfar, Isfahan University of Technology, Iran
A/ Prof. Gabriela B. Cazacu, Geotech Dobrogea, Romania
A/ Prof. Hadi Khabbaz, University of Technology, Sydney (UTS), Australia
A/ Prof. Homayoon Ganji, Herat Univercity Badghis, Afghanistan
A/ Prof. Hudson Jackson, US Coast Guard Academy, United States
A/ Prof. Inazumi Shinya, National Institute of Technology, Akashi, Japan
A/ Prof. John Smith, RMIT University, Australia
A/ Prof. Kasinathan Muthukkumaran, National Institute of Technology, India
A/ Prof. Lindrianasari Lindrianasari, Universitas Lampung, Indonesia
A/ Prof. Mahdi Karkush, Baghdad University, Iraq
A/ Prof. Mohamed Redha Menani, Batna University, Algeria
A/ Prof. Navid Khayat, Ahvaz Branch, Islamic Azad University, Iran
A/ Prof. Salam, Bash AlMaliky, AlMustansiriya University, Iraq
A/ Prof. Shailesh Kumar Jha, Indian Institute of Technology, India
A/Prof. Teodor Lucian Grigorie, University of Craiova, Romania
Dr. Abdul Karim M. Zein, University of Khartoum, Sudan
Dr. Abdull Halim Abdul, Universiti Teknologi MARA, Malaysia
Dr. Afshin Asadi, University Putra Malaysia, Malaysia
Dr. Ahmad Safuan A Rashid, Univeristi Teknologi Malaysia, Malaysia
Dr. Ahmad Safuan Bin A Rashid, Univeristi Teknologi Malaysia, Malaysia
Dr. Akindele Okewale, Federal University of Petroleum Resources, Nigeria
Dr. Akinola Johnson Olarewaju, Federal Polytechnic Ilaro, Nigeria
Dr. Ali Sobhanmanesh, Universiti Teknologi Malaysia (UTM), Malaysia
Dr. Alireza Bahiraie, Semnan University, Iran
Dr. Allan Manalo, Centre of Excellence in Engineered Fibre Composites, Australia
Dr. Aniza Ibrahim, National Defence University of Malaysia, Malaysia

Conference Correspondence:

Prof. Dr. Zakaria Hossain, Conference Director,
Dept. of Env. Sci. & Tech., Mie University, Japan,
Prof. Dr. Suksun Horpibulsuk (Chairman)
Dept. of Civil Engineering, Suranaree University of Technology, Thailand
Dr. Shinya Inazumi, General Secretary
A/Prof. National Ins. of Tech., Akashi, Japan
E-mail: conference@geomate.org
Tel & Fax: +81-59-231-9578

Editorial Committee and Executive Committee:

Keynote Paper

Sixth International Conference on Geotechnique, Construction Materials and Environment, Bangkok, Thailand, Nov. 14-16, 2016, ISBN: 978-4-9905958-6-9 C3051

SUSTAINABLE STABILIZATION OF MARGINAL LATERITIC SOIL FOR PAVEMENT APPLICAITONS

Suksun Horpibulsuk[1], Jeerapan Donrak[2], Itthikorn Phummiphan[3], Arul Arulrajah[4] and Menglim Hoy[5]
[1,2,5]Center of Excellence in Innovation for Sustainable Infrastructure Development, and School of Civil Engineering, Suranaree University of Technology Thailand; [3]Department of Rural Roads, Thailand; [4]Department of Civil and Construction Engineering, Swinburne University of Technology, Australia

ABSTRACT

Due to high rainfall, temperature and humidity with alternative wet and dry period, nearly 60% of the soils in Thailand are lateritic soil with colors ranging from red to yellowish red. The lateritic soil is found in dry flat lands and plains, throughout Thailand. This lateritic soil with suitable mechanical properties is commonly used as subbase materials in roads. However, lateritic soils are increasingly becoming scarce to source for road projects. Thus, the usage of marginal lateritic soil as a pavement subbase material leads to some challenging issues. This paper presents sustainable stabilization of marginal lateritic soil by Melamine Debris (MD) replacement and by geopolymer binders as unbound and bound pavement materials, respectively. MD is an industrial waste resulting from plate and cup manufacture. This MD cannot be reformed or reused for manufacturing plates and cups. Fly Ash (FA) is used a precursor to develop geopolymer binder. The test results on MD-lateritic soil blends shows that the MD replacement of lateritic soil reduces the fine content and increases the abrasion resistance of the soil particles, hence the reduction in liquid limit, plasticity index, LA abrasion and particle breakage. The physical and mechanical properties of the 20% MD replacement blend are found to meet the requirement of local road authority for engineering fill materials while the 50% MD replacement blend is found to be at the borderline for subbase course material. The test results on geopolymer stabilized lateritic soil show that the maximum early strengths at 7 days of curing were found at Na_2SiO_3:NaOH of 90:10, where Calcium Silicate Hydrate (C-S-H), cementitious products from high calcium FA and Na_2SiO_3, was found to play a significant role. The Sodium Alumino Silicate Hydrate (N-A-S-H) products, being time-dependent, however came into play after a longer duration. The maximum 90-day UCS was found at a Na_2SiO_3:NaOH ratio of 50:50. This research is significant in addressing the sustainable usage of MD and green geopolymer binder from engineering and environmental perspectives.

Keywords: marginal lateritic soil, geopolymer, melamine, calcium carbide residue, fly ash

INTRODUCTION

Due to high rainfall, temperature and humidity with alternative wet and dry period, nearly 60% of the soils in Thailand are lateritic soil with colors ranging from red to yellowish red. Quality lateritic soil for pavement subbase/base and engineering fill materials are becoming increasingly scarce to source for road infrastructure projects. Therefore, modification of soils on site is an attractive and economical option to improve their mechanical properties [1].

The most common soil improvement technique is to compact the locally available soil blended with high quality materials. Compaction is a practical and economical technique to improve the mechanical properties of soils by the application of either static or dynamic force [2]. The usage of recycled materials blended with high quality materials to stabilize marginal soils has significant engineering, economical and environmental benefits [3].

Melamine debris (MD) is an industrial waste resulting from plate and cup manufacture. This MD cannot be reprocessed for manufacturing plates and cups [4]. It was reported by Srithai Superware Public Co., Ltd, a largest melamine tableware company in Thailand, that the company releases 400 tons of MD annually. Presently, this MD is disposed by combustion at a very high temperature, which is costly and has significant negative environmental effects. The sustainable usage of MD in civil engineering applications will provide a lower carbon footprint and result in positive social and economical impacts for governments, industry and consumers. The usage of MD in marginal soil improvement for pavement application is innovative and of interest to the industrial sectors and national road authorities, particularly as road construction typically requires a large quantity of quality material.

Another alternative way, widely practiced around the world, is to compact the in-situ marginal soil mixed with Portland Cement (PC) [5]. The production of PC is however an energy-intensive process and emits a very large amount of greenhouse gas, particularly carbon dioxide (CO_2) into the atmosphere [6]. In the light of these problems, the utilization of low energy intensive cementing agents in civil engineering applications has been increasingly researched in recent years. Low energy intensive cementing agents include cement kiln dust [7] calcium carbide residue [8] granulated blast furnace slag [9] and geopolymer binder [10].

Geopolymer is an inorganic aluminosilicate material synthesized by alkaline activation of materials rich in alumina (Al_2O_3) and silica (SiO_2). Since Fly Ash (FA) offers the greatest opportunity given the plentiful worldwide stockpiles, it is frequently used as a precursor for producing geopolymers. Though there is readily available literature on the application of FA based geopolymer, they have been predominantly used as building materials while the studies on the application of FA based geopolymer to pavement materials are limited to date.

The paper attempts investigate physical and mechanical properties of marginal lateritic soil blended with MD at various replacement ratios to ascertain it as an engineering fill material and to investigate the possibility of using high calcium FA based geopolymer to stabilize a marginal lateritic soil to be a sustainable bound pavement material. This study is significant from engineering, economical and environmental perspectives.

MELAMINE DEBRIS REPLACEMENT

The lateritic soil studied is composed of 21.7% fine-grained particles and 78.3% coarse-grained particles in which 25.6% is gravel and 31% is sand. The specific gravity of coarse-grained particles is 2.67 and the liquid and plastic limits are 40.7% and 20.9%, respectively. This compacted lateritic soil has liquid limit (w_L) = 40.7%, plasticity index (I_p) = 19.7%, California Bearing Ratio (CBR) = 9.3, swelling percentage = 6.4), which does not meet the requirement of the Department of Highways, Thailand (required CBR are greater than 25% for subbase), and will require blending with a higher quality material if it is to be considered as a pavement subbase or fill material.

Fig. 1 and Fig. 3 show the particle size distribution curves of the lateritic soil/MD blends at MD replacement ratios of 50%, and 10%, respectively compared with the upper and lower boundaries of subbase materials specified by the Department of Highways, Thailand. It is noted that the MD particles larger than 3.80 mm (D_{60}) are above the upper boundary and MD particles finer than 1.05 mm (D_{20}) are below the lower boundary. The results indicate that MD replacement reduces fine content of the lateritic soil. It is noted that the reduction in fine content results in the decreases in the liquid limit (w_L) and plasticity index (I_p); i.e., w_L is 39.9%, 39.8%, 38.9%, 38.4% and 7.8% and I_p is 17.0, 16.6, 15.1, 12.6 and 11.1 for MD replacement ratios of 10%, 20%, 30%, 40% and 50%, respectively. Consequently, the lateritic soil/MD blends approach to a silty material type with increasing MD replacement ratio; i.e., they are classified as SM, SM, SM, SC and SC for MD replacement ratios of 10%, 20%, 30%, 40% and 50%, respectively while the lateritic soil is classified is SC. It is noted that w_L and I_p of these blends meet the consistency limits specified for engineering fill materials (w_L < 40% and I_p < 20%).

The MD replacement technique has the advantage of reduced particle breakage of the blends due to compaction as evident from Fig. 1 and 2. Besides the Atterberg limits and gradation, the durability of the lateritic soil particles is improved by the MD replacement. The MD has a relatively low LA abrasion of 11.3% compared to the lateritic soil with LA equal to 58.1%. Therefore, the MD replacement improves the LA abrasion of the lateritic soil by reducing the LA abrasion value for the blends. The LA abrasion of lateritic soil decreases from 58.1% (for 0% MD replacement) to 41.1% (for 50% MD replacement). Even without the MD replacement, this lateritic soil is considered as durable for subbase and engineering fill materials based on LA abrasion requirement of < 60% [11].

The modified compaction test results (Fig. 4) show that the blends at various MD replacement ratios exhibit bell-shaped compaction pattern, typical of traditional geo-materials [2], [12]. The Maximum Dry Density (MDD) values of the blends are between those of the lateritic soil and MD, which are 19.4 kN/m^3, 18.9 kN/m^3, 18.2 kN/m^3 and 17.3 kN/m^3 for 10%, 20%, 30% and 40% MD replacement, respectively. This significantly lower MDD, typical of a lightweight fill material, decreases the overburden on the foundation, which is an advantage over traditional pavement subbase materials.

Generally, bearing capacity as measured by CBR and swelling of the compacted materials are controlled by the fine content. Fig. 5 shows the soaked CBR values at different compaction energy levels in logarithm function. For a particular MD replacement ratio, the soaked CBR significantly increases with increasing compaction energy, E. There are two linear slopes and the slope change is found at E = 2681 kJ/m^3 (modified Proctor energy). The second slope (E > 2681 kJ/m^3) is steeper than the first one (E < 2681 kJ/m^3), indicating that the compaction energy is more significant on the increase in soaked CBR when E > 2681 kJ/m^3.

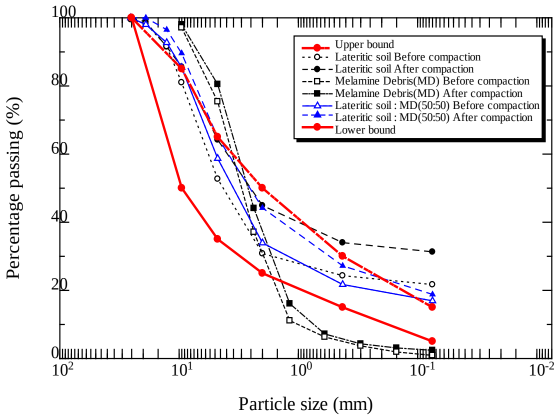

Fig. 1 Particle size distribution of lateritic soil/MD blend at 50% MD replacement.

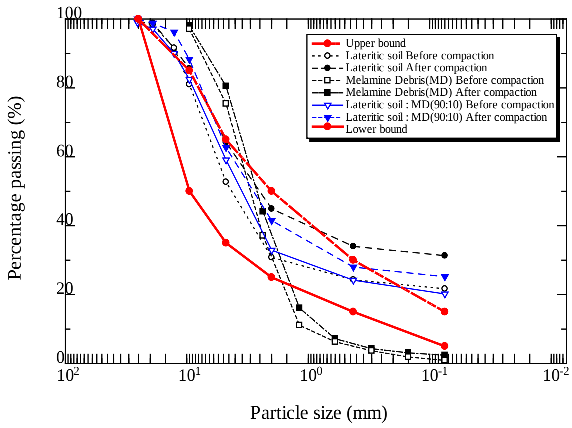

Fig. 3 Particle size distribution of lateritic soil/MD blend at 10% MD replacement.

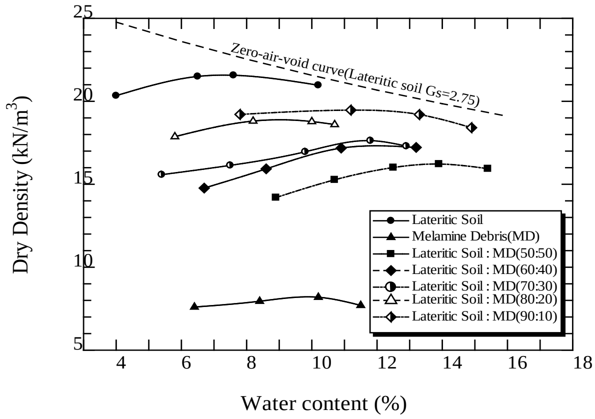

Fig. 4 Dry density versus moisture content relationship for various lateritic soil/MD blends.

For a particular energy, the soaked CBR increases with the MD replacement ratio; i.e., the 50% MD replacement exhibits the highest soaked CBR for all E values. It is obvious that the first slope of all the blends is essentially the same and the second slope of 50% replacement blend is the highest. This implies that the rate of soaked CBR development with MD replacement ratio at E < 2681 kJ/m^3 is essentially the same even with different MD

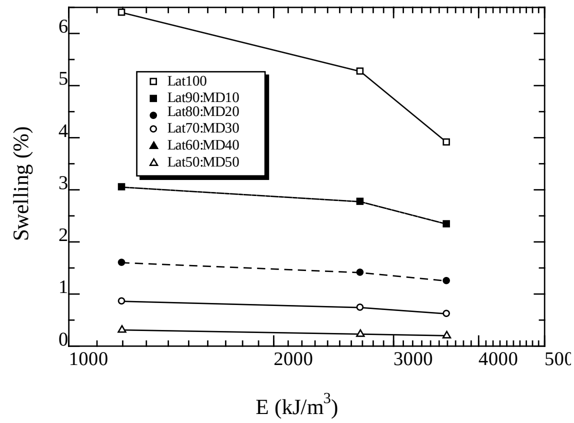

Fig. 2 Swelling versus compaction energy relationship for lateritic soil/MD blends.

replacement ratios.

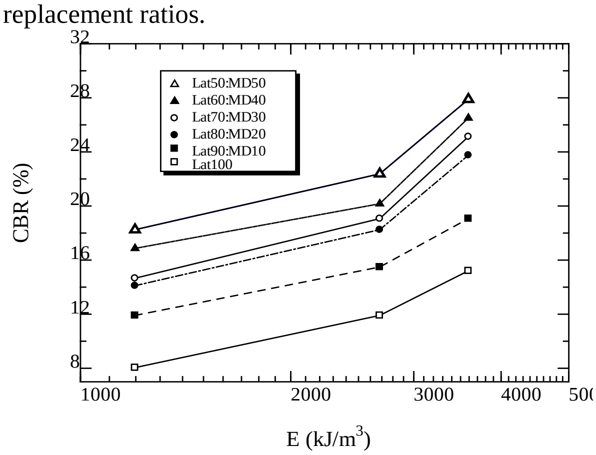

Fig. 5 Soaked CBR versus compaction energy relationship for lateritic soil/MD blends.

Fig. 2 shows the swelling versus logarithm of E relationship for various MD replacement ratios. Similar to the soaked CBR versus logarithm of E relationship, the E = 2681 kJ/m^3 is regarded as the threshold limit separating the first and second slopes of swelling versus logarithm of E relationship for lateritic soil.

Without MD replacement, E can reduce the swelling, especially when E > 2681 kJ/m^3 as seen that the second slope is remarkably lower than the first slope. The MD replacement significantly reduces the swelling; i.e., the swelling of lateritic soil reduces more than twice when only 10% MD is replaced. The first and second slopes of the blends are essentially the same and can be represented by a gentle linear function when MD replacement is greater 20%. It is noted that the swelling of the blends is significantly reduced even at a small E level unlike the marginal lateritic soil (without MD), which requires high E level to increase attractive forces among soil particles.

Based on an analysis of soaked CBR and swelling test results, it is practical to relate the soaked CBR and swelling of blends at various compaction energies in term of MD replacement. As such, the predictive equations (Fig. 6 and Fig. 7) for soaked CBR and swelling in term of MD replacement ratio are presented as follows:

$$\frac{CBR_{MD}}{CBR_0} = 1.365\exp(0.010MD)$$

for 1197 kJ/m^3 < E < 2681 kJ/m^3 (1)

$$\frac{CBR_{MD}}{CBR_0} = 1.231\exp(0.009MD)$$

for 2681 kJ/m^3 < E < 3591 kJ/m^3 (2)

$$\frac{S_{MD}}{S_0} = 10.867\exp(-0.06MD)$$

for 2681 kJ/m^3 < E < 3591 kJ/m^3 (3)

where CBR_{MD} and CBR_0 are the soaked CBR at different MD replacement ratios (ranging from 0% to 50%) and soaked CBR at 0% MD replacement, respectively and S_{MD} and S_0 are the swelling at different MD replacement ratios (ranging from 0% to 50%) and swelling at 0% MD replacement, respectively. These predictive equations are useful for predicting soaked CBR and swelling at different MD replacement ratios based on the values of lateritic soil (without MD replacement). The coefficients of correlation of these equations are greater than 0.91, confirming the validity of these equations.

The formulation of the predictive equation is on sound principle and can be fundamental to other marginal soils.

FA GEOPOLYMER STABILIZATION

The marginal lateritic soil was collected from a borrow pit in Rayong province, Thailand. The specific gravity is 2.58. The liquid limit, plastic limit, and plastic index are 27.72%, 21.65%, and 6.07%, respectively. This soil is classified as silty clayey sand (SC-SM) according to the Unified Soil Classification System and A-2-4(0) according to the AASHTO system. The compaction characteristics under modified Proctor energy are OMC of 8.0%, and MDD of 20.85 kN/m^3. CBR value is 14.7% at 95% of MDD. Los Angles (LA) abrasion is 52.9%. With low CBR and high LA abrasion compared to the specification of the Department of Highways, Thailand (required CBR and LA abrasion are greater than 25% and less than 60% for subbase materials, located below the base course, respectively), this lateritic soil is classified as a marginal soil. Fly Ash (FA) used in this study was obtained from Mae Moh power plant in Northern Thailand, which is the largest lignite power plant in Thailand.

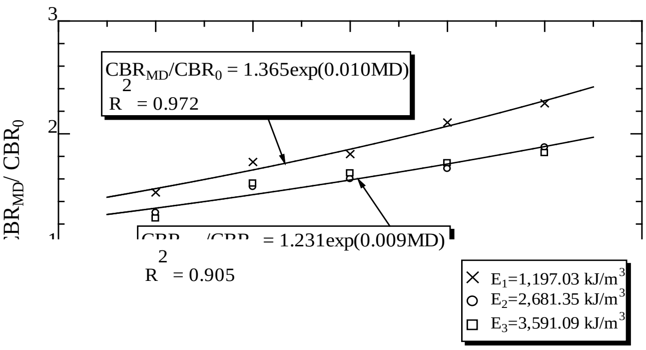

Fig. 6 Relationship between normalized soaked CBR and MD replacement ratio.

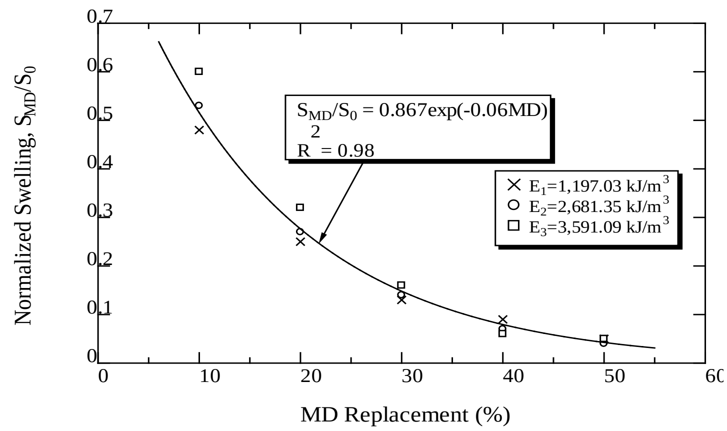

Fig. 7 Relationship between normalized swelling and MD replacement ratio.

The major components are 36.00% SiO_2, 26.73% CaO, 17.64% Fe_2O_3, and 16.80% Al_2O_3. According to ASTM C 618-12, it is categorized as class C high-calcium fly ash (CaO > 10%).

The liquid alkali activator was a mixture of sodium silicate (Na_2SiO_3) solution, composed of 15.50% Na_2O, 32.75% SiO_2, and 51.75% water by weight, and sodium hydroxide (NaOH) solution with 5 molars.

Fig. 8 shows the relationships between dry unit weight and liquid alkali activator content with various Na_2SiO_3:NaOH ratios of lateritic soil-FA geopolymer. The compaction curves of lateritic soil-FA geopolymer are different and depend on the Na_2SiO_3:NaOH ratio. For a particular Na_2SiO_3:NaOH ratio, the dry unit weight of lateritic soil-FA geopolymer increases with increasing liquid alkali activator content until MDD is attained at an optimum alkali activator content. Beyond this optimum value, the unit weight decreases as the alkali activator content increases. This characteristic is similar to a typical compaction behavior of coarse-grained materials. The optimum Na_2SiO_3:NaOH ratio exhibiting the highest DMM was found at 90:10.

Unconfined compressive strength

The UCS of geopolymers is attributed to the reaction between silica and alumina in the presence of alkali ions and in age of specimens [13]. The UCS values of the lateritic soil-FA geopolymer for various Na_2SiO_3:NaOH ratios (100:0 to 50:50) and curing times (7 to 90 days) are presented in Fig. 9. It is evident that the UCS values for all Na_2SiO_3:NaOH ratios increase as the curing time increases. At early stage of geopolymerization, the maximum 7-day UCS is found at Na_2SiO_3:NaOH ratio of 90:10 (about 7,100 kPa), which is greater than the strength requirement specified by the national road authority in Thailand (UCS > 1,724 kPa for light traffic and UCS > 2,413 kPa for high traffic) [14-15]. The 7-day UCS at Na_2SiO_3:NaOH ratio of 100:0 (no NaOH) is approximately 5,800 kPa. This moderately high UCS at Na_2SiO_3:NaOH ratio of 100:0 is contributed from the C-S-H, which is the cementitious product from the reaction between silica from Na_2SiO_3 and calcium from FA. In presence of Ca^{2+}, Na_2SiO_3 forms soluble calcium silicate, which polymerizes further to form gels that bind soil particles together and fill voids as the following equation [16]:

$$Ca^{2+} + Na_2SiO_3 + mH_2O \Downarrow \ CaO \ \beta SiO_2.mH_2O \ 2 \ 2Na^2$$
(4)

The effect of C-S-H is minimal when the curing time is greater than 28 days as seen that the UCS of sample at Na_2SiO_3:NaOH ratio of 100:0 is essentially constant when the curing time is greater than 28 days.

Since the N-A-S-H products are time-dependent, the UCS of geopolymer samples with the presence of NaOH (Na_2SiO_3:NaOH ratios of 90:10, 80:20, and 50:50) increases with curing time even after 28 days of curing. Due to the coexistence of C-S-H and N-A-S-H products, the geopolymer samples with Na_2SiO_3:NaOH ratios of 90:10 and 80:20 exhibit higher 7-day UCS than the geopolymer sample with Na_2SiO_3:NaOH ratios of 100:0 (its UCS is mainly contributed from C-S-H). The optimum coexistence of C-S-H and N-A-S-H products at 7 days of curing (providing the highest UCS) is found at Na_2SiO_3:NaOH ratio of 90:10.

Based on the strength data, it is suggested that the Na_2SiO_3:NaOH ratio of 50:50 is the best ingredient whose UCS is greater than 2,413 kPa (required for heavy traffic). The highest rate of UCS development of the geopolymer at this ingredient is also observed.

Microstructural analysis

Fig. 10 shows the microstructure of the four Na_2SiO_3:NaOH ratios of 100:0, 90:10, 80:20, and 50:50 at 7 days of curing (early stage of geopolymerization process) at ambient temperature.

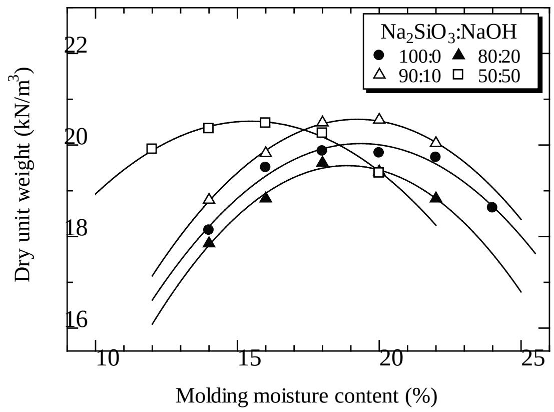

Fig. 8 Compaction curves of lateritic soil – FA geopolymer at different ingredients.

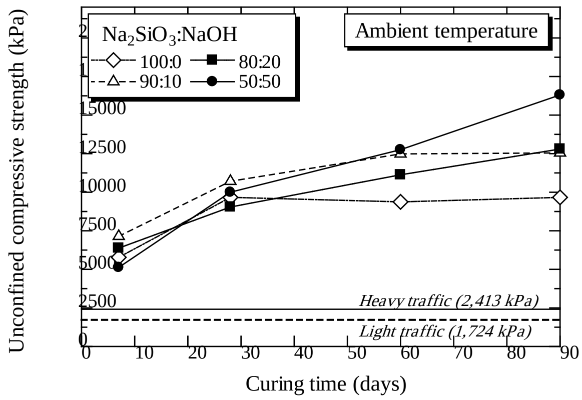

Fig. 9 Effect of curing time on UCS of lateritic soil – FA geopolymer

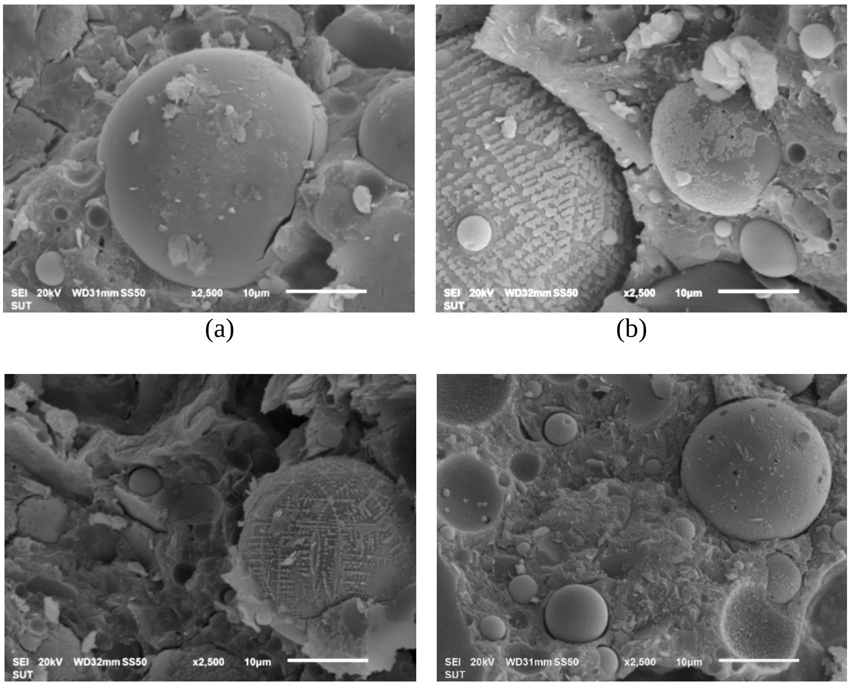

(a) (b)

(c) (d)

Fig. 10 SEM images of lateritic soil – FA geopolymer cured at 7 days of curing at ambient temperature for various Na_2SiO_3:NaOH ratios of (a) 100:0, (b) 90:0, (c) 80:20, and (d) 50:50.

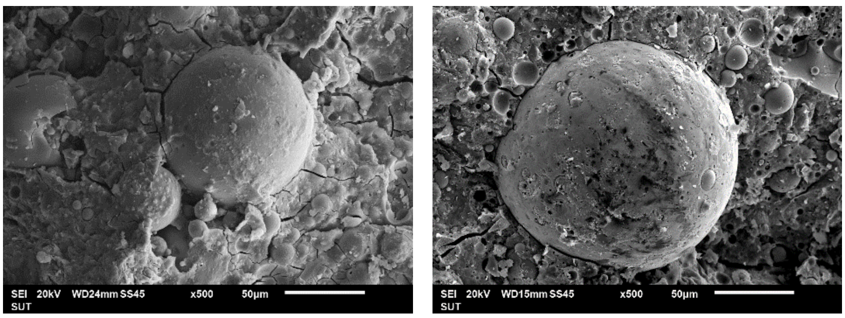

(a) (b)

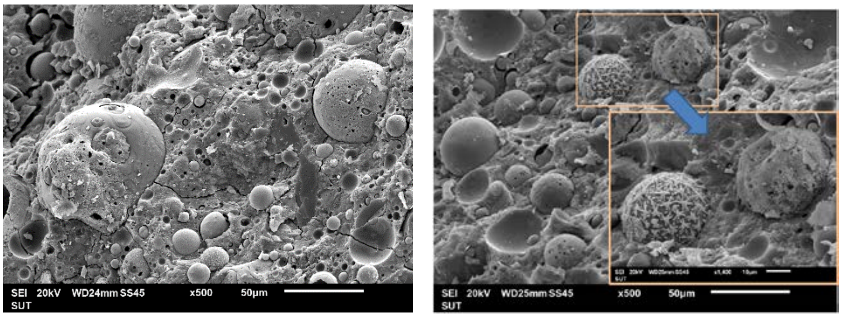

(c) (d)

Fig. 11 SEM images of lateritic soil – FA geopolymer cured at 90 days at ambient temperature for various ingredients of Na_2SiO_3: NaOH (a) 100:0, (b) 90:10, (c) 80:20, and (d) 50:50.

The cementitious (C-S-H and N-A-S-H) products on the high calcium FA surface are clearly observed at Na_2SiO_3:NaOH ratios of 90:10 and 80:20 when compared to those at Na_2SiO_3:NaOH ratios of 50:50 and 100:0, respectively Many holes on the FA surface are clearly observed for Na_2SiO_3:NaOH ratios of 50:50 due to strong alkaline reaction from NaOH while the least etched holes on FA surface are observed at Na_2SiO_3:NaOH ratio of 100:0.

The effect of Na_2SiO_3:NaOH ratio on the growth of geopolymerization products is illustrated by comparing Fig. 11a–11d, which show SEM images of the lateritic soil–FA geopolymer samples at various Na_2SiO_3:NaOH ratios of 100:0, 90:10, 80:20, and 50:50 after 90 days of curing. For Na_2SiO_3:NaOH ratio of 100:0 (no NaOH), the FA surface is approximately smooth and spherical with traces of C-S-H products. This indicates that the silica and alumina in FA was insignificantly leached out even after a very long curing time and the UCS of the samples is contributed from C-S-H (reaction of Na_2SiO_3 and CaO from FA) (Fig. 11a).

The NaOH content is not sufficient for leaching silica and alumina from FA for the sample at Na_2SiO_3:NaOH ratio of 90:10 as seen by the small amount of cementitious products on FA surface (Fig. 11b) when compared to the samples at Na_2SiO_3:NaOH ratios of 80:20 and 50:50 (Fig. 7c and d). For both samples at Na_2SiO_3:NaOH ratios of 80:20 and 50:50, the etched holes are mostly filled with other smaller size ash particles and the cementitious products fill up the pore space, resulting in a dense matrix. The cementitious products are more for the sample at Na_2SiO_3:NaOH ratio of 50:50. As such, the maximum UCS is found at Na_2SiO_3:NaOH ratio of 50:50 at 60 and 90 days of curing (*vide* Fig. 9)

The present study on the improvement of marginal lateritic soil by FA based geopolymer has significant impacts on sustainable pavement applications. The green geopolymer stabilized lateritic soil is proved as suitable where the 7-day UCS meets the specification for heavy traffic and the UCS increases with increasing curing time even after 28 days of curing due to the growth of geopolymerization product (N-A-S-H) over time.

CONCLUSION

This paper investigates physical and mechanical properties of marginal lateritic soil blended with MD at various replacement ratios to ascertain it as an engineering fill material as well as UCS and microstructural characteristics of the marginal lateritic soil stabilized with high calcium FA based geopolymer as low-carbon alternative green bound pavement material.

The marginal lateritic soil improvement by MD replacement is found to be a sustainable engineering fill material based on this research. The laboratory evaluation of the lateritic soil/MD blends at different MD replacement ratios included physical property tests such as particle size distribution, Atterberg limits and LA abrasion, as well as mechanical property tests such as soaked CBR and swelling. MD replacement can improve the mechanical property requirement for engineering fill material according to national local authority. The MD traditionally destined for landfill can be used as a replacement material to stabilize lateritic soil for developing the sustainable engineering fill material. With 20% MD replacement, the physical and mechanical properties of blends meet the requirement. The 50% MD replacement blend is at the borderline of the specification for subbase material.

It is evident from this study that the strength of lateritic soil-FA geopolymer meets the standard requirements for heavy and light traffic bound base materials specified by Department of Highways (DOH) and Department of Rural Roads (DRR), Thailand. FA based geopolymer can be used as an alternative binder to PC for sustainable pavement applications. This study indicates that the marginal lateritic soil can be stabilized by the high calcium FA based geopolymer to be a bound pavement material for both light and heavy traffic. This will leads to a usage reduction of PC and develop a possible environmentally sustainable material. The economical ingredient is suggested to be Na_2SiO_3:NaOH of 50:50.

ACKNOWLEDGEMENTS

This work was supported by the Thailand Research Fund under the TRF Senior Research Scholar program Grant No. RTA5680002 and Suranaree University of Technology.

REFERENCES

[1] Horpibulsuk S, Katkan W, Sirilerdwattana W, Rachan R, "Strength development in cement stabilized low plasticity and coarse grained soils: Laboratory and field study", Soils and Foundations, Vol. 46(3), 2006, pp. 351-366.

[2] Horpibulsuk S, Katkan W, Apichatvullop A, "An approach for assessment of compaction curves of fine-grained soils at various energies using a one point test", Soils and Foundations, Vol. 48(1), 2008, 115-125.

[3] Arulrajah A, Ali MMY, Disfani M.M. and Horpibulsuk S, "Recycled glass blends in pavement base/subbase applications: laboratory and field evaluation", Journal of Materials in Civil Engineering, 2014, doi: 10.1061/(ASCE)MT.1943-5533.0000966.

[4] Siwadamrongpong S, Wonglane K, and Mahai M, "Influence of water absorption the mechanical properties of recycled materials from waste melamine", South East Asian Technical University Consortium. 6 - 7 March 2012. KMUTT. Bangkok, Thailand.

[5] Chinkulkijniwat A, and Horpibulsuk S, (2012). "Field strength development of repaired pavement using the recycling technique", Quarterly Journal of Engineering Geology and Hydrogeology, Vol. 45(2), pp. 221-229.

[6] Davidovits J, Geopolymer Cement. *Geopolymer Cement, a review*, 2013.

[7] Ebrahimi A, Edil TB, and Son YH, "Effectiveness of Cement Kiln Dust in Stabilizing Recycled Base Materials. Journal of Materials in Civil Engineering", Vol. 24(8), 2012 pp. 1059-1066.

[8] Kampala A, Horpibulsuk S, Prongmanee N, and Chinkulkijniwat A, "Influence of Wet-Dry Cycles on Compressive Strength of Calcium Carbide Residue–Fly Ash Stabilized Clay", Journal of Materials in Civil Engineering, Vol. 26(4), 2014, pp. 633-643.

[9] Puppala AJ, Wattanasanticharoen E, and Punthutaecha K, "Experimental evaluations of stabilisation methods for sulphate-rich expansive soils", Ground Improvement, 7(1), 2003, pp. 25-35.

[10] Sukmak P, De Silva P, Horpibulsuk S, and Chindaprasirt P, "Sulfate resistance of clay-Portland cement and clay high-calcium fly ash Geopolymer", Journal of Materials in Civil Engineering, Vol. 27(5), 2015, pp.04014158(1-11).

[11] DH-S, Standard for Highway Construction. DH-S205/2532, 1996, Bangkok.

[12] Horpibulsuk S, Katkan W, Naramitkornburee A, "Modified Ohio's curves: A rapid estimation of compaction curve for coarse-and fine-grained soils", Geotechnical Testing Journal, Vol. 32(1), 2009, pp.64-75.

[13] Somna K, Jaturapitakkul C, Kajitvichyanukul P, and Chindaprasirt P, "NaOH-activated ground fly ash geopolymer cured at ambient temperature", Fuel, Vol. 90(6), 2011, pp. 2118-2124.

[14] DOH, DH-S204/2000 Standard of Soil Cement Base: Department of Highways, 2000.

[15] DRR, DRR244-2013 Standard of Soil Cement Base: Department of Rural Roads, 2013.

[16] Brykov AS, Danilov VV, Korneev VI, and Larichkov AV, Effect of hydrated sodium silicates on cement paste hardening. Russian Journal of Applied Chemistry, Vol. 75(10), 2002, pp. 1577-1579.

Sixth International Conference on Geotechnique, Construction Materials and Environment, Bangkok, Thailand, Nov. 14-16, 2016, ISBN: 978-4-9905958-6-9 C3051

ESTIMATION OF DYNAMIC BUCKLING STRENGTH OF CIRCULAR TUBE PILES WITH LIQUEFIED SOIL

Moeko Matoba[1], Tenshiro Goto[1] and Yoshihiro Kimura[1]
[1] Tohoku University, Japan

ABSTRACT

In current design criteria, the possibility of dynamic buckling of a pile foundation is not considered. Design codes have no prescription for limitations of a slenderness ratio for piles. However, pile buckling occurred when slender steel piles beneath buildings experience high axial compression forces as a result of vertical loads increased by the over turning moment of buildings, generated by inertia forces of buildings. With coincidence of liquefaction, the buckling risk is most likely to be even higher. In this study, centrifuge tests are conducted to assess the dynamic buckling behavior of circular tube piles with liquefied soil. Test parameters were the natural period of a superstructure–foundation system, input wave, pile slenderness ratio, and the material properties of the pile. Dynamic buckling stress measured using a centrifuge test can be evaluated approximately with an equivalent slenderness ratio of elastic buckling stress presented in the Limit State Design of Steel Structures.

Keywords: Steel pile, Dynamic buckling behavior, Liquefaction, Centrifuge tests

INTRODUCTION

Steel piles are believed to be able to sustain strong lateral and compressive forces and that no pile experiences flexural buckling because of the high compressive force attributable to the overturning moment in addition to the dead load of the building because of soil resistance against lateral deformation of the piles. In fact, no damage of steel piles, which have high strength and ductility, has been identified in surveys of past earthquake damage. However, during the 2011 Great East Japan Earthquake, many piles of buildings in Sendai city, sustained heavy damage because these buildings were used even though their piles had already sustained heavy damage during the 1978 Miyagi Earthquake [1]. It is difficult to assess damage to piles under the buildings in the soil if the piles can carry a vertical load after the earthquake, even after the piles have buckled during soil liquefaction. In the Japanese current design code, the possibility of steel pile buckling is not considered. Design codes have no prescription for limitations of the slenderness ratio for piles. The horizontal stiffness of the ground decreases drastically when liquefaction occurs during an earthquake. Moreover, when slender steel piles beneath buildings experience high axial compression forces caused by the overturning moment of the superstructure, which are generated by inertia forces of buildings, flexural buckling of piles occurs as presented in Fig. 1.

This study conducted centrifuge tests of superstructure-pile-liquefied soil systems to investigate the dynamic buckling behavior of circular tube piles subjected to compressive axial forces. The elastic flexural buckling equations of piles in liquefied soil were developed using the energy method. These equations are applied to the proposed equivalent slenderness ratio. Results show that experimentally obtained values agree well with the buckling curves having this slenderness ratio.

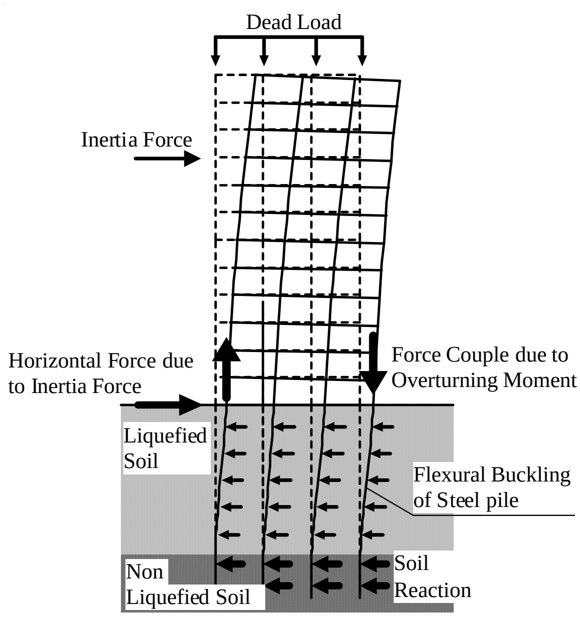

Fig. 1 Concept for Flexural Buckling of Steel Pile in Liquefied Soil

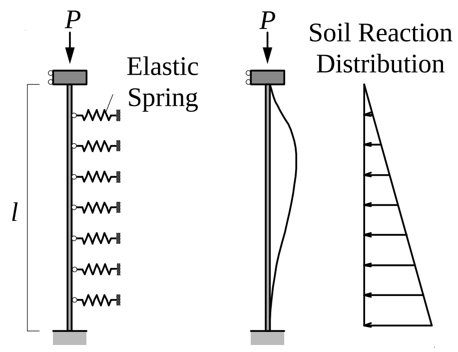

Fig. 2 Analytical Model of Steel Pile in Liquefied Soil and Distribution of Subgrade Reaction.

ELASTIC BUCKLING LOAD FOR A STEEL PILE IN LIQUEFIED SOIL

For this chapter, to develop the elastic buckling load of a steel pile in liquefied soil, the following are assumed. The external force subjected to a pile is only a vertical load such as Fig. 2. Both ends of the pile are fixed. The subgrade reaction is replaced by elastic horizontal springs.

When a steel pile in liquefied soil is buckled laterally, the potential energy is expressed as:

$$U = \frac{1}{2}\int_0^l \left(EIu''^2 - Pu'^2 + Ku^2 \right) dx \quad (1)$$

where EI stands for the steel pile flexural rigidity, l signifies the liquefaction layer thickness, and K denotes the subgrade reaction coefficient. Also, P and u respectively represent the pile vertical load and lateral displacement. The steel pile lateral deformation is expressed as a sine curve function.

$$u = a\left(1 - \cos\frac{2\pi x}{l}\right) \quad (2)$$

A triangular distribution is applied to the distribution of the subgrade reaction as in Fig. 2 and the following.

$$K = \frac{2K_c}{l}(l - x) \quad (3)$$

By substituting Eq. (3) into Eq. (2) and partially differentiating Eq. (2) the buckling load is obtained.

$$P_{cr} = \left(\frac{\pi}{l}\right)^2 EI\alpha \quad (4)$$

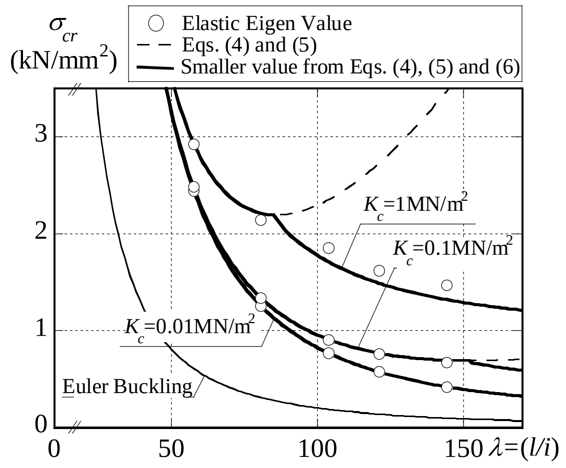

Fig. 3 Analytical Model of Steel Pile in Liquefied Soil and Distribution of Subgrade Reaction.

$$\alpha = 4 + \frac{3}{4}\left(\frac{l}{\pi}\right)^4 \frac{K_c}{EI} \quad (5)$$

The validity of the pile buckling load calculated from Eqs. (4) and (5) is ascertained by elastic eigenvalue analysis, where the pile is replaced by a line element divided into 50 parts in the longitudinal direction. The coefficient of the subgrade reaction is replaced by horizontal springs.

Figure 3 presents the relation between the elastic buckling stress for steel piles with the subgrade reaction and slenderness ratio. The plots represent elastic eigenvalue analysis results. The thin broken curves are drawn from Eqs. (4) and (5). The triangle subgrade reaction distribution is applied with the coefficient of the subgrade reaction, such as 1 MN/m^2, 0.1 MN/m^2, and 0.01 MN/m^2. When the slenderness ratio and the coefficient of the subgrade reaction are small, the pile buckling stresses calculated from Eqs. (4) and (5) are almost equal to numerical analysis results. However, when the slenderness ratio and the coefficient of the subgrade reaction are large, the pile buckling stresses calculated from Eqs. (4) and (5) are higher than numerical analysis results (e.g. K_c is 1 MN/m^2).

For a liquefaction layer thicker than the pile length, taking a local minimum of the buckling load, the closed form solution shown below is suggested.

$$\alpha = \left[8\left(1 - \frac{1}{\sqrt{3}}\right) + 2\left(\frac{l}{\pi}\right)^2\sqrt{\frac{K_c}{EI}}\right]\cdot\left[\frac{3}{4} + \frac{1}{2}\left(\frac{\pi}{l}\right)^2\sqrt{\frac{EI}{K_c}}\right]$$

$$\left(l > 2\pi\sqrt[4]{EI/3K_c}\right) \quad (6)$$

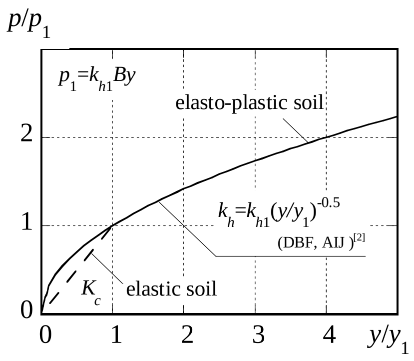

Fig. 4 Subgrade Reaction Curve.

Thick solid curves from Eqs. (4), (5), and (6) fit the numerical analysis results well. The subgrade reaction coefficient is adopted as the following in [2].

$$K_c = k_{h1} B (\mathrm{MN/m^2}) \tag{7}$$

$$k_{h1} = 80 E_0 B^{-\frac{3}{4}} (\mathrm{MN/m^3}) \tag{8}$$

In those equations, k_{h1} consists of the deformation modulus and the pile diameter.

Figure 4 shows the relation between the subgrade reaction and lateral displacement of the soil. The solid curve is the subgrade reaction curve as described in [2]. The broken line passes through the origin and point (1.0,1.0) of the coordinates has the gradient defined as K_c in Eq. (7). As described in this paper, soil having this curve or this line is designated as "elasto-plastic soil" or "elastic soil." The secant rigidity decreases as the lateral displacement of soil increases in Fig. 4. When the lateral displacement at the buckling of the piles is greater than reference displacement y/y_1=1, the coefficient of the subgrade reaction in elasto-plastic soil is smaller than that in elastic soil. Therefore, the coefficient of the subgrade reaction in elasto-plastic soil should be revalued when assessing lateral soil displacement.

As described in this paper, the lateral displacement at the buckling of the piles is assumed to be 0.002 l in [3]; this secant rigidity is designated as K_c'. The reduction ratio of the soil subgrade reaction, χ, is approximated as the ratio of K_c' to K_c.

$$\chi = \sqrt{l_0 / l} \tag{9}$$

Therein, l denotes the pile length, l_0 is 5 m. By substituting K_c' into K_c in Eqs. (4)–(6), the pile buckling stresses in elasto-plastic soil are calculated.

Furthermore, for centrifuge tests, the coefficient of the subgrade reaction decreases in liquefied soil when the piles buckle. Therefore, 0.1 or 0.2 for soil relative density of 30% or 60% is adopted as the reduction rate because of soil liquefaction [2].

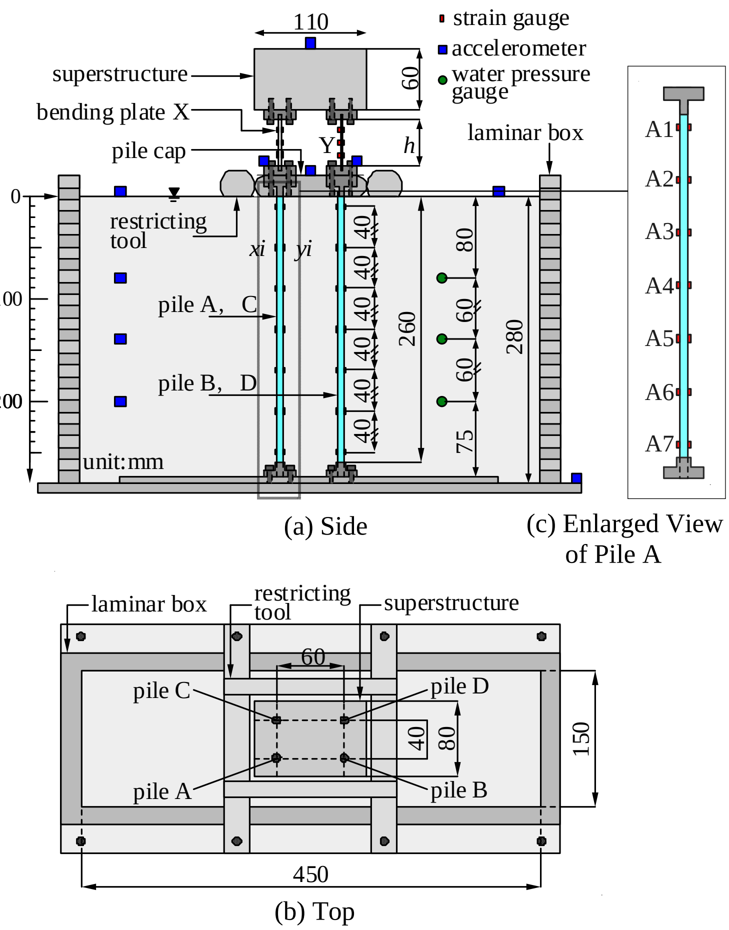

Fig. 5 Specimen and Instrumentation.

CENTRIFUGE TESTS

As described in this chapter, centrifuge tests of the superstructure–pile foundation model were conducted to clarify dynamic buckling behaviors of circular tube piles.

Outline of Centrifuge Test

Figures 5(a) and 5(b) show the specimen and the instruments. The specimen has a superstructure with mass, bending plates, four piles, and a saturated sand layer. The width of the foundation and superstructure is 80 mm. The superstructure height is 60 mm. The pile cap is laterally fixed to subject the piles to varying axial force caused by the superstructure weight and the overturning moment of the superstructure. As presented in Fig. 5, strain gauges on the left surface of piles and the bending plate are represented x_i, the gauges on the right surface are represented as y_i. Here, i represents 1–5 of each pile height, and 1–3 for each bending plate height. Accelerometers are put on upper surface of the superstructure and the pile foundation, the plate at bottom of the pile. Furthermore, accelerometers and water pressure gauges are placed at 80 mm, 140 mm, and 200 mm from ground level as presented in Fig. 5(a). The boundary condition of the piles is perfectly fixed. The pile cap is rotationally free, but laterally fixed. Centrifuge tests were performed under centrifugal acceleration of 40 g with a centrifugal loading device at the Disaster Prevention Research Institute, Kyoto University.

Table 1 presents the specimen specifications. The pile material is aluminum A1050S and brass C2680, the bending plate material is A5052; the others are SS400.

Figure 6 presents material properties of the piles. Therein, E is Young's modulus, σ_y is the yielding stress, and E_{st} is the strain hardening gradient.

Table 2 shows specimen parameters, which are the pile length, the initial axial force ratio, the natural period of the superstructure, the relative density, and the maximum input wave. Case 1 series and Case 2 series were conducted, respectively, without soil and with liquefied soil. The initial axial load ratio of aluminum piles, N_0/N_y is 0.37, issued from the design axial force of steel piles in actual structures. The initial axial load ratio of brass piles, N_0/N_y, is 0.13, to apply the same mass for specimens with aluminum piles. The pile length of the Case 1 series is 6000 mm or 9600 mm in full-scale. The pile length of Case 2 is 10400 mm. The natural period of the superstructure is presented in Table 2.

Figures 7(a) and 7(b) present the time history of the input waves. The sweep wave portrayed in Fig. 7(a) changes the period from 2.0 to 0.3 s in 50 s. The maximum input acceleration of the sweep wave is 1.0–5.5 m/s^2. The maximum input acceleration of

Table 1 Specification of the Specimens

Superstructure: m_1	Weight (N)	1.95×10^6
Bending plate	Thickness (mm)	80
Pile cap: m_2	Weight (N)	8.3×10^5
Pile	Diameter (mm)	240
	Thickness (mm)	20

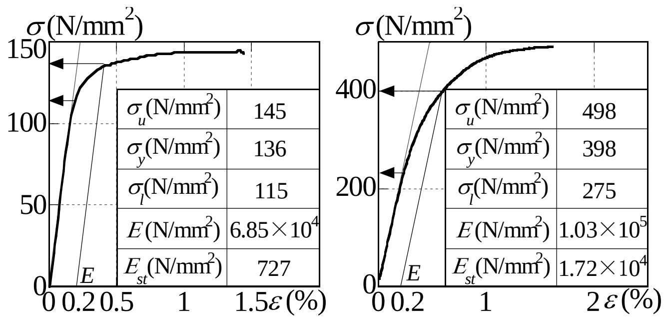

(a) Aluminum (b) Brass

Fig. 6 Material Properties of the Piles.

Table 2 Specimen Parameters

Specimen	Material	Pile length l (mm)	Initial axial force ratio	Plate length h (mm)	period of super-structure (s)	Relative Density Dr (%)	Input Wave	Maximum Input Wave (m/s^2)	State of vibration
Case 1-1	aluminum	6000	0.37	1800	0.79		Sweep	1.0	Elastic
								2.5	Collapse
Case 1-2								4.5	Collapse
Case 1-3				1400	0.59			1.0	Elastic
								2.5	Collapse
Case 1-4								3.0	Collapse
Case 1-5		9600		1800	0.79			1.0	Elastic
								1.8	Collapse
Case 1-6	brass		0.13	1400	0.59			1.0	Elastic
								5.5	Collapse
Case 2-1	aluminum	10400	0.37	1400	0.59	30	Sweep	3.0	Collapse
Case 2-2				1800	0.79	30			Collapse
Case 2-3				1400	0.59	60			Collapse
Case 2-4						30	Coastal Wave	6.9	Collapse
Case 2-5	brass		0.13			30	Sweep	3.0	Plasticized

※Full-scale

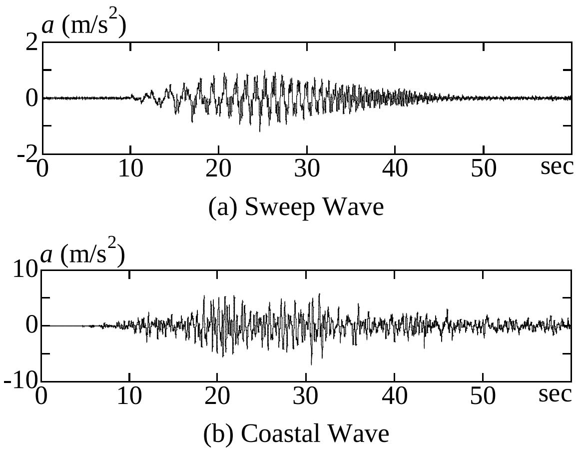

Fig. 7 Input Wave Time Histories.

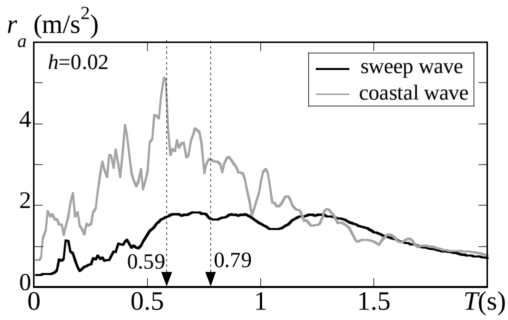

Fig. 8 Response spectrum of the input wave.

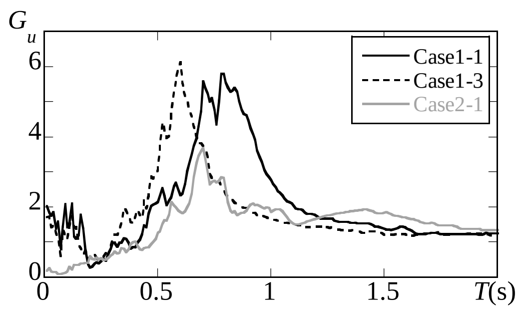

Fig. 9 Transfer Function of pile cap and Superstructure.

the coastal wave is 6.0 m/s^2.

Figure 8 portrays the acceleration response spectrum of the input wave. Figure 9 shows a transfer function of pile foundation and superstructure. The damping ratio is 0.02. The natural periods of Case 1-1 and Case 1-3 shown in Table 2 are 0.59 s and 0.79 s, which are close to the period at the maximum value of the coastal wave spectrum.

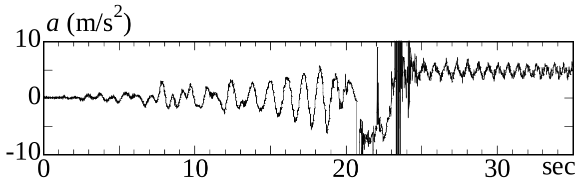

Fig. 10 Acceleration Response Time story of the Superstructure.

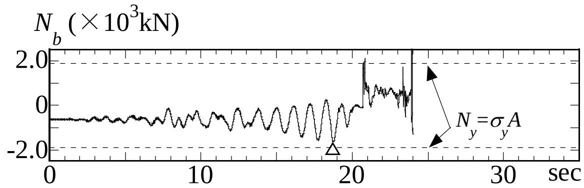

Fig. 11 Axial Force Response Time History.

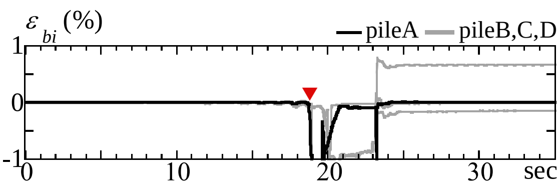

Fig. 12 Bending Strain Response Time History.

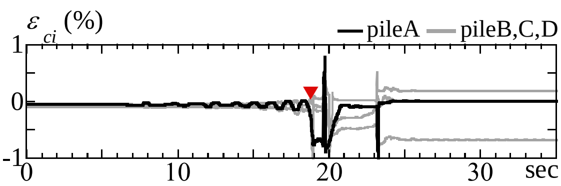

Fig. 13 Axial Strain Response Time History.

Dynamic Buckling Behavior of Superstructure–Pile Foundation System

For superstructure–pile models, this section clarifies the dynamic buckling behavior of circular tube piles.

Time history

Figures 10–13 present time histories of Case 1-1 shown in Table 2.

Figure 10 shows the acceleration response time history of the superstructure. Acceleration gradually increases. It reaches the maximum value at 19 s (1.06 Hz). Here, 1.06 Hz is the frequency of the sweep wave at dynamic buckling. Then the acceleration response fluctuates suddenly because of the pile collapse.

Figure 11 shows the axial force of pile response time history. The pile axial force is calculated as:

$$N_b = \frac{\varepsilon_{bxi} + \varepsilon_{byi}}{2} EA_b / 2 \; + \; m_2 g / 4 \tag{10}$$

where it is assumed that two piles uniformly carry varying axial force of the bending plate. Here, A_b denotes the bending plate cross-section ε_{bxi}, ε_{byi} represents the bending plate strain, and m_2 signifies the pile cap weight. Results show that the bending plates for all specimens remain elastic until the piles collapse. The horizontal broken line in Fig. 11 shows the piles' yield axial load. The white triangle symbol in Fig. 11 represents the maximum compression axial force before pile collapse. The maximum axial force is less than the yield axial force issued from dynamic buckling.

Figures 12 and 13 respectively depict bending strain and axial strain response time histories. These values are calculated with strain gauges at the pile center, as shown in Fig. 5. The bending strain and axial strain are calculated using the following equations.

$$\varepsilon_{bi} = \frac{\varepsilon_{pxi} - \varepsilon_{pyi}}{2} \tag{11}$$

$$\varepsilon_{ci} = \frac{\varepsilon_{pxi} + \varepsilon_{pyi}}{2} \tag{12}$$

The red triangle symbols in Figs. 12 and 13 indicate the times for the maximum bending strain increment. Black lines in Figs. 12 and 13 are the response time history of the pile that starts dynamic buckling first. Gray lines show the other piles' respective response time histories.

For Case 1-1, pile A buckled first. When pile A carries a maximum axial compressive force, the bending strain increment also reaches the maximum value. The bending strain of pile C increases immediately after the maximum bending strain increment of pile A. The bending strain of piles C and D is increased suddenly a few seconds later than that of pile A. Therefore, it can be inferred that pile C buckled immediately after dynamic buckling of pile A, and that piles B and D buckled dynamically. Results show that the maximum axial strain is reached after the maximum bending strain increment for all specimens.

Figure 14 shows the relation between axial force and axial strain for the pile of Case 1-1. The vertical axis is the pile's axial force calculated using Eq. (10). The horizontal axis is the axial strain at the center of piles calculated using Eq. (12). The black line represents the hysteresis loop of the pile buckled first. Gray lines represent the elastic gradient; N_y represents the yield axial load of the piles. The circle symbol in Fig. 14 shows the initial axial force. The triangle symbol shows the maximum axial force. Elastic hysteresis loops drawn with black lines are almost identical to the elastic gradient drawn with

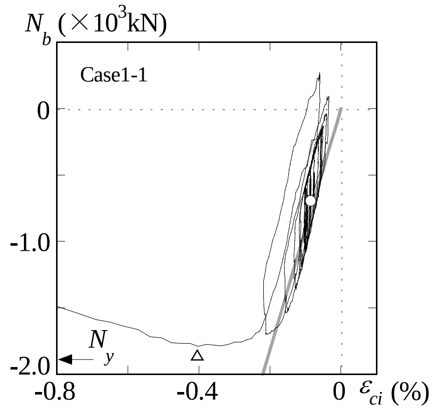

Fig. 14 Relation between Axial Force and Axial Strain

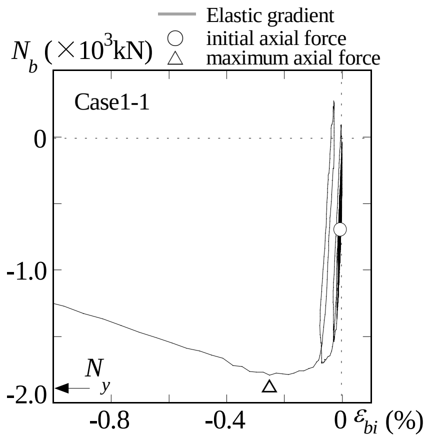

Fig. 15 Relation between Axial Force and Bending Strain

gray lines. Axial force for Case 1-1 with 76.8 of slenderness ratio decreases gradually after the axial force reaches the maximum value.

Figure 15 shows the relation between the axial force and the pile bending strain. For Case 1-1, the bending strain and axial force increase gradually until axial force reaches its maximum value. The hysteresis loops depicted in Figs. 14 and 15 are almost identical to the loops of the axial compressive members with static buckling.

Pile dynamic buckling behavior

Figure 16 shows the bending strain distribution of piles that buckled first for Case 1-1, Case 1-3, and Case 1-5. Each plot presents the bending strain at the measure point at 0.1% and 0.2% of the maximum bending strain increment and the maximum axial force. Maximum bending strain occurs at the pile center for all specimens. Bending strain of the pile end is less than that at the center of the pile.

Photo 1 shows the pile deformation of Case 1-6

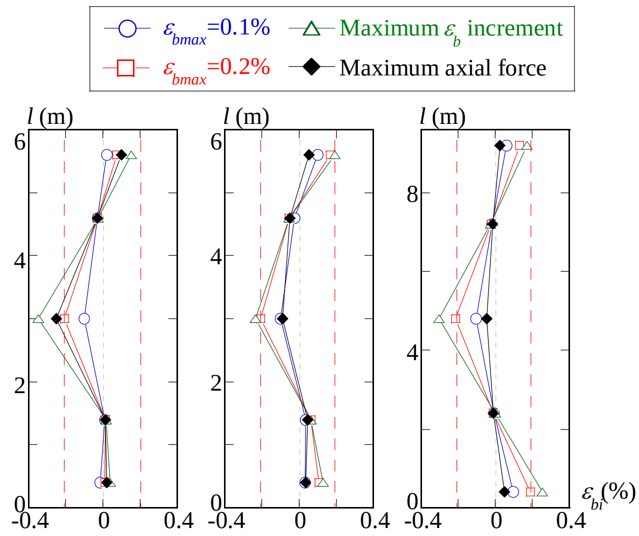

(a) Case 1-1 (b) Case 1-3 (c) Case 1-5

Fig. 16 Bending Strain Distribution of Pile.

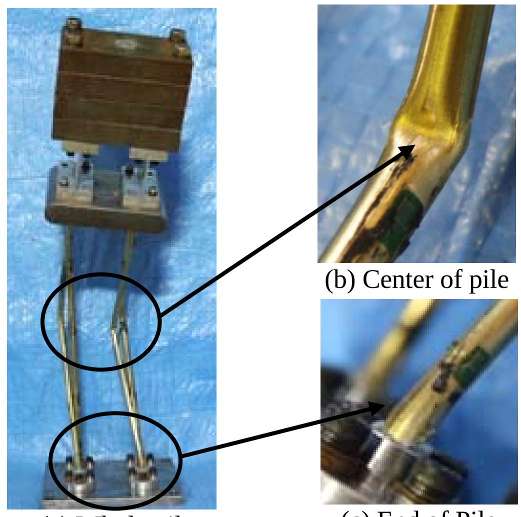

(a) Whole piles (b) Center of pile (c) End of Pile

Photo 1 Deformation of Piles (Case 1-6).

after vibration. All piles deform laterally at the center, which is similar to bending strain distribution of piles such as Case 1-1 in Fig. 16. Local buckling also occurred at the pile end because of the pile's large flexural buckling in Photo 1(c).

Results show that the bending deformation of all specimens appears to be almost identical.

Dynamic Buckling Behavior of Superstructure–Pile–Liquefied Soil System

In this section, the dynamic buckling behavior of circular tube piles is clarified with superstructure–pile–liquefied soil models.

Response time history

Figures 17–21 show the time history of Case 2-1 presented in Table 2. Figure 17 shows the superstructure acceleration response time history. Acceleration increases gradually and reaches a maximum value at 19 s.

Figure 18 shows the excess pore water pressure ratio time history. Black and gray curves respectively show data from water pressure gauges located on 80 mm and 140 mm from the ground surface depicted in Fig. 5(a). The dotted line in Fig. 18 shows the time at which the excess pore water pressure ratio reached 1.0. As described in this paper, soil liquefaction occurs when the excess pore water pressure ratio reaches 1.0.

Figure 19 portrays the axial force in the pile response time history, as calculated using axial strain gauges on bending plates (Fig. 5(a)). Figures 20 and 21 respectively show the bending strain and axial strain response time histories.

For Case 2-1, soil liquefaction occurs at about 16 s in Fig. 18. Furthermore, the bending strain increases suddenly at about 19 s, as marked by the red triangle symbol in Fig. 20, as soon as the axial force reaches the maximum value shown by the white triangle symbol in Fig. 19. For Case 2-1, pile B buckled first.

Figures 22–26 represent the time history of Case 2-2 presented in Table 2. Figure 22 shows the acceleration response time history of the superstructure. Acceleration increases gradually and reaches a maximum value at 13 s. Figure 23 depicts the excess pore water pressure ratio time history. Figure 24 portrays the axial force of the pile response time history, which is calculated from data of axial strain gauges on bending plates, as presented in Fig. 5(a). Figures 25 and 26 respectively display the bending strain and axial strain response time history.

For Case 2-2, soil liquefaction occurs at about 14 s, as presented in Fig. 23. Furthermore, then, the bending strain increases suddenly at about 15 s, as denoted by the red triangle symbol in Fig. 25 immediately after the axial force reaches the maximum value, as indicated by a white triangle symbol in Fig. 24. For Case 2-2, pile A buckled first. The response behaviors for Case 2-2 are similar to those for Case 2-1, even though the natural period of Case 2-2 is longer than that of Case 2-1.

Pile dynamic buckling behavior

Figure 27 portrays the relation between the excess pore water pressure ratio and the pile bending strain for Case 2-1. The vertical axis represents the excess pore water pressure ratio. The horizontal axis represents bending strain at the center of pile B, as calculated from Eq. (12). Gray dotted and black

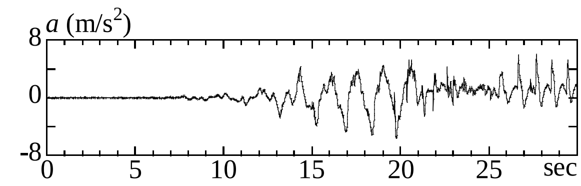

Fig. 17 Acceleration Response Time History of the Superstructure (Case 2-1).

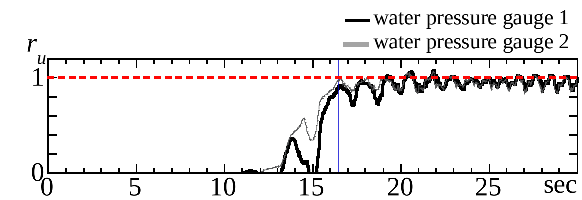

Fig. 18 Excess Pore Water Pressure Ratio Time History (Case 2-1).

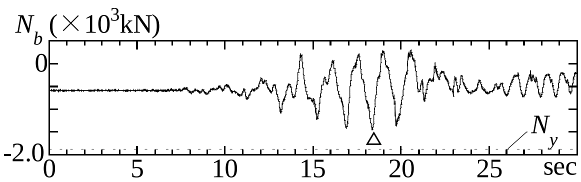

Fig. 19 Axial Force Response Time History (Case 2-1).

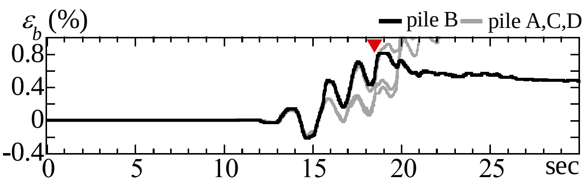

Fig. 20 Bending Strain Response Time History (Case 2-1).

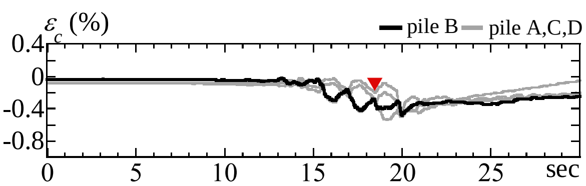

Fig. 21 Axial Strain Response Time History (Case 2-1).

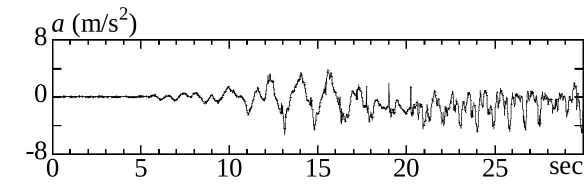

Fig. 22 Acceleration Response Time History of the Superstructure (Case 2-2).

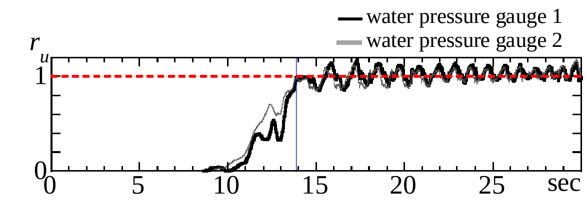

Fig. 23 Excess Pore Water Pressure Ratio Time History (Case 2-2)

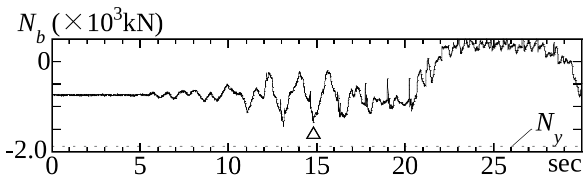

Fig. 24 Axial Force Response Time History (Case 2-2).

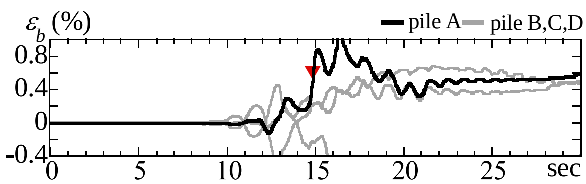

Fig. 25 Bending Strain Response Time History (Case 2-2).

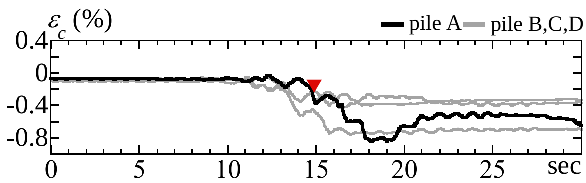

Fig. 26 Axial Strain Response Time History (Case 2-2).

solid curves respectively show the hysteresis loops before buckling occurs and after buckling occurs.

The bending strain increases only slightly before the excess pore water pressure ratio reaches 1.0. After liquefaction, the bending strain increases suddenly because of the reduction of the horizontal stiffness of the soil.

Figure 28 depicts the relation between the axial force and pile bending strain for Case 2-1. The vertical axis shows the axial force; the horizontal axis represents bending strain at the center of pile B. Gray dotted and black solid lines respectively show hysteresis loops before liquefaction and after liquefaction.

Before soil liquefaction, the bending strain increases only slightly, even if the axial force increases. After liquefaction, the axial force reaches a maximum value. Then dynamic buckling occurs. The more bending strain increases after buckling, the less axial force decreases. In contrast to the superstructure–pile models without soil in Fig. 15, the axial force decreases only slightly until the bending strain reaches about 0.15%.

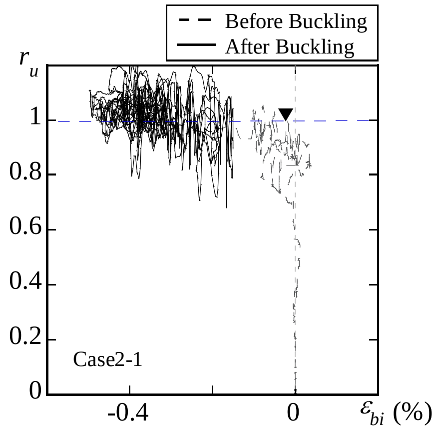

Fig. 27 Relation between Excess Pore Water Pressure Ratio and Pile's Bending Strain.

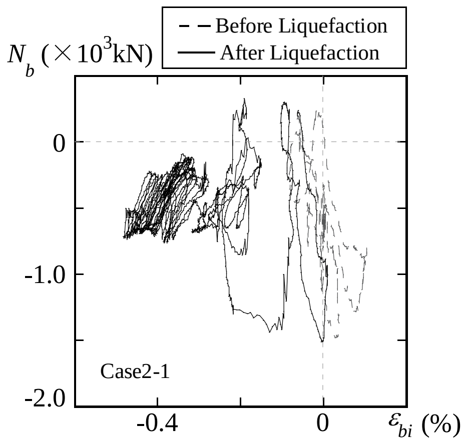

Fig. 28 Relation between Axial Force and Bending Strain.

Photo 2 shows the pile buckling deformation for the Case 2 series. For the specimens of Cases 2-1, 2-2 and 2-4, the piles' flexural buckling occurs with local buckling at the pile end. For Case 2-3, with soil relative density of 60%, pile buckling occurs laterally near the pile head. In contrast, although pile instantaneously becomes plastic for Case 2-5, which has a smaller initial axial force ratio than the others, the piles never buckle.

DYNAMIC BUCKLING STRENGTH OF STEEL PILES IN LIQUEFIED SOIL

Figure 29 portrays the relation between buckling stress and the equivalent slenderness ratio. The vertical axis represents the value of the dynamic buckling stress of the piles divided by the yielding stress. The horizontal axis shows the equivalent slenderness ratio of piles, calculated as:

$$\lambda_c = \sqrt{P_y / P_{cr}} \tag{13}$$

where P_y stands for the yield load and P_{cr} represents Euler's buckling load, as described in [4]. When steel piles are braced continuously by the soil, Euler's buckling load is replaced by the buckling load obtained from Eqs. (4)–(6). Then this equivalent slenderness ratio is defined as the modified equivalent slenderness ratio.

Figure 29 presents the relation between the

(a) Case 2-1 (b) Case 2-2 (c) Case 2-3 (d) Case 2-4 (e) Case 2-5

Photo 2 Deformation of Superstructure – Pile Cap Liquefied Soil System.

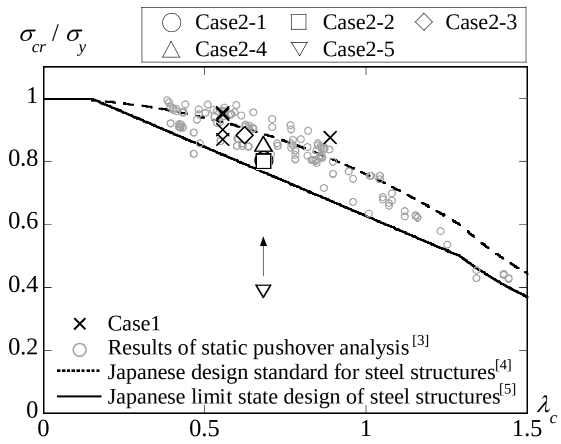

Fig. 29 Dynamic Buckling Strength and Buckling Stress Curves.

dynamic buckling strength of piles on centrifuge tests and the buckling stress curves for design criteria in [4] and [5]. In Fig. 29, the curves represent the buckling stress curves of the Japanese limit state design of steel structures and the Japanese design standard for steel structures. The cross symbols show results of Case 1. The other symbols show results of Case 2. The small gray circle shows results of static pushover analysis described in [3].

The results of centrifuge tests, except for Case 2-5, are exceeded for the curves of Japanese limit state design of steel structures, distributed as the upper-bound for the curve of Japanese design standard for steel structures. For Case 2-5, which shows no dynamic buckling behavior, the maximum compression axial force is substituted for the dynamic buckling strength for reference.

Results show that dynamic buckling stress for the steel piles in liquefied soil can be estimated approximately using the modified equivalent slenderness ratio by the curve of the Japanese limit state design of steel structures.

CONCLUSION

Superstructure–pile foundation systems were assessed using centrifuge tests to elucidate dynamic buckling behaviors and buckling loads of circular tube piles under compressive axial forces. Results show the following.

1) The flexural elastic buckling load for steel piles in liquefied soil can be calculated from Eqs. (4)–(6) developed using the energy method.
2) Results clarified that piles' dynamic buckling occurs after soil liquefaction because of the superstructure weight and the superstructure overturning moment.
3) Pile dynamic buckling occurs when the bending strain reaches a threshold value.
4) The axial force after dynamic buckling for Case 2 series with soil decreases less than that of Case 1 series without soil.
5) The dynamic buckling stress of steel piles in liquefied soil can be estimated using the modified equivalent slenderness ratio by buckling stress curves of the Japanese limit state design of steel structures.

ACKNOWLEDGMENTS

The authors appreciate the support of the Japan Iron and Steel Foundation.

REFERENCES

[1] Architectural Institute of Japan, Preliminary Reconnaissance Report of the 2011 Tohoku-Chiho Taiheiyo-Oki Earthquake, July, 2011. (in Japanese)

[2] Architectural Institute of Japan, Recommendation for Design of Building Foundations, 2001. (in Japanese)

[3] Kimura Y, Tokimatsu K, "Buckling Stress of Steel Pile with Vertical Load in Liquefied Soil", Jour. of Structural and Construction Engineering, No. 595, Sep. 2005, pp.73-79. (in Japanese)

[4] Architectural Institute of Japan, Design Standard for Steel Structures, 2005. (in Japanese)

[5] Architectural Institute of Japan, Limit State Design of Steel Structures, 1998. (in Japanese)

Technical Paper

Geotechnique

Sixth International Conference on Geotechnique, Construction Materials and Environment, Bangkok, Thailand, Nov. 14-16, 2016, ISBN: 978-4-9905958-6-9 C3051

STABILITY CHARTS FOR UNSUPPORTED PLAIN STRAIN TUNNEL HEADINGS IN UNDRAINED CLAY

Jim Shiau[1], Brian Lamb[1], Mathew Sams[1], Jay Lobwein[1] and Tin Nguyen[1]
[1]School of Civil Engineering and Surveying, University of Southern Queensland, Australia

ABSTRACT

This paper investigates the stability of plane strain tunnel headings in undrained soils. Using the factor of safety approach via the strength reduction technique, the idealised tunnel heading models are studied using the finite difference program *FLAC*. This problem is also similar to underground long wall excavations in plane strain condition. The finite difference results are presented alongside upper and lower bound limit solutions for validation. A thorough comparison between these two methods finds a very good agreement. Design charts are presented for a wide range of practical scenarios using dimensionless ratios, similar to Taylor's design charts used for slope stability. Typical examples are presented to illustrate the usefulness for practicing engineers.

Keywords: Plain Strain Heading, Undrained Clay, Stability, Strength Reduction Method, Design Chart

INTRODUCTION

The research of tunnel heading stability was initiated with [4] who studied the plastic flow of clay soil in vertical openings such as sheet pile walls and drew comparison to the stability of a tunnel heading face. The stability number was initially defined in Eq. (1).

$$\boldsymbol{N} = \frac{\sigma_s - \sigma_t + \gamma(C + D/2)}{S_u} \qquad (1)$$

Where σ_s is the uniform surcharge pressure on the surface and σ_t is the uniform internal tunnel pressure. The cover depth above the crown of the tunnel is C, whilst the tunnel diameter is D. The undrained shear strength of soil and the unit weight of the soil are represented by S_u and γ respectively.

During the 1970s at Cambridge University, numerous studies were completed on centrifuge models by [1]. The work was culminated by [9] who investigated the experimental and theoretical undrained collapse of three-dimensional cylindrical tunnel headings in normal consolidated kaolin under different geometry and gravity regimes. References [5], [12] built further on the stability ratio by using upper and lower bound solutions using the classical limit theorems for tunnel collapse in undrained cohesive conditions.

Reference [2] revisited the plane strain heading problem due to the recent improvements to finite element limit analysis methods developed in [7]-[8]. A number of papers were achieved in the area of tunnel stability by [10], [16] and [17]. In particular [10] extended the limit analysis theory on tunnel heading by investigating a three-dimensional multiblock failure mechanism for frictional and cohesive soil by the use of a spatial discretization technique.

All of these studies investigated the stability number as a function of dimensionless parameters. The problem was regarded as to find the limiting value of a pressure ratio $(\sigma_s - \sigma_t)/S_u$ that is a function of the independent parameters such as the depth ratio C/D and the strength ratio $S_u/\gamma D$. It is possible to simulate an unsupported excavation in green-field conditions by neglecting σ_s and σ_t, or a situation with equal surcharge and internal supportive pressure. It can also be a factor of safety problem that is a function of the depth ratio C/D and the strength ratio $S_u/\gamma D$ ~ a similar approach in Taylor's design charts for slope stability analysis [15].

This paper presents a comprehensive parametric undrained analysis for the stability of an unsupported plain strain heading in an unsupported excavation in green-field conditions. A strength reduction technique is used to determine the factor of safety in cohesive soils over a wide parametric range. Numerical results from the strength reduction technique using *FLAC* are compared to those obtained by the finite element limit analysis. Design stability charts are also presented for practical uses.

STATEMENT OF PROBLEM

The problem is a two dimensional plane strain heading condition by assuming the longitudinal section as a very long excavation [2]. Figure 1 shows the problem definition. The soil medium is considered as undrained and is modelled as a uniform Tresca material, which is the same as a Mohr-Coulomb material with no internal friction angle. The undrained shear strength (S_u) and the unit weight (γ) are soil properties used, whilst the excavation depth (D) has a cover depth (C) above the crown of the excavation.

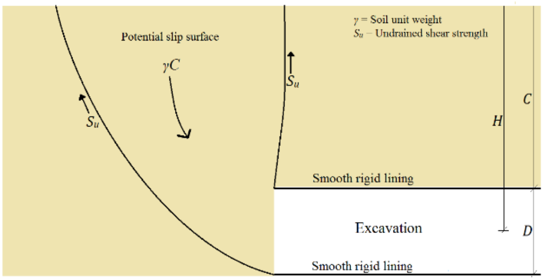

Fig. 1 Problem Definition

Similar to a slope stability analysis, the stability of the heading face is represented by the factor of safety (FoS) that is a function of the depth ratio (C/D) and strength ratio ($S_u/\gamma D$).

$$\boldsymbol{FoS = f\left(\frac{C}{D}, \frac{S_u}{\gamma D}\right)} \qquad (2)$$

These dimensionless ratios allow the results of this study to be used in scenarios that are physically different, but where the soil strength ratio and the depth ratio still fall in the parametric domain. To cover all possible realistic ranges, the parameters used in the study include $S_u/\gamma D$ = 0.1-2 and C/D = 1-6. This would ensure that the design charts produced can be applied to many different tunnel design and analysis problems, which are useful for design purposes.

MODELLING PROCEDURE

Figure 2 shows a typical finite difference mesh of the problem in this study. The soil domain size was elected to be large enough to validate the assumption of an infinite excavation. The boundary conditions within Fig. 2 are important to ensure that the entire soil mass is modelled accurately despite using a finite mesh. The smooth rigid lining above and below the soil excavation is restrained in the vertical (y) direction to reproduce the nature of the tunnel linings and mining supports. The base and sides of the model is restrained in the x and y directions.

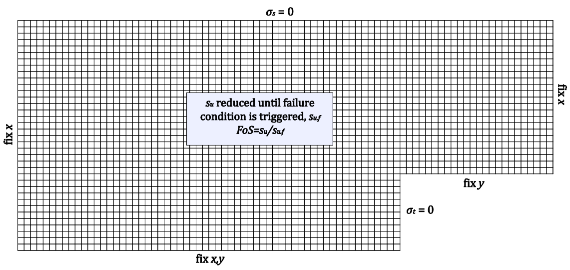

Fig. 2 Typical Mesh and Boundary Condition

The factor of safety for the many cases being studied is computed by using *FLAC* and the built-in implementation of the strength reduction technique. A built-in *FISH* language that enables automatic mesh generation was also developed to improve the efficiency in the parametric study. *FLAC* is based on the explicit finite difference method, but it is not very different from a nonlinear finite element program. This method has been widely used for slope stability analysis, but is rarely used for tunnel stability analysis. This strength reduction technique will yield a factor of safety (FoS), which is not unfamiliar with practicing designers.

Such a method involving factors of safety has been described by [3] for slope stability. The factor of safety is defined as a ratio of the strength necessary to maintain limiting equilibrium with the soil's available strength. The shear strength of the material is reduced until the limiting condition is found. This can be compared to the studies originated from [4] where the uniform surcharge pressure is increased until the limiting condition is found. If failure occurs initially, the shear strength of the soil is increased by amplifying the cohesion and friction angle until limiting equilibrium or failure state is reached. Once the actual and critical strength are known, the factor of safety can then be calculated.

RESULTS AND DISCUSSION

Using the strength reduction technique within the finite difference program *FLAC*, factor of safety (FoS) values were obtained for a range of parameters for an unsupported tunnel heading in undrained soil. The two dimensionless parameters used in the studies are the depth ratio (C/D) and the strength ratio ($S_u/\gamma D$).

It is important to compare the finite difference technique with another numerical investigation. Using finite element limit analysis, upper bound and lower bound, factors of safety have been calculated using *OptumG2* over the same parametric ranges. The numerical procedures used in *OptumG2* are based on the limit theorems of classical plasticity [7]-[8].

COMPARISONS WITH RIGOROUS UPPER AND LOWER BOUNDS

Dimensionless stability charts showing the numerical results obtained in this study are presented in Fig. 3 and 4. In Fig. 3, FoS increases linearly as the strength ratio $S_u/\gamma D$ increases, indicating that there exists a stability number where the effective FoS is equal to one, a critical stability number (N_c). This could be achieved by dividing the stability ratio

($S_u/\gamma D$) by the *FoS* result for each case. Also note that the rate of *FoS* increase is different for each *C/D* value. The gradient of the line is greater for smaller *C/D* values.

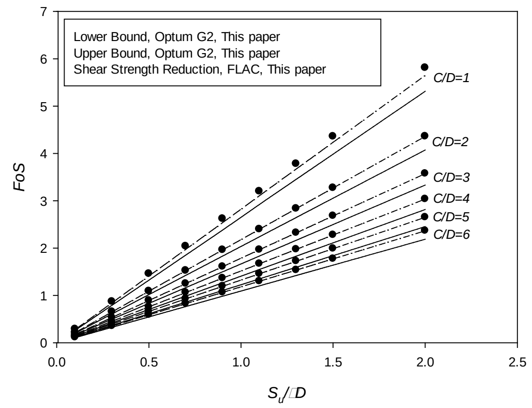

Fig. 3 Comparison of *FoS* results with respect to $S_u/\gamma D$ for various values of *C/D*

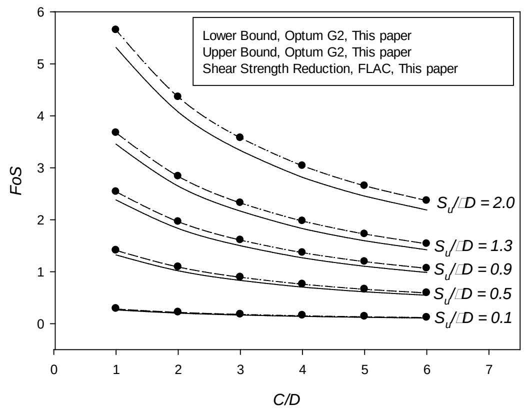

Fig. 4 Comparison of *FoS* results with respect to *C/D* for various values of $S_u/\gamma D$

Figure 4 shows that the *FoS* decreases nonlinearly with increasing depth ratio *C/D* for all strength ratios defined as $S_u/\gamma D$. The finite difference results are in good agreement with the upper bound solutions, but consistently produce results that are 3-5% larger than the lower bound solutions. Note the strength ratio is normalised with respect to the tunnel excavation depth (*D*), and therefore the undrained shear strength (S_u) remains constant throughout the increasing depth ratios. Owing to the increasing overburden pressure (*C/D* increase) and the constant undrained shear strength (S_u), it therefore results in *FoS* values decreasing. This is in contrast to the common belief that an increase to *C/D* always results in an increase to *FoS*.

A simple observation can be made from Fig. 1, where the active force is the weight of soil and the resisting force is given by the shear strength of the soil. Of two hypothetical tunnels in the same cohesive soil but at different depths, the tunnel with the smaller active force (γC) will have a higher probabililty of stability. This observation may not be true in a soil with internal friction angle ($\phi \neq \mathbf{0}$) due to the additional shear strength ($\sigma\tan\phi$) and geometrical arching effects. In purely cohesive soils, the latter still occurs, but its effect is not enough to overcome that subsequent increase in active force.

EXTENT OF FAILURE SURFACE

This area of investigation is related to the type of failure mechanism the tunnel heading encountered at certain depths. Reference [2] discusses the effects of increasing the soil weight and linear variation of the shear strength of the soil for increasing depth ratios. For homogenous shallow tunnels (depth ratios $C/D \leq 2$), the failure mode is predominantly through the vertical free movement wall. A trapdoor type mechanism is initiated, with the velocity vectors leading vertically down above the heading opening. For deeper tunnels the failure zone extends to the base of the tunnel. The velocity vectors are arched around the free moving heading vertical surface, compared to the vertical trapdoor mechanism for the shallow tunnels. Figures 5-8 show some typical plots of the shear strain rate and velocity field. Note that the cohesive strength of the soil appears to have no impact on the failure extent.

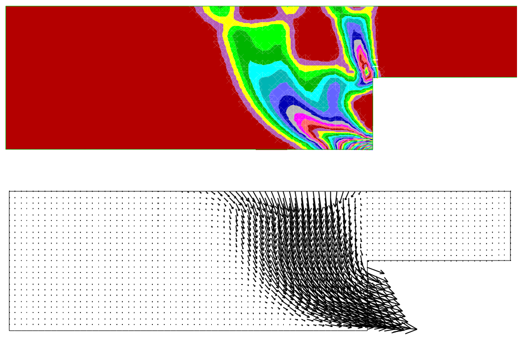

Fig. 5 Plots of shear strain rate and velocity field for *C/D*=1 and $S_u/\gamma D$ =0.1

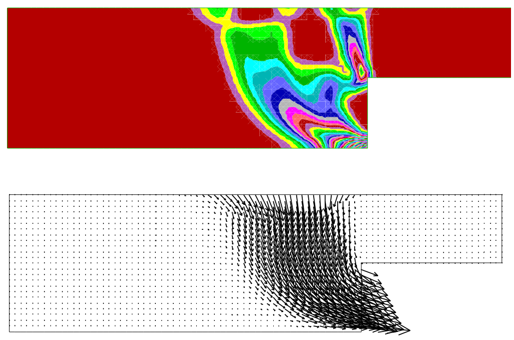

Fig. 6 Plots of shear strain rate and velocity field for *C/D*=1 and $S_u/\gamma D$ =2.0

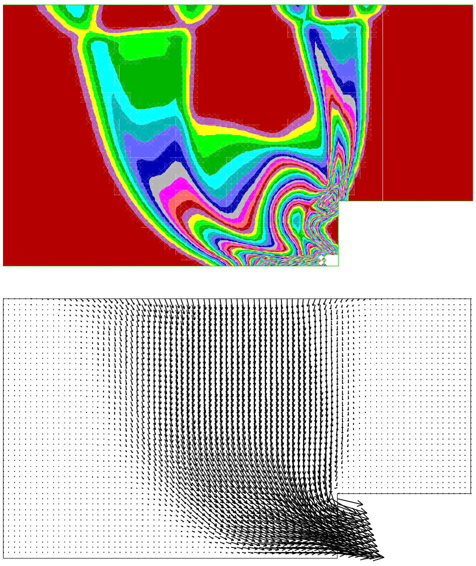

Fig. 7 Plots of shear strain rate and velocity field for C/D=3 and $S_u/\gamma D$ =0.1

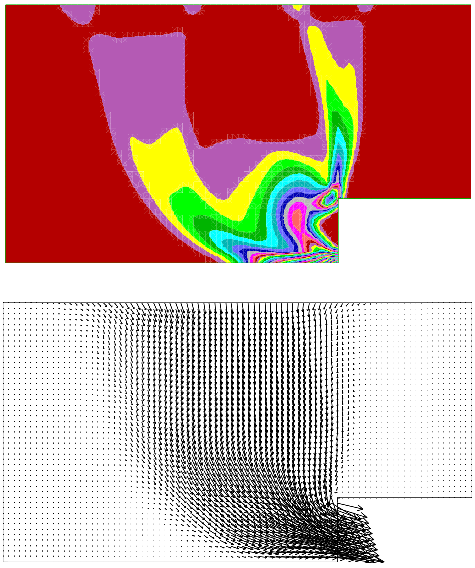

Fig. 8 Plots of shear strain rate and velocity field for C/D=3 and $S_u/\gamma D$ =2.0

Figures 9 and 10 show typical tensor plots for principal stresses. These plots show weak soil arching throughout the soil body and leading to the surface from the free excavation face. As discussed, soils with an internal friction angle ($\phi \neq 0$) would have more potential for stability, with the internal frictional angle adding to the strength of the material by the soil arch phenomena.

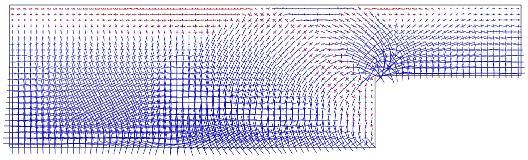

Fig. 9 Principle stress tensor plot at collapse for C/D=1 and $S_u/\gamma D$ =2.0

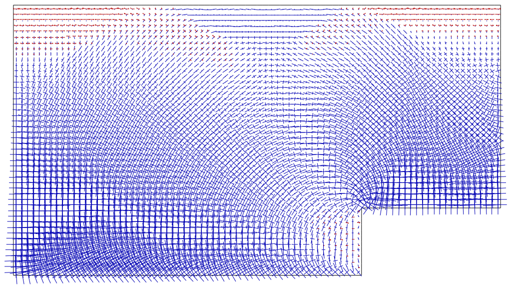

Fig.10 Principle stress tensor plot at collapse for C/D=3 and $S_u/\gamma D$ =2.0

In reality the deformation trough would be three dimensional, but with the assumptions made, the largest extent of plastic deformation in the heading cross-section can be reasonably estimated. This information of failure extent is important as it will assist practicing engineers in the decision making in monitoring ground movements.

USING THE STABILITY CHARTS

The stability design charts are best demonstrated through a number of examples. The numerical results have been used to produce design contour charts for factors of safety in Fig. 11. A designer will use the chart to relate the depth ratio (C/D), soil strength ratio ($S_u/\gamma D$) and factor of safety for the particular tunnel heading. This process would predominantly be used in the initial design procedure for the design engineers.

Fig. 11 presents the design chart where the factor of safety is a function of the depth ratio and strength ratio. Regression of the chart gives the following relationship with $r^2 = 0.99$.

$$\boldsymbol{FoS} = \mathbf{3}\left(\frac{\boldsymbol{s_u}}{\boldsymbol{\gamma D}}\right)\left(\frac{\boldsymbol{C}}{\boldsymbol{D}}\right)^{-\mathbf{0.47}} \qquad (3)$$

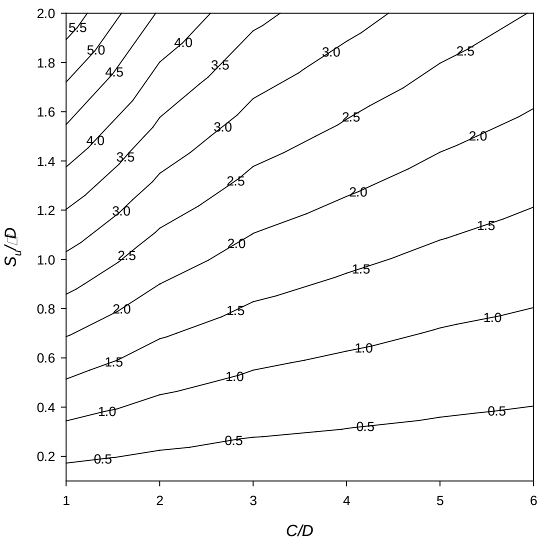

Fig.11 Stability chart for *FoS* with respect to *C/D* and $S_u/\gamma D$

EXAMPLES

Using the design chart and the regressed design equation, practical examples are presented for either analysis or design purposes.

Analysis of an existing unsupported tunnel

An existing mining excavation having no internal heading pressure and no surcharge pressure, determine the factor of safety for operations to continue. Parameters are given as S_u = 50 kPa, γ = 18 kN/m^3, C = 10 m, and D = 2.5 m.

1. Using C/D = 4.0, $S_u/\gamma D$ = 1.11, Eq. 3 gives a *FoS* of 1.74.
2. Using C/D = 4.0, $S_u/\gamma D$ = 1.11, Fig. 11 gives an approximate *FoS* of 1.75.

An actual computer analysis of this particular case gives a *FoS* of 1.76.

Analysis of a temporary unsupported tunnel heading

During the construction of a tunnel in soft soil, a factor of safety of 3 is targeted for a shallow tunnel maintenance job. While the machine requires maintenance, it will be unable to apply pressure to the tunnel face for a short period. A decision needs to be made whether stability will be maintained during this period. Parameters are given as: S_u = 30 kPa, $\boldsymbol{\gamma}$ = 18 kN/m^3, C = 20 m and D = 5 m

1. Using C/D = 4.0, $S_u/\gamma D$ = 0.33, Eq. 3 gives a *FoS* of 0.52.
2. Using C/D = 4.0, $S_u/\gamma D$ = 0.33, Fig. 11 gives an approximate *FoS* of 0.54.

An actual computer analysis of this particular case gives a *FoS* of 0.51. Therefore, in this case, a failure to supply heading pressure would result in collapse. Ground improvement is needed to increase the soil strength.

Design of an unsupported tunnel heading

The soil properties are known at the tunnel project site, and the diameter is specified. A target factor of safety is chosen, and the designers need to specify a maximum cover depth that will satisfy the target *FoS*.
Parameters are given as: S_u = 100 kPa, $\boldsymbol{\gamma}$ = 18 kN/m^3, D = 5m, and the target *FoS* = 2

1. Using *FoS* = 2 and $S_u/\gamma D$ = 1.11, Eq. 3 gives a C value of 14.8 m.
2. Using *FoS* = 2 and $S_u/\gamma D$ = 1.11, Fig. 11 gives an approximate C/D value of 3 and therefore C value of 15 m.

An actual computer analysis for this particular case (C value of 15m) gives a *FoS* of 2.07

CONCLUSION

Stability of plane strain headings was studied in this paper using a factor of safety approach with the strength reduction technique. Numerical results were obtained using both the finite difference software *FLAC* and the finite element software *OptumG2*. Design equation and charts were produced aligned with examples to determine the stability of excavated heading depths, such as idealised tunnel headings and long wall mining excavations. The factor of safety approach to plain strain heading stability is a useful approach to the initial design stage as it always provides direct information and understanding of tunnel stability.

REFERENCES

[1] Atkinson, JH, & Cairncross, AM 1973, 'Collapse of a shallow tunnel in a Mohr–Coulomb material', *In Proceedings of the Symposium on the Role of Plasticity in Soil Mechanics*, Cambridge, UK, 13–15 September 1973. Edited by A.C. Palmer. Cambridge University Engineering Department, University of Cambridge, Cambridge, UK. pp. 202–206.

[2] Augarde, CE, Lyamin, AV & Sloan, SW 2003, 'Stability of an undrained plane strain heading revisited', Computers & Geotechnics, vol.30, pp. 419-430.

[3] Bishop, AW 1955, 'The use of slip circle in the stability analysis of slopes', Geotechnique, vol. 5(1), pp. 7-17.

[4] Broms, BB & Bennermark, H 1967, 'Stability of clay at vertical openings', Journal of the Soil

Mechanic & Foundations Division, Proceedings of the American Society of Civil Engineers, vol. 93, pp. 71- 93.

[5] Davis, EH, Gunn, MJ, Mair, RJ & Seneviratne, HN 1980, 'The stability of shallow tunnels & underground openings in cohesive material', Geotechnique, vol. 30, pp. 397-416.

[6] FLAC 2003, Fast Lagrangian Analysis of Continua, Version 4.0, Itasca Consulting Group, Minneapolis, Minnesota, USA.

[7] Lyamin, AV, & Sloan, SW 2002(a), 'Lower bound limit analysis using non-linear programming', International Journal for Numerical Methods in Engineering, vol. 55, no. 5, pp. 573-611.

[8] Lyamin, AV & Sloan, SW 2002(b), 'Upper bound limit analysis using linear finite elements & non-linear programming', International Journal for Numerical & Analytical Methods in Geomechanics, **vol.** 26, no. 2, pp. 181-216.

[9] Mair RJ 1979, 'Centrifugal modelling of tunnel construction in soft clay', PhD thesis, University of Cambridge.

[10] Mollon, G, Dias, D & Soubra, AH 2010, 'Face Stability Analysis of Circular Tunnels Driven by a Pressurized Shield', Journal of Geotechnical & Geoenvironmental Engineering, Vol: 136, pp. 215-229.

[11] Optum G2 2013, Optum Computational Engineering, Version 1.2014.10.1, Newcastle, Australia.

[12] Sloan, SW, Assadi, A 1994, 'Undrained stability of a plane strain heading', Canadian Geotehcnical Journal, vol. 31, no. 3, pp. 443-450.

[13] Sloan, SW 1988, 'Lower bound limit analysis using finite elements & linear programming', International Journal for Numerical & Analytical Methods in Geomechanics, vol. 12, pp. 61-67.

[14] Sloan, SW 1989, 'Upper bound limit analysis using finite elements & linear programming', International Journal for Numerical & Analytical Methods in Geomechanics, vol. 13, pp. 263-282.

[15] Taylor, DW 1937, 'Stability of earth slopes.' Journal of the Boston Society of Civil Engineers, vol. 24, no. 3, pp. 197-246.

[16] Wilson, DW, Abbo, AJ, Sloan, SW, & Lyamin, AV 2014, 'Undrained Stability of Dual Circular Tunnels', International Journal of Geomechanics, vol. 14(1), pp. 69-79.

[17] Yamamoto, K, Lyamin, AV, Wilson, DW, Sloan, SW & Abbo, AJ 2011, 'Stability of a circular tunnel in cohesive-frictional soil subjected to surcharge loading', Computers & Geotechnics, vol. 38, pp. 504-514.

[18] Shiau, J., Sams, M. and Chen, J. 2016, 'Stability charts for a tall tunnel in undrained clay', Int. J. of GEOMATE, vol. 10(2), pp. 1764-1769

[19] Shiau, J., Sams, M. and Lamb, B. 2016, 'Introducing advanced topics in geotechnical engineering teaching – Tunnel modelling', Int. J. of GEOMATE, vol. 10(1), pp. 1698-1705

[20] Shiau, J., Lamb, B. and Sams, M. 2016, 'The use of sinkhole models in advanced geotechnical engineering teaching', Int. J. of GEOMATE, vol. 10(2), pp. 1718-1724

STRENGTH AND PERMEABILITY CHARACTERISTICS OF ROAD BASE MATERIALS BLENDED WITH FLY ASH AND BOTTOM ASH

Jonathan R. Dungca[1] and Julie Ann L. Jao[2]
[1,2]Civil Engineering Department, De La Salle University, Manila, Philippines

ABSTRACT

The Philippines has an extensive road network which handles most of its passenger and freight movements. Large volumes of aggregate embankment materials of good quality are required to primarily support these transport infrastructures, and this poses threat to the environment. Coal combustion by-products (CCPs) are seen to be its potential alternative mainly due to its vast production and disposal problems in the country. Representative samples of class C fly ash and bottom ash were gathered together with conventional road base materials. Fly ashes were substituted to act as fines; whereas, bottom ash substitutions were varied at different mixture ratios of 0%, 20%, 40%, 60%, 80%, and 100% of fine aggregates. Index properties (i.e. specific gravity, Atterberg limits, and maximum and minimum index densities), compaction characteristics, unsoaked and soaked California Bearing Ratios (CBR), and hydraulic conductivities were obtained for all the blends in order to produce empirical relationships with varying bottom ash content. Results show that the optimum strength can be produced at a blend of 100% bottom ash. However, permeability tests show a considerable decline in hydraulic conductivity with the addition of coal ashes to the typical aggregates. Thus, proper drainage must be carefully applied to these blended embankment materials so as to avoid substantial ingress of water.

Keywords: Fly Ash, Bottom Ash, Road Embankment, CBR, Permeability

INTRODUCTION

Transport infrastructure plays an important role in integrating the island economies of an archipelago such as the Philippines. Mostly comprising the highway embankment materials are the so-called aggregates. Due to the increasing public attention being paid to the environment, the coal combustion by-products (CCPs) are often looked upon as an attractive alternative to these aggregates mainly due to its large production and disposal problems. In fact, the coal-fired power plants which produce considerable amount of CCPs contribute the largest share of 27.06% of the total installed capacity of 15,571 MW last 2009 [1].

The main objective of this paper is to determine the optimum blending proportion of fly ash and bottom ash to the conventional road base materials used as highway embankments. Aside from illustrating the morphological characteristics of the materials in their pure forms, emphasis is given to the determination of their geotechnical properties when blended at different mixture ratios.

METHODOLOGY

Ash Properties

Using ASTM D854, the specific gravity of each soil blend was determined. The specific gravity of the soil mixtures was reduced by the addition of fly ash [2] since the usual of the specific gravity of fly ash is much lower compared with the soil.

The Particle Size Analysis was performed in accordance with ASTM D422 [3]. It determines the quantitative distribution of particle sizes of fly ash, bottom ash, and conventional materials used in the study. Sieve analyses were done for particle sizes larger than 75 μm (or those retained at No. 200 sieve); while hydrometer analyses were conducted for particle sizes smaller than 75 μm (or those passing No. 200 sieve).

Conventional materials, fly ash, and bottom ash samples were individually subjected to microscopic examinations in order to characterize their particle angularity, assemblage, and surface texture. These were performed using Scanning Electron Microscopy (SEM). With the purpose of characterizing the chemicals present on the introduced materials and their corresponding proportions, Energy-Dispersive X-ray Spectroscopy (EDS) was performed to both coal ashes. All three materials were subjected to X-ray Diffraction (XRD) Analysis so to investigate their structures.

To provide initial results, the following Index tests were conducted on all the pure materials conforming to the ASTM procedures.

a. Specific Gravity of Soils (ASTM D854)
b. Atterberg Limits (ASTM D4318 and D427)
c. Maximum and Minimum Index Densities (ASTM D4253 and D4254)

These tests were also performed on the blended materials while keeping its grain size distribution constant. It should be noted, however, that the grain size distribution curve (GSDC) used for all the specimens were arithmetically computed to comply with the requirements stipulated by Department of Public Works and Highways (DPWH) for sub-base and base courses. With this, fly ash was used to substitute the entire fines content constituting 10% of the total mass. On the other hand, the fine aggregates which comprise 32.5% of the total mass were replaced by bottom ash at different mixture ratios of 0%, 20%, 40%, 60%, 80%, and 100%.

Mechanical Properties

Following ASTM D698, Standard Proctor Test determined the OMC at which dry unit weight is greatest and compaction is best. The OMC that were obtained from these tests were used for sample preparation on strength and permeability tests for each blend.

Water was added to the sample to prepare the specimens such that the moisture contents are closed to 100% of OMC obtained in the Standard Proctor Test. After compaction, the compacted specimen in the mould was trimmed level with the top surface and then inverted to have the previously bottom surface tested under the Uniframe. CBR tests (ASTM D1883) were conducted under soaked and unsoaked conditions. The penetration test was performed immediately after the compaction for unsoaked condition.

Falling Head Permeability Tests (ASTM D5084) were conducted so as to illustrate the drainage behavior of all the blends under Relative Compaction, RC=100%. However, since the desired RC=100% is somehow unattainable in the laboratory due to tamping constraints, tests were instead conducted under varying relative compactions (i.e. 80%, 85%, and 90%) to produce a reliable empirical model.

RESULTS AND DISCUSSIONS

Gradation

It can be seen on Figure 1 that 57.5% of the total mass is composed of coarse aggregates, whereas 32.5% are fine aggregates and 10% are fines.

Fly ash is predominantly composed of silt- to clay-sized particles or those finer than 0.075 mm (No. 200 sieve). On the other hand, bottom ash has a better grain size distribution than the former with mostly sand-sized particle composition.

Soil Classification

Shown on Table 1 are the results of soil classification according to Unified Soil Classification System (USCS) [4, 5]. These were then verified using the AASHTO Soil Classification System following the Group Index Method.

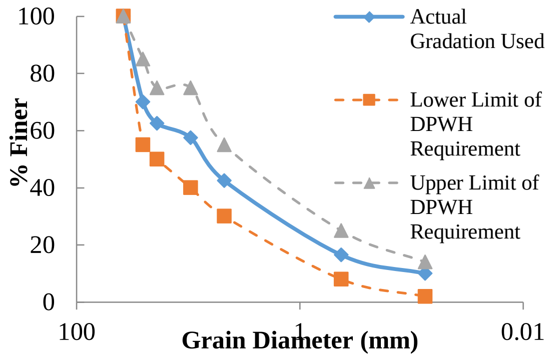

Fig. 1. Actual Grain Size Distribution Curve Used for All Tests

Table 1. USCS and AASHTO Soil Classifications of Pure Materials

Material	USCS (ASTM D2487)	AASHTO (Group Index Method)
Conventional Materials	Well-Graded Gravel with Silt and Sand (GW-GM)	Gravel and Sand
Fly Ash	Silt (ML)	Silty Soils
Bottom Ash	Poorly Graded Sand with Gravel (SP)	Fine Sand

Microscopic Examination

Apparently, its structure is composed of coarse and fine particle sizes with a few silt-sized ones shown on Figure 2. This supports the result of its soil classification which was "well-graded gravel with silt and sand". However, at higher magnification, flakes at random direction were detected to comprise its grains; while few inter-assemblage pore spaces were also noted.

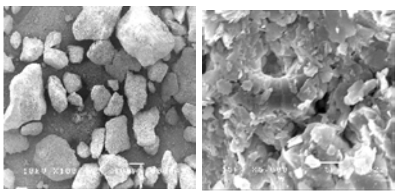

(a) (b)

Fig. 2. SEM Photomicrographs of Conventional Road Base Materials at (a) 100X and (b) 5000X Magnifications

Fly ashes are composed generally of spherical silt-sized particles with smooth surface as shown on Fig. 3. It can be seen that they flocculate with one another thereby producing larger and denser clustered particles. This tends to result in high volume of voids. Hence, at higher magnification, large inter-granular voids can be observed. This validates the high air void content, associated with its compaction behavior.

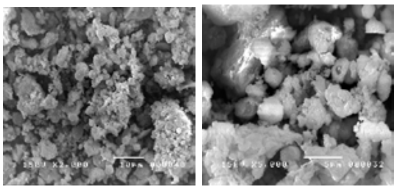

(a) (b)

Fig. 3. SEM Photomicrographs of Fly Ash at (a) 2000X and (b) 5000X Magnifications

As presented in Fig. 4, comparing its shape and surface characteristics, bottom ashes are seen comparable to the conventional materials in terms of particle sizes. However, the large grains can be observed to have clothed contacts since some of the silt-sized particles attach themselves to the much coarser grains. Few inter-assemblage pore spaces can also be observed with the 5000X magnification.

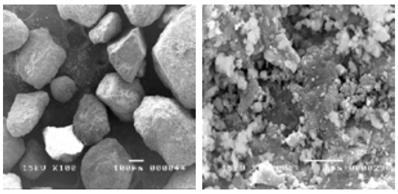

(a) (b)

Fig. 4. SEM Photomicrographs of Bottom Ash at (a) 100X and (b) 5000X Magnifications

Chemical Analysis

The chemical properties of the coal ashes greatly influence the environmental impacts that may arise out of their use/disposal as well as their engineering properties. The adverse impacts include contamination of surface and subsurface water with toxic heavy metals present in the coal ashes, loss of soil fertility around the plant sites, and the like. In practice, EDS is most often used for qualitative elemental analysis, simply to determine which elements are present on the materials and their relative abundance.

The bulk composition of fly ash is similar to many geologic materials. Fly ash is primarily composed of silicon, aluminum, iron, calcium, potassium, and rubidium, associated with oxygen as oxides, silicates, and aluminates. The combined silicon, aluminum, and iron content (reported as oxides) are frequently used to provide an indication of the pozzolanic or cementitious nature of fly ash. A combined value of 70% of these components indicates a pozzolanic fly ash, while a value of between 40% and 70% indicates a cementitious fly ash. Based on the results of EDS, fly ash samples are to be considered cementitious because the total content of oxides is 47.66%.

Table 2. EDS Results of Fly Ash and Bottom Ash

Elements	Fly Ash	Bottom Ash
Al	14.58	0.00
Si	30.37	6.83
K	4.77	0.00
Ca	6.58	16.40
Fe	2.71	2.66
Rb	34.29	7.54
Mo	1.06	0.00
I	1.10	2.28
Ba	1.44	0.88
Np	3.10	0.00
O	0.00	44.04
Mg	0.00	1.49
Sb	0.00	10.37
Er	0.00	7.51

Although similar in size and behavior to natural sand, the chemical composition of bottom ash provides unique pozzolanic properties that, as with cementitious materials, can result in a favorable time-dependent increase in strength. This is mainly due to its high calcium content which tends to react with water from which pozzolanic reaction occurs.

Geotechnical Properties of Pure Materials

Relevant geotechnical tests conforming to ASTM were individually conducted on all three materials in order to come up with the results, as shown on Table 3.

The obtained specific gravity of the aggregate samples is about 2.81, which is within the typical range of 2.40 to 3.60 depending on the nature of the mineral constituents. It can be seen that coal ashes have much lower specific gravities than the conventional aggregate materials. Bottom ashes have higher specific gravity than fly ash owing to the presence of heavier particles. It appears that ashes having high iron oxide content may have high specific gravity [6].

Atterberg Limits Test using the Percussion Cup Method was used to obtain the liquid limit (LL) of 15.60 and plasticity index (PI) of 1.96 for conventional road base materials. Both are within the restrictions of sub-base and base courses as per DPWH requirements.

With the results from the three materials, it is evident that coal ashes are indeed lighter than the conventional materials and is supported by the specific gravities obtained prior. The void ratio of a soil is largely associated with particle size distribution, particle size, shape, and texture. Lower maximum and minimum void ratios were observed for conventional materials; thus, indicating that it has better distribution of particle sizes.

Results demonstrate that fly ash has less variation of dry density compared to that for a well-graded soil. This is why fly ash is allowed to be compacted over a larger range of water content [7]. Furthermore, because of the generally low specific gravities of coal ash compared to soils, ash fills tend to result in lower dry densities. This decrease in the MDD is due to the extensive agglomeration of ash particles that prohibits the specimens to be compacted properly. Soils can be stabilized effectively by cation exchange using fly ash [8]. There are laboratory experiments using local samples [9, 10, 11, 12] of bottom ashes that can be used for validation. A noticeable decrease in CBR strength was manifested when the specimens were tested after soaking it in water for four (4) days [13].

Table 3. Geotechnical Properties of Pure Materials

Property	Conventional Materials	Fly Ash	Bottom Ash
Specific Gravity, G_s	2.813	2.335	2.519
Liquid Limit, LL	15.60	-	-
Plasticity Index, PI	1.96	-	-
Minimum Index Density, γ_{dmin} (kN/m^3)	16.960	5.614	11.785
Maximum Index Density, γ_{dmax} (kN/m^3)	22.289	8.330	16.869
Optimum Moisture Content, OMC (%)	4.938	46.164	14.058
Maximum Dry Density, MDD (kN/m^3)	23.621	10.184	17.298
Unsoaked CBR	43.05%	48.83%	30.27%
Soaked CBR	33.60%	-	-
Hydraulic Conductivity, k (cm/sec) at RC=100%	4.58E-4	4.35E-5	1.04E-5

Falling Head Permeability Tests were conducted at different relative compactions of RC=80%, 85%, and 90% in order to illustrate the effect of varying void ratios. Smaller particles come with smaller voids between them; and hence concluded that the resistance to flow of water increases with decreasing size of particles. As a result, the permeability decreases. Also, particles with a rough surface texture provide more frictional resistance to flow than smooth-textured particles.

Geotechnical Properties of Blended Materials

Specific Gravity of Blended Materials

Since specific gravity (G_s) is one of the most important physical properties required in characterizing the usability of coal ashes for geotechnical and other applications, it was obtained for all the blending proportions as shown on Fig. 5.

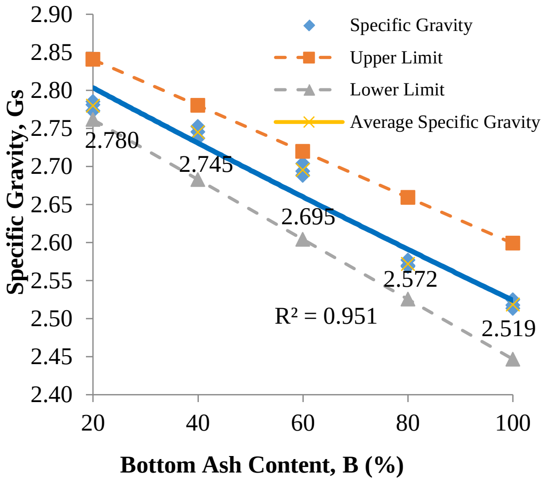

Fig. 5. Specific Gravity vs. Bottom Ash Content

Maximum and Minimum Index Densities of Blended Materials

To see and understand its behavior with varying bottom ash content, Equations 1 and 2 was generated. As observed, there is a significant decrease in both γ_{dmin} and γ_{dmax} when fly ash is present in mixture with aggregates, this is due to the significantly lighter weight of fly ashes which are hollow particles that were used to substitute the fines content of natural soil to complement the study of Kim [13].

Further addition of bottom ash tends to increase the values of both γ_{dmin} and γ_{dmax}. The addition of bottom ash leads to increasingly more well-graded size distributions, which allows the fly and bottom ash particles to pack more closely with the coarse aggregates, resulting in the increase in γ_{dmax}.

$$\gamma_{dmin} = 16.6277exp^{0.0004B} \quad (1)$$
$$\gamma_{dmax} = 20.4409exp^{0.0001B} \quad (2)$$

where: γ_{dmin} = minimum index density;
γ_{dmax} = maximum index density; and
B = bottom ash content (%)

Compaction Behavior of Blended Materials

In summary, Fig. 6 shows the behavior of the OMC with increasing bottom ash content. As observed, it shows a sudden increase in OMC when fly ash was introduced to the mixture to act as its fines content passing No. 200 sieve. This is mainly due to the capability of fly ash to contain large amount of water because of its high air void content nature. Further increase in bottom ash content slightly increases the OMC owing to the same reason. Moreover, an abrupt decrease in MDD was also noted with the use of fly ash because of its much lighter weight and the agglomeration of its particles prohibiting the specimens to be properly compacted.

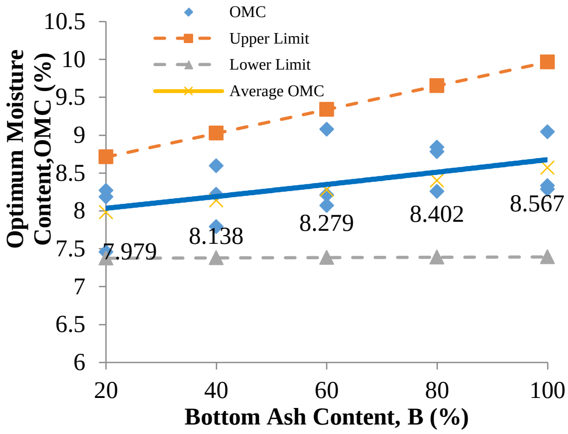

Fig. 6. Optimum Moisture Content (OMC) vs. Bottom Ash Content

The empirical equations correlating OMC and MDD with the bottom ash content are respectively illustrated in Equations 3 and 4.

$$\boldsymbol{OMC} \;\; = \mathbf{7.8816}\boldsymbol{exp}^{\mathbf{0.0010}\boldsymbol{B}} \qquad (3)$$

$$\boldsymbol{MDD} \;\; = \mathbf{22.7896}\boldsymbol{exp}^{-\mathbf{0.0005}\boldsymbol{B}} \qquad (4)$$

where: OMC = optimum moisture content (%);
MDD = maximum dry density (kN/m^3); and
B = bottom ash content (%)

Strength Behavior of Blended Materials

Presented on Figs. 7 and 8 are the corrected CBR values obtained for unsoaked and soaked conditions, respectively. These were plotted to clearly illustrate its behaviors with increasing bottom ash content while fly ash percentage was fixed at 10% of total mass.

It can be observed that there is a significant increase in CBR strength when fly ash was used to substitute the entire fines content constituting 10% of the total mass. The strength of fly ash generally improves with time due to cementitious reactions. Reactive silica and free lime contents are necessary for this reaction to take place. Given all these data, empirical relationships expressed in Equations 5 and 6 were established with which unsoaked and soaked CBR values can be respectively calculated at any given bottom ash content.

As affirmed, a continuous increase in CBR with increasing bottom ash content lead to a conclusion that the blend F10-B32.5-C57.5, in which 100% of fine aggregates are substituted by bottom ash, is the optimum blend which provided the highest CBR values. This blend provided a notable unsoaked CBR of 88.90% and a remarkable soaked CBR of 212.87%, indicating its strength to be more than twice that of crushed rock.

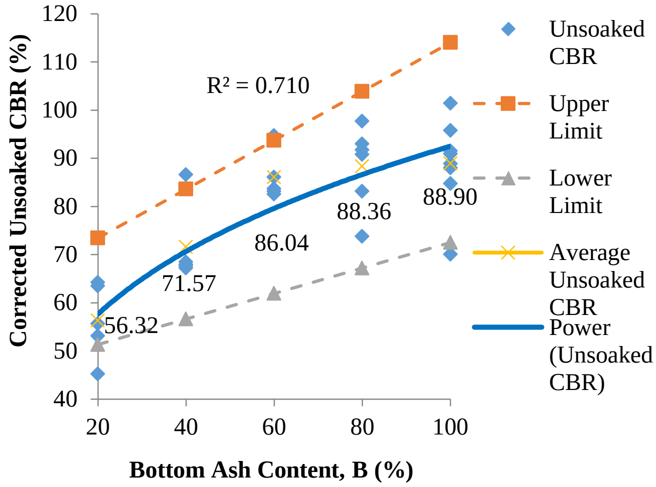

Fig. 7. Unsoaked CBR Values vs. Bottom Ash Content

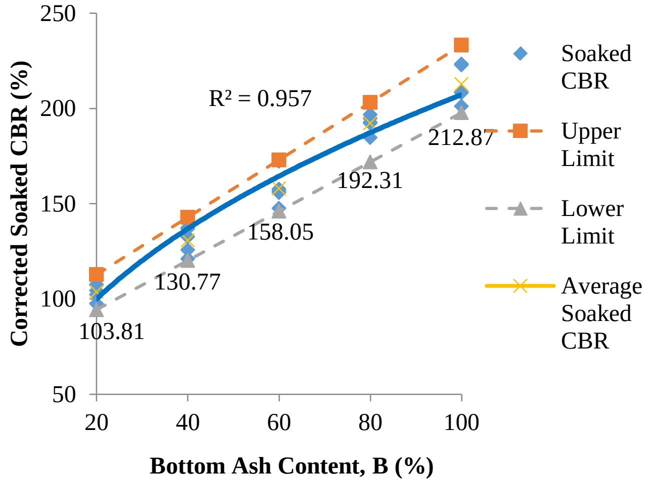

Fig. 8. Soaked CBR Values vs. Bottom Ash Content

$$\boldsymbol{CBR}_{\boldsymbol{unsoaked}} \;\; = \mathbf{23.8905}\boldsymbol{B}^{\mathbf{0.2940}} \qquad (5)$$

$$\boldsymbol{CBR}_{\boldsymbol{soaked}} \;\; = \mathbf{25.7953}\boldsymbol{B}^{\mathbf{0.4525}} \qquad (6)$$

where: $CBR_{unsoaked}$ = unsoaked CBR value (%);
CBR_{soaked} = soaked CBR value (%); and
B = bottom ash content (%)

Permeability Behavior of Blended Materials

Falling Head Permeability Tests in this study were conducted only under varying relative compactions of RC=80%, 85%, and 90% because samples with RC=95% and higher were found to be unattainable since specimens were only to be tamped using hands. Shown on Fig. 9 are the raw data obtained for all the blends.

$$\boldsymbol{k} = (\mathbf{2.99x10^{-7}})\boldsymbol{exp}^{(\mathbf{15.0522}\boldsymbol{e} + \mathbf{0.00796}\boldsymbol{B})} \qquad (7)$$

where: k = hydraulic conductivity (cm/sec);
e = void ratio of the material; and
B = bottom ash content (%)

Due to the large specific surface of fly ash, it causes more resistance to flow of water through the voids. With this, the addition of fly ash in the mixture resulted to a sudden decrease in permeability compared to the controlled mix which has a hydraulic conductivity of $4.58x10^{-4}$ at RC=100%.

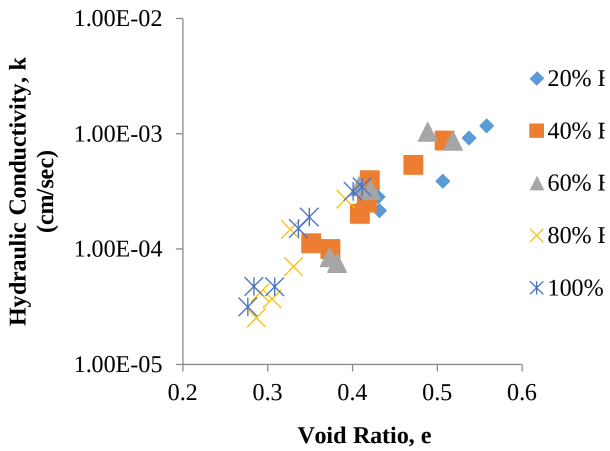

Fig. 9. Hydraulic Conductivity vs. Void Ratio

Subsequently, the results were compared to the drainage characterization as presented by Hazelton and Murphy [15] wherein it was found that all of the blended materials were categorized to have "very slow infiltration" at RC=100%.

CONCLUSIONS AND RECOMMENDATIONS

After performing all the necessary geotechnical tests, it can be concluded that both class C fly ash and bottom ash produced from burning local coals can be safely utilized as road embankment materials together with the natural aggregates typically used. Also, the self-cementing and pozzolanic hardening properties of class C fly ash and bottom ash impart additional strength to the road embankments. Since percolation of water through the soil is highly anticipated especially during rainy season, cementitious reaction can be expected to take place thereby strengthening the blended materials. The addition of bottom ash from 0% to approximately 50% of fine aggregates gave increasing hydraulic conductivity because they act just like the natural sands wherein water can flow freely. Ultimately, the utilization of coal ashes in highway embankment not only diminishes construction cost, but also helps in disposal problem of these previously regarded as waste by-products.

REFERENCES

[1] Department of Energy. (2010). Philippine Energy Plan: 2009 Update. Retrieved February 10, 2012 from http://www.doe.gov.ph/PEP/
[2] Prabakar, J., Dendorkar, N., & Morchhale, R. (2004). Influence of fly ash on strength behavior of typical soils. Construction and Building Materials, 18, 263-267.
[3] American Society for Testing and Materials. (2004). ASTM Standards on Transportation Applications. American Soc. for Testing & Mat.
[4] U.S. Army Military Soils Engineering (1997). Field Manual 5-410. http://www.adtdl.army.mil/cgi-bin/atdl.dll/fm/5-410/toc.htm
[5] U.S. Army Military Soils Engineering (1997). Field Manual 5-410. http://www.itc.nl/~rossiter/Docs/FM5-410/FM5-410_Ch12.pdf
[6] Seals R.K., Moulton L.K., and Ruth, B.E. (1972). Bottom Ash: An Engineering Material. JSMFD, ASCE, 98, 311-325.
[7] Pandian, N.S. (2004). Fly Ash Characterization with Reference to Geotechnical Applications. Indian Institute of Science, 84, 189-216. Retrieved from http://journal.library.iisc.ernet.in/
[8] Bhuvaneshwari, S., Robinson, R., & Gandhi, S. (2010). Stabilization of Expansive Soils Using Fly Ash. Fly Ash Bricks.
[9] Marques, J., Arvesu, M., & Aguila, B. (2003). A Study on Bottom Ash as Substitute for Fine Aggregates in the Production of Reinforced Pipe Culverts. (Undergraduate Thesis) De La Salle University, Manila, Philippines.
[10] Antonio, O. (2006). Lime-Fly Ash Stabilization of Calaca, Batangas Bottom Ash. (Masteral Thesis) University of the Philippines, Quezon City, Philippines.
[11] Asilo, M., Pamintuan, C., & Roque, A. (2004). Bottom Ash By-Product from Coal-Fired Power Plant in Pangasinan Used as a Substitute for Fine Aggregates in Concrete. (Undergraduate Thesis) De La Salle Univ., Manila, Philippines.
[12] Santos, F., Li, L., Li, Y., & Amini, F. (2011). Geotechnical Properties of Fly Ash and Soil Mixtures for Use in Highway Embankments. World of Coal Ash Conference, Denver, USA.
[13] Toth, S.P., Chan, H.T., & Cragg, C.B. (1987). Coal Ash as Structural Fill with Special Reference to Ontario Experience. Can. Geotech J., 25(1), 694-704.
[14] Kim, B., Prezzi, M., & Salgado, R. (2005). Geotechnical Properties of Fly and Bottom Ash Mixtures for Use in Highway Embankments. Journal of Geotechnical and Geoenvironmental Engineering ASCE, 131(7), 914-924. doi: 10.1061/(ASCE)1090-0241(2005)131:7(914)
[15] Hazelton, P., & Murphy, B. (2007). Interpreting Soil Test Results: What Do All the Numbers Mean?. CSIRO, Collingwood VIC.

DISCRETE ELEMENT MODELLING OF GEOCELL-REINFORCED SUB-BALLAST SUBJECTED TO CYCLIC LOADING

Ngoc Trung Ngo[1], Cholachat Rujikiatkamjorn[1] and Buddhima Indraratna[1]
[1]Centre for Geomechanics and Railway Engineering, Faculty of Engineering and Information Sciences, University of Wollongong, Wollongong, NSW 2522, Australia. ARC Centre for Excellence for Geotechnical Science and Engineering, Australia

ABSTRACT

Upon repeated train loading, sub-ballast aggregates, placed underneath a ballast layer in rail track, become degraded and fouled by the progressive accumulation of external fine particles such as mud-pumping of soft subgrade, seriously decreasing the shear strength and drainage capacity of the track. This paper presents a study of the load-deformation response of geocell-reinforced sub-ballast under cyclic loads using laboratory tests and discrete element method (DEM). A series of large-scale cubical triaxial tests with and without geocell inclusions are conducted in the laboratory and simulated in DEM to investigate the beneficial effect of the geocells in decreasing the lateral and vertical deformations of railway subballast. Irregularly-shaped particles of sub-ballast are modelled by connecting and bonding of many circular balls together at appropriate sizes and positions. The geogcell was simulated by bonding many small spheres together to build a desired geometry and structure. The load-deformation behaviour of the geocell-stabilised sub-ballast specimen at varied load cycles predicted from the DEM modelling agrees well with those measured experimentally, showing that the proposed DEM model in this study is able to capture the deformation behaviour of the sub-ballast stabilised by the geocell. Additionally, the DEM modelling also provides insight into the distribution of contact forces, average contact normal and shear forces, which cannot be determined experimentally. These observations clearly prove the reinforcement effect of the geocell in eliminating the deformation of sub-ballast from a micromechanical perspective.

Keywords: Discrete Element Method, Subballast, Geocell,Cyclic Loading

INTRODUCTION

In view of rapid urbanization, the demand for suitable ground improvement solutions is imperative, in order to construct roads and rail infrastructure over soft soils. This results in intensified stress on railway industry to find innovative approaches to maintain track stability and reduce maintenance cost. The use of planar geosynthetics (e.g. geogrids, geotextiles or geocomposites) has proven as a promising technique to strengthen the shear strength of granular media placed over weak and soft deposits [1]-[3]. Loss of track geometry that is often associated with excessive differential settlements due to localized failure of formation (capping and subgrade), often leads to decreased stability and reduced track longevity [4]. In this regard, planar geosynthetics has been effectively utilised to reduce excessive settlements and lateral displacements of ballasted rail tracks [5]. In recent times, three-dimensional cellular reinforcement, also known as geocell mattress, has been used for different applications. The improved performance of geocell-stabilised soil has been attributed to enhanced apparent cohesion between the infilled soil and the geocell [6]. Nevertheless, recent studies have proven that the additional confinement mobilised during cyclic loading, helps to enhance confinement and minimize lateral spreading of the aggregates, hence maintain stability of the infill granular material [7]. In order to determine the effects of geocells, different types of geocells have been widely used. Also, the effects of aperture size and shape and opening area have been investigated by employing large-scale direct shear box and assessing the shear strength of unreinforced and reinforced soil [6], [7].

There has been limited research carried out to study the effect of geocell mattress on railway substructure, where the benefits of geocell under cyclic loading have not been investigated in details either in laboratory or numerical modelling [8]. The development of computational models that have been validated appropriately by either laboratory or field measurements is thereby inevitable to study the enhanced performance of geocell-reinforced sub-ballast and to derive proper design guidelines for ballasted track, considering the confinement effect provided by geocells [9]. An extensive attempt has been made in this study to conduct large-scale cubical triaxial tests of geocell-reinforced sub-ballast and to develop a discrete element model (DEM) simulating the composite system, capturing the additional confinement provided by the geocell to the infilled sub-ballast.

The discrete element method (DEM) introduced by [10] has been widely used to study stress-strain behaviour of granular materials [11]-[15]. It is noted that there have been limited research on the use of DEM to simulate rail sub-ballast under cyclic loads with high numbers of load cycles. Lu and McDowell [16] carried out DEM analysis to model fresh ballast under 100 load cycles and showed that the DEM can capture the stress-strain behaviour of ballast that are comparable with 500,000 cycles in laboratory. Ngo et al. [12] conducted DEM analysis to investigate the performance of geogrid stabilised ballast fouled with coal, and presented that the interlock of the aggregates with geogrid was the main causes for improved performance of the composite assembly. It would also be noted that there has been limited past DEM studies on the behavior of geocell-reinforced ballast under a high numbers of load cycles and varied frequencies. Lobo-Guerrero and Vallejo [17] conducted DEM simulations of model tests for the ballast layer subjected to a total of 425 load cycles. Results indicated that stone-blowing was very effective while the use of geosynthetics was found to be less beneficial. This is because the DEM used circular bonded particles, and the simulations were limited to only a few hundred load cycles.

In this study, experimental tests were carried out and the discrete element method (DEM) was used to model geocell-reinforced sub-ballast subjected to cyclic train loading, capturing the deformation and corresponding micro-mechanical characteristics of this composite assembly. The current DEM analysis was able to include irregular shapes of particles to better represent the role of angularity, whereby up to 10,000 load cycles could be performed with different frequencies, and in this respect the current study is an original attempt to capture the more realistic behaviour of the plastic deformation of geocell-reinforced sub-ballast over a much longer cyclic loading duration.

EXPERIMENTAL STUDY

A large-scale cubical triaxial apparatus (800 mm long, 600 mm wide and 600 mm high) was designed and built at the University of Wollongong (Fig.1), and it was used to investigate the stress-strain behaviour of the unreinforced and geocell-reinforced subballast subjected to cyclic loading [6], [9]. The area of the test specimen in the cubical triaxial chamber was selected based on Australian standard gauge for heavy haul track with an approximate plan area of 800mm × 600mm, and 600 mm height. The sub-ballast material had a total depth of 450 mm, of which the upper 150mm was stabilised by geocell, as shown in Fig. 1. The material for sub-ballast used in this study was a locally available crushed basalt, collected from a quarry near Wollongong (NSW, Australia). The particle size distribution adopted for the sub-ballast was within the Australian rail industry specified range (D_{50} = 3.3 mm, D_{max} = 19

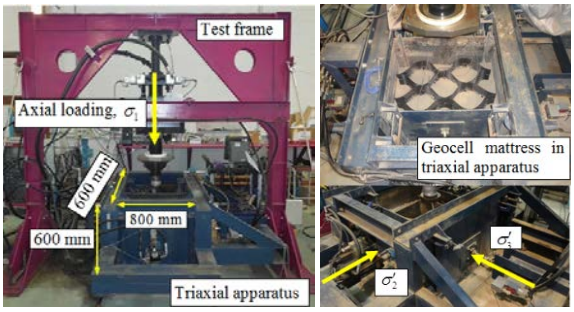

Fig. 1 Cubical triaxial apparatus used in this study.

mm, D_{min} = 0.075 mm, C_u = 16.3, C_c = 1.3, unit weight, γ = 18.5 kN/m^3). A geocell mattress made from polyethylene materials, that was connected at the joints to create a three-dimensional cellular form (i.e. depth = 150 mm, ultimate tensile strength = 9.5 kN/m, thickness = 1.3 mm, density = 950 kg/m3) was used. A predetermined mass of sub-ballast was placed inside the cubical box in several layers and compacted using a vibratory hammer to achieve a relative density (D_R) of about 77%, which is representative of the density of sub-ballast in the field [6]. A geocell mattress was placed onto the surface of the sub-ballast. All specimens were prepared until the layer of sub-ballast reached a final height of 450 mm.

The experiments were conducted under plane strain condition, where any lateral movement in the longitudinal direction (parallel to the track) was restricted (ε_2=0). The walls were allowed to move laterally in the direction parallel to the sleeper (or tie) ($\varepsilon_3 \neq 0$), to simulate a long straight section of track. Laboratory tests were carried out in a stress-controlled manner, where the magnitudes of the cyclic stresses were determined based on 30 tons/axle load. To investigate the influences of confining pressures on the load-deformation of sub-ballast, cyclic tests were conducted at varying confining pressures of, σ_3 = 5, 10, 15, 20, 30 kPa and frequencies of f =10, 20, 30 Hz. Initially, a monotonic strain-controlled load was applied to the specimen at a rate of 1 mm/min until a mean level of cyclic deviator stress was attained. Subsequently, a stress controlled cyclic loading using a positive full-sine waveform was applied to the specimens where a maximum and minimum stress of q_{max} = 166 kPa and q_{min} = 41 kPa was used to simulate subballast under a heavy haul freight network operating in NSW [7],[18], [19].

Laboratory test results showed that the confining pressure (σ_3) and frequency (f) induce a significant impact on the load-deformation behaviour of the sub-ballast under cyclic loading. The experimental data confirmed that under cyclic loading, geocell mattress can offer additional confinement ($\Delta\sigma_3$) to the infill material (i.e. other than the confining pressure available from sleepers and shoulder ballast), and help to decrease the axial and lateral deformations [9]. Also it is noted that due to cyclic loading, the magnitude of would be increase as the number of load cycle increases and when the densely compacted infill material dilates and thereby increases the magnitude of hoop stress. A summary of the key aspects of experimental outcomes can be brieftly summarised as: (i) the mobilised hoop stress of the geocell pockets is generated as a result of the dilation of the infilled soil during shearing; and (ii) the magnitude of hoop stress varies with the geocell modulus [6], [7],],[18].

DISCRETE ELEMENT MODELLING

In DEM, the force-displacement law derives the contact force acting on two particles (e.g *A* and *B*) in contact with the relative displacement between them. The force vector $\vec{F}$ is described into normal ($\vec{F}_N$) and shear component ($\vec{F}_T$) with respect to the contact plane:

$$\vec{F}_N = K_N \cdot U^n \tag{1}$$

$$\delta\vec{F}_T = -K_T \cdot \delta U^s \tag{2}$$

where, K_N and K_T are the normal and shear stiffnesses at the contact; δU^s is the incremental shear displacement, and $\delta\vec{F}_T$ is the incremental shear force.

The normal contact stiffness for the linear contact model used in this study was computed as:

$$K_N = \frac{k_n^{[A]} k_n^{[B]}}{k_n^{[A]} + k_n^{[B]}} \tag{3}$$

and the contact shear stiffness is given by:

$$K_T = \frac{k_s^{[A]} k_s^{[B]}}{k_s^{[A]} + k_s^{[B]}} \tag{4}$$

where, $k_n^{[A]}$, $k_n^{[B]}$, $k_s^{[A]}$, $k_s^{[B]}$ are the normal stiffness and shear stiffness of particle *A* and *B*, respectively.

The new shear contact force is determined by summing the old shear force existing at the start of the time-step with the shear elastic force increment

$$\vec{F}_T \leftarrow \vec{F}_T + \delta\vec{F}_T \le \mu \vec{F}_N \tag{5}$$

where, μ is the coefficient of friction.

DEM Modelling of Cubical Triaxial Test

A two-dimension DEM analysis was conducted to study the interaction between geocell and sub-ballast by simulating the cubical triaxial tests that were carried out in the laboratory, as illustrated in Fig. 2. The angular-shaped grains of sub-ballast were simulated by connecting a number of circular-shaped particles together, mimicking the actual sub-ballast shape and angularity. A total of 26567 particles, with sizes ranging from 0.5 to 19 mm, were generated to simulate actual sub-ballast gradation with a representative field unit weight approximately of 18.5 kN/m^3. Particles were generated in the assembly at random orientations to resemble experimental conditions. Micromechanical parameters to model sub-ballast (e.g. shear and normal contact stiffness, friction coefficient) selected in the current DEM analysis were determined based on the process of calibration of DEM results with the experimental data, as presented in Table 1. The geocell pocket structure was modeled by bonding balls of 20 mm-diameter and 10 mm-diameter to form vertical and horizontal

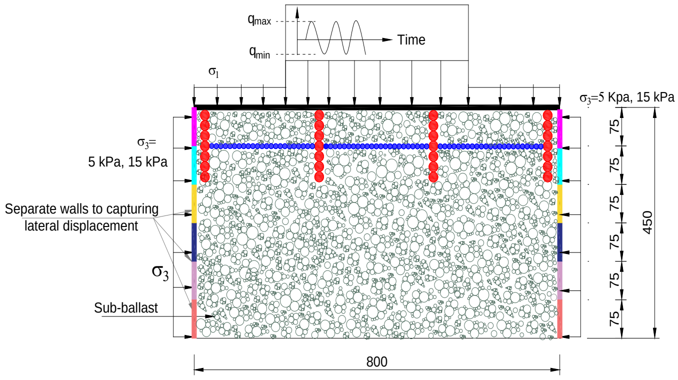

Fig. 2 Schematic DEM model used to calibrate sub-ballast micromechanical parameters (dimensions in mm).

Table 1 Micromechanical parameters used to simulate sub-ballast and geocell in DEM

Items	Sub-ballast	Geocell
Particle density (kN/m^3)	15.5	18.5
Coefficient of friction	0.72	0.45
Contact normal stiffness (N/m)	2.56 E8	6.51 E6
Contact shear stiffness, k_s (N/m)	2.56 E8	6.51 E6
Parameter of contact bond normal strength, ϕ_n(kN)	5.36 E6	43.2
Parameter of contact bond shear strength, ϕ_s (kN)	8.53 E6	43.2
Parallel bond radius multiplier, r_p	0.5	0.5
Parallel bond normal stiffness, k_{np} (kPa/m)	4.86 E7	4.86 ×10^7
Parallel bond shear stiffness, k_{sp} (kPa/m)	4.86 E7	4.86 ×10^7
Parallel bond normal strength, σ_{np} (MPa)	352	352
Parallel bond shear strength, σ_{sp} (MPa)	352	352

panels, respectively. This simplified geocell structure was presumed to be adequate to provide the confinement effect for the sub-ballast packed inside the cellular pockets. Micromechanical parameters (Table 1) to model the geocell were determined based on a series of simulated tensile tests and compared the tensile force-strain response with data measured experimentally.

RESULTS AND DISCUSSION

The DEM model for the plane strain cubical triaxial tests was used to simulate geocell-reinforced sub-ballast subjected to a confining pressure of σ_3=10 kPa and cyclic frequencies of 10, 20, and 30 Hz, similar to the loading conditions conducted in the laboratory. DEM simulations to model the sub-ballast with and without geocell inclusions were simulated up to 10,000 load cycles, where most of the sub-ballast deformation had taken place as observed in the laboratory. During loading, vertical positions and lateral movements of the sub-ballast assemblies were recorded to determine the associated settlements and lateral displacements at corresponding load cycles.

Settlements of Sub-ballast with and without Geocell

The average accumulated settlement at different load cycles obtained from DEM simulations compared to the experimental results are presented in Fig. 3. Results obtained from DEM analysis matched reasonably well with the experimental data at any given frequency and confining pressure. The predicted and measured data indicated that the settlement increased with an increase in frequency. Geocell-reinforced sub-ballast exhibited less settlement than that of the unreinforced assembly. Undoubtedly, this is a result of additional confining pressure provided by the geocell would decrease the deformation of sub-ballast. When the sub-ballast aggregates were compacted over a geocell, they were projected through the geocell pockets and generated a strong mechanical (i.e. acting as a non-displacement boundary) which results in reduced settlement. Additionally, the settlement accelerated significantly during the first few thousand cycles due to initial particle compression and rearrangement, and then the settlement increased at a diminished rate in the subsequent load cycles and approached an approximately constant rate at very high load cycle.

Contact Force Distributions of Geocell-reinforced Sub-ballast

Contact forces in a sub-ballast assembly are transferred through an inter-connected network of force chains via contact points. Fig. 4a presents contact force distributions of an unreinforced sub-

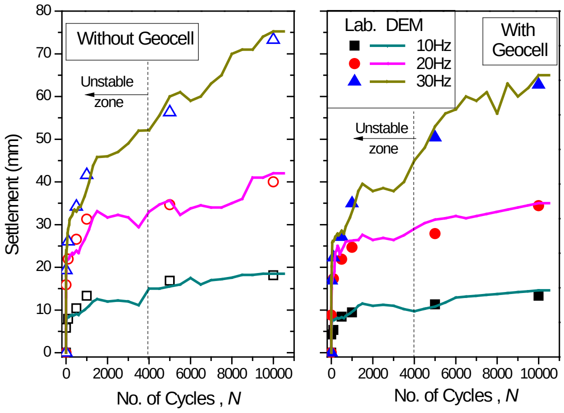

Fig. 3 Settlement versus load cycles measured experimentally and predicted in DEM (modified after Ngo *et al*. 2015).

ballast specimen subjected to the cyclic load at a given frequency of 20 Hz at a settlement (*S*) of 5 mm, while Figs. 4b-d show the contact force distributions of geocell-reinforced sub-ballast at settlements of *S=5* mm, 15 mm, and 20 mm, respectively. It is noted that the contact forces among particles are plotted as lines on the same scale, whose thickness is proportional to its magnitude, and for clarity, only those contacts with a magnitude exceeding the average force of the whole assembly are presented. They clearly show that the total number of contact forces and maximum contact forces increase as settlement increases, and this can be attributed to the assembly was compacted and compressed to sustain the external load. For instance, with reinforced sub-ballast, the number of contacts is 60,252 for the settlement of 5 mm, and it

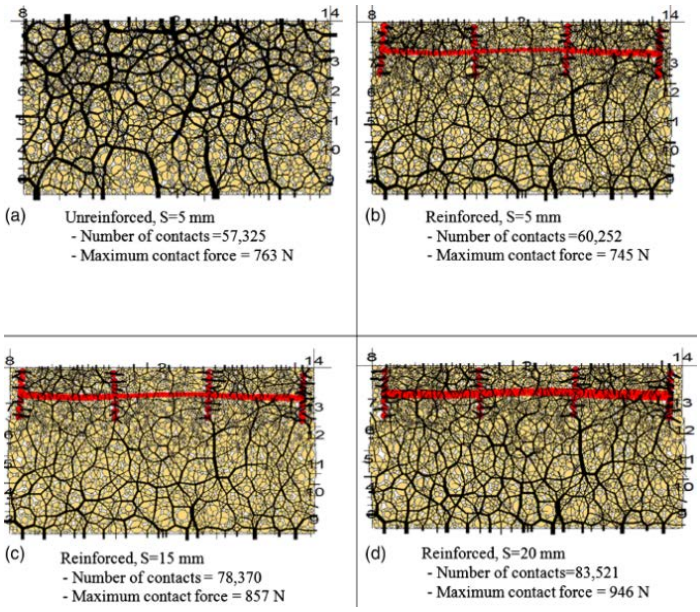

Fig. 4 Distribution of contact forces for unreinforced and reinforced subballast at varied settlements (modified after Ngo *et al*. 2015)

increases to 78,252 and 83,521 contacts for settlements of S=15 and 20 mm, respectively.

Maximum contact forces also increases with an increase of settlements, and these are 745 N, 857 N and 946 N for the settlements of S=5, 15 and 20 mm, respectively. Compared to the unreinforced sub-ballast (Fig. 3a), the reinforced assemblies created more contacts within the geocell regions, and this could be associate d with the confinement the geocell provided to the infilled sub-ballast. It can also be seen that the tensile forces (in red colour) in geocells are mobilised with an increased in settlement.

Variations of Contact Normal and Shear Forces

Fig. 5 presents the variations of contact normal and shear forces with depth for reinforced and unreinforced sub-ballast (at N=10,000 cycles). Compared to the unreinforced cases (Figs. 5c, 5d), geocell-reinforced sub-ballast assemblies exhibit a significant increase in the contact force within the geocell zone, but underneath the geocell the average normal and shear contact forces decrease with depth and approach almost constant values near the bottom of the assembly. Undoubtedly the inclusion of geocell decreases the shear and normal contact force in sub-ballast below the geocell. It is worth mentioning that the micro-mechanics of the geocell-reinforced sub-ballast conducted in this study was limited to the distribution of contact force chains and the average contact normal and shear force distributions. However, the comparison of the experimental observations with the 2D plane strain DEM analysis proves that to the current analysis was able to capture the load-deformation behaviour of geocell-stabilised sub-ballast in spite of these limitations. Generally, the authors have made a few simplifications to keep the micro-mechanical analysis fairly simples, as the requirements of brevity of this paper would not allow the reporting of more detailed DEM analyses that could capture other micro-mechanical aspects such as the evolution of fabric anisotropy and complex detailing of changing angularity with the high number of loading cycles.

CONCLUSION

A series of large-scale cubical triaxial tests were carried out on sub-ballast with and without geocell inclusion, and then the results were used to calibrate and compare with the DEM analysis. Irregular particles of sub-ballast were simulated by clumping several circular balls together to represent appropriate angularity. Geocell was modelled in 2D plane strain DEM model by bonding small balls together to form the cellular pockets with contact and parallel bonds. A set of micromechanical parameters to simulate sub-ballast and geocell were determined by comparing with laboratory test data.

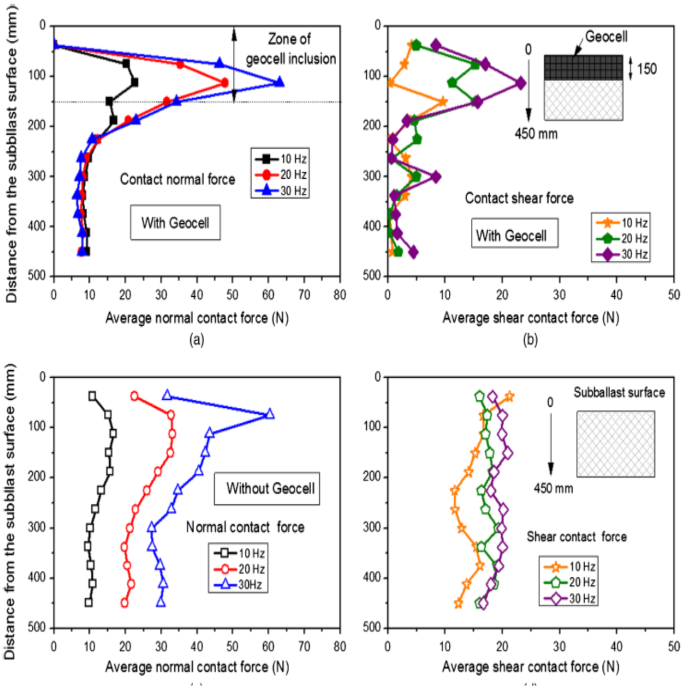

Fig. 5 Distributions of contact normal and shear forces: (a) and (b) - with geocell inclusion; (c) and (d) - without geocell.

Once these parameters were properly validated, they were used to simulate the cubical triaxial tests for testing sub-ballast subjected to cyclic loading at frequencies of 10 Hz, 20 Hz and 30 Hz. Experimental data of settlements and lateral displacements were comparable with those obtained from DEM simulations at a given frequency and confining pressure, indicating that the DEM model proposed in this study could simulate the load-deformation behaviour of a geocell-reinforced sub-ballast assembly. As the frequency increased, the settlement and lateral deformations of sub-ballast increased, but unlike the unreinforced sample, the geocell-reinforced sub-ballast exhibited remarkably less deformation. This was undoubtedly attributed to the confinement provided by geocell that prevented sub-ballast aggregates from free movement that would otherwise occur.

Contact force distributions of geocell-reinforced sub-ballast were presented. DEM results showed that the total number of contact force distributions and the maximum contact force increased with increased deformation. The contact normal and shear forces developed among sub-ballast particles at varied depths were also captured. The magnitudes of these forces within the geocell zone were considerably higher than at other locations. Underneath the geocell, these contact forces continuously decreased with depth and approached almost constant values near the bottom of the granular assembly.

ACKNOWLEDGEMENTS

The Authors would like to thank Australian Research Council (ARC) for providing funding to this study through the ARC Centre of Excellence in Geotechnical Science and Centre for Geomechanics & Railway Engineering (CGRE), University of Wollongong. The Authors thank to Dr Mahdi Biabani and laboratory assistance from technicians, Alan Grant and Ian Bridge during the laboratory tests. The Authors would also appreciate the kind permission from the Journal of Geotechnical and Geoenvironmental Engineering - ASCE for reproducing selected content in this paper.

REFERENCES

[1] Bergado, D. T., Chai, J. C., Abiera, H. O., Alfaro, M. C., and Balasubramaniam, A. S. (1993). "Interaction between cohesive-frictional soil and various grid reinforcements". Geotext Geomembranes. 12(4): 327-349.

[2] Indraratna, B., Ngo, N. T., and Rujikiatkamjorn, C. (2011b). "Behaviour of geogrid-reinforced ballast under various levels of fouling". Geotext and Geomembranes. 29(3): 313-322.

[3] Tutumluer, E., Huang, H. , and Bian, X. (2012). "Geogrid-aggregate interlock mechanism investigated through aggregate imaging-based discrete element modeling approach". Int J Geomech. 12(4): 391-398.

[4] Selig, E. T. , and Waters, J. M. (1994). “Track geotechnology and substructure management”, Thomas Telford, London.

[5] Indraratna, B., Ngo, N. T. , and Rujikiatkamjorn, C. (2013). "Studying the deformation of coal fouled ballast stabilised with geogrid under cyclic load". J. Geotech. Geoenviron. Eng., 139(8): 1275–1289.

[6] Biabani, M. M., Indraratna, B., and Ngo, N. T. (2016). “Modelling of geocell-reinforced subballast subjected to cyclic loading”. Geotext Geomembranes. 44(4), pp: 489-503.

[7] Biabani, M. M., Ngo, N. T., and Indraratna, B. (2016). “Performance evaluation of railway subballast stabilised with geocell based on pull-out testing”. Geotext Geomembranes.44(4): 579–591.

[8] Leshchinsky, B. and Ling, H., 2013a. Effects of geocell confinement on strength and deformation behavior of gravel. J. Geotech. Geoenviron. Eng., 139(2), 340-352.

[9] Ngo, N. T., Indraratna, B., Rujikiatkamjorn, C. , and Biabani, M. (2015). "Experimental and discrete element modeling of geocell-stabilized subballast subjected to cyclic Loading”, J. Geotech. Geoenviron. Eng.,42(4):04015100.

[10] Cundall, P. A. , and Strack, O. D. L. (1979). "A discrete numerical model for granular assemblies". Géotechnique. 29(1): 47-65.

[11] Lim, W. L. , and McDowell, G. R. (2005). "Discrete element modelling of railway ballast". Granular Matter. 7(1): 19-29.

[12] Ngo, N. T., Indraratna, B. , and Rujikiatkamjorn, C. (2014). "DEM simulation of the behaviour of geogrid stabilised ballast fouled with coal". Computers and Geotechnics. 55: 224-231.

[13] Indraratna, B., Ngo, N. T., Rujikiatkamjorn, C. , and Vinod, J. (2014). "Behaviour of fresh and fouled railway ballast subjected to direct shear testing - a discrete element simulation". Int. J. Geomech. , 14(1): 34-44.

[14] Indraratna, B., Ngo, N. T., Rujikiatkamjorn, C. & Sloan, S. W. (2015). Coupled discrete element–finite difference method for analysing the load-deformation behaviour of a single stone column in soft soil. Computers and Geotechnics, 63 267-278.

[15] Ngo, N. T., Indraratna, B. & Rujikiatkamjorn, C. (2015). A study of the behaviour of fresh and coal fouled ballast reinforced by geogrid using the discrete element method. In K. Soga, K. Kumar, G. Biscontin & M. Kuo (Eds.), Geomechanics from Micro to Macro (pp. 559-563). United Kingdom: Taylor & Francis. 2014.

[16] Lu, M. , and McDowell, G. R. (2010). "Discrete element modelling of railway ballast under monotonic and cyclic triaxial loading". Geotechnique. 60(6): 459-467.

[17] Lobo-Guerrero, S. , and Vallejo, L. E. (2010). "Crushing of particles under simulated static and centrifuge forces". GeoFlorida 2010: Advances in Analysis, Modeling & Design (Geotechnical Special Publication, 199), ASCE. 550-559.

[18] Indraratna, B., Biabani, M.M., Nimbalkar, S., 2015. Behaviour of geocell reinforced subballast subjected to cyclic loading in plane strain condition. J. Geotech. Geoenviron. Eng. 141 (1), 04014081-1-16.

[19] Ngo, N. T, and Tung, T. (2016). “Coupled discrete-continuum method for studying load-deformation of a stone column reinforces rail track embankments”. Procedia Engineering, 142 138-144.

ANALYSIS OF DCM WALL SUPPORTED EXCAVATION IN CLAY BY GROUND SPRING MODEL

Siriwan Waichita[1], Pornkasem Jongpradist[2] and Chanchai Submaneewong[3]
[1,2]Faculty of Engineering, King Mongkut's University of Technology Thonburi, Thailand;
[3]Soilcrete Technology Co., Ltd., Thailand

ABSTRACT

Nowadays, an application of Deep Cement Mixing (DCM) as a retaining structure in deep excavation works becomes gradually popular in very dense population areas because the construction process causes less noise and environmental impact than other systems. In addition, this new kind of retaining structure has various forms of utilization that depend on the designer’s experience and considerations. For better understanding of this system, full scaled test, down scaled physical model test, and numerical analysis are required to tackle the interested problem. To effectively discuss the behaviors observed from the full-scale numerical analysis and physical model test, the scaling factor must be seriously considered in the model test. However, it is difficult to scale down the properties of soft clay in the physical model test. Therefore, the soil and its lateral pressure transferred to the wall are modeled as series of springs and lateral forces in the model, respectively. To ensure the effectiveness of this modeling, preliminary evaluation is necessary. In this study, a 2D plane strain Finite Element model of an excavation with the DCM wall as a retaining structure was compared to a 3D Finite Element model with a series of ground springs to take the lateral stiffness of the in-situ soil behind the wall into consideration. The results of this numerical investigation reveal that the ground spring model has sufficient accuracy to represent the lateral soil-structure interaction.

Keywords: Deep Cement Mixing, Retaining Structure, Excavation, Ground-spring

INTRODUCTION

Thick layer of soft soil was found in many well known areas of the world, e.g., Thailand, Japan, and Sweden. Since the demand of land utilization in the city becomes increasing with time, large number of new buildings are commonly constructed with basement levels. During the excavation process, problem relevant to lateral movement is expectedly occurred. To control the excessive displacement that will affect to the adjacent structures, retaining wall is needed. The commonly used walls are either steel sheet pile, diaphragm wall, or contiguous pile wall.

Some of congested urban areas require extra conditions of construction method such as very low noise and vibrating [1]. Deep Cement Mixing wall, as an alternative of retaining structure is introduced to meet the requirements. There were several reports of case history using Deep Cement Mixing wall to support the excavation in various forms of applications, e.g., DCM wall without bracing [1], DCM wall with wall-strut [2], combination of DCM, sheet pile, and tie back supported excavation [3], and DCM cross walls installation with diaphragm wall [4] and shown in Fig. 1. Utilization of DCM in excavation were not only the support system, but also a ground improvement for soft soil in passive zone of an excavation [5]. However, they are still highly empirical in terms of analysis and design with several assumptions due to unclear understandings on DCM wall behavior. To fulfill this lack of knowledge, a series of numerical analysis, physical model test, and full-scale test are important to systematically tackle the problem. Despite that the full-scale test is the most reliable method to study the actual behaviors because the actual condition can be reproduced. The test expense is high and it is difficult to repeat the test with constant condition. While physical model requires the complicated scaling down technique, it can control the circumstances and the interested parameters can be varied. To compensate the limitations of full-scaled test, the study on DCM wall thus focuses on physical model test and numerical analysis.

In order to scale down the problem from the field for setting up the physical model in the laboratory, scaling law is the significant factor in the consideration. Because the test is to conducted under 1g condition, the properties of soft clay surrounding the wall cannot be correctly scaled down to meet the required values during the preparation if large scaling factor is considered. To solve this problem, set of springs is introduced to substitute the soil in the unexcavated side whereas point loads are represented as lateral loads of soil on the excavated side. Consequently, only the small scale DCM wall is to be prepared in the test. However, the continuously distributed pressures (both excavation and un-excavation sides) are discretely represented by numbers of springs and point loads in the physical

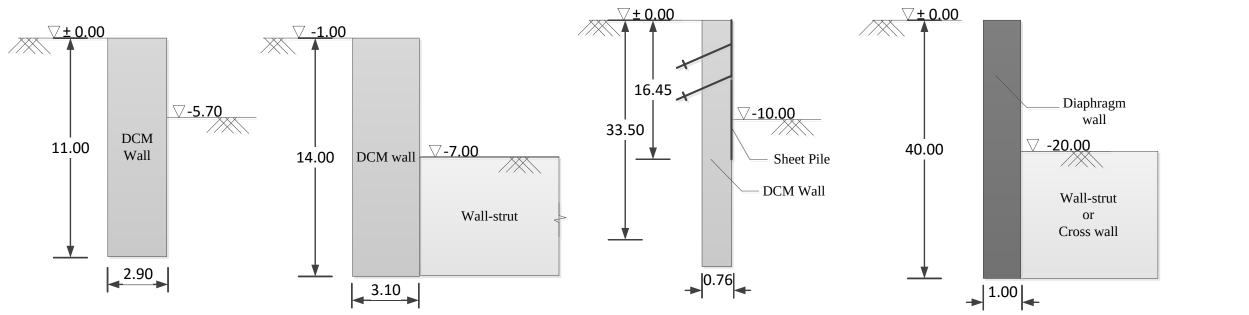

a) DCM wall without bracing [1]   b) DCM wall with wall-strut [2]   c) DCM with tie-back sheet pile wall [3]   d) Diaphragm wall with DCM Cross wall [4]

Fig. 1 Various patterns of DCM wall used in case histories.

model tests. It is thus necessary to evaluate the effect of numbers of springs and point loads on the model accuracy. Moreover, the minimum require numbers of both springs and point loads are preferred to minimize the effort during the preparation and test. To achieve this, preliminary analysis of DCM wall excavation using ground spring model in comparison to conventional continuum mechanics is carried out in this study. In the analyses with ground spring model, numbers of springs and point loads are varied and the results are discussed with those from the finite element analysis on the basis of same excavation problem.

2D NUMERICAL ANALYSIS OF THE REFERENCE CASE STUDY

The excavation with un-braced DCM wall was adopted to validate 2D numerical model used as a reference in this study. This excavation was constructed in Bangkok subsoil as shown in Fig. that the soil stratum consists of 2.5 m thick fill crust overlying 13.5 m thick soft clay. Stiff clay layer started at a level of -16.00 m with the thickness of 5 m. There is 1 m of clayey sand, sandwiched between the stiff clay layer and 12 m thick very stiff clay. The excavation was conducted to the maximum excavation depth and width of 5 m and 27 m, respectively. Three rows of 1 m in diameter deep cement columns were overlapped for the 2.8 m wide DCM block pattern wall with a depth of 15 m. The walls were installed by a jet grouting method with a cement content of 250 kg/m3 of soil to obtain the designed unconfined compressive strength of 1200 kPa at curing time of 28 days. During the construction process, horizontal movements along wall depth were observed by inclinometer for construction control and the validation.

Due to the symmetrical geometry of the excavation, half of the problem was modeled in plane strain condition using PLAXIS 2D software as shown in Fig. 2. The soil parameters were obtained from experimental and empirical data, listed on Table 1. Since the excavation was completed within less than 3 months, undrained analysis was used in the simulation. A retaining wall was classified as a small strain characteristic structure [6]. Numerical simulation of various cases of deep excavation in Bangkok subsoil revealed that the excavation simulation by using the Hardening soil model with small strain (HSS) provided high accurate results [7]. The HSS was thus adopted to represent the soft to stiff clay behaviors, while Mohr Coulomb model (MCM) was selected for fill crust, clayey sand and DCM wall. The excavation was simulated following the actual construction sequence. Figure 3 showed the comparison between analysis result and field observation of wall horizontal displacements

Table 1 Materials Properties

Materials	Model	c'	ϕ	E_u	E_{50}^{ref}	E_{oed}^{ref}	E_{ur}^{ref}	G_{max}	$\gamma_{0.7}$	υ_{ur}
		kPa	deg	MPa	MPa	MPa	MPa	MPa		
DCM	MC	c_u=600	0	300						
Fill Crust	MC	c_u=60	0	42						
Very Soft Clay	HSS	1	21		7.2	7.2	36	72	1×10^{-3}	0.2
Soft Clay	HSS	1	22		12.2	12.2	48	75	8×10^{-4}	0.2
Stiff Clay	HSS	15	26		45	45	150	170	1×10^{-5}	0.2
Clayey Sand	MC	0	36	E'=80						
Very Stiff Clay	HSS	40	26		80	80	300	350	1×10^{-5}	0.2

Remarks: MC was stand for Mohr Coulomb Model, and HSS was Hardening Soil Model with Small Strain. p_{ref} =100 kPa, and m=1for all materials using HSS.

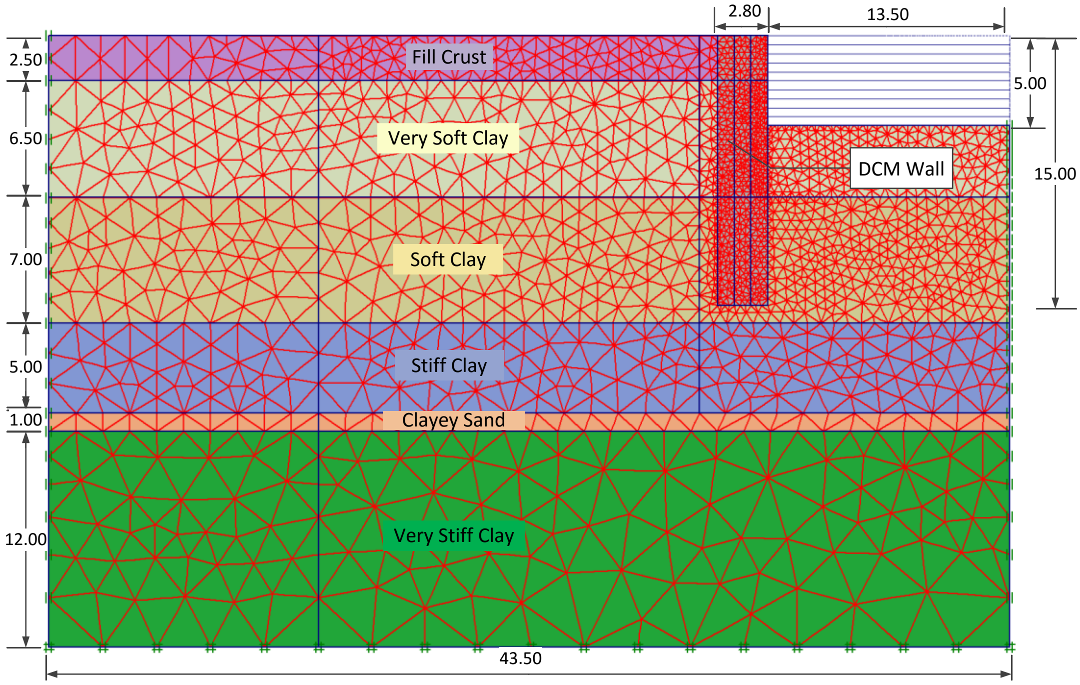

Fig. 2 Geometry and mesh of 2D plane strain model.

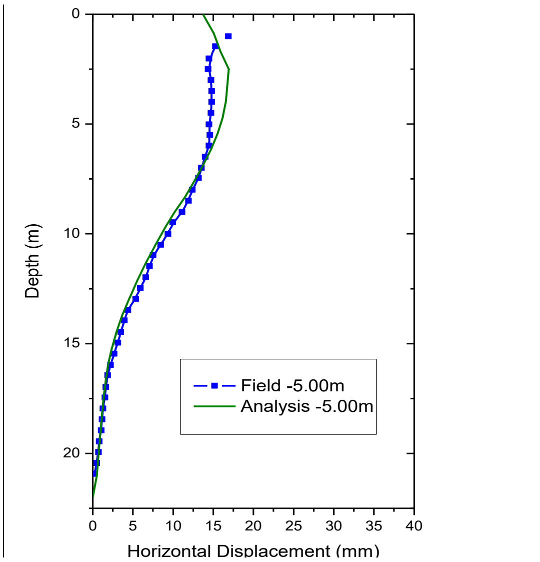

Fig. 3 Comparion of horizontal displacement from field observation and analysis.

occurred at the final level of excavation. It is seen from the figure that good prediction was provided in the validation, the analysis by 2D plane strain model together with the parameters used can reasonably use as a reference model.

3D NUMERICAL ANALYSIS WITH GROUND SPRING MODEL

Although field case study is the most reliable method to study the structural behaviors, it cannot provide the failure state of excavation and vary the influence parameters. Therefore, physical model test is preferable to overcome these limitations. In case that the test will be carried out in the laboratory under 1g condition, the scale down technique must be involved. Modeling of the studied problem is composed of DCM wall, surrounding clay layer, and earth pressure. Due to the fact that the height of wall in physical model is limited by the ceiling of the room and device capacity, the scaling factor must be large enough to scale down the actual 15 m high wall in laboratory test. The difficulties in the preparation of correctly scaled down clay layer thus occur. An idea of using set of springs and point loads instead of clay both sides of the scaled down wall was introduced and it is called as “ground spring model”. The set of springs and point loads are discretely applied on the wall. To do a feasibility study and ensure that this model can represent the excavation work, therefore the preliminary analysis of using the idea of ground spring model in excavation is performed.

The validated 2D model of field case study and input parameters in previous section were used as references in this analysis. ABAQUS program was utilized for a three dimensional analysis of a unit cell excavation. Mohr Coulomb Plasticity was employed for DCM wall properties. To reduce complexities of the problem, the soil layers are simplified as homogeneous layer in both of 2D and 3D models. Set of point loads was calculated from earth pressure of soil, which were varied in each excavation sequence. In the same manner, stiffness of spring in Eq. (1) is depended on horizontal subgrade reaction value and interval length. Vesic’s equation [8] was

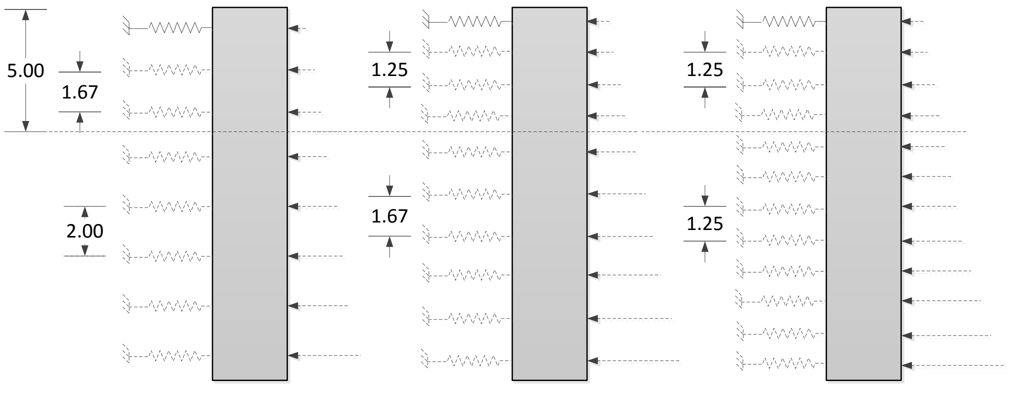

Fig. 4 Comparison of models in parametric study of spring quantities; (a) 8 springs case, (b) 10 springs case, and (c) 12 springs case.

was adopted for horizontal subgrade reaction calculation as shown in Eq. (2). Basis of horizontal subgrade reaction was applied in laterally loaded piles [9] and excavation [10].

$$K_h = k_{sh} \times B \times L \qquad (1)$$

$$k_{sh} = \frac{0.65 E_s}{B(1-\nu^2)} \sqrt[12]{\frac{E_s B^4}{E_w I_w}} \qquad (2)$$

Which K_h : Horizontal stiffness of spring
k_{sh} : Horizontal subgrade reaction
B : Width of wall
L : Interval length of spring
E_s : Soil's elastic modulus
ν : Poisson's ratio of soil
E_w : Wall's elastic modulus
I_w : Wall's moment of inertia

The purposes of this analysis are not only to check the reliability of spring model but also to be a prototype in the down-scaled physical model test. Parametric study of spring quantities was thus conducted. Figure 4 shows a comparison of each case in the parametric study including modeling with 8 springs, 10 springs, and 12 springs. As the wall depth is kept constant, an interval length of springs is varied by number of springs. Three different interval lengths of springs including 1.25 m, 1.67 m, and 2 m, was considered in the models. Rigid plate was used to improve the interaction between springs or loads to DCM wall. Assembled model was shown in Fig. 5, composing of rigid plates tied with springs in the ground (unexcavation) side and rigid plates tied with point loads in the excavation side. Following to the construction sequences, each spring was removed to simulate an excavation of soil layer. The final level of excavation was located at 5 m from wall top.

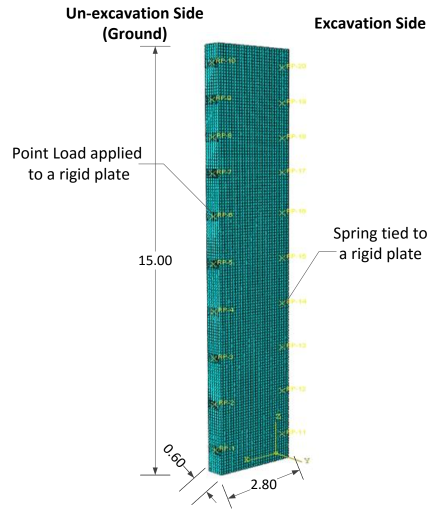

Fig. 5 Assembled model and mesh of 3D with ground spring model.

RESULTS

In this section, the analysis results from ground-spring model with different numbers of springs and point loads are compared together with that of the result from 2D plane strain continuum analysis. The results to be shown and discussed include horizontal displacement, principal and shear stresses. It is noted again that all analyses consider the same problem under homogeneous soil layer.

Horizontal displacement, a common parameter used in excavation monitoring, was shown in Fig. 6. It is seen from the figure that all cases with ground spring model represent a good tendency with the reference 2D continuum analysis. Not only the shape of horizontal displacement profile that are resemble, the predicted values are also in the same order with results from 2D analysis. The maximum horizontal displacement occurred at the top and decreased with depth. The inflection point of the horizontal displacement profile of all cases appear at the depth of about 5 m which is the excavation level. Among three cases of ground-spring analyses, the horizontal displacement decreases with increasing number of springs. However, only drastic increase of horizontal displacement was observed when spring quantity was changed from 8 to 10. In contrast, insignificant change can be seen in the region below the excavation level when the number of springs increased from 10 to 12. This implies that 10 springs are sufficient, for this case study, to simulate the DCM wall excavation.

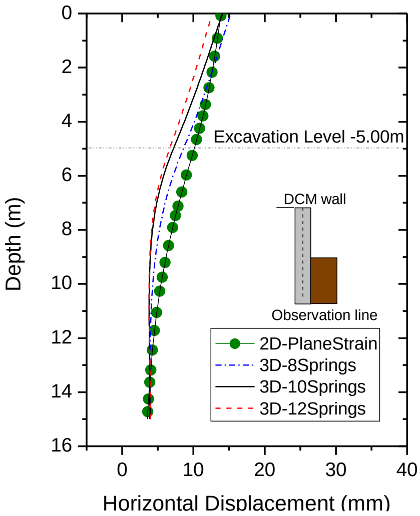

Fig. 6 Horizontal displacement results.

Considering at the center of wall thickness, the predicted major and minor principal stresses from three analysis cases by ground-spring model gave the same tendency with continuum analysis results as shown in Figs. 7-8. All analysis cases yield similar results, particularly for the depth located above the final excavation level. The results between 8 and 10 springs cases for the depth located below the excavation level was slightly different but almost the same value was obtained when increasing the number of spring from 10 to 12. This observation also suggests that the minimum required number of spring is 10. The maximum shear stress distribution along the wall height is shown in Fig. 9. The predicted results from all cases have good agreement to that from continuum analysis except those in the range of 5 m below excavation level. For the depth above excavation level, all cases gave nearly the same value. The results below the excavation level were much different from that of the continuum analysis. The predicted results by soil-spring model between using 10 and 12 springs were very close.

Since the excavation process reduces overburden pressure, vertical displacement results of 2D plane strain analysis (Fig. 10) showed that soil heave occurred at the excavated side of the wall. Note that, the 3D model with soil-spring does not consider this effect. In real practice, some counter measures, such as concrete lean, are utilized to suppress this adverse effect. Reanalysis of 2D continuum model with applying the overburden pressure back to the excavated level was performed and the comparison was shown in Fig. 11. When soil heave was eliminated, the maximum shear stress decreases to the same way of the 3D model results. The investigation prove that, if the effect of soil heave was eliminated or sufficiently minimized, the ground spring model can capture the shear stress distribution in the DCM wall.

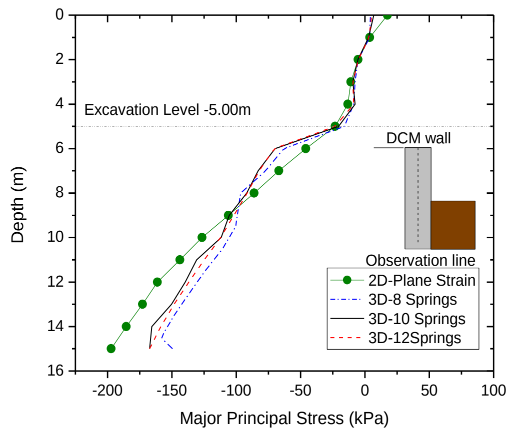

Fig. 7 Major principal stress at center of the wall.

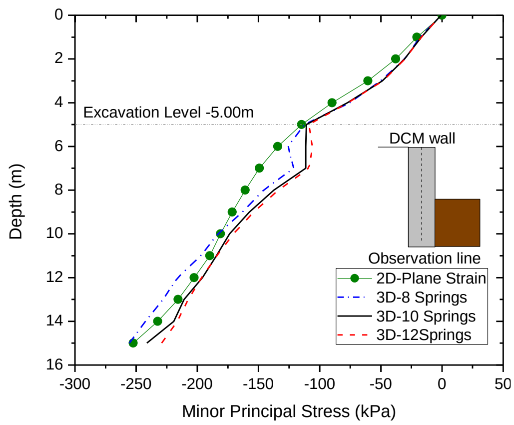

Fig. 8 Minor principal stress at center of the wall.

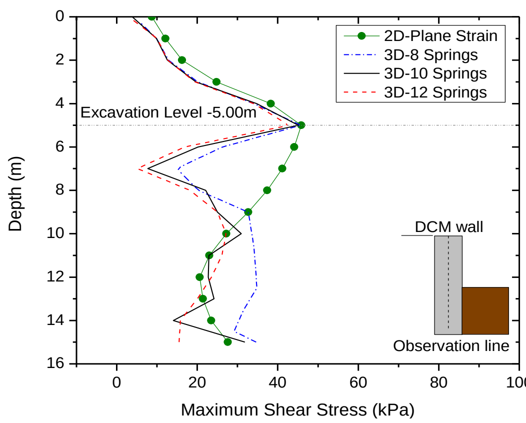

Fig. 9 Maximum shear stress at center of the wall.

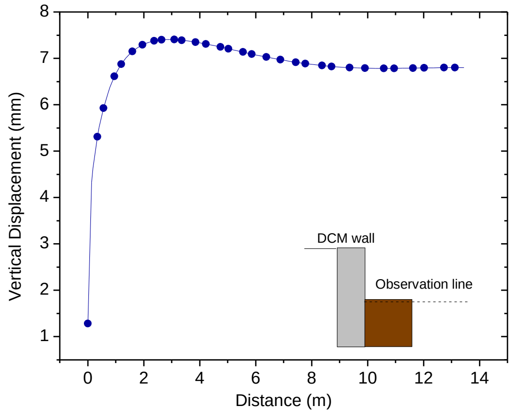

Fig. 10 Vertical displacement along excavation width from 2D continuum analysis.

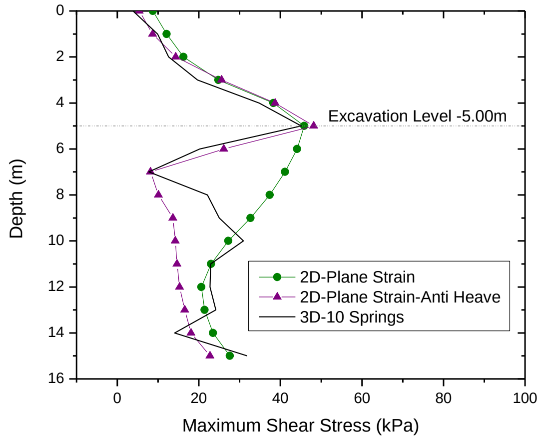

Fig. 11 Maximum shear stress at center of the wall and effect of soil heave.

CONCLUSION

A case study of Deep Cement Mixing wall as a retaining structure in deep excavation work in Bangkok subsoil was numerically simulated under 2D plane strain assumption and 3D approach using ground-spring model. The 2D simulation was validated by field observation using the monitored horizontal displacement of the wall. Then the 2D simulation can be used as a reference case to verify the proposed analysis method using the ground - spring model. The model is composed of a set of springs representing the ground in front of the wall (excavated side) and a series of point loads representing the lateral ground pressure applied to the wall (unexcavated side). Analyses by varying number of springs were carried out and both stress and deformation were observed in the study. According to the investigated results, the ground-spring model can reasonably reproduce the stressed induced in the wall as well as wall deflection behavior. However, the reproduced stresses in the wall can be much altered if the soil heave at the excavation bottom occurred. Under the reference excavation case, the minimum required number of springs is 10.

ACKNOWLEDGEMENTS

The authors gratefully acknowledge support from Research and Researchers for Industries (RRi) and The Thailand Research Fund (TRF) under contract grant PHD57I0076.

REFERENCES

[1] Tanseng P, “Soil-cement column wall without Bracing for Mat Foundation Construction in Bangkok Sub-Soils”, in Proc. 14th Asian Regional Conference on Soil Mechanics and Geotechnical Engineering, 2011.

[2] Tanseng P, “Soil-cement column wall with wall-strut to minimize ground movement for a road tunnel construction in Bangkok subsoil”, in Proc. 38th Int. Conf. At World Tunnel Congress, 2012.

[3] Yang DS, “Soil-Cement Walls for Excavation Support”, in Proc. Int. Conf. On Earth Retention Systems, 2003.

[4] Ou CY, Hsieh PG, and Lin YL, “A Parametric Study of Wall deflections in Deep Excavations with the installation of cross walls”, Computers and Geotechnics, Vol.50, pp. 55-65.

[5] Pavan A, and Tamilmani T, “Numerical Analysis on the Effect of Jet Grout Piles on an Excavation Located in an Urban Area”, Int. J. of GEOMATE, Vol.8, No.1, March 2015, pp. 1167-1171.

[6] Atkinson JH, and Sallfors G, “Experimental determination of stress – strain – time characteristics in laboratory and in situ tests”, in Proc. 10th European Conf. On Soil Mechanics and Foundation Engineering, 1991, pp. 915-956.

[7] Rukdeechuai T, et al., “Influence of Soil Models on Numerical Simulation of Geotechnical works in Bangkok Subsoil”, Journal of Research in Engineering and Technology, Vol.3, 2009.

[8] Vesic AS, “Beam on elastic subgrade and the winkler hypothesis”, in Proc. 5th Int. Conf. Soil Mechanics and Foundation Engineering, 1961.

[9] Bahrami A, and Nikraz H, “ Initial Soil Spring Stiffness for Laterally Loaded Piles” in Proc. 11th Australia New Zealand Conference on Geomechanics, 2012.

[10] Ou CY, Deep Excavation Theory and Practice. London: Taylor & Francis Group, 2006, ch. 7.

Sixth International Conference on Geotechnique, Construction Materials and Environment, Bangkok, Thailand, Nov. 14-16, 2016, ISBN: 978-4-9905958-6-9 C3051

PROBABILISTIC SAFETY ASSESSMENT OF ANCHORED SLOPE

Takashi Hara[1], Akira Tomioka[2], Nobuyuki Soga[3] and Atsushi Yashima[4]
[1]Department of Civil Engineering, Gifu University, Japan; [2-4] Gifu University, Japan

ABSTRACT

The maintenance of existing ground-anchored slopes has been traditionally carried out by experts' empirical judgment based on tensile force measurements of partial anchors composing the target-anchored slope. The experts' judgment is, however, more or less qualitative, so it is difficult to apply former maintenance experiences to other slope maintenance practices. Moreover, because the judgment is made through a technical committee, the present maintenance scheme takes long time and maintenance engineers cannot maintain the slope themselves rapidly. If the former maintenance experiences based on the judgments are organized quantitatively, rapid and reasonable maintenance of the slopes by maintenance engineers will be able to be achieved.

Therefore, the authors have conducted a study on development of a probabilistic safety assessment approach for existing ground-anchored slopes, which can reproduce the experts' judgments applied to former maintenances quantitatively. As the result, practicability of the proposed probabilistic safety assessment approach on the present stage of this study could be confirmed. This paper describes the practicability of the proposed approach from comparisons between the safety evaluation obtained from the proposed approach and made from experts' judgments with respect to actual existing anchored slopes as well as the detail of the proposed probabilistic safety assessment approach.

Keywords: Ground-Anchor, Existing Slope, Maintenance, Probabilistic Safety Assessment (PSA)

INTRODUCTION

Tensile forces acting in existing ground-anchors maintaining slope stability vary depending on the passage of time after the installation. The variation degree of the tensile forces with respect to design one differs due to several phenomena occurred in each site of existing slopes, such as creep of PC strand and/or slope ground, partial deformation of the slope, and so on. Furthermore, the existing excessive tensioned anchors let us know dangerous situation of the anchored slope. The danger level is different depending on the tension intensity, the distribution of the anchors with high tensile force and so on. Therefore, the safety judgment of existing ground-anchored slopes is difficult. Hence, the present maintenance has been traditionally carried out with experts' empirical safety judgment based on tensile force measurements of partial anchors composing of an entire existing anchored slope in a technical committee. The experts' empirical judgment is, however, qualitative, thus the application of accumulated former maintenance experiences to other slope maintenances is difficult. Moreover, because the judgment is made through a technical committee, the present maintenance takes long time and maintenance engineers cannot maintain the slopes themselves rapidly. If former maintenance experiences based on the judgments are accumulated quantitatively, rapid and reasonable maintenance of the slopes by maintenance engineers will be able to be achieved.

Therefore, the authors have conducted a study on development of a probabilistic safety assessment approach for existing ground-anchored slopes, which can reproduce the former maintenance experiences based on experts' empirical safety judgment quantitatively. This paper describes a proposed probabilistic safety assessment model for an anchored slope and its reproducibility of the present maintenance from several examples.

AIM OF THIS STUDY

Fig. 1 shows the present maintenance procedure of an existing ground-anchored slope in Japan.

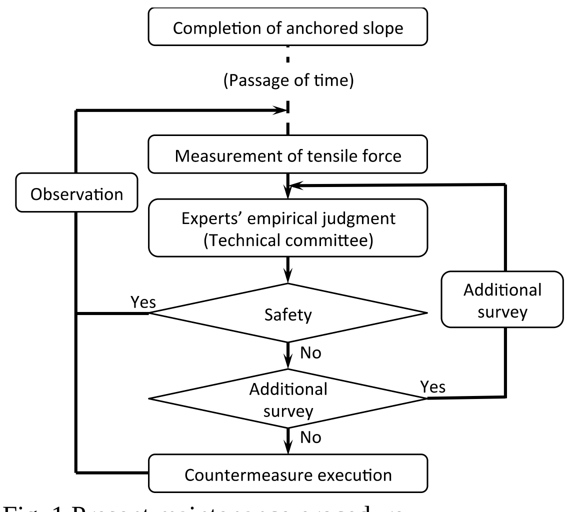

Fig. 1 Present maintenance procedure.

In the present procedure, the tensile force acting in partial ground-anchors, 5 - 10% of the entire target slope's ones, passed 10 - 20 years from the installation are measured and the safety level of the anchored slope is judged by experts in a technical committee qualitatively. In the safety judgment, the treatment is chosen from following ones; (1) observation, (2) additional survey, and (3) countermeasure execution. In additional survey, the target surveys are selected from following ones; (1) additional boring, (2) additional measurement of tensile forces acting anchors, (3) measurement of slope movement and etc., as well as their execution points and volumes are planned. Then the safety of the target slope is reevaluated based on the results of the additional surveys.

On the other hand, the present maintenance has several problems. The application of the accumulated former maintenance experiences to other existing slope maintenances is difficult because the experts' empirical judgment is more or less qualitative. The technical committee meetings for making the experts' empirical judgment are held three or four times a year, so the present maintenance takes long time and maintenance engineers cannot maintain the target slope themselves rapidly.

The authors, in order to solve these problems, have conducted a study on development of a probabilistic safety assessment approach for existing ground-anchored slopes, which can reproduce the former maintenance experiences of existing slopes quantitatively. Namely, the target of this study is to propose a future quantitative maintenance procedure, as shown in Fig. 2, with using the proposed approach.

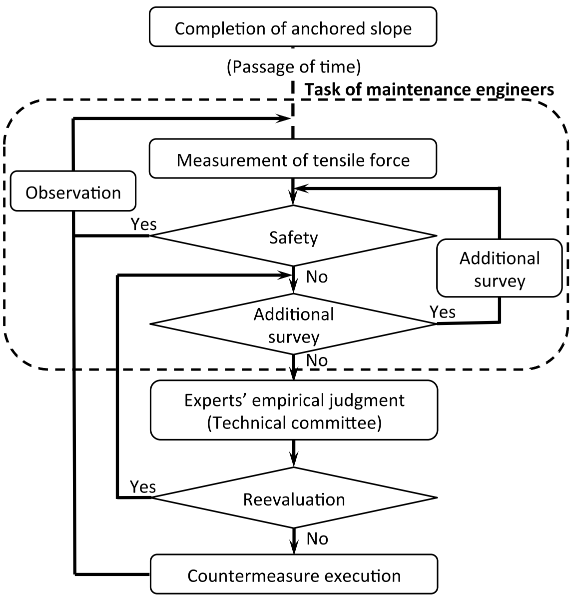

Fig.2 Future maintenance procedure.

In this procedure, maintenance engineers evaluate safety level of the target slope by using the proposed safety assessment approach, and if it is considered that additional surveys are necessary to reevaluate the safety level of the slope, it will be planned and carried out by maintenance engineers themselves before consulting to the technical committee. Consequently, it can be expected that the procedure achieve more rapid and reasonable maintenance of existing ground-anchored slopes.

The probabilistic safety assessment approach consists of a probabilistic model to estimate failure probability of the slope, and its threshold to evaluate the safety and decide the treatment of the target slope, which can reproduce the former maintenance experience based on experts' empirical judgments quantitatively. Fig. 3 shows the image of the model. In this figure, each plotted point is the combination of the failure probability of the slope, which is estimated by the proposed probabilistic model, and excessive tension rate, the ratio between mean tensile forces of an excessive tensioned anchor group and one before rising. If the thresholds drawn in the figure can reproduce the former maintenance experiences based on experts' empirical judgments, maintenance engineers will be able to evaluate the safety level of the target slope and plan the additional surveys from its failure probability estimated by the proposed probabilistic model.

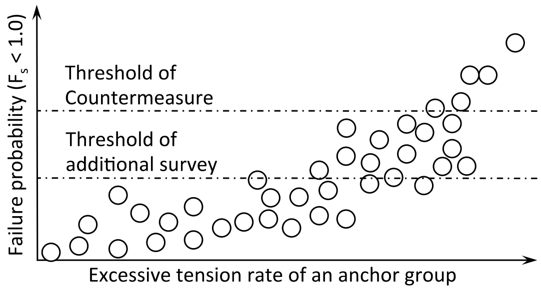

Fig. 3 Image of proposal model.

PROBABILISTIC SAFETY APPROACH OF ANCHORED SLOPE

Slope stability remains safe by ground-anchors functioning against the slope movement. This behavior indicates that tensile forces acting in the anchors of a stable slope continue to decrease from a design one due to the creep of PC strand and/or slope ground. On the other hand, the slope stability with excessive tensioned anchors remains safe by excessive tensile forces acting in anchors. Namely, the slope is in the sate in equilibrium of the moving force and the resistance, the apparent safety factor should be 1.0. Based on this consideration, safety evaluations of the slope with excessive tensioned anchors and one with decreased tension anchors are assumed as follows;

Slope with excessive tensioned anchors

Let us consider the case of the slope with two anchor groups, one consists of the anchors with near design level tensile forces and another one consists of the anchors with excessive tensile forces, as shown in Fig.4. This slope remains safe by the increase of tensile force, namely, the slope is in the state in which apparent safety factor is 1.0. Therefore, the safety level can be evaluated from following steps.

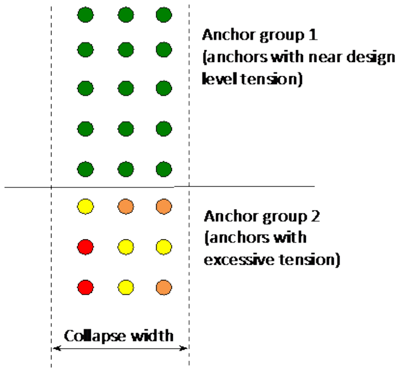

Fig.4 A slope consisting of two groups of anchors.

Step-1; estimating soil strength parameters, c and ϕ, from landslide analysis with using mean tension values of each anchor group, as reproducing the safety factor of 1.0.

Step-2; estimating failure probability, P_f, and actual safety factor of the slope by Eq. (1) with considering variations of tensile forces of each anchor group. Eq. (1) is a performance function, which means that the summation of the safety factors of one without considering the anchors' effect and the safety factor gain caused by setting ground-anchor is larger than 1.0. Furthermore, it was also defined that the tensile force acting in the anchors with considering the variation, $T_m * \delta_T$, does not exceed yield of PC strand, $T_L * \delta_{TL}$, and the ultimate capacity against pulling out the anchor body, $T_F * \delta_{FL}$. Here, although the apparent safety factor of the slope is 1.0 (Pf = 50%) from the viewpoint of equilibrium, because the probabilities of pulled out anchor body and broken PC strand exist, larger P_f than 50% and actual safety factor, which is smaller than 1.0, are obtained. Fig. 6 shows the concept of the safety evaluation.

$$F_s = F_{s0} \cdot \delta_{FS} + \left[\frac{\sum T_{m1} \cdot \delta_{T1} \cdot \left(\cos(\alpha+\theta) + \sin(\alpha+\theta) \cdot \tan\phi\right)}{\sum W_1 \cdot \sin\alpha} + \frac{\sum T_{m2} \cdot \delta_{T2} \cdot \left(\cos(\alpha+\theta) + \sin(\alpha+\theta) \cdot \tan\phi\right)}{\sum W_2 \cdot \sin\alpha} \right] \cdot \delta_{FS} \geq 1.0 \quad (1)$$

$$\left(\textit{subject to } \left[T_{m1} \cdot \delta_{T1}, T_{m2} \cdot \delta_{T2}\right] \leq T_L \cdot \delta_{TL} \textit{ and } \leq T_F \cdot \delta_{FL}\right)$$

where, F_s is the summation safety factor, F_{s0} is the safety factor without considering the effect of ground-anchors, δ_{FS} is the uncertainty of landslide analysis reproducibility with respect to actual land slide, a uniform distribution that lies between 0.9 and 1.1 [1], T_{m1} and δ_{T1}, T_{m2} and δ_{T2} are mean values and variations of tensile forces acting in each anchor group, α and θ are the angles between a tangential line of each land slide block surface and horizontal surface, and between anchor installation angle and horizontal surface (deg), as shown in Fig. 5, respectively, ϕ is the shear resistance angle (deg), W is each soil block weight of circular sliding (kN), T_L and δ_{TL} are nominal yield tensile force and its uncertainty of PC strand of the target anchor defined in quality control document, for instance [2], T_F is the ultimate capacity against pulling out anchor body, which is estimated by $T_F = U * \tau_f * L$ (kN), U is the circumference of anchor body (m), τ_f is the shaft resistance (kPa), L is the length of anchor body (m), δ_{FL} is the uncertainty of estimation method reproducibility of T_F, m = 1.07, COV = 0.49, lognormal distribution [3].

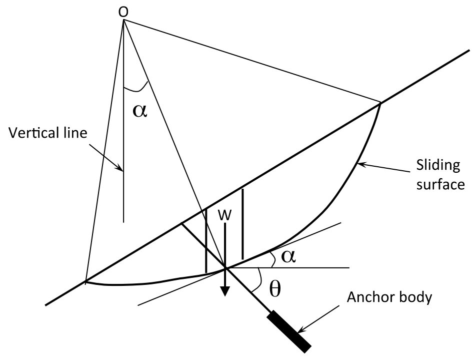

Fig. 5 α and θ.

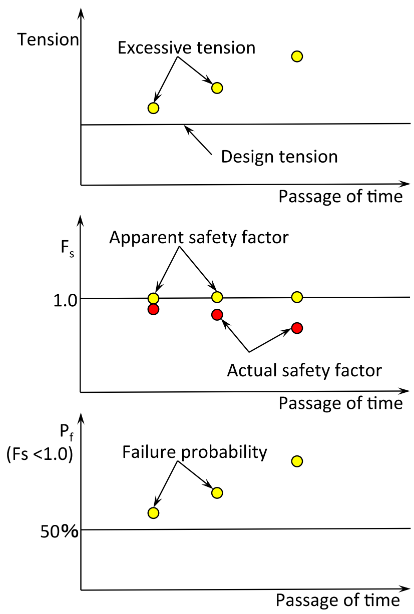

Fig. 6 Concept of the safety evaluation.

Slope with decreased tension anchors

As mentioned previously, if the slope was in stable state, tensile forces acting in anchors would tend to decrease due to the creep of PC strand and/or slope ground. Hence the slope with decreased tension anchors is not in dangerous state. On the other hand, if the decreased tensile forces acting in anchors reascended as shown in Fig. 7, the anchors would start to function for keeping stability of the slope, namely, the slope is in the state of equilibrium, the apparent safety factor is 1.0. In this situation, the safety of the slope has to be evaluated with using the same way of the slope with excessive tensioned anchors, in which the tensile forces before reascending is assumed to be the design one. The growth of P_f, however, is not so large, because the tensile forces acting in anchors is not so high.

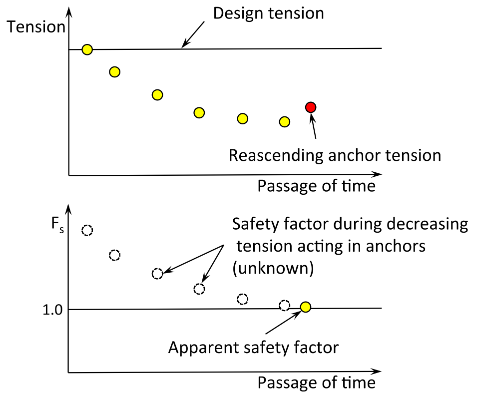

Fig. 7 Reascending anchor tension.

VALIDITY OF PROPOSED APPROACH

The validity of the proposed approach is confirmed from the application to actual anchored slopes.

Slope with excessive tensioned anchors

Target slope

The picture of the target slope for confirming the validity of the proposed approach is shown in Fig. 8. In this slope, tensile forces acting in partial anchors are measured. The measurement of tensile forces is carried out to 79 anchors (18.7% of 423 entire anchor numbers). The results and the safety evaluation area in this confirmation are shown in Fig. 9. The meaning of color in Fig. 9 is summarized in Tables 1 and 2. The numbers and the rate of each rank of measured 79 anchors are presented in Table. 3. The design tensile force of the slope's anchors is 350 kN.

This slope was judged as a dangerous one and the installing of additional anchors was proposed as a countermeasure in a technical committee.

Fig. 8 Picture of the target slope.

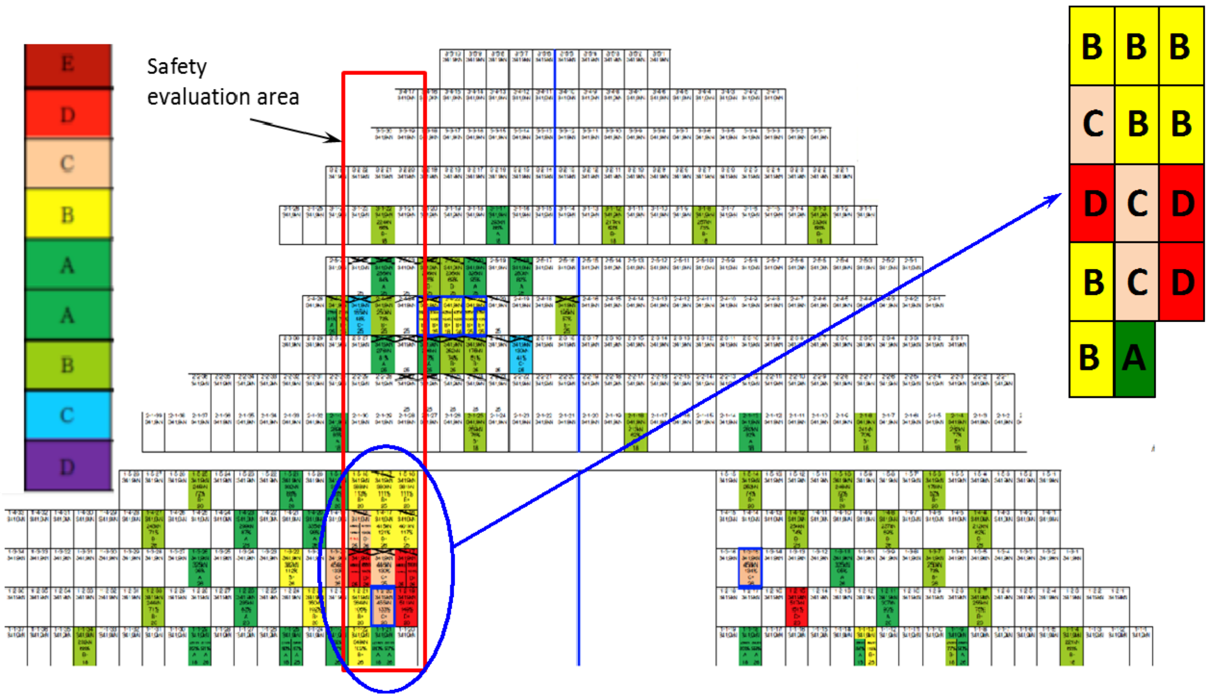

Fig. 9 Measurement results of tensile forces.

Table 1 High tensile force ranking

Rank	Color	Tensile force of anchor
A	Green	Setting force – Design one
B	Yellow	– 1.2 times of design force
C	Flesh	– 1.33 times of design force
D	Red	– 0.9 times of nominal yield
E	Brown	More than nominal yield force

Table 2 Low tensile force ranking

Rank	Color	Tensile force of anchor
A	Green	0.8 – 1.0 times of Setting force
B	Y-green	– 0.5 times of Setting force
C	Blue	– 0.1 times of Setting force
D	Purple	Less than C rank

Table 3 Measured tensile force ranks

		A	B	C	D	E
High tensile force	n	11	13	4	4	-
	%	14	16	5	5	-
Low tensile force	n	11	33	3	-	X
	%	14	41	4	-	X

Safety evaluation

The mean tensile force of upper 9 anchor lines in the safety evaluation area shown in Fig. 9 is 243 kN and one of excessive 5 anchor is 424 kN. The soil strength parameters estimated by landslide analysis as reproducing safety factor of 1.0 at step-1 are c = 5 kPa and ϕ = 31 degrees. Then actual safety factor and failure probability are estimated, as shown in Table 4 and Fig.10, by Eq. (1) with considering tensile forces variation of each anchor group shown in Table 5, which are estimated by Monte Carlo Simulation, MCS, with one million times. Fig. 11 shows the MCS plots to estimate probabilities of pulled-out anchor body and broken PC strand. From the results, although the slope remains safe due to the equilibrium of moving force and excessive tensile forces, the slope has dangerous of landslide potentially because of existing probabilities of pulled out anchor body and broken PC strand.

According to the result, it was considered that the proposed approach could reproduce the judgment made in a technical committee, in which the slope was judged as dangerous one.

Table 4 Apparent and actual F_s and P_f.

Apparent		Actual	
F_s	P_f (%)	F_s	P_f (%)
1.0	50	0.97	66

Table 5 Tension variations of anchors in each group

Group	Mean	Standard deviation
Upper 9 lines	0.69	0.135
Excessive 5 lines	1.22	0.187

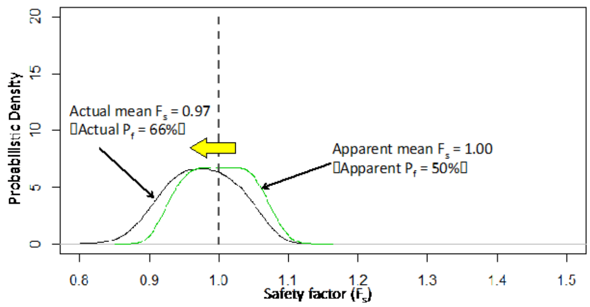

Fig. 10 Difference between apparent and actual ones.

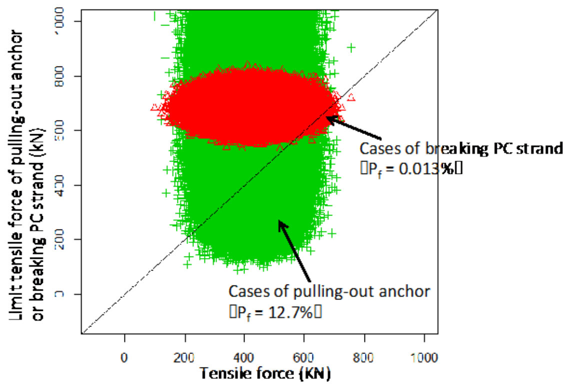

Fig. 11 MCS plots of pulled-out and broken anchor.

Slope with decreased tension anchors

Target slope

Figs. 12 shows the picture of the target slope for confirming the validity of the proposed approach with respect to the slope with decreased tension anchors. Fig.13 shows the tensile force measurement of the anchors composing of the anchored slope and the safety evaluation area. The tensile force measurement carried out to 15 anchors (30.6% of 49 entire anchors). The meaning of color in Fig. 13 is the same as presented in Tables 1 and 2. The design tensile force of the anchors is 750 kN.

Because the tensile forces of almost anchors are decreased, C of low tensile force ranking presented on Table 2, the slope is judged as safe one in a technical committee and follow-up observation of the tensile forces acting in anchors has been only continued.

Fig. 12 Picture of the target slope.

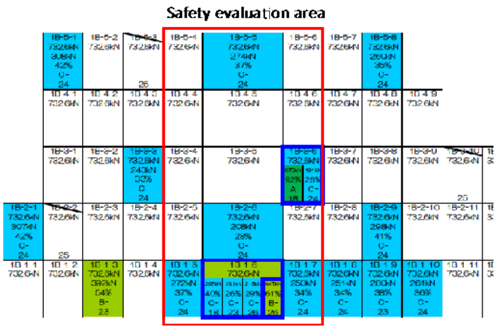

Fig. 13 Tensile force measurement results.

Safety evaluation

In order to confirm the proposed approach to this slope, the occurrence of reascenting tensile force is assumed. Namely, the apparent safety factor of the slope with the tensile forces acting in the anchors shown in Fig. 13 is assumed as 1.0.

The mean tensile force of the anchors in the safety evaluation area shown in Fig. 13 is 274 kN. The soil strength parameters estimated by landslide analysis as reproducing safety factor of 1.0 at step-1 are c = 13 kPa and ϕ = 35.5 degrees. Then actual safety factor and failure probability are estimated, as shown in Table 6 and Fig.14, by Eq. (1) with considering variation of tensile forces acting in anchors, the mean is 0.37 and standard deviation is 0.12, which are estimated by Monte Carlo Simulation, MCS, with one million times.

Table 6 Apparent and actual F_s and P_f.

Apparent		Actual	
F_s	P_f (%)	F_s	P_f (%)
1.0	50	0.999	51

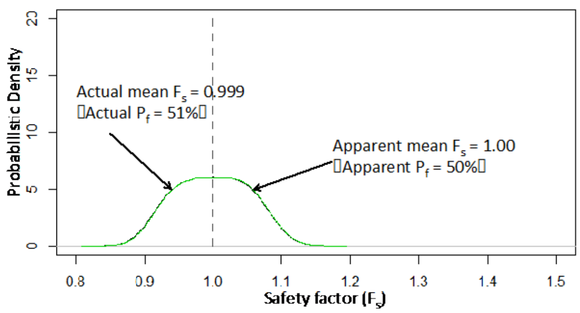

Fig. 14 Difference between apparent and actual ones.

According to the results, the actual safety is almost same as the apparent one in the case of the slope with decreased tension anchors. This reason is that the variation of the tensile forces acting in the anchors does not affect the probabilities of pulled-out anchor body and broken PC strand, as shown in Fig. 15 of MCS plots. This result reproduces the present judgment made in a technical committee, in which this slope is in the state of safety.

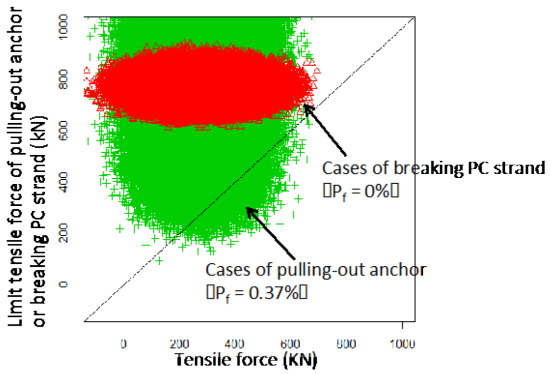

F.15 MCS plots of pulled-out and broken anchor.

CONCLUSIONS

A probabilistic safety assessment approach for ground-anchored slope has been studied in order to propose a future quantitative maintenance procedure of existing anchored slopes. The proposed probabilistic approach on the present stage of the study and the practicability confirmed from the application examples to the slope with excessive tensioned anchors and one with decreased tension anchors were introduced. As the result, it was considered that the proposed approach could reproduce the qualitative empirical judgments by experts. The authors are willing to propose the quantitative maintenance procedure from the application of the proposed approach to many existing anchored slopes and establishment of the threshold, as shown in Fig. 3, in the near future.

REFERENCES

[1] Matsuo, M. and Asaoka, A., “A statistical study on conventional safety factor method”, Soils and Foundation, Vol. 16, No.1, pp.75-90, 1976.

[2] VSLA (VSL Association), “A brochure of VSL permanent anchor method (rank A), 2012.

[3] Okahara, M., Takagi, S., Nakatani, S. and Kimura, Y., “A study on bearing capacity of a single pile and design method of cylinder shaped foundations”, Technical Memorandum of PWRI, 2919, 1991.

NEW CONCEPT FOR REASONABLE GEO-DISASTER RECOVERY

Takashi Hara[1], Akiho Inoue[2], Atsushi Yashima [3], Nobuyuki Soga [4] and Yoshihiro Yokota[5]
[1]Department of Civil Engineering, Gifu University, Japan; [2-4] Gifu University, Japan;
[5] MAEDA KOSEN CO., LTD., Japan

ABSTRACT

Various design and construction methods have been proposed and adopted in geo-disaster recovery projects. However, researches on optimum design and construction methods in geo-disaster recovery projects based on the comparison of the real recovery projects executed in the respective fields are very few. Because the number of geo-disasters, such as land slides, debris flows and so on, is predicted to increase due to the growth of the number of sudden heavy rainfalls caused by global climate change, it is considered that the research on optimum design and construction methods in geo-disaster projects will be necessary from the viewpoint of limited public investment.

Therefore, the authors have conducted a study on development of a future concept of reasonable geo-disaster recovery projects based on the real recovery projects executed in the respective fields. The proposed concept and examples of reasonable disaster recovery project on the present stage of this study as well as each consideration with respect to geo-disaster recovery in the several fields are discussed in this paper.

Keywords: Geo-Disaster, Recovery, Temporary Structure, Lifelong Duration, Permanent Measure

INTRODUCTION

The design and construction methods in geo-disaster recovery project have been different depending on the respective fields. For example, in the field of erosion control, permanent recovery structure is usually built independently. On the other hand, the temporal recovery structure is sometimes applied to a part of permanent recovery structure in the field of road management. Therefore, the temporal recovery treatment is called as the temporal-permanent recovery one in that case. However, researches studying on reasonable geo-disaster recovery projects from the comparison of the different respective considerations and real recovery projects executed in the respective fields are very few. Under the circumstance the increase of geo-disasters due to the growth of the number of sudden heavy rainfalls caused by global climate change, it is considered that the establishment of the concept of reasonable and optimum recovery geo-disaster project is necessary from the viewpoint of treating the geo-disasters by the limited public investment.

Therefore, the authors have started conducting a study on development of a future concept of reasonable geo-disaster recovery projects from the comparison of the considerations and real recovery projects executed in the respective fields. The proposed concept and examples of reasonable disaster recovery project on the present stage of this study as well as each consideration with respect to geo-disaster recovery in the several fields are discussed in this paper.

PRESENT GEO-DISASTER RECOVERY CONSIDERATIONS ON EACH FIELD

Erosion Control Field

In the field of erosion control, a temporary structure for emergent treatment is placed immediately just after the disaster by using large soilbags for instance, in order to protect human life from the occurrence of secondary disaster. Then a permanent recovery structure is planned and constructed with selecting the appropriate construction site of the structure, where the national government or local government purchases the necessary land for the construction. Namely, the construction sites for building temporary structure and that for permanent structure are in general different, as shown in Fig. 1.

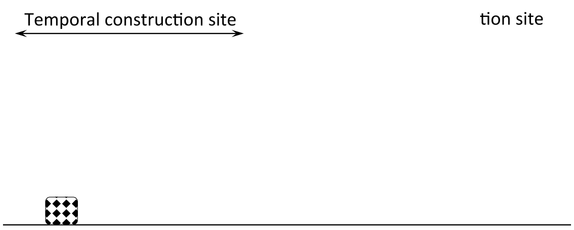

Fig. 1 Temporary and permanent recovery structure.

Hence, the temporal structure has not been applied to a part of permanent structure. Therefore, the temporary structure has been usually cleared away. The reason is that there is no time to select the appropriate construction site and purchase the necessary land right after the disaster.

Road Management Field

In the field of road management, building a temporary structure only for temporary recovery purpose has not been permitted in general.

(a) Case of landslide.

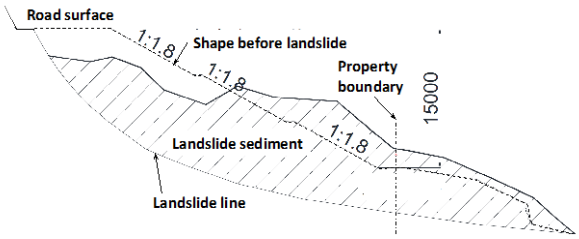

(b) Before and after landslide.

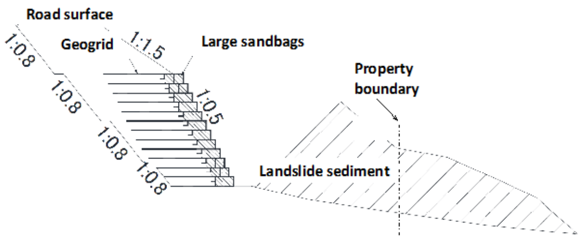

(c) Temporary-permanent recovery.

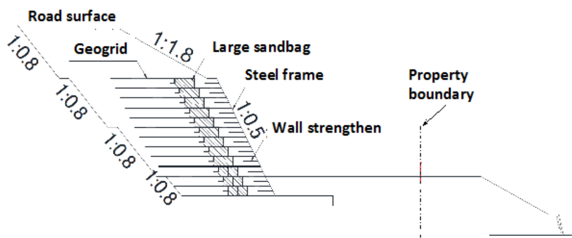

(d) Permanent recovery

Fig. 2 Application of temporary-permanent recovery.

The temporary recovery project is usually planed to build the temporary structure. At the same time, its temporary structure is often utilized to a part of the permanent recovery structure constructed in the permanent recovery project. In this consideration, the temporary recovery is called temporary-permanent recovery in the field.

Fig. 2 shows an example of adopting the temporary-permanent recovery [1-3]. In this example, reinforced soil wall composed of large soilbags and geogrids was adopted as the temporary-permanent recovery structure, as shown in Fig. 2(c). Then the permanent recovery structure was completed by adding another reinforced soil wall composed of steel frame and wall strengthen material to the temporary-permanent recovery structure.

Afforestation Field

Afforestation structures, as shown in Fig. 3, are placed to prevent a future erosion and to recover the mountain to nature condition. Therefore, the structures building in the afforestation field are basically permanent ones and it is not necessary for the national government or local government to purchase the land for building the structures.

Fig. 3 Example of afforestation structure.

NECESSITY OF A NEW CONCEPT FOR REASONABLE GEO-DISASTER RECOVERY

Variation of Temperature and Rainfall in Japan

According to data of Japan Meteorological Agency (JMA), the transition of average temperature of years and the frequency of heavy rainfall more than 50 mm/hr. observed at 1000 points have been increasing during recent decades in Japan, as shown in Fig. 4 and 5 [4]. The data indicate that the temperature raises 1.14 degrees centigrade a hundred year and the frequency of heavy rainfall more than 50 mm/hr. increases 21.3 times a decade as the trend. Namely, it is certainly considered that the heavy rainfall increases with the raise of the temperature in Japan.

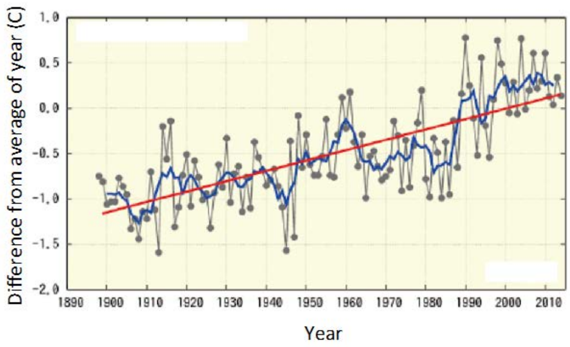

Fig. 4 Average temperature of years.

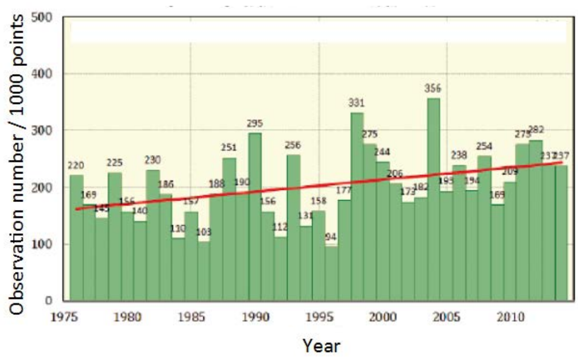

Fig. 5 Frequency of larger rainfalls more than 50mm/hr.

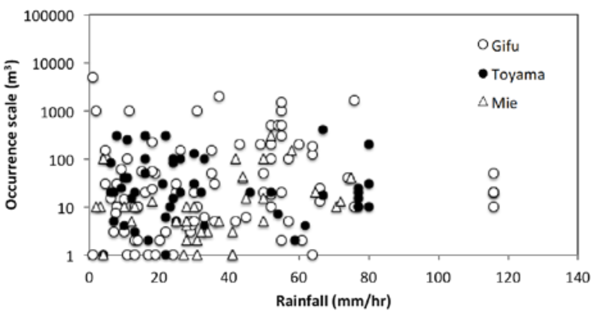

(a) Landslide

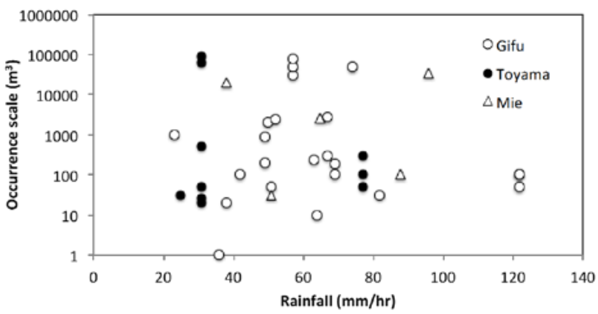

(b) Debris flow

Fig. 6 Relationship between geo-disaster occurrence scale and rainfall.

Geo-disaster Scale and Frequency with Rainfall

Figs. 6 and 7 summarize the relationships between occurrence scale and number of disaster and rainfall per hour with respect to landslide and debris flow, respectively [5]. The data were obtained from three prefectures such as Gifu, Toyama and Mie, as shown in Fig. 8. Although the data were obtained from a part of Japan, those can be representative ones as a mountainous country.

According to the results, both the occurrence scale and number of debris flows especially increase sharply with the increase of rainfall per hour. This result indicates that the occurrence scale and number of geo-disaster will increase with the increase of the frequency of heavy rainfall throughout Japan in the near future.

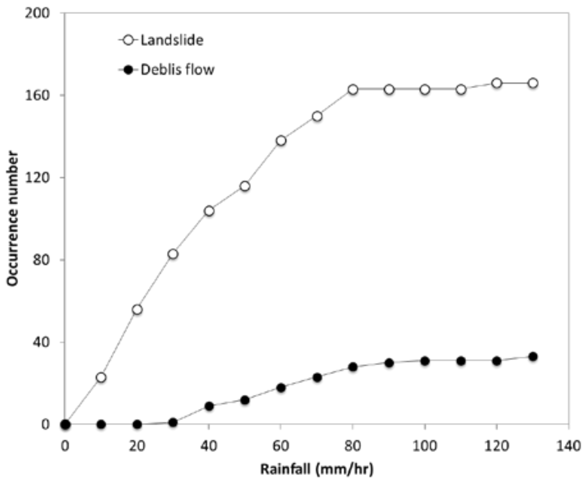

Fig. 7 Geo-disaster Occurrence number and rainfall.

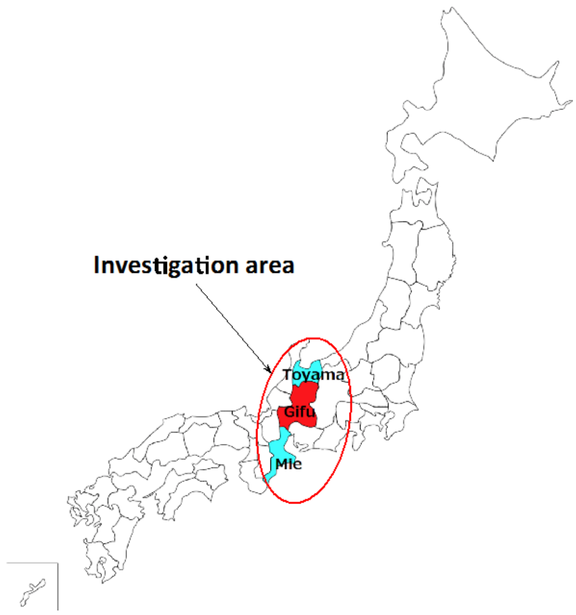

Fig. 8 Investigation area.

Fig. 9 shows the percentage of emergent treatments adopted after landslides and debris flows. Fig. 10 shows the percentage of the failed volume (m^3) by landslide with respect to each emergent treatment method from experiences in Gifu and Toyama prefectures [5]. In Figs. 9 and 10, CS is covering sheet, RS is removing soil, SB is setting soil bags, Fe is setting fences and Ot is others.

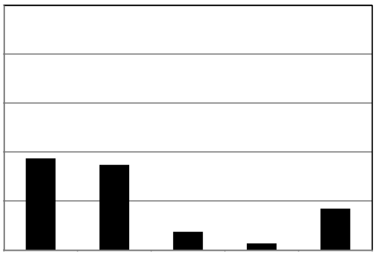

(a) Landslide

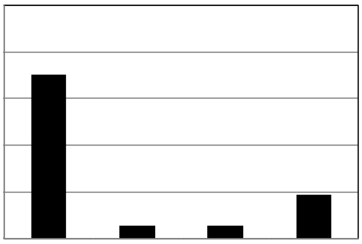

(b) Debris flow

Fig. 9 Adopted emergent recovery treatments.

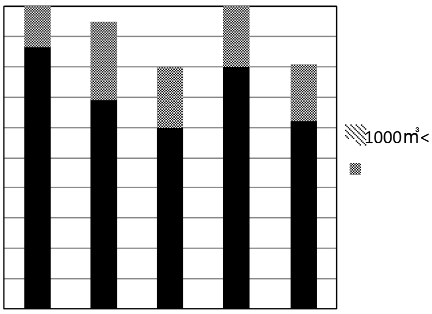

Fig. 10 Adopted treatments and scale of debris flow.

Necessity of a New Concept for Reasonable Geo-disaster Recovery

Under the circumstance of the increase of the occurrence number and the scale of geo-disaster in the near future, the establishment of a new concept for reasonable and optimum geo-disaster recovery scheme is very important in order to resist expected geo-disaster with using limited public investment. For example, the application of the temporary-permanent recovery consideration in the road management field to the erosion control field is very effective to decrease the disaster investment. Furthermore, the development of the technology for functionality enhancement and life prolongation of the structures built as a countermeasure against geo-disaster is also important.

A FUTURE CONCEPT OF REASONABLE GEO-DISASTER RECOVERY PROJECTS

The authors have started a study on the development of a concept for reasonable geo-disaster recovery projects from the viewpoints of previous study and preparation, in which the functionality enhancement and life prolongation, development of new recovery methods and their design methods will be discussed. The conceptual images for road, erosion control dam and embankment studied are shown in Fig. 11.

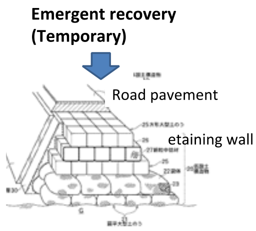

(a) One side filling (b) Both side filling

Fig. 11 Conceptual image of temporary and permanent structures.

As mentioned previously, temporary recovery structure and permanent recovery one are built on different place in the erosion control field, and the reason is that there is not enough time to select the appropriate construction site and to purchase the land for building the permanent structure. The problems, however, can be solved by previous studies on selecting the construction sites for building permanent recovery structure with the prediction of geo-disaster occurrence prediction and negotiations with the landowners.

If the prediction of geo-disaster and a-priori negotiation between officials and landowners are possible, the application of the temporal-permanent recovery consideration in the road management field to erosion control field will be possible.

Functionality Enhancement and Life Prolongation of Recovery Structures

There have been many cases in which a structure became to indicate a poor performance after receiving the geo-disaster impact such as a debris flow impact to an erosion dam. Thus the functionality enhancement has become one of the most important issues in the erosion control field. Furthermore, in the afforestation field, it is fundamental that all structures built in the field are aimed to recover the mountain greenery condition. The life prolongation of the structures has also become one of important issues from the viewpoint of reasonable afforestation.

Therefore, reasonable methods of functionality enhancement have been researched in this study. It is very important to make use of debris flow deposits for construction material. The authors propose the composite structure to enhance the exising dam by using debris flow deposits, soilbags and concrete cover, as shown in Fig. 12.

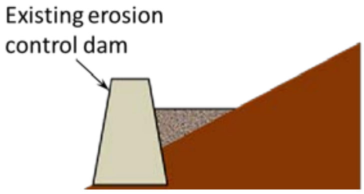

(a) Before debris flow

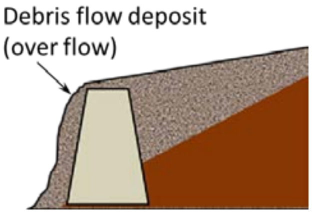

(b) After debris flow

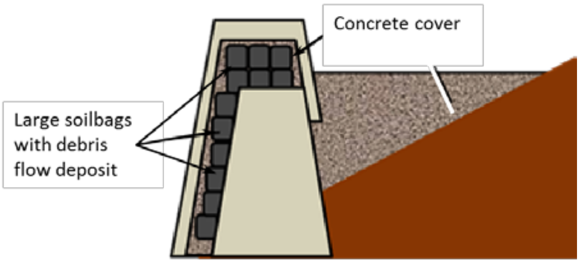

(c) Functionality enhancement with debris flow deposits

Fig. 12 A reasonable functionality enhancement.

Development New Recovery Methods and Their Design Methods

New reasonable recovery methods, as shown in Fig.9 for instance, are outlined in this chapter. Fig. 13 shows a simple application of temporary-permanent recovery consideration for a small-scale landslide disaster, in which large soilbags and covering soil will be only used.

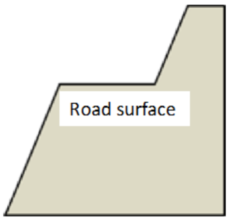

(a) Before landslide

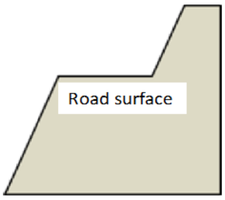

(b) Occurred landslide

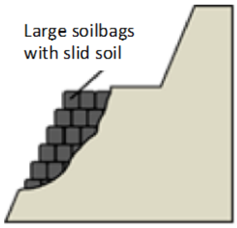

(c) Temporary-permanent recovery

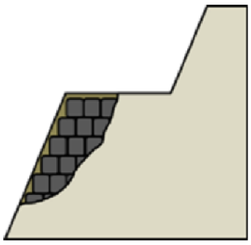

(d) Permanent recovery

Fig. 13 A simple temporary-permanent recovery.

Designs for recovery methods have been studied. For example, as far as the design of the permanent structure by making use of temporary soilbags for an erosion control dam concerned, a design model has been proposed as the composite element model with elastic beam and compression spring as shown in Fig.14. A design model shown in Fig. 14 is the case assumed for verification of internal stability. In this model, the covering concrete is modeled as an elastic beam and the interior soilbags are evaluated as spring with considering long-term compression of the soilbags. The arrangement of reinforcing bars should be designed next, as shown in Fig. 15. Meanwhile, the outer stability is verified from the viewpoints of rotation, sliding and bearing capacity, which is the same as retaining walls. The validity of a proposed design scheme will be confirmed by experiments and analyses in the near future.

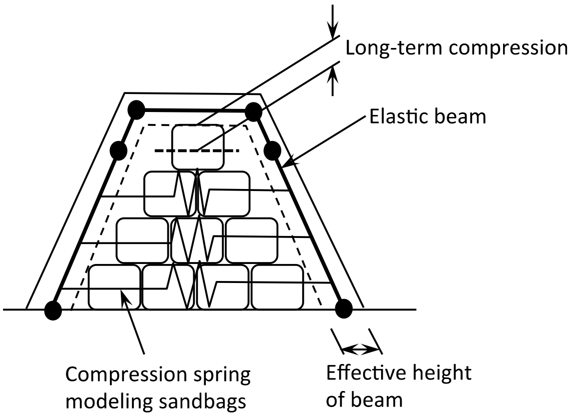

Fig.14 A design model for internal stability.

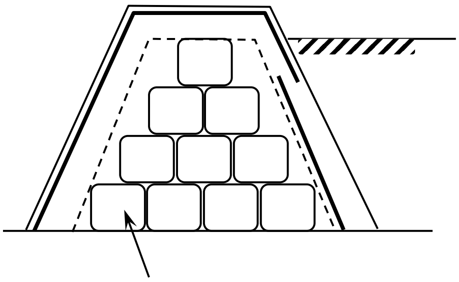

Fig. 15 An example of rebar's arrangement.

CONCLUSIONS

Geo-disaster recovery projects have been planned and carried out based on different considerations depending on several fields, such as erosion control, road management and so on. However, because the increase of geo-disaster occurrence number and growth of the disaster scale due to the global climate change is estimated, it is necessary for us to establish a future concept for reasonable geo-disaster recovery project from the viewpoint of efficient use of limited public investment.

Authors first summarized the trend of geo-disasters took place in Gifu, Toyama and Mie prefectures in Japan. The emergent treatments adopted were alkalized with respect to the disaster scale. Then authors proposed the new concept for the reasonable geo-disaster recovery in different fields. The conceptual design images were also mentioned for several temporary-permanent structures. The details of design methods for different structures will be introduced in the near future.

ACKNOWLEDGEMENTS

The authors would like to acknowledge the engineers of Etsumi-sankei erosion control (SABO) office of Ministry of Land, Infrastructure, Transportation (MLIT), Gifu prefecture, Toyama prefecture, Mie prefecture and Tono Forest Office of Ministry of Agriculture, Forestry and Fisheries (MAFF), who supplied us valuable data and ideas.

REFERENCES

[1] Kubo, T., Mori, Y. and Miyatake, H., "The behavior of the restoration method using the large-sized sand-bags", Geotechnical Journal

[2] Mori, Y., Kubo, T. and Miyatake, H., "A dynamic centrifuge test of disaster recovery technique with considering site condition", the 70th JSCE annual conference, 2015, pp.699-703.

[3] Kubo, T., Yokota, Y. and Tsuji, S., "Restoration and investigation of road embankment damaged by Noto-Hanto earthquake in 2007", Geosynthetics Engineering Journal, 2007, pp. 199-206.

[4] Japan Meteorological Agency (JMA), http://www.jma.go.jp/jma/kishou/books/hakusho/2015/index1.html.

[5] Inoue, A., "A study on efficient and economic concept of geo-disaster recovery", Graduation thesis of Gifu University, 2016.

Sixth International Conference on Geotechnique, Construction Materials and Environment, Bangkok, Thailand, Nov. 14-16, 2016, ISBN: 978-4-9905958-6-9 C3051

THE SOIL BLOCK APPROACH FOR VERIFYING HYD USING FEM

Georgios Katsigiannis[1, 2], Pedro Ferreira[1] and Raul Fuentes[3]
[1]University College London, UK; [2] Arup, UK, [3] University of Leeds, UK

ABSTRACT

The HYD limit state, as described in Eurocode 7, is caused by hydraulic gradients and is one of the most dangerous Limit States, resulting in sudden failure with serious consequences for people and structures. The hydraulic heave stability problem relates particularly to the upward flow of water through soil to a free surface such as may occur in front of a retaining wall in the base of an excavation. The simplest way to verify the oil stability against the HYD Limit State using Finite Element Methods is the so called Soil Block Approach. In this approach, which is based on the widely used Terzaghi's criterion, safety may be checked by studying the equilibrium of a rectangular block of soil. In this paper, the authors describe the Soil Block approach and discuss its advantages and disadvantages. Comparisons made using a benchmark geometry extensively studied and discussed between the members of the EC7 Evolution Group 9 on Water Pressures, illustrate that the calculated Terzaghi's factor directly depends on the upstream and downstream groundwater levels as specified by the ratio $\Delta h/t$ while for a given difference in the hydraulic head, the system becomes more critical for narrow excavations where confined space results in an increase in the groundwater pressures. Overall, the authors conclude that the HYD verification using numerical methods is straightforward and seems very promising.

Keywords: Eurocode 7, HYD, water pressures, FEM

INTRODUCTION

The HYD limit state, as defined in Eurocode 7 (EC7), relates to hydraulic heave, internal erosion and piping in the ground caused by hydraulic gradients [1]. This apparently covers a wide range of situations with stability problems caused by hydraulic gradients. This paper focuses on part of this definition, the hydraulic heave stability problem, which is illustrated in Fig 1. Hydraulic heave refers particularly to vertical upward flow of water to a free surface (e.g. water flow in front of a retaining wall) and is one of the most critical Ultimate Limit States, potentially causing sudden failures with serious consequences for both people and structures.

Nowadays, with the increasing popularity of the advanced numerical methods, more and more designers will use Finite Element methods, to verify soil stability against hydraulic heave. The HYD verification using FEM can be performed with the *Soil Block* approach. In this approach, safety is verified by studying the equilibrium of a rectangular soil mass. [5].

The use of the Soil Block approach has been recently discussed by the Evolution Group 9, and this work draws on those discussions to provide a better understanding and highlight the feasibility of the approach for verifying hydraulic heave using advanced numerical methods.

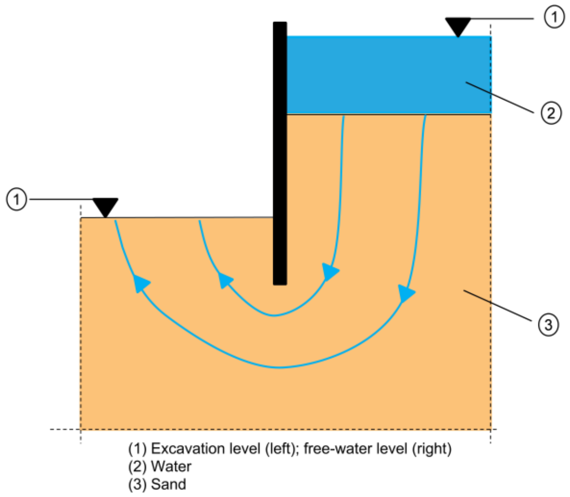

Fig. 1 Example of a HYD situation.

EUROCODE 7 REQUIREMENTS

Safety against failure by hydraulic heave is verified with Equation 2.9 as given by EC7, where stability of soil against heave shall be checked either in terms of forces or stresses [1]. More specifically, the equation is expressed in two different but equivalent forms, presented below as Equations 1 and 2. The first equation requires the design total vertical stress to be greater than the design pore water pressure at the bottom of a relevant soil column while the second requires the design buoyant weight of the column to be greater than the design seepage force.

$$u_{dst;d} \leq \sigma_{stb;d} \quad (1)$$

$$S_{dst;d} \leq G'_{stb;d} \quad (2)$$

The subscript *d* refers to *design* values of parameters while the subscripts *dst* and *stb* refer to *destabilising* and *stabilising* effects.

The partial factor values as specified in UK National Annex of EC7 are listed in Table 1 [1].

Table 1 Partial factors on actions (γ_F)

Action	Symbol	Value
Permanent Unfavourable[a] Favourable[b]	 $\gamma_{G;dst}$ $\gamma_{G;stb}$	 1,35 0,90
Variable Unfavourable[a]	 $\gamma_{Q;dst}$	 1,50
a Destabilising b Stabilising		

However, it is highlighted in the EC7, that the load factors might not be always suitable for ground water pressures. The code allows for direct assessment of the design value or application of a safety margin to the characteristic ground water table. Thus, by allowing three alternative methods, much of the responsibility for deriving the design value of water pressures is left with the designers [14]. Simpson & Katsigiannis recommend that factoring of water pressures should be generally be avoided and suggest the direct assessment of the design water pressures or the design water table level [2].

HYD VERIFICATION UDING FE METHODS

Methodology

The Soil Block approach for the HYD verification using FE methods, is now illustrated for the simple cofferdam problem presented in Fig 2. The software used is Plaxis 2015.02 and the following assumptions were made in the model:

- The wall is wished-in-place, impermeable and not allowed to deform in any direction.
- Only half the excavation width is considered, due to symmetry.
- Steady state conditions are assumed.
- The side and bottom boundaries are impermeable.
- The side model boundaries are fixed in the x direction while the bottom model boundary is fixed in both x and y directions.
- The unit weight of the soil γ is equal to 20kN/m^3
- Initial stress field conditions are based on hydrostatic water pressures and K_0=1-sinφ'.
- Interface elements are used between the soil and the wall with tanδ = 0.5tandφ', where δ is the wall friction angle.

The soil is homogeneous sand and its properties are given in Table 2. The generated finite element mesh is shown in Fig 3.

Table 2 Material properties of sand

Soil Properties	
Young's Modulus, E' (MPa)	25+6.5z
Angle of shearing resistance, φ' (°)	35
Effective cohesion, c' (kPa)	0
Poisson's ratio, v'	0.2
*where z is the depth below the ground level (m)	

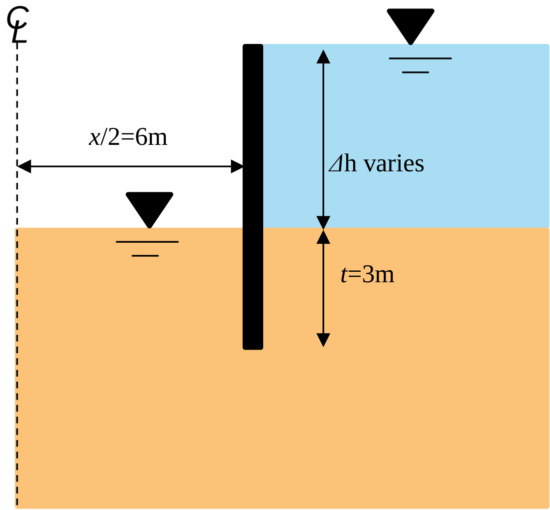

Fig. 2 Geometry of the cofferdam problem.

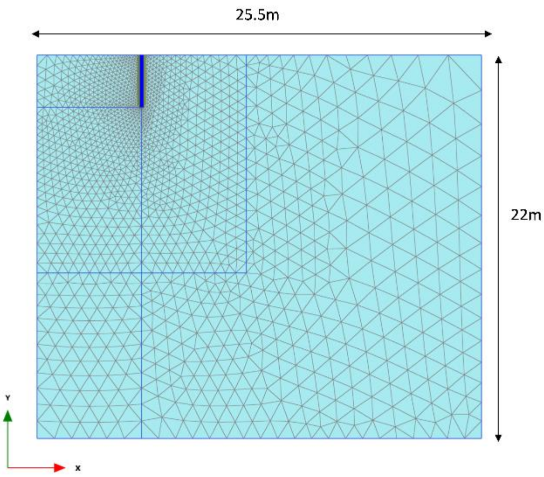

Fig. 3 Finite Element mesh

The Soil Block Approach

The Terzaghi's criterion

Terzaghi was the first to propose study of a soil block extending a depth *t* from the free surface to the toe of the wall and of width *b*=*t*/2 for isotropic and uniform materials [3], [4]. According to Terzaghi's criterion, soil stability is checked by verifying that the buoyant weight of the block is greater than the seepage force (see Fig. 4). The friction on the sides of the block at its interfaces with the wall and with the rest of the soil is ignored. Terzaghi's factor of safety is defined in Equation 3 below, where *W* is the weight of the block, *H* is the force on base of block due to hydrostatic pressure, *U* is the water force on base of block, *W-H* is the buoyant weight and *U-H* is the seepage forces.

$$F_T = \frac{W - H}{U - H} \qquad (3)$$

Although Terzaghi et al. give a worked example in which the acceptable factor required is F_T=2.5 [10], no direct recommendation from Terzaghi has been found, in previous publications, with the specification of a minimum factor of safety. Values taken from a survey of publications, generally based on the use of Terzaghi's diagram, are summarised in Table 2 [2].

Table 2. Published values for Terzaghi's factor of safety F_T [2]

Publication and any limitations	Values
Williams & Waite (1993) For clean sands	1.5 to 2.0
Kashef, Abdel-Aziz Ismail (1986)	4 to 5
Harr (1962)	4 to 5
German practice – unfavourable soils	1.9
(DIN 1054/A2 2014) – favourable soils	1.42
Swedish practice – coarse soils	1.5
(Ryner et al 1996) – silty material	2.5
Dutch practice	2.8
Das (1983), quoting Harr (1962)	4 to 5

The values for the required factor of safety shown in Table 2, range from 1.42 to 5. While some authorities require larger factors for finer soils than for coarser soils, no explanation of this range has been given by the authors.

Skempton & Brogan illustrate the significance of the grading curves of the materials in relation to safety considerations in presence of hydraulic gradients [9]. Even if water pressures are known with confidence, the achieved levels of safety highly depend on the grading curve of the material with poorly graded materials generally tolerating lower hydraulic gradients. This is because, in poorly graded materials, the effective stress may vary locally over distances of the order of a few soil particles, leaving some particles at much lower stresses than normally calculated from the depth of overburden.

Similarly, the German guide on erosion makes a distinction between poorly graded soils that are internally unstable and well graded soils where the soil particle mixtures are internally stable [8]. The critical failure mechanism depends on the grading curve with internal erosion and particularly suffusion (transport of the fine soil particles through the pores of the coarse particles) being critical for poorly graded soils and hydraulic heave for well graded soils.

This variability of the grading curves and the governing failure mechanisms among different soils, explains why different authors have proposed quite different values for the Terzaghi's factor with higher values typically suggested as an empirical way to account for the composition anomalies of internally unstable soils.

It is generally recommended that designers first investigate if the soil is internally stable before a verification of hydraulic heave can be done rather than generally use increased safety factors for the verification of hydraulic heave.

The Soil Block Approach with FEM

Calculating the Terzaghi's factor with FE methods is straightforward as the weight of the soil block and the hydrostatic pressure on the base of the block can be easily derived from hand simple calculations. The pore water pressures acting at the bottom of the block are obtained from the output of the FE calculations.

As mentioned before, Terzaghi recommended that a column of width *b*=*t*/2 should be used in the calculations of the factor of safety, taking no account of friction forces on its vertical sides. Simpson & Katsigiannis showed, however, that the hydraulic gradient would be higher if a narrower column were used [2]. It could be that Terzaghi considered that a narrower column is unlikely to fail because the favourable effect of the friction forces on its vertical sides would become significant. For this study, all the soil block calculations are based on the Terzaghi's block dimensions; the depth of the block is equal to the embedment depth *t* and the width *b* is equal to *t*/2.

As the buoyant weight, which is the stabilising force, only depends on the unit weight of the soil, γ and can be easily calculated for the Terzaghi's block as defined in Figure 3.5, the Terzaghi's factor is more sensitive to variations of the destabilising force which is the seepage force caused by the pore water pressures. The effects of different parameters on the pore water pressures and hence the Terzaghi's factor, are investigated in this study.

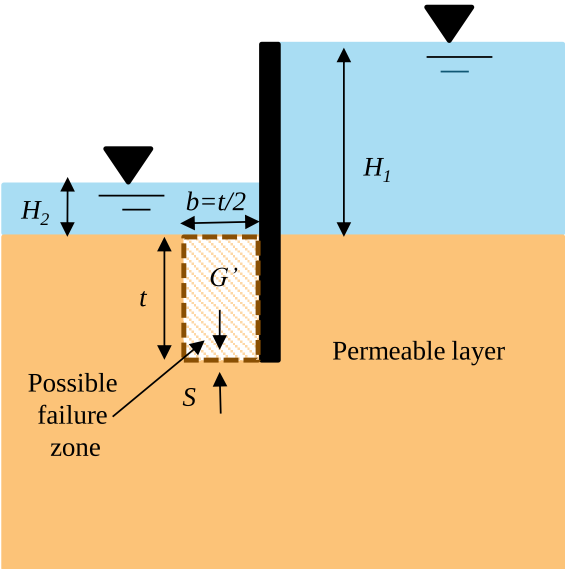

Fig. 4 The Terzaghi's criterion.

Effect of Δh/t

The calculation of the factor is now illustrated for a simple cofferdam problem for varying Δh/t ratio, where Δh is the difference in the hydraulic head and *t* is the embedment depth of the wall. By gradually increasing the Δh/*t* ratio, the analysis was driven to failure. Different hydraulic heads were achieved by specifying different levels of the free-water table behind the retaining wall and at the end of each analysis, the Terzaghi's factor was calculated. In Figure 5, the factor is plotted against the ratio of Δh/t and it can be seen that its value drops as Δh/t increases. This is because an increase in Δh gives rise to the groundwater pressures as shown in Fig 6. The system becomes unstable and the value of the factor less than unity for a ratio of Δh/t equal to 2.25. The corresponding vertical soil displacements vectors are presented in Fig. 7 where the well-defined failure mode can be observed. The results are consistent with the failure mechanisms presented by other authors for similar problems [12], [13].

It can be concluded that the calculated Terzaghi's factor directly relates to the specified upstream and downstream groundwater levels as expressed by the ratio Δh/t.

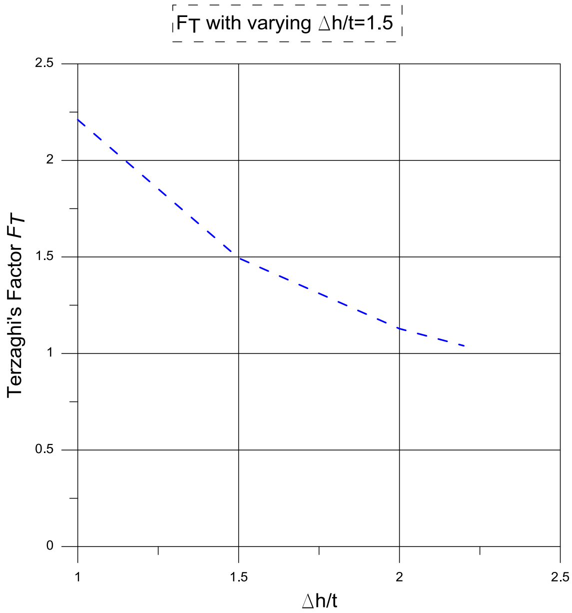

Fig. 5 Calculated Terzaghi's factor for varying Δh/t

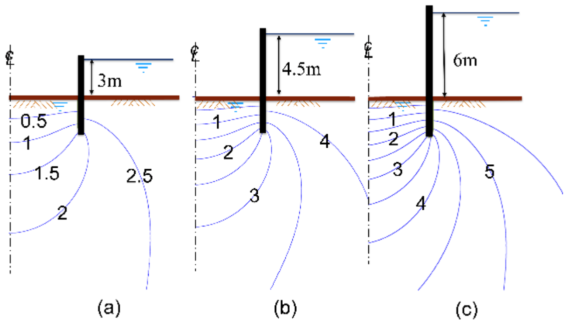

Fig. 6 Head equipotentials for a) Δh/t=1, b) Δh/t=1.5 and c) Δh/t=2

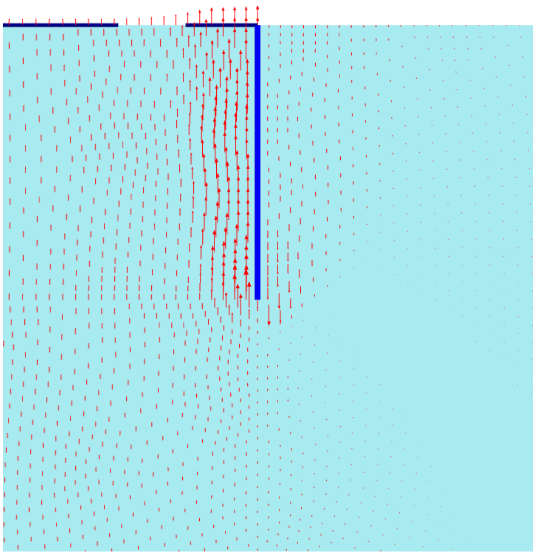

Fig. 7 Vertical displacement vectors for Δh/*t*=2.25

Effect of x/t

Simpson & Katsigiannis also illustrated the effect of the excavation width when calculating the Terzaghi's factor [2]. When plotting the head equipotentials for wide and narrow excavations, the authors observed that pore water pressures significantly rise when for small excavation widths.

To better illustrate this effect, the analysis is repeated for different excavation widths while the rest of the model parameters remain the same. More specifically, 5 different cases were considered for plain strain conditions: *x*/*t*=12, 8, 4, 2 and 1, where *x* is the excavation width (due to symmetry only half the excavation is modelled) and *t* is the embedment depth. At the end of each analysis, the Terzaghi's factor was calculated using the values of the pore water pressures acting at the bottom of the soil block from the output of the calculations. This study includes 5 different geometries each simulated using three different values of $\Delta h/t$, totalling 15 analyses.

In Figure 8, the Terzaghi's factor is plotted against the ratio *x*/*t* for $\Delta h/t=1.5$. It can be seen, that the narrower the excavation is, the lower the factor of safety becomes. The value of the factor of safety particularly drops for values of *x*/*t* lower than 4. Figure 9 gives the head equipotentials for varying the *x*/t parameter. It can be seen that the ground water pressures rise significantly as the excavation becomes narrower. This rise in the water pressures causes the drop in Terzaghi's factor value. This confirms the findings of Aulbach & Ziegler that when water is flowing upwards beneath a narrow excavation, the upward hydraulic gradients are higher than in the cases of wider excavations with little or no lateral restraint [11].

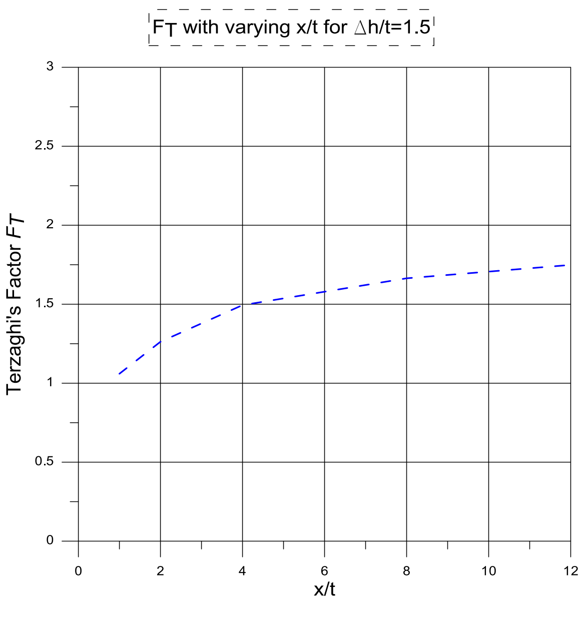

Fig. 8 Calculated Terzaghi's factor for varying *x*/t

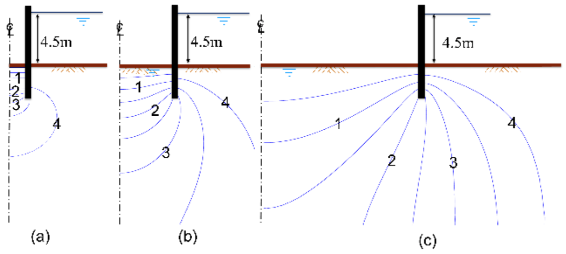

Fig. 9 Head equipotentials for *x*/t a) *x*/t =1, b) *x*/t =4 and c) *x*/t =12

CONCLUSION

Verification of stability against HYD using FE methods is straightforward and seems very promising. The *Soil Block* approach is simple and requires only the pore water pressures acting at the bottom of the soil block to be calculated from the FE analysis.

The calculated Terzaghi's factor directly depends on the upstream and downstream groundwater levels as specified by the ratio $\Delta h/t$. It was also noted that for a given difference in the hydraulic head, the system becomes more critical for narrow excavations where confined space results in an increase in the groundwater pressures.

While the *Soil Block* approach has the benefit of simplicity, it has the disadvantage that it can be applied only to the simple problems similar to the one studied in this paper, and not to more complex geometries such as slopes and embankments. Moreover, it provides no useful information about the soil stability at a very small scale but instead it pre-defines the critical failure mode.

In general, for HYD verifications it is considered good practice not to merely rely on factors of safety. Designers should always be aware that even small variations in permeability, which could very easily be overlooked in a ground investigation, could lead to instability [2].

ACKNOWLEDGEMENTS

The authors gratefully acknowledge the support of the project partners, EPSRC, Arup and UCL European Institute. Special thanks are extended to Brian Simpson from Arup Geotechnics for the useful discussions.

REFERENCES

[1] BS EN 1997-1 (2004). Eurocode 7 – Geotechnical design, Part 1 – general rules, British Standards Institution, London, 999pp

[2] Simpson, B. and Katsigiannis, G. (2015). Safety considerations for the HYD limit state. XVI ECSMGE, Edinburgh 2015

[3] Terzaghi, K. (1922). Der Grundbruch an Stauwerken and seine Verhiltung, Die Wasserkraft, Vol. 17, No. 24, pp. 445-449

[4] Terzaghi, K. (1943). Theoretical Soil Mechanics, J. Wiley and Sons, New York

[5] Evolution Group 9 - Water Pressures. (2014). Final report to TC250/SC7 Evolution of Eurocode 7 Part 1. July 2014

[6] Stelzer, O., & Odenwald, B. (2015). A New Stress-Based Approach for Verification of Safety Against Hydraulic Heave Based on EC7. XVI European Conference on Soil Mechanics and Geotechnical Engineering (pp. 4073-4078). Edinburgh: ICE Publishing.

[7] Simpson, B. (2012). Eurocode 7 – fundamental issues and some implications for users. 16th Nordic Geotechnical Meeting (pp. 29-52). Copenhagen: Danish Geotechnical Society.

[8] BAW (2013). Code of Practice: Internal Erosion (MMB). German Federal Waterways Engineering and Research Institute, Karlsruhe

[9] Skempton, A. W., & Brogan, J. M. (1994). Experiments on piping in sandy gravels. Géotechnique. 44, No. 3,449-460.

[10] Terzaghi, K., Peck, R., & Mesri, G. (1996). Soil Mechanics in Engineering Practice, 3rd edition. John Wiley & Sons, Inc.

[11] Aulbach, B., & Ziegler, M. (2013). Simplified design of excavation support and shafts for safety against hydraulic heave. Geotechnics and Tunnelling, 362-374.

[12] Benmebarek, N., Benmebarek, S., & Kastner, R. (2005). Numerical studies of seepage failure of sand within a cofferdam. Computers and Geotechnics, 264-273.

[13] Stelzer, O., & Odenwald, B. (2015). A New Stress-Based Approach for Verification of Safety Against Hydraulic Heave Based on EC7. XVI European Conference on Soil Mechanics and Geotechnical Engineering (pp. 4073-4078). Edinburgh: ICE Publishing.

[14] Simpson, B., Vogt, N. and Van Seters, A.J. (2011). Geotechnical Safety in Relation to Water Pressures. Proceedings of the 3rd International Symposium on Geotechnical Safety and Risk. Munich.

IMPROVEMENT OF HIGH EXPANSIVE SOILS BY DEEP SOIL MIXING METHOD IN THE SMALL SCALE LABORATORY EXPERIMENT

Yulvi Zaika[1] and Arief Rachmansyah[2]
[1,2]Faculty of Engineering, Brawijaya University, Indonesia

ABSTRACT

The expansive soil could damage on the pavement and other floor building because of its swelling characteristic, low strength and California Bearing Ratio. Improvements by adding stabilizing material is one alternative that could reduction swell potential and increasing of CBR. Because the thickness of expansive soils in Bojonegoro District, East Java, Indonesia are more than 1.5 m , the improvement by adding stabilizing material in the surface is less effective. Deep Soil Mixing (DSM) is ground modification technique can be done to depth up to 30 m. This paper will explain the result of laboratory experiment of deep soil mixing (DSM) method as suitable alternative. The small-scale experiments will be applied to observe the change of strength and swell potential. Implemented DSM requires consideration of the stabilized material (binder) with optimum value, water – binder ratio that provides maximum performance on DSM and geometric parameters (length, diameter and spacing of columns). The fly ash material will be used as the material will be made a series of experiments to get the optimum value. The optimum water content of expansive soil will be used and the configuration single square were implemented. The experiment showed that the strength of expansive soil increase and the swell potential decrease. The effect of DSM could increase the soil strength and reduce its swell potential.

Keyword: *expansive soil, Deep Soil Mixing, swelling, strength*

INTRODUCTION

One of geotechnical problems encountered in the construction of transportation infrastructure in the north part of East Java is wide spread expansive clayey soil (Fig.1). In this region it is founded two types of clayey soil.

Fig.1 Map of the spread of soft soil in the northern part of East Java, Indonesia and transportation infrastructure (Rachmansyah, 2014).

The first one is the sediment soil that as the product of sedimentation materials carried by the river Bengawan Solo and sedimentation in wetlands (Qa). This soil is generally fine-grained, and contains a lot of organic matter. The thickness of young soft sediment soil can reach 40 m depth (Wesley, 2010). The second type of clayey soil is the product of weathering process of mudstone (residual soil) of the Lidah Formation. The Lidah Formation (TQs) composed by blue grey mudstone with lenses of carbonatics sandstones and limestone. This geological formation is formed in a shallow marine environment during the Pliocene - Pleistocene (Ratman, et al., 1998). This residual soil type has generally high shrink-swell characteristics (known as high expansive soil), because of its high contents of montmorilonite minerals. Bojonegoro district is one of area in this formation. The expansive characteristics of the clayey soil can cause cracks in the floor of building and the road, and prone the landslide (Fig. 2).

Fig. 2 Typical cracks of the pavement that were built on the residual soil of Lidah Formation in the North East Java

To improve the soil properties, in this case to reduce shrink swell characteristics are used commonly cement, lime, silica and various chemicals compounds. In an industrial context, fly ash usually refers to ash produced during combustion of coal. Fly ash is generally captured by electrostatic precipitators or other particle filtration equipment before the flue gases reach the chimneys of coal-fired power plants. Because of its contains such as silica (SiO_2), iron oxide (Fe_2O3), aluminium oxide (Al_2O_3), and calcium oxide (CaO), fly ash can be categorized as pozzolanic materials.

Considering the successful and rapid nature of chemical based DSM in stabilizing soft soil and the same technology was considered to expansive soil. The purposed of this study was to explore the change of strength and swell potential of improvement with DSM in difference geometric parameters (length, diameter and spacing of columns) in small scale laboratory experiment. Laboratory result on field cores indicated that both field stiffness and strength are about 20% to 40% less than the corresponding laboratory prepared soil samples (Madhyannapu et al, 2010). Some of numerical studies have been carried out to understand the behavior column-supported embankment system, assuming linear elastic or linear elastic perfectly plastic but Yapage et al. (2014) obtained strain softening constitutive behavior for cement stabilized clay for DSM column. Application and evaluation of DSM was developed by Madhyannapu at al.(2014) to propose the stepwise design methodology.

The Bearing Capacity Improvement

How DSM improve soil characteristic is well understood by using Bearing Capacity Ratio or *Bearing Capacity Improvement* (BCI) that can be determined based on ultimate bearing capacity and bearing capacity of treated soil (DSM). Formulation of BCI can be written as

$$BCI = \frac{q_u(I)}{q_u} \quad (1)$$

Where:
qu (I) : ultimate bearing capacity with DSM
qu : ultimate bearing capacity native soil

Swell Potential

Determination of swell potential is quite important in design of foundations on expansive soils. The swelling tendencies of expansive soils are quantified by the swelling potential and/or free swell. Swell potential or volume change is defined as the ratio of increase in high to the initial high of the soil sample compacted at optimum moisture content in a consolidation ring and soaked under a surcharge of 6.9 kPa (1 psi) , Seed et al. (1962).

$$SP = \frac{H_i - H_f}{H_i}\, x100\% \quad (2)$$

where, H_i : initial height of sample, H_f : final height

Swell potential was percentage of swell under 1-psi surcharge of sample compacted at optimum water content to maximum density in Standard AASTHO Compaction Test. Set the swell gauge to zero and record the time of the start of test. The test will be stopped when the swell terminated.

Deep Soil Mixing (DSM)

The use of the soil mixing to improve the engineering properties of soft soil and contaminated soil is very well known for a long time. In this method soils are mixed in situ with stabilized binders. The stabilized material will produced the higher strength, lower permeability, and lower compressibility and lower swell potential than native soil. The improvement becomes possible by cation exchange at the surface clay minerals, bounding of soil particles and/or filling of void by chemical reaction product. The widely used binder are cement and lime, but slag, gypsum, fly ash and secondary products are also used.

The soil mixing can be divided into two general methods: the deep soil mixing and shallow soil mixing. The DSM is an applied for in situ stabilization of soil to minimum depth of 1.5 m (depend on mass stabilization). Generally DSM can be performed in two techniques of mixing, dry mixing and wet mixing. In the wet mixing, the soil is mixed with additives that have been in slurry, while the dry mixing soil mixed with additives in dry conditions.

The model for predicting the heave of expansive subsoil was based on the variation of swell pressures with depth and is presented in the following equation (Fredlund and Rahardjo 1993):

$$\Delta h = \sum_{i=1}^{n} \frac{C_{s,i} h_i}{1+e_{0,i}} \log \frac{p'_{f,i}}{p'_{s,i}} \quad (3)$$

Where:
$C_{s,i}$: swell index
$e_{o,i}$: initial void ratio
$p'_{f,i}$: final stress (overburden ± any change of total stress)
$p'_{s,i}$: initial swell pressure (suction).
h_i : thickness of each layer

According to Rao at. al. (1988) in unsaturated expansive soil the initial swell pressure could be measured as the corrected swell pressure, $p'_{s,i}$ from the constant volume type oedometer test. The final stress state, $p'_{f,i}$, accounts for the overburden stress, as well as any net change in total stress from either excavation or surcharge type loading. The Eq. (3) was modified into Eq. (4).

$$\Delta h = \sum_{i=1}^{n} \frac{C_{s,comp,i} h_i}{1+e_{0.i}^{comp}} \log \frac{p'_{f,comp,i}}{p'_{s,comp,i}} \quad (4)$$

Where the parameter $C_{s,comp,i}$, $e_{0.i}^{comp}$, $p'_{f,comp,i}$ and $p'_{s,comp,i}$ are composite properties of layer i in the treated ground. The parameter could be estimated as shown following:

$$C_{s,comp,1} = C_{s,col}.a_r + C_{s,soil}.(1-a_r) \quad (5)$$

$$p'_{s,comp,1} = p'_{s,col}.a_r + p'_{s,soil}.(1-a_r) \quad (6)$$

Where subscript soil= untreated soil properties and subscript col = treated soil.

Because of initial void ratio and bulk unit weight for treated and untreated are the same and constant with depth and the composite properties $C_{s,comp,i}$, $p'_{s,comp,i}$ were also constant with depth, the Eq.(4) became more simple:

$$\Delta h = \sum_{i=1}^{n} \frac{C_{s,comp,i} h_i}{1+e_{0.}} \log \frac{p'_{f,,i}}{p'_{s,comp,i}} \quad (7)$$

Bearing Capacity of Composite Ground

Besides the compressibility, the improvement bearing capacity of expansive soil also important in application DSM. Some methods to calculate bearing capacity of composite ground (end bearing column) are expressed:

(1) Weighted method

$$q_u = c_{uc}\alpha + (1-\alpha)c_{us} \quad (8)$$

(2) Broms (2000); Bouassida and Porbaha (2004) Method

$$q_u = 0.7q_{uc}\alpha + \lambda(1-\alpha)c_{us} \quad (9)$$

Where:
c_{uc}: undrained shear strength of column
c_{us}: undrained shear strength of soil(untreated)
q_{uc}:unconfined compressive strength of column
α: repalcement area ratio
λ : 5.5 (Bergado at al., 1994)

Volume Ratio (stabilized soil ratio)

Estimate the stabilized area or volume ratio (if the treatment was not end bearing column) is required to reduce overall swelling to tolerable swelling (heave).

The diameter of DSM column depend on the availability of local DSM rigs. The area ratio of square arrangement could be calculate based on Eq. 10.

$$a_r = \frac{a_{col}}{a_{soil}+a_{col}} = \frac{\pi d_{col}^2 / 4}{s_{cc} \cdot s_{cc}} \quad (10)$$

where a_{col} = area of column DSM, d_{col} = diameter of column DSM and s_{cc} is space between 2 columns. Volume Ratio is calculated by area and length of column.

MATERIAL AND METHOD

Soil Properties

The characteristics of expansive soil in this study were shown table 1.

Table 1. Characteristics of expansive soil

Characteristic	Value
Liquid Limit (LL)	73.9%
Plastic Limit(PL)	30.4%
Shrinkage Limit(SL)	2.8%
Plasticity Index (PI)	43.1%
USCS	CH

Based on specification of PI and LL was proposed by Horz (1956), Raman (1967), Chen (1988) and Snethen (1977) the degree expansion of soil is high.

Box Model and Soil Preparation of Loading Test

Prime element that used is box, made of fiber glass with length 100 cm, width 50 cm and height 30 cm. The box use L profile as the frame and it made to be rigid enough for maintain strain plane condition. Fiberglass used as box to make observation easier in laboratory (Fig.3).

The loading test performed on the untreated soil with 27.9 % moisture content and dry unit weight 1.288 gr/cm^3 and treated soil in 25.8% water content and 15% fly ash (based on previous research). Compaction is controlled from weight of soil that is loaded into the box with a volume that is required. The fly ash and soil are mix in dry condition.

The holes in treated soil test are made by using a steel pipe of the same size with a diameter of DSM column (2cm). In this experiment attempted to vary spacing and depth to the composition of a single square (Fig.4)

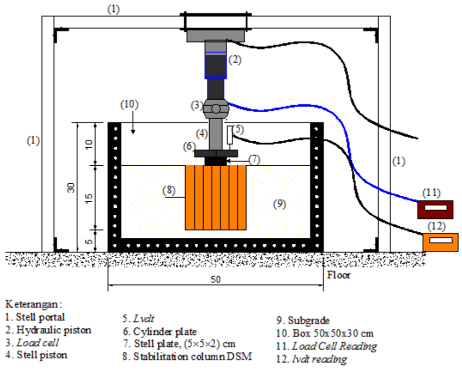

Fig. 3 Box experiment and loading test.

Treated soil is inserted into the hole with several layers. Each layer was compacted. The number of collisions is done by way of a preliminary study to obtain desirable density and curing in 3 days.

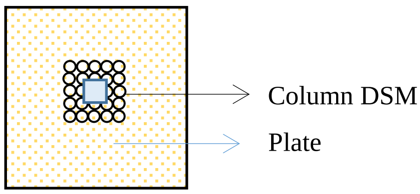

Fig. 4 Single square model

Variation of length and spacing of columns can be seen in Table 2.

Table 2 Length and Spacing of columns

Parameters	cm
Length (L)	B, 2B, 3B
Spacing(S)	D,1.25D, 1.5D

Where: B= width of loading plate (square) = 5 cm, D= diameter of column=2 cm.

Soil Preparation and Swelling Test

Swelling tests were applied for untreated and treated soil in the same condition (water content, dry density, cure time) in CBR mold. There are 1, 2, 3, 4, 5 and 6 column are made by treated soil and applied swelling test. The test is conducted to obtain relationship between volume ratio of stabilized soil and swelling potential. The relation will be used to estimate swell potential in small scale model.

Unconfined Compressive Strength Test

Unconfined Compressive Strength tests was applied to investigate the change of un-drained cohesive (cu) after improvement and also sensitivity of expansive soil.

RESULTS AND DISCUSION

Un-drained Cohesive Strength of soil Improvement

Clay soil exhibit significant increase in strength when treated with fly ash. The table 3 shows the measured value of un-drained shear strength in undisturbed, remolded, optimum water content without treated and treated sample.

Table 3 Un-drained shear strength of such condition expansive soil

Sample	Water content (%)	cu (kg/cm^2)
undisturbed	49.46	0.253
Compacted soil	27.8 (OMC)	0.643
Treated soil	25.8	0.981

The strength of expansive soil increase 155% by compaction method and increase 289% by mixed by fly ash in optimum content.

Spacing and Length Column Effect to Strength and Settlement

One the most important analyses of DSM is control of settlement of structure. Fig. 5 shown the relation between stress and settlement of soil. The untreated soil reached ultimate stress at 380 kN/m^2. At the same stress, the treated soil by DSM column establish small settlement. It made sense the treated soil was stiffer than untreated one.

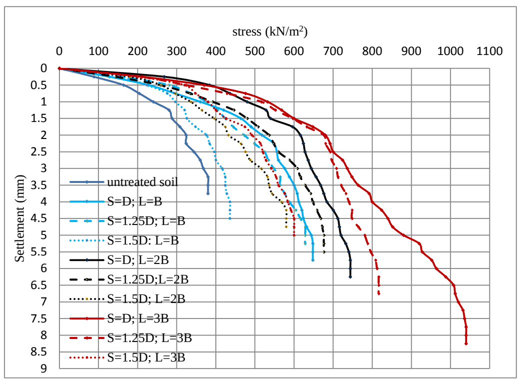

Fig.5 Relation between stress and settlement of length and column spacing of DSM

The longest and closest column reached peak load value. The result showed linear elastic perfectly plastic behavior of DSM columns. Based on Euro Soil Stab (2012), the curve is linear up to the long term strength (creep strength) and then the exceeded load is assumed to be constant as shown in Fig.6.

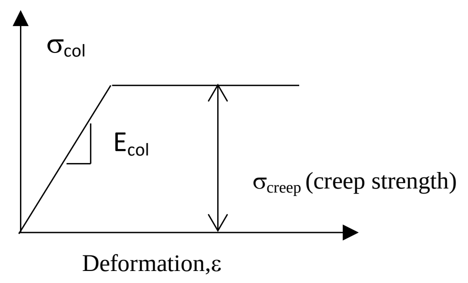

Fig. 6 Stress and deformation in column stabilized soil (Euro Soil Stab)

Bearing Capacity Improvement (BCI)

Bearing capacity improvement is a measure how high the improvement method to increase ultimate bearing capacity. Based on 3 variations of spacing and length of column, relation between Bearing Capacity Improvement and the parameters could be analyzed. The experiment give the result the highest BCI is 2.73 for the longest and nearest column spacing and the lowest one is 1.147 for the shortest and widest space column (Fig.7).

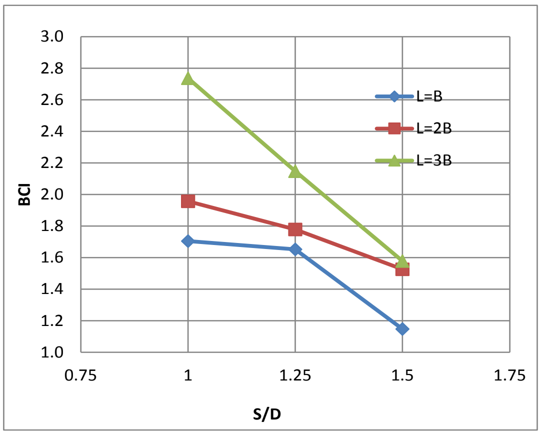

Fig. 7 BCI of soil for difference space and length of DSM column

Length and spacing of the columns have highly impact affect to the area or volume of soil improvement so as to give effect to an increase in the strength capacity of the soil as show in Fig.8. In this study the relation between volume of stabilized soil and bearing capacity was nonlinear. But based on Eq. 8 and 9, relations between bearing capacity and the ratio of the stabilized soil is linear for end bearing column.

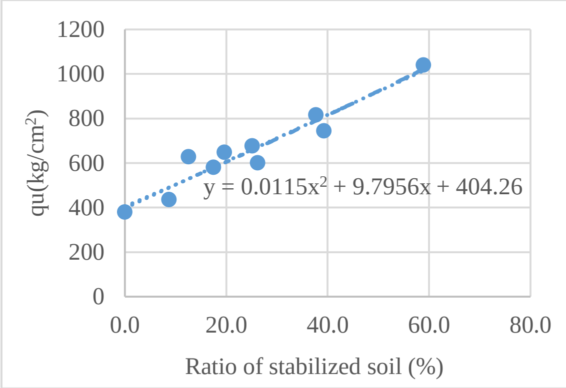

Fig. 8 Influence Stabilized Area to Bearing Capacity

The Swelling Potential of Improvement Soil

The swelling potential is comparison of volume change to initial volume in percentage. The observation of swell potential for DSM method was done by variation of number of column soil improvement. In this case the volume of soil improvement was change and the swell potential are measured.

The relationship between ratio of soil improvement volume and swell potential shown in Fig. 9.

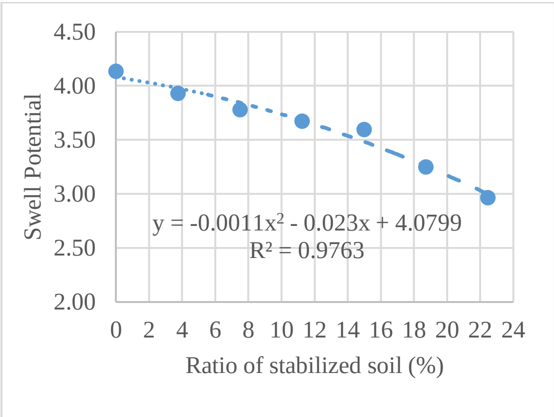

Fig. 8 Ratio of improvement soil and swell potential

The regression analysis was applied to data sample and gave the formulation as follows:

$$y = -0.0011x^2 - 0.023x + 4.0799 \qquad (11)$$

The equation was used to observe swell potential of DSM in scale model. The increasing ratio of volume of stabilized soil will decrease swell potential. There are some factors influence to decrease of swell potential such as characteristic expansive soil, type of binder, water content, curing time and mixing methodology.

The estimation of swell potential of DSM at square arrangement could be read in Table 4.

Table 4 Swell potential of square arrangement DSM

Spacing of column	Length of column	Ratio of Stabilized soil	Eq.11
untreated soil		0.00	4.08
D	B	19.63	3.20
2D	B	12.57	3.62
3D	B	8.73	3.80
D	2B	39.27	1.48
2D	2B	25.13	2.81
3D	2B	17.45	3.34
D	3B	58.90	-1.09
2D	3B	37.70	1.65
3D	3B	26.18	2.72

The tolerable heave for flexible pavement is generally on the order of 12 mm and the swell potential for untreated soil is 4.08%. If it assumed the depth of potential swelling in field is 1.5m= 150 cm and the ratio of stabilized was 45% then the swell potential was 0.8%, the tolerable condition can be reach.

SUMMARY AND CONCLUSION

This study is research a small scale in laboratory to evaluate DSM construction for stabilizing expansive soil to predict the condition in actual field.

Prior to DSM construction, laboratory mix design need to conduct such as swelling and strength untreated and treated soil in optimum dosage of binder.

The variation of space and depth of column are directly influence to ratio of stabilized soil and also strength and swell potential. The relation is not in linear function in which increasing of ratio will increase strength and decrease swelling.

To choose geometric parameter such as diameter and depth in installation pattern (square, triangular), it is needed study intensively about swell potential, binder content and also water content in field.

REFERENCES

[1] Asano, J, Ban, K and Azuma, K,” Deep mixing method of soil stabilization using coal ash”, Proc. The second international conference on grouting improvement geosystem, Balkema Rotterdam, 1996, pp.392-398.

[2] Bergado, D.T, Chai, J.C, Alfaro, M.C and Balasubramaniam, A.S,” Improvement techniques of soft ground in subsiding and lowland environment”, 1994, Balkema, Retterdam, 1-220.

[3] Boussida, M, Porbaha,”Ultimate bearing capacity of soft clays reinforces by a group of column application to a deep mixing technique”, Soils and foundations, 2004, vol.44, No.3, pp. 91-101.

[4] Broms, B.B,” Lime and lime/columns, summary and visions, Proceeding 4th international conference on ground improvement geo-system, 2000, vol. 1, 43.

[5] Chen, F.H.” The use of piers to prevent the uplifting of lightly loaded structure founded on expansive soil, Concluding Proc. Eng. Effects of moisture change in soils, Int. Res. Eng. Conf. expansive clay soil, 1965, Texas A&M Press, pp.152-171.

[6] Euro Soil Stab,” Development of design and construction methods to stabilize soft organic soil: Design guide soft soil stabilization, CT97-0351, Project no.BE-3177

[7] Fredlund, D G, Raharjo, H,” Overview of unsaturated soil behavior”, Proc. Unsaturated soil, 1993, ASCE, pp. 1-31.

[8] Holtz, W.G and Gibbs, ”Engineering properties of expansive clays’, Transaction ASCE, 1956, Vol.121, Issue 1,pp. 641-677.

[9] Madhyannapu, RS and Puppala, AJ, Nazarian, S, Yuan, D ,”Quality assessment and quality control of deep soil mixing construction for stabilizing expansive sub soils ”, J. Geotechnic & Geo-environment Engineering, 10.1061/(ASCE) GT.1943-5606.0000188, 2010, pp. 119 – 128.

[10] Madhyannapu, RS and Puppala, AJ ,”Design and construction guidelines for deep soil mixing to stabilize expansive soil”, J. Geotech. Geoenviron. Eng., 10.1061/(ASCE)GT.1943-5606.0001149, 2014, Pp. 04014051-1-04014051-14.

[11] Rahmansyah,A,” Improvement of expansive soil of east java, Indonesia by using industrial solid waste”, Proc. Int. Conf. on unsaturated soil UNSAT, 2014, Sydney, Australia.

[12] Raman,V,” Identification of expansive soils from plasticity index and the shrinkage index data”, Indian Eng., 1967, Calcuta 11(1), pp. 17-22.

[13] Ratman, N, Suwarti, T, and Samodra, H, “Peta Geologi Indonesia, Lembar Surabaya, skala 1:1000.000, Pusat Penelitian dan Pengembangan Geologi, 1998, Bandung (indonesia version)

[14] Rao, R.R, Rahardjo,H, Fredlund, D.G, Closed form heave solutions for expansive soils,

Journal Geotecnical Engineering, 1988, Vol.114, No.5, Pp. 573-588.

[15] Snethen, D.R, Johnson,L.D and Patrick,D.M," An evaluation of expedient methodology for identification of potentially expansive soil, soil and pavement lab.", US Army Eng.,1977, Waterway Exp.Sta, Vicksburg, MS,Rep. No. FHWA-RE-77-94,NTIS, PB-289-164.

[16] Seed,H.B, Woodward. R.J and Lundgren, R," Prediction of swelling pontential for compected clay", Journal ASCE, Soil Mechanics and Foundation Division, 1962,Vol. 88, Issue 3, pp. 53-88.

[17] Wesley, L D, " Fundamental of Soil Mechanics for Sedimentary and Residual Soils, 2010,John Wiley and Sons

[18] Yapage, N.N.S, Liyanapathirana, DS, Kelly, RB, Poulos, HG, Leo, CJ," Numerical Modeling of an Embankment over soft ground improved with deep cement mixed column: case story", Journal Geotech. Geoenviron Eng. 10.1061/(ASCE) GT.1943-5606.0001165, 2014, pp. 04014062-1-04014062-10.

Sixth International Conference on Geotechnique, Construction Materials and Environment, Bangkok, Thailand, Nov. 14-16, 2016, ISBN: 978-4-9905958-6-9 C3051

3D-FE ANALYSES OF PILED RAFT FOUNDATION WITH CONSOLIDATION IN BANGKOK SUBSOIL CONDITION

K. Watcharasawe[1], P. Kitiyodom[2] and P. Jongpradist[1]
[1,3]Faculty of Engineering, King Mongkut's University of Technology Thonburi, Thailand
[2]Geotechnical & Foundation Engineering Co., Ltd. (GFE), Thailand

ABSTRACT

This study focused on the investigation of influencing factors on behaviour of piled raft foundation in Bangkok subsoil. To evaluate the possibility of implementing this system in Bangkok subsoil condition, this research performed the consolidation analyses of piled raft foundation systems for low-rise (8-storey) and high-rise (25-storey) buildings with basement levels in clay soil, using three-dimensional Finite Element Method. The soils are modelled with Hardening Soil model and Mohr-Coulomb model. Evaluations of piled raft foundation, i.e., the load sharing ratio of piles, settlement behaviours in the foundation system are performed. The parametric study on the effect of raft depth, and load carried by piles of piled raft was done. The consolidation had a strong influence on the load carried by piles of the piled raft foundation in Bangkok. The load shared by piles can increase by up to 12% and 6% for low rise and high-rise buildings, respectively due to the consolidation effect. Therefore, the design of the piled raft foundation system in Bangkok subsoil essentially consider the consolidation effect.

Keywords: 3D-FEM, Bangkok subsoil, Consolidation, piled rafts, Piled-raft load sharing, Softs soil

INTRODUCTION

In Bangkok, there are many building projects constructed on soft soil. As the subsoil of this area consists 13-16 m thick soft clay and stiff clay interspersed with sand [1], the pile foundation must be used to transfer the load to stiff soil layers. Normally, the design and construction of foundation system on soft ground have posed various problems to geotechnical engineers, such as consolidation, excessive settlement, negative skin friction and bearing capacity failure. To avoid these problems, the structure of foundation in this area are relatively expensive.

In Thailand, the designers prefer to consider the pile group to support a structure [2]. The pile groups mostly focus on pile capacity and group settlement without considering the presence of the raft or mat. In fact the foundations are built using concrete and their bottom surfaces are attached to the soil beneath. Therefore, in most cases end up with overdesign of the foundation.

Typically, new office or residential buildings require 2 or more basements (depth10-20m.) for utilizing as a car park space. Meanwhile, the foundation has constructed in deeper level. This means that the mat foundations is placed on the stiff soil. Therefore, the soil bearing capacity are increasing at the bottom of the mat foundations. In recent years, the foundation engineers tend to combine these two separate systems (between shallow foundations (rafts) and deep foundations (piles)). Such a foundation system is referred to as piled raft foundation.

Recent years, the “Piled Raft Foundations” (PRF) have been widely accepted as one of the most economical methods of foundation systems [3, 4]. Thus, the piled raft systems have been used extensively in many parts of the world e.g. England [5], Japan [6], Germany [7, 9, 10]. The application of piled rafts on soft ground is becoming a significant issue in foundation design. A few successful applications and analysis of piled rafts on soft ground have been reported [8, 13]. However, the behaviour of piled raft foundation supporting the structure in clay soil was found that the long-term effect (consolidation) increases the load carried by piles and decreases raft contact pressure [5]. This means that the effect of consolidation in clay has influence on piled raft foundation system. Previous studies on numerical analysis of piled raft foundation in Bangkok subsoil condition indicated the potential of using PRF in Bangkok subsoil [2, 14]. However, they considered only short term behaviour.

To pay special to the consolidation effect, a coupled three-dimensional (3D) mechanical and hydraulic numerical model is used to analysis the behaviour of piled raft in Bangkok subsoil. The model considers the dissipation of excess pore water pressure in saturated clays. Two different building sizes, i.e., low-rise (8-storey) and high-rise (25-storey) buildings with basements are considered in this study to evaluate the potential of using the piled raft system. The main factor to be investigated its influence is the level of raft under long-term condition.

PILED RAFT WITH CONSOLIDATION

The PRF is a complex design of foundation that combines the bearing effect of both foundation elements (piles and raft) [11]. In Bangkok subsoil condition the characteristics of soft soils are high compressibility, low shear strength and high water content.

Consolidation is a process by which soils decrease in volume. In general, it is the process in which reduction in volume takes place by expulsion of water under long term static loads. When the consolidation settlement occurs, the soil at the bottom of the raft are deformed. Therefore, the consolidation may have a strong influence on the load carried by raft, which consequently affect the load carried by piles. In this study, only the settlement due to consolidation is of interest. The value of incremental of consolidation settlement "ΔS_{end}" is defined as shown in Fig 1.

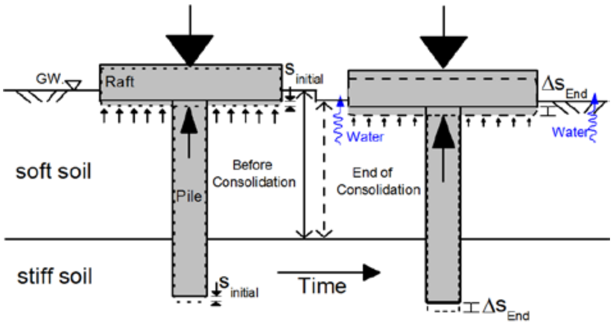

Fig. 1 Concept of piled raft foundation with consolidation.

Both, piles and raft are considered in the load distribution process:

$$P_{tot} = P_p + P_r \tag{1}$$

where P_{tot} = total load of the building; P_p = load carried by the pile group; P_r = load carried by the raft.

The bearing behaviour of the piled raft is commonly described by the piled raft coefficient or the load sharing ratio of piles α_{pr} which is defined by the ratio between the sum of load carried by pile and the total load of the building:

$$\alpha_{pr} = \frac{\sum R_{pile,i}}{R_{tot}} \tag{2}$$

$$\alpha_{PG} = 1 \tag{3}$$

where α_{pr} = the load sharing ratio of piles; $\sum R_{pile,i}$ = the amount of the pile loads; R_{tot} = total load of the structure. α_{PG} = the load sharing ratio of pile group.

$$\alpha_{\Delta} = \alpha_{final} - \alpha_{initial} \tag{4}$$

The effect of consolidation settlement is considered in load sharing ratio of pile. As mentioned previously α_{final} = the load sharing ratio of pile at end of settlement; α_{intial} = the load sharing ratio of pile before consolidation.

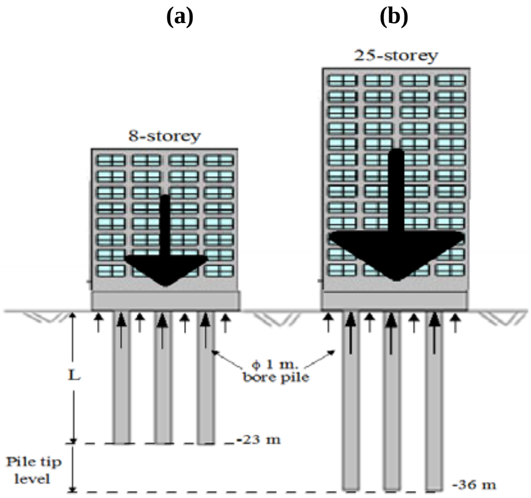

Fig. 2 Reference Case (a) LR-PR, (b) HR-PR

NUMERICAL MODELING OF PILED RAFT FOUNDATION ANALYSIS

Reference Case

A parametric study was considering 9 × 9 m, and 1 m. thick raft with 9 piles. The low-rise (8-storey) and high-rise (25-storey) buildings with basements are considered in this study. Both Low-Rise-Piled Raft (LR-PR) and High Rise-Piled Raft (HR-PR) having identical characteristics as shown in Fig 2 (a) and 2 (b), respectively.

The pile foundation in this study was designed following the pile group concept with a safety factor (FS) of 2.3 for each single pile, which is the current design in engineering practice. The raft level is varied from 0 to 10 m below the ground level. The bored piles have 1 m diameter (d) being arranged in the foundation with the spacing of 3 m. The level of pile tip is at 23 (1^{st} stiff clay layer) and 36 m (2^{nd} sand layer) below the ground surface for low-rise and high-rise buildings, respectively. Summary of the analysis cases is shown in Table 1.

Table 1. Summary of piled raft foundation of numerical analyses conducted.

Building	Pile spacing	Pile tip level (m)	Raft level (m)	Total load (kPa)
Low-rise 8-storey	3*d**	23^{f**}	0	140
			4	146
			8	152
			10	158
High-rise 25-storey	3*d**	36^{e**}	0	350
			4	356
			8	362
			10	368

* *d* (pile diameter): 1 m.

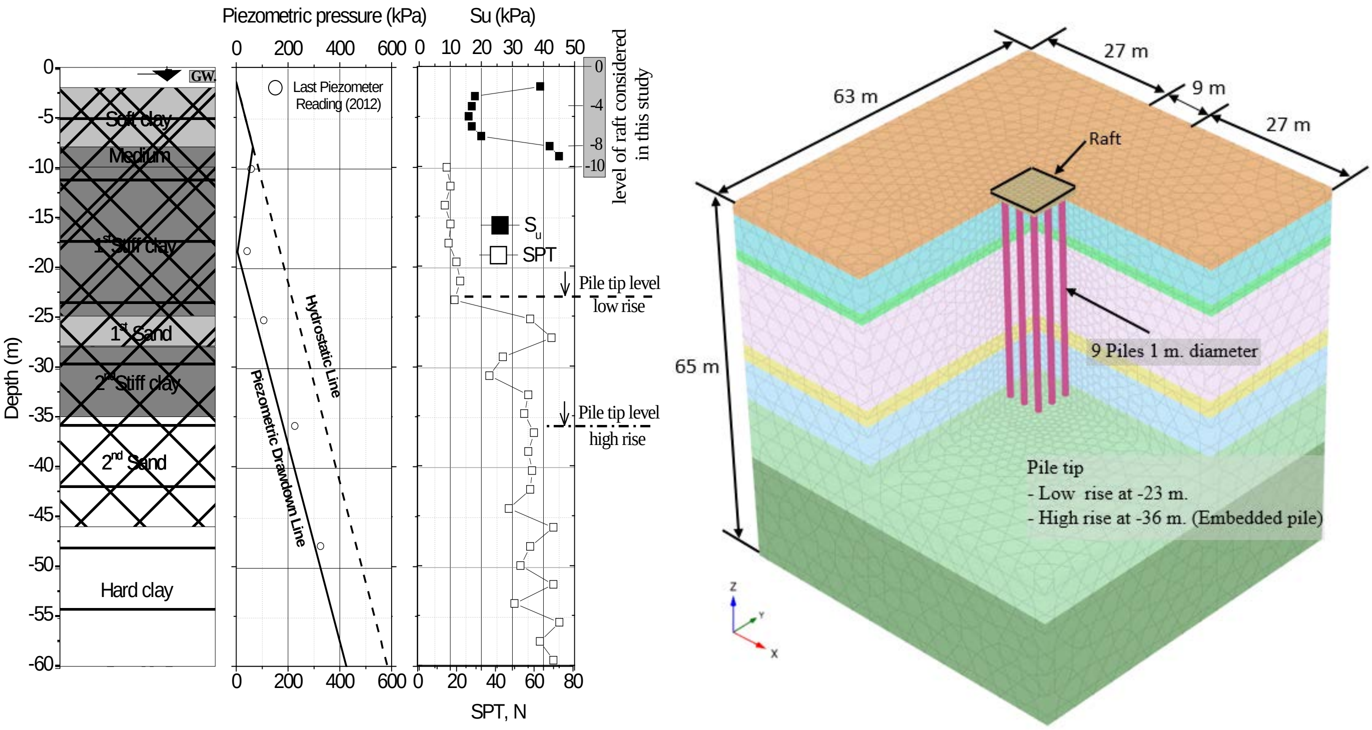

Fig 3 Soil profile and Piezometric line (a), Geometry of the problem and 3D Finite element mesh used in this study (b).

(a) (b)

** f: floating pile in clay; e: end bearing in sand layer.

Applied Load

Uniformly Distributed Loads (UDL) is used in this analysis. The weight of the structure and designed load were computed. These UDL are applied on top surface of the raft in analyses of PRF. The basement is considered to apply the load of 50 ton per level. The total applied loads on each foundation are listed in Table 1.

Subsoil Condition

The subsoil profile in this study are referred from that in the north of Bangkok. The generalized profiles of the stratified soil at the considered location are shown in Fig 3(a). The uppermost 2.0 m thick layer is the weathered crust, which is underlain by 6.0 m thick soft to medium clay layer. A medium clay layer is found at the depth of 8.0 m from the surface. Below the medium clay is stiff clay; the thickness is about 15m. The first sand layer is generally found at a depth of 25 to 30m. Below the upper first sand layer, there is stiff clay and further down alternating layers of dense sand and hard clay. The ground water table is below the ground surface at 1.5 m [14, 15]. The pore water pressure condition in Bangkok soft clay are hydrostatic from 1m below ground surface. Then the piezometric changed to drawdown near middle of clay layer as shown in Fig 3(a) [22]. The piezometric drawdown pressure was considered in this study.

Modeling and Boundary Condition

The geometry of the problem and FE mesh simulation of the piled raft foundation are shown in Fig. 3(b) and Fig. 4. The 3D-FEA using PLAXIS 3D version 2013 was carried out in this study. A coupled mechanical and hydraulic model was used for the consolidation analysis. The 3D model included a rigorous treatment of the soil and raft which were represented by volume elements. The piles are modeled as embedded piles in which the pile is assumed to be a slender beam element. The boundary conditions adopted for analyses are displacement restraints with roller supports applied on all vertical sides and pin supports applied to the base of the mesh. The layer surface (upper and bottom side) is allowed to drain while the other sides are kept undrained by imposing closed consolidation boundary conditions.

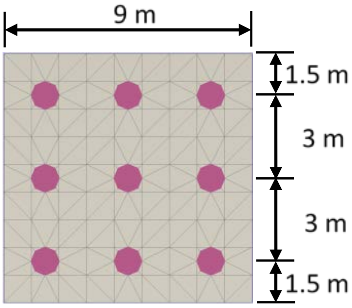

Fig 4 Adopted piled-raft geometry.

of pile reduces from 95% to 80% and 98% to 91% with increasing raft levels (0-10 m.) for the low-rise and high-rise buildings, respectively.

At the end of consolidation, the load sharing ratio of pile increases 2% to 12% and 1% to 6% with increasing raft levels (0-10 m.) for the low-rise and high-rise buildings respectively. Significant changes of load sharing by raft are obviously observed. This leads to the long-term load sharing by piles of 92% to 98% and 97% to 99% for the low-rise and high-rise buildings respectively. This means that the consolidation has a strong influence on the load carried by piles of the PRF in Bangkok subsoil.

Table 3 Constitutive models and model parameters used in analyses

Material		Model	γ_t (kN/m³)	Material behaviour	S_u (kPa)	C' (kPa)	ϕ (∘)	E_u, E' (kPa)	E_{50}^{ref}, E_{oed}^{ref} (kPa)	E_{ur}^{ref} (kPa)	G_0^{ref} (kPa)	Permeability coefficient, k (m/d)	$\gamma_{0.7}$	m	p_{ref} (kPa)	v, v_{ur}
Subsoil	**Depth (m.)**															
Weathered clay	0-2	MCM	17	Undrained	40			6000				-				0.3
Soft clay	2-8	HSS	15.2	Undrained		0	23		7000	23280	8954	5 x10^{-4}	1x10^{-4}	1	100	0.33
Medium clay	8-10	HSS	18.4	Undrained		0	24		10300	30900	22800	2.5 x10^{-4}	1x10^{-4}	1	100	0.32
1st Stiff clay	10-25	HSS	19	Undrained		0	26		25400	83900	32270	2.5 x10^{-4}	2x10^{-3}	1	552	0.32
1st Sand	25-28	MCM	20	Drained		-	36	85800				1.6				0.3
2nd Stiff clay	28-35	MCM	20	Undrained	192			96000				2.5 x10^{-4}				0.3
2nd Sand	35-46	MCM	20	Drained		-	37	96200				0.8				0.3
Hard clay	46-60	MCM	20	Undrained	223			111500				2.5 x10^{-4}				0.3
Foundation																
Bored Pile	Tip -23,-36	LEM	6-8	Non-porous				2.6x10^7								0.2
Raft	0,-4,-8,-10	LEM	24	Non-porous				2.8x10^7								0.2

Constitutive Models and Parameters

The soft clay, medium clay and first stiff clay layers were modelled with Hardening Soil Model with small strain [14, 16]. The 1st -2nd sand, 2nd stiff clay and hard clay layers were modelled with Mohr–Coulomb model. The soil properties used in the analyses are mainly determined from correlating local investigated data with comprehensive in situ tests of MRT projects [17] and previous laboratory tests from Asian Institute of Technology (AIT) [18-20]. Table 3 summarizes the material parameters used in the analyses.

COMPUTED RESULTS

Effect of the Load Sharing Ratio of Piles against Time with Differential Raft Level.

Fig. 5 shows the load sharing ratio of piles for different raft levels below the ground surface and time for both building types. The analysis results show that when the raft was placed on deeper soil layer, the load sharing ratio of pile has been decreased significantly. For subsoil condition and problem characteristics in this study, before consolidation, the load sharing ratio

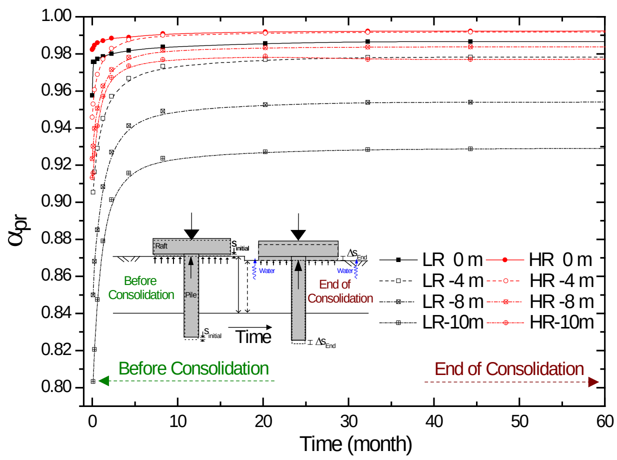

Fig. 5 Load sharing ratio of piles (α_{pr}) versus Time and raft level of different building types.

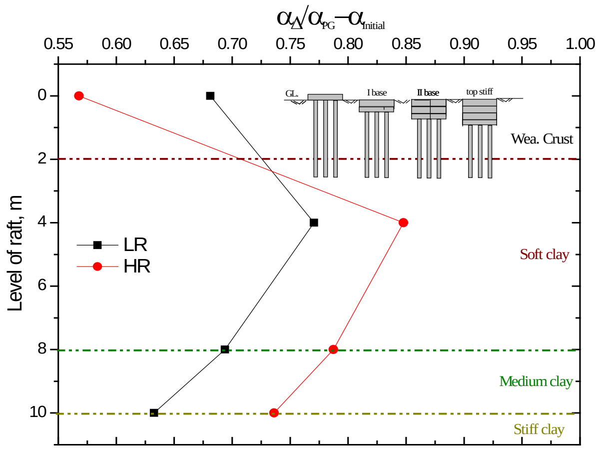

Fig. 6 Variation of load sharing ratio of piles versus raft level of different building types

Fig. 6 illustrated the computed variation of load sharing ratio of piles versus raft level with different building types. The variation is the difference load sharing ratio of pile between short term and end of consolidation process ($\alpha_\Delta = \alpha_{final} - \alpha_{initial}$ in Eq. (4)). The variation of load sharing ratio of piles seems to decrease with increasing raft level between -4 m to -10 m.

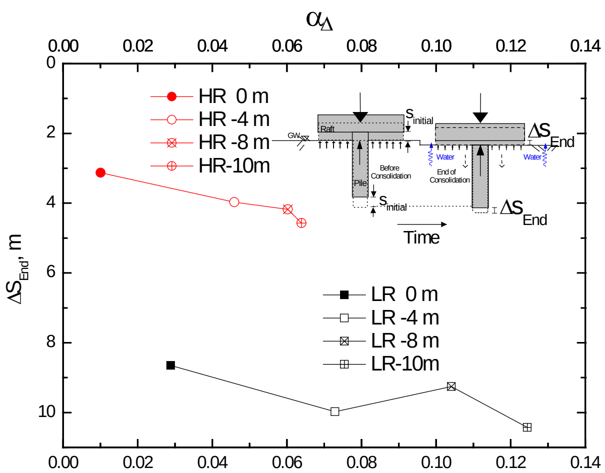

Fig. 7 Incremental settlement at end of consolidation ΔS_{end} versus the load sharing ratio of, α_Δ

Settlement of PRF and Load Sharing Ratio

The incremental settlement of consolidation ΔS_{end} and load sharing ratio of pile between short term and end of consolidation process (α_Δ) with different raft levels are shown in Fig 7. The analysis results show that the incremental consolidation settlement "ΔS_{end}" has significant influence on the incremental load sharing ratio of piles "α_Δ". For subsoil condition and problem characteristics in this study, the incremental consolidation settlement "ΔS_{end}" increases with increasing raft level. The incremental load sharing ratio of pile in consolidation process (α_Δ) increase with increasing incremental consolidation settlement ΔS_{end}. For low-rise building, the ΔS_{end} increase from 8.6 to 10.4 mm. with increasing α_Δ from 3% to 12% when increasing raft (0-10 m.). For the case of high-rise building, the ΔS_{end} increase from 8.6 to 10.4 mm. with increasing α_Δ from 1% to 6.5% with increasing raft level.

CONCLUSION

This article presents the results of numerical analyses of the PRF in the subsoil condition of north Bangkok, using 3-D FEM to investigate the effect of raft level on load shared by piles in Bangkok subsoil condition and paying special attention to the consolidation effect.

The analysis result in terms of load shared by piles with consolidation effect for the PRF case in this study in Bangkok subsoil condition can be summarized as follows:

- The consolidation had a strong influence on the load carried by piles of piled raft foundation in Bangkok. The load shared by piles can increase by up to 12% and 6% for low rise and high-rise buildings, respectively. Therefore, the design of the piled raft foundation system in Bangkok subsoil should consider the consolidation.

- The incremental consolidation settlement "ΔS_{end}" has significant influence on the incremental load sharing ratio of piles "α_Δ". The incremental load sharing ratio of pile in consolidation process (α_Δ) increase with increasing incremental consolidation settlement ΔS_{end}.

Since the pile foundation was designed using the pile group concept with high FS. The raft is not considered in the design of which the FS of the pile can be smaller. Higher efficiency of the system can be expected. Further study with less FS of pile should be done, to confirm effectiveness of PRF.

ACKNOWLEDGEMENT

The authors gratefully acknowledge financial support by Thailand Research Fund (TRF) and Geotechnical & Foundation Engineering Co., Ltd. (GFE) through the TRF-Rri Project under Contract No 5811005.

REFERENCES

[1] Thasnanipan N, Aye Z, Submaneewong C, and Teparaksa W, "Performance of Wet-Process Bored Piles Constructed with Polymer-Based Slurry in Bangkok Subsoil" Deep Foundations 2002, pp. 143-157.

[2] Amornfa K, Phienwej N, and Kitpayuck P, "Current practice on foundation design of high-rise buildings in Bangkok, Thailand", Lowland technology international, 2012, Vol. 14, pp. 70-83.

[3] Randolph M.F, "Design methods for pile groups and piled rafts" In Proceedings of the 13th International Conference on Soil Mechanics and Foundation Engineering, New Delhi, 1994, Vol. 5, pp. 1–82.

[4] Poulos H. G., "Piled raft foundations: design and application" Geotechnique, 2001, Vol. 51(2), pp. 95-113.

[5] Hooper J.A., "Observations on the Behaviour of a Piled-Raft Foundation on London Clay", Proc. Instn. Civil Engrs, 1973, Vol. 55, pp. 855- 877.

[6] Yamashita K., Yamada T, and Kakurai M, "Simplified method for analyzing piled raft foundations" In Proceedings of the Third International Geotechnical Seminar on Deep Foundation on Bored and Auger Piles, 1998, pp. 457–464.

[7] Poulos H. G, and Davis E. H., "Pile foundation analysis and design" *New York: Wiley*. 1980.

[8] Yamashita K, Kakurai M, and Yamada T, "Investigation of a piled raft foundation on stiff clay" Proceeding of the 13th International Conference on Soil Mechanics and Foundation Engineering, New Delhi, 1994, pp. 543-546.

[9] El-Mossalamy Y, El-Nahhas F, and Essawy A, "Innovative Use of Piled Raft Foundation to Optimize the Design of High-Rise Buildings" 10th Arab Structural Engineering Conference, 2006, pp. 13-15 November 2006, Kuwait

[10] Randolph M. F., "Design of pile raft foundations" Recent Development in Laboratory and Field Tests and Analysis of Geotechnical Problems, Bangkok, 1983, pp. 525-537.

[11] Katzenbach R, Arslan U and Moormann C, "Piled raft foundation in Germany In H. J.A. (Ed.)", Design applications of raft foundations, London, Thomas Telford Ltd, 2000, pp. 323-391.

[12] Poulos H.G., "Piled raft and compensated piled raft foundations for soft soil sites. Advances on designing and testing deep foundations" Geotech. Spec. Publ, ASCE, 2005, Vol.129, pp. 214–235.

[13] Tan Y.C., Cheah S.W., and Taha M.R., "Methodology for design of piled raft for 5-story buildings on very soft clay" Foundation analysis and design: innovative methods. Geotech, Spec. Publ. ASCE, 2006, Vol. 153, pp 226–233.

[14] Watcharasawe K, Kitiyodom P, and Jongpradist P., "Numerical Analyses of Piled Raft Foundation in soft soil using 3D-FEM", South-East Asian Geotechnical Society Journal, 2015, Vol. 46(1), pp. 109-116.

[15] Jamsawang P, Bergado D. T, and Voottipruex P, "Field behavior of stiffened deep cement mixing piles" Ground Improvement, 2010**,** Vol**.** 164(1)**,** pp. 33-49.

[16] Detkhong T, and Jongpradist P, "Impact of Constitutive model on the Numerical Analysis of Tunneling in Bangkok Clay", Conference on Advances in Civil Engineering for Sustainable Development, 2014, pp. 349-354.

[17] Prust R.E., Davies J, Hu S, "Pressuremeter investigation for mass rapid transit in Bangkok" Thailand, Journal of the transportation research board, Transportation research of the national academies, Washington, DC, 2005, pp. 207–217.

[18] Jamsawanga P, Yoobanpota N, Thanasisathita N, Voottipruex P, and Jongpradist P, "Three-dimensional numerical analysis of a DCM column-supported highway embankment", Computers and Geotechnics, 2016, Vol 72, pp. 42–56

[19] Bergado D.T, Youwai S, Teerawattanasuk C, and Visudmedanukul P, "The interaction mechanism and behavior of hexagonal wire mesh reinforced embankment with silty sand backfill on soft clay", Computers and Geotechnics, 2003, Vol. 30, pp. 517-534.

[20] Tanchaisawat T, Bergado D.T., and Voottipruex, P, "Numerical simulation and sensitivity analyses of full-scale test embankment with reinforced lightweight geomaterials on soft Bangkok clay", Geotextiles and Geomembranes, 2008, Vol. 26, pp. 498-511.

[21] Sawatparnich A, Sunitsakul J, and Kanhasing P, "Numerical Analysis of DOH Bearing Unit Sitting on Soft Bangkok Clay by Finite Element Method", Report No. RD. 256 Bureau of Road Research and Development, Department of Highways, Thailand, 2009,

[22] Department of Groundwater Resources, "A study on recovery of groundwater effect in Bangkok subsoil", Thailand, 2012

A STUDY ON PERMEABILITY OF SILICA MICRO-PARTICLES

Kentaro Uemura[1], Yukoh Hasunuma[1]
Takamitsu Sasaki[2], Koichi Nagao[3], Naoaki Suemasa[1] and Shunsuke Shimada[4]
[1]Tokyo City University Graduate Division, Japan; [2]Kyokado Engineering Co.,Ltd, Japan;
[3]Sato Kogyo, Japan; [4] Kyokado Co.,Ltd, Japan

ABSTRACT

Liquefaction has drawn an attention since the Niigata earthquake occurred in 1964. Since then, many construction methods for liquefaction countermeasures have been developed, and some of them are practically used at present. However, it is difficult for most of the countermeasures to be applied to the ground under existing buildings because the large equipment necessary for doing these methods cannot be set in narrow space. In this case, a permeable grouting method is generally adopted for the countermeasures, in which the injection material is required to be permeable to sandy ground and durable enough to maintain its effectiveness for long time. However, because the cost of such injection materials is expensive, silica micro-particles were chosen as an alternative injection material with relatively affordable and low cost in this study. In order to confirm the permeation characteristics of the silica micro-particles, a series of experiments and analysis using a proposed model of one-dimensional injection were carried out. As a result, the characteristics of permeating and clogging micro-particles in sand were confirmed through the experiments. In addition, the result of the analysis showed the clogging tendency similar to its experiment result

Keywords: Micro-particles, Permeability, Clogging, Liquefaction Countermeasure

INTRODUCTION

Not only the 2011 Tohoku earthquake but also the 2016 Kumamoto earthquake caused serious liquefaction damage to individual property. Though lots of researches and discussions have been done on liquefaction for long time, many existing buildings on alluvial plains and reclaimed land are still exposed to risks of liquefaction. It is, therefore, essential to devise countermeasures against liquefaction urgently.

Many construction methods for liquefaction countermeasures have been developed since the Niigata earthquake occurred in 1964 in Japan and some of them are practically used at present. Most of these methods, however, are applied only to important structures and buildings because large construction equipment is needed to perform it. Therefore, many existing buildings with high risk of liquefaction still remain not to be reinforced. In general, grouting methods are applied to the ground under such existing building because they can be executed even in narrow space as small-facilities are utilized for the construction and less construction byproduct is produced. A chemical grout [1] or a very fine cement grout [2] is widely used as an effective injection material for the grouting method. Their long term durability and high strength were verified through previous laboratory tests and field experiments, [3], [4]. In addition, recently developed suspension grouts such as an ultrafine cement grout with an average size of 1-3μm [5] and a superfine spherical silica grout with sub-micrometer scale [6] can permeate even in finer sand layers. Their durability and performance are confirmed to be as high as those of conventional cement grout. It is, however, difficult to apply these methods to detached houses because these grouting materials are still expensive. Therefore, the application of low-cost and affordable micro-particle with comparable performance is examined in this study. One of the improvement effects of permeating the micro-particles in sand layer is to increase the density of grouted sandy ground. Fig.1 shows the mechanism of ground improvement by the micro-particle permeation. According to the liquefaction evaluation method, so called F_L method, which is widely used as a simple ground liquefaction evaluation method in Japan [7], liquefaction resistance strength increases according as fine-grained soil fraction increases. On the contrary, several studies reported that liquefaction resistance of sand containing non-plastic fines was smaller than that without non-plastic fines at the same

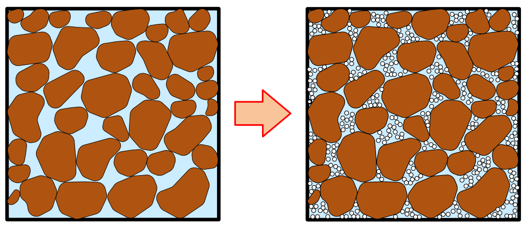

Fig.1 Ground improvement by injected micro-particles

Table 1 Physical properties of silica sand

-	Silica sand ♯4	Silica sand ♯5
ρ_s (g/cm^3)	2.638	2.640
ρ_{smax} (g/cm^3)	1.530	1.555
ρ_{smin} (g/cm^3)	1.305	1.300

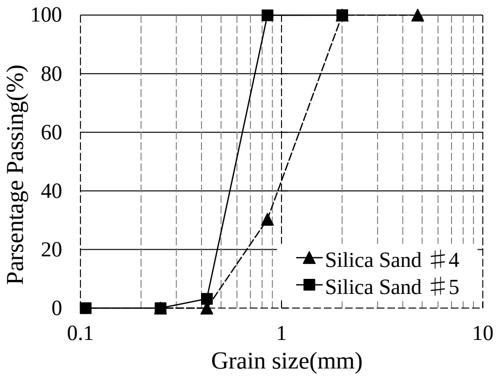

Fig.2 Grain size accumulation curve of silica sand #4 and #5

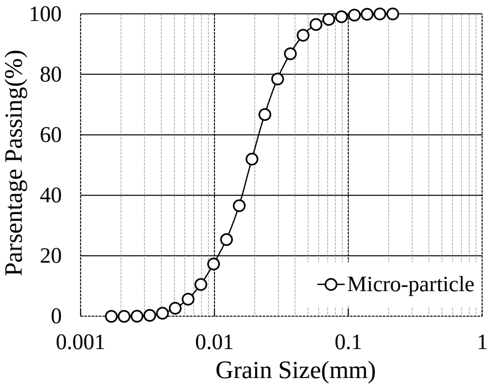

Fig.3 Grain size accumulation curve of micro-particles

Table 2 Conditions of experiment

Case	Silica sand	Concentration of micro-particle	Injection pressure
Case1	♯4	4.0%	10 kPa
Case2	♯4	4.0%	30 kPa
Case3	♯4	4.0%	60 kPa
Case4	♯5	4.0%	10 kPa
Case5	♯5	4.0%	30 kPa
Case6	♯5	4.0%	60 kPa

density [8], [9], [10]. At this point, it is not clear in what way micro-particles are permeated and deposited in sand layer and whether the deposited particles increase the liquefaction resistance of the sand. In particular, as ground layer conditions and the soil structures are so complex, the permeability of micro-particles is still unclear [11]. In this research, in order to confirm the permeation characteristics of micro-particles, experiments and simple analysis of one-dimensional injection were carried out.

ONE-DIMENSIONAL INJECTION EXPERIMENT

In this chapter, the characteristics of micro-particles on permeation were confirmed by the experiments using a short column and a multi-layer divided column. Here, volume compressibility of sand skeleton is neglected in these experiments. Table 1 and Fig.2 show the physical properties and the grain size accumulation curves of silica sand ♯4 and ♯5, respectively. A sand specimen was prepared by the air-pluviation method at specified relative density in an acrylic column, which was saturated by injecting de-aired water after inflow of CO_2 gas. Then, a series of permeation tests was examined by injecting water containing micro-particles. The grain size accumulation curve of the micro-particles is shown in Fig.3.

Experiments Using Short Columns

Conditions of Experiment

A series of injection laboratory experiments was conducted in order to confirm the permeability of micro-particles which way vary with the conditions of sand specimen and the initial injection velocity permeated into. In this test, silica sands ♯4 and ♯5 were used for the specimens and their physical properties and grain size accumulation curves are shown in Table 1 and Fig.2, respectively. The sand specimen with 5.0cm in diameter and 15.0cm tall was prepared by the air-pluviation method at relative density of 60%. The injection material mixed with water, which weight concentration of micro-particle in the mixed water was set to 4.0%, was permeated into the specimen. The volume of the injection material accumulated in the specimen was estimated by measuring the weight change of the specimen with a platform scale. Table 2 shows the conditions of these experiments. Different grouting velocity was set to each specimen by changing injection pressure. In this experiment, Injection pressure controlled so as not to be too high. And also, the concentration of the drained injection material obtained at each experiment was measured by evaporating in a drying furnace.

Results of Experiment

Fig.4 to Fig.6 show the results of permeation experiments. Broken lines in Fig.4 and Fig.5 indicate the approximate lines obtained from the rate of injection volume observed immediately after the start of injection. The results of Case1 to Case3 are shown in Fig.4, which indicates the change of the injection volume of water mixed with micro-particles with elapsed time. It is shown that the injection volume increased linearly with time in Case1, Case2 and Case3. Accordingly, it indicates that the clogging of the injected micro-particles did not occur at the pore of silica sand ♯4.

The results of Case4 to Case6 are shown in Fig.5. The injection volume increased linearly in Case5 and Case6. On the other hand, the rate of injection volume gradually decreased in Case4 whose injection velocity was set at the lowest of the three Cases. This result indicates that the clogging of permeated micro-particles was likely to be dependent on the velocity of permeation. In this experiment, however, it was not clear in which part of sand specimen the clogging occurred.

Fig.6 shows the change of weight concentration of injected micro-particles containing in the drain discharged from specimen. From the results that the concentrations of micro-particles in the drainage were constant at the initial value in all cases except for Case4, it was inferred that the micro-particles permeated uniformly in the sand specimen. In contrast, it was confirmed that the concentration in the drainage reduced with elapsed time in Case 4.

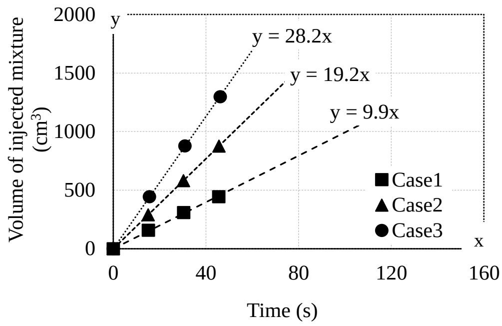

Fig.4 The result of Case1 to Case3

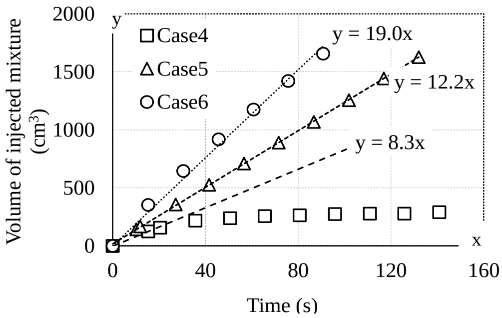

Fig.5 The result of Case4 to Case6

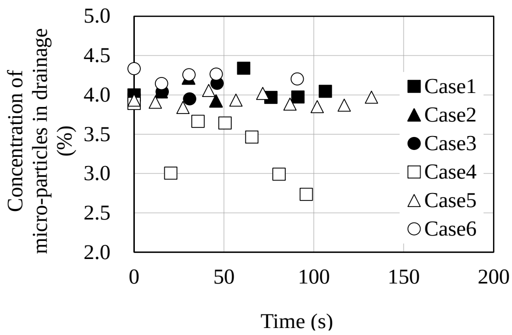

Fig.6 Concentration of micro-particles in drainage

Experiment Using a Multi-layer Divided Column

Conditions of Experiment

In order to obtain the clogging mechanism of micro-particles, it is necessary to disclose in which part of sand specimen clogging occurred. Experiments using a multi-layer divided column were performed to clarify the distribution of injected micro-particles concentration.

The multi-layer divided column made from acrylic resin are 5.0cm in diameter and 50.0cm tall and separable by 10.0cm. The experimental apparatus is shown in Fig.7. In this test, silica sand ♯5 was used for sand specimens, which physical properties and grain size accumulation curve are shown in Table 1 and Fig.2, respectively. The sand specimen was prepared in the column by the air-pluviation method at a relative density of 60%. The weight concentration of micro-particles in injected water was set to 4.0% or 6.0%, and the mixture was permeated into the specimen. In order to reveal difference of permeability due to initial injection velocity, different grouting velocity was set to each specimen by changing injection pressure. The conditions of experiments are shown in Table 3. The column was

Table 3 Conditions of experiment

Case	Silica sand	Concentration of mixture	Injection presure
Case7	♯5	4.0%	10 kPa
Case8	♯5	4.0%	20 kPa
Case9	♯5	4.0%	40 kPa
Case10	♯5	6.0%	10 kPa
Case11	♯5	6.0%	40 kPa

divided after the injection and then the concentration of micro-particles in pore water was measured by evaporating in a drying furnace. The concentration of the micro-particles measured was plotted at the center of the depth of each divided piece on graphs.

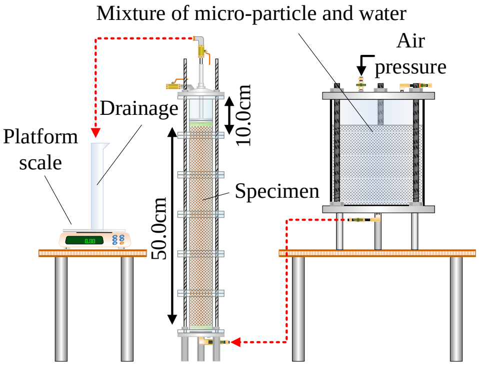

Fig.7 Experimental apparatus

Results of experiment

The results of experiments are shown in Fig.8 and Fig.9. Fig.8 are the relationship between the change of the injection volume of mixture with time. Fig.9 are the relationship between micro-particles in drainage and permeation distance. Fig.8 shows that the concentration of injected micro-particles in drainage was constant in Case9 whose velocity was the highest of the three Cases. It indicates that the injected micro-particles flowed through the pore of the specimen without clogging. In Case7 and Case8, on the other hand, the concentration in drainage tended to be higher in the order of shorter distance from the injection source. It indicates that clogging tended to occur at a short distance from the injection point in Case7 and Case8 whose velocities were lower than Case9.

The results of Relationship between micro-particles in drainage and permeation distance are shown in Fig.9. The comparison between Case7 and Case10 revealed that the highest concentration in Case10 was larger than that in Case7. In addition, the concentration in Case10 tended to develop significantly near the injection source. Therefore, it was also presumed that the trend of clogging depends on the concentration of injected micro-particles.

From these results, it was confirmed that clogging was affected by the properties of sand and micro-particles, injection velocity, injection volume and the concentration of micro-particles. Particularly, in the cases whose injection velocity was low, since the micro-particles clogged in the sand layer near the injection source, the rate of injection volume became low.

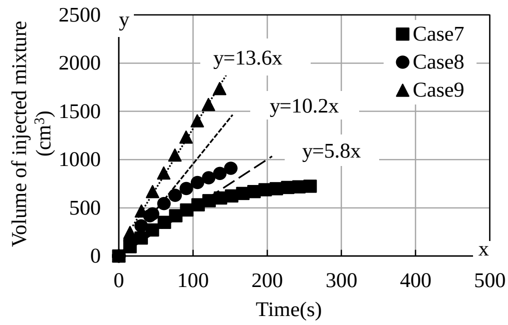

(a) Results of Case7 to case9

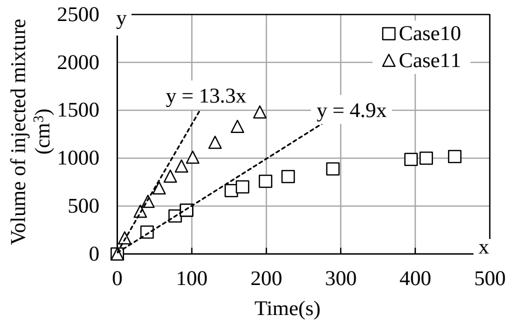

(b) Results of Case10 to Case11

Fig.8 The change of injection volume of mixture with time

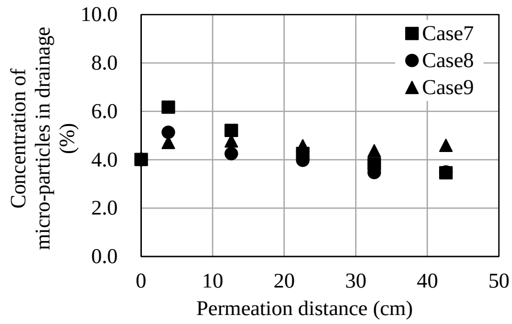

(a) Results of Case7 to case9

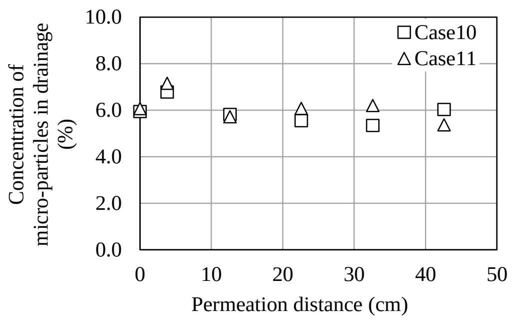

(b) Results of Case10 to Case11

Fig.9 Relationship between micro-particles in drainage and permeation distance

ANALYSIS OF ONE-DIMENSIONAL PERMEATION

Conditions of Analysis

One-dimensional permeation analysis was performed to understand the influence of clogging by micro-particles. A model was created based on the results from the previous one-dimensional injection experiments. Here, volume compressibility of sand skeleton was neglected in this chapter. Simulation was carried out under the same conditions as the injection experiments. The analytical model is shown in Fig.10. The analysis object region was 50.0cm tall and divided into 100 elements. A permeability coefficient was determined depending on the amount of micro-particles storage in each divided element. In the analysis, the concentration of permeated micro-particles is expressed as the volumetric concentration *C*, which is equal to the initial concentration of micro-particles C_0 at the boundary of injection source and decreases with permeation distance depending on the amount of micro-particles storage.

From the experimental results, it was revealed that the amount of micro-particles storage increased when some of the permeated micro-particles were caught in the void of sand skeleton. Therefore, the concentration of micro-particles, some of which are adhered in the pore of sand and others of which are advected, is formulated by the following advection diffusion equation (1).

$$\frac{\partial C}{\partial t} + \upsilon \frac{\partial C}{\partial x} = -\frac{\partial C_s}{\partial t} \qquad (1)$$

where C : the volumetric concentration of micro-particles in injected mixture, C_s : the adhesion concentration obtained by dividing the volume of accumulated micro-particles in an element with the pore volume of the element; x : the permeation distance from the injection source; t : time; υ : the seepage velocity. From the results of the experiments, it was suggested that clogging of micro-particles was affected by injection volume, injection velocity and the concentration of micro-particles. Therefore, in the analysis, the clogging was simulated by using the pass length *I* which means how many micro-particles passed through a boundary surface. The pass length was obtained by dividing the total volume of injected water mixture flowing through a boundary surface with the area of the surface. Moreover, assuming that the seepage velocity of water mixture follows the Darcy's low, a permeability coefficient k_e for each element which is reduced by clogging is defined as Eq. (2).

$$k_e = k_0 e^{-a \cdot I} \qquad (2)$$

where k_e : the reduced coefficient of permeability by clogging, k_0 : the initial coefficient of permeability, *e* :Nepier's constant, a : the parameter of clogging, *I* : the pass length. According to Eq. (2), the more the amount of micro-particle in an element became, the smaller permeability coefficient tended to be. As the volume of injected water mixture increases, the amount of accumulated micro-particles increases in sand void. The accumulation of the micro-particles is expressed in Eq. (3).

$$C_s = C_{smax} \times \tanh(b \cdot I) \qquad (3)$$

where C_{smax}: the limit accumulation volume of micro-particle, b : the accumulation parameter. In Eq. (4), the accumulation of micro-particles in an element increased by increasing the amount of water containing micro-particles that flowed through the element. The experiments of Case7 to Case9 using the multi-layer divided column were simulated in this analysis. The parameters used in this simulation are shown in Table 4.

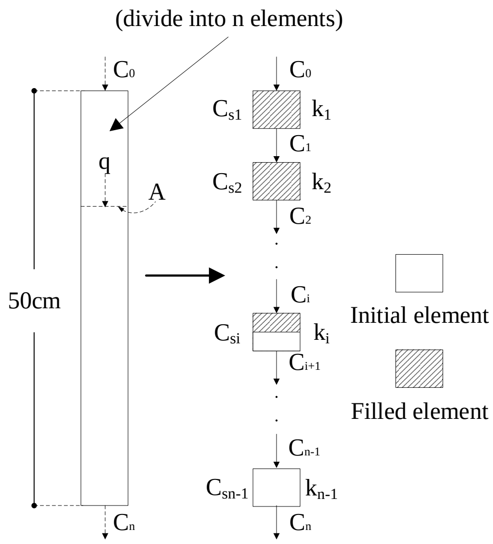

Fig.10 Analytical model

Table 4 Condition of analysis

Case	Parameter a	Parameter b
Case7	4.00	0.07
Case8	2.20	0.04
Case9	0.40	0.01

Results of Analysis

Analysis results are shown in Fig.11. In Fig.11 (b), *C* and C_0 are the concentration of micro-particles in an element and the initial concentration in mixture, respectively. Moreover, the plots indicate the results of experiments and the broken lines that of analysis. From all cases, it was confirmed that the results of experiments and analysis closely matched each other. Particularly in Case7 and Case8, non-linear behavior was observed in the concentration rate C/C_0 and larger value was seen near the injection source.

It is considered that the results of experiments were able to be simulated by the proposed model. However, an interrelationship among the parameters is unclear. To solve this problem, further studies are required.

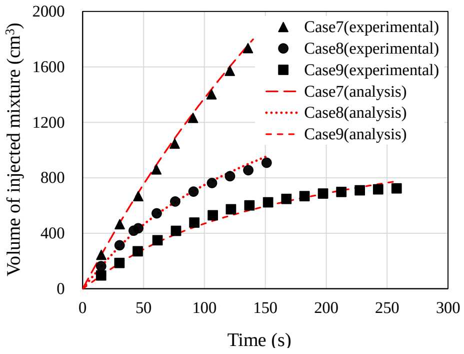

(a) Relationship volume of injected mixture and time

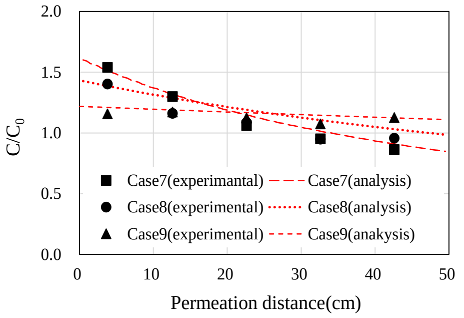

(b) Relationship C/C_0 and permeation distance

Fig.11 Results of analysis

CONCLUSION

Experiments using a short column and a multi-layer divided column were carried out to confirm the characteristics of micro-particles permeating and clogging. Permeability of micro-particles was influenced by seepage velocity, injection volume and the concentration of micro-particles. In particular, if the seepage velocity of injected water mixture was high, clogging scarcely occurred because of its sweeping action. On the other hand, when the seepage velocity of the mixture was low, decreasing the sweeping action occurred the clogging of micro-particles. From the results of experiments, it was also revealed that clogging of micro-particles significantly grew near the injection point.

An one-dimensional permeation analysis was performed to understand the influence of clogging of micro-particles. It was confirmed that the results of experiments and analysis closely matched each other. However, further studies are required because an interrelationship among the parameters is unclear.

REFERENCE

[1] Yonekura R, Shimada S, “Long Term Durability of Chemical Grouts”, Tsuchi-to-Kiso, Vol.40 No.12, Japanese Geotechnical Society, 1992, pp. 17–22. (In Japanese)

[2] Zebovltz S, Krizek R J, Atmatzidis D K, “Injection of Fine Sands with Very Fine Cement Grout”, Journal of Geotechnical Engineering, Vol.115 No.12, 1989, pp. 1717-1733

[3] Nakayama T, Sawada R, Hiraoka Y, Akagi H, “Evaluation of Long Term Stability of Chemically Stabilized Sand with Grouting”, J.JSCE Ser.C Geotechnical Engineering, Vol.69 No.2, 2013, pp. 162-173. (In Japanese)

[4] Fukushima K, Kwachi T, “Evaluation about Durability of Soil Grouted with Metal-Acrylate on Site”, Proceedings of the 33th Annual Conference of the Japanese Geotechnical Society, 1998, pp. 2181-2182. (In Japanese)

[5] Koizumi Y, Tanaka T, Takeuchi J, Kanazawa T, Nishigaki M, “Development of Grouting Method of Fine Sand with Ultrafine Cement Grout”, Journal of the Society of Materials Science, Vol.61 No.1, 2012, pp. 52-57. (In Japanese)

[6] Yamada T, Sekine I, Sekiguchi T, Ishida H, Seki H, Fukushima N, “The Project for Grouting Development for High Level Radioactive Waste Repository, 4; Development of Superfine Spherical Silica Grout”, Proceedings of the 65th Annual Conference of the Japan Society of Civil Engineers, 2010, pp. 89-90, (In Japanese)

[7] Architectural Institute of Japan, Recommendations for Design of Ground Improvement for Building Foundations: Maruzen.Inc, 2008, pp. 313-342. (In Japanese)

[8] Polito C P, Martin J R, ”Effects of Nonplastic Fines on the Liquefaction Resistance of Sands”, Journal of Geotechnical and Geoenvironmental Engineering, 2001, pp. 408-415.

[9] Kuwano J, Sapkota B K,Hasizume H, Takahara K, “Liquefaction Characteristics of Sand Containing Fines”, Tsuchi-to-Kiso, Vol.47 No.7, The Japanese Geotechnical Society, 1993, pp. 23-28–22. (In Japanese)

[10] Sato M, Oda M, Kazama H Ozeki K, “Fundamental Study on the Effect of Fines on Liquefaction Strength of Reclaimed Ground”, J.JSCE Ser.III Geotechnical Engineering, No.561, 1997, pp. 271-282. (In Japanese)

[11] Yoneda S, Nakagawa K, “Basic Properties and Penetration of Cement Suspension Grouts with Different Grain Sizes”, J.JSCE Ser.IV Infrastructure Planning and Management, No.462, 1993, pp. 101-110. (In Japanese)

DOUBLY ASYMPTOTIC OPEN BOUNDARY CONDITION FOR MODAL RESPONSES OF PORE WATER PRESSURE

Suriyon Prempramote
Department of Civil Engineering, Kasetsart University, Thailand

ABSTRACT

The doubly asymptotic open boundary condition has been developed for solving the modal transient seepage equation of any isotropically saturated soil layer with a constant depth. The continued fraction technique is adopted to formulate the doubly asymptotic continued fraction solution in the frequency domain. All constants of the solution are determined at both high- and low-frequency limits. The convergence rate of the solution is much faster in comparison with the high-frequency continued fraction solution. By introducing the auxiliary variables and the doubly asymptotic continued fraction solution to the relationship between the modal seepage flow and the modal response of pore water pressure, the open boundary condition is constructed first in the frequency domain. After transformed to the time domain, the open boundary condition is in terms of a system of fractional differential equations that can be solved by the direct integration methods. The convolution integral is no longer required. The results of modal responses of pore water pressure obtained from the doubly asymptotic open boundary condition with merely low orders of continued fraction are very accurate.

Keywords: Seepage, Open boundary condition, Continued fraction, Modal dynamic permeability, Doubly asymptotic

INTRODUCTION

One of the important issues in simulation of wave propagation in an elastodynamic system is the modeling of the unbounded domain e.g. foundation soil [1]. The responses of the structure on the unbounded domain are often affected by the size of the unbounded domain used in the analysis. If the size is very large, the analysis results of responses are more accurate, but if the size is not large enough, the results may be polluted by the spurious reflection at the truncated boundary of the unbounded domain [2]. This is a common issue when using the finite element method (FEM) as a tool in modeling.

To cope with this issue, a non-reflecting boundary condition have to be imposed on the truncated boundary to satisfy the boundary condition at infinity, in other words, the radiation condition [3]. This non-reflecting boundary condition is actually an approximation based on mathematical formulations. Today, there are several non-reflecting boundary conditions called by different names e.g. artificial boundary condition [4], absorbing boundary condition [5], open boundary condition [6], etc.

Besides the responses of the structure, the responses of the unbounded domain are also important, especially the response of pore water pressure that may significantly affect the embedded part of the structure in transient seepage problems. Many approaches have been proposed to solve such problems [7-9]. Apart from such approaches, there is an interesting one proposed in terms of a high-frequency open boundary condition of transient seepage equation for semi-infinite layers with a constant depth [10]. The high-frequency open boundary condition is expressed as a system of fractional differential equations in the time domain that can be solved by the Newmark method with the improved numerical method of Riemann-Liouville fractional derivative [11]. The concept of formulation of this open boundary condition is from the open boundary condition of scalar wave equation in [6].

Recently, a high-frequency open boundary for two-dimensional transient seepage problems in saturated soil layers with a constant depth has been successfully developed by extending the scaled boundary finite element method (SBFEM) [12] with the concept used in [10]. Under either a short-term flow or a long-term flow, the responses of pore water pressure obtained from the high-frequency open boundary are very accurate as long as the order of continued fraction chosen by the user is high enough. Even though it provides accurate results of responses, it may be inefficient if a very high order of continued fraction is chosen.

Thus, the objective of this paper is aimed at presenting the doubly asymptotic open boundary condition, which is more efficient, for modal responses of pore water pressure in saturated soil layers with a constant depth. The convergence rate of the solution obtained from this open boundary condition is much faster, and only a few orders of continued fraction are required to obtain an accurate result.

MODAL DYNAMIC PERMEABILITY COEFFICIENT

For any isotropically saturated soil layer with a constant depth h underlain by an impervious layer as shown in Fig. (1), the governing equation of two-dimensional transient seepage in the time domain is given by

$$\nabla^2 u = \frac{1}{c}\dot{u} \quad (1)$$

where $u = u(x,z,t)$ is the response of pore water pressure and c is the hydraulic diffusivity, which is equal to the ratio of the permeability k to the specific storage S_s. Note that the arguments of the function u in Eq. (1) are omitted for simplicity in the nomenclature. The initial and boundary conditions are given by $\dot{u}(0,z,0) = 0$ at the vertical boundary Γ_V. At the upper boundary Γ_U, $u(x,0,t) = 0$. And at the lower boundary Γ_L, which is adjacent to the impervious layer, $u(x,h,t),_z = 0$.

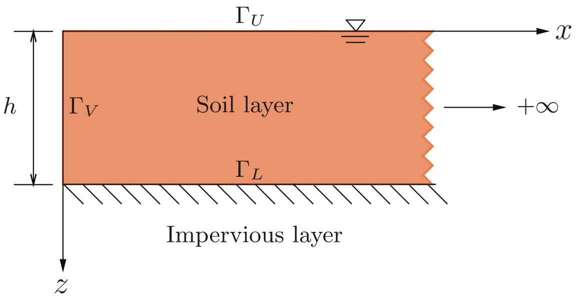

Fig. 1 Saturated soil layer with constant depth.

Equation (1) can be rewritten in the frequency domain as

$$U,_{xx} + U,_{zz} - \frac{1}{c}(\mathrm{i}\omega)U = 0 \quad (2)$$

where $U = U(x,z,\omega)$ is the amplitude of pore water pressure, $\mathrm{i} = \sqrt{-1}$ is the imaginary unit, and ω denotes the excitation frequency. The solution of Eq. (2) is determined from the method of separation of variables as expressed in the following equation:

$$U = \tilde{X}\,\tilde{Z} \quad (3)$$

where $\tilde{X} = \tilde{X}(x,\omega)$ and $\tilde{Z} = \tilde{Z}(z)$. Substituting Eq. (3) into Eq. (2) and multiplying the equation by h^2 yield

$$h^2 \frac{\tilde{X},_{xx}}{\tilde{X}} - (\mathrm{i}a_0) = -h^2 \frac{\tilde{Z},_{zz}}{\tilde{Z}} \quad (4)$$

where the introduced a_0 denotes the dimensionless frequency, which is defined as

$$a_0 = \frac{\omega h^2}{c} \quad (5)$$

Both sides of Eq. (4) must be equal to the same constant which is denoted as λ^2. This allows Eq. (4) to be separated into the following equations:

$$\tilde{Z},_{zz} + \left(\frac{\lambda}{h}\right)^2 \tilde{Z} = 0 \quad (6)$$

$$\tilde{X},_{xx} - \frac{1}{h^2}((\mathrm{i}a_0) + \lambda^2)\tilde{X} = 0 \quad (7)$$

The solution of Eq. (6) is in the form of

$$\tilde{Z} = C_1 \cos\left(\frac{\lambda}{h}z\right) + C_2 \sin\left(\frac{\lambda}{h}z\right) \quad (8)$$

where C_1 and C_2 are constants that can be determined from substituting the initial condition $\tilde{Z} = 0$ at $z = 0$ into Eq. (8). The constant C_1 is found to be zero while C_2 is arbitrary and negligible because it never be calculated. As a result, Eq. (8) is reduced to be the eigenfunction,

$$\tilde{Z}_j = \sin\left(\frac{\lambda_j}{h}z\right) \quad (9)$$

where the eigenvalue is determined from

$$\lambda_j = \frac{(2j+1)\pi}{2} \quad (10)$$

for each mode number i.e. $j = 1, 2, 3, \ldots$, and so on. This implies that Eq. (7) must depend on λ_j as well. Therefore, Eq. (7) can be rewritten in the frequency domain for each mode as

$$\tilde{X}_j,_{xx} - \frac{1}{h^2}((\mathrm{i}a_0) + \lambda_j^2)\tilde{X}_j = 0 \quad (11)$$

which is the modal seepage equation in the x-direction. The solution of Eq. (11) can be determined from the relationship between the modal amplitude of prescribed seepage flow $\tilde{Q}_j$ and the modal amplitude of pore water pressure $\tilde{X}_j$ on the vertical boundary Γ_V as expressed in the following equation:

$$\tilde{Q}_j = \tilde{S}_j^{\infty}\tilde{X}_j \quad (12)$$

where $\tilde{S}_j^\infty = \tilde{S}_j^\infty(a_0)$ denotes the modal dynamic permeability coefficient, and $\tilde{Q}_j = \tilde{Q}_j(x,a_0)$ is equal to

$$\tilde{Q}_j = -h\tilde{X}_{j,x} \tag{13}$$

Substituting Eq. (13) into Eq. (12) and rearrange the equation as

$$\tilde{X}_{j,x} = -\frac{1}{h}\tilde{S}_j^\infty \tilde{X}_j \tag{14}$$

Differentiating Eq. (14) with respect to x and substituting Eq. (14) into the differentiated equation lead to

$$\tilde{X}_{j,xx} = \frac{1}{h^2}(\tilde{S}_j^\infty)^2 \tilde{X}_j \tag{15}$$

Substituting Eq. (15) into Eq. (11) and eliminating $\tilde{X}_j$ in the equation lead to the modal dynamic permeability equation,

$$(\tilde{S}_j^\infty)^2 - \lambda_j^2 - (\mathrm{i}a_0) = 0 \tag{16}$$

The exact solution of Eq. (16) is of the positive form

$$\tilde{S}_j^\infty = \sqrt{\lambda_j^2 + (\mathrm{i}a_0)} \tag{17}$$

to satisfy the boundary condition at infinity. On the vertical boundary Γ_V, the response of modal pore water pressure $\tilde{x}_j = \tilde{x}_j(t)$ due to prescribed modal seepage flow $\tilde{q}_j = \tilde{q}_j(t)$ in the time domain can be determined from the following convolution integral:

$$\tilde{x}_j = \int_0^t (\tilde{s}_j^\infty)^{-1}\tilde{q}_j d\tau \tag{18}$$

where $(\tilde{s}_j^\infty)^{-1} = (\tilde{s}_j^\infty(t-\tau))^{-1}$ is the inverse Fourier transform of $(\tilde{S}_j^\infty)^{-1}$.

DOUBLY ASYMPTOTIC CONTINUED FRACTION SOLUTION

In the derivation of the doubly asymptotic continued fraction solution, the high-frequency continued fraction solution is derived first and then followed by the low-frequency continued fraction solution.

High-frequency Continued Fraction Solution

The continued fraction solution at the high-frequency limit ($a_0 \to \infty$) is defined as

$$\tilde{S}_j^\infty = (\mathrm{i}a_0)^{1/2}\tilde{C}_{\infty,j} - \lambda_j^2(\tilde{Y}_j^{(1)})^{-1} \tag{19}$$

with the recurrence relation

$$\tilde{Y}_j^{(i)} = (\mathrm{i}a_0)^{1/2}\tilde{Y}_{1,j}^{(i)} - \lambda_j^2(\tilde{Y}_j^{(i+1)})^{-1} \tag{20}$$

for i = 1, 2, 3, …, M_H where $\tilde{C}_{\infty,j}$ and $\tilde{Y}_{1,j}^{(i)}$ are constants while $\lambda_j^2(\tilde{Y}_j^{(1)})^{-1}$ and $\lambda_j^2(\tilde{Y}_j^{(i+1)})^{-1}$ are residual terms. Substituting Eq. (19) into Eq. (16) leads to an equation of a power series ($\mathrm{i}a_0$) including the following terms:

$$(\mathrm{i}a_0)(\tilde{C}_{\infty,j}^2 - 1) + (-\lambda_j^2 - (\mathrm{i}a_0)^{1/2}2\tilde{C}_{\infty,j}^2\lambda_j^2(\tilde{Y}_j^{(1)})^{-1} + \lambda_j^4(\tilde{Y}_j^{(1)})^{-2}) = 0 \tag{21}$$

Setting the 1st term (($\mathrm{i}a_0$) term) equal to zero leads to

$$\tilde{C}_{\infty,j} = 1 \tag{22}$$

Note that the positive root of $\tilde{C}_{\infty,j}$ is chosen to satisfy the boundary condition at infinity. Multiplying the last term by $-(\tilde{Y}_j^{(1)})^2/\lambda_j^2$ and substituting Eq. (22) into it result in

$$(\tilde{Y}_j^{(i)})^2 + (\mathrm{i}a_0)^{1/2}b_{1,j}^{(i)}\tilde{Y}_j^{(i)} - \lambda_j^2 = 0 \tag{23}$$

which is a residual equation with the introduced constant

$$b_{1,j}^{(i)} = 2 \tag{24}$$

for the case of i = 1. If substitute Eq. (20) into Eq. (23), the following equation:

$$(\mathrm{i}a_0)((\tilde{Y}_{1,j}^{(i)})^2 + b_{1,j}^{(i)}\tilde{Y}_{1,j}^{(i)}) + (-\lambda_j^2 - (\mathrm{i}a_0)^{1/2}\lambda_j^2(b_{1,j}^{(i)} + 2\tilde{Y}_{1,j}^{(i)})(\tilde{Y}_j^{(1)})^{-1} + \lambda_j^4(\tilde{Y}_j^{(i+1)})^{-2}) = 0 \tag{25}$$

which is also a power series of ($\mathrm{i}a_0$) is obtained. Again, set the 1st term (($\mathrm{i}a_0$) term) equal to zero to obtain

$$\tilde{Y}_{1,j}^{(i)} = -b_{1,j}^{(i)} \tag{26}$$

Then, multiply the last term by $-(\tilde{Y}_j^{(i+1)})^2/\lambda_j^2$ and substituting Eq. (26) into it to obtain the recursive equation,

$$(\tilde{Y}_j^{(i+1)})^2 + (\mathrm{i}a_0)^{1/2}b_{1,j}^{(i+1)}\tilde{Y}_j^{(i+1)} - \lambda_j^2 = 0 \tag{27}$$

with the introduced constant

$$b_{1,j}^{(i+1)} = -b_{1,j}^{(i)} \tag{28}$$

Low-frequency Continued Fraction Solution

For simplicity in notation, $\tilde{Y}_j^{(M_H+1)}$ and $b_{1,j}^{(M_H+1)}$ are rewritten as $\tilde{Y}_{L,j}$ and $b_{L1,j}$, respectively. Thus, Eq. (27) with $i = M_H$ can be rewritten as

$$(\tilde{Y}_{L,j})^2 + (\mathrm{i}a_0)^{1/2} b_{L1,j}\tilde{Y}_{L,j} - \lambda_j^2 = 0 \tag{29}$$

The continued fraction solution at the low-frequency limit ($a_0 \to 0$) is defined as

$$\tilde{Y}_{L,j} = \tilde{Y}_{L0,j} + (\mathrm{i}a_0)^{1/2}\tilde{Y}_{L1,j} - (\mathrm{i}a_0)(\tilde{Y}_{L,j}^{(1)})^{-1} \tag{30}$$

with the recurrence relation

$$\tilde{Y}_{L,j}^{(i)} = \tilde{Y}_{L0,j}^{(i)} - (\mathrm{i}a_0)(\tilde{Y}_{L,j}^{(i+1)})^{-1} \tag{31}$$

for i = 1, 2, 3, …, M_L where $\tilde{Y}_{L0,j}$, $\tilde{Y}_{L1,j}$ and $\tilde{Y}_{L0,j}^{(i)}$ are constants while $(\mathrm{i}a_0)(\tilde{Y}_{L,j}^{(1)})^{-1}$ and $(\mathrm{i}a_0)(\tilde{Y}_{L,j}^{(i+1)})^{-1}$ are residual terms. Substituting Eq. (30) into Eq. (29) leads to an equation of a power series ($\mathrm{i}a_0$) including the following terms:

$$\begin{aligned}&(\tilde{Y}_{L0,j}^2 - \lambda_j^2) + (\mathrm{i}a_0)^{1/2}(2\tilde{Y}_{L0,j}\tilde{Y}_{L1,j} + b_{L1,j}\tilde{Y}_{L0,j}) + (\mathrm{i}a_0)(\\ &\tilde{Y}_{L1,j}^2 + b_{L1,j}\tilde{Y}_{L1,j}) - 2\tilde{Y}_{L0,j}(\tilde{Y}_{L,j}^{(1)})^{-1} - (\mathrm{i}a_0)^{1/2}(b_{L1,j} + \\ &2\tilde{Y}_{L1,j})(\tilde{Y}_{L,j}^{(1)})^{-1} + (\mathrm{i}a_0)(\tilde{Y}_{L,j}^{(1)})^{-2}) = 0\end{aligned} \tag{32}$$

This equation is satisfied by setting all terms equal to zero. The 1st term (constant term) leads to

$$\tilde{Y}_{L0,j} = \pm\lambda_j \tag{33}$$

In Eq. (33), if M_H is an odd number, the positive sign is chosen. On the contrary, the negative sign is chosen when M_H is an even number. The 2nd term ($(\mathrm{i}a_0)^{1/2}$ term) leads to

$$\tilde{Y}_{L1,j} = -b_{L1,j}/2 \tag{34}$$

The last term (($\mathrm{i}a_0$) term) can be reduced to

$$-1 - 2\tilde{Y}_{L0,j}(\tilde{Y}_{L,j}^{(1)})^{-1} + (\mathrm{i}a_0)(\tilde{Y}_{L,j}^{(1)})^{-2} = 0 \tag{35}$$

after Eq. (34) is substituted into it. Then, multiply Eq. (35) by $-(\tilde{Y}_{L,j}^{(1)})^2$ to obtain

$$(\tilde{Y}_{L,j}^{(i)})^2 + b_{L0,j}^{(i)}\tilde{Y}_{L,j}^{(i)} - (\mathrm{i}a_0) = 0 \tag{36}$$

which is a residual equation with the introduced constant

$$b_{L0,j}^{(i)} = 2\tilde{Y}_{L0,j} \tag{37}$$

for the case of i = 1. If substitute Eq. (31) into Eq. (36), the following equation:

$$\begin{aligned}&((\tilde{Y}_{L0,j}^{(i)})^2 + b_{L0,j}^{(i)}\tilde{Y}_{L0,j}^{(i)}) - (\mathrm{i}a_0)(1 + b_{L0,j}^{(i)}(\tilde{Y}_{L,j}^{(i+1)})^{-1} + \\ &2\tilde{Y}_{L0,j}^{(i)}(\tilde{Y}_{L,j}^{(i+1)})^{-1} - (\mathrm{i}a_0)(\tilde{Y}_{L,j}^{(i+1)})^{-2}) = 0\end{aligned} \tag{38}$$

which is also a power series of ($\mathrm{i}a_0$) is obtained. Again, set the 1st term (constant term) equal to zero to obtain

$$\tilde{Y}_{L0,j}^{(i)} = -b_{L0,j}^{(i)} \tag{39}$$

Then, multiply the last term by $(\tilde{Y}_{L,j}^{(i+1)})^2$ and substituting Eq. (39) into it to obtain the recursive equation,

$$(\tilde{Y}_{L,j}^{(i+1)})^2 + b_{L0,j}^{(i+1)}\tilde{Y}_{L,j}^{(i+1)} - (\mathrm{i}a_0) = 0 \tag{40}$$

which is a residual equation with the introduced constant

$$b_{L0,j}^{(i+1)} = -b_{L0,j}^{(i)} \tag{41}$$

The doubly asymptotic continued fraction solution, for example, with M_H = M_L = 1 can be constructed by using Eqs. (19), (20), (30) and (31) as expressed in the following equation:

$$\tilde{S}_j^{\infty} = (\mathrm{i}a_0)^{1/2}\tilde{C}_{\infty,j} - \cfrac{\lambda_j^2}{(\mathrm{i}a_0)^{1/2}\tilde{Y}_{1,j}^{(1)} - \cfrac{\lambda_j^2}{\tilde{Y}_{L0,j} + (\mathrm{i}a_0)^{1/2}\tilde{Y}_{L1,j} - \cfrac{(\mathrm{i}a_0)}{\tilde{Y}_{L0,j}^{(1)}}}} \tag{42}$$

Note that the residual term $(\mathrm{i}a_0)(\tilde{Y}_{L,j}^{(i+1)})^{-1}$ in Eq. (31) is approximated as zero when $i = M_L$.

DOUBLY ASYMPTOTIC OPEN BOUNDARY CONDITION

To construct the doubly asymptotic open boundary condition in the frequency domain, first substitute Eq. (19) into Eq. (12) and rearrange the equation to obtain

$$(\mathrm{i}a_0)^{1/2}\tilde{C}_{\infty,j}\tilde{X}_j - \lambda_j\tilde{X}_j^{(1)} = \tilde{Q}_j \tag{43}$$

where the introduced auxiliary variable $\tilde{X}_j^{(1)}$ is

$$\tilde{X}_j^{(1)} = \lambda_j(\tilde{Y}_j^{(1)})^{-1}\tilde{X}_j \tag{44}$$

Then, substitute Eq. (20) with i = 1 into Eq. (44) and rearrange the equation as

$$-\lambda_j\tilde{X}_j + (\mathrm{i}a_0)^{1/2}\tilde{Y}_{1,j}^{(1)}\tilde{X}_j^{(1)} - \lambda_j\tilde{X}_j^{(2)} = 0 \tag{45}$$

where the introduced auxiliary variable $\tilde{X}_j^{(2)}$ is

$$\tilde{X}_j^{(2)} = \lambda_j(\tilde{Y}_j^{(2)})^{-1}\tilde{X}_j^{(1)} \tag{46}$$

Again, if the same procedure done previously is repeated for i = 2, 3,…, M_H, equations with the same pattern as Eq. (45), that is,

$$-\lambda_j\tilde{X}_j^{(i-1)} + (\mathrm{i}a_0)^{1/2}\tilde{Y}_{1,j}^{(i)}\tilde{X}_j^{(i)} - \lambda_j\tilde{X}_j^{(i+1)} = 0 \tag{47}$$

for i = 2, 3,…, M_H are also obtained. For simplicity in notation, $\tilde{X}_j^{(M_H+1)}$ is rewritten as $\tilde{X}_{L,j}$. Thus, Eq. (47) with $i = M_H$ can be rewritten as

$$-\lambda_j\tilde{X}_j^{(M_H-1)} + (\mathrm{i}a_0)^{1/2}\tilde{Y}_{1,j}^{(M_H)}\tilde{X}_j^{(M_H)} - \lambda_j\tilde{X}_{L,j} = 0 \tag{48}$$

where the introduced auxiliary variable $\tilde{X}_{L,j}$ is

$$\tilde{X}_{L,j} = \lambda_j(\tilde{Y}_{L,j})^{-1}\tilde{X}_j^{(M_H)} \tag{49}$$

Next, substitute Eq. (30) into Eq. (49) and rearrange the equation as

$$\begin{aligned}&-\lambda_j\tilde{X}_j^{(M_H)} + \tilde{Y}_{L0,j}\tilde{X}_{L,j} + (\mathrm{i}a_0)^{1/2}\tilde{Y}_{L1,j}\tilde{X}_{L,j}\\ &-(\mathrm{i}a_0)^{1/2}\tilde{X}_{L,j}^{(1)} = 0\end{aligned} \tag{50}$$

where the introduced auxiliary variable $\tilde{X}_{L,j}^{(1)}$ is

$$\tilde{X}_{L,j}^{(1)} = (\mathrm{i}a_0)^{1/2}(\tilde{Y}_{L,j}^{(1)})^{-1}\tilde{X}_{L,j} \tag{51}$$

Next, substitute Eq. (31) with i = 1 into Eq. (51) and rearrange the equation as

$$-(\mathrm{i}a_0)^{1/2}\tilde{X}_{L,j} + \tilde{Y}_{L0,j}^{(1)}\tilde{X}_{L,j}^{(1)} - (\mathrm{i}a_0)^{1/2}\tilde{X}_{L,j}^{(2)} = 0 \tag{52}$$

where the introduced auxiliary variable $\tilde{X}_{L,j}^{(2)}$ is

$$\tilde{X}_{L,j}^{(2)} = (\mathrm{i}a_0)^{1/2}(\tilde{Y}_{L,j}^{(2)})^{-1}\tilde{X}_{L,j}^{(1)} \tag{53}$$

Again, if the same procedure done previously is repeated for i = 2, 3,…, M_L, equations with the same pattern as Eq. (52), that is,

$$-(\mathrm{i}a_0)^{1/2}\tilde{X}_{L,j}^{(i-1)} + \tilde{Y}_{L0,j}^{(i)}\tilde{X}_{L,j}^{(i)} - (\mathrm{i}a_0)^{1/2}\tilde{X}_{L,j}^{(i+1)} = 0 \tag{54}$$

for i = 2, 3,…, M_L are also obtained. Note that the residual term $(\mathrm{i}a_0)(\tilde{Y}_{L,j}^{(i+1)})^{-1}$ in Eq. (31) is approximated as zero when $i = M_L$. Then, combine Eqs. (43), (45), (47), (48), (50), (52), (54) and use Eq. (5) to form the following equation in matrix form:

$$([K_h] + (\mathrm{i}\omega)^{1/2}[C_h])\{X\} = \{Q\} \tag{55}$$

where $\{X\} = [\tilde{X}_j, \tilde{X}_j^{(1)},\ldots, \tilde{X}_j^{(M_H)}, \tilde{X}_{L,j}, \tilde{X}_{L,j}^{(1)},\ldots, \tilde{X}_{L,j}^{(M_L)}]^T$, $\{Q\} = [\tilde{Q}_j, 0,\ldots, 0, 0, 0,\ldots, 0]^T$ and the time-independent matrices,

$$[K_h] = \begin{bmatrix} & -\lambda_j & & & & & & \\ -\lambda_j & & -\lambda_j & & & & & \\ & -\lambda_j & & \ddots & & & & \\ & & \ddots & & -\lambda_j & & & \\ & & & -\lambda_j & \tilde{Y}_{L0,j} & & & \\ & & & & & \tilde{Y}_{L0,j}^{(1)} & & \\ & & & & & & \ddots & \\ & & & & & & & \tilde{Y}_{L0,j}^{(M_L)} \end{bmatrix} \tag{56}$$

$$[C_h] = \frac{h}{\sqrt{c}}\begin{bmatrix} \tilde{C}_{\infty,j} & & & & & & & \\ & \tilde{Y}_{1,j}^{(1)} & & & & & & \\ & & \ddots & & & & & \\ & & & \tilde{Y}_{1,j}^{(M_H)} & & & & \\ & & & & \tilde{Y}_{L1,j} & -1 & & \\ & & & & -1 & & \ddots & \\ & & & & & \ddots & & -1 \\ & & & & & & -1 & \end{bmatrix} \tag{57}$$

Equation (55) can be transformed into the time domain as

$$[K_h]\{x\} + [C_h]D^p\{x\} = \{q\} \tag{58}$$

which is the doubly asymptotic open boundary condition for solving the modal responses of pore water pressure $\tilde{x}_j$ where $\{x\} = [\tilde{x}_j, \tilde{x}_j^{(1)},\ldots, \tilde{x}_j^{(M_H)}, \tilde{x}_{L,j}, \tilde{x}_{L,j}^{(1)},\ldots, \tilde{x}_{L,j}^{(M_L)}]^T$ and $\{q\} = [\tilde{q}_j, 0,\ldots, 0, 0, 0,\ldots, 0]^T$, and D^p denotes the fractional derivative of an order p which is equal to 1/2. The vector $\{x\}$ in Eq. (58) can be solved by the direct integration methods e.g. the Newmark method with γ = 0.5 and β = 0.25 (the average acceleration scheme) in association with the improved numerical method of Riemann–Liouville fractional derivative [11].

NUMERICAL EXAMPLES

Two soil layers are chosen for the analyses in the frequency and time domains. The 1st soil layer is of the following properties: h = 1 m and c = 1 m^2/s, while the 2nd soil layer is assumed to be deeper and less permeable, that is, h = 10 m and c = 0.01 m^2/s.

Frequency Domain Analysis

The accuracy of the doubly asymptotic continued fraction solution obtained from using Eqs. (19), (20), (30) and (31) is evaluated and compared with that of the high-frequency continued fraction solution proposed in [10]. The exact solution (Eq. (17)) is used for verifying the accuracy of both solutions. For the 1st soil layer, the doubly asymptotic continued fraction solution with M_H = M_L = 1 is tested at the high mode j of 1,000 with λ_j = 2,001(π/2). The result normalized by λ_j is plotted in Fig. 2(a) for the real part and Fig. 2(b) for the imaginary part. It is clear that both real part and imaginary part match those of the exact solution throughout the entire range of a_0. In comparison with the high-frequency continued fraction solution with the same number of fractions i.e. M_H = 3, they both yield the same result. However, when tested at the lowest mode j of 0 with λ_j = π/2, the high-frequency continued fraction solution with M_H = 3 is very inaccurate (see Fig. 3). In order to gain the accurate result, the order M_H must increase to 19. In contrast, the doubly asymptotic continued fraction solution with M_H = M_L = 1 is still accurate.

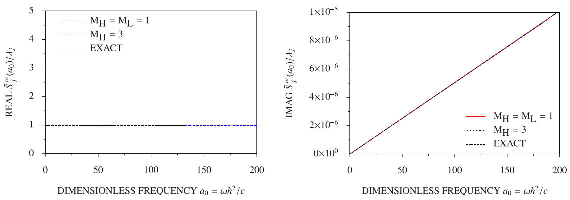

(a) (b)

Fig. 2 Continued fraction solutions: (a) real part and (b) imaginary part for mode j = 1,000.

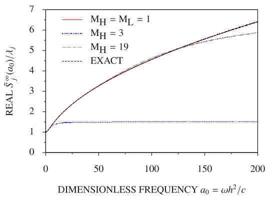

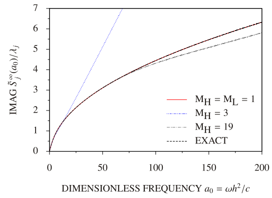

(a) (b)

Fig. 3 Continued fraction solutions: (a) real part and (b) imaginary part for mode j = 0.

For the 2nd soil layer, the higher mode j of 50,000 with λ_j = 100,001(π/2) and the very low mode j of 5 with λ_j = 11(π/2) are chosen for the test. The results of continued fraction solutions normalized by λ_j for such modes are plotted in Figs. 4 and 5, respectively. Again, at the higher mode, both continued fraction solutions with the same number of fractions yield the same accurate result as shown in Fig. 4. However, at the very low mode, the high-frequency continued fraction solution with M_H = 3 yields the very poor result as shown in Fig. 5. As the order M_H increases from 3 to 51 and 51 to 113, the accuracy of the solution is continuously improved. By contrast, the doubly asymptotic continued fraction solution with merely M_H = M_L = 1 is enough to gain the accurate result. It is noted that in the case of the deeper and less permeable soil layer, the order M_H used for the high-frequency continued fraction solution is much higher when tested at the very low mode.

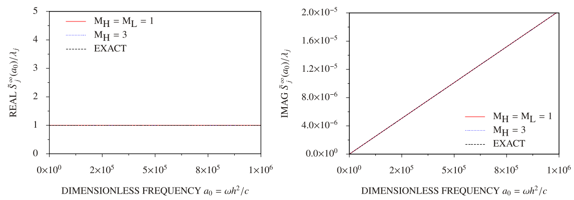

(a) (b)

Fig. 4 Continued fraction solutions: (a) real part and (b) imaginary part for mode j = 50,000.

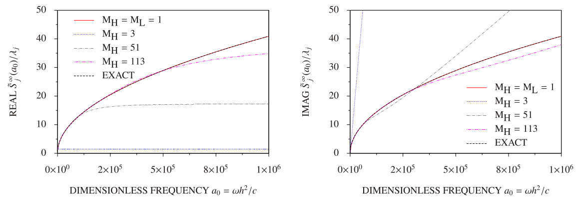

(a) (b)

Fig. 5 Continued fraction solutions: (a) real part and (b) imaginary part for mode j = 5.

Time Domain Analysis

The accuracy of the modal responses of pore water pressure $\tilde{x}_j$ obtained from the doubly asymptotic open boundary condition in Eq. (58) is evaluated and compared with that of the high-frequency open boundary condition proposed in [10]. The convolution integral in Eq. (18) as the exact response is used for verifying the responses. The small time increment Δt of 0.005 sec. is used in the analysis to ensure the accuracy of the results.

Modal seepage flow as double impulse function

In the 1st example, the 1st soil layer is tested at the high mode j of 1,000 with λ_j = 2,001(π/2) and the lowest mode j of 0 with $\lambda_j = \pi/2$ under a short-time $\tilde{q}_j$ which is the double impulse function as prescribed in Fig. 6(a) with its Fourier transform in Fig. 6(b). At the high mode, both doubly asymptotic and high-frequency open boundary conditions using the same number of fractions yield the same accurate response as their curves match the curve of the exact response in Fig. 7(a). At the lowest mode, the high-frequency open boundary condition with M_H = 3 does not provide an accurate result (see Fig. 7(b)). Only M_H of 19 is enough to gain the accuracy. On the contrary, the doubly asymptotic open boundary condition with merely $M_H = M_L = 1$ still provides the accurate result.

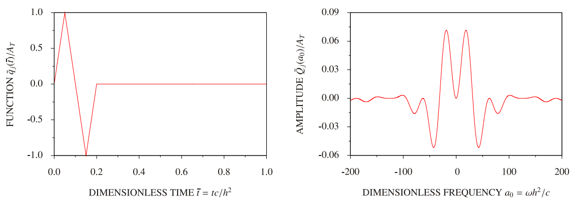

(a) (b)

Fig. 6 Double impulse function: (a) time history and (b) Fourier transform.

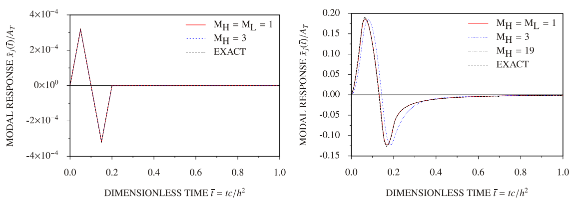

(a) (b)

Fig. 7 Modal responses of pore water pressure to double impulse function: (a) for mode j = 1,000 and (b) for mode j = 0.

Modal seepage flow as Bessel function of 1st kind

In the 2nd example, the 1st soil layer is tested again at the same modes but under a long-time $\tilde{q}_j$ which is the Bessel function of the 1st kind for order 1/2 i.e. $J_{1/2}(\overline{\omega}\bar{t})$ where $\overline{\omega} = 30\pi$ as shown in Fig. 8(a) with its Fourier transform in Fig. 8(b).

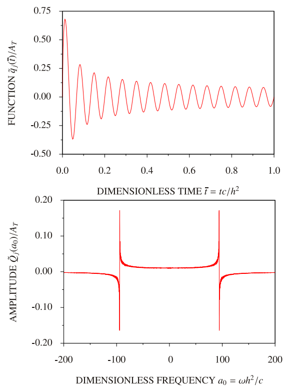

(a) (b)

Fig. 8 Bessel function of 1st kind: (a) time history and (b) Fourier transform.

Both open boundary conditions still provide the very good results at the high mode as shown in Fig. 9(a). At the lowest mode, the doubly asymptotic open boundary condition with $M_H = M_L = 1$ performs better as its response matches the exact response while the high-frequency open boundary condition with M_H = 3 yields the poorer result as compared in Fig. 9(b). Only M_H of 19 can match the exact response.

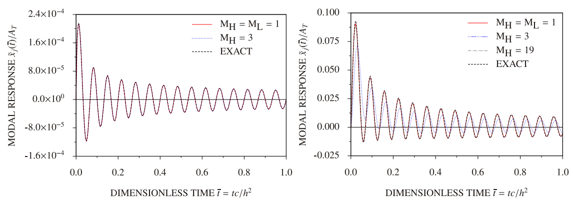

(a) (b)

Fig. 9 Modal responses of pore water pressure to Bessel function of 1st kind: (a) for mode j = 1,000 and (b) for mode j = 0.

Modal seepage flow as single impulse function

In the 3rd example, the 2nd soil layer is tested at the higher mode j of 50,000 with λ_j = 100,001(π/2) and the very low mode j of 5 with λ_j = 11(π/2) under a short-time $\tilde{q}_j$ which is the single impulse function as given in Fig. 10(a) with its Fourier transform in Fig. 10(b). For the deeper and less permeable soil layer, both open boundary conditions also yield the same result at the higher mode as shown in Fig. 11(a). As expected, the doubly asymptotic open boundary condition with $M_H = M_L = 1$ still performs very well at the very low mode as the response curve fits the exact response as shown in Fig. 11(b). For the high-frequency open boundary condition, the order M_H of 3 is not enough to gain the accurate result. It turns out that the order M_H must increase to 51 in order to fit the exact curve. This shows that when h increases and c decreases, only the high-frequency open boundary condition is affected because the order M_H used must be higher to guarantee the accuracy of responses.

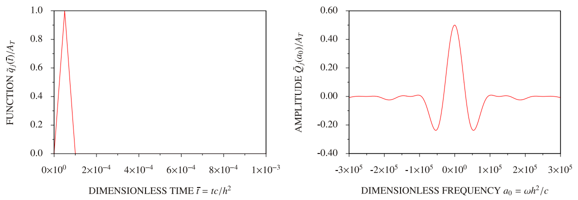

(a) (b)

Fig. 10 Single impulse function: (a) time history and (b) Fourier transform.

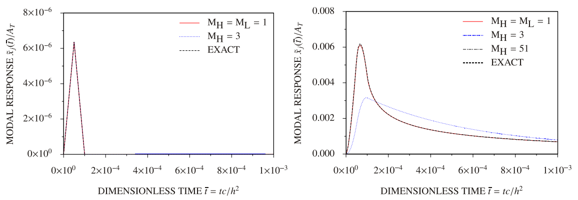

(a) (b)

Fig. 11 Modal responses of pore water pressure to single impulse function: (a) for mode j = 50,000 and (b) for mode j = 5.

Modal seepage flow under earthquake excitation

In the last example, the 2nd soil layer is analyzed again at the same modes, but using a long-time $\tilde{q}_j$ under earthquake excitation in Fig. 12(a) with its Fourier transform in Fig. 12(b). For the high mode, the results obtained from both open boundary conditions are identical as plotted in Fig. 13(a). Again, at the very low mode, the high-frequency open boundary condition is no longer efficient because the order M_H used is very high, that is, 113 in order to fit the exact curve (see Fig. 13(b)). But in the case of the doubly asymptotic open boundary condition, merely $M_H = M_L = 1$ is enough to fit the exact curve. This also confirms that for the deeper and less permeable soil layer, only the high-frequency open boundary condition is affected as the order M_H used must be higher to guarantee the accuracy of responses.

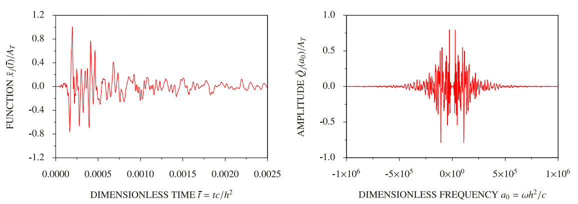

(a) (b)

Fig. 12 Earthquake excitation: (a) time history and (b) Fourier transform.

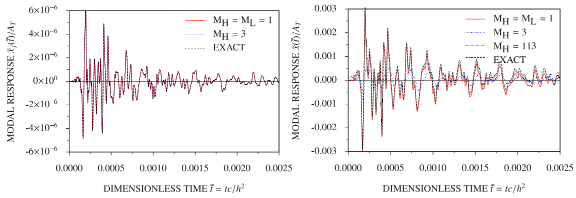

(a) (b)

Fig. 13 Modal responses of pore water pressure to earthquake excitation: (a) for mode j = 50,000 and (b) for mode j = 5.

CONCLUSIONS

The doubly asymptotic open boundary condition proposed herein is expressed as a system of fractional differential equations in the time domain. It can be solved by the Newmark method with the improved numerical method of Riemann-Liouville fractional derivative, and the convolution integral, which is an expensive task, is no longer required.

In the frequency domain analysis of both soil layers, the convergence rate of the doubly asymptotic continued fraction solution is much faster than that of the high-frequency continued fraction solution, especially at the low modes. In the time domain analysis under the short-time and long-time flows, all the results of modal responses of pore water pressure obtained from the doubly asymptotic open boundary condition using the less number of continued fraction orders are more accurate, in other words, the doubly asymptotic open boundary condition is more efficient than the high-frequency open boundary condition.

REFERENCES

[1] Wolf JP, Song C, Finite-element Modelling of Unbounded Media. John Wiley & Sons: Chichester, 1996, ch. 1.

[2] Givoli D, "Non-reflecting boundary conditions: a review", J. of Computational Physics, Vol. 94, May 1991, pp. 1-29.

[3] Keller JB, Givoli D, "Exact non-reflecting boundary conditions", J. of Computational Physics, Vol. 82, May 1989, pp. 172-192.

[4] Tsynkov SV, "Artificial boundary conditions for the numerical simulation of unsteady acoustic waves", J. of Computational Physics, Vol. 189, Aug. 2003, pp. 626-650.

[5] Hagstrom T, De Castro ML, Givoli D, Tzemach D, "Local high-order absorbing boundary conditions for time-dependent waves in guides", J. of Computational Acoustics, Vol. 15, Mar. 2007, pp. 1-22.

[6] Prempramote S, Song C, Tin-Loi F, Lin G, "High-order doubly asymptotic open boundaries for scalar wave equation", Int. J. for Numerical

Methods in Engineering, Vol. 79, Jul. 2009, pp. 340-374.

[7] Zhao C, Valliappan S, "Transient infinite elements for seepage problems in infinite media", Int. J. for Numerical and Analytical Methods in Geomechanics, Vol. 17, May 1993, pp. 323-341.

[8] Jie Y, Jie G, Mao Z, Li G, "Seepage analysis based on boundary-fitted coordinate transformation method", Computers and Geotechnics, Vol. 31, Jun. 2004, pp. 279-283.

[9] Chen B, Song E, "An artificial boundary approach for unbounded transient seepage problems", Int. J. for Numerical and Analytical Methods in Geomechanics, Vol. 39, May 2015, pp. 762-774.

[10] Prempramote S, "High-frequency open boundary condition of transient seepage equation", in Proc. 19th National Convention on Civil Engineering, 2014, pp. 1-8.

[11] Zhang W, Shimizu N, "The improved numerical method of Riemann-Liouville fractional derivative for FE formulation", in Proc. WCCM VI in conjunction with APCOM'04, 2004, pp. 1-7.

[12] Prempramote S, "A high-frequency open boundary for transient seepage analyses of semi-infinite layers by extending the scaled boundary finite element method", Int. J. for Numerical and Analytical Methods in Geomechanics, Vol. 40, Apr. 2016, pp. 919-941.

Sixth International Conference on Geotechnique, Construction Materials and Environment, Bangkok, Thailand, Nov. 14-16, 2016, ISBN: 978-4-9905958-6-9 C3051

3D FINITE ELEMENT ANALYSIS OF EARTH PRESSURE BALANCE SHIELD TUNNEL EXCAVATION USING SHELL ELEMENT AND GROUTING LAYER

P. Lueprasert[1], P. Jongpradist[2], N. Heama[1], K. Ruengwirojjanakul[1] and S. Suwansawatt[1]
[1]*Faculty of Engineering, King Mongkut's Institute of Technology Ladkrabang, Bangkok, Thailand*
[2] *Faculty of Engineering, King Mongkut's University of Technology Thonburi, Bangkok, Thailand*

ABSTRACT

With the advancement of computer sciences and researches on tunneling simulation in the past, the 3D finite element analysis of tunnel excavation by tunnel boring machines (TBMs) has been extensively used over the last decade. Due to the complicated construction sequences and relevant loads can be taken into account, complex interaction problems can then be performed. Many simulation techniques have been proposed depending on the assumptions used in the modeling. For modeling the tunnel lining, solid elements are commonly used due to the ratio between the width and thickness of the lining is not large. In addition, most studies focused on the ground deformation, not the lining forces. In the circumstance that the lining forces are essentially observed, the structural elements that directly provide the values are preferred. Therefore, this research attempts to propose the shell elements as tunnel lining together with the grouting layer in the analysis. The analysis results from the proposed method and the conventional one are compared and discussed in terms of ground deformation and lining forces. The analysis focuses on the characteristics of the MRTA tunnel project, (e.g. tunnel diameter and positions, soil profile and construction process) including the operations of TBMs in the project (e.g. face pressure, shield element or shield weight, tunnel lining and grouting pressure).

Keywords: 3D FEM, Tunnel boring machines, Tunnel lining, Shell element, Lining force

INTRODUCTION

The construction of tunnels in urban areas can induce ground movements, which have harmful effects on existing structures. To limit soil disturbance and resultant surface settlement, tunnel boring machines (TBMs) combined with the earth pressure balance shield (EPBS) method are popularly employed in tunnel construction projects as shown in Fig. 1. Analyses on ground movement due to tunneling by TBM or induced structural forces in the lining are necessary during the design stage. Among various analysis methods, Finite Element Method (FEM) is one of the most widely used tool for tunneling works.

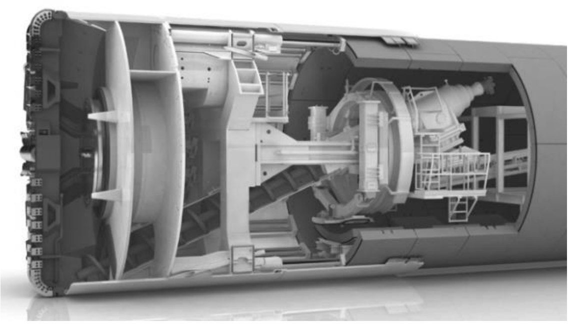

Fig. 1 Schematic section of a Herrenknecht TBM–EPB machine [1]

At the beginning, the simulations of tunneling using TBMs were analyzed in 2D finite element (FE) models [2]-[5]. In these models, the different stages of the TBMs advancement are considered by stress-relief method. The 3D FE models for TBMs tunneling were first applied in the early 1990s. Various simulation methods considering different factors and simplifications have been developed [6]-[10]. Among different factors considered in the analysis by each researcher, the tunnel lining element and the tail void grout process have not been considered yet. These two parameters were measured and emphasized by [11] and [12]. The complicated simulations of 3D EPBS tunneling models using several parameters e.g., face pressure, shield element or shield weight, tunnel lining element, tail void grout process, hydraulic jack, steering control, and backup trailer loads were gradually introduced [13], [14]. The 3D FE models using face pressure, shield element, tunnel lining element, and grouting process as the parameters are used in studies [15], [16]. As the studies mentioned above, only four main parameters (face pressure, shield element, grouting process and lining element) are generally used to model the 3D EPBS tunneling. Thus, these parameters are used to simulate the 3D EPBS tunneling in the present work.

However, various methods to model the grouting process have been proposed in the simulation of the excavation by EPBS in the past. For example, the method which uses a distributed pressure to represent the grouting process was introduced by [17], [18]. In the grouting process in engineering practice, the grouting will change from the liquid state to solid. In order to realistically model this characteristic, solid elements having different stiffness are represented to simulate the grouting process [12], [15] and [19]. However, an actual behavior of initial grout is in a fluid state with no stiffness. In practice, it is then difficult to specify the modulus of grouting during liquid state. The pressure boundary may thus be more appropriate than the solid elements.

In simulation of ground movement due to tunneling, the solid elements or the brick elements are generally adopted to represent the tunnel lining [13], [14] and [17]. The lining which has a certain width and the actual excavated periphery of the soil can then properly be modeled. By using the solid elements, the structural forces (i.e., bending moment, normal force and shear force) cannot directly be obtained. In circumstances that the structural forces are needed to be investigated, the modeling by the solid elements becomes inconvenient. In this situation, shell elements which offer the direct quantification of lining structural forces are preferable. The shell elements have been also used in the past researches, e.g., the influence of ground stratification on lining force and settlement due to tunneling [19], the effects of tunneling on adjacent building and existing tunnel respectively [15]-[16] and [20]. However, using the shell elements to model the tunnel lining causes a problem due to that the shell elements have no thickness in the process of meshing. It is reasonable to model the shell element (as line on cross sectional plane) at the mid plane. Consequently, the treatment on the gap between the excavated soil periphery and mid plane during meshing is essential.

This study introduces the grouting layer as solid element in the gap to represent the solid-state grouting while using pressure boundary to represent the liquid-state grouting. The comparison of three tunneling simulation methods using 3D FE models are made and discussed. The first method follows one suggested in PLAXIS 3D 2013.1 manual [18]. The second method is similar to the first method but the solid elements as tunnel lining are replaced by the shell elements assuming the excavated boundary at the mid plane. The final method, the shell elements used to represent the tunnel lining together with the adapted grouting process mentioned above. The results are discussed in terms of surface settlement profiles and the structural forces in tunnel lining

SITE DESCRIPTION

The section CS-8B of Mass Rapid Transit Authority (MRTA) Blue Line Project is chosen to simulate in this study as shown in Fig. 2. The geotechnical conditions for the study site are detailed by [21]. Geological conditions can be described as follows:

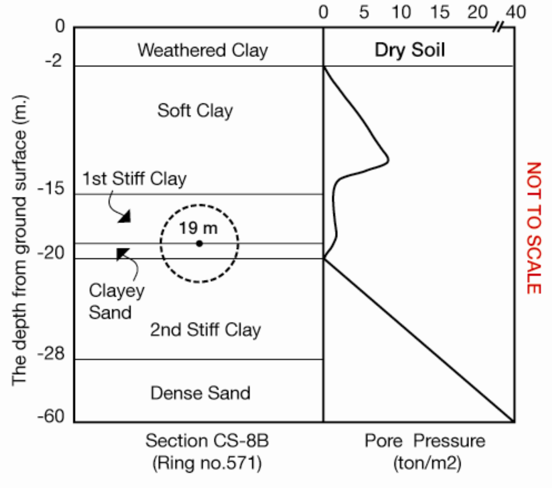

Fig. 2 Soil profile and pore pressure of case study in MRTA Blue Line Project

The uppermost first layer consists of weathered crust or fill material. The second layer is the very soft clay layer. The first stiff clay is located in the third layer. A thin seam of clayey sand is found below the first stiff clay as a fourth layer. The second stiff clay is found below the upper sand. Tunnel with inner and outer diameter of 5.7 and 6.3, respectively, is located in the stiff clay layers at the depth of about 19 m from ground surface. A typical pore water pressure profile in Bangkok is a piezometric drawdown as shown in Fig. 2. The pore water at the depth of about 20 m is almost zero and restored condition to hydrostatic pressure at the depth about lower than 20 m.

FINITE ELEMENT ANALYSIS

Numerical model

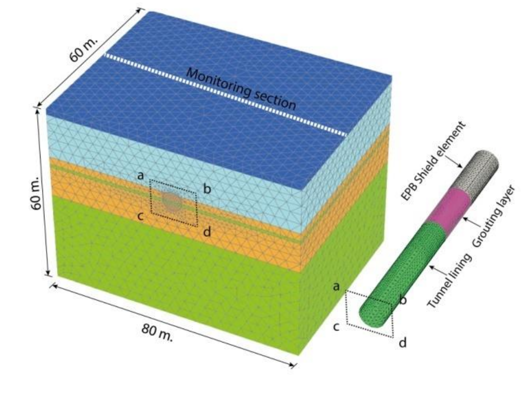

Fig. 3 The mesh in FE model (the proposed method)

The 3D FE mesh presenting the sample case of the proposed method (the final method) is depicted in Fig.3. The soil layers were discretized into the six-node bricks or the solid elements with a suitable aspect ratio. The simulation of tunnel components consisted of three layers, EPB shield layer, grouting layer and tunnel lining layer. The four-nodes shell elements were used to model the tunnel lining and EPBS. The hardened grouting layer was simulated by the solid elements. Their information will be detailed in next section. The dimension of model is 80 m (≈12.5D_T) in the transverse direction, 60 (≈ 9.5D_T) in the longitudinal and vertical directions. The monitoring section is at the center of longitudinal direction. The distance of 5D_T ahead and behind the monitoring section are enough to fully simulate the tunneling problem. The PLAXIS 3D 2013.1 software was implement to analyze and adopt for mesh generation.

Earth pressure balance shield advancement and simulation procedures

The tunneling process of EPBS was simulated using a step-by-step approach. Each excavation step corresponded to an advancement of the tunnel face of 1.2 m which is equal to the width of tunnel lining. A simplified geometry of EPBS is assumed with the original cone-shaped replaced by a cylindrical shape. The schematic of simulated process with EPBS was shown in Fig. 4. The simulation process can be described as follows.

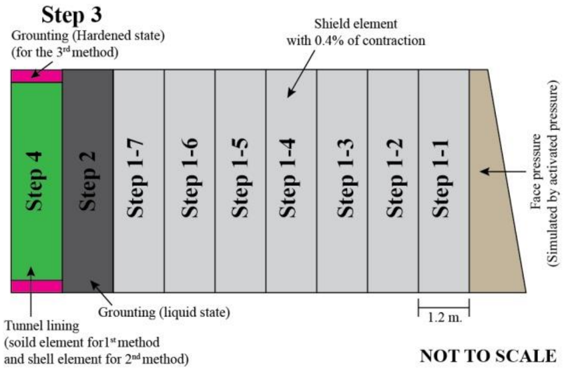

Fig. 4 The tunneling simulation process

Step 1, the soil elements were deactivated as the EPBS diameter which the over cutting of shield did not simulate in this study. The support of excavation face was modeled by applying a pressure distribution with linear increase of pressure with depth. The face pressure in this study is about 150 to 200 kPa at crown and invert of tunnel respectively [21]. The shell elements were activated to represent the EPB shield with contraction ratio of 0.4%, which was calibrated from the previous FE analysis of tunneling projects in Bangkok subsoil. These procedures were repeated until the advancement of shield was completed with seventh rings for the width of about 8.4 m in longitudinal direction. Step 2, the simulation of tail void grouting in a first phase, the grout has not yet fully hardened, the liquid state of grouting was simulated by applying a radial pressure with 200 kPa [21] acting on soil around tunnel. The simulation of tunneling process in steps 1 and 2 follows ones recommended by manual of PLAXIS 2013.1 [18]. Step 3, the tail void grouting in a second phase is considered to be hardened, the grouting layer was simulated by the solid elements. Step 4, the shell or solid elements representing the tunnel lining was activated in the same grouting layer section. These steps, 3 and 4, are differed for the simulation by each method in this study. The details are described in next section.

The patterns of simulation method

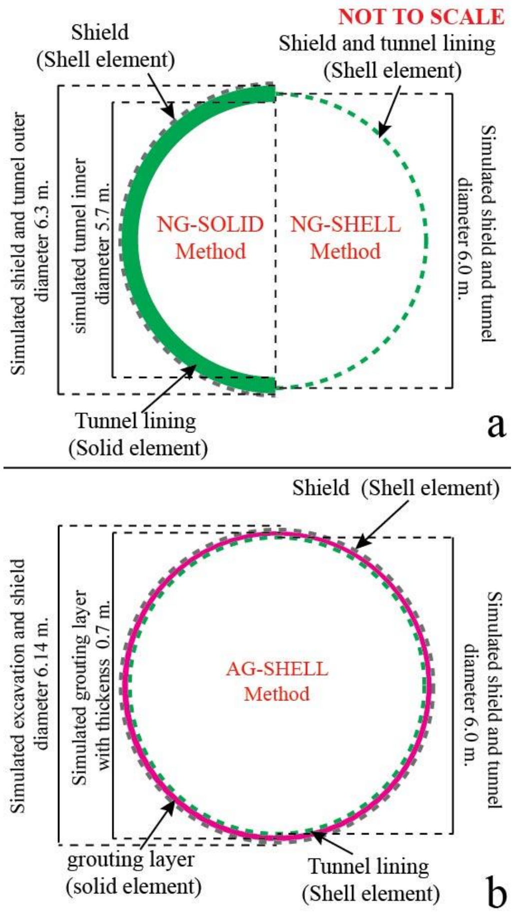

Fig. 5 The cross sections of simulation patterns

The simulation method with EPBS tunneling is divided into three patterns. The difference of patterns is that the different techniques are selected to simulate the tunnel lining and grouting layer section as shown in Fig. 5.

The first method that is called “NG-SOLID method”, the tunnel linings are modeled by the solid elements with thickness of 0.30 m. The step 3 of simulation procedures is not considered in this method. The second method, that is called “NG-SHELL method”, is similar to the first method. The shell elements are represented to simulate the tunnel linings, the geometry of simulation is thus different. The difference between using the solid or shell elements is that the geometry of thin shell element is modeled as zero-thick line at mid plane. Thus, the diameter of excavated soil periphery in this modeling is 6.0 m with the same as shield diameter. The details of two simulation methods are depicted in Fig 5.

The final method was suggested in this study. The shell elements are used to represent the tunnel lining together with the grouting layer, that is called "AG-SHELL method". The thickness of grouting layer is 0.07 m which is equal with the thickness of EPB shield in the case that the pitching angle of excavation process and over cutting of EPBS is not considered in this study. The cross section of AG-SHELL method is depicted in Fig. 5b.

Analysis condition

The initial distribution of vertical effective stress and horizontal effective stress are controlled by the given soil unit weight, the coefficient of earth pressure at rest, K_0 for all strata and the hydrostatic pore water pressure conditions in equilibrium with a water table at the ground surface. The undrained analysis was considered.

The displacement boundary was adopted in this study. The sides of the mesh including the front side and rear side are restrained against lateral movements but free to move vertically, so no movement perpendicular to their side of meshes. The bottom of the mesh is fixed (no vertical and horizontal movements). These conditions were used for all finite element meshes throughout of the analysis.

Material properties

Table 1 Soil parameters for modeling [22]

Soil layer	**Wea. crust**	**Soft clay**	**Stiff clay**	**Sand**
Material model	MC	Hardening Soils (HS) model		MC
E' **(kPa)**	6,000	-	-	80,000
E_{oed}^{ref} **(kPa)**	-	5,000	60,000	-
E_{50}^{ref} **(kPa)**	-	5,000	60,000	-
E_{ur}^{ref} **(kPa)**	-	15,000	180,000	-
γ_{sat} **(kN/m³)**	17	16	18	20
υ' **(-)**	0.32	0.33	0.33	0.3
ϕ' **(º)**	22	22	22	36
c **(kPa)**	8	5	18	0
m **(-)**	-	1	1	-
p_{ref} **(kPa)**	-	100	95	-

The properties of soil are determined from the MRTA projects [22]. The soil layers, stiff and soft clays, were assumed by hardening soil model (HS) [23]. The Mohr-Coulomb model (MC) was assumed to represent the weathered clay and sand layer. The soil properties in this study are calibrated material parameters for the accuracy of simulations of geotechnical work in Bangkok subsoil [24] as shown in Table 1.

Table 2 Material properties of EPB shield, tunnel lining and grouting layer.

EPB Elements	**Young modulus [E] (kN/m²)**	**Poisson's ratio [υ]**	**Unit weight [γ] (kN/m³)**
Tunnel lining	31×10^6	0.20	24
EPB shield	210×10^6	0.28	78
Grouting layer	1×10^6	0.30	21

Table 2 shows the properties of the components of EPBS tunneling simulation. The EPB shield, tunnel lining and grouting layer were assumed to be linear elastic. The properties of grouting layer at 28 days of curing are obtained from [13], [14] while those of EPBS are acquired from [19].

ANALYSIS RESULT

The results in terms of surface settlement and lining forces from the three simulation methods are compared and discussed together with the measurement data if available. The observations of FE analysis results are carried out after the process of tunneling simulation is completed.

Surface settlement

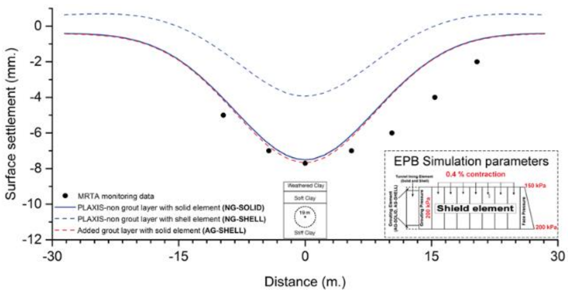

Fig. 6 Comparing transverse settlement profile from MTRA section CS-8B with FEM analyses

Figure 6 shows the surface settlement profiles compared between FE analyses and MRTA monitoring data in section CS-8B. The surface settlement profiles analyzed by FEM are similar in shape but quantitatively different. The surface settlement profile of the NG-SOLID method is noticeably deeper than the surface settlement obtained from the NG-SHELL method. It is clear, the selection of simulation method significantly affects on the nature of the computed surface settlements. The difference of the surface settlement profiles may be presumed to be associated with properties of the elements or the excavated cavity of tunneling.

Although the excavated cavity of NG-SOLID is larger than the AG-SHELL method, the surface settlement profile of the AG-SHELL method is close to that of the NG-SOLID and the MRTA monitoring data. This may attribute to the grouting layer (solid element) adapted in the AG-SHELL method.

Lining force

The comparison of the computed structural forces in the tunnel lining for three methods is presented hereafter. The structural forces are plotted from the reference lining ring located at the mid-section of model.

Bending moment

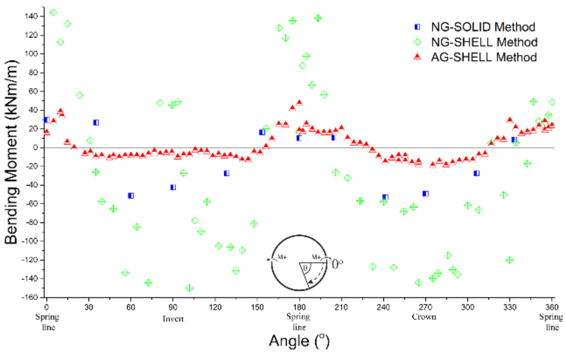

Fig. 7 The computed bending moment in linings for three different methods

Figure 7 shows the computed bending moment resulted by the three simulation methods. From this figure, the significant differences of computed bending moment are revealed. Especially, the distribution of the computed bending moment by the NG-SHELL method is drastically different with those by the others. The computed bending moment of tunneling simulation located in soft clay (K_0 < 1.0) is positive values at the spring line and negative values at crown and invert. This behavior obtained by the computed bending moment of NG-SOLID and AG-SHELL methods. Although the trends of the computed bending moment for NG-SOLID and AG-SHELL methods are similar, the magnitudes are different. However, the ranges of magnitude of computed bending moment obtained from the NG-SOLID and AG-SHELL methods are close to those reported in the previous studies [25], [26].

Axial force

Figure 8 depicts the computed axial force resulted by three simulation methods. The tendency of the computed axial force is similar to the computed bending moment. The computed axial force of the NG-SOLID and the AG-SHELL methods is in the same range. This range agrees well with the previous researches [25], [26], which should be in the range of 0 to 1000 kN/m. In contrast, the distribution of the computed axial force of the NG-SHELL method is in much higher.

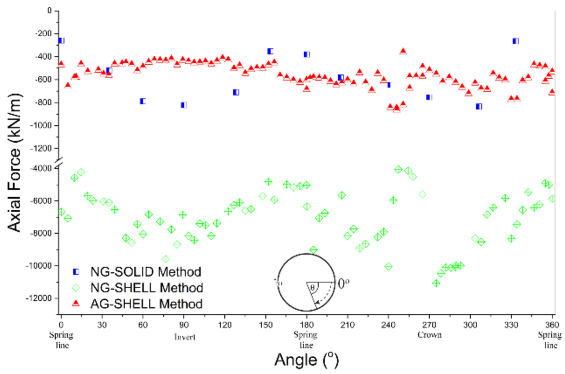

Fig. 8 The computed axial force in linings for three different methods

CONCLUSION

In this study, we proposed to model the tunnel lining with the shell elements together with the grouting layer in tunneling analysis by TBM in soft ground. The grouting is modeled as pressure boundary and solid elements in liquid and solid state, respectively. By the proposed method, grouting process and actual excavated boundary of the soil can then be realistically modeled. Analysis of tunnel excavation using the proposed method in conjunction to 4 main factors (face pressure, shield element, grouting process and lining element), provides good agreement with results from the conventional method. Besides, the structural forces obtained from the current method are in ranges of history records.

ACKNOWLEDGEMENT

The financial support provided by the research funding from the Thailand Research Fund (TRF) and 1D2 Group Co. Ltd. under Grant PHD56I0057 is acknowledged.

REFFERENCES

[1] Herrenknecht AG, "Herrenknecht" [Online], Germany,Available:https://www.herrenknecht.com/en/products/core-products/tunnelling/epb-shield.html [5 April 2016].

[2] Clough GW, Sweeney BP, Finno RJ, “Measured soil response to EPB shield tunneling”, J. of Geotechnical Engineering-ASCE, 109(2), 1983, pp. 131-149.
[3] Finno RJ, Clough GW, “Evaluation of soil response to EPB shield tunneling”, J. of Geotechnical Engineering-ASCE, 111(2), 1985, pp. 155-173.
[4] Bernat S, Cambou B, “Soil-structure interaction in shield tunnelling in soft soil”, Computers and Geotechnics, 22(3/4), 1998, pp. 221-242.
[5] Bernat S, Cambou B, Dubois P, “Assessing a soft soil tunnelling numerical model using field data”, Geotechnique, 49, 1999, pp.427-452.
[6] Lee KM, Rowe RK, “Finite element modelling of the three-dimensional ground deformations due to tunnelling in soft cohesive soils: part I – method of analysis”, Computers and Geotechnics, 10, 1990, pp.87–109.
[7] Lee KM, Rowe RK, “Finite element modelling of the three-dimensional ground deformations due to tunnelling in soft cohesive soils: part II - results”, Computers and Geotechnics, 10, 1990, pp.111-138.
[8] Lee KM, Rowe RK, “An analysis of three-dimensional ground movements: The Thunder Bay tunnel”, Canadian Geotechnical Journal, 28, 1991, pp.25-41.
[9] Lee KM, Rowe RK, Lo KY, “Subsidence owing to tunnelling. I. Estimating the gap parameter”, Canadian Geotechnical Journal, 29, 1992, pp.929-940.
[10] Rowe RK, Lee KM, “Subsidence owing to tunnelling. II. Evaluation of a prediction technique”, Canadian Geotechnical Journal, 29, 1992, pp.941-954.
[11] Abu-Krisha A. Numerical modelling of TBM tunnelling in consolidated clay. Ph.D. Thesis, University of Innsbruck, 1998.
[12] Swoboda G, Abu-Krisha A, “Three-dimensional numerical modelling for TBM tunnelling in consolidated clay”, Tunnelling and Underground Space Technology, 14(3), 1999, pp. 327-333.
[13] Kasper T, Meschke G, “A 3D finite element simulation model for TBM tunnelling in soft ground”, J. Int. for Numerical and Analytical Methods in Geomechanics, 28, 2004, pp.1441-1460.
[14] Kasper T, Meschke G, “A numerical study of the effect of soil and grout material properties and cover depth in shield tunneling” Computers and Geotechnics, 33, 2006, pp. 234-247.
[15] Chakeri H, Ozcelik Y, Unver B, “Effects of important factors on surface settlement prediction for metro tunnel excavated by EPB”, Tunnelling and Underground Space Technology, 36, 2013, pp. 14-23.
[16] Zheng G, Zhang T, Diao Y, “Mechanism and countermeasures of preceding tunnel distortion induced by succeeding EPBS tunnelling in close proximity”, Computers and Geotechnics, 66, 2015, pp. 53-65.
[17] Broere, W, Brinkgreve, R.B.J., ‘‘Phased simulation of a tunnel boring process in soft soil’’, in Proc. Conf. on Numerical Methods in Geotechnical Engineering, in Mestat (Ed.), Presses de 1’ENPC/ LCPC, Paris, 2002, pp.529-536.
[18] PLAXIS Version 8 Manual. A.A. Balkema Publishers, 2013
[19] Katebi H, Rezaei A, Hajialilue-Bonab M, Tarifard A, “Assessment the influence of ground stratification, tunnel and surface buildings specifications on shield tunnel lining loads (by FEM)”, Tunnelling and Underground Space Technology, 49, 2015, pp. 67-78.
[20] Comodromos EM, Papadopoulou MC, Konstantinidis GK, “Numerical assessment of subsidence and adjacent building movements induced by TBM-EPB tunneling”, J. of Geotechnical and Geoenvironmental Engineering, 140 (11), 2014
[21] Suwansawat. S. “Earth Pressure Balance (EPB) Shield Tunneling in Bangkok: Ground Response and Prediction of Surface Settlements Using Artificial Neural Networks”, Ph.D. Thesis, Massachusetts Institute of Technology, USA, 2002.
[22] Jongpradist P, Kaewsri T, Sawatparnich A, Suwansawat S, Youwai S, Kongkitkul W, Sunitsakul J, “Development of tunneling influence zones for adjacent pile foundations by numerical analyses”, Tunnelling and Underground Space Technology, 34, 2013, pp. 96-109
[23] Schanz T, Vermeer PA, Bonnier PG, “The hardening soil model: formulation and verification”, in Proc. Conf. on Beyond 2000 in Computational Geotechnics-10 years of Plaxis, Balkema, Rotterdam, 1999, pp. 281–296.
[24] Prust RE, Davies J, Hu S, “Pressure meter investigation for mass rapid transit in Bangkok, Thailand”, J. of the transportation research board, Transportation research of the national academies, Washington, DC, 1928, 2005, pp. 207–217.
[25] Working Group No. 2, ITA, “Guidelines for the Design of Shield Tunnel Lining”, Elsevier Science Ltd: Published, 2000
[26] Moller S, “Tunnel induced settlements and structural forces in linings” Doctoral Thesis, University of Stuttgart, Germany, 2006

ANALYSIS OF TUNNELING CONSTRUCTION WITH GROUND-SPRING MODEL

P. Chaipanna [1], P. Jongpradist [1] and M. Sugimoto [2]
[1] *King Mongkut's University of Technology Thonburi, Bangkok, Thailand*
[2] *Nagaoka University of Technology, Niigata, Japan*

ABSTRACT

The shield tunnel has been extensively implemented for underground transportation of urban areas. Many reports of tunnel segment damage during tunnel construction. The jack thrust force is the essential causes of damage to the segment. The objective of this article is to present the model which analyzes the behavior of tunnel lining during construction. This model consists of five rings and ten segments for each ring. The segments are connected with the shear springs which represent the segment joint and ring joint. The zero thickness interface elements assigned is used to model the segments interface behavior. The jack trust force is applied at the first ring. The lubricant pressure, grout pressure and soil pressure are taken into account in this model. The ground spring model is implemented into FEM program ABAQUS, then the soil stiffness is represented by mean of spring. This analysis is separated into two cases; straight alignment and curve alignment. From the analysis result, the analysis result agrees with the measurement, the stresses of tunnel segment are governed by jack thrust force. The ground-spring model has been proven to be appropriate for analysis of suitable behavior of the tunnel segment.

Keywords: 3D FEM, Soil-Tunnel Interaction, Ground spring model, and Tunneling construction

INTRODUCTION

The shield tunneling technology is continuously developed, the shield tunneling is possibly constructed in the difficult ground conditions at increasing soil and water pressures, and various cross-section of the tunnel. The segmental lining is popularly used in the shield tunneling. The segments are sequentially erected as tunnel boring advances, which are consecutively coupled with the bolts in the longitudinal and circumferential direction of the tunnel. The packing materials are used between segments with the purpose of load distribution.

During the shield tunnel excavation, the tunnel linings are subjected to the construction loads, such as, the jack thrust, the shield tail pressure, the grouting pressure and ground pressure. Many reports of shield segment damage during construction have been increasingly presented and these indicate the significance of construction load [1, 2]. However, the conventional design of tunnel lining takes into account only the serviceability loads in shield tunneling [3, 4].

Nowadays, analysis of shield tunneling has been already achieved by mean of three-dimensional (3D) model [5,6]. These analyses take into account the step of tunnel construction, but the tunnel lining is modeled by means of continuous element. Katebi et al.,[7] and Blom et al.,[8] model tunnel lining by segmental lining, but the surrounding soil is characterized by elastic behavior which is not rational to represent the natural soil.

Although, it is commonly realized that the effect of the tunnel construction loads on the tunnel lining must be taken into account in the analysis and design of shield tunnels, only few research has been carried out to grasp the effect of tunnel construction loads [5, 6, 8]. This paper presents a three-dimensional analysis model to enhance the appreciation of tunnel lining behavior due to the construction loads. The measurement data were taken from the literature of Nishin-Shinjuku [9] tunnel allows the verification of the present analysis.

FIELD MEASUREMENT

In order to verify the appropriateness of the present analysis, the field measured data during the construction of Nishin-Shinjuku tunnel have been used to validate the proposed model [9]. The Nishin-Shinjuku tunnel is a part of the Metropolitan Expressway Central Ring Shinjuku Line. The Nishin-Shinjuku Tunnel comprises of twin tunnels and a total length of 600 m. The outer diameter of tunnel is 13.0 m, thickness is 0.55 m and segmental width is 1.2 m. For field instrumentation, strain gauges were installed in first three tunnel rings, 10 positions for each ring.

The tunnel crown is located at the depth of 22 m while groundwater table is at 13 m below the ground level. The tunnel was excavated through very dense gravel and very dense sand. The geotechnical data are tabulated in Table 1.

Table 1 Soil properties of analysis [9]

Earth layer	Value
Wet density (kN/m^3)	18.6
Adhesive force (kN/m^2)	38.0
Internal friction angle (deg)	37.0
Subgrade reaction coefficient (MN/m^3)	91.0
N value	50

ANALYSIS STRATEGY

This section presents a three-dimensional analysis for shield tunneling, which takes into account the soil and water pressure, the tail void grouting pressure, the wire brush grease pressure, the jack thrust and soil-tunnel interaction. The analysis is performed by means of FE analysis.

The tunnel lining considered in the analysis includes five rings, each ring comprises of ten segments, which are staggered alignment along the tunnel axis. The segments are coupled with the segment joints and ring joints in longitudinal and circumferential directions, respectively. These joints are considered using the shear spring elements. The assembly of tunnel lining is illustrated in Fig.1(a). The attribution of packer material is represented with the interface element which involves the normal and tangential behaviors.

There are various loads acting on the tunnel lining, such as, jack thrust, wire brush pressure, tail void grouting pressure and earth pressure. These loads influence on the performance of the tunnel lining. For this reason, these loads are taken into account in the analysis, as seen Fig.1(b).

The soil-tunnel interaction is modeled by means of a series of radial spring [10], the stiffness of radial spring is regarded using nonlinear elastic behavior (Fig. 2). The stiffness of radial springs are varied along the longitudinal tunnel, as seen in Fig.1(c).

The Ring1 in the model is only subjected by the jack thrust in longitudinal direction, no any loads acting on radial direction. The grease is injected into the gap between shield tail and the extrados of tunnel lining to prevent the external water flow into the shield. The grease pressure acts on the Ring2. Ring3 is subjected by tail void grouting pressure. The grout material is filled the gap between the extrados of tunnel lining and surrounding soil. The constant pressure is kept over the hydrostatic pressure of 90 kPa. Ring4 and Ring5 are subjected to the surrounding ground pressure which comprises the soil pressure and water pressure.

The simulation of shield tunneling is divided in two categories, the shield tunneling for straight forward alignment and the curve forward alignment. The hydraulic jack pattern for both categories are illustrated in Fig.3. The black circles are represented the active jack thrust, in the other hand, the white circles are represented the inactive jack thrust.

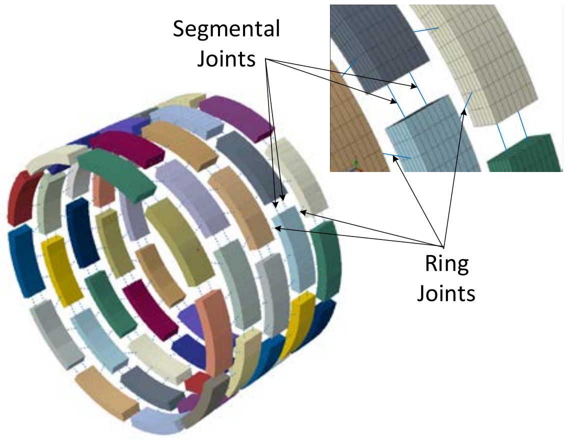

(a) Configuration of ring and segment joints

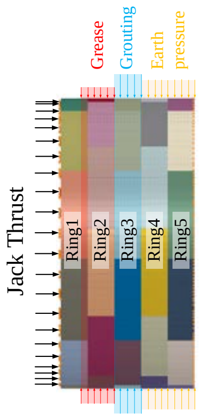

(b) Loads distribution

(c) Radial springs

Fig. 1 Loads distribution and boundary condition of analysis model

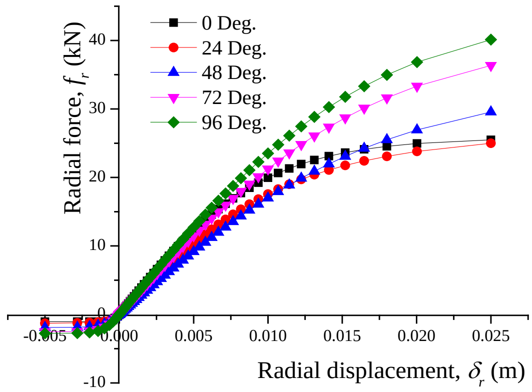

Fig. 2 Modeling of the soil-tunnel interaction

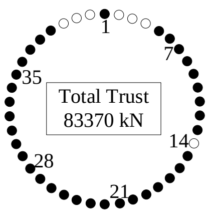

(a) Straight alignment

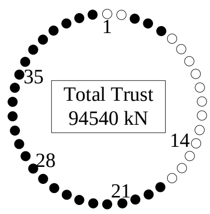

(b) Curve alignment

Fig. 3 Configuration of jack thrust.

ANALYSIS RESULT

The simulation results of Ring1, Ring2, and Ring3 are compared to the field measurements taken from literature to validate and calibrate this analysis method.

The measured and analysis results from Figs.4 to 7 are traced from centerline of tunnel segments. The measured and computed results are compared by mean of plotting the results (bending moment, forces and deformation) in the circumferential direction against the circumferential angle. The contour shedding of stress distribution are also depicted as illustrated in Figs.8 to 10.

Fig. 4 shows the comparison between the measured and computed of circumferential bending moment of the tunnel Ring1, Ring2 and Ring3. The left figures represent results of simulation during straight alignment, and the right figure is for shield tunneling during curve alignment. The circumferential bending moment occurs slightly in the Ring1 because there is no external force in circumferential direction; only gravitational force of the segments themselves exists. The jact thrusts are in longitudinal direction. The moment becomes increasing in Ring 2 and Ring 3due to the grease and grouting pressures, respectively. Comparison between the computed and measured results, it is seen that the analysis can reproduce the moment distribution in a fair agreement with te measured ones. The difference between the straight and curve alignment can be also reflected.

Fig. 5 summarizes the computed circumferential bending from all 5 rings. The maximum circumferential bending occur in the Ring 5 as a result of different vertical and horizontal pressure of surrounding soil. The influence of jack thrust (as straight or curve alignment) on the bending is clearly seen as shown in Figs. 5(a) – (b).

Fig. 6 shows distribution of circumeferential force comparing between the measured and computed values. The maximum circumferential force appears in Ring2. For Ring 1 and Ring 2, it is seen that the computed forces are in good agreement with the measured one, whereas, the computed forces in Ring 3 are larger than those of the measurement.

From figs.4 and 6, it indicates that the analysis results satisfactorily correspond to the measurement for both bending moment and circumferential force.

Fig. 7 depicts the computed circumferential forces from all 5 rings. The maximum circumferential load occurs at the invert of Ring5. The jack thrust does not only affect the axial load, but also the the circumferential load. Furthermore, a circumferential load of Ring5 is affected from the jack thrust too. The distribution of circumferential of Ring5 of straight alignment (Fig. 7(a)) differ slightly from curve alignment (Fig. 7(b)).

The distribution of the circumferential stress is shown in Figs.8 (a)-(b) for straight and curve alignments, respectively. The jack thrust has strong influence on the circumferential stress. The circumferential stress mostly concentrated on the

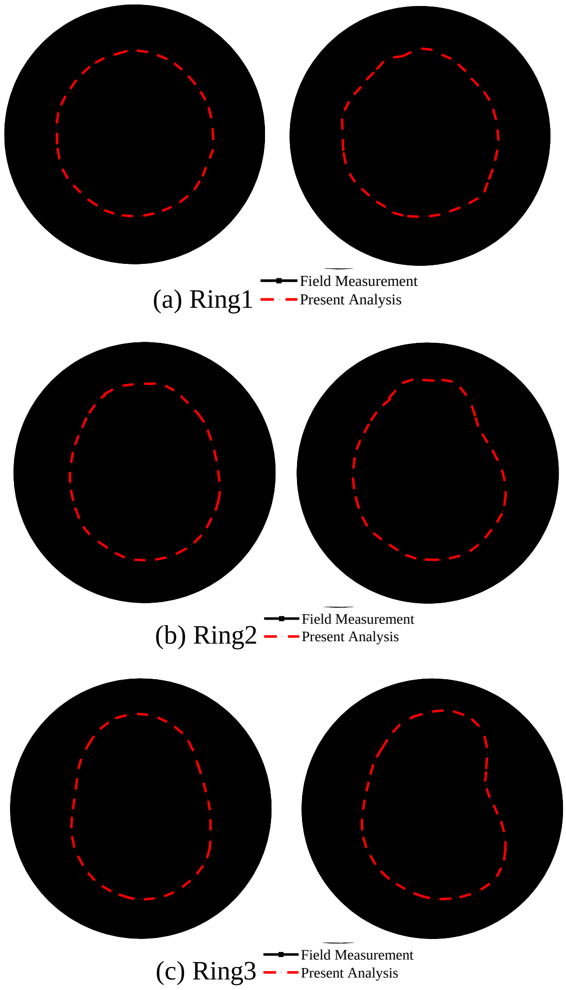

Fig.4 Comparison of bending moment (kN-m) between field measurement and present analysis (Left side for straight alignment and right for curve alignment).

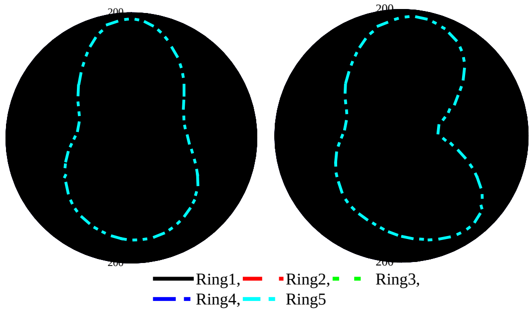

(a) Straight alignment (b) Curve alignment

Fig. 5 Computed bending moment distribution (kN-m).

front face of Ring1 which is in accordance with the position of hydraulic jacks. The circumferential stress decreases in Ring2 and Ring3. The circumferential stress increases again in Ring4 and Ring5 due to radial pressure. The eccentric jack thrust obviously shows the difference of stress intensity between the straight and curve alignment. The jack thrust directly affects to the longitudinal stress, this stress concentrates at the hydraulic jack position on the front face of Ring1. The longitudinal stress gradually decreases in the other rings. The contour shading of longitudinal stress of straight and curve alignments obviously differ between the straight and curve alignment of the analysis, see Figs.9(a)-(b).

The computed shear stress of tunnel lining is shown in Figs.10(a)-(b). Due to the tunnel lining is segmental, the shear stress of adjacent segments are transferred by mean of interface elements and tunnel joint. The maximum shear stress occurs at the position of hydraulic jack.

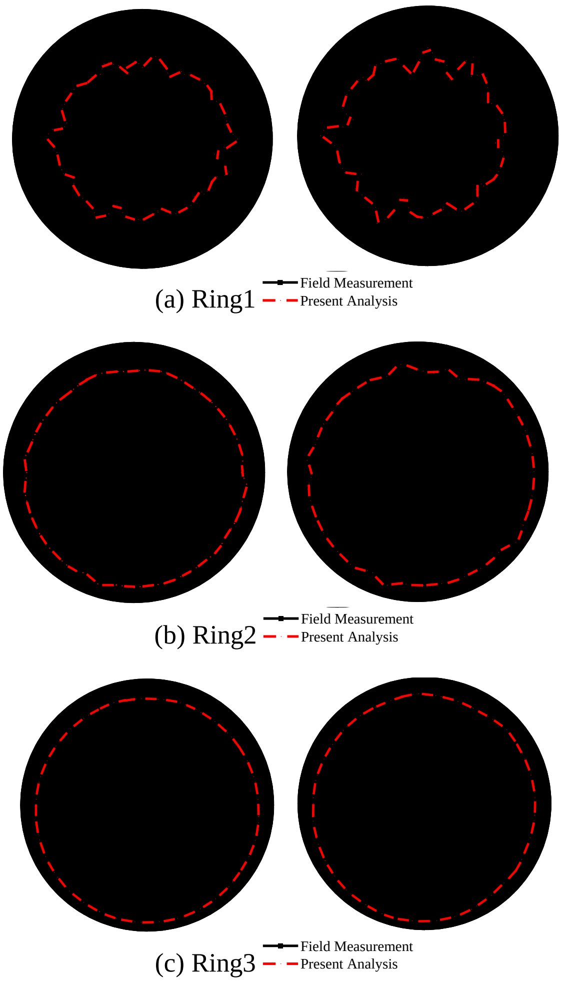

(a) Ring1

(b) Ring2

(c) Ring3

Fig. 6 Comparison of circumferential force (kN) between field measurement and present analysis (Left side for straight alignment and right for curve alignment).

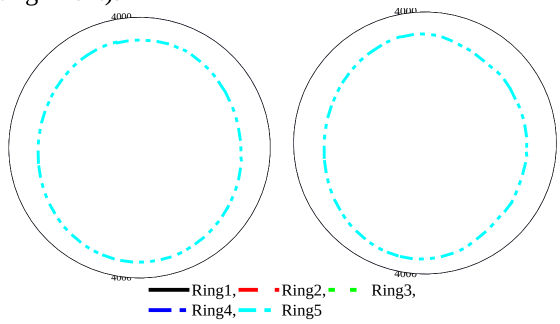

(a) Straight alignment (b) Curve alignment

Fig. 7 Computed circumferential force (kN).

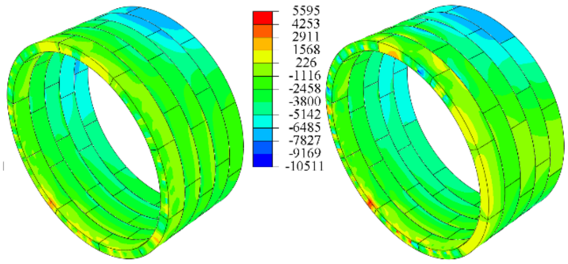

a) Straight alignment b) Curve alignment

Fig. 8 Distribution of circumferential Stress (kPa).

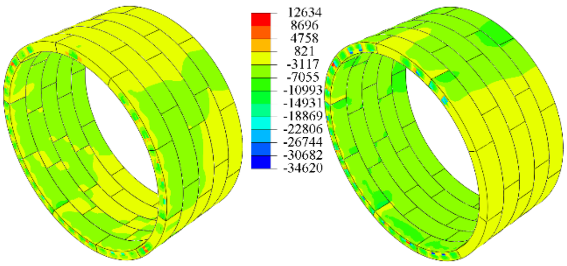

a) Straight alignment b) Curve alignment

Fig. 9 Distribution of longitudinal stress (kPa).

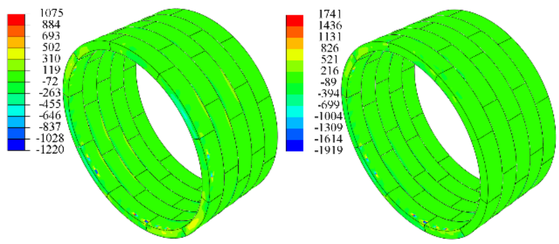

a) Straight alignment b) Curve alignment

Fig. 10 Distribution of shear stress (kPa).

Fig. 11, the differential pressure acts on the extrados of tunnel rings that heavily affect to its radial displacement. The Ring5 shows maximum radial displacement that is induced by the ground pressure. The diameter of tunnel lining increases in the horizontal direction and decreases in the vertical direction. The overall tunnel diameter reduces due to surrounding pressure.

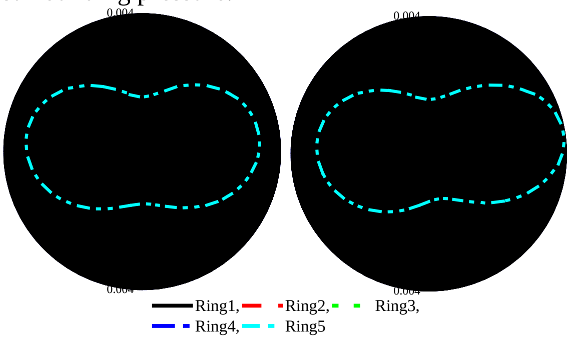

(a) Straight alignment (b) Curve alignment

Fig. 11 Computed radial displacement of the analysis

CONCLUSIONS

A three-dimensional analysis of shield tunnel segments during construction has been presented, which takes into account all relevant interactions and loads, i.e., soil and water pressures, the grouting pressure, the jack thrust force and the grease pressure. The conclusions from this study are as follows:

- The present analysis satisfactorily correspond to the field measurement of case study.
- The analysis results can reproduce the influence of jack thrust on the tunneling behavior.
- The jack thrust influence on both displacement and structural forces of tunnel lining.
- The jack thrust is the main cause of the maximum stress in the segment. Therefore, the internal stress of tunnel lining is governed by the jack thrust.

REFERENCES

[1] Sugimoto, M., “Causes of Shield Segment Damages During Construction”, in Proc. Int. Symp. On Underground Excavation and Tunnelling, Bangkok, 2006,Thai, pp.67-74

[2] Wu M.Q., “Application study on steel fiber concrete segment in metro tunnel engineering”, Guangdon Building Materials 3, 2004

[3] ITA-WG2, “Guidelines for the Design of Shield Tunnel Lining”, Tunnelling and Underground Space Technology, Vol.15, No.3, 2000, pp.303-331

[4] Japanese Society of Civil Engineerings (JSCE), “Japanese Standard for Shield Tunneling”, 3rd ed. 1996, Tokyo, Japan

[5] Kasper T. and Meschke G., “A 3D finite element simulation model for TBM tunnelling in soft groung”, Int. J. Numer. Anal. Meth. Geomech. 28, 2004

[6] Katebi H., Rezaei A.H., Hajialilue-Bonab M. and Tarifard A., “Assessment the influence of ground stratification, tunnel and surface buildings specifications on shield tunnel lining loads (by FEM)”, Int. J. Tunn. Undergr. Space Techno. 49, 2015

[7] Blom C.B.M., van der Horst E.J. and Jovanovic P.S., “Three-dimensional Structural Analyses of the Shield-Driven Green Heart Tunnel of the High-Speed Line South”, Int. J. Tunn. Undergr. Space Techno. 12, 1999

[8] Mo H.H. and Chen J.S., ”Study on inner force and dislocation of segments caused by shield machine attitude”, Int. J. Tunn. Undergr. Space Techno. 23, 2008

[9] Tajima M., Kishida M., Fukai N. and Saitou M., “Study on shield tunnel construction loads using a three-dimensional FEM model”, in Proc. Tunnel Engineering, JSCE Vol.14, 2004, pp.353-360

[10] Chaipanna P., Jonpradist P. and Kalasin T., “3D FEA of Shield Segmental Lining with Ground Spring Model”, in Proc. ITA-AITES World Tunnel Congress 2012

SixthInternational Conference on Geotechnique, Construction Materials and Environment, Bangkok, Thailand,Nov. 14-16, 2016, ISBN: 978-4-9905958-6-9 C3051

THERMO-MECHANICAL ANALYSIS OF GEOTHERMAL PILES IN DENSE SAND

Anant Aishwarya Dubey[1], Suresh Kumar[2]
[1,2]Department of Civil Engineering, Indian Institute of Technology (BHU), Varanasi, India.

ABSTRACT

Increasing population and leading development has impacted the surrounding environment with multiplied pollution in the attempt to meet the energy demands. To reduce the harm causing pollutant, the advancement of sustainable and renewable energy sources, is essential. One of the most reliable source of renewable energy is geothermal energy and with geothermal structures, it is possible to transfer energy from the ground to fluid-filled pipes casted in concrete and then to building environments. For efficient design of geothermal piles, it is necessary to evaluate the thermo-mechanical behavior of geothermal piles in local conditions. The aim of this study is to evaluate the behavior of geothermal pile subjected to thermo-mechanical loading. First, in this study the field results are validated and then parametric study by varying mechanical and thermal loading on the geothermal pile placed in dense sand, is performed. In this study the sand-geothermal pile is modeled as axis-symmetrical model where pile is considered to be thermo-elastic in nature and sand is modeled as Mohr-Coulomb elastic-plastic material. Coupled Temperature-Displacement step is applied in order to simulate the observed experimental results. It is shown that the numerical model is able to reproduce the major thermo-mechanical effects approximately.

Keywords: Geothermal Piles, Numerical Modelling, Thermo-Mechanical Analysis, thermal response of pile.

INTRODUCTION

The geothermal piles function as sub-structural support to the building and also fulfill the building's heating–cooling requirements. For manufacturing of energy piles, the reinforced concrete drilled shafts are often preferred over the steel pipe piles because of good thermal storage capacity and thermal conductivity of concrete that make these piles an ideal medium for geothermal energy absorber (Brandl 2006). In spite of the growing acknowledgement on the benefits of energy piles, there is still knowledge cavity in understanding the load transfer mechanism of these piles under thermo-mechanical loading (Laloui et al, 2006).

There are three major ways to analyse the behaviour of geothermal piles, first one is full scale field in-situ tests; the second is, Laboratory scale modelling tests and Centrifuge Modelling tests; and the third way is Theoretical analysis and Numerical Simulations.

First full scale field in-situ test on thermo-mechanical behaviour of geothermal pile was performed at Bad Schallerbach, Austria by Brandl et Al (1998, 2006). An instrumented pile, forming part of an operational GSHP system of 143 piles, was installed during construction works for a rehabilitation centre in Bad Schallerbach, Austria (Brandl, 1998, 2006). The piles are part of a piled raft, supporting a seven-storey building that is benched into a sloping site. The test pile was equipped with pressure cells at the toe and the head, 'fissure meters' at three levels, and 'thermo-elements' at five levels. Data were collected intermittently at different times of the year over several years' operation of the GSHP system.

Second field trial on geothermal piles was undertaken at E´cole Polytechnique Fe´de´rale de Lausanne (EPFL) by Laloui et al. (2003, 2006), Switzerland, during the construction of a new building on the campus. They reported pile uplift and temperature-induced axial stress in the pile is higher as compared to that caused by the mechanical load.

Later Amis et al. (2008) and Bourne-Webb et al. (2009) performed energy pile field trials in Lambeth College, London, UK. The test site is located within the grounds of the Clapham Centre of Lambeth College in South London.

McCartney et al. (2010) performed centrifuge model tests of thermo-active foundations under 60 °C heating and subsequent cooling to 25 °C and observed an increase in shaft capacity of the piles due to heating. Wang et al. (2011) analysed the effect of coupled thermo-mechanical loading on the load carrying capacity of laboratory scale model geothermal energy piles. They reported that temperature is an important parameter which influences the load carrying capacity of the piles. McCartney and Murphy (2012) performed experiments on two full-scale energy foundations installed at the new Denver Housing Authority Senior Living Facility in Denver, Colorado. Upward expansion of the piles during heating was observed for end-bearing piles. Centrifuge test on energy piles in sand has been performed by Goode et al. (2014). They observed upward displacement of the pile head and uniform thermal axial strain in the pile due to heating of the pile.

Kramer and Basu (2014) at The Pennsylvania State University performed laboratory scale modelling of geothermal pile by applying thermal load on pile via fluid (ethyl-glycol and water) through a inbuilt PVC pipe in the energy pile model itself to simulate the real phenomena of thermal load transfer mechanism of energy piles. They concluded increase in velocity of circulating fluid increases the thermal performance of the energy pile, however, since higher velocity of fluid consumes more electricity, it may have unfavorable effect on seasonal performance factor on the system. They also reported that variation of circulation speed doesn't affect the temperature of surrounding soil significantly. It was confirmed by the laboratory scale model testing that the positive and negative temperature gradient have equal and opposite effects on the heat transfer and on soil temperature increment.

Another effective way to analyse the Thermo-Mechanical behaviour of energy pile is by theoritically studying the complex behavior of energy pile, and/or Numerical Simulation. Professor Lyesse Laloui, Alice Di Diona, M. E.Suryatriyastuti, Knellwolf, and Prof. Guney Olgun have performed the simulation and analysis of Geothermal Piles on various software packages like Lagamine finite element software, Ansys, COMSOL and Abaqus Simulia. They have reported on various aspect of geothermal piles like Shaft resistance, Axial Load. Stress behavior and Thermal Performance of energy piles. Laloui et al. (2006) performed finite element (FE) analyses of energy piles. They noted that the thermal piles may undergo uplift as opposed to the mechanical piles which settles when subjected to static dead weight of building. Knellwolf et al. (2011) proposed a new finite difference analysis method for geothermal piles considering elastic pile behavior and neglecting the radial strain in pile during heating and cooling. Amatya et al. (2012) analyzed the results obtained from field tests on energy piles during heating and cooling. They observed that the pile temperature after a thermal recovery cycle was always slightly higher than the initial temperature in each test phase, indicating a build-up of thermal mass around the test pile. The Ground Source Heat Pump (GSHP) association proposed design charts (GSHP 2012) for predicting axial stress and pile head displacement of thermal piles in London clay using a thermal pile software. They predicted that the axial stress in the pile and pile uplift increase with increasing pile temperature. Ghesami-Fare and Basu (2013) performed heat transfer analysis on geothermal energy piles using finite difference method & reported that heat transfer from energy piles happens in radial direction. Mimouni and Laloui (2013) studied the effect of radial strains in thermal piles on the associated soil–structure interaction numerically. Arson et al. (2013) investigated the effect of debonding and presence of air pocket at the soil– pile interface in heat propagation from the geother- mal piles in dry sand. They observed that air pocket at the pile–soil interface has an insulating effect and thus, less heat is transmitted to the ground than in the case of perfect adhesion, which results in higher temperature in the pile and lesser temperature in the soil. They also observed that debonding has a critical effect on the mechanical performance of the pile due to loss of frictional resistance. Di Donna and Laloui (2013) studied the settlement behavior of energy pile due to cyclic heating of the pile and noted that the pile settlement increases only for the first five cycles of heating and then settlement becomes constant. They also reported that thermal load may cause an additional settlement in the order of 10 % of the settlement induced due to mechanical load. Wang et al. (2012, 2014) performed coupled thermo-pore-mechanical FE analysis of centrifuge experiments on energy piles in saturated and partially saturated silt, respectively. They investigated the strain and displacement response of the pile and temperature distribution surrounding the pile considering the soil domain as linear elastic and isotropic. Rajnee Saggu and T. Chakroborty (IIT, Delhi) , 2014 studied stresses and displacement of the energy piles in sand and the surrounding soil under cyclic thermo-mechanical loading" on abaqus simulia using Abaqus Simulia. They applied 50 cycles of thermal loading of $\Delta T = 21°C$ on different load magnitudes and concluded that Negative Shear stress is generated near the pile head in the soil and The ultimate capacity (limit load) of the energy pile is unaffected by temperature changes.

Simulation and Parametric Studies

In this study, nonlinear transient thermo-mechanical axisymmetric FE analyses have been carried out for floating energy piles in dense sands. The pile and soil geometries are created as separate parts using FE software Abaqus. Figure 1 shows pile–soil geometry and the FE mesh for the pile–soil domain. The vertical far-field soil boundary in the model has been placed at a distance of fifteen times of the pile diameter from the pile–soil interface. The bottom soil boundary is placed at a distance of one pile length from the bottom of the pile.

The far-field vertical soil boundary has been restrained in horizontal direction using roller support and the bottom soil boundary has been restrained in both vertical and horizontal directions using pinned support. The thermal boundary conditions applied in the model include heat flow through the far-field vertical and the bottom boundaries of the mesh. Heat flux is assumed to be zero along the axis of symmetry of pile and soil. The ambient soil temperature is assumed to be 15 °C (Laloui et al. 2006). The FE domain has been discretized using four node, axisymmetric, thermally coupled, bilinear displacement and temperature elements (CAX4T) for both soil and pile. At the pile–soil interface, shear strain localization may happen and as a result, shear band formation may take place in the first column of elements next to the pile shaft. Therefore, a refined mesh has been used near the pile–soil interface in soil and coarser mesh in the far-field regions.

The interfaces between the pile and the soil surfaces have been modelled as frictional contact in the tangential direction with a coefficient of friction (μ) between soil and concrete pile = tanϕ where ϕ is the internal friction angle of sand (saggu et al, 2012). In the normal direction between the pile and the soil, hard contact with zero penetration has been considered.

Heat conduction between pile and soil has been made possible by defining a linearly varying gap conductance value. It is assumed that when the distance between the pile and the soil is zero, then the conductance of contact between sand and pile is assumed to be perfect and this value reduces linearly to zero for a gap size of 0.1m between the pile and the soil. However, it is observed from the analyses that no gap formation takes place between pile and soil during thermal cycling. Thus, the gap conductance at the pile–soil interface may be considered uniform and same as soil thermal conductivity.

Validation of Finite Element Model under Thermo-Mechanical Loading

For this study nonlinear transient thermo-mechanical axisymmetric FE analyses of Energy Pile is performed on Software Abaqus Simulia. For the checking the simulated programmes reliability first a full scale in-situ pile was simulated and the results were found to be in good agreement with the field results. The Full scale test chosen for validation was the test performed at EPFL by Lyesse Laloui as the availability of data and extensive work done on the Model.

The FE analysis results of geothermal energy piles under combined mechanical and thermal loading have been validated by comparing the simulation results with the field pile load test data and numerical simulation results given by Laloui et al. (2006).

Laloui et al. (2006) performed thermal pile load tests in Lausanne, Switzerland for a duration of 28 days in which heating period consisted of 12 days and cooling period consisted of 16 days. The length and diameter of the pile were 26 m and 1 m, respectively. The change in temperature was on the order of ΔT = 21 °C induced in the pile. The pile was placed in a layered soil deposit consisting of alluvial soils, sandy gravelly moraine and mollase. An axial load of 1,300 KN was applied at pile head. Laloui et al. (2006) modelled the field pile load test numerically using the Drucker–Prager thermo-elastoplastic model for soil and linear elastic constitutive model for pile. In the present simulation, axisymmetric, thermo-mechanical FE analysis of a 26 m long pile with 1 m diameter is performed using the coupled temperature-displacement procedure in Abaqus. The elastic and thermal material properties for the concrete pile and the soil layers have been taken from Laloui et al. (2006) and reported in Table 3. The soil stress–strain response is simulated using Mohr–Coulomb model. The pile is assumed to be thermo-elastic in Nature.

Properties	Soil A1	Soil A2	Soil B	Soil C	Soil D	Pile
Mechanical Parameters						
Poisson's Ratio (υs)	0.146	0.146	0.2	0.2	0.15	0.2
Elastic modulus (Es) (MPa)	259	259	451	634	3865	27800
Mohr–Coulomb plasticity parameters						
Frictional angle (ϕ)	30°	27°	23°	27°	-	-
Dilation angle (ψ)	0	0	0	0	-	-
Apparent cohesion (c_s) (Pa)	5000	3000	6000	20000	-	-
Thermal Properties						
Thermal conductivity (k_s) (W/m °C)	1.8	1.8	1.8	1.8	1.1	2.1
Specific heat (C_s) (J/°C)	1200	1230	1200	1091	785	800
Coefficient of thermal expansion (α_s)(/°C)	10^{-5}	10^{-5}	10^{-4}	10^{-4}	10^{-6}	10^{-5}

Table 1: Material Properties Used for First Validation

The results of Simulation were found to be in good agreement with experimental results.

A total of 10645 element are used for simulation of three different sizes with minimum being 0.005625 m^2 in near regions to the pile and maximum is 0.0675 m^2 in far field regions while in the finite element analysis by Laloui et al, coarse 634 elements were consider

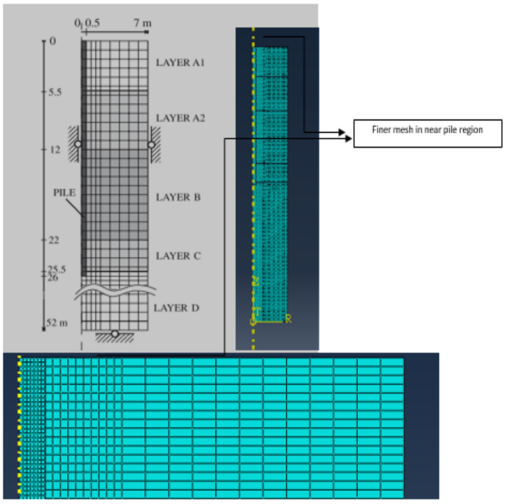

Figure 1: EPFL energy pile-soil profile, Mesh elements used for simulation (mesh elements near pile element are kept finer and in far boundary the mesh is coarser)

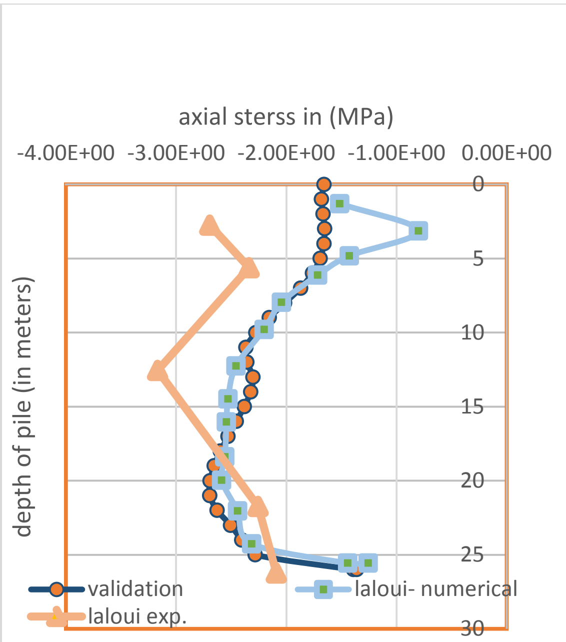

Figure 2: Comparison between Present Simulation Results and Experimental and Numerical Simulation Performed by Laloui et al, 2006.

Thus, the results of Simulation were found to be in good agreement with experimental results.

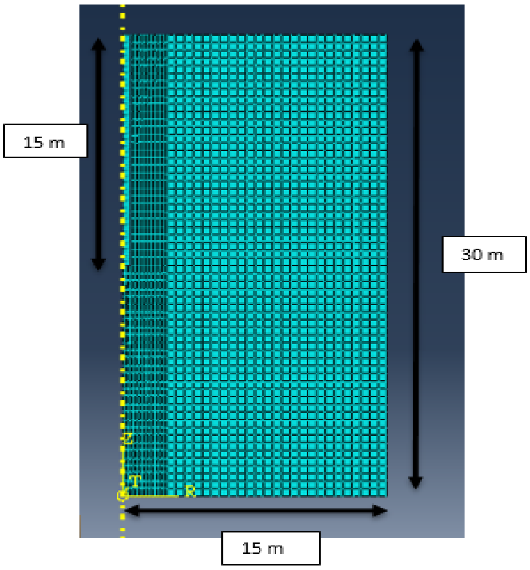

Figure 3: Pile soil Geometry and the FE mesh for pile soil domain for present simulation.

A total of 3800 CAX4T elements were generated with minimum size of 0.005625 m^2 in near regions of pile and maximum mesh size of 0.0675m^2 in far field regions. The material properties used for the simulation and parametric studies are given as follow:

Properties	**Homogeneous sand**	**Geothermal Pile**
Mechanical Parameters		
Poisson's Ratio (υs)	0.2	0.2
Elastic modulus (Es) (MPa)	70	27800
Mohr–Coulomb plasticity parameters		
Frictional angle (ϕ)	30°	-
Dilation angle (ψ)	0	-
Apparent cohesion (c_s) (Pa)	5000	-
Thermal Properties		
Thermal conductivity(k_s) (W/m °C)	1.8	2.1
Specific heat (C_s) (J/°C)	1200	800
Coefficient of thermal expansion (α_s)(/°C)	10^{-5}	10^{-5}

Table 2: Material Properties Used for Parametric studies.

The thermo-mechanical analyses is done on a single pile by for 6 load cases 50 KN, 250 KN, 500 KN, 1000 KN, 1500 KN and 2000 KN for 3 thermal variation in the pile ΔT = 15 °C, ΔT= 25 °C, ΔT=35°C.Three aspects were mainly analysed in the study, Axial Stress behaviour along the length of pile, Radial Stress and Radial Strain Behaviour.

Results and Discussion:

1. Axial Stress in Pile after a complete cycle of Heating and Cooling cycle

(a). At 50 KN Axial axial Load

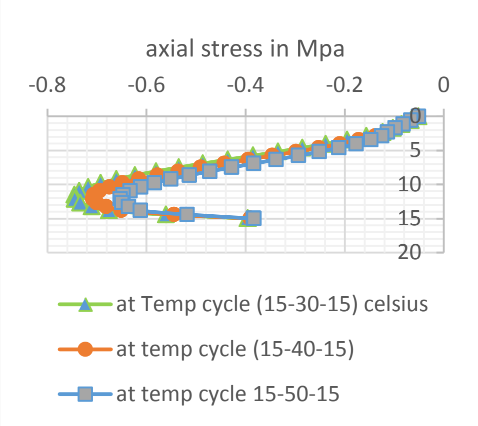

(b). At 250 KN axial Load

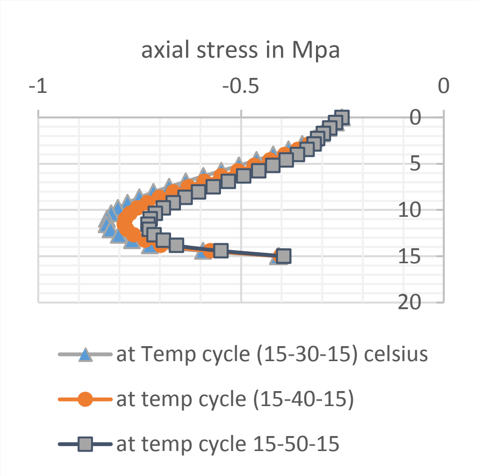

(c). At 500KN axial load

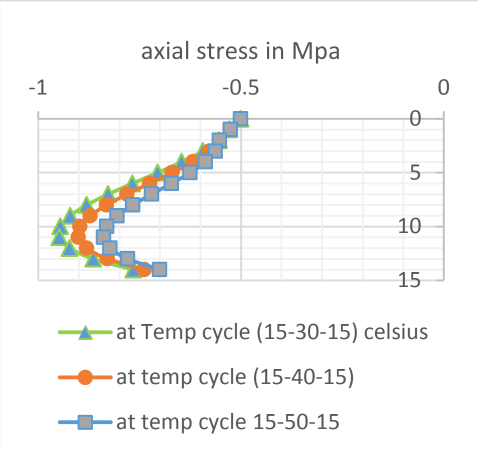

(d). At 1000 kN load

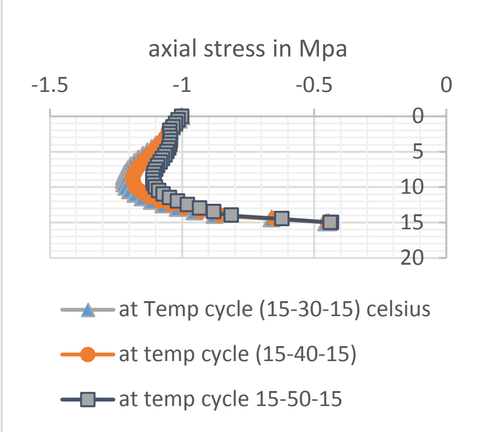

(e). At 1500 KN axial load

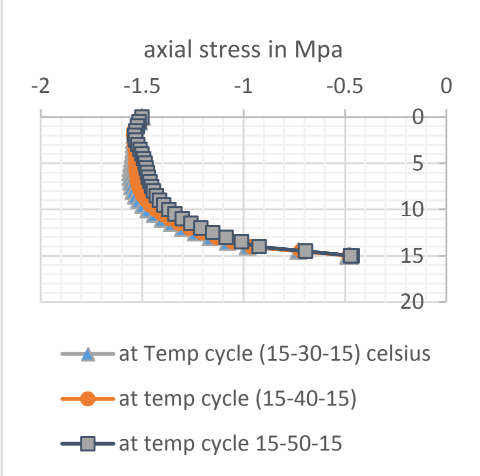

(f). At 2000 KN axial load

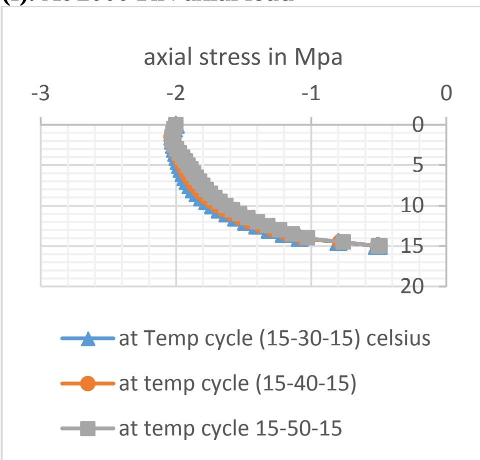

Figure 4: Axial Stresses in Pile after Complete Heating Cooling Cycle at different loading (a). At 50 kN load (b). At 250 kN load (c). At 500 kN load (d). At 1000 kN load (e). At 1500 kN load (f). At 2000 kN load

2. Axial Strain in Pile after Complete Heating and Cooling Cycle

(A). At 50KN Load

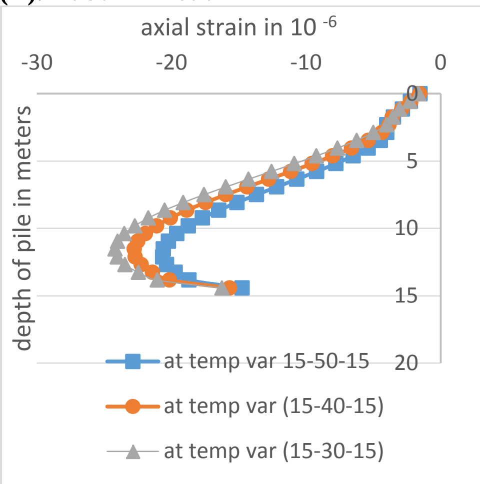

(d). At 1000 KN load

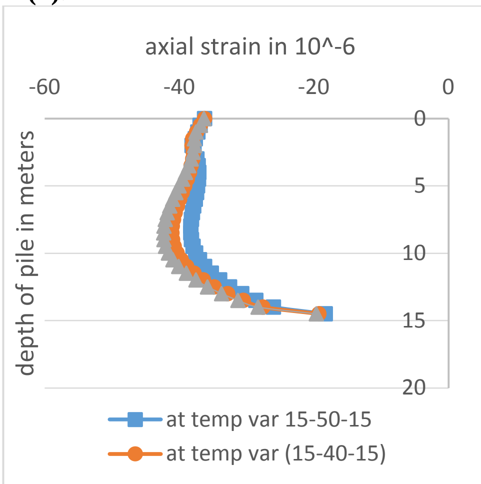

(b). At 250 KN Load

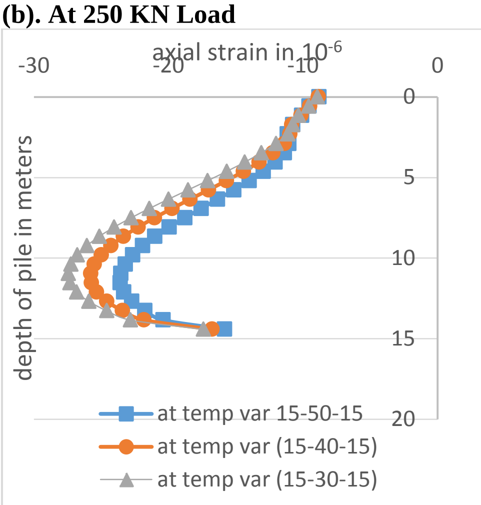

(e). At 1500 KN Load

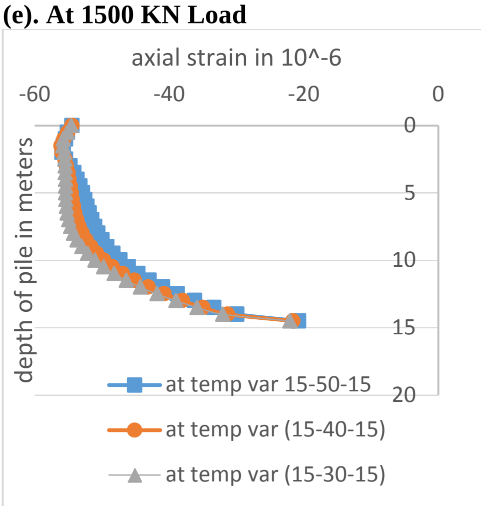

(c). At 350 KN Load

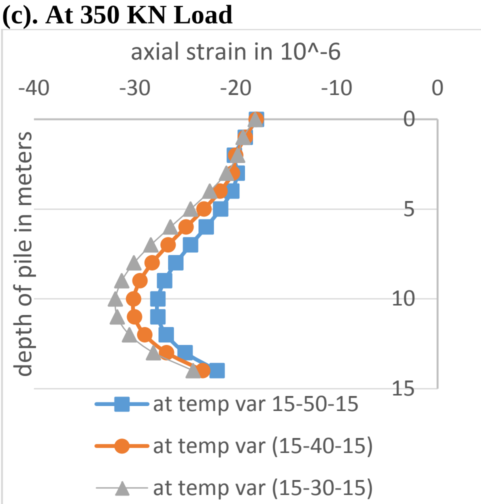

(f). At 2000 KN Load

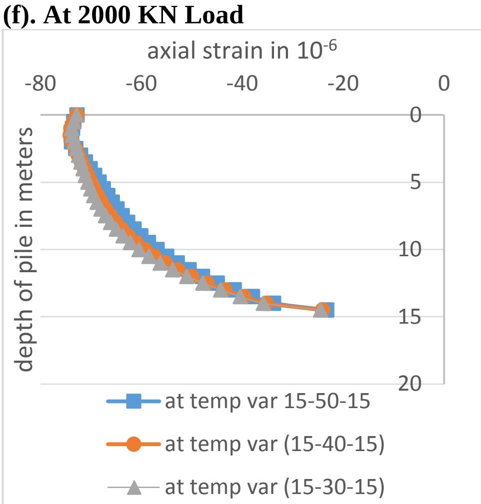

Figure 5: Axial Strain in Pile after Complete Heating Cooling Cycle at different loading (a). At 50 kN load (b). At 250 kN load (c). At 500 kN load (d). At 1000 kN load (e). At 1500 kN load (f). At 2000 kN load

3. Radial Strain in Pile after Complete Heating and Cooling Cycle

(a). At 50 KN Load

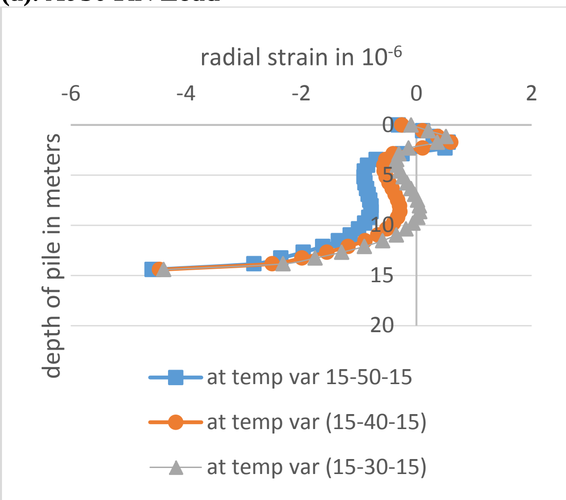

(b). At 250 KN Load

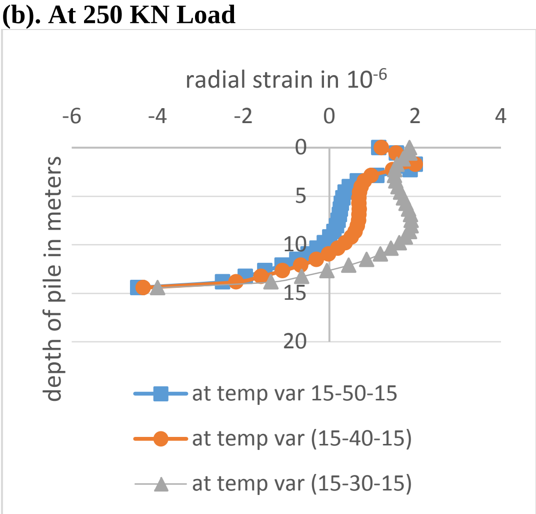

(c). At 500 KN Load

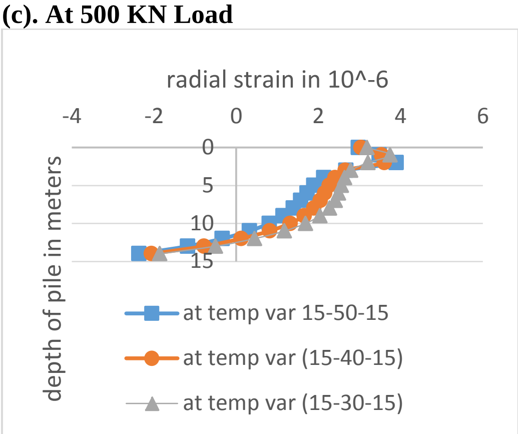

(d). At 1000 KN Load

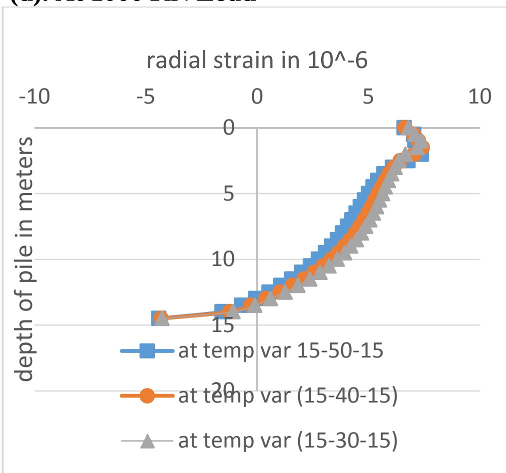

(e). At 1500 KN Load

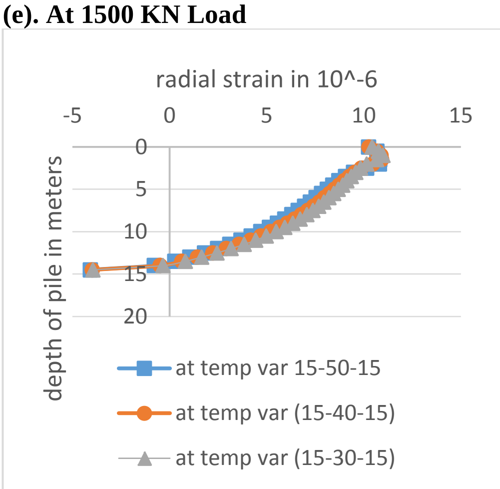

(f). At 2000 KN Load

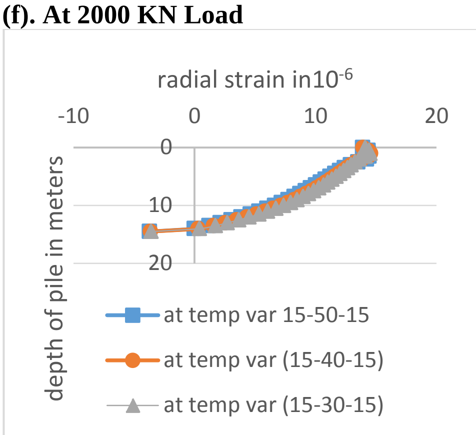

Figure 6: Radial Strain in Pile after Complete Heating Cooling Cycle at different loading (a). At 50 kN load (b). At 250 kN load (c). At 500 kN load (d). At 1000 kN load (e). At 1500 kN load (f). At 2000 kN load

Summary and Conclusion

Geothermal Pile subjected to heating at different loading, varying both thermal load and mechanical load was analysed for a floating pile of diameter 1 meter and length 7.5 meter in dense sand.

The stress strain behaviour was analysed and it may be concluded that-

- At low mechanical load the axial stress generated on the pile varies much on applying thermal loading while when Mechanical Load is high, the axial stress along the depth varies lesser. So it may be concluded that when mechanical load value is low the thermal variation influences the axial stress produced and at higher mechanical load the stress behaviour is nearly constant at different temperature variation, so the axial stress along the pile is majorly due to applied mechanical load.
- The radial strain in the pile was also influenced only at low mechanical load, at higher loads the value of radial stress and strain is nearly same.
- Larger axial strain were noted at the tip of pile and sand surrounding the energy pile near head of pile.

References:

Abaqus/Standard User's Manual, Version 6.11 (2011) Dassault Syste`mes Simulia Corporation, Providence, Rhode Island, USA.

Amis, A., Bourne-Webb, P., Amatya, B., Soga, K. & Davidson, C. (2008), "The effects of heating and cooling energy piles under working load at Lambeth College". Proc. 33rd Ann. and 11th Int. DFI Conf., New York, article no. 1620.

AMATYA, & Laloui, L. (2012). Thermo-mechanical behaviour of energy piles, (6), 503–519.

Arson, C., Berns, E., Akrouch, G., Sanchez, M., & Briaud, J. (2013). Heat Propagation around Geothermal Piles and Implications on Energy Balance, 628–635.

Brandl, H. (1998). "Energy piles and diaphragm walls for heat transfer from and into the ground." Proc. 3rd Int. Symp. on Deep Foundations on Bored and Auger Piles, BAP III, Ghent, 37–60.

Brandl, H. (2006). "Energy foundations and other thermo-active ground structures". Ge´otechnique 56, No. 2, 81–122, http:// dx.doi.org/10.1680/geot.2006.56.2.81.

Bourne-Webb, P., Amatya, B. L., Soga, K., Amis, T., Davidson, C. & Payne, P. (2009). "Energy pile test at Lambeth College, London: geotechnical and thermodynamic aspects of pile response to heat cycle". Ge´otechnique 59, No. 3, 237–248, http:// dx.doi.org/10.1680/geot.2009.59.3.237.

Donna, A. Di, Torino, P., Loria, A. F. R., Donna, A. Di, Loria, A. F. R., & Laloui, L. (2015). Numerical study of the response of a group of energy piles under different combinations of thermo-mechanical loads different combinations of thermo-mechanical loads, (February 2016). http://doi.org/10.1016/j.compgeo.2015.11.010

Kramer, C., & Basu, P. (2014). Performance of a model energy pile in sand. *International Conference on Physical Modelling in Geotechnics*, (August 2014), 1–6. http://doi.org/10.1201/b16200-106

Laloui, L., Nuth, M., & Vulliet, L. (2006). Experimental and numerical investigations of the behaviour of a heat exchanger pile. *International Journal for Numerical and Analytical Methods in Geomechanics*, *30*(8), 763–781. http://doi.org/10.1002/nag.499

Loria, A. F. R., Gunawan, A., & Ng, C. W. W. (2015). Numerical modelling of energy piles in saturated sand subjected to thermo- mechanical loads. *Geomechanics for Energy and the Environment*, *1*(June), 1–15. http://doi.org/10.1016/j.gete.2015.03.002

Loveridge, F. (2012). The Thermal Performance of Foundation Piles used as Heat Exchangers in Ground Energy Systems, 206.

Suryatriyastuti E., Mroueh, B. (2006). Thermo-mechanics behavior of energy pile subjected by monotonic thermal loading Abstract : *20Ème Congrès Français De Mécanique [Cfm2011]*, (2005), 4–9.

Saggu, R., & Chakraborty, T. (2014). Cyclic Thermo-Mechanical Analysis of Energy Piles in Sand. *Geotechnical and Geological Engineering*, *33*(2), 321–342. http://doi.org/10.1007/s10706-014-9798-8

Marto, A., Teknologi, U., Mahir, A., & Universiti, M. (2015). Comparisons on the response of shallow geothermal energy pile embedded in soft and firm soils Jurnal Teknologi C OMPARISONS ON THE R ESPONSE OF S HALLOW, (February 2016). http://doi.org/10.11113/jt.v77.6433

Mimouni, T., & Laloui, L. (2014). Towards a secure basis for the design of geothermal piles. *Acta Geotechnica*, *9*(3), 355–366. http://doi.org/10.1007/s11440-013-0245-4

Mimouni, T., Dupray, F., & Laloui, L. (2014). Estimating the geothermal potential of heat-exchanger anchors on a cut-and-cover tunnel. *Geothermics*, *51*, 380–387. http://doi.org/10.1016/j.geothermics.2014.02.007

Ng, C., Shi, C., Gunawan, A., Laloui, L., & Liu, H. L. (2015). Centrifuge modelling of heating effects on energy pile performance in saturated sand. *Canadian Geotechnical Journal*, *1057*(December 2014), 1045–1057. http://doi.org/10.1139/cgj-2014-0301

MODEL TEST ON THE REINFORCING EFECT OF THE FACE BOLTS IN THE UNCONSOLIDATED SANDY LAYER TUNNEL

Yoshifumi Taguchi[1]

[1]Department of Comprehensive Engineering, Urban Environment Course, Kindai University Technical College, Japan

ABSTRACT

In the tunnel excavating unconsolidated sandy layer in NATM, it is important to stabilize the tunnel cutting face and to prevent the surface settlement. Therefore, various auxiliary methods of tunnel construction are used by this purpose, but it becomes the effective method to drive the long face bolts recently. As the effect of the face bolts for the cutting face stability and the surface settlement control, it is thought that reinforcing effects are different according to length and the interval. In this study, we changed the length and the interval of the face bolts by the two-dimensional model test used Toyoura-sand and examined the influence level on the effect of the face stability and the surface settlement. As a result, face stabilizing effect is higher better installation interval of the face bolt is small. When the length of the face bolt is longer than 0.3D（D: cutting face height）, the reinforcing effect of the cutting face becomes higher. It is small in length 0.2D. When the length of the face bolt is longer than 0.5D, about the surface settlement, a reinforcing effect becomes higher. In addition, the influence range of the surface settlement is 1.3-2.0D before from the tunnel cutting face.

Keywords: Tunnel, Face bolt, Model test, Unconsolidated sandy soil, Reinforcement effect

INTRODUCTION

In the tunnel excavating unconsolidated sandy layer in NATM as shown in Fig.1, it is important to stabilize the tunnel cutting face and to prevent the surface settlement. Therefore, the various auxiliary methods of tunnel construction are used by this purpose, and it becomes the effective method to drive the long face bolts recently.

As the effect of the face bolts for the cutting face stability and the surface settlement control, it is thought that reinforcing effects are different according to length and the interval. In this study, we changed the length and the interval of the face bolts by the two-dimensional model test used Toyoura-sand and examined the influence level on the effect of the face stability and the surface settlement[1]-[6].

OUTLINE OF MODEL TEST

Model Test Equipment

A model test equipment shown in Fig. 2. The size of the soil tank is 65cm in height, 80cm in width, and 15cm in depth. As shown in Fig. 3, Tunnel part of the model is the two-dimensional cross section of the longitudinal direction taken along the center of the actual tunnel cross section, a rectangular cross-section of the cutting face model is 15cm in height and 15cm in width.

The actual tunnel is a three-dimensional cross-section of a circular, but the reason for the two-dimensional, a scale of the soil tank becomes large in three-dimensional tunnel model, the test becomes difficult, but the two dimensional section is because easy to do experiments or analysis.

In this test, a cutting face bolt modeled with a thin Kent paper thicknesses 0.12mm of a flat plate shape, was placed at a predetermined interval in cutting face, as shown in Fig. 3.

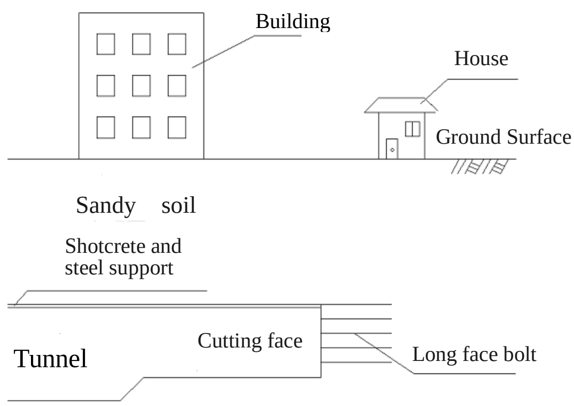

Fig.1 MATM tunnel in unconsolidated ground (face bolt combination)

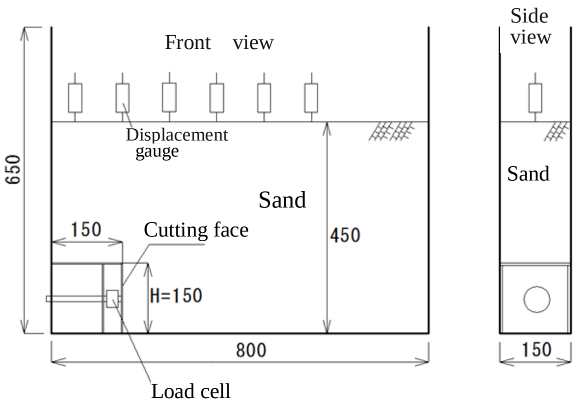

Fig.2 Model test equipment

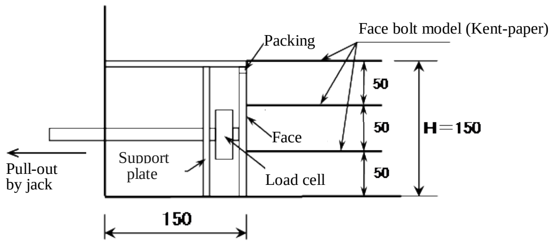

Fig.3 Cutting face part enlarged view (unit mm)

Experimental Method

The model test reproduced the excavation by pulling out the tunnel cutting face model by a screw jack. Upon reaching a predetermined pull-out amount was measured the load acting on the tunnel cutting face and the surface settlement. The load acting on the tunnel cutting face sets the load-cell on the back side of the tunnel cutting face, was measured change of the load in accordance with the pull-out.

Table 1 shows the case of the model test. The length of the face bolt model (Kent paper) was changed 15cm (1.0H, H: cutting face height of model tunnel), 7.5cm (0.5H) and 3cm (0.2H). Further, the installation interval was changed 7.5cm (1- stage), 5cm (3 -stage), 3cm (5- stage), and investigated the influence.

The model of the face bolt used a flat plate shape of Kent paper instead of rod-type bolt is because easy simply compare the effect of the length or interval of the bolts, also because the model preparation near the tunnel cutting face is easy.

Model ground was used Toyoura-sand of the air-dried state. The model sand was free-fall from the outlet of a fixed size at the position of the height 60cm, and the model ground was introduced to overburden thickness 30cm (2.0H). The density of the sand is 1.54g/cm^3.

The pull out of the tunnel, one by 0.2mm up to 0～2mm, one by 0.5mm up to 2～10mm, one by 1mm up to 10～15mm was carried out. The measurement of the surface settlement used a displacement gauge. It was placed in five locations in the 10cm interval.

Table 1 Case of model test

Model test case	Length（ℓ）	Installation interval
1	Non reinforced	
2	15.0cm (1.0H)	1,3,5-stage
3	7.5cm (0.5H)	1,3,5-stage
4	3.0cm (0.2H)	5-stage

EXPERIMENTAL RESULT

Case of Non Face Bolt

Figure 4 shows the change of the load acting on the tunnel cutting face due to the pull out of the cutting face model when there is no face bolt. From this figure, the load acting on the cutting face decreases rapidly in the pull-out of about 1.0mm, then, it converges to 4～5N. This may be because the earth pressure of the cutting face is made from the earth pressure at rest to active earth pressure state.

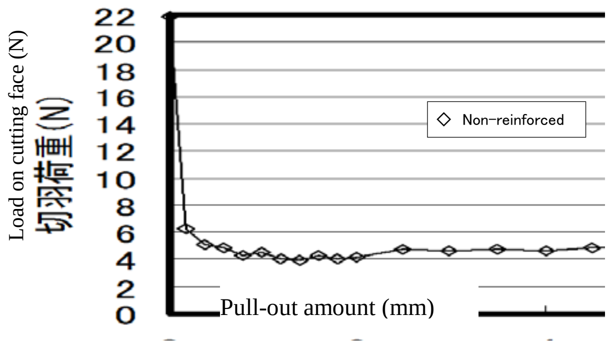

Fig.4 Load on cutting face due to pull-out (non-reinforced)

Similarly, it shows the change in surface settlement due to tunnel cutting face pull out in Fig.5. The measurement point just above the face, and front 10cm, 20cm, 30cm and 40cm from the cutting face just above. It is the point of the rear 10cm from the cutting face just above. The surface settlement of the point of the cutting face immediately above and the front 10cm is large. With the pull-out amount of the cutting face increases, the surface settlement is increasing linearly.

The reason for this surface settlement has increased because its position is within the range of the sliding surface of the ground. The surface settlement amount at the position of the cutting face behind 10cm and face forward 20cm~40cm is small and the surface settlement is not significantly increased even if the pull-out amount of the cutting face is increased. The reason is because the surface settlement is not significantly increased in order to that position the outside than the range of the sliding surface.

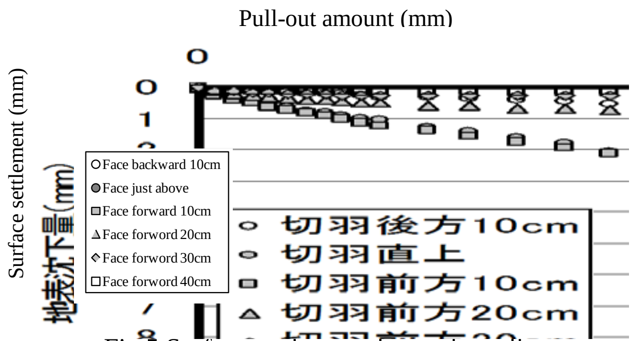

Fig.5 Surface settlement due to the pull-out (non-reinforced)

Case of Using Face Bolts

Figure 6 shows the change in the load acting on the cutting face due to the tunnel face pull-out in the case of the face bolt installed 5-stage at the installation interval 3cm and length 15cm. From this figure, the load acting on the cutting face decreases rapidly in the pull out of about 1.0mm, then, it converges to about 2N. This value is smaller than the value of non-reinforced case, have appeared reinforcing effects of the cutting face bolts.

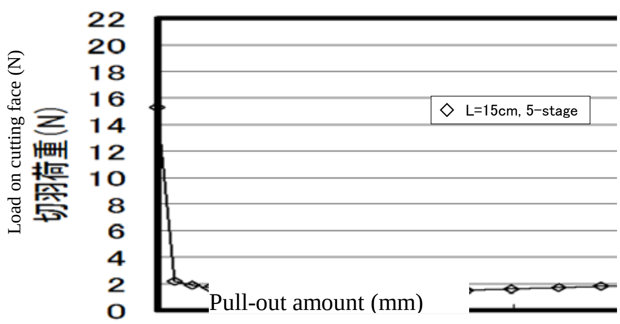

Fig.6 Load on face due to pull-out (Bolt length 15cm, 5-stage)

Figure 7 shows the change in surface settlement due to cutting face pull-out. The settlement measurement points are the same as described above the non-face bolt case. The surface settlement amount of point of the face above and face the front 10cm is slightly larger. The maximum surface settlement at the time of pull-out 15mm of tunnel face is about 2 mm, surface settlement than non-face bolt is considerably suppressed.

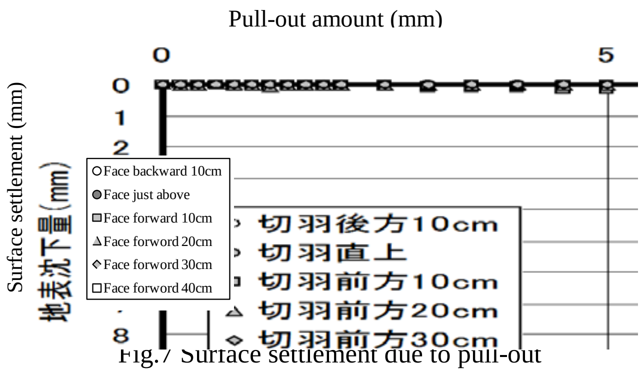

Fig.7 Surface settlement due to pull-out (Bolt length 15cm, 5- stage)

Influence of Number of Bolts on the Load Acting Cutting Face

In the case of length 15cm (1.0H)

Figure 8 shows the comparison of the difference in load acting on the cutting face due to the difference of the face bolt installation interval in the case of face bolt's length 15cm (1.0H). Installation interval of the face bolt is three types of 1-stage, 3-stage and 5-stage. In all cases, the cutting face load in the pull-out of about 1.0mm is reduced rapidly, has converged constant value as the pull-out amount increases. In the case of the face bolt 5-stage, cutting face load has become the smallest, the face stabilizing effect is higher. In the case of 3-stages, the cutting face load has become slightly larger than in the case of 5-stages, it is substantially equal.

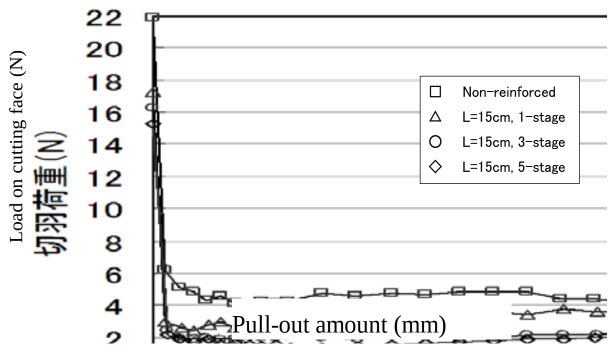

Fig.8 Load on cutting face due to pull-out (Bolt length 15cm (1.0H))

Even if the face bolt 1-stage, the face load is smaller than the case of non-face bolt in the cutting face pull-out early stage, the face stabilizing effect is observed. However, as the pull-out amount of the face is increased, it has become almost equivalence in the case of non-face bolt, the reinforcing effect is small.

In the case of length 7.5cm (0.5H)

Figure 9 shows a comparison of differences of load acting on the cutting face due to the difference in the installation interval of the face bolt when the length 7.5cm face bolt (0.5H). Installation interval of the face bolt is three types of 1-stage, 3-stage and 5-stage. In all cases, the load acting on the face rapidly decreases with the pull-out of about 1.0 mm, is converged to a constant value with the pull-out amount is increased.

In the case of face bolt 5-stages, the load acting on the face has become the smallest, high face stabilizing effect. In the case of the 3-stages, this face load is larger slightly than in the case of the 5-stages. In the case of face bolt 1-stage is almost the same tendency as in the case of face bolt 15cm (1-stage) of the above-mentioned. In the case of face bolt 5-stage, the difference due to the length 15cm (1.0H) and 7.5cm (0.5H) in length it is not seen so much.

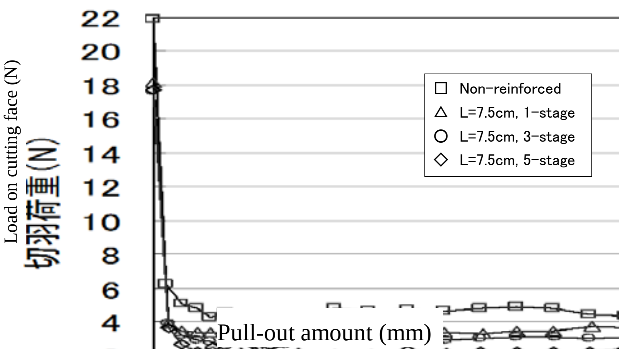

Fig.9 Load on cutting face due to pull-out (Bolt length 7.5cm (0.5H))

Influence of Length on the Load Acting Cutting Face

Figure 10 shows the difference in load acting on the cutting face due to the difference in length of the face bolts when the installation interval of the face bolt is 5-stages. The length of the face bolt is three types of 15cm, 7.5cm and 3cm. In all cases, the load acting on the face rapidly decreases with the pull-out of about 1.0 mm, is converged to a constant value with the pull-out amount is increased. In the case of the length of 15cm, the load acting on the face become the smallest, the face stabilizing effect is higher.

On the other hand, in the case of the length of 3cm, the face load is smaller than in the case of non-reinforced in the face pull-out early stage. However, as the pull-out amount of the face is increased, it has become almost equivalence in the case of non-reinforcing, the reinforcing effect is small. In the case of the length 7.5cm it is almost equal to that of the length 15cm.

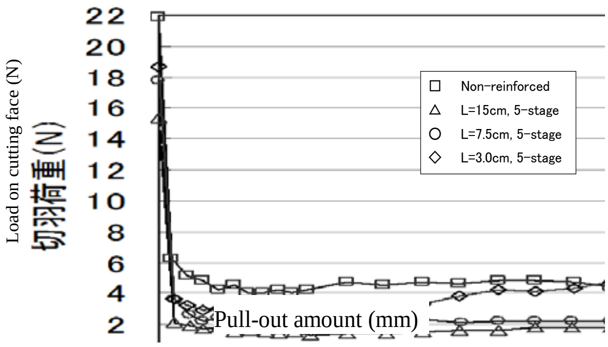

Fig.10 Load on cutting face due to pull-out (Bolt installation interval 5-stages)

Influence of the Installation Number of Face Bolt to Surface Settlement

In the case of bolt length 15cm

Figure11 to 13 shows the surface settlement of the tunnel longitudinal direction in the case of changing the installation interval of the face bolt when the case of face bolt length is 15cm (1.0H). The tunnel cutting face position as 0cm, at the position of the face front 10cm, 20cm, 30cm, 40cm and face backward 10cm, shows the surface settlement value of each case.

Figure 11 shows the surface settlement when pulled out 5mm (0.03H) the cutting face. Although in the case of non-reinforcement are about 2mm settlement at the point of the face front 10cm from the face just above the part, hardly settlement in the face bolt 5-stage and 3-stage. In the case of the face bolt 1-stage, slight settlement occurs.

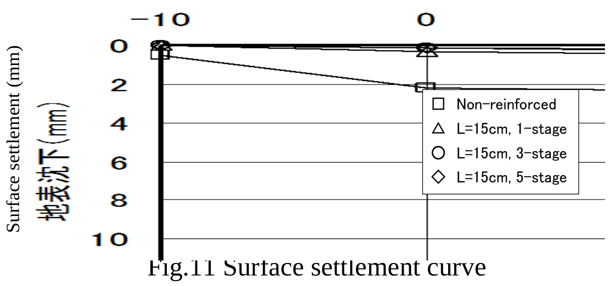

Fig.11 Surface settlement curve (Longitudinal direction, on 5mm pull-out)

Similarly, Fig.12 shows the surface settlement when the cutting face was pulled out 10mm (0.07H). In the case of non-reinforced, at the point of the face front 10cm from the face above, it is about 4mm settlement. On the other hand, in 5-stage and 3-stage hardly subsidence, about 1mm settlement in the face just above even 1-stage, the surface settlement control effect is clearly evident.

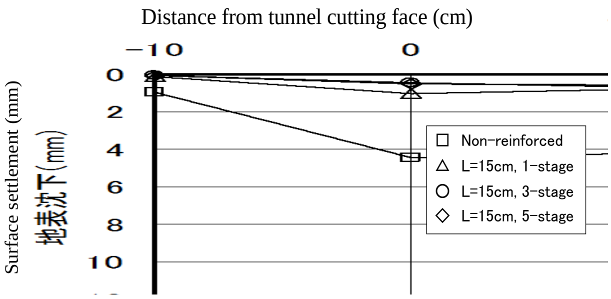

Fig.12 Surface settlement curve
(Longitudinal direction, on 10mm pull-out)

Figure 13 shows the surface settlement when pulled out 15mm (0.1H) the cutting face. In the case of non-reinforcement is about 6～7mm settlement at the point of the face front 10cm. Although the 5-stage and 3-stage have been settlement of about 2mm, increased sharply settlement just above the cutting face in the case of 1-stage, there is no reinforcing effect. In addition, from these figures, the range of influence of surface settlement is about face forward 20 ~ 30cm (1.3 ~ 2.0H).

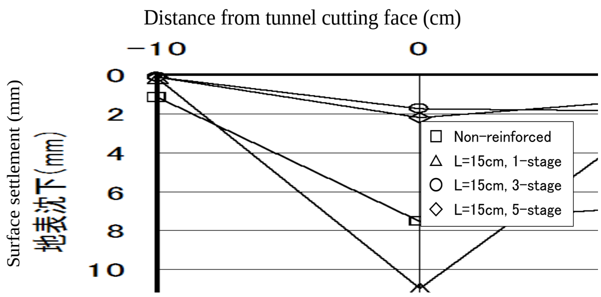

Fig.13 Surface settlement curve
(Longitudinal direction, on 15mm pull-out)

In the case of bolt length 7.5cm

Similarly, Fig.14 to 15 shows the surface settlement of the tunnel longitudinal direction changing the installation interval of the face bolt in the case of face bolt length 7.5cm (0.5H). Figure 14 shows the surface settlement when pulled out 5mm (0.03H) the cutting face. Although in the case of non-reinforcement is about 2mm settlement at the point of the face front 10cm from the face just above the part, in the case of face bolt 5-stage and 3-stage is less than the half. In the case of the face bolt 1-stage, the settlement is about 1mm.

Figure 15 shows the surface settlement when pulled out 15mm (0.1H) . In the case of non-reinforcement are about 6～7mm settlement at the point of the face front 10cm. On the other hand, in the 5-stage and 3-stage is a settlement of about 2mm, a settlement of about 3mm in the 1- stage.

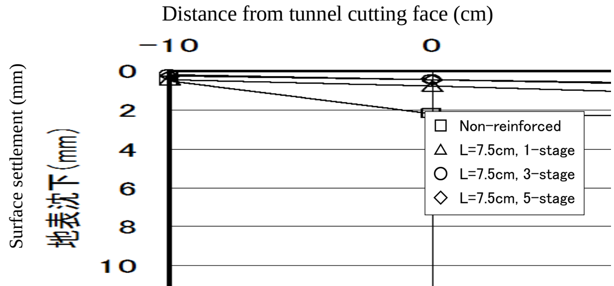

Fig.14 Surface settlement curve
(Longitudinal direction, on 5mm pull-out)

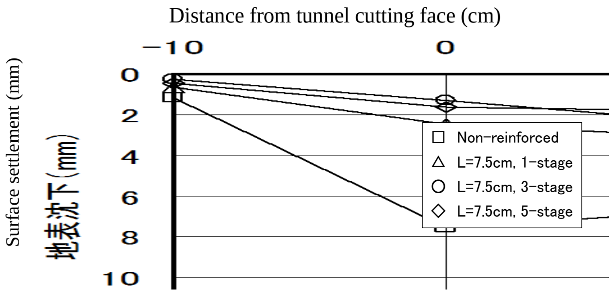

Fig.15 Surface settlement curve
(Longitudinal direction, on 15mm pull-out)

Influence of the Length on the Surface Settlement

Figure 16 to 17 shows the surface settlement of the tunnel longitudinal direction changing the face bolt length 15cm (1.0H), 7.5cm (0.5H) and 3cm (0.2H) in installation interval 5-stages.

Figure 16 shows the surface settlement when pulled out 5mm (0.03H) the cutting face. Although in the case of non-reinforcement are about 2mm settlement at the point of the face front 10cm from the face just above the part, hardly settlement in the case of installing face bolts.

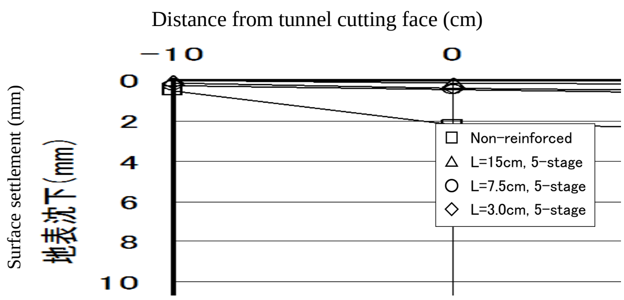

Fig.16 Surface settlement curve
(Longitudinal direction, on 5mm pull-out)

Similarly, Fig.17 shows the surface settlement when pulled out 15mm (0.1H) the cutting face. In the case of non-reinforcement are about 7～8mm settlement at the point of the face front 10cm. Although the settlement amounts of the same degree in the face bolt length 15cm and length 7.5cm are about 2mm settlement, the surface settlement control effect of is high. On the other hand, in the face bolt length 3cm (0.2H), the settlement amount has been increased to about 4mm just above tunnel face, the surface settlement control effect is small.

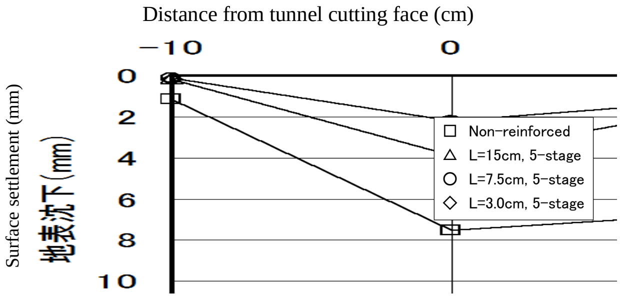

Fig.17 Surface settlement curve
(Longitudinal direction, on 15mm pull-out)

CONCLUSION

In this paper, by the two-dimensional longitudinal direction of the model test using Toyoura-sand, by changing the installation interval and length of the tunnel cutting face bolt, examined surface settlement controlling effect and tunnel face stabilizing effect. As a result, it was found that the following.

(1)Small installation interval of the face bolt and more the number of installations is often the smaller the load acting on the face, the face stabilizing effect becomes higher. In the bolt length 15cm (1.0H, H: face height), the face stabilizing effect is higher in the installation interval 5-stage and 3-stage, but it is small in the 1-stage.

(2)When the length of the face bolt is longer than 0.5H (H : face height), the load acting on the face is small, the reinforcing effect is increased. In the case of installation interval 5-stages, in bolt’s length 15cm (1.0H) and 7.5cm (0.5H) the face stabilizing effect is high, the bolt’s length of 3cm (0.2H) is small.

(3)When the number of installations of the face bolt is larger, the surface settlement control effect is higher. In the case of bolt length 15cm (1.0H), although in the 5-stage and 3-stage surface settlement control effect is large, settlement is increased in 1-stage.

(4)When the length of the face bolt is longer than 0.5H, the surface settlement control effect of becomes higher. In the installation interval is 5-stage, although the length of 15cm (1.0H) and 7.5cm (0.5H) are almost the same settlement control effect, is large settlement in bolt’s length 3cm (0.2H).

REFERENCES

[1] The Japan Geotechnical Society, **“**To construction from the design of the mountain tunnel construction method”, 2007, pp.140-141. (in Japanese)

[2] Japan Society of Civil Engineers,”Practice of model experiments and numerical analysis in the mountain tunnel”, 2006,pp.22-59. (in Japanese)

[3]Fukusima S, Mochizuki Y,Kagawa K, Yokoyama A, “Model test on pre-reinforcement of shallow tunnel in sandy ground”, Japan Society of Civil Engineers, No.406, Ⅲ-11, JUN.1989,pp.79-86.(in Japanese)

[4] Taguchi Y, Kagawa K, Sagara M, Yoshikawa K, “Reinforcing effects of thin flexible pre-lining”, Japan Society of Civil Engineers, No. 645,Ⅲ-50,Mar.2000, pp.125-135. (in Japanese)

[5]Mitarasi Y, Matsuo T,Tezuka T,Okamoto T,Nisimura S,Matsui T,”Evaluation of effect of long face reinforcement method in tunneling”, Japan Society of Civil Engineers, No.743,Ⅲ-64, SEP.2003,pp.213-222.(in Japanese)

[6]Domon T, Seo K, Nishimura K, ”Simplified design method for face bolting based on the reinforcing effect”, Journal of Japan Society of Civil Engineers, Ser. F1,Tunnel Engineering, vol. 66, No. 1,NOV.2010,pp.29-39.(in Japanese)

[7] Tanaka T, Taguchi Y, ” Model Test on reinforcing effect of the long face bolt in unconsolidated sand”, Chubu branch Japan Society of Civil Engineering,Mar.2010, pp 297-298. (in Japanese)

[8] Taguchi Y, Tanaka T,” Model test on the effect of reinforcing the face bolt in unconsolidated sand tunnel”, Kindai University Technical College Research Reports, vol.4, JAN.2011, pp.79-84. (in Japanese)

[9] Taguchi Y, Tabira T,”Model test on tunnel face stabilizing effect of the face bolt”, Kindai University Technical College Research Reports, vol.6, MAR.2013, pp.71-76. (in Japanese)

Sixth International Conference on Geotechnique, Construction Materials and Environment, Bangkok, Thailand, Nov. 14-16, 2016, ISBN: 978-4-9905958-6-9 C3051

TUNNEL LINING RESPONSES DUE TO ADJACENT LOADED PILE – NUMERICAL INVESTIGATION

N. Heama[1], P. Jongpradist[2], P. Lueprasert[1] and S. Suwansawatt[1]
[1] *Faculty of Engineering, King Mongkut's Institute of Technology Ladkrabang, Bangkok, Thailand*
[2] *Faculty of Engineering, King Mongkut's University of Technology Thonburi, Bangkok, Thailand*

ABSTRACT

Underground structures are popularly utilized in urban development, especially tunnels for both transportation and utilities. The interaction problem between existing tunnel and piles from new constructed structures thus becomes unavoidable in dense area. The tunnel would deform or even lose its stability if the additional forces (due to adjacent piles under loading) in lining are drastically high. This depends on many factors, such as the clearance and pile tip level with respect to tunnel position. For preliminary assessment during the first stage of design, it is necessary to estimate this impact. The concept of tunnel protection zone is commonly adopted. However, to establish the tunnel protection zone for adjacent loaded pile, the understanding on this interaction problem is essential. This study analyzes the effect of adjacent pile under loading on the existing tunnel by 3D finite element method. The case study is the tunnel of MRTA project subjected to an adjacent 1 m bored pile under loading with various lengths and clearances. The additional forces (bending moment and axial force) are investigated. The results show that the additional forces increase when the tunnel affected by adjacent loaded pile. the maximum value occurs at invert and right spring line.

Keywords: 3D FEM, Tunnel lining deformation, Structure forces, Adjacent pile

INTRODUCTION

The underground structures increase in urban development, especially tunnels for both transportation and utilities. The Mass Rapid Transit Authority of Thailand (MRTA) has used the tunnel to solve the traffic congestion problems in Bangkok, Thailand. Generally, the MRT tunnels are aligned below major road and pass indirectly under buildings. In recent years, numbers of building constructions are increasing. Some new construction projects using a deep pile foundation are close to existing tunnels. The new constructed adjacent piles under loading as shown in Fig.1 may induce the adverse effect on tunnel lining.

In recent years, 3D finite element method (FEM) was used to analyze the effect on existing tunnel due to loaded bore pile in London [1], the effect of surface construction of multi-storey commercial building on two existing tunnels of Toronto subway in Canada [2] and the effect of a deep open face excavation on existing tunnel in Prague-Czech Republic [3]. In Bangkok, Thailand, the new influence zone considering the pile tip position with respect to tunnel position was presented by [4].

However, those researches focused only on the tunnel deformation and did not consider the additional forces in lining. Only a few works considered the effect on the structural forces in lining. The 2D and 3D FEM are used to study the structural forces during tunnel excavation or even additional forces in tunnel lining affected by ground stratification, surface buildings and tunnel depth [5]. The numerical and finite element analyses have also been utilized in design of tunnel lining [6-8].

Although the current design practice for tunnel lining considers all possible load scenarios during service of the tunnel, however, the future activities have not been included. It is then necessary to evaluate the possible effect of adjacent pile under loading on tunnel lining in terms of additional structure forces. The appropriate mean can then be prepared to tackle this problem.

Therefore, this study investigates the effects of adjacent pile under loading on existing tunnel in terms of the structural forces (bending moment and axial force) by 3D FEM program.

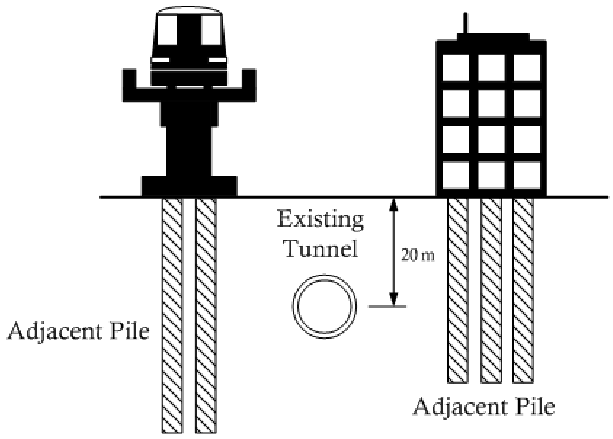

Fig. 1 New construction adjacent to existing tunnel in urban environment.

METHODOLOGY

Considered Problem and Variables

The evaluation of the effects of adjacent single pile on existing tunnel is accomplished with the 3D-finite element program- PLAXIS3D. Undrained conditions were used in this study. The analysis did not consider the influence of pile construction. The length and applied working load of the single pile are varied in the analysis. The working loads are derived using the α – method [9]. In this paper, the geometric parameters in the study case are depicted in Fig. 2a. The tunnel diameter *(D_T)* of 6.3 m, the lining thickness *(T)* of 0.3 m and the tunnel depth *(L_T)* of 20.0 m below the ground surface, the bored pile dimeter *(D_P)* of 1.0 m and the interface of 0.9 which is interaction between soil and pile elements were considered. In addition, two case studies are taken into account. The first case (CASE 1) considered the tunnel located in soft clay. The second case (CASE 2), the tunnel is located in stiff clay. In the analysis, the clearance *(C)* between the bored pile to edge of tunnel and the bored pile length *(L_P)* are varied as shown in Fig 2b.

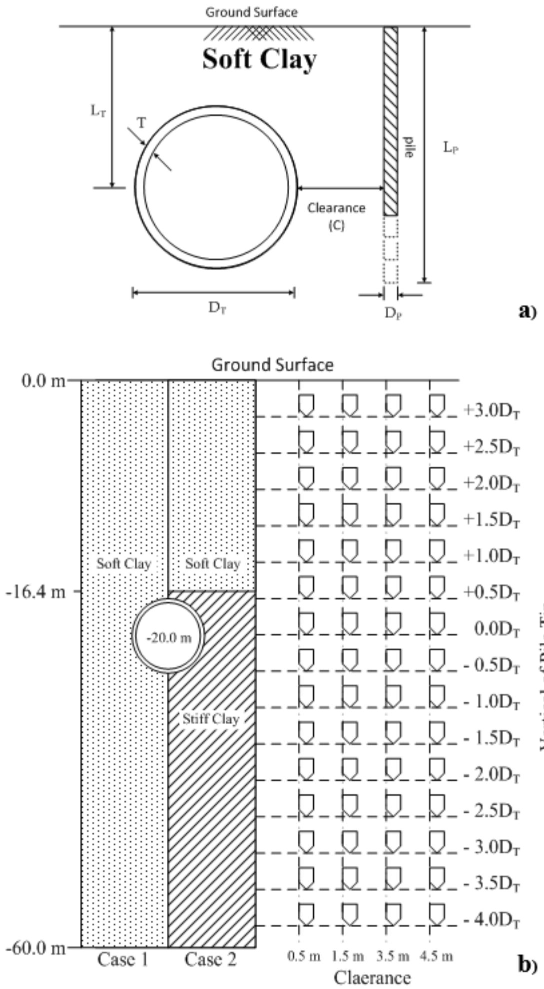

Fig. 2 Geometric parameters, the tunnel and bored pile installed.

Numerical model

The 3D-finite element mesh and numerical modeling in this paper are shown in Fig.3. The dimension of model is 80 m *(≈ 12.5D_T)* in the transverse direction, 60 *(≈ 9.5D_T)* in the longitudinal direction and 60 m *(≈ 9.5D_T)* in the vertical direction. The monitoring plane was assigned at the center of longitudinal direction. To directly obtain the structural forces, shell elements are used to model tunnel lining with grouting layer, which is obtained from [10, 11]. The detail of this technique is presented in the companion paper [12].

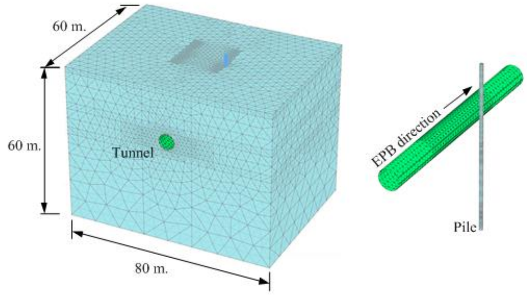

Fig. 3 Model and meshes for tunnel construction in soft clay.

Boundary condition and initial conditions

Boundary conditions

Displacement boundary conditions are used in simulation of this study. The left and right side and bottom boundaries are sufficiently extended from the effect of tunnel excavation and pile settlement in the three dimensional analysis. The sides of the mesh including rear side and front side are free to move vertically but restrained against lateral movements. Left and right sides of mesh are controlled against perpendicular movement. The bottom of the mesh is fixed to both horizontal and vertical movement. The surface is allowed for free horizontal and vertical movement.

Initial conditions

The initial stress state, horizontal effective stress and vertical effective stress are controlled by the coefficient of earth pressure at rest, K_o and unit weight of soil layers. A typical pore water pressure profile from case study in MRTA Blue Line Project in Bangkok, Thailand in term of piezometric drawdown [7] with a water table at depth of 2.0 m below ground surface.

Model parameters

The linear elastic model is assumed for tunnel lining, pile and grouting layer. The soft and stiff clay is modeled by hardening soil model (HS) [13]. The properties of soil are determined form MRT projects [14]. The material parameters for the simulations of geotechnical work in Bangkok subsoil are calibrated by [15].

Table 1 Soil model parameters [16]

Soil layer	Soft clay	Stiff clay
Material model	HS	HS
E_{oed}^{ref} (kPa)	5,000	60,000
E_{50}^{ref} (kPa)	5,000	60,000
E_{ur}^{ref} (kPa)	15,000	180,000
γ_{sat} (kN/m^2)	16	18
υ' (-)	0.33	0.33
ϕ' (°)	22	22
c (kPa)	5	18
m (-)	1	1
p_{ref} (kPa)	100	95

Table 2 Material properties of the bore pile, tunnel lining and grouting layer.

	Young modulus [E] (kN/m^2)	Poisson's ratio [υ]	Unit weight [γ] (kN/m^3)
Bored pile	3.1 x 10^7	0.20	24
Tunnel lining	3.1 x 10^7	0.20	24
Grouting layer	1 x 10^6	0.30	21

Measurement of Structural forces in lining

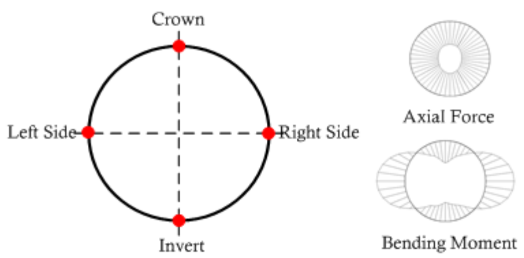

Fig. 4 Positions to observe the structural forces in tunnel lining.

Based on previous studies on impact of adjacent loaded pile on existing tunnel [5,7], the tunnel deformation is generally considered in term of the changed tunnel diameter on the tunnel axis with vertical (tunnel crown and Invert) and horizontal (tunnel spring line) directions. Therefore, the maximum bending moment and axial force were measured from the corresponding positions as shown in Fig 4. The considering method of the change of bending moment and axial force are shown in Eq. (1) and (2). When ϕ_1 and ϕ_2 are structural forces in tunnel lining before and after pile under loading, respectively.

$\Delta\phi_M$ = change of bending moment

$$\Delta\phi_M = \phi_{M2} - \phi_{M1} \tag{1}$$

$\Delta\phi_N$ = change of axial force

$$\Delta\phi_N = \phi_{N2} - \phi_{N1} \tag{2}$$

ANALYSIS RESULT

Structural forces in tunnel lining

The structural forces (bending moment and axial force) of tunnel ling induced by adjacent pile under loading are observed and presented in this section.

Bending Moment

Figure 5 depicts the bending moment at crown, invert and spring line in non-dimensional form when the tunnel is located in soft clay and the clearances between the pile and the tunnel are 0.5 and 4.5 m. The values shown in the figure are normalized by the initial bending moment (M_i) values (after completion of tunnel construction) at their positions. When the pile tip is above the tunnel axis, the bending moment gradually increases with pile length and the maximum value occurs when the pile tip is at the depth of 0.7-075L_T (0.75-0.5D_T above the spring line). The maximum values happen at the invert with the value of 35% of the initial moment. After that, the moment gradually decreases with increasing pile length. The minimum value occurs at a depth in the range of 1.0-1.25L_T. When the pile tip extends to the depth of 1.25L_T to 1.75L_T, the bending moment becomes increasing again and gradually decreases until constant or remains unchanged with extending pile tip position underneath this level. Note that the values of change of bending moment in case of clearance of 4.5 m are much smaller than those in case of clearance of 0.5 m.

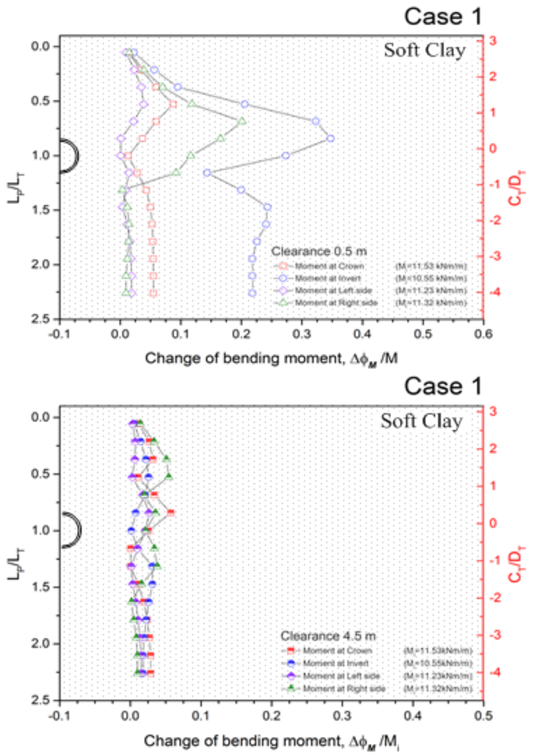

Fig. 5 The change of bending moment in tunnel lining due to adjacent loaded pile in soft clay.

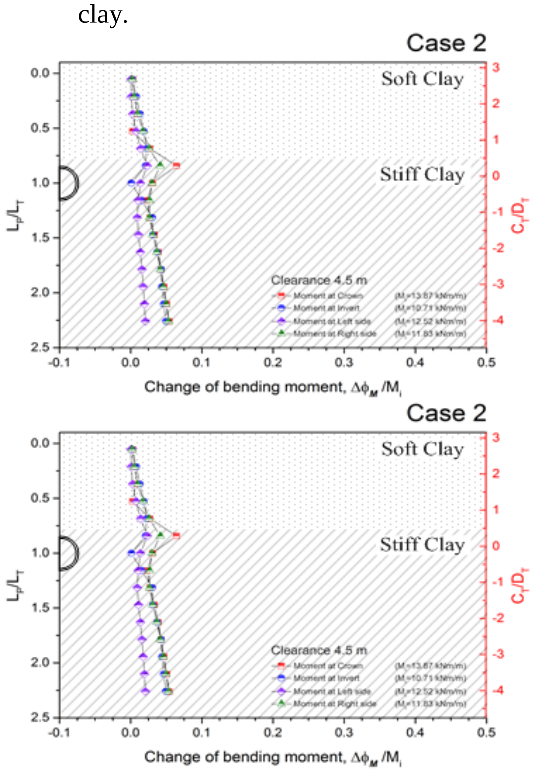

Fig. 6 The change of bending moment in tunnel lining due to adjacent loaded pile in stiff clay.

Figure 6 depicts the analysis results when the tunnel is located in stiff clay. With increasing depth of the pile tip above the tunnel axis, the bending moment gradually increases and the maximum value occurs at a depth of $0.8L_T$, where the pile tip penetrates into the stiff clay layer. After that the moment decreases until the pile tip is located at depth in the range of 1.0-1.25 L_T before increasing with pile length again. However, the ratios of increase of moment ($\Delta M/Mi$) in this case is much smaller than those of the previous case (tunnel in soft clay). Note that the maximum value appears at the crown for this case.

CASE 1, the maximum increments of bending moment at crown and invert increase 8-10 and 5-35 percent, respectively. While at the left and right sides of spring line, 3-5 and 10-25 percent of maximum additional bending moment are observed.

CASE 2, the maximum increments of bending moment at crown and invert increase 10-20 and 10-55 percent, respectively. While at the left and right sides of spring line, 5-10 and 8-50 percent of maximum additional bending moment are observed.

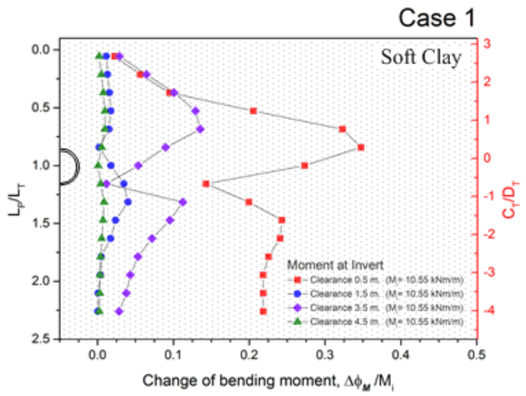

Fig. 7 The change of bending moment in tunnel lining at invert due to adjacent loaded pile in soft clay.

To investigate the effect of clearance on induced bending moment, the change of bending moment in tunnel lining due to adjacent pile with various clearance are shown in Fig.7. Only the case of tunnel located in soft clay and at the invert is shown. The change of bending moment decreases when clearance increases. From the figure, it is seen that only small change in tunnel lining moment occurs if the clearance is larger than 3.5 m. This agrees well with the previous study [7] on tunnel lining deformation. The clearance of 3.5 m seems to be the safe distance for this condition.

Axial Force

Figure 8 depicts the axial force at crown, invert and spring line in non-dimensional form when the tunnel is located in soft clay and the clearances between the pile and the tunnel are 0.5 and 4.5 m. The values shown in the figure are normalized by the initial axial force (N_i) values (before having a loaded pile) at their positions. When the pile tip is above the tunnel axis, the axial force dramatically increases with pile length and the maximum value occurs when the pile tip is at the depth of $0.8L_T$ ($0.5D_T$ above the tunnel spring line). Unlike the bending moment, the maximum value occurs at the right side of spring line. After that, the axial force gradually decreases with increasing pile length. The minimum value occurs at a depth in the range of 1.0-1.25L_T. When the pile tip extends to the depth below the tunnel axis, the axial force becomes constant or remains unchanged in all clearance. Note that the values of change of axial force in case of clearance of 4.5 m are much smaller than those in case of clearance of 0.5 m. In CASE 2 (tunnel located in stiff clay), the ratios of increase of axial force ($\Delta N/N_i$) is much smaller than those of the CASE 1.

CASE 1, the maximum increments of axial force at crown and invert increase 1-2 and 0.5-1 percent, respectively. While at the left and right sides of spring line, 0.5-1 and 1-4 percent of maximum additional bending moment are observed.

CASE 2, the maximum increments of axial force at crown and invert increase 1-7 and 0.5-1 percent, respectively. While at the left and right sides of spring line, 5-10 and 0.5-10 percent of maximum additional bending moment are observed.

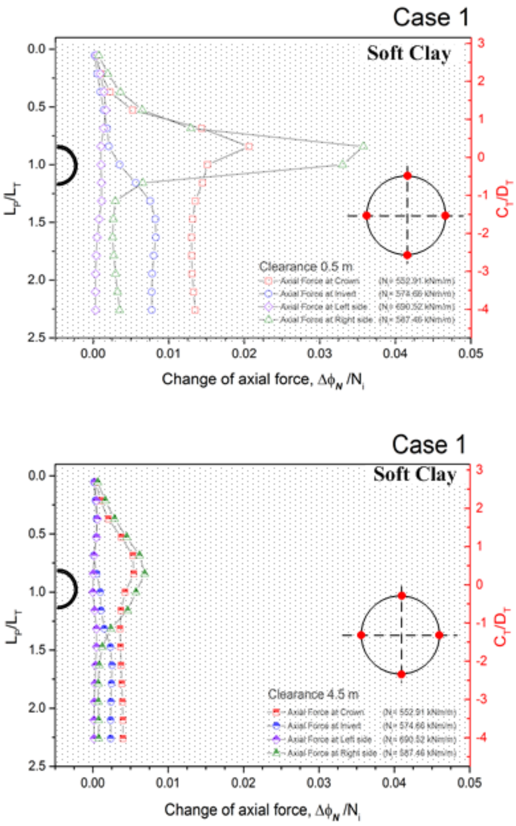

Fig. 8 The change of axial force in tunnel lining due to adjacent loaded pile in soft clay.

By comparing with the result form previous study [17] on tunnel deformation as shown in Fig.9. The position of pile tip to induce maximum deformation agrees well that in this study.

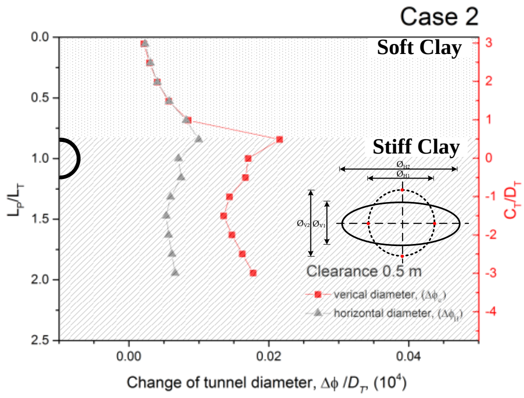

Fig. 9 The change of tunnel diameter due to adjacent loaded pile in stiff clay. (modified from [17])

CONCLUSION

This paper analyzes the effect of existing tunnel due to adjacent single pile under loading by 3D finite element method. The single pile is positioned with various lengths and clearances. The changes of structural forces in tunnel lining are observed. The main results of the analysis are as follows:

1. The structural forces in tunnel lining that is located in stiff clay are larger than those of tunnel located in soft clay. This is due to that the working load on pile in stiff clay (CASE 2) is larger than that in soft clay (CASE 1).
2. The structural forces decrease when clearances increase and become insignificantly increasing when the clearance is larger than 3.5 m. The maximum structural forces in tunnel lining occur when the pile tip is located at the depth of about $0.8L_T$ in all clearance and all cases.
3. It is possible that the increase in structural forces in the lining due to adjacent pile is significant and cannot be neglected. The possible increasing structural forces due to future construction should be considered in tunnel lining design. Otherwise, the lining must be checked if it can resist the additional forces due to the planned construction.

ACKNOWLEDGEMENTS

The authors wish to express their gratitude to the Ladkrabang Underground and Tunneling Innovation Center (LUTIC), Thailand Research Fund (TRF) and 1D2 Group Co. Ltd. for the financial support to the first author through Grant MSD58I0075.

REFERENCES

[1] Schroeder FC, Potts DM and addenbrooke TI, "The influence of pile group loading on existing tunnels", Vol. 54, Geotechnique, 2004, pp. 351-362.

[2] Abdel M-Meguid, Rowe RK and Lo KY, "3D effects of surface construction over existing subway tunnels", Vol. 2, Geomechanics, 2002, pp. 447-469.

[3] Dolezalova M, "Tunnel complex unloaded by a deep excavation" , Vol. 28, Computer Geotechnics, 2001, pp.469-493.

[4] Lueprasert P, Jongpradist P, Charoenpak K, Chaipanna P and Suwansawat S, " Three dimensional finite element analysis for preliminary establishment of tunnel influence zone subject to pile loading", Vol. 9, Maejo Int. J. of science technology, 2015, pp. 209-223.

[5] Katebi H, Rezaei AH, Hajialilue M-Bonab and Tarifard A, "Assessment the influence of ground stratification, tunnel and surface buildings specifications on shield tunnel lining loads (by FEM)" Vol. 49, Tunnelling and Underground Space Technology, 2015, pp. 67-78.

[6] Bakker KJ, " Structural design of linings for bored tunnel in soft ground", Vol. 48, Delft University of technology, 2003.

[7] Suwansawat S, "Earth Pressure Balance (EPB) Shield Tunneling in Bangkok: Ground Response and Prediction of Surface Settlements Using Artificial Neural Networks", Ph. D. Thesis of Massachusetts Institute of Technology, 2002.

[8] Bobbier PG, Moller SC and Vermeer PA, "Bending moments and normal forces in tunnel linings", Conf. on 5th European Conference of Numerical Methods in Geotechnical Engineering, 2002.

[9] Skempton AW, " Cast in- situ bored piles in London Clay", Geotechnique, 2, 195*9, pp. 153-173.*

[10] Kasper T and Mescgke G, "A 3D finite element simulation model for TBM tunnelling in soft ground", Vol. 28, Int. J. for Numerical and Analytical Methods in Geomechanics, 2004, pp. 1441-1460.

[11] Kasper T and Mescgke G, "A numerical study of the effect of soil and grout material properties and cover depth in shield tunnelling", Vol. 33, Computers and Geotechnics, 2006, pp. 234-247.

[12] Lueprasert P, Jongpradist P, Heama N and Suwansawat S, "3D-FEM of EPB shield tunnel excavation using shell element and grouting layer" , Int. Conf. on GEOMAT, 2016. [submitted]

[13] Schanz T, Vermeer PA and Bonnier PG, "The hardening soil model: Formulation and verification", in Proc. of PLAXIS symposium on Beyond 2000 in Computational Geotechnics, Rotterdam, Netherlands, 1999, pp. 281-296.

[14] Prust RE, Davies J and Hu S," Pressure meter Investigation for Mass Rapid Transit in Bangkok, Thailand" Transport. Res. Res. J. of the Transportation Research Board, 2005, pp. 207-217.

[15] Rukdeechuai T, Jongpradist P, Wonglert A and Kaewsri T, " Influence of soilmodels on numerical simulation of geotechnical works in Bangkok subsoil", Vol. 20, EIT Research and Development Journal, 2009, pp. 17-28.

[16] Jongpradist P, Kaewsri T, Sawatparnich A, Suwansawat S, Youwat S, kongkitkul W and Sunitsakul J, " Development of tunneling influence zones for adjacent pile foundations by numerical analyses", Vol. 34, Tunnelling and Underground Space Technology, 2013, pp. 96-109.

[17] Heama N, Suwansawat S, Lueprasert P and Jongpradist P, "Study of lining behavior affected by adjacent loading pile in MRTA Blue Line Project", paper on National Concention on Civil Engineering, 2015.

LIFE CYCLE ASSESSMENT ON LEAKAGE RISK FROM CONTAINMENT STRUCTURES AT COASTAL LANDFILL SITES

Misato Sekitani[1], Shinya Inazumi[2], Suttisak Soralump[3] and Ken-ichi Shishido[4]

[1]Advanced Course of Architecture and Civil Engineering, Akashi College, National Institute of Technology, Japan; [2]Department of Civil Engineering, Akashi College, National Institute of Technology, Japan; [3]Department of Civil Engineering, Kasetsart University, Thailand; [4]TOMEC Corporation, Japan

ABSTRACT

The enclosure function of toxic substances that originate in waste is expected, and the evaluation of achieving the enclosure function has been obtained in previous research on waste landfill sites. However, the initial construction cost is the prime factor for the structural selection of the landfill site in the current approach. Toxic substances are thought to not leak from coastal landfill sites, and most research has not advanced countermeasures for when the toxic substances do leak out in the maintenance management planning. The risk concerning the leakage of toxic substances is assumed to be a decision making standard by especially adapting the risk assessment in the coastal landfill sites. This is especially relevant when the leakage of the toxic substances is presumed to occur according to deterioration in the side impervious walls and by the use of repair methods of the coastal landfill sites.

Keywords: Coastal landfill site, Life cycle cost, Risk management, Side impervious wall

INTRODUCTION

The enclosure function of the toxic substances that originates in waste is expected at the coastal landfill site. In the coastal landfill site, it has been understood that the leakage risk of the toxic substances increases by considering deterioration of the side impervious wall by previous studies [1]. Therefore, it is necessary to conduct an appropriate maintenance repair to achieve the enclosure function of the toxic substances from which the coastal landfill site is requested at the life cycle. However, an initial construction cost is the prime factor for the structural selection of the landfill site in the current state. In other words, the factor for damage level generating the leakage of the toxic substances due to deterioration in an impervious wall is considered as few [2]. The toxic substances have been thought to be no leakage from the coastal landfill site, and most researches have not been advanced of the countermeasures and so on when the toxic substances leak out in the maintenance management planning [2].

In this research, utilization of the risk evaluation according to a concept of asset management on the leakage of toxic substances with deterioration of a steel-made side impervious wall to selection of a repairing method in a coastal landfill site is proposed.

ASSESSMENT OF WATER LEAKAGE RISK IN COASTAL LANDFILL SITES

Fragility function

It proposes a standard exceedance probability as one of the risk assessment, and this technique refers to the fragility function [3]. The fragility function is the one defined as the conditional probability of occurrence to the specified suffering scale.

In this research, the concentration and the total flux of the toxic substances that leaks to the sea area as indexes that shows the leakage risk in the coastal landfill site are applied. The probability to exceed the limit reference set in these indexes is defined as a performance function (X) and a standard exceedance probability (F_X) such as Eqs. (1) and (2).

$$X = \frac{C_A}{C_t} \tag{1}$$

$$F_X = Rrob.(X \le 1) \tag{2}$$

Where, X is the performance function, C_t is the concentration or the total flux of the toxic substances that leaks to the sea area after use t year passes, C_A is the limit reference setting in each index, and F_X is the standard exceedance probability.

C_t (concentration or total flux of the toxic substances that leaks to the sea area after use t year passes) and C_A (limit reference in each index) adopt the lognormal distribution function because of non-negative conditions. When the concrete example is shown for the concentration of the leaking toxic substances, F_X means that the concentration of the leaking toxic substances calculates a probability beyond the closure and abandonment of coastal landfill sites, and it assumes as C=0.1 in this research. Therefore, because the lognormal distribution function is set to the probability density distribution, F_X is expressed as Eq. (3). By the above-mentioned calculation, F_X exceeding the specified limit reference value when uses t year passes is calculated. A similar calculation is performed in the evaluation periods of 30 years, and F_X to the age of service and the index is obtained.

$$F_X = \int_0^1 \frac{1}{\sqrt{2\pi}\zeta_X} \exp\left\{-\frac{1}{2}\left(\frac{\ln x - \lambda_X}{\zeta_X}\right)^2\right\} dx \tag{3}$$

The average (λ_X) and the standard deviation (ζ_X) in the performance function (X) can be led such as Eqs. (4) and (5) by the median value and the coefficient of variation of C_t and C_A previously introduced.

$$\lambda_X = \ln \mu_{CA} - \ln \mu_{Ct} \tag{4}$$

$$\zeta_X = \sqrt{\ln\left(1 + v_{CA}^2\right)\left(1 + v_{Ct}^2\right)} \tag{5}$$

Where, λ_X is the average value in the performance function (X), μ_{CA} is the median value in the limit reference set in each index, μ_{Ct} is the median value in the concentration or the total flux of toxic substances leaking into sea area after use t year passed, ζ_X is the standard deviation in performance function (X), υ_{CA} is the variation coefficient in the limit reference set in each index, υ_{Ct} is the variation coefficient in the concentration or the total flux of toxic substances leaking into sea area after use t year passed.

Loss function

The loss function is a function that showed the expected loss value corresponding to the damage level and the standard deviation of the expected loss [3]. The calculating the expected loss (R) by Eq. (6) requires the amount of the damage loss (C_i) at the damage level and the occurrence probability (P_i) of the damage level. In this research, the total flux of the leaking toxic substances is suitable as an index that calculates the damage level of the coastal landfill site.

The occurrence probability of damage level k ($Prob(k)$) based on the total flux in the toxic substances that leak from the coastal landfill site can be calculated using the standard exceedance probability. Moreover, it is necessary to adopt the LIME for converting it into monetary value to facilitate the comparison with the cost, when the damage loss in the total flux of the leaking toxic substances quantifies it [4]. The estimation of damage cost on the damage level due to the total flux of the toxic substances is shown by Eq. (6).

$$E_k = \sum_t J_k \times e_i \tag{6}$$

Where, E_k is the damage cost related the total flux of the toxic substances in damage level k, J_k is the total flux of toxic substances in damage level k, e_i is the coefficient converted into monetary value by the kind of the toxic substances, i is the kind of the toxic substances.

Because it is assumed the leakage of the toxic substances to the sea area in the coastal landfill site, the coefficient converted into monetary value in its discharge to an area of the sea is adopted in this research. Moreover, because the target that the toxic substances influences are to the ecosystem and to the human body, the damage coefficient calculated by adding both of them each other is set as a coefficient converted into monetary value.

The expected loss value is indicated by Eq. (7).

$$NEL = \sum_i^k Prob(k) \times E_k \tag{7}$$

Where, NEL is the expected loss value relating to toxic substances in coastal landfill sites, $Prob$ (k) is the damage occurrence probability in damage level k, and E_k is the damage cost related to the total flux of the toxic substances in damage level k.

The leakage risk of toxic substances considering the uncertainties to degradation of impervious wall in the coastal landfill site is estimated by adopting the risk assessment in the above-mentioned.

Application method of leakage risk assessment in coastal landfill sites

In the leakage risk of the toxic substances in the coastal landfill site based on deterioration in impervious wall, the probability density distribution is calculated in each index, and also a standard exceedance probability.

When the concentration of the toxic substances that leaks to the sea area is assumed to be an index, C=0.1 is set as a limit reference. Moreover, when the total flux of the toxic substances that leaks to the sea area is assumed to be an index, the damage level is set as shown in Table 1, and the limit reference is set at each damage level. The limit reference based on the closure and abandonment of coastal landfill sites in the total flux is set as the value obtained by using the flow rate becoming C=0.1 that is the concentration of the toxic substances in seepage water under the hydraulic conductivity with 1.0×10^{-6}cm/sec in technical guidelines of impervious walls. Moreover, the limit reference based on technical guidelines of impervious walls is set from the total flux when the value of technical guidelines of impervious walls (hydraulic conductivity with 1.0×10^{-6}cm/sec of the side impervious walls and with 1.0×10^{-5}cm/sec of the clay layers) is adopted. In addition, the probability density distribution is not set, because it is thought that the environmental quality standard value in the closure and abandonment of coastal landfill sites is as appropriate as limit reference (C_A) set in the above-mentioned.

Based on the above-mentioned assumption, it proposes to the coastal landfill site where the leakage risk can be decreased by evaluating the leakage risk of the toxic substances in the coastal landfill site, and understanding quantitatively the influence of each analytical condition from the viewpoint of the risk.

Results of risk assessment concerning leakage

Figure 1 shows a standard exceedance probability by the concentration in each model. The standard exceedance probability by the total flux of the leaking toxic substances is shown in Fig. 2. The standard exceedance probability by the concentration rapidly increases after the elapse of 13 years in analyzed model with the steel-made side double impervious wall (*see* Fig. 1). The standard exceedance probability of 10% in 50 years is adopted as an important probability value on safety in the infrastructure [3]. This is equivalent to the standard exceedance probability at the elapsed time of 1 year is equivalent to 0.2105%. The standard exceedance probability of an analyzed model with the steel-made side double impervious wall after the elapse of 12 years is equivalent to 0.04%, and exceeds the above index. Also in an index of the total flux by leaking toxic substances, as shown in Fig. 2, when the closure and abandonment of coastal landfill sites (rank3) by total flux exceeds the standard exceedance probability of 10% at the elapse of 50 years, the point is equivalent to the elapse of 15 years in analyzed model with the steel-made side double impervious wall. In other words, it is difficult to say that analyzed model with the steel-made side double impervious wall satisfies the containment function of the toxic substances considering the deterioration of impervious walls in coastal landfill sites.

Table 1 Loss level at total flux of seepage pollution materials

	Loss level	Annual seepage flax [cm³/year]
Rank 0	No leaking	0
Rank 1	Abolished seepage concentration: 10%	1.65 E+06
Rank 2	Abolished seepage concentration: 50%	8,26 E+06
Rank 3	Abolished standard of seepage concentration	1.65 E+07
Rank 4	Abolished standard of impervious work	1.13 E+08

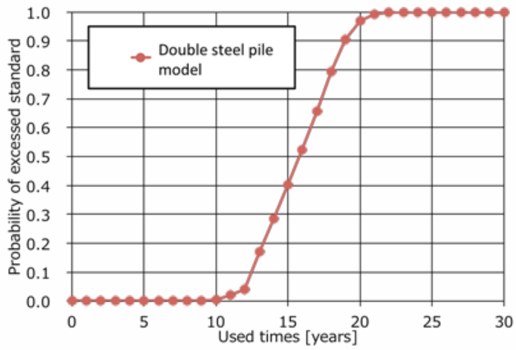

Fig. 1 Probability of excessed standard about seepage pollution concentration

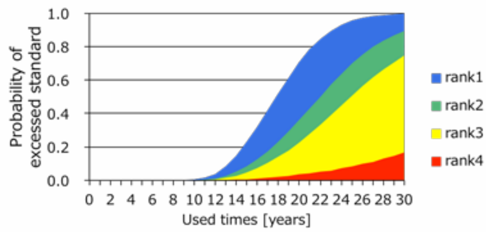

Fig. 2 Probability of excessed standard about total flux of seepage pollution materials

DECISION OF OPTIMAL MAINTENANCE STRATEGIES BASED ON RISK ASSESSMENT CONCERNING LEAKAGE

Outline

In the coastal landfill site, it has been understood that the leakage risk of the toxic substances increases by considering deterioration of the side impervious wall. Therefore, it is necessary to conduct an appropriate maintenance repair to achieve the enclosure function of the toxic substances from which the coastal landfill site is requested at the life cycle.

When the maintenance strategy of social infrastructures is planned, it is necessary to select an appropriate repairing method, time and so on from the concept of an asset management. Moreover, whether it is necessary to repair by using the life cycle cost (LCC) and the cost benefit ratio including the repairing cost and the damage cost as a decision making index concerning the maintenance strategy when repairing is judged. However, when the manifestation of the environmental risk is shown, it is necessary to repair because it is top priority that the landfill site achieves the function to enclose the toxic substances contained in waste.

In this research, deterioration in the side impervious wall is assumed as a factor that causes to increases the environmental risk in the coastal landfill site, and it is proposed as a countermeasure method of repairing the side impervious wall. The leakage risk of the toxic substances is adopted as a decision making index concerning the repair. That is, an appropriate maintenance strategy that considers the decrease of the leakage risk according to the repair is examined.

Assumptions

The leakage risk of the toxic substances according to deterioration in impervious wall is assumed to be a decision making standard in the examination of the maintenance strategy of the coastal landfill site, and the judgment index and the repairing method are examined in this research The assumptions in the decision of appropriate maintenance strategies is shown below.

(1) As seawall form of coastal disposal sites, to adopt a steel-made side double impervious wall. The evaluating the cross-sectional view assumes analyzed model with the steel-made side double impervious wall (*see* Fig. 3).
(2) The evaluation period is assumed to be 30 years.
(3) Because assume the water-level difference in the inside and outside the landfill site to be 200cm, so the relationship between concentration distribution and the total flux of the leaking toxic substances obtained in the previous study is used in examination of the maintenance strategy (*see* Fig. 4).
(4) The concentration, the total flux of the toxic substances leaks, and the hydraulic conductivity of the side impervious wall are adopted as a judgment index to repair.
(5) Propose a strategy to repair steel-made side impervious walls on sea side only as a repairing method in coastal landfill site, also a strategy to repair steel-made side impervious walls on the both sides (sea side and landfill site side), in analyzed model with the steel-made side double impervious wall. Moreover, the repair of the steel-made side impervious wall is made only once.
(6) The hydraulic conductivity of the steel-made side impervious wall after repairs is assumed to be a recovery to the hydraulic conductivity at the time of initial. The deterioration curve of the steel-made side impervious wall after repairs adopts the curve of the best case where deterioration progresses least.
(7) The maintenance strategy sets six patterns in total as shown in Table 2, by set defining point as the time to repair that exceeded the standard in each judgment index.

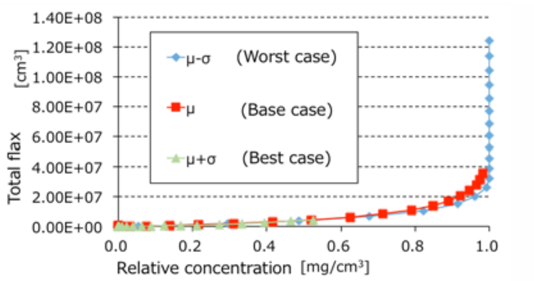

Fig. 3 Relation between total flux and relative concentration

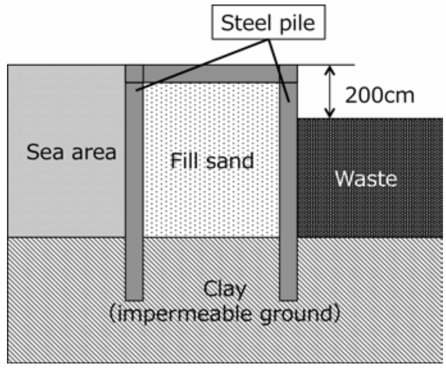

Fig. 4 Double steel pile model at evaluated risk

Table 2 Proposing plan of maintenance and repair in this study

	Decision index	Repairing time	Repairing method
No repairing			No repairing
Plan ①	Concentration	Point in time when the density of the sea area becomes the abolition :C=0.1	Repairing side impervious work (sea side)
Plan ②			Repairing side impervious work (both sides)
Plan ③	Total flax	Point in time when total flax becomes the abolition	Repairing side impervious work (sea side)
Plan ④			Repairing side impervious work (both sides)
Plan ⑤	Coefficient permeability	Point in time when coefficient permeability becomes the abolition :1.0×10^{-6}cm/sec	Repairing side impervious work (sea side)
Plan ⑥			Repairing side impervious work (both sides)

Table 3 Point in time when the standard about decision index

Decision index	Used years [years]		
	μ-σ	μ	μ+σ
Concentration	11	16	24
Total flax	15	23	44
Coefficient permeability	9	22	52

Examination of appropriate maintenance strategy based on risk assessment

In the case that repairing method is not applied, the result indicating a relationship between the concentration and the total flux is assumed to be a "base-plan". In the base-plan, point over the standard set in each judgment index is shown in Table 3. Set point over the standard becomes early by Table 3 in order of the concentration, the total flux, and the hydraulic conductivity. In each repairing method, it is assumed that the side impervious wall is repaired at the elapsed time of showing in Table 3.

In each repairing plan, the transition of a standard exceedance probability for the concentration of the leaking toxic substances is shown in Fig. 5. The effect of the repair is not confirmed from showing no differences with base-plan in plans 2 and 4. At the elapse of 30 years, plans 1 and 2 are able to suppress a standard exceedance probability most. It can be said that it is necessary to adopt the concentration of the leaking toxic substances as the judgment index for the repair. When the side impervious wall on both sides is repaired, the decrease of the leakage risk can be attempted by the difference of the repairing methods.

In each repairing strategy, the expected loss value for the leaking toxic substances and the standard deviation in the expected loss is calculated by the loss function. In addition, the comparative results in the effect of the risk reduction in each repairing strategy is shown by plotting it in the plane indicating risk-expectation that used in the financial engineering field (*see* Fig. 6). In Fig. 6, the base-plan is plotted in upper right. On the other hand, each repairing strategy is plotted in under left. In the plane indicating risk-expectation of this research, plotted in upper right mean it is high risk because the effect caused in leaking toxic substances and differences are large. On the other hand, it means the expectation and the standard deviation are controlled, and it can be called a low-risk to be plotted under the left.

The leakage risk was able to be decreased compared with the base-plan to not repair one, and the effect of the repair could be confirmed in each repairing strategy. It was shown the plans 1 and 2 are able to decrease expectations most in each repairing strategy by the viewpoint of the loss expectation. Moreover, same as a standard exceedance probability, it can be said that it is a method to which the method that repairs the side impervious wall on both sides decreases the loss expectation most. The difference is not confirmed in all repairing strategies from the viewpoint of standard deviation. This is because, the deterioration curve of the side impervious wall after it is repaired is united to the curve of the best case with the latest progress of deteriorate, it is convergence the difference concerning the leakage of the toxic substances.

The concentration of the toxic substances that leaks to the sea area is the most suitable for a judgment index for the repair. The decrease in a water interception performance of the side impervious wall is suppressed because the repairing strategy of which the judgment index is the concentration of the sea area compared with other judgment indices repairs at the early stage. And, it

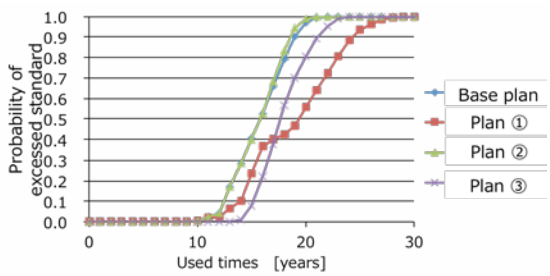

(a) Repairing side impervious work (sea side)

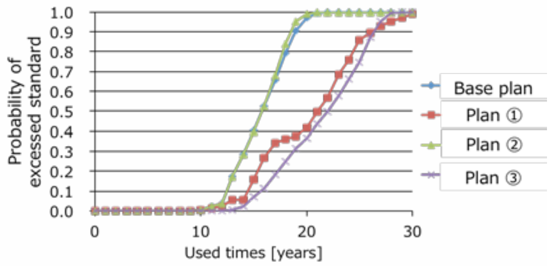

(b) Repairing side impervious work (both side)
Fig. 5 Probability of excessed standard about relation concentration

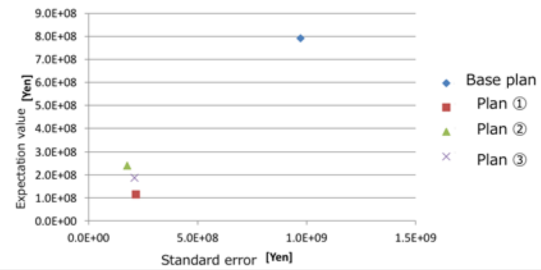

(a) Repairing side impervious work (sea side)

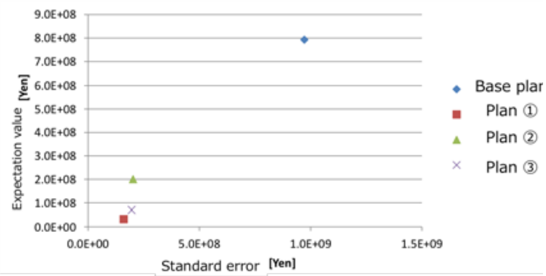

(b) Repairing side impervious work (both side)
Fig. 6 Risk-expectation plane about repair plan

Table 4 Repair and cost effect in repair plan

	Repair effect NEL [Yen]	Repair effect σ [Yen]	Repair cost [Yen]	Cost effect
Plan①	6.77E+08	7.55E+08	2.20E+06	**3.08E+03**
Plan②	5.52E+08	7.96E+08	2.20E+06	2.51E+03
Plan③	6.06E+08	7.62E+08	2.20E+06	2.75E+03
Plan④	**7.60E+08**	**8.12E+08**	4.40E+06	1.73E+03
Plan⑤	5.92E+08	7.70E+08	4.40E+06	1.35E+03
Plan⑥	7.22E+08	7.76E+08	4.40E+06	1.64E+03

can be shown to decrease the leakage risk of the toxic substances by repairing the side impervious wall on both sides in the repairing method.

Because the repairing cost and the achieved effect vary by the difference of the repairing method, an appropriate repairing strategy is selected by using a net present value (NPV) and the life-cycle cost (LCC) in asset management. The repairing cost is not considered because it pays attention only in the effect of the risk reduction of the repair. It will be necessary to select the repairing method from the viewpoint of cost-effectiveness because it is thought that the investment assigned to the maintenance of social infrastructures in Japan decreases in the future. The cost-effectiveness in the repairing strategy of the coastal landfill site is calculated by Eq. (8) [5].

$$Effect\ of\ cost\ measure = \frac{of\ the\ leaking\ risk\ of\ to\ toxic\ substance}{repair\ cost} \tag{8}$$

For calculating the cost-effectiveness of each repairing strategy, it is defined as the amount of the decreasing the leakage risk for the toxic substances on the effect of repairing the coastal landfill site. In other words, a repairing cost is assumed to be the material cost of required water swelling material to repair the joint section of sides impervious wall with a cross section model (horizontal 1m × vertical 13m × width 5m) . Table 4 shows the effect of the repair and cost-effectiveness in each repairing strategy based on the above-mentioned definition. It can be said that the repairing method that repairs the side impervious wall on both sides is appropriate because plan 4 is the largest for the effect of the repair. However, it is shown that plan 1 is appropriate in the viewpoint of cost-effectiveness. That is, it is interpreted that the effect of the repair of corresponding to the repairing cost is not achieved though the leakage risk can be decreased by repaired the side impervious wall on both sides.

It is understood that an appropriate repairing strategy varies by the decision making standard in planning an appropriate maintenance strategy. In the maintenance of the coastal landfill site, it is necessary to repair only the side impervious wall on the sea side under the limited budget constraint though it is necessary to repair the side impervious wall on both sides if it locates with top priority when putting the decrease of the leakage risk.

CONCLUSIONS

A quantitative evaluation on the leakage of the toxic substances in the coastal landfill site where the decrease in a water interception performance due to deterioration in the side impervious wall had been considered was performed. The results and the findings achieved in this research are shown as follows.

(1) To consider the uncertainties in the prediction for a future in the coastal landfill site, the application of risk assessment was proposed. In the risk assessment, a "loss function" that is applied generally in earthquake risk analysis could show over standard probability, the probability that index exceed the limited standard, loss expectation value in leaking toxic substances, and standard deviation.

(2) To perform an evaluation of water leaking risk, it was proposed that an important probability value on safety in social infrastructures is the exceedance probability of 10% during 50 years, and that exceeds at the elapse of 15 years in an analyzed model with the steel-made side double impervious wall was confirmed. However, it is difficult to say that the steel-made side double impervious wall is satisfied the containment function of toxic substances as the structure of landfill sites considered the deterioration of the water interception.

(3) The superiority of the strategy to repair when the concentration of the toxic substances that leaked to the sea area exceeded the closure and abandonment of coastal landfill sites was shown. Moreover, it was confirmed that the strategy to repair only the side impervious wall on the sea area side was suitable when considering the viewpoint of cost-effectiveness.

It is clear that the leakage risk of the toxic substances increases because it considers deterioration in impervious wall in the coastal landfill site. It is a critical issue to decide the strategy on design and the maintenance to consider the leakage risk of the toxic substances at the life cycle of the coastal landfill site.

REFERENCES

[1] Ministry of the Environment: Study Results Report Towards the Costal Waste Landfill Site Closure or Abolished Apply Manual Developed (Draft), 2008.

[2] Waterfront Vitalization and Environment Research of Center: Management Type Waste Landfill Seawall Design, Construction, and Management Manual (Revised edition), 2008.

[3] Aoto, H. and Yoshikawa, H.: A Study of Fragility Curve and Seismic Loss Function for Reinforced Concrete Pier, Japan Concrete Institute, Vol.30, No.3, pp.43-48, 2008.

[4] Itsubo, T. and Inaba, A.: Life Cycle Environmental Impact Assessment Method, MARUZEN, 2005.

[5] Miyagawa, T., Yasuda, K., Iwashiro, I., Yokota, H. and Hattori, A.: Asset Management for Civil Engineers -From a Concrete Structures Viewpoint-, Japan Society of Civil Engineers F, Vol.64, No.1, pp.24-43, 2008.

ANALYTICAL EVALUATION OF THE INFLUENCE OF HOLES FORMED BY PULLING OUT PILE FOUNDATIONS ON THE MECHANICAL CHARACTERISTICS OF THE SURROUNDING GROUND

Kazuki Nosho[1], Shinya Inazumi[2], Suttisak Soralump[3], Shuuichi Kuwahara[4] and Yusuke Torigoe[5]

[1]Advanced Course of Architecture and Civil Engineering, Akashi College, National Institute of Technology, Japan; [2]Department of Civil Engineering, Akashi College, National Institute of Technology, Japan; [3]Department of Civil Engineering, Kasetsart University, Thailand; [4]Marushinn Co., Ltd., Japan; [5]Department of Earth Sciences, Okayama University, Japan

ABSTRACT

Teardowns of social infrastructure, including civil structures, have been increasing in number in recent years because these structures have aged and their utilization has decreased along with the decrease in population. The number pile foundations being pulled out is now far greater than that being newly installed. However, after a pile foundation is pulled out, the mechanical characteristics of the surrounding ground may be affected by the existence of the resulting hole formed by pulling out. There are no regulations yet on injecting fillers into pull-out holes, and the influence of filler strength on the surrounding ground is yet to be elucidated. This study considers the influence of a pull-out hole on the static and dynamic characteristics of the surrounding ground using two-dimensional dynamic finite-element analysis. The special qualities required by fillers injected into such holes are also clarified.

Keywords: existing pile foundation, pull-out hole, surrounding ground, two-dimensional dynamic finite-element analysis

INTRODUCTION

In Japan, many cities are located on soft ground, and many structures use pile foundations. Therefore, for land to be reutilised in places where existing structures are present, it is necessary to remove the existing piles supporting the structure as well as the structure itself for construction of a new structure. Further, existed piles and concrete husk become industrial waste, be left of these industrial waste in the ground is a very difficult problem. In addition, the presence of such piles remaining in the ground is seen as a hidden defect in land transactions [1]. Accordingly, it can be said that the removal of existing piles is essential.

Methods of removing existing piles include the pull-out method and the crushing-removal method [2]. The crushing-removal method suffers from vibration, noise and environmental problems, and hence, the pull-out method is more widely used. However, the pull-out method also has certain problems; in particular, a hole is formed when an existing pile is pulled out of the ground, and if this hole is left unattended, it is possible that the ground surface may subside as earth and sand collapse into the hole. Therefore, it is necessary for filler to be injected into the pull-out hole. Conventionally, mountain sand or sand recycled from construction is used as filler, as these materials are simple and inexpensive. However, as such materials cannot ensure reliable filling or stable strength, the use of processing soil and cement–bentonite has increased in recent years. However, there are no regulations yet on the filler that are injected into pull-out holes, and the influence of filler strength on the surrounding ground is yet to be elucidated.

This study considers the influence of the pull-out holes of pile foundations on the static and dynamic characteristics of the surrounding grounds using two-dimensional dynamic finite-element analysis. The special qualities required by fillers for being injected into pull-out holes are also clarified in this study.

SUMMARY OF THE STUDY OF THE DYNAMIC BEHAVIOUR OF THE PULL-OUT HOLE AND THE ORIGINAL GROUND

The tasks involved in this study are described in points (1) to (5) (as shown in Fig. 1).

(1) Select the study cross section and the input ground-motion waveform.
(2) Create an analytical model based on the cross section selected in point (1), and set the mesh division of the analytical area.
(3) Select an analytical constant. Set the application configuration model and material parameters in the initial stress analysis and the dynamic total

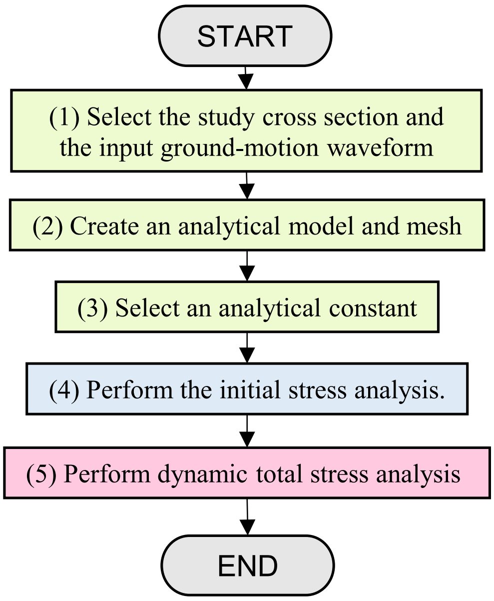

Fig. 1 Analytical procedure

stress elastic–plastic analysis.

(4) Perform the initial stress analysis. The analysis technique used is total stress analysis. In this study, an HD model for the ground material and an elastic model for the hollow portion are applied.

(5) Took over the calculated ground in stress at (4), perform dynamic total stress analysis. Again, as with the initial stress analysis, the HD model for the ground material and the elastic model for the hollow portion are applied. Enter the seismic acceleration at the bottom of the analytical model.

DYNAMIC BEHAVIOUR OF THE PULL-OUT HOLE AND THE ORIGINAL GROUND, THE ANALYTICAL MODEL AND THE INPUT GROUND-MOTION WAVEFORM

Analytical model

In the analysis, the analytical cross section has two layers. The upper layer has clay as a soft stratum, for which the N-value is approximately 4. The lower layer consists of a strong formation of gravel serving as a support layer, for which the N-value is approximately 50. The width of the analytical cross section is set at 50 m, the thickness of the clay layer is 18 m, the thickness of the gravel layer is 8 m and the total depth of the cross section is 26 m. Two pull-out holes exist in the model at a spacing of 4 m; the pore diameter is 1 m, depth is 20 m and the depth of embedment in the gravel layer is 2 m. To improve the accuracy of the analysis, a finer mesh spacing is used near the pull-out hole. This finer mesh continues to be used even when the pull-out holes are filled in order to examine the behaviour of the filling. As a boundary

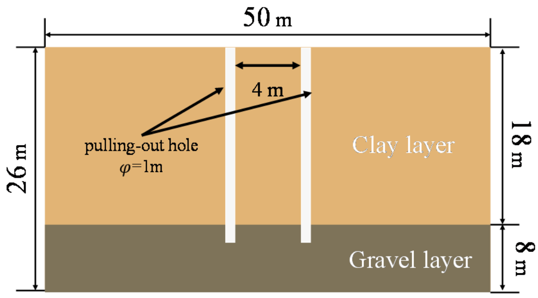

(a) Empty pull-out hole

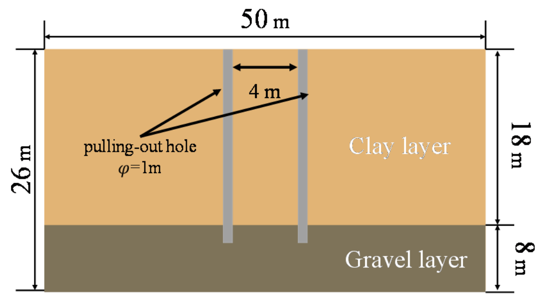

(b) Filled pull-out hole

Fig. 2 Sectional view

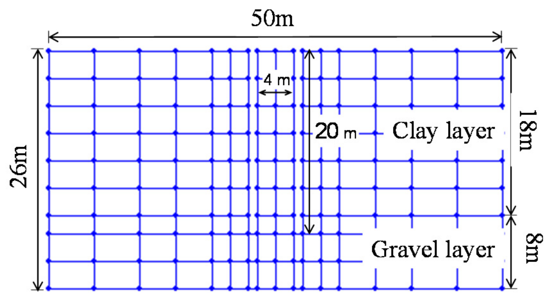

(a) Empty pull-out hole

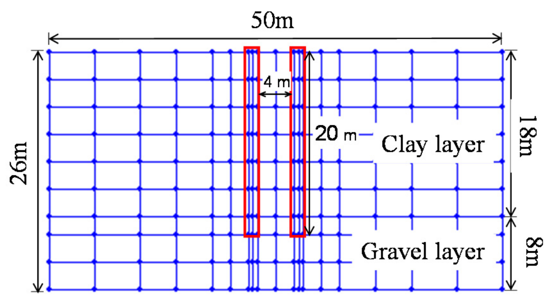

(b) Filled pull-out hole

Fig. 3 Analytical model

condition, in the dynamic analysis, the bottom is a fixed fulcrum and the lateral boundary is the equal-displacement boundary. When the moving node on the side of the left side, node of the other side to the

Table 1 HD model parameters

Parameters	Clay layer	Gravel layer
G_0 (kPa)	27900	298485
σ'_m (kPa)	90	234
v (-)	0.45	0.40
c (kPa)	25	0
φ (°)	0	50

Table 2 Elastic model parameters

Parameters	Pull-out holes (filler)		
	filler 1	filler 2	filler 3
q_u (N/mm^2)	0.1	0.5	1.0
E (kN/m^2)	25280	126400	252800
v (-)	0.48	0.46	0.44

Table 3 Element parameters

Parameters	Clay layer	Gravel layer	Pull-out holes (filler)
γ_t (kN/m^3)	15	21	15
γ_w (kN/m^3)	9.8		
Constitutive law	HD model	HD model	Elastic model

displacement is the same movement as the node on the side of the left. Therefore, it is possible to express whether the stratum has spread to the left or right.

Analysis is performed on three types of ground: one with no pull-out holes, one with empty pull-out holes and one where the pull-out holes are filled. The analytical cross-sectional view of the ground is shown in Fig. 2. A similar analytical model is shown in Fig. 3. In the case of filled pull-out holes in Figure 3, the portion surrounded by a red frame is the pull-out hole portion. The parameters of the HD model in the clay and gravel layers are shown in Table 1. Table 2 shows the parameters of the elastic model of the pull-out hole.

Constitutive law and material parameters

The parameters in the clay and gravel layers used in the analysis as well as the soil parameters in the pull-out hole are shown in Table 3. In this analysis, a fluidising processing soil is used as a filler; experimental values of its properties can be seen in the literature [3], [4]. In addition, three fillers with different elastic moduli and different Poisson ratios are analysed in order to examine the effect of filler strength on the ground. The strengths of the fillers increase in the order filler 1, filler 2, filler 3. Parameters used in the analysis is to determine the anamnestic literature reference [5].

γ_t represents the weight per unit volume of soil; γ_w represents the weight per unit volume of water; G_0 represents the initial shear stiffness; σ'_m represents the initial average active confining pressure; v represents Poisson's ratio; c represents the adhesive force; φ represents the internal friction angle; q_u represents the compressive strength; and E represents the elastic coefficient.

Input ground-motion waveform

In the analysis, the waveform of the El Centro 1940 NS earthquake (which was provided by the Building Centre of Japan) is exerted on the substrate's surface. The maximum acceleration is 341.7 cm/s^2.

ANALYTICAL RESULTS AND STUDY OF THE DYNAMIC BEHAVIOUR OF THE PULL-OUT HOLE AND THE ORIGINAL GROUND

The results of the dynamic analysis for the three types of ground are shown as follows.

Results of the dynamic analysis

Figure 4 shows the diagrams of the maximum displacement for each of the three ground types. In addition, Fig. 5 shows the X-direction displacement contour diagrams, and Fig. 6 shows the Y-direction displacement contour diagrams. Figure 7 shows the time history view of the X-direction displacement of the ground centre in the cases where no pull-out holes are present and where the pull-out holes have been filled.

Study of the results of the dynamic analysis

It can be seen that the ground wave causes significant horizontal displacement in all cases when it is allowed to act on the base surface. From Figure 4, it can be seen that a large ground subsidence occurs in the vertical direction when the pull-out hole is empty. The maximum subsidence in ground surface is approximately 60 cm, which is very dangerous. However, this subsidence does not occur in the case where the pull-out holes are filled. Thus, it can be said that filling the pull-out hole is an effective way to prevent subsidence.

From Fig. 4, it can be seen that, using filler 1, the maximum horizontal displacement is on the left side, unlike in the other cases. Figure 5 clearly shows that the behaviour of the horizontal displacement under filler 1 is different from that of the other cases.

In the other cases, displacement to the right occurs rapidly at approximately 5 seconds and displacement have continued while the displacement remained. However, if the displacement at 5 seconds is small,

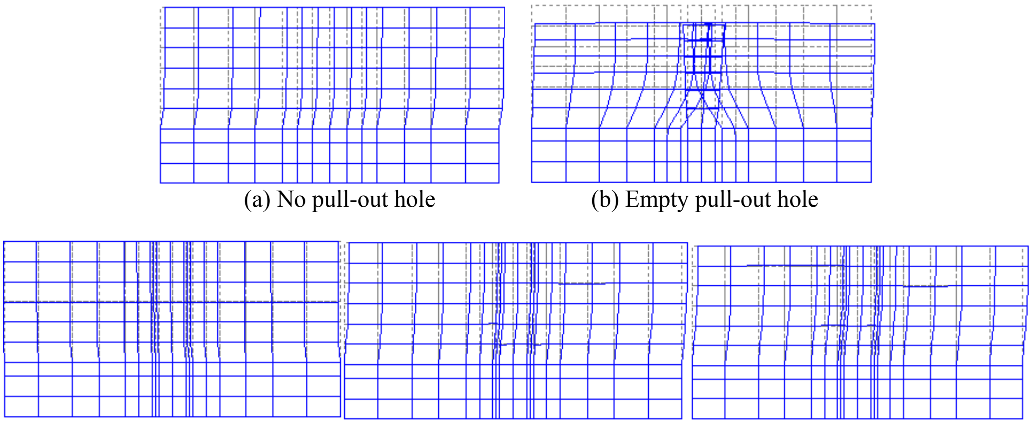

(a) No pull-out hole (b) Empty pull-out hole

(c) Filler 1 (d) Filler 2 (e) Filler 3

Fig. 4 Displacement diagram (The amount of displacement is three times)

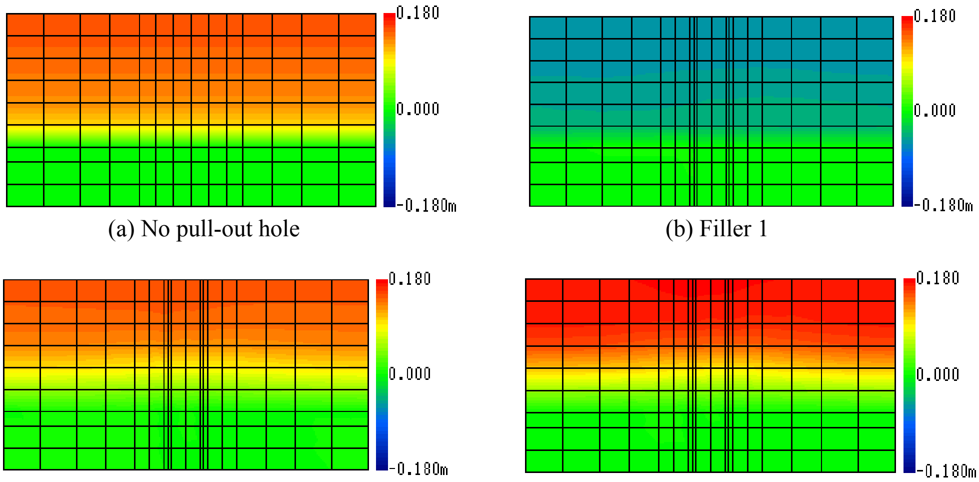

(a) No pull-out hole (b) Filler 1

(c) Filler 2 (d) Filler 3

Fig. 5 X-direction displacement contour diagrams

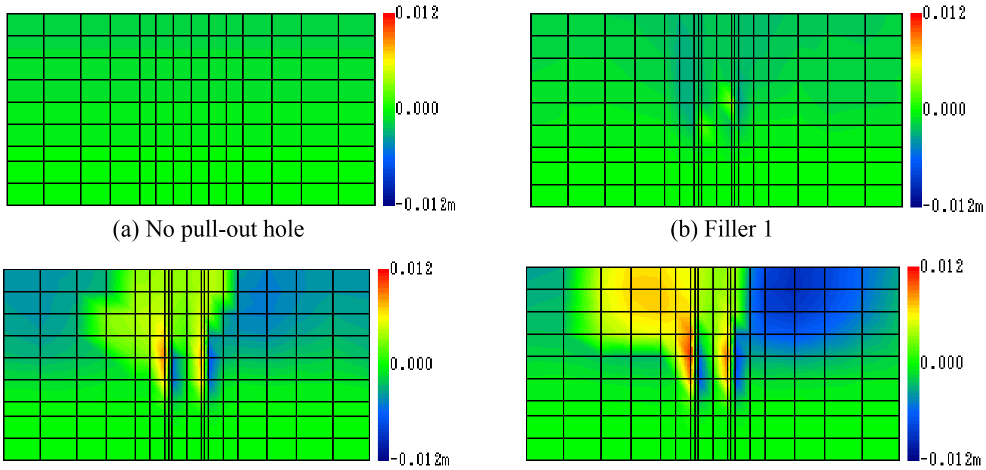

(a) No pull-out hole (b) Filler 1

(c) Filler 2 (d) Filler 3

Fig. 6 Y-direction displacement contour diagrams

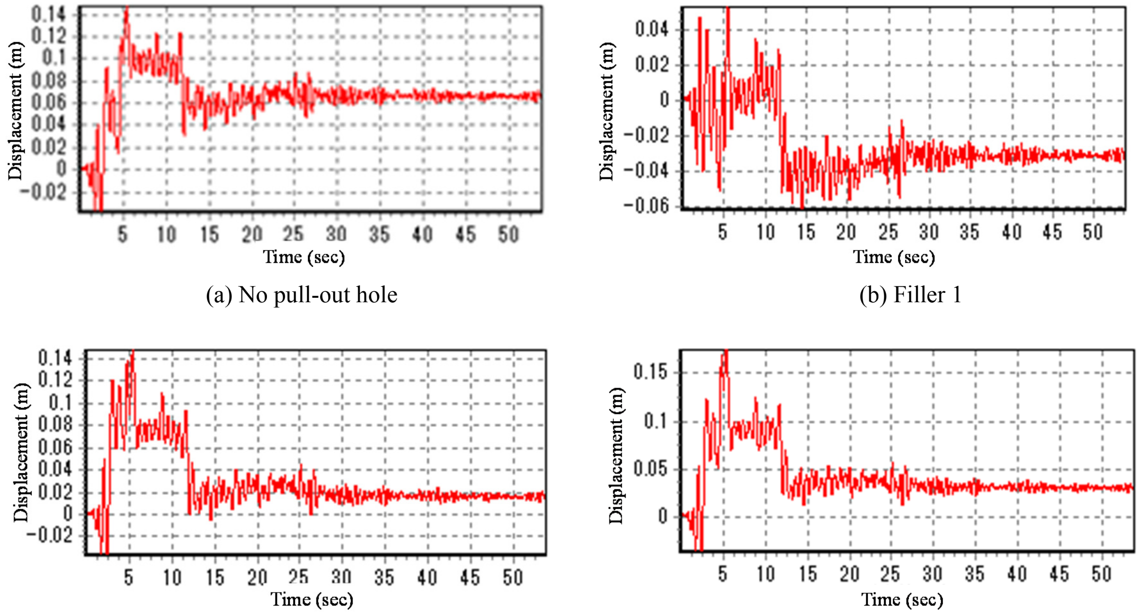

(a) No pull-out hole (b) Filler 1

(c) Filler 2 (d) Filler 3

Fig. 7 Time history view of the X-direction displacement of the ground centre

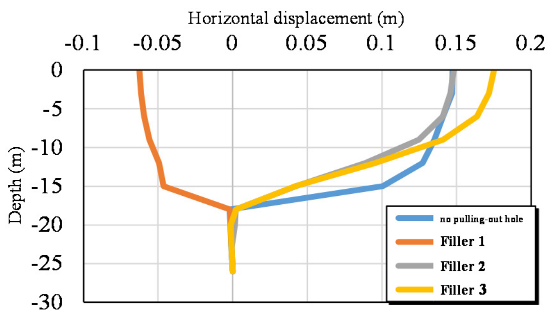

Fig. 8 Graph comparing the horizontal displacements of the ground centre line

then the system will soon return to its original configuration. From this fact, it is believed that the behaviour of the horizontal displacement of the ground varies greatly when the filling material strength is too small. From Fig. 5, it can be seen that the horizontal displacement is greatest in the case where filler 3 is used and the displacement is approximate in the case where no pull-out holes and filler 2 are used. Figure 8 shows a comparison of the horizontal displacements of the ground centre line. From Fig. 8, it can be seen that rapid displacement of the clay layer bottom occurs in all cases. In addition, the behaviour of the ground with holes filled by filler 2 is considered to be closest to the behaviour of the ground without pull-out holes. In the vertical direction, bulging occurs on the left side of the filling portion and subsidence occurs on the right side when fillers 2 and 3 are used. Furthermore, it can be seen that the displacement increases as the filler strength increases.

CONCLUSIONS

In this study, two-dimensional dynamic finite-element analysis was used to elucidate the effect of pull-out holes of foundation piles on the dynamic behaviour of the ground.

The results obtained from the analysis are shown below.

(1) Ground subsidence occurs in the vicinity of a pull-out hole when the hole is left empty, particularly in the area sandwiched between two pull-out holes. A very large subsidence occurs in a wide range of ground surfaces if ground motion is applied .

(2) When the pull-out holes are filled, ground subsidence does not occur in the dynamic or static analyses. For this reason, it is clear that filling pull-out holes is effective.

(3) When the filling strength is too small relative to the strength of the original ground, the ground may behave in a significantly different way from the case with no pull-out holes. For this reason, it is necessary to change the filler strength to suit the ground conditions.

This study has not taken account of the influence of different compounding filler materials or different hole shapes. Therefore, there is a need to investigate these conditions as the subject of future analysis.

REFERENCES

[1] Murakami T, “Leaving the foundation pile, backfilling denied the defects of ground support force of the part, agent of accountability violation was also negative case”, RETIO, No.82, pp.166-167, 2011.

[2] Marushicn Co., Ltd., “About the PG Methods”, http://marushinn.jp/about_chacking.html, 2016.

[3] Furugaki Y, Nakasawa F, Utaka Y, Tokuda K, “Study on the Young's modulus of the fluidized processing soil”, Summaries of Technical Papers of Annual Meeting Architectural Institute of Japan, pp.591-592, 2014.

[4] Furugaki Y, “Deformation properties of the backfill material which has a fluidity and self-hardening”, TowN-value-up Management Report, No.37, pp.41-44, 2011.

[5] Ministry of Land, Infrastructure, Transport and Tourism (MLIT), “Public Building Construction Standard Specification (Building Work) 2013 Edition”, MLIT, 2014.

DEVELOPMENT OF SILICA-BASED SOLIDIFICATION MATERIALS MADE FROM INORGANIC SOLID WASTES

Yuuya Nakase[1], Shinya Inazumi[2], Suttisak Soralump[3], Takashi Shinsaka[4], Jun-ichi Yamazaki[4], Ryo Hashimoto[5], Tomoyuki Mizuta[6] and Yoshihiro Nakagishi[7]

[1]Advanced Course of Architecture and Civil Engineering, Akashi College, National Institute of Technology, Japan; [2]Department of Civil Engineering, Akashi College, National Institute of Technology, Japan; [3]Department of Civil Engineering, Kasetsart University, Thailand; [4]Sanshin Corporation, Japan; [5]Doboku Chishitsu Co., Ltd., Japan; [6]Nippon Steel & Sumikin Slag Products Co., Ltd., Japan; [7]Amangu. Corporation, Japan

ABSTRACT

In a series of studies, the authors have developed a powdery silica-based solidification material composed of heat-treated inorganic solid wastes with a high content of silica products (such as waste glass and waste fly ash) mixed with alkali aids. This material is most suitable for use with iron or steel slag, such as that which comes from a blast furnace or a steel-making process. The powdery silica-based solidification material mixed with iron and steel slag can be expected to exhibit higher mechanical strength and more predominant characteristics than a powdery cement-based solidification material. In this study, the solidification mechanism for the mixture of the silica-based solidification material, blast furnace slag and water is clarified from the viewpoints of chemistry and mineralogy by conducting X-ray diffraction analysis, X-ray fluorescence spectrometry and inductively coupled plasma spectroscopy.

Keywords: silica-based solidification material, solidification mechanism, waste glass

INTRODUCTION

In Japan, while natural resources are being steadily depleted, emissions of waste are increasing year after year. In a series of studies, the authors have developed a new solidification material using waste glass discharged from glass industries for the purpose of reducing and effectively using waste glass and blast furnace slag to prevent the depletion of natural resources [1]. However, although the mechanism for curing the mixture of silica-based solidification material, blast furnace slag, and water has been clarified, the solidification mechanism has not. In this study, the solidification mechanism is clarified from the viewpoints of chemistry and mineralogy by conducting X-ray diffraction analysis (XRD analysis), X-ray fluorescence spectrometry (XRF analysis) and inductively coupled plasma spectroscopy (ICP analysis). The applicability of ground-improvement methods, such as mechanical stirring and high-pressure injection mixing, to the material is also clarified through laboratory blended tests with sandy and clayey materials.

Table 1 The results of XRF analysis of the silica-based solidification material

Chemical composition	SiO_2	Na_2O	CO_2	CaO	MgO	Al_2O_3
Contents (%)	41.7	37.8	9.1	5.8	2.5	1.3

A POWDERY SILICA-BASED SOLIDIFICATION MATERIAL COMPOSED OF INORGANIC SOLID WASTES AND BLAST FURNACE SLAG

Basic composition of a powdery silica-based solidification material

The new powdery silica-based solidification material is composed of heat-treated inorganic solid wastes with high contents of silica products (such as waste glass and waste fly ash) mixed with alkali aids for drying and grinding. The main chemical components of this material are clarified by XRF analysis, and the results are shown in Table 1. As shown in the table, the main chemical components include silicon dioxide, sodium oxide and carbon dioxide. Further, the main mineral components of the powdery silica-based solidification material are clarified by XRD analysis; as shown in Fig. 1, these components are sodium metasilicate and calcium carbonate. The clear peak in the figure indicates that the powdery material has a crystalline structure. Therefore, the material has a dense structure, which is excellent for preventing acid infiltration [2].

Basic composition of blast-furnace slag powder

Blast-furnace slag powder is blast-furnace slag

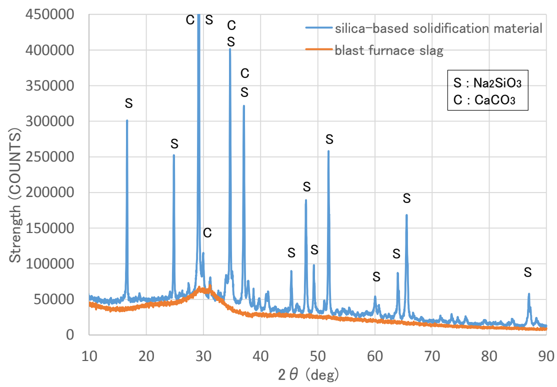

Fig. 1 The results of XRD analysis of the silica-based solidification material

Table 2 The results of XRF analysis of the cement-based solidification material

Chemical composition	CaO	SiO_2	Al_2O_3	MgO	CO_2	SO_3
Contents (%)	42.0	29.6	13.8	5.2	5.2	2.0

Table 3 The results of ICP analysis of the silica-based solidification material

	extract from NaOH solution (30 min)	extract from water (30 min)	extract from water (7days)
Si	m	m	m
Na	17000	4800	3900
Ca	2800	27000	3500
Mg	2600	33000	2500
Al	2100	1500	390
Ti	71	1200	70
Remarks	"m" cannot measure because of eluting much more, unit (ppm)		

Table 4 The results of ICP analysis of blast-furnace slag

	extract from NaOH solution (30 min)	extract from water (30 min)	extract from water (7days)
Si	4300	1800	7800
Na	16000	27	27
Ca	21000	13000	31000
Mg	210	3200	990
Remarks	unit (ppm)		

with a specific surface area that has been adjusted to be more than 4,000 or 6,000 cm^2/g. It is used in concrete admixtures for its high-strength, high-flow and low-heat-build-up properties. Powder with a specific surface area of 3,000 to 4,000 cm^2/g is used as a material in general blast-furnace cement. Japanese Industrial Standards (JIS) has manufactured concrete blast-furnace slag powders with specific surface areas of 3,000, 4,000, 6,000 and 8,000 cm^2/g [3]. We clarify the main chemical components of this powder by XRF analysis and find that they include calcium oxide, silicon dioxide, aluminium oxide and magnesium oxide (*see* Table 2). Furthermore, Fig. 1 shows that blast-furnace slag powder lacks the clear peaks of the powdery silica-based solidification material. Because a low-strength broad peak is found, the powder is suggested to be unstable and amorphous, with good reactivity.

SOLIDIFICATION MECHANISM OF THE MIXTURE OF THE SILICA-BASED SOLIDIFICATION MATERIAL AND BLAST-FURNACE SLAG

From the results of the ICP analysis of the silica-based solidification material, as presented in Table 3, the elution of large quantities of Si, Na and Ca is observed. ICP analysis of blast-furnace slag powder, as presented in Table 4, indicates the elution of large quantities of Ca. In the initial stage of the reaction, the eluted Na and Ca atoms become ionised and combine with hydroxide ions to form sodium hydroxide and calcium hydroxide. Because of the creation of sodium hydroxide, the liquid phase shows high pH, and the amorphous blast-furnace slag powder is stimulated and activated. Furthermore, calcium hydroxide made from the blast-furnace slag powder participates in a hydration reaction with silica in high-alkaline surroundings to create calcium silicate hydrate (C-S-H) [4]. It is believed that filling voids in soil structures with calcium silicate hydrate condenses and cures the soil structures. Furthermore, the soil surface is activated by alkaline ions created during the initial stage of the reaction, and Si eluted from the silica-based solidification material creates a silica colloid. It is considered that silica colloid fills the voids in soil structures to adhere to activated soil surface, and cure. It is further supposed that the long-term strength of the silica-based solidification material is due to a pozzolanic reaction.

TEST DESCRIPTION

Sample soil and mixing condition

A list of test cases is shown in Table 5. The mixture of the silica-based solidification material and blast-furnace slag is used as a solidification material. The silica-based solidification material is white and powdery and has a SiO_2 content of approximately 50%, a density of 2.56 g/cm^3 and a grain size of 20 to 100 μm.

The slag consists of blast-furnace slag powder. The compounding ratios of a silica-based solidification material (H) and blast-furnace slag powder (SL) are SL/H = 5, 10 and 15 by weight. For comparison, a powdery cement-based solidification material (C) used in high-pressure injection mixing methods is also tested. Each solidification material is used with slurry. The compounding ratio of water (W) and a solidification material (M) is W/M = 130%. In the case of the powdery cement-based solidification material, M = C. In the case of the mixture of the silica-based solidification material and blast-furnace slag, the volume of the solidification material is the total volume of each component (M = H + SL).

Sandy and clayey materials are selected for the test. The sandy material is *Toyoura* silica sand (ρ_s = 2.367 g/cm^3), and its water content, w, is adjusted to w = 10%. The clayey material is *Tochi-cray*, made in Tochigi prefecture, (ρ_s = 2.724 g/cm^3, w_L = 34.0%, w_p = 17.0%, I_p = 17.0), and its water content is adjusted for over 12 hours to be w = 40%. The compounding ratios of the soil material (S) and solidification material (M) are set to S/M = 2.0 and 1.5 by volume.

The testing method

In order to confirm the strength characteristics of improved ground, a compression test is conducted. Test pieces are created using a mould of diameter 50 mm and height 100 mm. The uniaxial compression test is conducted after the test pieces are cured for 1, 3, 7, 28 and 56 days.

THE RESULTS OF THE TEST

Differences between soil materials

The relationship between compressive strength and age for each solidification material is shown in Fig. 2. In the case of the powdery cement-based solidification material, the sandy material case has a higher strength than the clayey material case. This behaviour accords with what has been observed in the literature [5]. On the other hand, in the case of the silica-based solidification material, clayey material cases have higher strengths than sandy material cases after approximately 20 days. Because the grain size of *Tochi-cray* is very small, its specific surface area is large. Furthermore, *Tochi-cray* contains soluble SiO_2 and Al_2O_3 eluted from the clay mineral. Therefore, the adhesion effect of silica is greater in clayey materials than in sandy materials. Because increased strength also occurs because of a pozzolanic reaction, *Tochi-cray* has a higher strength than sandy materials.

Long-term strength

The relationship between compressive strength and age under each of the compounding ratios is shown in Fig. 3. In the case of the powdery silica-based solidification material, a strength increase is found after 28 days. It is believed that the silica-based solidification material includes more silica, alumina

Table 5 List of test cases

No.	solidification material				compounding conditions			
	SL/H			C	ground material		S/M	
	5	10	15		cray	sandy	2.0	1.5
1	x				x		x	
2	x					x	x	
3		x			x		x	
4		x				x	x	
5		x			x			x
6		x				x		x
7			x		x		x	
8			x			x	x	
9				x	x		x	
10				x		x	x	
11				x	x			x
12				x		x		x

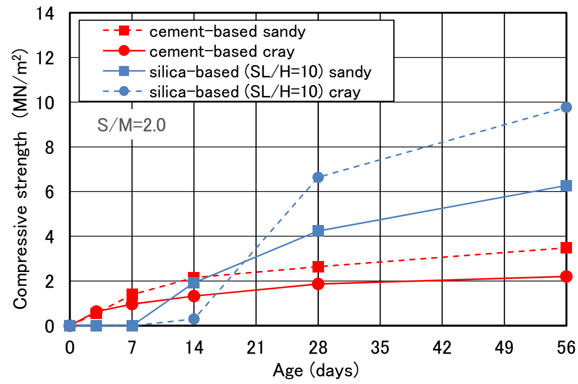

Fig. 2 Change of compressive strength as a function of time for each solidification material

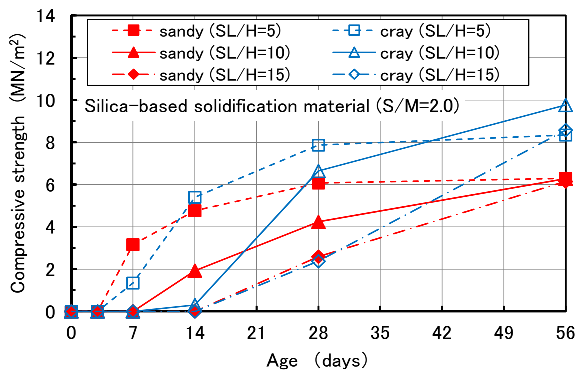

Fig. 3 Comparison by compounding ratio

and calcium hydroxide than the powdery cement-based solidification material, because the pozzolanic reaction advances briskly after 28 days, increasing strength. Furthermore, it is believed that the pozzolanic reaction would continue to increase strength after 56 days.

Efficiency of the delay of strength development

As shown in Fig. 2, in the case of the powdery silica-based solidification material, the strength increases with age even after 28 days, but the increment is small. On the other hand, strength development of the silica-based solidification material is slower than that of the powdery cement-based solidification material, and the test pieces do not stand without support until 7 or 14 days later. Considering the solidification mechanism of the powdery cement-based solidification material, hydration occurs immediately and strength increases slowly. However, because the silica-based solidification material needs time to develop latent hydraulic properties of blast-furnace slag and for silica to adhere between soil particles, the test pieces do not stand without support until 7 or 14 days after their creation.

CONCLUSIONS

In this study, the authors developed a silica-based solidification material and clarified its solidification mechanism. The following results were obtained.

(1) From XRD analysis, the blast-furnace slag powder was found to be amorphous and caused by curing mixture with silica-based solidification material and a blast furnace slag powder.
(2) ICP analysis showed that, during the initial stage of the reaction, Na and Ca were eluted from the silica-based solidification material, causing the pH of liquid phase to increase and activating the blast-furnace slag powder. Si becomes silica colloid, and an adhesion effect occurs between soil particles.
(3) ICP analysis also showed that large quantities of Ca were eluted from the blast-furnace slag powder, creating $Ca(OH)_2$ and C-S-H and causing hardening through areaction with Si.
(4) Because the adhesion of the effect between soil perticles due to silica and the development of long-term strength due to pozzolanic reactions, clayey materials have higher strengths than sandy materials, and effect of the improvement is large.
(5) The silica-based solidification material undergoes a brisk pozzolanic reaction due to the inclusion of much silica, alumina and calcium hydroxide. The increase in strength is large after 28 days, and continues even after 56 days.
(6) Strength development of the silica-based solidification material is slower than that of the cement-based solidification material, because there is efficiency of delay, it is possible to apply to ground improvement method to need overlap.

This study indicates that the silica-based solidification material has excellent delay efficiency but that the delay in strength development is a general problem. The reaction is promoted by increasing the amount of silica-based solidification material. It may be possible to advance strength development, but the exact compound involved in early strength development is unclear, making this a problem for future research.

REFERENCES

[1] Amano K, Ito M, Yanagisaw Y, “According to environmental load considered reuse of waste and a by-product”, Study of environmental system, vol.25, pp.255-259, 1997.

[2] Matumoto K, Yonekura A, Ito H, “Development acid resistance mortar by mixing admixture”, Proceedings of the Japan Concrete Institute, vol.27, No.1, pp.883-885, 2005.

[3] Yamada T, Nishigata T, “Strength characteristics of improved soil used mixed solidification material made from magnesium oxide and a blast furnace slag powder”, Vol.10, No.1, pp.57-65, 2014.

[4] Kasai J, “Unburnable cement”, Inorganic Materials, Vol.1, No.252, pp.144-149, 1994.

[5] Japan Cement Association, “The ground improvement manual by the cement-based solidification material [the second edition] ”, pp.17-48, 1994.

HYDRAULIC MODEL EXPERIMENTS ON DIMENSIONS OF ARMOR UNITS FOR THE RESILIENT BREAKWATAERS

Shota Inoue[1], Kiyonobu Kasama[2], Mitsunari Hirasawa[3],
Kouki Zen[4], Zentaro Furukawa[5] and Yuichi Yahiro[6]
[1,2,5,6] Graduate School of Engineering, Kyushu University, Japan;
[3,4] Department of Joint Research on Environment and Disaster in Offshore and Poat Areas,
Kyushu University, Japan

ABSTRACT

The Tohoku-Pacific Ocean Earthquake and tsunami gave serious damages to many breakwaters in Tohoku region, Japan. The major cause of failure is the tsunami wave force. However, a new type of failure is confirmed: caused by scouring of the harbor side mound by overflow and seepage flow. In fact, the cause of failure of 9 among the 22 destroyed breakwaters was scouring of the mound and any effective measurement against that cause has not been invented. Therefore, in the previous research we developed a new method to calculate the stable weight of a wave dissipating blocks in consideration of the overflow and seepage flow from the view point of the geotechnical engineering. In this paper, using this method, the most effective shape of the wave dissipating block will be described. Furthermore, some sort of hydraulic model experiments with Kamaishi bay breakwater as a subject have been done in order to see the difference of damage in terms of different 3 height ratio (given by height divided by radius of blocks) shapes of blocks and 2 ways of laying blocks. Thorough this methodology the optimum proportion of the block which has a hole like annulus was found. The hydraulic model experiments also revealed that the most effective height ratio was 1/2 out of 1/4, 1/2 and 3/4. In conclusion, it can be reasonable to use this methodology to determine the optimum shape of wave dissipating blocks for much stronger breakwaters to the future tsunami.

Keywords: Armor Units, Tsunami breakwater, Seepage flow, Overflow

INTRODUCTION

Many breakwaters were damaged by the March 11, 2011 Tohoku Earthquake off the Pacific coast and studies about breakwater stability at the time of tsunami overflow are needed. The breakwaters were destroyed or deformed by roughly three causes; scouring of mound by tsunami overflow and seepage flow, horizontal force caused by wave and surface elevation difference between sea and harbor side, and reduction of bearing capacity of mound induced by seepage flow. Among them, scouring of harbor-side mound by overflow and seepage flow has been studied and developed recently [1], [2]. In our previous research the equation to calculate stable weight W_s for rubble constituting mound has been proposed in consideration of overflow and seepage flow [3]. Stable weight is defined as the minimum weight which enables a rubble or an armor unit to be stable to a tsunami and armor units which have smaller stable weight are more resistant to tsunamis and more economical.

It is assumed that installing armor units which can let seepage flow out and be stable against overflow at harbor-side mound is effective in order to prevent the scouring by overflow and seepage flow. In this paper, using our method, the most effective shape of armor units is discussed and some sort of hydraulic model experiments with Kamaishi bay breakwater as a subject have been done. The model armor units were hollow cylinder shaped because it is pointed out by previous study that such a shape enables to reduce seepage force. the hollow cylinder-shaped block is assumed as armor units as shown in Fig. 1 and the optimal proportion was examined. Furthermore, the stability of hollow cylindrical armor units was investigated thorough the hydraulic model experiments. This result will be applicable to general caisson type composite breakwaters because the parameters such as overflow water depth or dimensions of mound can be changed in accordance with each breakwater.

The goal of this research is proposing the most effective and economical shape for armor units which can improve existing breakwaters in order to prevent damage from huge tsunamis assumed in the future.

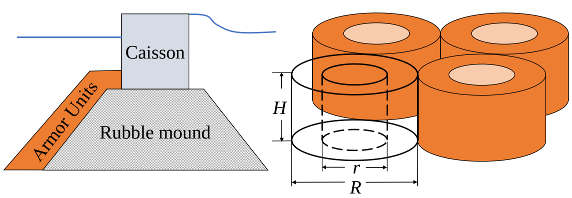

Fig. 1 Image of armor units application

STUDY ON THE OPTIMAL SHAPE OF AN ARMOR UNIT

Equations to estimate seepage failure and calculate stable weight for armor units

Figure 2 illustrates that the overflow and seepage flow through the rubble mound strike the harbor-side armor units and its detail situation is shown in Fig. 3. Since seepage flow can cause the seepage failure of armor units before the overflow, the judgement of whether seepage flow occurs should be performed at first. That failure can occur when seepage force exceeds the slope vertical weight of armor unit. Therefore, the critical hydraulic gradient i_c was calculated theoretically based on this mechanism. This eq. (1) can be compared with measured hydraulic gradient in order to judge whether seepage failure occurs or not.

$$i_c = \frac{G_S - 1}{1+e}\cos\theta \tag{1}$$

: where e is void ratio, θ is mound gradient and G_s is specific weight of an armor unit.

Hudson's equation which can find the stable weight W_s for armor units hit by overflow was reconsidered because it was developed without the idea of seepage flow. According to Fig. 2 and 3, the eq. (2) which calculates critical weight when harbor-side armor units start moving because of overflow and seepage flow (stable weight W_s) was developed theoretically.

$$W_s = \frac{k_a^{\,3}\gamma_s C_D^{\,3} u^6}{8k_v^{\,2} g^3 \left[\left\{ f_r\left(\cos\theta - \dfrac{1+e}{G_S-1} i\right) - \sin\theta \right\}(G_s - 1)\right]^3} \tag{2}$$

: where C_D is resistance coefficient, u is overflow velocity plunging into mound, g is gravitational acceleration, f_r is frictional coefficient, γ_s is unit weight of armor units, i is hydraulic gradient, k_v is volume coefficient and k_a is area coefficient. Based on the Nakamura's [4] and Sawaraki's [5] assumption, in this study, tsunami is regarded as in a steady state because tsunamis are very long waves. In this paper, this eq. (2) is used for calculation of stable weight of armor units.

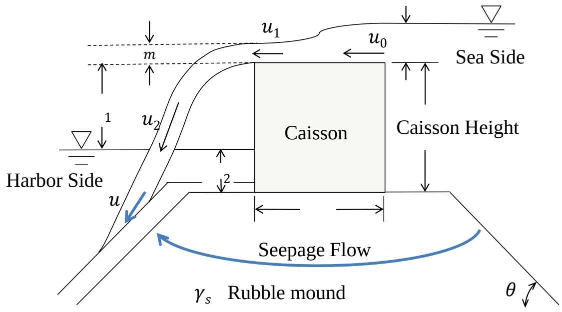

Fig. 2 Overflow and seepage flow around breakwater

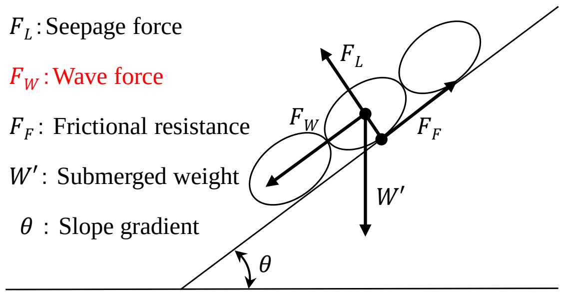

Fig. 3 Force diagram about armor units

Study on the optimal shape of armor units

In this section, the most effective shape for armor units described in Fig 1. is discussed by using eq. (2).

At first, external diameter R in Fig.1 is assumed to be constant and void ratio

e is calculated. That armor units are placed on the harbor-side mound and their two different ways of placement are shown respectively in Fig4.

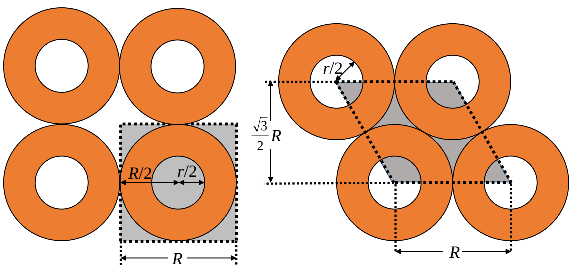

Fig. 4 Placement ways (left: square placement, right: triangle placement)

Since void ratio e is the ratio of the volume of voids to the volume of solids, each one is calculated as below.

$$e_{square} = \frac{4}{\pi}\frac{1}{1-\left(\dfrac{r}{R}\right)^2} - 1 \tag{3}$$

$$e_{triangle} = \frac{2\sqrt{3}}{\pi} \frac{1}{1-\left(\frac{r}{R}\right)^2} - 1 \qquad \textbf{(4)}$$

Because these two eq. (3) and (4) have little differences in form, the void ratio for the triangle placement is discussed in the following paper. Therefore, the eq. (2) is expressed as below by inserting eq (4).

$$W_{s,triangle} = \frac{\pi \gamma_s C_D{}^3 u^6}{32\left[gf_r\left\{(G_s - 1) - \frac{2\sqrt{3}}{\pi}\frac{i}{1-(r/R)^2}\right\}\right]^3}\left(\frac{R}{H}\right)^2\left\{1-\left(\frac{r}{R}\right)^2\right\} \qquad (5)$$

For simplicity, the armor units located on the crest of the mound are examined and the slope gradient θ is 0. k_v, k_a were calculated with representative length R, height H and inner diameter r of armor units. As a result, because stable weight is inversely proportional to the square of H, the higher armor blocks are, the smaller stable weight can be obtained.

Furthermore, eq. (5) was taken the partial derivative with r regarding outer diameter R as constant. The inner diameter r which gives the extreme value of W was named r_0. Therefore, the most suitable ratio r_0/R was obtained as blow.

$$\frac{r_0}{R} = \sqrt{1 - \frac{8\sqrt{3}i}{\pi(G_s - 1)}} \qquad (6)$$

This equation shows that when hydraulic gradient increases due to the seepage flow the hollow should be made larger in order to let the seepage flow out.

HYDRAULIC MODEL EXPERIMENTS ON THE SHAPE OF ARMOR UNITS

Outline of the model experiments

Kamaishi bay breakwater was selected as the model of experiments and its scale is 1/100. It is the deepest breakwater in the world whose depth is 63 m. The height of caissons is around 20 m and the range of rubble-mound foundation is from -60 m to -27 m. Therefore, the effect of seabed can be ignored and only those of overflow and seepage flow can be seen.

Test conditions

In order to understand how the stability of armor units depends on those dimensions, the three types of armor units and two ways of placement were adopted.

Boundary conditions on this experiment are shown in fig. 5. As is shown in this figure, the water level difference Δh was kept by the balance of inflow and outflow and the bottom line was regarded as impermeable.

Figure 6 describes the outline of the experimental equipment and Table 1 shows the specifications of the experimental materials and other conditions. The mound consists of rubble whose diameter is 2 ~ 19 mm and weight is 0.004 ~ 0.027 [N/each]. When mound was created, compactions by a rammer were done for each 150 mm layer of rubble. In order to model tsunamis, the pumps generated circulating flow and the gates adjusted the water surface elevation. The sea-side level was raised 1 mm per 10 seconds while the harbor-side level was kept fixedly. Video cameras recorded the breakwater and armor units under tsunami. The results from water pressure gages and water velocity gages were used to conduct analysis. Three different types of model armor units were hollow cylinder-shaped and made by three different flat-washer in order to make the difference due to height ratio H/R obvious. Table 2 shows the property of armor units. With the experimental limitation, weights of model armor units are not exactly the same each other but set close values. and Table 3 shows the experimental cases. Aperture ratio O is ratio of void area per unit area. Experiment in each case was conducted twice.

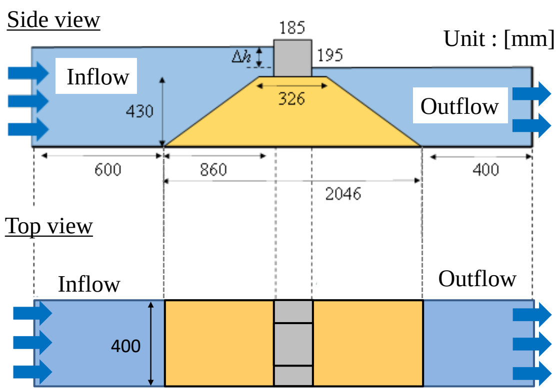

Fig. 5. Boundary conditions

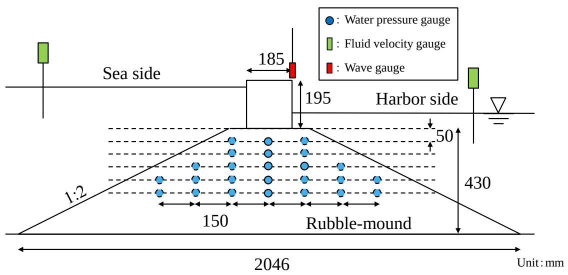

Fig. 6. Schematic of experimental devices

Table 1. Test conditions

Model		Kamaishi bay brealwater (1/100)
Caisson	Size	Height 195mm ×Breadth 185mm ×Depth 190mm
	density	2.03g/cm^3
Rubble-mound	dimensions	Upper base 326mm Lower base 2046mm Height 430mm Gradient 1:2
	Particle size	2mm-19mm
	Saturated density	1.81g/cm^3
Water level difference		0mm, 40mm, 80mm, 120mm, 145mm, 185mm, 210mm
Water level at harbor side		25mm (from the crest of the mound)

Table 2. Specification of armor units

Shape		Hollow cylinder		
Density [g/cm^3]		7.66		
Height ratio *H*/*R*		1/4	1/2	3/4
Height *H* [mm]		7.2	9.6	13.2
Outer diameter *R* [mm]		30	22	18
Inner diameter *r* [mm]		15	10.5	8.5
Weight [N]		0.250	0.235	0.186
Aperture ratio *O*	Square placement	0.411	0.394	0.390
	Triangle placement	0.320	0.300	0.295

Table 3. Experimental cases

	Height ratio *H*/*R*	Ways of placement
CASE 1	1/4	Square
CASE 2		Triangle
CASE 3	1/2	Square
CASE 4		Triangle
CASE 5	3/4	Square
CASE 6		Triangle

Results of the model experiments

Figure 7 and 8 illustrate the damage ratio *D* of armor units for each case with water level difference between sea and harbor side. When an armor unit is moved horizontally, that is judged to be damaged. Equation (6) was used to calculate damage ratio.

$$D = \frac{\text{The number of damaged armor units}}{\text{The total number of armor units}} \times 100\ [\%] \tag{6}$$

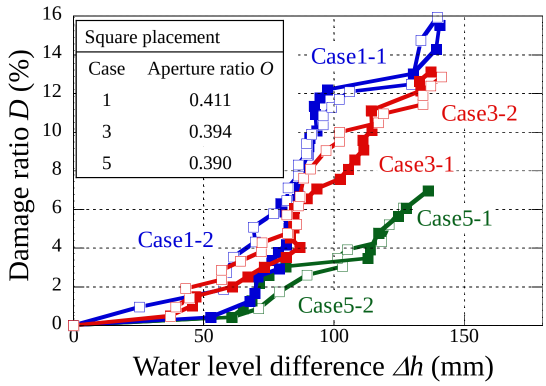

Fig. 7 Damage ratio of armor units placed square

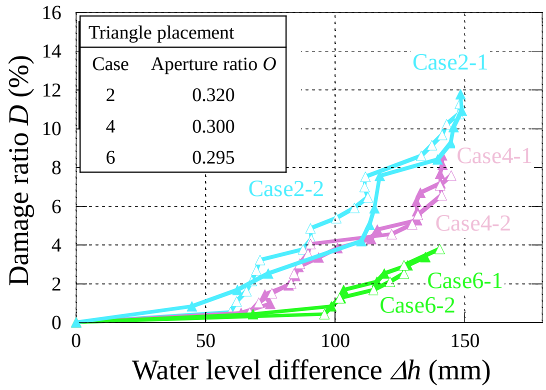

Fig. 8 Damage ratio of armor units placed triangularly

Regardless of the difference in the ways of placement, it is obvious that the larger the height ratio *H*/*R* is, the less the damage ratio can be. Moving armor units were seen in any case before Δh is around 120 mm at which overflow occurred. This is because they were floated by seepage flow through the rubble mound. After that, each damage ratio jumped and many armor units placed at the point where overflow water dives were damaged.

Relationship between the result and parameters

As a result of the experiments, it was found that there were differences in damage ratio. In fig. 7 and 8, it is obvious that larger height ratio *H*/*R* makes damage ratio lower, which is supported by the eq (5). Moreover, comparing fig 7 with 8, it was also confirmed that less aperture ratio *O* (void ratio *e*) makes the armor units stable.

Safety assessment for the seepage failure

Contour graphs illustrating safety factors for the seepage failure when Δh is 40, 80 120 140 mm are shown in Fig. 9. The safety factor is defined to be ratio of the critical hydraulic gradient i_c which can be calculated by eq. (1) to measured hydraulic gradient i thorough the model experiments. Seepage failure is assumed to occur when safety factor is less than 1.

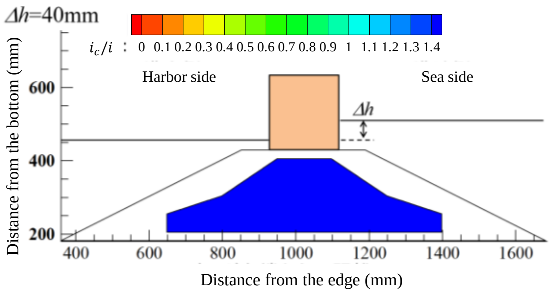

a) Δh = 40 mm

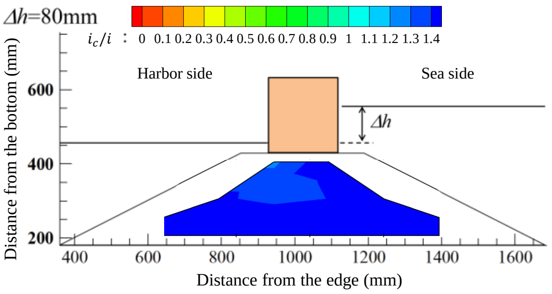

b) Δh = 80 mm

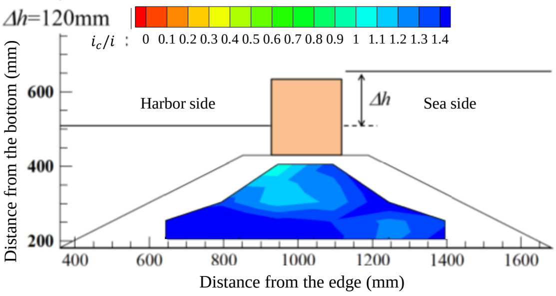

c) Δh = 120 mm

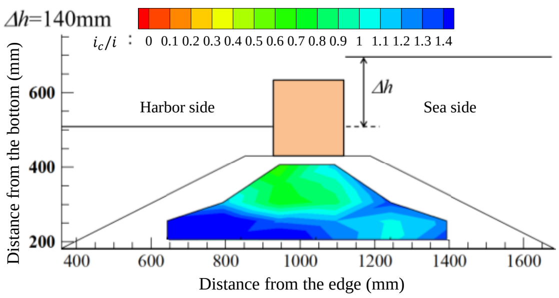

d) Δh = 140 mm

Fig. 9 Safety factor for seepage failure (Case6-1)

Even though overflow did not occur when Δh is 80 mm, the safety factor around the crest of the harbor-side mound is less than 1. This also confirms the fact that seepage failure can occur before overflow.

Safety assessment for the seepage failure

Figure 10 shows the relationship between the safety factor for overflow and seepage failure and overflow depth h in each case. The safety factor is defined to be ratio of the weight of a model armor unit W to the stable weight W_s which can be calculated by eq. (2). Overflow and seepage failure is also assumed to occur when safety factor is less than 1.

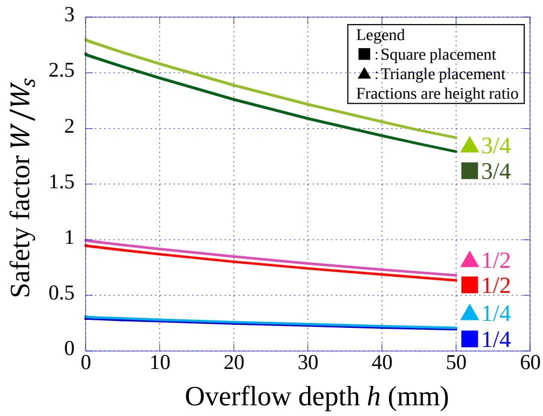

Fig. 10 Comparison of the safety factor for the overflow and seepage failure

It is found that the larger the height ratio H/R is, the more stable against overflow and seepage failure can be. This is consistent with the theoretical study and the experimental result stated above. The fact that experiments performed with the same height ratio have almost the same value implies that the stability against overflow and seepage failure depends on height ratio rather than difference in ways of placement. Some of the armor units whose height ratio is 3/4 were damaged in the experiments, however, the safety factor is more than 1. This is because that overturning or sliding of armor units was not considered in theoretical equation.

The model armor units had different unit weight and the one which had height ratio 3/4 had the largest unit weight. Therefore, experiments with armor units which have the same unit weight are needed in order to reveal the effect of weight.

CONCLUSION

In this paper, the formula for a stable weight of the hollow cylinder shaped armor units has been developed. This has made clear that armor units should be as high as possible to a constant diameter in order to be stable against tsunamis with smaller weight. Furthermore, the ratio of optimal outer diameter to inner diameter against overflow and seepage failure has been found by the equation.

Hydraulic model experiments with three different shapes of model armor units and two ways of placement were performed. This resulted in that the armor units whose height ratio was 3/4 were more stable than the others. It is also found that seepage failure can happen before overflow. Moreover, analysis with the proposed equation was consistent with the experimental results. However, because the experimental cases are not still enough, further studies are needed to more accurately estimate the optimal shape of armor units

In conclusion, the proposed equation is effective to determine the optimal shape of armor units in order to improve existing breakwaters against the bigger tsunamis in the future. More detailed studies or experiments are needed to develop the new methodology.

ACKNOWLEDGEMENTS

This study is a part of the achievement of Research Grants Basic Research Science (B): research issue 25289149 "Development of new-style tsunami breakwater that utilize disaster prevention blocks made of dredged soil" (research leader: Kiyonobu KASAMA).

REFERENCES

[1] T. Arikawa, et al., “Failure mechanism and resiliency of breakwaters under tsunami”, Technical note of the Port and Airport Research Institute. Port and Airport Research Institute, Japan, No. 1269, 2013.

[2] S. Maruyama, et al., “Experimental study on stability of armor units for harbor-side rubble mound of composite breakwater against tsunami”, Journal of JSCE, Ser. B3 (Civil Engineering in the Ocean), Japan Society of Civil Engineers, Vol. 68, No. 2, I 7-I 12, 2012.

[3] S. Inoue, et al., “A model experiment for the stable weight of rubble-mound considering the overflow and seepage flow”, Journal of JSCE, Ser. B3 (Civil Engineering in the Ocean), Japan Society of Civil Engineers, Vol. 71, No. 2, 2015.

[4] T. Sawaraki, A. Onisi (1982) “Destruction mechanism due to the resonance phenomenon on the riprap breakwater slope”, Coastal Engineering Papers, Vol.35, 1982, pp. 428-432.

EVALUATION OF POROSITY IN BIOGROUTED SAND USING MICROFOCUS X-RAY CT

Shumpei Mitsuyama[1] , Kazunori Nakashima[2], Satoru Kawasaki[2]

[1]Graduate School of Engineering, Hokkaido University, Sapporo, Japan
[2]Faculty of Engineering, Hokkaido University, Sapporo, Japan

ABSTRACT

Biogrouting is a method employed for ground improvement based on microbially induced calcium carbonate precipitation. It is commonly believed that biogrout has environmental and economic benefits. However, there remains the need to clearly understand the internal structure of biogrouted soil. In this study, we use microfocus X-ray computed tomography (CT) to evaluate the porosity in biogrouted sand. X-ray CT is useful as a non-distractive inspection tool. First, we prepare small specimens using coral sand at different dilution rates of culture solution. After carrying out a solidification test for 2 wks., we perform an unconfined compressive strength (UCS) test and measure the porosity of the specimens. Our aim is to investigate the influence of the dilution rate on the UCS and the porosity of sand specimens. The results show that a lower dilution rate resulted in a lower sand-specimen porosity and an increase in the UCS. We investigate the precipitation that fills a void. Then, we investigate the relationship between UCS and the ratio of porosity. There was a negative correlation between UCS and porosity, which closely agrees with previous research. We confirm the validity of the result, and we determine the UCS from the porosity.

Keywords: Sand Solidification, X-ray CT, Ureolytic Bacteria

INTRODUCTION

Recently, artificial beachrock obtained by biogrout solidification through microbially induced carbonate precipitation (MICP) [1]–[5] has attracted a great deal of attention. This method can be applied to ground improvement and coastal protection[6]–[8], and it is believed that it is environmentally friendly and low cost. In previous studies, precipitation in sand specimens was evaluated by measuring the unconfined compressive strength (UCS). However, the amount of precipitation varies depending on the location [9]. Improving the UCS is key to enabling us to understand the internal quantity of calcium carbonate. In this study, we determine experimentally the porosity, which indicates the proportion of pores in the total volume in the specimen. There are several ways to measure the porosity, including the mercury intrusion technique and the liquid saturation method [10]. However, these methods result in the deformation of internal structures. In this study, we evaluate the porosity using microfocus X-ray computed tomography (CT). X-ray CTs can visualize the internal structure quantitatively without any deformation. Therefore, UCS and porosity can be measured using the same sample.

As shown in Figure 1, Microbial urease catalyzes the hydrolysis of urea into ammonium and carbon dioxide (Eqs. (1) and (2)).

$$\mathbf{CO(NH_2)_2 + 3H_2O \rightarrow 2NH_4^+ + 2OH^- + CO_2} \quad (1)$$

$$\mathbf{CO_2 + H_2O \rightarrow HCO_3^- + H^+} \quad (2)$$

The carbonate ions react with calcium ions. Then, calcium carbonate precipitates between sand grains and form cementing bonds (Eq. (3)).

$$\mathbf{Ca^{2+} + HCO_3^- + OH^- \rightarrow CaCO_3 + H_2}\mathrm{O} \quad (3)$$

The byproduct, which is the ammonium ion, can result in an increased pH. In addition, the carbonate ion can increase the pH. The precipitation of calcium carbonate tends to take place at higher pH values.

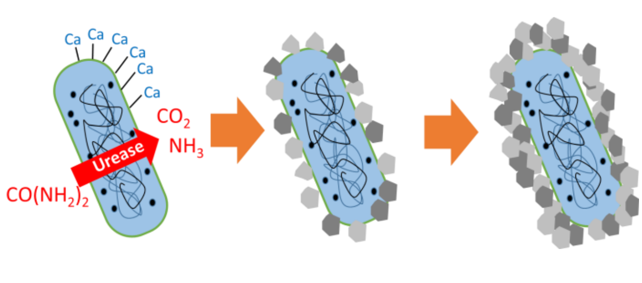

Fig. 1 Urea hydrolysis reaction.

METHOD

We used *Pararhodobacter* sp., which was isolated from the beach sand in Sumuide, Nago, Okinawa, Japan [11]. The grain size is shown in Figure 2. We obtained 1 g of bacteria cultivated on ZoBell 2216E plate medium (polypeptone 5.0 g/L, yeast extract 1.0 g, and $FePO_4$ 0.1 g/L with artificial seawater) and placed it in 100 mL of ZoBell medium solution. Then, we shook it at 30°C, 160 rpm for 24 h. In the meanwhile, 40 g of coral sand was dried at 110°C for 24h.

Table 1 Composition of cementation solution (solvent: artificial seawater).

Reagent	Content (g / L)
Nutrient broth	3.00
NH_4Cl	10.00
$NaHCO_3$	2.12
$CO(NH_2)_2$	30.00
$CaCl_2$	55.5

We separated the cells by centrifugation at 30°C, 3000 rpm for 10 min. We extracted 10 mL at the bottom and moved it to a 90 mL ZoBell medium. As indicated in Figure 3, we set the syringes at 30°C in an incubator. On the first day, we diluted the culture solution with ZoBell 2216 medium. The test conditions of the syringe test are shown in Table 2. Sixteen mL of culture medium solution and 20 mL of the cementation solution were added to each syringe. Then, we injected 20 mL of cementation solution and drained every 24 h for 2 wks. We measured the pH and concentration of Ca^{2+} every 3 d. At the end of the experiment, we drained all of the solution in the specimens.

We also measured the needle-penetration inclination (diameter = 2.5 cm, height = 7 cm). The UCS was estimated using a needle penetration device (SH-70, Maruto Testing Machine Company, Tokyo, Japan). Equation (4) describes the relationship between the UCS (y) and the needle penetration inclination (x) determined from 114 natural rock samples and 50 improved soils with cement.

$$\log(y) = 0.978\log(x) + 2.621 \tag{4}$$

In addition, we observed samples using a microfocus X-ray CT. After performing the solidification test for 2 wks., we also measured the porosity in order to investigate the influence of the dilution rate on the UCS and the porosity of sand specimens. In the X-ray CT images, the smallest unit is called a voxel [12]. A voxel has a CT value as given in Eq. (5).

$$\text{CT value} = S\mu + B \tag{5}$$

where S is the slope, B is the bias and μ is attenuation coefficients of X-ray beams. In this study, S = 200 and B = 0. The voxel size is 25 μm ×25 μm × 40 μm. In the experiment, we obtained 80 slice images using a TOSCANER 31300 μhd (Toshiba IT & Control Systems Co., Ltd.), which is installed at Hokkaido University, Japan. The applied tube voltage was 130 kV, and the maximum tube current was 62 μA. In this experiment, we used the cone-beam scanning mode, and the number of pixels was 1024 × 1024. The brighter areas represent lower density regions, while the darker areas represent higher density regions. Using the maximum-likelihood thresholding method [10], we then determined the threshold.

Table 2 Test conditions for syringe tests.

Case number	Dilution rate
Case 1	1
Case 2	2
Case 3	5
Case 4	10

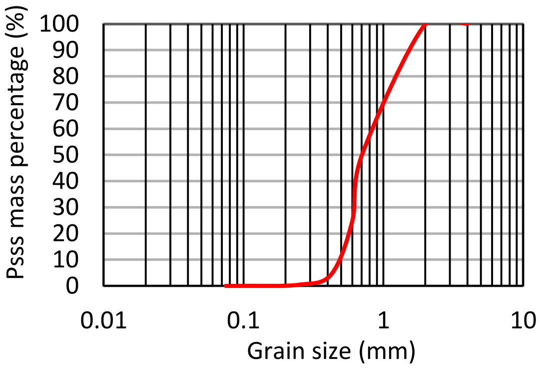

Fig. 2 Grain size distribution of coral sand.

Fig. 3 Syringe cementation test.

RESULTS

The sand was cemented, as shown in Figure 4, and as shown in Figure 5, the UCS increase as the dilution rates decrease. One explanation for this is that the UCS is related to the number of bacteria. Moreover, the sand in Case 4 was cemented only at the surface (2-cm thick). For cases 1 and 2, the estimated UCS value tended to be higher than in cases 3 and 4. For case 1, the UCS at the upper edge is a maximum of 7 MPa. For case 4, the UCS at the bottom edge is 0 MPa. This point was not solidified. The bottom UCS is markedly low since the amount of bacteria is sufficiently small. In addition, we estimated the amount of $CaCO_3$ in the sand based on the Ca^{2+} concentration of the drainage at 3, 6, 9, 12, and 14 d. From Figure 6, the amount of $CaCO_3$ increased for all cases. However, the slope of Case 1 on the graph is highest. The amount of $CaCO_3$ tended to rise significantly when we used dilution rates of 1 and 2. We also measured the pH at the drainage. As shown in Figure 7, the pH decreases with time. From the above, the amount of bacteria decreased with time. For the duration of the test period, the pH of all specimens tended to be lower than the pH at the beginning. Figure 8 shows X-ray CT images of all cases. Further, the porosity values for all cases are shown in Table 3. The results clarified that a lower dilution rate results in a decreased porosity of the sand specimen and an increase in the UCS.

Fig. 4 Syringe specimen of Case 1 after 14 d of curing.

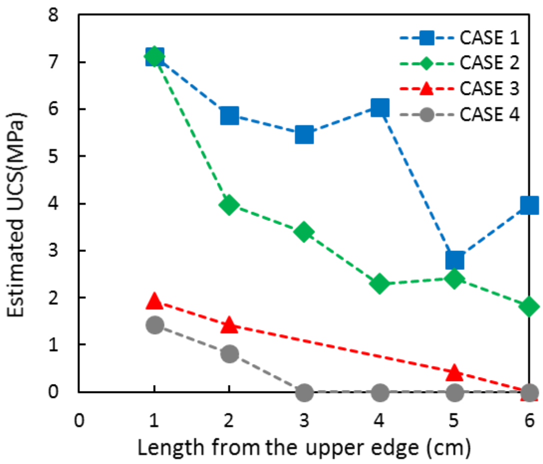

Fig. 5 The UCS of each specimen

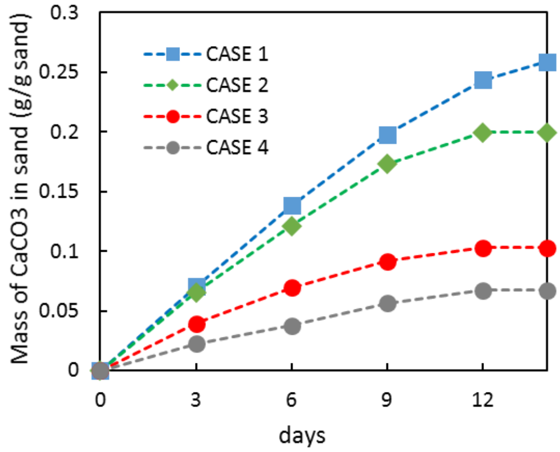

Fig.6 The amount of $CaCO_3$

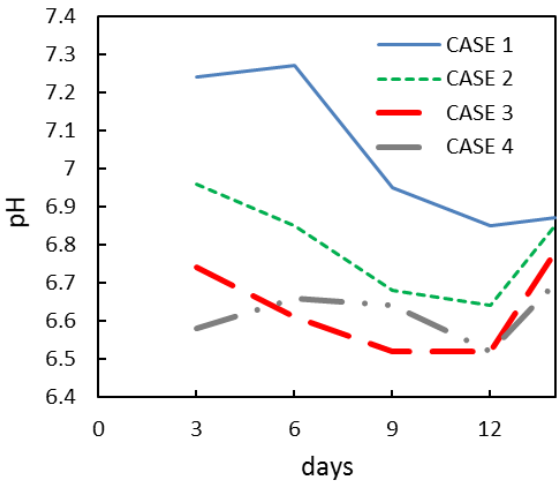

Fig.7 Variation in the pH values of drainage.

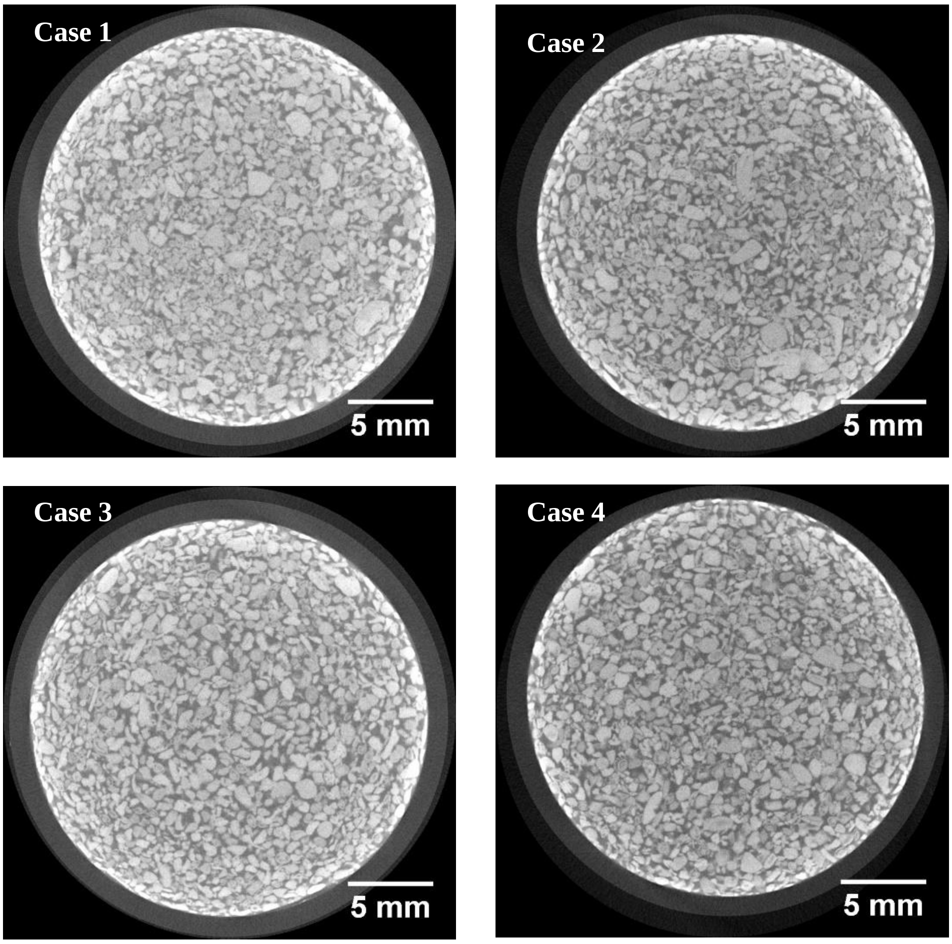

Fig. 5 X-ray CT images at the upper edgr.

Table 3 The porosity based on the syringe test.

Case number	Porosity at the upper edge (%)	Porosity at the bottom edge (%)
without bacteria	42.9	50.6
Case 1	31.0	32.7
Case 2	31.8	34.8
Case 3	31.6	40.0
Case 4	33.0	39.6

DISCUSSION

As shown in Figure 9, there is a relationship between the porosity (n) and UCS (q_u) (Eq. (6)) (correlation coefficient: 0.5956).

$$q_u = -0.6092\, n + 23.787\ (R^2 = 0.5956) \quad (6)$$

There is a negative correlation between UCS and the porosity. This negative correlation closely agrees with previous research. Miyagi and Komiya [13] reported the relationship between UCS and porosity (Eq. (7)) (correlation coefficient: 0.291) of natural sandy limestone in Okinawa, Japan.

$$q_u = -0.7616\, n + 30.55\ (R^2 = 0.291) \quad (7)$$

The porosity and UCS is found to be smaller than the values for natural beachrock. From this graph, if all voids are filled with precipitation, the strength will increase to 23.8 MPa. In the case where the porosity is greater than 39.0%, the specimen is not solidified. For the same porosity, UCS is different, and this is because the initial porosity is different. The number of samples is low, and more samples are therefore needed.

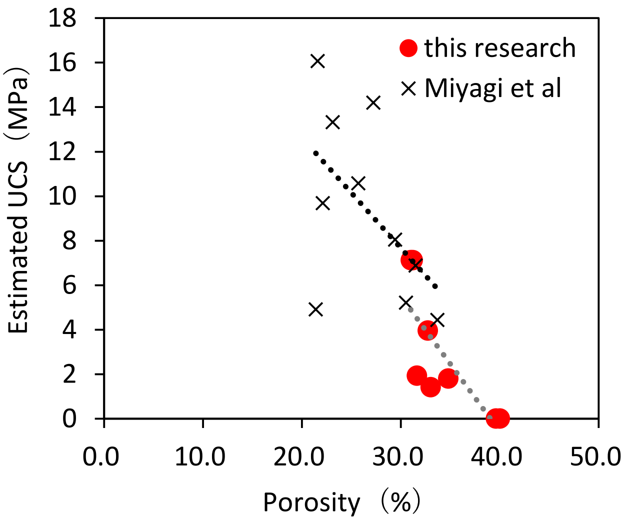

Fig. 6 Relation ship between Estimated UCS and Porosity

CONCLUSION

In this study, we cemented sand specimens using different dilution rates with a culture solution to determine the effects of various conditions on the USC and porosity. The main findings of this study are as follows:

(1) The sand specimens were cemented up to 7 MPa after 14 d using one dilution rate. The dilution rate is lower and the UCS is higher.

(2) We observed the filling of the pore with precipitation.

(3) There is a negative correlation between UCS and porosity.

REFERENCES

[1] A. Al Qabany, K. Soga *et al.*, “Factors Affecting Efficiency of Microbially Induced Calcite Precipitation,” Jounal Geotech. geoenvironmental Eng., Vol. 138, No. 8, pp. 992–1001, 2012.

[2] L. A. Van Paassen, R. Ghose *et al.*, “Quantifying Biomediated Ground Improvement by Ureolysis : Large-Scale Biogrout Experiment,” Jounal Geotech. geoenvironmental Eng., Vol. 136, No. 12, pp. 1721–1728, 2010.

[3] V. Achal and S. Kawasaki, “Biogrout : A Novel Binding Material for Soil Improvement and Concrete Repair,” Front. Microbiol., Vol. 7, No. 3, pp. 9–11, 2016.

[4] M. Li, Q. Fu *et al.*, “Bio-grout based on microbially induced sand solidification by means of asparaginase activity,” Sci. Rep., Vol. 5, pp. 1–9, 2015.

[5] J. T. Dejong, M. B. Fritzges *et al.*, “Microbially Induced Cementation to Control Sand Response to Undrained Shear,” Jounal Geotech. geoenvironmental Eng., Vol. 132, no. 12, pp. 1381–1392, 2006.

[6] T. Danjo and S. Kawasaki, “Microbially Induced Sand Cementation Method Using Pararhodobacter sp Strain SO1, Inspired by Beachrock Formation Mechanism,” Min. Mater. Process. Inst. Japan, No. 1, 2016.

[7] T. Danjo and S. Kawasaki, “A Study of The Formation Mechanism of Beachrock in Okinawa, Japan: Toward Making artificial Rock,” Int. J. GEOMATE, Vol. 5, No. 1, pp. 634–639, 2013.

[8] M. nakibul H. Khan, S. Shimazaki *et al.*, “Coral Sand Solidification Test Through Miceobial Calcium Carbonate Precipitation Using Pararhodobacter sp.,” Int. J. GEOMATE, Vol. 11, No. 26, pp. 2665–2670, 2016.

[9] V. S. Whiffin, L. a. van Paassen *et al.*, “Microbial Carbonate Precipitation as a Soil Improvement Technique,” Geomicrobiol. J., Vol. 24, No. 5, pp. 417–423, 2007.

[10] M. Kato, M. Takahashi *et al.*, “Evaluation of Porosity and Its Variation in Porous Materials Using Microfocus X-ray Computed Tomography Considering the Partial Volume Effect,” Mater. Trans., Vol. 54, No. 9, pp. 1678–1685, 2013.

[11] Takashi Danjo, “Fundamental study on development of artificial rock learnt from

beachrock formation mechanism," Grad. Sch. Eng. Dr. Thesis, 2015.

[12] H. Yamanaka, Satoru Kawasaki *et al.*, "Segmentation of internal structure of two-phase materials using micro-focus X-ray CT," Japanese Geotech. J., Vol. 6, No. 2, pp. 273–284, 2011.

[13] N. Miyagi and Y. Komiya, "Effective porosity and compression strength of Ryukyu limestone in Pleistocene Epoch in the Quanternary period," Univ. Ryuku Acad. Rep., Vol. 50, pp. 131–135, 2003.

Sixth International Conference on Geotechnique, Construction Materials and Environment, Bangkok, Thailand, Nov. 14-16, 2016, ISBN: 978-4-9905958-6-9 C3051

UNIAXIAL COMPRESSION TEST OF UNSATURATED MASADO UNDER CONSTANT DEGREE OF SATURATION CONDITION AND ITS MODELING

Yuhei Kurimoto[1], Seiji Kobayashi[1], Takashi Tsunemoto[2] and Feng Zhang[2]
[1] Department of Scientific and Engineering Simulation, Nagoya Institute of Technology, Japan;
[2] Department of Civil Engineering, Nagoya Institute of Technology, Japan

ABSTRACT

Soils in surface ground are usually unsaturated. Proper modeling of the characteristics of unsaturated soil is therefore absolutely needed. However, due to its complicated mechanical behavior, establishing a constitutive model for unsaturated soil is far more difficult than that for saturated soil. In this research, uniaxial compression tests were firstly conducted on unsaturated Masado (Decomposed granite) under constant degree of saturation condition to investigate the mechanical behavior of the soil at different degree of saturation. Then, based on the test data, the performances of previously proposed elastoplastic constitutive model for unsaturated soil were checked carefully, taking the Bishop-type skeleton stress and the degree of saturation as the state variables. It is found that the mechanical behavior of the unsaturated Masado can be properly described by the proposed elastoplastic constitutive model that takes the skeleton stress and the degree of saturation as the state variables.

Keywords: Unsaturated Soil, Degree of Saturation, Constitutive Model, Uniaxial Compression Test

INTRODUCTION

Soils, especially in surface layer, may exist at unsaturated state, whose void is occupied with water and air. Because of the complicated mechanical behavior of unsaturated soil, the application of constitutive models for unsaturated soil in numerical analysis for practical engineering problem is much less than those for saturated soil. However, an unsaturated soil is not a special soil but the soil whose degree of saturation, a state variable, is smaller than 1.0. It is necessary to establish a constitutive model that can describe both unsaturated state and saturated state under any stress condition so that it can properly evaluate the deformation and the failure behavior, such as slope failure, due to increase and decrease of the water content of the geomaterials.

Since the pioneering work by Reference [1], in which Barcelona Basic Model (BBM) was proposed and regarded as one of the basic models for unsaturated soil, a number of elastoplastic constitutive models have been proposed to describe the mechanical behavior of unsaturated soil [2]-[7]. In recent years, some constitutive models, using the effective stress (or skeleton stress) and the degree of saturation as the independent state variables, have also been established by Reference [8]-[10]. The model has been verified by some tests but is not sufficient enough. In order to make it applicable in practical engineering, it is needed to give an appropriate unifying evaluating method for the parameters involved in the proposed constitutive model, which is proved to be time consuming and needs advanced testing technique. The main purpose of this research is to find out the fundamental behaviors of unsaturated soil, especially the influence of the degree of saturation with laboratory test, and establish a unified constitutive model for unsaturated/saturated geomaterials. In this paper, uniaxial compression tests were firstly conducted on unsaturated Masado under constant degree of saturation condition and then the performances of previously proposed elastoplastic constitutive model for unsaturated soil were checked carefully with the test data.

OUTLINE OF ELEMENTARY TESTS AND ANALYSES

Uniaxial Compression Test of Unsaturated Masado under Constant Degree of Saturation Condition

Masado, typical decomposed granite that widely distributed in southwest Japan, was used as the specimen in uniaxial compression test. Physical properties and the grain size distribution curve of Masado, which has been sieved to the soil particles less than 2.0 mm, are shown in Table 1 and Fig. 1. The specimens (60 mm in diameter and 10 mm height) were compacted in one layer directly into the oedometer ring at target void ratio e = 0.50. Based on the compaction curve of Masado, as shown in Fig. 2, as a fundamental test condition, the target water content was set to w = 9, 12, 15, 18, 21%, in which the optimum water content is w_{opt} = 15%, and dry side is w = 9, 12%; wet side is w = 18, 21%.

Table 1 Physical properties of Masado

	Unit	Value
Specific gravity, G_s	-	2.66
Liquid limit, w_L	%	NP
Plasticity index, I_p	%	NP
Maximum dry density, ρ_d	g/cm^3	1.85
Optimum water content, w_{opt}	%	13.7

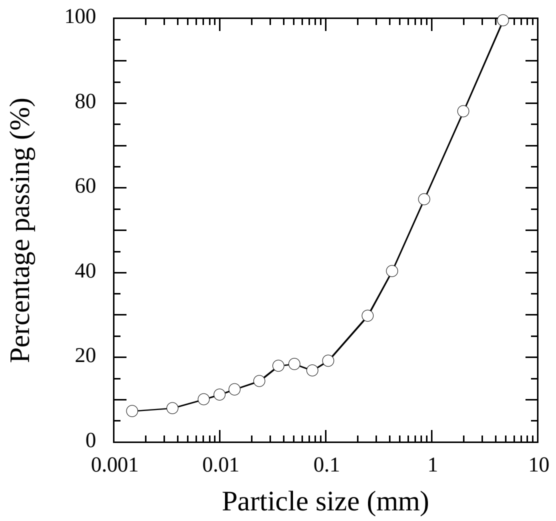

Fig. 1 Grain size distribution curve of Masado

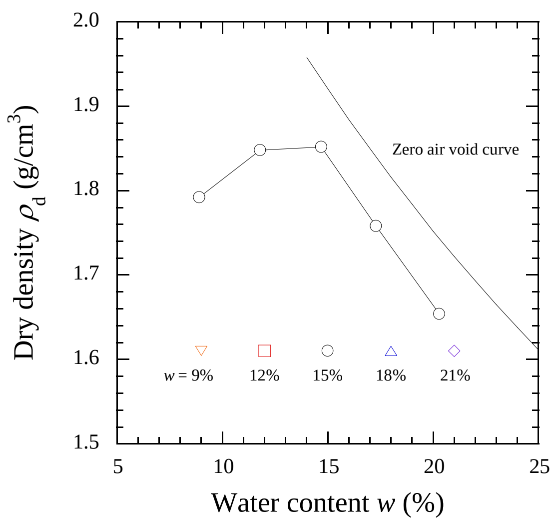

Fig. 2 Compaction curve of Masado

In order to verify the influence of the initial degree of saturation on the mechanical behavior of Masado, uniaxial compression tests of the unsaturated Masado under the condition of constant degree of saturation with pressuring method were conducted. Fig. 3 shows the test apparatus for uniaxial compression tests. Pore water pressure was controlled and measured through a ceramic disc with an air entry value (AEV) of 1500 kPa, installed at the bottom of the specimen. Pressure/volume controller (PVC, GDS product), which can control the pore pressure or the pore water volume according to the usage, was implemented in the uniaxial compression test in order to be able to conduct the tests under constant degree of saturation condition. On the other hand, pore air pressure was applied using a pneumatic regulator at the top of the specimen.

In the tests, the net stress ($\sigma_v^{net} = \sigma_v - u_a$, σ_v: total stress, u_a: pore air pressure) was applied to 20 kPa at the beginning, and then the suction ($s = u_a - u_w$, u_w: pore water pressure) was applied to 100 kPa (u_a = 500 kPa, u_w = 400 kPa). After confirming that the drainage of water from the specimen became stable, switch on the control unit to keep the degree of saturation being constant, and simultaneously start applying the net stress from 20 kPa to 965 kPa with a rate of 60 kPa/h. The control technique proposed by Reference [11], which can adjust the drainage of water from the specimen by increasing/decreasing the pore water pressure under constant pore air pressure, was adopted in order to keep the degree of saturation being constant. The expression for the controlling of the degree of saturation is given as,

$$dV_w - S_{r(init.)}dV_v = 0 \quad (1)$$

where, dV_w is the change in pore water volume, $S_{r(init.)}dV_v$ is the product of the initial degree of saturation and the change in volume of the voids. In the uniaxial compression test, dV_w is obtained from the product of the cross-sectional area and the vertical displacement of the specimen. Meanwhile, dV_w is adjusted using the PVC to keep the degree of saturation.

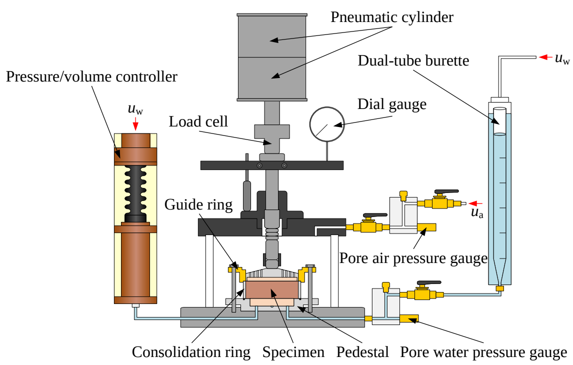

Fig. 3 Schematic illustration of the test apparatus for uniaxial compression tests

Performance of Proposed Elastoplastic Constitutive Model for Unsaturated Soil

In the simulations, an elastoplastic constitutive model proposed by Reference [8], was used in theoretical simulation of the tests. The model is based on the modified Cam-Clay model [12], in which the Bishop-type skeleton stress ($\sigma'' = \sigma_v^{net} + S_r s$) and the degree of saturation are used as the state variables, can take into consideration wetting-drying moisture hysteresis of an unsaturated soil. The material parameters for the constitutive model and the parameters of moisture characteristic curve (MCC) are listed in Table 2. Here, it is assumed that normally consolidated line in unsaturated state (*N.C.L.S.*) is parallel to the normally consolidated line in saturated state (*N.C.L.*) but in a higher position than *N.C.L.*, which means that under the same mean skeleton stress, the unsaturated soil can keep higher the void ratio than those of saturated soil. In other words, compression index λ is always constant with the degree of saturation. The *N.C.L.S.* and the *C.S.L.S.* are given in the following relations as,

$$N.C.L.S.:\ e = N(S_r) - \lambda \ln \frac{p}{p_r},\quad \left(\eta = \frac{q}{p} = 0\right) \tag{2}$$

$$C.S.L.S.:\ e = \Gamma(S_r) - \lambda \ln \frac{p}{p_r},\quad \left(\eta = \frac{q}{p} = M\right) \tag{3}$$

where, $N(S_r)$ and $\Gamma(S_r)$ are the void ratios at *N.C.L.S.* and *C.S.L.S.* under the reference mean skeleton stress (p_r = 98 kPa) and certain degree of saturation. p and q are the mean skeleton stress and the second invariant of deviator skeleton stress tensor. M is the stress ratio at critical state and has the same value for saturated and unsaturated states. $N(S_r)$ is expressed as,

$$N(S_r) = N + \frac{N_r - N}{S_r^s - S_r^r}\left(S_r^s - S_r\right) \tag{4}$$

where, S_r^s is the saturated degrees of saturation and S_r^r is the residual degrees of saturation, which have definite physical meaning and can be determined by water retention test easily. N_r is the void ratio at *N.C.L.S.* under the reference mean skeleton stress when the degree of saturation is at residual dry state.

RESULTS AND DISCUSSION

Fig. 4 shows the comparison between the test data and the simulated data of the water retention test based on the pressuring method. In the figure, it is very clear that there is a good agreement between the test data and the simulated data. It should be noted that the material parameters for elastoplastic constitutive model and the parameters of MCC have been unified in all simulation cases.

Table 2 Material parameters for constitutive model and parameters of MCC of Masado

Material parameters for constitutive model	Compression index, λ	0.089
	Swelling index, κ	0.0080
	Critical state parameter, R_{cs}	4.01
	Void ratio, N (p' = 98 kPa on *N.C.L.*)	0.69
	Poisson's ratio, ν	0.25
	Parameter of overconsolidation, a	60.0
	Parameter of suction, b	20.0
	Parameter of overconsolidation, β	2.0
	State variable of overconsolidation, ρ_e	0.040
	Void ratio, N_r (p' = 98 kPa on *N.C.L.S.*)	0.71
Parameters of moisture characteristic curve	Saturated degrees of saturation, S_r^s	0.85
	Residual degrees of saturation, S_r^r	0.27
	Parameter corresponding to drying AEV (kPa), S_d	5.0
	Parameter corresponding to wetting AEV (kPa), S_w	1.0
	Initial stiffness of scanning curve (kPa), k_{sp}^e	2000
	Parameter of shape function, c_1	0.014
	Parameter of shape function, c_2	0.060
	Parameter of shape function, c_3	50.0

Note: *N.C.L.* is the normally consolidated line at saturated state; *N.C.L.S.* is the normally consolidated line at unsaturated state.

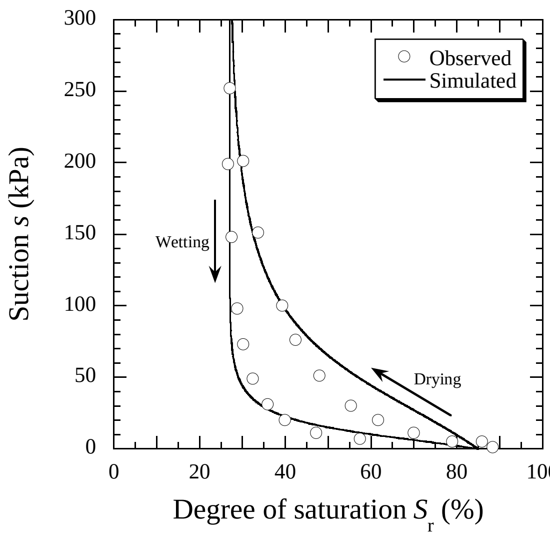

Fig. 4 Moisture characteristic curve of Masado

Table 3 Physical properties at different stages

Target water content	Initial condition			Stage beginning			Stage end		
	w_0 (%)	e_0	S_{r0} (%)	w (%)	e	S_r (%)	w_f (%)	e_f	S_{rf} (%)
w = 9%	8.5	0.642	35.2	7.4	0.613	31.6	5.3	0.453	31.1
w = 12%	12.1	0.650	49.3	9.6	0.625	40.7	7.3	0.479	41.0
w = 15%	15.0	0.650	61.7	11.0	0.625	46.8	8.0	0.446	47.7
w = 18%	17.8	0.651	72.8	11.1	0.613	48.0	7.9	0.441	48.8
w = 21%	21.8	0.660	87.8	11.5	0.623	49.0	8.5	0.455	49.6

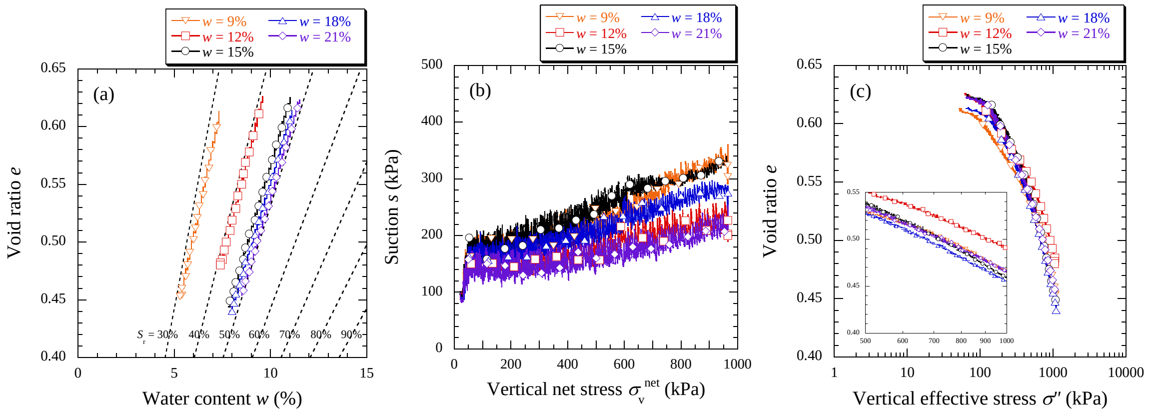

Fig. 5 Uniaxial compression tests results under constant degree of saturation; (a) e vs. w, (b) s vs. σ_v^{net}, (c) e vs. σ''

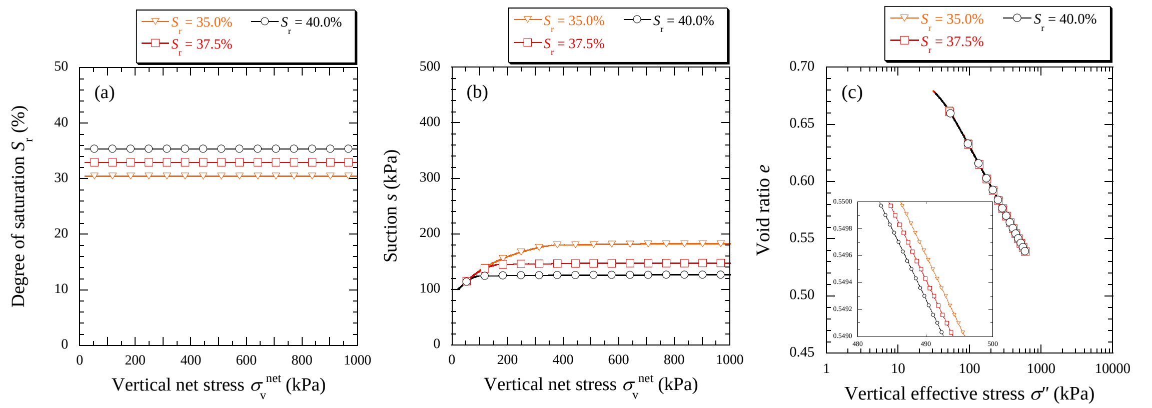

Fig. 6 Simulated results of uniaxial compression tests under constant degree of saturation; (a) S_r vs. σ_v^{net}, (b) s vs. σ_v^{net}, (c) e vs. σ''

Fig. 5 shows the test results obtained from the uniaxial compression tests under constant degree of saturation. The constant degree of saturation lines were drawn based on $eS_r = wG_s$. See Table 3 for the physical properties of Masado in each test. From these results, it is known that the water content declines with the decreasing of the void ratio, while the degree of saturation is kept constant. In Fig. 5(b), the suction is built up along with the increasing of the net stress, and the increment of suction is depending on the initial degree of saturation. In two cases (w = 18, 21%), even the degrees of saturation at the beginning of suction are almost the same, the specimen with higher initial degree of saturation shows lower increment of suction. As shown in Fig. 5(c), the *N.C.L.* of dry side (w = 9, 12%) is located above those of wet side (w = 18, 21%) and the optimum water content (w_{opt} = 15%). In other words, the lower the initial degree of saturation is, the more the *N.C.L.* will be shifted upward.

Fig. 6 shows the simulated results of uniaxial compression tests under constant degree of saturation. The simulated loading path is the same as that of the tests. In the simulations, the target degrees of saturation were set into three cases (S_r = 35.0, 37.5, 40.0%), which are corresponded to the value located in the inner side of MCC from Fig. 4. From these results, the degree of saturation decreases due to the suction, after then the degree of saturation is kept constant by the increment of the net stress. In Fig. 6(b), it can be observed that the simulated data is on the whole agreed with the test data. As shown in Fig. 6(c), the proposed model can qualititatively describe the parallel upward moving of *N.C.L.* along with the decreasing of the initial degree of saturation, though quantitatively there still exists some discrepancies.

CONCLUSIONS

In this paper, uniaxial compression tests were conducted to verify the importance of proper selection of the state variables, that is, the skeleton stress and the degree of saturation as the state variables, in proposing constitutive model for unsaturated soil. Corresponding theoretical simulation were also conducted with proper MCC. The following conclusions can be drawn:

1. By using the skeleton stress as a state variable, the influence of the degree of saturation on the deformation and the strength of unsaturated soil can be identified.
2. In the simulations, it is proved that the proposed model can describe the mechanical behaviors of unsaturated soil under different degrees of saturation to some extent on the whole. However, the comparison between the test data and the simulated data has not been checked directly yet, because the range of the degree of saturation depending on the suction can be applied for the simulation is limited. In future study, it is necessary to determine the parameters, especially for MCC in a more accurate way, based on more test cases.

REFERENCES

[1] Alonso EE, Gens A, Josa A, “A constitutive model for partially saturated soils”, Géotechnique, Vol. 40, No. 3, Sep. 1990, pp. 405-430.

[2] Kohgo Y, Nakano M, Miyazaki T, “Theoretical aspects of constitutive modelling for unsaturated soils”, Soils and Foundations, Vol. 33, No. 4, Dec. 1993, pp. 49-63.

[3] Cui YJ, Delage P, “Yielding and plastic behaviour of an unsaturated compacted silt”, Géotechnique, Vol. 46, No. 2, June 1996, pp. 291-311.

[4] Loret B, Khalili N, “An effective stress elastic-plastic model for unsaturated porous media”, Mechanics of Materials, Vol. 34, No. 2, Feb. 2002, pp. 97-116.

[5] Chiu CF, Ng CWW, “A state-dependent elasto-plastic model for saturated and unsaturated soils”, Géotechnique, Vol. 53, No. 9, Nov. 2003, pp. 809-829.

[6] Sun DA, Cui HB, Matsuoka H, Sheng DC, “A three-dimensional elastoplastic model for unsaturated compacted soils with hydraulic hysteresis”, Soils and Foundations, Vol. 47, No. 2, Apr. 2007, pp. 253-264.

[7] Sheng D, Fredlund DG, Gens A, “A new modelling approach for unsaturated soils using independent stress variables”, Canadian Geotechnical Journal, Vol. 45, No. 4, Apr. 2008, pp. 511-534.

[8] Zhang F, Ikariya T, “A new model for unsaturated soil using skeleton stress and degree of saturation as state variables”, Soils and Foundations, Vol. 51, No. 1, Feb. 2011, pp. 67-81.

[9] Zhou AN, Sheng D, Sloan SW, Gens A, “Interpretation of unsaturated soil behaviour in the stress-saturation space: II: Constitutive relationships and validations”, Computers and Geotechnics, Vol. 43, June 2012, pp. 111-123.

[10] Zhou AN, Sheng D, Sloan SW, Gens A, “Interpretation of unsaturated soil behaviour in the stress - Saturation space, I: Volume change and water retention behaviour”, Computers and Geotechnics, Vol. 43, June 2012, pp. 178-187.

[11] Burton GJ, Pineda JA, Sheng D, Airey DW, Zhang F, “Exploring one-dimensional compression of compacted clay under constant degree of saturation paths”, Géotechnique, Vol. 66, No. 5, May 2016, pp. 435-440.

[12] Schofield AN, Wroth CP, Critical State Soil Mechanics, McGraw-Hill, 1968.

AN ANALYTICAL EVALUATION OF RADIAL CONSOLIDATION WITH RESPECT TO DRAIN DEGRADATION

Thanh Trung Nguyen[1], Buddhima Indraratna[2] and Cholachat Rujikiatkamjorn[3]
[1,2,3] Faculty of Engineering and Information Sciences, University of Wollongong, Australia

ABSTRACT

The use of synthetic prefabricated vertical drains over the past decades for soil improvement has had a negative ecological effect on the natural environment due to their long-term existence in soil. The emergence in recent years of Natural Fibre Drains (NFDs) made from biodegradable materials such as jute, coir, and straw is believed to be an environmentally friendly approach to treating soft soil. However, when subjected to adverse conditions such as pyritic acidic and/or biologically active soil, natural fibres can decay rapidly, and that results in a significant deterioration of the engineering characteristics of drains during consolidation. This deterioration can particularly reduce the discharge capacity of the drains, which retards the dissipation of excess pore pressure and delays consolidation. This paper represents an analytical method which can capture the effect that drain degradation has on the radial consolidation of soil over time, and then applies this method to an exponential reduction of drain discharge capacity. This analytical method, with supporting evidence from experimental data, reveals that there is a significant retardation in excess pore pressure dissipation due to drain degradation. The study indicates there is a potential risk when using NFDs in adverse soils and suggests that caution is needed in practice.

Keywords: Soil Consolidation; Discharge Capacity; Natural Fibre Drains; Prefabricated Vertical Drains; Biodegradable Materials

INTRODUCTION

Prefabricated vertical drains (PVDs) have been used worldwide to accelerate soil consolidation, and over the years have undergone extensive technical improvements such as combining vertical drains with surcharge and vacuum loading [1]. Rather than using polymeric PVDs which can damage the natural environment, natural fibre drains (NFDs) have been widely used in South and Southeast Asia in recent years, ever since the first NFDs were introduced by Lee et al. [2] in 1987 while a significant effort [3-5] has been made to convenience the application of those naturally occurring materials in geoengineering. Most field observations [4, 6] indicated that NFDs have engineering characteristics that are comparable to synthetic prefabricated vertical drains and hence accelerate consolidation very affectively. However these NFDs had been used in more inert soft soils which might not harm the engineering features of the drain seriously, but in highly acidic and/or bio-active soils such as acidic sulphate soil where the sulphate reducing bacteria consume organic compounds for their metabolism, natural fibres potentially decay much faster, and therefore the degradation of NFDs in adverse soils needs urgent evaluation.

Natural fibre drains can be made from agriculture products such as jute, coir, and straw with either circular or band shaped cross-sections. Of these, jute and coir are preferred in practices due to their favorable engineering characteristics and sheer abundance in developing countries. Coir fibre extracted from coconut husks has approximately 30% lignin [7] making it more robust and durable than other natural fibres such as jute which contains more than 80% cellulose and only around 12% lignin [8]. Straw has also been employed in several studies [4] but the drain made from this fibre showed relatively smaller discharge capacity than those composed of jute and coir.

The degradation of jute fibre basically depends on the environmental conditions, particularly the acidity and biological activities of soil. For example, jute fibre can degrade much faster where the pH value is less than 5.2 or higher than 9 [8, 9]. Since acidic soil can be found in many regions around the world, as reported by [10, 11], the effect of this soil on the performance of NFDs must be considered. Moreover, bacteria and fungi in their preferred environment can also enhance the biodegradation of natural fibres, as shown by [4, 9]. Several anaerobic bacteria can decompose organic matters faster when they have access to oxidants such as Fe^{3+}, Mn^{2+} and SO_4^{2-} [12].

This paper discusses the effect that drain degradation has on the radial consolidation of soil, based on an analytical approach. The result from this analytical method is then compared with those obtained from an experimental investigation.

ANALYTICAL APPROACH FOR RADIAL CONSOLIDATION WITH RESPECT TO DRAIN DEGRADATION

Degradation of natural fibre drains

Since the major function of NFD is to discharge the excess pore pressure (EPP) of soil, the engineering characteristics of the drain are expected to remain until the design target of consolidation is achieved (Fig. 1). However previous studies ([4, 8, 9]) indicated that natural fibres (i.e., jute, straw) can decay rapidly in adverse environments, leading to a considerable retardation in the dissipation of EPP. Therefore the over decay of NFDs on consolidation needs serious evaluation.

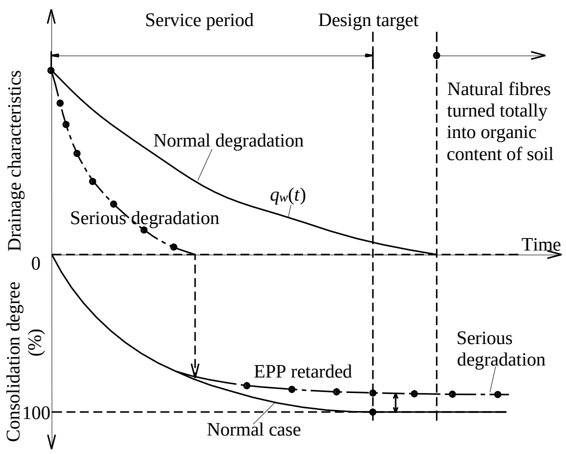

Fig. 1 Degradation of NFDs in relation to consolidation process of soil

The biodegradation of NFDs is complicated and depends on a number of factors such as: (*i*) the environmental conditions of soil such as pH, temperature, activities of micro-organisms and so on; (*ii*) the properties of natural fibres in the drain e.g., their chemical components. A pilot investigation in the field carried out by Kim and Cho [6] on the reduction in the discharge capacity of several natural fibre drains made from straw and jute installed in saturated clay indicated that the rate of degradation varied considerably over different seasons where the temperature and humidity changed.

For simplicity in this study, a number of assumptions were made: (*i*) the NFDs began to degrade immediately after installation; (*ii*) the geometric parameters (i.e., equivalent diameter and length) of drains were constant while the discharge capacity varied over time; (*iii*) degradation was uniform over the installation depth; and (*iv*) the reduced discharge capacity reached a limit level in which the jute fibres were converted completely into organic components of soil.

Incorporating Drain Degradation into the Radial Consolidation of Soil

Based on numerous studies into the consolidation of soil, the radial consolidation theory proposed by Barron [13] and later improved by Hansbo [14] is the preferred approach ([15, 16]). According to this method, the dissipation of EPP is described by:

$$\frac{u(t)}{u_o} = exp\left(\frac{-8T_h}{\mu}\right) \tag{1}$$

In the above, T_h is the time factor for horizontal drainage: $T_h = (c_h t)/(d_e^2)$ where c_h is the consolidation coefficient for horizontal drainage, and d_e is the diameter of the influence zone. u_o is the initial EPP. $\mu = \mu_q + \mu_{n,s}$ where $\mu_q = (2\pi k_h l^2)/(3q_w)$ represents the influence of the discharge capacity q_w of a drain with a length l; and $\mu_{n,s}$ denotes the effect of geometry (i.e., the size of the smear and influence zones), and is estimated as follows:

$$\mu_{n,s} = \frac{n^2}{n^2-1}\left[ln\left(\frac{n}{s}\right) + \frac{k_h}{k_s} ln(s) - \frac{3}{4}\right] + \frac{s^2}{n^2-1}\left[1 - \frac{s^2}{4n^2}\right] + \frac{k_h}{k_s}\left(\frac{1}{n^2-1}\right)\left[\frac{s^4-1}{4n^2} - s^2 + 1\right] \tag{2}$$

In the above, $n = r_e/r_w$; $s = r_s/r_w$ where r_e, r_s and r_w are the radius of the influence, smear and well zones, respectively; k_h and k_s are the coefficient of permeability in the undisturbed and smear zones, respectively.

By assuming that the geometric parameters of NFD are constant and only the discharge capacity of the drain decreases over time when natural fibres are decaying, a time-dependent function of discharge capacity $q_w(t)$ is introduced to the conventional method of Hansbo. According to Indraratna et al. [15], the average excess pore pressure of a unit cell at time t can be written by:

$$u = \frac{\int_0^l \int_{r_w}^{r_s} u_s(2\pi r)drdz + \int_0^l \int_{r_s}^{r_e} u_u(2\pi r)drdz}{V} \tag{3}$$

In the above, V is the total volume of the unit cell. By integrating Eq. [3] with the constant geometric parameters and varying the discharge capacity over time, and then re-arranging yield:

$$u + h(t)\frac{du}{dt} = 0 \tag{4}$$

where $h(t)$ is written as:

$$h(t) = \chi\left(\mu_{n,s} + \frac{\lambda}{q_w(t)}\right) \tag{5}$$

where

$$\lambda = \frac{2\pi k_h l^2}{3} \tag{6}$$

$$\chi = \frac{d_e^2}{8c_h} \tag{7}$$

Solving the ordinary differential equation Eq. [4] and re-arranging result in:

$$\frac{u(t)}{u_o} = exp\left(-\int_0^t \frac{1}{h(t)}dt\right) \tag{8}$$

Note that this equation describes the radial consolidation of soil with respect to any given degradation function of the discharge capacity $q_w(t)$ incorporated into Eq. [4]. In order to demonstrate the proposed solution, a specific form of $q_w(t)$ is required. By referring to biological studies [17-19] which used mathematical models to predict an exponential decay of organic matters (e.g., jute, straw), this paper assumes an exponential reduction in the discharge capacity over time, particularly:

$$q_w(t) = q_{wo}e^{-\omega t} \tag{9}$$

where ω is the decay coefficient that represents the rate at which the drain discharge capacity degrades, and q_{wo} is the initial discharge capacity of the drain. Apparently ω should be within the range [0, +∞].

Replacing Eq. [9] into $h(t)$ of Eq. [8] and integrating lead to:

$$\frac{u(t)}{u_o} = exp\left\{\frac{-8T_h}{\mu_{n,s}} + \frac{1}{\chi\mu_{n,s}\omega}\left[ln\left(\frac{\frac{\mu_{n,s}}{\mu_{qo}} + e^{\omega t}}{\frac{\mu_{n,s}}{\mu_{qo}} + 1}\right)\right]\right\} \tag{10}$$

The above describes the dissipation of EPP over time with respect to an exponential reduction in the discharge capacity of a drain. Note that when ω approaches zero (no degradation of drain), Eq. [10] turns into Hansbo's solution which assumes a constant discharge capacity.

Results and discussion

A prefabricated vertical jute drain (PVJD) with an equivalent diameter d_w of 70 mm was used to demonstrate the proposed model with respect to the approximation $d_w = 2(a_w + b_w)/\pi$ where a_w and b_w are the thickness and width of the drain. A typical PVJD is normally 80-110 mm wide and 6-12 mm thick (Fig. 2). The drain had an initial discharge capacity q_{wo} of 0.43 m^3/day determined by carrying out the discharge capacity test in the laboratory. Note that PVJDs can be installed using the same method as conventional drains, so the smear behaviour of soil using PVJDs should be identical to conventional cases already clarified by Indraratna and Redana [20]. In this investigation, a ratio of k_s/k_h = 3 was used, and the soil properties were assumed.

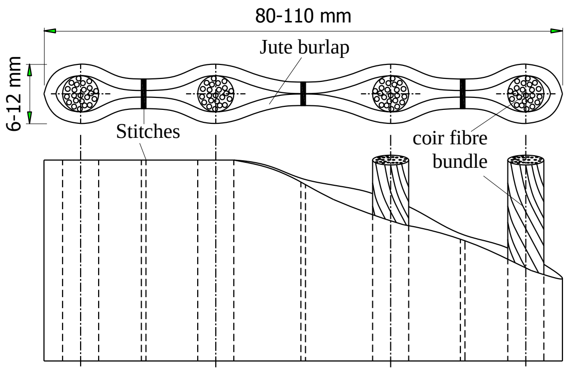

Fig. 2 Structure of a typical prefabricated vertical jute drain (PVJD)

Fig. 3 shows how the proposed analytical solution could capture the retardation of the dissipation of EPP due to drain degradation compared to the conventional method without degradation. In this comparison, the exponential degradation of the drain discharge capacity with ω = 0.02 day^{-1} was considered. In the period where the drain discharge capacity was large enough (initially 50 days), degradation had almost no influence on the dissipation of EPP, so deviation between the two curves is not clear, but after this period when the discharge capacity of the drain was less than 0.1 m^3/day, dissipation of EPP induced by the degradable drain definitely deviated from the conventional drain. The proposed solution indicated there was a serious obstruction of EPP discharged after approximately 200 days meanwhile this trend could not be shown in the conventional solution which did not consider any drain degradation. This result also showed a critical state of decay where the predicted curve was almost horizontal after nearly

300 days at a residual EPP of almost 20%. In this critical state the discharge capacity of the drain reached an extremely low value (i.e., below 0.01 m^3/day), leading to a very low rate of dissipation of EPP.

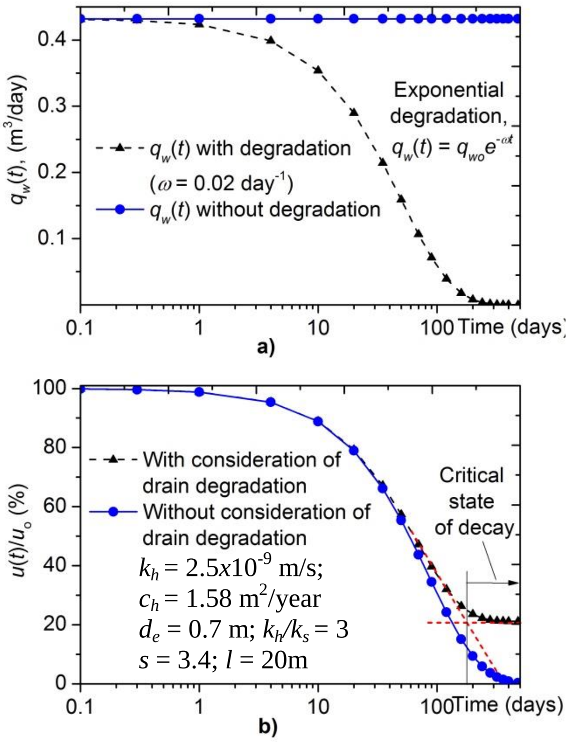

Fig. 3 Degradation versus no-degradation of drain: *a*) Discharge capacity; and *b*) Dissipation of EPP

The radial consolidation of soil induced by a degradable drain with respect to various rates (ω = 0.01; 0.02; and 0.03 day^{-1}) of degradation is represented in Fig. 4. The fastest drain decay occurred (ω = 0.03 day^{-1}) where the drain discharge capacity decreased to 7.0x10^{-3} m^3/s in 150 days; here the dissipation of EPP began slow after almost 60 days and then turned into a critical state of decay after only 160 days with a residual EPP of 35%. In the smaller range of degradation rates i.e., ω = 0.02 and 0.01 day^{-1}, the consolidation curves reached a critical state after 200 days and 400 days with a residual EPP of approximately 20% and 5%, respectively. Unlike the case where the drain did not decay, the degradable drain caused an obvious retardation in the consolidation process.

This study also showed that the negative influence of drain degradation only became obvious when the discharge capacity decreased to a certain small value which varies with the properties of soil (e.g., c_h) and geometric parameters such as the length and space of the drain. In this investigation, the discharge capacity that began to markedly obstruct the dissipation of EPP was approximately 0.08 m^3/day.

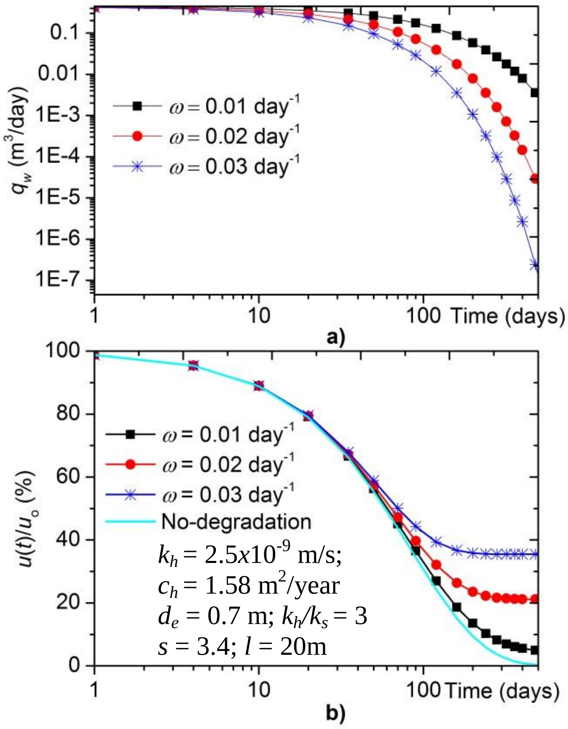

Fig. 4 Degradation with different decay rates: *a*) Discharge capacity; and *b*) Dissipation of EPP

Fig. 5 compares the consolidation curves obtained by the proposed analytical solution and the experimental work conducted in the laboratory by Kim et al. [21]. A unit cell with d_e = 0.6 m; d_s = 0.3 m; d_w = 0.05 m and l = 2 m was adopted for computation with reference to the laboratory data measured by Kim et al. [21]. The drain with an initial discharge capacity of q_{wo} = 0.014 m^3/day and a degradation coefficient of ω = 0.260 day^{-1} (Fig. 5a) was also obtained from the work by Kim et al. [21]. The soil parameters, including k_h = 3.6x10^{-10} m/s and c_h = 3.154 m^2/year, and the ratio k_h/k_s = 1.05 were used in this study.

Fig. 5b shows a good agreement between the analytical method and the laboratory data measured by Kim et al. [21]. In the first 7 days, the analytical curve was almost 5% higher than the laboratory curve, but it gradually became closer to the experimental curve over the next 10 days before turning into a smaller range. This deviation is understandable because of a difference in the drain discharge capacity between the measured and fitted curves, as shown in Fig. 5a. With ω = 0.260 day^{-1} of the exponential degradation adopted, the sharp drop in discharge capacity in the first days of the experiment could not be captured accurately, resulting in a gap between the two curves, as shown in Fig. 5b. When the degradation of drain discharge capacity observed in the experiment was described better by the exponential curve, the dissipation of EPP was captured more accurately by the proposed method.

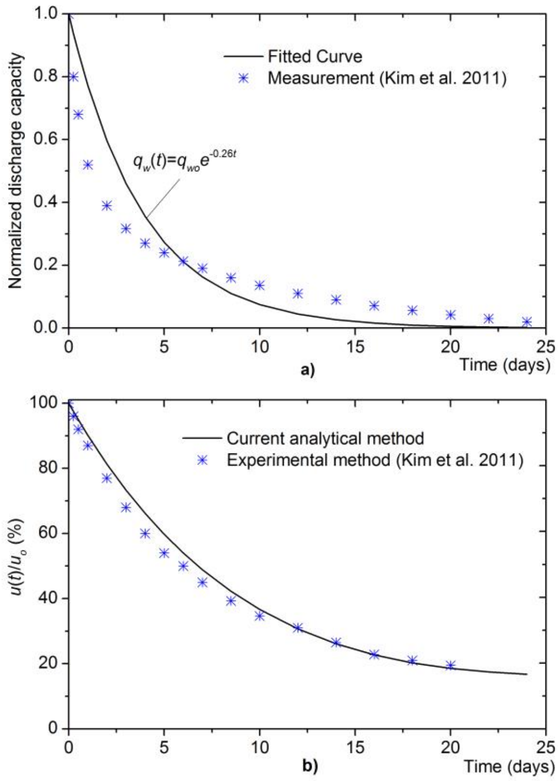

Fig. 5 Model verification by comparing with experimental work: *a*) Exponential curve fitting experimental data; *b*) Dissipation of EPP

This investigation also indicated that the form of the degradation function $q_w(t)$ played a decisive role in accurately predicting the influence of drain degradation on the consolidation of soil. In this paper, only the exponential degradation of the drain was considered but it is noteworthy that the proposed analytical solution (Eq. 8) can be applied to any given form of $q_w(t)$, such as convex and concave curves. To determine $q_w(t)$, it requires an extensive investigation into the degradation of NFDs subjected to specific environmental conditions of soil.

CONCLUSION

An analytical approach which incorporated the degradation of natural fibre drain into the radial consolidation of soil was represented in this study, and then the solution was applied to an exponential degradation of drain discharge capacity. The results showed that the dissipation of excess pore pressure (EPP) could be retarded significantly when the discharge capacity of the drain decreased to less than 0.08 m^3/day. Consolidation of soil could be slowed down seriously when the decay of a drain turned into a critical state where the discharge capacity became very small. This study also indicated there is a need to determine the exact form of the degradation function $q_w(t)$ with respect to specific soil conditions in order to optimise the accuracy of this method.

ACKNOWLEDGEMENTS

The authors acknowledge the Australia Research Council for funding this research. The 1st author's PhD scholarship is sponsored by the Australia Endeavour Scheme.

REFERENCES

[1] Indraratna B, Rujikiatkamjorn C, Kelly C, Buys H. Soft soil foundation improved by vacuum and surcharge loading. Ground Improvement 2012; 165(2): 87-96.

[2] Lee SL, Ramaswamy SD, Aziz MA, Das Gupta NC, N. C. & Karunaratne GP. Fibredrain for consolidation of soft soils. In: Post- Vienna Conference on Geotextiles, Singapore 1987; vol. 2: p. 238-58.

[3] Nguyen TT, Indraratna B. Hydraulic behaviour of parallel fibres under longitudinal flow: a numerical treatment. Canadian Geotechnical Journal 2016.

[4] Kim JH, Cho SD. Pilot scale field test for natural fiber drain. Geosynthetics in civil and environmental engineering. In: Li G., Chen Y., Tang X., Editors. Springer Berlin Heidelberg; 2009. p. 409-414.

[5] Asha BS, Mandal JN. Absorption and discharge capacity tests on natural prefabricated vertical drains. Geosynthetics International 2012; 19: 263-271.

[6] Lee SL, Karunaratne GP, Ramaswamy SD, Aziz MA, Das Gupta NC. Natural geosynthetic drain for soil improvement. Geotextiles and Geomembranes 1994; 13(6–7): 457-474.

[7] Asasutjarit C, Hirunlabh J, Khedari J, Charoenvai S, Zeghmati B, Shin UC. Development of coconut coir-based lightweight cement board. Construction and Building Materials 2007; 21(2): 277-288.

[8] Som N, Chattopadhyay BC, Sanyal T. A manual on use of jute geotextiles in civil eingieering, 4th Edition. Jute Manufactures Development Council, Kolkata, India 2009.

[9] Saha P, Roy D, Manna S, Adhikari B, Sen R, Roy S. Durability of transesterified jute geotextiles. Geotextiles and Geomembranes 2012; 35: 69-75.

[10] Dent DL, Pons LJ. A world perspective on acid sulfate soils. Geodarma 1995; 67: 263-276.

[11] Fitzpatrick R, Shand P. Inland acid sulfate soil systems across australia. In: CRC LEME Open File Report 249. CRC LEME. Perth. 2008. p. 1-309.

[12] Inglett PW, Reddy KR, Corstanje R. Anaerobic soils. Encyclopedia of Soils in the Environment. In: Hillel D., Editor. Elsevier: Oxford; 2005. p. 72-78.

[13] Barron RA. The influence of drain wells on the consolidation of fine-grained soils. Trans ASCE 1948; 113(2348): 718-54.

[14] Hansbo S. Consolidation of fine-grained soils by prefabricated drains and lime column installation. In: Proceedings of 10th International Conference on Soil Mechanics and Foundation Engineering, Stockholm, A.A. Balkema, Rotterdam, The Netherlands 1981; vol. 3: p. 677-682.

[15] Indraratna B, Rujikiatkamjorn C, Sathananthan I. Analytical and numerical solutions for a single vertical drain including the effects of vacuum preloading. Canadian Geotechnical Journal 2005; 42(4): 994-1014.

[16] Indraratna B, Sathananthan I, Rujikiatkamjorn C, Balasubramaniam AS. Analytical and numerical modeling of soft soil stablization by prefabricated vertical drains incorporating vacumm preloading. International Journal of Geomechanics, ASCE 2005; 5:2(114).

[17] Means JE, Kermit Cromack J, Macmillan PC. Comparison of decomposition models using wood density of Douglas. fir logs. Canadian Journal of Forest Research 1985; 15(6): 1092-1098.

[18] Gamage NPD, Asaeda T. Decomposition and mineralization of Eichhornia crassipes litter under aerobic conditions with and without bacteria. Hydrobiologia 2005; 541(1): 13-27.

[19] Manzoni S, Piñeiro G, Jackson RB, Jobbágy EG, Kim JH, Porporato A. Analytical models of soil and litter decomposition: solutions for mass loss and time-dependent decay rates. Soil Biology and Biochemistry 2012; 50: 66-76.

[20] Indraratna B, Redana IW. Development of the smear zone around vertical band drains. Ground Improvement 1998; 2(4): 165-178.

[21] Kim R, Hong SJ, Lee MJ, Lee W. Time dependent well resistance factor of PVD. Marine Georesources & Geotechnology 2011; 29(2): 131-144.

A STUDY ON INJECTING MICRO BUBBLE WATER MIXED WITH CRUSHED SILICA

Yukoh Hasunuma[1], Kentaro Uemura[1]
Takamitsu Sasaki[2], Koichi Nagao[3], Naoaki Suemasa[1] and Shunsuke Shimada[4]
[1]Tokyo City University Graduate Division, Japan; [2]Kyokado Engineering co.,Ltd, Japan;
[3]Sato Kogyo, Japan; [4] Kyokado co.,Ltd, Japan

ABSTRACT

Liquefaction has been a serious problem in Japan for a long time and many technical countermeasure methods have been developed until now. However, it is still difficult to improve the ground in a narrow place such as residential land. This is because most of the methods generally used for liquefaction countermeasures need both large-scale construction machinery and a high cost per unit area.

Therefore, it has been demanded to develop a method with a low cost and better operability. In this study, Bubble White was proposed as a new grouting material for a chemical grouting method, which is a mixture of silica micro-particles and micro bubble water. This report describes the result of injection experiments where silica micro-particles were injected into sand specimens in order to verify the permeation characteristics of micro-particles. As a result of the experiments, it was confirmed that the permeability of micro-particles in soil changed depending on both injection speed and amount.

Keywords: Micro-particles, Micro bubble, Liquefaction countermeasures

INTRODUCTION

Japan is one of the countries where earthquakes occur most frequently in the world. Large earthquakes in the past caused a lot of damage directly to existing structures such as shear failure of reinforced concrete bridge piers. In particular, liquefaction damage has become a major social issue after the 2011 off the Pacific coast of Tohoku Earthquake.

Photo. 1 Liquefaction damage overview

Photo. 1 [1], taken after the earthquake, shows the damage situation of underground structures. Ground subsidence occurred due to liquefaction and accordingly the manholes buried under the ground came out from the ground to the surface. In addition, sand boil phenomena were observed in several areas, where sand in the ground gushed on the ground. One of the reasons why such widespread damage was caused was that the liquefaction countermeasures for existing structures have not been pushed forward sufficiently on account of a high cost performance. In this study, therefore, a low-cost material, Bubble White was focused on as a grouting material for a chemical grouting method with excellent operability. Bubble White is able to be obtained only by mixing inexpensive silica micro-particles and micro bubble water.

New grouting material Bubble White

Photo. 2 shows micro bubbles. As the characteristics of the micro bubbles, the surface area of micro bubbles is quite large in comparison with that of a normal air bubble with the same volume. Also, the bubbles have an advantage that they tend to rise slower and accordingly diffuse horizontally. The micro bubbles can reduce both saturation degree and pore water pressure in the ground during an earthquake [2].

Photo. 2 Micro bubbles

While silica micro-particles are obtained by crushing solidified silica sol which is made by neutralizing alkali contained in silica glass with acid. By injection of the silica particles, the density of the ground increases. In addition, the silica particles are viscous enough to stay in the voids of the ground. They can increase the density of the ground efficiently. By combining these excellent materials: the micro-bubble water and the silica micro-particles, it was expected to increase the effectiveness of preventing ground from liquefaction [3].

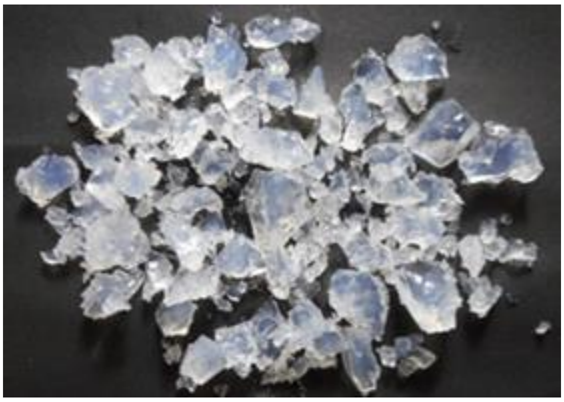

Photo.3 Solid silica

Photo. 3 shows solid silica. Because the solid silica was too coarse to be injected into a granular material such as the ground, it was necessary to crush solid silica into infinitesimal grains by a crushing device.

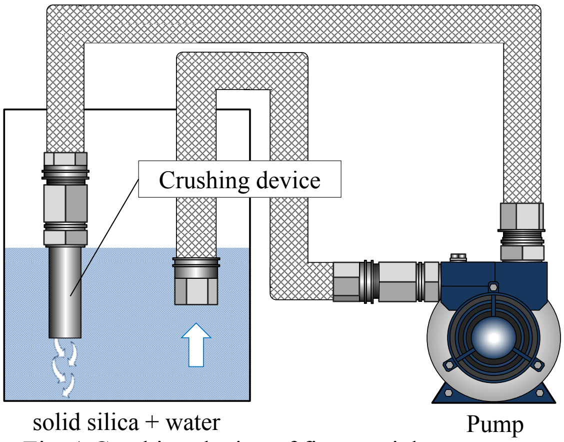

Fig. 1 Crushing device of fine particle

Fig. 1 shows a crushing device of fine particles. The crushing device attached to the discharge port of a pump was used to crush solid silica and generate micro bubbles. The crushing device has a structure which produces a turning flow and releases a pressure when a liquid passes. Silica micro-particles and micro bubbles were produced by a shear force generated by the device when a mixture of water with both solid silica and air released a pressure. Incidentally, air dissolved water was used for the experiments.

CRUSHING EXPERIMENT OF SOLID SILICA

Conditions of Experiment

A problem of silica micro-particles as a grouting material was that their grain sizes were too large to be injected into the ground. When a grain size is large, clogging tends to occur in ground voids at the early stage of injection and prevent from injecting uniformly in the ground. In this study, therefore, two different types of solid silica were examined, which were cured under different conditions. Their grain sizes were measured after being crushed in order to study grain refining mechanism. Table 1 and Fig. 2 show the test conditions of samples and the grain size accumulation curves of micro-particles, respectively.

Table 1 Test conditions of samples

case	case1	case2
sample	solid silica	
chemical liquid concentration	12%	
curing time	7days	
heat curing time	120min	-
crush time	50min	

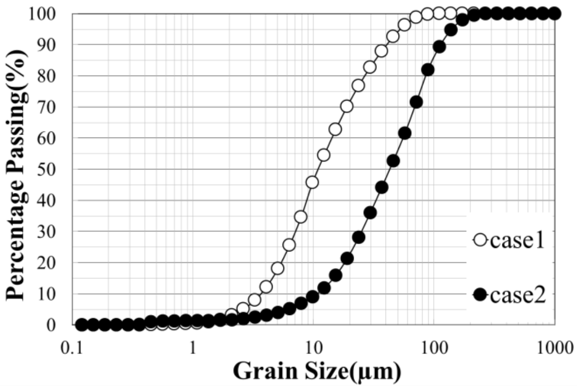

Fig. 2 Grain size accumulation curves of microparticles

Results of Experiment

As a result of comparison between Case1 and Case 2, it was confirmed that Case 1 provided with heat curing was able to be crushed into finer grains than Case 2. It was assumed that the gel structure was disrupted by the effect of volume expansion and contraction caused by both heat curing and temperature change after heat curing, and accordingly solidified silica body became easy to be crushed. On the contrary, when provided with heat curing until being dried completely, the solid silica became too hard to be crushed. It was revealed from the result that the crushing efficiency of solid silica increased by proper degree of heat curing. However, since a particle size of solid silica was still too large to be used as an injection material, it is necessary to continue pursuing optimum curing and crushing method.

Samples for Experiment

Fig. 3 and Fig. 4 show the grain size accumulation curves of silica sands and those of micro-particles, respectively, which were used for one-dimensional injection experiments and undrained triaxial tests.

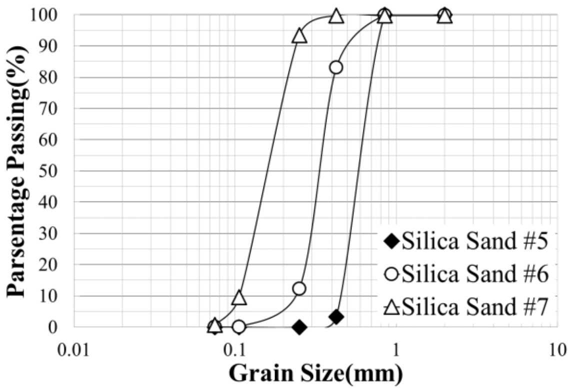

Fig. 3 Grain size accumulation curves of Silica Sand

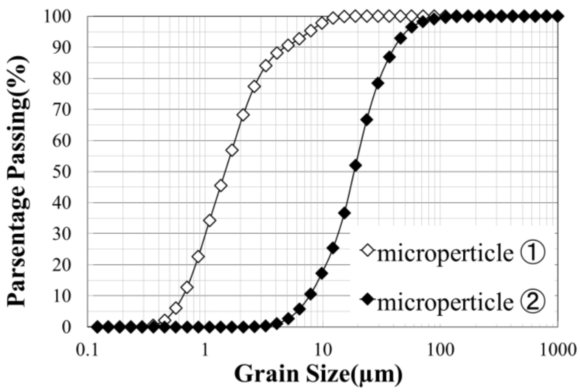

Fig. 4 grain size accumulation curves of micro-particles

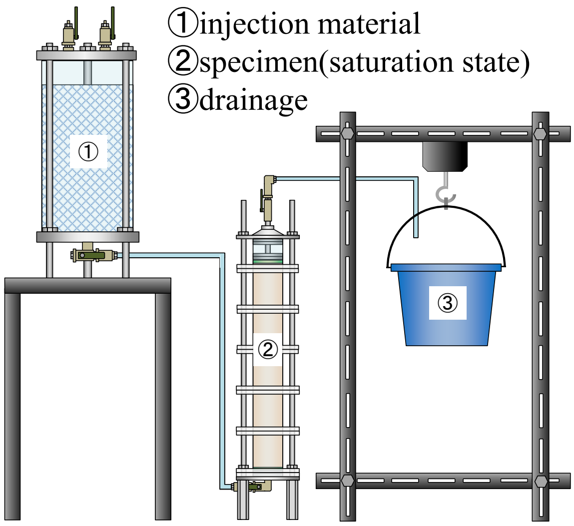

Fig. 5 Schematic of injection experiment

Table 2 Conditions of experiment

case	case1	case2	case3	case4
silica sand	#5	#6	#7	
injection material	microparticle①			
diameter	5.0cm			
height	50cm			30cm
concentration of injection material	4.0%			
injecting pressure	20kPa	20kPa	40kPa	40kPa
relative density	60%			

ONE-DIMENSIONAL INJECTION EXPERIMENT

Conditions of Experiment

The injection experiment was conducted in order to confirm the permeability of micro-particles which may differ depending on sand types. A long specimen was prepared for the experiment by combining separable columns with the height of 10.0 cm. Fig. 5 and Table 2 show a schematic and the conditions of injection experiment, respectively.

The sand specimen with 5.0cm in diameter and 50.0cm in height was prepared by the air-pluviation method at a relative density of 60% and completely saturated. And also, the drainage from the outlet of the container was sampled and its material concentration was measured after drying.

Results of Experiment

Results of experiment are shown in Fig. 6 to Fig. 8. In these figures, the index C / C_0 is the ratio of the concentration of material in drained C to the initial concentration of material in injected mixture C_0. The term “replacement rate” is defined as the ratio of injected mixture volume divided by total void volume in the specimen.

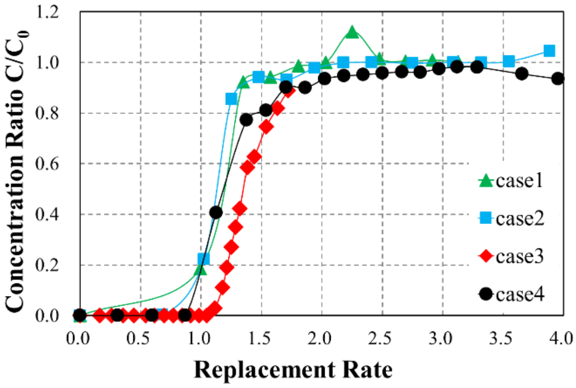

Fig. 6 Relationship between replacement rate and concentration ratio

Fig. 6 shows the relationship between replacement rate and concentration ratio. The concentration ratio increased in the replacement rate of 1.0 in all cases except Case 3. On the other hand, the concentration ratio of Case 3 increased after the replacement rate exceeds 1.0. This result is thought to be caused by using silica sand C for Case 3, which is finer in particle size than sands for Case 1 and Case 2. Silica sand #7 is likely to clog micro-particles because the void diameter is smaller than the other sands. Therefore, it is considered that the increase in concentration ratio was suppressed because the amount of micro-particles discharged was reduced. In Case 4 with silica sand #7, however, its upward trend of concentrations was similar to the other cases. Because the permeation distance was shorter than those of the two cases, it was found that the effect of particle size of sand was balanced by the influence of permeation distance.

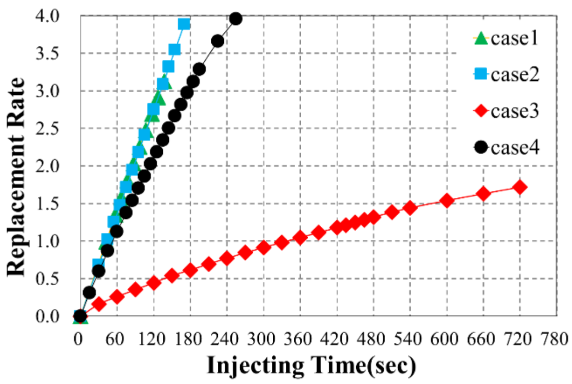

Fig. 7 Relationship between injecting time and replacement rate

Fig. 7 shows the change of replacement rate with time. Case 1 and Case 2 showed almost the same behavior, as they were injected at the same constant speed. After the replacement rate exceeded 1.0, the injection volume of Case 4 gradually decreased. This is considered that clogging occurred even in the case of the short permeation distance because the particle diameter of silica sand #7 was small. In Case 3, the injection speed was extremely lower than those of the other cases because the flow resistance of the mixture was larger than those of the other cases when the micro-particles passed through narrower void of silica sand #7. From the results, it seems that the factors on whether the clogging of the micro-particles occurs are attributed to the size of sand where the micro-particles pass through, the replacement rate of the mixture and the distance of the micro-particles passing through.

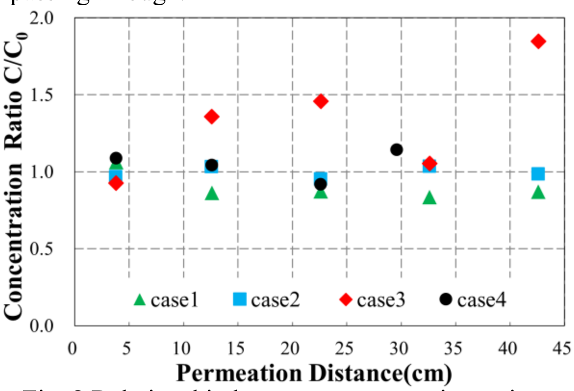

Fig. 8 Relationship between concentration ratio and permeation distance

Fig. 8 shows the distribution of concentration ratio of silica particle in pore water with permeation distance. As the concentration ratios in all cases except Case 3 are plotted around 1.0, which means injected materials were uniformly injected and deposited. On the other hand, the concentration ratio in Case 3 has a large variation. It is presumed that the injected material is not uniformly injected in the case that injection speed is slow. In other words, there is a possibility that the concentration ratio became locally high in the position where clogging occurred. Photo. 4 shows clogging of the specimen.

Photo. 4 Clogging of the specimen

UNDRAINED CYCLIC TRIAXIAL TEST

Conditions of Experiment

A series of cyclic triaxial tests were performed to study the liquefaction strength on the specimen improved by injecting micro-particles and micro bubbles. Table 3 and 4 show the conditions of experiments. All of the specimens except Case 2 were prepared at the relative density of 60%. Case 1 and Case 2 were conducted to obtain the liquefaction strength of unimproved sand specimens at the relative density of 60% and 70% for comparison with improved sand specimens. As for Case 3 to 6, grouting material was injected after the specimens were fully saturated. Incidentally, silica micro-particles used in Case 3 and 4 had an average diameter of about 20μm. In addition, a localized necking was observed in the specimen at the situation of DA= 5% during the test of Case 6 where the bubble white was injected. Photo. 5 shows localized necking of the specimen. The necking failure was thought to be shear failure at the tensile side in the triaxial test rather than liquefaction. Therefore, the test results were estimated at the double amplitude of axial strain: DA=3% not to cause the localized necking failure in all cases.

Photo. 5 Localized necking of the specimen

Table 3 Conditions of specimens

sample	silica sand #5
diameter	5.0cm
height	10.0cm
relative density	60%,70%(case2)

Table 4 Conditions of experiments

case	injection material	Concetration of injection material	Injection pressure
case1	-	-	20kPa
case2			
case3	microparticle②	6%	
case4		12%	
case5	microparticle①		
case6	microparticle① + Micro Bubble		

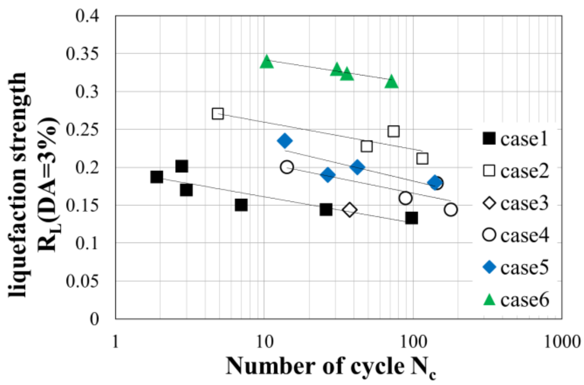

Fig. 9 Liquefaction strength curves

Results of Experiment

Fig. 9 shows the liquefaction strength curves of both improved and unimproved sand specimens.

The relative density of each improved specimen was calculated by a difference between specimen weights before and after the injection experiment which was carried out in another process. The relative density of Case 3 was 63% and those of Case 4 and 5 increased to 69%. As for Case 3, however, the liquefaction strength was almost the same as those of unimproved sands. Although the liquefaction strength of Case 4 and 5 increased, it was lower than that of unimproved sand whose relative density was 70%. It was expected that the soil skeleton was not strengthened by the injected particles because the injected particles didn't adhere to the contact portion of the soil skeleton. From this experiment, it was confirmed that a portion of the injected particles strengthened soil skeleton. Furthermore, the effect of suppressing liquefaction increased more by injecting Bubble White than injecting only fine particles.

CONCLUSION

Solid Silica was found to be crushed efficiently by moderate heat curing.

The permeability of micro-particles was affected by not only penetration speed and injection volume but also the particle size of sand injected. Especially when the particle size of the sand was small, permeability was greatly affected by permeation distance.

Liquefaction strength was found to increase by the injection of micro-particles and Bubble White. However, the liquefaction strength of improved sand, whose relative density increased by injection, became lower than that of unimproved sand with same relative density. Therefore, it was cleared that even relative density of specimen increased by injecting particles, not all the injected particles increased liquefaction strength. Moreover, since liquefaction strength increased more by injecting Bubble White than injecting only micro-particle, it was figured out that Bubble White was effective to suppress liquefaction.

REFERENCE

[1]Katori City website, http://www.city.katori.lg.jp 2016/01/07

[2]Koichi N, Naoaki S, Tosiyuki K, Saeka Y,‘‘Applicability of soil improvement with using Micro-Bubbles mixing water against soil liquefaction’’ J.JSCE Ser.C 2015 Vol.71 No.4 pp.395-406. (in Japanese)

[3]Shota M, Kentaro U, Naoaki S, Takamitu S, Koichi N, ‘‘Ultrafine particles of silica grouting method for liquefaction countermeasure ’’The Japanese Geotechnical Society, 2015, p.307. (in Japanese)

Sixth International Conferenc e on Geotechnique, Construction Materials and Environment, Bangkok, Thailand, Nov. 14-16, 2016, ISBN: 978-4-9905958-4-5 C3051

SOIL BEARING CAPACITY REFERENCE FOR METRO MANILA, PHILIPPINES

Jonathan R. Dungca[1], Ismael Concepcion Jr.[1], Moises Christian Mickail Limyuen[1], Terence Oliver See[1] and Marion Ryan Vicencio[1]

[1]Gokongwei College of Engineering, De La Salle University, Philippines

ABSTRACT

This study focuses on the analysis of the soil bearing capacities of the various cities and municipalities of Metro Manila, Philippines. The allowable soil bearing capacities to be used for foundation design were calculated through various theories and studies using geotechnical parameters, such as relative density and angle of internal friction. Standard Penetration Test (SPT) results were used to estimate these geotechnical parameters in order to obtain a good approximation of the soil‘s bearing capacity.

Because of economic constraints, not all low-rise construction projects choose to perform soil exploration. Due to this, soil data are usually lacking and may cause problems when designing shallow foundations of these kinds of structures. In line with this kind of situation, the study can help engineers in designing shallow foundations by providing them a reference of the allowable bearing capacity of any area within Metro Manila. This will be able to give them a good idea of the soil‘s strength in supporting shallow foundations.

The allowable bearing capacity of the soil shown in the reference is obtained from collected borehole data within Metro Manila and by using several geotechnical engineering theories. Contour maps of the bearing capacities are then made in order to provide an overview of the soil‘s bearing capacity for shallow foundations. A Geographic Information System (GIS) software database was also made so as to store all the borehole location‘s data as well as serving another basis for estimation. This can be updated whenever new data is available.

Keywords: Soil Bearing Capacity, Foundation Design, Standard Penetration Test, Geotechnical Properties of Metro Manila

INTRODUCTION

Foundation design requires engineers to understand how the soil interacts with the foundations. But, foundations are situated underground, wherein engineers cannot explicitly describe the interactions of the soil underground without conducting some tests. As soil exploration is a very costly test to conduct, engineers cannot always perform these tests; therefore, they rely on previous explorations done by their peers that are close to the project site to approximate the value for the bearing capacity for the aforementioned.

Since soil exploration is too costly and mere guessing will not suffice when making foundations, the author decided to come up with a way to fill in the dire needs of engineers. Using the borehole logs available within the Metro Manila, Philippines, the study analyzed the SPT borehole logs, calculated the required soil parameters and compiled everything into a reference that shows the bearing capacities of the covered areas.

The study aims to create a reference that will provide structural engineers the estimated allowable soil bearing capacities at any point in Metro Manila Philippines through the use of contour maps.

METHODOLOGY

With Metro Manila having an approximate size of 624.33 square kilometers, a density of one borehole log per square kilometer was used to describe the geotechnical characteristics and possible foundation design parameters of the said area. Borehole logs were collected for a total of 486 locations all over Metro Manila.

The amount of borehole logs alone is not the only criterion in gathering data for the study. It is just as important as, that the locations of the borehole logs be properly distributed. To check their distribution, each of the locations of the borehole logs was plotted in a map of Metro Manila. After this, the distribution was visually inspected and the areas that needed more data were determined. Aside from these, borehole logs that seemed erroneous were removed and disregarded.

In properly designing shallow foundations, the geotechnical characteristics and allowable bearing capacity of the soil must be known. This is because the design would largely depend on the strength and the behavior of the soil. The bearing capacities are computed using the SPT N values found in the borehole logs which were corrected using the procedures discussed in [1]-[4], also shown in Equation 1.

$$N_{60} = \frac{E_m C_B C_S C_R C_N N}{0.6} \qquad \text{(Eq. 1)}$$

Where: N_{60} is the corrected SPT-N value (blows/ft), E_m is the hammer efficiency, C_B is the borehole diameter correction, C_S is the sampler correction, C_R is the rod length correction, C_N is the overburden pressure correction and N is the SPT-N recorded in the field.

The corrected SPT, N_{60}, values were then used to compute for various geotechnical parameters such as relative density, undrained shear strength and angle of internal friction using different correlation factors [5]-[9]. As such, the group computed the ultimate bearing capacity. The Terzaghi‘s and Vesic‘s bearing capacity formulas, shown on Equations 2 and 3 respectively, were used to achieve this [10]-[12].

$$q_{ult} = 1.2cN_c + \gamma DfN_q + 0.4\gamma BN_\gamma \quad \text{(Eq. 2)}$$

Where: q_{ult} is the ultimate bearing capacity, γ is the effective unit weight, B is the width of foundation, Df is the depth of foundation below ground surface, N_c, N_γ and N_q are the Terzaghi's factors.

$$q_{ult} = c'^{N_c s_c d_c i_c b_c g_c} + \sigma'_{zD} N_q s_q d_q i_q b_q g_q + 0.5\gamma' N_\gamma s_\gamma d_\gamma i_\gamma b_\gamma g_\gamma \qquad \text{(Eq. 3)}$$

Where: s_c, s_q, s_γ are shape factors; d_c, d_q, d_γ are depth factors; i_c, i_q, i_γ are load inclination factors; b_c, b_q, b_γ are base inclination factors; and g_c, g_q, g_γ are ground inclination factors.

A factor of safety of 3.0 was divided to ultimate bearing capacity to determine the allowable soil bearing capacity of the soil. The allowable soil bearing capacities at different locations were then plotted on to the maps at 1-meter, 2-meters, 3-meters , 4-meters and 5-meter depths. Contour maps were created to visually classify and analyze the allowable bearing capacities at different locations in Metro Manila. With the ever growing technology in data processing, it has become more convenient to show the reference through the use of a Geographic Information System (GIS) program. The map of Metro Manila was first loaded into the GIS program. After this, the locations and all the relevant, data such as the bearing capacities, were placed inside a .csv file.

ANALYSIS AND DISCUSSION

Metro Manila or the National Capital Region of the Philippines is composed of 16 cities and 1 municipality. It is bounded by the province of Bulacan in the North, Manila Bay at the West, Rizal Province and Laguna Bay in the East, and Cavite Province in the South. It has a total land area of 597.47 km^2.

Soil Characteristic

Manila used to be a submerged area at one time in the geologic past. Intermittent volcanic activities followed and after which, volcanic materials were deposited. During the intervening period of inactivity, transported sediments were deposited on top of previously-laid volcanic materials. Thus, alternating beds and transported sediments became a characteristic feature of the geologic deposit. [13]-[14]

Available geologic information about Metro Manila and the areas surrounding it indicated that Quaternary volcanic rocks generally known as the Guadalupe Formation, locally known as "adobe", is the predominant rock unit underlying it. It consists of the Lower Alat Conglomerate Member and the Upper Diliman Tuff Member. The Diliman Tuff includes the tuff sequence in the Angat-Novaliches region and along Pasig River in the vicinity of Guadalupe, Makati and extending to some areas of Manila and most of Quezon City. Its upper surface ascends gently from Manila Bay outward Caloocan, Makati, Mandaluyong and Quezon City in which rock exposures can be found. The entire sequence is almost flat lying, thin to thickly bedded and consist of medium to coarse grained vitric tuffs and welded volcanic breccias with subordinate amounts of tuffaceous medium to coarse-grained sandstone, silty and clayey tuffs and tuffaceous conglomerates. These types of tuff are distinguished from their textual characteristics. Silty and clayey tuffs are very fine-grained while conglomerates contain coarse particles. In some areas, this rock formation is overlain by minimal alluvial deposits which tend to thicken towards Manila Bay. The high elevation areas are generally composed of dense sands and tuffaceous clay, while the low-lying areas are generally composed of loose sands and soft clays [13]- [14].

Topography and Elevation

Figure 1 shows that majority of the Metro Manila area rest on high elevations. The low lying areas are the coastal areas.

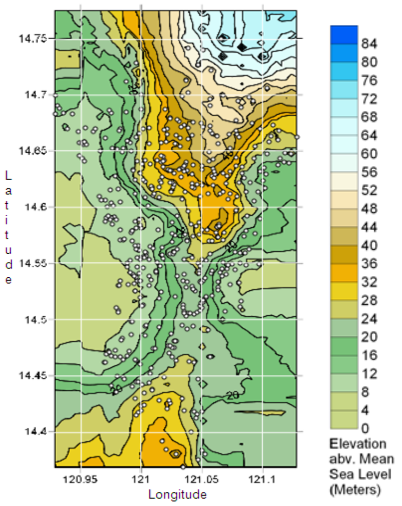

Fig. 1 Surface Elevation Contour

Borehole Locations

Figure 2 shows the location of the data points that were obtained in the area while Table 1 shows the number of borehole location in each area of the study and density of data per one square kilometer.

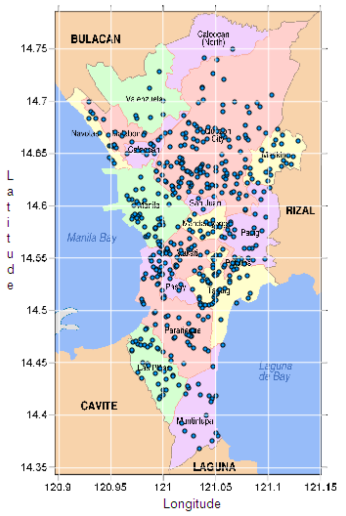

Fig. 2 Map of the Data Points in Metro Manila

Table 1 Number of Borehole Locations and its Density

City or Municipality	Area (km^2)	Borehole Locations (BH)	Density, BH/Area
Manila	38.55	39	1.00
Mandaluyong	11.25	14	1.00
Marikina	21.50	26	1.00
Pasig	31.00	24	0.77
Quezon City	134.26	130	0.97
San Juan	5.94	3	0.51
Caloocan	53.33	15	0.28
Malabon	15.71	12	0.76
Navotas	10.69	11	1.00
Valenzuela	44.59	9	0.20
Las Pinas	41.54	38	0.91
Makati	27.36	28	1.00
Muntinlupa	46.70	17	0.36
Paranaque	46.57	40	0.86
Pasay	18.50	24	1.00
Pateros	2.10	8	1.00
Taguig	47.88	48	1.00
TOTAL	**597.47**	**486**	**81.34%**

SOIL BEARING CAPACITY

Figure 3 shows the bearing capacity of the region at 1-meter depth. It can be seen that many areas where elevation is high have larger bearing capacities compared to the lower elevated areas. It is observed that the fault line is directly below the part where the bearing capacity is high. SPT N values of the outer 1-meter depth have a usual value in the range of 2 to 10 for both sands and clays. A reason why the outer areas have low bearing capacity is due to sediment deposits that are left by the rivers and creeks over time.

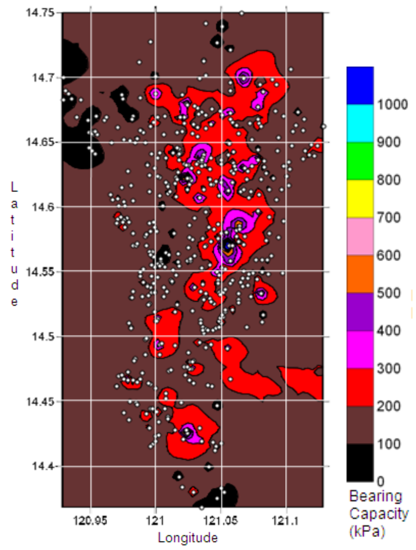

Fig. 3 Bearing capacity at a Depth of 1 meter in Metro Manila

The allowable bearing capacities of a depth of 2 meters below the ground surface are shown in

Figure 4. It can be seen in the central part of the region that refusal (SPT N-values greater than 50) has been achieved. Bearing capacities of the outer portions has also increased but not as much compared to the center of the map. The blue areas represent the places where the soil has hardened to a point that SPT is not advisable anymore. These blue areas are very near, if not above, the fault line and thus have a large bearing capacity.

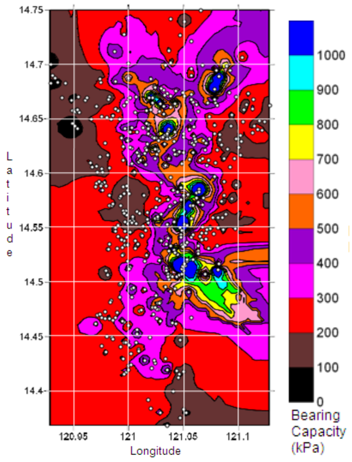

Fig. 4 Bearing capacity at a Depth of 2 meters in Metro Manila

Figure 5 shows the bearing capacities of a depth of 3 meters below the ground surface. More areas have now achieved refusal. SPT N values of the areas around the blue areas have increased but the outer areas of Metro Manila still have a small bearing capacity as compared to the center.

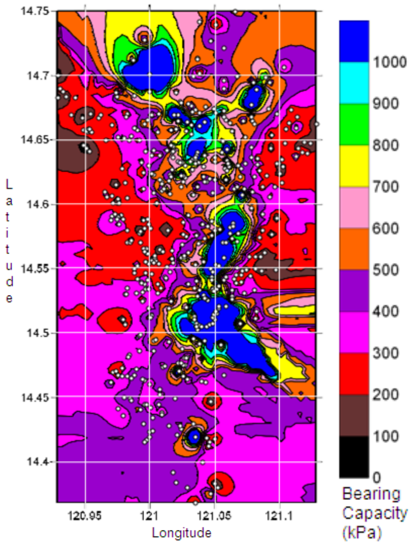

Fig. 5 Bearing capacity at a Depth of 3 meters in Metro Manila

Figure 6 shows the bearing capacity at a depth of 4 meters below the ground surface. Almost all areas have a bearing capacity of 300 kPa or greater except in the northwestern and eastern portion.

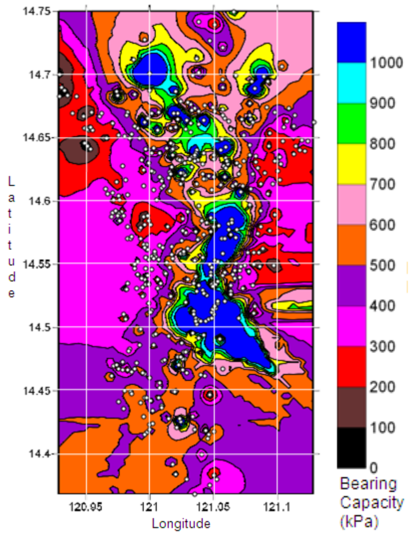

Fig. 6 Bearing capacity at a Depth of 4 meters in Metro Manila

Figure 7 shows the bearing capacity at a depth of 5 meters below the ground surface. Almost all areas have reached an allowable bearing capacity of 300 kPa and above, as expected, due to consolidation of soil over time.

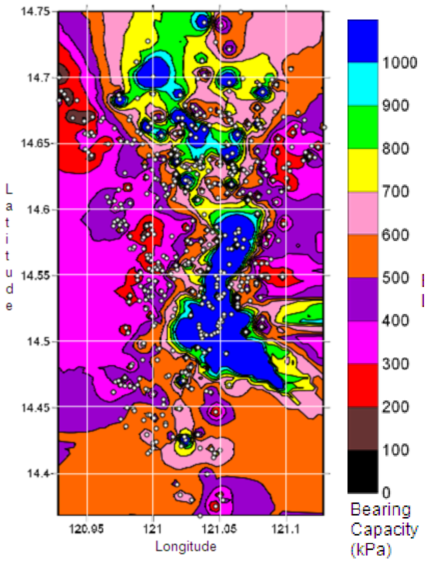

Fig. 7 Bearing capacity at a Depth of 5 meters in Metro Manila

Figure 8 shows the geological map of Metro Manila [13]. Looking at this map, deposits are seen in the western and eastern side of the region, while the tuff formation is seen in the central region.

With this information, the region can be further divided into 3 parts: the west coast, the east coast and the central area as shown in Figure 9. The west coast is composed of cities that are near the Manila Bay, which are Navotas, Malabon, South Caloocan, Manila, Pasay, Paranaque and Las Pinas. The east coast is composed of cities that are near the Laguna Bay, which are Marikina, Pasig, Pateros, Taguig and

Muntinlupa. The remaining cities of North Caloocan, Valenzuela, Quezon City, San Juan, Mandaluyong, and Makati are the cities that comprise the central area.

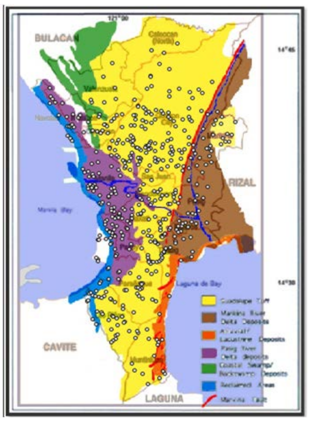

Fig. 8 Geologic Map of Metro Manila [13]

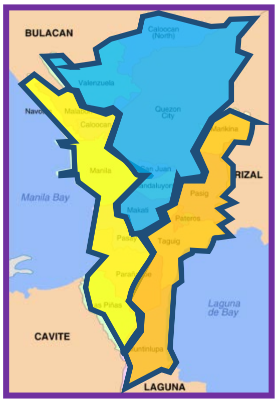

Fig. 9 Division of Cities

Looking at the west coast, as shown in Figure 10, the surface geology of this area is mostly composed of quarterly alluvial soil. SPT N- values on these areas are also very low (2-10) at the surface and average (20-30) as the soil goes deeper. The east coast is generally the same compared to the west coast, having quarterly alluvium soil in the surface as well as having the same SPT value patterns. SPT refusal was not achieved below a depth of 5 meters. Due to the fact that the surface geology of the soil of the aforementioned areas is generally loose, the resulting bearing capacities also reflected the composition of the soil. Allowable bearing capacities of the area at shallow depths of 1 to 2 meters have values ranging from 0 to 200 kPa.

The central area of Metro Manila has a different surface geology compared to its neighboring sides. Tuff was primarily observed in this area, and rock formations are common below the surface. SPT blows depend on the amount of deposits that are present and increase as the soil goes deeper. SPT refusal was achieved at shallow depths of 2 to 3 meters in the outer regions and as shallow as the ground surface in the inner regions.

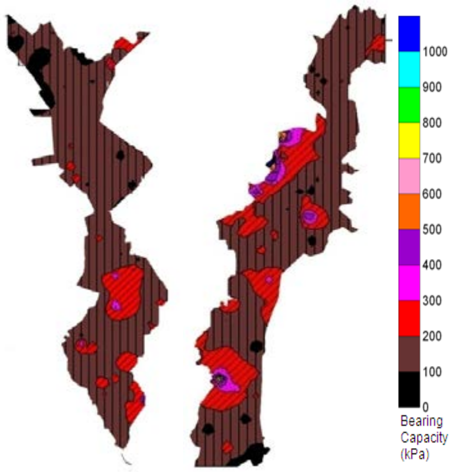

Fig. 10 Bearing Capacity Contour Map of West and East Coast of Metro Manila (depth of 1m)

Since the surface geology of this area is reported as tuff, it can be generalized that the land is mostly made up of rocks. Comparing rocks to soil, rocks are generally stronger than soil. In accordance to this, the bearing capacities of the rocks should have high values compared to soils which is clearly noticeable in Figure 11. Calculations have shown that the bearing capacities of the area have a range of 200 to 300 kPa.

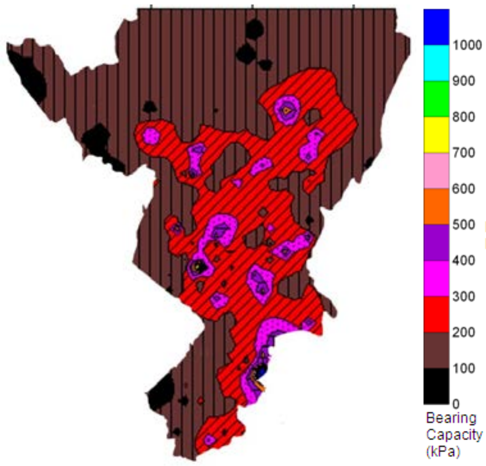

Fig. 11 Bearing Capacity Contour Map of Central Area of Metro Manila at a depth of 1 meter

CONCLUSION

Borehole logs were collected for a total of 486 locations all over Metro Manila, Philippines. Maps were also created in order to show the locations of the collected boreholes throughout Metro Manila.

Using an excel program, different geotechnical properties of the collected boreholes were computed. Some examples of this are the unit weight and the angle of internal friction. Also using the same excel program, bearing capacity of the 16 cities and 1 municipality were estimated and evaluated per meter depth until a depth of 5 meters. Contour maps of the allowable bearing capacities at each of the depths were also made and analyzed. Based on the results of the study, it was found out that several locations in Metro Manila were composed of soil with allowable bearing capacities suitable for shallow foundations.

Cities which are near the bodies of water, such as Manila, Navotas, and Marikina, have low bearing capacities. Thus, the use of shallow foundations on these areas is recommended only for structures that have lower design loads, such as residential houses. As the soil is not capable of carrying heavy loads, using shallow foundations for high rise buildings and other large structures should be avoided or a deep foundation is recommended. According to research [13], the western part of Metro Manila was once underwater. Due to this, some of the soils in the area contained seashells. Also, the surface geology of the western and eastern area is composed mostly of quarterly alluvium, a loose type of soil that is in its early ages. Also, it should be noted that the river system determines the direction of the sediments being washed out from its origins. Marikina River flows from north to south. Pasig River then carries the river water from Marikina River, splitting it into two: one in the west direction with the Manila Bay as its last stop, while the other in the east direction with the Laguna Bay as its endpoint. Because of this, sediments from high elevation areas were deposited by rivers and creeks into low lying areas along their paths. This happens because water slowly scours the soil and carries it to the areas where the slope is mild. Gravity then takes effect and sediments are left behind, resulting in a composition that is generally loose and soft for sands and clays.

Cities with rock formations beneath the surface, such as Quezon City, North Caloocan, and Muntinlupa, have soils with high bearing capacities at shallow depths. It is recommended to place the foundations on these refusal levels since it is more than capable of carrying loads that are suited for shallow foundations. Nevertheless, caution must be taken when placing structures in these areas, as the Valley Fault System is nearby, making the area prone to earthquakes.

REFERENCES

[1] Dungca J R and Chua RAD, "Development of a Probabilistic Liquefaction Potential Map for Metro Manila", Int. Journal of GEOMATE, April 2016, Vol. 10, No. 2, pp. 1804-1809 teJohn Wiley, 1943. Terzaghi K, "Theoretical Soil Mechanics", John Wiley, 1943.

[2] Clayton CRI " SPT Energy Transmission:Theory, Measurement, and Significance", Ground Engineering, Vol. 23, No. 10, 1990, pp 35-43.

[3] Skempton AW " Standard penetration Test Procedures and the Effects in Sands of Overburden Pressure, Relative Density, Particile Size, Aging and Over Consolidation" Geotechnique, Vol 36, No. 3 1986, pp. 425-447.

[4] Tokimatsu k and Seed HB "Simplified Procedures for the Evaluation of the Settlements in Clean Sand. Report No. UCB/EERC-84/16. University of California , Berkely, CA, 1984.

[5] Das B. "Fundamentals of Geotechnical Engineering, 3rd Ed., Toronto, Canada, Thomson Learning, 2008

[6] Coduto DP " Foundation Design Principles and Practices, 2nd Ed., New Jersey, USA, Rentice Hall, 2001.

[7] Sowers G. and Sowers G. "Introductory soil Mechanics and Foundation, New York, USA Macmillan, 1961.

[8] Gibbs HJ and Holtz WG "Research on Determining the Density of Sands by Spoon Penetration Testing, In the Proceedings of the 4th International Conference on Soil Mechanics, Vol. 1, London, 1957, pp. 35-39.

[9] Kulhawy FH and Mayne PW "Manual on Estimating Soil Parameters for Foundation Design. Report No. EL-6800, Electric Power Research Institute, Palo, Alto, CA, 1990.

[10] Terzaghi K, "Theoretical Soil Mechanics", John Wiley, 1943. Terzaghi K, "Theoretical Soil Mechanics", John Wiley, 1943.

[11] Vesic' AS "Analysis of Ultimate Loads of Shallow Foundations," ASCE Journal of the Soil Mechanics and Foundation Division, 1973, Vol. 99, No. SM1, pp. 45-73.

[12] Vesic' AS "Bearing Capacity of Shallow Foundations," Foundation Engineering Handbook. 1st ed., p 121-147, Winterkorn, Hans F. and Fang, Hsai-Yang, eds., Van Nostrand Reinhold, New York., 1975.

[13] Oca G. "The Geology of Greater Manila and Its Bearing to the Catasthropic Earthquake of August 2, 1968" the Philippine Geologist, Vol 22 No. 4, pp. 171-192.

[14] Tan R. "Engineering Properties of Manila Subsoil" Quezon City Philippines: University of the Philippines Press, 1985.

[15] Bureau of Mines and Geo-Science," Geology and mineral resources of the Philippines", 1981.

Sixth International Conference on Geotechnique, Construction Materials and Environment, Bangkok, Thailand, Nov. 14-16, 2016, ISBN: 978-4-9905958-6-9 C3051

VALIDATION OF METHOD FOR ESTIMATING LONG-TIME STRENGTH OF CHEMICAL GROUT COMPOSITION WITH HEAT CURING

Shunsuke Takiura[1], *Naoaki Suemasa*[1] *and Takamitsu Sasaki*[2]
[1]Urban and Civil Engineering, Tokyo City University, Tokyo, Japan
[2]Research and Development, Kyokado Engineering Co., Ltd, Tokyo, Japan

ABSTRACT

The Great East Japan Earthquake on March 11, 2011 caused terrible liquefaction damage especially in reclaimed lands and soft grounds. Under the circumstances, there has been a growing demand for a liquefaction countermeasure in Japan. In this study, a chemical grouting method was focused on as a liquefaction countermeasure method because it is excellent in performance compared to other methods. Although the chemical grouting method used to be only a temporary and supplementary construction method, it has become one of the most effective liquefaction countermeasures in recent years since the performance of the chemical solution has been improved and is capable to make long-term performance in the ground. However, the mechanism of the chemical solution has not been clarified yet, because it would require quite a long time to verify the long-term durability of the improved ground. It is urgent and essential to find out an efficient method to verify it in a short period of time. In this study, the possibility to predict the change of long-term strength was examined by a short-term laboratory test where heat curing was provided the improved ground model in a thermostatic tank. Here, the acceleration mechanism by heat curing is based on the chemical reaction rate theory of Arrhenius. The predicted values calculated from the Arrhenius equation showed similar strength change to the measured values obtained from the test. As a result, it was confirmed that it was possible to calculate the future change of the durability with this method.

Keywords: Chemical grouting method, Long-term durability, Heat curing

INTRODUCTION

Chemical Grouting Method for Liquefaction Countermeasure

The Great East Japan Earthquake disaster happened on March 11, 2011 and the maximum acceleration of 2933 gal was recorded in Kurihara city in Miyagi prefecture. Liquefaction occurred in many regions from Tohoku to Kanto district and the total damage throughout Japan reached42 square kilometers. The liquefaction countermeasures using a chemical grouting method were performed in several places along the Pacific coast in 2008 after Niigata Chuetsu-oki earthquake in July 2007. It was revealed through the damage survey of the 2011 Earthquake that the chemical grouting method was quite effective as a liquefaction countermeasure [1].

Improvement Principle and Characteristic

The improvement principle of the chemical grouting method is to replace pore water in sand skeletons with a gelatinous silica compound in order to prevent both contraction of the sand skeletons and a rise in excess pore water pressure caused by the seismic vibration. In addition, the silica compound gives cohesion between sand particles and accordingly increases the cyclic shear resistance of the sand against earthquake vibration [2]. The advantages of the method are less vibration and less noise than other methods during the construction. In addition, this method provides small equipment for space saving, which can drill a hole not only in a vertical but also in an oblique and a curved lines.

Durability of chemical improved body

A human-initiated accident took place in 1974 where the groundwater was contaminated at the ground improvement work injecting the materials of Acrylic Alumite origin. The former Ministry of Construction prohibited the use of the macromolecule-based infusion materials promptly after the accident and only water glass-based grout materials have been used since then. However, it is well known that the durability of water glass-based grout infusion materials is not strong enough to support the ground for a long time that they are generally used only for temporary constructions [3].

Recently, the effect of water glass-based grout infusion materials has been improved through some new technology, and consequently a new type of durable grout material has been developed. However, there are still problems for this new material. One of these is that most of previous studies on the chemical grouting have focused on the development or the choice of durable infusion materials. Furthermore, sufficient proof experiments for the material have not been carried out because it has been only ten and several years since the permanent grout material was developed. It is, therefore, essential to establish a practical way to estimate the strength change of the improved soil with elapsed time [3].

Purposes of this study

Athough a chemical grouting method of construction has been proved to be effective for liquefaction countermeasures, the long-term strength of the improved soil has been unexplained. Therefore, the method in which the long-term strength is able to be verified in a short term is suggested in this study. In the study, a heat and cure process have been provided for the chemical improved specimens in a thermostatic tank in order to promote the chemical reaction. The strength change of the specimens applied the process of heating and curing for 1000 days is reported in this paper.

EXPERIMENTAL PROCEDURE

Physical characteristics of sample

Toyoura sand was used for this experiment. Table 1 shows the maximum and the minimum densities of Toyoura sand and Fig. 1 shows the result of grain size analysis.

Characteristics of grout material

The grout material used for the experiments were active colloidal silica with 29% of concentration in weight and silica sol with 6%. The active colloidal silica is based on the active silica, which is obtained by removing alkali from water glass by an ion exchange technique in order to exclude its deterioration factor. Therefore, the active colloidal silica is considered to become a sort of permanent grouting materials that could keep its effectiveness without eluviation of silica for a long time. While, the silica sol is based on the non-alkaline water glass solution which is obtained by neutralizing alkali of the water glass with acid [4]. As shown in the Fig 2, the active colloidal silica has hardly changed in volume for a long time. On the other hand, the silica sol has remarkably changed (decreased) in volume immediately after it was solidified. And also, the unconfined compression strength of the improved soil tended to gradually decrease. It seemed to be because the cohesion of the gel decreased or disappeared by the decrease in volume.

Table 1. Physical properties of Toyoura sand

Density test of soil particle (g/cm^3)	Maximum void ratio e_{max}	Minimum void ratio e_{min}
2.634	0.986	0.621

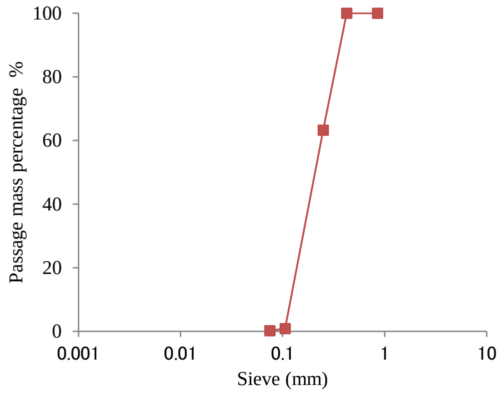

Fig.1 Grain size accumulation curve of Toyoura sand

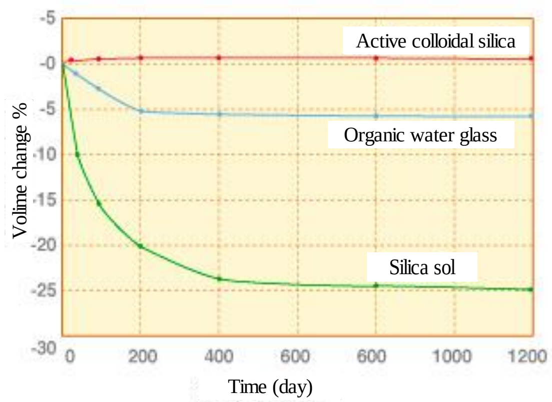

Fig.2 Volume change of plain gel (Geo-grouting development Organization: HP)

Methods of making a specimen and curing

Two kinds of specimens, sand gel and plain gel, were prepared as follows. For the sand gel, Toyoura sand was air-pluviated in a mold of 5 cm in inside diameter so as to be the sand specimen with 60% of the relative density. The sample was set 10cm in height by putting a weight on top of the sample and taping a side of the mold with a wooden hammer. Then the chemical grout was injected into a specimen deaerated in a vacuum pump. After confirming that the specimen was fully solidified after 24 hours, the specimen was removed from the mold. Photo. 1 and Photo. 2 describes the situation of injecting the chemical grout solution. For the plain gel, 200 ml of chemical grout was poured into a glass container with 5cm in inside diameter and the specimen molded by the solidification of the grout was removed from the container.

A process of curing was carried out under the conditions of three different temperatures of 25, 45 and 50 degrees Celsius. All of the specimens wrapped in a wrap film were covered with wet papers and put in an airtight container to prevent from being dried. As for the curing at 25 degrees Celsius of temperature, the specimen was cured in the room where the temperature was constantly controlled at 25 degrees Celsius with an air-conditioner. For the heat curing, the specimens in the containers were set in the constant temperature tanks whose temperatures were continuously adjusted at 45 and 55 degrees, respectively. An experiment case is shown in Table 2.

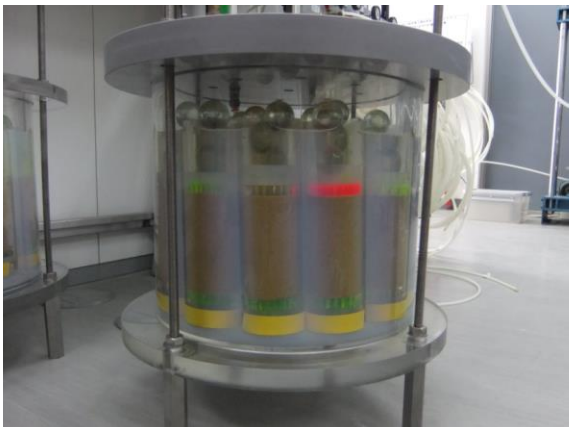

Photo.1 Infusion situation

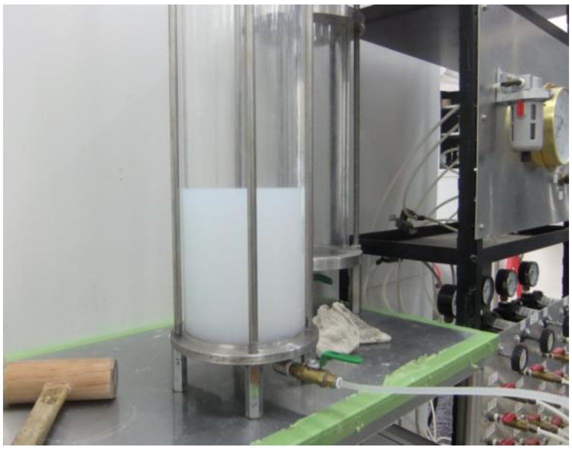

Photo.2 Infusion situation

Table 2. Experiment case

Grouting	Test piece	Curing temperature	site
Active colloidal silica	sand gel	25℃	A
		45℃	B
	plain gel	25℃	C
		45℃	D
Silica sol	sand gel	25℃	E
		45℃	F
		55℃	G
	plain gel	25℃	H
		45℃	I
		55℃	J

RESULTS AND DISCUSSION

Unconfined compression test result

Fig. 3 shows the change of unconfined compression strength for the sand gel specimen of the active colloidal silica with time and temperature. The specimen of heating curing showed higher unconfined compression strength than that of ordinary temperature curing. Fig. 4 shows the change of unconfined compression strength for the plain gel specimen of the active colloidal silica. In the same way as the sand gel, the specimen of heating curing showed higher unconfined compression strength than that of ordinary temperature curing. From the result mentioned above, a reaction acceleration effect by the heating curing was confirmed.

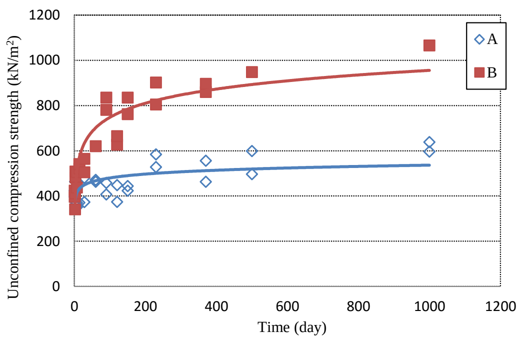

Fig.3 Unconfined compression strength of active colloidal silica sand gel

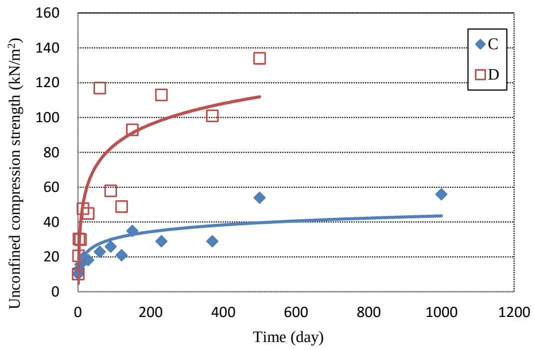

Fig.4 Unconfined compression strength of active colloidal silica plain gel

Fig. 5 shows the change of unconfined compression strength for the sand gel of the silica sol. The specimen of heating curing showed lower unconfined compression strength than that of ordinary temperature curing. In addition, the sand gel specimen of the silica sol had gradually decreased in strength. Similar results were obtained in all cases for the silica sol. Fig. 6 shows the change of unconfined compression strength for the plain gel specimen of the silica sol. In the same way as the sand gel, the specimen of heating curing showed lower unconfined compression strength than that of ordinary temperature curing. The specimen of ordinary temperature curing had gradually increased in strength. On the other hand, as for the specimen of heating curing, the strength had gradually decreased after having increased at an initial stage.

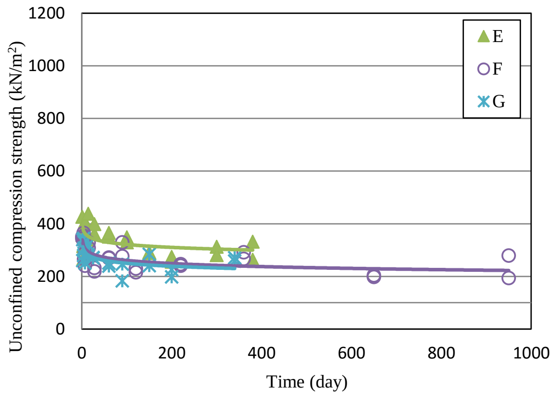

Fig.5 Unconfined compression strength of silica sol sand gel

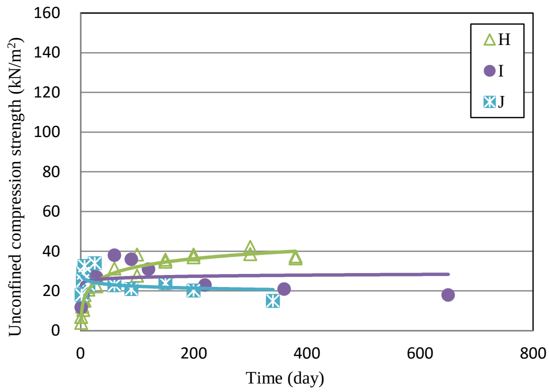

Fig.6 Unconfined compression strength of silica sol plain gel

Volume change of plain gel

Fig. 7 and 8 show the changes in the rate of volume change of specimen for the plain gel of the active colloidal silica and silica sol over the time, respectively. As for the active colloidal silica, the rate of volume change was constantly near -2.5% in both cases of ordinary temperature curing and heating curing. While, as for the silica sol, the rate of volume change in the case of heating curing grew larger than that in the case of ordinary temperature curing. In addition, when comparing the specimens of heating curing, the amount of volume change was larger at a higher temperature. As shown in Fig. 2, the silica sol tends to change in volume easily. Therefore, it appeared that heating curing promoted the volume change more effectively than ordinary temperature curing.

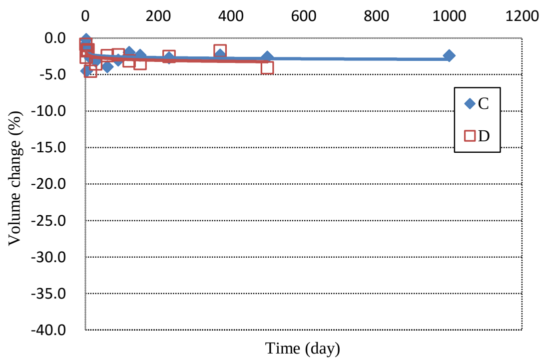

Fig.7 Volume change in active colloidal silica plain gel

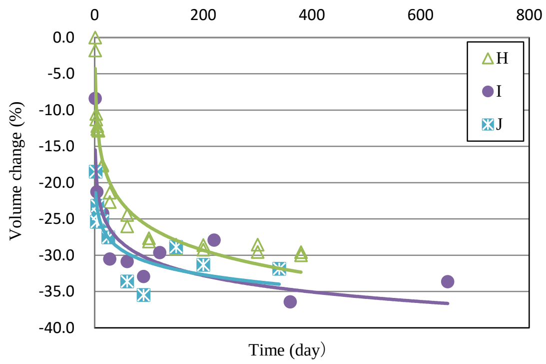

Fig.8 Volume change in silica sol plain gel

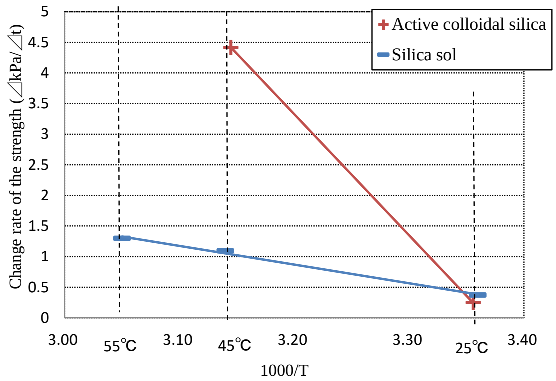

Fig.9 Arrhenius plot of sand gel

Long age strength estimation

In order to estimate the long age strength, the strength increment (Δqu) from the initial strength (qu_0) for the sand gel specimen of active colloidal silica and silica sol was calculated using the latest test data. The strength incremental rate (Δqu/Δt) obtained by dividing the strength increment (Δqu) by the elapsed days (Δt) was shown in a vertical axis. The curing temperature was shown in a horizontal axis as a reciprocal number of the absolute temperature (T). As a result, the inclination of Arrhenius plot was obtained as shown in Fig. 9. The acceleration coefficient calculated from this Arrhenius plot was multiplied by the sand gel age of heating curing. Then the standard curing strength was able to be predicted from the heating curing.

The change of predictive strength for the active colloidal silica sand gel is shown in Fig. 10, which was calculated using the acceleration coefficient obtained from Arrhenius plot in Fig. 9. A measured value was defined as the compression strength of the ordinary temperature curing specimen. While a predictive value was defined as the compression strength which was derived from both the acceleration coefficient calculated from Arrhenius plot and the material age of the heating curing specimen. The measured values and predictive values showed similar strength change in the specimens whose material age was between 14 and 1, 000 days. In addition, increase of compression strength was able to be observed in both the measured value and the predictive value of the specimens whose material age was more than 60 days.

The predictive strength of the silica sol sand gel was shown in Fig. 11, which was obtained using the acceleration coefficient from Arrhenius plot in Fig. 9. The results of measured values and predicted values showed similar strength change, too.

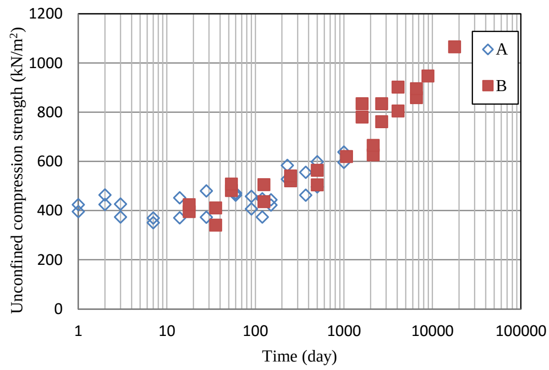

Fig.10 Predictive strength of active colloidal silica sand gel

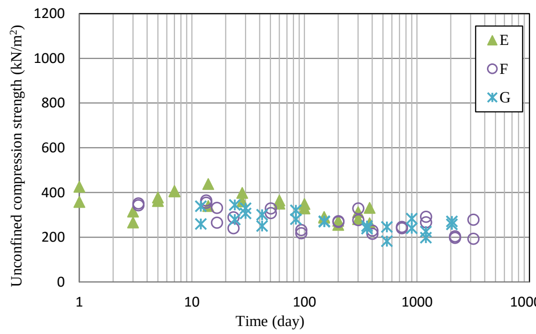

Fig.11 Predictive strength of silica sol sand gel

From the results mentioned above, it was confirmed that the predictive strength was able to be derived from the heating curing. Table 3 shows the results of the promotion testing in each case. From the result, the strength of up to approximately 50 years later at the longest was able to be predicted by measuring the strength of the specimen whose age was 1, 000 days. That is, it was cleared that there was a possibility of long-term strength prediction in a short term.

Table 3. Forecast result

	Test piece	Curing temperature	Acceleration factor	Predictive time (year)
Active colloidal silica	sand gel	45℃	17.84	48.9
	plain gel		6.30	17.3
Silica sol	sand gel	45℃	3.35	9.2
		55℃	6.01	16.5
	plain gel	45℃	3.25	8.9
		55℃	4.32	11.8

CONCLUSION

The efficiency of the promotion test with heating curing was confirmed in all cases through the experiments.

(1) It was proved that the active colloidal silica was a permanent grout material without loss of strength with time elapse.

(2) The predictive value derived from Arrhenius plot showed similar strength change to the measured value.

(3) The prediction method for long-term strength of improved soil by chemical injection in a short term was accomplished through the laboratory experiment with a constant temperature tank.

REFERENCES

[1] Sasaki, T., Oyama, T., Shimada, S., Suemasa,N (2012). “ Influence of Gelling Time On Permeability And Strength of Ground Improved By Chemical Grouting Method, ” The Twenty-second International Offshore and Polar Engineering Conference, 17-22 June, Rhodes, Greece

[2] Sasaki, T (2013). “Liquefaction measures of ground seen in the case, ” Kindaikagakusha, pp 158-159.

[3] Nakayama, T., Sawada, R., Hiraoka, Y., Akagi, H (2013). “ Evaluation of Long Term Stability of Chemically Stabilized Sand with Grouting. ” Japan Socuety of Civil Engineering Memoirs C (Ground Zone Engineering), Vol69, No.2, pp162-173.

[4] Geo-grouting development Organization HP: http://www.jckk.jp/kokyu.php

Sixth International Conference on Geotechnique, Construction Materials and Environment, Bangkok, Thailand, Nov. 14-16, 2016, ISBN: 978-4-9905958-6-9 C3051

VERIFICATION OF ELASTO-PLASTIC MODEL FOR CEMENT-TREATED SOIL BEHAVIOR UNDER TRIAXIAL TENSION CONDITION

Tsutomu Namikawa[1]
[1]Department of Civil Engineering, Shibaura Institute of Technology, Japan

ABSTRACT

This paper presents the numerical simulation of the triaxial tension behavior of cement-treated soils. An elasto-plastic model is adopted to simulate the triaxial tension behavior of the cement-treated soils. In the triaxial tension test results, tensile failure is observed under low confining pressures and shear failure is observed under high confining pressures. Thus two failure surfaces, tensile and shear failure surfaces, are assumed to express the two failure modes observed in the laboratory tests. The simulation results agree reasonably with the laboratory test results, indicating that the adopted elasto-plastic model can properly describe the tension and shear behaviors of cement-treated soil under effective confining pressures.

Keywords: Cement-treated Soil, Triaxial Tension Behavior, Elasto-plastic Model, Numerical Simulation

INTRODUCTION

Ground improvement by cement mixing has been widely used for structure foundation, retaining wall, liquefaction mitigation and so on. Recently column and wall shaped ground improvements are often adopted to reduce construction cost. When external forces apply to the cement mixing column, tensile stress possibly occurs in the column under a low confining stress condition. Thus the evaluation of tensile behavior of cement-treated soils is required to design the ground improvement rationally. However there is little study clarifying the tensile behavior of cement-treated soil under a confining pressure.

The author has conducted the drained triaxial tension tests of cement-treated soil to investigate the tension and shear failure behaviors under effective confining pressures [1][2]. This paper presents the numerical simulation of the triaxial tension test of cement-treated soils. The elasto-plastic model proposed by Namikawa and Mihira (2007) [1] is adopted to simulate the triaxial tension behavior of the cement-treated soils. In the triaxial tension test results, tensile failure is observed under low confining pressures and shear failure is observed under high confining pressures. Thus two failure surfaces, tensile and shear failure surfaces, are assumed to express the two failure modes observed in the laboratory tests. The simulation results agree reasonably with the laboratory test results, indicating that the elasto-plastic model can properly describe the tension and shear behaviors of cement-treated soil under effective confining pressures.

ELASTO-PLASTIC MODEL

A brief description of the elasto-plastic model proposed by Namikawa and Mihira (2007) [1] is given here.

General Formulation

It is assumed that a total strain increment $\dot{\varepsilon}_{ij}$ is a sum of the elastic component $\dot{\varepsilon}_{ij}^{e}$ and plastic component $\dot{\varepsilon}_{ij}^{p}$, that is,

$$\dot{\varepsilon}_{ij} = \dot{\varepsilon}_{ij}^{e} + \dot{\varepsilon}_{ij}^{p} \qquad (1)$$

The elastic strain increment is linearly related to an effective stress increment $\dot{\sigma}_{ij}$ as

$$\dot{\varepsilon}_{ij}^{e} = E_{ijkl}^{-1}\dot{\sigma}_{kl} \qquad (2)$$

where E_{ijkl} is the matrix of elastic constant. The stress-strain relationship of the elasto-plastic model can be described as

$$\dot{\sigma}_{ij} = E_{ijkl}\,\dot{\varepsilon}_{kl} - \frac{\dfrac{\partial f}{\partial \sigma_{mn}} E_{mnop}\dot{\varepsilon}_{op}}{H + \dfrac{\partial f}{\partial \sigma_{qr}} E_{qrst} \dfrac{\partial Q}{\partial \sigma_{st}}} E_{ijkl} \frac{\partial Q}{\partial \sigma_{kl}}$$

(3)

where f is the yield function, Q is the plastic potential function and H is the plastic modulus.

Form of Failure and Yield Surface

In this model, two different failure surfaces are defined to describe the tensile and shear failures. The failure function for the shear F_s is defined as

$$F_s(\sigma_{ij}) = \sqrt{J_2} - \Gamma(\theta)(c/\tan\phi + p)k_f = 0,$$
$$k_f = \frac{6\sin\phi}{\sqrt{3}(3-\sin\phi)}, \quad \Gamma(\theta) = \frac{2\xi}{(1+\xi)-(1-\xi)\sin 3\theta},$$
$$\xi = \frac{3-\sin\phi}{3+\sin\phi}, \quad -\frac{\pi}{6} \le \theta \le \frac{\pi}{6} \qquad (4)$$

where $\sqrt{J_2}$ is the invariant of deviator stress, ϕ is the friction angle, c is the cohesion coefficient, θ is the Lode angle and p is the mean effective stress. It is assumed that tensile failure occurs when a minor principal stress reaches the tensile strength T_f. Thus the tensile failure function F_t is described as

$$F_t(\sigma_{ij}) = \frac{2\sqrt{J_2}}{\sqrt{3}}\sin\left(\theta + \frac{2}{3}\pi\right) - p - T_f = 0 \qquad (5)$$

Based on the failure surfaces, two different yield surfaces, the shear yield surface f_s and the tensile yield surface f_t, are introduced to describe the tension and shear strain-hardening/softening behaviors. The shear and tensile yield surfaces are expressed in a form that is similar to the failure surfaces. Then the yield functions f_s and f_t are expressed as

$$f_s(\sigma_{ij}, k_y, \Omega) = \sqrt{J_2} - \Gamma(\theta)\left(\frac{c(1-\Omega)}{\tan\phi} + p\right)k_y = 0$$

(6)

$$f_t(\sigma_{ij}, \Omega) = \frac{2\sqrt{J_2}}{\sqrt{3}}\sin\left(\theta + \frac{2}{3}\pi\right) - p - T_f(1-\Omega) = 0$$

(7)

where k_y is the internal variable denoting degree of hardening and Ω is the internal variable denoting degree of softening. While k_y is used for the shear yield surface to describe the strain-hardening response, Ω is used in the strain-softening process. k_y and Ω are defined as

$\Omega = 0, \quad 0 \le k_y < k_f$ before $F_s = 0$ or $F_t = 0$

$0 < \Omega \le 1, \quad k_y = k_f$ after $F_s = 0$ or $F_t = 0$ (8)

The elastic region is assumed to be defined as

$$f_0(\sigma_{ij}) = \sqrt{J_2} - \frac{\Gamma(\theta)}{\Gamma(-\pi/6)}\frac{T_f}{\sqrt{3}} < 0 \qquad (9)$$

Hardening and Softening Rules

In the strain-hardening process, the stress lies on f_s defined by Eq. (6). Then the internal variable k_f is defined as the following hyperbolic function of the deviator plastic strain invariant :

$$\frac{k_y - k_0}{k_f - k_0} = \alpha\frac{\bar{\varepsilon}^p/e_y}{1+\bar{\varepsilon}^p/e_y}, \quad \bar{\varepsilon}^p = \sqrt{\frac{1}{2}\varepsilon_{ij}^{sp}\varepsilon_{ij}^{sp}},$$
$$k_0 = \frac{T_f}{\sqrt{3}\Gamma(-\pi/6)(c/\tan\phi + p)} \qquad (10)$$

where ε_{ij}^{sp} is the deviator plastic strain tensor. α and e_y are the material parameters. Here it is assumed that the plastic volumetric strain does not occur in the strain-hardening process. After the strain reaches the shear failure surface, the strain-softening behavior is controlled by the internal variable Ω defined as

$$\Omega = 1 - \exp\left\{-\frac{R_l\left(\bar{\varepsilon}^p - \bar{\varepsilon}^p_{peak}\right)}{e_r}\right\}, \quad R_l = \frac{l_c}{t_{s0}} \qquad (11)$$

where $\bar{\varepsilon}^p_{peak}$ is $\bar{\varepsilon}^p$ at peak stress state, e_r is the material parameter, t_{s0} is the thickness of shear band and l_c is the characteristics length related to the mesh size. In the strain-softening process, the plastic volumetric strain is assumed to occur due to dilatancy. The plastic volumetric increment $\dot{v}^p$ is defined as

$$\dot{v}^p = D_c\dot{\bar{\varepsilon}}^p \qquad (12)$$

where D_c is the dilatancy coefficient.

After the stress reaches the tensile failure surface, the strain-softening behavior is controlled by Ω. Here the strain-softening behavior is defined by the bilinear function. Thus, Ω is defined as

$$\Omega = -l_c\frac{T_f}{G_f}\left(\varepsilon_3^P - \varepsilon_{3peak}^p\right) if\ 0 \le \Omega \le 0.75 \qquad (13)$$

$$\Omega = \frac{12}{17} - \frac{1}{17}l_c\frac{T_f}{G_f}\left(\varepsilon_3^P - \varepsilon_{3peak}^p\right) if\ 0.75 \le \Omega \le 1$$

(14)

where G_f is the fracture energy, ε_3^p is the minor principal plastic strain and ε_{3peak}^p is the minor principal plastic strain at the tensile peak stress state.

TRIAXIAL TENSION TEST

Namikawa and Hiyama (2014) have conducted the drained triaxial tension and compression tests for a cement-treated soils [2]. A brief description of the experimental procedure and result is described here.

Test Procedure

The material used in this study is a mixture of Toyoura sand (D_{50} = 0.18 mm, Uc = 1.6), Portland cement, water and Kaolin clay. The mixing proportions are listed in Table 1. Two kinds of binders are prepared in the test. The specimen is made by vibration after mixing thoroughly all the materials that composed the cement-treated sand. The cylindrical mold is used for preparing the specimens. The curing time is 7 days. The unconfined compressive strengths q_u are around 1300 kPa and 500 kPa for Binder A and B. Before the shearing process, the specimen is consolidated isotropically to the prescribed effective confining pressures. Thereafter the axial load is applied under a drained condition. The experimental program is summarized in Table 2.

Test Results

Stress-strain relationship

The typical stress-strain relationships for Binder A are shown in Fig. 1 and Fig. 2. Fig. 1 shows the results of the triaxial tension tests. It can be seen that all the samples show an approximately linear stress-strain relationship during the initial loading process. For the sample tested at the value of p_c' = 100 kPa (AT-1), the deviator stress increased almost linearly with the strain until the failure occurs and the strain at the peak stress is around -0.015%. For the sample tested at the value of p_c' = 500kPa (AT-5), although the slight strain hardening is observed before the peak stress, the sample reaches the peak stress at small strain level. Fig. 2 shows the results of the triaxial compression tests. It can be seen that all the samples show a strain hardening behavior before the peak stress. The absolute values of strain at the peak stress are around 0.7% and 1.1% for AC-1 and AC-3. For Binder A, the absolute strain values at the peak stress in the triaxial compression tests are significant larger than those in triaxial tension tests.

The typical stress-strain relationships for Binder B are shown in Fig. 3 and Fig. 4. Fig. 3 shows the results of the triaxial tension tests. It can be seen that the sample shows a failure at small strain level at the value of p_c'= 30kPa (BT-1). This behavior is similar to that observed in the result of Binder A. Conversely, for the sample tested at higher values of p_c' (BT-6), the strain hardening is observed before the peak stress and the absolute value of strain at peak stress becomes

Table 1 Mixing properties of cement-treated soil

Binder	Sand	Cement	Clay	Water
A	69.3%	7.0%	5.0%	18.7%
B	71.2%	4.5%	5.6%	18.7%

Table 2 Summary of triaxial tests

Case	Binder	p_c': kPa	Loading
AT-1	A	100	Tension
AT-2	A	200	Tension
AT-3	A	300	Tension
AT-4	A	400	Tension
AT-5	A	500	Tension
AC-1	A	50	Compression
AC-2	A	50	Compression
AC-3	A	100	Compression
AC-4	A	100	Compression
AC-5	A	150	Compression
AC-6	A	200	Compression
BT-1	B	30	Tension
BT-2	B	100	Tension
BT-3	B	200	Tension
BT-4	B	300	Tension
BT-5	B	400	Tension
BT-6	B	500	Tension
BC-1	B	50	Compression
BC-2	B	100	Compression
BC-3	B	200	Compression

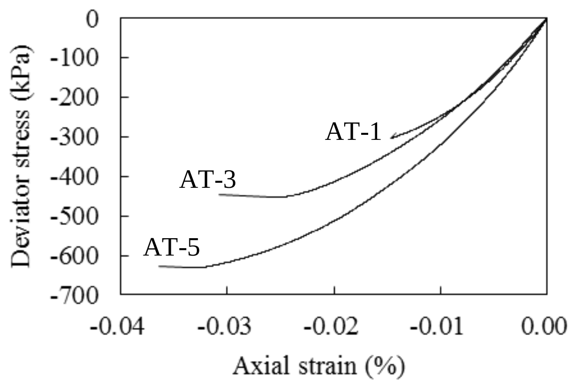

Fig. 1 Stress-strain relationships of triaxial tension test for Binder A.

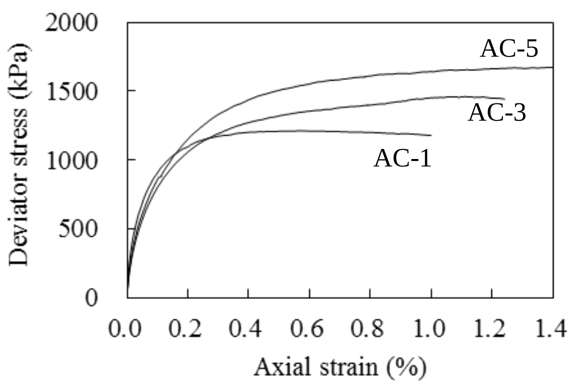

Fig. 2 Stress-strain relationships of triaxial compression test for Binder A.

significantly larger than that for BT-1. Such difference between the pre-peak behaviors may be induced by the difference between the failure modes depending on p_c'. The failure modes under triaxial tension condition is discussed in the following section. Fig. 4 shows the results of the triaxial compression tests. Similar to the result in Binder A, all the samples show a strain hardening behavior before the peak stress. The absolute value of strain at the peak stress is around 1.8% for BC-1.

The triaxial tension and compression test results show the difference of the stress-strain relationships. For Binder A in which q_u = 1300 kPa, the pre-peak stress-strain relationship is approximately linear under the tiaxial tension condition while the strain hardening behavior is observed under the triaxial compression condition. For Binder B in which q_u = 500 kPa, the strain hardening behavior is observed even under the triaxial tension condition. These results indicate that the constitutive model for cement-treated soil should describe such variation of the stress-strain relationships under the triaxial tension and compression conditions.

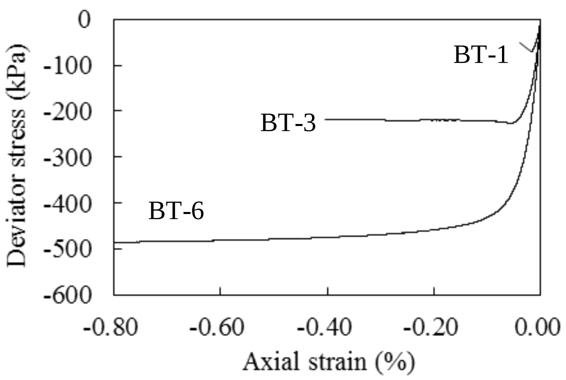

Fig. 3 Stress-strain relationships of triaxial tension test for Binder B.

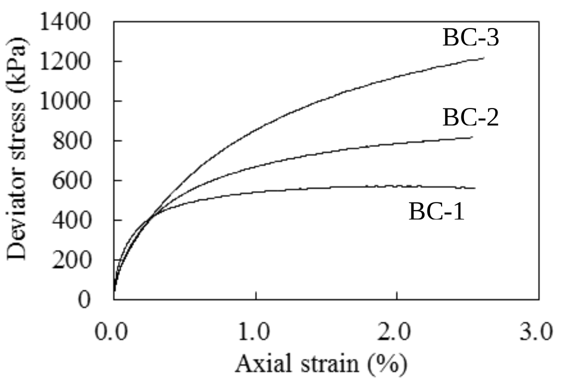

Fig. 4 Stress-strain relationships of triaxial compression test for Binder B.

Failure surfaces

The peak stress states of all the cases are shown in Fig. 5 and Fig. 6. In the results for BC-2 and BC-3, since the peak stress state is not obtained clearly from the stress-strain relationships, the stress at the axial strain of 2 % is defined as the peak stress. The shear and tension failure surfaces defined by Eqs. (4) and (5) are plotted in these figures. The material parameters of the failure surfaces are shown in Table 3. The values of c and ϕ which are required for the shear failure surface are determined from the triaxial compression test results. The value of T_f is determined from the uniaxial tension test results. For Binder A, the triaxial compression test results lie on the shear failure surface defined by Eq. (4) while the triaxial tension test results lie on the tension failure surface defined by Eq. (5).

The difference of the failure modes may induce the difference of the pre-peak stress-strain relationships as mentioned in the previous section.

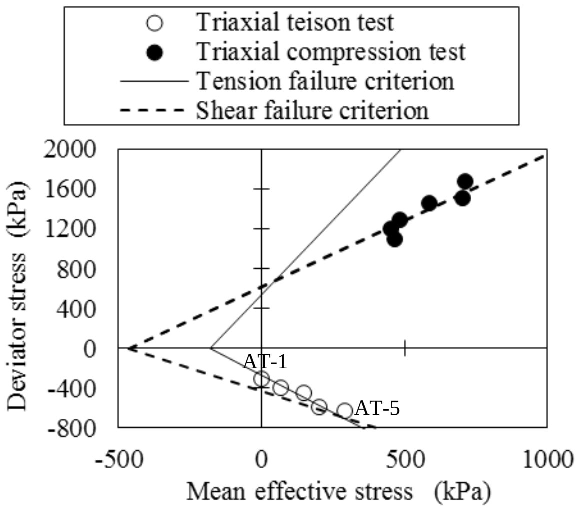

Fig. 5 Peak stress state and failure surfaces for Binder A.

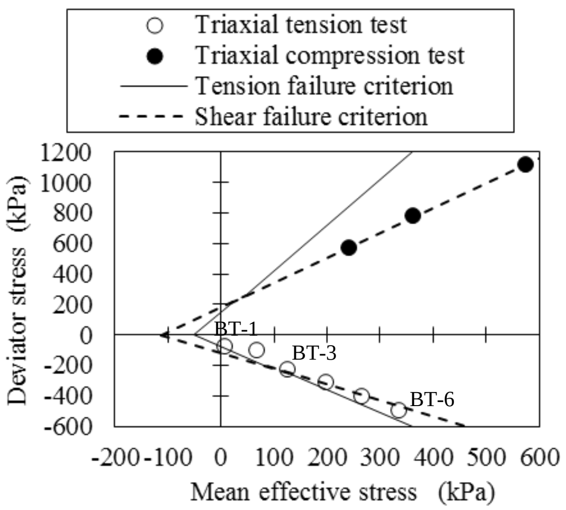

Fig. 6 Peak stress state and failure surfaces for Binder B.

For Binder B, the triaxial compression test results lie on the shear failure surface. In the triaxial tension test results, the peak stress states lie on the shear failure surface under the high confining pressures while those lie on the tension failure surface under low confining pressures. It can be seen that the failure mode changes with the confining pressure for Binder B. This difference of the failure modes in the triaxail tension test results is consistent with the difference between the stress-strain relationships in Fig. 3.

SIMULATION OF TRIAXIAL TESTS

Simulation Conditions

The laboratory tests presented in the previous section are simulated by the elasto-plastic model proposed by Namikawa and Mihira (2007). The elasto-plastic model is implemented as a user's subroutine in the finite element software DIANA. The iterative initial stress method is used in solving the problem incrementally. In the laboratory tests, the specimens exhibit complex failure patterns after the peak stress state and the global stress-strain relationships depend on the failure patterns. It is difficult to consider such complex failure pattern in the analysis. Therefore the specimen is modeled as an element and the predictions are restricted to the pre-peak stress-strain relationships. Moreover one phase formulation is used in the analysis by assuming the perfectly drained condition.

The material parameters used in the simulation are shown in Table 3. Since the simulation is restricted to the pre-peak regime, the parameters for the softening behavior are omitted from this table. The values of the elastic modulus E are determined from the experimental stress-strain relationship shown in the previous section. As mentioned above, the values of the friction angle ϕ and cohesion c are determined from the peak stress states obtained from the triaxial tests in this study. The values of the tensile strength T_f are determined from the uniaxial tension test results. The values of Poisson's ratio ν, the hardening parameters α and e_y are determined based on the previous test results [1].

Table 3 Material parameters

Parameter	Binder A	Binder B
E	3000 MPa	1000 MPa
ν	0.167	0.167
ϕ	33 degree	40 degree
c	300 kPa	90 kPa
T_f	180 kPa	50 kPa
α	1.05	1.05
e_r	0.0002	0.0002

Simulation results

The comparison between the experimental and numerical results for triaxial tension tests (AT-1, AT-5, BT-1, BT-3, BT-6) are shown in Fig. 7 and Fig. 8. Fig. 7(a) and Fig. 8(a) show that the numerical simulation result reasonably agree with the experimental result of tests AT-1 and BT-1 in which the values of p_c' are low. This indicates the elasto-plastic model can describe the tensile stress-strain behavior under a low confining pressure. Fig. 7(b) and Fig. 8(b) shows that there is some difference between the simulation and experimental results of test AT-5 and BT-3. In these cases, it seems that the shear failure occurs in the simulation while the tension failure occurs in the laboratory test. Fig. 5 and Fig. 6 show that the peak stress lies on the transition region in those tests. These results indicate that further research is required to simulate accurately the stress-strain relationship in the transition region. Fig. 8(c) shows that the numerical simulation result reasonably agrees with the experimental result in test BT-6. In this case, Fig. 6 shows that the shear failure occurs in the test. It is clear that the elasto-plastic model can simulate such shear hardening under the tiaxial tension condition.

The comparison between the experimental and numerical results for triaxial compression test (AC-1, BC-1) is shown in Fig 9 and Fig. 10. Althought there

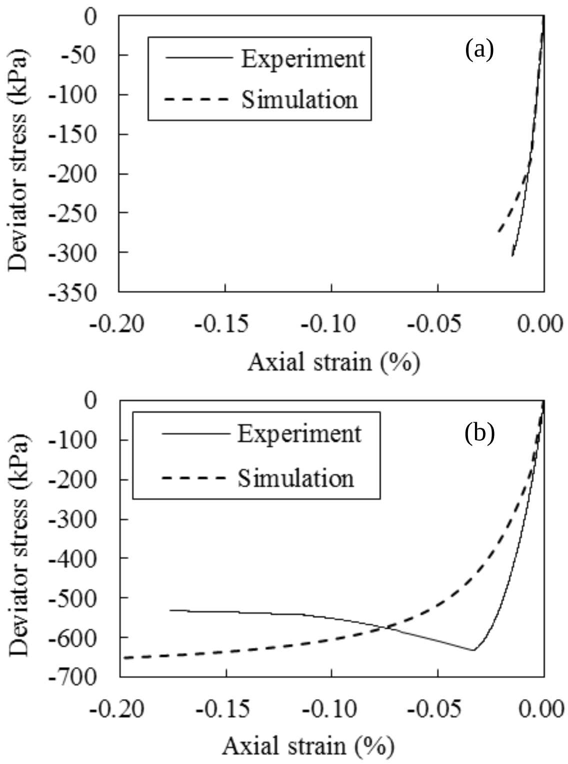

Fig. 7 Comparison of stress-strain relations for triaxial tension tests in Binder A: (a) AT-1 and (b) AT-5.

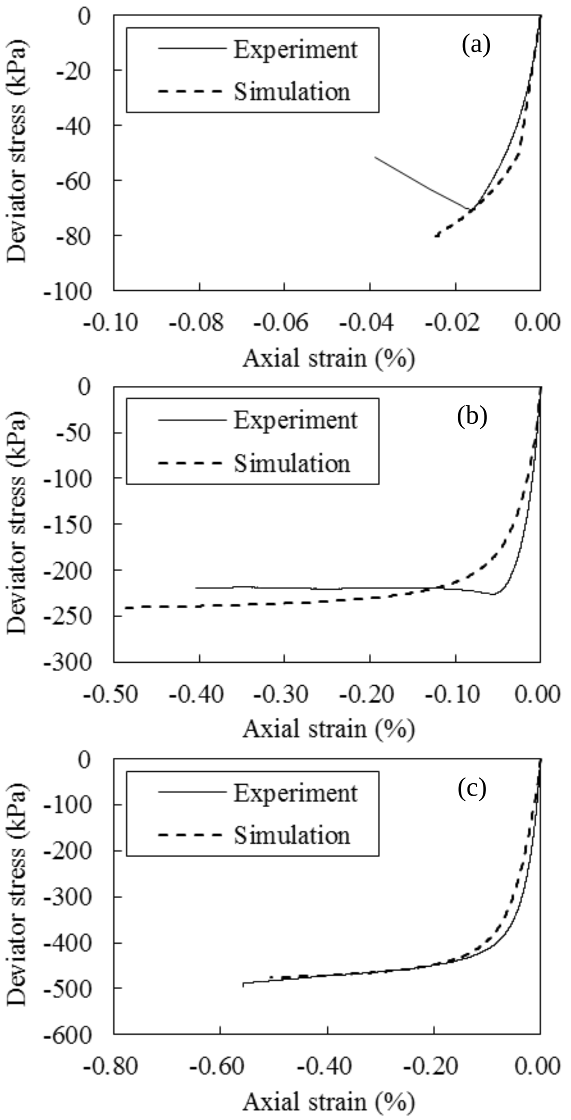

Fig. 8 Comparison of stress-strain relations for triaxial tension tests in Binder B: (a) BT-1, (b) BT-3 and (c) BT-6.

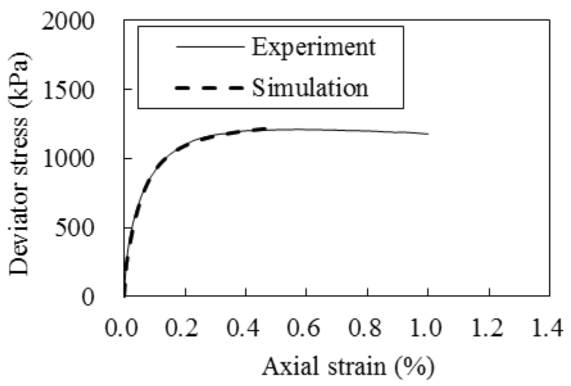

Fig. 9 Comparison of stress-strain relation for triaxial compression test (AT-1).

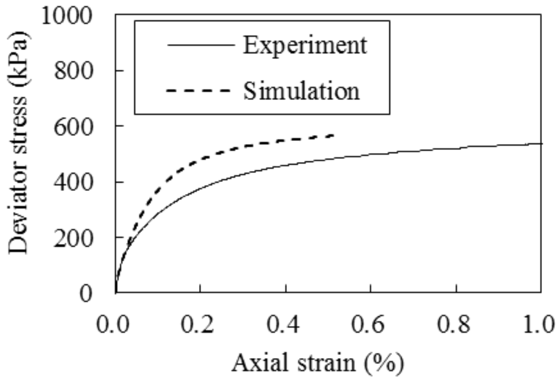

Fig. 10 Comparison of stress-strain relation for triaxial compression test (BT-1).

is some difference between the experimental and simulated stress-strain relationships in the case of BC-1), the simulation result agree reasonably with the experimental result. This indicates that the elasto-plastic model can also describe the triaxial compression behavior of the cement-treated soil.

CONCLUSION

This paper presents the numerical simulation of the triaxial tension test of cement-treated soils. The elasto-plastic model proposed by Namikawa and Mihira (2007) is adopted to simulate the triaxial tension behavior of the cement-treated soils. The simulated stress-strain relationships reasonably agree with those obtained from the laboratory tests, indicating that the elasto-plastic model can describe the tension and shear behaviors under the effective confining pressures. In particular, it is clear that the adopted model can simulate the shear hardening observed in the triaxial tension tests under high effective confining pressures.

ACKNOWLEDGEMENTS

The author acknowledges the support of the Japan Society for the Promotion of Science (JSPS KAKENHI Grant No. 25420509).

REFERENCES

[1] Namikawa T and Mihira S, “Elasto-plastic model for cement-treated sand”, Int. J. Numer. Anal. Meth. Geomech., Vol. 31, No.1, 2007, pp. 71–107.

[2] Namikawa A and Hiyama S, “Triaxial tension test of cement-treated soil”, Proceedings of the 15th Danube – European Conference on Geotechnical Engineering, Vienna, Austria, Vol. 1, 2014, pp. 329-334.

ASSESSMENT OF PHYSICAL AND MECHANICAL PROPERTIES OF COMPOSITE TILE MADE OF WOOD CHIPS AND CERAMIC POWDER REINFORCED WITH BAMBOO FIBERS

Hermie M. del Pilar[1,] Marisol E. Manarin[1], Clevin John V. Santos[1],Krizza Diane M. Santos[1],
[1]Department of Civil Engineering, Malayan Colleges Laguna,
Pulo Diezmo Road Cabuyao City, 4025, Philippines

ABSTRACT

Innovatıons in composite materials prompted this study to assess the physical and mechanical properties of three layer wood–ceramic composite tile. Specimens of 200 mm x 200 mm wood tiles having 2.5 mm top and bottom face layers and 5mm thickness core layer were produced to make up a 10 mm thickness of composite tile. Face layers made of fine wood chips and ceramic powder mixture, having 70:30 weight ratio. Core layers made of coarse wood chips binded with UF 12% by weight resin were prepared in 3 mix ratios with bamboo fiber yielding ratios 80:20, 70:30, 60:40. Bamboo fibers reinforcement has a nominal diameter between 1.0 mm – 2.0 mm cross-oriented in one direction interfaced between face layers and core layers. The composite board was hot-pressed 150^{O}C at 1.38MPa in 5 minutes using Carver Laboratory Press of RI Chemicals Corporation. The property of the boards were tested using Thickness Swelling (TS), Water Absorption (WA), Modulus of Rupture (MOR) and Impact Strength (IS). The 60:40 ratio yields the highest MOR and IS tests at 37.55 MPa and 83.42 Kpa-m respectively, while the 80:20 ratio is the lowest at 18.43 MPa and 59.49 KPa-m respectively. For the physical property tests, there were no significant differences on TS having values close at 0%. WA resulted to 8% - 9% for all mix ratios with no significant difference. This study concluded that the incorporation of bamboo fibers will improve the mechanical properties in terms of MOR and IS.

Keywords: Composite Board, Bamboo Fibers, Urea Formaldehyde, Ceramic Powder, Bending Strength

INTRODUCTION

Manufactured composite boards are widely used in the construction industry. The attainment of optimum strength is one of the concerns in the continuous development of the products. One way to enhance the strength of composite boards is to introduce a reinforcing component.

Recently, researchers reported the great potential use of bamboo for composite boards. Bamboo is an ideal material for construction due to its characteristics, such as: fast growing, widely-distributed, excellent performance, and sustainable [1]. Bamboo is a porous material with axially arranged fibers that causes its mechanical and physical properties to be directionally dependent [2]. Because of these properties, several research studies were done using bamboo-based composite materials [3].

In the study of Chen, et.al[4].,a three-layer composite board has improved its strength with the aid of bamboo- reinforced fibers, determined when the mechanical properties of bamboo fiber reinforced polypropylene (PP) composite were tested. Deshpande and Rao [5] also used extracted bamboo fibers as reinforcement in polyester composites. Okubo,et.al [6] reported an improvement in tensile strength and Young's Modulus of Composite made from bamboo fiber and polypropylene. Takagi and Ichihara [7] reported that both tensile and flexural strength of composite manufactured boards with a mixture of starch- based degradable resin and short bamboo fiber were strongly affected by fiber ratio and fiber content. Currently, the utilization of bamboo earned its place on many researches for structural materials such as composite boards.

This study aimed to determine the effects of increasing weight ratio of the bamboo fiber reinforcement on the physical and chemical properties of composite tiles made of wood chips and ceramic powder reinforced with bamboo fibers. A comparison on the physical and mechanical properties of the produced composite tiles and the commercially available wood tile was also conducted.

METHODOLOGY

2.1 Raw Materials Preparation

Bamboo fiber reinforcement with a nominal diameter between 1.0 mm – 2.0 mm were drawn from commercially available raw sticks product (Figure 1). These sticks are domestic product usually with a nominal diameter of 0.5 cm and length of 30 cm. With the aid of a thin knife, the bamboo sticks can be further reduced to the desired nominal diameter of 1.0 – 2.0 mm fibers.

The ceramic powder material used for the face layer of the board was sourced from Mariwasa Siam Ceramics Incorporated (Figure 2). The ceramic powder is an inorganic non-metallic solid powdered, which is the same material in manufacturing ceramic tile products. Ceramic powder together with the fine wood chips was mixed using a common adhesive.

Fig.1 Bamboo Fibers

Fig. 2 Ceramics Powder

In this study, Urea formaldehyde (UF) was used as adhesive (Figure 3), manufactured and purchased from RI Chemicals Corporation located in Pasig City, Metro Manila, Philippines. This adhesive was used to bind the wood chips (Figure 4), powdered ceramic and bamboo reinforcement together (Figure 7).

Wood chips collected from Southern Sky Construction Supply Cabuyao Laguna were used as raw material for the face and core layer of the composite boards. Fine wood chips were used for the face layer base material and coarse wood chips were used for core layer. Wood chips were oven-dried at 105 Celsius for twenty-four hours (24h) and then cured at room temperature for two weeks.

Fig. 3 Urea Formaldehyde

Fig 4. Wood Chips

2.2 Board Production

Three-layer composite tiles reinforced with bamboo fibers were manufactured. The manufacturing criteria of the boards are listed in Table 1.

Table 1
Board Manufacturing Criteria

Target	**Raw Density**	**Weight Materials Content**	**Orientation Ratio (%)**	**Resin (%)**
0.80g/cm^3	**Core Layer: Bamboo Fibers**	**80:20 70:30 60:40**	**Cross Section**	**12 %**

The target density and dimensions of the board were used to compute for the total mass of the composite tile. Based on the total mass, 70% of the mass constitute the face layers while 30% is covered by the core layers and bamboo fibers were manufactured based on the total mass. Likewise, the face layers had 70% fine wood chips and 30% ceramic powder. The total mass of the core layer and bamboo fibers were varied according to three weight ratios, 80:20, 70:30 and 60:40. Bamboo fibers were oriented in a cross section manner interfaced between the face layers and core layer. Urea formaldehyde with a resin content of 12% and 1% of the catalyst was used as a binder for the composite tile.

2.3 Machines for the composite board production

The machines used in the production of three layer composite tiles were mixers and the heat press. As shown in Figure 5, the Ross mixer from RI Chemicals Corporation consisted of a double planetary mixer equipped with classic rectangular stirrer blades mounted at the mix vessel. The machine runs at a fixed speed set at 60 rpm for mixing operations. Figure 6 shows the heat press machine used – the Carver Laboratory Press from RI Chemicals Corporation. Each platen was aluminum with 8 square inches size installed with a dial type temperature gauge and manual temperature adjusted to 150^{O}C.

Fig. 5. Ross Mixer

Fig. 6 Carver Laboratory Press

2.4 Board Manufacturing Process

After the materials and equipment preparation, ceramics, fine and coarse wood chips, urea formaldehyde and bamboo fibers were weighed using a digital electronic balance for proper proportioning. Figure 7 shows the ceramic powder, fine wood chips weighed together to form the face layer composition placed in a Ross Mixer for mixing operation. Figure 8 shows the UF applied quickly to avoid forming colloids due to the reaction of the catalyst. The materials were mixed for five minutes to allow homogeneous mix.

Fig.7. Face Layer Composition in the Ross Mixer

Fig. 8. Face Layer in Mixed Proportion

Figure 9 shows the mixture placed in form seats prepared for the face layers of the board. The metal mold has eight inches square in size and twelve inches height. The surface of the face layer was flattened using a heavy metal cover to spread the mixture uniformly. In Figure 10, bamboo fibers were placed mutually perpendicular on face layer seats. Urea formaldehyde was spread over the bamboo fibers. Two layers of bamboo fibers in cross oriented manner were formed. The bamboo fibers were placed slowly to avoid disruptions of the face layer.

Fig. 9. Bottom Face Layer Seat

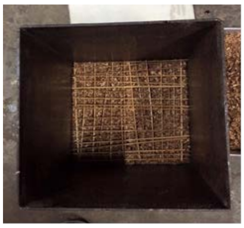

Fig. 10. Bamboo Fibers at the Face Layer

The wood chips and adhesive were mixed using the Ross Mixer forming the core layer of the board. The mixture was evenly spread on top of the bamboo fibers reinforcement. Another set of bamboo fiber reinforcement was placed on top of the core layer.

The top face layers were added with the same composition of the bottom face layer. The top face layer was the final part of the three-layer composite tile. The three layers of the composite tile initially pressed inside the mold using a heavy metal cover to combine all 3 layers as one (Figure 11). The composite tile was removed from the mold and placed in the aluminum sheet for hot pressing.

The forming size of the board was 200 mm wide and 200 mm long and the thickness was calibrated at 10 mm thickness. The hot plate Carver Laboratory Press temperature was adjusted to 150 degree Celsius with pressure of 1.38MPa, and the hot press time was adjusted to 12 minutes.The resulting boards were allowed to cure at room temperature (Figure 12).

Fig. 11. Combined Layers for Pressing

Fig. 12. Hot-pressed composite board

2.5 Preparation of Test Specimen.

Specimens were prepared to determine the physical and mechanical properties of the composite tile product. In this study, 4 tests were conducted, 2 for each property. The boards were tested for water absorption and thickness swelling for physical property tests, while the modulus of rupture and impact strength account for the mechanical property tests

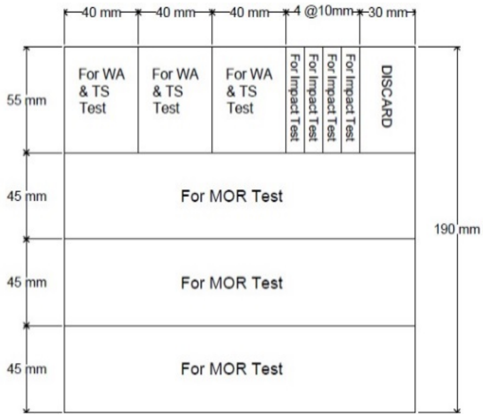

Fig. 17. Cutting pattern for test specimens testing

2.6.1 Physical Property Test

Water Absorption (ASTM D1037-99, 100-107)

The specimens with dimension 40mm x 55mm are first weighed individually for this test, then submerged to distilled water for the next 24 hours, after which it was weighed again to determine the water absorption of each specific sample. Water absorption is defined as the increase in weight percent and was determined using:

$$\mathrm{WA}(\%) = \frac{\text{Wet Weight} - \text{Dry Weight}}{\text{Dry Weight}} \text{ x } 100\% \qquad (1)$$

Thickness Swelling (ASTM D1037-99, 100-107)

The specimen with dimensions 40mm x 55mm were subjected for this test. First, the specimen's thickness was measured, and then submerged in distilled water for the next 24 hours. Next, the samples were taken from the container and the adsorbing water on surface was removed. The thickness of the specimen was again measured to determine the thickness swelling. Thickness swelling is determined by the formula:

$$\text{TS (\%)} = \frac{\text{Final Thickness} - \text{Initial Thickness}}{\text{Initial Thickness}} \text{ x } 100\% \quad (2)$$

2.6.2 Mechanical Property Test

Modulus of Rupture

A static bending test was conducted using the Shimadzu, Universal Testing Machine. Three specimens (190mm x 45mm x 12 mm) were prepared for the static bending test using the 3 point bending with effective span of 160 mm at a loading speed of 5 mm/min. The Modulus of rupture can be determined using the formula:

$$\text{MOR} = \frac{3PL}{2bd^2} \quad (3)$$

Impact strength (ASTM A370)

The impact strength (IS) test measured the amount of energy or load required to break the board specimens. The Charpy impact test, also known as the Charpy V-notch test, is a standardized high strain-rate test which determines the amount of energy absorbed by a material during fracture. This absorbed energy is a measure of a given material's notch toughness.

2.7 Statistical Tool

The One Way Analysis of Variance (ANOVA) was utilized to determine if there is a significant difference on the performance of composite boards produced using the 3 mix ratios for the physical tests (WA and TS) and the Mechanical Tests (MOR and IS).

3. RESULTS AND DISCUSSION

3.1 Physical Property Tests Results

Thickness Swelling Test

Figure 19 shows the changes in for each of the weight ratios. The thickness swelling of the composite tile is less than the commercial wood tile. The results showed that the thickness swelling increases with the increase on bamboo fiber content.

“Bamboo is able to absorb all fluids of different densities over the time most likely due to the capillary forces within the pore structure” [8], which is consistent of the result.

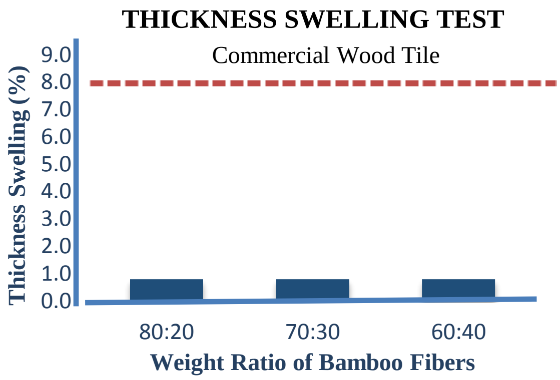

Fig. 19. Thickness Swelling with Varying Bamboo Fibers Weight Ratio

Water Absorption Test

Figure 20 shows the variations in water absorptions measured for each weight ratio. The water absorption of the composite tile was less compared to the commercial wood tile. The water absorption increases with the increase in weight of the bamboo fiber. Yang, et.al. found that “Bamboo fibers are highly hydrophilic due to their chemical constituents such as lignin which can decrease adhesion with hydrophobic matrix materials” [9], which is consistent with result.

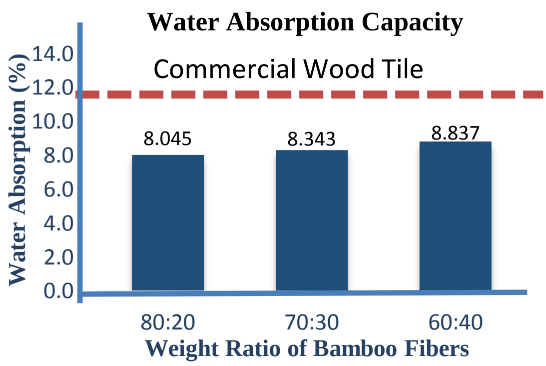

Fig. 20. Water Absorption with Varying Bamboo Fiber Weight Ratio

3.2 Mechanical Property Tests Results

Modulus of Rupture

Figure 21 shows the results of Modulus of Rupture for each weight ratio. The means of Modulus of Rupture increases as the weight ratio increased. The increasing Modulus of Rupture affirms the claim of Hermawan et.al (2011) relating the uniform dispersion of the fibers in the face layer of the board which leads to the even distribution and transfer of stress from the face layer to the fibers [10].

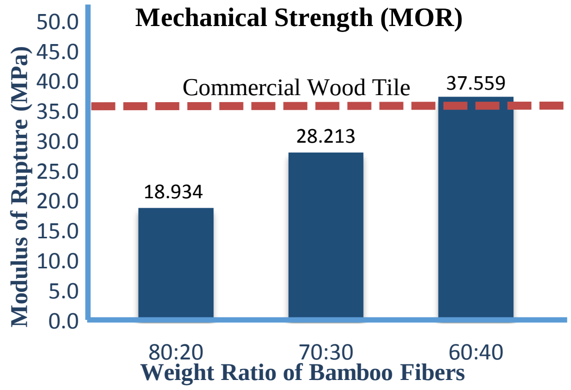

Fig. 21. Modulus of Rupture with Varying Bamboo Fibers Weight Ratio

Figure 22 shows the result recorded from Charpy Impact Strength Test on nine specimens for each weight ratio. The means of the impact strength increase as the weight ratio of the bamboo fibers increased. This shows that the reinforcement provided by the bamboo fibers results to a significant increase in the impact strength of the composite tile. "The increased fiber content is improving its capability to absorb impact, which is consistent with the findings of Jena and Pradhan [11].

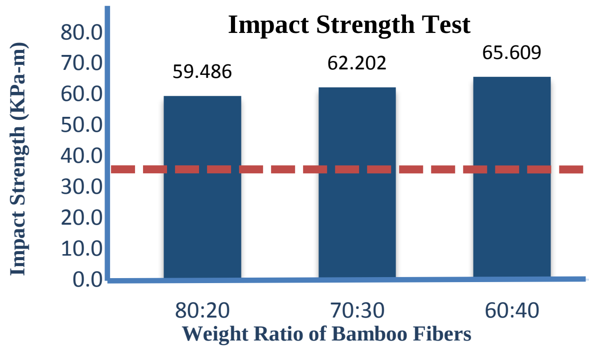

Fig.22 Impact Strength with Varying Bamboo Fibers Weight Ratio

Statistical Results

The statistical results using One-Way ANOVA showed that the use bamboo strips significantly affect the Mechanical Property but not the Physical Property. This is using an $\alpha = 0.05$. Table 2 summarizes the result for the test of significance.

Table 2: Test for the difference in properties of the composite tile

Comparison Between	Mechanical Property		Physical Property	
	MOR	**IS**	**WA**	**TS**
3 Types of bamboo reinforced tile board	**Significant**	**Significant**	**Not Significant**	**Not Significant**

4. CONCLUSIONS

In terms of the physical properties, the produced composite board had lower values for both thickness swelling and water absorption. For mechanical properties, the board exhibited excellent results with the variation of weight ratio of the bamboo fibers.

Based on the outcomes, several conclusions were drawn.

1.) The water absorption and thickness swelling of the composite board had shown good quality regardless of the weight ratio used. The thickness swelling was almost 0%. The low values of water absorption and thickness swelling implied that the boards have high resistance to moisture content.

2.) The bending strength of the board is significantly affected by weight ratio of bamboo fibers. The Modulus of Rupture shows larger value with increased weight ratio of bamboo fibers. Among the weight ratios 60:40, 70:30 and 80:20, the best value of MOR is 37.55 MPa from the 60:40 ratio, while the lowest value is 18.43 MPa from 80:20 ratio.

3.) The Impact Strength increased as the weight ratio of the bamboo fibers increased. The 60:40 ratio exhibits the highest value of 65.609 KPa-m while the ratio 80:20 exhibits the least value of 59.49 KPa-m. The increased fiber content is improving its capability to absorb more energy. This shows that the reinforcement provided by the bamboo fibers results to a significant increase in the impact strength of the composite tile. Impact strength of the composite tile with bamboo reinforcement exhibited excellent quality when compared with commercial wood tile whose impact strength measures 35.47 KPa-m on average.

4.) The physical appearance and property of the composite board are comparable to the quality of a commercial wood tile due to its surface glaze and rigidity. The tapestry brought by the compressed ceramic powder and fine wood chips at the face layer significantly add to the aesthetic value of the composite board.

REFERENCES:

[1] Yao, W. & Zhang, W. (2011). Study on Bamboo Conditions for Processing Bamboo Fiber. *Fourth International Conference on Intelligent Computation Technology and Automation.* 10.1109, 198-202. 62

[2] Prieto, M.G., Vidal, N.J., & Rojas, J.T., (2013). Bamboo as a Sustainable Material for Several City Uses.*Fourth International Conference on Intelligent Computation Technology andAutomation.* 978-1-4799-2911-5/13.

[3] Suhaily, S., Khalil, A., Nadirah, W., & Jawaid, M. (2013). Bamboo Based Biocomposites Material, Design and Applications.Creative Commons Attribution License. 10.5772/56057.

[4] Chen X., Guo Q., &Mi Y. (1998) Bamboo Fiber-Reinforced Polypropylene Composites: A Study of the Mechanical Properties.*JApplPolym Sci*.69:1891–1899.

[5] Deshpande A., Rao L., & Rao B. (2000). Extraction of Bamboo Fibers and Their Use as Reinforcement in Polymeric Composites. *JApplPolym Sci*. 76:83–92.

[6] Okubo, K., Fujii, T., Yamamoto, Y. (2004) Development of Bamboo-Based Polymer 59 , Composites and their mechanical properties. Composite: Part A 35:377 – 83

[7] Takagi, H., Ichihara, Y. (2004). Effect of fiber length on mechanical properties of green composite using a starch based resin and short bamboo fibers. JSMEIntJ : Series A 47:551-5

[8] Sobrinho, A., Aragao, J.L., Torres, S.M., Barros, S., Ortiz, S.R. & Barbosa, N.P. (2009). Bamboo PH and Absorption in Different Liquids.

[9] Yang, H., Kim,H., Park, H., Lee,B., & Hwang, T. (2006). Water Absorption Behavior and Mechanical properties of Lignocellulosic filler-polyolefin bio-composites. Composite Structures. Vol. 72, no. 4 , pp.429-437, 2006

[10] Hermawan,A., Ohuchi,T., & Fujimoto, N. (2010). Manufacture of Three-Layer Wood Porcelain Stone Composite Board Reinforced with Bamboo Fiber. Materials and Design. 32, 2485-2489

[11] Jena, H., Pandit, M., & Pradhan, A. (2012). Study the Impact Property of Laminated Bamboo Fibre Composite Filled with Cenosphere. *International Journal of Environmental Science and Development*, Vol. 3, No. 5. 457-458.

Sixth International Conference on Geotechnique, Construction Materials and Environment, Bangkok, Thailand, Nov. 14-16, 2016, ISBN: 978-4-9905958-6-9 C3051

UNCONFINED COMPRESSIVE STRENGTH OF COMPACTED DISTURBED CEMENT-STABILIZED SOFT CLAY

Mohamed Ayeldeen[1], Yuki Hara[2] and Masaki Kitazume[3]
[1] Environmental Engineering Department, Egypt–Japan University of Science and Technology (E-JUST), Alexandria, Egypt.
[2, 3] Civil and Environmental Engineering Department, Tokyo Institute of Technology, Tokyo, Japan.

ABSTRACT

Pneumatic flow mixing method is a new land reclamation method, developed in Japan to meet the persistent lack of space. In this method dredged soft soil is mixed with a small amount of stabilizing material (such as cement) during transporting the soft soil in a pipe using compressed air to be used for land reclamation. In some cases, the soil/cement mixture is stored in temporary place for days and then transported and compacted at the required place. Basically, the cement chemical reaction starts immediately after the mixing with the soft soil and the mixture starts to gain its strength, therefore disturbing the mixture after days from the mixing influences the mixture strength. However, the soil/cement mixture is still able to gain extra strength after disturbance, transportation, and compaction. This study aims to evaluate the effect of dynamic compaction on the shear strength of disturbed cemented soft soil mixture experimentally. The mixture was fully disturbed after one week from mixing with cement. Three cement/soil ratios were used in this study under different dynamic compaction energies. Unconfined compression test was conducted at various curing times for both disturbed and non-disturbed specimens.

Keywords: Pneumatic flow mixing, Stabilized soft clay, Compaction, Unconfined compressive strength, Soil disturbance

INTRODUCTION

Soft soil deposits can be found in many places all over the world especially coastal areas, which are recognized by the high compressibility and low shear strength. Where it became essential to find appropriate method to improve the softy soil characterizations to meet the needed engineering requirements for construction. One of the new methods used to improve the soft soil for land reclamation is pneumatic flow mixing method, which depends on mixing the dredged soft soil with cement during transporting the soil through pipes to the construction site [1], [2], [3], [4]. However, in some cases the soil/cement mixture has to be stored in other place for days and then transported again to the construction site. In that case the soil/cement mixture become disturbed, where the cement chemical reaction already started as soon as the cement has been mixed with the soil. The disturbance process, which is necessary to transport the mixture after days to the site, shall change the mixture behaviour especially after using compaction to place the mixture in its final site.

Hence the chemical reaction of the cement already started once the cement has been mixed with the soil, the efficiency of the connections reformed after the disturbance is affected by the time period spent from mixing paste till the disturbance and setting up again. The longer this period is, the weaker this reformed connection will be. In this study the disturbed period has chosen to be as long as possible, to represent optimum reduction of the soil strength after disturbance, where the chosen period is 7 days from mixing the paste till the disturbance and the molding.

This study is an attempt to understand and evaluate the unconfined compressive strength of compacted disturbed cement-stabilized soft clay. Three cement/clay ratios were used in this study (5, 10 and 15%). Different compaction energies were used to compact the disturbed soil, while tapping was used for non-disturbed soil. Unconfined compression test was performed for both disturbed and non-disturbed specimens after different curing times.

MATERIALS AND TEST PROCEDURE

Material properties and specimen preparation

In order to have a clear understanding of the effect of compaction on the mechanical properties of disturbed cement-stabilized soft clay, Kaolin clay (w_L of 77.5% and w_P of 30.3 %) and ordinary Portland cement were used in this study.

Kaolin clay was mixed with tap water for one hour in a vacuum mixer at a water content ratio of 120%. Ordinary Portland cement was added after to the slurry at cement content varying from 5 to 15%, and both clay slurry and ordinary Portland cement were mixed for 10 mins. Cement content, *aw*, can be defined as the ratio between the weight of cement and the weight of clay in dry case. The paste was then split in two parts (one part for non-disturbed specimens and the other for disturbed specimens). For non-disturbed specimens, the paste was used immediately after mixing and molded by tapping in a plastic mold, 50 mm diameter and 100 mm height at three layers [5]. Each layer was tapped 100 times to grantee the homogeneity of the specimens. The non-disturbed specimens were kept in humidity curing chamber and were tested after 7, 28, 35 and 42 days from mixing the paste.

For disturbed specimens, the paste was kept airtight in plastic bag for 7 days before it fully disturbed for 5 mins in the mechanical mixer. Specimens were molded in the same plastic molds as in the non-disturbed case, however various dynamic compaction energies were used to mold the disturbed specimens. The molds were filled at three layers; each layer was dynamically compacted by 1 kg cylinder hummer falling free from a height of 1 meter. Different numbers of blows (5, 10, 20 and 40) were used to compact each layer to obtain different compaction energies. The tapping technique was also used to compact disturbed specimens at compaction energy, *C.E.* of zero. The specimens were kept also in humidity curing chamber and were tested after 28, 35 and 42 days from the initial mixing.

Test procedure

Unconfined compressive strengths were obtained using a strain rate of approximately 1 %/min for all specimens. Corrections to the cross-sectional area were made prior to calculating the compressive stress on the specimen. All tests were accomplished three times at least for each case. Curing time was a fundamental parameter for understanding the behavior of compacted disturbed cemented-soft clay; therefore, experimental schedule was arranged to perform the tests at different time periods (7, 28, 35, and 42 days) from mixing the clay with the cement.

RESULTS AND DISCUSSION

Effect of disturbance on the stress strain behaviour

Figure 1 shows the difference in behaviour between disturbed and non-disturbed cemented clay for cement ratio, *aw* of 15% tested after curing period, *t* of 28 days. For non-disturbed specimen, a clear brittle behaviour with peak strength and quite small residual strength can be notice with unconfined compressive strength, $q_{un\_Non\_28}$ of 270 kPa at axial strain at failure of 2%, while the unconfined compressive strength for disturbed specimen, $q_{un\_D\_28}$ does not exceed 50 kPa regardless the compaction energy, *C.E*, and with failure stain of 6-7 % in a ductile behaviour with unclear peak strength.

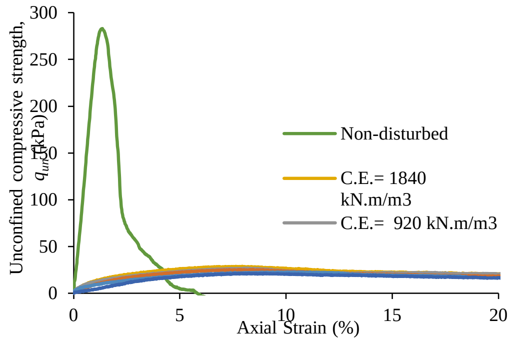

Fig. 1 Stress strain curve for disturbed and non-disturbed specimen (*aw* = 15%, 28 curing days).

The effect of compaction energy on the behaviour of disturbed cemented clay can be observed in Figure 2 for the same conditions as in Figure 1 (*aw* = 15%, *t* = 28 days). The ductile behaviour for disturbed cemented clay changed to be more brittle with increasing the compaction energy. It can be noticed that the unconfined compressive strength increased with increasing the compaction energy, while the axial strain at failure decreased. For non-compacted specimen, the peak unconfined compressive strength, q_{un} was about 21 kPa at axial strain at failure of 12%. However, the peak strength increased to 24 kPa with increasing the compaction energy to 460 kN.m/m^3, where also the axial strain at failure reduced to 8%, which reflects increasing the brittle behaviour with increasing the compaction energy. The brittle behaviour became more clear for specimen compacted with higher dynamic energy, at compaction energy of 1840 kN.m/m^3, the peak unconfined compressive strength reached 28 kPa with axial strain at failure of 6%.

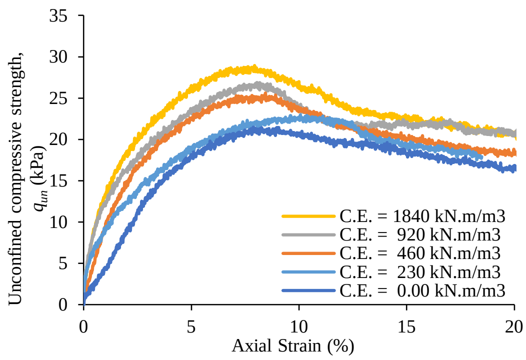

Fig. 2 Stress strain curve for disturbed specimen with different compaction energies (*aw* = 15%, 28 curing days).

Effect of curing time on both unconfined compressive and modulus of deformation

Figure 3 clarifies the variation of q_{un} under five different compaction energies with time for cement content of 15%. Increasing the compaction energy reflected to a positive increasing in the unconfined compressive strength. At curing time of 28 days, q_{un} increased from 25 kPa at zero compaction energy to about 35 kPa at compaction energy of 1840 kN.m/m^3 (i.e. the percentage of increasing is about 140%). The same percentage of increasing can be also notice at curing time of 42 days, where q_{un} increased from 32 kPa to 46 kPa (increasing percentage of about 143%) by increasing the compaction energy from zero to1840 kN.m/m^3. It can be observed also that doubling the compaction energy from 920 to 1840 kN.m/m^3 did not have the considerable effect on the compressive strength, where q_{un} at curing period of 28 days had increased from 33 to 35 kPa after increasing the compaction energy from 920 to 1840 kN.m/m^3. The same trend can be notice at curing time of 42 days, where increasing the compaction energy from 920 to 1840 kN.m/m^3 effected on increasing the compressive strength from 43 to 46 kPa, *i.e.* increasing the compaction energy from 920 to 1840 kN.m/m^3 caused an increasing in q_{un} with a percentage of 5-6 %. The unconfined compressive strength improved by percentages of 135, and 142 % by increasing the compaction energies from zero to 920 and from zero to 1840 kN.m/m^3 respectively. This can be interpreted due to the high water content and the very low permeability of clay which affected the efficiency of compaction after certain compaction energy.

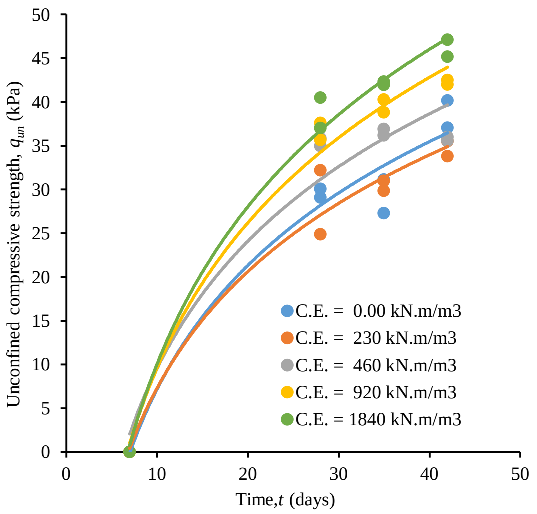

Fig. 3 Variation of unconfined compressive strength with time under different compaction energies (*aw* = 15%).

For more understanding to the effect of compaction energy and curing time on the disturbed cemented clay, Figure 4 displays the effect of compaction energy on modulus of deformation, E_{50} for *aw* = 15% with different curing periods. It can be seen from the figure the increasing in modulus of deformation, E_{50} with increasing the compaction energy. At curing time of 28 days, E_{50} has increased from 1000 to 1250 kPa by increasing the compaction energy from zero to 920 kN.m/m^3 and it has increased again to be 1500 kPa at compaction energy of 1840 kN.m/m^3 with increasing percentage of 125 and 150 % for both compaction energies of 920 and 1840 kN.m/m^3 respectively.

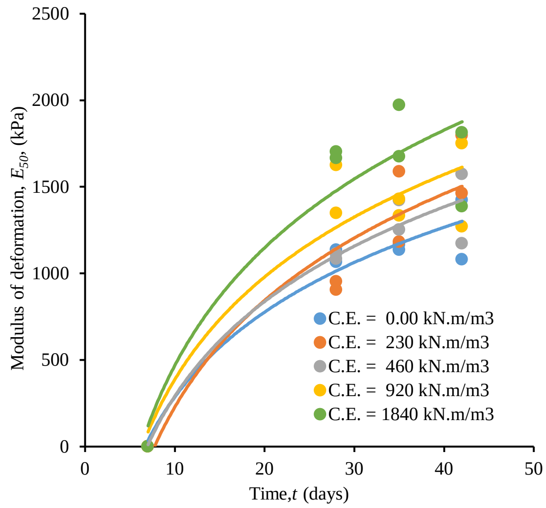

Fig. 4 Variation of modulus of deformation with time under different compaction energies (*aw* = 15%).

The same trend still exists at curing period of 42 days, where E_{50} has augmented comparing the zero compaction case with increasing percentage of 123 and 142 % for both compaction energies of 920 and 1840 kN.m/m^3 respectively. Unlike unconfined compressive strength, the effect of doubling the compaction energy are more effective on E_{50} than q_{un}, where E_{50} has increased from 123-125% to 142-150% by increasing the compaction energy from 920 and 1840 kN.m/m^3.

Relationship between unconfined compressive strength and modulus of deformation for both disturbed and non-disturbed specimens

According to previous studies [1] [6] for undisturbed cemented Japanese clays and Bangkok clay, It was found that E_{50} can be taken as approximate value of 50 to 300 × q_{un}. However, in this study the correlation value of E_{50} can be considered as 160 q_{un} as it can be seen in Figure 5 (a). This difference between the current study and the previous studies can be explained due to the difference in used clay and water content, however both values can be acceptable to estimate E_{50} from the corresponding q_{un}.

Figure 5 (b) shows the relation between E_{50} and the corresponding q_{un} for disturbed compacted cemented clay with different cement ratios and different compaction energies. As mentioned before in Figure 1, that the disturbance process reduced the unconfined compressive strength of the cemented clay and transferred the behaviour to be ductile, this behaviour can be seen clearly form the approximate function between E_{50} and the corresponding q_{un}. The multiplier factor to estimate E_{50} has considerably reduced from (E_{50} =160 q_{un}) for non-disturbance cemented clay to (E_{50_D} = 25 - 50 q_{un_D}) for disturbance cemented clay.

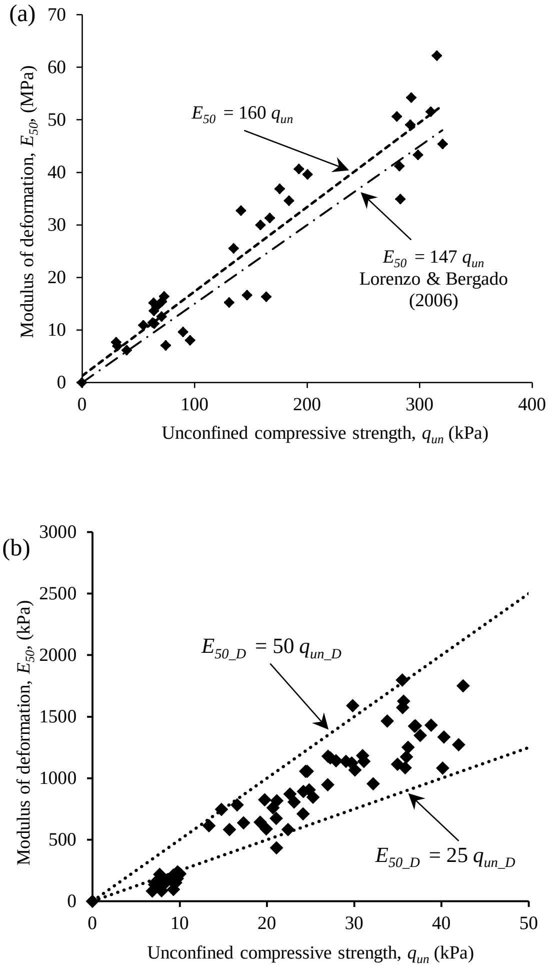

Fig. 5 Modulus of deformation versus unconfined compressive strength of: (a) non-disturbed cemented clay; (b) disturbed cemented clay

Effect of compaction energy on dry density

The plot of dry density against compaction energy for various cement ratios is shown in Figure 6, where increasing the soil density is the key target for compaction process. Increasing the soil density will lead to reduction in the ground settlement, increasing in shear strength, and increasing in the bearing capacity. From Figure 6, increasing the compaction energy affected positively on dry density, where the average dry density - at *aw* = 10% - has increased from 7.0 to 7.3 kN/m^3 by increasing the compaction energy from zero to 460 kN.m/m^3, and has reached 7.5 kN/m^3 at compaction energy level of 920 kN.m/m^3. Increasing dry density with increasing the compaction energy was expected due to the effect of compaction on reducing void space between particles, which leaded to increasing in the density. However, the compaction efficiency can affect by some factors such as high water content, where it can be notice at low level of compaction energy.

Increasing the compaction energy from zero to 230 kN.m/m^3 did not have the noticeable effect on increasing the dry density, while this effect started to be obvious at starting from compaction energy of 460 kN.m/m^3. Cement content affected the dry density, where increasing the cement content was followed by raising in the dry density. Dry density increased from 6.7 to 7.5 kN/m^3 by increasing *aw* from 5 to 10%, and to 8.1 kN/m^3 at *aw* of 15%. This can be explained due to increasing the cemented pozzolanic formations inside the soil gaps, which increased by increasing the cement ratio.

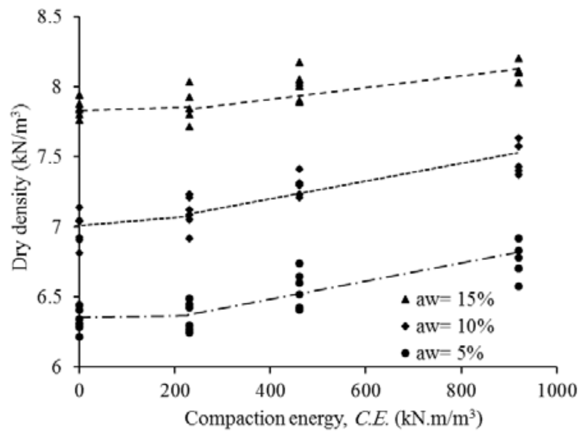

Fig. 6 Effect of compaction energy on dry density

Relationship between unconfined compressive strength and both dry density and voids ratio

Figure 7 displays the relationship between dry density and disturbed unconfined compressive strength for different cement ratios. This relationship was effected by changing the cement content, and this can be notice clearly from the slope of the three trend lines (A, B and C). The slope of trend line A with the horizontal projection is almost neglectable, which means that changing the dry density does not have considerable effect on q_{un} for *aw* = 5%, where the dry density changed from 6.3 to 6.9 kN/m^3 with average change in q_{un} was from 6.5 to 8.5 kPa. The slope of trend line B is more apparent than the trend line A, which clarifies the relationship between dry density and q_{un_D} for aw = 10%, where the average dry density has changed from 6.9 to 7.7 kN/m^3 accompanied by changing in q_{un_D} from 15 to 27 kPa. That relationship reached the utmost clarity in case of trend line C (aw = 15%), where the changing in dry density – just from 7.8 to 8.2 kN/m^3 - was followed by high changing in q_{un_D} – from 26 to more than 40 kPa.

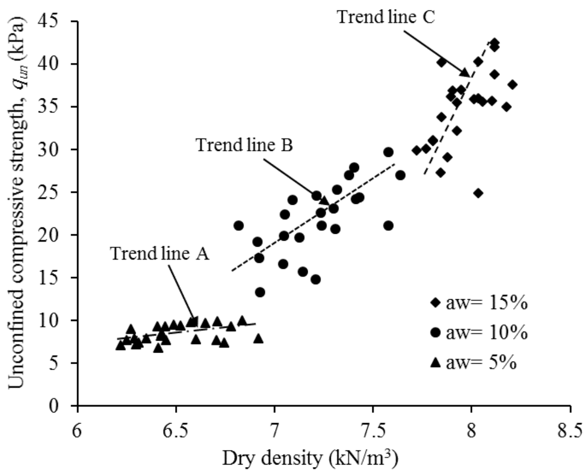

Fig. 7 Relationship between dry density and disturbed unconfined compressive strength.

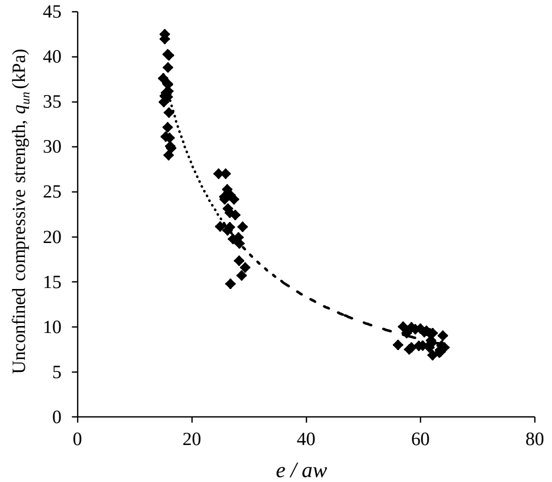

Fig. 8 Unconfined compressive strength versus e/aw.

The final void ratio corresponding to each dry density - which takes into consideration the effect of water content, curing time, and compaction energy- can be calculated as follows:

$$e = \frac{(1+wc)\times G_s \times \gamma_w}{\gamma_t} - 1 \quad (1)$$

where γ_t = the total unit weight after curing, wc = the water content corresponding to γ_t, γ_w = water unit weight, and G_s = the mixture specific gravity.

The formation of e/aw has already collected the effect of several variables such as water content, curing time, cement ratio, and compaction energy. The reason behind the division of e by aw that some specimens can have different cement ratios and compaction energies, however it may chance to have the same void ratio, and for sure not the same value of q_{un_D}. The following empirical relationship has been delivered to estimate the value of q_{un_D} as clear in Figure 8:

$$q_{un\_D} = 700 \times {}^{e}\!/_{aw} \quad (2)$$

Estimating the value of the increasing factor *i*

It is important to find a strategy to estimate both unconfined compressive strength and modulus of deformation for disturbed cemented clay under different compaction energies for various curing periods. A clear relationship between unconfined compressive strength for non-disturbed specimens at curing time t , $q_{un\_Non\_t}$ and unconfined compressive strength for disturbed non compacted specimens at the same curing time t, $q_{un\_D\_T\_t}$ can be figured out from Figure 9, where it can be written as following:

$$q_{un\_D\_T\_t} = 0.1 \times q_{un\_Non\_t} \quad (3)$$

where both $q_{un\_Non\_t}$ and $q_{un\_D\_T\_t}$ have the same cement ratio, water content and curing time.

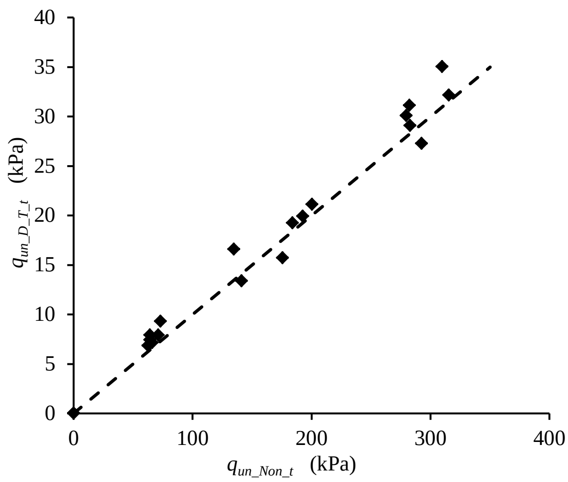

Fig. 9 Unconfined compressive strength for non-disturbed specimens versus unconfined compressive strength for disturbed non compacted specimens

For disturbed cemented clay, the unconfined compressive strength will increase than q_{un_D} with increasing the compaction energy as mentioned before in Figure 2. This increasing can be represented by the factor *i*, as following:

$$q_{\text{un\_D\_comp\_t}} = i \times q_{\text{un\_D\_28}} \quad (4)$$

where, $q_{\text{un\_D\_comp\_t}}$ is the unconfined compressive strength for disturbed cemented clay under compaction energy, after curing period of *t*. $q_{\text{un\_D\_T\_28}}$ is the unconfined compressive strength for disturbed cemented non compacted clay after 28 days curing period for the same cement ratio, and *i* the increasing factor as percentage.

It was not possible to figure out a formula to estimate *i* statistically, thus using neural network tool will be essential to estimate the value of *i* as a function of both curing time and compaction energy, which will be discussed in future.

CONCLUSIONS

This study focuses on investigating the behavior compacted disturbed cemented soft clay under different compaction energies and curing periods. Three different cement contents are used in this study with water content of about 120%. Within the experimental range of this investigation, the following conclusions can be drawn:

Disturbing the soil has a serious effect on the stress strain behaviour, where the behaviour changes from being brittle with peak to more ductile, with a huge reduction in the compressive strength and modulus of deformation.

The stress strain behavior has changed slightly due to the compaction, where increasing the compaction energy changed the behaviour to be more brittle with increasing both unconfined compressive strength, q_{un} and modulus of deformation, E_{50}. The relationship between q_{un} and E_{50} for undisturbed cemented clay has an acceptable matching with the previous test results.

Increasing the compaction energy reflects to increase the soil dry density, however the compaction mechanism can affect by some factors such as high water content and soil particles size especially at low levels of compaction energy.

The relationship between unconfined compressive strength, q_{un} and both dry density and voids ratio affects by many factors such as the cement ratio, water content, and the compaction energy, therefore using the term *e*/*aw* can be more reliable to relate q_{un} with the soil void ratio *e*.

Obtaining a formula for the increasing factor *i* shall be helpful to estimate the value of unconfined compressive strength for disturbed cement clay for different cement ratio, compaction energy, and curing time.

ACKNOWLEDGEMENTS

The first author would like to thank Egyptian Ministry of Higher Education (MoHE) for providing the financial support (PhD scholarship) for this research as well as the Egypt–Japan University of Science and Technology (E-JUST) for offering the facility and tools needed to conduct this work. The first author wishes to express his gratitude to Tokyo Institute of Technology for providing the needed materials and apparatuses where this work would not have been possible without that valuable support.

REFERENCES

[1] Ministry of Transport, The Fifth District Port Construction Bureaus, "Pneumatic flow mixing method", Yasuki Publishers, 157p. (in Japanese).

[2] Kitazume, M., & Hayano, K., " Strength properties and variance of cement-treated ground using the pneumatic flow mixing method", Proc. Institution of Civil Engineers - Ground Improvement, 2007, Vol. 11, No. 1, pp. 21–26.

[3] Kitazume, M. & Satoh, T., "Development of a pneumatic flow mixing method and its application to Central Japan International Airport construction". Proc. Institution of Civil Engineers - Ground Improvement, 2003, Vol. 7, No. 3, pp. 139–148.

[4] Kitazume, M. & Satoh, T., "Quality control in Central Japan International Airport construction", Proc. Institution of Civil Engineers - Ground Improvement, 2005, Vol. 9, No. 2, pp. 59–66.

[5] Japanese Geotechnical Society, "Practice for making and curing stabilized soil specimens without compaction", JGS 0821-2009. Japanese Geotechnical Society. 2009, Vol. 1, pp. 426-434 (in Japanese).

[6] Lorenzo, G. A., & Bergado, D. T.,"Fundamental characteristics of cement-admixed clay in deep mixing", Journal of Materials in Civil Engineering, 2006, Vol. 18, No. 2, pp. 161–174.

Sixth International Conference on Geotechnique, Construction Materials and Environment, Bangkok, Thailand, Nov. 14-16, 2016, ISBN: 978-4-9905958-6-9 C3051

A MODIFIED HARDENING SOIL MODEL FOR ROCKFILL MATERIALS

R. Sukkarak[1], and P. Jongpradist[1]

[1] King Mongkut's University of Technology Thonburi, Bangkok, Thailand

ABSTRACT

The hardening soil (HS) model is widely utilized for simulating the stress-strain behavior for different soil type, because many essential features of rockfills have been included in the hardening soil model (i.e., nonlinearity, stress-dependent stiffness and shear dilatancy). More recently, this model is adopted to characterize the behavior of rockfill materials. However, several significant features of rockfill material have not included in the current model, since the model was originally developed for fine grained soils (i.e., sands and clays). In this paper, an existing HS model is modified for simulating the stress-strain-volumetric strain response of rockfill material. A new hardening parameter, which is the stress-dependent stiffness value, is derived in order to improve the simulation capability. A modification of Rowe's stress-dilatancy theory is proposed to account for the influence of particle breakage. The modified model predicts in very consistent manner with the triaxial response of different type of rockfill materials.

Keywords: Hardening soil model, Rockfill materials, Stress-dependent stiffness value, Rowe's stress-dilatancy theory, Particle breakage

1. INTRODUCTION

Rockfill material is widely used in many geotechnical applications, especially rockfill dams. Based on several experimental studies [1]-[5] it has widely been recognized that (1) the stress-strain behavior of rockfill materials is non-linear and stress dependent, (2) the behavior of the rockfill materials is affected by many factors as mineralogical composition, particles grading, size and shape of particles, (3) the confining pressure is significant that affects to stress-strain behavior of rockfill materials, increase of confining pressure have an influence to increase in deviator stress, axial strain and volumetric strain at failure, (4) the shear dilatancy phenomenon occurs when confining pressure is low. For simulating these behaviors, the preferred constitutive models must be based on an elasto-plasticity theory [6], intense shear dilatancy behaviors of dense granular materials and stress-dependence of stiffness.

The Hardening Soil (HS) model is the one of the kind of an elasto-plasticity model which is extensively used for simulating the stress-strain behavior of many soil types. Several researchers have reported that the HS model can be applied in numerical simulations of rockfill behavior by comparing with the experimental data [7]-[8], and implemented in rockfill dam stress-deformation analyses [9]-[11]. Since, the HS model simulations give a good agreement with experimental result or dam monitoring data. However, some of model parameters are often obtained by the back-calculation method or can be difficult to detemine due to lacking of experimental result (i.e. oedometer test). Although many essential features of rockfills have been included in the HS model (i.e., nonlinearity, stress-dependent stiffness and shear dilatancy), the model was originally developed for soils (i.e., sands and clays) [12]. Based on experimental studies [5], [13], these studies indicated that the particle breakage happen even low confining pressure condition and changes in the particle during shearing. This feature may the result in different behavior between rockfill material and fine grained soils.

In this study, the HS model is developed for simulating the stress-strain-volumetric strain $(q-\varepsilon_1-\varepsilon_v)$ response of rockfill materials. The comprehensive testing results of Nam Ngum 2 rockfill materials, which have been well documented (including triaxial and oedometer tests), are used to investigate the significance of the effects of the stress-dependent stiffness and particle breakage. A modification to Rowe's dilatancy equation is introduced in the current work to account for particle breakage. The capability of the model has been assessed by comparing between the predicted results and test data.

2. HARDENING SOIL MODEL

The Hardening Soil (HS) model has been adopted to characterize the behaviour of different kinds of soil. The HS is the developed constitutive model which has been implemented in the finite element code PLAXIS. The constitutive model associated with the elasto-plastic theory by introducing two yield surfaces as shown in Fig. 1(a). First, the Mohr–Coulomb yield surface f has been specified in the following form:

$$f = \overline{f} - \gamma^{p} \tag{1}$$

$$\overline{f} = \frac{2}{E_i}\frac{q}{1-q/q_a} - \frac{2q}{E_{ur}} \tag{2}$$

$$\gamma^{p} = -(2\varepsilon_1^{p} - \varepsilon_v^{p}) \approx -2\varepsilon_1^{p} \tag{3}$$

where $\overline{f}$ and γ^{p} are the function of stress and plastic strains respectively. The second yield surface (cap yield surface) is taken to close the elastic region in isotropic compression defined as follows:

$$f^{c} = \frac{\tilde{q}^2}{\alpha^2} + p'^2 - p_p^2 \tag{4}$$

Where α is an auxiliary model parameter that is related to K_0^{nc}.

Following [14], a principle hyperbolic function is used to express the stress-strain relations of HS model in primary triaxial loading which can be expressed as:

$$-\varepsilon_1 = \frac{1}{E_i}\frac{q}{1-q/q_a} \text{ for: } q < q_f \tag{5}$$

Here, ε_1 is the vertical strain and q is the deviatoric stress. q_a and E_i are the asymptotic value and the initial stiffness.

For the stiffness dependent, the primary deviatoric loading and primary compression are controlled by E_{50} and E_{oed}, respectively, as shown in Figs. 1(b)-(c):

$$E_{50} = E_{50}^{ref}\left(\frac{c\cos\varphi - \sigma_3'\sin\varphi}{c\cos\varphi + p^{ref}\sin\varphi}\right)^{m} \tag{6}$$

$$E_{oed} = E_{oed}^{ref}\left(\frac{c\cos\varphi - \dfrac{\sigma_3'}{K_0^{nc}}\sin\varphi}{c\cos\varphi + p^{ref}\sin\varphi}\right)^{m} \tag{7}$$

where E_{50}^{ref} and E_{oed}^{ref} are the reference modulus from the triaxial (Secant modulus) and oedometer (Tangent modulus) tests, φ is the friction angle, c is the cohesion, p^{ref} is the reference confining pressure and m is the defined as the power for the stiffness dependent.

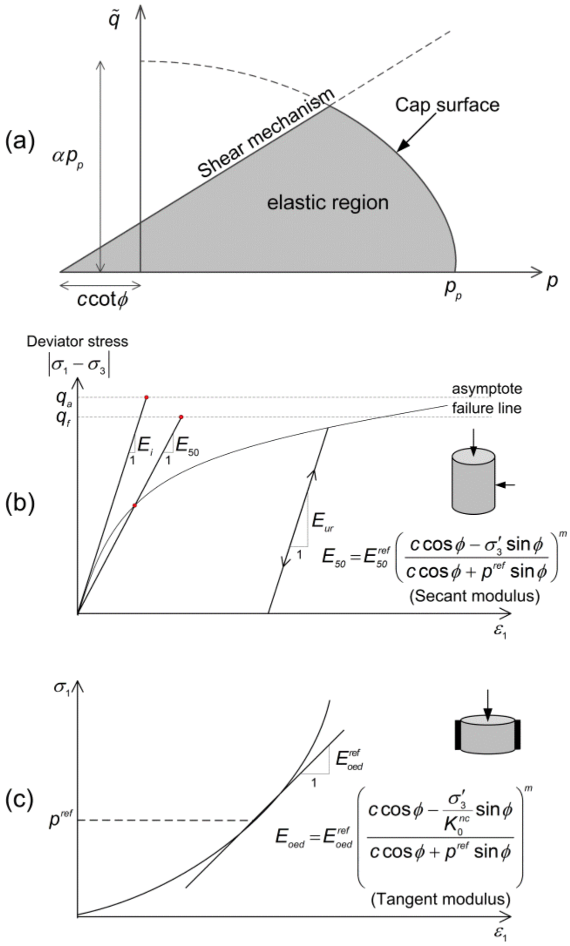

Fig. 1 (a) yield surface of the hardening soil model on the $p-q$ plane (b) stiffness dependent from triaxial test (c) stiffness dependent from oedometer test

The plastic strain increment can be determined following relationship between $\dot{\varepsilon}_v^{p}$ and $\dot{\gamma}^{p}$, and the flow rule is given as:

$$\dot{\varepsilon}_v^{p} = \sin\psi_m \dot{\gamma}^{p} \tag{8}$$

According to the original Rowe's stress-dilatancy theory [15], the dilatancy equation can be written as follows:

$$\sin\psi_m = \frac{\sin\varphi_m - \sin\varphi_{cv}}{1-\sin\varphi_m \sin\varphi_{cv}} \tag{9}$$

where ψ_m is the mobilized dilatancy angle, φ_{cv} and φ_m are the critical state friction angle and the mobilized friction angle respectively.

3. EXPERIMENTAL EVIDENCE AND MODEL MODIFICATION

In the previous section, the detail of HS model has been described. To better adapt the model for application to rockfills, based on experimental data, some additional features of which still have not yet been considered. In this section, several key features were identified and a new constitutive parameter is introduced.

The experimental data (including data from triaxial and oedometer tests) used in this research were based on those for the construction of the Nam Ngum 2 dam by the Institute of Water Resources and Hydropower Research (IWHR) and the Asian Institute of Technology (AIT). The rockfills in this project consisted of blended rockfill materials containing sandstone and siltstone (six types) [16] as listed in Table 1. The confining pressures were varied from 0.5 to 2 MPa in the triaxial tests, whereas a maximum vertical stress of 3.2 MPa was applied in the oedometer tests.

Table 1 Characteristics of rockfill materials used

Type	Materials	Densities (g/cm^3)	D_{max} (mm)
I	Sandstone	2.15	40
II	Sandstone	2.15	60
III	Sandstone	2.15	60
IV	Sandstone: 85%, Siltstone: 15%	2.15	60
V	Sandstone: 70%, Siltstone: 30%	2.10	60
VI	Sandstone: 55%, Siltstone: 45%	2.10	60

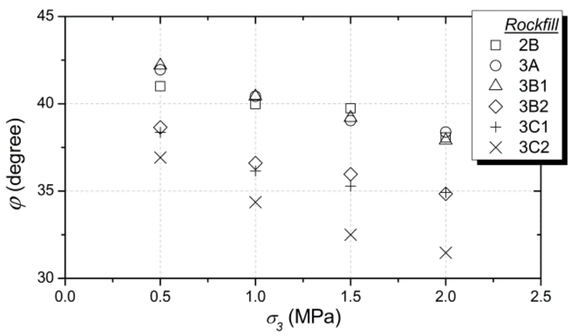

Fig. 2 Relationship between φ and σ_3

First, one of the important features to be considered in rockfill behavior is the variation of φ. Fig. (2) shows the relationship between the φ and σ_3. Inspection of this figure shows that φ decreases with an increasing of σ_3 and can be derived as:

$$\varphi = \varphi_0 - \Delta\varphi \log\left(\frac{\sigma_3'}{p_a}\right) \tag{10}$$

where p_a is the atmospheric pressure, φ_0 is the reference friction angle, and $\Delta\varphi$ is the reduction factor.

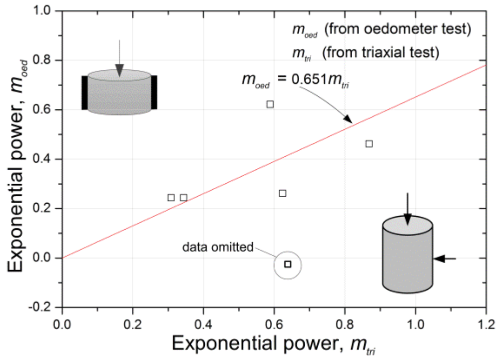

Fig. 3 Relationship between m_{oed} and m_{tri}

Secondly, in this work the new model parameter taking into account the stiffness dependent is derived from the experimental data. As mentioned in previous section, E_{50} and E_{oed} vary with the evolution of the stress state in a power-law form (m). For fine grained soils, m values were approximately the same values corresponding to both triaxial and oedometer tests. The HS model assumes the same degree of evolution with the stress state m for both E_{50} and E_{oed}. The power parameter m is typically determined from the results of triaxial tests and used for both E_{50} and E_{oed}. However, no study has yet discussed the validity of these stiffness moduli for rockfill materials because very few authors have reported data from both triaxial and oedometer tests. As illustrated in Fig. 3, m_{tri} values (from triaxial test) are higher than m_{oed} values (from oedometer test) the relationship of the aforementioned data can be estimated as the linear function as:

$$m_{oed} = 0.651 m_{tri} \tag{11}$$

To take an account for separate degree of stress dependent stiffness, the model constant m_{oed} needed to be defined separately and denoted by n in this study:

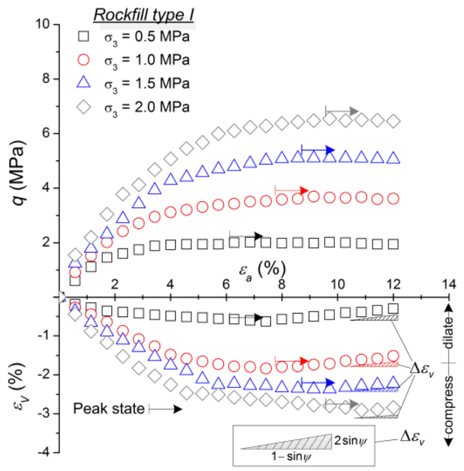

Fig. 4 Rockfill material (type I) observed at various confining pressures

Finally, the present paper presents a simplified method of considering the effect of particle breakage on the dilatancy of rockfill materials. Fig. 4 shows the $q-\varepsilon_1-\varepsilon_v$ response of rockfill materials type I (RF I). Obviously, the $\delta\varepsilon_v / \delta\varepsilon_1$ gradient (dilation) decreases after the peak state with an increasing degree of particle breakage (higher confining pressure). The volumetric strain response of rockfill material under shearing has been directly correlated with the degree of particle breakage [13], [17]. For this present paper, a modification of Rowe's stress-dilatancy equation that incorporates particle breakage behavior is proposed as $\psi_{m,bg}$:

$$\sin\psi_{m,bg} = \frac{(\sin\varphi_m - \sin\varphi_{cv})\cdot(1-B_g^{\lambda})}{1-\sin\varphi_m \sin\varphi_{cv}} \tag{12}$$

where $\psi_{m,bg}$ is the modified mobilized dilatancy angle, B_g is the particle breakage index, and λ is the power-law parameter for breakage. To quantify the particle breakage, the modified definition proposed by Einav (2007) [18] is adopted in this study to represent the change in the particle distribution, as shown in Fig. 5:

$$B_g = \frac{\int_{d_m}^{d_M} [F_u(d)-F_0(d)]\, d(\log d)}{\int_{d_m}^{d_M} [F_c(d)-F_0(d)]\, d(\log d)} \tag{13}$$

where F_0, F_c and F_u are the initial, current and ultimate gradation curves, respectively:

$$F_0(d) = \left(\frac{d}{d_M}\right)^{3-\alpha_0} \tag{14}$$

$$F_c(d) = \left(\frac{d}{d_M}\right)^{3-\alpha_c} \tag{15}$$

$$F_u(d) = \left(\frac{d}{d_M}\right)^{3-\alpha_u} \tag{16}$$

where α_0, α_c and α_u are the fractal dimensions for the initial, current and ultimate gradation curves, respectively, and d, d_m and d_M are the particle diameter, minimum particle diameter and maximum particle diameter, respectively. α_0 and α_c can be determined by fitting the gradation curve before and after the test. For rockfill materials, a value of α_u = 2.7 is generally used [19]. The particle breakage evolution related to plastic work W_p can be defined in terms of a hyperbolic function (see Fig. 6):

$$B_g = \frac{W_p}{\chi + W_p} \tag{17}$$

where W_p can be written in the following form:

$$W_p = \int p' d\varepsilon_v^p + q d\varepsilon_s^p \tag{18}$$

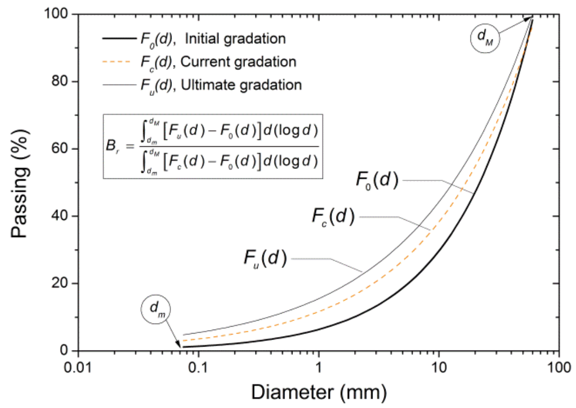

Fig. 5 Definition of the particle breakage index [18]

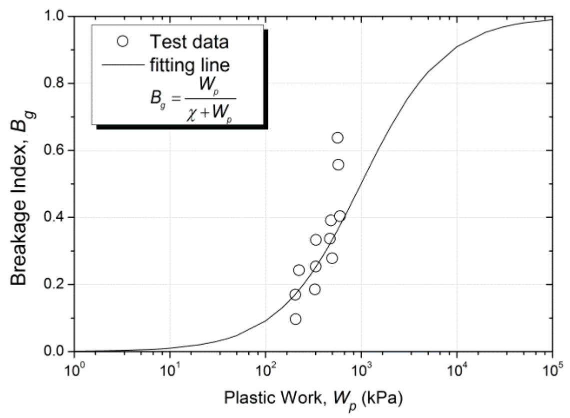

Fig. 6 Relationship between B_g and W_p

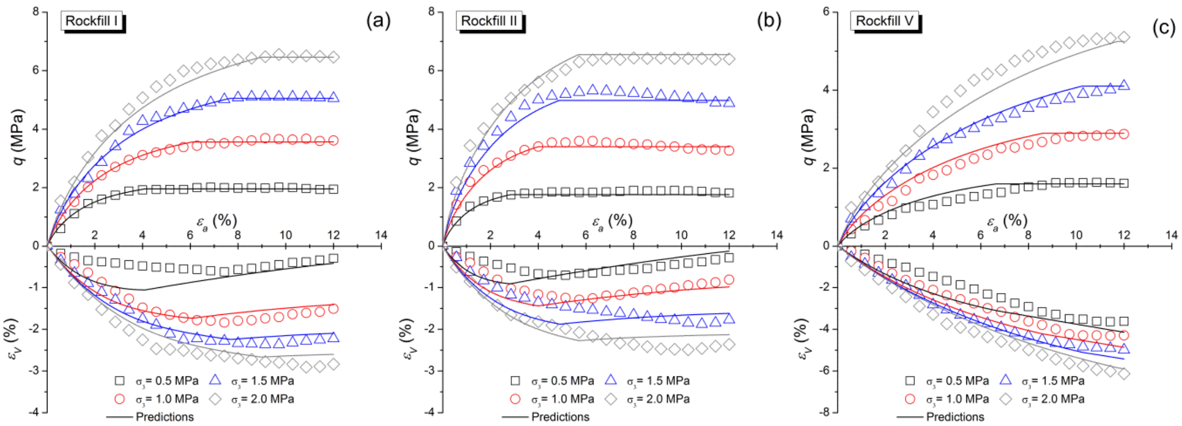

Fig. 7 Model predictions and triaxial test results

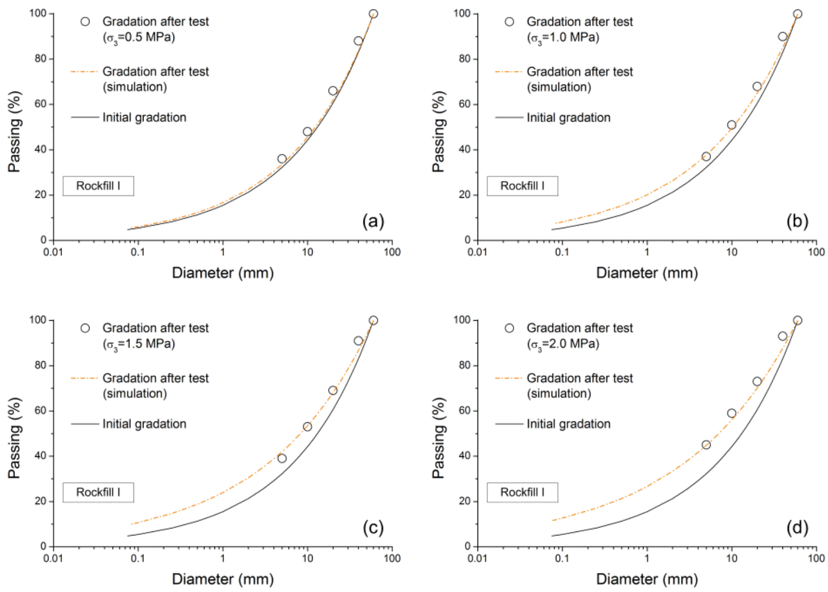

Fig. 8 Model predictions and evolution of the particle distribution after the test

Table 2 Model parameters used for this study

Parameter	Type					
	I	II	III	IV	V	VI
φ_0 (degree)	46.08	43.23	47.09	42.60	42	43.30
$\Delta\varphi$	2.59	1.16	2.99	2.55	2.45	3.95
ψ_0 (degree)	3.2	3.2	3.2	0.5	-5	-5
E_{50}^{ref} (MPa)	65	65	80	32	20	12
E_{oed}^{ref} (MPa)	52	50	55	24	17	10
m	0.34	0.45	0.29	0.69	0.68	0.70
n	0.24	0.25	0.14	0.42	0.32	0.26
R_f	0.75	0.74	0.78	0.82	0.68	0.65
Other	$E_{ur}^{ref} = 3E_{50}^{ref}$, $p^{ref} = 100$ kPa, $c = 1$ kPa, $OCR = 1$, $K_0^{NC} = 1 - \sin\varphi$, $\upsilon_{ur} = 0.3$					
Breakage parameter	$\chi = 993$, $\lambda = 0.268$					

4. CALIBRATION

In this current study, the modified model was implemented in the ABAQUS program through a user-defined material subroutine (UMAT). The 1-element FEM simulation was performed in order to demonstrate the validity and the capability of the modified constitutive model. The model parameters for NN2 rockfill materials used in FEM simulation are listed in Table 1.

Figs. 7(a)-(c) show the comparisons between the predicted results and test data for different rockfill types and confining pressures. The test data are presented by the symbols for each confining levels, while the predicted results are displayed by the solid lines. For overall comparisons, there is a good agreement between the predicted results and test data. In additions, for the evolution of the particle distribution (RF I) for various confining pressures (after test), the comparisons show that the prediction is generally satisfactory as illustrated in Figs. 8(a)-(d).

5. CONCLUSIONS

In this study, an existing HS model is modified for simulating the stress-strain-volumetric strain response of rockfill material. The comprehensive testing results of Nam Ngum 2 rockfill materials are used to investigate the significance of the effects of the stress-dependent stiffness and particle breakage. Based on the previous statement and observation, according to the HS model was originally developed for fine grained soils. For rockfill materials, the model is developed by taking into account following features:

- The friction angle decreases following an increasing of confining pressure.
- The degree of stress dependent stiffness values (for triaxial and oedometer tests) separately and defined by the new hardening parameter.
- A modification of Rowe's stress-dilatancy theory is proposed to account for the influence of particle breakage in conjunction with the particle breakage index (B_g) developed by Einav (2007).

The validation of the modified model was confirmed by the comparing between the predicted results and experimental data. Overall comparisons, the modified model is able to predict reasonable well a $q-\varepsilon_1-\varepsilon_v$ response of rockfill materials.

ACKNOWLEDGEMENTS

The authors gratefully acknowledge the financial support of the Thailand Research fund (TRF) and King Mongkut's University of Technology Thonburi through the Royal Golden Jubilee Ph.D. program, under contract grant PHD/0006/2556. The authors also extend their appreciation to the Office of the Higher Education Commission for granting financial support through the Higher Education Research Promotion and National Research University (NRU) Project of Thailand. They are also indebted to the CK Power Public Company Limited and Nam Ngum 2 Power Company Limited for providing the valuable data.

REFERENCES

[1] Marsal RJ, "Large Scale Testing of Rockfill Materials" Journal of Soil Mechanics and Foundation Engineering Division, ASCE, Vol. 93, No. SM2, 1967, pp. 27–43.

[2] Marachi ND, Chan CK, Seed HB and Duncan JM, "Strength and deformation characteristics of rockfill materials" Rep. No. TE 69-5, Civil Engineering Dept., Univ. of California, Berkeley, California, 1969.

[3] Charles JA and Watts KS, "The influence of confining pressure on the shear strength of compacted rockfill" Géotechnique, Vol. 30. No. 4, 1980, pp. 353–367.

[4] Thiers GR and Donovan TD, "Field density gradation and triaxial testing of large-size rockfill for little blue run dam" Laboratory Shear Strength of Soil, ASTM, STP, 740, R. N. Yong and F. C. Townsend, eds., ASTM, Philadelphia, 1981, pp. 315–325.

[5] Varadarajan A, Sharma K, Venkatachalam K and Gupta A, "Testing and modeling two rockfill materials." *Journal of Geotechnical and Geoenvironmental Engineering*, Vol. 129, No. 3, 2003, pp. 206–218.

[6] Zhang G, Zhang JM and Yu Y, "Modeling of Gravelly Soil with Multiple Lithologic Components and its Application," *Soils and Foundations*, Vol. 47, No. 4, 2007, pp. 799-810.

[7] Loupasakis CJ, Christaras BG, Dimopoulos GCh and Hatzigogos TN, "Evaluation of plasticity models ability to analyze typical earth dams soil materials." *Geotechnical and Geological Engineering*, Vol. 27, No. 1, 2009, pp. 71–80.

[8] Araei A, "Artificial Neural Networks for Modeling Drained Monotonic Behavior of Rockfill Materials." *International Journal of Geomechanics*, Vol. 14, No. 3, 2014, 04014005.

[9] Özkuzukiran S, Özkan MY, Özyazicioğlu M and Yildiz, GS, “Settlement behaviour of a concrete faced rock-fill dam.” *Geotechnical and Geological Engineering*, Vol. 24, 2006, pp. 1665–1678.

[10] Soroush A and Araei AA, “Analysis of behaviour of a high rockfill dam.” *Proceedings of the ICE - Geotechnical Engineering*, Vol. 159, No. 1, 2006, pp. 49-59.

[11] Mahabad NM, Imam R, Javanmardi Y and Jalali H, “Three-dimensional analysis of a concrete-face rockfill dam”, *Proceedings of the ICE - Geotechnical Engineering*, Vol. 167, No. 4, 2014, pp. 323-343.

[12] Schanz T, Vermeer PA and Bonnier PG, “The hardening soil model – formulation and verification.” *Proceedings Plaxis Symposium "Beyond 2000 in Computational Geotechnics*, Amsterdam, Rotterdam, Balkema, 1999.

[13] Xiao Y, Liu H, Chen Y and Jiang J, “Strength and Deformation of Rockfill Material Based on Large-Scale Triaxial Compression Tests. I: Influences of Density and Pressure” *Journal of Geotechnical and Geoenvironmental Engineering*, Vol. 140, No. 12, 2014, .04014070

[14] Duncan JM and Chang CY, “Nonlinear analysis of stress-strain in soils”, *Journal of the Soil Mechanics and Foundations Division*, ASCE, Vol. 96, No. 5, 1970, pp. 1629–1653.

[15] Rowe PW, "The Stress-Dilatancy Relation for Static Equilibrium of an Assembly of Particles in Contact." *Proceedings of The Royal Society A*, Vol. 269, 1962, pp. 500-527.

[16] IWHR., *Report on Laboratory Tests of the Rockfill Materials of Nam Ngum 2 CFRD*. Institute of Water Resources and Hydropower Research, Beijing, China, 2007.

[17] Liu H and Zou D, “Associated Generalized Plasticity Framework for Modeling Gravelly Soils Considering Particle Breakage.” *Journal of Engineering Mechanics*., Vol. 139, No. 5, 2013, pp. 606–615.

[18] Einav I, "Breakage mechanics-Part II: modelling granular materials." *Journal of the Mechanics and Physics of Solids*, Vol. 55, No. 6, 2007, pp. 1298-1320.

[19] Yang ZY and Juo JL, "Interpretation of sieve analysis data using the box-counting method for gravelly cobbles." *Canadian Geotechnical Journal*, Vol. 38, No. 6, 2001, pp.1201-1212.

Sixth International Conference on Geotechnique, Construction Materials and Environment, Bangkok, Thailand, Nov. 14-16, 2016, ISBN: 978-4-9905958-6-9 C3051

LONG TERM MECHANICAL AND LOAD TRANSMISSION PROPERTIES OF SOIL-CONCRETE BLOCK

Kayo Doumoto[1], Kiyonobu Kasama[2], Mitsunari Hirasawa[2], Kouki Zen[2], Zentaro Furukawa[2], Yuichi Yahiro[2], Masato Nakamichi[3], Makoto Yamaguchi[3], Takashi Umeyama[3], Masaaki Katagiri[4], Osamu Kawahara[5] and Toshiyuki Nagano[6]

[1]Graduate School of Engineering, Kyushu University, Japan; [2]Division of Civil and Structural Engineering, Faculty of Engineering, Kyushu University, Japan; [3]Ministry of Land, Infrastructure, Transport and Tourism, Kitakyushu, Japan; [4]Nikken Sekkei Civil Engineering Ltd., Japan; [5]Coastal Development Institute of Technology, Japan; [6]Rinkai Construction Co., Ltd., Japan

ABSTRACT

In order to recycle dredged soil, our research group developed interlocking blocks from dredged soil. Dredged soil interlocking blocks (350 mm in width, 350 mm in depth and 100 mm-150 mm in height) were made from soft clay dredged from the Kanmon Waterway. They were produced with the constant dewatering pressure 5 MPa and cement content of 15 %, 20 % and 25 % per the dry weight of clay. The unconfined compression test was carried out to investigate material characteristics of dredged soil interlocking blocks in the water for six months and one year respectably. In order to check the effect of interlocking blocks, a road was constructed by using interlocking blocks on the surface. As a roadbed material, dredged and dewatered soil and crushed stone for mechanical stabilization were used. Characteristics of dispersion of traffic load and settlement were evaluated by running experiments. Stress was measured by four earth pressure gauges and settlement was measured. The following conclusions are obtained: (1) There was close relationship between unconfined compressive strength and water-cement ratio. The correlation became stronger with curing period. (2) Dredged and dewatered soil can disperse traffic load effectively. (3) When using crushed stone for mechanical stabilization as roadbed material, soil-concrete blocks can disperse traffic load effectively after one year from the construction. When using dredged and dewatered soil as roadbed material, sinking suppressing effect was observed.

Keywords: Soil, Cement, Unconfined compressive strength, Stress, Settlement

INTRODUCTION

The soft clay piled on the bottom of the ocean or bay is problematical against the in-service of ship navigation. This soft clay is regularly dredged out, but the shortage of disposal sites has become a serious problem.

At the Kanmon Waterway, an important international seaway, dredging work is carried out for deepening seabed every year. Dredged soil is transported to Shinmojioki disposal site, but the capacity will be full in the middle of 2018 [1]. Construction of new disposal site is inevitably necessary, but it takes time.

In order to recycle dredged soil, our research group has conducted basic study and Yamashita et al. [2] succeeded making soil block (Φ 53.4 cm × H 50 cm) that has strength equals to concrete from dredged soil.

In this study, we developed interlocking blocks from dredged soil. Cement was mixed with soft clay dredged from the Kanmon Waterway and the mixture was dewatered. To investigate mechanical properties, the unconfined compression test was carried out on interlocking blocks after immersed in the water for six months and one year. A road was constructed by using interlocking blocks on the surface and characteristics of dispersion of traffic load and the settlement were evaluated by running experiments.

EXPERIMENT OUTLET

Material Experiment

The material used in this study is soft clay dredged from the Kanmon Waterway (called Kanmon clay). The physical properties of Kanmon clay is shown in Table 1.

Table 1 Physical properties

	Kanmon clay
Soil particle density ρ_s (g/cm^3)	2.697
Liquid limit w_L (%)	95.0
Plastic index I_p (%)	59.1

Cement content is 15 %, 20 % and 25 % of blast furnace slag cement type B per the dry weight of clay. The test conditions are shown in Table 2.

Kanmon clay was prepared with initial water content of 300 % and mixed with cement. The mixture was poured into the dewatering equipment (*W* 350 mm × *D* 350 mm × *H* 1000 mm) shown in Fig. 1.

Table 2 Test conditions

Clay	Kanmon clay
Cement type	Blast furnace slag cement type B
Cement content	15, 20, 25 %
Dewatering mode	2 MPa: 30 min. → 5 MPa: 265 ~ 755 min.
Initial water content	300%
Curing condition	Water curing (Temperature: 20℃)
Curing period	6 months, 1 year

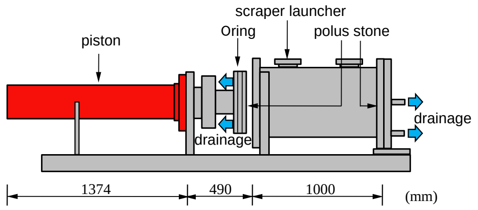

Fig. 1 The dewatering equipment

The mixture was dewatered with dewatering pressure of 2 MPa for 30 min. followed by constant dewatering pressure of 5 MPa. In order to investigate material characteristics, the unconfined compression test (JIS A 1216) was carried out.

Running Experiment

The sectional view of road is shown in Figure 2 and the horizontal projection of road is shown in Figure 3.

The earth pressure gauges were set in base course for measuring vertical earth pressure. After spreading each layer (20 cm), pressure was given 8 times by rolling machine (4 t.). These works were repeated 5 times and roadbed of 1 meter in height was constructed. Dredged and dewatered soil (called "dewatered soil) and crushed stone for mechanical stabilization (called "crushed stone") were used as roadbed materials. On the surface of the road, soil blocks were used as interlocking blocks. The earth pressure gauges were set in four points to investigate differences of roadbed materials and to check the effect of interlocking

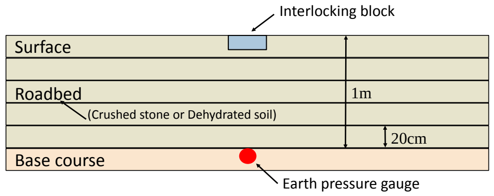

blocks. Loaded cars and empty cars were used as traffic loads. The settlement was measured.

Fig. 2 The sectional view of road

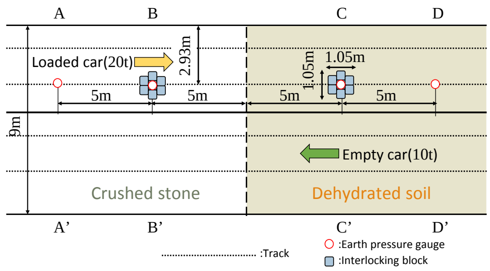

Fig. 3 The horizontal projection of road

STRENGTH PROPERTY

Figure 4 shows the relationship between unconfined compressive strength and cement content. Unconfined compressive strength cured for 6 months increased with increasing cement content. Average unconfined compressive strength for cement content of 20 % was 8.06 MPa (Curing period 6 months) and 10.80 MPa (Curing period 1 year). Unconfined compressive strength increased with curing period because of solidification of cement.

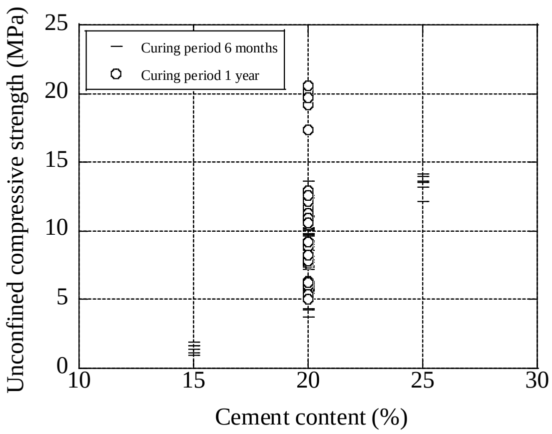

Fig. 4 Unconfined compressive strength and cement content

Figure 5 shows the relationship between unconfined compressive strength and dry density. Change of dry density by passage of curing period wasn't observed much. Unconfined compressive strength increased with increasing dry density regardless of cement content. From this, increase of unconfined compressive strength is related to not only density but also solidification of cement. Increase of unconfined compressive strength by curing period was observed remarkably with high dry density for cement content of 20 %.

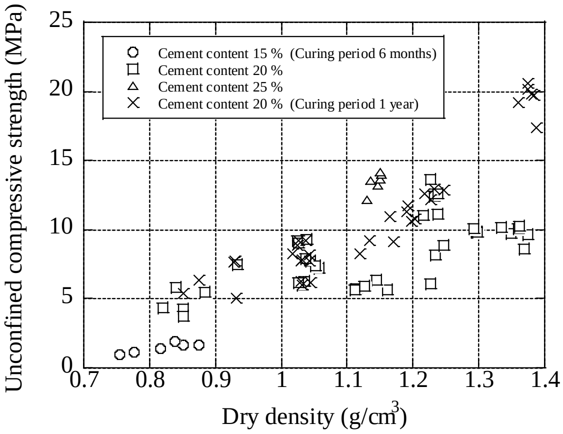

Fig. 5 Unconfined compressive strength and dry density

Figure 6 shows the relationship between unconfined compressive strength and water content. Change of water content by passing of curing period wasn't observed much. Unconfined compressive strength decreased with increasing water content regardless of cement content. This is because of water left as gap. Increase of unconfined compressive strength by passing of curing period was observed remarkably with low water content for cement content of 20 %.

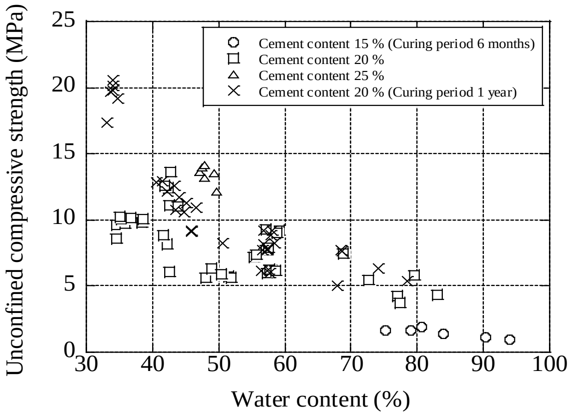

Fig. 6 Unconfined compressive strength and water content

The relationship between unconfined compressive strength and water-cement ratio is shown in Figure 7. In this paper, the water-cement ratio is defined as weight ratio of water and cement. Unconfined compressive strength increased with decreasing water-cement ratio. Following equations between unconfined compressive strength and water-cement ratio for cement content of 20 % were obtained:

$$q_{u6month} = 17.71(w/c)^{-0.912} \tag{1}$$

$$q_{u1year} = 39.22(w/c)^{-1.517} \tag{2}$$

Eq. (1) shows the result of relationship between unconfined compressive strength and water-cement ratio of soil blocks cured for 6 months. Eq. (2) shows the result of cured for 1 year. q_u is the unconfined compressive strength and *w/c* is the water-cement ratio. The coefficient of correlation R in Eq. (1) and Eq. (2) were 0.69 and 0.96 respectively. Correlation became stronger with curing period.

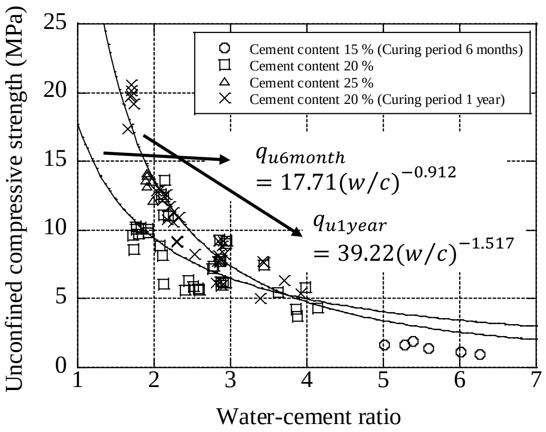

Fig. 7 Unconfined compressive strength and water-cement ratio

LOAD TRANSMISSION

Figure 8 shows the relationship between height of roadbed and vertical stress measured in base course when constructing roadbed. As the height of roadbed grew, vertical pressure increased linearly. Increasing rates of stress were 27.96 kPa/m (crushed stone) and 3.91 kPa/m (dewatered soil). The increasing rate of vertical stress for crushed stone was 7 times higher than that of dewatered soil. The increasing rates of stress calculated by wet unit weight were 17.36 kPa/m (crushed stone) and 11.23 kPa/m (dewatered soil). Therefore, it is considered that dewatered soil can disperse traffic load effectively.

Fig. 8 Height of roadbed and vertical stress

The relationship between vertical stress and running frequency right after the construction and after one year from the construction are shown in Figure 9 and Figure 10 respectively. From Fig. 9, vertical stress was about 30 kPa smaller when dewatered soil was used as roadbed compare to the case when crushed stone was used. And the vertical stress became larger when soil blocks were set on the surface of the road. Vertical stress where blocks were set on the surface was 1.04 times (crushed stone) and 2.83 times (dewatered soil) larger compare to where no block was set on the surface [3]. From Fig. 10, vertical stress became smaller when using soil blocks on the surface and crushed stone was used as roadbed. Vertical stress where blocks were set on the surface was 0.85 times (crushed stone) and 1.97 times (dewatered soil) larger compare to where with no block setting on the surface. From Fig. 9 and 10, change of vertical stress wasn't observed much when using dewatered soil as roadbed and negative pressure wasn't measured one year from the construction. This is because of stability of the foundation.

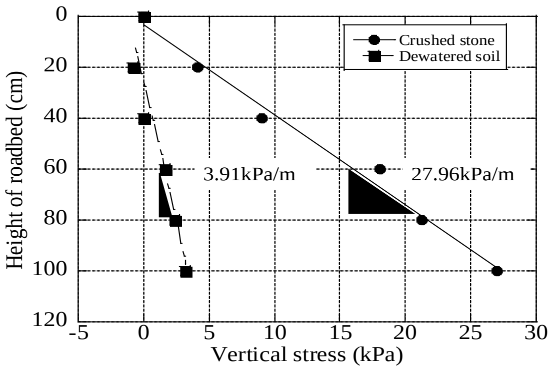

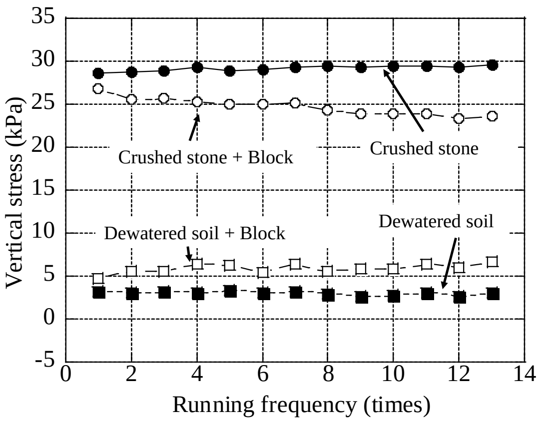

Fig. 9 Running frequency and vertical stress (right

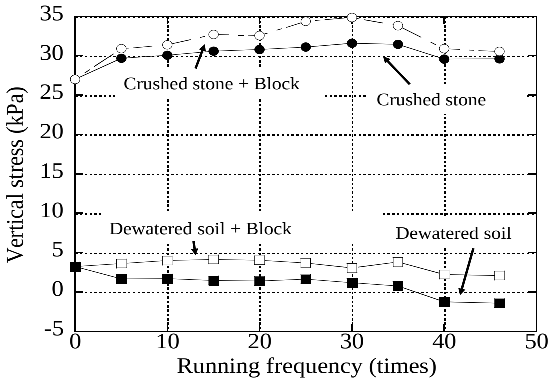

after the construction)

Fig. 10 Vertical stress and running frequency (after one year from the construction)

The relationship between traffic stress amplitude and running frequency right after the construction and after one year from the construction are shown in Figure 11 and Figure 12 respectively. Traffic stress amplitude is defined as the gap of maximum stress and minimum stress measured by traffic load. Fig. 11 shows that traffic stress amplitude increases where with block setting on the surface. Traffic stress amplitude tended to decrease due to increase of traffic frequency. The traffic stress amplitude was smaller when dewatered soil was used as roadbed compare to the case when crushed stone was used [3]. From Fig. 12, traffic stress amplitude also increased when setting blocks on the surface. Traffic stress amplitude where with blocks on the surface was 2.32 times (crushed stone) and 3.09 times (dewatered soil) larger compare to when setting no block on the surface. Traffic stress amplitude tended to converge constant value compare to Fig. 11 and deference of whether soil blocks were set or not could observe clearly.

Fig. 11 Traffic stress amplitude and running frequency (right after the construction)

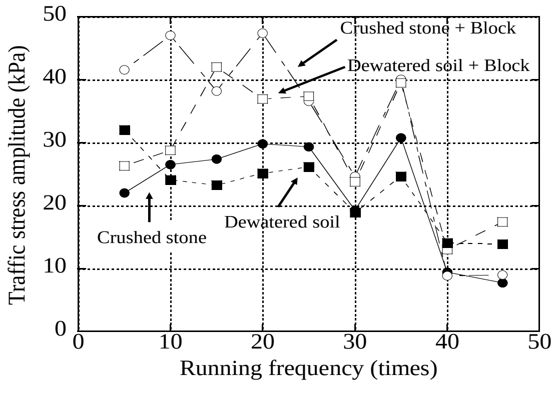

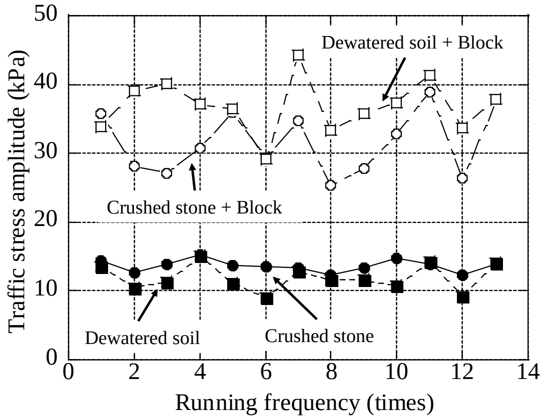

Fig. 12 Traffic stress amplitude and running frequency (after one year from the construction)

The relationship between settlement and running frequency just after the construction is shown in Figure 13. The settlement increased with the increase of running frequency. Especially, the settlement was large when dewatered soil was used as roadbed. The effect of soil block could not be confirmed when using crushed stone as roadbed material, but when using dewatered soil, soil block reduced the settlement more than 1 cm. This is because of occlusion of blocks.

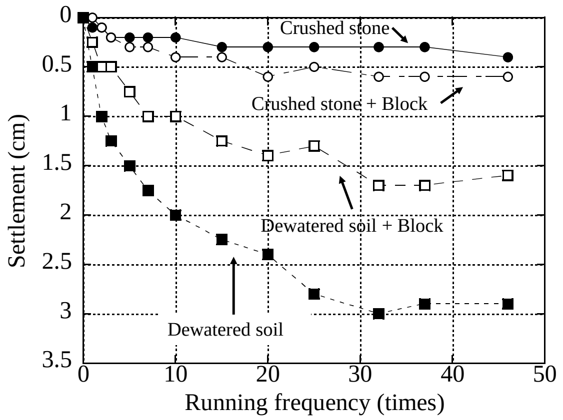

Fig. 13 Settlement and running frequency (just after the construction)

CONCLUSION

In order to investigate mechanical and load properties of soil interlocking blocks, the unconfined compressive strength was examined and running experiments were carried out. The following conclusions are obtained: 1) There was close relationship between unconfined compressive strength and water-cement ratio. The correlation became stronger by passage of curing period. 2) Dredged and dewatered soil can disperse traffic load effectively. 3) When using crushed stone for mechanical stabilization as roadbed material, soil-concrete blocks can disperse traffic load effectively after one year from the construction. When using dredged and dewatered soil as roadbed material, sinking suppressing effect was observed.

ACKNOWLEDGEMENTS

We appreciate the generous support received from SCOPE for research development of this study. We gratefully acknowledge the “Shin-Mojioki disposal site construction project III technology investigative commission” for their professional advice. We also express our deepest gratitude to all who were involved in this study for their time and help.

REFERENCES

[1] Ministry of Land, Infrastructure, Transport and Tourism Kyushu Regional Development Bureau, “Shin-Mojioki Disposal Site (Second Period) Public Ownership Water Surface Land Fill Project Environmental Impact Assessment Preliminary Documents”, 2015, 2-1.

[2] Yamashita Y, Kasama K, Zen K and Chen G, “Dehydration and Strength Properties of Cement-mixed and Dehydrated Clay”, The International Conference on Advances in Geotechnical Engineering (ICAGE 2011), 2011, pp. 151–155.

[3] Doumoto K, Kasama K, Hirasawa M, Zen K, Furukawa Z, Yahiro Y, Nakamichi M, Sakamoto M, Ueda T, Katagiri M, Yamamoto S, Kawahara O, and Nagano T, “Mechanical and Load Transmission Properties of Soil-concrete Block”, 6th Japan-China Geotechnical Symposium, 2015.

Sixth International Conference on Geotechnique, Construction Materials and Environment, Bangkok, Thailand, Nov. 14-16, 2016, ISBN: 978-4-9905958-6-9 C3051

EFFECTS OF VERTICAL WALL BARRIER DUE TO RIGID PAVEMENT DEFLECTION OF FULL SCALE 1-PILE ROW NAILED-SLAB SYSTEM ON SOFT SUB GRADE BY COMPRESSION LOADINGS

Anas Puri[1,a], Hary C. Hardiyatmo[2,b], Bambang Suhendro[2,c], Ahmad Rifa'i[3,d]

[1]Associate Professor Department of Civil Engineering, Islamic University of Riau, Indonesia
[2]Professor Department of Civil and Environmental Engineering, Gadjah Mada University, Indonesia
[3]Associate Professor Department of Civil and Environmental Engineering, Gadjah Mada University
[a]anaspuri@eng.uir.ac.id, [b]harychistady@yahoo.com, [c]bbsuhendro@yahoo.com, [d]ahmad.rifai@ugm.ac.id

ABSTRACT

The weaker part of rigid pavement when it is loaded is the edge of slab. Vehicle wheels that are often running in/out from/to pavement can cause void in the sub base-pavement interface for a long time loading period. Flexural moment caused by temperatures also precipitate the damages of pavement edge. To avoid the damage of pavement edge, the vertical wall barrier is added. This research is aimed to learn the contribution of vertical wall barrier on the pavement of Nailed-slab System to reduce the slab deflection. Full scale observation was done over models in soft clay soil. The full scale of 1 pile row Nailed-slab System was conducted on soft clay which consisted of 6.00 m x 1.20 m slab area with 0.15 m in slab thickness, 5 short micro piles (0.20 m in diameter, 1.50 m in length, and 1.20 m in pile spacing) as slab stiffeners which were installed under the slab. Piles and slab were connected monolithically, then in due with vertical concrete wall barrier on the two ends of slab. The system was loaded by compressive loadings on the center and the end of slab. Deflection of model without vertical wall barrier was analyzed by finite element method. Results show that the vertical wall barrier cannot significantly reduce the deflection for edge loading. It is opposite to the model test result from Puri, et.al. [1] where the vertical wall barrier can reduce 74% deflection for edge loadings. It is to be expected that numerical application program could not model the vertical wall barrier which lower position than slab level.

Keywords: rigid pavement, soft clay, Nailed-slab System, vertical wall barrier, deflection.

INTRODUCTION

The edge of a rigid pavement is the weaker part in bearing the traffic load. This part tends to get maximum deflection and to damage the pavement such as broken pavement, developed voids between sub grade and pavement, and can be followed by pumping. The edge of rigid pavement is also the weaker part in the Nailed-slab System [1]. Hence, in this research the edge of the pavement is reinforced by a vertical wall barrier. Furthermore, the behavior of Nailed-slab System and the contributions of vertical wall barrier will be studied.

A vertical wall barrier is usually reinforced concrete that is 10 cm – 20 cm in thickness and it is conducted in a vertical position that is 40 cm – 50 cm in height. Figure 1 shows an example of a vertical wall barrier. Some benefits of a vertical wall barrier are [2]: (1) it acts as a slab stiffener for edge of pavement because this part will be a weaker part of pavement, (2) to avoid the void between sub grade and pavement due to the effect of the tires which often exit/ enter to/ from pavement, (3) to reduce the disturbing on berm, and (4) as a vertical wall barrier to isolate the negative effects of water changing in sub grade. It prevents the water infiltration to the soil under the pavement slab.

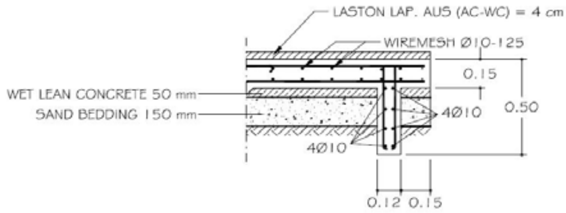

Fig. 1 An example of vertical wall barrier [3] (The Indonesian Research and Development Center for Highway and Bridge, 2007)

Puri, et.al. [1] (2011) conducted the 1-pile row Nailed-slab model tests on the soft clay to learn the effects of vertical wall barrier. The vertical wall barrier can reduce deflection 34% and 74% for concentric and edge loadings respectively.

This paper is aimed to discuss the comparison of the slab deflection behavior between the Nailed-slab with a vertical wall barrier and without a vertical wall barrier. The Nailed-slab models consider the vertical wall barrier on each end of the slab. The experimental study was conducted by full scale model tests of one row pile Nailed-slab system and analyzed by finite element method.

INVESTIGATED 1-PILE ROW FULL SCALE NAILED-SLAB

Detail of the procedure on 1-pile row full scale Nailed-slab is presented in Puri, et.al. [4] and briefly described in Puri, et.al. [5]. In this paper, it will be presented again comprehensively.

Soil Pond and Materials

A full scale model of Nailed-slab was conducted on soft clay. A 6 m x 3.6 m soil pond was conducted by digging the existing soil until the depth of 2.5 m. On the two longer sides it was retained by masonry walls and supported by some temporarily bamboo girder. The anchorage system was built near the pond. Separator sheets were set on the pond walls and base to avoid the effects of surrounding existing soils. A 2.15 m of pond depth was filled by soft clay which was taken from District Ngawi, East Java, Indonesia. The soft clay properties are presented in Table 1. The slab and piles were reinforced concrete. The concrete strength characteristic of the slab and piles was 29.2 MPa and 17.4 MPa respectively. The flexural strength of the slab was 4,397.6 kPa.

Dimension of Nailed-slab Prototype

The Nailed-slab System Prototype dimension was 6.00 m × 3.54 m, 0.15 m in slab thickness, and the slab was reinforced by micro piles 0.20 m in diameter and 1.50 m in length. The spacing between piles was 1.20 m. This model was obtained by cutting the 600 cm × 354 cm × 15 cm Nailed-slab to 3 parts where each part consisted of one pile row. The tested 1 pile row Nailed-slab was the middle one with slab dimension 600 cm × 120 cm × 15 cm as shown in Figure 2. All piles were installed under the slab and connected monolithically by using thickening slab connectors (0.40 m × 0.40 m and 0.20 m in thickness). Each end of slab is equipped by the vertical concrete wall barrier. There was a 5 cm lean concrete thickness under the slab. The slab was loaded by compression loadings with different load positions. Loads were transfered to the slab surface by using a circular plate 30 cm in diameter (the plate represents the wheel load contact area). Then the instrumentations were recorded. Details about testing procedure is presented in Puri, et.al. ([4], [5]). Some photographs in construction and testing are presented in Fig. 2.

Table 1 Soft Clay Properties [4]

Parameter	Unit	Average
Spesific gravity, G_s	-	2.55
Consistency limits:		
- Liquid limit, *LL*	%	88.46
- Plastic limit, *PL*	%	28.48
- Shrinkage limit, *SL*	%	9.34
- Plasticity index, *PI*	%	59.98
- Liquidity index, *LI*	%	0.36
Natural water content, w_n	%	50.49
Water content, *w*	%	54.87
Clay content	%	92.93
Sand content	%	6.89
Bulk density, γ	kN/m^3	16.32
Dry density, γ_d	kN/m^3	10.90
Undrained shear strength, s_u		
- Undisturbed	kN/m^2	20.14
- Remolded	kN/m^2	11.74
CBR	%	0.83
Soil classification:		
- AASHTO	-	A-7-6
- USCS	-	CH

Analysis of Deflections

In the 2D finite element analysis (FEM), Mohr-Coulomb soil model was employed in the study. Likewise, soil parameters and idealization of structural elements are presented in Table 2 and 3, respectively. The material properties were adjusted due to the plain strain case [6]. The slab width is 120 cm and the length of considered section is 20 cm (perpendicular to cross section). Numerical analysis was conducted by 2D Plaxis version 8.6. The soft clay was modeled by Mohr-Coulomb in undrained condition. All structural elements were modeled by plate element in linear-elastic behavior. Lean concrete was modeled by soil with linear-elastic non-porous material. The thickening slab was ignored since it could not be modeled by numerical application program.

The used mesh in plain strain FEM analysis is shown in Fig. 3. Fig. 4 shows one of deformed shape outputs.

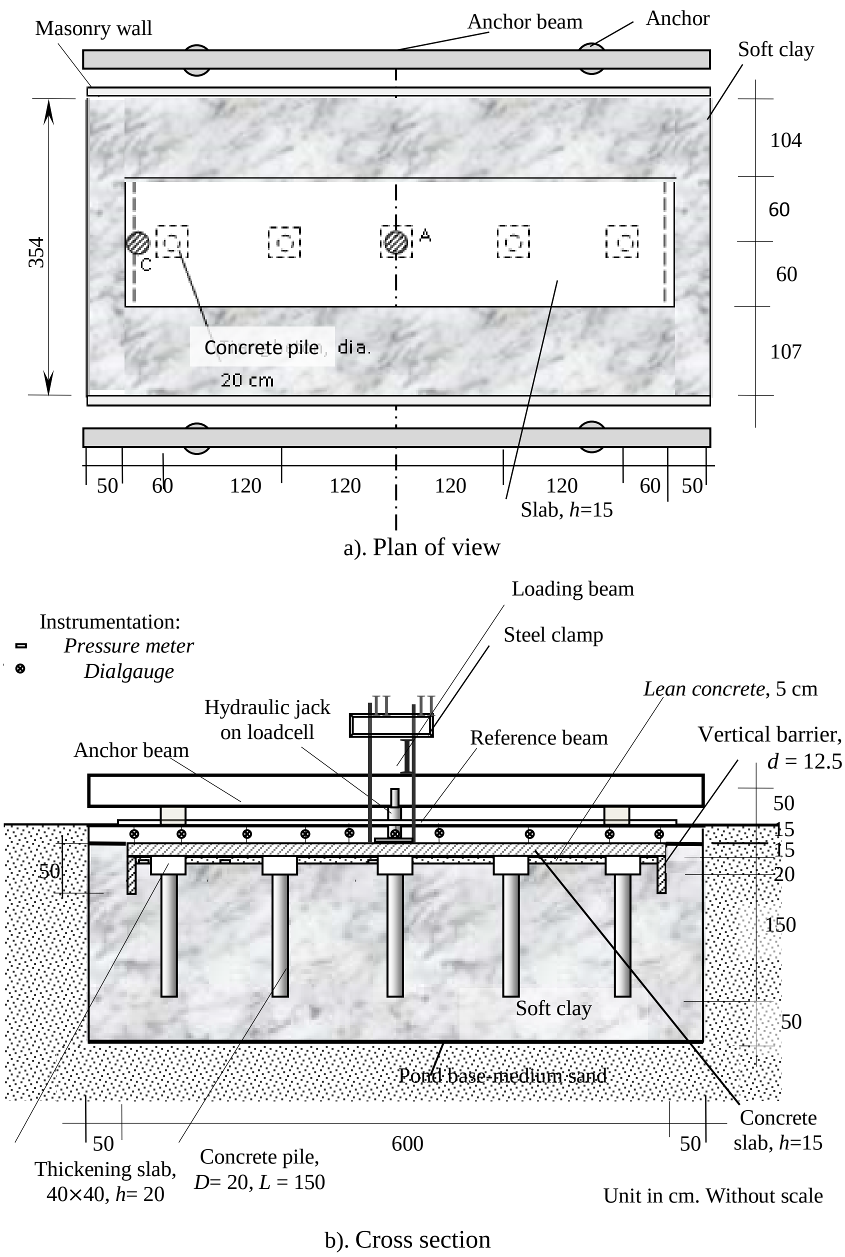

Fig. 2 Schematic diagram of full scale Nailed-slab with 1 pile row.

Table 2 Model and parameters of soil

Parameters	Name/ Notation	Soft clay	Sand	Unit
Material model	Model	Mohr-Coulomb	Mohr-Coulomb	-
Material behavior	Type	*Undrained*	*Drained*	-
Saturated density	γ_{sat}	16.30	18.00	kN/m^3
Dry density	γ_d	10.90	20.00	kN/m^3
Young's Modulus	E	1,790.00	42,750.00	kPa
Poisson's ratio	v	0.45	0.35	-
Undrained cohesion	c_u	20.00	1.00	kPa
Internal friction angle	ϕ	1.00	47.80	^{o}
Dilatancy angle	ψ	0.00	2.00	^{o}
Initial void ratio	e_0	1.19	0.50	-
Interface strength ratio	R	0.80	0.70	

Table 3 Model and parameters of structural elements in FEM 2D plain strain

Parameters	Name/ Notation	Lean concrete (LC)	Structural elements			Unit
			Slab	Vertical wall barrier	Pile	
Material model	Model	Volume element	*Plate*	*Plate*	*Plate*	-
Material behavior	Type	Elastic	Elastic	Elastic	Elastic	-
Normal stiffness	*EA*	-	4,554,000	3,795,000	616,696	kN/m
Flexural rigidity	*EI*	-	8,539	4.941	75,655	kNm^2/m
Equivalent thickness	*d*	-	0.15	0.125	0,027	m
Weight	*w*	-	3.60	3.00	29.12	kNm/m
Poisson's ratio	v	0.2	0.15	0.15	0.20	-
Density	γ	22	24	24	24	kN/m^3
Young's Modulus	*E*	17,900	25,300	25,300	19,600	MN/m^2
Interface strength ratio	*R*	0.80	0.80	0.80	0.80	-

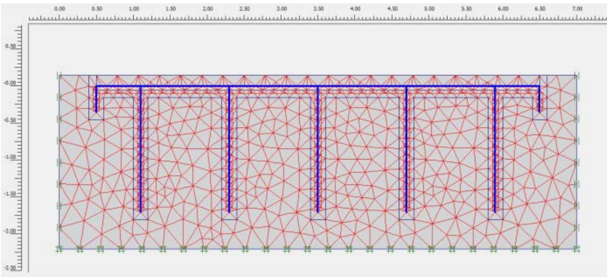

Fig. 3 A used mesh in plain strain FEM analysis.

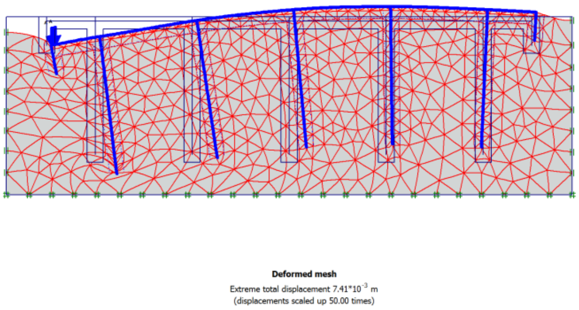

Fig. 4 A deformed shape output of numerical analysis for edge loading.

RESULTS AND DISCUSSION

P-δ Relationship for Nailed-Slab with Vertical Wall Barrier

Fig.5 shows deflection shape along the slab (cross section in field condition). It is seen that the deflection shape is a bowl shape. Analysis results show that maximum displacement occured under the loading point and decreased as you move further away from the loading point. This phenomenon fulfilled the expectation. The maximum deflections were appropriate with the observations. But the end of slab was uplifted. Both ends of the slab were uplifted for concentric loading (Fig. 5a). However, the opposite end of the slab was uplifted caused by edge loading (Fig. 5b).

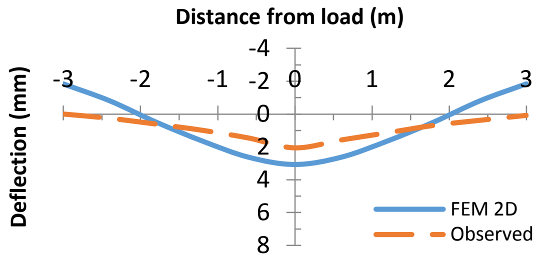

a)

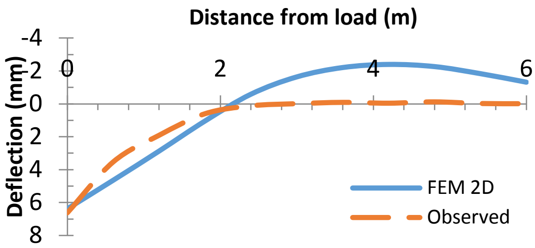

b)

Fig. 5 Deflection shape along the slab for load *P* = 80 kN; a) centric load, b) edge load.

According to Figure 6, the maximum shear between soil and pile occured around the pile tip of the middle piles (Fig. 6a) and the left pile for edge loading (Fig. 6b). The extreme shear stresses on pile were 12.63 k/m^2 and 10.46 kN/m^2 for concentric loading and edge loading, respectively. Both shear stresses did not reach the ultimate value of 16.00 kN/m^2 (=$R_{inter}c_u$).

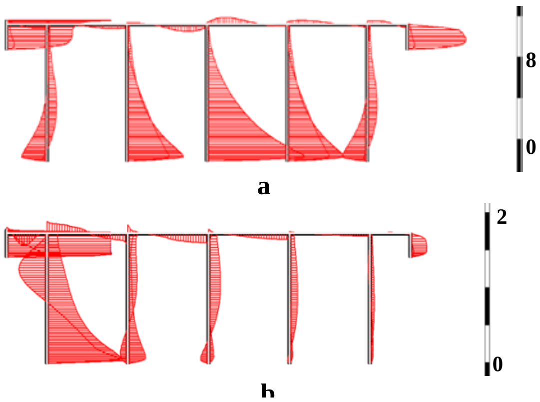

Fig. 6 Shear stress on the interface of structural elements; a) concentric load, P = 150 kN, b) edge load, P = 80 kN.

Effects of Vertical Wall Barrier

Figure 7 shows the P-δ relationship for edge loading. It seems that the vertical wall barrier can reduce deflection 5.25% only. It is an insignificant reduction if it is compared to the model test. The vertical wall barrier can reduce 74% deflection for edge loadings in model test [1].

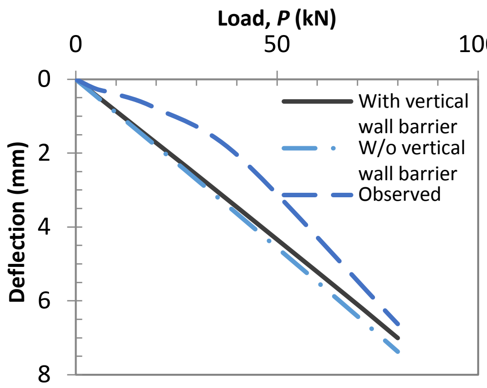

Fig. 7 P-δ relationships for load on C (edge load).

CONCLUSION

In this paper, observations for pavement of Nailed-slab System which are equiped by vertical wall barrier on the end of slab were conducted and numerical analysis for both systems with and without vertical wall barrier has been done. Numerical results show that the vertical wall barrier gave insignificant reduction to the slab deflection. It is opposite to the model test result from Puri, et.al. [1] where the vertical wall barrier can reduce 74% deflection for edge loadings. Soil shear stresses did not reach the ultimate value for both load positions.

ACKNOWLEDGEMENTS

The authors acknowledge the financial support from the Directorate General of Research and Technology and Higher Education Republic of Indonesia number SP DIPA-023.04.1.673453/2015.

REFERENCES

[1] Puri, A., Hardiyatmo, H.C., Suhendro, B., and Rifa'i, A., 2011, Contribution of Wall Barrier to Reduce the Deflection of Nailed-Slab System in Soft Clay, *Proc. of 9th Indonesian Geotech. Conf. and 15th Annual Scientific Meeting (KOGEI IX & PIT XV) HATTI*, HATTI, Jakarta, 7-8 December 2011, pp. 299-306 (in Bahasa Indonesia).

[2] Suhendro, B., dan Hardiyatmo, H.C., 2010, Modified Chicken Foot Pavement System as an Alternative Solution for Road Construction on Soft Soils, Expansive, and Embankment, *Proc. of One Day Seminar and Exhibition 2010 New Innovative Technology on Highway and Bridge*, DPD HPJI Jatim, Surabaya, 31 March 2010 (in Bahasa Indonesia).

[3] The Indonesian Research and Development Center for Highway and Bridge, 2007, *Uji Coba Skala Penuh Teknologi Cakar Ayam Modifikasi, Bab-7 Gambar Rencana*, Satuan Kerja Pusat Litbang Jalan dan Jembatan, Departemen Pekerjaan Umum Republik Indonesia.

[4] Puri, A., Hardiyatmo, H.C., Suhendro, B., and Rifa'i, A., 2013, Behaviour of Full scale Nailed-slab System with Variation on Load Positions, *Proc. 1st Intl. Conf. on Infrastructures Development (ICID)*, Surakarta, 1-3 November 2013, pp. 26-36.

[5] Puri, A., Hardiyatmo, H.C., Suhendro, B., and Rifa'i, A., 2014, Behavior of Nailed-slab System on Soft Clay Due to Repetitive Loadings by Conducting Full Scale Test, *IJCEE-IJENS*, Vol. 14 No. 06, pp. 24-30.

[6] Plaxis 3D Foundation, *Material Models Manual version 1.5*.

AN EVALUATION OF OSMOTIC TECHNIQUE UNDER ULTRAVIOLET GERMICIDAL IRRADIATION EXPOSURE

Mohd Yuhyi Mohd Tadza[1], Nurhidayah Mahazam[1] and Snehasis Tripathy[2]
[1]Faculty of Civil Engineering and Earth Resources, Universiti Malaysia Pahang, Malaysia[1] School of Engineering, Cardiff University, United Kingdom[2]

ABSTRACT

The osmotic technique, which uses polyethylene glycol (PEG) solutions of varying concentrations with semipermeable membranes of different molecular weight cutoffs (MWCO), is commonly used to apply suction in soils. Cellulose acetate membranes which are most commonly used, are susceptible to microbial attacks. This in turn will lead to the intrusion of PEG into soil specimens. Osmotic and vapour equilibrium techniques are often used to establish drying suction-water content soil-water characteristic curves (SWCC). In this study, suctions of 0.11 to 300 MPa were applied on Andrassy bentonite slurries. At higher applied suctions, the osmotic tests were carried under short length ultraviolet germicidal irradiation (UVGI). In addition, Atomic Force Microscopy (AFM) and Fourier Infrared (FTiR) were employed to evaluate the changes in the semipermeable membranes and PEG molecules, respectively. The water content of the clay obtained from the osmotic tests was found to be greater at the overlapping suction region. Interestingly, under UVGI exposure, the water content was found to be in good agreement with the water content determined using the osmotic technique at low suctions and the vapour equilibrium technique at higher suctions. FTiR spectrum and AFM results revealed that some changes had occurred on both the PEG and in the membrane pore sizes. However, these changes did not affect the final water content in the bentonite and therefore, more precise suction-water content SWCC for the clay could be established.

Keywords: Clay, Suction, Osmotic, Microbes, PEG, UV, Cellulose Acetate

1.0 INTRODUCTION

Bentonite is expansively used in various geo-environmental applications. Bentonite in various forms such as loose powder, compacted and slurry have been used in the construction of liners, engineered barriers, isolation walls and backfill material [1][2]. Bentonites have been considered due to their unique containment properties (i.e. low permeability, high sorption capacity, self-sealing membrane characteristics, and durability in a natural environment) [3][4]. As of late, the study of soil microbes and their interactions in bentonite buffer has been of interest in nuclear waste repository applications [5]. Previous studies have shown that the presence of microbes can affect the geochemistry of bentonites and thus, influence their properties and engineering behavior [6][7][8][5].

The engineering behavior of unsaturated soils (viz. shear strength, volume change, permeability) due to changes in the water content are commonly predicted by establishing the suction-water content soil-water characteristic curves (SWCCs). In the laboratory, the suction-water content SWCCs are commonly established using various techniques to predict the changes in the water content in soils [9][10]. Recently, the vapour equilibrium and osmotic techniques have gained widespread acceptance as reliable methods for controlling suction in soil specimens [11]. The vapour equilibrium technique, which utilizes thermodynamic principles to control the relative humidity of various acid and salt solution vapours in a closed system, is used to apply suction in soil [9]. In the osmotic technique, on the other hand, the soil specimen is placed in semipermeable membrane and is brought into contact with polyethylene glycol (PEG) of predetermined concentration. In this technique, two polymers are commonly used, namely aqueous solution of (PEG) and cellulose acetate semipermeable membrane [12].

One of the main drawbacks of the osmotic technique when using PEG 6000 along with molecular weight cut-off (MWCO) 3500 semipermeable membrane, is the intrusion of PEG solution into the soil specimen particularly at higher applied suction [13]. This problem occurs due to the breakage of the semipermeable membrane by soil fungi [14]. As soil hosts a diversity of microbes, the breakage of the semipermeable membrane in osmotic tests is found to be inevitable. Removal of soil microbes prior to conducting osmotic tests is therefore crucial to ensure precise determination of soil-water SWCCs.

The main focus of this paper is to evaluate the use of short-length ultraviolet germicidal irradiation (UVGI) to remove soil microbes prior to conducting osmotic tests. In this study, the suction-water content SWCC for Andrassy bentonite was established using both osmotic and vapour equilibrium techniques. The microbial characteristics of the bentonite were established before the removal of said microbes by exposing both PEG solutions and the soil specimens to UVGI. Atomic Force Microscopy (AFM) and Fourier Transform Infra-red (FTiR) spectroscopy were employed before and after exposure of UVGI. to determine if there any changes to PEG molecules and cellulose semipermeable membrane as a result of the irradiation.

2.0 LITERATURE REVIEW

2.1 Suction-Water Content SWCC

PEG is a hydrophilic polymer made up of molecular chains having the chemical formula: HO-$[CH_2\text{-}CH_2\text{-}O]n\text{-}H$ [9]. The use of PEG–water mixtures along with suitable semipermeable membranes enables the application of osmotic gradients in an osmotic system. During the commencement of an osmotic test, a soil specimen is enveloped by a semipermeable membrane and immersed in an aqueous solution of PEG of varying concentrations. Cellulose acetate, an acetate ester of cellulose ($C_6H_7O_2(OH)_3$) is commonly used for this purpose [14]. In some cases, polysulfonate membrane is also used [9]. The semipermeable membrane is expected to prevent the passage of PEG molecule to soil–water systems. A review of literature suggested that, the osmotic technique has been successfully used for applying suctions in soils up to 1.5 MPa. Although the technique can be further extended to 12 MPa using smaller molecular weight PEGs (i.e. PEG 1500) [12], the application of osmotic technique at higher applied suction appears to be limited to PEG 6000 only. This could be due to unavailability of lower MWCO semipermeable membranes [14]. For suctions higher than 10 MPa, the vapour equilibrium technique is often opted for. The vapour equilibrium technique has been used to apply total suction from 3 up to 1000 MPa [9][11].

In order to obtain a continuous suction-water content SWCC that covers a wide range of suction for any given soil, suction-water content from both techniques are commonly plotted together. Studies in the past have shown disagreement between the test results from both vapour equilibrium and osmotic tests at higher applied suctions [15][10]. The differences were mainly attributed to alterations of the membrane pore sizes which enabled the crossing of PEG molecules into soil specimens [13]. The magnitude of the alteration was found to be significant for lower MWCO membranes.

2.2 Intrusion of PEG

Soil microbes (i.e. bacteria and fungi) exist in both naturally occurring and commercially available bentonites [8][5]. The biodegradation of cellulose acetate based material by soil microbes has been studied for a long time by number of authors [16][17]. It is anticipated that, these microbes were responsible for the degradation of the membrane. The antibacterial property of PEG was found to be insufficient in removing soil microbes [14]. In geotechnical application, Kassif & Ben Shalom [18], recommended the usage of penicillin during laboratory tests to eliminate the bacteria to ensure long-term performance of cellulose acetate membranes. However, a recent study revealed that the breakage of the membrane is due to biodregadation of cellulose acetate by soil fungi [14]. Mohd Tadza et al. [14] also noted that the use of penicillin is ineffective in removing soil fungi. Thus, other methods of disinfection may be required to eliminate the presence of cellulose degrading fungi in soil specimens.

2.3 Ultra Violet Germicidal Irradiation

The application of short-length UVGI in disinfection and removal of microbes is widely used and accepted in the microbiology community [19]. This method was also applied in disinfection of medical instruments and operation theaters [20]. The UV exposure at 200-280 nm for a certain period of time damages cell's DNA and RNA, thus destroying the ability of the microbes to reproduce [21]. The germicidal effectiveness peaks at UVC, which is the subdivision of the UV wavelength (between 260-265 nm) [22]. Various types of soil bacteria and fungi were completely eliminated when exposed directly to UV lamp under laboratory conditions [23][21].

The main concern of using UVGI in osmotic technique is that the UV exposure may also lead to degradation of both the PEG molecules and cellulose acetate membrane. PEG can be photochemically degraded when exposed to UV. However, prolonged exposure is required. Das & Gupta (2005) noted that some changes in the FTiR spectrum of PEG when exposed under UV lamp for more than 1 hour. In the presence of oxidation chemicals such as hydrogen peroxide and titanium oxide, the degradation of PEG in aqueous form was found to occur at shorter periods of exposure [25][26].

Direct degradation of cellulose acetate under UVGI has not been reported elsewhere. However, previous researches have shown that, cellulose acetate based materials were found to degrade under

UV exposure at different wavelengths (i.e. 275-390 nm) in the presence of photo sensitizers and oxidation catalysts [17]. Thus, the objective of this study is to explore the effect of UVGI exposure within this context.

3.0 EXPERIMENTAL TECHNIQUES

3.1 Determination of Geotechnical and Microbiological Properties of Bentonite Samples

The physical and microbiological properties of the Andrassy bentonite was first determined following standard laboratory procedures described in [10][14]. The microbiological properties of the bentonite, namely bacteria and fungi determination were carried out following plating, slide culture, streaking and isolation techniques [19]. Potato dextrose agar (PDA) was used for culturing fungi, whereas Nutrient agar (NA) was used to culture bacteria. The clay specimen was initially suspended in 0.9% NaCl solution to separate the microbes from the soil [27]. Isolation of each microbe was carried out in an independent laboratory using the polymerase chain reaction (PCR) protocol and identification of the specific strain was done by referring to the international microbiological characterization database.

3.2 Establishing the drying suction-water content SWCC

Bentonite slurry was initially prepared by mixing bentonite powder thoroughly with deionized water to slightly greater than liquid limit (i.e. 1.2 x LL). The bentonite–water mixture was stored in sealed plastic bags and kept in an air-tight container to allow for water equilibration to take place for about 7 days prior to preparing the specimens for the laboratory tests.

Osmotic tests were carried out by applying suctions of 0.15, 0.25, 0.42, 1.03, 1.7, 3.65, 5.08, 6.64, 7.74, and 9.96 MPa using two types of PEG. PEG 20 000 was used for applying lower suctions up to 2.67 MPa, whereas PEG 6000 was used for applying suctions greater than 2.67 MPa. The applied suctions in vapor equilibrium were 3.6, 14.58, 23.58, 39.38, 111.77 and 262.75 MPa corresponding to the relative humidities (RHs) of saturated solutions of K_2SO_4, KNO_3, KCl, NaCl, K_2CO_3, and LiCl, respectively. The suctions of each PEG and saturated salt solutions were measured using a chilled mirror dew-point hygrometer. Decagon WP4C was used for this purpose.

PEG 20 000 and Spectra/Por semipermeable membranes with MWCO value of 14 000 were used for applying suctions lower than 3.0 MPa, whereas PEG 6000 and Spectra/Por membranes with MWCO value of 3500 were used for applying higher suctions. Specimens for the osmotic tests were prepared using the bentonite slurry in cellulotic tubes of the semipermeable membranes (MWCO 14 000 and MWCO 3500). Both ends of the semipermeable membrane tubes were then securely fastened using polypropylene clips prior to immersing the specimens in PEG solutions. For applied suction higher than 3.0 MPa using PEG 6000, duplicate tests were conducted under UVGI exposure. For this purpose, the tests were conducted using Esco Airstream Horizontal Laminar Flow Clean Bench (Glass Side Wall). The UV lamp automatically switched off after 10 minutes. For establishing suction-water content relationship using vapor equilibrium, bentonite slurries were initially prepared in 38 mm diameter stainless steel rings. Once prepared, the slurry specimens were carefully extruded and transferred directly into test desiccators.

3.3. AFM Analyses

After completion of the osmotic tests, the membranes were carefully removed and rinsed before being directly transferred to a Nanowizard II scanning probe AFM from JPK Instruments for morphological scanning.

3.4 FTiR Analyses

A PerkinElmer Spectrum 100 spectrometer was used for studying the chemical and molecular changes of the PEG solutions. FTIR spectroscopy generates spectrum patterns according to the infrared intensity (i.e. wavenumber or wavelength) and the fraction of infrared transmitted by certain chemical bonds [28]. The spectrum patterns were then interpreted following methods described by Morrison & Boyd [29]. A sudden shift or distortion to the spectrum will generally indicate degradation or changes to either chemical bonds or molecule structure [13]. PEG 6000 solutions at the end of osmotic tests (i.e. with and without UVGI exposure) were collected and tested.

4.0 RESULTS AND DISCUSSION

4.1 Geotechnical and Microbiological Properties of Andrassy Bentonite

The properties of Andrassy bentonite is presented in Table 1. The bentonite in this study was found to exhibit a large surface area and high surface charge characteristics which make it ideal for soil microbes [34]. Referring to Table 1, it was found out that eight microbes were present within the soil, (i.e. Bacteria: *Bacillus anthracist, Staphylococcus aureus,* *Micrococcus luteus, Achromobacter Xylosoxidans;* Fungi: *Paecilomyces lilacinus, Trichoderma atroviridae, Fusarium proliferatum, Rhodotorula mucilaginosa*). All eight microbes are considered to be common soil microbes. Interestingly, two strains of fungi (i.e. *Paecilomyces lilacinus* and *Trichoderma atroviridae*) found in the soil specimen has the potential to degrade cellulose [14]. Remarkably, no presence of microbes were observed on both PDA and NA plates after UVGI exposure, indicating that complete removal of microbes were obtained after 10 minutes of UVGI exposure.

Table 1 Geotechnical properties of Andrassy bentonite

Geotechnical properties	
Specific gravity, G*s*	2.78
Liquid limit, *wl* (%)	129.30
Plastic limit, *wp* (%)	46.12
Shrinkage limit, *ws* (%)	34.00
Specific surface area, *S* (m^2/g)	734.27
Cation exchange capacity, *B* (meq/100g)	42.77

4.2 Suction-water content SWCC

Figure 1 shows the equilibration plot at applied suction of 3.65 MPa using PEG 6000. Some differences were noted between the equilibration time for specimen with and without UVGI exposure.

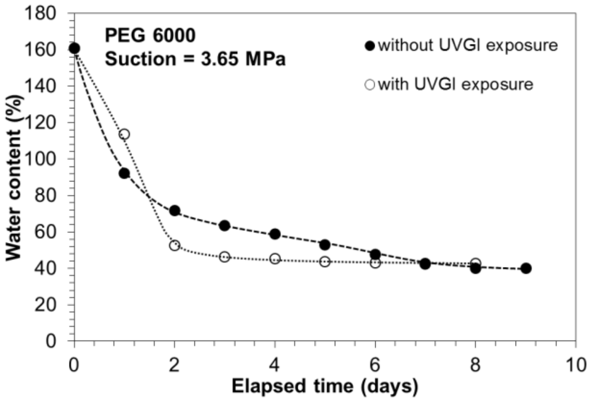

Fig 1 Time equilibration plot in osmotic test at suction 3.65 MPa.

The specimen that has undergone UVGI was found to equilibrate much longer (i.e. 8 days) as compared to 6 days for the specimen without UVGI exposure. Interestingly, the final water content attained for the specimen exposed under UVGI was slightly greater compared to the specimen that has not been exposed to UVGI. It is expected that a much faster equilibration was obtained due to alteration of the membrane pore sizes.

The drying suction-water content SWCC is shown in Fig. 2. The final water contents of the soil specimens were found to decrease with an increase in the applied suctions. Smooth curve joining the osmotic test at lower suctions (i.e. PEG 20 000), and higher suctions (i.e. vapor equilibrium). However, some disagreements were noted between osmotic test results (see PEG 6000 without UVGI exposure) and vapor equilibrium test results. The osmotic tests results at the overlapping suction region were found to remain lower than that of water contents obtained from vapour equilibrium. Similar observation was reported by Tripathy et al. [10] for other types of bentonites. The lower water contents are primarily attributed to the intrusion of PEG solution into the bentonites specimens. On the contrary, water contents obtained using PEG 6000 that has undergone UVGI were found to complement the test results of both osmotic test at lower suctions and vapour equilibrium at higher applied suctions.

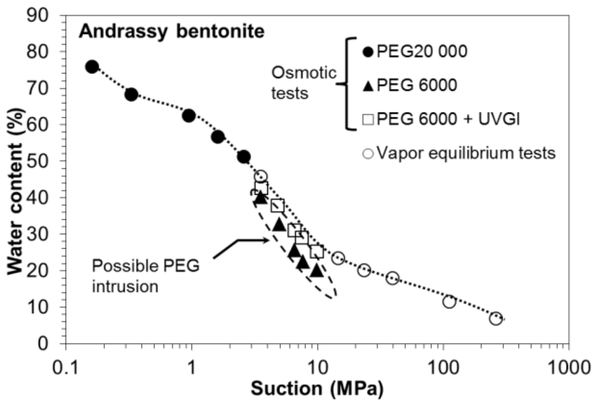

Fig 2 Drying suction-water content SWCC

4.3 Effect of UVGI on Membrane Pore Size

Figure 3a and 3b present typical AFM images of MWCO 3500 membrane with and without UVGI exposure at the end of the osmotic tests. The membrane is composed of series of well-organized regenerated cellulose acetate strands to form a mesh like formation. AFM images revealed that both membrane pore sizes were larger than that specified by the manufacturer. It is believed that these differences were caused by degradation caused by cellulose degrading microbes present within the soil. Similarly, degradation also occurred due to UVGI exposure.

Some differences were noted between the pore size of membrane after the test and the pore size of membrane exposed to UVGI. Differences in the structural arrangements of the strands were also observed. Alteration of the membrane pore sizes by cellulose degrading microbes in this study (i.e.

without UVGI) was found to be greater than those that have undergone UVGI exposure. Surprisingly, although alteration of the membrane pore sizes occurred after UVGI exposure, the final water contents determined in the osmotic tests were found to be in better agreement with those of the osmotic test at lower suctions and the vapour equilibrium water contents.

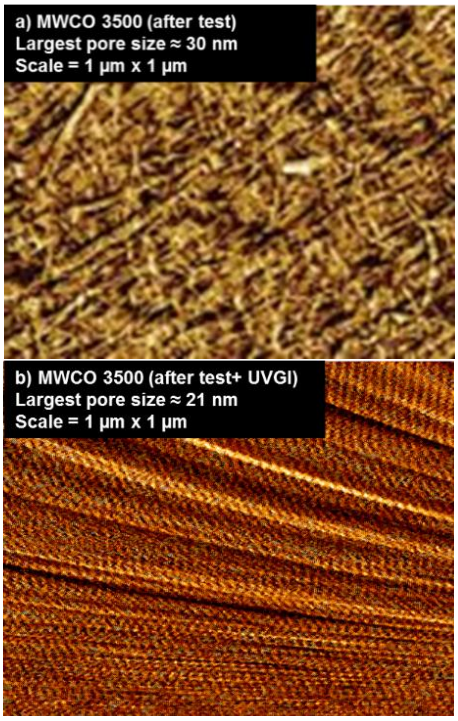

Fig. 3 AFM images of MWCO 3500 semi-permeable membrane after osmotic tests (a) without UVGI and (b) with UVGI exposure

4.4 Effect of UVGI on FTiR Spectrum

Comparison of FTiR spectrums for PEG 6000 solutions after completion of osmotic tests with and without UVGI exposure is shown in Fig. 3.

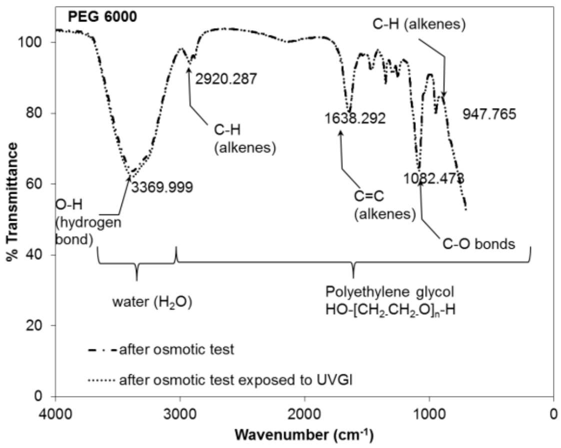

Fig. 4 Comparison of FTiR spectra for PEG 6000 with and without UVGI exposure

Slight differences were noted on 3369 cm-1 peaks corresponding to O-H bond. It is noted that a slightly higher transmittance were obtained for PEG solution after osmotic tests without UVGI exposure. Apart from that, the primary molecular structure of PEG remained somewhat unaffected by the exposure of UVGI, indicating that no degradation occurred.

5.0 CONCLUSION

Results of the investigation after conducting osmotic test under UVGI exposure have been presented in this paper. Based on the test results, the following conclusions were drawn:

i. All soil microbes in this study were completely eliminated by 10 minutes of UVGI exposure, and thus degradation of membrane by microbes is prevented.
ii. Water contents obtained after UVGI complemented vapour equilibrium and osmotic tests results at lower suctions, and more precise SWCC were established.
iii. the FTiR Spectrum showed that UVGI had some effects on the O-H bond and pore size of the cellulose acetate semipermeable membrane. These effects were found to be insignificant in the determination of final water contents of the bentonite.

ACKNOWLEDGEMENTS

The authors would like to express their gratitude to Universiti Malaysia Pahang for providing financial support under RDU 130384. The authors would also like to thank the Malaysian Nuclear Agency for providing AFM service for this study.

REFERENCES

[1] Shackelford C.D, “Membrane behavior in engineered bentonite-based containment barriers: state of the art”. In Proceedings of Coupled Phenomena in Environmental Geotechnics (CPEG 2013), 1–3 July 2013, Torino, Italy, Taylor & Francis Group, London, UK, 2013, pp. 45–60.
[2] Tripathy S., Thomas H., and Bag R, “Geoenvironmental Application of Bentonites in Underground Disposal of Nuclear Waste: Characterization and Laboratory Tests”, J. of Hazardous, Toxic, and Radioactive Waste, 2015.
[3] Pusch R. and Yong R.N. Microstructure of Smectite Clays and Engineering Performance. 1st Edition, Taylor and Francis, 2005.
[4] Plotze M., Kahr G., Dohrmann R. and Weber H. P. Hydro-mechanical, geochemical and mineralogical characteristics of the bentonite

buffer in a heater experiment: The HE-B Project at the Mont Terri Rock Laboratory - Elsevier, Physics and Chemistry of the Earth, Vol. 32, 2007, pp. 730-740.

[5] Stone W., Kroukamp O., Moes A., McKelvie J., Korber D.R and Wolfaardt G.M, Measuring microbial metabolism in atypical environments: Bentonite in used nuclear fuel storage, Journal of Microbiological Methods, Vol. 120, 2016, pp. 79-90

[6] Pedersen K., Motamedi M., Karnland O., and Sandén T, Cultivability of microorganisms introduced into compacted bentonite clay buffer under high-level radioactive waste repository conditions, Engineering Geology, Vol. 58, 2000, pp.149–161.

[7] Stroes-Gascoyne S., Hamon C.J., Maak P., and Russell S, The effects of the physical properties of highly compacted smectitic clay (bentonite) on the culturability of indigenous microorganisms, Applied Clay Science, Vol.47, 2010, pp. 155-162.

[8] Lopez-Fernandez M., Fernandez-Sanfrancisco, O., Moreno-Garcia., Martin-Sanchez., Sanchez-Castro I and Merroun M.L, Microbial communities in bentonite formations and their interactions with uranium, Applied Geochemistry, Vol. 49, 2014, pp. 77-86.

[9] Delage, P., Romero, E. and Tarantino, A, Recent developments in the techniques of controlling and measuring suction in unsaturated soils. In Saturated Soils: Advances in Geo-Engineering, Taylor and Francis Group, London, 2008, pp. 33-52.

[10] Tripathy S., M. Tadza M.Y. and Thomas H.R, Soil-water characteristic curves of clays, J. of Canadian Geotechnical Journal, Vol. 51, No. 8, 2014, pp. 869-883.

[11] Blatz J.A., Cui Y. J., and Oldecop L, Vapour equilibrium and osmotic technique for suction control, J. of Geotechnical and Geological Engineering, Vol. 26, No. 6, 2008, pp. 661–673.

[12] Tripathy S. and Rees S.W, Suction of Some Polyethylene Glycols Commonly Used for Unsaturated Soil Testing, Geotechnical Testing Journal, Vol. 36, No. 5, 2013, pp.768-780.

[13] Tripathy S., Tadza M.Y.M. and Thomas H.R, On the intrusion of polyethylene glycol during osmotic tests, Geotechnique Letters, Vol. 1, No. 3, 2011, pp. 47–51

[14] Mohd Tadza M.Y., Farida Asras M.F., Mohd Tadza M.A., Ismail J., Mahazam N. and Mohd Azmi S.M, Intrusion of Polyethylene Glycol During Osmotic Tests: Identifying Cellulose Acetate Degrading Microbes, Jurnal Teknologi (Sciences & Engineering), Vol. 72, 2016, pp. 1-6.

[15] Fleureau J. M., Kheirbek Saoud S., Soemitro R. and Taibi, S, Behavior of clayey soils on drying–wetting paths, J. of Canadian Geotechnical Journal, Vol. 30, No. 2, 1993, pp. 287–296.

[16] Lenz R.W, Biodegradable polymers, Advances in Polymer Science, Vol. 107, 1993, pp. 1-40.

[17] Puls J., Wilson, S.A and Holter. D, Degradation of Cellulose Acetate-Based Materials: A Review, J. Polym. Environment, Vol. 19, 2011, pp. 152-165.

[18] Kassiff G. and Ben Shalom A, Experimental relationship between swell pressure and suction, J. of Géotechnique, Vol. 21, No. 3, 1971, pp. 245–255.

[19] Benson H. J, Microbiological Applications: A Laboratory Manual in General Microbiology. McGraw-Hill Science, 2001.

[20] Katara G, Hemvani M, Chitnis S, Chitnis V, Chitnis D.S, Surface disinfection by exposure to germicidal UV light. Ind J Med Microbiol, Vol, 26, 2008, pp. 241–242.

[21] Kowalski W, Ultraviolet Germicidal Irradiation Handbook, Springer-Verlag Berlin Heidelberg, 2009.

[22] Harm W, Biological Effects of Ultraviolet Radiation, New York: Cambridge University Press, 1980.

[23] Johnson M.L., Berger L., Philips L and Speare R, Fungicidal effects of chemical disinfectants, UV light, desiccation and heat on the amphibian chytrid Batrachochytrium dendrobatidis, Diseases of Aquatic Organisms, Vol. 57, 2003, pp. 255-260.

[24] Das I and Gupta S.K, Polyethylene glycol degradation by UV irradiation, Indian Journal of Chemistry, Vol. 44A, 2005, pp. 1355-1358.

[25] Giroto J.A, Teixeira A.C.S.C, Nascimento C.A.O and Guardani R, Degradation of Poly(ethylene glycol) in Aqueous Solution by Photo-Fenton and H2O2/UV Processes, Ind. Eng. Chem. Res., Vol. 49, No. 7, 2010, pp 3200–3206.

[26] Santos L.C., Schmitt C.C., Poli A.L and Neumann M.G, Photo-Fenton Degradation of Poly(ethyleneglycol), J. Braz. Chem. Soc., Vol. 22, No. 3, 2011, pp. 540-545.

[27] Zborowski M., Malchesky P. S., Jan, T. and Hall G. S, Quantitative separation of bacteria in saline solution using lanthanide Er(II1) and a magnetic field, J. of General Microbiology, Vol. 138, 1992, pp. 63-68.

[28] Roberts J. D. and Caserio, M. C, Basic principles of organic chemistry, California: W. A. Benjamin, Inc., 1965.

[29] Morrison R. T. and Boyd, R. N, Organic chemistry. Allyn and Bacon Inc. 1983.

Sixth International Conference on Geotechnique, Construction Materials and Environment, Bangkok, Thailand,Nov. 14-16, 2016, ISBN: 978-4-9905958-6-9 C3051

STABILITY ANALYSIS OF SLOPES ON CLAY SOIL FOUNDATIONS BY LIMIT EQUILIBRIUM AND FINITE ELEMENT ANALYSIS METHODS

Abdul Karim M. Zein[1] and Waleed Abdul Karim[2]
Building and Road Research Institute, University of Khartoum, Khartoum, Sudan

ABSTRACT

This paper presents an evaluation and comparative study on the stability analysis of simple slope models founded on undrained clay soils. The analysis was performed according to the limit equilibrium (LE) and finite element (FE) methods utilizing "Slide 2D" and "Plaxis 2D" computer programs respectively. Forty five slope models with different geometries based on soft, medium stiff and very stiff clay soil foundations were considered for stability analysis. The comparison made between four LE methods indicated that the Bishop and Spencer methods produced practically similar FOS results whereas the Fellenius and Janbu methods gave FOS values lower than the Spencer method by 3.0% and 7.4% respectively. For slopes founded on soft clays, the difference in FOS computed by the LE and FE methods is negligible but the FOS values computed by the LE methods were 8.5% higher than the FE method for slopes on medium and very stiff clays. Based on the results of linear regression analysis of all data, the Fellenius, Bishop, and Spencer methods gave FOS values higher than the FE method by 1.4, 5.3 and 5.7% respectively whereas the Janbu method gave FOS lower than the FE method by 4.3%. Evaluation of the effects of slope geometry and foundation soil properties on slope stability revealed a reliable relationship between FOS and a variable combining four slope and soil parameters.

Keywords: Slope Stability Analysis, Factor of Safety, Undrained Clay Soils, Limit Equilibrium, Finite Element

INTRODUCTION

Slope stability problems are normally encountered when the balance of natural or engineered soil slopes is disrupted. The stability of a slope may be defined as the resistance of an inclined surface within the soil mass to failure by sliding, overturning or collapsing. Soil stability analysis is performed to assess equilibrium conditions and achieve safe design of slopes. The factor of safety (FOS) against slope instability is defined as the ratio of the resisting forces (strength) to the driving forces (loading) along a potential failure surface. The slope is said to be in a limit equilibrium condition when FOS = 1 whereas higher values correspond to stable slopes.

Slope stability analysis can be evaluated by the limit equilibrium (LE) and finite element (FE) methods. The LE methods are based on the static equilibrium of the forces and/or moments whereas the FE methods utilize the constitutive law or stress-strain relationship concept. The LE approach involves different methods depending on the type of problem to be solved and the required accuracy of analysis results. More attention has been directed in the recent decades to the use of the FE in slope stability analysis to model cases with complex slope geometry, soil behavior and loading sequences and to visualize soil deformations in place. Many design computer software packages have been developed to enhance the application of the LE and FE methods in slope stability analysis.

This paper presents an evaluation and comparison of the results of slope stability analysis carried out according to certain LE and FE methods for a simple slope with variable geometries founded on undrained clay soils with different strength characteristics. The analysis was performed utilizing the "Slide" and "Plaxis" computer software programs for the LE and the FE approaches respectively. Some important aspects are given below on the LE and FE slope stability analysis methods.

METHODS OF SLOPE STABILITY ANALYSIS

In the LE slope stability analysis, the soil mass above the slip surface is divided into slices and the shear and normal inter-slice forces are determined by applying appropriate forces and/or moment equilibrium equations for each slice to satisfy the static equilibrium conditions. The FOS computation procedure involves comparing the available soil shear strength along the sliding surface with the force required to maintain the slope in equilibrium. The LE methods are commonly adopted in routine design due to their simplicity, accuracy and the small number of parameters required for analysis. The first LE method, known as the Fellenius method or the ordinary method of slices, was developed in 1927 by the Swedish engineers and is applicable to circular slip surfaces [1]. A revised method of circular slip analysis was developed by Bishop in 1955 [2] for improving the accuracy of FOS computations. The latter requires an iterative procedure to calculate the minimum FOS. To undertake analysis of non-circular slips, Janbu's method [3] is normally used. More refined LE methods which account for both force and moment equilibrium [4] have been developed to further improve the FOS calculation accuracy.

Finite Element Stability Analysis Methods

The main feature of the FE is using soil stress-strain behavior for slope stability modeling which changes the problem from a static-indeterminate to a static-determinate one. In FE methods there is no pre-assumption about the shape and location of the failure surface. FE modeling starts by dividing the slope into a finite number of zones or elements. Forces and strains are then calculated for each element using the appropriate constitutive laws for the materials in the slope.

The FE method uses the strength reduction method (SRM), to calculate/simulate failure limit state of slope and safety factor. The SRM is based on progressive reduction of soil strength parameters; φ and c, by a "strength reduction factor" (SRF) until convergence occurs within a specified number of iterations and tolerance or failure of slope occurs. The SRF which corresponds to the point at the last convergence state is equivalent to the safety factor.

MODELLING OF SLOPE STABILITY PROBLEM

A description of the methodology followed for modeling the various aspects of slope stability problem analyzed is given hereunder. The main aspects included the slope geometry, characteristics of slope and foundation soils and the computer programs used for FOS computations.

Slope Geometry and Soil Properties

The slope geometry assumed in this study is comprised of a two soil layers model with variable strength parameters as schematically illustrated in Fig. 1. The upper slope layer comprises a sandy soil whereas the lower foundation layer is a homogeneous clay of variable shear strength. The clay soils were modeled in an undrained condition with zero internal friction angle (φ=0) and cohesion values of 20, 40 and 140kN/m^2 representing soft, medium stiff and very stiff soils. Table 1 lists the input parameters used for stability analysis which include the properties of the slope material and foundation soil types. These properties are typical of those normally obtained from testing of such soil materials.

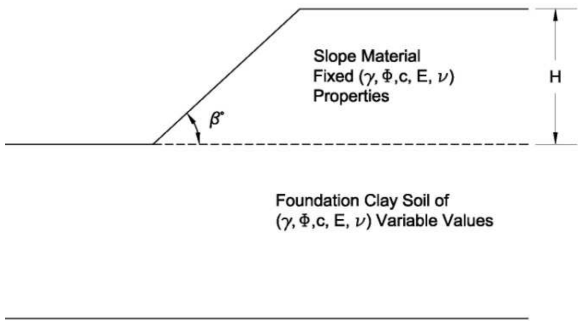

Fig. 1 Two soil layers model assumed for slope stability analysis.

Table 1 Properties of the slope material and foundation soil types used for stability analysis

Soil properties		c_u kN/m^2	Φ_u (°)	γ_b kN/m^3	E MPa	ν
Slope material		10	30	18.0	15	0.17
Base Soil	Soft clay	20	0	17.3	14	0.30
	Med. stiff clay	40	0	18.9	33	0.30
	Very stiff clay	140	0	20.4	75	0.30

Simple slope geometries of variable heights (H) and inclination angles (β) were assumed such that different slope models are covered in the analysis. Slope heights of 12m, 20m and 28m were chosen to represent low, medium and high slopes and for each case the angle β was varied from 10° to 24°. In total, forty five study cases were considered for analysis.

Slope Stability Analysis Computer Software Used

Limit Equilibrium "Slide 2D" Software

The LE methods chosen in this study included the Fellenius's (FM), Bishop's method (BM), Spencer's method (SM) and Janbu's method (JM). The input and features of models included the slope geometry and soils parameters, selection of the number of slices (25 slices) and adoption of the Mohr-Coulomb soil shear strength model without tension cracks. The slope models were analyzed using “Slide 2D” computer Software from Rocscience Inc. [5] for computing FOS using vertical slice limit equilibrium methods of circular or non-circular failure slip surfaces. The Slide software is simple to use, and yet complex models can be created and analyzed quickly and easily. Searching of the critical slip surface is realized with the help of a grid or as a slope search in user-defined area. Individual slip surfaces can be analyzed, or search can be applied to locate the critical slip surface for a given slope.

Finite Element “Plaxis 2D” Software

The stability of the slope was analyzed using the finite element Plaxis 2D software [6] normally used with plane strain model for stability and deformation analysis to determine the minimum FOS for assumed slope models. The models were drawn with 15 nodes and the standard fixities were used to define the boundary conditions. Plaxis 2D uses a convenient graphical user interface that enables users to quickly generate a geometry model and finite element mesh based on a representative vertical cross section of the situation in question. Standard boundary conditions are automatically generated by the program. All soil types are modeled through Mohr-Columb yield criterion in Plaxis. Once the geometry model and boundary conditions are defined, automatic mesh generation is applied with the bandwidth optimizer for the finite element discretization refinement.

RESULTS AND DISCUSSION

Stability Analysis Results

The results of FOS computed according to the LE and FE stability analysis methods are presented in Tables 2, 3 and 4 for the slopes founded on soft, medium stiff and very stiff clays respectively. The discussion presented herein is focused on comparisons of FOS computed using LE and FE methods and evaluation of the effects of slope geometry and soil properties on slope stability.

For slopes founded on soft clays it may be noted from Table 2, that the LE and FE methods yielded values of FOS less than 1 in all cases indicating that the slopes are unstable due to their inadequate shear strength. The analysis results showed that the slopes were even more unsafe for the cases with higher H and β values. The FOS values in Table 2 may be useful when it is required to improve the resistance of such weak soils against slope failures through application of certain soil stabilization techniques.

The FOS pertaining to slopes on medium stiff clay foundations (Table 3) varied from 0.45 to 1.15 with the lower and upper values pertaining to inclination angles of 24° and 10° respectively. Such a slope foundation represents a marginal stability situation for the analyzed slope models. The results indicated that stability could be achieved (FOS ≥ 1) by some methods only in slopes with small heights (H = 12-14m) and mild inclinations (β = 12-14°).

For slopes on very stiff clay foundation soils, the FOS (Table 4) varied from 1.23 to 3.7 indicating that all analysed models were stable even for the cases of maximum H and β values. The highest and lowest FOS values pertain to slope geometries with the lowest and highest values of H and β respectively.

Comparisons of FOS Computed by LE and FE Methods

General

For all slopes founded on soft clays there is a very good agreement between the FOS values computed according to the LE methods except for the JM which gave consistently low FOS with a discrepancy reaching 10% for the 12m high slope. Generally, the FE method indicated FOS values that are similar to or slightly lower than those of the LE methods for slopes founded on these soils. Therefore, both approaches seem to produce similar FOS values.

For slopes founded on medium stiff clays, there is a perfect agreement between the FOS computed by the BM and SM methods; both methods gave the highest FOS followed by the FM whereas the JM gave the lowest values. The FE method showed a reasonable comparison with the LE methods for slopes of low to moderate heights but gave significantly lower FOS for relatively high slopes.

As noted for the slopes founded on soft and medium stiff clays, the BM and SM gave the highest FOS values for very stiff clays, followed by the FM whereas among the LE methods the JM indicated the lowest values. There is a very good agreement between the FOS values deduced from the FE

Table 2 Computed FOS values for slope models founded on soft clay soil foundations

Slope Geometry	H	12m					20m					28m				
	β	10°	14°	18°	20°	24°	10°	14°	18°	20°	24°	10°	14°	18°	20°	24°
Limit Equilibrium Methods Slide 2D	BM	0.60	0.56	0.54	0.54	0.53	0.46	0.39	0.36	0.35	0.34	045	0.33	0.29	0.28	0.26
	SM	0.60	0.56	0.54	0.54	0.53	0.46	0.39	0.36	0.35	0.34	0.45	0.33	0.29	0.28	0.27
	FM	0.59	0.56	0.54	0.54	0.53	0.47	0.39	0.36	0.36	0.34	0.46	0.36	0.31	0.30	0.28
	JM	0.55	0.51	0.50	0.50	0.50	0.43	0.36	0.33	0.32	0.31	0.42	0.31	0.27	0.26	0.25
FEM Plaxis 2D		0.61	0.57	0.54	0.53	0.52	0.45	0.38	0.36	0.35	0.33	0.39	0.36	0.30	0.28	0.26

Table 3 Computed FOS values for slope models founded on medium stiff clay soil foundations

Slope Geometry	H	12m					20m					28m				
	β	10°	14°	18°	20°	24°	10°	14°	18°	20°	24°	10°	14°	18°	20°	24°
Limit Equilibrium Methods Slide 2D	BM	1.16	1.09	1.07	1.06	1.05	0.84	0.84	0.69	0.68	0.66	0.73	0.77	0.55	0.53	0.50
	SM	1.16	1.09	1.06	1.06	1.04	0.84	0.73	0.68	0.67	0.66	0.77	0.61	0.55	0.53	0.50
	FM	1.12	1.06	1.03	1.03	1.01	0.81	0.70	0.66	0.65	0.63	0.73	0.59	0.52	0.51	0.49
	JM	1.05	0.99	0.97	0.96	0.95	0.77	0.67	0.62	0.61	0.60	0.72	0.56	0.50	0.48	0.46
FEM Plaxis 2D		1.09	1.01	1.04	1.03	1.01	0.75	0.66	0.62	0.61	0.59	0.60	0.51	0.47	0.45	0.43

Table 4 Computed FOS values for slope models founded on very stiff clay soil foundations

Slope Geometry	H	12m					20m					28m				
	β	10°	14°	18°	20°	24°	10°	14°	18°	20°	24°	10°	14°	18°	20°	24°
Limit Equilibrium Methods Slide 2D	BM	3.85	3.24	2.60	2.37	2.02	2.61	2.34	2.24	2.13	1.80	2.16	1.83	1.70	1.66	1.61
	SM	3.84	3.23	2.60	3.37	2.02	2.60	2.33	2.22	2.12	1.80	2.14	1.81	1.68	1.64	1.60
	FM	3.76	3.12	2.49	2.27	1.94	2.51	2.23	2.12	2.05	1.73	2.04	1.71	1.58	1.54	1.48
	JM	3.38	3.10	2.46	2.24	1.92	2.32	2.04	1.94	1.91	1.72	1.93	1.60	1.47	1.43	1.38
FEM Plaxis 2D		3.82	3.31	2.60	1.76	1.61	2.62	2.34	2.19	1.52	1.33	2.14	1.83	1.68	1.39	1.23

method on one hand and the BM and SM methods on the other for slopes of low to moderate inclinations (β =12 to 18°). For slopes with β =20°and steeper, the FE method gave FOS significantly lower than the LE methods. The differences in FOS computed by the LE and FE methods become more pronounced for slopes with relatively steep inclinations (β =24°) and greater heights (H >20m).

LE – LE Comparisons

In the LE-LE comparison, the FOS values computed from the Spencer method (SM) were compared to those obtained from by the other three LE methods. The SM was selected as a basis for comparison because it satisfies both the force and moment requirements for static equilibrium. Moreover, the SM can be applied for circular as well as non-circular slip surfaces [4]. The comparison criterion was the discrepancies between FOS values deduced from the SM and other methods. The LE-LE comparison results show that the FOS values computed by the BM and the SM are practically the same for all slope models and foundation conditions. The FOS values computed using the FM were on average 3% lower than SM values for slopes on clays with different strength characteristics. The JM gave FOS values lower than the SM by 4.5 to 9.1% with an average of 7.4%. For the medium and very stiff clay foundations, the discrepancy between the JM and SM methods were higher than the previously reported maximum difference of 6% [7] between various LE methods.

LE-FE Comparisons

The average FOS values obtained for the LE methods for each slope model were compared to the values deduced from the FE method. The results indicated that the FE method gives FOS values which in all cases are smaller than the average LE values. The difference in FOS computed by the LE and FE methods is negligible (0.9%) for slope models founded on soft clays. However, the discrepancy between the two approaches becomes more pronounced (8.5%) for slopes founded on medium and very stiff clays.

To examine whether the FOS computed from the LE methods can be related to the FOS according to the FE method the two data sets were analyzed by the regression method. Four linear equations were established between the FOS data pertaining to each LE method and the LE method. Equations of the best fit lines indicated that the Fellenius, Spencer and Bishop methods gave FOS higher than the FE method by 1.4, 5.3 and 5.7% respectively whereas the Janbu method gave FOS lower than the FE method by 4.3%. The coefficient of determination R^2 varied from 0.958 to 0.967 indicating a perfect linear relationship between the LE and FE methods .

It has been reported in a previous study [8] that the differences in FOS computed by the FE and LE are negligible for simple slopes founded on undrained clay soils. The results of this study reveal that such a finding is only applicable for the slopes founded on soft clays. For slopes founded on medium and very stiff clays the FEM tends to give FOS values lower than the LE methods. The difference may be attributed to the degree of accuracy of the inter-slice forces calculation [9]. The inter-slice forces are more accurately calculated by the FE software packages which take into account the local stress distribution in the soil mass. On the other hand, the LE methods have limitations with regards to the inter-slice shear forces computation. It has been indicated that the forces computed in the FE method are higher than in the LE methods; thus lower FOS are produced by the former.

Prediction of FOS for Simple Slopes Founded on Undrained Clay Soils

The effects of slope geometry and foundation soil characteristics on the computed FOS were evaluated using the data pertaining to the LE and FE slope stability methods. The parameters considered for evaluation included the slope height (H) and inclination angle (β) and the undrained cohesion (c) and bulk unit weight (γ) of foundation soils. For a given slope the stability increases with soil strength and unit weight (c and γ) and deceases with slope height and inclination angle (H and β). Hence, the FOS may be expressed as a function of slope and soil parameters by the following equation:

$$\mathbf{FOS} = \boldsymbol{f}\left(\frac{\boldsymbol{\gamma * c}}{\mathbf{H * tan\,\beta}}\right) \quad (1)$$

To define the type of relationship in above equation, the FOS values computed by each method were plotted against the results of the product of (γ*c/H*tan β) as shown in Fig. 2 with H, c and γ expressed in m, kN/m^2 and kN/m^3units respectively

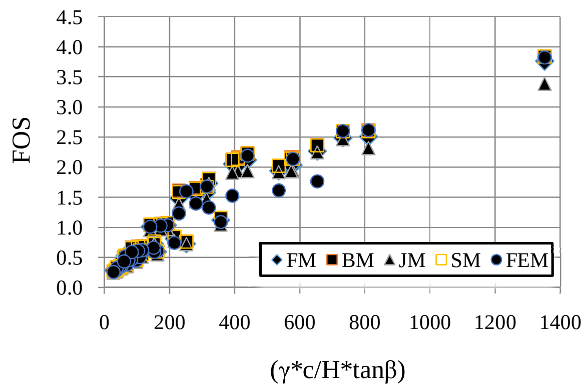

Fig. 2 Relationship between FOS and (γ*c/H*tan β)

The trends depicted in Fig. 2 indicate that a sound linear relationship exists between the FOS and (γ*c/H*tan β) variables for each analysis method. Linear regression analysis was carried out using data pertaining to different slope and foundation conditions to quantify such relationships. The following general equation was developed for estimating the FOS from slope and soil parameters:

$$\mathbf{FOS} = \mathbf{A}\,\frac{\boldsymbol{\gamma * c}}{\mathbf{H * tan\,\beta}} + \mathbf{B} \quad (2)$$

For each method of analysis, the constants A and B are dependent on the slope geometry and soil properties and they respectively represent the slope and y-intercept of the best fit lines for the data sets plotted in Fig. 2. Their values were determined for each method as given in Table 5. The data in Table 5 confirm the previously stated conclusion that the FE method tends to give FOS that are lower than all LE methods (particularly the BM and SM).

Equation 2 may be used in conjunction with the values of A and B in Table 5 to predict the FOS using the LE and FE methods for slopes of simple geometry founded on homogeneous clay soils with similar characteristics.

Table 5 Values of A, B and R^2

Analysis Method		A	B	R^2
LE methods based on Slide software	BM	0.003	0.361	0.902
	SM	0.003	0.361	0.904
	FM	0.002	0.353	0.913
	JM	0.002	0.336	0.903
FE Plaxis 2D method		0.002	0.317	0.921

CONCLUSIONS

The stability of simple slope models founded on clay soils with variable undrained strength characteristics was analyzed using the LE and the FE methods utilizing the "Slide" and "Plaxis" software programs respectively. The main conclusions drawn from analysis and discussion of study results are given below.

The results of comparison between the FOS computed using four LE analysis methods revealed that the Bishop and Spencer LE methods produced similar FOS values; whereas the Fellenius and Janbu methods gave FOS lower than the Spencer's method by 3.0% and 7.4% respectively.

The FOS computed using LE and FE methods compared very well for the slope models founded on soft clays. However for slopes on medium and very stiff clay foundations, the LE methods tend to give FOS values higher than the FE method.

The results of linear regression analysis of data deduced from the LE and FE methods showed that the FOS obtained from Bishop, Spencer and Fellenius LE methods are higher by 1.4 to 5.7% compared to those from the FE method.

The effects of soil geometry and foundation soil properties on the FOS computed according the two stability analysis approaches were evaluated. A simple and reliable mathematical linear relationship was developed from regression analysis of data between FOS and a variable combining four parameters of slope geometry and soil properties as given in Eq. 2. The constants A and B in this equation are dependent on slope geometry, soil properties and applied method of analysis.

Finally, the study results indicate that the LE slope stability analysis methods which are simple and relatively fast can produce accurate and reliable results. Such methods may be applied with confidence in routine design for slopes with simple geometry founded on undrained clays. The FE method is an advanced and reliable analysis tool of great value in modeling design cases with complex slope geometry, heterogeneous soil behavior and different loading patterns.

REFERENCES

[1] Fellenius, W. "Erdstatische Berechnungen mit Reibung and Kohaesion", Ernst, Berlin, 1927.

[2] Bishop, A.W. "The Use of the Slip Circle in the Stability Analysis of Slopes". Géotechnique, , Vol. 5, No. 1, 1955, pp. 7-17

[3] Janbu, N. "Slope stability computations", Soil Mech. Found. Engng Report, Trondheim: Technical University of Norway, 1968.

[4] Spencer, E. "A Method of Analysis of the Stability of Embankments Assuming Parallel Interslice Forces" Géotechnique, Vol. 17, No. 1, 1967, pp. 11-26

[5] Rocscience Inc., 2008, SLIDE version 5.0 User Manual

[6] PLAXIS, "Finite Element Code for Soil and Rock Analysis," PLAXIS-2D Version 8, 2004, Manual, DUT, Netherlands,

[7] Duncan, J., M. State of the art: Limit equilibrium and finite element analysis of slopes. J.of Geotech. Engng., Vol. 122 (7), 1996, 577-596.

[8] Khabbaz, B., Fatahi, B. and Nucifora C "Finite Element Methods against Limit Equilibrium Approaches for Slope Stability Analysis" Proc. ANZ Conf. , 2012, pp. 1293-1298.

[9] Aryal, K.P., Differences between LE and FE Methods used in Slope Stability Evaluations, The 12th Int. Conf. of Int. Association for Computer Methods and Advances in Geomechanics , 2008.

EFFECT OF PERIODICAL RAINFALL ON SHALLOW SLOPE FAILURES: FINITE ELEMENT ANALYSIS

Avirut Chinkulkijniwat[1], Somjai Yubonchit[2], Rajeshwar Goodary [3] and Duc Bui Van[4]
[1,2,4] School of Civil Engineering, Suranaree University of Technology, Nakhon Ratchasima, Thailand.
[3] Faculty of Sustainable Development and Engineering, Université des Mascareignes, Mauritius.

ABSTRACT

Assessment of rainfall-induced shallow slope failures is vital to mitigate damages of infrastructures, and loss of people life in the hazardous areas. The usual tool for prediction of shallow slope failures is critical rainfall concept due to its simplicity and faster assessment. However, this concept has been developed based on statistical approach from historical slope failure data, in which many factors those might trigger shallow slope failures are disregarded. Assessment of the probable factors triggering shallow slope failures is presented in this paper. A set of parametric study was numerically conducted under finite element environment. The rainfall periods to slope failures (D_f) under various rainfall intensity (I_f) were recorded. The relationships between I_f and D_f for initiation of shallow slope failures (ID thresholds) were presented. The results indicate that periodical rainfall plays role on failure state of shallow slope. The D_f under assigned I_f decreases with increasing dry period.

Keywords: Periodical rainfall, Shallow slope, ID thresholds

INTRODUCTION

A critical rainfall concept is a common tool for mitigating the slope failure worldwide. This concept has been developed based on a statistical approach related to historical slope failure data, and shown in form of rainfall thresholds that trigger the failures (ID thresholds). It is presented by a relationship between rainfall intensity and duration at the state of slope failure [1]-[8]. The advantages of critical rainfall concept are their simplicity and fast assessment. It is therefore implemented as a part of early warning system in various countries, for example in Hong Kong [9], USA [10], [11] and Italy [12]-[14].

Although the critical rainfall concept has been used worldwide, possible factors triggering the slope failures have been disregarded [15]. Rahardjo et al. [16] performed a set of parametric study using numerical model to investigate influential factors on instability of homogenous soil slopes. The results indicated that the stability of homogenous soil slope or safety factor (FS) is affected by many factors including saturated permeability of soil, rainfall intensity, slope angle, and also initial water table location. Rahimi et al. [17] studied effect of hydraulic properties on instability of slope subjected to rainfall events. They stated that the soil-water characteristic (SWC) play an important role on *FS* especially in poor drainage soil. While the saturated coefficient of permeability play a vital role on the stability of homogenous slope both for good and poor drainage soil slopes. In addition, the effect of antecedent rainfall on instability of soil slopes has been examined [18], [19].

Previous researches have recognized that many factors could trigger instability of slopes. However, they conducted stability analysis only under a specific period of rainfall. None of them performed the analysis with continuous rainfall until the slope failure takes place. Set of parametric study were performed via finite element based software to evaluate the influential factors on the shallow slope failure. The factor focused in this study was periodical condition of rainfall. The slope failure were triggered by assigned continuous rainfall with various rainfall intensities. Times to failure according to the assigned rainfalls were recorded and the ID thresholds were plotted accordingly.

THEORETICAL BACKGROUND

Finite element PLAXIS code with a fully coupled flow-deformation analysis was used in this study. The code to rainfall infiltration problems was verified by Hamdhan and Schweiger [20]. Mohr-Coulomp failure criterion with Bishop's effective stress [21] for unsaturated soil is used:

$$\tau = c' + (\sigma_n - u_w)tan\varphi' + \chi(u_a - u_w)tan\varphi' \quad (1)$$

where τ is shear strength of unsaturated soil, σ_n is total normal stress, u_a is pore air pressure, u_w is pore-water pressure, $(\sigma_n - u_a)$ is net normal stress, $(u_a - u_w)$ is metric suction, c' is effective cohesion, φ' is internal soil friction angle and χ is scalar multiplier which was assumed equal to the effective degree of saturation(θ_e).

Richard's equilibrium was used to simulate transient flow through unsaturated soil. The equilibrium states of flow in x, y and z directions is:

$$\frac{\partial}{\partial x}\left(k_x(h)\frac{\partial h}{\partial x}\right)+\frac{\partial}{\partial y}\left(k_y(h)\frac{\partial h}{\partial y}\right)+\frac{\partial}{\partial z}\left(k_z(h)\frac{\partial h}{\partial z}+1\right)=\{C(h)+S.S_s\}\frac{\partial h}{\partial t} \quad (2)$$

where k_x, k_y, k_z are coefficients of permeability in directions of x, y and z respectively, $C(h) = (\partial\theta/\partial h)$ is differential between volumetric moisture content(θ) to pressure head(h) which represent the specific moisture capacity, and S_s is the specific storage of a material.

Permeability of unsaturated soil depends mainly on soil-water characteristics (SWC). The SWC is the relationship between moisture content and pressure head, which can be explained by van genuchten [22] and the permeability function is explained by Mualem [23] as respectively shown as Eq. 3 and Eq. 4.

$$\theta_e = \frac{\theta_W-\theta_{res}}{\theta_{sat}-\theta_{res}} = \frac{1}{[1+(\alpha h)^n]^m} \quad (3)$$

$$k(h) = k_{sat}\left\{\theta_e{}^{1/2}\left[1-\left(1-\theta_e{}^{1/m}\right)^m\right]^2\right\} \quad (4)$$

where θ_w is volumetric moisture content, θ_{res} is residual volumetric moisture content, θ_{sat} is saturated volumetric moisture content, k_{sat} is saturated permeability of soil and α are related to air-entry value of soil, which is the matric suction value that must be exceeded before air recedes into the soil pores, n is the rate of water extraction from the soil once the air entry has been exceed, respectively, $, m$ is parameter related to value of $n(m = n - 1/n)$.

These two group of material parameters including shear strength parameters ($i.e.\, c', \varphi'$) and three hydraulic related parameters $(i.e.\, \alpha, n, k_{sat})$ are the required parameters to perform an analysis of rainfall-induced slope failures in PLAXIS. In this study, these parameters were obtained by pervious research works and discussed in the following section.

MATERIALS AND METHODS

Shallow slope failure is common found in many parts of the world. The geological conditions in each hazardous area are different depending on climate conditions, soil type, slope geometry, etc. This paper gathered the soil properties reported from the relevant literatures [24]-[30] and they are summarized in Table 1. Typical range of the parameters are as following: the parameter α is between 0.016 and 0.360 kPa^{-1}, the desaturation parameter n is between 1.290 and 2.780, θ_{sat} is from 0.286 to 0.480, θ_{res} is from 0 to 0.250, and the saturated permeability of soil is between 1.0x10^{-6} and 2.1x10^{-4} m/s.

Previous literatures [15], [16] reveal that the saturated permeability plays a major role on the stability of slope. Hence, it was mainly focused in this paper. The remained parameters were kept constant at c' = 6.74 kN/m^2, φ' =33.6°, α = 0.162 kPa^{-1} and n = 1.564. These parameter values were deducted from the average values reported in Table 1. In this study, variation of the saturated permeability is represented by type of soil, i.e. the soils A, B and C stand for low (K_{sat}=1x10^{-6} *m/s*), medium (K_{sat}=1x10^{-5} *m/s*) and high (K_{sat}=1x10^{-4} *m/s*) drain ability, respectively.

Eighteen cases of simulation run were conducted to evaluate the effect of periodical rainfall on time to failures of shallow slope. Rainfalls assigned in this paper were composed of two rainfall events having the equal rainfall intensity. The first rainfalls were assigned for 24 hr followed by dry period and the second rainfall which were assigned until the slope failure. The durations of dry period taken place between rainfall events (t_b) were 2 and 7 days. In this study, the effect of time between rainfall events is evaluated under three rainfall intensities and two types of soil, while slope angle was also kept constant as summarized in table 2.

SET UP OF EXPERIMENTS

Slope geometry, boundary conditions and fixity used in this paper are shown in Figure 1. The model composed of two layers: natural soil and bedrock. Bedrock layer is overlaid by soil layer of 3 meters thickness, which gives a soil depth over slope length of 3/100. Standard fixities were prescribed to allow only vertical movement along the boundary sides, while lateral and vertical movements were fixed at bottom boundary. Fifteen-node triangles finite element mesh was assigned. The finer elements was generated at the soil layer, and the finest mesh was generated at interested zone.

A prescribed flux, which is used to represent the desired intensity of rainfall, was assigned along the slope surface BC. Based on the rainfall intensity specified in Table 2, a range of pore pressure was between -0.05 m and 0.05 m. By this maximum pore water pressure of 0.05 m, the pounding water due to the excess of rainfall intensity over the drainage capacity at soil saturation state could be developed up to 5 cm. over the slope surface. While the minimum pore water pressure of -0.05 m was used to represent a depth where the negative flux due to evaporation is no longer occur. The boundaries AB and CD were assigned as no flux boundary, while the boundaries AHG, DEF and GF were prescribed as impervious boundary. The initial conditions of the model is according to no groundwater table exists in the soil layer. Table 3 summarizes parameters required for calculation.

Table 1 Summary of soil parameters from previous study

Data No.	Author/Year	Hydrualic property			Strength property	
		k_{sat} (m/s)	α $(kPa)^{-1}$	n	c' (kN/m²)	φ' (°)
1	Jotisankasa et al.(2008) & Jotisankasa A. and Mairaing W.(2010)	-	0.360	1.290	6.5	37.0
2		2.1x10^{-4}	0.290	1.316	12.8	33.1
3		1.0x10^{-5}	0.265	1.596	8.7	38.6
4		-	0.066	1.298	17.6	28.7
5	Bordoni et al.(2015)	2.0x10^{-5}	0.016	1.300	0	32.0
6	Dahal et al.(2009)	4.9x10^{-5}	-	-	4.9	31.5
7	Oh H. and Lu N.(2015)	5.6x10^{-6}	0.044	1.370	0	34.1
8	Vieira et al.(2010)	1.0x10^{-6}	-	-	6	34
9	Godt JW. and MaKenna JP (2008)	5.0x10^{-5}	0.096	2.780	4.2	33.6
MEAN	-	4.29x10^{-5}	0.162	1.564	6.74	33.6

Table 2 Summary of numerical experiments

Rainfall intensity related to soil type i, (mm/hr)			Time between rainfall events t_b, (day)
A	B	C	-
0.36	1	1	2,7
3.6	10	10	

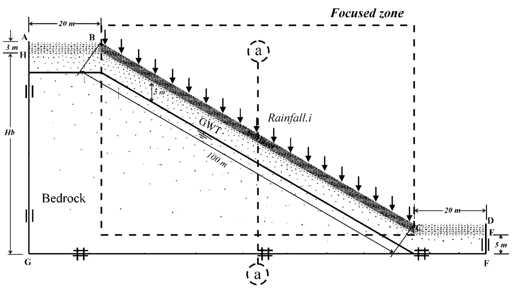

Fig. 1 Slope geometry and boundary conditions

NUMERICAL RESULTS AND DISCUSSIONS

The results from numerical experiments are represented in this section, including 1) the possible failure mechanism related to pore-water pressure responses, and 2) rainfall threshold for the initiation of shallow slope failure.

General Mechanism of Rainfall-induced Shallow Slope Failures

Two cases of simulation results were used to explain the shallow slope failure mechanism. Rainfall intensity of 10 and 36 mm/hr were assigned to soil type B (k_{sat} =1x10^{-5} m/s). Figure 2 shows the variation of *FS* with period of the second rainfall. For the rainfall intensity of 10 mm/hr, a small rate of FS reduction is found at the beginning. The *FS* decreases sharply to critical value after 48 hours. In case of rainfall intensity equals to saturated permeability (saturated permeability of soil type B is 1x10^{-5}m/s = 10^{-5} x 10^{3} mm/m x 3600 s/hr =36 mm/hr), the *FS* decreases sharply since the beginning of rainfall period.

Figure 3 shows pore water pressure profile (section a-a in Figure 3) related to rainfall intensity of 10 and 36 mm/hr. For the rainfall intensity of 10 mm/hr, the development of pore water pressure is divided into two stages. The first stage is according to the rainfall infiltration process. The pore water pressure increases from its initial value to about -3 kPa. The stability of slope shown in Figure 2 is still stable during this process because of the remained matric suction in the soil slope.

After the first stage, rising of water table and the positive pore water pressure take place at the second stage which is taking place when the rain water infiltrates to soil-bedrock interface. The positive pore water pressure results in the reduction of the soil shear strength especially at the soil-bedrock interface.

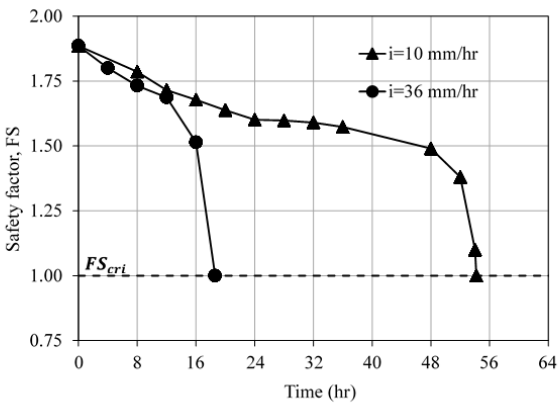

Fig. 2 Relationship between safety factor and time under rainfall intensities

Table 3 Material parameters required in PLAXIS

Parameter	Symbol	Soil layer	Bedrock layer	Unit
General parameters				
Material model	Model	Morh Coulomb	Morh Coulomb	-
Type of material behavior	Type	Undrained A	Non-porous	-
Dry unit weight	γ_{unsat}	17.36	23^{a*}	kN/m^3
Total unit weight	γ_{sat}	17.36	23^{a*}	kN/m^3
Strength parameters				
Cohesion	c'	6.74	25^{a*}	*kPa*
Friction angle	φ'	33.62	50^{a*}	°
Flow parameters				
Unsaturated flow model	-	Van Genuchten	-	-
Soil type	-	*A* *B* *C*	-	-
Saturated permeability of soil	$k_{sat,x} = k_{sat,y}$	$1x10^{-6}$ $1x10^{-5}$ $1x10^{-4}$	-	*m/s*
n	n	1.564	-	-
α	α	0.162	-	kPa^{-1}

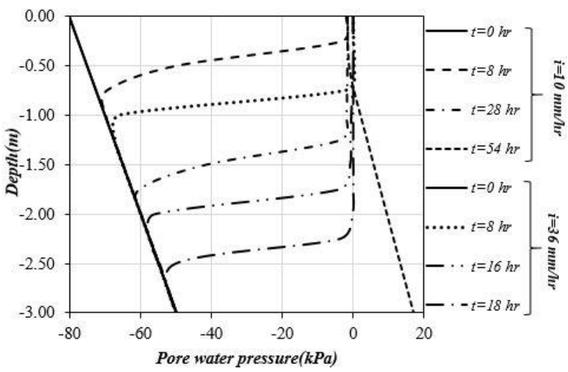

Fig. 3 Pore water pressure profile under different rainfall intensity of soil type B

For the rainfall intensity of equal to saturated permeability, the development of pore water pressure increases from its initial value to reach null pore water pressure immediately since rainfall started. In the other word, the matric suction was dissipated during rainfall infiltration process. It is therefore resulting in drop of *FS* and then slope failures as shown in Figure 2.

Rainfall Thresholds for Initiation of Shallow Slope Failure (ID thresholds)

Generally, the ID thresholds is established by plotting the relationship between rainfall intensity I_f versus duration D_f at failure states of slope on double logarithm relationship, which can be explained as:

$$I_f = a + cD_f^m \tag{5}$$

where a, c, and m are model parameters, which represent the curvature, interception and gradient of ID threshold, respectively. Figure 4 presents the ID thresholds plotted from all simulation results. A Single linear relationship between log(I_f) and log (D_f) could be drawn regardless the magnitude of permeability of the soil. The effect of periodical rainfall on ID thresholds is also presented in Figure 4. Times between the rainfall events were 2 and 7 days. The smaller D_f is encountered for the shorter the dry period. It is found that the effect of time between rainfall events results in the vertically shift of the ID thresholds plot.

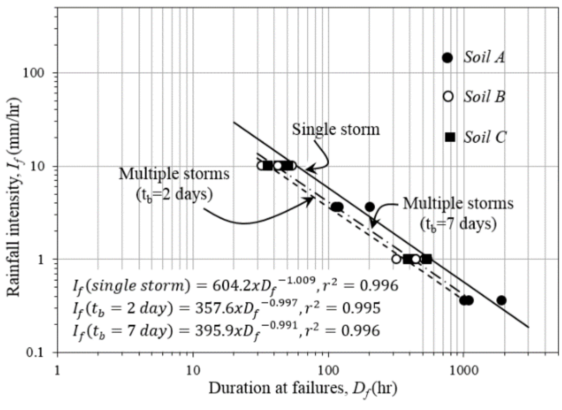

Fig. 4 ID thresholds with varying in time between rainfall events

CONCLUSIONS

1) Under a certain slope geometry, shallow slope failure can be triggered under either the rainfall infiltration or the rising of water table modes depending on the soil properties and rainfall intensity. The soil saturated permeability is one of the primary factored control the range of rainfall intensity. The lower rainfall intensity comparing

with the saturated permeability, the higher stability of the slope during infiltration stage. For rainfall intensity equals to or greater than saturated permeability, the matric suction will completely disappear during infiltration stage, and hence the slope failure is possibly found during the infiltration state.

2) The periodical rainfall plays an important role on failure state of shallow slope. The time to slope failure (D_f) subjected to assigned rainfall intensity (I_f) decreases with a short period between rainfall events. Furthermore, it also results in the fitting parameter representing interception of rainfall intensity-duration for initiation of shallow slope failures (ID thresholds).

REFERENCES

[1] Aleotti P. 2004. A warning system for rainfall-induced shallow failures. Engineering Geology 73(3-4):247-265.

[2] Caine N. 1980. The rainfall intensity-duration control of shallow landslides and debris flows. Geografiska Annaler Series A-physical Geography 62:23-27.

[3] Calcaterra D, Parise M, Palma B, and Pelella L. 2000. The influence of meteoric events in triggering shallow landslides in pyroclastic deposits of Campania. Proceedings 8th International Symposium on Landslides, (Bromhead E, Dixon N, Ibsen ML, eds) Cardiff: AA Balkema 1:209-214.

[4] Cannon SH, and Gartner JE. 2005. Wildfire-related debris flow from a hazards perspective. In: Debris flow Hazards and Related Phenomena (Jakob M, Hungr O, eds). Springer Berlin Heidelberg:363-385.

[5] Chien YC, Tien CC, Fan CY, Wen CY, and Chun CT. 2005. Rainfall duration and debrisflow initiated studies for real-time monitoring. Environmental Geology 47:715-724.

[6] Corominas J. 2000. Landslides and climate. Keynote lecture- In: Proceedings 8th International Symposium on Landslides, (Bromhead E, Dixon N, Ibsen ML, eds) Cardiff: AA Balkema 4:1-33.

[7] Crosta GB, and Frattini P. 2001. Rainfall thresholds for triggering soil slips and debris flow. In: Proceedings 2nd EGS Plinius Conference on Mediterranean Storms (Mugnai A, Guzzetti F, Roth G, eds) Siena:463–487.

[8] Guzzetti F, Peruccacci S, Rossi M, and Stark CP. 2007. Rainfall thresholds for the initiation of landslides in central and southern Europe. Meteorology and Atmospheric Physics 98:239-267.

[9] Brand EW. 1984. State-of-the-art report of landslides in Southeast Asian. In: 4th International Symposium on Landslides, Toronto, Canada 1:377-384.

[10] Keefer DK, Wilson RC, Mark RK, Brabb EE, Brown WM-I, Ellen SD, Harp EL, Wieczorek GF, Alger CS, and Zatkin RS. 1987. Real-time landslide warning during heavy rainfall. Science 238:921-925.

[11] Wilson RC, Mark RK, and Barbato G. 1993. Operation of a real-time warning system for debris flows in the San Francisco Bay area, California. International Conference Hydraulics Division, ASCE 2:1908-1913.

[12] Sirangelo B, and Braca G. 2004. Identification of hazard conditions for mudflow occurrence by hydrological model. Application of FLaIR model to Sarno warning system. Engineering Geology 73:267-276.

[13] Sirangelo B, Versace P, and De Luca DL. 2007. Rainfall nowcasting by at site stochastic model PRAISE. Hydrology and Earth System Science 11:1341–1351.

[14] Versace P, Sirangelo B, and Capparelli G. 2003. Forewarning model of landslides triggered by rainfall. 3rd International Conference on Debris-flow Hazards Mitigation: Mechanics, Prediction and Assessment, Davos, Switzerland 2:1233–1244.

[15] Rahardjo H, Ong TH, Rezaur RB, and Leong EC. 2007. Factors controlling instability of homogeneous soil slopes under rainfall. Journal of Geotechnical and Geoenvironmental Engineering 133(12):1532-1543.

[16] Rahardjo H, Nio AS, Leong EC, and Song NY. 2010. Effects of Groundwater Table Position and Soil Properties on Stability of Slope during Rainfall. Journal of Geotechnical and Geoenvironmental Engineering 136(11):1555-1564.

[17] Rahimi A, Rahardjo H, and Leong E-C. 2010. Effect of hydraulic properties of soil on rainfall-induced slope failure. Engineering Geology 114(3-4):135-143.

[18] Rahardjo H, Li XW, Toll DG, and Leong EC. 2001. The effect of antecedent rainfall on slope stability. Geotechnical and Geological Engineering 19:371-399.

[19] Rahimi A, Rahardjo H, and Leong EC. 2011. Effect of Antecedent Rainfall Patterns on Rainfall-Induced Slope Failure. Journal of

Geotechnical and Geoenvironmental Engineering 137(5):483-491.

[20] Hamdhan IN, and Schweiger HF. 2013. Finite Element Method–Based Analysis of an Unsaturated Soil Slope Subjected to Rainfall Infiltration. International Journal of Geomechanics 13(5):653-658.

[21] Bishop AW, and Blight GE. 1963. Some aspects of effective stress in saturated and partly saturated soils. Géotechnique 13(2):177-197.

[22] van Genuchten MT. 1980. A closed-form equation for predicting the hydraulic conductivity of unsaturated soil. Soil Science Society of American Journal 44:615–628.

[23] Mualem Y. 1976. A new model predicting the hydraulic conductivity of unsaturated porous media. Water Resources Research 12:513-522.

[24] Jotisankasa A, and Mairaing W. 2010. Suction-Monitored Direct Shear Testing of Residual Soils from Landslide-Prone Areas. Journal of Geotechnical and Geoenvironmental Engineering 136(3):533-537.

[25] Jotisankasa A, and Vathananukij H. 2008. Investigation of soil moisture characteristics of landslide-prone slopes in Thailand. Proceeding of International Conference on Management of Landslide Hazard in the Asia-Pacific Region, Sendai Japan:1-12.

[26] Bordoni M, Meisina C, Valentino R, Bittelli M, and Chersich S. 2015. Site-specific to local-scale shallow landslides triggering zones assessment using TRIGRS. Natural Hazards and Earth System Science 15(5):1025-1050.

[27] Dahal RK, Hasegawa S, Nonomura A, Yamanaka M, Masuda T, and Nishino K. 2008. Failure characteristics of rainfall-induced shallow landslides in granitic terrains of Shikoku Island of Japan. Environmental Geology 56(7):1295-1310.

[28] Oh S, and Lu N. 2015. Slope stability analysis under unsaturated conditions: Case studies of rainfall-induced failure of cut slopes. Engineering Geology 184:96-103.

[29] Vieira BC, Fernandes NF, and Filho OA. 2010. Shallow landslide prediction in the Serra do Mar, São Paulo, Brazil. Natural Hazards and Earth System Science 10(9):1829-1837.

[30] Godt JW, and McKenna JP. 2008. Numerical modeling of rainfall thresholds for shallow landsliding in the Seattle, Washington, area. Review in Engineering Geology 20:121-136.

EXPRESSION OF AIR PRESSURE DISTRIBUTION USING SOIL/WATER/AIR COUPLED ANALYSIS

Katsuyuki KAWAI[1], Takuya KAWAKATSU[2] and Atsushi IIZUKA[3]
[1]Dept. Of Civil and Environmental Engineering, Kindai University, Japan; [2] Shimizu Corporation, Japan;
[3] Research Center for Urban Safety and Security, Kobe University, Japan

ABSTRACT

Recently, the frequency of torrential rainfall has increased due to global climate change, and these events cause sediment potential failure. It is difficult to predict when and where a slope failure will occur because of the concentration of heavy rain. Knowing precursory phenomena, however, is effective for disaster reduction. Nonetheless, some of these phenomena have not been explained in the framework of geotechnical engineering. Organic smells and strange sounds, known as precursory signs of slope failure, propagate through the atmosphere. Therefore, it is important to monitor air movement within earth structures. This study focuses on pore air behavior within the ground due to rainfall infiltration. Here, the infiltration column test combined with monitoring smell, as conducted by Tsuchida et al., was first simulated using the soil/water/air coupled finite element code, DACSAR-MP. Next, a sloping earth structure exposed to rainfall was simulated. Consequently, it was found that distribution of pore air pressure was dependent on drainage conditions of air, and that pore air behavior influenced rainfall infiltration behavior.

Keywords: Unsaturated Soil, Soil/water/air Coupled Analysis, Slope Stability, Rainfall, Air Pressure

INTRODUCTION

Recently, torrential rainfall events have tended to occur locally, and it is difficult to predict damage from landslides due to rainfall. Therefore, increasing citizen awareness about disasters is needed to reduce disaster damage. In this regard, understanding precursory phenomena for landslides is effective. There are a lot of successful cases in which precursory phenomena acted as an alert. Because of this, precursory phenomena were introduced onto a hazard map published by Japanese government. However, some of these phenomena are difficult to explain theoretically in soil mechanics. In particular, the generating mechanism of unusual sound and smell before a landslide has not been clarified. These phenomena likely result from rainfall influencing air within the ground, since both sound and smell are transmitted by air. In this study, rainfall infiltration into sloped ground was simulated with soil/water/air coupled analysis to investigate localization of air within the ground.

PRIOR INVESTIGATIONS OF AIR BEHAVIOR WITHIN THE GROUND

Tsuchida et al. conducted soil column testing to investigate the relationship between rainfall infiltration and smell occurrence [1]. The soil column was installed with a profile moisture meter to measure the seepage line generated by a sprinkler fitted above the sandy soil column (Fig. 1). Smell was generated

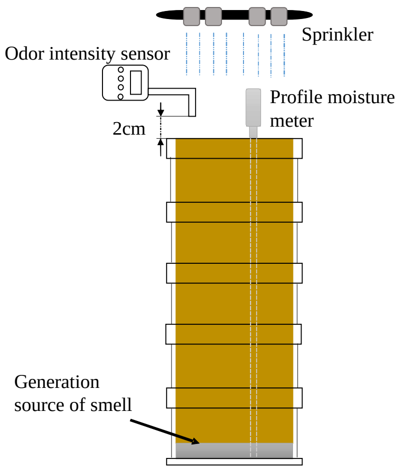

Fig. 1 Rainfall infiltration test by Tsuchida et al.

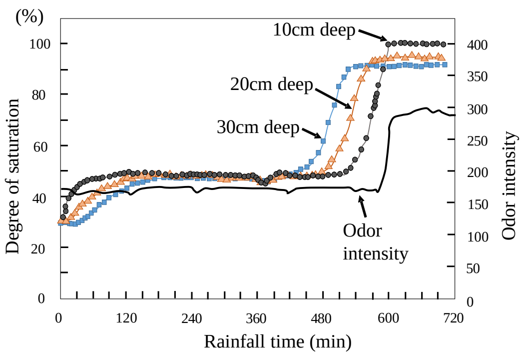

Fig. 2 Distribution of degree of saturation and odor intensity at the ground surface during rainfall

by a source at the bottom of the soil column, and leakage of smell from the surface of the soil column was measured with an odor intensity sensor. In this way, the distribution of the degree of saturation and odor intensity due to rainfall infiltration were monitored (shown in Fig. 2). First, it was found that degree of saturation started to increase from the bottom of the column, and the rise of the ground water level was more remarkable than the descent of the wetting front at the given rainfall condition. The odor intensity at the surface of the column drastically increased after an increase in the degree of saturation at each depth, a phenomena correlated to the rise of the groundwater level. Tsuchida et al. concluded that the groundwater level, determined by arriving to the bottom of infiltrated rain water, pushed air within the ground upwards, thus odor generation before a landslide signifies that the groundwater level is rising. However, their investigation was limited to one-dimensional infiltration. In this study, the soil column test performed by Tsuchida et al. was first simulated, followed by simulation of rainfall infiltration into virtual sloping ground.

SOIL/WATER/AIR COUPLED ANALYSIS

The soil/water/air coupled simulation code, DACSAR-MP [2], was used for rainfall simulation. The constitutive model for unsaturated soil, proposed by Ohno et al. [3], was adopted and formulated with the theory of three phase's mixture material proposed by Borja [4]. In this way, effective stress is expressed as follows.

$$\boldsymbol{\sigma}' = \boldsymbol{\sigma}^{net} + p_s \mathbf{1} \tag{1}$$

$$\boldsymbol{\sigma}^{net} = \boldsymbol{\sigma} - p_a \mathbf{1}, \;\; p_s = S_e s \tag{2}$$

$$s = p_a - p_w, \;\; S_e = \frac{S_r - S_{rc}}{1 - S_{rc}} \tag{3}$$

Here, $\boldsymbol{\sigma}'$ is the effective stress tensor; $\boldsymbol{\sigma}^{net}$ is the net stress tensor; $\mathbf{1}$ is the second-order unit tensor; $\boldsymbol{\sigma}$ is the total stress tensor; s is suction; p_s is suction stress; p_a is pore air pressure; p_w is pore water pressure; S_r is degree of saturation; S_e is effective degree of saturation; and S_{rc} is degree of saturation at $s \to \infty$. The yield function is expressed as follows.

$$f\left(\boldsymbol{\sigma}', \zeta, \varepsilon_v^p\right) = MD \ln \frac{p'}{\zeta p'_{sat}} + \frac{MD}{n_E}\left(\frac{q}{Mp'}\right)^{n_E} - \varepsilon_v^p = 0 \tag{4}$$

$$\zeta = \exp\left[(1 - S_e)^{n_s} \ln a\right], \;\; MD = \frac{\lambda - \kappa}{1 + e_0} \tag{5}$$

$$p' = \frac{1}{3}\boldsymbol{\sigma}' : \mathbf{1}, \; q = \sqrt{\frac{3}{2}\mathbf{s} : \mathbf{s}}, \; \mathbf{s} = \boldsymbol{\sigma}' - p'\mathbf{1} = \mathbf{A} : \boldsymbol{\sigma}', \; \mathbf{A} = \mathbf{I} - \frac{1}{3}\mathbf{1} \otimes \mathbf{1} \tag{6}$$

Here, n_E is a shaping parameter; ε_v^p is plastic volumetric strain; M is the stress ratio q/p' at the critical state; D is the dilatancy coefficient; p'_{sat} is the yield stress at saturated state; a and n_s are the parameters expressing the yield stress increment due to desaturation; and λ and κ are compression and expansion indices, respectively. Darcy's law is assumed for pore water and air flow as follows.

$$\tilde{\mathbf{v}}_{\mathbf{w}} = -\mathbf{k}_{\mathbf{w}} \cdot \mathrm{grad} h \tag{7}$$

$$\tilde{\mathbf{v}}_{\mathbf{a}} = -\mathbf{k}_{\mathbf{a}} \cdot \mathrm{gradh}_a, \;\; h_a = \frac{p_a}{\gamma_w} \tag{8}$$

Here, $\tilde{\mathbf{v}}_{\mathbf{w}}$ and $\tilde{\mathbf{v}}_{\mathbf{a}}$ are the velocity of water and air, respectively; $\mathbf{k}_{\mathbf{w}}$ and $\mathbf{k}_{\mathbf{a}}$ are permeability of water and air, respectively; h is total water head; γ_w is unit weight of water; and h_a is air pressure head. Permeability of water and air are expressed by Mualem's equation [5] and Van Genuchten's equation [6] as follows.

$$\mathbf{k}_{\mathbf{w}} = k_{rw}\mathbf{k}_{\mathbf{wsat}} = S_e^{1/2}\left[1 - \left(1 - S_e^{1/m}\right)^m\right]^2 \mathbf{k}_{\mathbf{wsat}} \tag{9}$$

$$\mathbf{k}_{\mathbf{a}} = k_{ra}\mathbf{k}_{\mathbf{ares}} = \left(1 - S_e\right)^{1/2}\left(1 - S_e^{1/m}\right)^{2m} \mathbf{k}_{\mathbf{ares}} \tag{10}$$

Here, k_{rw} and k_{rw} are the relative permeability of water and air, respectively; m is Mualem's coefficient; and $\mathbf{k}_{\mathbf{wsat}}$ and $\mathbf{k}_{\mathbf{ares}}$ are water permeability at a saturated state and air permeability at a perfectly dry state, respectively. The continuous equation of water and air are expressed by the application of three phases' mixture theory.

$$n\dot{S}_r - S_r\dot{\varepsilon}_v + \mathrm{div}\tilde{\mathbf{v}}_{\mathbf{w}} = 0 \tag{11}$$

$$\left(1 - S_r\right)\dot{\varepsilon}_v + n\dot{S}_r - n\left(1 - S_r\right)\frac{\dot{p}_a}{p_a + p_0} - \mathrm{div}\tilde{\mathbf{v}}_{\mathbf{a}} = 0 \tag{12}$$

Here, n is porosity; ε_v is volumetric strain; and p_0 is atmospheric pressure. The elasto-plastic constitutive model can be obtained from equation (4) and the force equilibrium equation as follows.

$$\dot{\boldsymbol{\sigma}}' = \mathbf{D} : \dot{\boldsymbol{\varepsilon}} - \mathbf{C} \cdot \dot{S}_e \tag{13}$$

Here, $\mathbf{D}$ is the elasto-plastic stiffness matrix; $\boldsymbol{\varepsilon}$ is the strain increment tensor; and $\mathbf{C}$ is the tensor expressing change in stiffness due to desaturation. The soil/water/air coupled problem was formulated by equations (11), (12) and (13). The soil water retention characteristic curve (SWRCC), which demonstrates the relationship between suction and soil moisture, is dependent on suction history. This hysteresis influences compaction behavior. In this study, the SWRCC model proposed by Kawai et al. [7] was used.

ONE-DIMENSIONAL RAINFALL INFILTRATION SIMULATION

Tsuchida et al. studied air behavior within ground exposed to relatively small rainfall. In this study, rainfall intensity large enough to generate a wetting front was simulated. The soil parameters used for the simulation are summarized in Table 1, and the soil water retention characteristic curves are shown in Fig. 3. Here, a sandy soil commonly used for general earth structures was assumed. The analytical mesh shown in Fig. 3 was assumed in accordance with Tsuchida et al. The undrained water and undrained air boundaries were provided for right and left side boundaries. A flux boundary, corresponding to rainfall intensity, and a drained air boundary ($p_a = 0$) were applied to the upper boundary. On the bottom of the analytical area, two kinds of boundary were investigated. One

Table 1 Soil parameters used for simulation

λ	κ	M	p'_{sat} (kPa)	k_{wx} (m/h)	k_{wy} (m/h)	S_{ri}
0.087	0.009	1.375	1500	0.156	0.078	0.15
m	a	n	n_E	k_{ax} (m/h)	k_{ax} (m/h)	e_i
0.8	10	1.0	1.00	15.6	7.8	0.7

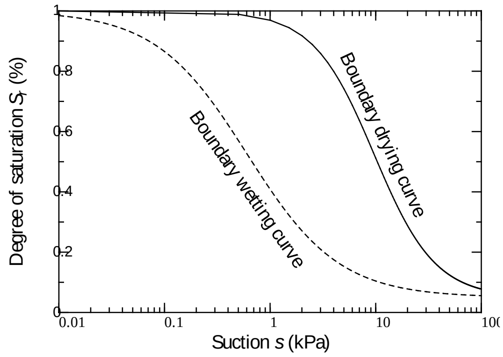

Fig. 3 Soil water retention characteristic curves

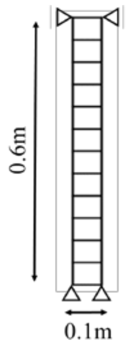

Fig. 4 Analytical mesh for one dimensional infiltration simulation

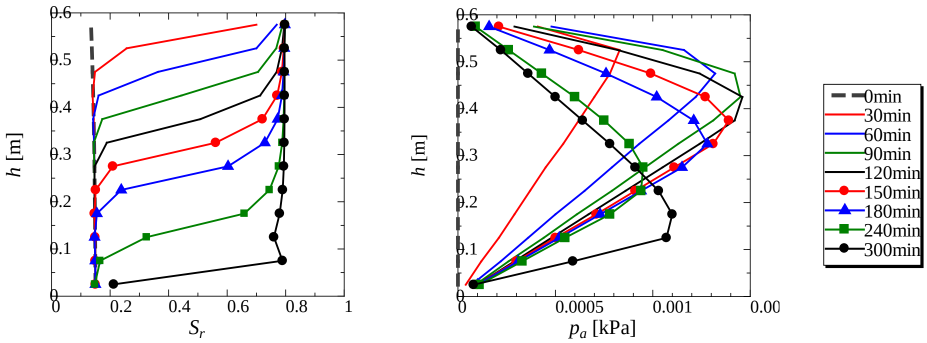

(a) Degree of saturation (b) Air pressure

Fig. 5 Rainfall intensity 30mm/h (Case DD)

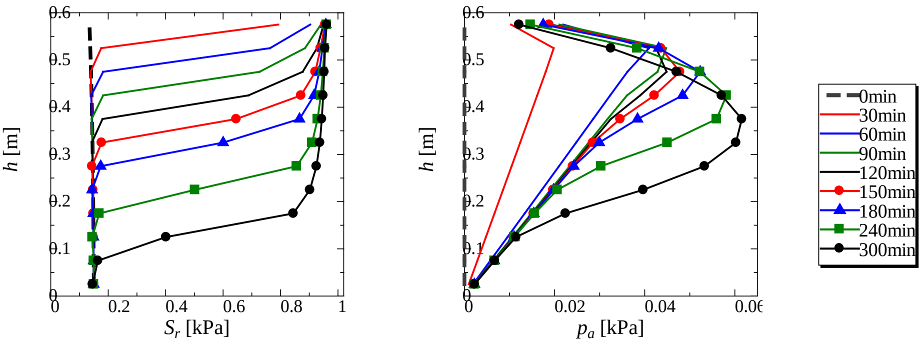

(a) Degree of saturation (b) Air pressure

Fig. 6 Rainfall intensity 60mm/h (Case DD)

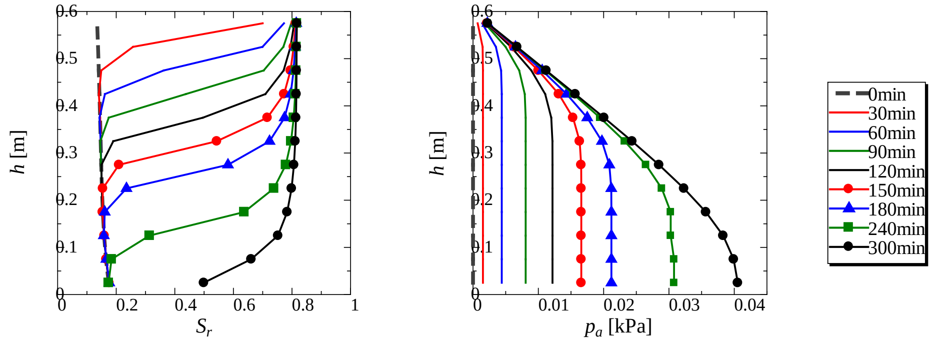

(a) Degree of saturation (b) Air pressure

Fig. 7 Rainfall intensity 30mm/h (Case UU)

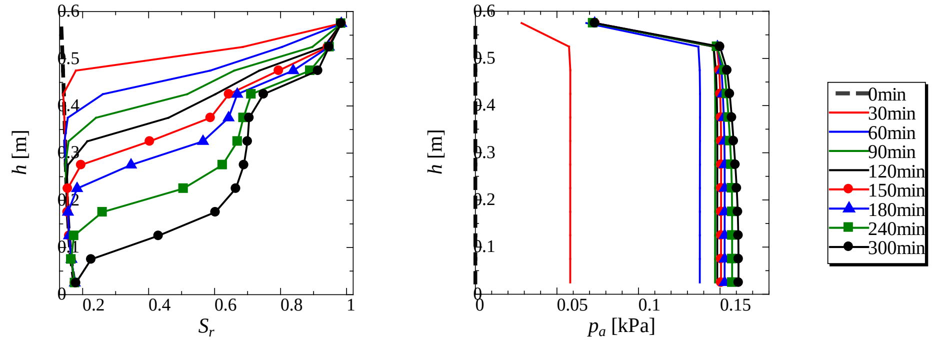

(a) Degree of saturation (b) Air pressure

Fig. 8 Rainfall intensity 60mm/h (Case UU)

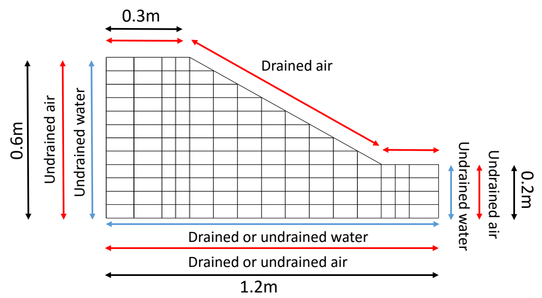

Fig. 9 Analytical mesh for rainfall simulation on sloping ground

case, named Case DD, investigated the condition of drained air and drained water, using a value of $p_w = -5.5(\text{kPa})$ to indicate an initial distribution of suction. The other case, named Case UU, investigated undrained water and undrained air conditions. Rainfall intensities of 30 and 60 mm/h were simulated.

Figures 5 and 6 show the distribution of the degree of saturation and air pressure in Case DD. These results demonstrate that differences in infiltration behavior depended on rainfall intensity. Degree of saturation of the wetting front, indicating rainfall infiltration, was 0.8 for a rainfall intensity of 30mm/h, while it was over 0.9 for a rainfall intensity of 60mm/h. However, the time at which the degree of saturation started to increase at each depth was earlier for the 30mm/h than the 60mm/h rainfall intensity. This tendency can be explained due to the distribution of air pressure. The descent of the wetting front compressed air within the ground and increased the degree of saturation at the surface. Here, entrapment of air was more remarkable for the 60mm/h rainfall intensity, and compressed air prevented infiltrated water from descending. The wetting front for the 30mm/h rainfall intensity case exhibited a 0.8 degree of saturation, and air was easily exhausted from the surface. Consequently, air pressure gradually decreased after peaking at 90 minutes.

Figures 7 and 8 show simulation results obtained from Case UU. Because the bottom boundary was undrained water, infiltrated water accumulated here after the wetting front reached the bottom. Moreover, air pressure monotonically increased. In this case, the higher air pressure that was generated can predict a burst of compressed air from the ground surface.

RAINFALL INFILTRATION INTO SLOPING GROUND

On an actual slope, the direction of groundwater

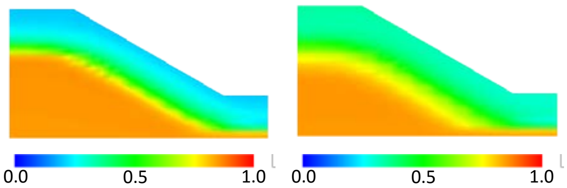

(a) 1.5 hour rainfall (b) 1 hour settling

Fig. 10 Degree of saturation (Case DD, 30mm/h)

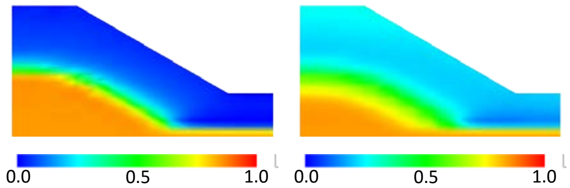

(a) 1.5 hour rainfall (b) 1 hour settling

Fig. 11 Degree of saturation (60mm/h, Case DD)

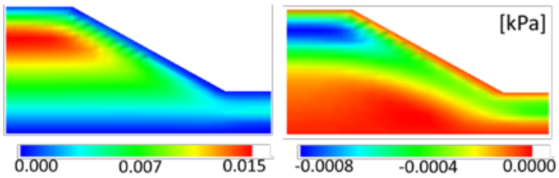

(a) 1.5 hour rainfall (b) 1 hour settling

Fig. 12 Air pressure (Case DD, 30mm/h)

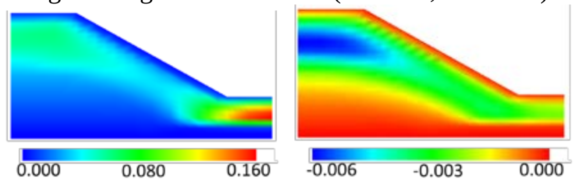

(a) 1.5 hour rainfall (b) 1 hour settling

Fig. 13 Air pressure (60mm/h, Case DD)

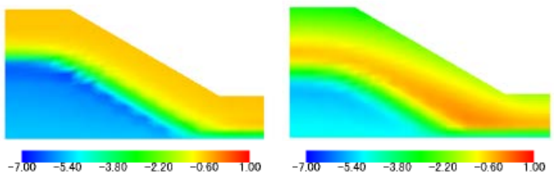

(a) 1.5 hour rainfall (b) 1 hour settling

Fig. 14 Water pressure (Case DD, 30mm/h)

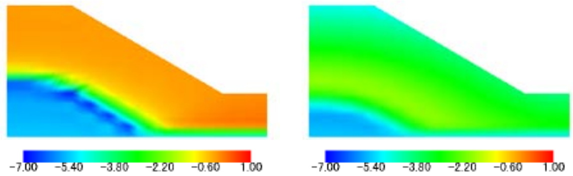

(a) 1.5 hour rainfall (b) 1 hour settling

Fig. 15 Water pressure (60mm/h, Case DD)

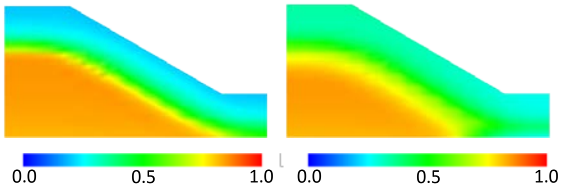

(a) 1.5 hour rainfall (b) 1 hour settling

Fig. 16 Degree of saturation (Case UU, 30mm/h)

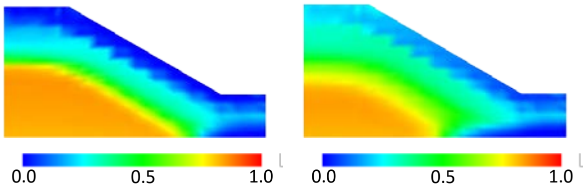

(a) 1.5 hour rainfall (b) 1 hour settling

Fig. 17 Degree of saturation (60mm/h, Case UU)

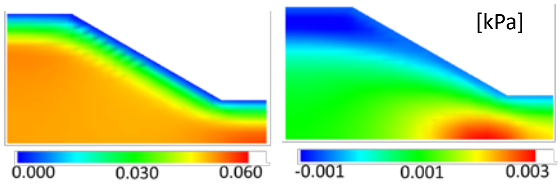

(a) 1.5 hour rainfall (b) 1 hour settling

Fig. 18 Air pressure (Case UU, 30mm/h)

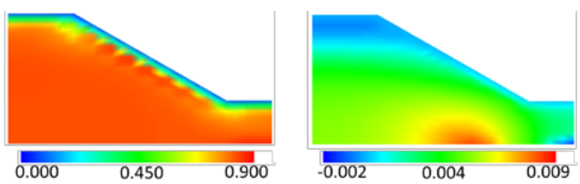

(a) 1.5 hour rainfall (b) 1 hour settling

Fig. 19 Air pressure (60mm/h, Case UU)

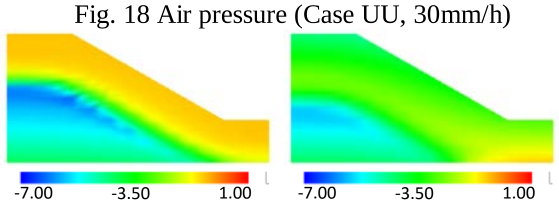

(a) 1.5 hour rainfall (b) 1 hour settling

Fig. 20 Water pressure (Case UU, 30mm/h)

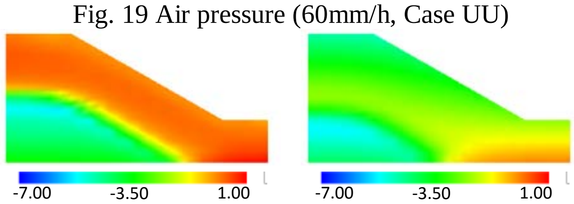

(a) 1.5 hour rainfall (b) 1 hour settling

Fig. 21 Water pressure (60mm/h, Case UU)

flow depends on slope shape. In this study, rainfall infiltration into sloping ground was simulated. Figure 9 shows the analytical mesh used in simulations. The right and left side boundaries were undrained water and air boundaries. The ground surfaces, including the crown and the slope, were both flux boundaries corresponding to rainfall intensity. The drainage condition of the bottom was changed with one-dimensional infiltration simulation. Input soil parameters are summarized in Table 1 and Fig. 3. Rainfall duration was 1.5 hour, and the settling time after rainfall is provided for each case.

Figures 10 and 11 show the distribution of the degree of saturation in the case of a drained bottom boundary (Case DD) under rainfall intensities of 30mm/h and 60mm/h, respectively. Rainfall of 60mm/h saturated the slope surface after 1.5 hours, while rainfall of 30mm/h did not saturate the surface in the same time period. Infiltrated water concentrated around the toe of slope during the settling term. This tendency was more remarkable for the higher rainfall intensity, shown in Fig. 11. This can be explained from equation (9). Unsaturated permeability depends on degree of saturation. Rainfall increases the degree of saturation around the slope surface first, resulting in an increase in the permeability around the slope surface. Consequently, flux parallel to slope becomes easier than vertical flux.

Figures 12 and 13 show the distribution of air pressure under rainfall intensities of 30mm/h and 60mm/h, respectively. An high air pressure area first appeared around the crown under a rainfall intensity of 30mm/h. This was because rainfall caused downward flux and pushed air toward the bottom as a drained boundary. Figures 14 and 15 show the distribution of water pressure. Rainfall increased the water pressure at the surface. However, the high water pressure area descended during the settling term, and negative water pressure appeared at the surface. This was because air permeability around the surface decreased due to saturation around the surface, and entrapped air expanded by downward flux. This led to negative air pressure around the crown. On the other hand, under a rainfall intensity of 60mm/h, since infiltrated water flowed parallel to the slope, the highest air pressure appeared around toe of slope.

Next, the same rainfall simulation was conducted under a condition of an undrained bottom boundary (Case UU). Figures 16 and 17 show the distribution of the degree of saturation under rainfall intensities of 30mm/h and 60mm/h, respectively. Since the bottom boundary was undrained, water infiltrating from the slope surface flowed towards the toe of slope and accumulated under the berm, especially under 60mm/h rainfall intensity. During the settling term, accumulated water spread to the left-hand side. However, in Case UU, the saturated area from the slope surface due to rainfall was smaller than in Case DD. This was because air was entrapped more easily and prevented rainfall from infiltrating. Figures 18 and 19 show the distribution of air pressure. In these figures, an area of high air pressure covered the whole of the sloping ground during rainfall, and it moved toward the toe of the slope during the settling term. This tendency was more remarkable and higher air pressure was generated under the higher rainfall intensity. Figures 20 and 21 show the distribution of water pressure. These results show that infiltrated water reached the bottom and tended to function as the phreatic surface.

CONCLUSIONS

In this study, rainfall infiltration was simulated with a soil/water/air coupled analysis to investigate rainfall effects on the behavior of air within the ground. Results show that the geometric condition and the drainage condition of water air strongly influenced the distribution of air pressure. Moreover, it was found that high pressure air entrapped by infiltrated water prevented rainfall from infiltrating. These results predict that compressed air will move towards a drained boundary and be finally exhausted. However, further considerations are needed to clarify the precursory phenomena of landslides.

REFERENCES

[1] Tsuchida, T., Yuri, A., Kano, S., Nakayabu, K., Yabuki, K., Hanaoka, N. & Kawabata, S. ‘Consideration of odor intensity within the ground and odor generation on landslide’, Journal of JGS, Vol.8, No.2, 2013, pp.339-348.

[2] Kanazawa, S. ‘Numerical evaluation of mechanical behavior of compacted soil structures based on a mathematical modelling for unsaturated soils’ Doctoral dissertation, Department of Civil Engineering, Kobe University, 2010 (in Japanese).

[3] Ohno S., Kawai K. & Tachibana S., ‘Elasto-plastic consti-tutive model for unsaturated soil applied effective degree of saturation as a parameter expressing stiffness’ Journal of JSCE, Vol. 63, No.4, 2007, pp.1132-1141 (in Japanese).

[4] Borja, R. I., ‘A mathematical framework for three-phase deformation and strain localization analysis of partially saturated porous media’ Computer methods in applied mechanics and engineering, Vol.193, 2004, pp.5301-5338.

[5] Mualem, Y., ‘A new model for predicting the hydraulic conductivity of unsaturated porous media’ Water Resources Research, Vol.12, No.3, 1976, pp.514-522.

[6] Van Genuchten, ‘A closed-form equation for predicting hydraulic of unsaturated soils’ Soil Science Society American Journal, Vol.44, 1980, pp.892-898.

[7] Kawai, K., Iizuka, A., Hayakawa, E. & Wang, W. ‘Non-uniform settlement of compacted earth structures caused by the deformation characteristics of unsaturated soil on wetting’ Soils and Foundations, Vol.47, No.2, 2007, pp. 195-206.

CYCLIC LATERAL RESPONSE OF MODEL PILE GROUPS FOR WIND TURBINES IN CLAY SOIL

Werasak Raongjant [1], Meng Jing [2]

[1] Assistant Prof., Department of Civil Engineering, Faculty of Engineering, Rajamangala University of Technology Thanyaburi, Thailand.

[2] Assistant Prof., Department of Civil Engineering, Faculty of Engineering, Rajamangala University of Technology Thanyaburi, Thailand.

ABSTRACT: Due to the large diameter and the cyclic loading, it is necessary to investigate the lateral response of pile groups for wind turbines in clay soil. This paper presents an experimental research on 2x2 model pile groups embedded in different types of clay soil, relatively density of 90% and 10%, subjected to one-way lateral cyclic loading. Analysis on the experimental results, such as load–deflection curves and bending moment profiles, were processed. It is found that the magnitude of the head level deflections and the maximum bending moment increased with the number of loading cycles. The group interaction effect under cyclic lateral loading is more significant in loose soil.

Keywords: Pile groups, Cyclic Lateral Loading, Relatively Density, Wind Turbines, Model Test

1. INTRODUCTION

Wind energy is now the popular energy resource all over the world due to its clean and renewable advantages. Also in Thailand, the government has planned to install the wind energy capacity to 800 MW by the year 2022 [1]. The pile group foundation consisting of a number of smaller piles connected by a platform plate is one of the suitable solutions for supporting wind turbine. The pile groups supporting these structures are subjected to cyclic lateral loading generated by wind, which is quite large and will governs the design of pile groups. Pile group behavior under cyclic lateral loading is nonlinear and involves complicated group interaction [2],[3]. Inevitably, group interaction has significant effect on the behavior of pile groups also.

Fig. 1 The Danish offshore wind farm in the North Sea [1]

Limit research experiences of pile group foundations under cyclic lateral loading could be reviewed. Rollins et al. [4] tested series of full scale pile groups with various spacing to study the effect of pile spacing under cyclic lateral loading on the behavior of pile groups. It was concluded that the group interaction effect decreases considerably with increase of spacing from 3.3 to 5.65 times the diameter of pile. Peng et al. [5] summarized various devices used for applying cyclic lateral load to model piles. Chandrasekaran et al. [6] reported experimental investigation on 1×2, 2×2 and 3×3 model pile groups, having different length or spacing and embedded in soft marine clay under lateral cyclic loading. From the test results it could be seen that, the lateral capacity of the pile group increased with the number of pile. Piles in closely spaced groups carry considerably higher moments at deeper depths. Basak S. and Mastorakis Nikose [7] performed the experiment on 2×2 pile group, each pile being hollow circular stainless steel bar. During cyclic loading in progress, a pair of gaps appeared in front and the back of the pile with the increasing number of loading cycles. The degradation factor decreased with number of cycles and increased with frequency nonlinearly.

Also there are some researches on the lateral behavior of pile groups using numerical analysis. Abbas et al. [8] reported the numerical studies on the lateral behavior of three pile group configurations (i.e. 2×1, 2×2 and 3×2 pile groups) with four values of pile spacing (i.e. 2D, 4D, 6D and 8D). It can be observed that, the group configuration has significant effect on the lateral pile displacement and ultimate soil resistance under the same lateral load. Chore et al. [9] used finite element method to analyze two pile groups subjected to lateral loads by considering the non-linear behavior of soil. It was concluded that the of soil due to non-linear behavior of soil, the top displacement of the pile group was increased 66.4% to 145.6%, while the fixed moments was reduced 2% to 20% and the positive moments 54% to 57%.

There are limited literature presented the experimental results of the pile groups in clay soil with different relative density under cyclic lateral loads. The effects of soil on pile groups under cyclic loading have not previously been studied extensively. Hence, in the present study, four model pile groups embedded in clay soils were tested under one-way cyclic lateral load to study the effects of soil density and number of cycles on load–deflection and bending behavior of pile group.

2. TEST PROGRAM

2.1 Soil Used

Clay used in this study is mined from the area in Pathum Thani province in Thailand. The properties of the clay are: liquid limit = 54.5%, plastic limit= 35.48%, plasticity index= 18.92%. According to the determined value, dense soil with relative density of 90% and loose soil with relative density of 10% were prepared in the test, following the compaction standard method. Clay was put into the test tank and compacted well. The placement density of dense clay soil (relative density of 90%) is 1.425 g/cm^3. The placement density of loose clay soil (relative density of 10%) is 1.253 g/cm^3. The conformed moisture content of both type of soil is 29.5%, according to that in Pathum Thani province of Thailand.

2.2 Pile Groups

The origin of the model pile group is the pile group foundation for wind turbine with the tower of 25 m high and the rotor diameter of 10 m. Four concrete piles, 19 m long and in 50×50 cm solid section, were arranged in the case of 2×2 pile group with the hanging space of 1.9 m. The pile cap is in 2.80×2.80 m square section with the thickness of 45 cm. Similitude laws proposed by Wood DM and Crewe A. [10] are followed to select the material and dimensions of model pile.

$$\frac{\boldsymbol{E_m I_m}}{\boldsymbol{E_p I_p}} = \frac{\mathbf{1}}{\boldsymbol{n^5}}$$

in which E_{m} is the modulus of elasticity of model pile, which was recorded as 69 GPa for aluminum in this study; E_{p} is the modulus of elasticity of prototype pile, corresponding to the reinforced concrete of f_c' = 25 N/mm^2 in this study; I_{m} is the moment of inertia of model pile; I_{p} is the moment of inertia of prototype pile; and $1/n$ is the scale factor for length of model pile to prototype pile, which equal to 1/30 in this study.

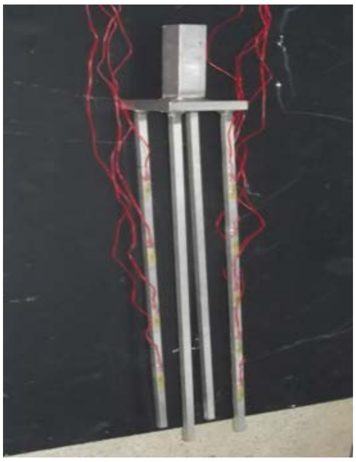

Fig.2 Model pile

750 mm long aluminum stick having square section of 10×10 mm was used as model pile to arrange 2×2 pile group with spacing of 63 mm in this study. Aluminum plate in 93× 93cm square section and in 15 mm thick was used as pile cap. Aluminum stick in size of 30×30 mm and 150 mm long was welded above the pile cap to subject lateral load from hydraulic jack. Four strain gauges at the interval of 150 mm were pasted on selected pile in leading row or rear row to record the bending moment at different depth of pile groups (see in Fig.2).

2.3 Test Loading Pattern

The steel tank used in test is 750 mm high with the section diameter of 650 mm (see in Fig.3). The model pile was then plug into the soil, leaving 120 mm above the soil surface. Then the cyclic lateral load was then applied by pneumatic cylinder attached on the loading frame. The one-way cyclic lateral load was increased from a minimum value of P_{min} = 0 to a maximum of P_{max} =20N, and return to P_{min} = 0 (no reversal of loading direction). The maximum lateral load P_{max} was taken as 80% of the ultimate lateral loading capacity of 25N, which has determined from static test when the corresponding deflection is equal to 20% of pile diameter. The lateral load was repeated for 50 times (cycles) and then increased monotonically until failure.

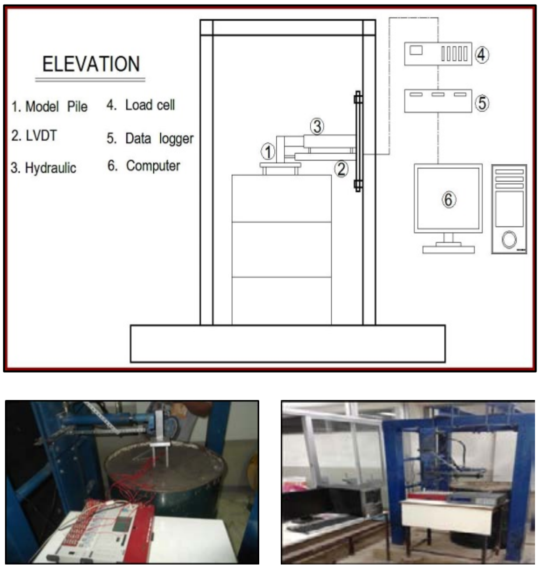

Fig.3 Test set-up

3. DISCUSSION ON TEST RESULTS

3.1 Load-Deflection Curves

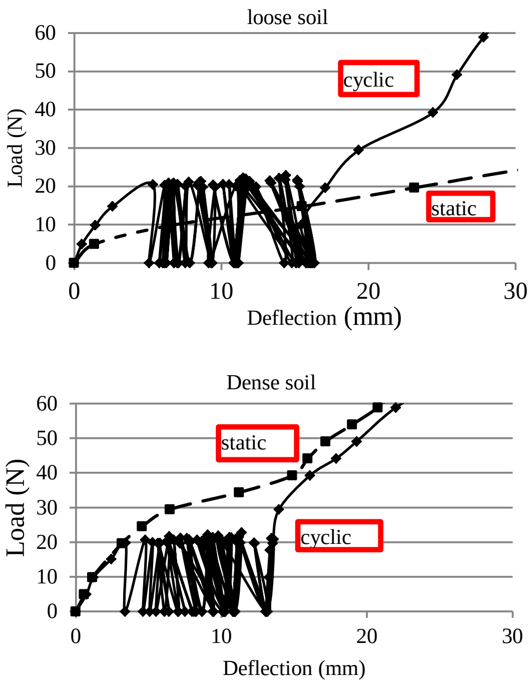

Fig. 4 Load versus head level deflection curves of pile groups in different soil

The lateral deflection of model pile groups under lateral static or cyclic loading, measured at the level of pile caps, were drawn in Fig. 4. The deflection increased nonlinearly with the number of loading cycles. It shows that, for pile group embedded in dense soil, the load-deflection curves under cyclic or static load behaved similar trend. The deflection of pile group in dense soil after 50 loading cycles was about 4.27 times more than the value for the same static load. However, the deflection of pile group in loose soil after 50 loading cycles was about 65% of the value for the same static load. It can also be seen that the deflection of pile group in dense soil, developed in the first 15 loading cycles, is accounted for 66% of the deflection at 50 cycles. For pile group in loose soil, this value is 50%.

3.2 Bending Moment Profiles

Based on the strain data measured along the depth of the pile in leading row and rear row of the pile group, the bending moment at various depth can be calculated by the expression: $M = \frac{EI\varepsilon}{r}$, in which E is the young's modulus of the model pile; I is the moment of the inertia of the model pile; $\mathcal{E}$ is the measured strain; and r is the horizontal distance between strain gauge position and neutral axis, equal to half width of the section of pile.

3.2.1 Effect of loading cycles

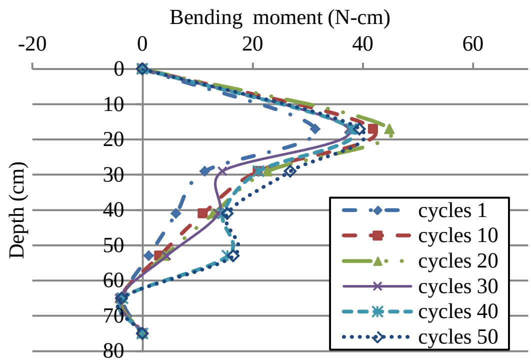

(a) Loose soil

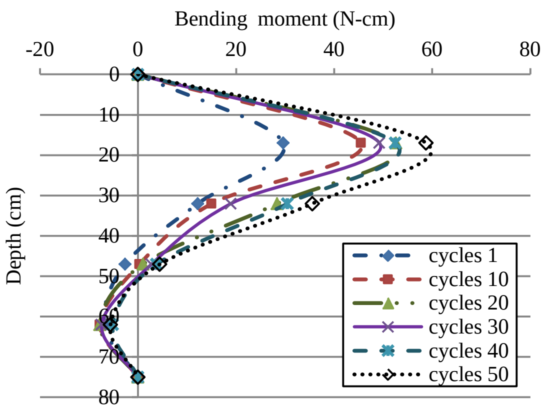

(b) Dense soil

Fig.5 Bending moment of piles in dense or loose soil

For the cyclic loading test, Fig.5 presents lateral response of model pile at the same position in pile groups. The bending moments at various depths increased with the number of loading cycles. From 50cm below the soil surface down, the pile in dense soil subjected to bending moment in inverse direction. The maximum bending moment in pile embedded in loose soil after 50 loading cycles was about 1.6 times of that at the first cycle. However, for pile in dense soil, the maximum bending moment for 50 cycles was 2 times of that at the first cycle. The depth corresponding to the maximum bending moment acted on pile group in loose soil at 50 loading cycles were measured at about 5 cm below the corresponding depth at the first cycle. However, marginal increase in the depth corresponding to the maximum bending moment was observed for pile embedded in dense soil.

3.2.2 Effect of loading program

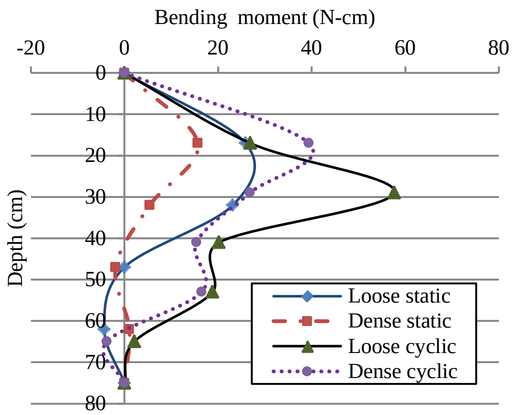

(a) Pile in leading row of the pile group

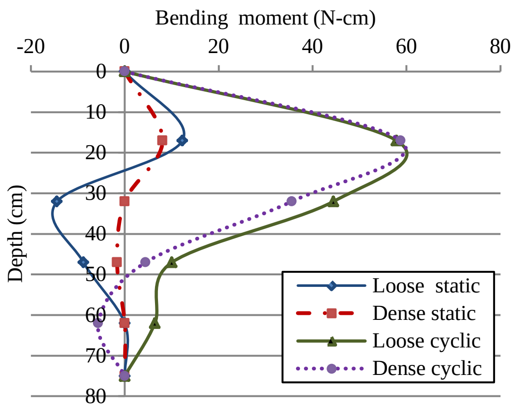

(b) Pile in rear row of the pile group

Fig.6 Bending moment behavior for pile groups under static and cyclic loading (cycles = 50)

Fig.6 shows the bending moment along the depth of piles under static and cyclic loading at 50 cycles. It is noted that, for pie in leading row of the pile group, the maximum bending moment subjected by pile at 50 loading cycles in either loose or dense soil was more than 2 times of the value for the same static load. Moreover, for pile in loose soil, the maximum bending moment occurred at the deeper depth. For pile in rear row of the pile group, the maximum bending moment subjected by pile at 50 loading cycles in either loose or dense soil was more than 6 times of the value for the same static load. However, depth of the maximum bending moment undergoes little change.

3.2.3 Effect of the position of pile in pile group

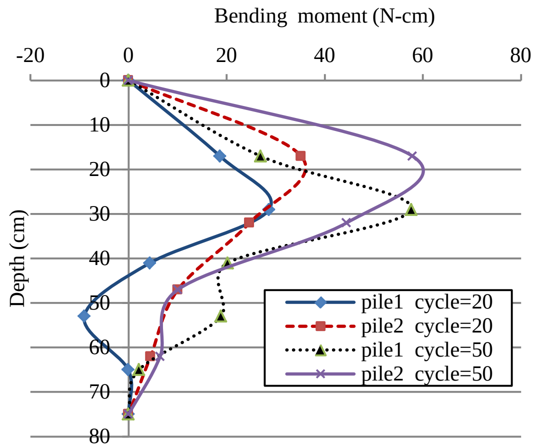

Loose soil

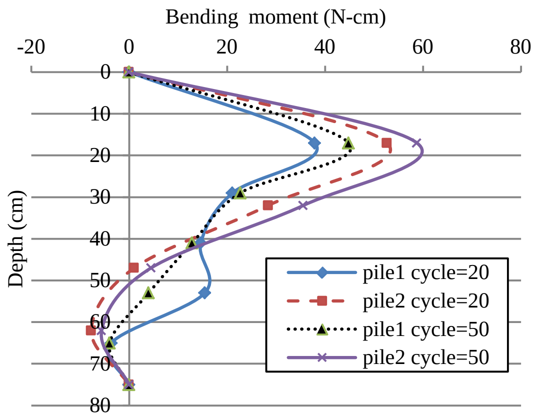

Dense soil

Fig.7 Bending moment for piles in leading or rear rows

The bending moment profiles for piles at different positions in the pile groups embedded in dense or loose soil are shown in Fig.7. More bending moment was carried by pile 2 in rear row under cyclic lateral loading. When embedded in loose soil, the maximum bending moment subjected by pile 2 at 20 loading cycles was 50% more than that of pile 1 in leading row. The magnitude of this difference decreased to 5% at 50 cycles. When embedded in dense soil, the maximum bending moment subjected by pile 2 at 20 loading cycles was 38% more than that of pile 1 in leading row. The magnitude of this difference changed little at 50 cycles. This indicated that more load was reacted by the rear row piles under cyclic lateral loading. Especially for pile group embedded in dense soil, the design will be governed by the pile in the rear row.

3. 3 Effect of soil

Development of the deflection with the number of loading cycles for pile groups in dense or loose soil is shown in Fig.8. The deflection increased nonlinearly with the number of loading cycles. It can be seen that, with the increasing of loading cycles, deflection of pile groups increased quickly to a certain value. Then after 22 cycles, the increasing became slow. It can also be observed that the soil had a significant effect on the deflections. As the relative density of soil decrease from 90% to 10%, there was approximately 4% to 16% increase in the deflection level. The deflection for pile group in loose soil is 6.16 mm and 15.96 mm for the first and 50th cycles, respectively. The corresponding values for dense soil were 3.42 mm and 13.60 mm, respectively. Plastic soil deformation around the pile was noted (Fig.9). A ‘gap’ occurred under the cyclic loading.

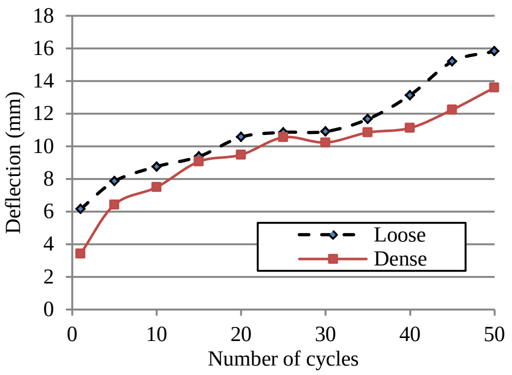

Fig.8 Deflection for pile groups in different soils

Fig.9 Gap occurred under cyclic loading

4. CONCLUSION

Based on the discussion of the test results aforementioned, some conclusions were summarized here.

(1) The deflection of pile group in dense soil after 50 loading cycles was about 4.27 times more than the value for the same static load. However, the deflection of pile group in loose soil after 50 loading cycles was about 65% of the value for the same static load.

(2) With the increasing of loading cycles, the deflection of pile groups increased quickly to a certain value. Then after 22 cycles, the increasing became slow. More than 50% of the total deflection at 50 cycles occurred in the first 15 cycles.

(3) More loads were reacted by the rear row piles under cyclic lateral loading. For pile in rear row of the pile group, the maximum bending moment subjected by pile at 50 loading cycles in either loose or dense soil was more than 6 times of the value for the same static load. Especially for pile group embedded in dense soil, the design will be governed by the pile in the rear row.

(4) The depth corresponding to the maximum bending moment acted on pile group in loose soil at 50 loading cycles is deeper than that at the first cycle. However, marginal increase in the depth corresponding to the maximum bending moment was observed for pile embedded in dense soil.

5. ACKNOWLEDGEMENTS

The work described in this paper was carried out with generous financial assistance RMUTT Annual Government Statement of Expenditure in 2014 provided by the Rajamangala University of Technology Thanyaburi (Thailand).

6. REFERENCES

[1] Das Manish Kumar and Leephakpreeda Thananchai, “A review study on trends to wind energy in a global and Thailand context”, Sura. J. Sci. Tech. 2011 (1), pp.1-13.

[2] Cuellar Pablo, “Pile Foundations for Offshore Wind Turbines: Numerical and Experimental Investigations on the Behaviour under Short-term and Long-term Cyclic”. Doctor Thesis, 2011, Berlin University of Technology, Germany.

[3] Li Z., Haigh S. K. and Bolton M. D., “Centrifuge modeling of mono-pile under cyclic lateral loads”. In: 7th International Conference on Physical Modeling in Geotechnics, Zurich. 2010. Vol. 2, pp.965-970.

[4] Kyle M. Rollins, Ryan J. Olsen, Jeffery J. Egbert, “Derek H. Jensen, Kimball G. Olsen and Brian H. Garrett. Pile spacing effects on lateral pile

group behavior: load tests". J. Geotech. Geoenviron. ASCE (2006a), 132(10), pp.1262–1271.
[5] Peng J.R., Clarke B.G., Rouainia M., "A device to cyclic lateral loaded model piles". Geotech. Test. J., ASTM. 2006, 29(4), pp.1-7.
[6] Chandrasekaran S., Boominathan A. and Dodagoudar G. R., "Experimental investigations on the behaviour of pile groups in clay under lateral cyclic loading". Geotech. Geol. En. 2010, Vol. 28, pp.603–617.
[7] Basak S. and Mastorakis Nikose, "Experimental investigation of pile group under lateral cyclic load in soft cohesive soil". Proceedings of the 4th IASME/WSEAS International Conference on Continuum Mechanics (CM'09). 2009. pp.50-55.
[8] Abbas Jasim M, Chik Zamri and Tah Mohd Raihan, " Influence of group configuration on the lateral pile group response subjected to lateral load". Electoron. J. Geotech. En. 2010, Vol. 15, pp.761-772.
[9] Chore H.S., Ingle R.K. and Sawant V.A., "Non-linear analysis of pile groups subjected to lateral loads using 'p-y' curve". Inter. Multi. Mech. 2012, Vol. 5, pp.57-73.
[10] Wood DM, Crewe A., "Taylor C. Shaking table testing of geotechnical models". Int. J. Phys. Model. Geotech.. 2002, Vol 1, pp.1-13.

Sixth International Conference on Geotechnique, Construction Materials and Environment, Bangkok, Thailand, Nov. 14-16, 2016, ISBN: 978-4-9905958-6-9 C3051

THE USE OF POLYURETHANE TO MAINTAIN STRENGTH OF ROAD SUBGRADE FOR FLOOD DAMAGE CONTROL

Safawati Mohd Radzi[1], Abdul Naser Abdul Ghani[2], Muhd Shahril Nizam Ismail[1], Ahmad Hilmy Abdul Hamid[2] and Khalid Ahmad[2]
[1]Postgraduate, School of Housing Building and Planning, Universiti Sains Malaysia, MALAYSIA
[2]School of Housing Building and Planning, Universiti Sains Malaysia, MALAYSIA

ABSTRACT

The strength of subgrade soil or foundation can influence the design of road pavement structures. Flood can be one of the causes of road damages. Since the condition of subgrade layer is critical in the road pavement stability, a study was carried out to ascertain the use of polyurethane insertion as a stabilization mechanism in road subgrade. This study was conducted based on two types of soil that are usually used as soil embankment in road construction. California Bearing Ratio (CBR) test was conducted to the various categories of soaking days and repeated submerged conditions to determine the strength of subgrade soil with and without polyurethane layer. It can be concluded that polyurethane layer can be used to increase or maintain the strength of subgrade soil from the inundation effect.

Keywords: Subgrade, Road, Flooding, California Bearing Ratio (CBR)

INTRODUCTION

Floods have great impacts on road infrastructure and people as their activity may be disrupted and the impacts, in most cases, can last for more than one week. In the coming years, climate change could make the situation become more challenging [1]. Floods are also among the most costly natural disasters in terms of returning occurrence, economic loss and human suffering. These flooding damage the roads, environmental surrounding, and livelihood. The impact of the flood can take the long term effect in maintenance works since the whole range of civil infrastructures are usually involved. The continuous flood submersion to the roads would bring damage on large part of any city or village infrastructures [2]. However, damage to road pavement and roadway could create disconnection of people movement and emergency supply or evacuation works. Road subgrade is the most prone to the flood effect because it is at the lower level of road structure, having the largest exposure to flood. Ghani et al. [3] found that the CBR values for subgrade strength decreases due to the higher number of inundation days of the subgrade soil.

Subgrade soil can be strengthened by the stabilization agents such as cement, lime and fly ash. Besides the three agents, polymer or polyurethane has also been used to stabilize sand clay mixtures in the soil slope erosion [4]. The impact of flooding can be disastrous to the infrastructure and the environment. On top of that there will be huge expenditure for the rehabilitation process and it may take some time to make things back to normal. Soil stabilization is one method for soil improvement which help to improve the subgrade soil strength hence reducing the impact of flooding on road infrastructures. There are few types of existing subgrade improvement using chemical, geotextile and mechanical. Poor quality of the subgrade soil can be improved by the treatment of the soil using stabilizing agents cement or lime [5], [6]. For example, soft clay mixed with cement will strengthened the subgrade because cement and water react to form cementitious calcium silicate and aluminum hydrates which can bind the soil particles together [7].

Geotextiles can also be used for subgrade stabilization because it can maintain physically the integrity of pavement layer boundaries and it enables water to move in an unrestricted manner. Subgrade alone, when it is weak, cannot support layer interface because of the interpenetration of soft subgrade with granular layer under the high traffic loading. As solution, geotextiles can be placed at an interface of the soft subgrade and granular layer to prevent the two materials intermixing and function to stabilize the interface between two materials and enable the granular layer to maintain the compacted strength [8].

There are many application of polyurethane in the manufacturing and construction industry. Polyurethane has been used to improve the safety and performance of railway track infrastructure due to the stiffness and ductility [9] and has become a solution to the settlement problem with the injection of polyurethane to the pile and slab in order to replace the conventional underpinning pile [10].

Polyurethane has also been used to fill void in the soil and reduced settlement issues [11]. The advantage of polyurethane is it is durable and have shorter time to complete remediation which may gain 90% compressive strength within 15 minutes from injection. In order to determine the feasibility of using polyurethane in road subgrade, there is a need study on the existing application of polyurethane related to soil and how it can be applied in case of road subgrade.

MATERIALS AND METHOD

The use of polyurethane is simulated in the lab using CBR mould and test. Two (2) types of commonly used or found soil as subgrade layer were used in the CBR test. Details of the soils are shown in Fig.1, 2, 3 and 4.

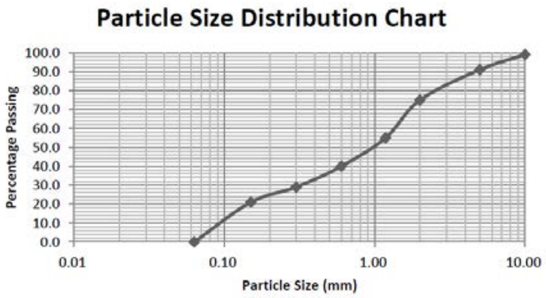

Fig 1: PSD for Soil 1

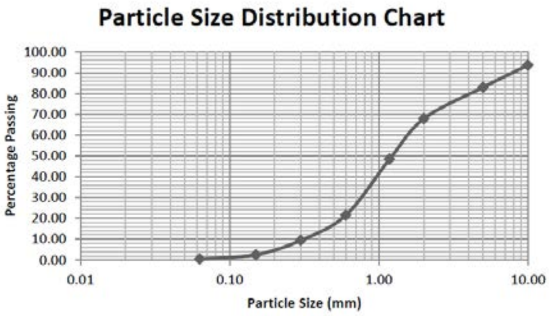

Fig 2: PSD for Soil 2

Fig 3: Soil 1

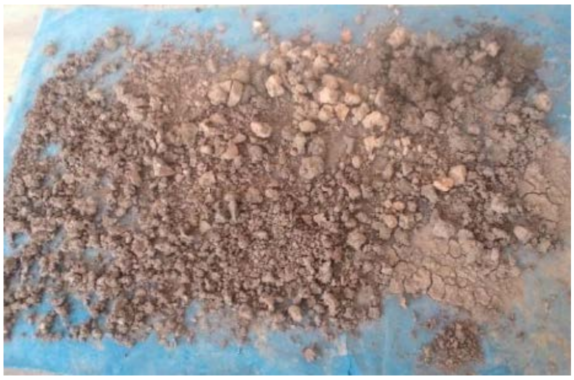

Fig 4: Soil 2

Other basic properties of the soils used in this study are shown in the following Table 1.

Table 1: Basic Properties of Soils

Properties	Soil 1	Soil 2
Specific Gravity	2.64	2.60
Maximum Dry Density (kg/m3)	1964	1510
Plasticity Index	Non Plastic	28.5%
Grading	Well Graded Sand (SW)	Poorly Graded Sand With Clay (SP-SC)

The Polyurethane

The polyurethane layer used in this study was produced from mixing two (2) compounds namely polyol and polyisocyanates at a ratio of 1:1.2. The compound that can be obtain from local supplier is shown in Fig 5 below.

Fig 5: Mix ratio of polyurethane compounds

Cured polyurethane in a PVC mould were then cut into sizes as shown in Fig 6 for placement in the CBR mould together with the subgrade soil samples as shown in Fig 7.

Fig 6: Polyurethane

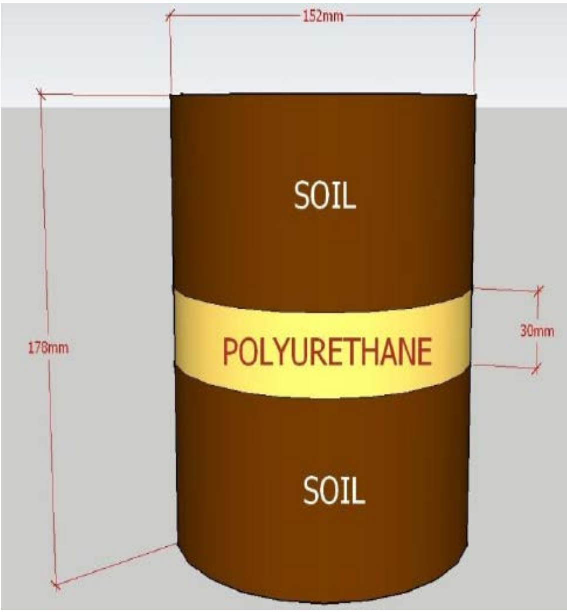

Fig 7: Placement of Polyurethane Layer

Specimen and Test Preparation

CBR specimens with and without polyurethane were prepared in the lab. Altogether 24 specimens were prepared from Soil 1 and Soil 2 (12 each). The specimens were intended for control, continuous soaking and repeated submerge conditions. Fig 8 shows specimens kept under water.

Fig 8: Specimen under water to simulate flood

Specimens were kept under water according to the specified inundation period of 1, 3, and 7 day duration. Another set were repeatedly inundated for one hour only on day 1, 3, and 7 to simulate repeated flood submerge.

California Bearing Ratio (CBR) tests were conducted on all the samples of soil according to BS 1377 using instrumented CBR equipments.

RESULT AND DISCUSSION

Soil 1

Fig 9 shows the difference between the strength of the soil that unsoaked and soaked conditions for sample of soil that normal and there is an additional of polyurethane. The samples of soil left to soak in water for different days which are 1, 3 and 7 days. The graph shows the CBR value of the sample of soil that does not soaked is higher than the samples of soil that soaked. This is because the saturated period of the soil sample. The CBR value to the sample of soil that not immersed is 50.35%. The result CBR values for the samples of soil that soaked for 1, 3, and 7 days is 3.65%, 6.45% and 3.8% respectively. These results show that the presence of water during the immersion causes the degradation of the soil sample.

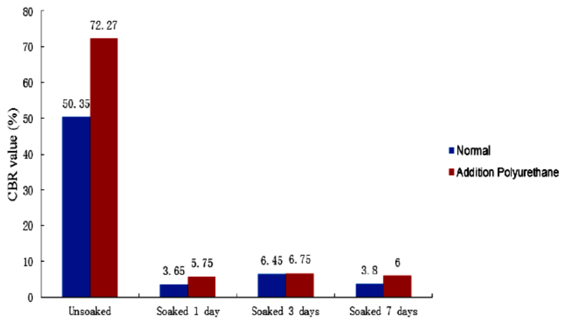

Fig 9: Inundation days and CBR strength (Soil 1)

However, with the presence of polyurethane in the soil sample, the CBR value can be increased slightly. This is means the strength of soil can be increased. For the sample that not immersed in the water, the CBR value is 72.27%. It shows a significant increase to the soil sample. Besides that, in the 1 day of soaked condition, the value of CBR rise from 3.65% to 5.75%. On the other, CBR values for soil sample 3 days of soaked is 6.75% and for 7 days of soaked is 6%. The CBR values for three samples with polyurethane in the soaked conditions have shown higher than the CBR values for normal samples. It can be concluded that polyurethane can help to maintain or increase the strength of the soil.

Graph bar in Fig 10 shows the comparison on the soil samples containing polyurethane between two different situations which is repeated soaked and unsoaked conditions. The soil samples are soaked for 1 hour at Day 1, Day 3 and Day 7.

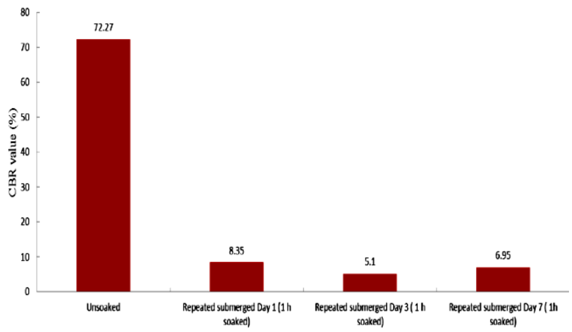

Fig 10: Repeated submergence CBR (Soil1)

The CBR values on the bar chart show the different patterns of the result. It shows that the result on unsoaked condition is 72.27% and for the repeated submerged condition for 1 hour on Day 1, Day 3 and Day 7, the CBR result is 8.35%, 5.1% and 6.95% respectively. In this repeated submerged case, the CBR value was reduced on Day 1 and the value subsequently also reduced on Day 3 compared to the unsoaked sample soil. It can be seen that the CBR values are compatible with the continuous inundation specimens from Fig 9 before.

Soil 2

Fig 11 shoes the comparison of the CBR value for the soil sample that contains polyurethane and the normal based on the two different conditions which are for unsoaked and soaked condition. For the normal sample soil, the bar graph shows the CBR value for unsoaked condition higher than the CBR value to the soaked conditions. The strength for unsoaked condition soil sample is 44.39% while the CBR value for the soaked condition for 1, 3 and 7 days is 4.3%, 1.7% and 1.3% respectively. The strength of soil tends to decrease due to the inundation of the days.

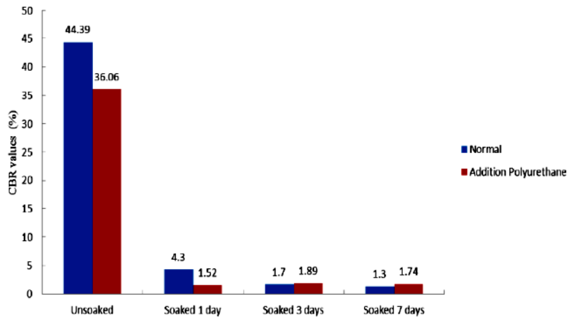

Fig 1: Inundation days and CBR (Soil 2)

However, for the soil sample that containing polyurethane, CBR value for unsoaked condition seen as 36.06% which is obviously higher than CBR value for soaked conditions. In the graph, the CBR value for 1 day soaked is 1.52%, while CBR value for 3 days soaked is 1.89% and for 7 days soaked, the reading of CBR is 1.74%. Generally, the value of CBR for soil samples in 3 and 7 days soaking period is increase.

Subsequently, in Fig 12, the graph shows the result of Soil 2 samples for CBR value for control and repeated submerged sample containing polyurethane. The repeated submerged sample is soaked for 1 hour on Day 1, Day 3 and Day 7. The control sample shows the highest result with CBR value of 36.06% compare to the repeated submerge sample. CBR value for the repeated submerge samples are decreasing respectively from day 1 to day 7 in which the result are 2.35% on Day 1. Then it is reduced to 1.65% on Day 3 and 1.30% on Day 7. So, it can be seen that CBR value become lower when the soil was submerged again and again under water.

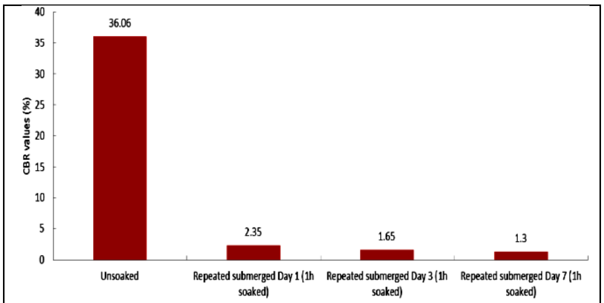

Fig 12: Repeated submergence CBR (Soil 2)

Other Observation

It is also important to note that the movement of the CBR plunger downward is also contributed by the compressible effect of the polyurethane layer itself. This can be observed when the soil and the polyurethane layer are removed from the mould as shown in Fig. 13 and 14. If this movement can be predicted and control, the ultimate actual subgrade strength improvement is actually higher than what is shown above.

Fig 13: Polyurethane layer before test

Fig 14: Polyurethane layer after test becomes thinner

CONCLUSION

This experimental study had been conducted in order to determine the strength of soil sample containing polyurethane and its capability to maintain the strength when the soil samples are kept in different inundation conditions. From the result of this study, it can be concluded that the soil samples that have been kept in longer duration of inundation tends to loss the strength as expected. Polyurethane that was placed in the soil samples and tested in the different days of inundation indicated that it can help to increase and maintain the strength of the soil. The reduction of subgrade strength once it is inundated can be very significant. In this study, polyurethane layer helps recover at least 3% of the strength loss due to inundation.

However, there is one issue that requires further investigation. The issue is about the compressibility of the polyurethane layer under load. This issue must be comprehended and resolved before actual application on site.

ACKNOWLEDGEMENTS

This work is supported by the Universiti Sains Malaysia RUI Grant Scheme No. 1001/PPBGN/814283.

REFERENCES

[1] NFRA, Flood National Risk Assessment. December 2011.
[2] Bowoputro, H. et al. (2009): Temperature Influence and Lapindo Mud Submersion towards the Stability Value of Asphaltic Concrete Mix, Rekayasa Sipil Journal.
[3] Ghani, A.N.A., Roslan, N.I.,and Hamid, A.H.A., (2016). Road Submergence During Flooding and Its Effect on Subgrade Strength. Int. J. of GEOMATE, May 2016, Vol.10, Issue 21, pp 1848-1853.
[4] Liu J, Shi B, Huang H, Jiang H (2009) Improvement Of Water-Stability Of Clay Aggregates Admixed With Aqueous Polymer Soil Stabilizers.
[5] Bell FG (1995) Cement Stabilization and Clay Soils, with Examples. Environmental & Engineering Geoscience.
[6] Bell, F.G. (2007). Engineering Geology. 2nd Edition, Elsevier Science Publishers, Oxford, United Kingdom
[7] Gueddouda, M. K., Goual, I., Lamara, M., Smaida, A., & Mekarta, B. (2011). Chemical Stabilization of Expansive Clays from Algeria, Journal Of Researches In Engineering. 11(5).
[8] Lawson, C.R., (1995), “Subgrade Stabilisation With Geotextiles”, Geosynthetics International.
[9] Woodward, P.K., Kennedy, J. And Medero, G. (2009). Three-Dimensional Track Reinforcement Using Polymer Geocomposites, Proceedings Of The 2009 American Railway Engineering And Maintenance Of Way Association (AREMA), Chicago, Illinios, USA
[10] Philip. M. (2010). Uretek Ground Engineering http://www.uretek.com.au/pages/pdf/32_Page_Book.pdf
[11] Diana, Ismacahyadi, Nor Azizah, Mohamed Khatif (2014) Evaluation Of Performance For Polyurethane Injection Pile System As A Ground Improvement Using Plaxis 2nd International Conference On Innovation And Technology For Sustainable Built Environment.

EVALUATION OF CONSTRAIN MODULUS-BULK STRESS RELATIONS OF PAVEMENT STRUCTURE MATERIALS BY USING CBR MOULD

Sawanya Dararat[1] and Warat Kongkitkul[2]
[1,2] Department of Civil Engineering, Faculty of Engineering,
King Mongkut's University of Technology Thonburi, Thailand

ABSTRACT

Resilient modulus (M_R) of pavement structure materials is an important parameter used in the mechanistic pavement engineering design. In general, M_R is evaluated by applying a number of repeated loads at various stress states in a triaxial test which is complicated and expensive. This paper presents an alternative method to determine the constrain modulus (M) of a dry sand, a lateritic soil and a crushed rock, under one-dimensional deformation. At various vertical stress levels, M values were determined by applying small strain-amplitude cyclic loadings to the compacted soil specimen prepared in a CBR mould. In the present study, the CBR mould was made special in that it can measure lateral stress confined the specimen during a test. Hence the bulk stress (θ) can then be determined, and M-θ relations for the tested materials were presented. In addition, an analytical method for eliminating the effects of bedding error was attempted so as to obtain the true M value. It is found that M is not constant but increases with θ, similar to M_R-θ relations found with the resilient modulus test. And bedding error is important and can result in significant underestimation of the true M value.

Keywords: Pavement structure materials, Constrain modulus, Resilient modulus, Coefficient of lateral earth pressure, Bedding error

INTRODUCTION

Resilient modulus (M_R) of pavement structure materials is an important parameter used in the mechanistic pavement engineering design. Resilient modulus is a property of the pavement system corresponding to repeated traffic loadings. The resilient modulus laboratory testing of soil and aggregate materials has been recommended by AASHTO T307 [1]. Triaxial apparatus is widely used for evaluation of resilient modulus of pavement structure materials [2]-[5]. To utilise the M_R from triaxial results, k-θ model is the most commonly used for granular materials in the pavement engineering design (Eq.1).

$$M_R = K_1 \theta^{K_2} \tag{1}$$

where K_1 and K_2 are regression constants

However, preparation of test specimens and shearing loading history employed in the triaxial tests for evaluation of M_R are complicated, and therefore it is difficult, expensive and time consuming. On the other hand, the resilient modulus can be estimated from correlations with California Bearing Ratio (CBR), as in [6], [7]. It is of great interest in the present study to determine the resilient modulus or a similar parameter that reflects the elastic stiffness directly from the specimen prepared with the standard CBR mould.

To this end, many researchers have developed alternative methods to evaluate the material's stiffness for the pavement design purpose, for example, the K-Mould [8], Springbox [9], and PUMA [10]. One-dimensional cyclic loading test on a specimen prepared in a CBR mould is easy to conduct in laboratory. Then constrain modulus (M) can be determined. However, this test method could not measure the lateral stress. It is therefore necessary to modify the standard CBR mould so that the measurement of lateral stress is possible. In this study, a CBR mould was attached with strain gauges to measure the hoop strain and converts to the lateral stress. Then the coefficient of lateral earth pressure at rest (k_0) was determined. Hence, the bulk stress (θ), which is summation of all the normal stresses, can then be determined. Then, at the same θ, M and M_R could be compared, and if there are correlations, M_R could be estimated from M which can be reliably determined in a much easier method. In addition, the usual measurement of specimen's deformation always includes the so-called bedding error which significantly affects the determined material's stiffness. In this study, it was attempted to prepare test specimens with different heights and used the correction procedures proposed by Koseki et al. [11] to determine the true M value that is free from any bedding error.

Summarising the above, in this study, it was attempted to evaluate the constrain modulus of pavement structure materials, and eliminate the bedding error from one-dimensional cyclic load tests. A special CBR mould was used to evaluate lateral stress confined to the test specimen.

MATERIALS AND APPARATUSES

Test Materials

Three materials used in the test program were KMUTT sand, lateritic soil, and crushed rock. Fig 1 shows their particle size distributions. KMUTT sand is in air-dry condition and used to verify the test program and the special CBR mould (explained later). The lateritic soil and crushed rock materials are prepared at 100% of maximum dry density (MDD) and optimum moisture content (OMC). The compaction curves are shown in Fig.2. Table 1 lists the OMC and MDD of lateritic soil and crushed rock.

Apparatuses

A cylindrical metal mould with an inner diameter of 152.4 mm and a height of 177.8 mm (without the collar) was used. This mould is in accordance ASTM D 1883-99. By using this mould, the lateral deformation of specimen is confined (1D condition). A special CBR mould that was attached strain gauges is shown in Fig.3. To measure the hoop strain, two strain gauges attached on side of the mould, and then connected with other two fix resistors to form a full Wheatstone bridge circuit (opposite side 2-active-gauge) (Fig. 3).

TEST METHOD

Specimen Preparation

A KMUTT sand specimen was prepared by pluviation through air. The density thus obtained is around 1.52 g/cm^3. The lateritic soil and crushed rock materials were prepared by compacting these materials that were laid layer-to-layer into the mould. Three heights of specimens of 177.8 mm, 142.2 mm, and 106.7 mm were prepared.

Test Program

Two loading patterns were employed as shown in Fig. 4. They are: i) continuous monotonic loading with a constant strain rate (ML); and ii) sustained loading and then followed by cyclic loading (CL). In the latter loading pattern, monotonic loading is applied firstly until the target vertical stress has reached, and then sustained loading is performed for 30 minutes. Next, cyclic loading with a double stress-amplitude of 30 kPa are applied for 10 cycles, subsequently monotonic loading is applied again to the next target vertical stress (Fig 4). Test program in the present study is shown in Table 2.

Table 1 Compaction lateritic soil and crushed rock

Materials	OMC (%)	MDD (g/cm^3)
Lateritic soil	7.22	2.163
Crushed rock	6.26	2.289

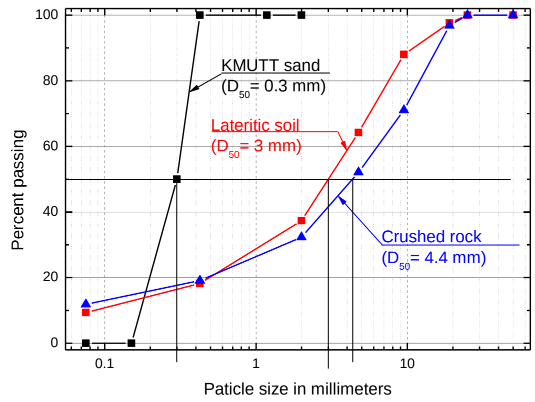

Fig. 1 Particle size distributions of tested materials.

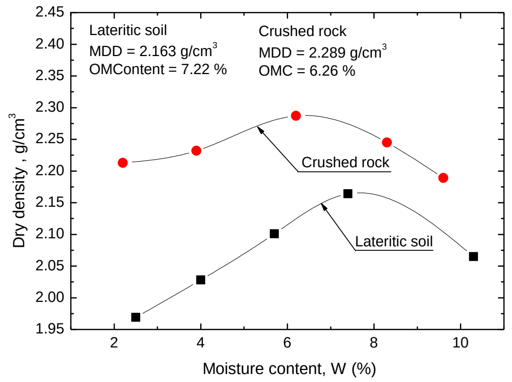

Fig. 2 Compaction curves of lateritic soil and crushed rock.

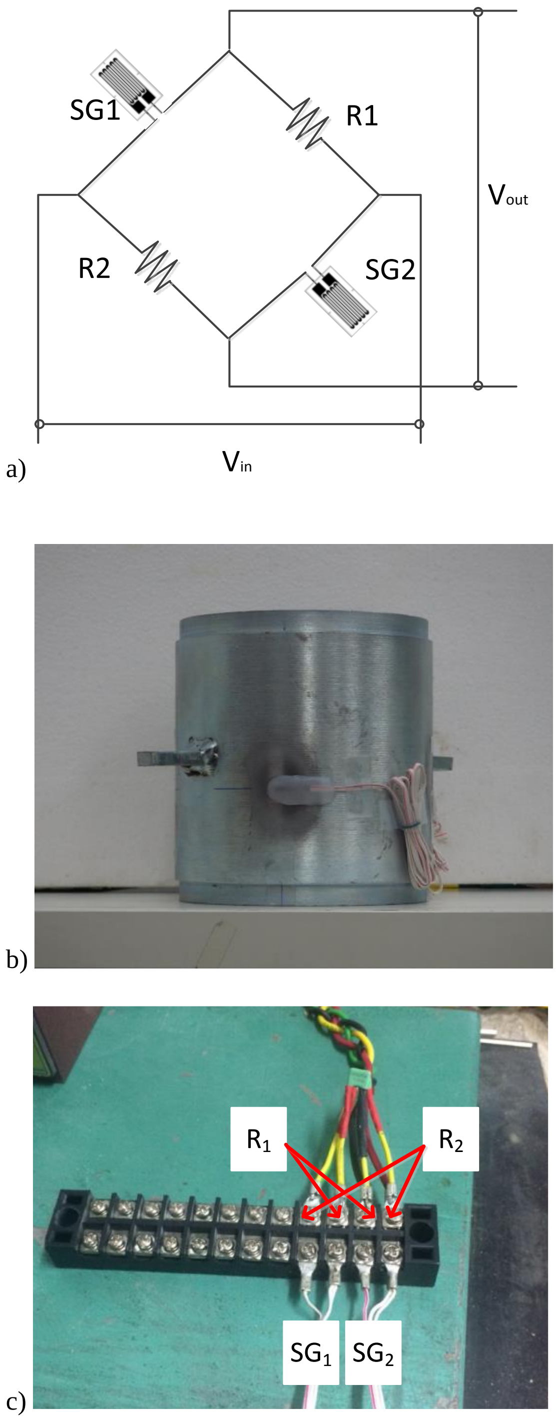

Fig. 3 Configurations of the special CBR mould: (a) a full Wheatstone bridge with two active gauges and two fix resistors; (b) strain gauges attached on the side; and (c) connections of strain gauges and fix resistors

Table 2 Test program used in the present study

Materials	Initial height, H	Load Patterns, LP
KMUTT	H	ML
Sand	H, 0.8H, 0.6H	ML, SL ,CL
Lateritic soil	H	ML
	H, 0.8H, 0.6H	ML, SL ,CL
Crushed rock	H	ML
	H, 0.8H, 0.6H	ML, SL ,CL

Note: H = Initial height specimen is 177.8 mm

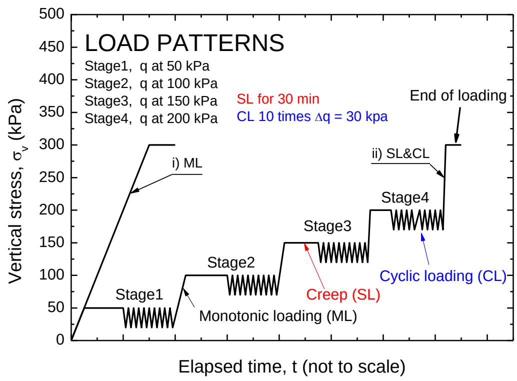

Fig. 4 Loading histories.

TEST RESULTS AND DISCUSSIONS

Monotonic Loading Test Results

Figures 5(a), 5(b), and 5(c) show the variation of vertical stress (σ_V) and horizontal stress (σ_h) with vertical strain (ε_V) from ML tests on KMUTT sand, lateritic soil, and crushed rock, respectively. In these tests, stress-strain curves exhibit continuous strain-hardening behaviour. Here, it was assumed in the present study that the tangential strain (ε_θ) mobilised on surface of the CBR mould during a test is uniform along the height and the periphery. The ε_θ value measured by the strain gauges is therefore the representative of the entire CBR mould. Then, the horizontal stress can be calculated from Eq. 2, based on the theoretical of stress in cylindrical.

$$\sigma_h = \frac{\varepsilon_\theta \mathrm{E} t}{r} \tag{2}$$

where E is Young's modulus, t is a thickness, and r is a radius of CBR mould. It may be necessary to calibrate the horizontal stress determined by the technique described above with other relevant techniques that can directly measure the horizontal stress so as to assure the measurement accuracy and precision. However, it is not presently known to the authors how this calibration shall suitably be performed.

Coefficient of lateral earth pressure at rest ($K_0 = \sigma_h / \sigma_V$) of materials are shown in Figs. 6a, 6b, and 6c, for KMUTT sand, lateritic soil, and crushed rock, respectively. For a simulation in the pavement engineering analysis, K_0 of the base and subbase courses are typically selected at 0.30-0.42 [12], [13]. However, K_0 of lateritic soil and crushed rock measured from this test are around 0.4-0.5. Further investigation on accuracy of the use of lateral stress measurement technique used in this study is necessary to find out the slight discrepancies mentioned above.

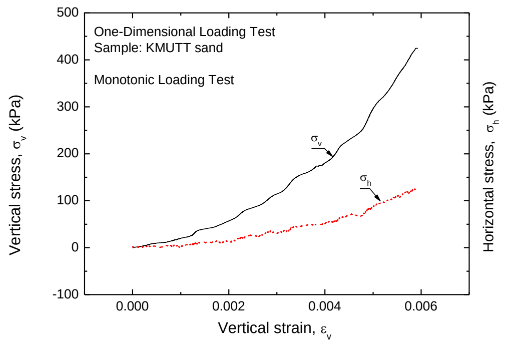

a)

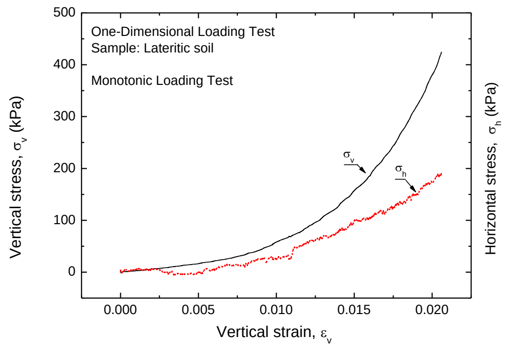

b)

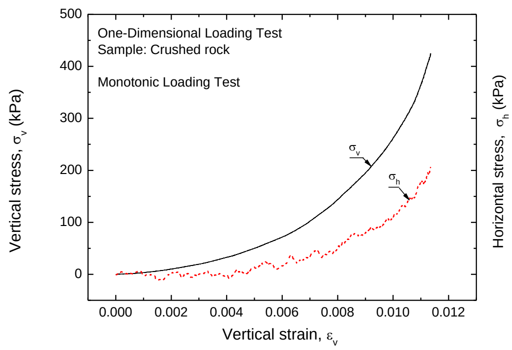

c)

Fig. 5 Vertical stress and horizontal stress – axial strain relations from monotonic one-dimensional tests on: (a) KMUTT sand; (b) Lateritic soil; and (c) crushed rock.

Constrain Modulus from CL Tests

Figures 7(a), 7(b), and 7(c) show the unloading braches Nos. 6-10 at the stress level of 100 kPa for KMUTT sand, lateritic soil, and crushed rock, respectively. The stress-strain behaviour along these branches is highly linear only for a smaller range of stress increment of the stress-strain loop. Lines were best-fitted to the respective unloading branches presented in Fig. 7 to obtain the constrain modulus (M). Then, the relationship between M and bulk stress ($\theta = \sigma_V + 2\sigma_h$) where $\sigma_h = K_0 \sigma_V$ for each stress level with different materials are plotted in Fig. 8. It can be

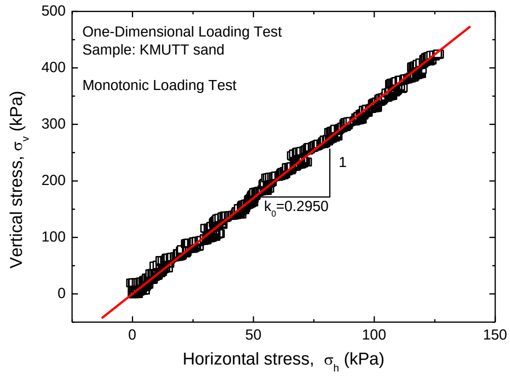

a)

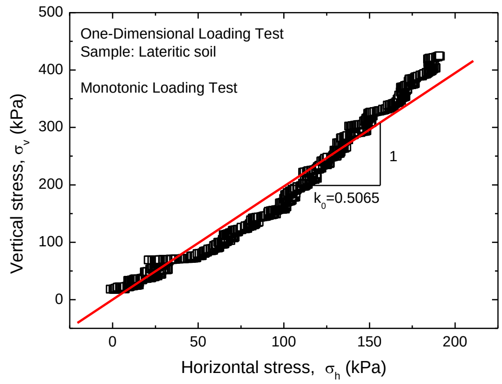

b)

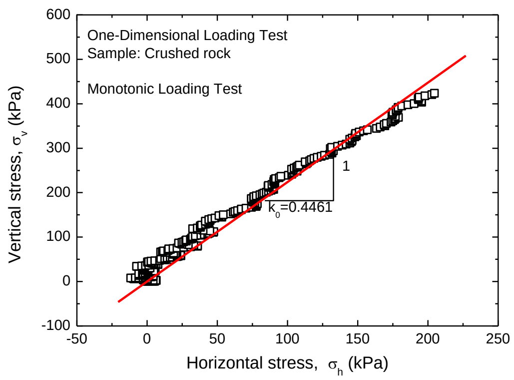

c)

Fig. 6 Relationship between vertical stress and horizontal stress of: (a) KMUTT sand; (b) lateritic soil; and (c) crushed rock.

clearly seen that the M value increases significantly with an increase in the stress level [2], [4], [6]. Due to the errors of axial deformation found with tests on KMUTT sand and lateritic soil using the specimens with the heights of 0.6H and 0.8H, the M value can be confidently determined only for the stress level of 100 kPa. The data points at the higher stress levels for these two materials were obtained by extrapolations using the relation obtained for the specimen with the height of H to pass through the only data point measured at the stress level of 100 kPa, as shown in Figs. 8a and 8b.

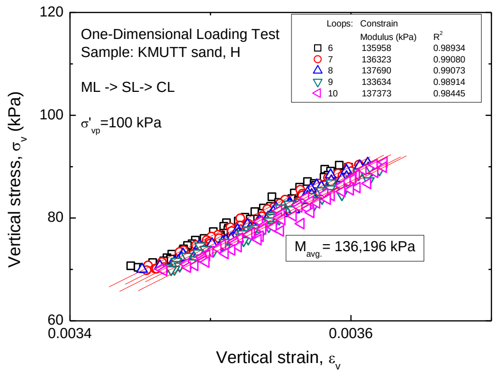

a)

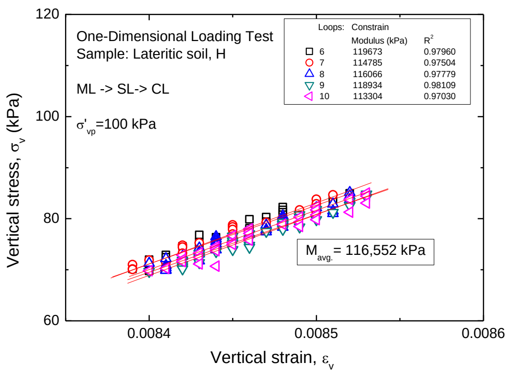

b)

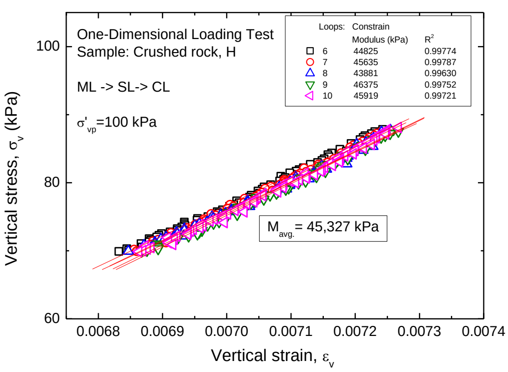

c)

Fig. 7 Relationships between vertical stress and vertical strain during unloading branches to determine the constrain modulus at stress level 100 kPa on: (a) KMUTT sand; (b) lateritic soil; and (c) crushed rock.

Evaluation of Effects of Bedding Error on Constrained Modulus

In order to evaluate effects of bedding error on the measured constrain modulus, the analytical procedures proposed by Koseki et al. [11] was used. According to Eq.3, a constrain modulus of a bedding error layer (M_1) and the constrain modulus of the normal layer (M_2) can be evaluated from relationships between $1/M_0$ and $1/H$ [11].

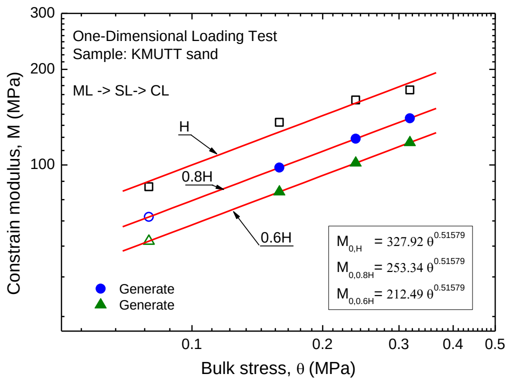

a)

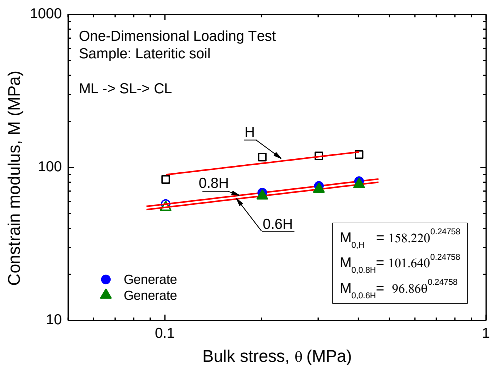

b)

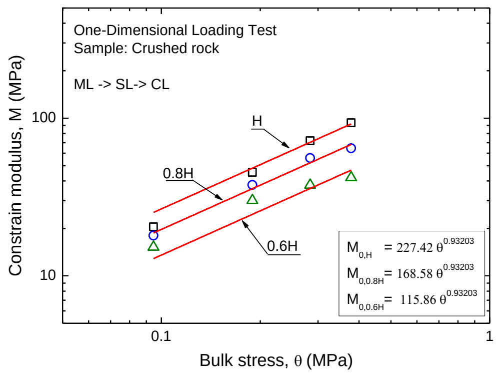

c)

Fig. 8 Relationship between constrain modulus and bulk stress on: (a) KMUTT sand; (b) lateritic soil; and (c) crushed rock.

$$\frac{1}{M_0}=\left(\frac{1}{M_1}-\frac{1}{M_2}\right)\frac{D_{50}}{H}+\frac{1}{M_2} \quad (3)$$

where M_0 is a nominal value of the constrain modulus evaluated in conventional manner for whole specimen height, H is a height of a specimen, and D_{50} is a particle mean diameter. In the present study, M_0 is therefore the measured M value shown in Fig. 8, which is dependent on the specimen's height, and M_2 is the constrain modulus of test material that is free from any bedding error and independent of the specimen's height.

Figures 9(a), 9(b), and 9(c) show relationships between $1/M_0$ and 1/H for KMUTT sand, lateritic soil, and crushed rock, respectively. It can be seen that value of $1/M_0$ increased with an increase with the value of 1/H. Lines were best-fitted by assuming that slopes for different stress levels are the same.

Table 3 Nominal constrained modulus and estimated results for bedding error layers and normal layer

Tested material	Stress Level (kPa)	M_0 (MPa)	M_1 (MPa)	M_2 (MPa)
KMUTT sand	50	57, 68, 85	0.33	128
	100	82, 98, 136	0.33	322
	150	101, 120, 160	0.33	769
	200	117, 140, 172	0.33	2500
Lateritic soil	50	55, 57, 83	2.02	200
	100	65, 68, 116	2.04	500
	150	72, 75, 119	2.04	1000
	200	77, 81, 121	2.04	3333
Crushed rock	50	15, 18, 20	1.16	34
	100	30, 37, 45	1.20	333
	150	37, 56, 72	1.32	-14
	200	42, 64, 93	1.22	-98

The value of constrain modulus are summarised in Table 3. The M_2 values are significantly larger than the respective M_0 values. On the other hand, the constrain modulus of bedding error M_1 values are noticeably lower than M_2.

The M_2 values of crushed rock at the stress levels of 150 and 200 kPa exhibit negative. It may be affected from larger particles [11]. However, all the M_2 values obtained from the present study should be compared/calibrated with the triaxial test results. However, this work is beyond the scope of the paper.

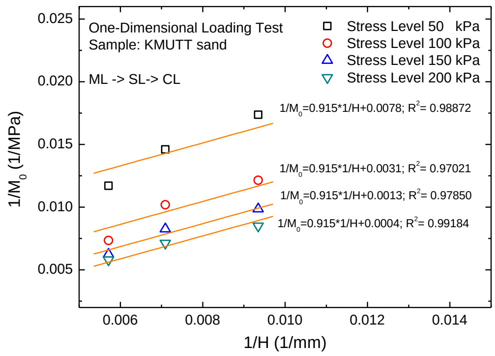

a)

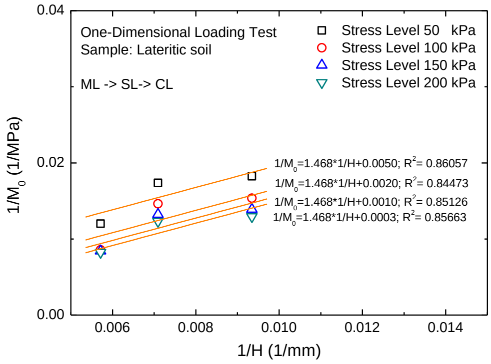

b)

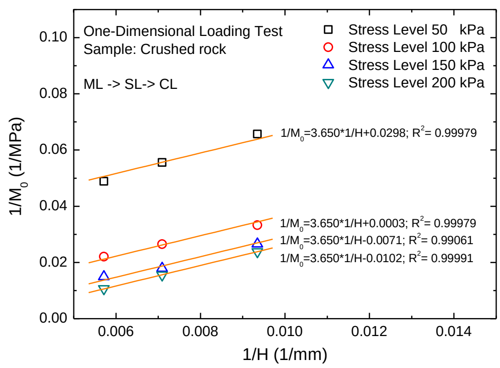

c)

Fig. 9 Relationship between $1/M_0$ and 1/H : (a) KMUTT sand; (b) lateritic soil; and (c) crushed rock.

CONCLUSION

The following conclusions can be derived from the test results presented in this study:

1. Coefficient of lateral earth pressure at rest can be measured from the special CBR mould attached with strain gauges for the measurement of tangential strain.
2. Constrain modulus of KMUTT sand, lateritic soil, and crushed rock are not constant but increases with an increase in the vertical stress level.
3. Constrain modulus that is free from bedding error can be determined by performing tests with different specimen's heights. By using an analytical method reported in the literature, it is found that bedding error can result in a significant underestimation of constrain modulus.

ACKNOWLEDGEMENTS

The authors are grateful to The Thailand Research Fund (TRF) via The Royal Golden Jubilee (RGJ) and King Mongkut's University of Technology Thonburi (KMUTT) for financial support (Contract number PHD/0187/2556)

REFERENCES

[1] AASHTO T307-99, "Standard method of test for determining the resilient modulus of soils and aggregate materials", American Association of State Highway and Transportation Officials, Washington, DC, USA., 2000.

[2] Chummuneerat S, Jitsangiam P, and Nikraz H, "Mechanical characteristics of hydrated cement treated crushed rock base", Advances in Transportation Geotechnics II, 2012, pp. 296-301.

[3] Ibrahim SF, "Bagdad Subgrade Resilient Modulus and Liquefaction Evaluation for Pavement Design using Load cyclic Triaxial Strenght", J. of Environment and Earth Science, Vlo. 3, 2003, pp. 125-141.

[4] Yoshida N, Sugisako Y, Nakamura H, and Hirotsu E, "Resilient modulus of hydraulic mechanically stabilized slag base-course material", Deformation Characteristics of Geomaterials, 2003, pp. 293-298.

[5] Vuong TB, "Precision studies of resilient modulus and permanent strain testing", Unbound Granular Materials, 1999, pp. 63-83.

[6] Sawangsuriya A, "Assessment of Modulus and CBR of Pavement Materials for Design and Construction", Bureau of Materials, Analysis and Inspection, Department of Highways.

[7] Louay MN, Huang B, Puppala AJ, and Allen A, "Regression Model for Resilient Mokulus of Subgrade Soils", J. of the Transportation Research Board, No. 1687, 1999, pp. 47-54.

[8] Semmelink CJ, and de Beer N, "Rapid determination of elastic and shear properties of road-building materials with the K-mould, In Unbound Aggregates in Roads ,University of Nottingham, 1995, pp. 70-77.

[9] Eswards JP, Thom NH,Fleming PR, and Williams J, "Axxelerated laboratory base mechanistic testing of unbound layers within the mewly developed NAT Spingbox", J. of Transportation Research Board,2005, pp. 32-40.

[10] Thom NH, Cooper A, Grafton P, Ealker C, Wen H, and Sha R, "A New Test for Base for Base Material Characterisation", Porceedings of the International Symposium on Heaby Duty Asphalt Pavements and Bridge Deck Pavements, 2012.

[11] Koseki J, Mikami T, and Sato T, "Deformation Characteristics of Granular Materials in Cyclic One-Dimensional Loading Tests", J. of Transportation Infrastructure Geotechnology, Volume 1, Issue 1, Jan. 2014. pp. 54-67.

[12] Nega A, Nikraz H, and AI-Qadi I, "Simulation of Shakedown Behavior for Flexible Pavement's Unbound Granular layer", J of American Society of Civil Engineers, Jul 7 2015, pp. 801-812.

[13] Djellali A, Ounis A, and Saghafi B, "Behavior of Flexible Pavements on Expansive Soils", J of Transportation Engineering, Volume 1, 2012.

RATE-DEPENDENT DEFORMATION CHARACTERISTICS OF EPS BEAD-MIXED SAND

Agawit Thaothip[1] and Warat Kongkitkul[2]
[1, 2] Department of Civil Engineering, Faculty of Engineering,
King Mongkut's University of Technology Thonburi, Thailand

ABSTRACT

This research studies the deformation characteristics of expended polystylene (EPS) bead-mixed sand. A set of standard Proctor compaction test was conducted to determine the proper amount of water for use in the mixing between EPS bead and sand at the volumetric ratio of 1:1. A special series of air-drained triaxial compression tests was performed on the sand-EPS bead mixture (SEM) specimens. Various loading histories, which are: i) monotonic loading (ML) at constant strain rates; ii) sustained (creep) loading (SL); iii) cyclic loading with small strain-amplitude (CL); and iv) stepwise changes in the strain rate during otherwise ML, were employed in this study. These loading histories were used to evaluate the elastic and viscous properties of the SEM. Then these properties were also compared with the ones obtained from sand alone under similar loading conditions. It is found that the elastic and viscous properties of the SEM are qualitatively similar to those of sand alone. They are different in terms of quantity. A non-linear three-component (NTC) model was used to simulate the elasto-viscoplastic of the SEM. The simulations are well successful by using model parameters determined especially for the SEM under the conventional model framework.

Keywords: Creep, Elastic, EPS bead, EPS bead-mixed sand, Non-linear three-component, Strain rate, Triaxial compression test.

INTRODUCTION

Settlement of road embankment constructed on the soft clay layer due to its primary consolidation is a crucial problem. This is in particular for the bridge approach where differential settlement can result, and thus leads to danger for the drivers. At present, there are many mitigation techniques proposed which can be categorised into two groups; i.e., i) improvement of the soft clay layer by mixing with cement or other relevant additives [1]-[4]; and ii) reducing the surcharge on the soft clay layer by using the lightweight fill materials [5], [6]. This research interests on the strength and deformation of properties of the latter group. A sand-expanded polystyrene (EPS) bead mixture (SEM) [7] was prepared by mixing at the ratio of 1:1 by volume, and therefore, the unit weight of SEM became about a half of the sand alone. When used as a refilling material to replace the original sand fill, the unit weight of SEM is sufficient low so as to not allow the primary consolidation settlement of the soft clay to continue, if the degree of consolidation of more than a certain level had been achieved.

In view of the above, a series of special air-drained triaxial compression tests [8] were performed in this study. Various loading histories including: i) continuous monotonic loading with constant strain rates; ii) sustained (creep) loading; iii) cyclic loading; and iv) stepwise change in the applied shearing strain rate, were used to evaluate strength properties, and elastic and viscous properties of SEM. Test results of SEM are presented and compared with those of sand alone. Lastly, an elasto-viscoplastic non-linear three-component (NTC) model was used for simulations of test results of SEM observed in the present study.

TEST MATERIALS

There are two test materials used to perform triaxial tests in the present study. They are sand and EPS bead.

Sand

A cleaned riverbed sand was used. To control its gradation, the portion that passes through sieve No. 40 but retains on sieve No. 50 was mixed with the other portion that passes through sieve No. 50 but retains on sieve No. 100 at the ratio of 1:1 by mass. The gradation curve thus obtained is shown in Fig. 1.

EPS beads

A type of EPS bead was used. Its diameter is around 1-2 mm. The absolute density is 32.9 kg/m^3.

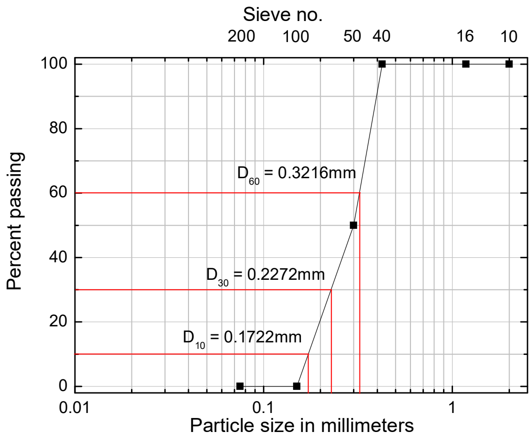

Fig. 1 Particle size distribution of sand.

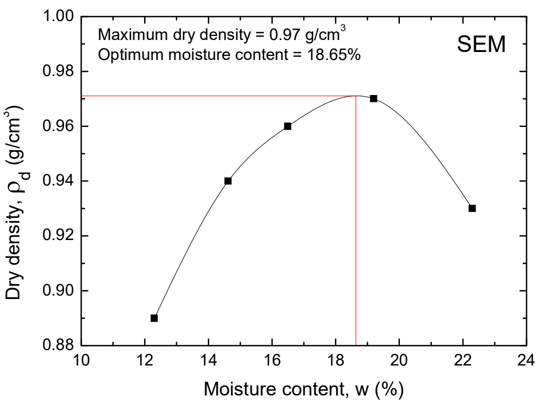

Fig. 2 Compaction curve by standard Proctor compaction test on SEM.

TEST METHODS

Standard Proctor Compaction Test

The purpose of this test is to determine the maximum dry density and the optimum moisture content of SEM. Fig. 2 shows the compaction curve which defines the optimum moisture content (OMC) of 18.65% and the maximum dry density of 0.97 g/cm^3.

Air-Drained Triaxial Compression Tests

The purpose of this test is to evaluate the strength and deformation properties of SEM. The specimen is cylindrical in the shape. It is 150 mm high by 70 mm in diameter. Triaxial specimens were prepared by tamping the SEM layered in the mould such that the density meets the target value (0.97 g/cm^3). Four loading patterns were employed. They are: i) continuous monotonic loading with constant strain rate (ML); ii) sustained loading (SL); iii) cyclic loading (CL); and iv) stepwise change in the applied shearing strain rate (SS). Triaxial compression test program is shown in Table 1.

Table 1 Triaxial compression test program

Test	S	E	W	SP	σ_3	$\dot{\varepsilon}_v$
SND01	875	-	163	ML	25	0.15
SND02	875	-	163	ML	50	0.15
SND03	875	-	163	ML	75	0.15
SND04	875	-	163	ML	100	0.15
SEM01	550	12	105	ML	25	0.15
SEM02	550	12	105	ML	50	0.15
SEM03	550	12	105	ML	75	0.15
SEM04	550	12	105	ML	100	0.15
SEM05	550	12	105	ML	100	0.05
SEM06	550	12	105	SL,CL	100	0.05
SEM07	550	12	105	SL,CL	100	0.05
SEM08	550	12	105	ML	100	0.50
SEM09	550	12	105	SL,CL	100	0.50
SEM10	550	12	105	SL,CL	100	0.50
SEM11	550	12	105	SS	100	0.05
SEM12	550	12	105	SS	100	0.05

Note: S = sand (g); E = EPS bead (g); W = water (g); SP = shearing patterns; σ_3 = confining pressure (kPa); $\dot{\varepsilon}_v$ = basic vertical strain rate (%/min); SND = tests on sand alone; SEM = tests on sand-EPS bead mixture

TEST RESULTS AND DISCUSSIONS

Monotonic loading test results

From ML tests, deviator stress (q)-axial strain (ε_a) characteristics between sand alone (Fig. 3(a)) and SEM (Fig. 3(b)) can be compared. It can be observed from Figs. 3(a) and 3(b) that the q-ε_a relations exhibit a strain-hardening behaviour until achieving the respective peaks, and then show a strain-softening behaviour toward the residual states. The behaviours described above are qualitatively similar between the sand alone and the SEM specimens. This may imply that sand in the SEM matrix play a major role to control the global behaviours of SEM.

Shear strength parameters at the peak and the residual states of sand alone and SEM are listed in Table 2. The peak and residual friction angles of sand alone are noticeably greater than the corresponding values of SEM. On the other hand, cohesion at the peak state of sand is smaller than that of SEM.

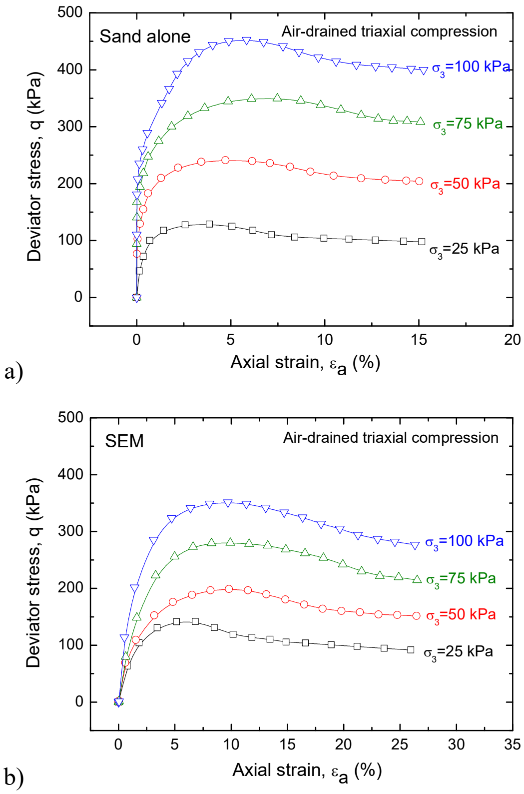

Fig. 3 Deviator stress (q)-axial strain (ε_a) relations from continuous ML triaxial compression tests on: (a) sand alone; and (b) SEM

Table 2 Shear strength parameters of sand alone and SEM

Sample	State	Cohesion (kPa)	Friction angle (°)
Sand alone	Peak	5.0	43.1
	Residual	0.0	42.0
SEM	Peak	16.5	36.0
	Residual	0.0	34.5

Elastic modulus from CL tests

Two patterns of loading histories, used to evaluate the elastic modulus and the creep behaviours of SEM, are shown in Figs. 4(a) and 4(b). In these tests, ML was firstly applied until the specified deviator stress at 100, 150, 200 or 250 kPa was achieved, and then sustained loading (SL) which lasted for two hours was applied. Next cyclic loadings (CL) with a double stress-amplitude of 50 kPa were applied for 10 cycles. Two values of strain rate which are 0.05 and 0.5 %/min were employed during ML and CL in their courses (Figs. 4(a) and 4(b)). Test results thus obtained are shown in Figs. 5(a) and 5(b) for the strain rate of 0.05 and 0.5 %/min, respectively. It can be

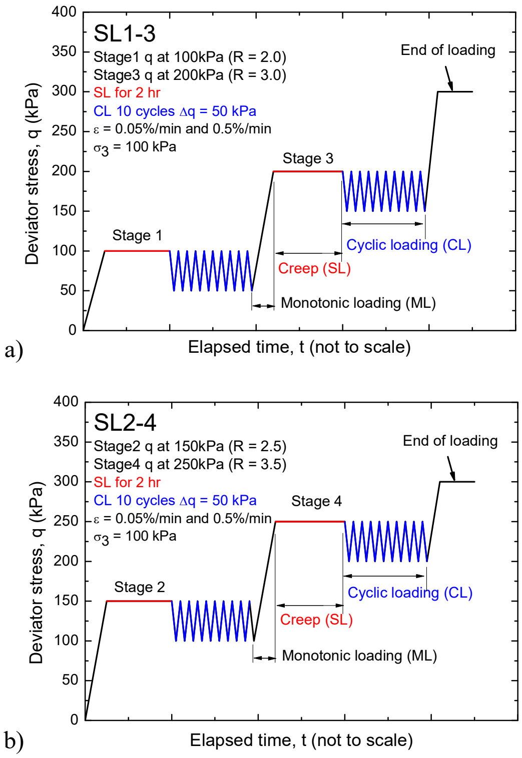

Fig. 4 Loading histories used to evaluate elastic modulus and creep behaviours of SEM at: (a) R =2.0 & 3.0 (SL1-3); and (b) R =2.5 & 3.5 (SL2-4).

clearly observed that upon the restart of ML after the last CL at the highest deviator stress level, the q-ε_a relation tends to rejoin to the relation that is obtained from the respective continuous ML test, and importantly, the peak deviator stress is maintained. Thus it can be postulated that although creep strain of SEM is obvious, it does not degrade the SEM's shear strength.

Unloading braches of CL of the last five loops were exaggerated as shown in Fig. 6. To determine the values of quasi-elastic Young's modulus (E_{eq}) [9], lines were best-fitted to these respective unloading branches. Then these slopes were averaged and accounted as the representative of E_{eq} for the deviator stress level at which it was determined. Next the E_{eq} value was converted to be represented in terms of R, where R is the stress ratio equal to σ_1/σ_3. Fig. 7 shows the relation between E_{eq} (expressed in terms of R) and R, plotted in the full-log scale. It can be seen that E_{eq} is not constant but increases with an increase in the stress ratio. For the same stress ratio, the E_{eq} of sand alone is noticeably greater than that of SEM. The dependency of elastic modulus with the stress level observed with sand alone and SEM is qualitatively similar and can be expressed with hypo-elasticity expressed by Eq. 1.

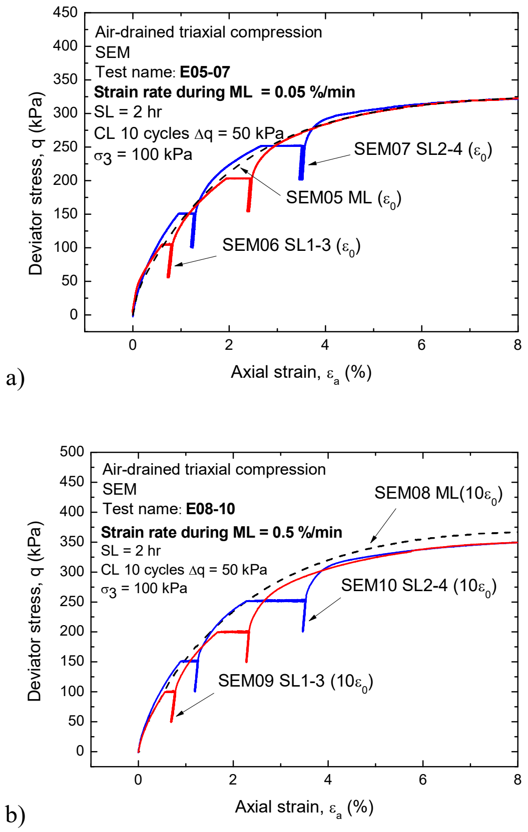

Fig. 5 Deviator stress-axial strain relations of SEM obtained from tests with the intermissions of SL and CL; the strain rate during ML and CL is: (a) 0.05 %/min; and (b) 0.5 %/min

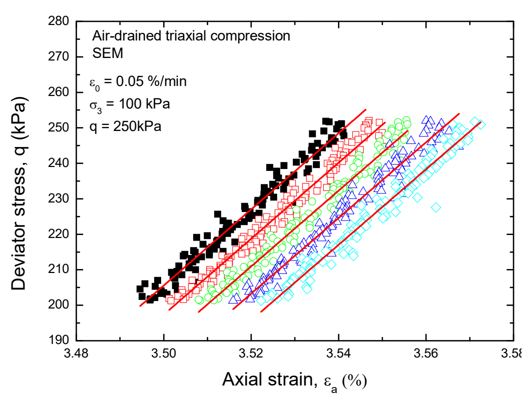

Fig. 6 Unloading branches of the last five loops of a CL course with the respective best-fitted lines to determine the quasi-elastic modulus

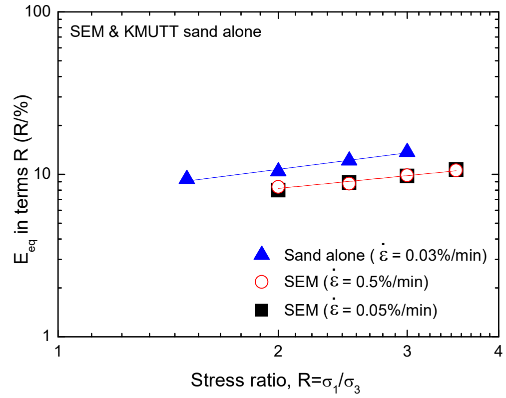

Fig. 7 Comparison of $E_{eq} - R$ relations between sand alone and SEM

$$E_{eq} = E_0 \left(R\right)^m \tag{1}$$

where $E_0\left(R/\%\right)$ = 7.20 and 5.66 for sand alone and SEM, respectively; m = 0.576 and 0.485 for sand alone and SEM, respectively

Creep loading

Fig. 8 compares creep axial strain of SEM developed after two hours between the sustained loadings with the initial strain rates of 0.05 %/min and 0.5 %/min. The test results reveal that creep axial strain increases with time. However, the creep strain rate decreases with time towards nearly zero at the end of creep. Creep strain developed by sustained loading for two hours increases with the stress ratio, and at the same time, creep of SEM obtained with the initial strain rate of 0.5 %/min is significantly larger than the one with the initial strain rate of 0.05 %/min. This shows the influence of strain rate at the start of creep on the development of creep strain with time. In order to compare the creep axial strains having different initial strain rates, they were corrected to the initial strain rate of 3.5 x 10^{-4} %/min. Then the comparison of creep axial strains between the sand alone and the SEM under the same initial strain rate condition is shown in Fig. 9. The two different relations for SEM shown in Fig. 8 are now becoming close to each other in Fig. 9. The trend of increasing of creep axial strain with the increasing stress ratio is obvious for both sand alone and SEM. However, creep of SEM is noticeably greater than the one of sand alone as shown in Fig. 9.

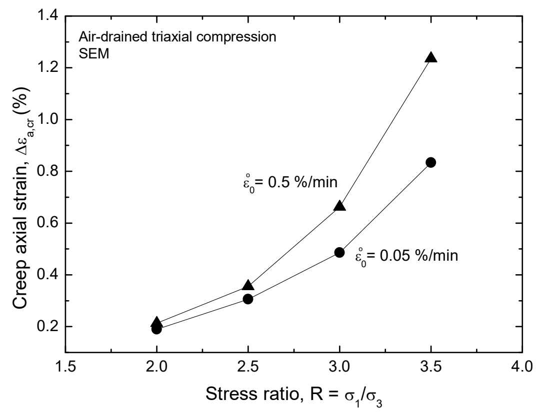

Fig. 8 Comparison of creep axial strains of SEM for two hours between the initial strain rates of 0.05 %/min and 0.5 %/min

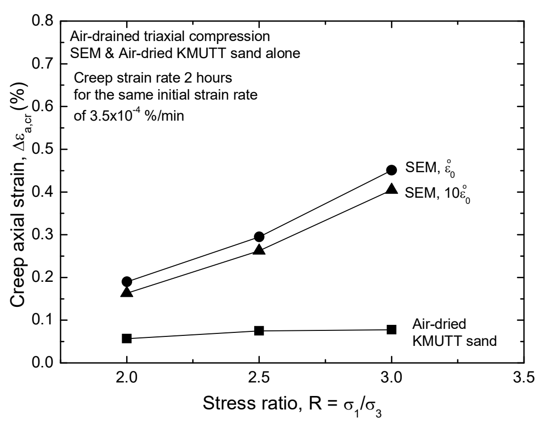

Fig. 9 Comparisons of creep axial strains after having been corrected for the same initial strain rate of 3.5 x 10^{-4} %/min between sand alone and SEM

Strain rate responses of SEM

Responses of SEM to changes in the strain rate were also studied in this research. To quantify the viscous responses, stepwise changes in the applied shearing strain rate were performed. In these tests, the basic reference strain rate ($\dot{\varepsilon}_0$) of 0.05%/min was firstly selected. Different strain rates that are slower and faster than $\dot{\varepsilon}_0$ for 10 and 100 times and also the $\dot{\varepsilon}_0$ were then specified into a set. During a test, the shearing strain rate was stepwise changed many times from a value to the other value specified in the set. Fig. 10 shows relationship between the stress ratio and the irreversible axial strain obtained with the above-mentioned changings in the strain rate. It can be readily seen that upon stepwise changes in the strain rate, the stress-strain relation exhibited stress jumps. These stress jumps are responses due to the viscosity of SEM. To quantify the viscosity of SEM, jump in the stress ratio upon a stepwise increase or decrease in the strain rate was defined as shown in Fig. 11. Then the measured stress ratio jumps were normalised with the stress ratio immediately before the jump (ΔR/R), and then plotted against the ratio of strain rate after and before stepwise change, as shown in Fig. 12. The slope of the line best-fitted to the data points shown in Fig. 12 (Eq. 2) is called the rate-sensitivity coefficient (β) [10], [11].

$$\frac{\Delta R}{R} = \beta \log_{10}\left(\frac{\dot{\varepsilon}^{ir}_{after}}{\dot{\varepsilon}^{ir}_{before}}\right) \quad (2)$$

The β value of SEM determined from this study is 0.0619. On the other hand, from previous studies on other standard sands by performing stepwise changings in the strain rate during triaxial tests [12], [13], the β values are equal to 0.0226, 0.0195, and 0.0195 for Toyoura sand, Albany sand, and Monterey sand, respectively. Therefore, SEM is more sensitive to changes in the strain rate than typical sands for about three times, which may due to the inclusion of EPS bead into the matrix.

Non-linear Three-component Model

A non-linear three-component (NTC) (Fig. 13) was used to simulate rate-dependent characteristics (e.g., creep, jump in the stress ratio) of SEM. The three components are elastic, inviscid, and viscous components. Total stress ratio (R) consists of the inviscid and the viscous components (R^f and R^v) while strain rate ($\dot{\varepsilon}$) the elastic ($\dot{\varepsilon}^e$) and the irreversible ($\dot{\varepsilon}^{ir}$) components.

Elastic modulus (E_{eq}) of the elastic component, which is dependent of stress ratio level (Fig. 7), is determined by a hypo-elasticity model (Eq. 1). The elastic strain rate can then be calculated from Eq. 3 [14].

$$\dot{\varepsilon}^e = R/E_{eq} \quad (3)$$

Inviscid stress ratio (R^f)-irreversible axial strain (ε_a^{ir}) relation of the inviscid component, which is independent of any strain rate effect and called the reference curve, is determined from the functional form shown in Eq. 4.

$$R^f = P_1 + \left(P_2 + P_3\varepsilon_a^{ir}\right)\left\{1-\exp\left[-P_4\left(\varepsilon_a^{ir}\right)^{P_5} - P_6\frac{\varepsilon_a^{ir}}{P_2}\right]\right\} \quad (4)$$

where $P_1 - P_5$ are constants that are determined from the regression analysis such that Eq. 4 is best-fitted to the respective R- ε_a^{ir} relation that is extrapolated to zero-strain rate.

The rate-dependent responses of SEM can be observed not only with creep by sustained loading (Fig. 5) and stress ratio jumps by changes in the strain rate (Fig. 10) but also with R-ε_a relations by continuous ML tests with different strain rates as shown in Fig. 14. At the same ε_a, it is obvious that R for the faster strain rate is greater than the value for the slower strain rate. This difference in the R value along continuous ML R-ε_a relations with different strain rates is referred as residual state of rate-dependency [12]. In Fig. 14, imaginary stress ratio jumps were imposed between the two R-ε_a relations, and then coefficient of rate-sensitivity at the residual state (β_r) is then determined as shown in Fig. 12. Then the viscosity type parameter (θ) [12] can then be determined from Eq. 5.

$$\theta=\beta_r/\beta \tag{5}$$

It was also found with SEM that, similar to many other geomaterials [12], the θ value is not constant but dependent on the irreversible strain, and can be expressed with Eq. 6.

$$\theta(\varepsilon^{ir})=\frac{\theta_{ini}+\theta_{end}}{2}+\frac{\theta_{ini}-\theta_{end}}{2}\cos\left[\pi\left(\frac{\varepsilon^{ir}}{\varepsilon^{ir}_{\theta}}\right)^{c}\right];\ \varepsilon^{ir}<\varepsilon^{ir}_{\theta} \tag{6a}$$

$$\theta(\varepsilon^{ir})=\theta_{end};\ \varepsilon^{ir}\geq\varepsilon^{ir}_{\theta} \tag{6b}$$

where θ_{ini} and θ_{end} are the initial and residual values of transition of the θ value; c and $\varepsilon^{ir}_{\theta}$ are constants. The viscous stress ratio (R^v) can be determined from Eq. 7 [12].

$$R^{v}(\varepsilon^{ir},\dot{\varepsilon}^{ir},h_s)=\theta(\varepsilon^{ir})\cdot R^{v}_{iso}(\varepsilon^{ir},\dot{\varepsilon}^{ir})+\{1-\theta(\varepsilon^{ir})\}\cdot R^{v}_{G.TESRA}(\varepsilon^{ir},\dot{\varepsilon}^{ir},h_s) \tag{7a}$$

$$R^{v}_{iso}(\varepsilon^{ir},\dot{\varepsilon}^{ir})=R^{f}(\varepsilon^{ir})\cdot g_{v}(\dot{\varepsilon}^{ir}) \tag{7b}$$

$$R^{v}_{G.TESRA}(\varepsilon^{ir},\dot{\varepsilon}^{ir},h_s)=\int_{\tau=\varepsilon^{ir}_{1}}^{\varepsilon^{ir}}\left[dR^{v}_{iso}\right]_{(\tau)}\cdot[r_1(\varepsilon^{ir})]^{\varepsilon^{ir}-\tau} \tag{7c}$$

$$g_{v}(\dot{\varepsilon}^{ir})=\alpha\cdot[1-\exp\{1-(\frac{|\dot{\varepsilon}^{ir}|}{\dot{\varepsilon}^{ir}_{r}}+1)^{m}\}] \tag{7d}$$

where α, m, $\dot{\varepsilon}^{ir}_{r}$, and r_1 are constants.

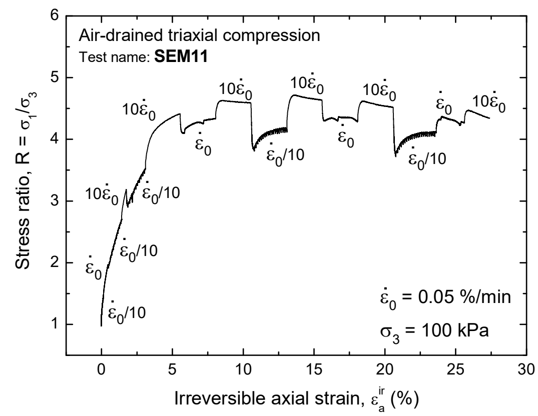

Fig. 10 Relationship between stress ratio and irreversible axial strain of SEM obtained from a test with multiple changes in the strain rate

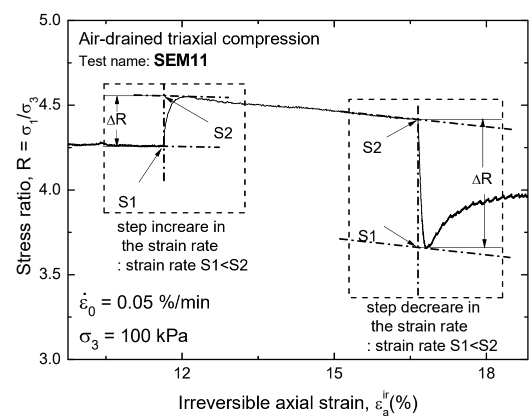

Fig. 11 Definitions of stress jumps upon a step increase and a step decrease in the irreversible strain rate

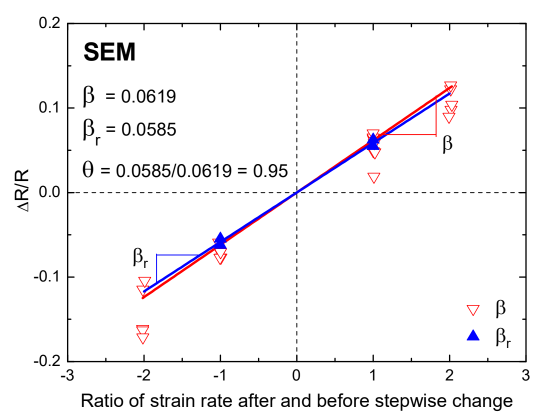

Fig. 12 Determination of rate-sensitivity coefficient from relationship between the normalised stress ratio jump and the ratio of strain rate after and before stepwise change

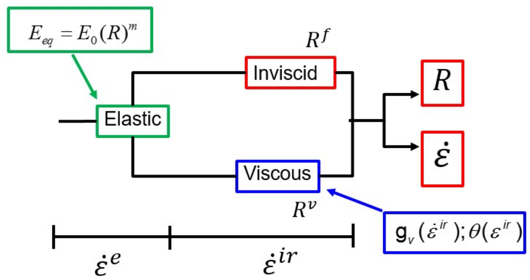

Fig. 13 Non-linear three-component model [10]-[12]

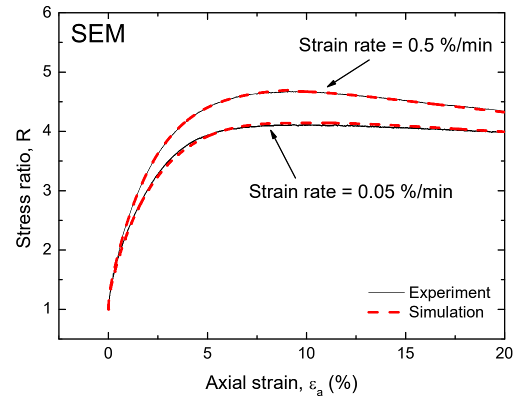

Fig. 14 Simulations of continuous ML tests on SEM with different but constant strain rates of 0.05 and 0.5 %/min

Simulation Results

Fig. 14 compares the R-ε_a relations between the experimental and simulation results from continuous ML on SEM with strain rates equal to 0.05 and 0.5 %/min. It can be readily seen that the NTC model can well-successfully simulate all the R-ε_a characteristics that are different by the strain rate effects.

Fig. 15(a) compares R-ε_a relations of SEM subjected to SL during otherwise ML at the strain rate of 0.5 %/min between the experimental and simulation results. It can be seen that not only the development of axial strain (creep) under a constant stress ratio condition but also the behaviour in that the R-ε_a relation re-join to the one that would be obtained from continuous ML can successfully be simulated. Fig. 15(b) compares the creep axial strains for different stress ratio values. The behaviours in that the creep axial strain increases with an increase in the stress ratio and also with an increase in the initial strain rate at the start of creep can be well-simulated. Thus the NTC can be used to predict the time-dependent (rate-dependent) creep deformation of SEM.

Fig. 16 compares R-ε_a relations of SEM subjected to stepwise changes in the strain rate between the experimental and simulation results. All the sudden increases and decreases of stress ratio by stepwise increases and decreases in the strain rate can be well-simulated. The NTC model therefore has a great potential to predict the rate-dependent deformation characteristics of SEM evaluated by the experiments in the present study.

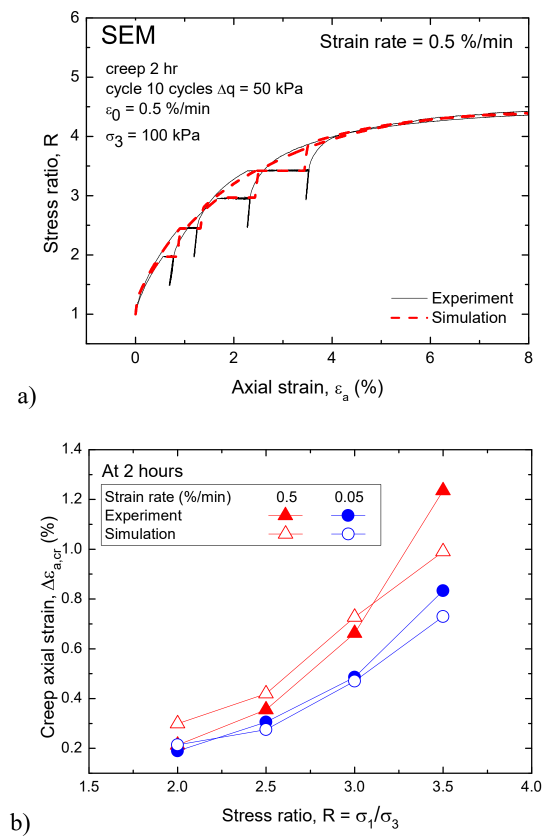

Fig. 15 Simulations of 2-hr SL tests on SEM during otherwise ML: a) comparisons of R-ε_a relation with the strain rate during ML of 0.5 %/min; and b) comparisons of creep axial strain for different stress ratios

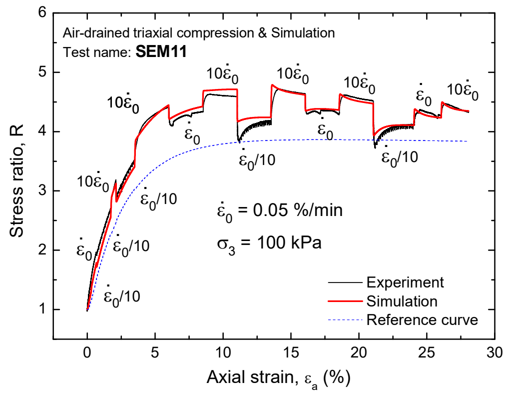

Fig. 16 Simulations of stepwise changes in the strain rate applied to SEM

CONCLUSIONS

The following conclusions can be derived from the air-drained triaxial compression test results and their simulations.

1. Peak and residual friction angles of SEM are noticeably smaller than those of sand alone.
2. Elastic Young's moduli of air-dried sand alone and SEM are not constant but increase with an increase in the axial stress. At the same axial stress, the elastic Young's modulus of SEM is quite smaller than that of air-dried sand alone.
3. SEM exhibited creep strain significantly upon the applied sustained loading. The creep strain increases with an increase in the shear stress level and also increases with an increase in the strain rate at the start of creep. Creep strain of SEM is significantly larger than the one of sand alone. Yet, by ML at the end of creep, the stress-strain relation of SEM rejoins to the one that is obtained by continuous ML with the same strain rate, and thus, the peak shear strength is maintained. Therefore, creep of SEM is not a degradation phenomenon.
4. SEM is more sensitive to the strain rate than the air-dried sand alone. This also results in a greater amount of creep developed under otherwise the same conditions
5. NTC model can successfully simulate the stress-strain-time behaviours of SEM, taken into account the dependency of elastic Young's modulus with the axial stress and the evaluated and quantified viscous properties. Moreover, this model can successfully predict the creep strain developed during sustained loading.

REFERENCES

[1] Chida S, "Dry jet mixing method-State of the Art on Improvement Methods for Soft Ground", J. of Japan Soc. Soil mechanics and foundation engineering., 1982, pp.69-76,

[2] Kawasaki T, Niina A, Saitoh S, Suzuki Y, and Honjo Y, "Deep mixing method using cement hardening agent", Proceedings of 10th International conference on soil mechanics and foundation engineering, Stockholm, 1981, pp.721-724.

[3] Miura N, Koga Y, and Nishida K, "Application of a deep mixing method with quicklime for Ariake-clay ground", J. of Japan Soc. Soil Mech. and Found. Eng'g, Vol.34 (4), 1986, pp.5-11.

[4] Terashi M, Tanaka H, and Okumura T. "Engineering properties of lime treated marine soils and deep mixing method", Proceedings of 6th Asian regional conference on soil mechanics and foundation engineering, Vol.1, 1979, pp.191-194.

[5] Horvath J, "The compressible-inclusion function of EPS geofoam: analysis and design methodologies", Res Rpt No CE/GE-98, 1998.

[6] NCHRP, Guideline and Recommended Standard for Geofoam Applications in Highway Embankments, NCHRP Report 529, Transportation Research Board, 2004.

[7] A. Edincliler , A. T. Ozer. "Effects of EPS bead inclusions on stress–strain behaviour of sand". J. of Geosynthetics International, Vol.21(2), 2014, pp.89-102.

[8] Das, B. M. (2013). Triaxial test. In Fundamentals of Geotechnical Engineer. Canada: Cengage.

[9] Kongkitkul W, Tabsombut W, Jaturapitakkul C, and Tatsuoka F, "Effects of temperature on the rupture strength and elastic stiffness of geogrids", J. of Geosynthetics International, Vol.19, No.2, April 2012, pp.106-123.

[10] Tatsuoka F, Ishihara M, Di Benedetto H, and Kuwano R, "Time-dependent shear deformation characteristics of geomaterials and their simulation", J. of Soils and Foundations, Vol.42, No.2, 2002, pp.103-129.

[11] Di Benedetto H, Tatsuoka F, and Ishihara M.: "Time-dependent shear deformation characteristics of sand and their constitutive modelling", J. of Soils and Foundations, Vol. 42, No.2, 2002, pp.1-22.

[12] Tatsuoka F, Di Benedetto H, Enomoto T, Kawabe S, and Kongkitkul W, "Various viscosity types of geomaterials in shear and their mathematical expression", J. of Soils and Foundations, Vol.48, No.1, February 2008, pp. 41-60

[13] Kiyota T and Tatsuoka F, "Viscous property of loose sand in triaxial compression, extension and cyclic loading", J. of Soils and Foundations, Vol. 46, No.5, 2006, pp.665-684.

[14] Hoque E and Tatsuoka F, "Anisotropy in elastic deformation of granular materials", J. of Soils and Foundations, Vol.38, No.1, 1998, pp.163-179.

GEOTECHNICAL REQUIREMENTS FOR CAPTURING CO_2 THROUGH HIGHWAYS LAND

M. Ehsan Jorat[1], Ben W. Kolosz[1], Mark A. Goddard[1], Saran P. Sohi[2], Nurten Akgun[1], Dilum Dissanayake[1] and David A.C. Manning[1]
[1]School of Civil Engineering and Geosciences, Newcastle University, UK;
[2]School of Geosciences, University of Edinburgh, UK

ABSTRACT

Roadside verges in Britain support 238,000 hectares of vegetated land and approximately 10 hectares of vegetated central reserves. These areas have the potential to be engineered in such a way that they deliver a range of ecosystem services such as flood regulation and biodiversity conservation in addition to their primary functions such as comfort of sidewalk users (mostly un-vegetated), protection of spray from passing vehicles, a space for benches, bus shelters, street lights and other public amenities, and visual improvement of the roads and designated green belts. Previous research has shown that in soils, calcium-rich materials such as recycled crushed concrete or crushed dolerite undergo carbonation. This effectively captures CO_2 from the atmosphere and stores it in the form of $CaCO_3$ precipitated between soil particles. Engineering this process can potentially assist the UK in achieving its ambitious target to reduce CO_2 emissions by 80% of 1990 levels by 2050. Rates of carbonation measured at urban brownfield sites in the UK suggest that treating 12,000 ha of land containing suitable amendments could remove 1M t CO_2 annually. However, brownfield sites are often subjected to re-construction activities which would reduce the rate of CO_2 absorption from the atmosphere by sealing. To optimize the rate of carbonation, engineered soils need to be constructed at locations subjected to least post-construction activities and roadside verges and central reserves represent a key opportunity in this regard. This paper calculates limits to $CaCO_3$ formation within the first 1 m of pore spaces of soils at roadside verges and central reserves in Britain considering soil porosity of 20%.

Keywords: Britain roads, engineering soil, CO_2 capture, roadside verges and central reserves

INTRODUCTION

Roadside verges and central reserves are an integral part of road construction. Pieces of land between the road-surface and the boundary line, e.g. adjacent hedgerows, fences or hard development, are called roadside verges [1]. Central reserves are the areas that separates the carriageways of a dual carriageway exclusive of any hardstrips [2].

There are estimated to be 238,000 hectares of roadside verges in Britain [3]. In 2014, the United Kingdom's Department of Transport estimated the length of roads (Motorways and type A, B, C and U roads) in Britain to be 245,800 miles. Considering the length of roads and central reserves associated with it, there are nearly 31,200 miles of central reserves along the roads in Britain.

Roadside verges and central reserves are areas of great potential to capture carbon in addition to their primary functions, if managed and designed appropriately. The ambitious UK target of reducing CO_2 emissions by 80% by 2050, compared to a 1990 baseline, can only be achieved by engaging diverse sectors of society. It is likely that major CO_2 emission reduction will be achieved through improved efficiency in the energy system (e.g. [4]). However, capturing and storing atmospheric carbon in a form of carbonate in urban soil also appears to be an economically and environmentally effective method [5], [6], [7]. Measurements at an urban brownfield site in the UK suggest that in a few years, each 12,000 ha of engineered land could remove 1 Mt CO_2 yr^{-1} [7]. The formation of pedogenic carbonates, which are predominately composed of the mineral calcite ($CaCO_3$), depends on two main factors (i) the availability of calcium; and (ii) carbonate in solution.

Calcium is naturally derived from the weathering of silicate minerals (plagioclase feldspars, pyroxenes etc.) that commonly occur in basic igneous rocks (e.g. basalts and dolerites), or from artificial calcium silicate and hydroxide minerals within concrete and cement [8], [9]. Carbonate carbon is predominantly derived from photosynthesis, based on stable isotope studies [10]. During the process, silicate minerals, in particular calcium silicates, react with dissolved CO_2 to form carbonates (Equation 1).

$$CaSiO_3 + CO_2 + 2H_2O \longrightarrow CaCO_3 + H_4SiO_4 \quad (1)$$

This leads to the removal of atmospheric carbon and its subsequent storage in a stable, inorganic state [6], [7], [8], [11], [12], [13], [14], [15]. Once formed, this is a stable store for CO_2 since it will only be naturally removed by dissolution, when carbon would normally stay stable in solution, entering surface and groundwater systems.

In this paper, we investigate possible constraints to realising the potential for $CaCO_3$ sequestration in roadside verges and central reserves of Britain. The result of this investigation will assist in designing more sustainable roads which would provide their primary functions while also sequestering CO_2 emissions discharged into the atmosphere partly from vehicles using internal combustion engines. We also highlight the implications of engineering roadside verges and central reserves to capture carbon on their ability to also deliver a range of additional ecosystem services, such as flood regulation and biodiversity.

THEORETICAL BACKGROUND

$CaCO_3$ formation occurs within soil pore spaces. The porosity of soils ranges between 20–60%, depending on soil type and degree of compaction [16]. Pore spaces within coarser soils provide higher potential for carbon sequestration because larger pore spaces having lower surface areas result in decreased friction and provide higher permeability. Higher permeability results in faster weathering of silicate minerals and provides sufficient H_2O for the chemical reaction (Equation 1) to take place.

For roadside verges and central reserves to provide their primary functions, they should reach a certain degree of compaction that leads to significant reduction of porosity. However, optimum compaction of soil with small grains fitting within the larger grain pores would give a porosity of around 20% [16]. This means that even at the highest degree of compaction, 20% of the total soil volume is comprised of voids which can provide a potential location for $CaCO_3$ formation.

Based on previous measurements by [6] at the Science Central development site in Newcastle, UK, the majority of carbonation occurs in the top 1 m of the soil profile, depending on soil type and precipitation. Based on that result, the first 1 m soil depth is also considered for roadside verges and central reserves. The porosity of the soil at roadside verges and central reserves is considered to be 20%.

RESULTS

Cross-sections and dimensions for rural and urban roads in Britain are shown in Fig. 1. Based on the dimensions provided, the total volume of the soil associated with the first 1 m of road central reserves is calculated and presented in Table 1.

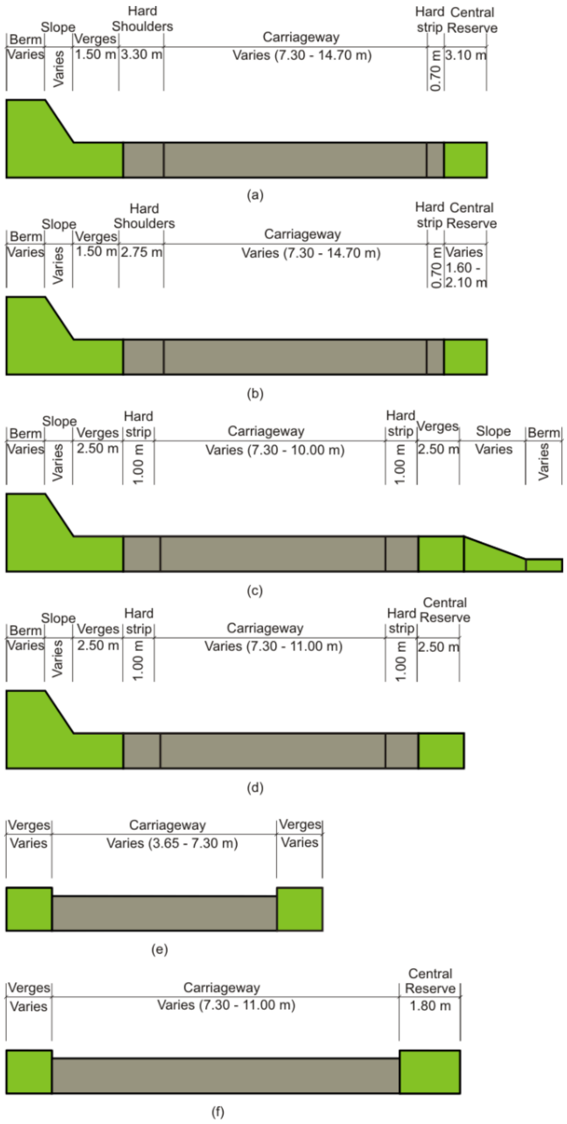

FIG. 1 Dimensions of cross-section components for (a) rural motorway, (b) urban motorway, (c) rural single carriage all-purpose, (d) rural dual carriage all-purpose, (e) urban single carriage all-purpose and (f) urban dual carriage all-purpose roads mainline [2].

Based on an estimated density of pure $CaCO_3$ as 2715 kg/m^3 [17] for soil at roadside verges and central reserves, maximum ranges of $CaCO_3$ deposition within pore spaces are calculated and presented in Table 2. For the calculations, the porosity of 20% is considered and it is assumed that 100% of the pore spaces are filled with $CaCO_3$. Therefore, potentially 543 kg of $CaCO_3$ for each cubic metre of soil could be stored within soil pore spaces in roadside verges and central reserves.

Table 1 Total volume of soil present within the first 1 m of soils along road central reserves in Britain

Type of roads	Total length of central reserve (mile) [18]	Volume of soil present in the upper 1 m of central reserves (m^3)
Rural/urban motorway	2212	8815
Rural dual carriage	22122	88710
Urban dual carriage	6882	19870
Rural/urban dual carriageway	Not available in urban roads	Not available in Dual carriage roads

Table 2 Total potential $CaCO_3$ storage capacity within the top 1 m of soil depth along roadside verges and central reserves in Britain. For the calculations of this table, porosity of 20% is considered

Type	Volume of soil present in the top 1 m (m^3)	Potential $CaCO_3$ storage (Mt)
Roadside verges	2,380,000,000[1]	1292
Road central reserves	117,395	0.06
		$\sum = 1292$

DISCUSSION

Results from Table 2 show that roadside verges have a great potential for $CaCO_3$ deposition compared with road central reserves which devote a very small and negligible portion to potential $CaCO_3$ deposition.

Table 2 indicates the limit to the formation of $CaCO_3$ within the first 1 m of sediments at roadside verges and central reserves, which is defined by porosity and hence particle size and degree of compaction. Considering the porosity of 20% and assuming all of the void spaces within the top 1 m of soil within roadside verges and central reserves are filled with $CaCO_3$, they have the capacity to deposit an estimated maximum of 1,292 Mt $CaCO_3$ (Table 2), equivalent to 150 Mt C. However, in reality, other factors such as solution pH, the presence of organic complexes and fluid flow rate also play an important role in the formation of $CaCO_3$ [11].

Clearly, engineering all roadside verges and central reserves for carbon sequestration in Britain is not feasible since they are mostly operational and reconstruction to implement carbon capture design into the roadside verges and central reserves requires significant funding and time. However, Department of Transport statistics in 2014 show that total road length in Britain increased 2% over ten years, compared with 2004 baseline [18]. Considering a similar rate for the next ten years, if roadside verges and central reserves of new roads are engineered for carbon capture purposes during construction they have the potential to deposit nearly 25 MT of $CaCO_3$ which equates to 11 MT of CO_2. This figure is separate from roads which will be upgraded and resurfaced in future providing further opportunity to implement the carbon capture design during re-construction. The calcium source required for new engineered soils could be partly acquired through recycling of concrete from the demolition of bridges and other concrete structures associated with roads as they reach the end of their life. Remaining calcium sources could be acquired from local demolition sites or dolerite quarries.

Green infrastructure needs to be multifunctional (e.g. [19]) and carbon capture is only one of a number of ecosystem services that roadside verges and central reserves can provide. Although roads generally have a negative impact on animal populations (e.g. [20], [21]), sympathetically managed or restored roadside verges make an important contribution to the conservation of grassland species (e.g. [22]) and pollinating insects [23]. For instance, Highways England are committed to the implementation of the National Pollinator Strategy for England [24] and will undertake a programme of works to achieve a significant area of species rich grasslands estimated at 3500 hectares by 2021.

The choice of planting and management of vegetation on roadside verges and central reserves could also influence calcite formation. Carbon stored in carbonates is plant derived, implying that encouraging plant growth on engineered urban soils may facilitate carbon capture [8], as well as providing other ecosystem services associated with vegetated land.

If fully carbonated, the permeability of soil approaches zero and roadside verges would no longer have the capacity to drain water, possibly (depending on specific design) leading to flooding during periods of heavy rainfall. For roads in general and motorways in particular, if it occurs, such flooding might lead to damaging events. Accordingly, a proper drainage system such as SUDS [25], [26] should be considered for roadside verges and central reserves if engineered to capture carbon in addition to their primary functions. A further benefit of SUDS is that the created wetland can provide habitat for supporting biodiversity.

Predicting the saturation point for the $CaCO_3$ formation between soil particles is an essential factor which largely controls the geotechnical properties of the substrate such as permeability and this can be done using multiple regression modelling. Through regression analysis, quantitative dependent variable distribution would be created based on one or more quantitative independent variables [27] which take into account the conditional distribution of the dependent variable as a function of independent variables.

The continuous quantitative dataset of possible independent predictors which could be used in the multiple regression model include substrate porosity, grain size, degree of compaction, permeability, Ca content, organic content, pH and vehicle traffic flow. Using the independent variables, the dependent variable can be defined. This will be used for the prediction of $CaCO_3$ formation in the soil. The model would provide an understanding of the saturation point in which the engineered soil at roadside verges stops sequestering CO_2.

By adding significant variables in a regression model, the accuracy of the dependent variables will increase. However, overloading the model with excessive variables could lead to inefficiency of the model and result in overfitting of the results. In contrast, having only a few variables would result in biased results. To determine the risk profiles of the variables, which are used in the multivariable model, the effective index is commonly used in the regression models [28].

The dependent and independent variables' lower limits need to be specified in order to develop an accurate prediction by a multiple regression model. The minimum sample size is determined by the relationship between the number of independent variables and the squared multiple correlation coefficient (R^2) [29]. Determining the sample size increases the accuracy of results and will facilitate progress planning and cost management.

CONCLUSIONS

Limits to $CaCO_3$ formation within pore spaces of sediments at roadside verges and central reserves have been calculated and we show that roadside verges have the greatest potential deposition rate. Considering a porosity of 20%, the top 1 m of soil at roadside verges and central reserves along rural and urban roads in Britain has a theoretical capacity of 1,292 Mt $CaCO_3$, equivalent to 150 Mt C, of which almost all is in verges. Road length in Britain is expected to increase by 2% over the next ten years. This will lead to increase vehicle movements and CO_2 emissions. If managed and engineered appropriately, roadside verges and central reserves associated with new roads have the theoretical capacity to store 25 Mt $CaCO_3$ (from 11 Mt CO_2; 3 Mt C). Recycling of concrete from demolition of bridges and other concrete structures associated with roads as they reach the end of their life could be an appropriate calcium source for new engineered soil.

This study indicates that road components such as roadside verges and central reserves have potential to provide the function of passive CO_2 removal. However, considering the possibility that deposition of $CaCO_3$ within soil pore spaces may reduce permeability, efforts to maintain proper drainage in the soil profile may be required to avoid flooding. Engineering a carbon capture function into roadside verges needs to be sympathetic to the provision of other ecosystem services, such as biodiversity conservation.

ACKNOWLEDGMENTS

The authors thank funding of the Engineering and Physical Sciences Research Council (EP/K034952/1 and EP/I002154/1). We thank the United Kingdom Department of Transport for providing the necessary resources and information.

REFERENCES

[1] Thomas C, "ROADSIDE VERGES", Warwickshire, Coventry and Solihull Local Biodiversity Action Plan, 2005, pp.8.

[2] Department for Transport, "Design Manual for Roads and Bridges - Cross-Sections and Headrooms", Volume 6, Section 1, Part 2, 2005.

[3] Department for Transport, "Road lengths in Great Britain", 2013, available from: https://www.gov.uk/government/uploads/system/uploads/attachment_data/file/208692/road-lengths-in-great-britain-2012.pdf.

[4] Pacala S, Socolow R, "Stabilization wedges: Solving the climate problem for the next 50 years with current technologies", Science 305, 2004, pp. 968– 972.

[5] Manning DAC, "Biological enhancement of soil carbonate precipitation: passive removal of atmospheric CO_2", Mineralogical Magazine 72, 2008, pp. 639-649.

[6] Washbourne CL, Renforth P, Manning DAC, "Investigating carbonate formation in urban soils as a method for capture and storage of atmospheric carbon", Science of the Total Environment 431, 2012, pp. 166-175.

[7] Washbourne CL, Lopez-Capel E, Renforth P, Ascough PL, Manning DAC, "Rapid removal of atmospheric CO_2 by urban soils", Environmental Science and Technology 49, 2015, pp. 5434-5440.

[8] Manning DAC, Renforth P, "Passive sequestration of atmospheric CO_2 through

coupled plant-mineral reactions in urban soils", Environmental Science and Technology 47(1), 2013, pp. 135-141.
[9] Jorat ME, Goddard MA, Kolosz BW, Sohi S, Manning DAC, "Sustainable Urban Carbon Capture: Engineering Soils for Climate Change (SUCCESS)", In: 16th European Conference on Soil Mechanics and Geotechnical Engineering (XVI ECSMGE 2015). 2015, Edinburgh, pp. 2559 – 2564.
[10] Cerling TE, "The stable isotope composition of modern soil carbonate and its relationship to climate", Earth and Planetary Science Letter 71,1984, pp. 229-240.
[11] Renforth P, Manning DAC, Lopez-Capel E, "Carbonate precipitation in artificial soils as a sink for atmospheric carbon dioxide", Applied Geochemistry 24, 2009, pp. 1757-1764.
[12] Renforth P, Edmondson J.; Leake, J. R.; Gaston, K. J.; Manning, D. A. C. Designing a carbon capture function into urban soils. Proc. Inst. Civ. Eng.: Urban Design Plann. 2011, 164 (2), pp. 121−128.
[13] Kolosz BW, Goddard MA, Jorat ME, Aumonier J, Sohi SP, Manning DAC, "A Sustainability Framework for Engineering Carbon Capture Soil In Transport Infrastructure", International Journal of Transport Development and integration 2017, 1, pp. 74-83 (In-press).
[14] Kolosz BW, Manning P, Goddard MA, Jorat ME, Sohi SP, Manning DAC, "A Multifunctional Soil Inorganic Carbon Prediction Model", In: 8th International Congress on Environmental Modelling and Software. 2016, Toulouse France (In-press).
[15] Kolosz BW, Goddard MA, Jorat ME, Sohi S, Manning DAC, "Developing Lifecycle Inventory Indices for Estimating the Carbon Sequestration of Artificially Engineered Soils and Plants", In: 5th Asian conference on Sustainability, Energy, and the Environment, 2015, pp. 93-112.
[16] Jorat ME, Kolosz BW, Sohi S, Lopez-Capel E., Manning DAC, "Changes in geotechnical properties of urban soils during carbonation", In: 15th Pan-American Conference on Soil Mechanics and Geotechnical Engineering, 2015, Buenos Ares, Argentina, pp. 912 – 918.
[17] Deer WA, Howie RA, Zussman J, "An introduction to the rock forming minerals", Longman Scientific & Technical, Essex, 2013, 3rd Edition.
[18] Department for Transport, "Road lengths in Great Britain", 2014, available from: https://www.gov.uk/government/uploads/system/uploads/attachment_data/file/428857/road-lengths-in-great-britain-2014.pdf.
[19] Lovell ST, Taylor JR, "Supplying urban ecosystem services through multifunctional green infrastructure in the United States", Landscape Ecology, 28, 2013, pp. 1447-1463.
[20] Muñoz P, Torres F, Megías A, "Effects of roads on insects: a review", Biodiversity and Conservation, 24, 2015, pp. 659-682.
[21] Benítez-López A, Alkemade R, Verweij PA, "The impacts of roads and other infrastructure on mammal and bird populations: A meta-analysis", Biological Conservation, 143, 2010, pp. 1307-1316.
[22] Auestad I, Rydgren K, Austad I, "Road verges: Potential refuges for declining grassland species despite remnant vegetation dynamics", Annales Botanici Fennici, 48, 2011, pp. 289-303.
[23] Hopwood JL, "The contribution of roadside grassland restorations to native bee conservation", Biological Conservation, 141, 2008, pp. 2632-2640.
[24] DEFRA, "The National Pollinator Strategy: for bees and other pollinators in England", 2014.
[25] Poleto C, Tassi R, "Sustainable Urban Drainage Systems", Drainage Systems, Prof. Muhammad Salik Javaid (Ed.), ISBN: 978-953-51-0243-4, InTech, 2012, available from: http://www.intechopen.com/books/drainage-systems/sustainable-drainage-systems.
[26] Zhou Q, "A Review of Sustainable Urban Drainage Systems Considering the Climate Change and Urbanization Impacts", Water 6, 2014, pp. 976-992.
[27] Fox J, "Applied Regression Analysis, Linear Models, and Related Methods", Published by Sage Publications, Inc., ISBN: 0-8039-4540-X, the United Stated of America, 1997, Chapter 2, pp.15.
[28] Harrell F E Jr, "Regression Modelling Strategies: With Application to Linear Models, Logistic Regression and Survival Analysis", published by Springer Science Business Media ISBN-10: 0-387-95232-2, United States of America, 2011.
[29] Knofczynski GT, Mundfrom D, "Sample Sizes When Using Multiple Linear Regression for Prediction", published by Educational and Psychological Measurement, 68(3), 2008, pp 431-442.

COMPOSITIONAL CHARACTERISTICS OF SAND MATRIX SOILS

Choy Soon Tan[1], Aminaton Marto[2] and Ali Sobhanmanesh[1]
[1]Faculty of Engineering, Technology and Built Environment, UCSI University, 56000 Cheras, Malaysia
[2] Faculty of Civil Engineering, Universiti Teknologi Malaysia, 81310 UTM Skudai, Malaysia

ABSTRACT

Previous study always assumes that the typical engineering characteristic of clean sand was remarkably representing as to all types of sand matrix soils. However, the primary physical characteristics are varying with the amount of presenting fine particles within the matrix of sand grain. Empirical evidences revealed that the sand matrix soils are also liquefiable besides the clean sand. Hence, the typical engineering characteristic of clean sand could not represent as to all types of sand matrix soils. The aim of this paper is to examine the primary physical characteristics of sand matrix soils through experimental study.

Keywords: particle size distribution, particle density, limiting density, void ratio

INTRODUCTION

Chinese Criteria [1] is the best known liquefaction susceptibility identification founded following the 1975 Haichang Earthquake and the 1976 Tangshan Earthquake. The criteria are: (1) fraction finer than 0.005mm ≤ 15%; (2) liquid limit ≤ 35% and (3) natural water content ≥ 0.9 liquid limit. Some modification and amendment have been done over the years. Seed et al. [2] combined the criteria into a plasticity chart while Finn [3] suggested some adjustments to suit globally recognised ASTM standard. The Modified Chinese criteria are now the basic groundwork of liquefaction susceptibility criteria.

In the 20th century, researchers started to question and debate on the usability of Modified Chinese Criteria owing to the presence of fines (which supposed to be non-liquefiable) in some field evidences which deviated from the criterion. Both academicians and engineers believed that the Modified Chinese Criteria that is conceptually based on empirically oriented, which is inadequate to define the vulnerability of sand with some fines towards soil liquefaction. Thus, the re-examination is vital to introduce some necessary correction factors in the criteria in order to adjust in accordance with the influence of fines [4].

Kramer [5] reviewed and concluded that there are four important criteria in liquefaction susceptibility which are historical criteria, geologic criteria, compositional criteria and state criteria. Compositional characteristic is the most important criteria out of the other three criteria because it is associated with volume change behaviour. These compositional characteristics include particle size, shape and gradation. The presence of plastic fines in sand matrix soils gives significant influences to the compositional characteristic. It is believed that this is the main reason why current empirical evidences show that sand with limited percentages of fines is also liquefiable. Numerous researchers initiated their research to characterize on which type of sand matrix soils is the most susceptible to soil liquefaction. The boundary limit on liquefaction susceptibility criteria have been broadened since then. Therefore, it is essential to be able to describe the physical characteristics of soils more concisely in order to express the real engineering behaviour of sand matrix soils [6]. The plasticity behaviour of sand matrix soils have been described in companion paper of [7]. Therefore, the aim of this paper is to examine the primary physical characteristics of sand matrix soils through experimental study. The primary physical characteristics are the particle density (ρ_s), particle size distribution and limiting densities (ρ_{max}/ρ_{min}).

EXPERIMENTAL TESTING

In order to quantify the physical characteristics of various kinds of sand matrix soils, the reconstituted sand matrix soils were mixed by adding two types of commercially available plastic fines to the parent sand at various percentages by weight. The clean sand used to form the sand matrix soils in this study is the natural sand obtained from a river in Johor Bahru, Malaysia. The plastic fines are (i) low plastic fines, white kaolin (MI) by Kaolin (Malaysia) Sdn Bhd and (ii) highly plastic fines, green bentonite (CE) by Halliburton (Malaysia) Sdn Bhd. Four main types of reconstituted sand matrix soils was summarised in Table 1.

Table 1 Compositional percentages of reconstituted sand matrix soils

Sand Matrix Soils	Percentages by weight (%)			Label
	Sand	Kaolin	Bentonite	
Clean Sand	100	0	0	SAND100
Sand-Kaolin Mixtures	95	5	0	SK05B00
	90	10	0	SK10B00
	85	15	0	SK15B00
	80	20	0	SK20B00
	75	25	0	SK25B00
	70	30	0	SK30B00
	60	40	0	SK40B00
Sand-Fines Mixtures	90	5	5	SK05B05
	80	15	5	SK15B05
	80	10	10	SK10B10
	80	5	15	SK05B15
	75	12.5	12.5	SK13B12
	70	15	15	SK15B15
	60	20	20	SK20B20
Sand-Bentonite Mixtures	95	0	5	SK00B05
	90	0	10	SK00B10
	85	0	15	SK00B15
	80	0	20	SK00B20
	75	0	25	SK00B25
	70	0	30	SK00B30
	60	0	40	SK00B40

The soil classification test that was carried out in this study to investigate the physical characteristics of sand matrix soils are (i) particle density test using the small pycnometer method; (ii) particle size distribution test by combining the results of wet sieving method and hydrometer test and (iii) limiting density test. All tests were carried in accordance with British Standard (BS) 1377-2:1990 [8] except for the limiting density test. In fact, the limiting densities of sand should be determined in accordance with Clause 4.2 for a maximum density of sands and Clause 4.4 for a minimum density of sands in BS1377-4:1990 [9]. However, the general requirement in both clause states that both methods is suitable only for sand containing a small amount of fine material, usually not exceeding 15 % of material finer than a 63μm test sieve, by mass. Due to that the soil sample used in this study, the sand matrix soils are mostly having more than 10 % of fines by weight based on the results of particle size distribution; the techniques recommended by [10] were used to determine the limiting densities.

Particle Density

Particle density of the soil, G_S is the ratio of the mass density of the mineral soils in soil normalised relatively to the mass density of water. The small pycnometer method is more suitable for the soils fines than 2 mm, as chosen to be conducted in this research. All soil samples with approximately 100 g were oven dried at 105 °C prior to testing. The soil was divided into three portions to carry out the test concurrently to ensure the repeatability and precision of the results. The test was carried out in accordance with Clause 8.3 in Part 2 BS1377.

Particle Size Distribution

Soil consists of individual particles or grains. Grain size refers to the size of an opening in a square mesh through which a grain will pass. Since all of the grains in a mass of soil are not the same size, it is convenient to quantify grain size in terms of a gradation curve. The particle size distribution is the percentages of the various grain sizes present in a soil. Since the soil samples in this study are ranging from sand size down to clay soils, the particle size distribution need to be determined by combining the results of wet sieving method and the results of the sedimentation test by using the hydrometer method. All soil samples were oven dried at 105 °C prior to testing. The wet sieving method was carried out in accordance with Clause 9.3 in Part 2 BS1377 while the hydrometer method was carried out in accordance with Clause 9.5.

Limiting Density

The limiting density is the dry densities corresponding to the extreme states of packing of particles of a granular soil. The maximum density is defined as when the soils at the densest practicable state of packing while the minimum density is when the soils at the loosest state of packing. In fact, neither British Standard (BS) nor American Society of Testing Material procedure (ASTM) is suitable for the determination of the maximum density and minimum density for sand matrix soils; most standard are limited to soils with maximum fines content of 10% to 15% only. Due to that the soil sample used in this study, the sand matrix soils are mostly having more than 10% of fines by weight; the techniques recommended by Lade and Yamamuro [10] were used to determine the limiting densities in this study. The soil samples were oven dried at 105 °C prior to testing.

RESULTS AND DISCUSSION

The results of the soil classification test to describe the primary physical characteristics of sand matrix soils are presented in this section. The secondary physical characteristics which are obtained by correlate with the primary physical characteristics are also included.

Particle Density

Particle density (G_S) is typically expressed using three significant figures. The G_S for sands is often assumed to be 2.65 and higher for the clay, normally between 2.70 to 2.80 depending on mineralogy. However, the pure soil used in this research has lower value of G_S compared to the typical values. The G_S value for the clean sand is 2.63 while the G_S for the kaolin and bentonite are 2.61 and 2.35 respectively. The results of G_S values for sand matrix soils are shown in Fig. 1.

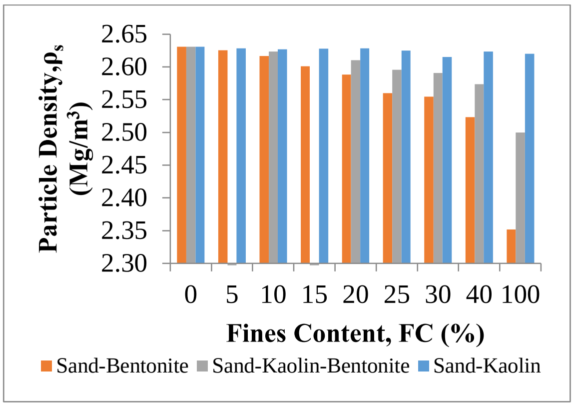

Fig. 1 Particle density of sand matrix soils

As the clean sand used in this study is the river sand, and hence, the presence of other organic material in the sand grain causes a lower value of particle density in this study. Both the plastic fines also reported a lower particle density than the typical values. The reason is because the manufacture process of these commercially available fines had eliminated the presence of heavy metals, in order to keep the purity of the material. In fact, particle density is remarkably influenced by its mineralogy composition while the natural soil often consists of a variety of minerals. Therefore, chemical tests which are beyond the scope of this study should be conducted in the future to determine the mineralogy of the clean sand and both plastic fines.

Particle Size Distribution

The sieving method is not practical for soils smaller than silt size. By combining the results of wet sieving and sedimentation procedure using hydrometer, the particle size distribution of the whole sand matrix soils is achievable. The grading curve from sand size down to clay size is shown in Fig. 2. The composition percentages of the sand matrix soils are listed in Table 2 together with its grading characteristics, including the coefficient of uniformity, C_u and coefficient of curvature, C_c. The sand matrix soils were then classified in accordance with the British Soil Classification System for Engineering Purposes (BSCS) as described in clause 41 to Clause 43 of BS 5930:1981 [11]. Although most of the classification tests in this study are carried out in accordance with BS, the classification based on the Unified Soil Classification System (USCS) was adopted in this study for comparison purpose. The USCS [12] is more commonly used in the industry to describe the texture and grain size of most unconsolidated materials. The composition characteristics of sand matrix soils at various percentages of fines content are more obvious by using the USCS.

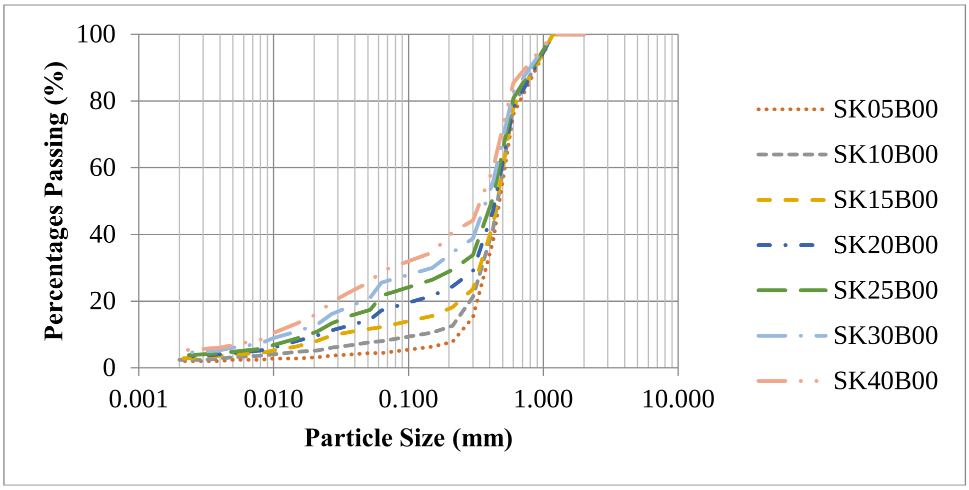

(a) Sand-kaolin mixtures

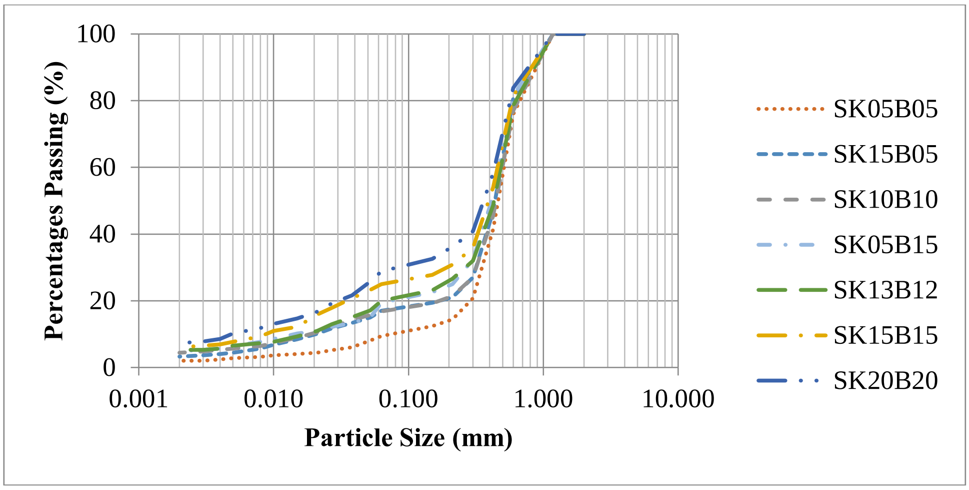

(b) Sand-fines mixtures

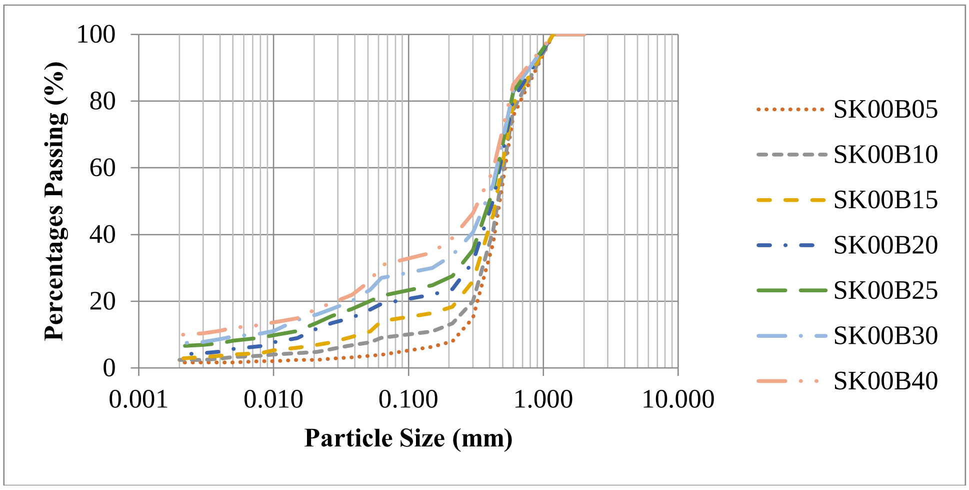

(c) Sand-bentonite mixtures

Fig. 2 Particle size distribution of (a) sand-kaolin mixtures pure soils; (b) sand-fines mixtures; (c) sand-bentonite mixtures

Table 2 Grading Characteristics of sand matrix soils

Series	Soil composition			Gradation		
	Sand	Silt	Clay	Cu	Cc	D50
		%			-	mm
SAND100	100	0	0	2	1	0.500
SK05B00	96	2	2	2	1	0.500
SK10B00	92	6	2	3	1	0.470
SK15B00	88	9	3	10	5	0.450
SK20B00	83	14	3	16	7	0.420
SK25B00	78	18	4	20	5	0.410
SK30B00	75	21	4	23	3	0.400
SK40B00	71	24	5	32	1	0.350
SK05B05	91	7	2	6	3	0.480
SK15B05	83	14	3	25	12	0.460
SK10B10	84	12	4	24	11	0.440
SK05B15	80	15	5	23	10	0.420
SK13B12	80	15	5	22	10	0.400
SK15B15	75	19	6	48	10	0.380
SK20B20	72	21	7	84	2	0.360
SK00B05	96	2	2	2	1	0.500
SK00B10	91	7	2	2	1	0.450
SK00B15	86	11	3	8	3	0.400
SK00B20	81	15	4	32	11	0.380
SK00B25	78	15	7	46	14	0.350
SK00B30	73	20	7	88	7	0.320
SK00B40	69	21	10	430	4	0.300

Limiting Density

The maximum and minimum density of the sand matrix soils are plotted against percentages of fines by weight in Fig. 3. The negative hyperbolic curve is noticeable from the plot of limiting densities. During the filling-of-void phase, the density of soil is increasing with fines content. The fine particles is filling the void spaces between sand grains, increasing the overall density of soil. The liquefaction resistance would be lower because the permeability is low; the rate of pore pressure build up due to the external loading is therefore faster. Replacement-of-void stage occurs when the void spaces are almost completely filled. Addition of fine particles would displace the sand grains from each other; therefore, the density is decreasing with the addition of fines content. The limiting value of fines content at the transition from these two phases is known as the threshold fines content (f_{th}), which normally is located within 20% to 40% of fines content. The threshold fines content of sand-bentonite and sand-fine mixtures are both 20% of fines by weight while for sand-kaolin is 25% of kaolin by weight.

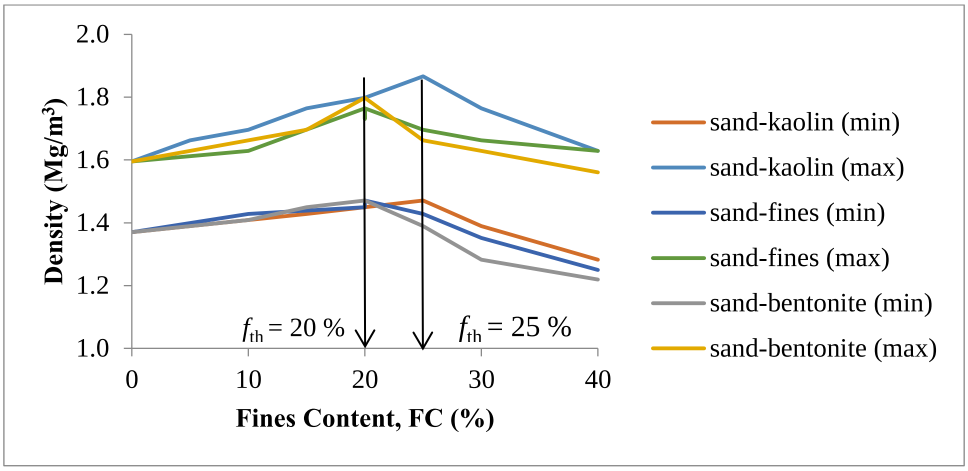

Fig. 3 Limiting densities of sand matrix soils

CONCLUSION

In this study, both primary and secondary physical characteristics of sand matrix soils were investigated through laboratory testing. The primary physical characteristic including particle density, particle size distribution, limiting densities were examined. Based on the results, the following conclusions are achieved:

1. The particle density of the clean sand, white kaolin and green bentonite used in this study are 2.63, 2.62 and 2.35 respectively.
2. The threshold fines content of sand-bentonite and sand-fine mixtures are 20% of fines by weight while for sand-kaolin is 25% of kaolin by weight.
3. The physical characteristics are varying with the amount of fines present within the matrix of sand grain.
4. Typical engineering characteristic of clean sand could not represent as to all types of sand matrix soils.

ACKNOWLEDGEMENTS

The authors gratefully acknowledged the financial supports given by the Ministry of Education (MOE) under the Fundamental Research Grant Scheme in undertaking this research.

REFERENCES

[1] Wang, W. S. Some Findings in Soil Liquefaction. Chinese Jounal of Geotechnical Engineering, 1980.

[2] Seed, H. B., Idriss, I. M., & Arango, I.. Evaluation of liquefaction potential using field performance data. Journal of Geotechnical Engineering, 1983, 109(3), pp. 458–482.

[3] Finn, W. D. L.. Assessment of liquefaction potential and post-liquefaction behavior of earth structures: developments 1981-1991. In Second International Conference on Recent Advances in Geotechnical Earthquake Engineering and Soil Dynamics, 1991, 1833–1850 .

[4] Prakash, S., and Puri, V. K. Recent advances in liquefaction of fine grained soils. In 5th international conference on recent advances in geotechnical earthquake engineering and soil dynamics, San Diego, California, 2010.

[5] Kramer, S. L. Geotechnical earthquake engineering (1st ed) New Jersey: Prentice Hall, 1996.

[6] Tan, C. S., Marto, A., Leong, T. K., and Teng, L. S.. The role of fines in liquefaction susceptibility of sand matrix soils. Electronic Journal of Geotechnical Engineering, 2013, 18 L, pp. 2355–2368.

[7] Tan, C. S., Marto, A., Makhtar, A. M., and Pakir, F. Plasticity Behaviour of Sand Matrix Soils. Applied Mechanics and Materials, 2015, 695, pp. 734–737.

[8] British Standards Institution. BS1377-2:1999 Classification tests. (2010a).

[9] British Standards Institution. BS1377-4:1999 Compaction-related tests, 2010b.

[10] Lade, P. V. and Yamamuro, J. A. Effects of nonplastic fines on static liquefaction of sands. Canadian Geotechnical Journal, 1997, 34(6), pp. 918–928.

[11] British Standards Institution. BS5930:1999 Code of practice for site investigations, 2010c.

[12] American Society for Testing and Materials. D2487-11: Standard practice for classification of soils for engineering purposes (Unified Soil Classification System), 2011.

Sixth International Conference on Geotechnique, Construction Materials and Environment, Bangkok, Thailand, Nov. 14-16, 2016, ISBN: 978-4-9905958-6-9 C3051

EFFECT OF FLY ASH ON THE STRENGTH DEVELOPMENT OF BANGKOK SOIL-CEMENT

Keeratikan Piriyakul[1]
[1]Center of Excellence in Structural Dynamics and Urban Management, Department of Civil and Environmental Engineering Technology, College of Industrial Technology, King Mongkut's University of Technology North Bangkok, Thailand

ABSTRACT

This research presents the effect of fly ash on the strength development of Bangkok soil-cement mixing. The Bangkok clay samples were prepared with 20 % of the Portland cement type 1 by weight of dry soil and varied the replacement of fly ash type F 10, 15, 20, 25 and 30 % by weight of cement. Then, these samples were cured to 7, 14, 28 and 90 days respectively and the bender element and the unconfined compression tests were performed. The research found that the optimum percent replacement of fly ash was about 15-20 %. The V_s result of 20 % replacement of fly ash at 90 days was the maximum V_s result, showing the long term behaviour of fly ash mixed with cement. From the saturation equation, the $V_{s(max)}$, the K_{Vs}, the $G_{0(max)}$ and the K_{Go} parameters showed that the optimum percent replacement of fly ash was about 15-20 %. In a similar way, the $S_{u(max)}$ and K_{Su} parameters showed that the optimum percent replacement of fly ash was about 15-25 %.

Keywords: Bangkok Clay, Fly-ash, Bender Element Test, Soil-cement

INTRODUCTION

The shear wave velocity measurement technique was used to determine the initial shear modulus, G_0, by means of elastic shear wave. This measurement technique used the principles of wave propagation showing a direct correlation between the shear wave velocity and G_0 as described in [1]. Piriyakul [2] used similar piezoelectric ceramic sensors to assess the disturbance of soil samples. Piriyakul [3] used piezoelectric ceramic sensors to examine the anisotropy of clay soils by shear wave velocity. Piriyakul and Gi-nga [4] and Piriyakul and Pochalard [5] used piezoelectric ceramic sensors to determine the cementation of soft Bangkok clay mixed with cement and with fly ash, respectively. This initial shear modulus is widely considered to be an important parameter in earthquake engineering and the prediction of soil-structure interaction. The shear wave is generated and received by piezoelectric transducers placed at opposite ends of the soil specimen. The shear wave velocity is calculated from the tip to tip distance between the two transducers and the time required by the shear wave to cover this distance as shown in Eq. (1).

$$V_s = L/t \tag{1}$$

where V_s is the shear wave velocity in m/s, L is the tip to tip distance between two transducers in mm, and t is the required time to cover this distance in µs. After obtaining the shear wave velocity, the initial shear modulus, G_0, in MPa is calculated using the relationship of elastic continuum mechanics as shown in Eq. (2).

$$G_0 = \rho . V_s^2 \tag{2}$$

where ρ is the mass density of the material in kg/m^3.

The saturation equation, the so called Michaelis-Menten equation [6], was used to predict the strength development of Bangkok soil-cement as shown in Eqs. (3) to (5).

$$\frac{s(max) \times t}{K_{Vs} + t} \tag{3}$$

where $V_{s(max)}$ is the maximum shear wave velocity and K_{Vs} is the constant for shear wave velocity.

$$\boldsymbol{G_0} \quad \frac{G_{0(max)} \times t}{K_{Go} + t} \tag{4}$$

where $G_{0(max)}$ is the maximum shear modulus and K_{Go} is the constant for shear modulus.

$$\boldsymbol{S_u} \quad \frac{S_{u(max)} \times t}{K_{Su} + t} \tag{5}$$

where $S_{u(max)}$ is the maximum undrained shear strength and K_{Su} is the constant for undrained shear strength.

BENDER ELEMENT TEST

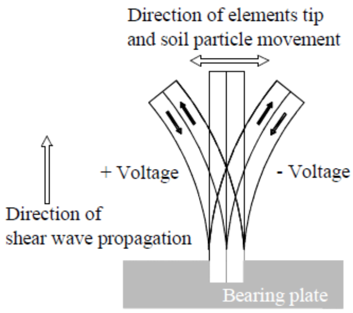

Fig. 1 Operation of piezoelectric ceramic sensor [1].

Bender element sensors were piezoelectric sensors. The principle of piezoelectric sensor is based on the properties of piezoelectric ceramic materials. A voltage applied to faces of a combination of two piezoelectric ceramic materials causes one to expand while the other contracts, causing the entire element to bend as described by [7] and shown in Figure 1. Similarly, a lateral disturbance of the piezoelectric sensor will produce a voltage so the piezoelectric sensor can be used as both shear wave transmitter and receiver. Measurement of time delay between sending and receiving of the shear wave will provide the shear wave velocity.

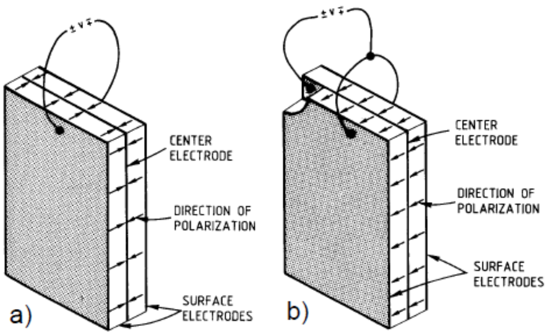

Fig. 2 a) Series and b) Parallel connected elements [7].

There are two types of piezoelectric transducers. One is a series connected piezoelectric transducer and the other is a parallel connected piezoelectric transducer. The series connected piezoelectric transducer is shown in Fig. 2a. Noting that the polarization is oriented in opposite directions for each plate. An electrical wire lead is attached to each of the outer electrode surfaces. The parallel connected piezoelectric transducer is shown in Fig. 2b. In this second type of piezoelectric transducer, the polarization has the same direction for both plates. The electrical connections are attached such that the two outer electrode surfaces are the same pole and the center electrode is the other pole. To attach an electrical wire lead to the center electrode, a portion of the element must be ground away. The series connected piezoelectric transducer is better to use as receiver. On the other hand, the parallel connected piezoelectric transducer is better to use as transmitter. However, this research uses only the parallel type for both transmitter and receiver transducers due to the advantage in measurement of sending signal.

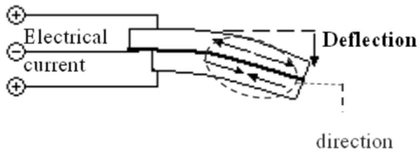

Fig. 3 Schematic of the piezoelectric ceramic sensor.

Figure 3 shows the piezoelectric transducer used in this research. This sensor is a non-magnetic piezoceramic with non-magnetic electrodes and non-magnetic reinforcing materials. This sending sensor (T220-A4NM-303Y) is manufactured from the Piezo System, Inc. The size of the sending sensor is 12.7 mm in width, 15.9 mm in length and 0.51 mm in thickness. The research uses this sensor to send the shear wave because of the strong sending signal.

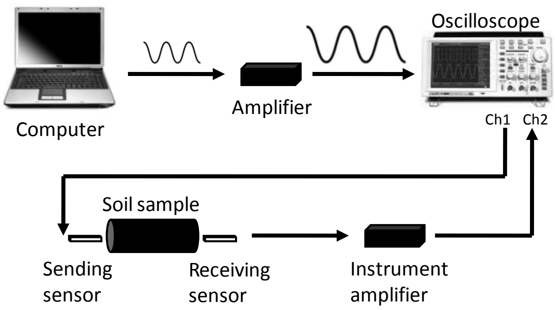

Fig. 4 Schematic of shear wave measurement and associated electronics.

Figure 4 shows the schematic test set-up. A personal computer generates a signal through a sound card with 5V peak to peak as suggested by [8]. This signal is amplified to 40V peak to peak. An oscilloscope is used to measure the arrival time between a sending signal and a receiving signal. A voltage pulse is applied to the sending sensor. This causes it to produce a shear wave. When the shear wave reaches the other end of the soil sample, distortion of the receiving sensor produces another voltage pulse. The receiving sensor is directly connected to the oscilloscope to compare the difference in time between the sending and the receiving signals. The shear wave velocity measurements are usually performed with frequencies ranging between 2 to 12 kHz, at strains estimated to be less than 0.0001 %. At low frequencies, signals can be influenced by a near-field effect. At high frequencies, the receiving signal is very weak and difficult to interpret. In most cases, signals are averaged 32 times in order to get a clear signal. The measurement of shear wave velocity in soil sample by means of piezoelectric ceramic sensors is clearly described by [9] and [10].

BANGKOK CLAY MATERIAL

The geological condition of Bangkok is reported by [11] and shows that Bangkok is situated on a large plain underlain by alluvial and deltaic sediments of the Chaophraya basin. This plain is about 13,800 km2 in area and is generally known as "the lower central plain". The plain was under a shallow sea 3,000 to 5,000 years ago and the regression of the sea took place around 2,700 years ago, leaving the soft deposits, which form the lower central plain. This plain consists of thick clay known as Bangkok clay on its top layer, and its thickness is about 15 to 20 m in the Bangkok city area. The soft clay has very low shear strength, and is highly compressible, as it has never been subjected to mechanical consolidation.

The soft Bangkok clay at 10-12 m depth is sampled for this research. The engineering properties are found where that the specific gravity is 2.72, the natural water content is 66.3%, the mass density is 1,470 kg/m3 and the liquid limit is 88%. 60 experiment soft Bangkok clay samples are prepared at the liquid limit by mixing 20% by weight of Portland cement Type 1 and varying the replacement fly ash of 0, 10, 15, 20, 25 and 30%. This research uses the fly ash Type F from Mae Moh Lignite Power Plant in Lampang. Then, these samples are cured 7, 14, 28 and 90 days in order to perform the bender element test and the unconfined compression test.

TEST RESULTS

Figure 5 shows the shear wave velocity, V_s, versus the percent replacement of fly ash. From the test results, the research found that the optimum percent replacement of fly ash was about 15-20 %. From the 90 days results, the V_s of 20 % replacement of fly ash was the maximum value which reports the long term behaviour of fly ash and cement mixed.

In a same way, Fig. 6 shows the shear modulus, G_0, versus the percent replacement of fly ash. From the experimental results, the research found that the optimum percent replacement of fly ash was 20 %.

In a similar ways, Fig. 7 shows the undrained shear strength, S_u, versus the percent replacement of fly ash. From the experimental results, the research found that the optimum percent replacement of fly ash was about 15 %. From the 90 days results, the S_u of 15 % replacement of fly ash was the maximum value which reports the long term behaviour of fly ash and cement mixed.

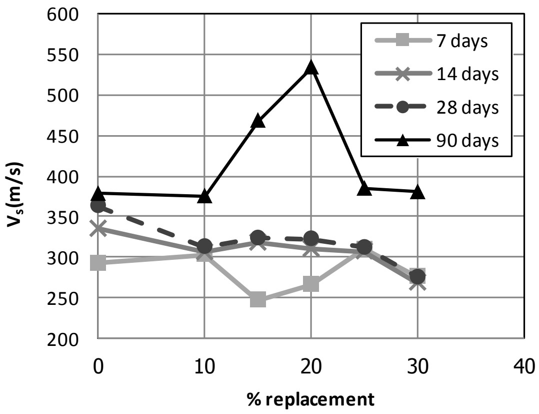

Fig. 5 V_s versus the % replacement of fly ash.

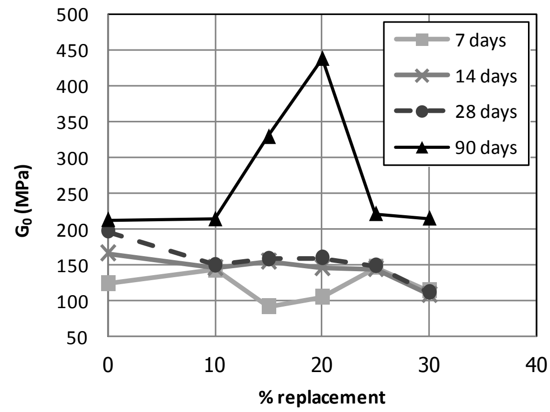

Fig. 6 G_0 versus the % replacement of fly ash.

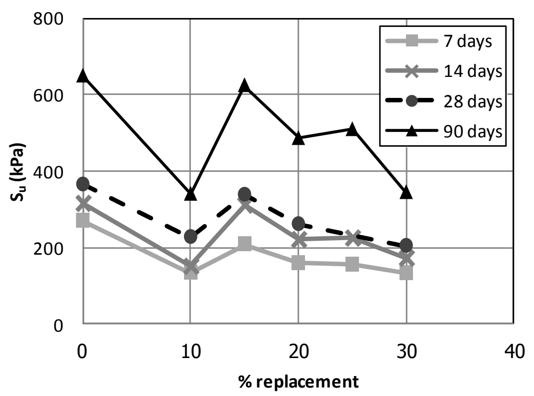

Fig. 7 S_u versus the % replacement of fly ash.

Figure 8 shows the plot of the $1/V_s$ versus the 1/t varied with the percent replacement of fly ash. The control Bangkok soil-cement sample data with 0 % replacement of fly ash depicted a Y-intercept of 0.00256. The invert of the Y-intercept value was the $V_{s(max)}$ of 390.63 m/s and the K_{Vs} of 2.36 was calculated by using the $V_{s(max)}$ of 390.63 m/s multiplied with the slope of 0.00603. Table 1 shows all results of $V_{s(max)}$ and K_{Vs} parameters varied with the percent replacement of fly ash. From the test results, the research found that the optimum percent replacement of fly ash was about 15-20 %. The maximum value of shear wave velocity $V_{s(max)}$ of 20 % replacement of fly ash was 452.49 m/s and the K_{Vs} was 5.43 day for the Bangkok soil-cement to develop strength half of $V_{s(max)}$.

In a similar way, Fig. 9 shows the plot of the $1/G_0$ versus the 1/t varied with the percent replacement of fly ash. Table 2 showed all results of $G_{0(max)}$ and K_{Go} parameters varied with the percent replacement of fly ash.

In a same way, Fig. 10 shows the plot of the $1/S_u$ versus the 1/t varied with the percent replacement of fly ash. Table 3 shows all results of $S_{u(max)}$ and K_{Su} parameters varied with the percent replacement of fly ash.

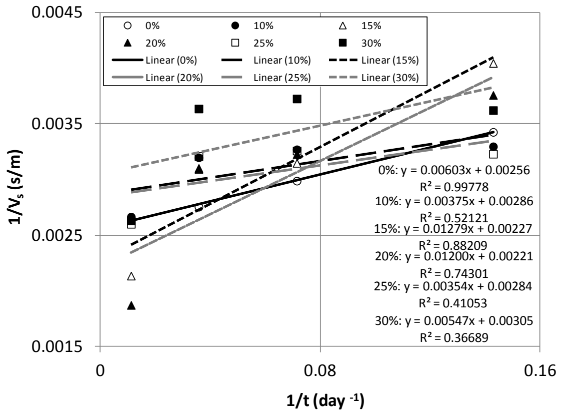

Fig. 8 The relationship between $1/V_s$ and 1/t.

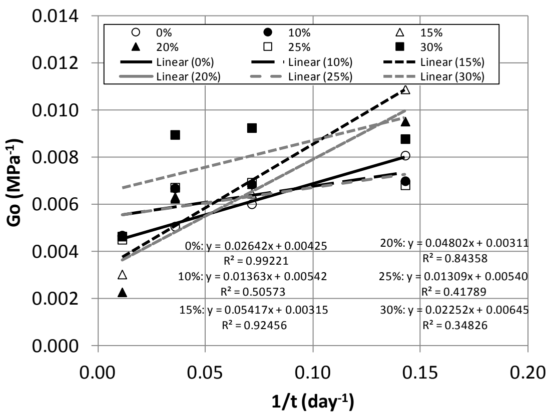

Fig. 9 The relationship between $1/G_0$ and 1/t.

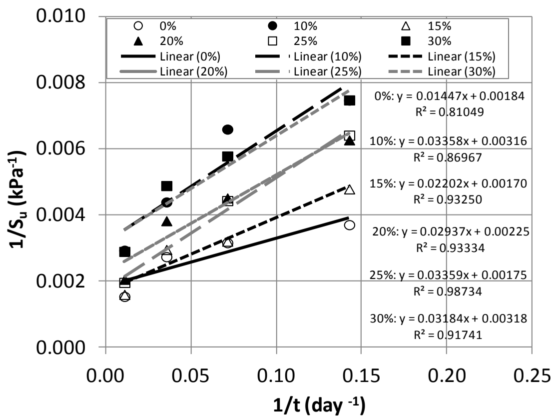

Fig. 10 The relationship between $1/S_u$ and 1/t.

Table 1 Results of $V_{s(max)}$ and K_{Vs} parameters varied with the percent replacement of fly ash

% Fly ash	V_s (max) [m/s]	K_{Vs} [day]
0	390.63	2.36
10	349.65	1.31
15	440.53	5.63
20	452.49	5.43
25	352.11	1.25
30	327.87	1.79

Table 2 Results of $G_{0(max)}$ and K_{Go} parameters varied with the percent replacement of fly ash

% Fly ash	G_0 (max) [MPa]	K_{Go} [day]
0	235.29	6.22
10	184.50	2.51
15	317.46	17.20
20	321.54	15.44
25	185.19	2.42
30	155.04	3.49

Table 3 Results of $S_{u(max)}$ and K_{Su} parameters varied with the percent replacement of fly ash

% Fly ash	S_u (max) [KPa]	K_{Su} [day]
0	543.48	7.86
10	316.46	10.63
15	588.24	12.95
20	444.44	13.05
25	571.43	19.19
30	314.47	10.01

CONCLUSION

From the test results, the research found the conclusions as follows:

- The optimum percent replacement of fly ash was about 15-20 %. From the 90 days results, the V_s of 20 % replacement of fly ash was the maximum value which reports the long term behaviour of fly ash and cement mixed.
- From the saturation equation, the $V_{s(max)}$ and the K_{Vs} parameters showed that the optimum percent replacement of fly ash was about 15-20 %.
- From the saturation equation, the $G_{0(max)}$ and the K_{Go} parameters showed that the optimum percent replacement of fly ash was about 15-20 %.
- From the saturation equation, the $S_{u(max)}$ and the K_{Su} parameters showed that the optimum percent replacement of fly ash was about 15-25 %.

ACKNOWLEDGEMENTS

The author is grateful to the scientific research fund of the College of Industrial Technology and the King Mongkut's University of Technology North Bangkok (KMUTNB).

REFERENCES

[1] Dyvik R & Madshus C, "Laboratory measurement of G_{max} using bender elements", The ASCE Annual Convention, 1985, pp. 186-196.

[2] Piriyakul K, "Soil disturbance assessment in soil sampling of open tube sampler and rotary core drilling", The Journal of Industrial Technology, Vol.6, 2010, pp. 1-6.

[3] Piriyakul K, "Examination of anisotropy of clay using shear wave velocity", The Journal of Industrial Technology, Vol.6, 2010, pp. 25-29.

[4] Piriyakul K & Gi-nga T, "Using shear wave velocity to determine the cementation of soft Bangkok clay mixed with cement", Proceedings of International Symposium on Sustainable Geosynthetics and Green Technology for Climate Change (SGCC), 20-21 June 2012, Bangkok, Thailand, pp. 339-342.

[5] Piriyakul K & Pochalard, S, "Using shear wave velocity to determine the cementation effect of soft Bangkok clay mixed with cement and fly ash", Multiphysical Testing on Soil and Shales, Springer Series in Geomechanics and Geoengineering, 2012, pp. 311-316.

[6] Michaelis L & Menten M, "Die kinetik der invertinwirkung", Biochemistry Zeitung, Vol. 49, 1913, pp. 333-369.

[7] Kramer SL, "Geotechnical Earthquake Engineering. Prentice-Hall International Series", Prentice Hall, Upper Saddle, New Jersey, 1996.

[8] Mohsin AKM & Airey DW, "Automating G_{max} measurement in triaxial tests", The Prefailure Deformation Characteristics of Geomaterials, 2003, pp. 73-80.

[9] Brignoli EGM, Gotti M & Stokoe KH, "Measurement of shear waves in laboratory specimens by means of piezoelectric transducers", Geotechnical Testing Journal, Vol. 19, 1996, pp. 384-397.

[10] Piriyakul K, "A development of a bender element apparatus", Journal of King Mongkut's University of Technology North Bangkok, Vol. 20, 2010, pp. 363-369 (in Thai).

[11] Tuladhar R, Yamazaki F, Warnitchai P & Saita J, "Seismic microzonation of great Bangkok area using microtremor observations", J.of Earthquake Eng Struct Dynam, Vol. 33, 2004, pp. 211-225.

DRAINED SHEAR STRENGTH OF COMPACTED KHON KAEN LOESS

R. Nuntasarn[1] and W. Wannakul[2]
[1,2] Faculty of Engineering, Khon Kaen University, Thailand

ABSTRACT

The objective of this study was to determine the relationship between drained shear strength and matric suction of compacted Khon Kaen loess. Khon Kaen loess in this study was compacted at 95% by modified method. This soil sample was investigated a soil water characteristic curve (SWCC) from the pressure plate test. Moreover the relationship between drained shear strength and matric suction was determined from the consolidated drained triaxial test (CD Test) under saturated and unsaturated condition. Three saturated specimens were tested to determine an effective friction angle (ϕ´) and an effective cohesion (c´). Another three unsaturated specimens were tested with various matric suction of 30, 180 and 280 kPa, respectively. The net confining pressures of these specimens were constant at 100 kPa. To determined drained shear strength at unsaturated condition, an effective friction angle (ϕ´) was assumed to be constant with a matric suction value. The SWCC of compacted Khon Kaen loess showed a bimodal curve. The first air-entry value and the first residual volumetric moisture content was 4 kPa and 20%, respectively. The results of saturated consolidated drained triaxial test (CD Test) presented that an effective friction angle (ϕ´) and an effective cohesion (c´) was 31 degree and 54 kPa, respectively. Moreover the unsaturated triaxial test showed a linear relationship between drained shear strength and matric suction with the ϕ^b angle of 28 degree.

Keywords: Unsaturated Soil, Compacted Soil, Khon Kaen Loess, Consolidated Drained Triaxial Test, Soil Water Characteristic Curve

INTRODUCTION

The unsaturated soil has three phases which are solid, liquid and air. Therefore, the Terzaghi's effective stress law for saturated soil is not appropriate for unsaturated soil. Reference [1] formulated the shear strength equation for an unsaturated soil as given in Eq. (1).

$$\tau_{ff} = c' + (\sigma_n - u_a)\tan\phi' + (u_a - u_w)\tan\phi^b \quad (1)$$

Where τ_{ff} is a shear stress at failure. c' is an effective apparent cohesion, which is the shear strength intercept when the effective stress is equal to zero. σ_f is total normal stress at failure. u_{af} is pore-air pressure at failure. u_{wf} is pore-water pressure at failure. ϕ' is an effective angle of internal friction. And ϕ^b is an angle indicating the rate of increase in shear strength relative to the soil suction at failure.

Reference [2] was investigated the shear strength parameters of unsaturated residual soils by consolidated drained test. This study found that the values of ϕ^b are generally lower than ϕ′.

Reference [3] was studied consolidated drained test on a residual soil, which was classified as CL according to USCS. This study found that the effective friction angle of 31.5 degree and a ϕ^b of 29 degree before air entry value. After Air entry value the relationship between cohesion intercept (c) and matric suction was non-linear as shown in Figure 1.

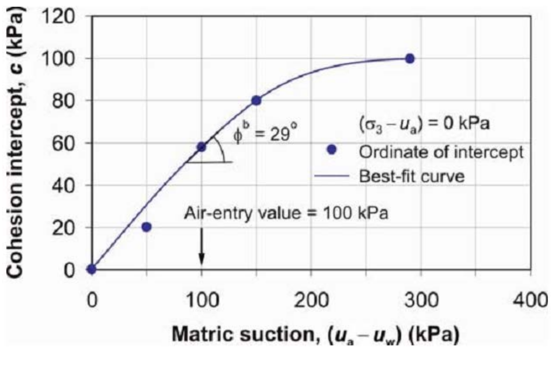

Fig. 1 the relationship between cohesion intercept (c) and matric suction (Ref [2])

BASIC PROPERTIES

The soil used in this study was Khon Kaen loess, which was classified as silty sand (SM) according to USCS. The basic properties of Khon Kaen loess were present in Table1. Percent passing sieve No. 4 and No.200 of this soil sample was 100% and 47%, respectively as shown in Fig.2. Moreover, a liquid limit and a plastic limit of this soil were 13% and of 12%, respectively, which gave the plastic index of 1%. The specific gravity was 2.65.

The maximum dry density and optimum moisture content were 2.06 t/m^3 and 8.5%, respectively, which was determined by standard compaction effort [4]. However, the specimen in this study was prepared at 95% of maximum dry density, which was 1.95 t/m^3, and moisture content of 6.5%.

Table 1 Basic Properties of Khon Kaen loess

Properties	
Liquid limit (LL), %	13
Plastic limit (PL), %	12
Plasticity index (PI), %	1
Specific gravity	2.65
Optimum moisture content (OMC), %	8.5
Maximum dry density (ρ_d), t/m^3	2.06
Sand (%)	53
Silt (%)	27
Clay (%)	20
USCS classification	SM

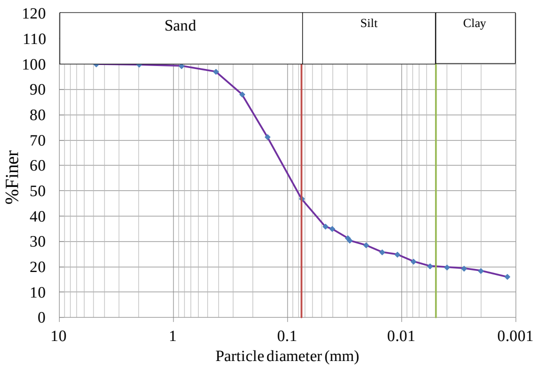

Fig.2 Grain size distribution

SOIL WATER CHARACTERISTIC CURVE

The drying soil water characteristics curve (SWCC) for the compacted Khon Kaen loess was determined by two methods. According to [3], the pressure plate method was used to establish SWCC for a suction values between 1 to 1,500 kPa. Moreover, SWCC at suctions above 1,500 kPa were determined from the isopiestic humidity method. In this method, three solutions, which were Copper Sulphate (CuSO4), Ammonium Chloride (NH4Cl) and Sodium Hydroxide (NaOH.H2O), were used to determine SWCC at a suction value of 3,900 kPa, 30,900 kPa, and 365,183 kPa, respectively. Data points above 1,500 kPa were total suction values.

The test result of a pressure plate and isopiestic humidity showed the soil water characteristic curve (SWCC) as illustrated in figure 3. The soil sample was compacted at the dry side of optimum moisture content (6.5% or 95% of OMC). The SWCC of compacted Khon Kaen loess showed a bimodal curve, which indicated two distinct air-entry values and two distinct residual points [6]. The first and second air entry value is 8 and 5,000 kPa, respectively. Moreover, the first and second residual volumetric moisture content are 10 and 2%, respectively. Therefore, the soil suction value of saturation regime and transition regime was between 0 to 8 kPa and 8 to 200 kPa, respectively. The soil suction, which was higher than 200 kPa, was a residual regime.

The cause of bimodal curve might be the specimen was compacted at the dry side. Because the SWCC of the undisturbed sample showed a unimodal curve with two bending points as illustrated in Fig 4.

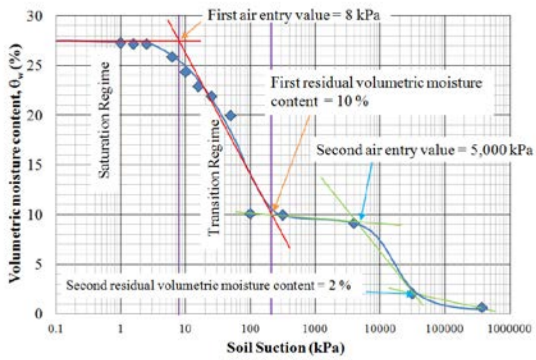

Fig. 3 Soil water characteristic curve of compacted Khon Kaen loess

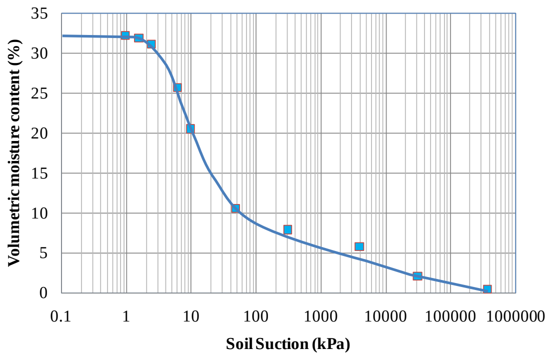

Fig.4 Soil water characteristic curve of undisturbed Khon Kaen loess

CONSOLIDATED DRAINED TEST

Soil sample was mixed with water to achieve 1.95 t/m^3 in dry density and 6.5% of moisture content. Then soil sample was equally separated in two parts and statically compacted in a mold diameter of 50 mm and 100 mm of height.

Each samples were saturated by applied backpressure, which was lower than confining pressure (i.e. σ'_c = 20 kPa) prior to consolidate and drained shear. B-values were observed to be greater than 98% to complete saturation.

Three net confining pressures of 100, 200 and 300 kPa were investigated in this study. For the saturated series, three specimens were tested to determine the effective friction angle (ϕ') and cohesion (c'). Pore air pressure (u_a) and pore water pressure (u_w) of these three samples were controlled at 20 kPa. For the unsaturated series, three samples were observed at net confining pressures of 100 kPa. Pore air pressures were controlled at 50, 200 and 300 kPa and pore water pressures were controlled at 20 kPa to achieve a matric suction of 30, 180 and 280 kPa. The shear rate in this study for both saturated and unsaturated series was 0.01 mm per minute.

The failure of both saturated and unsaturated sample showed a failure plane of 60 degree as shown in Fig.5. For both saturated and unsaturated series, the stress-strain relationship showed the strain hardening behavior as illustrated in Fig.6. Thus the failure was defined at 20% strain. The test result of saturated sample was present at Table 2. Then the Mohr's Circle was drawn in Fig.7. The Mohr's circle showed that the effective friction angle and cohesion was found as 31 degree and 44 kPa, respectively.

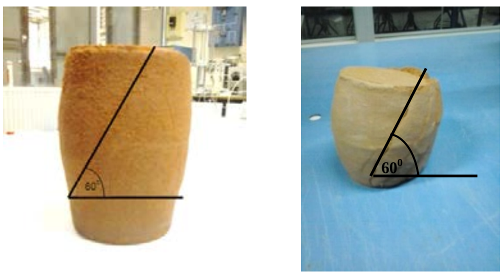

(a) Saturated series (b) Unsaturated series

Fig.5 A shear failure of compacted Khon Kaen loess

The drained shear strength of unsaturated soil was calculated by assumed constant ϕ' (ϕ' = 31 degree) as present in Fig.8. The shear stress (τ_{ff}) and the net stress (σ_{netf}) at failure plane of unsaturated soil were calculated from the maximum shear stress (τ_{max}) as shown in Eq.(2) and Eq.(3), respectively. Then the cohesion intercepted (c") was determined from Eq.(4). And a ϕ^b angle was determined from Eq.(5).

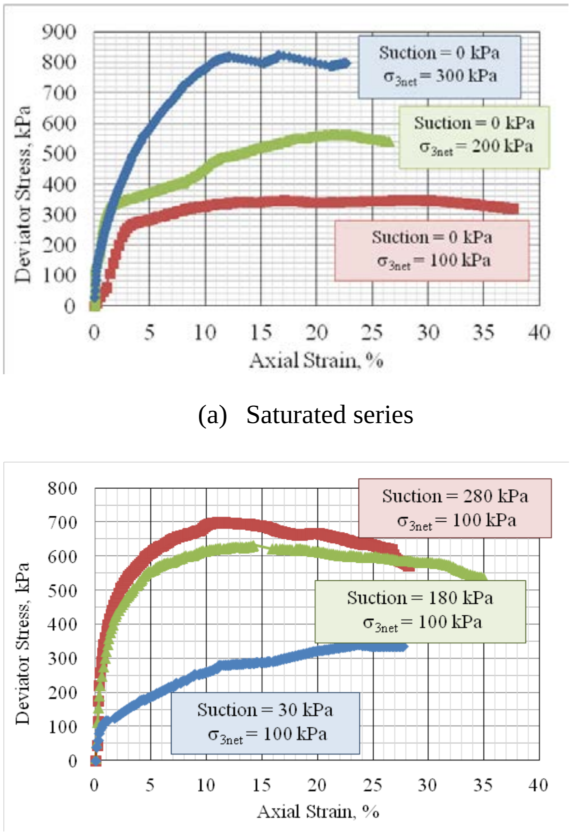

(a) Saturated series

(b) Unsaturated series

Fig. 6 The relationship between stress and strain of compacted Khon Kaen loess

Table 2 A saturated sample result

σ_3 (kPa)	u_a (kPa)	u_{wf} (kPa)	σ_d (kPa)	τ_{max} (kPa)
120	20	20	350	174
220	20	20	565	282
320	20	20	799	399

$$\tau_{ff} = \tau_{max}.\cos\phi' \quad (2)$$

$$\sigma_{netf} = \frac{(\sigma_{1netf} + \sigma_{3netf})}{2} - \tau_{max}.\sin\phi' \quad (3)$$

$$c'' = \tau_{ff} - \sigma_{netf}.\tan\phi' \quad (4)$$

$$\phi^b = \tan^{-1}\left[\frac{c'' - c'}{(u_a - u_w)_f}\right] \quad (5)$$

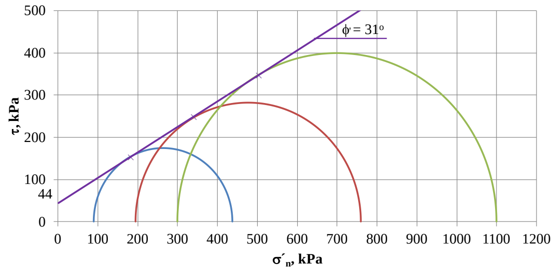

Fig.7 The Mohr's circle of compacted Khon Kaen loess at saturated condition

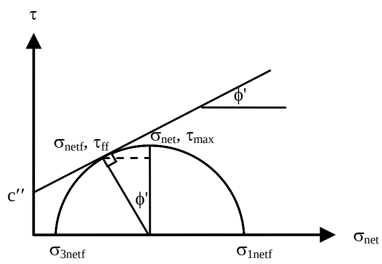

Fig.8 The interpretation of unsaturated drained shear strength

The test results of unsaturated sample were present in Table 3. The plot between drained shear strength and matric suction was illustrated in Fig.9. Figure 9 showed that the drained shear strength of this study was investigated at saturated, transition and residual regime. In addition, Fig.9 presented a non-linear relationship between cohesion intercept and matric suction. Table 3 showed that ϕ^b was slightly lower than ϕ'. Moreover, ϕ^b was constant at 30.5 degree for the matric suction range between 0 and 180 (ϕ^b was constant before residual regime). Then matric suction was higher than 180 kPa, a ϕ^b angle value was dropped from 30.5 to 28 (ϕ^b was decreased after the transition regime).

Moreover, the relationship between the total volumetric strain and axial strain showed the dilation behavior of both saturated and unsaturated series as illustrated in Fig.10 and Fig.11, respectively. The dilation behavior is the characteristic of dense soil.

The relationship between the water volume change and axial strain of unsaturated sample as present in Fig.12 showed that water was suction into a specimen.

Table 3 An unsaturated sample results

σ_3 (kPa)	u_a (kPa)	u_{wf} (kPa)	σ_d (kPa)	τ_{max} (kPa)	τ_{ff} (kPa)	σ_{netf} (kPa)	c'' (kPa)	ϕ^b (°)
150	50	20	437	219	187	206	63	30.5
300	200	20	759	379	325	283	154	30.5
400	300	20	896	448	383	317	193	28.0

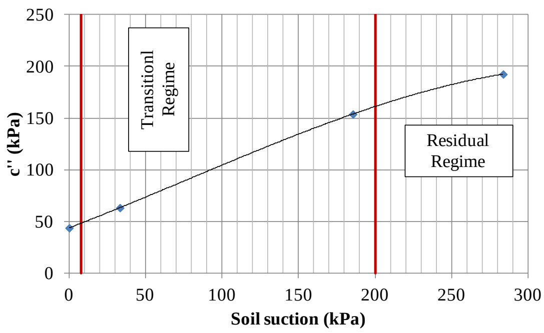

Fig. 9 The relationship between drained shear strength and matric suction

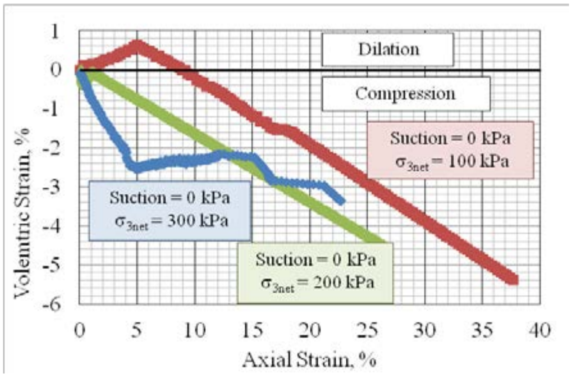

Fig. 10 The relationship between the total volumetric strain and axial strain of saturated sample

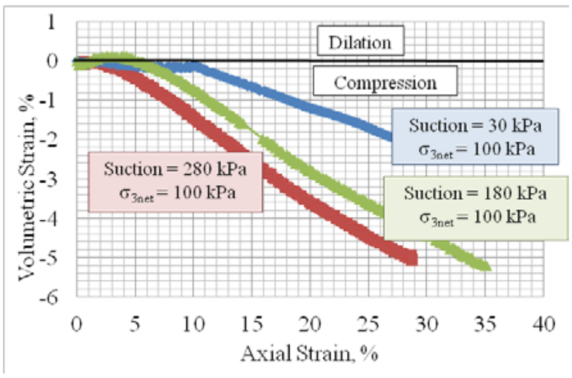

Fig.11 The relationship between the total volumetric strain and axial strain of unsaturated sample

CONCLUSIONS

The soil sample in this study was Khon Kaen loess, which was classified as silty sand. This study found that the SWCC of compacted Khon Kaen loess was a bimodal curve. The cause of bimodal curve might be the specimen was compacted at the dry side. The first and second air entry value is 8 and 5,000 kPa, respectively. Moreover the first and second residual volumetric moisture content is 10 and 2 %, respectively. The stress-strain behavior of compacted Khon Kaen loess for both saturated and unsaturated series showed a strain hardening. In addition the relationship between the volumetric strain and axial strain of both saturated and unsaturated series showed the dilation behavior. The consolidated drained triaxial test of saturated compacted Khon Kaen loess presented the effective angle and cohesion of 31 degree and 44 kPa, respectively. The unsaturated drained shear strength was determined by assumed a constant friction angle (ϕ'). ϕ^b was constant before residual regime. After the transition regime, ϕ^b was decreased.

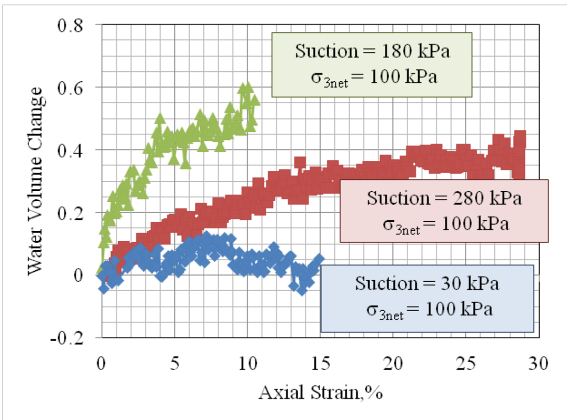

Fig.12 The relationship between the water volume change and axial strain of unsaturated sample

ACKNOWLEDGEMENTS

Acknowledgement is given to Faculty of Engineering, Khon Kaen University for the support of this re-search. Sincere thanks are extended to Dr. Ketsuda Dejbhimon and Mrs Pornpis Chuson, for the favor of using instruments in this study.

REFERENCES

[1] Fredlund, D.G. and Rahardjo, H. Soil Mechanics for Unsaturated Soils. Wiley. New York. 1993

[2] Huat, Bujang BK, Faisal Hj Ali, Affendi Abdullah, Saravanan Mariappan, and Soenita Hashim. Shear Strength Parameters of Unsaturated Residual Soils. Jurnal Kejuruteraan 17. 2005

[3] Rahardjo, H., Ong, B.H. and Leong, E.C. Shear Strength of Compacted Residual Soil From Consolidated Drained and Constant Water Content Traxail Test. Canadian Geotechnical Journal, 41: 421-436. 2004

[4] ASTM - American Society for Testing Material. Standard Test Method for Laboratory Compaction Characteristics of Soil using Standard Effort (12,400 ft-lbf/ft3 (600 kN-m/m^3)) (ASTM D698-00a). Ann Arbor. Michigan. 2000

[5] ASTM - American Society for Testing Material. Standard Test Method for Capillary-Moisture Relationships for Coarse- And Medium-Textured Soils By Porous-Plate Apparatus (ASTM D2325-98). Ann Arbor. Michigan. 1998

[6] Gitirana Jr., Gilson de F.N. and Fredlund, D.G. Soil –Water Characteristic Curve Equation with Independent Properties. Journal of Geotechnical and Geoenvironmental Engineering. 2004.Vol. 130. No.2. pp.209-211

A CASE STUDY ON SOIL IMPROVEMENT FOR REFORMING THE BED OF A CYLINDRICAL STORAGE TANK USING MICROPILES.

Mohammad reza Atrchian[1], Ali NisariTabrizi[1]

[1]Department of Geotechnic Engineering, Faculty of civil engineering, Islamic Azad University, Zanjan, Iran.

ABSTRACT

Problem statement: Unsymmetrical immediate settlement is one of the defects from storage tanks located in the bed composed of different subsurface soil. In this study, the tank was established in the bed of marl layers and coral limestone layers with many holes. Moreover, gaps in the boundary both kinds of layers (marl layers and limestone coral layers) have also been observed. These gaps could lead to increase in the contingency of an unsymmetrical immediate settlement following loading of the tank. The aim of this study is to select a suitable method of soil improvement for reforming the bed of a cylindrical storage tank. **Approach/methodology:** There was a limitation on development of the options as the tank structure had already been established. Therefore, the most appropriate of remedial option, micropile along with injection under the pressurewas detected. **Results:** The process of micropile along with injection under pressure leds to reduction of the soil settlement, as loads were appropriately distributed to ground. In addition, with filling holes, without appearance of the unsymmetrical immediate settlement, loads were transferred to the lower layers. **Conclusions:** Clearly, with the performance of micropiles along with injection under pressure have also been improved the soil characteristics.

Keywords: *Soil improvement, Unsymmetrical immediate settlement, Micropiles*

INTRODUCTION

There are generally two methods in front of the geotechnical engineer for dealing with problematic soils such as loose soils with low bearing capacity, soils with high consolidation capacity, liquefaction potential, and loose fills:

1- Utilization of load bearing elements in soil
2- Soil improvement and modification of the physical-mechanical properties of the soil mass[1], [2].

In this regard, one of the methods of soil improvement is by using micropiles [3]. Micropiles are used to improve the properties of the soil and reinforcement of the ground beneath a foundation [4]. In the current study, the soil underneath the site in the vicinity of a tank, mainly consisting of coral limestone with a lot of pores on a bed of Marl is being investigated. The site had to be leveledin order to build the tank, and some parts of the ground had to be filled and excavated subsequently. The studied tank is located between the excavated and filled ground parts. According to inspections and site investigations, existence of large voids, and lots of pores is evident in the coral limestone layer. Furthermore, some openings have been detected in the boundary between the Marl and coral limestone layers. Due to the existence of these openings, there is a high probability of primary consolidation after the tank being loaded.

The proper method of soil improvement for the location of the tank has to be selected according to special conditions of the site. In the situation when the tank had not been built, there were more options for the soil improvement plan. There will be fewer options now that the tank has been built and the structure is located on the specified area.

There are two important issues which have to be solved by the proper improvement method design:

1- Filling the pores present in the coral limestone layer and in the boundary between the coral limestone and Marl.
2- Proper load transference to the lower layers of the ground.

According to the soil model underneath the tank (with the assumption of the pores being filled), and the results of the analysis of the soil under the tank using PLAXIS software, primary consolidations were found to be greater than the allowed value.

As seen by the results, an appropriate method has to be used to reduce the sum of primary consolidation and secondary compression in the soil beneath the foundation of the tank.

In the current study, the selected solution for the two mentioned issues is by using micropiles along with grouting.

METHOD AND MATERIAL

Construction Method

As specified by the existing reports and the state of the tank due its location in the boundary region of excavated and filled zones, there is a probability of non-uniform consolidation underneath. Furthermore, the pores which are distributed in an unspecific manner have to be filled with the proper materials. According to the suggested improvement plan which consists of implementing micropiles with appropriate grouting, PLAXIS 8.2 for two dimensional modeling has been used to simulate the soil under the tanks and the micropiles with grouting (Fig. 1). Mechanical properties of the soil from the boreholes of the site have been used to model the soil under the tank. It has to be noted that the properties of the improved coral limestone are used in the modeling process; and also the micropilesare located at angles of 45, 70, and 85 degrees to the horizon around the tank.

Properties of the modeled soil layers and the grout surrounding the micropile are given in Figure 2. Sum of the primary and secondary consolidation under the tank is equal to 20.4 centimeters based on the results from the program calculations. Additionally, the sum of the acceptable minimum primary and secondary consolidation, which can occur under the tank in, is 9.5 centimetersfor the filled area, and 6 centimeters for the excavated area subsequently.

Drilling the micropiles

In consistence with the design plan, 345 micropiles were drilled in the vicinity of the tank. The amount of drilling operations for the execution of the micropiles is listed in table 1.

Table 1
Amount of drilling operations of the micropiles

Angel of micro piles to the horizontal (Degree)	Number	Length (M)	Sectional area (M^2)	Volume (M^3)
45	115	23	0.07	185
70	115	20	0.07	161
85	115	20	0.07	161
	Sum total (M^3)			~510

Grouting

Existing pores in the limestone layer and also the drilled boreholes have to be filled with proper material based on the soil improvement design plan. Information obtained from the drilled boreholes have been used to calculate the volume of grouting material, which might be subject to some variations (due to undetermined state of soil and rock layers under the tank). A summary of the calculations is given in Table 2.

Table 2

Tank area (M^2)	Thickness of rock layer (M)	Porosity (%)	Pores volume (M^3)	Injection volume of micropiles (M^3)
4663	2	25.4	2368	*500
4663	8	20	14921	
Sum total (M^3)			~18000	

Volume of the grouting operations for tank.
*- Volume of the grouting has been calculated with the reduction of the area of the bar and casing (if used any) taken into account.

Weight of the bars

No. 32 bars have been used for the micropiles. Weight of the bar and the casing used for micropile construction of the tanks is given in Table 3.

Table 3

Angel of micro piles to the horizontal (Degree)	Length of the bar (M)	Number	Weight of the bar (Kg)
45	23	115	16642
70	20	115	14523
85	20	115	14523
Sum total (Kg)			~ 46000

An estimate of the bars used for the micropiles

Micropile construction briefing

The following steps have been taken for the construction of the micropiles:

- Preparation of the tools and utilities for the construction of the micropiles including boring and grouting machines.
- Installation of the central grout mixing station.
- Drilling the boreholes according to technical specifications.
- Installation of permanent steel casing and No. 32 bar in the micropile
- Installation of spacers inside the casing for grouting the micropiles.

- Preparation of the grout mixture (water to cement ratio of around 0.35 to 0.6)
- Grouting with maximum pressure of up to 5 atmospheres (0.5 KPa) of the micropiles.

RESULTS

After performing the soil improvement plan under the tank, excavated and filled zones were locked together and all the existing pores have been filled either with a mix of cement and stone dust mortar or a mix of cement and soft sand. Micropiles of 300 millimeters in diameter, 23 meters in length, with 45 degrees to the horizon; and also some other with 70 and 85 degrees to the horizon and 20 meters long have been implemented under the tank with center to center distances of 3 meters. Spacing of the micropiles with 45, 70, and 85 degrees to the horizon is equal to 1 meter as indicated in Figure 3. Micropile spacing and angles have been determined based on the significance of mortar penetration in the vicinity of the tank, and also its penetration extent under the tank. The various degrees of micropiles cause the mortar to be distributed in a wider range.

It has to be noted that the length of the piles has been designed to penetrate into the strong Marl layer and transfer the load in a sufficient length. During the execution of these piles, grouting was done to fill the pores and continued until they were filled completely.

After the execution of the micropiles, hydrostatic test was performed according to segment 5-6-3-7 of API 650 guidelines, which showed an improvement in the settlement conditions based on the results from settlement analysis of primary and secondary consolidations,as well as the output from PLAXIS software (Fig. 4 and 5). Therefore, execution of the micropiles has caused the overload to be transferred to stronger lower layers of soil, limit the settlement, seismic improvement, reinforcement of foundation and the soil under the tank, and improvement of the area soil. Mechanical properties of the soil in the project site and around the micropiles have changed using the micropiles, and mechanical parameters such as compactness, load bearing capacity, permeability, and compressibility modulus of the soil have been improved.

DISCUSSION

Micropiles are used to improve the properties of the soil and reinforce the ground under a foundation [3]. Soil improvement is achieved by pushing a sufficient number of micropiles and the resulting effect is assumed to be the generation of strong composite materials. Micropiles have diameters less than 300 millimeters and their performance depends on the grouting method in the soil. There are multiple ways to construct a micropile but it always leads to inserting a bar or a tube with a few centimeters in diameter which is secured in the ground by means of grouting. Hence, construction method of micropiles is such as the regular piles [5]. The main forces which are generated in the micropiles are mainly compression and tension [6]. Due to small diameter of micropiles, small force on the tip of the micropile is assumed to be negligible and hence the interaction between the soil and micropile is most frictional [6].

Piles are categorized into two main groups:

1. Displacement piles: piles which are driven into the ground by means of vibration and pressing, which cause the surrounding soil to be displaced [6].
2. Replacement piles: these piles are inserted into pit holes previously dug, and replace the soil within the hole [7].

In the current study, micropiles are built using the second method (replacement method) by means of drilling the hole.

Load beating capacity of the micropiles are often dependent on the steel components with high load bearing capacity inside, which are capable of bearing most of the load.

Furthermore, in the current study, single micropiles or a group of micropiles were used which are loaded directly and the main part of the load is supported by the reinforcement and can be used as an alternative for regular piles for transferring the over load to lower layers of the soil.

Using micropiles has some advantages over using other soil improvement methods which are:

1- Using micropiles causes the least amount of disturbance for nearby structures, soil, and the environment.
2- Micropiles can be constructed in every type of soil, landfill, rock, ground conditions and areas with limited access.
3- Micropiles can be constructed with any angle in the soil.
4- The equipment used to for micropile construction is the same as the tools used for construction of tiebacks, soil nail walls, and grouting projects.

CONCLUSION

In the current study, due to the limitations in the soil improvement method imposed by existence of the tank, the best solution was recognized as utilization of micropiles with grouting.Construction of micropiles lead to the loads being transferred to the layer with a sufficient bearing capacity and hence, a reduction in settlement under the tank. Furthermore, pressurized grouting lead to the pores in the soil being properly filled which helped the load be transferred to the lower layers of the soil without creating any unacceptable primary consolidation. Additionally, Soil properties also improved with construction of the micropiles.

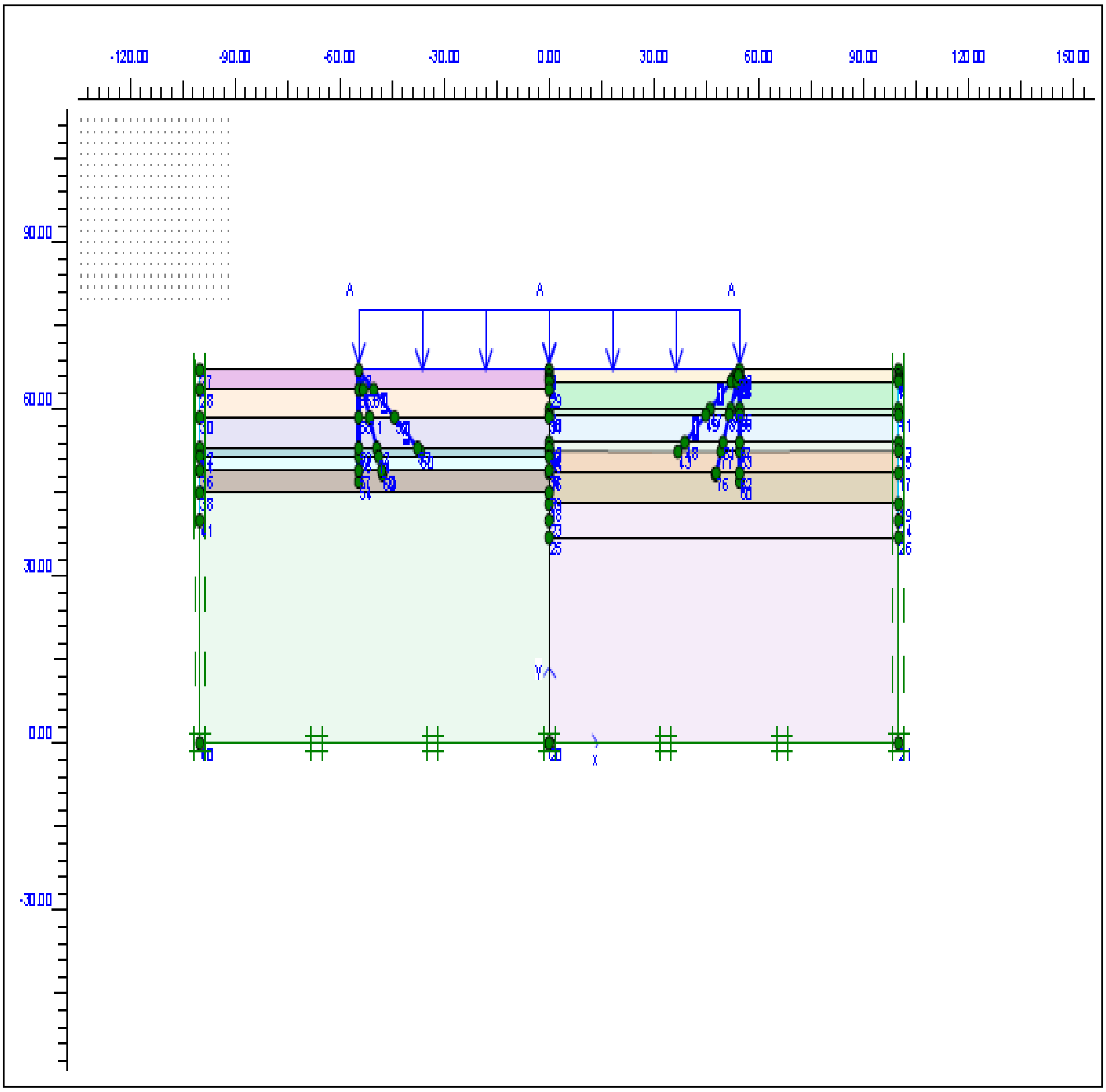

Fig.1. Simulation of the tank No.With PLAXIS

ID	Name	Type	γ_{unsat} [kN/m^3]	γ_{sat} [kN/m^3]	k_x [m/s]	k_y [m/s]	ν [-]	E_{ref} [kN/m^2]	c_{ref} [kN/m^2]	φ [°]	ψ [°]
1	rock	Drained	17.0	18.0	1.0000E-3	1.0000E-3	0.30	1.5E5	2.1E3	27.0	0.0
2	2	Drained	15.5	16.8	5.0000E-8	5.0000E-8	0.30	17500.0	145.0	20.0	0.0
3	3	Drained	16.9	18.2	1.0000E-3	1.0000E-3	0.30	55000.0	2.3	32.2	0.0
4	4	Drained	14.8	16.0	5.0000E-8	5.0000E-8	0.30	17500.0	5.0	22.0	0.0
5	5	Drained	15.5	17.0	1.0000E-5	1.0000E-5	0.30	50000.0	65.0	18.9	0.0
6	6	Drained	16.0	17.0	1.0000E-8	1.0000E-8	0.30	60000.0	24.9	11.7	0.0
7	7	Drained	15.0	16.0	1.0000E-8	1.0000E-8	0.30	60000.0	27.0	0.0	0.0
8	8	Undrained	17.1	18.4	1.0000E-8	1.0000E-8	0.30	65000.0	166.0	0.0	0.0
9	9	Undrained	15.1	16.4	1.0000E-8	1.0000E-8	0.30	60000.0	28.0	0.0	0.0
10	space	Drained	1.0	11.0	0.1000	0.1000	0.00	100.0	1.0	5.0	0.0
11	a	Drained	17.0	18.0	1.0000E-3	1.0000E-3	0.30	55000.0	0.1	36.0	0.0
12	b	Drained	18.0	19.0	1.0000E-3	1.0000E-3	0.30	1.75E5	22.8	36.9	0.0
13	c	Drained	14.5	15.6	5.0000E-8	5.0000E-8	0.30	17500.0	31.5	19.3	0.0
14	d	Drained	16.8	17.9	1.0000E-4	1.0000E-4	0.30	40000.0	68.0	20.0	0.0
15	e	Drained	15.0	16.4	5.0000E-8	5.0000E-8	0.30	1.75E5	60.0	15.0	0.0
16	f	Drained	16.0	18.0	1.0000E-8	1.0000E-8	0.30	60000.0	65.0	0.0	0.0
17	g	Undrained	16.0	18.0	1.0000E-8	1.0000E-8	0.30	60000.0	65.0	0.0	0.0
18	aa	Drained	19.5	20.5	1.0000E-3	1.0000E-3	0.30	4E5	200.0	42.0	0.0
19	bb	Drained	20.5	21.5	1.0000E-3	1.0000E-3	0.30	5.25E5	223.0	42.0	0.0
20	cc	Drained	17.0	18.1	5.0000E-8	5.0000E-8	0.30	52500.0	232.0	22.3	0.0
21	rockrock	Drained	19.5	20.5	1.0000E-3	1.0000E-3	0.30	5.5E5	2.3E3	42.0	0.0
22	22	Drained	18.0	19.2	5.0000E-8	5.0000E-8	0.30	52500.0	345.0	23.0	0.0
23	33	Drained	19.4	20.7	1.0000E-3	1.0000E-3	0.30	4E5	202.0	42.0	0.0
24	44	Drained	17.4	18.5	5.0000E-8	5.0000E-8	0.30	50250.0	205.0	25.0	0.0

Fig. 2. Properties of the soil used in the modeling with PLAXIS

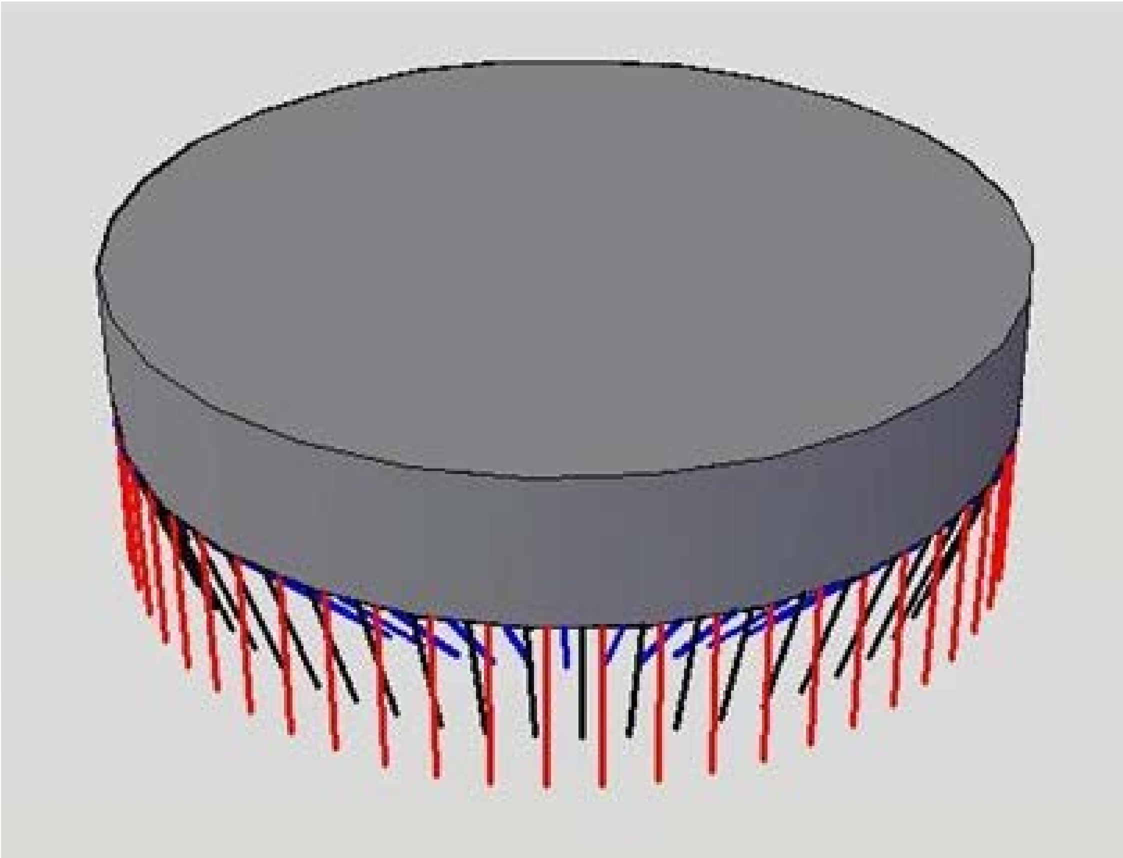

Fig. 3. Three dimensional view of the micropile execution under the tank.

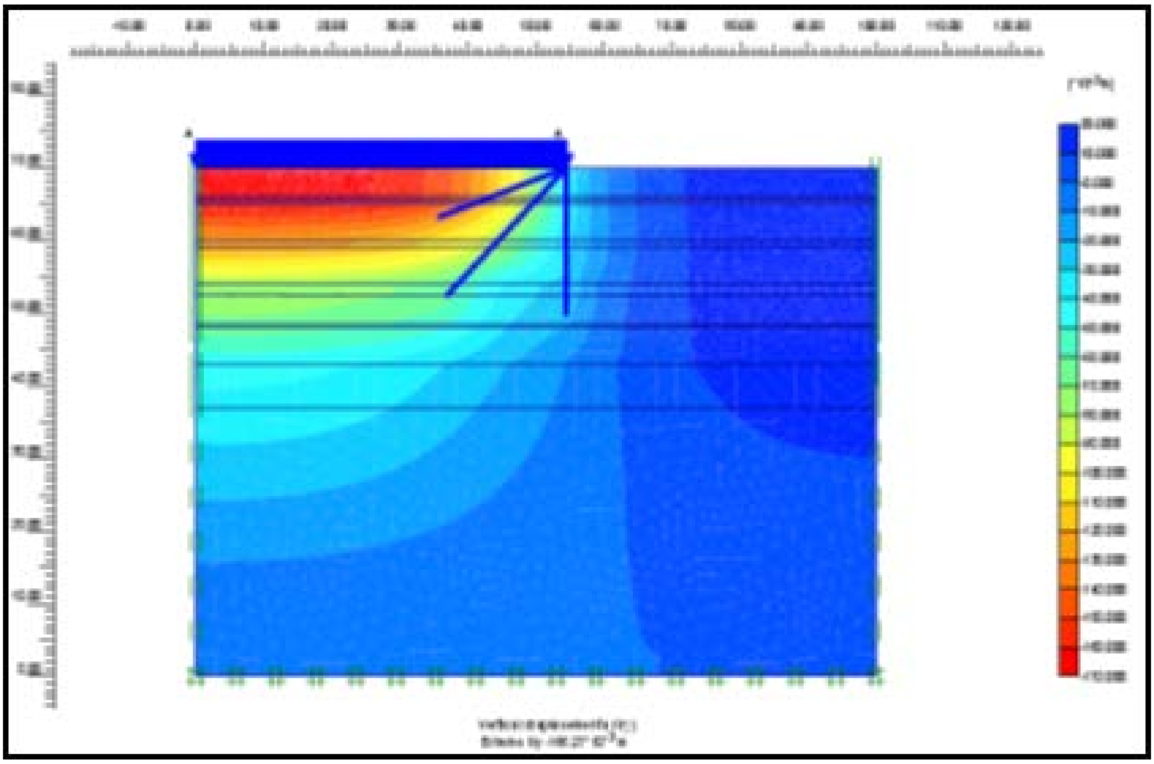

Fig. 4. Primary consolidation under the tank with micropiles

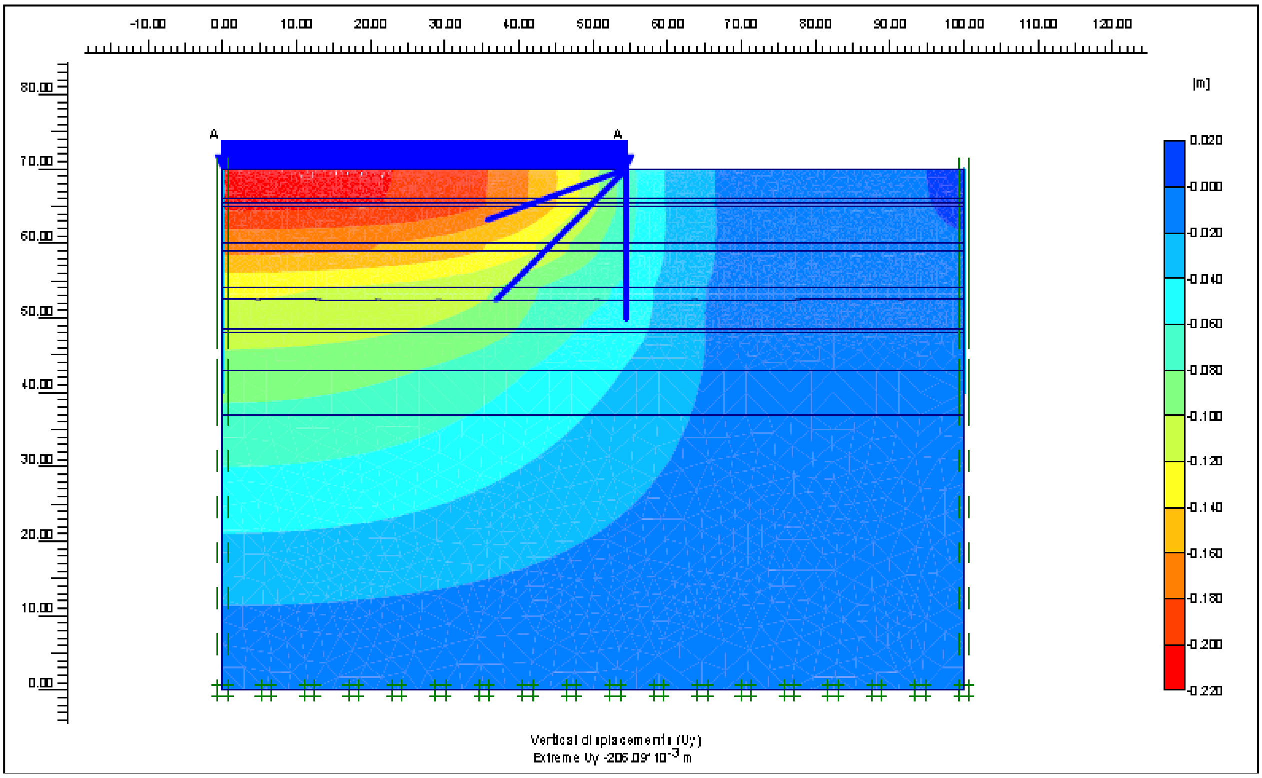

Fig.5. Secondary consolidation under the tank with micropiles

REFERENCES

[1] Horn R, Taubner H, Wuttke M, Baumgartl T. Soil physical properties related to soil structure. Soil and Tillage Research.30. 1994, pp.187-216.

[2] Meyerhof GG. Some recent research on the bearing capacity of foundations. Canadian Geotechnical Journal.1. 1963, pp.16-26.

[3] Babu SG, Murthy SB, Murthy D, Nataraj M. Bearing capacity improvement using micropiles a case study. American Society of Civil Engineers. proceedings of sessions of the geosupport conference 2004, pp.1-8

[4] Alnuaim A, El Naggar M, El Naggar H. Performance of micropiled raft in clay subjected to vertical concentrated load: centrifuge modeling. Canadian Geotechnical Journal. 52. 2015, pp.2017-2029.

[5] Juran I, Bruce D, Dimillio A, Benslimane A. Micropiles: the state of practice. Part II: design of single micropiles and groups and networks of micropiles. Proceedings of the Institution of Civil Engineers-Ground Improvement. 3. 1999, pp.89-110.

[6] Han J, Ye S-L. A field study on the behavior of micropiles in clay under compression or tension. Canadian Geotechnical Journal.43. 2006, pp.19-29.

[7] Nogami T, Novák M. Soil pile interaction in vertical vibration. Earthquake Engineering & Structural Dynamics. 4. 1976; pp.277-293.

BEHAVIOR OF STEEL NAILS-REINFORCED STONE COLUMN MADE OF MIXTURE OF TYRE CHIPS AND STONE AGGREGATES

Tanwee Mazumder[1], Nishant Neeraj[2] and Ramanathan Ayothiraman[3]
[1]Ph.D. Scholar, [2]Former M.Tech Student, [3]Associate Professor, Dept. of Civil Engg, IIT Delhi, New Delhi, India

ABSTRACT

Scrap tyre generated from passenger cars, light and heavy trucks, heavy equipment, aircraft, and off–road vehicles have many good engineering properties and hence has been effectively utilized for civil engineering applications such as lightweight material for backfill of retaining structures, drainage layer and thermal insulation layer etc. Typically stone aggregates of size 15 mm to 75 mm are used in the construction of stone column. A few studies reported use of spent ballast and construction debris as a substitute to stone aggregates in stone columns. In the present study an attempt has been made to investigate the behavior of stone columns reinforced with vertical steel nails and constructed with mixture of stone aggregates and shredded tyre chips through a series of small scale model experiments. Model stone column of diameter (*d*) 100 mm and *l/d* ratio of 4.5 is used to simulate floating stone column. The stone columns were reinforced with vertical steel rods to the entire length of column. Loading is applied through a hydraulic jack and reaction loading frame. Different mix proportions of stone aggregates and tyre chips: 100S, 70S+30T, 50S+50T, 30S+70T and 100T were used in model testing. Results of model tests indicates that the conventional columns can be replaced by columns made up entirely of shredded tyre chips when reinforced with vertical rods as encasement along the column circumference.

Key Words: Tyre Chips; Stone Column; Encasement; Soft clay.

INTRODUCTION

Soft soil necessitates improvement of the ground so that the ground can be used beneficially for various projects that serve to mankind. Thus, to render it useful for various construction or such other purposes, soft soil needs to be stabilized/reinforced so that it can bear the loads coming from superstructure. Ground improvement by the installation of stone columns have been a widely accepted technique as it results in reduced settlements and accelerates the rate of consolidation settlement [1]. Various studies have been carried out on the mechanism of failure of stone columns and the load settlement behavior as well as on the design of ordinary and encased stone columns [2-17].

Also the disposal of scrap tyres produced in huge quantities every year across the globe poses huge environmental threat. The amount of scrap tyres produced every year is also increasing at an alarming rate. Thus, this study looks into the viability of using scrap tyres as an alternative to stone aggregates in stone columns. It is seen in the literature that apart from the stone aggregates used in conventional stone columns, various other recycled materials like spent railway track ballast and crushed concrete debris are being used as aggregates in stone columns [18]. Tyre chips can be beneficially used in geotechnical applications due to its advantageous properties (low density, hydrophobic nature, durability, resilience and high frictional strength) [19]. However, limited studies on the application of shredded tyre shreds as aggregates in ordinary stone columns have been carried out [20-21]. Therefore, in this study vertical steel nails are used to encase the columns made of different mix proportions of shredded tyre chips and stone aggregates through model tests.

MATERIALS USED

The various materials used in the model experiments and their properties and characteristics are presented below.

Soil

The clay bed in the model experiments was constructed of Kaolinite clay. Kaolinite clay is shown in fig. 1. The properties of clay is given in Table 1.

Fig. 1. Kaolinite clay

Table 1 Properties of Kaolinite Clay

Property	Value
Liquid limit	45%
Plastic Limit	23%
% Clay	62%
% Silt	38%
Optimum moisture content	21%
Maximum dry density	1620 kg/m^3
Shear strength at w = 38%	7.5 kPa

Stone aggregates and shredded tyre chips

Stone aggregates and shredded tyre chips passing thorough 12.5 mm sieve and retained on 10 mm sieve was taken to construct stone column in the test tank. Laboratory tests were conducted to determine the various index and engineering properties of the stone aggregates and tyre chips. Stone aggregate and shredded tyre chips are shown in figs. 2 and 3 respectively. The properties are listed in Table 2.

Table-2. Properties of Tyre Chips and Stone Aggregates

Property	Tyre Chips	Stone Aggregates
Average Size	10 mm	10 mm
Specific Gravity	1.10	2.78
Maximum Density (kg/m^3)	575	1608
Minimum Density (kg/m^3)	527	1367

Fig. 2. Stone aggregates

Fig. 3. Shredded tyre chips

Encasement/Reinforcement

Vertical rods, having 8 mm diameter were provided around the circumference of the stone column to encase the stone column constructed at the centre of the clay bed. The typical view of nail-reinforced column in both plan and section is shown in fig. 4. The image of nails used is shown in fig. 5.

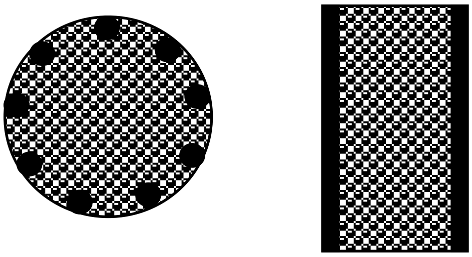

Fig. 4. Top view and cross-sectional view of nail-reinforced column

Fig. 5. Vertical steel nails

Test Setup

A cylindrical tank of wall thickness 10 mm having a diameter 550 mm and height 750 mm was taken to conduct model experiments. For the stone columns, a scaling of 4 to 10 has been adopted as the column diameter in the field varies between 400 to 1000 mm. As for the steel rods a scaling factor of 4 is assumed, that is the 8 mm diameter used in the model tests can be replaced by 32 mm rods in the field. Also it is difficult to ensure complete vertical installation of steel rods of small diameters like 8 mm over great depths. Hence bigger size diameter steel rods e.g. 32 mm rods can be installed to greater depths. The loading arrangement involves loading through a reaction loading frame.

In this study, tests were performed on 100 mm diameter columns having *l/d* ratio of 4.5. Replacement method was employed to construct the stone column at the center of the clay bed. A sand blanket of 30 mm thickness was placed over the equivalent circular loading area (2 times the diameter of the stone column) to facilitate better stress transfer. Above the sand blanket, a loading cap having a diameter of 200 mm and 15mm thickness was kept to apply the load centrally and uniformly. The load was applied through a hydraulic jack and a reaction frame. These arrangements are shown in fig. 6.

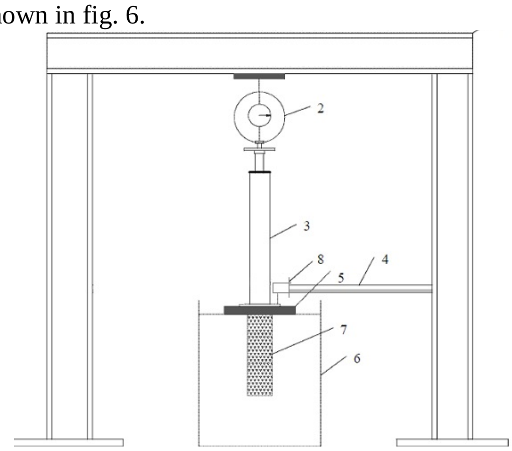

1-Loading frame, 2-Proving Ring, 3-Hydraulic jack, 4-Reference frame for fixing the Dial gauge, 5-Sand Mat, 6-Cylindrical test tank with clay bed, 7-Stone column, 8-Dial gauge.

Fig. 6. Test setup.

Clay bed preparation

The soft clay bed was made of remoulded soft Kaolinite clay. The water content was maintained at 38 % to obtain very soft clay bed (c = 7 kPa) of shear strength 7.5 kPa. Clay was uniformly mixed with water until no lumps were present. The test tank was filled in layers with the paste and each layer was compacted by hand kneading. The finished clay bed was covered with wet clothes and left for 24 hours. The moisture content readings and shear strength were taken at every 100 mm depth of clay layer. The typical variation of moisture and shear strength over the depth of clay bed for 100T column is illustrated in figs. 7 and 8 respectively. It is seen from figs. 7 and 8 that the water content and shear strength are uniform throughout the depth of tank, thus ensuring homogeneity of clay bed.

Stone column construction

The stone column was constructed by replacement method. The centre of the cylindrical tank was properly marked. Silicon grease was applied on the inner and outer surface of a thin open-ended seamless Perspex cylindrical pipe of outer diameter 100 mm the pipe was pushed into the centre of the clay bed upto a depth of 450 mm. Iron rods of diameter 8 mm were then pushed into the clay bed along the circumference of the perpex pipe to install these rods vertically. A clear spacing of 27 mm was maintained between the consecutive rods. The clay was scooped out in stages using a helical auger. Tyre chips/stone aggregates were charged into the hole in layers of 50 mm and each layer was given light uniform compaction. Casing pipe was raised in stages ensuring minimum 10 - 20 mm penetration below the tyre chip/aggregates placed.

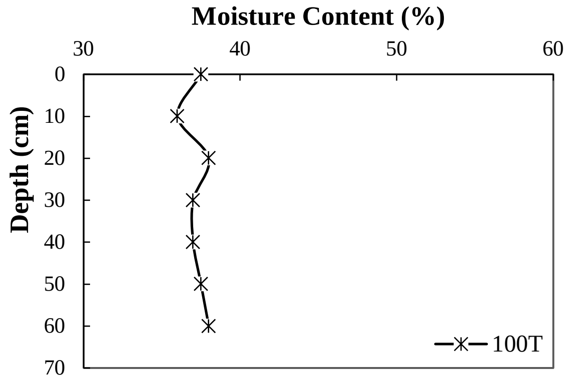

Fig. 7. Variation of moisture content with depth of clay bed

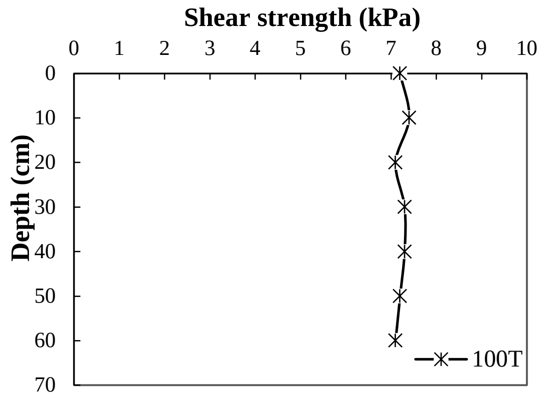

Fig. 8. Variation of shear strength with depth of clay bed.

Loading of stone column

A sand mat is placed over the column and it is topped with a loading cap of 15 mm thickness and 200 mm diameter. The load was applied through a hydraulic jack and pump system supported by a reaction loading frame. The settlements were recorded by a dial gauge. Load settlement and time settlement curves were plotted for analyzing the behavior of model the stone columns. The complete arrangement is already shown in above Fig. 6.

DISCUSSION OF RESULTS

The model tests were performed on vertical mild steel nails-reinforced stone column made of different mix proportions of stone aggregates and shredded tyre chips to study the time dependent load settlement behavior. Similar load tests were also carried on pure unreinforced clay bed and clay bed without stone columns but provided with steel nails circumferentially over a circular area located centrally over the clay bed and having a diameter of 100 mm. The typical measured time-settlement response for 100S, 50S+50T and 100T are shown in figs. 9-11. Figures 9 - 11 demonstrate that the settlement for each load increment is found to stabilize at around 70 to 100 mins, for various mix proportions of stone aggregate and shredded tyre chips.

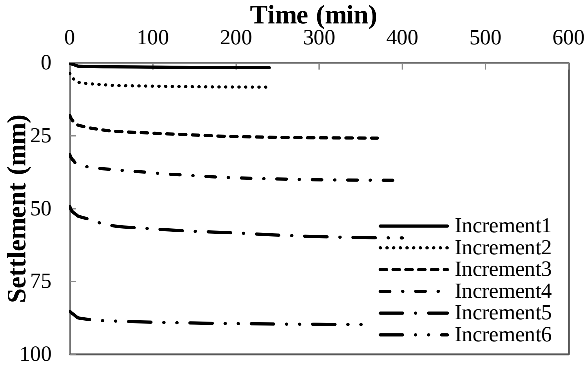

Fig. 9. Time-Settlement response of 100S column

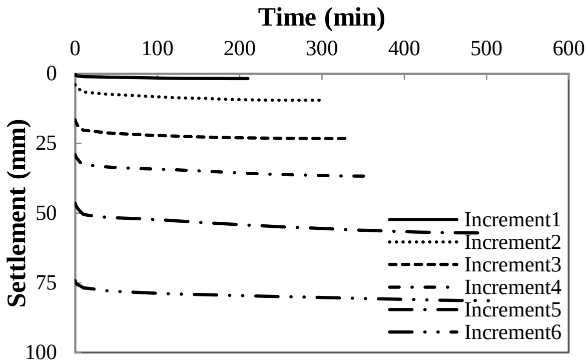

Fig. 10. Time-Settlement response of 50S+50T column

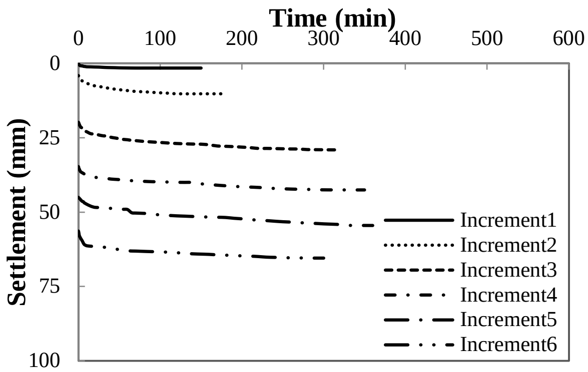

Fig. 11. Time-Settlement response of 100T column

The load-settlement curve for 100S, 50S+50T and 100T is shown in fig. 12. It is seen from the figure that the columns made of 100S and 50S+50T undergo lesser settlement, while 100T column undergo higher settlement for the same load. This indicates that as the percentage of tyre chips increases, the columns settle relatively high. Nevertheless, the load carried by the stone columns is always higher than the load carried by only clay bed and clay bed reinforced with nails only.

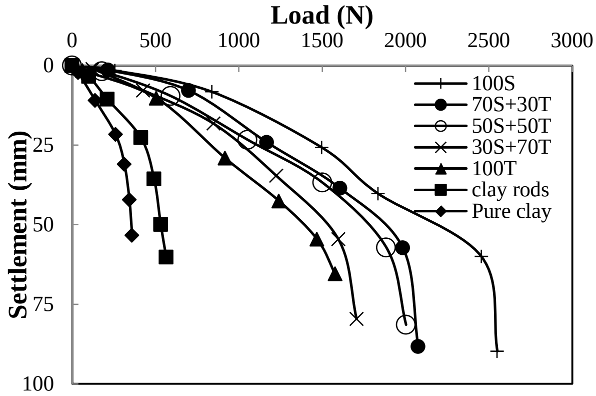

Fig. 12. Comparative study of load-settlement behavior of different stone columns.

The load carrying capacity of stone columns are taken by double tangent method for stone columns made of various mix proportions as well as that of clay bed with iron rods and pure clay beds, and the values are presented in Table 3.

Table 3 Ultimate load carrying capacity of various stone column.

Stone column type	Experimental capacity (N)
100S	2471
70S+30T	1952
50S+50T	1750
30S+70T	1492
100T	1208
Clay bed with iron rods	413
Pure clay bed	313

From Table 3 it can be seen that encasing the column with vertical nails cause a significant rise in the ultimate load carrying capacity for each of the mix proportion. The load carrying capacity of ordinary stone column made of 100S and 100T is theoretically calculated using IS code method (IS: 15284, 2003) and the values are 1137 N and 653 N respectively. It is seen that reinforced column made of all mix proportions exhibits higher capacity than ordinary column. Thus, reinforcing the stone columns increases the stiffness and reduces the severe lateral bulging significantly and hence enables the encased columns to exhibit higher load carrying capacities for same settlement. It can also be seen that iron rods increases the ultimate load capacities especially for 50S+50T (more than 50%) and more than 100 % for 100S. It is also noted from the Table 3 that clay bed reinforced with nail only has only marginal increase of load capacity (32 %) due to skin friction along the nails. But when these nails were used in stone columns, the load was initially taken by the aggregates in the column at low settlement, and at high settlement, the columns tend to bulge, which is confined by steel nails. This lateral confinement of nails lead to an increase of 85% for 100T and 117 % for 100S. This increase is much higher than 32 % increase observed in bed with nails only. Thus, it may confirm that the steel nails interact efficiently in stone column when it tend to bulge laterally. It is also seen from Table 3 that the capacity of steel rod-encased 100T column is 1208 N, which is higher than the theoretical capacity of ordinary stone column made of 100% stone aggregates (1137 N). This indicates that with steel nail-reinforcement, complete replacement of stone aggregates is possible with tyre chips.

For understanding the performance of stone columns made of different mix proportions and the effect of nail-reinforcement, a parameter: "Efficiency" is defined. Efficiency is defined as a factor: ratio of load carrying capacity of either OSC or ESC made of any mix proportion to the load carrying capacity of OSC made of 100S. The comparison plot of efficiency of the stone columns in the present study to that reported in literature is shown in fig. 13.

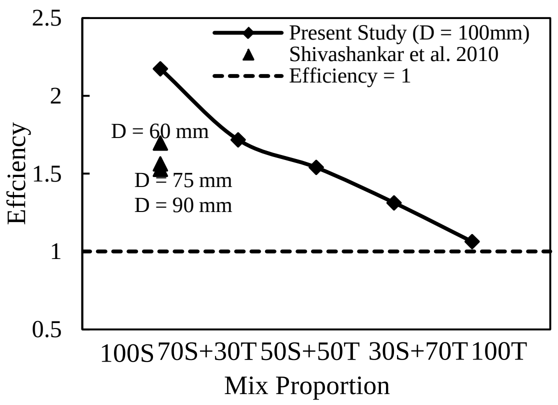

Fig. 13. Comparative study of efficiency of different stone columns.

The efficiency for conventional stone columns (100S) of different diameter reinforced with steel nails upto 3*d* (*d* = diameter of the stone column) conducted by Shivashankar et al. [15] is also calculated and compared with the present study. It is seen from fig. 13 that the efficiency of each of the column in the present study as well as obtained from literature is greater than 1.0. The efficiency for 100S stone columns measured from present study is higher than that was measured by Shivashankar et al. [15]. This may due to the fact that the model tests by these authors were conducted on smaller diameter columns and the diameter of nails were 2 mm, therefore the stiffness of nail-reinforced column might be lesser than that was used in the present study. IT is also seen from fig. 13 that columns reinforced with vertical steel nails exhibit efficiency greater than 1 even when the stone aggregates are completely replaced by tyre chips. Thus this ensures that complete replacement of stone aggregates with shredded tyre chips is possible when the columns are provided with vertical nails as encasement/reinforcement. However, there is an issue of corrosion of these steel nails, which require proper anti-corrosive treatment/protection when these nails are used in practice and it needs to be examined through field studies. Possible use of shredded tyre chips as backfill in retaining walls, vibration absorbers, drainage media in landfill leachate collection systems and as insulators beneath roads had been explored by Humphrey and his co-workers, thus it is evident that the shredded tyre chips has its applicability in wide range of civil engineering problems.

CONCLUSIONS

The results obtained from the model tests in the present study show that 100S column exhibits highest capacity. However, it is seen that complete replacement of the stone aggregates with shredded tyre chips is possible when the columns are provided with the steel rods as encasement over the entire depth of the column. This is due to the higher stiffness of the composite ground. The tensile strength of steel rods also plays an important role in significant increase in the overall stiffness. Corrosion of the steel nails used may be a concern, which needs to be taken care, when this technique is adopted in practice. The durability of the columns is a concern especially when the columns are exposed to saline water or marine and coastal water. In such cases, galvanized rods may replace the usual steel nails. However, field studies are essential to examine the durability of corrosion-treated nails and galvanized nails for confirming its field applications.

REFERENCES

[1] Murugesan, S., and K. Rajagopal, "Geosynthetic-encased stone columns: numerical evaluation", Geotextiles and Geomembranes, Volume 24, Issue 6, December 2006, pp. 349-358.

[2] Greenwood, D. A, "Mechanical improvement of soils below ground surface", Institution of Civil Engineers Proceedings, London/UK/, 1970, pp-1900.
[3] Hughes, J. M. and Withers, N. J, "Reinforcing of soft cohesive soils with stone columns", Ground Engineering, 1974, pp. 42-49.
[4] Bergado, D. T., Anderson, L. R., Miura, N. and Balasubramaniam, A. S,. "Soft ground improvement in lowland and other environments", ASCE, 1996.
[5] Alamgir, M., Miura, N., Poorooshasb, H.B. and Madhav, M.R, "Deformation analysis of soft ground reinforced by columnar inclusions", Computers and Geotechnics, Volume 18, Issue 4, 1996, pp. 267–290.
[6] IS: 15284 – 2003, "Design and construction for ground improvement—Guidelines. Part 1: Stone columns", Bureau of Indian Standards, New Delhi, India.
[7] McKelvey, D., V. Sivakumar, A. Bell, and J. Graham, "Civil Engineers Geotechnical Engineering", Volume 157, Issue GE3, July 2004.
[8] Ambily, A.P. and Gandhi, S.R, "Behavior of stone columns based on experimental and FEM analysis", Journal of Geotechnical and Geoenvironmental Engineering, ASCE, Volume 133, Issue 4, 2007, pp. 405–415.
[9] Black, J.A., Sivakumar, V., Madhav, M. R. and Hamill, G. A, "Reinforced Stone Columns in Weak Deposits: Laboratory Model Study", Journal of Geotechnical and Geoenvironmental Engineering, ASCE, Volme 133, Issue 9, 207, pp. 1154-1161.
[10] Deb, K., Chandra, S. and Basudhar, P. K, "Response of multilayer geosynthetic-reinforced bed resting on soft soil with stone columns", Computers and Geotechnics, Volume 35, 2007, pp. 323-330.
[11] Malarvizhi, K. and Ilamparuthi, S. N, 2007. "Comparative study on the behavior of encased stone column and conventional stone column", Soils and Foundation, Japanese Geotechnical Society, Volume 47, Issue 5, 2007, pp. 873-885.
[12] Borges, J. L., Domingues, T. S. and Cardoso, A. S, "Embankments on Soft Soil Reinforced with Stone Columns: Numerical Analysis and Proposal of a New Design Method", Geotechnical and Geological Engineering, Volume 27, 2009, pp. 667–679.
[13] Gniel, J. and Bouazza, A, "Improvement of soft soils using geogrid encased stone columns", Geotextiles and Geomembranes, Volume 27, 2009, pp. 167-175.
[14] Murugesan, S. and Rajagopal, K, "Studies on the behavior of single and group of geosynthetic encased stone columns", Journal of Geotechnical and Geoenvironmental Engineering, Volume 136, Issue 1, 2010, pp. 129-139.
[15] Shivashankar, R., Babu, M. D., Nayak, S. and Manjunath, R, "Stone columns with vertical circumferential nails: Laboratory model study", Geotechnical and Geological Engineering, Volume 28, Issue 5, 2010, pp. 695-706.
[16] Shahu, J. T. and Reddy, Y. R, "Clayey Soil Reinforced with Stone Column Group: Model Tests and Analyses", Journal of Geotechnical and Geoenvironmental Engineering, ASCE, Volume 137, Issue 12, 2011, 1265-1274.
[17] Hanna, A.M., Etezad, M. and Ayadat, T, "Mode of Failure of a Group of Stone Columns in Soft Soil", International Journal of Geomechanics, ASCE, Volume 13, Issue 1, 2013, pp. 87-96.
[18] Serridge, C. J, "Achieving sustainability in vibro stone column techniques", Proceedings of the Institution of Civil Engineers-Engineering Sustainability, Volume 158, Issue 4, Thomas Telford Ltd, 2005, pp. 211-222.
[19] Humphrey, Dana N., Thomas C. Sandford, Michelle M. Cribbs, and William P. Manion, "Shear strength and compressibility of tire chips for use as retaining wall backfill", Transportation Research Record, Volume 1422, 1993.
[20] Ayothiraman, R., Soumya, S, "Model tests on the use of tyre chips as aggregate in stone columns", Ground Improvement, Proceedings of ICE, UK, DOI: 10.1680/grim.13.00006, 2014
[21] Ayothiraman, R., Rolaniya, A. K. and Mazumder, T, "Load-settlement behaviour of encased stone columns made of waste tyre chips", proceedings of 6th International Geotechnical Symposium on Disaster Mitigation in Special Geoenvironmental Conditions, January 21-23, 2015, IIT Madras, Chennai, India, pp. 241-244.

INCREASE OF EFFICIENCY OF CONSOLIDATION OF WEAK WATER-SATURATED SOIL VERTICAL SANDY DRAINS AND DINAMIC LOADINGS

Usmanov R. A., Dr. Sci. Tech., prof., vice-president of Geotechnical society of Tajikistan,

Dushanbe, Republic of Tajikistan

ABSTRACT

Results of field pilot studies on consolidation of weak water-saturated loessial soil of Central Asian regions by vertical sandy drains are given in article. In the first part efficiency of application of this method is proved in soil conditions of the Republic of Tajikistan. In the second part features of carrying out experimental works in field conditions, a technique of the appendix of static loadings and imitation of seismic influences are considered. In the third part results of researches, changes of strength and deformation characteristics of the condensed soil are analysed. In the fourth part the corresponding conclusions by results of researches are drawn. At the end of article the bibliography is provided.

Keyword: Weak water-saturated loessial soil, Vertical sandy drains, Loading embankment weight, Static influences, Seismic and seismic-explosive influences, Consolidation.

INTRODUCTION

Experience of construction shows that at a considerable thickness of a weak water-saturated layer of earth (h > 10 m), fluidity indicator $I_L \geq 0.8$ and the module of deformation of soil E ≤ 5.0 MPa the method of consolidation of soil by vertical sandy drains from the subsequent loading condensed thickness the weight of an embankment or other materials from which payload is equal is widely used or exceeds loading from the projected construction.

In seismically active regions of the Republic of Tajikistan, as well as in some other the Central Asian countries, in connection with flooding of territories, platforms of construction can be often presented by big thicknesses of weak water-saturated loessial soil (h = 12-20 m), with very low values of physics and mechanicals characteristics ($I_L \geq 0.8$; $e \geq 0.8$; $R \leq 100$ KPa; $E \leq 5.0$ MPa). Design and ensuring operational reliability of buildings in the specified conditions is connected with application of various methods of preparation of the artificial bases (consolidation, fixing, replacement of weak soil, etc.) and the device of the deep foundations, including pile foundations. The existing experience shows that the method of consolidation of this soil vertical sandy drains and the loading territory [1]-[5] can be one of effective, and sometimes the only thing.

It should be noted what experience of design and materials of researches on consolidation of weak water-saturated loessial soil by this method in the conditions of the republic and other countries us isn't established. For studying of an opportunity and efficiency of application of this method in the conditions of the Republic of Tajikistan field (natural) pilot studies which purpose was research of features of their consolidation by sandy drains at static and dynamic (seismic) influences have been conducted.

TECHNIQUE OF TESTS

Researches have been conducted on an experimental site, the weak water-saturated soil put by big thickness with the following physicяs and mechanicals properties: density of dry soil - ρ_d = 1.54 t/m^3, natural humidity - w = 32%, degree of humidity - S_r = 0.98, coefficient of porosity - e = 0.79, consistency - I_L = 0.8, module of deformation - E = 2-2.7 MPa. Level of underground waters is at a depth of 1.5 m from a day surface, and on depth more than 16 m soil is presented by water-saturated loessial loams.

Prior to the beginning of the device of sandy drains static tests by means of round rigid stamps by square A_{st} = 1.0 m^2 (d_{st} = 1.13 m) which have been established directly on a layer of weak soil have been carried out (on a mark of level of underground waters). By results of tests value of settlement resistance of soil of the basis has made R = 90 KPa, and the deformation module - E = 2-2.7 MPa.

On an experimental site the ditch of 10 x 30 m in size to the level of underground waters on which surface the sandy pillow with h thickness h = 0.5 m from the coarse-grained washed sand has been arranged has been dug. This pillow provided traficability of mechanisms on a ditch surface, and further served as a horizontal drainage for removal of the wrung-out water from thickness of soil. The prepared platform has been divided on 3 separate speed up the sizes of 10 x 10 m everyone. The plan and a section of the experimental platform is given in Figure 1.

For comparison of results of experimental researches the first site was loading embankment weight without device of sandy drains in the basis, in the second sandy drains on a grid 2 x 2 m, in the third – on a grid 3 x 3 m have been arranged. Vertical sandy drains have been arranged with diameter of d = 0.4 m on depth h = 6.0 m from a ditch bottom. The scheme of a vertical sandy drain is shown in Figure 2a.

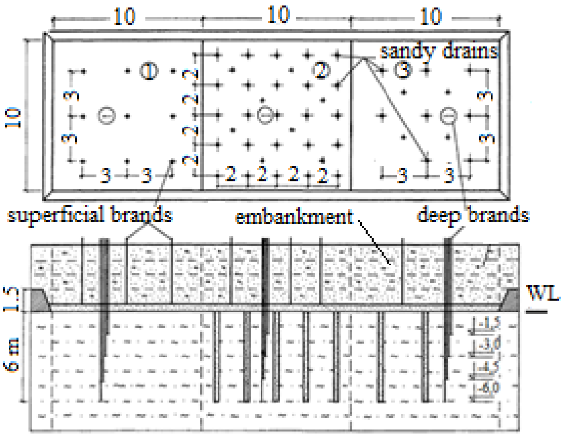

Fig. 1 Plan and section of the experimental platform

For measurement of the general and layer-by-layer deformations of thickness of weak soil on depth, on all three sites special designs of superficial and deep brands have been established (the scheme of placement of brands is given in Fig. 1, and their designs in Fig. 2b and 2c). Superficial brands have been placed on a grid 3 x 3 m, and deep brands are established through each 1.5 m up to the depth of 6.0 m. Supervision over movements of all brands were carried out by means of leveling concerning two motionless reference points located at distance of 40 m from the experimental platform.

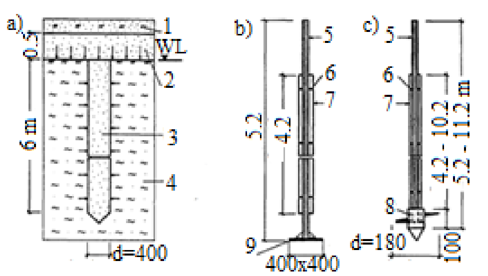

Fig. 2 Scheme of a sandy drain (a), design of superficial (b) and deep brands (c): 1- prigruzochny embankment; 2- sandy pillow; 3- sandy drain; 4- weak soil; 5- reperny pipe; 6- epiploons; 7- upsetting pipe; 8- pipe d = 76 mm; 9- metal plate

Loading of experimental sites static pressure was made by embankment weight by dumping of layers of earth 1.0 m thick everyone, with endurance of each step before the conditional stabilization of deformations accepted equal 1.0 mm/days. After a loading of thickness of soil static influences, have also conducted researches on studying of influence of the seismic forces imitated by seismic-explosive influences.

Imitation of seismic influence has been carried out with the help of camouflage explosions of charges of explosive weighing 8-10 kg in (a way of detonation of electric). Charges of explosive with a gross weight of 384 kg was established in special metal containers and plunged into boreholes on depth of 8-10 m from the Earth's surface. Explosive wells in number of 40 pieces have been located 3 concentric rows (13+13+14 wells) at distance of 20, 25 and 30 m from experimental sites. This method is widely used in practice of researches of the Republic of Tajikistan [6].

After completion of all works changes of physics and mechanicals properties of soil of the condensed thickness in laboratory and field conditions have been studied, and also static tests by means of metal round rigid stamps by a standard technique are carried out.

Results of researches

Before a loading of the territory provisions of all superficial and deep brands of rather motionless reference points have been recorded. Loadjng of the territory static pressure has been made by layer-by-layer dumping of a soil embankment from mix of gravel and pebble and loamy soil by density ρ = 1.8 t/m^3. When dumping an embankment there were great difficulties in this connection only 4 layers and the general static load of the condensed thickness of soil have been poured out has made p = 75 KPa. Dependence of deformations of the condensed thickness of "s" on time of "t" and weight of a load of "p" for all experimental sites are given in Figure 3.

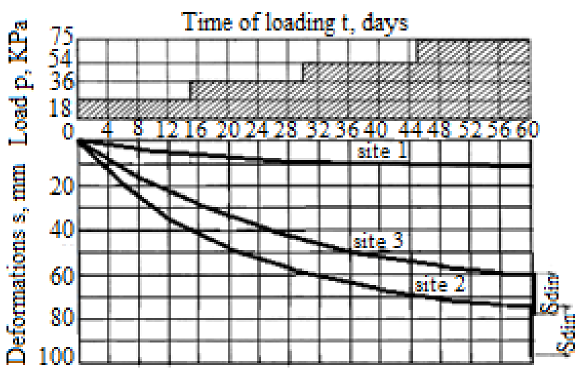

Fig. 3 Development of deformations of experimental sites in time

The greatest values of deformations have been recorded on a site where sandy drains are located on a grid 2 x 2 m (site 2). Rather good effect of consolidation is also gained at the device of drains on a grid 3 x 3 m (site 3). By researches it has been established that the main part of deformations happens in the first 5-6 days after the appendix of each step of loading. Apparently from the schedule application of vertical sandy drains allows to increase considerably quality of consolidation of thickness of weak water-saturated loessial soil (by 5-8 times) that testifies to rather high efficiency of application of this method in the conditions of weak water-saturated loessial soil.

Features of development of layer-by-layer and relative deformations of soil in depth of the basis of a site 2 are given in Figure 4. The analysis of a diagram of layer-by-layer movements demonstrates that the main part of deformations of soil thickness happens at a depth up to -3.0 m where more than 70% of the general draft of soil thickness are recorded. At the same time, more than 50% of their size are the share of depth of -1.5 m, and the deep brand located on a mark of -6.0 m practically didn't move. Obviously, it is connected with the insufficient size of the operating pressure, as well as with the fact that on depth of the basis the structural durability of compression of soil increases.

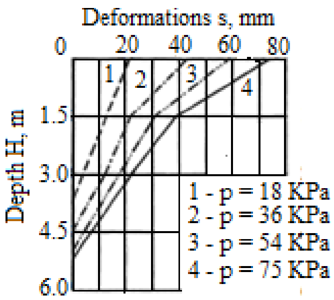

Fig. 4 Development of layer-by-layer and relative deformations in basis depth

After completion of tests for action of static loadings, researches of influence on the massif of the condensed thickness of soil of the seismic loadings imitated by seismic-explosive influences by the above-stated technique have been conducted. At the same time intensity of seismic influence has made 8 points (on the 12th mark scale of MSK-64) [7].

Results of tests are given in fig. 1 and show that seismic-explosive influences promote development of considerable additional deformations (S_{din}) which can make up to 30% of the general deformations recorded at a static loadings. Obviously, this circumstance is connected with increase of excessive hydrodynamic pressure in steam water which brings to additional their wring into a body of sandy drains and to consolidation of thickness of soil.

The following is established by the conducted pilot studies:

- seismic (dynamic) influences allow to accelerate process of filtrational consolidation and promote improvement of quality of consolidation of thickness of weak water-saturated soil when using vertical sandy drains;

- at design of the specified method in the conditions of weak water-saturated soil and high seismic activity of territories of construction, it is necessary to consider a possibility of additional consolidation of thickness of soil and, therefore developments of additional deformations in foundation of buildings when passing a seismic (dynamic) wave. Not accounting of this factor can significantly affect operational reliability of buildings after their delivery in operation.

It should be noted that imitation of seismic (dynamic) influences by means of seismic-explosions is labor-consuming and expensive action. For acceleration of process of consolidation and improvement of quality of consolidation of weak water-saturated loessial soil by more expedient use of energy of small charges (micro-explosions) [8] which mass for preservation of integrity of sandy drains by production of explosions has to be accepted within 0,3-0,5 kg is. At the same time charges of explosive should be placed in space between drains and at 2-3 levels on height of a sandy drain (schemes of an arrangement of charges on the example of an experimental site 2 are given in Figure 5a and 5b).

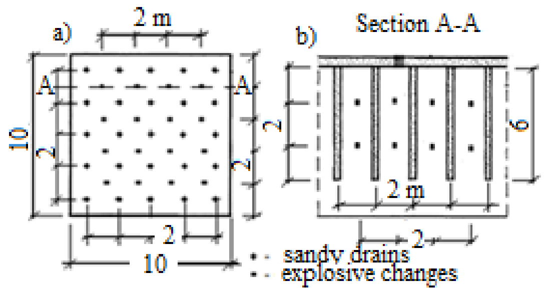

Fig. 5 Schemes of an arrangement of charges of explosive in respect of (a) and on height (b) between sandy drains

After completion of all researches on consolidation of loessial water-saturated soil sandy drains, on sites 2 and 3, for definition of strength and deformation characteristics of the condensed soil, have carried out static tests by means of metal rigid round stamps by square A_{st} = 1.0 m^2 and diameter of d_{st} = 1.13 m. Tests were carried out by a simultaneous loadings of two stamps located at distance not less 5,0dsh from each other through a metal platform by means of reinforced concrete calibrated blocks steps of loadings on p = 25-50 KPa. In Figure 6 dependences of deformation of stamps of "s" on loading "p" are given in the condensed sites. For comparison of the received results on the same schedule results the stamps of tests of soil before their consolidation are given by sandy drains (in the natural basis)

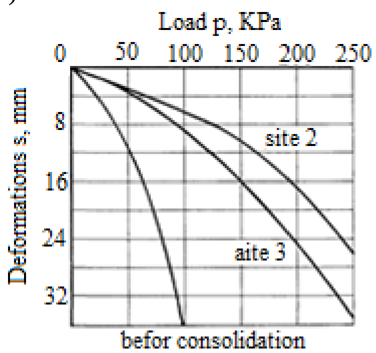

Fig. 6 Dependence a deposit of stamps from loading on the condensed bases

The received results demonstrates that consolidation of thickness of weak soil with use of vertical sandy drains allows:

- to increase values of settlement resistance (to increase the bearing ability) basis soil to R = 250 kPa that almost by 3 times exceeds these values before consolidation;

- to increase values of the module of deformation of the condensed soil to 4 times;

- to increase values of specific coupling of the condensed soil twice (by results of static sounding).

Conclusions

1. In general, the conducted pilot studies testify to efficiency of application of vertical sandy drains for consolidation of the bases put by water-saturated loessial soil, even at small sizes the static loadings.
2. The main lack of this method is complexity of dumping of a prigruzhayushchy embankment of big height in the extensive territory that demands use of considerable volume of soil and labor expenses. Therefore it is necessary to find more effective ways of a prigruzka of thickness of soil (for example, to use a zagruzheniye of the condensed territory water weight by analogy with hydrotests of metal tanks for storage of oil and oil products).

3. Seismic (dynamic) influences significantly increase efficiency of consolidation of weak water-saturated loessial soil when using vertical sandy drains. For their imitation by more expedient use of micro-explosions by placement of charges of explosive in space between drains and at various levels on height of a sandy drain is. Besides, use of micro-explosions will allow to increase quality of consolidation at rather small values of static pressure, i.e. will promote decrease in height of the poured-out embankment (loading).

4. Results of researches also testify to need of the accounting of seismic and dynamic influences when using vertical sandy drains for consolidation of weak water-saturated soil since at the same time development of additional deformations, considerable in size, in foundation of buildings after their delivery in operation is quite possible that can negatively affect operational reliability of buildings.

Bibliography

[1] Abelev MYu, “Construction of industrial and civil buildings on weak water-saturated soil”, Moscow: Stroyizdat, 1983.

[2] Mangushev RA, Usmanov RA and etc., “Methods of preparation and device of the artificial bases”, Manual, Moscow – St. Petersburg: Publishing house of Association of Construction Higher education institutions, 2012.

[3] “Recommendations about rational methods of consolidation of weak water-saturated soil by means of sandy vertical drains and limy columns for the device of the bases and the foundations, Espoo, Finland, 1984.

[4] “Recommendations about consolidation of weak soil temporary loading with application of sandy and paper drains”, Yaroslavl, 1978.

[5] “Recommendations about consolidation of weak water-saturated soil temporary loading with application of tape drains”, Moscow, 1985.

[6] Lekarkin VK, “A technique of research of influence of seismic-explosive impacts on the bearing ability of the bases”, in Proc. of the international scientific conference "Modern Aspects of Development of Aseismic Construction and Seismology", Dushanbe, 2005.

[7] Set of rules of the joint venture 14.13330.2014 "Construction in seismic countries", the staticized edition Construction Norms and Regulations of II-7-81*, Moscow, 2013.

[8] Ivanov P L, “Consolidation of low-coherent soil explosions”, Moscow: Nedra publishing house, 1983.

INFLUENCE OF CLAYSTONE DETERIORATION ON SHEAR STRENGTH OF BACKFILL

Pisut Rodvinij[1] and Pitiwat Wattanachai[1]

[1] Department of Civil Engineering, Chiang Mai University, Thailand

ABSTRACT

Claystone in Mae Moh mine after excavation has been used as a backfill material to counterweight instability slope. However, claystone deteriorates when it has been exposed to wet-dry process in the natural condition. The investigation on the properties of claystone under natural condition and control condition can clarify the deterioration effect due to wet-dry process. Deterioration can be defined as the alteration process on size distribution and strength of claystone. Sieve analysis test and unconfined compression test were conducted on claystone samples to investigate the deterioration effect on size distribution and strength of claystone. Claystone exposed to natural condition having a decrease of an average particle size (D_{50}) to be approximately 50 mm in 12 weeks and unconfined compressive strength of claystone was decreased 45% in 3 weeks. In contrast, claystone under control condition gave the same size distribution and unconfined compressive strength slightly decreased. Thus, the result demonstrated wet-dry process in natural condition was the main cause of claystone deterioration. The decrease on size distribution of claystone due to deterioration can be the cause of reduced on backfill shear strength. In order to clarify this assumption, direct shear test was conducted on 3 different particle sizes of claystone to simulate the effect of size reduction on shear strength of backfill. The experimental results demonstrated shear strength of the larger particle size samples was higher than the smaller especially under high normal stress. In conclusion, the deterioration of claystone significantly affects on shear strength of backfill.

Keywords: claystone, deterioration, shear strength, size distribution, unconfined compressive strength

INTRODUCTION

Study area located at the northeast side of the pit wall in Mae Moh mine, called area 4.1. This area will become problematic because a normal fault separated the layers have been displaced in a dip direction to the normal fault. Fig. 1 shows a cross section of area 4.1. According to the mine plan, K and Q seams (green layer and red layer in Fig.1) of lignite must be excavated [1]. K and Q lignite layers have supported the potential mass (gray layer in Fig.1). Thus, after excavating K and Q seams of lignite, the potential mass over the lignite layer becomes a sliding. The suitable method to solve this problem is cut and fill method.

The cut and fill method was used to excavate lignite in this area. The area will be mined and partially undercut. Thus, the G1 weak plane interface is also partially daylight. After completion of mining, backfilling will begin to support the slope face and maintaining adequate room for mining activities. The mining- backfilling cycle is iterative until all the lignite in area 4.1 is completely mined out. It is necessary to fill the current pit and cut the neighboring slope in subsequent procedure [1], [2].

Claystone has been used as a backfill material to counterweight and supported the potential mass. However, claystone deteriorated when it has been exposed to weather change. The deterioration of claystone can be the cause of reduced in the stability of backfill slopes. Deterioration can be defined as the alteration process of claystone occurring under the direct influence of atmosphere and hydrosphere [3]. The alteration process can be in form of either physical and/or chemical deterioration. The physical deterioration causes disintegration (or breakdown) of original fabrics and also imposes new fabric features. While the chemical deterioration, which usually takes a long time, forms discoloration of the affected rock and change in mineralogy [4].

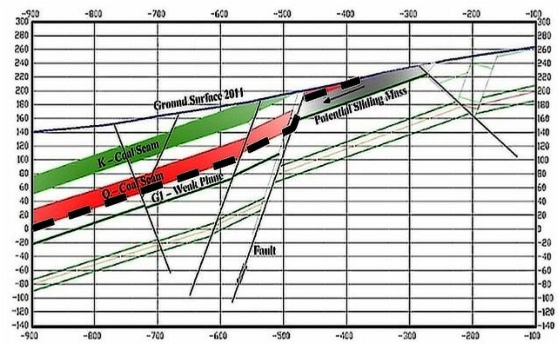

Fig. 1 Cross section plot of area 4.1 [1]

In its fresh condition, claystone usually stiff or hard and quite difficult to excavate without mechanical equipment. The occurrence of physical and chemical changes in deterioration process can lead to significant reduction in strength value [5]. Moreover, claystones have specific characteristics, mainly found to exhibit slake-deterioration within a short period of time when exposed to the atmosphere and/or moistened. This will induce some significant problems in varied engineering activities [6].

Shear strength behavior of claystone backfill was similar to rockfill or granular soil that most depend on friction angle [7]. Thus, the decrease on size distribution of claystone due to deterioration can be lead to the reduced friction angle of backfill. Eventually, stability of claystone backfill can be reduced due to deterioration of claystone.

SCOPE

The investigation on claystone properties under the natural condition and control condition can characterize the deterioration behaviors of claystone. Natural condition, claystone samples were exposed to the natural weathering process. In contrast, claystone samples under control condition were located in laboratory room (The temperature was between 25-28 °C) and they were not exposed to the weather change. The alteration process of claystone under two different conditions can be suggested that wet-dry process in natural condition was the causes of claystone deterioration. The alteration process on the size distribution of claystone was investigated by sieve analysis test. The alteration process on the strength of claystone was investigated by unconfined compression test.

The influence of claystone deterioration to the shear strength of backfill was investigated by shear strength test. Direct shear test was conducted on 3 different particle sizes of claystone samples in order to simulate the decrease of claystone particle size due to the deterioration affected shear strength of backfill.

VISUAL CHARACTERISTIC OF DETERIORATED CLAYSTONE

Physical characteristics of the deteriorated claystone can be observed by visible. Claystone samples were exposed to the natural weathering process during 0-9 weeks. Claystone samples dimension between 10-25 cm were collected from Mae Moh mine. The deterioration effect to a characteristic of claystone in natural condition was shown in Fig. 2 When time passed, the deterioration effect was demonstrated by breakdown of original claystone.

Physical characteristics of original claystone are generally gray and it is relatively stiff or hard. After claystone exposed to natural weathering process in 1 week, it was starting to intensively slake and generally followed by noticeable heaving. Some of claystone samples were started break to small particles and showed some visible fractures on the samples. In 3 weeks, the visible fractures on claystone were increased and most of the samples disintegrated into small pieces. When the samples were in natural condition during 6-9 weeks, almost all of claystone samples was broken down into very small pieces and could not classify the pieces of the sample before breakdown.

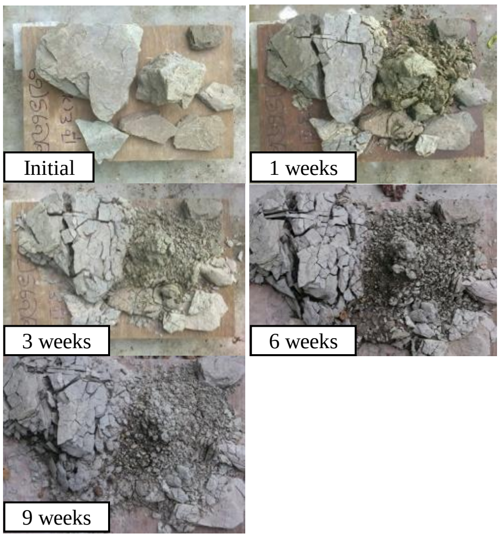

Fig. 2 Deterioration effect on characteristic of claystone under natural condition

THE EFFECT OF DETERIORATION ON SIZE DISTRIBUTION OF CLAYSTONE

The physical characteristic of deteriorated claystone demonstrated breakdown of claystone when exposed to natural weathering processes. Size distribution of claystone backfill was changed due to deterioration effect. In order to investigate the deterioration effect on size distribution of claystone. Sieve analysis was conducted on claystone samples in a natural condition and a control condition during 1-12 weeks to clarify the alteration of size distribution.

Fig. 3 indicated the size distribution of claystone decreased under natural environment during 1-12 weeks. Size distribution of the samples was decreased with increasing elapse time. Considering the average particle size (D_{50}) of claystone samples, D_{50} of claystone samples decreased from 60.0 mm remaining to 9.0 mm in 12 weeks. The deterioration greatly affected during 2 weeks as D_{50} of the samples in 2 weeks was decreased from the first week approximately 40 mm. After 2 weeks, the average particle size of claystone was slightly decreased as D_{50} of the samples was decreased approximately 11 mm during 2-12 weeks.

In contrast, claystone under control condition gave the same size distribution when the time passed as shown in Fig 4. The results can be concluded that claystone deteriorated, specifically under natural condition. Thus, wet-dry process in natural condition was the main cause of claystone deterioration.

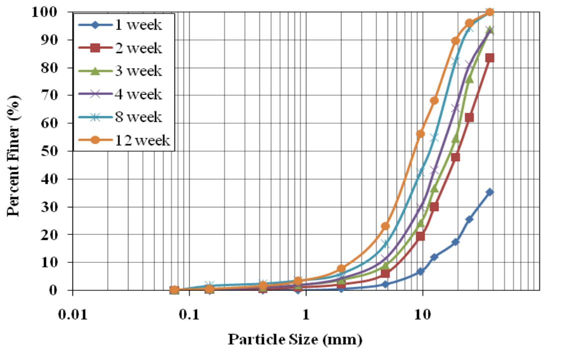

Fig. 3 Size distribution of claystone samples under natural condition

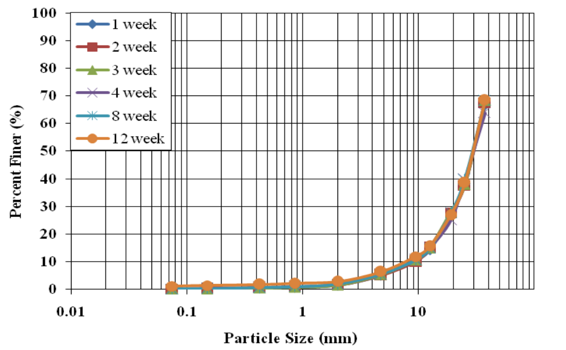

Fig. 4 Size distribution of claystone samples under control condition

THE EFFECT OF DETERIORATION ON STRENGTH OF CLAYSTONE

In fresh condition, claystone is usually stiff or hard materials. However, the deterioration process can lead to significant reduction in strength value [5]. In order to investigate the deterioration effect on strength of claystone, unconfined compression test was conducted on claystone samples under a natural condition and a control condition during 1-12 weeks to reconfirm a strength reduction of claystone. Size of trimmed claystone specimens that used in this test was 5 cm in diameter and 10 cm height as shown in Fig 5.

The experimental results of the deterioration effect on a strength of claystone was shown in Fig. 6. Unconfined compressive strength of claystone samples under natural condition decreased from 3.2 MPa remaining to 1.8 MPa or reduced approximately 45% in 3 weeks. After 3 weeks could not be prepared the specimens for the dimension that used in the test because claystone specimens deteriorated into small pieces.

Fig. 5 Unconfined compression test on claystone

On the other hands, the strength of claystone samples under control condition decreased from 2.8 MPa remaining to 2.4 MPa or reduced approximately 15% in 4 weeks. After 4 weeks, the strength of samples was slightly decreased. Unconfined compressive strength was remaining 2.1 MPa in 12 weeks. Hence, unconfined compressive strength of claystone samples in control condition has decreased approximately 25% during 12 weeks.

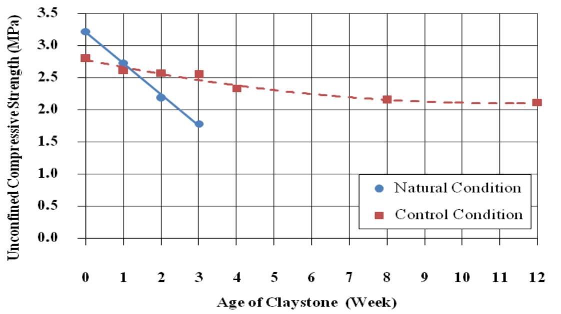

Fig 6. The results of unconfined compressive test

Regarding the age of samples at 3 weeks, unconfined compressive strength of the samples under natural condition reduced approximately 45% but unconfined compressive strength of the samples under control condition reduced approximately 10%. Thus, the strength reduction rate of claystone under natural condition was higher than claystone under control condition. The results can demonstrate the influence of wet-dry process due to weather change extremely affected the strength of claystone.

SHEAR STRENGTH OF CLAYSTONE BACKFILL

Shear strength of claystone backfill was mostly depended on friction angle of materials. Then, the decrease of size distribution due to the claystone deterioration was lead to reduce shear strength of backfill. In order to verify the decrease of particle size affect on shear strength of backfill, direct shear test was conducted on the various particle sizes of claystone samples. The experimental results express the deterioration effect on shear strength of backfill.

Table 1 Size of claystone samples

Size of samples	D_{50} (mm)
Passing sieve 25.4 mm retained on sieve 19.0 mm (50%) + Passing sieve 19.0 mm retained on sieve 12.7 mm (50%)	19.0
Passing sieve 12.7 mm retained on sieve 9.5 mm (50%) + Passing sieve 9.5 mm retained on sieve 4.75 mm (50%)	9.5
Passing sieve 4.75 mm retained on sieve 2.0 mm (50%) + Passing sieve 2.0 mm retained on sieve 0.85 mm (50%)	2.0

Direct shear test was carried out on the samples to obtain shear strength properties under unconsolidated undrained condition. Size of claystone specimens was prepared according to table 1 and normal stress that used in this test was 0-930 kPa. Direct shear test was conducted on 6 inches in diameter of specimen by rock direct shear testing machine as shown in Fig 7, Fig 8 and compacted specimens at moisture contents same as sampled in the field (moisture contents 26%).

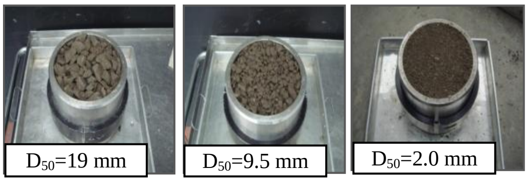

Fig. 7 Claystone samples prepared for direct shear test

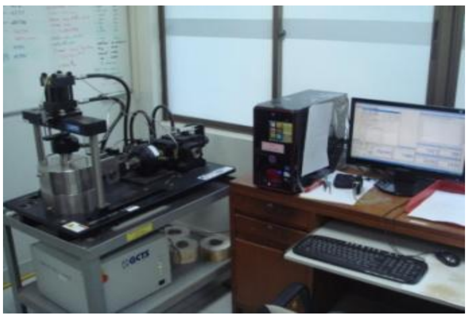

Fig. 8 Rock direct shear testing machine

The reduction of claystone particle size affects on shear strength of backfill

Shear strength characteristic of claystone backfill was similar to granular soil or rockfill. Thus, shear strength behavior is actually nonlinear. This nonlinear can be approximated a straight line in the range of low normal stress (0-254 kPa) and a straight line in the high normal stress (254-930 kPa). The higher effective normal stress will yield lower values of friction angle.

Fig 9 shown the reduction of particle size affected shear strength of backfill. Shear strength envelope of the samples at D_{50} equal to 19.0 mm was higher than the samples at D_{50} equal to 9.5 mm and 2.0 mm, especially under high normal stress. Under low normal stress, shear strength envelope of the samples at D_{50} equal to 19.0 mm, 9.5 mm and 2.0 mm was similar. The maximum shear stress of the samples at D_{50} equal to 19.0 mm was higher than the samples at D_{50} equal to 9.5 mm and 2.0 mm approximately 120 kPa and 140 kPa respectively.

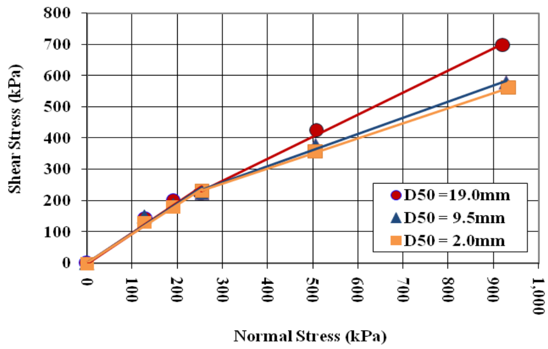

Fig. 9 Size of claystone affect to shear strength of backfill

The Influence of deterioration affects to shear strength parameter

Shear strength parameter of claystone backfill samples at various particle sizes which were cohesion and friction angle was shown in Table 2.

Table 2 Shear strength parameter of the samples

D_{50} (mm)	Low Normal Stress (0-254 kPa)		High Normal Stress (254-930 kPa)	
	c (kPa)	ϕ (˚)	c (kPa)	ϕ (˚)
19.0	0	44.1	53	35
9.5	0	43.8	103	27
2.0	0	43.1	109	26

Table 2 shown friction angle of the samples at D_{50} equal to 19.0 mm was more than D_{50} equal to 2.0 mm approximately 1° under low normal stress. Under high normal stress, friction angle of the samples at D_{50} equal to 19.0 mm was more than the samples at D_{50} equal to 9.5 mm and 2.0 mm approximately 8° and 9° respectively. Cohesion of the samples at D_{50} equal to 19.0 mm was less than the samples at D_{50} equal to 9.5 mm and 2.0 mm approximately 50 kPa and 56 kPa respectively.

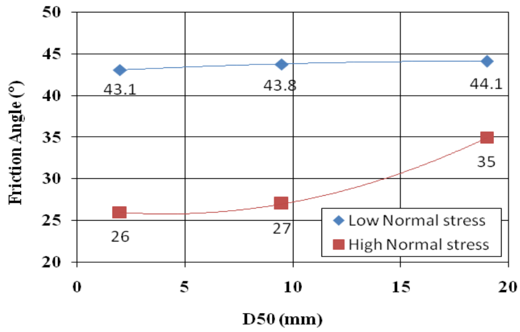

Fig. 10 Relationship between friction angle and D_{50}

Fig. 10 shown the correlation between friction angle and D_{50} of the samples. Friction angle reduced by the decline of claystone particle sizes. In the range of low normal stress, friction angle was slightly decreased when the particle size of claystone was smaller. In contrast, friction angle in the range of high normal stress was rapidly decreasing when D_{50} of the samples equal to 19.5 mm reduced to 9.5 mm. However, the average particle size of the samples which lower than 9.5 mm, a trend of friction angle was slightly decreased. The results can be described the decrease of claystone particle size due to deterioration was a cause of reduced backfill shear strength especially under high normal stress.

CONCLUSION

Claystone has been used as backfill material to counterweight and supported instability slope in Mae Moh mine. In its fresh condition, claystone usually stiff or hard. However, claystone deteriorated when it has been exposed to weather change. The deterioration of claystone can be the cause of reduced in the shear strength of backfill.

Deterioration can be defined as the alteration process on size distribution and strength of claystone. The investigation on claystone properties under natural condition and control condition can characterize the deterioration behaviors of claystone. Size distribution and strength of claystone under natural condition decreased due to deterioration effect. In contrast, claystone under control condition can maintain size distribution and strength. Thus, the investigation on claystone properties suggested that the deterioration effect occurs only under natural condition due to claystone has been exposed to wet-dry process.

Stability of claystone backfill slope depended on shear strength of backfill material. The reduction on size distribution of claystone due to deterioration can be the cause of reduced backfill shear strength. Therefore, shear strength test was conducted on 3 different particle sizes of claystone to simulate the effect of size reduction on shear strength of backfill. The experimental results demonstrated shear strength of backfill reduced by the decline of claystone particle size, especially under high normal stress. Overview of this study can be concluded that claystone deteriorated under natural condition due to wet-dry process and the deterioration of claystone significantly affects to decrease shear strength of backfill.

REFERENCES

[1] Leelasuksaree C, Mavong N, Khosravi M H, Pipatpongsa T, "Physical and Numerical Models of Undercut Slope Lying on Steeply Inclined Bedding Plane", 17th National Convention on Civil Engineering, 2012, pp. GTE045-1 -GTE045-10.

[2] Mavong N, Tunkeaw S, Mungpayabal N, Boonsritun N, "Mining Plan and Progressive Excavation in Lowwall Area 4.1 of Mae Moh Mine", International Symposium on Earthquake Hazard Potential and Preparedness for Safety in Coal Mining, 2011.

[3] Sounders M K, and Fookes P G, "A review of the relationship of rock weathering and climate and its significance to foundation engineering", Eng. Geol, 4, 1970, pp. 289-325.

[4] Sadisun I A, Shimada H, Matsui K, "Characterization of Weathered Claystone and Their Engineering Significance", Indonesian Scientific Meeting 2000, 2000, pp. 1-8.

[5] Sadisun I A, Shimada H, Matsui K, "Determination of Strength of Subang Formation Claystone Due to Weathering", Proceeding of the 3rd Asian Symposium on Geology and the Environment (ASEGE), 2001, pp. 37-46.

[6] Sadisun I A, Shimada H, Ichinose M, Matsui K, "Study on the physical disintegration characteristics of Subang claystone subjected to modified slaking index test", Geotechnical and Geological Engineers, 2005, pp. 199-218.

[7] Das Braja M, "Shear Strength of Soil", Advanced Soil Mechanics, Singapore : McGraw-Hill, 1985, pp. 402-416.

[8] Budhu M, "Some Causes of Slope Failure", Soil Mechanics and Foundation, New Jersey : John Wiley & Sons, 2000, pp. 525-528.

[9] Mitchell J K, Soga K, "Physical Process of Weathering", Fundamentals of Soil Behavior, New Jersey : John Wiley & Sons, 2005, pp. 8.

[10] Naderian A R, William D J, "Bearing Capacity of Open-Cut Coal-Mine Backfill Material" Transactions of the Institution of Mining and Metallurgy, Section A-Mining Industry, 1997, pp. A30-A34.

[11] Shakoor A, Gautam T P, "Assessing the Slaking Behavior of Clay-Bearing Rock", 10th Annual Technical Forum Geohazards Impacting Transportation in the Appalachian Region, 2010.

FINITE DIFFERENCE ANALYSIS OF A CASE STUDY OF VACUUM PRELOADING IN SOUTHERN VIETNAM

Cong-Oanh Nguyen[1], Thanh Thi Tran[2] and Van-Tram Thi Dao[3]
[1,2]Division of Soil Mech. & Foundation Eng., Southern Institute of Water Resource Research, Vietnam; [3]Faculty of Civil Engineering, Transportation College 3, Vietnam

ABSTRACT

The vacuum preloading method was first developed in 1952, since then it has become a commonly used method all over the world in general and in Vietnam in particular to accelerate the consolidation of the soft ground. However, there is still misunderstanding of the variation of vacuum pressure over the depth of prefabricated vertical drain (PVD) among researchers. The paper presents a case study of soft ground improvement by vacuum preloading method for a land development project in Sothern Vietnam. A series of finite difference analysis (FDA) of the improved ground with multi-layer models to get insight into the effectiveness of the method are conducted. Input parameters are characterized from constant rate of strain (CRS) consolidation tests on undisturbed samples retrieved by stationary piston sampler. Vacuum pressure is considered as equivalent surface load in the analyses. In comparison with field monitored data, the analyses show good agreement for magnitude vs. time for both settlement and dissipation of excess pore water pressure as well as strength gain for the first 10-m soft ground while the bottom part shows little or no improvement.

Keywords: Consolidation, CRS, FDA, PVDs, settlement, soft clay, un-drained strength, vacuum preloading

INTRODUCTION

Recent advances in ground improvement all over the world allow geotechnical engineers to deal with the soft soil treatment with large thickness in general. Vietnam is located in the Holocene soil deposit from the North to the South part of the country especially in Red River and Mekong Delta. Among the most popular soft ground treatment methods, vacuum preloading assisted with prefabricated vertical drains (PVDs) has been increasingly utilized for the recent years.

First introduced by Kjellman [1], the method of vacuum preloading with and without surcharge assisted by PVDs has become one of the most popular way of ground improvement over the soft clayey deposits [2]. The use of PVDs is to reduce the drainage path length to speed up the consolidation process which may take many years to complete [3] & [4]. With the use of surcharge the soft ground deposit may undergo long time of construction and risk of instability and there has been lack of sand supply source, therefore vacuum has been applied in conjunction with surcharge to reduce the volume of surcharge sand and has proved the efficiency of the soft ground improvement work [2] & [5]. Even there has been development in theory and application of vacuum preloading over the past few years, there is still misunderstanding and misleading of the use of the vacuum distribution over the whole length of PVDs despite the length of PVDs may exceeds the effective depth of vacuum distribution in the formulation of the analytical equations, which is not complied with the Pascal’s law for the cases of PVDs deeper than 10 m [6], [7] [8], and [9].

It had been stated [10] that below z_0, there is no effective vacuum pressure, which confirm the work of Pascal’s law on the distribution of vacuum pressure over the soft soil deposit and PVDs length. This means that there is still disputed research on the distribution of vacuum pressure over the improved zone. However, this issue has not been clearly confirmed by full scale testing of the method. The paper presents a case study of soft ground improvement by vacuum preloading assisted by surcharge and PVDs in the Southern area of Vietnam by simulation of the one dimension problems with multi-layer soil model in a finite difference code named CONSOPRO [11]. A new concept of vacuum pressure distribution over the soft soil deposit and PVDs is proposed. Various finite difference analyses (FDA) is carried to prove the correctness of the proposed distribution.

THE SITE AND SOIL PROFILE

The site is located in the South part of Vietnam and within Mekong delta as indicated in Fig. 1. The considered area is 100 m by 250 m. The area is around 30 km from the East Sea, which is affected by fluctuated seasonal tide. The original ground elevation is lower than the average sea level.

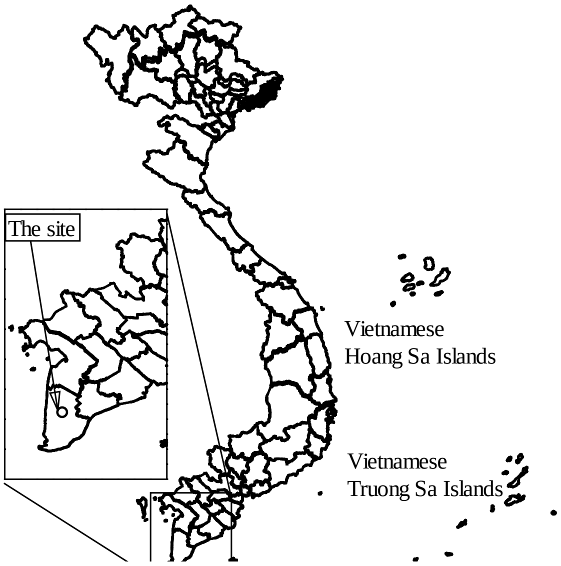

Fig. 1 Site location

The area was designed to be improved by vacuum and surcharge preloading to reduce post construction settlement and to ensure the slope stability during the construction of the surcharge fill by hydraulic method. Prefabricated vertical drains (PVDs) were used in conjunction with the preloading method the acceleration of the consolidation of the soft clay deposit.

Even there was geotechnical investigation done in 2014 for Front-End Engineering Design (FEED), the contractor was requested to do the additional soil investigation just before the start of the soil improvement work to determine the compressibility and consolidation characteristics of the soft soil deposit in order to estimate the ground settlement under surcharge load and during the time of operation. For the considered area, there was one borehole CRS with application of the stationary piston sampler to avoid disturbance to the soft samples, one electrical vane shear test FVT-01 and one electrical piezocone penetration test CPTu-01 as indicated in Fig. 2. The soft soil has natural water content close to liquid limit and ranging from 50 % to 75 % in Fig. 3(a). The thickness of the deposit is around 16 m. CRS consolidation tests are used to determine the compressibility indices and consolidation characteristics of the soft ground with the application of the method in [11]. The compressibility indices are presented in Fig. 3(c). The compressibility indices in normally consolidated state is average of 0.6 for the top 3 m of soft clay while the below show values ranging from 0.9 to 1.1.

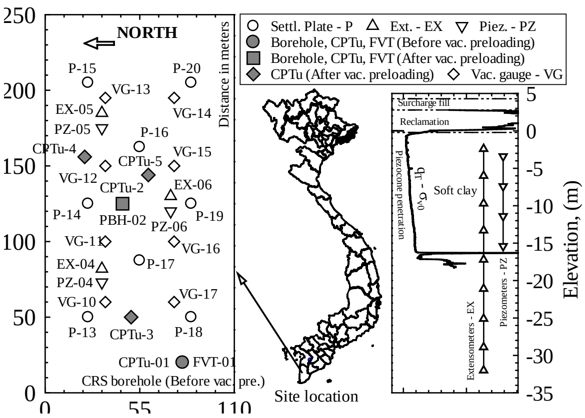

Fig. 2 Layout of instruments and investigation

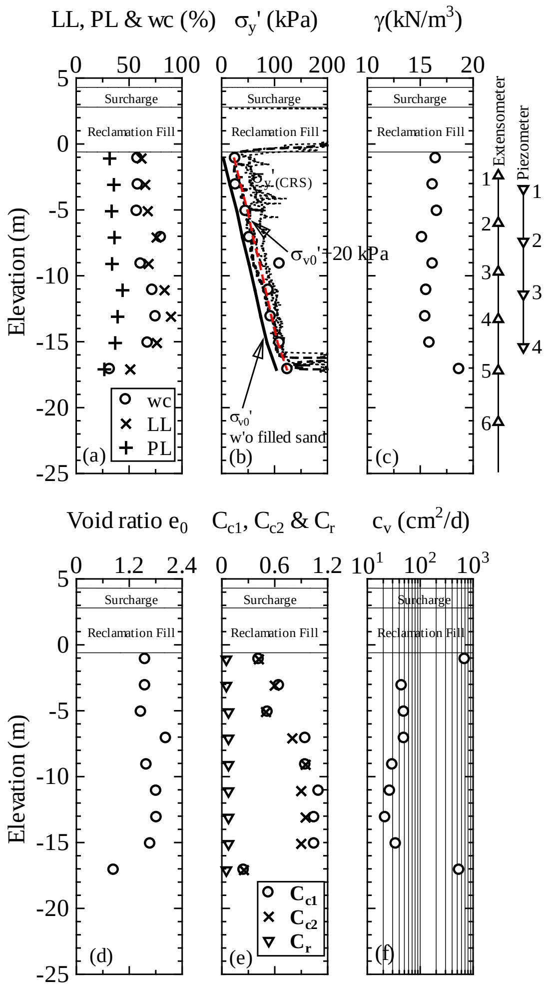

Fig. 3 Soil profile and consolidation characteristics

Table 1 Compressibility and consolidation characteristics of soft soil sub-layers

Sample	Depth (EL.)	Ho	σ'_{v0}	e_0	σ'_y	σ'_b	C_r	C_{c1}	C_{c2}	$c_{v(NC)}$	$c_{v(OC)}$
N^0	m (mCD)	(cm)	(kPa)		(kPa)	(kPa)				(cm^2/d)	
1	3.9 (-1.1)	160	3	1.566	26	400	0.050	0.42	0.42	7000	700
2	5.9 (-3.1)	200	16	1.565	27	175	0.050	0.65	0.60	450	45
3	7.9 (-5.1)	200	29	1.472	46	300	0.075	0.52	0.50	500	50
4	9.9 (-7.1)	200	39	2.037	53	200	0.075	0.95	0.80	500	50
5	11.9 (-9.1)	200	52	1.598	110	200	0.075	0.95	0.95	300	30
6	13.9 (-11.1)	200	63	1.816	89	200	0.075	1.10	0.90	270	27
7	15.9 (-13.1)	200	74	1.823	93	200	0.075	1.05	0.95	220	22
8	17.9 (-15.1)	200	86	1.681	110	200	0.075	1.05	0.90	350	35
9	19.9 (-17.1)	100	103	0.852	125	300	0.050	0.25	0.25	5500	550

Notes: The coefficient of consolidation in OC is 10 times of that in NC state $c_{v(OC)}=10c_{v(NC)}$.

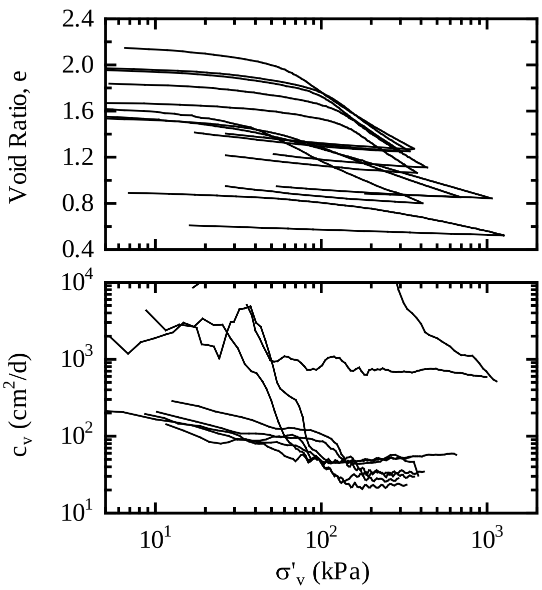

Fig. 4 CRS consolidation test results

Consolidation yield stress varies as much as linear over depth, which is shown in Fig. 3(b). Pre-overburdened pressure POP, which is the difference between consolidation yield stress σ'_y and overburdened pressure σ'_{vo} is found to be 20 kPa and OCR larger than 1.0 for the site. This confirms that soft clay deposit is in slightly over consolidated state and in consistence with data found in [12] & [13], which stated that there is no Holocene deposit in Mekong Delta having OCR less than 1.0. Void ratio for the whole clay layer is larger than 1.5, resulted in high compressibility of the clayey soil as plotted in Fig. 3(d). Summary plots of CRS test results are shown in Fig. 4 upon which the determination of compressibility and consolidation yield stresses is complied with the method found in [11]. Determined values of the soft clay properties are tabulated in Table 1.

INSTRUMENTATION

The monitoring instruments consist of 8 surface settlement plates from P13 to P20, 3 piezometer groups (PZ-04 to PZ-06) of 4 tips at each group; 3 extensometer groups (EX-04 to EX-06) of 9 magnetic rings at each group and 8 vacuum gauges from VG-10 to VG-17 as indicated on Fig. 2. The average installation elevation of surface settlement plate is +2.700 (mCD). The installation elevation of piezometer tips and extensometer rings is presented in Table 2.

Table 2 Elevation of PZ tips and EX magnetic rings

EX-04	EX-05	EX-06
-2.37 (mCD)	-2.43 (mCD)	-2.15 (mCD)
-5.99 (mCD)	-6.01 (mCD)	-5.98 (mCD)
-9.67 (mCD)	-9.75 (mCD)	-9.85 (mCD)
-13.31 (mCD)	-13.54 (mCD)	-13.75 (mCD)
-17.17 (mCD)	-17.34 (mCD)	-17.68 (mCD)
-21.08 (mCD)	-21.21 (mCD)	-21.61 (mCD)
-25.07 (mCD)	-25.11 (mCD)	-25.57 (mCD)
-28.90 (mCD)	-28.96 (mCD)	-28.91 (mCD)
-32.01 (mCD)	N/A	-31.93 (mCD)
PZ-04	**PZ-05**	**PZ-06**
-3.38 (mCD)	-3.43 (mCD)	-3.39 (mCD)
-7.38 (mCD)	-7.43 (mCD)	-7.39 (mCD)
-11.38 (mCD)	-11.43 (mCD)	-11.39 (mCD)
-15.38 (mCD)	-15.43 (mCD)	-15.39 (mCD)

The piezometer tips were all installed within the soft clay deposit while extensometer rings were installed down to the elevation of -30.xx (mCD), of which 5 elevated rings are within the soft clay deposit. Vacuum gauges were installed underneath the impervious membrane in order to monitor the vacuum pressure transmitted from pumps to the drainage sand fill.

Correction of the settlement of piezometer tips is taken into account to evaluate the excess pore water pressure measurement. The piezometer tip elevation is different from that of extensometer rings; therefore interpolation of measured settlement of these rings is used with consideration of initial installation elevation of the tips and magnetic rings. In order to calculate the excess pore water pressure, the ground water elevation, which is related to the reduction in level during operation of vacuum pumps in the treated area, is considered. The ground water level inside the vacuum treated area can be calculated by using the initial ground water level to subtract the reduction of its elevation caused by the effect of vacuum pump operation.

CONSOLIDATION ANALYSIS

Analysis Method and Software

The authors apply the finite difference method and the coded software which has been coded and copyrighted by the authors. An axisymmetric unit cell around the vertical drain is considered in the analysis. As soon as the vertical drains are installed in the ground, the consolidation boundary condition is introduced at the vertical drain. The finite difference code named CONSOPRO version 1.0 allows users to consider up to 20 subsoil layers and 50 loading steps including ramp and sudden increase in loading, which is the same procedure applied in [11]. There is no clear data about the correlation between the vertical and horizontal coefficient of consolidation; therefore, assumption of the ratio of horizontal values over vertical values is 3, which means $c_h=3c_v$ which was reported in [11].

Construction Sequences

From the original ground elevation of -0.8 (mCD), a reclamation fill was conducted by hydraulic method. The fill thickness was averaging of 2.8 m. A drainage sand fill of 0.5 m, which is used for acceleration of the drainage of pore water in the ground, was carried after the reclamation fill. Then prefabricated wick drains were installed by statically pressing with the rectangular mandrel size is 60 mm by 120 mm in 1 m by 1 m square grid pattern. Impervious HDPE membrane was installed to cover all the treated area, then vacuum pumps were started to generate the atmospheric pressure difference between underneath the membrane and outside air. After the vacuum pressure was measured stably within the targeted range from 70 kPa to 80 kPa as average values, the surcharge fill was loaded in a ramp increase until the thickness reached 1.5 m. The design dwelling time is 160 days from the start of site reclamation.

New Procedure for Vacuum Load

Fig. 5 shows the comparison between field testing before and after ground improvement. There is considerable increase in un-drained shear strength from the top of soft clay down to elevation of -8 m Chart Datum Level (mCD) while there is almost no strength gain for the deposit below -8 m (mCD), which means that the effectiveness of vacuum preloading could be within 10 m down from the vacuum pump elevation.

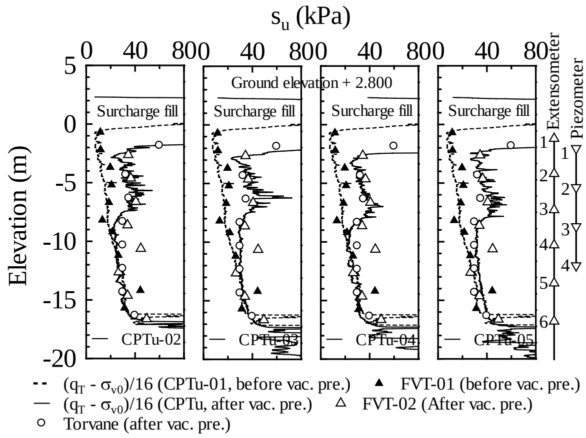

Fig. 5 Piezocone after vacuum preloading

Therefore, the authors propose vacuum loading distribution over depth as the following:

1. Constant distribution of vacuum loading from pump elevation down to the effective depth which does not exceed 10 m. This means that the Pascal law is true;
2. Linear distribution of vacuum preloading from the effective depth to the maximum depth which follows Pascal law;
3. The effective depth is dependent on vacuum pump efficiency;
4. The vacuum load is equivalent to the surcharge load in the same amplitude;

Consolidation Analysis

Consolidation analyses are carried out at the monitoring instruments. The proposed distribution of vacuum pressure vs. depth within the effective zone, which accounts for Pascal law, is applied in

and c_h=3c_v which was reported [11] is used.

Excess pore water pressure

Fig. 6 shows the results of finite difference analysis of excess pore water pressure dissipation at 3 piezometers PZ-04, PZ-05 and PZ-06. A correction of pressure, which is equivalent to the vacuum pressure distribution over depth, is applied. The results indicate that the distribution of vacuum pressure from the first to the second piezometer tip is almost constant and ranges from 70 kPa to 90 kPa; however, below the elevation of -7.30, the vacuum pressure reduce considerably.

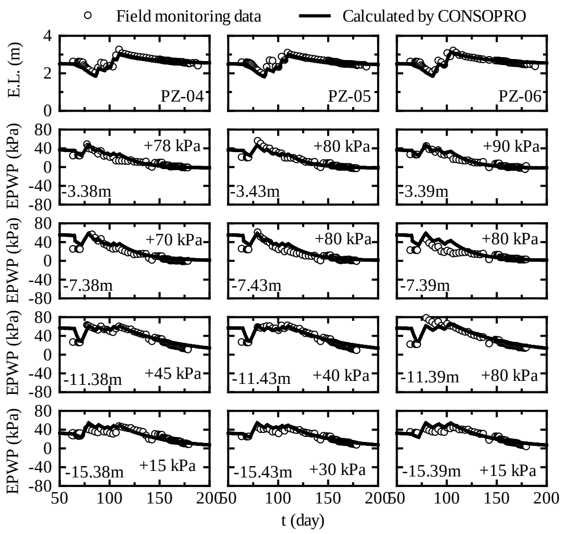

Fig. 6 Analysis of excess pore water pressure

The reduction of vacuum pressure for deeper zone of the soft clay can reach 50% at depth deeper than -7.30 and 80% for elevation deeper than -15.30. It is clear that the vacuum pressure is not transmitted constantly over the depth of prefabricated vertical drains (PVDs) in such cases where PVDs are installed deeper than 10 m from the vacuum pump base elevation. The vacuum pressure distribution over depth from piezometer data is consistent with those from piezocone penetration data presented in Fig. 5.

The plots show that the field monitoring data of excess pore water pressure are consistent with the calculated values. Right at the time (t=xx days) of starting vacuum pump, the excess pore water pressure increase rapidly and followed by the dissipation process.

the calculation. Input parameters are presented in

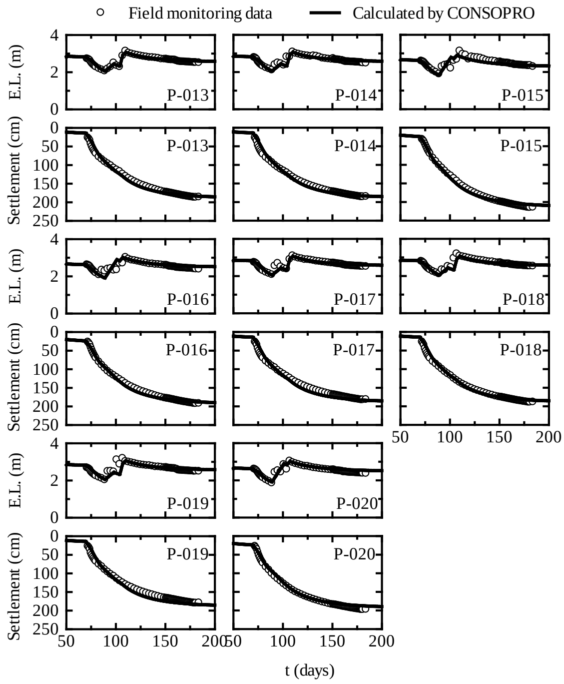

Fig. 7 Analysis of surface settlement

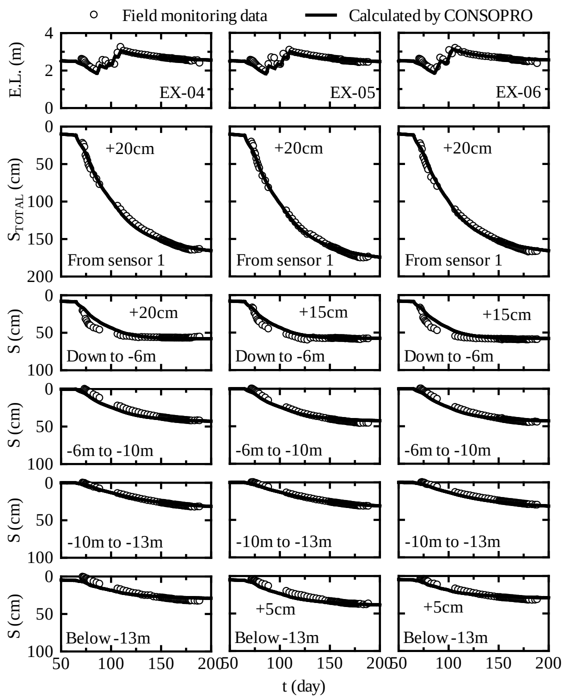

Fig. 8 Analysis of multi-layer settlement

Surface and multi-level settlement

The results of finite difference analysis shows, in Fig. 7, the consistence between the calculated and monitored data except at settlement plate P-013 and P-020 where there is underestimation of surface settlement. However, in general the calculated results at settlement plates are best fit with the field monitoring data. The settlement at plates ranges from 188 cm to 213 cm from plates P-013 to P-020. The difference in magnitude of settlement can be designated to the discrepancy of soft clay thickness over the installation location of the plates.

The compressibility of the soft clay deposit determined from CRS testing results show good agreement in magnitude of settlement of the sub-layers of soft soil as indicated in Fig. 8. This proves the appropriateness of the strain rate of 0.02%/min. used in CRS tests to obtain consolidation characteristic of the soft soil.

CONCLUSION

There are the following conclusions

1. Pre-overburdened pressure of the considered soft soil deposit is 20 kPa. The soft clay deposit is in lightly over consolidated state.
2. Compressibility and coefficient of consolidation derived from constant rate of strain (CRS) consolidation test at 0.02%/min. can be utilized directly into the consolidation analysis whose results consistent with those from field monitoring.
3. Horizontal coefficient of consolidation is as much as three times of vertical value determined by CRS test results $c_h=3c_v$. The vertical coefficient of consolidation in over-consolidated stage is almost 10 times as much as that in normally consolidated stage $c_{v(OC)}=10c_{v(NC)}$.
4. The soft ground should be divided into vacuum zone which extends to the maximum depth of 10 m from the elevation of vacuum pump, which follows Pascal's law. The ground is improvement much on the top 10 m, while the below part is not effectively improved because the vacuum pressure cannot be transmitted effectively deeper than 10 m from vacuum pump elevation.

REFERENCES

[1] Kjellman, W., Consolidation of clayey soils by means of atmospheric pressure, in Proceedings of the conference on soil stabilization, MIT, Editor. 1952: Boston. p. 258-263.

[2] Indraratna, B., X. Geng, and C. Rujikiatkamjorn, Review of methods of analysis for the use of vacuum preloading and vertical drains for soft clay improvement. Geomechanics and Geoengineering, 2010. 5(4): p. 223-236.

[3] Bo, M.W., et al., Soil Improvement: Prefabricated Vertical Drain Techniques. 2003: Thomson Learning, Singapore.

[4] Saowapakpiboon, J., D.T. Bergado, and S. Youwai, Measured and predicted performance of prefabricated vertical drains (PVDs) with and without vacuum preloading. Geotextiles and Geomembranes, 2010. 28(1): p. 1-11.

[5] Mesri, G. and A.Q. Khan, Ground improvement using vacuum loading together with vertical drains. Journal of Geotechnical and Geoenvironmental Engineering, 2012. 138(6): p. 680-689.

[6] Chai, J., S. Hayashi, and J.P. Carter, Vacuum consolidation and its combination with embankement loading, in Ground Modification and Seismic Mitigation - GSP 152, ASCE, Editor. 2006.

[7] Chai, J., Z. Hong, and S. Shen, Vacuum-drain consolidation induced pressure distribution and ground deformation. Geotextiles and Geomembranes, 2010. 28: p. 525-535.

[8] Indraratna, B., R. Cholachat, and I. Sathananthan, Analytical and numerical solutions for a single vertical drain including the effects of vacuum preloading. Canadian Geotechincal Journal, 2005. 42: p. 994-1014.

[9] Tran, T.A. and T. Mitachi, Equivalent plane strain modeling of veritcal drains in soft ground under embankment combined with vacuum preloading. Computers and Geotechnics, 2008. 35: p. 655-672.

[10] Qiu, Q.C., H.H. Mo, and Z.L. Dong, Vacuum pressure distribution and pore water pressure variation in the ground improved by vacuum preloading. Canadian Geotechincal Journal, 2007. 44: p. 1433-1445.

[11] Nguyen, C.O. and T.T. Tran, Consolidation analysis of Vietnam soft marine clay by finite difference method with application of constant rate of strain consolidation test, in Fifth International Conference on Geotechnique, Construction Materials and Environment, H. Zakaria, Editor. 2015, The GEOMATE International Society: Osaka, Japan. p. 271-276.

[12] Bui, T.M., Initial Evaluation of Consolidation Characteristics of Mekong Soft Clay and Their Use in Engineering Practice, in Hanoi Engineering Geology Workshop. 2003: Ha Noi. p. 1-13.

[13] Takemura, J., Y. Watabe, and M. Tanaka, Characterization of alluvial deposits in Mekong Delta, in Characterisation and Engineering Properties of Natural Soils. 2007, Taylor & Francis Group, London. p. 1805-1829.

EARTHQUAKE ATTENUATION MODELS AND ITS RESPONSES TO EARTH ZONE DAM IN UPPER NORTHERN PART OF THAILAND

Tawatchai Tanchaisawat[1]*, Sirikanya Laosuwan[2] and Nutapong Hirano[3]
[1]*Lecturer (tawatchai@eng.cmu.ac.th), [2]Doctoral Student, [3]Master Student
Department of Civil Engineering, Faculty of Engineering, Chiang Mai University,
Chiang Mai, THAILAND

ABSTRACT

The upper northern part of Thailand is mountainous area which classified as moderate risk by earthquake. This study was focused on the earthquake attenuation model of Abrahamson and Silva (2008). Exciting quake source from the Chiang Rai 2014 earthquake was recorded at earth zone dam site study. The accelerometer was installed in the bottom of dam which is 59 m height, 9 m width and 1,950 m length. The attenuation model is the relationship between acceleration, distance, size of earthquake, period of stabilization, characteristics of seismic sources and geological conditions. This research aims to compare the peak ground acceleration (PGA) between the attenuation models and the data measurement at the dam to check the accuracy of the model. And to study the dynamics analysis in the dam by using two selected time history records with different wave characteristics as: short period (EQ1) and long period (EQ2) to analyze the behavior of the pore water pressure, the stress and displacement in the dam. The results of this study revealed that the Peak Ground Acceleration (PGA) from the attenuation model of Abrahamson and Silva equal to 0.017787 g. And the percentage error of calculated PGA when compared to the PGA from measurement was 6.38. The analysis of the dynamics by using seismic waves with different time duration. EQ1 have made the pore water pressure on the dam higher when the effective stress in the dam decrease, which makes the displacement of the dam more than EQ2.

Keywords: Earthquake Attenuation Model, Finite Elements Method, Dynamic Analysis, Dam Behavior

INTRODUCTION

Earthquakes are natural disasters that cause direct damage to engineered constructions such as buildings, roads, bridges, and dams, causing loss of life and property. And in the northern part of Thailand has many active faults that causing earthquake. From seismic records, in the North part has more frequent earthquakes than the other part. But currently, Thailand still does not have much research on the decreasing energy of seismic that depends on the distance. In the past, Warnitchai [1] studied the attenuation model of foreign soil compared with Bangkok soil. And Attapon [2] studied for the attenuation model, but also focus on the areas in Chiang Mai.

When the earthquake occurred. The building structure had effected, particularly the building is located close to the epicenter of the earthquake. So this research aims to study the attenuation model by using the Chiang Rai (6.3 on Richter scale) earthquake that has epicenter in Phan district, Chiang Rai province (Latitude 19.748 ºN Longitude 99.692 ºE) on May 5, 2014. The data has collected by Seismological Bureau of Thai Meteorological Department as shown in Fig. 1.

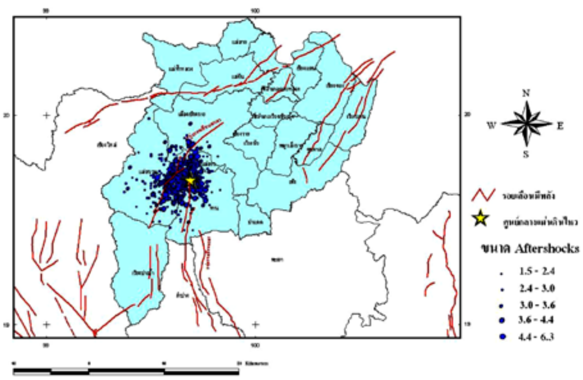

Fig. 1 The Chiang Rai earthquake datas (Main shock and aftershock) have collcted by Seismological Bureau, TMD

The Abahemsan equation is the attenuation model that has been used in the research. The calculated PGA has been compared with the dam instrumentation (accelerometer) that is installed in the Mea Ngud Somboon Chon Dam. After that, the dam model will be used to analysis the dam behaviors (pore pressure, stress and displacement) after effected by using the earthquake waves that have short-period and long-period waves. The Hardening-Soil Model will be used in this analysis.

SITE DESCRIPTION AND INSTALLATION

Mae Ngat Dam

Mae Ngat Dam was an earth-filled embankment dam with a clay core. It is a zoned earth dam consisting of 4 parts: (1) Core zone, (2) Random Zone, (3) Miscellaneous, (4) Filter zone and (5) Rock fill zone. The dam was built to block the Mae Ngat waterway at Cho lae sub district, Mae Taeng district, Chiang Mai. The dam's height is 59 meters and the length is 1,590 meters. The types of soils used in the construction of Mae Ngat Dam were CL and MH. The dam's construction began in 1977 and was completed in 1984. The cross section of the main dam and its layout is shown in Fig. 2.

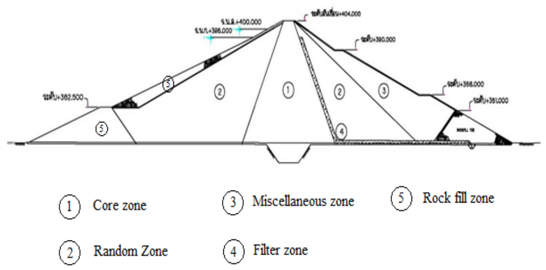

Fig. 2 Typical cross section of the Mae Ngat Dam.

The Dam's Materials and Properties

The data of the zoned-earth dam in this study was collected to acquire detailed information of both the construction and the timing of water retention by testing the qualities of the materials both on the field and in the laboratory by Vikrom [3] and collecting the samples of soil in the core zone for additional laboratory testing. The acquired information was analyzed to select representatives of the current materials to be able to set properties in creating a model that is the closest to the current soil conditions, so it can be used to analyze the behavior of the dam when affected by Dynamic force. Properties of materials of the dam are displayed in Table 1 and Table 2.

Table 1. Properties of soil in Mae Ngat Dam

Zone	E	C	ϕ	μ	γ	Ψ
Clay Core	8,171	49	16	0.48	19.72	0
Random	9,620	32	30	0.350	18.56	0
Miscellaneous	22,750	0	42	0.3	19.0	5
Filter	9,620	18	28	0.350	15.5	5

When γ = Unit weight (kN/m^2), E = Young's modulus(kN/m^2), ν = Poisson's ratio, φ = Friction angle (°), c = Cohesion (kN/m^2), ψ = Dilatancy angle (°)

Table 2. Properties of soil in Mae Ngat Dam (continue)

Zone	Permeability (cm/sec)	Permeability Ratio
Clay Core	0.13 x 10-6	1
Random	0.96 x 10-6	1
Miscellaneous	0.94 x 10-6	1
Filter	1.3 x 10-4	1

Instrumentation

With the cooperation of Royal Irrigation Department, the dam instrumentations (accelerometers) were installed to measure the acceleration at Mae Ngat Dam in January 2014 in the middle, on the crest of the dam and the mountain next to it as shown in Fig. 3.

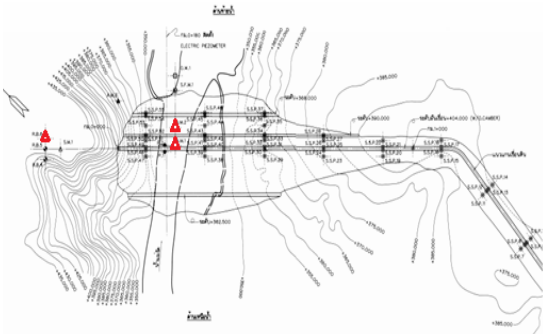

Fig. 3 Position of Accelerometer installation

The accelerometer model is the 130-SMA (Standard) (Fig. 4). The collected data from installed instrument can be output in Acceleration-Time graph. The Peak Ground Acceleration (PGA) can be analyzed at time period = 0.01. For the Chiang Rai earthquake (magnitude 6.3 on Richter scale), PGA can be measured equal to 0.187 m/s^2 or 0.019g (Fig. 5).

Fig. 4 The accelerometer model

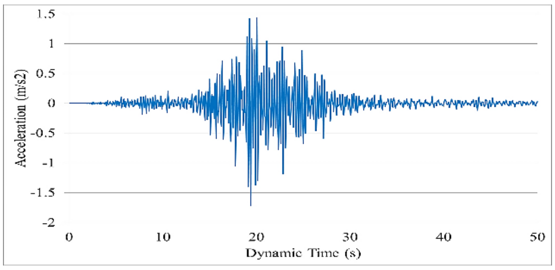

Fig. 5 The acceleration-time graphs from accelerometer.

From the earthquake (magnitude 6.3 on the Richter scale), which has a distance from the epicenter to Mea Ngud Somboon Chon Dam about 110 kilometers, shown in Fig. 5. The acceleration in the dam can be measured while the earthquake acted to the dam. The acceleration-time data records are shown in Fig. 6.

Fig. 6 the distance between the Epicenter to Mea Ngud Somboon Chon Dam

For this event. The analysis results from Global CMT Catalog conclude that the type of fault is strike slip and show the parameter of strike, dip, slip and moment tensor, as shown in Fig. 7.

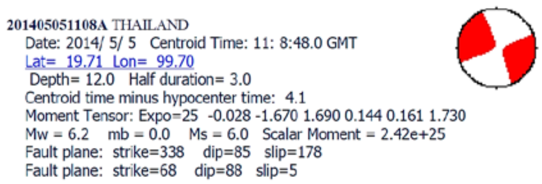

201405051108A THAILAND
Date: 2014/ 5/ 5 Centroid Time: 11: 8:48.0 GMT
Lat= 19.71 Lon= 99.70
Depth= 12.0 Half duration= 3.0
Centroid time minus hypocenter time: 4.1
Moment Tensor: Expo=25 -0.028 -1.670 1.690 0.144 0.161 1.730
Mw = 6.2 mb = 0.0 Ms = 6.0 Scalar Moment = 2.42e+25
Fault plane: strike=338 dip=85 slip=178
Fault plane: strike=68 dip=88 slip=5

Fig. 7 Analysis of earthquake mechanisms from Global CMT Catalog [4].

THEORY

In this research was conducted to study the appropriate model for attenuation equation in the northern part of Thailand. The previous research, Nutapong [5] studied the attenuation model and concluded that the equations of Abrahamson and Silva [6], the one of the NGA model developed from the Abrahamson and Silva model (1997), is suitable for use to analyze the attenuation model in the northern part of Thailand.

So the Abrahamson and Silva equation shows in Eq. (1).

$$ln(PGA) = f_{base} + f_{fault+AS} + f_{site} + f_{TOR} + f_{dist} \quad (1)$$

The 1st function is the variant of the magnitude and distance term (f_{base}), as shown in Eq. (2).

$$a_1 + a_4(M - c_1) + a_8(8.5 - M)^2 + \left[a_2 + a_3(M - c_1)\right]\ln\left(\sqrt{R_{rup}^2 + c_4^2}\right) \quad (2)$$

The 2nd function is the pattern of impact fault and aftershocks ($f_{fault+AS}$) as Eq. (3).

$$a_{12}F_{RV} + a_{13}F_{NM} + a_{15}F_{AS} \quad (3)$$

The 3rd function is the soil characteristics that set (f_{site}), shown in Eq. 4.

$$(a_{10} + bn)\ln\left(\frac{V_{s30}}{V_{LIN}}\right) \quad (4)$$

The 4th function is the effect of depth to the moving plane (f_{TOR}), as Eq. 5.

$$a_{16}F_{RV} + a_{17}(1 - F_{RV})\left(\frac{Z_{TOR} - 2}{8}\right) \quad (5)$$

The 5th function is the affected for small to medium earthquake at long distances (f_{dist}), shown in Eq. 6.

$$a_{18}(R_{rup} - 100)(6.5 - M) \quad (6)$$

When M=Moment magnitude, R_{rup}=Rupture distance (km), R_{jb}=Joyner-Boore distance (km), R_x=Horizontal distance (km) from top edge of rupture, Z_{top}=Depth-to -top of rupture (km), F_{RV}=Flag for reverse faulting earthquakes, F_{NM}=Flag for normal faulting earthquakes, F_{AS}=Flag for aftershocks, F_{HW}=Flag for hanging wall sites, Dip=Fault dip in degrees, V_{S30}=Shear-wave velocity over the top 30 m (m/s) $Z_{1.0}$ =Depth to V_S=1.0 km/s at the site (m), $\hat{PGA}_{1100}$=Median peak acceleration (g) for V_{S30}=1100 m/s and W=Down-dip rupture width (km). The value for the Peak Ground Acceleration (PGA) that comes from the definition of Abrahamson and Silva (2008)

Table 3. The coefficient of Peak Ground Acceleration (PGA) [4]

c_1	c_4	a_3	a_4	n	V_{LIN}	b	a_1	a_2	a_8
6.75	4.5	0.265	-0.231	1.18	865.1	-1.186	0.725	-0.968	0

a_{10}	a_{12}	V_{S30}	a_{13}	a_{15}	a_{16}	a_{17}	a_{18}
0.9485	-0.12	1100	-0.05	-0.405	0.65	0.6	-0.0067

Calculation of the PGA of an earthquake in Chiang Rai.

$$f_{base} = -4.28256$$
$$f_{fault+AS} = 0$$
$$f_{site} = -0.10833$$
$$f_{TOR} = 0.375$$
$$f_{dist} = -0.0134$$

$$\ln(PGA) = (-4.28256) + (0) + (-0.10833) + (0.375) + (-0.0134)$$
$$PGA = 0.017787$$

RESULTS

Attenuation Model

From using the Abrahamson and Silva equation in the attenuation model analysis, the PGA from Chiang Rai earthquake at Mea Ngud Somboon Chon can be resolve. The parameters that were used in the calculation consists of M is equal to 6.3 on the Richter scale, ZTOR equal to the depth of 7 km, RRUP than 110 km from the spot. The Chiang Rai earthquake occurred at Payao fault which is horizontal movement (Strike slip). The result found that the Peak Ground Acceleration (PGA) from calculation equal to 0.017787 g. And the percentage error of calculated PGA when compared to the PGA from measurement was 6.38.

Dynamic Analysis

The data used in the analysis came from the soils used in the dam construction which were tested in the field and the laboratory. The datas were used to create the model dam by using the Hardening-Soil model (2D shear plane) with the Finite Element Method to study the response of the dam under earthquake loads. The PLAXIS program [7] was used to analyze the model. The selected elements were triangular with 15 Nodes and 12 Stress points (Fig. 8) from Brinkgreve and Vermeer [8]. The water level in the dam was analyzed while the water retention level was normal. The water pressure was set to Hydrostatic Pressure. Then, the experiment was analyzed under Dynamic force.

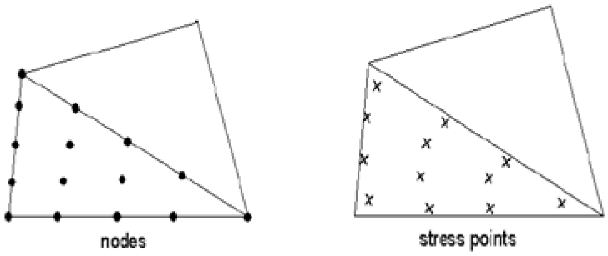

Fig. 8 Triangular elements with 15 Nodes and 12 Stress points.

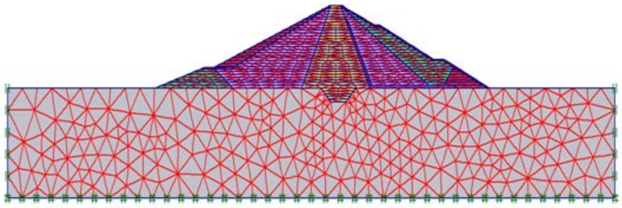

Fig. 9 Mae Ngat Dam model using finite element method (FEM) consists of 845 elements and 6947 nodes.

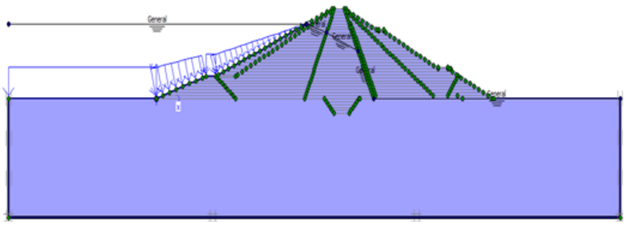

Fig. 10 The model using finite element method shows the Phreatic line of Mae Ngat Dam.

The 2 difference earthquake waves (short-time period; EQ1 and long-time period; EQ2) (Table 4) was used to analyze for study the behavior of pore water pressure, stress and displacement that occurs in the dam during earthquake occurs. The excess pore water pressure was considered at 37 m depth from the dam crest. The results were shown in Fig. 11-18.

Table 4 The data of seismic waves used in the analysis.

Earthquake	Victoria Mexico (EQ1)	Borrego Mth. (EQ2)
Year (A.C.)	1980	1968
PGA (g)	0.130	0.120
Time (sec)	15.58	40
Magnitude (M)	6.33	6.63
Distance (km.)	58.87	70.75
Predominant period	0.30	0.33
Type of earthquake	Short period	Long period

The study found that the pore water pressure in the dam was increasing during the seismic force acted to the dam. The long period of earthquake (EQ2) make the pore water pressure is worth more than the short period of earthquake (EQ1) when the PGA of two difference waves are similar. In Fig. 11-12, the range of changing in pore water pressure of approximately 102.5-107.5 kPa under EQ1 and 116.75-121.5 kPa under EQ2. The excess pore water pressure occurring in the dam of EQ1 is equal to 66.48 kN/m^2 and EQ2 is equal to 89.17 kN/m^2, respectively in Fig. 13-14.

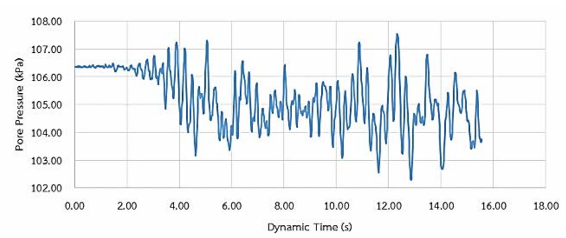

Fig. 11 The pore water pressure changing under short period earthquake (EQ1).

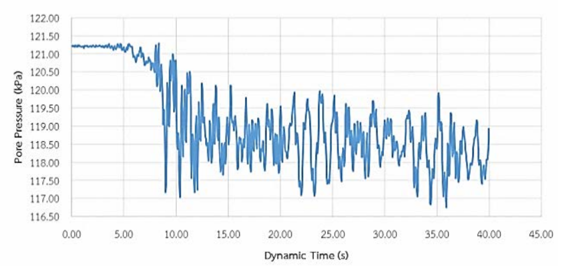

Fig. 12 The pore water pressure changing under long period earthquake (EQ2).

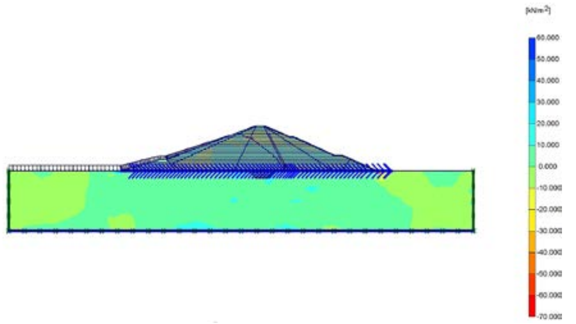

Fig. 13 The excess pore water pressure occurring in the dam under short period earthquake (EQ1).

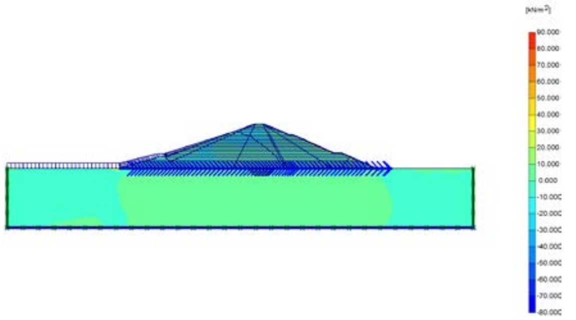

Fig. 14 The excess pore water pressure occurring in the dam under long period earthquake (EQ2).

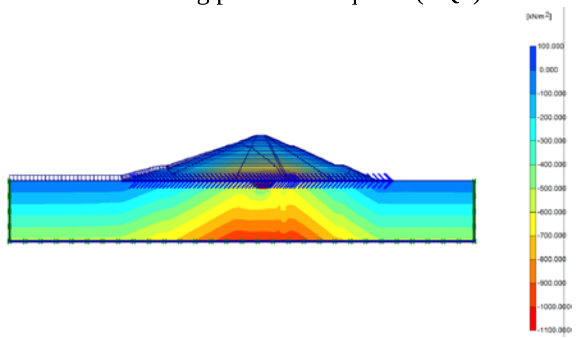

Fig. 15 The effective stress of the dam under short period earthquake (EQ1).

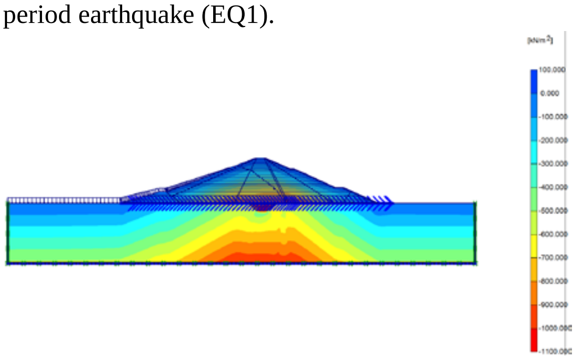

Fig. 16 The effective stress of the dam under long period earthquake (EQ2).

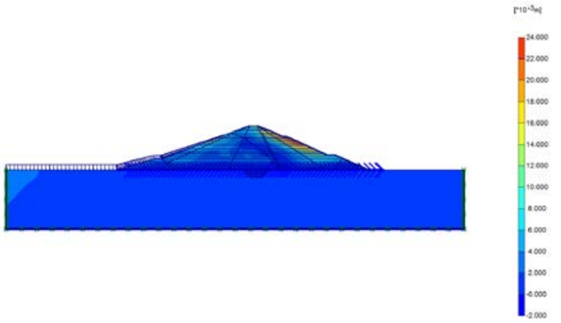

Fig. 17 The total displacements of the dam under short period earthquake (EQ1).

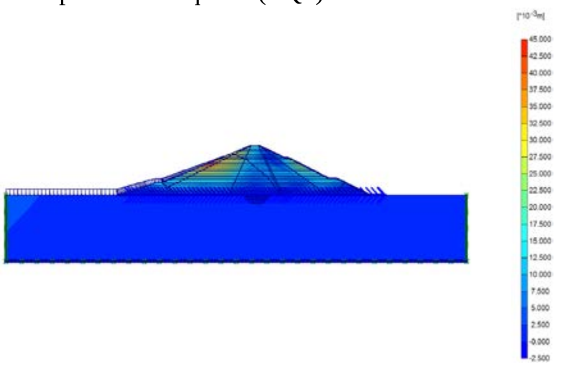

Fig. 18 The total displacements of the dam under short period earthquake (EQ2).

From the seismic force, not only caused the pore water pressure in the dam increase but it also affects to the effective stress. The maximum effective stress that could be calculated at core zone at the base of the dam during the earthquake was 1980 kN/m^2 for EQ1 and 1080 kN/m^2 for EQ2. In Fig. 15-16 show the shade area to present the effective stress in the earth zone dam.

The maximum total displacement equal to 23.23 mm and 43.01 mm for EQ1 and EQ2 condition respectively. The displacement from these earthquakes are shown in Fig. 17-18. The results showed that the maximum total displacement of the model affected by the short period of earthquake occurred in the downstream side of random zone and changed to upstream side when it affected by the long period of earthquake.

CONCLUSION

After comparing the analysis results with the measurement value from the accelerometer found that the attenuation model of Silva and Abrahamson (2008) can calculated the Peak Ground Acceleration (PGA) equal to 0.017787 g and the percentage error was 6.87.

From study the pore water pressure in the zone earth dam in dynamic condition by using finite element method found that the pore water pressure in dam under the long period earthquake wave (EQ2) is greater than the short period earthquake wave (EQ1). Under the seismic waves that have the PGA about 0.12-0.13g, they make the excess pore water pressure the pore water pressure increases about 12-15%, the maximum effective stress is equal to 1980 kN/m^2 and 1080 kN/m^2 for EQ1 and EQ2 respectively. When the pore water pressure and stress in the dam were changed by the seismic force, they are important factors that cause the displacement of the dam and cause a decrease in the strength of the soil. So the total displacement can be analyzed equal to 43.01 mm. and 23.23 mm. for EQ1 and EQ2 respectively.

ACKNOWLEDGEMENTS

Thanks to all the professors in the civil engineering department who provided fundamental knowledge on geotechnology and thank you to the Mae Ngat Dam Royal Irrigation Department, The Ministry of Agriculture and Cooperatives, the Construction Management Department, and the Regional Irrigation Office 1 Chiang Mai, Dam-instrument Ltd., Part., who was the supervisor, and for the information and convenience provided while conducting field work for this study.

REFERENCES

[1] Warnitchai P, Sangarayakul C and Ashford S, “Seismic Hazard in Bangkok Due to Long-Distance Earthquake”, Proceedings of the 12th World Conference on Earthquake Engineering, Auckland, New Zealand, 2000

[2] Attapon A, “Earthquake attenuation model for Chiang Mai subsoil”, Chiang Mai University, Thailand, 2011.

[3] Vigrom V, “The behavior of Mae Gnad earthfill dam during construction”, Kasetsart University, Thailand 1987.

[4] Global CMT Catalog Search, Available at: http://www.globalcmt.org/CMTsearch.html, 2016

[5] Nutapong H, “Analysis of the earthquake attenuation model to the 2014 Chiang Rai earthquake affected to Mae Ngud Somboon Chon dam in Chiang Mai”, The 21st National Convention on Civil Engineering, 28-30 June 2016, Songkhla, Thailand.

[6] Abrahamson N.A. and Silva W.J., “Summary of the Abrahamson & Silva NGA Ground Motion Relations”. Earthquake Spectra. 24, 1: 67–97, 2008

[7] PLAXIS 2D version 8.2, Version 8.0 Plaxis BV, Delft.

[8] R.B.J Brinkgreve and P.A. Vermeer., “Finite element code for soil and rock Analysis”, PLAXIS 8.0 manual, Balkema, Rotterdam, The Netherlands, 1998.

Sixth International Conference on Geotechnique, Construction Materials and Environment, Bangkok, Thailand, Nov. 14-16, 2016, ISBN: 978-4-9905958-6-9 C3051

VIBRATION CHARACTERISTICS OF DEFORMED STONE WALLS OF JAPANESE TRADITIONAL CASTLE

Minoru Yamanaka[1], Hayato Ishigaki[2], Katsuhiko Koizumi[2], Shuichi Hasegawa[1] and Hiroyuki Araki[3]

[1]Department of Safety System Construction Engineering, Kagawa University, Japan;
[2]Graduate School of Engineering, Kagawa University, Japan;
[3]Department of civil and Environmental Engineering, Chuo University, Japan

ABSTRACT

The non-destructive survey technique is required to estimate quantitatively the deterioration level of a stone wall at a traditional castle site. Microtremor measurement method is one of the non-destructive survey technique to estimate geotechnical characteristics of the ground. In this study, microtremors are measured at the stone wall of the Marugame castle, in order to evaluate vibration characteristics of deformed or non-deformed stone wall; the method to extract the deformation part of the stone wall is discussed based on the measurement results. The results showed that the value of H/V and H/H spectral ration increased with the increase of deformation of wall but also by the elevation of a measurement point. It was observed that the values of energy ratio were scattered widely. It is concluded that the H/H spectral ratio is a suitable index to indicated the deformation level of a stone wall. By setting the adequate threshold value, deformed walls were extracted roughly by the value of H/H spectral ratio at the Marugame castle.

Keywords: Microtremor measurement, stone wall, H/V spectral ratio, H/H spectral ratio, Japanese castle

INTRODUCTION

Japanese traditional castles have been often constructed at a crest of soil embankment. The wall face of the soil embankment was commonly protected with stones. These stone walls should be left for posterity as a part of cultural heritage.

However, stone walls deteriorated with ageing are affected sometimes seismic damage. For example, the stone walls of Sendai castle ruin and the Komine-Shirakawa castle ruin was collapsed by The 2011 off the Pacific coast of Tohoku Earthquake. Recently, stone wall of the Kumamoto castle was collapsed by The 2016 Kumamoto Earthquake.

In order to keep for posterity, a stone wall should be maintained according to its deterioration level. The deterioration level of a stone wall is ordinary judged based on visual observations in appearance condition.

In-situ tests such as boring and sounding test have been hardly used in survey of stone walls to avoid disturbance of a wall [1]. Especially the influence of in-situ tests for a stone wall which is collected in the cultural asset must be minimized from the viewpoint of cultural property protection. Therefore, the non-destructive survey technique is required to estimate quantitatively the deterioration level of a stone wall.

Microtremor measurement method is one of the non-destructive survey technique to evaluate vibration characteristics of the ground and structures [2],[3]. A predominant period is evaluated from spectrum of microtremor. S-wave response of the measuring target is estimated approximately based on the ratio of horizontal and vertical spectrum of the microtremor, H/V spectral ratio.

A few study on application of microtremor measurement method for evaluation of vibration characteristics of stone wall has been conducted, while the microtremor measurement method was sometimes applied to the evaluation of the ground and structures. For example, the microtremor measurement method was applied to the stone wall at the Kochi castle. The measurement results explained that the H/V spectral ratio was one of the deterioration index of the stone wall [4]. However, the microtremor of stone walls with highly deformation has not been

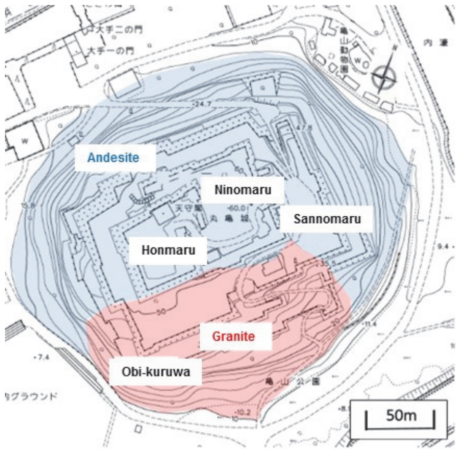

Fig. 1 The layout of the Marugame Castle plotted on geological map.

a) Swelling and opening (Sannomaru)

b) Habaki stone wall (south-west part of Honmaru)

Fig. 2 Typical deformed stone wall a) and Habaki stone wall b)

measured in the previous study.

In this study, microtremor measurement method is applied to the stone walls with highly deformation at the Marugame castle, Kagawa prefecture in Japan. The method to extract the deformation part of the stone wall is discussed based on the measurement results

OUTLINE OF MARUGAME CASTLE SITE

Figure 1 is the layout of the Marugame castle plotted on geological map [5]. The Marugame castle built in 1602, is located on the crest of Mt. Kameyama consisting of andesite and granite. The Marugame castle is composed of Honmaru (donjon), Ninomaru (first outer citadel), San-nomaru (second outer citadel) and Obikuruwa (outermost citadel). Each citadel is supported by a stone wall. The height of the whole stone wall is tallest in that of Japanese castle.

Figure 2 shows typical deformation of stone wall observed at the Marugame castle. Figure 2a shows swelling of a wall face and opening of the joint between stones. The reason of these deformations are estimated to earth pressure and rain water seepage. 'Habaki' stone wall was built at the foot of stone walls in order to restrain the deformation of the walls, as shown in Fig. 2b.

Figure 3 shows a schematic of a cross section of typical stone wall at the Marugame castle. A stone wall composed of a wall face stone, a crushed stone zone, backfill and bed rock. The width of the crushed stone zone is assumed to be 1 to 2 m approximately.

MICROTREMOR MEASUREMENT OF A STONE WALL

The location of microtremor meters, McSEIS-MT NEO made by OYO corporation in Japan, are also shown in Figure 3. Microtremor meters were put directly on a wall face stone, a crushed stone and bed rock, which were named as MWS, MCS and MBR in this paper, respectively. The distance between MWS and MCS was 2 m approximately. MBR were typically put on the midpoint between a top of a wall and a toe of a wall behind in order to ensure to be reference point.

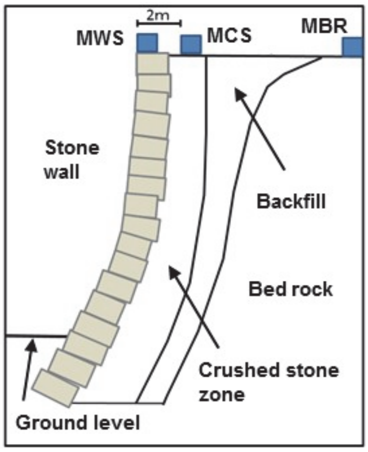

Fig. 3 Schematic of a cross section of a typical stone wall at the Marugame castle

Figure 4 shows the planform of microtremor meters location. The numbers of MWS, MCS and MBR are 133, 131 and 9, respectively. The distances of each MWS and each MCS were 5 m approximately.

The data of microtremor were measured at MWS, MCS and MBR at the same time. The measurement time was about 1 hour to avoid effects of vibration of pedestrians.

Microtremors were measured at the geological cliff of the Sendai castle in previous study [6], which showed that the ground motion amplification of the perpendicular direction to the cliff was larger than that of the horizontal direction. Referring to the previous study, N-S direction of a microtremor meter was set to the perpendicular direction to a stone wall in this study, N-S component of microtremors was analyzed mainly in order to observe the motion in perpendicular direction to a stone wall.

MICROTREMOR MEASUREMENT RESULTS AND DISCUSSION

Analysis method of microtremor records

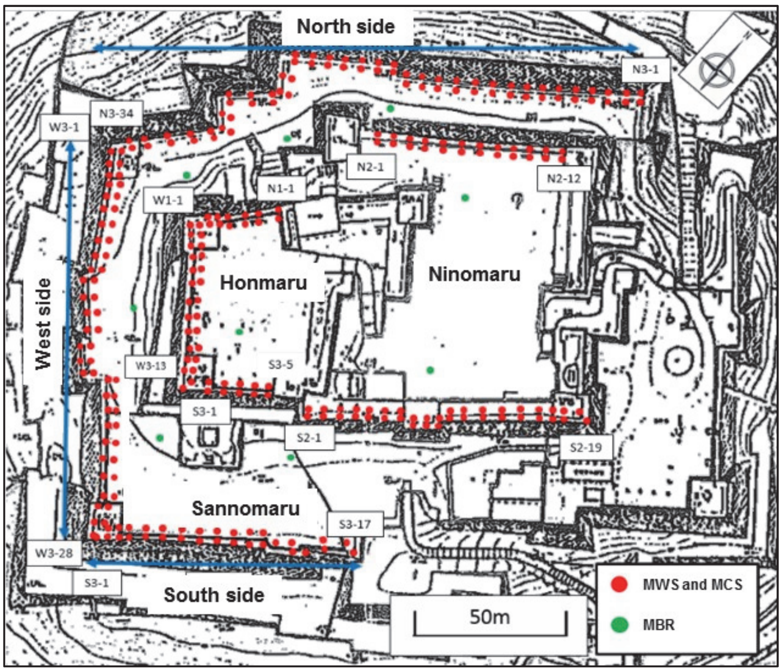

Fig. 4 The location of microtremor meters at the Marugame castle

Microtremor records were used to analysis the vibration characteristics of Marugame castle. All microtremor spectrum (Fourier amplitude spectrum) were obtained in a frequency range of 1 to 10 Hz, then those were smoothed separately with Parzen window with a band width of 0.3 Hz. In order to found the normalized result explaining clearly the relationships between vibration characteristic and deformation of stone wall, three kinds of normalized result of microtremor records, as H/V spectral ratio, H/H spectral ratio and energy ratio were calculated based on the microtremor records.

H/V spectral ratio and H/H spectral ratio

H/V spectrum is a ratio of horizontal component and vertical component of a Fourier amplitude spectrum in perpendicular direction to a stone wall (NS component of a microtremor). The H/V spectral ratio is the H/V spectrum obtained at MWS or MCS normalized by the H/V spectrum obtained at MBR. The H/H spectral ratio, defined in this study, is horizontal component of a Fourier amplitude spectrum obtained at MWS or MCS normalized by horizontal component of a Fourier amplitude spectrum obtained at MBR in perpendicular direction to a stone wall.

Figure 5 shows typical spectral ratios of H/V and H/H obtained at 2 sites where the stone walls were judged to be largely deformed (W3-27) and be slightly deformed (W3-10) based on the visual observation in appearance condition. Black circles shown in Figure 5 indicate the peak values of the spectra. The peak values of spectral ratio were obtained in all observation points in the same manner.

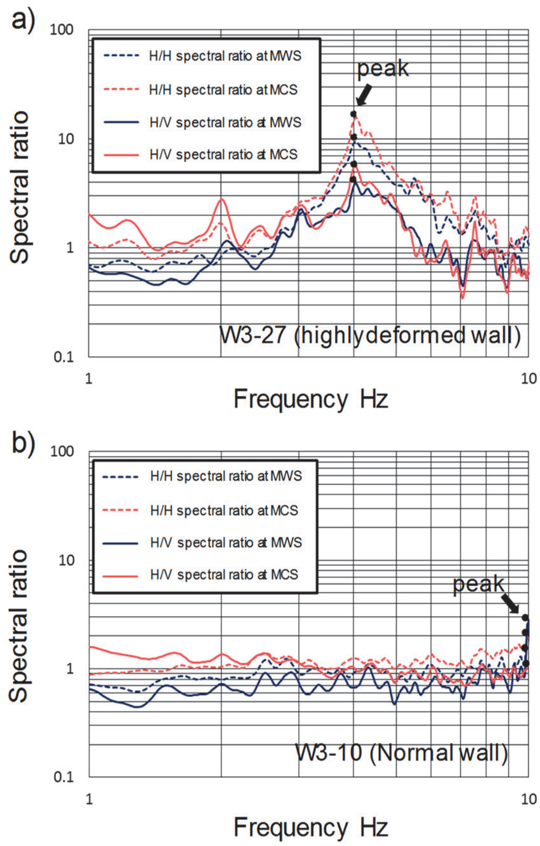

Fig. 5 Typical H/V and H/H spectral ratios obtained at W3-27 a) and W3-10 b)

Energy ratio

Yamauchi *et al.* [7] pointed out that the value of a Fourier amplitude which was obtained at unstable rock increased in all frequency range before the rock slid down. In order to clarify the increase of the amplitude values which were obtained at unstable stone of a stone wall, the value of energy was obtained by integration of Fourier amplitude spectra of 3 components, vertical and 2 horizontal components. Then the value of energy at MWS or MCS was normalized by the value of energy at MBR, which was defined as energy ratio in this paper.

Comparison of spectral ratios and energy ratio

The results of H/V spectral ratio and H/H spectral ratio are shown in Fig.6 and Fig. 7, respectively. The results measured at highly deformed site and small deformation site were plotted with red legend and blue legend, respectively.

The value of H/V spectral ratio obtained at highly deformed site was slightly larger than that at small deformation site, while the value scattered widely (Fig.6). A similar trend was observed also in the results of H/H spectral ratio (Fig.7). The variation of the value of H/H spectral ratio smaller than that of the value of H/V spectral ratio (Fig.6 and 7). The values of H/V and H/H spectral ratio increased with the increase of deformation.

In addition, the value of H/V spectral ratio obtained at Honmaru was larger than those at Ninomaru and Sannomaru (Fig.6). The elevation of Honmaru is higher than those of Ninomaru and Sannomaru. Hence, the value of H/V spectral ratio was affected possibly by the effect of not only deformation but elevation of a measurement point. On the other hand, the results of H/H spectral ratio were less affected by elevation of a measurement point. Therefore, H/H spectral ratio is assumed to be one of suitable index to extract highly deformed site.

The values of energy ratio obtained at all measurement points are shown in Fig. 9. The value of energy ratio obtained at MWS varies widely and is totally larger than that obtained at MCS. This trend explains the amplitude of micromotion at MWS is larger than that at MCS. The value of MWS which is remarkably large compared with the value of MCS might suggest existing of unstable stone in the stone wall. However, it is difficult to use the value of energy ratio for extraction of a deformed part of a stone wall.

Extracting method of a deformed stone wall by using H/H spectral ratio

As described above, the value of H/H spectral ratio was assumed to be one of an index to extract highly deformed site. The value of H/H spectral ratio was compared with the deformation state of a stone wall in order to conform the availability of this value.

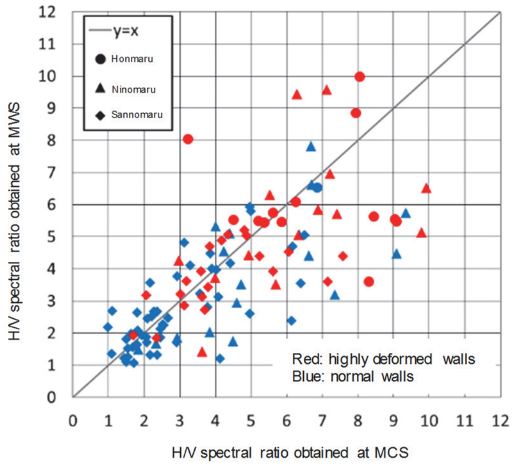

Fig. 6 H/V spectral ratio obtained at MWS and MCS

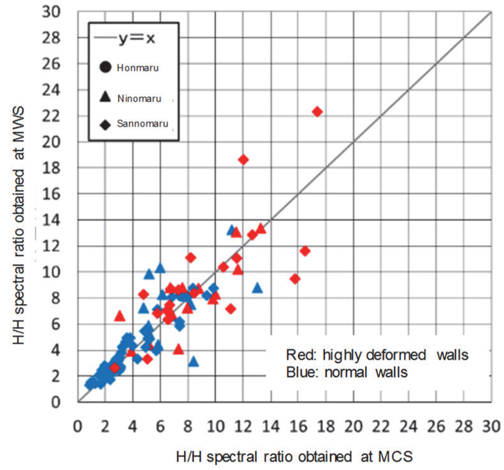

Fig. 7 H/H spectral ratio obtained at MWS and MCS

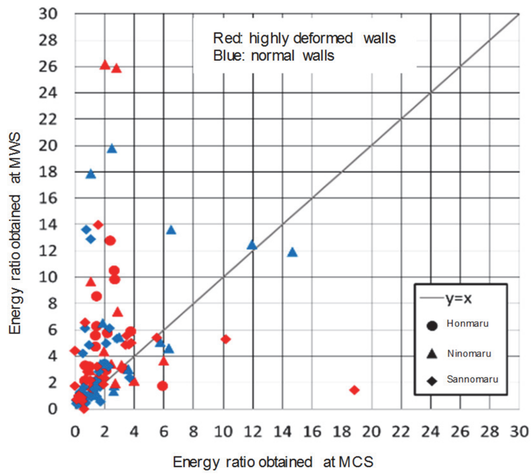

Fig. 8 Energy ratio obtained at MWS and MCS

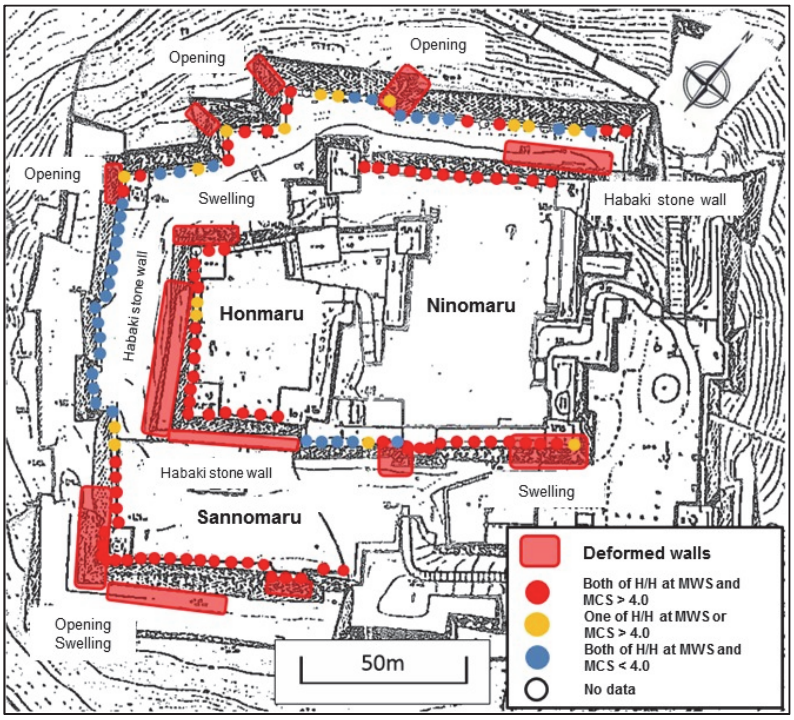

Fig. 9 The location of deformed wall and the distribution of the thresholded value of H/H ratio

Figure 9 shows the location of deformed stone wall. The 60% of the whole stone walls was judged as highly deformed by visual observations.

Based on this rate, upper 60 % of the value of H/H spectral ratio was assumed to be obtained at the highly deformed wall. The lower threshold value of H/H spectral ratio including upper 60 % was obtained as 4.0 in both cases of MWS and MCS, then the threshold value was set to 4.0 to extract highly deformed wall. Figure 9 also shows the distribution of the threshold value of H/H spectral ratio. The measurement points were classified into 3 types, both values at MWS and MCS exceeding 4.0 (red circle), one value at MWS or MCS exceeding 4.0 (yellow circle) and both values at MWS or MCS falling behind 4.0 (blue circle). The number of red circle, yellow circle and blue circle was 78, 16 and 32, respectively.

The deformed walls were observed at 47 sites in 78 red circles, 6 sites in 16 yellow circles and 2 sites in 32 red circles. When the both value of H/H spectral ratio at MWS and MCS exceed 4.0, the stone wall under the measurement point was highly deformed with a probability of about 60 %. This result suggest the deformed walls are extracted roughly by the value of H/H spectral ratio and adequate threshold value. Further study is required to reveal the setting method of threshold value.

CONCLUSIONS

In this study, microtremors were measured at the stone wall of Marugame castle in order to evaluate vibration characteristics of deformed or non-deformed stone wall. The following conclusions could be derived from the results of the microtremor measurement.

1) The values of H/V spectral ratio scattered widely and slightly increased with the increase of the deformation. The value of H/V spectral ratio was also affected possibly by the effect of the elevation of a measurement point.

2) The values of H/H spectral ratio increased with the increase of deformation. In addition, the values of H/H spectral ratio were less affected by the elevation of a measurement point.

3) The H/H spectral ratio is a suitable index to indicate the deformation level of a stone wall. The deformed walls are extracted by the value of H/H spectral ratio and adequate threshold value, 4.0 at the Marugame castle. When the both values of H/H spectral ratio at MWS and MCS exceed 4.0, the stone wall might be highly deformed with a probability of about 60 %.

4) It is difficult to use the value of energy ratio for extraction of a deformed part of a stone wall because the value scattered widely.

REFERENCES

[1] Nishida K., Ohshima K. Kanaoka M. and Kitazono K. “Geotechnical survey on the stone wall at Takamatsu castle”, in Proceedings of the 46th Annual Conference of the Japanese Society

of Civil Engineering, No. 4, 2009, pp.171‐172. (in Japanese)
[2] Yamanaka M., Hachimura T. and Hasegawa S. “Estimation of thickness of landfill by geophysical exploration methods at illegal industrial wastes disposal site”, Proceedings of 4th International Conference on Geotechnique, Construction Materials and Environment; GEOMATE2014, Brisbane, pp.232-237, 2014.
[3] Putra R.R., Kiyono J., Yoshimoto Y., One Y. and Syahril, “Determined soil characteristic of Palu in Indonesia by using microtremor observation”, International Journal of GEOMATE, Vol.10, No.2, pp.1737-1742, 2016.
[4] Yamanaka M., Nishiwaki D., Koizumi K. and Hasegawa S. “Detection of dynamic unstable point of stone wall at Kochi Castle by microtremor”, Proceedings of 50th Annual Conference of Japanese Geotechnical Society, 2015, pp. 203–204 (in Japanese).
[5] National Institute of Advanced Industrial Science and Technology, Geological Survey of Japan, “Geological map display system Geomap Navi”, https://gbank.gsj.jp/geonavi/geonavi.php#latlon/16,34.28567,133.80458
[6] Motosaka M. and Watanabe T. “Ground vibration characteristics of geological cliff structure at the Sendai castle site based on microtremor and earthquake observations and prediction of strong ground motion spectra for past earthquake”, Journal of Structural Engineering B, Architectural Society of Japan, Vol.47B, 2001, pp.167–172. (in Japanese)
[7] Yamauchi Y., Jiang Y. and Tanabashi Y. “Monitoring management of the unstable rock blocks aimed at the changes of a dynamic characteristic”, Proceedings of symposium on geological environment and geotechnical survey, Japanese Geotechnical Society, 2006, pp.21–26. (in Japanese)

DETERMINATION OF THE POST-CYCLIC YIELD STRENGTH AND INITIAL STIFFNESS OF TWO PEAT SOILS

Adnan Zainorabidin[1], Habib Musa Mohamad[2]
[1]Faculty of Civil and Environmental Engineering, Universiti Tun Hussein Onn Malaysia, Malaysia[2]

ABSTRACT

The post-cyclic yield shear strength and initial stiffness of a peat soil after subjecting to cyclic loading is a major topic in this study. Due to the effects of cyclic loading, post-cyclic shear strength decreases lower than its initial strength. A series laboratory static and cyclic triaxial test followed by post-cyclic monotonic tests carried out to determine the yielding parameters. Tests were carried out on the undisturbed samples taken from Parit Nipah, Johor and Lumadan, Sabah within west and east Malaysia peat soils. Post-cyclic loading test conducted with effective stress 100 kPa with frequency 1.0Hz. The initial stiffness is the initial tangential modulus with yield shear strength was half of the deviator stress in which two tangential lines intersect. The post cyclic yield shear strength of undisturbed peat soil is considerably lower compared to static at the axial strain of only 1.4% and 1.5%. The Parit Nipah and Lumadan peat are classified as Hemic.

Keywords: Post-cyclic, Peat, Yield shear strength, Initial stiffness

INTRODUCTION

Peats occur as extremely soft, wet and unconsolidated surficial deposits. Peats are geotechnically problematic due to their high compressibility and low shear strength [1]. In a moderate load increment, it may lead to large volume changes that shows high compressibility. Deep peats exhibit high compressibility, medium to low permeability, low strength and volume instability [2]. Peats are also characterized by high initial void ratio, organic content and water holding capacity [3].

Since the main component is an organic matter, peats are very spongy, highly compressible and combustible in characteristics [4]. These characteristics make the peats to pose its own distinctive geotechnical properties as compared to other inorganic soils like clay and sandy soils which are made up of only soil particles [3]. Peats which are formed from the accumulation of organic materials over thousands of years, are characterised by its high water content, compressibility and low shear stiffness and shear strength [5]. However, the overburden pressure of peats are very low [6].

Nonetheless, the effective shear strength of peat soils are essentially a frictional material and that it behaves closely in accordance with the principles of effective stress. Past researchers conclusively explained that standard tests that consolidates undrained triaxial test with the measurement of pore water pressure does not required over 50% axial strain to fail [6]. The undrained shear strength (su) refers to the strength of soil in situations where the excess pore water pressures developed during shearing cannot dissipate and failure takes place [7].

Post-cyclic behaviour of soil is generally considered to depend on the maximum strain developed during cyclic loading [8]. Post-cyclic as tests carried out on the sample by allowing the cyclic pore pressure to develop during cyclic loading to either dissipate or without dissipation [9]. While the samples are then subjected to post-cyclic monotonic loading without dissipation of cyclic pore pressure. Post-cyclic monotonic shear strengths were evaluated after various numbers of cycles of dynamic loading [10].

The studies of post-cyclic behaviour of soils includes the loss of static undrained shear strength and strain softening of soils under cyclic loads [11]. There is a considerable reduction in the undrained strength after cyclic loading [12]. There were effects from the number of loading cycles on the test respectively involved. Similar trends were observed for the test, and it shows that there were increases with continuing loading cycles from 1 to 100 cycles [9]-[13] findings.

The initial stiffness is the initial tangential modulus, which is in turn the slope of the curve of deviator stress versus axial strain at the axial strain of 0%. To get the yield shear strength, two tangential lines were plotted [14]. The yield shear strength was half of the deviator stress at an axial strain, in which those two tangential lines intersect [15]. The shear strength and stiffness at small deformation were called as yield shear strength and initial stiffness while, the shear strength and stiffness at large deformation were called as undrained shear strength and secant modulus, respectively.

Figure 1 shows the illustration of method for determination of yield shear strength (S_y) and initial stiffness (E_i) suggested by Wang (2011). The initial stiffness is the initial tangential modulus, which is in turn the slope of the curve of deviator stress versus axial strain at the axial strain of 0%. Two tangential lines were plotted to get the yield shear strength. The yield of shear strength was half of the deviator stress at an axial strain and intersect with two tangential lines [15]. This research work deals with a study on the post cyclic behaviour of peat soils analyzed using dynamic and static methods. The application of effective stresses and frequencies are critically reviewed using triaxial tests.

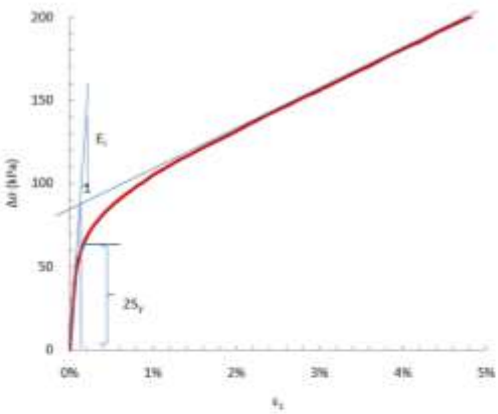

Fig. 1 Determination of yield shear strength and initial stiffness (Wang, 2011).

A series of triaxial tests were carried out to investigate the influence of dynamic loading on shear strength. The post-cyclic yield shear strength and initial stiffness of peat soil after subjecting to cyclic loading is presented in this research. The procedure used to determine the stress-strain threshold is proposed using the reduction of post-cyclic strength after 100 cycles of loading.

MATERIAL AND EXPERIMENTAL METHOD

This paper had conducted investigation on the post-cyclic shear strength of peat soil. All tests have been conducted using undisturbed peat soil specimen. The sampling location was located in Parit Nipah, Johor and Lumadan, Beaufort, Sabah. Ground water table was found at the depth of less than 1 meter during the sampling. The soil was excavated to a depth of 0.5 m below the ground surface and numbers of tube sampler with the size of 50mm diameter and 100mm height were pushed slowly into the soil. The undisturbed peat soils were waxed both at the end of the tubes and sealed with the aluminium and plastics to prevent the loss or gain of moisture. Jolting during transport was avoided.

The samples were kept in the laboratory under constant temperature in the air conditioned room. Dynamic triaxial apparatus or popularly known as Dynamic Triaxial Testing System (ELDYN) was used in the determination of shear strength of peat soil using an electronic controlled system. Sample preparation for the post-cyclic triaxial test is similar to the monotonic test. The specimens was mounted on the base of the pedestal sealed with a rubber membrane and ends with filter paper and porous stone at each end. All samples were consolidated 100 kPa effective confining stress and cyclic tests were performed under 1.0 Hz frequency in order to determine the shear strength. The index properties tests conducted on undisturbed specimens.

Monotonic loading was seriate applied at a 0.10mm/minute loading rate, and lasted till the soil specimens exhibited an axial strain of 20%. The specimens were subjected to 100 cycles. After cyclic loading, the specimens were immediately subjected to post-cyclic loading or known similar to standard consolidated undrained triaxial monotonic loading to failure.

Peat sample was obtained from Malaysia peat deposit area. Under reserved land area and far from agricultural activity. As seen in Table 1, the index properties of Parit Nipah fairly significant that natural moisture content is about 593% higher than Lumadan peat about 455.51%. The natural water content of peat in Malaysia ranges from 200 % to 700 % and with organic content in the range of 50 % to 95 % [1]. Therefore, the recorded values for Parit Nipah and Lumadan fulfil this statement. Specific gravity recorded 1.3 for Parit Nipah and Lumadan recorded 1.37 were within the range as reported by [1]. In addition to basic characterization tests, the Parit Nipah and Lumadan peat identified as Hemic.

Table 1 Index properties of peat soil

Properties	Lumadan	Parit Nipah
Moisture content, %	455.51	593
Liquid limit w_l, %	211	243
Specific Gravity, G_s	1.37	1.3
pH test	4.3	4.0
Organic Content, %	95.51	95.6
Fiber Content, %	66	38.5
Von Post Scale	H7	H5

DETERMINATION OF YIELD STRENGTH AND INNITIAL STIFFNESS

In order to evaluate the post-cyclic yield strength and initial stiffness, an extensive series of static and cyclic tests were carried out on large 50 mm diameter cylindrical specimens of peat soil materials using consolidated undrained triaxle tests and followed by post-cyclic shear test after cyclic loading. This paper presented the behaviour of peat soil subjected cyclic loading and effect to post-cyclic shear strength while compared to static results.

The shear strength and stiffness at small deformation were called as yield shear strength and initial stiffness, respectively and the shear strength and stiffness at large deformation were called as undrained shear strength and secant modulus [14]. This research carried out to study the shear strength and stiffness at small deformation. Static results are compared to the post-cyclic shear strength and stiffness. The reduction of shear strength and stiffness measured and there are significant behaviour when peat imposed with cyclic loading.

Figure 2 shows the consolidated undrained static results for both sample. Parit Nipah peat has maximum shear strength at 92.04 kPa and higher than Lumadan peat where about 58.44 kPa. The variations of index properties of both sample resulting in different shear strength property. The West Malaysia peat moisture content varied in the ranges 676.30% to 735.45% [16] while, 710.44% [17], 460% [18]. Undoubted, tropical peat has high water content and most of peat deposit are in moderately decomposed condition. However, the shear strength of intact peat is made up of interparticle friction as well as tension in the peat fibres [19].

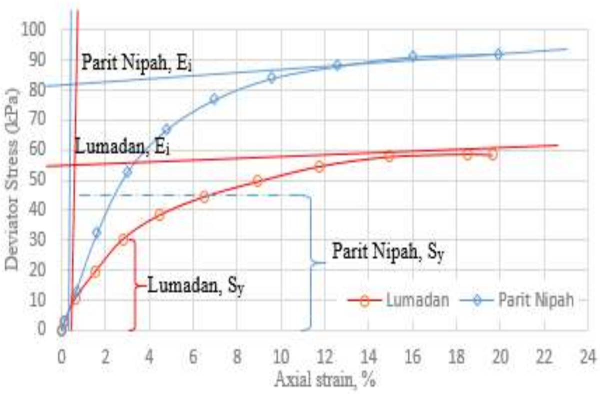

Fig. 2 Consolidated undrained static results

This study focuses on the shear strength and initial stiffness of peat soil in post-cyclic behaviour. Figure 3 shows the results of consolidated undrained post-cyclic for both sample. This test carried out after 100 numbers of cycles in dynamic stage. This test similar to static test arrangement. From the results, it can be seen clearly that, the shear strength of peat significantly decreased when subjected to cyclic loading. This statement in line with [16] where, the shear strength of peat soil decreased after 100 number of cyclic loading in post-cyclic compared to the monotonic tests and post-cyclic peak shear strength decreased substantially with frequencies applied.

Table 2 indicates the initial stiffness and shear strength (Sy) results for static and post-cyclic test conducted. In post-cyclic, Lumadan peat shear strength 21.55 kPa, decreased compared to static about 29.37 kPa. This reduction of shear strength Lumadan peat fairly lost in shear strength about 26.63% from the initial strength. Parit Nipah peat in certain patterns keep popping up in same behaviour. Those relationship offers decreases in shear strength after subjected to cyclic loading. Initial shear strength of Parit Nipah peat 46.02 kPa, decreased to 60.13% and remaining shear strength about 18.35 kPa. The static undrained shear strength decreased significantly after 15 loading cycles and softening behaviour occurred when the specimen exhibited ± 1.5% axial strain [10].

The initial stiffness (E_i) of both samples expressly decrement in post-cyclic compared to static results. The reduction of initial stiffness of Lumadan and Parit Nipah peat about 60.80% and 31.92%, respectively. The initial stiffness slope tangential get passes through the curve of deviator stress and pointed 10.45 for Lumadan peat and 10.73 for Parit Nipah.

Tangential slope for both sample almost closed where the curves derived from deviator stress in post-cyclic notched same patterns. The decrement of initial stiffness due to cyclic loading. On the other hand, if peat soil has experienced cyclic loading, the deformation of soil structure and alteration of void will resulted in decreasing in yield shear strength.

The existence of yield strength, where softening starts, is determined from post-cyclic tests. The level of post-cyclic yield strain occurred in ±0.62% of axial strain for Parit Nipah peat and ±0.58% for the undisturbed peat soils. The shear deformations increase rapidly in post-cyclic, exceeding the curves after 9%. The reduction properties of initial stiffness and yield shear strength due to soil softening during cyclic loading. Softening behaviour occurred after 12 cycles, in this study the softening behaviour outgrow at 100 number of cycles [10].

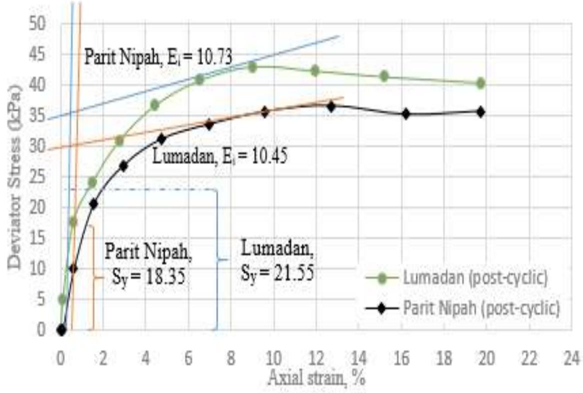

Fig. 3 Consolidated undrained post-cyclic results

Table 2 Initial stiffness and shear strength results for static and post-cyclic

Test	Location	Initial stiffness (E_i)	Shear strength (S_y)
Static	Lumadan	26.66	29.37
	Parit Nipah	15.76	46.02
Post-cyclic	Lumadan	10.45	21.55
	Parit Nipah	10.73	18.35
Reduction (%)	Lumadan	60.80	26.63
	Parit Nipah	31.92	60.13

Yield shear strength decreases by the number of cyclic loadings, and exceeds a failure limit in 100 cycles with 9% and 12% of an axial strain for Lumadan and Parit Nipah peat. Allowing the deviator stress developed an increase during post-cyclic loading, initial stiffness decrease significantly and more pronounced in knee point at the axial strain of only 1.4% and 1.5% intersect in turn the slope of the curve of deviator stress until the end of the test.

CONCLUSION

In summary, the main contributions to research in the determination of the post-cyclic yield shear strength and initial stiffness of Lumadan and Parit Nipah peat soil can be included as follows:

1. The post cyclic yield shear strength of undisturbed peat soil is considerably lower compared to static while cyclic loading are imposed to specimens after 100 numbers of cycles.
2. The initial stiffness of post cyclic of peat soil is governed by the softening behaviour that occurred when the specimen exhibited ± 1.5% axial strain.
3. The level of post-cyclic yield strain occurred in ±0.62% of axial strain for Parit Nipah peat and ±0.58% for the undisturbed peat soils.
4. Cyclic loading causes deformation of soil structure and alteration of void will resulted in decreasing of yield shear strength.

REFERENCES

[1] Huat, B. B.K. (2004). Organic and Peat Soils Engineering. Universiti Putra Malaysia Press, Serdang, Malaysia, pp. 20-80.

[2] Wong L.S, Hashim R. and Ali F.H (2008). Strength and Permeability of Stabilized Peat Soil.

[3] Deboucha S. Hashim R. and Alwi A. (2008). Engineering properties of stabilized tropical peat soils. Electron. J. Geotechn. Eng., 13E.

[4] Shafiee A., Scott J. B. and Jonathan P. S. (2013). Laboratory Evaluation of Seismic Failure Mechanisms of Levees on Peat. Department of Civil and Environmental Engineering University of California, Los Angeles. Report UCLA-SGEL 2013/04 Structural and Geotechnical Engineering Laboratory Department of Civil & Environmental Engineering University of California, Los Angeles September 2013. Ph.D Thesis.Wang S. (2011). Postcyclic behavior of low-plasticity silt. A dissertation presented to the faculty of the Graduate School of the Missouri University of Science and technology. Doctor Philosophy.

[5] Boylan N. and Long M. (2012). Evaluation of Peat Strength for Stability Assessments. Proceedings of the Institution of Civil Engineers, Geotechnical Engineering. University College Dublin, Ireland. 166: 1-10.

[6] Gosling D. and Keeton P. (2006). Problems with Testing Peat for Stability Analysis. Peat Seminar. Edinburgh, 11 March 2008.

[7] Boylan N., Jennings P. and Long M. (2008). Peat slope failure in Ireland. Quarterly Journal of Engineering Geology and Hydrogeology 2008; v. 41; p. 93-108 doi:10.1144/14709236/06-028.

[8] Diaz-Rodriguez J. A., Moreno P. and Guadalupe S. (2000). Undrained Shear Behaviour of Mexico City Sediments during and After Cyclic Loading. 12 WCEE. 2000. 1653.

[9] Rakesh J. P., Nazeeh K. M., Robinson R. G. (2013). Post-Cyclic Behaviour of Clayey Soil. Indian Geotechnical Journal. March 2014, Volume 44, Issue 1, pp 39-48.

[10] Erken A. and M.B.C. Ülker. (2008). The Post-Cyclic Shear Strength of Fine Grained Soils. The 14th World Conference on Earthquake Engineering October 12-17, 2008, Beijing, China.

[11] Alex G. G. (2014). Shear resistance degradation of lime –cement stabilized soil during cyclic loading. Division of Soil- and Rock Mechanics Department of Civil, Architectural and the Built Environment Stockholm 2014. Independent thesis Advanced level (degree of Master.

[12] Yasuhara K., Hirao K. and Hyde A.F.L. (1992). Effects of cyclic loading on undrained strength and compressibility of clay. Soils and Foundations 32 (1), 100-116.

[13] Moses G. G. and Rao N. S. (2003). Degradation in Cemented Marine Clay Subjected to Cyclic Compressive Loading. Marine Georesources and Geotechnology. 21(1), 37-62.

[14] Wang S., (2011). Postcyclic behavior of low-plasticity silt. Department: Civil, Architectural and Environmental Engineering. Doctoral Dissertations.Paper 2009. Missouri University of Science and Technology

[15] Wood, D. M. (1990). Soil Behavior and Critical State Soil Mechanics, Cambridge University Press.

[16] Adnan Z. and Habib M. M. (2015). Pre- and Post-Cyclic Behavior on Monotonic Shear Strength of Penor Peat. Electronic Journal of Geotechnical Engineering. Vol. 20 (2015), Bund. 15. 6928.

[17] Zolkefle S. N. A. (2014). The Dynamic Characteristic of Southwest Johor Peat under Different frequencies. Degree of Master in Civil Engineering Thesis.

[18] Zainorabidin, A. and Bakar I. (2003). Engineering Properties of in-situ and Modified Hemic Peat Soil in Western Johore. In Proceedings of 2nd International Conference on Advances in Soft Soil Engineering and Technology (pp. 252 - 261). Putra Jaya, Malaysia.

[19] Michael T. H., Jitendra S. S. C. Derek M. S. and Lee B. (2011) Effect of fibre content and structure on anisotropic elastic stiffness and shear strength of peat. Canadian Geotechnical Journal, 2012, 49(4): 403-415, 10.1139/t2012-003.

PROMOTION OF ICT UTILIZATION BY ELECTRIC RESISTIVITY MANAGEMENT IN FLUIDIZATION TREATMENT PROCESS FOR GROUND IMPROVEMENT

Yasuhide Mochida [1], Indra Hardi [2]

[1] Professor of Department of Architecture and Urban Design, Graduate School of Science and Engineering, Ritsumeikan University, Japan; [2]Master Degree Student of Department of Architecture and Urban Design, Graduate School of Science and Engineering, Ritsumeikan University, Japan

ABSTRACT

This research introduced a new method for monitoring the quality of ground improvement body by measuring the electrical resistibility of the ground improvement body using the ICT device attached on the bucket mixer. This method shows the engineers the unevenness of electrical resistivity of the ground improvement body, which means imperfection in mixing process or inconsistency of the compound within the ground improvement body. The monitoring is intended to perform real-time two-dimensional cross-section observation of the ground improvement body. This method is expected to be useful to minimize the vague judgment in the decision-making process on the ground improvement stirring states.

Keywords: Ground improvement, electrical resistivity, shallow foundation, ICT

INTRODUCTION

In application of the fluidization treatment method for the ground improvement work, the most common method to make the final decision to ensure the performance of the ground improvement body are by confirmation of the rotation number or mixing device's tachometer and flow value of the stirrer control and also by visual observation of the engineers on the color and consistency of the mixture. However, it is difficult to confirm the entire parts of ground improvement body and it cannot be denied that there is a possibility of inhomogeneous mixture inside the ground improvement body.

With the utilization of the ICT (Information and Communication Technology), by performing management procedure by attaching an electrical resistivity sensor on the bucket mixer and measure the electrical resistivity of the ground improvement body, it is possible to monitor and determine the unevenness of the ground improvement body mixture and understand the performance of the ground improvement body in real-time.

FLUIDIZATION TREATMENT METHOD OF GROUND IMPROVEMENT

Figure 1 shows the flowchart of the ground improvement work. The first step is to perform a feasibility study such as building's shape, necessary loads to be transferred directly to the foundation and soil properties to perform a design process for ground improvement. Subsequently, perform an indoor compound examination using local materials and determine the design for the compound to be used on ground improvement work. Then perform construction plans at the execution stage, such as construction order and quality control and continued by inspection stage and completion of the construction process.

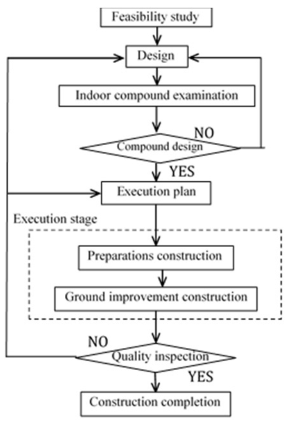

Fig. 1 Ground improvement work flow

Figure 2 shows the flow chart of the execution stage, which are describes as follows.

1. Confirmation of ground improvement position by planting steel rod in the boundary area..
2. Removing excessing unsuitable for construction soil by excavation work.
3. Excavation of soil within the boundary area of the ground improvement site to the expected depth.
4. Verify the support soil/ground by measure the geometry of the cavity. Determine the fluidization treatment agent volume to be use based on the calculated cavity's volume

5. Decide the reference line on the ground improvement area range using a backhoe and the backhoe's tip as the reference

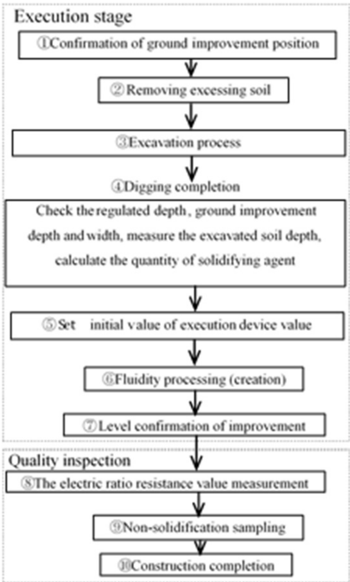

Fig. 2 Execution stage

6. Fluidization treatment process (construction)
7. Confirm the improved level of the ground improvement body.
8. Electrical resistivity measurement.
9. Sample collection for laboratory test.
10. Completion of the process.

ELECTRICAL RESISTIVITY APPLICATION

The Degree of Mixing Process Investigation by Electrical Resistivity Measurement

This investigation method is using the measurement of electrical resistivity of the soil and solidifying agent compound and estimates the mixing degree from the change of the electrical resistivity of the parts of ground improvement body.

Electrical resistivity is the opposite of the electric current flow, which is expressing the resistor for electric current. Cement, waterglass injection, bentonite clay, etc., are the main material used for construct the ground improvement. If the ion concentration of those materials is high, the electrical resistivity became lower and changes because of the mixing process with the soil. Therefore, if the compound perfectly stirred/mixed the electrical resistivity become lower and when there are a high value of electrical resistivity it may indicate that there are slumps or incompletely stirred compound at that part. This method allows engineers to verify the mixing degree of the ground improvement body with less time needed.

Electrical Resistivity Ratio

According to Ohm's law electric resistant ρ described by equations (1). With the measurement units follows; voltage (V): V, resistant (Ω): R, and electric current (A): I.

$$\text{Voltage}: E(V) = R \times I$$
$$\text{Electric current}: I(A) = \frac{E}{R}$$
$$\text{Resistance}: R(\Omega) = E/I \qquad (1)$$

Figure 3 shows the cone type sensor (4-electrode) that was used in a mixing investigation. This cone type sensor flows the electric current (A) from two of the four electrodes (outside electrodes) while the 2 electrodes located inside measuring the voltage. With knowing value of current and voltage, electric resistant and electrical resistivity can be calculated.

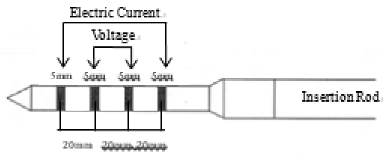

Fig. 3 Cone type sensor (4 electrodes type)

The cone type sensor have a diameter approximately 25mm, with the length of the sensor unit of 100mm, the electrode thickness of 5mm and spacing between the electrodes are 20mm.

Measuring Method (Insertion Rod Measurement Method)

Measurements of the electrical resistivity perform immediately after completion of stirring process or after the expected rotation counter number is satisfied, by sinking the cone sensor at certain points on the depth direction. Investigation method performs by suspending the sensor on the hydraulic shovel available at the construction site, and penetrates at a constant speed. Investigate two or three points in one area and control by make relationship between average moving value and depth distribution and between average electrical resistant value and depth distribution. The interval of measurement points is set to 10cm while one side of the investigation point decides using 1meter length triangle ruler marker and three investigation points decide using the range of 50cm equilateral triangle ruler.

Application Example of Construction Management by the Electric Resistivity Utilization Method

The examination conducted in five locations with different type of soil; Kanto loam soil on two location (Chofuyagumodai-Tokyo, Tokorozawa-Saitama (Pre fecture), sandy silt soil on one location (Nagai-Yamagata Prefecture), decomposed granite (DG) soil on one location (Koriyama-Fukushima Prefecture) and clay soil on one location (Nagaoka City-Niigata Prefecture).

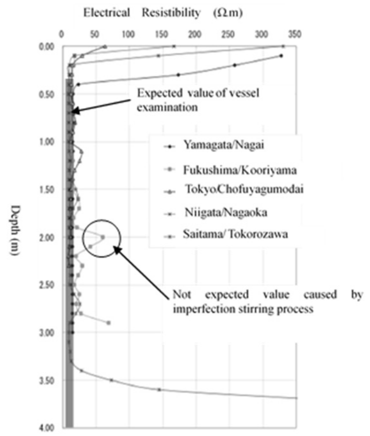

Fig. 4 Vessel Test Result

Cement-based solidifying material has been used to the ground improvement as an additive material with the addition of sandy silt and Kanto loam soil with an amount of 200~350 kg/m3. The basic process for ground improvement on this research is by performed solidifying process to several soil layers that need to improve and finally performed the fluidization treatment process to the entire part of ground improvement body. Vessel test has been performed at each position in order to set the target value for the mean electrical resistivity value due to fluidization process.

According to vessel test results (Figure 4), the target of electrical resistivity value of the improved body was set on 10 ~ 20 (Ω · m) and the average resistivity value of each investigation points has satisfied the expected value. The examination results in DG soil on Fukushima Prefecture and Kanto loam on Tokyo shows the big difference of average electrical resistivity value partially. Thus, there was imperfection of the stirring process and the value changed into expected range after another stirring process.

Variation of the Electrical Resistivity of the Final Stage in the Ground Improvement Work

Figure 5 shows the relationship between strength of ground improvement body and the coefficient of variation of the electrical resistivity value of the site core. Local soils are selected for experiment from total 31 locations: sandy soils (sand from three locations, DG soils from one location, fine sands from one location), clay group (clay from 11 locations, sandy silt from six locations, silt from three locations) and loam (Kanto loam from six locations). The strength of ground improvement body mixture in the site core was calculated using coefficient of variation of unconfined compressive strength after curing (material age of 28 days). Coefficient of variation of electrical resistivity is defined as coefficient of variation based on electrical resistivity value where the sample for compressive strength test was taken. In this construction method of ground improvement, coefficient of variation for the compressive strength was set at 30% as a target and experiment results has satisfied the target. On the other hand, the trend of coefficient of variation of the electrical resistivity is not due to the soil type, and the result satisfies the value of 20%.

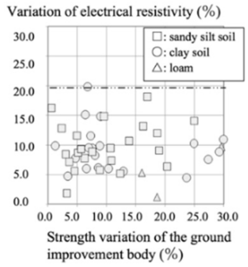

Fig. 5 Relation between electrical resistivity value and cement amount

Relationship between Compression Strength of Ground Improvement Body and Electrical Resistivity Value of Field Core.

Figure 6 shows relationship between strength of the improvement of the electrical resistivity and the field core. The strength of ground improvement body on full-length core is using uniaxial compressive strength after curing (28 days) and electrical resistivity of the location where the sample for uniaxial compressive was taken is used for electrical resistivity value. If the linear approximation formula and regression analysis in each three types of soil is calculated, the following formula is derived.

$(Sand) \quad y = -989.1x + 223 \qquad (2)$

$(Clay) \quad y = -12.7x + 3272 \qquad (3)$

$(Loam) \quad y = -42.3x + 3087 \qquad (4)$

Compressive strength is increased as electrical resistivity value increases is the mutual trend of every type of soil. In particular, this tendency is significant when sandy soil (Equation 2) is compared with clay and loam soil.

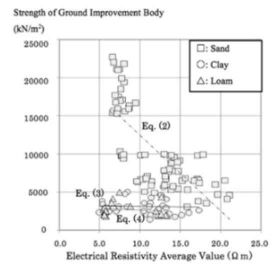

Fig. 6 Relation between electrical resistivity value and compressive strength of ground improvement body

ELECTRICAL RESISTIVITY APPLICATION OF ICT UTILIZATION IN CONSTRUCTION MANAGEMENT

Electrical resistivity measurements in the past research gave an example how to understand the ground properties by gathering electrical resistivity value at a specific location using the stationed electrical resistivity measurement sensor. The technology used in this research provides a method in how to understand the ground properties on a two-dimensional cross section of ground improvement body by measuring the compound's electrical resistivity using electrical resistivity sensor attached on moving bucket mixer in order to perform a stirring process. This paper shows the basic concept of promoting ICT technology described as follows.

· Made the possibility to observe the visually invisible underground situation
· Speeding up the performance identification by utilize the electric signal
· Allows instant observation by display method

Therefore, this technology application capable of enhancing certainty of ground improvement performance identification by eliminate the lack of the information on the performance on the conventional method by human eye visual observation and improve productivity by eliminating the ambiguous judgment of the stirring rotation counter number method. Finally, this technology is expected to reduce the misjudgment on the management process made by recent lack of skill engineers.

Fluidization Treatment Process of Ground Improvement Construction Management

Figure 7 shows diagram of wireless communication system and Figure 8 shows diagram of attached electrical resistivity sensor on the pail part of the bucket mixer. Mixing rotor and solidifying material liquid discharge device configures the pail part of the bucket mixer device to be used in this construction method. Furthermore, the pail part is equipped with depth gauge, tachometer, and an electric resistivity sensor, which has a function for transmitting the mixing situation of the mixture inside the ground improvement body to the surface.

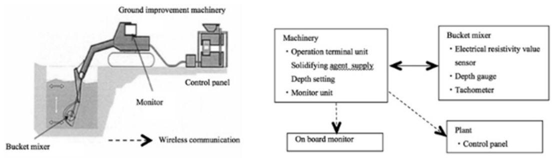

Fig. 7 Wireless communication system diagram

Monitoring procedure will be conduct by the operator using electric signals sent from equipment attached on the pail to the control unit. Operator judges the compound mixture condition of the ground improvement body based on information displayed on the monitor and able to understands the shape and the compound uniformity degree of the ground improvement body. Measured electrical resistivity value will be display on the monitor screen on different colors based on its value and divide the ground improvement body into 25cm x 25cm grid shape.

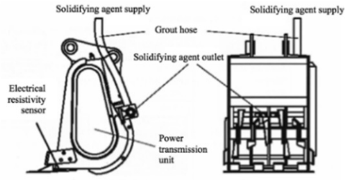

Fig. 8 Bucket mixer configuration

Calibration

Calibration procedure for the method and equipment describes as follows.

1. Put distilled water in the mud balance instruments to manage the specific gravity of the solidifying material liquid, ensure the specific gravity value is 1.0. Measure the specific gravity of the solidifying material liquid measured in mud balance instruments and ensure the specific value is 99%. Ensure the pail if the bucket mixer in the predetermined shape.
2. Store the solidifying material liquid into the vessel and ensure the value of electrical resistivity is less than 10Ω.
3. Inspection of the horizontal position movement and orientation of the bucket mixer by actual measurement and monitor observation as a reference and ensure the different is ± 5cm in 2 meters horizontal movement. As well for inspection of vertical movement, the different is ± 5cm in 1meter vertical movement.

Monitoring

Data including compound uniformity level displays on the monitor in real-time to be use for evaluating the process. Monitoring situation and electrical resistivity distribution show in photo 1. The electrical resistivity distribution in the entire of ground improvement body displays in the different color according to its value. The ground improvement body displays on cross section view in 25cm x 25cm grid form and the measured electrical resistivity appears in colored-dot shape. The stirring process completed if electrical resistivity distribution displayed uniformly in pink or yellow dot indicators.

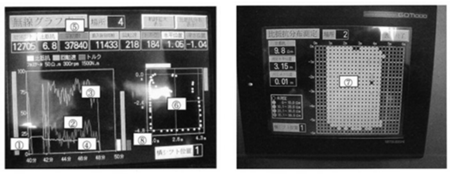

1. Quantity of solidification materials
2. Rotation torque
3. Rotation speed
4. Electrical resistivity value
5. Propeller blade rotation counter
6. Improvement trace
7. Electric resistivity value distribution
8. Ground improvement depth

Photo 1 Monitoring and the electric resistivity value distribution

Control Device

Figure 9 and Figure 10 show the depth gauge used for measuring the coordinates of the pail part of bucket mixer and ground improvement traces monitoring. The coordinate management procedure describes as follows.

1. Set the position of the pail from the length and angle of each arm using inclination sensor.
2. Define a reference line using one side of a backhoe inside area range of ground improvement and set the tip of the bucket mixer pail in this position.
3. From this position, calculate the pail part position by angle and length of each arms and display the trajectory.
4. Input the dimension of ground improvement area range and depth calculated from reference line, and display them on the monitor.

Ground improvement trajectory shows the outer periphery of the body and it is assumed as the maximum trajectory. Ensure that this maximum trajectory sufficiently satisfied the ground improvement body geometry by observing the monitor. Quality control performs by measuring electrical resistivity inside the ground improvement body using electrical resistivity sensor attached on the tip of bucket mixer pail. Ground improvement cross-section displays into 25cm x 25cm grids pattern and the electrical resistivity will be measured continuously at each grid so the change of its value can be observed in real-time. The construction control procedure describes as follows.

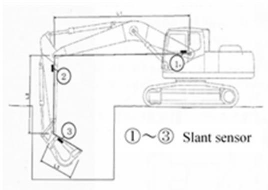

Fig. 9 Coordinated measurement

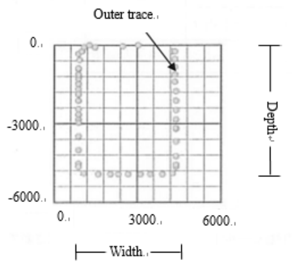

Fig. 10 Ground improvement trajectory

1. Electrical resistance measurement of solidifying agent liquid.

The value has tendency express the compound stirring state. Measure the solidifying agent resistivity prior to examination and assume it as the minimum value.

2. Electrical resistivity measurement of ground improvement body.

Measuring the electrical resistivity value of the entire ground improvement body, using a sensor attached on the pail part of the bucket mixer and performs monitoring process.

3. Monitor observation.

Electric signals sent by the sensor transmitted to the control unit cabin monitored. The operator will understand the stirring state of the ground improvement body compound by judging its condition based on the information displayed on the monitor.

Electrical resistivity value varies depending on the soil type, but in the homogeneous stirring/mixing state converge within 7 ~ 20Ωm. Hence, maximum value is set on 20Ωm. If the measurement value exceeds 20Ωm or there is significant variation seen in the resistivity value of the measurement in the depth direction, the existence of not completely stirred part is become a concern. In this occasion, re-stirring process must be performed immediately until the electrical value uniformly distributed within the expected range. Subsequently, perform a quality control process by measuring electrical resistivity value in the depth direction by inserting electrical resistivity sensor using insertion rod into the ground improvement body.

QUALITY CONTROL OF UNSOLIDIFIED SPECIMEN

Quality investigation of the ground improvement mixture due to fluidization treatment process is commonly conducted by performing unconfined compressive strength test of the specimens taken from solidified ground improvement body using core cutter or core boring. This method allows engineers to understand the performance of the ground improvement body at early stage and assuming the next progression.

However, in this research, sample is collected by collecting unsolidified specimens from ground improvement body and also allows collecting specimens by using both of remixing mold core and insert mold core. Subsequently perform comparison of compressive strength between remixing core and insert core, and estimating the strength of boring core due to remixing core, and shows that proposed method collecting sample using mold core was reliable.

Experiment on Performance Confirmation of Unsolidified Sampler

Experiment on performance confirmation is conducted in total 9 locations, which are loam in 6 locations, sandy silt in 1 location, silt in 1 location and sandy clay in 1 location. Terms and conditions of each of the ground improvement are W/C = 80 ~ 150 (%), additive amount of 250 ~ 300 (kg/m3), design strength criteria of 450 ~ 1050 (kN/m2) and the thickness of ground improvement body from 1.6 m to

4.5 m. As a reference, 3 locations from total 9 locations of boring core and remixing core was performed boring core (48 ϕ ~ 72 ϕ), remixing core (50 ϕ) and insert core (100 ϕ). Both of boring core and mold core was subjected to compressive strength test in moist air (20 ℃ ± 3 ℃) based on Japan compressive test standard (JIS A 108).

Strength comparison of boring core and the mold core

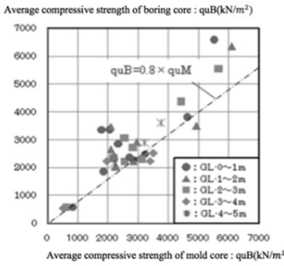

Fig. 11 Comparison of average compressive strength between mold core and boring core (remixing mold core)

Figure 11 shows the comparison of average compressive strength between mold core (remixing core) and boring core. The average compressive strength of mold core is roughly considered about 80% of the average compressive strength of the boring core.

Strength Comparison of Remixing Core and Insert Core

Figure 12 shows the comparison of average compressive strength between mold (remixing, insert core) and boring core. As been shown in previous research on compressive strength of the concrete core, the compressive strength and coefficient of variation of core's strength increase due decreasing in core's diameter, and on concrete core with maximum aggregate size (5 mm to 20 mm), its compressive strength decrease due to increasing in core's diameter. Compressive strength test result in this research also shows the trends that compressive strength of the insert core has more variation and compressive strength of remixing core has the higher value.

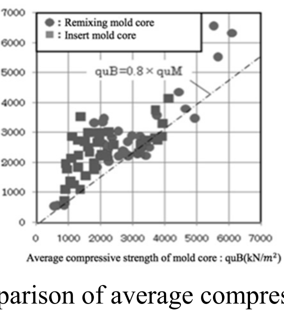

Fig. 12 Comparison of average compressive strength between mold core (remixing, insert core) and boring core

CONCLUSION

This research showed an example of practical utilization of ICT technology in construction management by investigating the two-dimensional cross-section monitoring to observe the mixing degree of the entire ground improvement body in real-time by electrical resistivity value measurement using devices attached on the pail part of bucket mixer. The technology is aiming for the realization of production improvement with adding a user-friendly device to deal with ambiguous judgment or inaccurate observation result made by the engineers in verifying the ground improvement body stirring states.

This research has proved that quality control using electrical resistivity measurement of ground improvement body provides great accuracy due to 2 dimensional monitoring of ground improvement body along with dot colored indicators that indicates electrical resistivity value of ground improvement body mixture.

Furthermore, by understanding the differences in electrical resistivity value due to soil type, relationship between cement amount and electrical resistivity value, and relationship between strength of ground improvement body and coefficient of variation of electrical resistivity, this method has satisfied targeted value of 30% on both of coefficient of variation and quality control.

In addition, due to mold core on unsolidified sample of ground improvement body and performed compressive strength test at early stage, with the sample taken at any depth, allows engineers to estimate the strength of ground improvement body at any material age.

REFERENCES

[1] "Design ground improvement and quality control guidelines for buildings", Japan Architecture Center,2006
[2] Sakai Y, "Quality control method (underground stake and consecutive underground walls) using electrical resistivity", Japanese Geotechnical Society, July 2007, the 42nd conference
[3] Mochida Y, "Quality control method (ground improvement and fluidity processing) using electrical resistivity", Japanese Geotechnical Society, July 2007, the 42nd conference
[4] Mochida Y, "A study about electric ratio resistance and it relations to mixture degree", Japanese Geotechnical Society, July 2008, the 43rd conference
[5] Tamura T, "Field experiment on the quality evaluation of improved body by electrical resistivity", Architectural Institute of Japan, May 2000, structure system papers no.531

GROUT PROPERTIES OF MICROPILE UNDER DIFFERENT SOIL CONDITIONS

Putli Yasmeen Nadeah M. Y.[1], Hassanel Zachary A.[2] Julinda Hena J.[3] Siti Aishah M. S.[2]

[1]Mariwangsa Maju Sdn. Bhd., Malaysia ; [2]Faculty of Engineering, Universiti Malaysia Sabah, Malaysia ; [3]STL Geotechnical Engineering Sdn. Bhd., Malaysia.

ABSTRACT: Micropiles application have grown widely as a foundation options especially for underpinning of existing structures, strengthening of foundations and supports for buildings and bridges. Buried underground, the grout of micropiles may encounter aggressive environment that may detrimental to its properties. The essential of this research is due to the increasing number of micropiling applications throughout countries and to investigate the grout properties of micropiles under different soil conditions through soil sample testing, water chemical testing and grout cube testing. This paper found that grout specimens cured in treated water which have higher sulfate content have the highest percentage of ettringite with 43.18% and 20% of the percentage of hydration products, specifically portlandite (Calcium Hydroxide) are the lowest compared to the other curing conditions. The formation of ettringite may develop tensile stress and micro cracks inside the grout cube, thus lead to strength loss and allow more sulfate ingress that can add into further deterioration. Conclusively, the grout cubes cured in untreated water with lower sulfate content are more likely to produce higher early and 28 days compressive strength.

Keywords: Micropile; Foundations; Grout; Sulfate;

1. INTRODUCTION

Micropiles had been used throughout the world since their development in Italy in 1952 (FHWA, 1997). The micropiling method was introduced in Malaysia in the early 1980s and gained acceptability since then particularly in difficult ground conditions, limited working area and treacherous limestone areas. However, there is only limited number of studies concerning micropiles especially in Malaysia.

The micropile must be designed to satisfy the general criteria of the foundations design which it must be located properly so as not to be adversely affected by outside influences (Liu and Evett, 2005). The outside influences that may affect the foundations are water, significant volume change, underground defects (caves, for example), frost and groundwater, adjacent structures and property lines. In accordance to the micropile design, grout plays the critical part of micropiles during its lifetime. Nonetheless, the study on micropiles and laboratory data are very few, thus the behaviour of the grout properties of micropiles under different soil conditions remains unclear.

The aims of this research are to study the mechanical properties of micropiles grout subjected under different soil conditions. After being casted in different soil conditions, the microstructures of the micropiles grout samples will be analyzed to study the effects of different environment towards its composition.

2. METHODOLOGY

In order to imitate the actual environments that will surround the micropiles grout, 16 test cubes are prepared and cured into 4 different conditions. The conditions are as follows:

i. Condition 1: Curing of 4 nos of test cube; water sourced from the daily water supply (treated water)

ii. Condition 2: Curing of 4 nos of test cube; water sourced from river (untreated water)

iii. Condition 3: Curing of 4 nos of test cube; sandy soil and immersed with water sourced from river (untreated water)

iv. Condition 4: Curing of 4 nos of test cube; sandy silt soil and immersed with water sourced from river (untreated water)

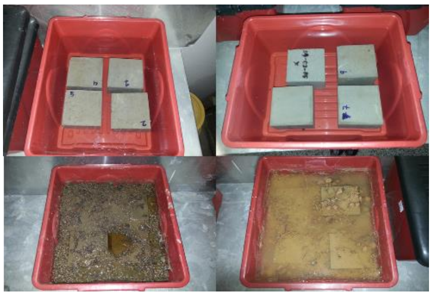

Fig. 1: (Top Left) Curing Condition 1. (Top Right) Curing Condition 2. (Bottom Left) Curing

Condition 3. (Bottom Right) Curing Condition 4.

Laboratory test conducted are divided into three groups namely soil sample testing, water chemical testing and cement grout testing. The grout cube testing is performed on 16 cement grout cubes both for 7 days and 28 days curing period. For soil sample testing, two soil samples were taken for analysis. There are four major tests conducted for the soil samples such as Sieve Analysis, Hydrometer Test, Atterberg Limits and Specific Gravity.

For water chemical testing, both treated and untreated water samples are analyzed in terms of sulfate content and chloride content. Water chemical testing were conducted to study the effect of the chemical contents in the two water samples towards the grout cube properties. The water chemical testing includes the Sulphate Content and Chloride Content.

Finally, the parameters of grout cubes are obtained from bulk density test, compressive strength SEM images and X-Ray Diffraction analysis for all grout cubes.

Table 1 Grout cube tagging

Condition	Days of Curing	Cube Tag
1 (Treated water)	7	C1a
		C1b
	28	C1c
		C1d
2 (Untreated water)	7	C2a
		C2b
	28	C2c
		C2d
3 (Untreated water + sandy soil)	7	C3a
		C3b
	28	C3c
		C3d
4 (Untreated water + sandy silt soil)	7	C4a
		C4b
	28	C4c
		C4d

3.

RESULTS AND DISCUSSION

3.1 Soil Sample Testing

3.1.1 Sieve Analysis

Based on visual observation, the soil samples for the purpose of conditions preparations as mentioned in methodology of research are expected to be sandy soil and clay soil. The position and shape of the grading curve determines the soil class and the soil sample No. 1 are classified as gravely sand.

3.1.2 Hydrometer Test

This soil sample No.2 are considered to be clay based on visual observation. The wet sieving procedure separate the silt and clay sized particles for hydrometer testing. The value of percentage finer (passing) is then plotted in the particle size distribution graph. From the graph, it was found that the soil samples are categorized as sandy silt. The soil sample can be further categorized by textural classification by referring to USDA Soil Textural Triangle, thus can be classified into silt loam category.

3.1.3 Atterberg Limits

Table 2 Summary of Attenberg limit test data

Summary	
Liquid Limit	35
Plastic Limit	14
Plasticity Index	21

The Atterberg Limits are carried out by Cassagrande method. The soil sample used for the condition 4 (Sample No. 2) has the average of Plastic Limit of 13.55% whereas the Liquid Limit is 34.16%. The soil samples are categorized as organic silt based on USCS (ASTM D 2487).

3.1.4 Specific Gravity

The first soil sample, Sample No. 1 is categorized as Sandy Soil and the value of the specific gravity is assumed from the range of the sandy soil which is from 2.63–2.67. The range for the silt soil type is 2.65-2.7. From this test, the specific gravity for this sandy silt soil type is 2.655 which are under the range of silt soil specific gravity.

3.2 Water Sample Testing

In this research, there are two types of water sample used in the 4 curing conditions of the grout cube which is from treated water and untreated water, which is sulfate and chloride content. The chloride content of both water samples is nearly the same which is 23 mg/L and 24 mg/L. whereas the sulfate content of the untreated water is lower compared to treated water. The sulfate content in the treated water is relatively higher, could be resulted from the use of Aluminium Sulfate from the water treatment plant.

3.3 Grout Cube Testing

In this research, there are a total of 16 nos. of micropile grout cube that will be analyzed according to the bulk density, moisture absorption, compressive strength, microstructure and chemical composition.

3.3.1 Bulk Density

For the grout cube with 7 days of curing, it was found that grout C3b has the highest bulk density which is 1.981 Mg/m3 whereas grout C3a has the lowest value with 1.86 Mg/m3. Meanwhile for 28 days of curing, grout C4d has the highest bulk density which is 1.989 Mg/m3 whereas grout C3a has the lowest value with 1.877 Mg/m3.

3.3.2 Moisture Absorption

At 7 days curing ages, grout C3a has the lowest moisture absorption with 1.45% while C4b has the highest value with 3.03%. For the 28 days of curing, it showed C3d has the lowest moisture absorption with 1.44% while grout cube C4c has the highest value with 2.80%.

3.3.3 Compressive Strength

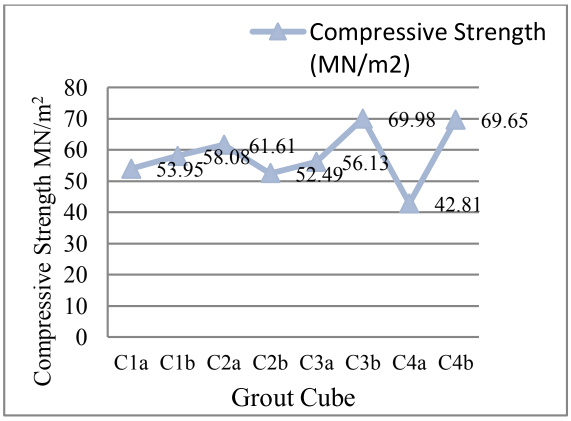

Fig. 2 Graph of compressive strength of grout cubes (7 days curing)

After 7 days of curing in the 4 conditions as specifically prepared in this research, 2 cubes for each condition are crushed to determine the compressive strength. It was found that the grout cube C3b which is cured in untreated water and sandy soil has the highest compressive strength of 69.98 MN/m2. On the other hand, the grout cube which has the lowest strength is C1a with 53.95 MN/m2 which is cured in a conventional method from daily water supply.

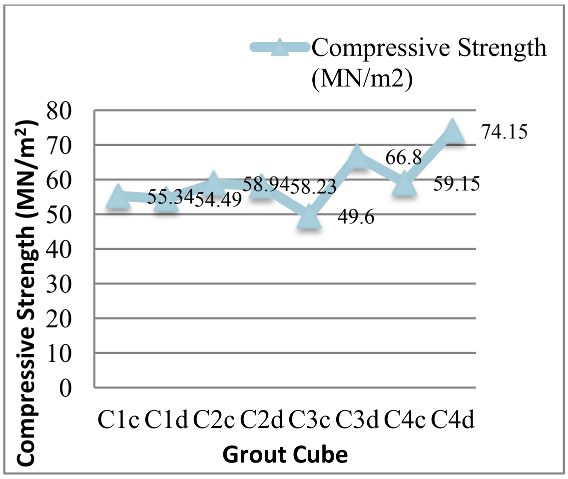

Fig. 3 Graph of compressive strength of grout cubes (28 days curing)

At 28 days of curing, it is found that grout cube c4d which is cured in condition 4 (untreated water and sandy silt soil) has the highest compressive strength with 74.15 MN/m2. The cube with the lowest strength is C3c, 49.6 MN/m2 which is cured in untreated water and gravely sand.

By referring to the grout cube average compressive strength, the cubes which is cured in Condition 2, 3 and 4 is higher than cubes cured in Condition 1. In general, the grout cubes cured in untreated water with lower sulfate content are more likely to produce higher early and 28 days' compressive strength. The possible cause for lower strength for grout cube cured in treated water may be due to the formation of expansive compounds as a result of chloride and sulfate attack. Yet, the long term performance of the grout cubes cured in this water samples are still uncertain.

3.3.4 Microstructure (SEM & EDX)

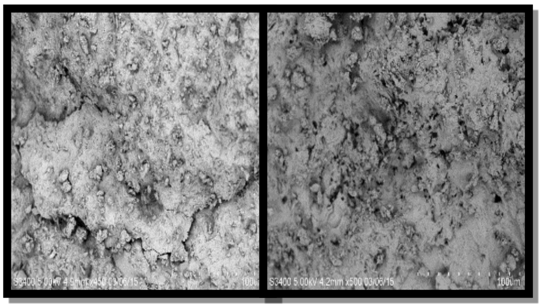

Fig. 4 The overview of the microstructure of grout sample from grout cube C1a and C1b

From the overview, the grout of C1b has a relatively smaller void than grout C1a. Meanwhile, the distant view of specimens C1d shows a great deal of larger air void.

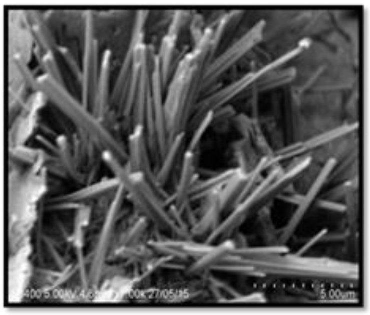

Fig. 5 Ettringite formation in specimen C1a

Generally, in cement-based material, sulfate attack mainly occurs from the exterior and internally. External attack arises from increased sulfate sulfate concentration from the outside environment (Menendez et. Al, 2013) and is more common and occurs when water contain dissolved sulfate penetrate or come into contact with the cement-based material. The microstructure of the sample experiences some changes that vary and the common signs are the formation of ettringite.

In this research, ettringite formation is observed from SEM and confirmed by EDX. From larger SEM magnification, it was found that from sample C1a, show presence of prismatic fine needle shaped crystals as shown in figure below. The structure is identical to the ettringite that are commonly found in cement based materials.

From SEM imaging of the grout cube specimens, the ettringite formation is present in almost all grout cube specimens. Nonetheless, the intensity of the entringite formation may vary depending on the curing conditions. Additionally, the results and severity of the sulfate attack might be different with higher sulfate concentration.

Fig. 6 Formation of ettringite inside an air void in specimen C2d

3.3.5 X-Ray Diffraction and Quantitative Phase Composition of Grout Specimens

For the phase identification to determine the chemical compositions of the grout cube specimens, each X-Ray patterns of the 16 grout cube specimens are analyzed by using software and the phase assumed to be present will be selected based on the figure-of-merit and visual inspection of their agreement with the experimental pattern.

In this analysis, it is important to pay attention to the hydration products and the percentage of the expansive crystalline presents in the specimen as both of these are the main factors in the mechanisms of the external sulfate attack. In external sulfate attack, the waterborne sulfates from medium such as soil and water, reacts with hydration products to form expansive crystalline products such as the ettringite, monosulfate and gypsum.

Table 3 The average percentage of phase present in grout cube specimens

Sample	Ettringite (%)	Gypsum (%)	Portlandite (%)	Tricalcium Aluminate (%)	Thaumasite (%)	Calcite (%)
Condition 1	43.18	17.13	20.20	3.33	1.28	14.88
Condition 2	33.43	14.57	29.33	4.67	1.60	16.40
Condition 3	30.43	9.93	34.25	1.00	1.08	23.33
Condition 4	28.30	16.90	35.00	3.38	1.25	15.20

From the table, the average of each phase obtained from 16 grout cube specimens and compared with respect to the curing conditions. It is found that grout specimens cured in Condition 1 possess the highest percentage of ettringite with 43.18%. Correspondingly, the percentage of hydration products, specifically portlandite (Calcium Hydroxide) are the lowest with 20.20% compared to the other curing conditions. This shows that most of the hydration products have reacted with waterborne sulfates resulting in the high percentages of the ettringite and low percentages of portlandite.

Comparatively, grout specimens cured in Condition 4 have the lowest percentage of ettringite with 28.30%. Correspondingly, the percentage of hydration products, specifically portlandite (Calcium Hydroxide) are the highest with 35% compared to the other curing conditions. This shows that most of the hydration products have yet to react with waterborne sulfates resulting in the high percentages of the portlandite and low percentages of ettringite.

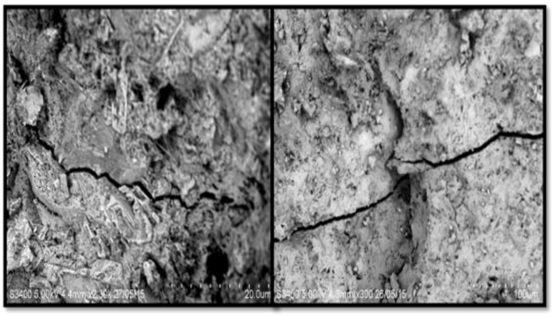

Fig. 7 Examples of Micro Cracks as found in Specimen C1a (Left) and C4a (Right)

Apparently, the average of the compressive strength for grout cubes cured in Condition 1, Condition 2, Condition 3 and Condition 4 are 55.47, 57.82, 60.63 and 61.44 MN/m^2 respectively. When comparing the phase identification results to the compressive strength, it shows that the percentages of ettringite presents in the grout cube relatively affecting the performance of grout cube in terms of strength. The formation of ettringite may develop tensile stress and micro cracks inside the grout cube, thus lead to strength loss and allow more sulfate ingress that can add into further deterioration.

4. CONCLUSION

In this research, consideration has been given to the grout properties of micropile in different soil conditions. The following are the general concluding remarks to define this research:

a) Primarily, the micropile grout is a setting material, normally cement and water, sometimes containing additives or a limited amount of fine aggregates that transfers load from the bearing element. During its service life, deterioration may occur as a result from aggressive chemical penetration into the grout. It is important to assess the type of exposure, strength and microstructural in order to achieve the specified micropile grout criteria.

b) There are many factors that may cause deterioration and degradation of the micropile grout, therefore, consideration should be taken to agents such as water and soils as it may contain aggressive chemical that can reacts with the unstable cement phases. The performance of the grout mainly depends on the environmental exposure, chemicals that may diffuse through its mass and the design quality.

c) In terms of compressive strength, the cubes which is cured in Condition 2, 3 and 4 is higher than cubes cured in Condition 1. Therefore, the grout cubes cured in untreated water with lower sulfate content are more likely to produce higher early and 28 days compressive strength.

d) Based on the ACI 318 exposure classes, the sulfate content and the chloride content in the water used as curing conditions are negligible. The sulfate exposure in this research is less than 150 ppm and the chloride content is less than 0.30 % as specified by ACI. Therefore, the sulfate and chloride exposure in all the curing conditions gave not as much effect to the grout cube properties.

5. ACKNOWLEDGEMENTS

Above all, I would like to offer my sincerest gratitude to my supervisor and co author, Mr. Hassanel Zachary Amaludin for his kind help, motivation and effort. Very special thanks to STL Geotechnics for the generous cooperation and collaboration in this research and Engineer Miss Julinda for taking time from her busy schedules to advise me on my project. The technical supports and encouragements offered are very crucial throughout the completion of this research. Not to forget, to both of my parents and family members for the unconditional support and understanding.

6. REFERENCES

[1] FHWA Micropile Design and Construction Guidelines Implementation Manual Priority Technologies Program (PTP) Project. 2000. Washington: Publication FHWA-SA-97-070.

[2] C. Liu and J. Evett. 2005. Soils and Foundations SI Ed.: Prentice-Hall.

[3] E. Menendez, T. Matschei and F. P. Glasser (2013), Sulfate Attack of Concrete, Performance of Cement-Based Materials in Aggressive Aqueous Environments, 10(1), 7-74.

[4] ACI 318: Building Code Requirements for Reinforced Concrete. 2008. American Concrete Institute, Farmington Hills.

Sixth International Conference on Geotechnique, Construction Materials and Environment, Bangkok, Thailand, Nov. 14-16, 2016, ISBN: 978-4-9905958-6-9 C3051

EXPERIMENTALLY MEASUREMENT AND ANALYSIS OF STRESS UNDER FOUNDATION SLAB

M. Mohyla[1] and K. Vojtasik[1] and M. Stolarik[1] and M. Pinka[1] and H. Lahuta[1]
[1] Faculty of Civil Engineering, VSB - Technical University of Ostrava, Ostrava, Czech Republic

ABSTRACT

Understanding of a load redistribution into subsoil below building foundation is an important knowledge for reliable design and its economy too. The article presents the results of a physical model of a foundation slab and its interaction with the subsoil. The interactions were investigated comprehensively by monitoring the developments of stress in the subsoil and foundation slab settlement during its loading. The load acting on the foundation was applied by strutting the hydraulic press against heavy steel frame which was established by the Department of Building Structures, Faculty of Civil Engineering of VSB -TU Ostrava for this purpose. The preparatory phase of the present experiment involved the homogenization of soil during which trio pressure cells in three horizons were gradually fitted. The quality of homogenization was checked on an ongoing basis through field tests: dynamic penetration load test, dynamic plate load test and seismic measurement of foundation slab response. Finally, the homogenized soil was subjected to mechanical analysis to determine the strength and deformation parameters for basic Mohr-Coulomb constitutive model.

Keywords: Physical model, foundation slab, foundation-subsoil interaction, subsoil pressure

INTRODUCTION

Surface foundation slab transfers the load from the building into the subsoil (or foundation environment). The load is transferred into the subsoil by contact stress on the physical surface interface between the foundation slab and the subsoil. From this interface, stress extends further into the subsoil and the stress increment in the subsoil caused by the load is progressively reduced with increasing distance from the physical interface. The extent and value of stress increments below the foundation in the subsoil caused by the load are determined by the appropriate analytical methods of force balance, and deformation or numerical methods. Direct stress measurements are only carried out on the horizon of the foundation base in the case of major building structures [1]-[3]. Experimental measurements on the horizons below the foundation base were conducted rarely based on in situ physical models at 1:1 scale on the original subsoil [4], [5]. So far, the calculation of stress values at different subsoil horizons below the foundation has not been verified at points such as the centre of gravity, characteristic point, edge and corner of the foundation slab surface. The installation of measuring pressure cells into the original subsoil above each other at different horizons is impossible without disturbing the subsoil structure, thereby affecting measurement results. Installing pressure cells distributed across the subsoil in the desired scheme is only possible if the subsoil is artificially created, where pressure cells may be installed gradually in the course of subsoil creation. This paper deals with the direct experimental measurement of stress below the foundation slab, as this measurement was performed on a real foundation built on artificial subsoil. The paper documents in detail the preparation and verification of the quality of artificial subsoil, a system of measuring pressure cells installed at three horizons, conditions during measurement, the recorded data, and data processing.

Fig. 1 Heavy steel test frame

EQUIPMENT

The Faculty of Civil Engineering, VSB-TU Ostrava has an external heavy steel test frame used to conduct experiments on building structural elements. Figure 1 shows a photograph of the test frame. The steel frame was designed by the

Department of Building structures in cooperation with Department of Geotechnics and Underground Engineering. The aboveground part of the test frame is a steel frame assembled from steel I beams.

The underground part consists of two foundation wall strips which are, additionally, anchored by 5m long steel tube micro-piles (89/10mm). Each of the wall strips is anchored into the subsoil by five micro-piles. Three of them are vertical and the two remaining ones are inclined at both ends of the wall strip.

The total bearing capacity of the micro-piles in tensile load is 1MN. A detailed diagram of the test frame structure is shown in fig. 2.

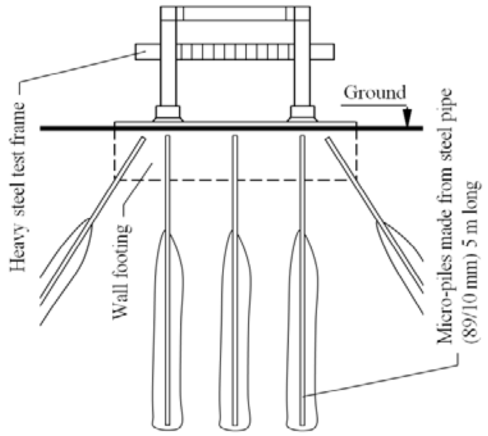

Fig. 2 Structure scheme of the heavy steel test frame

PREPARATION OF ARTIFICIAL SUBSOIL

For the progress of the experiment to be successful, it was desirable that the subsoil influenced by interactions with the experimental model foundation slab showed homogeneous properties (descriptive, stress and strain properties). Partial results of experiments for example [6], [7] and subsequent field tests, however, showed that the subsoil does not show such homogenous properties. The inhomogeneity of subsoil properties was due to the geological profile in the region of interest [8] and the technology used to build the test frame foundations. These foundations are monolithic and have been built in a sloped excavation by depositing concrete into the formwork. Backfill was built using the original soil; however, it has not been compacted to the original state, which had the largest impact on the inhomogeneity of the environment. Figure 3 shows the heterogeneity of the original soil; the wall of the excavation contains the original subsoil and fills, and the side sections next to the concrete foundations contain backfill of the sloped excavation from the time the test frame foundations were built. Based on the identified circumstances, homogenization was performed as follows:

- Complete excavation of soil from under the test frame, which was defined by the position of the frame test foundation and the depth of the test frame foundation base (fig. 1).
- Backfill: excavated soil was gradually (in layers with a thickness of up to 15cm) deposited back into space under the test frame. The backfill was performed manually, with the stochastic selection of sampling points from the excavated soil. It was then evenly spread over the entire area under the test frame. The thickness of layers was modified as necessary depending on the desired location horizon of pressure cells.
- Compaction: compaction was performed using vibration rammer with compaction force of 12.0kN (fig. 3). The quality of compacting of each layer was continuously verified by a light dynamic plate (impact modulus of elasticity E_{vd} [MPa]). In the case of surface areas with lower parameters, the area was re-compacted and verified.

Fig. 3 Completion of sub-layers by compaction

As a result of the above manner to perform the backfill, it was possible to build a foundation environment with quasihomogeneous layers exhibiting homogeneous properties, especially in the horizontal plane. This led to the creation of an environment with the vertical direction of anisotropy. To ensure a homogeneous isotropic subsoil, the excavated soil (approx. 20m^3) would have to be homogenized as a one part. Given that complete homogenization would be time consuming and due to the absence of the required technology (machines), homogenization of the foundation subsoil was performed as described above. The layout of the experiment and the method of applying load on the experimental foundation allowed the above method of homogenization to be used.

Installation of pressure cells

As part of the backfill of the homogenized subsoil, pressure cells (Geokon, Model 4800 and 4810) were continuously fitted, successively in two depth horizons (-0.800m, -0.350m) below the future foundation base and in the foundation base (0.000m).

The cells were fitted at three locations in each of the horizons: the centre, the centre of the edge and corner of the experimental foundation slab. The cells in the centre of the edge and corner of the foundation slab were placed 5cm from the edge of the foundation slab, i.e. 0.835m from the centre of the slab. A total of 9 pressure cells in three horizons and three vertical axes were fitted (fig. 4). The placement of the pressure cells in various depth horizons was derived by comparing the nominal bearing capacity of the pressure cells used (2x170kPa, 6x350kPa, 1x700kPa) and the expected developments of stresses in the subsoil beneath the loaded experimental foundation according to the theory of elastic half-space defined by Boussinesq.

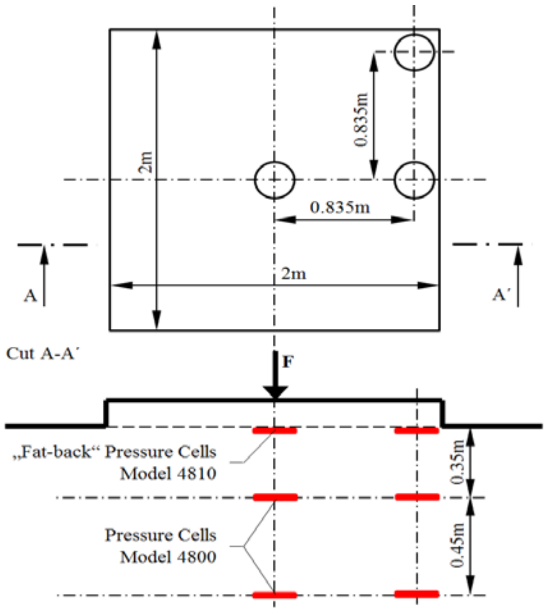

Fig. 4 Layout of pressure cells

The thickness of backfill layers was modified as necessary always to have the pressure cells placed in an additional groove with a depth of about 100mm in the freshly compacted layer. The bottom of the groove was levelled off with a steel scraper, filling up with soil was not accepted due to the potential creation of a local site with a different degree of compaction. Although the risk of a possible occurrence of stone or boulder was eliminated during homogenization, the site where the pressure cell was placed was subjected to a subjective penetration check by a thin steel needle to a depth of about 5cm at 9 locations. The fitted pressure cell was gradually covered by homogenized soil and continuously compacted up to the level of the surface of the currently compacted layer. When compacting the backfill of the cell, the emphasis was placed on keeping a consistent degree of compaction with the surrounding environment. Backfill with sand was excluded due to the different strain parameters compared with the original soil. This could negatively affect the registered stress in the pressure cell. The foundation base was fitted with cells (fat-back pressure cell, type 4810) intended for contact with the soil and the slab. The side of the cell touching the slab is reinforced with a steel plate due to specific developments in the stress on the interface between the soil and the slab. The method of mounting pressure cells was adapted to the layout conditions under the foundation of the present experiment, while respecting the recommendations made by the pressure cell manufacturer.

Pressure cells intended for the monitoring of the stress in the soil environment record stress, which is calculated as the sum of total stress (σ) and atmospheric pressure (P). Effective stress (σ') can be calculated using the following Terzaghi’s Eq. (1), provided that the place where the pressure cell is located is fitted with a piezometer for monitoring pore pressures (u), and total stress (σ) is free from the influence of atmospheric pressure:

$$\sigma' = \sigma - u \tag{1}$$

The measured values are affected by numerous factors distorting the results, some of which can be corrected (from a temperature of the atmospheric pressure). One of the factors which, however, cannot be affected, is the ratio of strain parameters (stiffness) of the pressure cell and the surrounding soil environment, which should ideally be identical. The pressure cell with higher stiffness as compared to the soil environment registers higher values of stress which do not correspond to the geostatic stress including any incremental stress due to the load. Moreover, the situation is complicated by the different stiffness of the pressure cell itself, which has a substantially higher circumferential stiffness than surface stiffness. Generally, there is a direct correlation between the thickness of the pressure cell and the degree to which pressure is affected due to the different ratios of elasticity moduli of the pressure cell and the environment. The thinner the pressure cell, the less the measurement is affected by error due to differences in strain parameters of the cell and the environment.

The technology used to fit the pressure cells into the soil environment also affects the measurement significantly. The environment around the pressure cells must be homogeneous and evenly compacted. Pressure readings on cells may show lower stress values than in the case where the soil environment near the cell is less compacted. The cell does not register all stresses due to the non-compacted soil, which becomes consolidated during loading. Therefore, stress is transferred to the vicinity of the cell and the stress tensor above the pressure cell takes the form of an arch. Conversely, if the immediate vicinity around the cell is compacted more than the surrounding environment, this leads to stress becoming concentrated in this region; consequently, the cell registers a higher stress which does not correspond to geostatic stress including any incremental stress due to the load.

DESCRIPTION OF THE EXPERIMENT

The design of experimental slab was developed by the Department of Building Structures and was based on the results of existing experiments [9], [10], [11] and the layout constraints of the test frame structure. Larger sizes of the experimental basis would lead to the interaction between the foundation and the subsoil being affected by the existing test frame foundations. A model foundation slab was made of plain concrete of 2x2m and a thickness of 0.2m. The class of the concrete according to the compressive strength was C35/45. During slab casting, three samples were made for later analysis of strain parameters (table 1).

Table 1 Foundation slab properties

$f_{ck,cyl}$ [N/mm^2]	$f_{ck,cube}$ [N/mm^2]	Young's modulus [GPa]		
35	45	29	30,5	28

The load was applied to the foundation slab by means of a hydraulic press leaning against the test frame structure. Loading took place in several steps, each taken every 0.5 hours. Each loading step was about 80kN, with a total of 7 steps taken, i.e. the slab was subjected to a theoretical maximum load of about 600kNm. These load values could not be achieved with total precision due to gross dosing of the press used. The real values of the load in individual steps and are summarized in Table 2. Each loading step involved the following steps:

- the increase in load ΔF=80kN (the load increment was achieved in about 1 minute),
- stress readings on pressure cells made immediately after loading (about 3 minutes),
- stress readings on pressure cells made before terminating the loading step (about 3 minutes),
- the increase in load in the next step.

The experimental foundation was loaded by the proposed scheme regardless of any defects occurring during loading. Continuously with measuring, temperatures were recorded on individual pressure cells, including atmospheric pressure, which was later used to calibrate the measured data. Also, settlement of the foundation slab was recorded using electronic linear path sensors. Pore pressures were not recorded.

Hydraulic equipment used by the implementation team during the experiment did not allow keeping constant pressure during one loading step. As a result of the above, the pressure in the hydraulic load decreased depending on the subsoil being strained. Therefore, the experimental slab was not subjected to loading by constant force within one loading step.

During the period from subsoil homogenization until the actual experiment, the test frame was covered with a tent which prevented potential saturation of the subsoil as a result of precipitation. The groundwater level during the experiment was also not encountered; it can be thus assumed that the environment was not 100% saturated. The load test on the described experiment was performed around 4 months after the subsoil homogenization. During this period, dissipation of potential local pore pressures occurred and humidity anisotropy with defining vertical axis was created.

Table 2 Load steps of experimental slab

Step	1	2	3	4	5	6	7
Load [kN]	82	166	244	310	385	471	616

DISCUSSION

The course of the interaction between the foundation slab and the subsoil is primarily affected by the dimensions of the foundation and the ratio of strain parameters of the foundation and the subsoil. The experimental foundation slab which, at this stage of research, was not reinforced had the character of a pliable foundation, where uneven settlement can be expected. As a consequence of low stiffness of the foundation slab, loading was accompanied by uneven settlement and uplift of the corners above the ground, and a gradual reduction in the contact area between the foundation and the subsoil. Due to the low tensile strength of concrete (approximately 10x less than the compressive strength), very soon (in the third step) the first tensile cracks emerged, developing from the foundation base (at a load of approximately 250kN). During the subsequent loading step, the cracks spread over the entire height of the foundation slab, resulting in a significant reduction of the contact area between the foundation and the subsoil. The load of the slab redistributed to a smaller area then resulted in a significant increase in stress in this reduced contact area between the foundation and the subsoil.

The following figures show the results of monitoring total vertical pressure on cells located in the subsoil under the experimental foundation slab according to figure 4. The pressure distribution diagrams are already free from the influence of atmospheric pressure, temperature and stress due to the weight of the overlying strata, i.e. they are total incremental stresses developed in the subsoil only due to load. The results are systematically divided into diagrams according to the depth location of the pressure cells and their horizontal position about the foundation slab.

Figure 5 (z=0.00m) summarizes the progress in stress acting on the three cells located in the foundation base. The solid line characterizes stress below the middle, where a significant increase in stress during the third loading step is evident (1.5 hours). The cell located under the corner simultaneously stopped recording stress due to the uplift of the corners of the experimental slab described above.

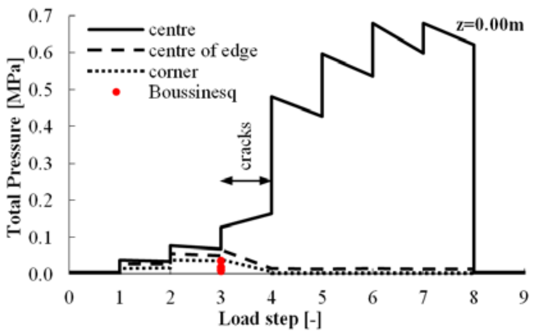

Fig. 5 Total pressures in foundation base during loading

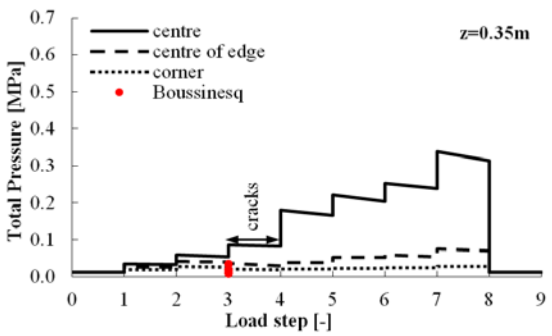

Fig. 6 Total pressures in horizon -0.35 during loading

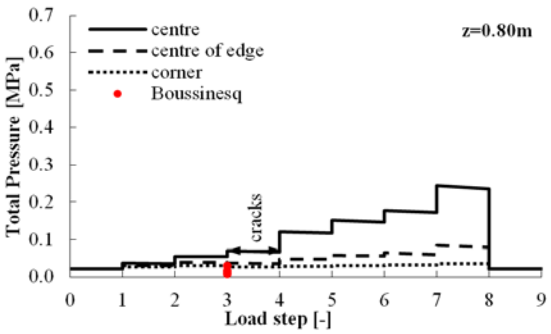

Fig. 7 Total pressures in horizon -0.80 during loading

Figure 6 and 7 presents the results of the trio cells located at a depth of 0.35m and 0.80m, respectively. Here, the qualitative development of stress is similar, differing only in absolute pressure values. Even at these depths, a sharp rise in stress is evident, due to the reduction of the foundation base.

The red dot in diagrams presents the stress for loading step before the rupture of the foundation slab, determined based on the theory of elastic half-space (Boussinesq).

CONCLUSION

The paper aimed to present the results of a physical model, including preparatory work involving the preparation of subsoil (homogenization) and mounting pressure cells to monitor total stress. In particular, stress redistribution in the subsoil below the loaded experimental foundation slab was monitored. During these activities, several facts have been confirmed, which should be summarized in the conclusion.

The importance of the correct positioning of the pressure cell in the soil environment proved to be crucial. It is essential that material and state homogeneity of the immediate environment around the cell is observed when the pressure cells are being fitted. Failure to observe this will significantly affect the monitoring of total stress in the subsoil. The ratio of strain parameters of pressure cells and subsoil also has a significant influence. Generally, the stiffer the cell compared to the soil environment, the higher total stress it reads. The above information must be observed when fitting pressure cells as well as when interpreting the readings.

The readings of incremental pressures in the selected loading step were evaluated and compared with the readings based on the elastic half-space theory (Boussinesq). The above comparison was performed using the loading step before the disruption of the experimental foundation slab. After the disruption of the experimental basis, the contact area at the foundation base was reduced, which greatly affected the interaction between the foundation slab and the subsoil. It should be borne in mind that the theory does not allow taking account of the stiffness of the foundation slab, which significantly affects the settlement and the redistribution of stress in the subsoil. The comparison must, therefore, be considered as indicative.

In the course of the experiment, there were a few questions that will need to be answered during further research in this area. The physical model will be extended to include the possible influence of groundwater level with a possible modification of its depth. For these purposes, it will be necessary to increase the permeability of the subsoil. To increase the permeability by e.g. mixing the original soil with sand, it would be necessary to add an amount of sand larger than the volume of the original soil, which would inter alia, increase the strain parameters of the subsoil. This is not desirable due to changes in relative stiffness in the foundation–subsoil system. The effort to increase the settlement of the experimental foundation as a result of a load applied to it could, therefore, lead to the bearing capacity of the test frame being exceeded. Another problem involves the fact that controlled saturation of the subsoil is time-consuming and that it is affected by capillary elevation, which is problematic. One possible solution to that situation is to create a sandwich of layers of the original soil (approx. 0.20m thick) and a drainage layer (approx. 0.05m thick). Any internal erosion of the original soil is prevented by inserting a non-woven geotextile beneath the drainage layer. Such a layer structure would allow changing the groundwater level in 0.25m increments in a relatively short period thanks to a significantly shortened drainage path, while preserving the strain parameters of the original subsoil.

ACKNOWLEDGMENTS

This outcome has been achieved with the financial support of the project GACR No. 16-08937S „State of stress and strain of fiber reinforced composites in interaction with the soil environment“. In this undertaking, theoretical results gained by the conceptual development of research, development, and innovations for 2015 at the VŠB-Technical University of Ostrava (granted by the Ministry of Education, Youths and Sports of the Czech Republic) were partially exploited.

REFERENCES

[1] Milev N., Kostov V. “Monitoring of the foundation of an existing RC building and some modelling approaches“, NZSEE Conference 2015, Wellington, New Zealand, pp. 199-206.

[2] Mendoza M. J., Rufiar M., Ibarra E., Mendoza S.A. “Performance of a pioneer foundation of the skirt type for the Metro-Line 12 overpass“, Proceedings of the 18th International Conference on Soil Mechanics and Geotechnical Engineering, Paris 2013.

[3] Sokolic I., Ivsic T. “Analysis and measurements of settlement for heavy loaded rigid footing“, 8th European Young Geotechnical Engineers' Conference / Fratalocchi, Evelina (ur.). - Ancona: Universita Politecnica delle Marche, Associazione Geotecnica Italiana, ISSMGE, 2007.

[4] La Gatta D. P., Keller T. O. “Vertical Load Tests of Footings on Silt“, First International Conference on Case Histories in Geotechnical Engineering, Missouri University of Science and Technology.

[5] Anderson J. B., Townsend F. C., Rahelison L. “Load Testing and Settlement Prediction of Shallow Foundation“, Journal of Geotechnical and Geoenvironmental Engineering, American Society of Civil Engineers, 2007, Vol. 133, Issue. 12, pp. 1494-1502. ISSN: 1943-5606.

[6] Cajka R., Buchta V., Burkovic K., Fojtik R. “Experimental Measurement of Ground Base Plate“ Transactions of the VŠB - Technical University of Ostrava, Civil Engineering Series, 2012, Vol. 12, Issue 2, pp. 1-6, ISSN: 1804-4824 (Online), DOI: 10.2478/v10160-012-0014-6.

[7] Stolarik, M., Hrubesova, E., Pinka, "M. Dynamic Response of the Experimental Foundation Slab - Seismic Measurement and Analysis". 15 th GeoConference on Science and Technologies in Geology, Exploration and Mining, SGEM International Multidisciplinary Scientific GeoConferences, Vol. 2, no. 1, p. 261-268. Albena, 2015.

[8] Cajka R., Krivy V., Sekanina D. “Design and Development of a Testing Device for Experimental Measurements of Foundation Slabs on the Subsoil“, Transactions of the VŠB - Technical University of Ostrava, Civil Engineering Series, 2011, Vol. 11, Issue 1, pp. 1-5, ISSN: 1804-4824 (Online), DOI: 10.2478/v10160-011-0002-2.

[9] Cajka, R., Labudkova, J., Mynarcik, P. “Numerical solution of soil - foundation interaction and comparison of results with experimetal measurements“, International Journal of GEOMATE, vol. 11, no. 1, pp. 2116-2122.

[10] Lahuta, H., Hrubesova, E., Duris, L., Petrasova, T. “Behaviour Subsoil of Slab Foundation under Loading“ 15th Geoconference on Science and Technologies in Geology, Exploration and Mining, SGEM International Multidisciplinary Scientific GeoConferences, Albena, 2015. Vol. 2, no. 1, pp. 119-126. ISSN: 1314-2704.

[11] Cajka, R., Mynarcik, P., Labudkova, J. “Experimetal measurement of soil-prestressed foundation interaction“, International Journal of GEOMATE, vol. 10, no. 4, pp. 2101-2108.

RELATING TRADITIONAL DYNAMIC SHEAR MODULUS TO NANOINDENTATION MODULUS OF ASPHALT BINDERS

Rafiqul A. Tarefder[1], Hasan M. Faisal[2], Umme A. Mannan[2]
[1]Professor of Civil Engineering, University of New Mexico, USA
[2]PhD Candidate and Graduate Research Assistant, University of New Mexico, USA

ABSTRACT

Traditionally, asphalt binder is characterized by a dynamic shear rheometer, which applies a shear load on a bulk volume of liquid asphalt binder to determine shear modulus (*G**). Recently, a nanoindentation test can characterize an asphalt binder film in the form of a coating around roadway aggregates, which is more practical. In a nanoindentation test, a sharp tip is used to indent an asphalt film while residing on an aggregate surface to determine nanoindentation modulus (*E*). This study evaluates whether there is a relation between *G** and *E*. For both tests, replicate samples were conditioned in three ways: unaged, rolling thin film oven aged, and pressure vessel aging. Results show that the E-value is approximately 2 to 6 times larger than the *G**-value based on all samples/conditioning.

Keywords: Nanoindentation, Asphalt, Aging, Modulus, Binder, Dynamic, Shear.

INTRODUCTION

Asphalt concrete's dynamic modulus (*E**) is one of the key input the parameters for the structural design of flexible pavement according to the Mechanistic-Empirical Pavement Design Guide (MEPDG, currently packaged as DARWin-ME software). Currently, asphalt binder shear modulus G*-based Witczak equation is used in MEPDG Level 2 analysis to estimate *E** of asphalt concrete from Hot Mix Asphalt (HMA) mix volumetrics and binder information. Specifically, asphalt binder's dynamic shear modulus (*G**) and phase angle (δ) are used in G*-based Witczak equation to predict *E** mastercurve at Level 2 MEPDG analysis.

While Asphalt Concrete's (AC) *E** testing is conducted using an axial compression (or tension), asphalt binder's *G** is conducted in shear mode. Because, over the years, test methods developed and performed to characterize asphalt binders have been limited to a few rheological tests. Moreover, the existing tests cannot be performed on asphalt binder film while they are integral parts of AC. Rather those tests are performed on bulk liquid asphalt separately. Nanoindentation has created an opportunity to determine the stiffness (*E*) of asphalt binder while they are parts of AC and under compression loading [].

To this end, this study conducts dynamic shear modulus (*G**) and nanoindentation stiffness (*E*) testing of selected Performance Grade (PG) asphalt binders of New Mexico sources. In addition, the study examines possible correlation between *G** and *E*. It is expected that asphalt binder's *E* will a better estimator of asphalt concrete's *E** for Level 2 MEPDG analysis.

THEORY OF NANOINDENTATION

A typical nanoindentation load displacement curve is shown in Fig. 1(a). A sitting load of 0.005 mN is typically applied initially to facilitate a contact between the tip and sample surface. Next, the load is increased gradually from point *a* to *b*. The tip is unloaded at the maximum load point *b*. The unloading path is assumed to be elastic for most of the elastoplastic material. The unloading curve does not come back to point *a* due to plastic deformation in elastoplatic materials. The slope of the unloading curve at point *b* is usually equal to the slope of loading curve at point *a*.

Fig. 1(b) shows the surface profile as a function of penetration depth during loading and unloading. Here, h_{max} is the total depth of indentation at a maximum load, h_p is the total depth of indentation that is unrecovered, h_s is the depth of the surface at the perimeter of the indenter contact and h_c is the vertical depth along which contact is made between the indenter and the sample. Therefore,

$$h_c = h_{\max} - h_s \qquad (1)$$

The depth of impression that is recovered is,

$$h_e = h_{\max} - h_p \qquad (2)$$

Hertz found the contact radius *a* is related to the indenter radius *R*, applied load *P* and the reduced elastic modulus E^* of a sample by (Fig. 2):

$$a^3 = \frac{3}{4}\frac{PR}{E^*} \qquad (3)$$

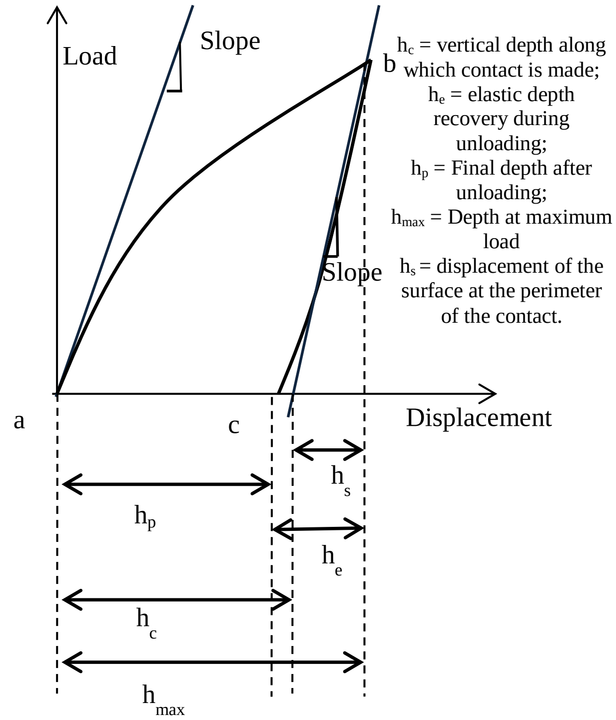

(a) Load –displacement curve

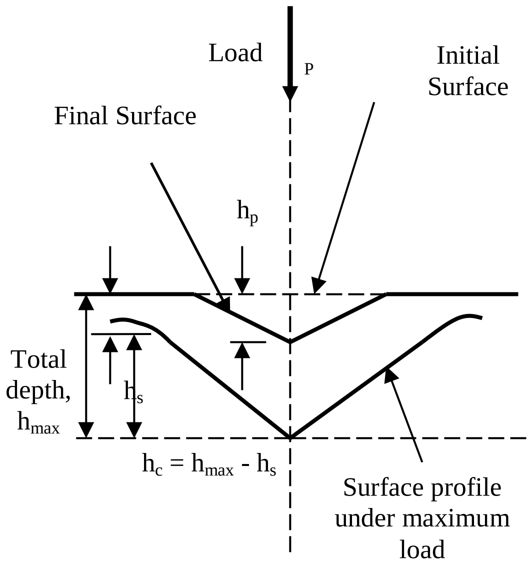

(b) Indentation Depth

Fig. 1. Schematic of Indentation Test.

Contact radius *a* is also related to the indenter radius *R* and penetration depth by:

$$a = \sqrt{Rh} \tag{4}$$

From Eq. (2) and (3) the applied load can be written as:

$$P = \frac{4}{3}E^* R^{1/2} h^{3/2} \tag{5}$$

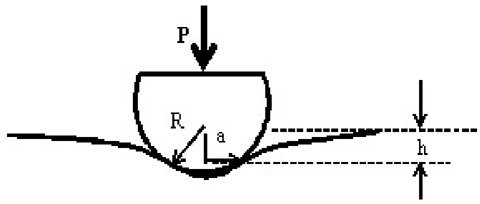

Fig. 2. Indenter Geometry.

Determination of *E**

By differentiating Eq. (5) with respect to the penetration depth h. Using the relation in Eq. (4):

$$\frac{dP}{dh} = 2E^* \sqrt{Rh} = 2E^* a \tag{6}$$

The projected area at the maximum load can be defined as: A $=\pi a^2$

Therefore,

$$S = \frac{dP}{dh} = \frac{2}{\sqrt{\pi}} E^* \sqrt{A} \tag{7}$$

where S is the unloading stiffness or slope of the unloading curve; Therefore,

$$E^* = \frac{\sqrt{\pi}}{2\sqrt{A}}(S) \tag{8}$$

Oliver and Pharr (1992) used a power law function to fit the unloading path of the load-displacement curve [5]. The power law function used by Oliver-Pharr is shown in Eq. (9):

$$P = \alpha (h - h_f)^m \tag{9}$$

where h is the depth of penetration,
$\mathbf{h_f}$ is plastic depth,
α and **m** are curve fitting parameters related to tip geometry.
m = 1 for flat ended cylindrical tip, m = 1.5 for spherical tip, and m = 2 for conical tip (Berkovich tip). The slope is measured by differentiation the in above Eq. (9) at the onset of unloading.

Determination of *A*

Oliver and Pharr (1992) defined the projected area A as a function of h_c defined in Eq. (1) [5]. Oliver and Pharr (1992) extrapolated the tangent line to the unloading curve at the maximum loading point down to zero load. This yields an intercept value for depth which estimates the h_s by:

$$h_s = \varepsilon \frac{P_{\max}}{S} \tag{10}$$

Therefore,

$$h_c = h_{\max} - \varepsilon \frac{P_{\max}}{S} \tag{11}$$

where **ε** is a geometric constant.
ε = 0.72 for conical tip, ε = 0.75 for Berkovich tip, and ε = 0.72 for spherical tip.

Determination of *E*

Timoshenko and Goodier found the reduced elastic modulus, E^* is related to the modulus of the indenter and the specimen and given by:

$$\frac{1}{E^*} = \frac{1-\nu}{E} + \frac{1-\nu_i}{E_i} \tag{12}$$

where E is Young's modulus of the material,
ϑ is Poisson's ratio of the material,
E_i is Young's modulus of the indenter and
ϑ_i is Poisson's ratio of the indenter,
E^* is the reduced modulus. One can find the elastic modulus of the sample, E using Eq. (12).

Determination of *H*

Hardness, H, is defined by the maximum load divided by the projected area (3):

$$H = \frac{P_{\max}}{A} \tag{13}$$

where P_{max} = peak load and A = projected area of contact at the peak load. The unit of hardness is given in N/m^2=Pa.

MATERIALS AND SAMPLE PREPARATION

Collection

A total of four performance grade (PG) binders available in New Mexico were collected in five one-gallon buckets per PG binder.

Table 1: Asphalt binders collected so far

PG 58-22	PG 64-22	PG 70-22	PG 76-22

Some performance graded asphalt binder such as PG 58-34, PG 64-34, PG 70-34 are not used in New Mexico. These binders could not be collected.

Conditioning

One PG binders were subjected to three conditioning – (1) unaged/ original binder and (2) RTFO (Rolling Thin Film Oven) and (3) PAV (Pressure Aging Vessel) aged before DSR testing. The conditioned binder is PG 76-22. The Rolling Thin Film Oven (RTFO) Test simulates the short-term aging of asphalt binders that occurs during the hot-mixing process. Asphalt binder was exposed to an elevated temperature to simulate manufacturing and placement aging according to AASHTO T 240-09 (2009) test procedure. Unaged asphalt binder was taken in cylindrical glass bottles and placed in a rotating carriage within an oven which rotates within the oven at 325°F (163°C) temperature for 85 minutes. After the RTFO aging, 50gm sample was placed in the PAV plate and then aged at 100°C and 2.10 MPa for 20 hours according to the AASHTO R 28-12. Fig. 3 shows the PAV apparatus.

Fig. 3. Pressure Aging Vessel (PAV) for long term aging simulation on asphalt binder.

Nanoindentation Sample Preparation

Fig. 4 shows a laboratory prepared asphalt binder film on glass substrate. As the first step, a glass slide surface 0.5 in × 0.5 in was selected and weighed in scale up to 4 significant decimal digits of grams. Next, the glass slide was wrapped with high temperature resistant tape. The tape was placed so that it formed the 0.25 inch square gap area previously outlined for the binder. Then, hot polymer modified liquid asphalt binder was poured into the gap between the tape strips. The polymer-modified binders were melted by heating them to 163°C for an hour. The asphalt coated surface was placed in the oven at 163°C for 10 min in order to have a smooth surface, cooled at room temperature and the tapes were removed. Finally, the glass slide with the asphalt coating was weighed again to measure the amount of asphalt binder. From the known area, the density of the asphalt binder and mass the thickness of the binder film was measured. The film thickness varied within a range of 40 µm to 80 µm to avoid the substrate effect on test results.

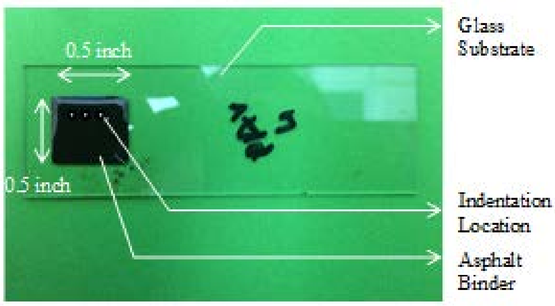

Fig. 4. Asphalt Binder Sample for Nanoindentation.

TESTING

Dynamic Shear Rheometer (DSR) Testing

Dynamic Shear Rheometer (DSR) was conducted on the conditioned binders. The test measures the dynamic shear modulus or complex modulus, G* and phase angle (δ) of asphalt binders under a continuous sinusoidal loading using a dynamic shear rheometer and parallel plate test geometry. Fig. 5 shows the DSR test device. The G* and δ were measured at room temperatures and a loading frequency of 10 rad/sec. A thicker sample (2 mm) with a smaller diameter plate (8 mm) was used so that the phase angle (δ) becomes measurable. All the tests were conducted following the AASHT0 T 315-09 (2009) test protocol within the linear viscoelastic range under strain-controlled mode. Three replicate samples were tested and the average of the three tests was used to develop the master curve.

Fig. 5. Dynamic Shear Rheometer.

Nanoindentation Testing

Indentation experiments were performed by using a nanoindenter manufactured by MicroMaterials Ltd. Wrexham, UK. In all the tests the nanoindenter was equipped with the pyramidal Berkovich tip. The indentation tests were conducted in load control mode. In load control mode, the indentation includes a constant loading, unloading rate and a holding segment at maximum load. A maximum load of 0.055 mN was applied with an initial load of 0.005 mN. Thirty indentations for loading rate 0.002 mN/sec, unloading rate 0.002 mN/sec and dwell time of 200 sec is selected. The loading, unloading rate and dwell times were selected so the tests could be performed in the thin film without hitting the glass substrate and also according to the study of Tarefder and Faisal [1]. The indentation depth remained small compared to the total material thickness so that the substrate effect on determining the mechanical property of the material could be avoided. The indenter moved at a rate of 1µm/sec to make the initial contact. In all the tests, the camber test temperature was kept at 26˚C, within a fluctuation of ±0.2˚C. After the test, the temperature corrections were also provided to the analysis. In the test, for each sample a set of 5 indentations (see Fig. 6) were made on the sample with a distance of 300µm. The distance was selected to avoid the pile up and sink in effect for successive indentations. However, according to ASTM guidelines, the required distance needed to be at least six indent radii away from the previous indentation point [6]. Because of the soft bulk of the asphalt binder, the pile up effect could be more. Furthermore, there was no limitation of space in the sample in nanoscale. For these reasons, a substantial distance was chosen for testing the material. Three different aging condition of the samples of the asphalt binder were introduced 20 indentations were conducted for each.

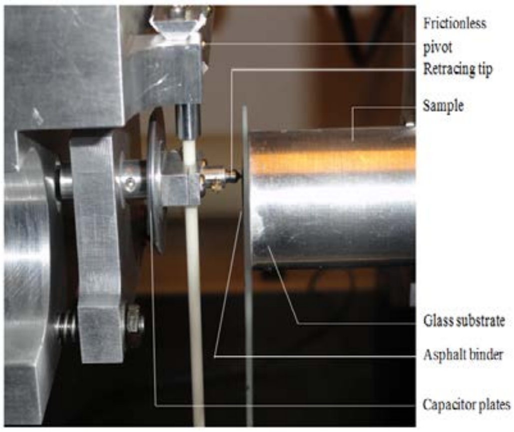

Fig. 6. Nanoindentation on Unaged Sample.

RESULTS AND DISCUSSIONS

In the current study a comparative analysis has been conducted between complex modulus of the binder *G** and nanoindentation modulus *E* of the material.

Figure 7 shows the Complex modulus *G** of four different binders and three different aging conditions. The figure shows with an increase in aging the complex modulus of the binder increases, however the increase is comparatively higher for PAV aging condition. Since PAV aging condition simulates long term aging in asphalt binder, the complex modulus is almost 3 to 5 times higher for PAV aging condition, however that is for RAFO aged condition is only 1.1 to 1.9 times higher.

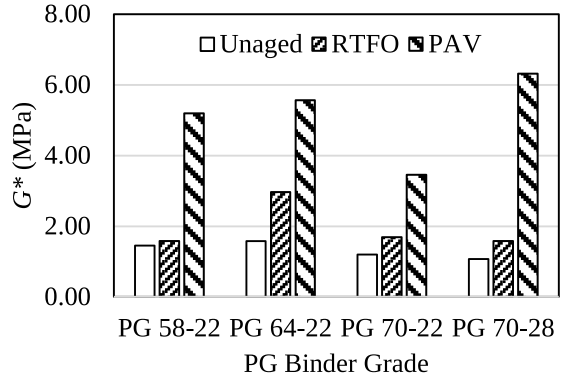

Fig. 7. G^* of different PG grades and two different aging conditions

Figure 8 shows the load displacement curves obtained from unaged PG 70-22 asphalt binder. Twenty indentations are conducted on each binder sample. The load displacement curve shows maximum displacement is restricted to 7200 nm.

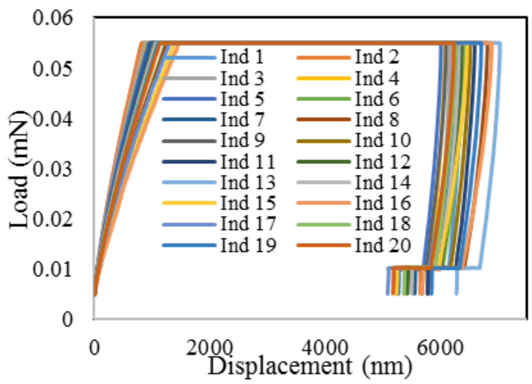

Fig. 8. Load displacement behavior of PG 70-22 unaged asphalt binder.

The selection high unloading rate and extended dwell time made the unloading portion of the load displacement curve positively sloped. Therefore, it was possible to analyze the unloading data in Oliver-Pharr framework. Figure 9 shows the modulus determined from nanoindentation test. Results show again with an increase in aging condition the modulus of the material increases. The increase in modulus is 4 to 8 times higher in the case of RTFO aged condition, however it is for PAV condition is 10 to 23 times. Therefore, for all cases of the nanoindentation modulus found higher than compared to complex modulus G^* of the material. Because of the scale different also the surface energy the nanoindentation. Comparison between E and G* shows nanoindentation E of the material is 1.5 to 6 times higher than the G* of the material.

However the increase in the factor n (=E/G*) shows decreasing trend for PAV aging condition of PG 58-22 and PG 70-28. E might have been showed higher values compared to the G^* of the material.

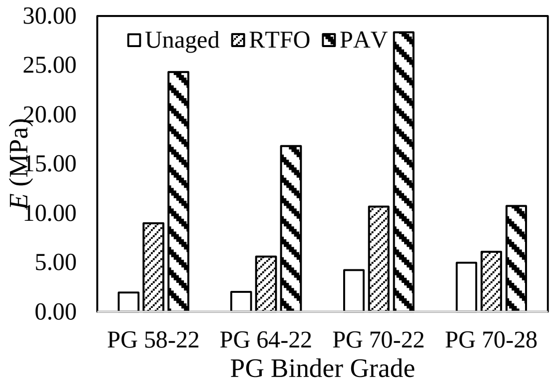

Fig. 9. E from nanoindentation test for different PG binder grade and aging condition

Since both of these binders are manufacture with polymer modification in the binder industry, the polymer structure may reduce the effect of aging on nano scale structure of the binder material.

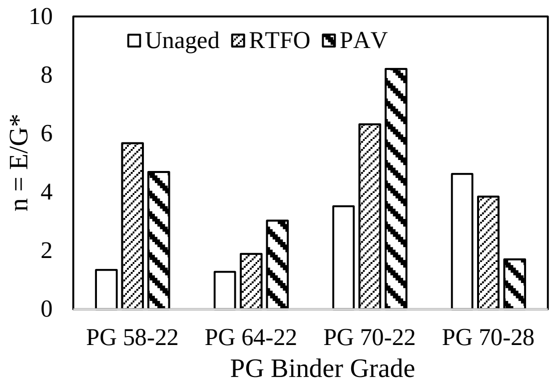

Fig. 10. n-value comparison for different PG binder grade and aging condition

CONCLUSION

Following conclusions can be drawn from the current study:

i) Both Complex modulus and nanoindentation modulus increases with increase in aging condition of the material.

ii) Nano scale modulus of the binder is 2 to 6 times higher than micro scale modulus or complex modulus of the material irrespective of aging condition.

iii) Nano scale modulus increases 4 to 8 times for RTFO aging condition where micro scale modulus shows an increase of 10 to 23 times for PAV aging condition with respect on unaged asphalt binder.

ACKNOWLEDGEMENTS

The authors would like to express their sincere gratitude and appreciation to the Safety and Operations of Large-Area Rural/Urban Intermodal Systems (SOLARIS), a tier 1 university transportation center led by the University of Nevada, Reno, for providing the funding of this research project.

REFERENCES

[1] Tarefder RA and H. Faisal, Effects of Dwell Time and Loading Rate on the Nanoindentation Behavior of Asphaltic Materials. Journal of Nanomechanics and Micromechanics, ASCE, Vol. 3, No. 2, 2013, pp. 17–23.

[2] Tarefder, RA and H. M. Faisal, Nanoindentation Characterization of Asphalt Concrete Aging. Journal of Nanomechanics and Micromechanics, ASCE, 2013, Vol.4, No.1, 2013 A4013003.

[3] Tarefder, RA and H. M. Faisal, Modeling Nanoindentation Creep Behavior of Asphalt Binder. Advances in Civil Engineering Materials, ASTM, Vol. 2, No.1, 2013, pp. 418-440.

[4] Faisal HM, R. A. Tarefder, and M. I. Hossain. A Nanomechanical Characterization of Vapor Condition and Unconditioned Asphalt. Transportation Research Record: Journal of the Transportation Research Board, No. 2506, Transportation Research Board, Washington, D.C., 2015, pp. 126–136, DOI: 10.3141/2506-14.

[5] Oliver, WC, and GM Pharr, An improved technique for determining hardness and elastic modulus using load and displacement sensing indentation experiments, J. Mater. Res., 1992, Vol. 7, No.6, pp.1564–1583.

[6] ASTM Standard E2546 – 07, Standard Practice for Instrumented Indentation Testing, ASTM International, West Conshohocken, PA, DOI: 10.1520/E2546-07, www.astm.org.

Sixth International Conference on Geotechnique, Construction Materials and Environment, Bangkok, Thailand, Nov. 14-16, 2016, ISBN: 978-4-9905958-6-9 C3051

SLOPE FAILURE MODEL TESTS CONTROLLED AGAINST THE FAILURES BY USING A FILTERING MATERIAL AND THEIR SIMULATIONS

Anusron CHUEASAMAT[1], Toshikazu HORI[2], Hirotaka SAITO[1] and Yuji KOHGO[1]
[1]United Graduate School of Agricultural Science, Tokyo University of Agriculture and Technology, Japan
[2]National Institute for Rural Engineering, Japan

ABSTRACT

The slope failures caused by heavy rainfall have frequently occurred in many countries. In order to investigate the mechanism of the failures, we conducted a series of slope failure model tests. It was found from the model tests that the slope failures initiated at the toes of the slopes where the rainwaters infiltrated were accumulated and the pore water pressures changed to be positive or be larger than the air entry value of the surface soil. In order to control the slope failures, drainage of the accumulated rainwaters is important. In this paper, a filtering material filled within gabions was used to drain the rainwaters. Four model test cases with the different sizes of gabions were carried out. It was found from the results that the slope failures highly depend on the ratios of the heights between gabions and the slopes. The higher ratio, it took the more time to failure. The failures always only occurred above the gabions. The simulations of the tests were conducted by using the saturated and unsaturated consolidation method with an elastoplastic model considering two suction effects. The simulation results could well express the experimental ones.

Keywords: Slope Failure, Pore Water Pressure, Filtering Material, Saturated and Unsaturated Consolidation Method, Elastoplastic Model with Two Suction Effects

INTRODUCTION

The slope failures caused by heavy rainfall have frequently occurred in many countries (e.g. Tohari et al., 2007). Most of the failure slopes had following common features: the depths of the failures were less than 2m, the inclines of the slopes were 30–50 degrees and the slopes consisted of permeable residual layers on relatively firm rock foundations (Rahardjo et al., 2005; Orense et al., 2006). It was found from some model failure tests, which simulated typical natural slopes, that the slope failures initiated at the toes of the slopes where the rainwaters infiltrated were accumulated and the pore water pressures changed to be positive (Orense et al., 2004; Tokoro et al., 2012). In order to control the slope failures, drainage of the accumulated rainwaters at the toes is important.

In this paper, a filter material filled within gabions was used to drain the accumulated rainwaters at the toe. Gabions are usually used to stabilize shorelines, stream banks or slopes against erosion. In this paper, in order to investigate the drainage performance of the gabions, four different sizes of filter gabions were used.

EXPERIMENTAL METHODS

The slope model test framework consists of two parts: an artificial rainfall instrument and an iron soil tank shown in Fig. 1. The artificial rainfall instrument was mounted about 4 meters above the soil tank to supply rainwater as uniformly as possible. Square spray nozzles (IKEUCHI Co., Ltd) were used to supply rainwater. These nozzles could supply uniform rainfalls to the slopes and the size of each rain drop was so small that it had little influence to slope failures. Some calibration rainfall tests were conducted to adjust the nozzle layouts. As the result, we could obtain 49.95 mm/h for the target 50 mm/h rainfall intensity.

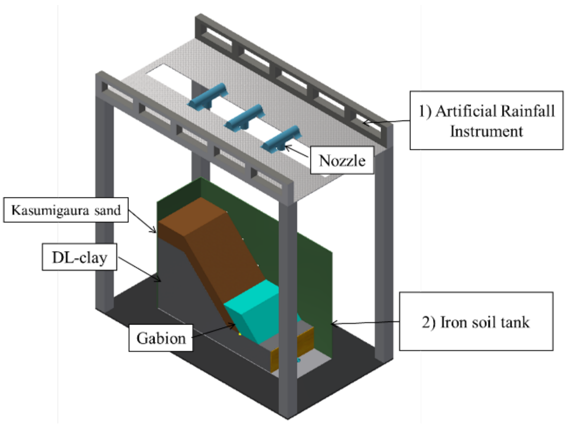

Fig. 1 Slope model test framework

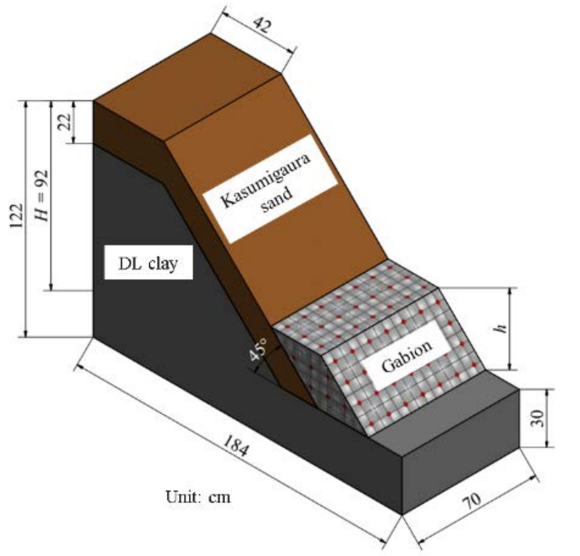

Fig. 2 Slope model dimensions and shapes

The slope models used in this series of tests are shown in Fig. 2. The models consist of three materials: Kasumigaura sand for the surface layers, DL clay for the firm foundations of the slopes and a filter material within gabion parts. Each slope model had a shape where a shallow surface sand layer lay on a relatively hard foundation like typical natural slopes. The grading curves of three materials are shown in Fig. 3 and all grading curves are almost parallel. Each slope model was constructed in a steel soil tank with a transparent glass surface in the front of the tank. The dimensions of the model slopes were 122 cm in height (including the 100 cm height DL clay and the 22 cm height Kasumigaura sand), 42 cm in crest width, 70 cm in depth, and 184 cm in base length. The gradients of slopes were 45 degrees. Four different sizes of gabions were employed. The difference of the sizes is expressed in the height ratio h/H, where h is a height of the gabion and H is a height of the surface slope, respectively.

At first, the base foundation was constructed by compacting DL clay in the maximum dry density, namely compaction ratio D = 100 %, and the water content w = about 17 %. The thickness of each DL

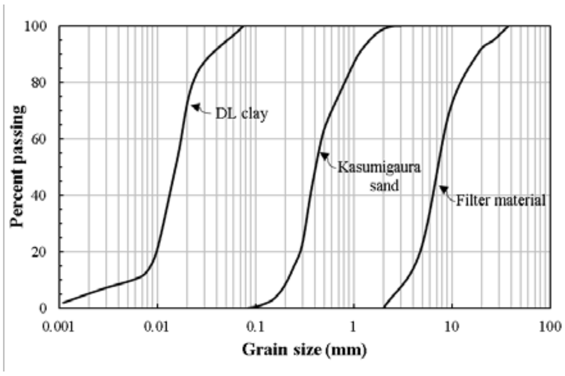

Fig. 3 Grading curves of the slope materials

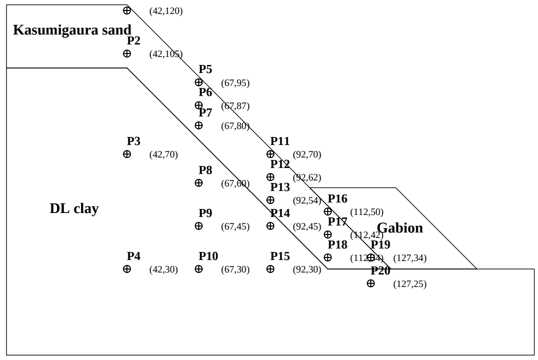

Fig. 4 Pore water pressure transducer positions

Table 1 Initial condition of slope models

Case	Height ratio h/H	Rainfall intensity I (mm/h)	*Relative density D_r (%)	*Water content w (%)	*Dry density ρ_d (g/cm^3)	*Degree of saturation S_r (%)
1	0.05	50	25	9.5	1.429	28.9
2	0.1	50	25	9.4	1.431	28.7
3	0.2	50	25	9.9	1.424	29.9
4	0.3	50	25	9.8	1.425	29.7

* for the surface layer

clay layer after the compaction was 5 cm and the necessary number of layers until the completion was 20 layers. After the construction of DL clay layer, the sand layer was laid on the DL clay foundation. Relative densities D_r = 25 % of the sand layers were employed with the water content w = about 10 %. The rolled thickness of each sand layer was 4 cm, and 23 layers were constructed. The filter material was filled in the gabions in a minimum density: about 1.60 g/cm^3 and each gabion lay on the toe part of the sand layer as shown in Fig. 2. The sizes of gabions and the initial conditions of models are shown in Table 1.

During the tests, pore water pressures and displacements were measured. The pore water pressures (PWPs) were monitored with 20 pore water pressure transducers (Capacity = 150 kPa). Each transducer was connected to each ceramic cup with a thin tube (Outer diameter = about 3 mm) filled with de-aired water. The dimensions of each ceramic cup were 12.5 mm in diameter and 25 mm in length and the air entry value was about 200 kPa. The ceramic cups were saturated with de-aired water under a vacuum. The 20 ceramic cups were installed into each soil slope. The installed positions (P1 – P20) are shown in Fig. 4 and the install level of each ceramic cup was the same as that of each associated transducer mounted on the back board of the soil tank. To measure the displacements of the slopes, pictures were taken through the transparent glass of the soil tank with a digital camera. The displacements were calculated by using Particle

Image Velocimetry (PIV) analysis method (White et al., 2003).

SIMULATION PROCEDURES

We conducted simulations of the model tests just mentioned before to clarify the mechanism of the slope failure. In simulation process, compression stresses assume to be negative and the following three assumptions are assumed to be valid: (i) The soil consists of soil particles, pore water and pore air, (ii) Pore air is always in contact with the atmosphere, (iii) The permeability of pore air is much higher than pore water. According to these assumptions, the following two field equations in weak forms are valid:

$$\int_V \left(\sigma'_{ij,j} + \delta_{ij} u_{eq,j} + \gamma F_i\right)\delta u_i^* \mathrm{d}V = 0\,, \tag{1}$$

$$\int_V \left(q_{i,i} - \dot{a}_{st} + S_r \dot{\varepsilon}_{ii}\right)\delta u_w^* \mathrm{d}V = 0\,. \tag{2}$$

Equation (1) is the force equilibrium equation and the Equation (2) is Richard's mass conservation equation of pore water. Here σ'_{ij} = effective stress tensor, δ_{ij} = Kronecker's delta, u_{eq} = equivalent pore pressure, γ = unit weight of soil, F_i = components of the body force vector, q_i = components of the relative displacement velocity vector of water with respect to soil skeleton, a_{st} = change of storage of water due to change of degree of saturation (S_r), ε_{ii} = volumetric strain of soil skeleton, δu^*_i = increment of the virtual displacement vector, δu_w^* = increment of virtual pore water pressure. Subscripts after a comma denote spatial differentiation. A superposed dot denotes differentiation with respect to time.

Unknown variables in these equations are displacements of soil skeleton and pore water pressures. The field equations are introduced to the discrete system using the finite element method and solution procedure base on the modified Newton-Raphson method is adopted.

In the elastic range, the elastic moduli are assumed to be functions of p' and the second deviator stress invariant J_2 as follows:

$$K = \frac{-2.3(1+e_0)}{\kappa} + K_i \tag{3}$$

$$G = G_i + \gamma_J \sqrt{J_2} - \gamma_p p'\,, \tag{4}$$

where K = the bulk modulus, G = the shear modulus and K_i, G_i, γ_J and γ_p = material parameters.

An Elastoplastic Model for Unsaturated Soil

In conducting consolidation analysis, material nonlinear properties: stress-strain relationship, permeability, soil water retention curves have to be considered. In this analysis, an elastoplastic model with two suction effects (Kohgo et al., 1993a, 1993b, 2007) was adopted as a stress-strain relationship. The two suction effects are that (i) an increase in suction increases effective stresses, and (ii) an increase in suction enhances yield stresses and affects the resistance to plastic deformations.

The first suction effect can be evaluated by describing the relationship between suction and shear strength at the critical state as follows:

$$\sigma'_{ij} = \sigma_{ij} - \delta_{ij} u_{eq}\,, \tag{5}$$

$$u_{eq} = u_a - s \qquad (s \le s_e)\,, \tag{6}$$

$$u_{eq} = u_a - \left[s_e + \frac{a_e}{s^* + a_e} s^*\right] \qquad (s > s_e)\,, \tag{7}$$

$$s = u_a - u_w\,, \tag{8}$$

$$s^* = \langle s - s_e \rangle\,. \tag{9}$$

Where σ_{ij} = total stress tensor, u_a = pore air pressure, u_w = pore water pressure, s = matric suction, s^* = effective suction, s_e = air entry suction, a_e = a material parameter, the brackets < > denote a Heaviside function: the operation $< z > = 0$ at $z < 0$ and $< z > = z$ at $z \geq 0$.

The second suction effect can be formulated by evaluating the state surface, which expresses elastoplastic volume changes behavior in unsaturated soils (Kohgo et al., 1993b). The state surface can be plotted in the space with the axes: mean effective stress p', effective suction s^*, and void ratio e. The shapes of state surfaces depend on the types of soils. Here, when $s^*_m = \infty$, state surface is expressed as follows (Kohgo et al., 2007):

$$e = -\lambda^* \log(-p') + \Gamma^*\,, \tag{10}$$

$$\lambda^* = \lambda + \frac{\lambda^*_{f1} s^*}{s^* + a_1^*}\,, \tag{11}$$

$$\Gamma^* = e_{01}^0 + \frac{\left(\Gamma - e_{01}^0\right)\lambda^*}{\lambda}\,. \tag{12}$$

Where $\lambda=\lambda^*$ in saturation; $\Gamma=\Gamma^*$ in saturation, λ^* = the slopes of e - log (- p') curves in the elastoplastic range, Γ^* = void ratios of the e - log (- p') curves in the elastoplastic range at p'= unit, s^*_m, λ^*_{f1}, a_1^* and e^0_{01} = material parameters.

Finite Element Mesh

Figure 5 shows the finite element mesh (FE mesh) and boundary conditions used in the simulation. Dimensions of the FE mesh are the same as the experimental slope models. The FE mesh consists of 230 elements and 759 nodal points. The 8-node isotropic elements were used for the displacement field and super-parametric elements were used for the pore water pressure filed. At first, built-up analyses were carried out from 1 layer to 14 layers, then, consolidation terms were set and after that rainfalls were subjected to the surface of the slope as constant flux values. The value was 50 mm/ h. At the bottom of the model slope, both directions of displacements were fixed and impervious condition was set. On the left and right side surfaces of the model slope, only the horizontal direction of the displacement was fixed. The material parameters of permeability model, SWR model, and other parameters are shown in Table 2.

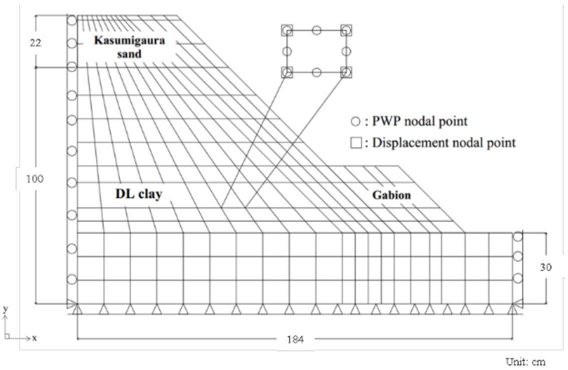

Fig. 5 Finite element meshes and boundary conditions used for the model simulation

Table 2 Material parameters of slope model simulation

	Elasticity					Plasticity			
Parameter	κ	K_i (kPa)	G_i (kPa)	γ_j	γ_p	α_h	φ'	φ'_{cs}	R
DL clay	0.020	0.0	0.10	0.0	70.0	5.0×10^4	26.2	32.0	1.0
Kasumigaura sand	0.0079	0.0	77.0	0.0	80.0	1.0×10^4	30.0	33.4	1.7
Filter	0.005	3,500	5,300	0.0	100.0	1.0×10^4	42.3	42.5	1.0
	State Surface					Effective Stress		Permeability	
Parameter	λ	Γ	e^0_{01}	λ^*_{f1}	a_1^* (kPa)	a_e		k_s (m/min)	m_p
DL clay	0.152	1.306	0.508	0.044	17.4	33.3		4.0×10^{-5}	1000.0
Kasumigaura sand	0.042	0.915	0.760	0.037	0.91	15.0		7.5×10^{-3}	1.3
Filter	0.158	0.872	0.20	0.093	0.403	15.0		1.0×10^{2}	3.0
	Soil Water Retention								
Parameter	S_{re}	S_{rm}	S_{rf}	s_e (kPa)	s_m (kPa)	s_f (kPa)	c_m	c_f	c_e
DL clay	0.99	0.60	0.16	10.0	13.0	120.0	1.0×10^{-2}	9.0×10^{-4}	1.0×10^{-3}
Kasumigaura sand	0.92	0.35	0.15	0.50	2.90	10.0	6.0×10^{-1}	8.0×10^{-4}	1.0×10^{-3}
Filter	0.85	0.50	0.20	0.07	0.50	5.00	1.0×10^{0}	4.0×10^{-3}	1.0×10^{-3}

RESULTS

Experimental Results

The experimental results are shown in Figs. 6 – 9. Figure 6 shows pore water pressure distributions when the first failures occurred. In all the cases, positive PWP values appear in the surface layers. In Case 1, the positive PWP values were seen at only the toe and the boundary between the sand layer and the foundation. Meanwhile, in Case 4 the positive pore water pressure values were monitored in almost the all areas of the surface layer. Thus the larger size of the filter gabions, the more rainwater could be stored within the slopes. Times t_f when the first failures occurred were 73 min in Case 1, 99 min in Case 2, 115 min in Case 3 and 148 min in Case 4, respectively. The times increased with an increase in the height ratio *h*/*H* (see Fig. 7).

Figure 7 shows the relationship between the first failure occurrence time t_f and the height ratio *h*/*H*. The relationship was linear and t_f increased with an increase in *h*/*H*. From the figure, the value of t_f in the case without the filter gabion could be read 63 minutes that is almost the same as 55 minutes obtained from our previous experimental test.

Figure 8 shows displacement vectors during failures. The large displacements could be only seen within the surface layer. Especially the displacements concentrated on the failure parts that started from the almost the same levels as those of the tops of filter gabions and extended to the upper parts. The areas where the large displacements were monitored became smaller in order of the height ratios. In all the cases, the displacements occurred almost along the slopes.

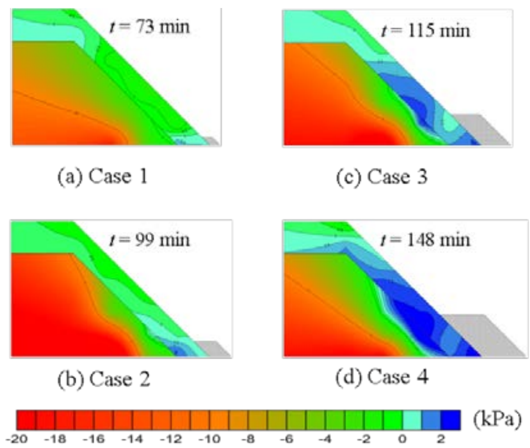

Fig. 6 Pore water pressure distributions when the first failures occurred

Figure 9 shows pictures at the final situations taken from diagonally above the slopes. In all the cases, the surface failures appeared. Types of slope failures depend on the cases. In Case 1, relatively large and clear failures could be seen. In other cases, the failure areas became mud and the failures were like flows.As mentioned before, the failures started from the almost the same levels as those of the tops of filter gabions and extented to the upper part. The sizes of failure areas were smaller as the height ratio increased. Thus, the filter gabions could make not only the failure size smaller but also the duration time of rainfall until the failure longer. But they did not express the drainage performance.

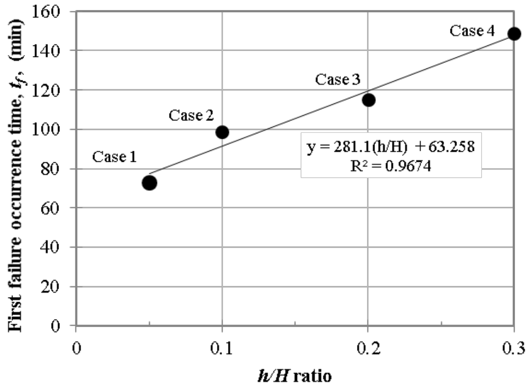

Fig. 7 First failure times versus the height ratios

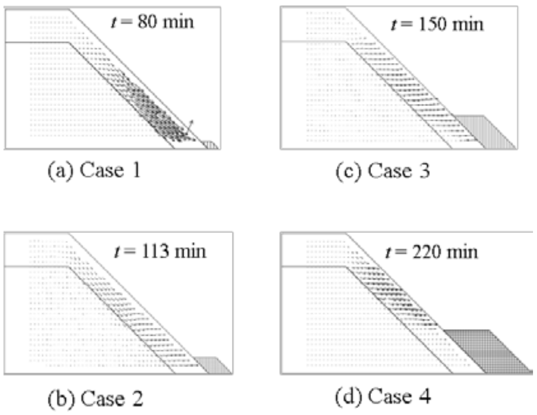

Fig. 8 Slope displacement vectors during failures

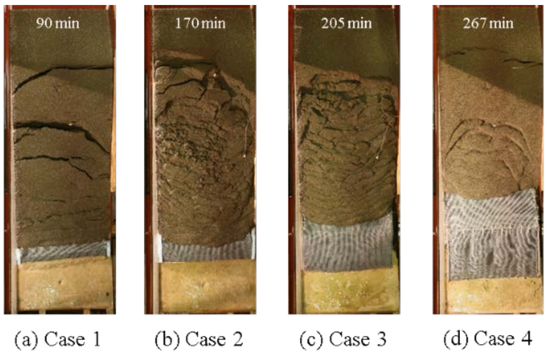

Fig. 9 Slope failure patterns at the end of the tests

Simulation Results

A model test: Case 2 was simulated by using a saturated and unsaturated consolidation analysis method coupled with an elastoplastic model for unsaturated soils (Code name: GEOCUP). The model had I = 50 mm/h and D_r = 25 %. Figure 10 shows the distributions of PWP values in both experimental and simulation results for Case 2. Comparing the results at the same elapsed time t = 60 minutes, in both positive PWP values appeared almost behind the gabion. In other parts there were negative PWP values. In DL clay layer most of areas were smaller than -10 kPa that was the air entry value of DL clay. At t = 100 mininutes, there was a clear seepage surface (u_w = 0 kPa on this surface) and the surface appeared at a relatively upper position of the slope surfaces. The seepage level calculated was slightly higher than that measured.

Figure 11 shows a comparison of simulation and experimental results of displacement vectors in Case 2. It was found that large displacements were calculated or measured within the surface layer, especially they were remarkable at the toe of the slope. The both situations were almost similar. At t = 99 minutes, the first failure occurred at the toe within the surface layer and the failures gradually progressed to the upper parts of the slope. At t = 120 minutes, they advanced to the whole surface slope.

Figure 12 shows the simulation result of shear strain distributions. At t = 80, 100 minutes, shear strains were still small. At t = 120 minutes, large shear strains were calculated within the surface layer and the area where large shear strains calculated started

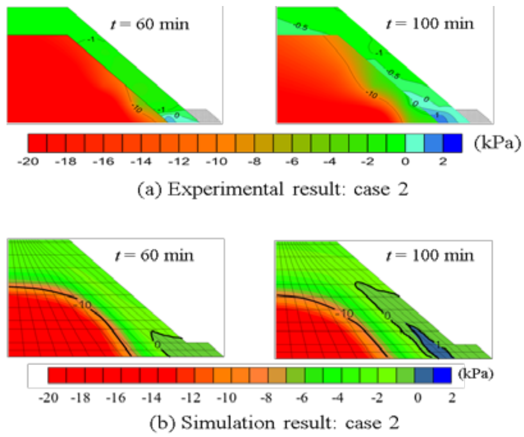

Fig. 10 Pore water pressure distributions in Case 2

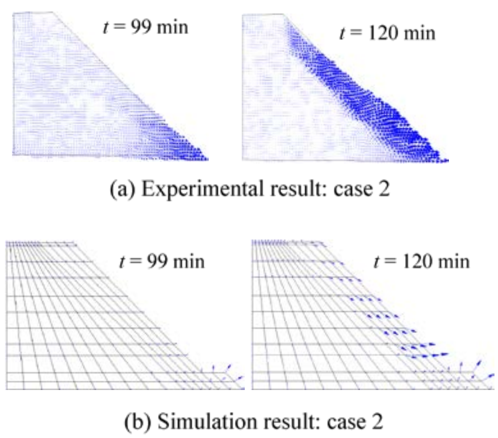

Fig. 11 Slope displacement vectors in both results comparison of Case 2

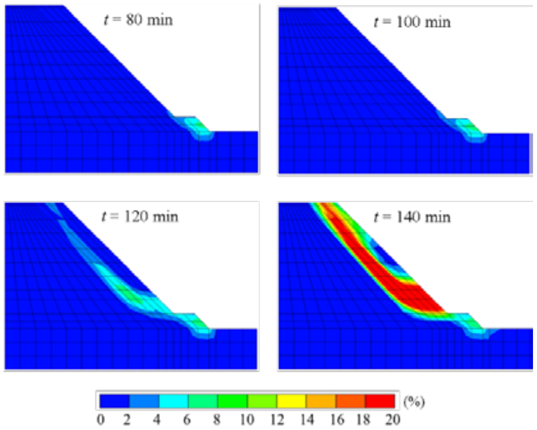

Fig. 12 Simulation result: Shear strain distributions with elapsed time of Case 2

from the same level as that of top of the gabion and extended to the crest of the slope. At t = 140 minutes, the area where the values of shear strains reached about 20 % made a band and the band reached the crest of the slope. The area where large amounts of shear strain calculated were almost consistent with the area where failures were measured from the experimental test.

CONCLUSION

We conducted a series of slope model tests with different sizes of filter gabions under a heavy rainfall condition. Each slope model had a shallow and loose surface sand layer on a relatively hard foundation as often seen in natural slopes. The filter material filled in gabions were used to control against slope failures. A model test was simulated by using a saturated and unsaturated consolidation analysis method coupled with an elastoplastic model for unsaturated soils (Code name: GEOCUP). We could obtain the following results: (i) Negative pore water pressure dissipated from the toes of the slopes and the saturated zones progressed to the upper part of the slopes, (ii) Large displacements were only accumulated in the surface layer, (iii) The failures started from the saturated toes at the top of the filter gabion and the failure zones progressed to upper part of the sand layer, (iv) The larger size of the filter gabion (high value of *h/H* ratio) could contain more water infiltrated inside of the slopes before a failure occurring, and (v) These situations mentioned above were consistent with both of the experimental and simulation results.

The filter gabions could make not only the failure size smaller but also the duration time of rainfall until the failure longer. But they did not express the drainage performance.

ACKNOWLEDGEMENT

The research herein was supported by the Japan Society for the Promotion of Science (JSPS) (the grant No. 23580327). Finally, we would like to express gratitude to members of our laboratory and staffs of National Institute for Rural Engineering, Tsukuba, Japan for their help and contributions to this series of experimental model tests.

REFERENCES

[1] Kohgo, Y., Nakano, M. and Miyazaki, T. 1993a. Theoretical aspects of constitutive modeling for unsaturated soils, *Soils and Foundations* 33(4), 49-63.

[2] Kohgo, Y., Nakano, M. and Miyazaki, T. 1993b. Verification of the generalized elastoplastic model for unsaturated soils, *Soils and Foundations* 33(4), 64-73.

[3] Kohgo, Y., Asano, I. and Hayashida, Y. 2007. An elastoplastic model for unsaturated rockfills and its simulations of laboratory tests, *Soils and Foundations* 47(5), 919-929.

[4] Orense, R. P., Shimoma, S., Maeda, K. and Towhata, I. 2004. Instrumented model slope failure due to water seepage, *J. Natural Disaster Science* 26(1): 15-26.

[5] Orense, R. P., Sapuay, S. E., Billedo, E. B. and Matsuoka, K. 2006. The 2004 sediment disasters in Quezon province, Philippines triggered by heavy rainfall, *Soils and Foundations* 46(6): 701-711.

[6] Rahardjo, H., Lee, T. T., Leong, E. C., Rezaur 2005. Response of a residual soil slope to rainfall, *Can. Geotechnical J.*, 42(2), 340-351.

[7] Tohari, A., Nishigaki, M. and Komatsu, M. 2007. Laboratory rainfall-induced slope failure with moisture content measurement, *J. Geotechnical and Geoenvironmental Eng*. ASCE 133(5), 575-586.

[8] Tokoro, N., Tanikawa, K., Saito, H., Kohgo, Y. and Hori, T. 2012. On 1G slope failure model tests due to rainfalls - Difference of failure patterns due to difference of densities of a subsurface sand layer, *Proc. 2nd Advances in Transportation Geotechnics*: 755-760.

[9] White, D.J., Take, W.A. and Bolton, M.D. 2003. Soil defor- mation measurement using particle image velocimetry (PIV) and photogrammetry, *Geotechnique* 53(7): 619-631.

SETTLEMENT PREDICTION OF LARGE-DIAMETER BORED PILE IN BANGKOK SOILS

Thayanan Boonyarak[1], Zaw Zaw Aye[1], Nutthapon Thasnanipan[1], Sahapap Supawo[2], Sereyroath Chea[1] [1]Seafco Public Company Limited, Thailand; [2]Faculty of Engineering, Khon Kaen University, Thailand

ABSTRACT

For large-diameter pile design, in addition to analysis of allowable bearing capacity, pile settlement calculation is required for minimizing differential and excessive settlements of a building. The objective of this paper is to evaluate and compare capability of each approach for pile settlement estimation. Data in this study was obtained from instrumented static pile load test results on 25 large-diameter bored piles and barrettes constructed in Bangkok. Thus, pile head settlement, pile base settlement and load distribution in each soil layer can be investigated. The pile settlement data was back-analyzed using analytical solutions and numerical modeling. Factors that influenced pile settlement behavior, consisting of soil type at pile base, shape of pile and drilling slurry, were analyzed. According to measured data, pile constructed using bentonite slurry had larger settlement than those excavated with polymer slurry. This is because shaft friction reduction in the former was larger than the latter, resulting in larger load transferred to the pile base and caused higher toe settlement. For pile settlement more than 2% of pile diameter, axial load transferred to pile toe. In these settlement regions, analytical approaches substantially underestimate the measured results while the numerical modeling still reasonably captured the measured one. Guidelines for adopting each method for pile settlement calculation are also proposed.

Keywords: Pile settlement prediction, Load transfer mechanism, Bangkok soils, Load-settlement database, Numerical modeling

INTRODUCTION

For deep foundation, apart from capacity of pile, accurate settlement calculation is also a key factor to be considered. To calculate pile settlement, analytical solution is commonly adopted for simplicity. Tomlinson (1995) [1] proposed an equation to calculate pile settlement as shown in Eq. 1. For brevity of the paper, detail of each parameter is not described. To sum up, the first and second terms refer to elastic shortening of the pile and settlement of soil at pile base, respectively.

$$\delta = \frac{(W_s+2W_b)L}{2A_sE_p} + \frac{\pi W_b B(1-\nu^2)I_p}{4A_bE_s} \quad (1)$$

Bowles (1996) [2] considered pile shortening according to each layer of soil along pile shaft and calculate soil settlement at pile toe (refer to Eq. 2).

$$\delta = \Sigma\left[\frac{P_{av}\Delta L}{A_{av}E_p}\right] + \Delta q D\frac{(1-\nu^2)}{E_s} m I_S I_F F_1 \quad (2)$$

Vesic (1977) [3] adopted three components of pile settlement as stated in Eq. 3. In this equation, the first, second and third terms are pile settlement due to elastic shortening, soil compression at pile base and soil compression along the pile shaft, respectively.

$$\delta = \frac{(Q_{wp}+\xi Q_{ws})L}{A_pE_p} + \frac{Q_{wp}C_p}{Dq_p} + \frac{Q_{ws}D(1-\nu^2)I_{ws}}{pLE_s} \quad (3)$$

Alternatively from analytical solutions, numerical analysis can be adopted for computing pile settlement. Elaziz and Naggar (2014) [4] presented finite element method by back-analyzing results from hollow steel pile load testing. Shooshpasha et al. (2013) [5] conducted three-dimensional finite element analyses for determining bearing capacity of a pile and validated with measured result.

Construction technique of bored pile also influences the pile capacity. Thasnanipan et al. (1998) [6] reported that if the exposure time of bentonite slurry in each borehole is more than 48 hours without agitating, filter cake thickness is high. This resulted in substantial reduction in load-bearing capacity of the pile. To minimize this problem, Thasnanipan et al. (2003) [7] and Boonyarak et al. (2015) [8] found that bored pile constructed using polymer slurry had larger load bearing capacity than those constructed with bentonite slurry. Submaneewong (1999) [9] studied effect of barrette shape on load bearing capacity and reported empirical equation to estimate pile behavior in each type of soil.

This paper presents a method for estimating pile settlement based on load testing database of piles constructed in Bangkok soils. Factors influenced pile settlement behavior was analyzed. Limitation and recommendation of each method is explained and discussed.

BACK-ANALYSIS OF PILE LOAD TESTS

Data analyzed in this study is obtained from 25 instrumented pile load tests in Bangkok soils. Pile diameters are ranging from 0.80 m to 1.65 m and depth of pile tip are varying between 41.0 m and 59.3 m. All piles were tested using slow maintained load test method [10] with maximum test load of 2.5 times the design safe working load.

Analyzed data can be categorized into four groups. These groups are circular bored pile with pile tip in sand and clay, barrette with tip embedded in sand and clay.

For estimation of pile settlement, Young's modulus of sand and clay are assumed to be 2000N and 800C_u, respectively (adopted from [11]). Poisson's ratio of soil is assumed to be 0.25. For concrete pile, modulus of elasticity is 27 GPa.

NUMERICAL ANALYSIS OF LOAD TESTING

Finite element method using software PLAXIS 2D 2015 was adopted for computing pile settlement.

Finite element mesh and boundary conditions

To model a single pile behavior, axis-symmetry analysis was carried out using finite element mesh as shown in Fig. 1a. One project from load testing database was selected considering the same soil conditions as load testing. The pile had a diameter of 1.0 m and depth of 43 m.

Boundary conditions at the right side and the bottom of the mesh were roller and hinge, respectively. The boundary at the left side was the axis of symmetry. The width of the model is 30 m and depth is 80 m which is greatly larger than the required distance of six times the pile diameter at the side and the pile base.

Figure 1b shows details of pile and applied load. Pile was model using linear elastic material having Young's modulus, Poisson's ratio and unit weight of 27 GPa, 0.15 and 24 kN/m^3, respectively. Reduction factor of 0.75 was applied at the interface between the pile and the surrounding soil at the side as there is a slip between the soil and pile. However, no interface was adopted at the pile base as the soil and pile always attached to each other.

Soil model and parameters

Soil was modeled using Hardening soil with small strain stiffness [12 & 13]. Unlike other conventional elastic-perfectly plastic model, this model can simulate stiffness dependent on stress, strain and path. Parameters were adopted and modified from [14] and [15], who studied and calibrated the model parameters for Bangkok soils. All parameters are summarized in Table 1.

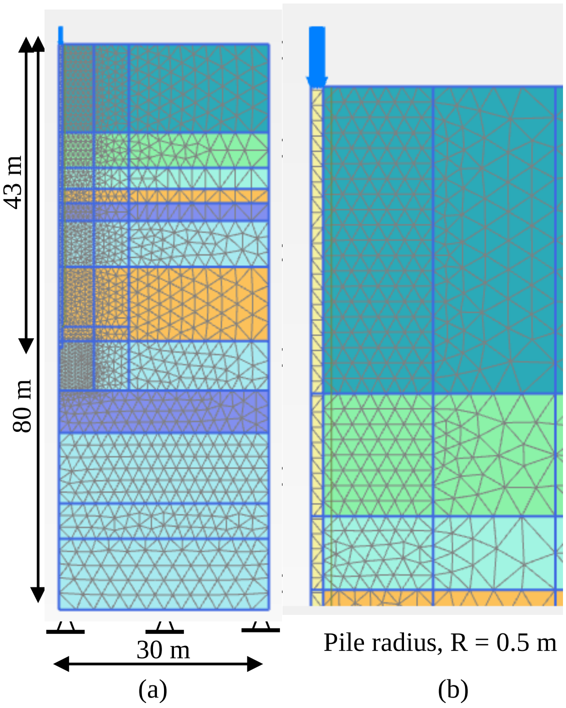

Fig. 1 (a) Finite element mesh; (b) Details at pile head and surrounding soils

Table 1 Parameters for numerical analysis

Parameter	Soft clay	Medium stiff clay	Stiff to very stiff clay	Dense sand	Hard clay
c'	1	5	11.5	0.1	11.5
ϕ'	27	27	28	33	28
Ψ	0	0	0	5	0
$E_{ref,50}$	800	5150	5150	27000	9500
$E_{ref,oed}$	850	6425	6425	27000	12000
$E_{ref,ur}$	8000	19000	19000	162000	30000
R_f	0.9	0.9	0.9	0.9	0.9
m	1	1	1	0.5	1
$K_{0,NC}$	0.74	0.74	0.5	0.5	0.5
ν_{ur}	0.2	0.2	0.2	0.2	0.2
$\gamma_{0.7}$	0.0005	0.001	0.001	0.014	0.0015
G_{max}	5000	16000	48000	200000	124000

Modeling procedures

In the first stage, stress in soil is initialized according to $K_{0,NC}$ of each soil. After that, bored pile is constructed by changing material properties from soil to concrete. It is assumed that there is no soil displacement during bored pile installation. For pile load testing, line load (P) is applied on cross section area of pile (A_b). Load is increased by 1% step until reaching the maximum test load of 100% in each pile.

INTERPRETATION OF RESULTS

Settlement of circular bored pile

Results of load-settlement relationship of circular bored pile are shown in Fig. 2. For comparison of data in each test, applied load is divided by shaft area (P/A_s) and settlement at pile head is normalized by its pile diameter (δ/D). General trend of load-settlement curves can be described by bi-linear relationship. The first part of linear is where normalized settlement is within 2%. After that, load settlement relationship becomes curved or so-called transition zone. The second part of linear is the zone of higher settlement rate than the first part of linear.

For bored pile constructed using bentonite slurry with pile tip in sand, P/A_s at normalized settlement at 2% is between 70 and 90 kN/m^2. By comparing with pile constructed using polymer slurry having pile tip in sand, the P/A_s of this type of pile at the same δ/D was ranging from 90 to 120 kN/m^2. It suggests that shaft friction of bored pile using bentonite slurry is smaller than those with polymer slurry. This is because thicker filter cake in the former than in the latter [7], resulting in smaller shaft friction. Note that only one set of data from pile using polymer shows a bi-linear behavior as axial load did not transfer to the toe of most of piles of this type.

The effects of drilling slurry on pile settlement also influenced the piles with tip in clay. At settlement of 2%D, P/A_s for piles constructed using bentonite slurry and polymer slurry are 50-70 kN/m^2 and 70 kN/m^2 (data only from one pile), respectively.

Considering type of soil at pile base, it is found that pile with tip in sand had smaller settlement than those having tip in clay (given the same type of drilling slurry). This is because soil stiffness (e.g. Young's modulus) of sand (at depth of more than 40 m) is substantially larger than clay as stiffness proportionally increases with depth for sand.

Settlement of barrette

Figure 3 shows load-settlement relationship of barrettes with tip in sand and clay. All barrettes were constructed using bentonite slurry as polymer slurry was not applicable to stabilize the trench of barrette.

From the comparison, settlement of barrette with pile tip in clay was substantially larger than those in sand. For example, at P/A_s of 60 kN/m^2, settlements of barrette with tip in sand and clay were 0.5%D and 5.5%D, respectively. This observation was consistent with those of circular bored pile (refer to Fig. 2).

For effects of shape on settlement of barrette, at δ/D of 2%, P/A_s of barrette with tip in sand was about 80 kN/m^2, which is in the same range of those for circular bored pile (constructed using bentonite slurry) of from 70 to 90 kN/m^2. When tip of barrette was in clay, P/A_s was about 50 kN/m^2, which is similar to those of bored pile (50-70 kN/m^2). This finding suggests that shape of barrette does not significantly affect the settlement behavior.

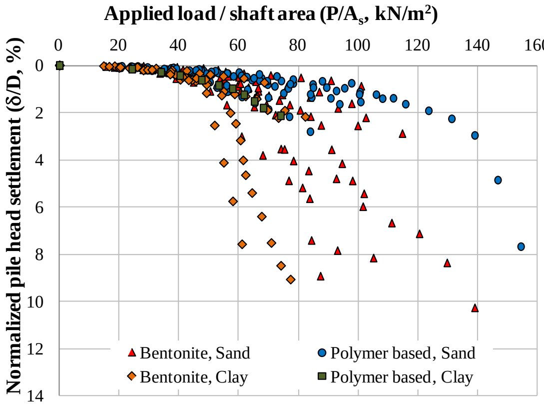

Fig. 2 Load-settlement curves of circular bored pile with different soil types at pile tip and drilling slurries

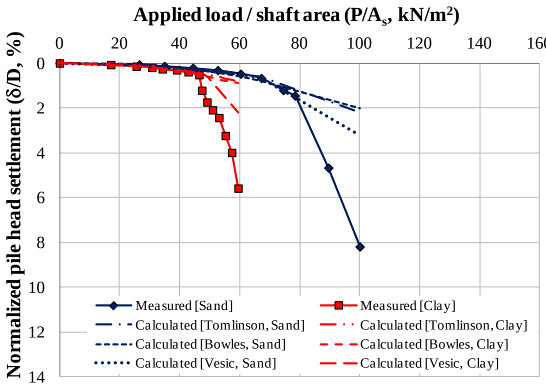

Fig. 3 Comparison of effects of soil type at pile tip on settlement of barrettes

The three approaches for calculating deep foundation settlements were compared with the measured results (refer to Fig. 3). In the region where pile head settlement was between 1%D and 2%D, the three methods reasonably captured the measured results as elastic shortening of the pile was the major factor of pile head settlement. As the load was increased, settlements calculated by Tomlinson (1995) and Bowles (1996) were significantly underestimated. The calculated result obtained from

Vesic (1977) had a larger settlement than the other two but still underestimated the measured one. This is because shear modulus of soil considered in the analytical solution was assumed constant, resulting in underestimation of settlement at higher load. This effect of stiffness on pile settlement is explained later in the topic shear modulus degradation modeling in numerical analysis.

Comparison between numerical analysis and analytical solution

Measured results of pile load test compared with three analytical solutions and numerical analysis are shown in Fig. 4. This pile had a diameter of 1 m, depth of 43 m and was constructed by using bentonite slurry.

From the comparison, analytical solution acceptably predicted the measured result up to P/A_s of 42 kN/m^2 or at 125% of designed safe working load. When the test load reached its maximum at P/As of 96 kN/m^2, measured settlement was more than two times larger than those obtained from the analytical solutions.

Settlement obtained from numerical analysis slightly overestimated the measured result in the small settlement region. At higher testing load, finite element method result was very similar to the measured result. Relatively small discrepancy in the region of P/As from 60 to 80 kN/m^2 between computed and measured one may be due to inconsistent stiffness degradation modeling in the numerical analysis.

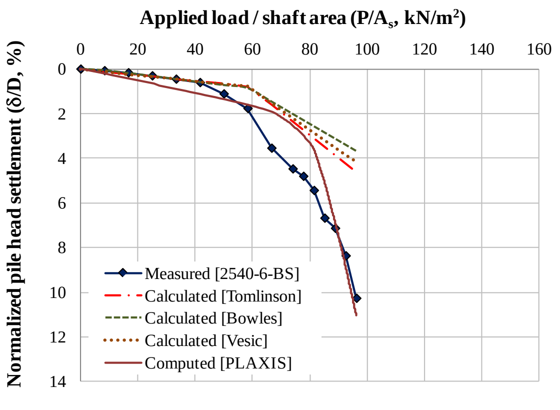

Fig. 4 Measured load settlement curve compared with three analytical solutions and numerical analysis

Proportion of pile settlement

Pile shortening and toe settlement of the pile which is discussed in the previous section is shown in Figure 5. Measured result of normalized pile shortening was 1.4% or equivalent to 0.52 PL_p/A_bE_p; where P is maximum test load, L_p is the pile length, A_b is the cross-sectional area of the pile and E_p is Young's modulus of the pile. Pile shortening calculated from Tomlinson (1995), Bowles (1996) and Vesic (1977) were ranging from 1.8%D to 2.0%D. Similarly, pile shortening obtained from numerical analysis was 1.9%D. It is found that both approaches provided reasonable value of pile shortening compared with the measured result.

The normalized toe settlement from measured result was 8.9%D but the calculated results using analytical solution substantially underestimated the measured one. However, toe settlement computed using numerical analysis was closed to the measured result, resulting in reasonable estimation of pile settlement calculation (refer to Fig. 4).

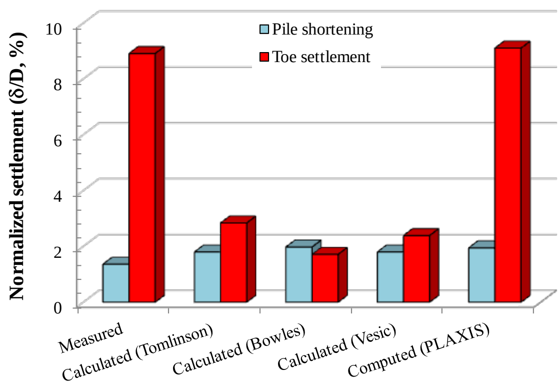

Fig. 5 Proportion of pile settlement

Effects of shear modulus degradation of soil on pile settlement

Figure 6 shows normalized shear modulus of soil (G_{After}/G_{Before}) at each normalized pile settlement (δ/D). Note that G_{Before} and G_{After} refer to shear modulus of soil before and during pile load test, respectively. Shear modulus used in the analytical solutions is constant by using an average or lower bound value. For numerical analysis, the normalized shear modulus reduced from 1 to 0.34 at pile settlement of 1.1%D. This settlement is where friction is almost fully mobilized (between 1-2%D). As an advanced soil model is adopted in this study, the effect of soil stiffness degradation can be considered.

As shown in Figs. 4 and 5, analytical approaches substantially underestimate the measured results while the numerical modeling still reasonably captured the measured one. This is due to constant soil stiffness and stiffness degradation adopted for the former and the latter, respectively.

ACCURACY OF PILE SETTLEMENT ESTIMATION BY ANALYTICAL SOLUTION

Comparisons of maximum measured pile head settlement and calculated result from the three analytical solutions are shown in Figure 7.

Figure 7a shows comparison of pile settlement estimation using Tomlinson (1995)'s approach with measured results. At pile head settlement not more than 2%D, calculated settlement was slightly larger than the measured one. For this settlement region, the analytical solution was still reasonably estimated the measured settlement with error of from 0.5%D to 1.0%D.

However, for pile with settlement larger than 5%D, the calculated settlement significantly underestimated the measured result by 3%D to 8%D. In addition, estimation of pile settlement constructed by using polymer slurry was more accurate than those constructed with bentonite slurry and barrette. Thus, one should be aware when using the analytical solution to estimate settlement of pile that has a tendency to be larger than 5%.

There are also comparisons between two analytical solutions of pile head settlement using Bowles (1996) and Vesic (1977) and the measured results as shown in Figure 7b and 7c, respectively. These two analytical solutions provided similar trend to those obtained from Tomlinson (1995). Thus, to predict pile settlement, any of the three analytical solutions can be adopted up to pile settlement of 5%D.

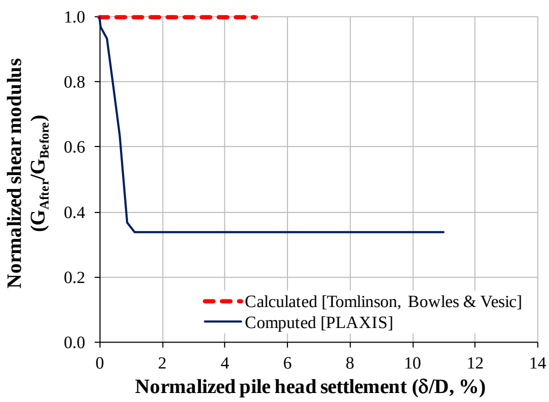

Fig. 6 Shear modulus degradation and pile head settlement

IMPLEMENTATION OF LOAD SETTLEMENT DATABASE FOR PILE CAPACITY DETERMINATION

According to relationship between applied load per shaft area (P/A_s) and normalized pile head settlement (δ/D) as refer to Figures 2 and 3, pile capacity can be determined. If pile settlement of 5%D is set as an ultimate load bearing capacity settlement, average P/A_s can be obtained for each type of pile. For example, bored pile with diameter of 1.5 m, depth of 50 m, embedded in sand and constructed using polymer slurry is estimated to have P/A_s of 140 kN/m^2. Thus, the ultimate load bearing capacity and a safe working load of this pile are about 32,000 kN and 12,800 kN, respectively given that factor safety of 2.5 is adopted.

Table 2 summarizes average load per unit area at normalized settlement of 2% and 5%, which are settlement at fully mobilized shaft friction and ultimate bearing capacity, respectively.

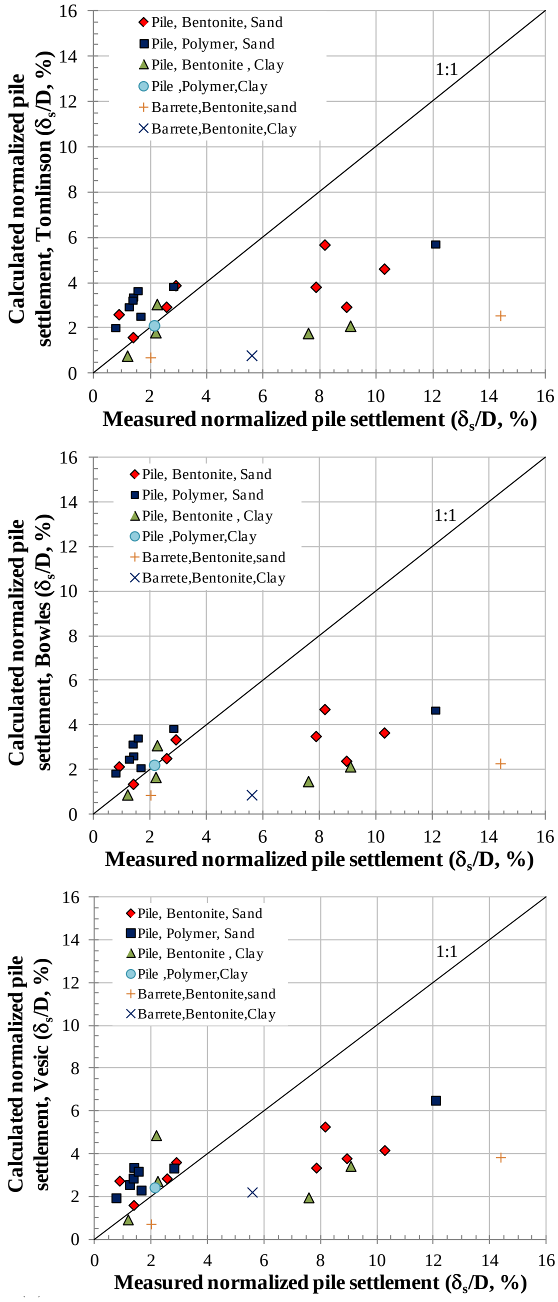

Fig. 7 Comparison of settlement prediction using following approach: (a) Tomlinson, 1995; (b) Bowles, 1996; (c) Vesic, 1977

Table 2 Summary of load-settlement relationship

Pile type	Slurry type	P/A_s , kN/m^2 at δ/D of 2%	P/A_s , kN/m^2 at δ/D of 5%
Bored pile, sand	Bentonite	70 - 90	80 - 100
Bored pile, sand	Polymer	90 - 120	140
Bored pile, clay	Bentonite	50 - 70	60 - 80

Pile type	Slurry type	P/A_s , kN/m^2	
		at δ/D of 2%	at δ/D of 5%
Bored pile, clay	Polymer	70	N/A*
Barrette, sand	Bentonite	80	90
Barrette , clay	Bentonite	50	60

Note: * Pile settlement did not reach 5%D

CONCLUSIONS

Based on back-analyzed data from 25 numbers of instrumented pile load test, following conclusions may be drawn:

(a) For deep foundation embedded in the same soil type, settlement of bored pile constructed using bentonite slurry is substantially larger than those constructed with polymer slurry. This is because of thicker filter cake in former than the latter, causing reduction in shaft friction.

(b) By comparing bored pile constructed using the same type of slurry, bored piles embedded in clay have larger pile settlement than those embedded in sand. This is due to smaller soil stiffness in the former than the latter.

(c) There is no significant difference in settlement between barrette and circular bored pile. Thus, load-settlement relationship of bored pile can be adopted to estimate the settlement in barrette, given that bentonite slurry is used in bored pile and soil type at pile toe is the same.

(d) Pile settlement estimated using analytical solutions proposed by Tomlinson (1995), Bowles (1996) and Vesic (1977) provided reasonable result in the range where resistance is mainly provided by shaft friction. This range is within pile settlement of 2% the pile diameter.

(e) At settlement larger than 5% the pile diameter, the three analytical solutions substantially underestimate the measured result. On the other hand, numerical analysis still reasonably predicts the measured result. This is because soil stiffness degradation was modeled in the latter while stiffness was assumed constant in former.

REFERENCES

[1] Tomlinson M.J.,"Pile foundation, The carrying capacity of piles and pile groups", Foundation design & Construction 6th edition, 1995, pp. 265-316.

[2] Bowles. J. E., "Pile settlement ", Foundation analysis and design 5th ed., 1996, pp. 907-909.

[3] Vesic, A. S., "Design of Pile Foundations", National Cooperative Highway Research Program, Synthesis of Practice No. 42, Transportation Research Board, Washington DC, 1977, 68 pp.

[4] Elaziz, A. Y. A. and Naggar, M. H. E., "Geotechnical capacity of hollow-bar micropiles in cohesive soils", Can. Geotech. J. 51: 1123–1138, 2014, dx.doi.org/10.1139/cgj-2013-0408

[5] Shooshpasha, I., Hasanzadeh, A. and Taghavi, A. "Prediction of the axial bearing capacity of piles by SPT-based and numerical design methods", Int. J. of GEOMATE, June, 2013, Vol. 4, No. 2 (Sl. No. 8), pp. 560-564

[6] Thasnanipan, N., Baskaran, G. & Anwar, M.A. "Effect of construction time and bentonite viscosity on shaft capacity of bored piles", Proceeding of the 3rd international geotechnical seminar on bored and auger piles, Ghent, Belgium (ed. Van Impe), 1998, pp. 171-177

[7] Thasnanipan, N., Aye, Z. Z. and Boonyarak, T. "Behavior of Polymer-based Slurry for Deep-seated Bored Piles in Multi-layered Soil of Bangkok", Proceedings of the 4th International Geotechnical Seminar on Deep Foundations on Bored and Auger Piles. Ghent, 2003, Belgium

[8] Boonyarak, T., Prongmanee, N., Boonchaiyo, C., Aye, Z. Z. and Thasnanipan, N. The assessment of design parameters of wet-processed bored pile in Bangkok subsoil. The 20th National Convention on Civil Engineering, Chonburi, Thailand. 2015, ID 348 (in Thai).

[9] Submaneewong C. (1999). Behavior of instrumented barrette and bored piles in Bangkok subsoils, (in Thai), M.Eng. Thesis, Department of Civil Engineering, Faculty of Engineering Chulalongkorn University, Bangkok, Thailand.

[10] ASTM D 1143, "Standard test method for piles under static axial compressive load", 1994; West Conshohoken, P.A.

[11] Aye, Z. Z., Boonyarak, T., Maung, A. W., Thasnanipan, N. and Prongmanee, N. "Back-analysis of design parameters for bored pile in Yangon". International Conference in Soft Ground Engineering, Singapore (ICSGE), 2015, pp 563-570

[12] Schanz, T., Vermeer, P.A. and Bonnier, P.G. "Formulation and verification of the Hardening soil model", in Beyond 2000 in computational Geotechnics, A.A. Balkema, Roterdam, Netherlands, 1999, pp. 281-290

[13] Benz, T. "Small-strain Stiffness of Soils and Its Numerical Consequences". Volume 55 of Institut für Geotechnik Stuttgart, Mitteilung. Inst. für Geotechnik, 2007

[14] Surarak, C., Likitlersuang, S., Wanatowski, D., Balasubramaniam, A., Oh, E., Guan, H.,. "Stiffness and strength parameters for hardening soil model of soft and stiff Bangkok Clays". Soils and Foundations 52 (4), 2012: 682–697.

[15] Likitlersuang, S., Teachavorasinskun, S., Surarak, C., Oh, E. and Balasubramaniam, A. "Small Strain Stiffness and Stiffness Degradation Curve of Bangkok Clays". Soils and Foundations. 53(4), 2013: 498–509

INFLUENCE OF NONWOVEN GEOTEXTILE ON THE HYDRAULIC RESPONSE OF MECHANICAL STABILIZED EARTH WALL

Duc Bui Van[1], Avirut Chinkulkijniwat[2], Suksun Horpibulsuk[3], Arul Arulrajah[4], Somjai Yubonchit[5], Artit Udomchai[6], Irin Limrat[7], Tulasi Ram Bhattarai[8]

[1] School of Civil Engineering, Suranaree University of Technology, Thailand. Email: buivanduc@humg.edu.vn
[2,3] Center of Excellence in Civil Engineering, School of Civil Engineering, Suranaree University of Technology, Thailand;
[4] Swinburne University of Technology, Melbourne, Australia
[5,6,7] School of Civil Engineering, Suranaree University of Technology, Thailand;
[8] Senior Divisional Engineer at Ministry of Irrigation, Government of Nepal.

ABSTRACT

The use of improper drainage system may cause the instability, even failure of Mechanical Stabilized Earth (MSE) walls. Due to the shortcoming of conventional methods, the drainage system made of geocomposite has been widely employed as an alternative mean once dealing with the seepage problem. Some of previous works reported that the water retention characteristic (WRC) of geotextile is similar to that of the coarse-grained soil, however, the influence of WRC of geotextile on the flow behavior of MSE wall is still not clearly understood. In this research, the laboratory and numerical investigation was chosen to examine the effect of nonwoven geotextile on the hydraulic response of MSE. Firstly, a large scale physical model of MSE wall was conducted under two conditions including with and without installation of geocomposite layer. Next, a series of numerical calculation was performed by using finite element method so as to examine the effect of some soil water characteristics of non-woven geotextile on seepage responds including the effective saturation, and phreatic surface in the MSE wall reinforced by geogrids. Results from experiment shows that there is a significant reduction in water level in reinforced zone once the geocomposite employed hence higher stability of MSE obtained. Similarly, parametric study is also found out that the distribution of effective saturation at the interface between backfill and geocomposite material is influenced by the g_a parameter whereas the gn plays a little role on the distribution of effective saturation at the interface. In conclusion, the profile of effective saturation is mainly affected by the WRC of geotextile, whereas the impact of van Genuchten parameters of geotextile on the phreatic surface is found insignificantly. The second factor that affects the distribution of effective saturation along the interface between soil and geocomposite was observed is that “capillary barrier”.

Keywords: Mechanical Stabilized Earth wall, Geocomposite Drain, Unsaturated Flow, Soil Water Retention.

1. INTRODUCTION

The use of improper drainage system may cause the instability even failure of Mechanical Stabilized Earth (MSE) walls. Seventeen of 26 collected case histories of failure of MSE wall associated to low permeability of backfill material was investigated by Koerner, R.M., et al (2001) [1]. After carrying out an investigation of the disastrous failure of a reinforced earth wall Yabu city in 2004 Shibuya, S., et al. [2] concluded that the conventional drainage system is not applicable for high level of ground water.

Due to the shortcomings of the conventional drainage method such as cost expensive, requires large site preparation, the use of an artificial drainage material consisting of a core element having large flow channel (geonet) sandwiched by nonwoven geotextile is necessary to provide a drainage system [1]. Despite having many reports on the use of geocomposite as a drainage system, limited numerical analysis of MSE walls using geocomposites has been stated. Similarly, the effect of WRC of non-woven geotextile has not been taken into account yet, even many of studies [1], [3], [4] indicate that the geotextiles has WRC similar to those of coarse-grained soils. Currently, various methods have been introduced to estimate WRC of geotextile including a hanging column test; a capillary rise test approach; an outflow capillary pressure cell, and modified outflow capillary pressure cell [5], [6]. In fact, WRC of geotextile is now more common; however, the design of geocomposite drains in MSE wall does not incorporate WRC of geotextiles. This paper aims to investigate the influence of some soil water parameters of non-woven geotextile, a large scale of MSE wall with L-shape geocomposite drains was employed in this research. A set of instruments were used to observe flow and deformation responses during tests. Lastly, parametric study was chosen to carry out the numerical experiments. The outcomes of this research will lead to a better understanding of which parameters affect the performance of the geocomposite. This finding can contribute to the effectiveness of the selection of drainage material, backfill material as well once dealing with seepage water through the mechanically stabilized earth wall.

2. PHYSICAL AND NUMERICAL OUTLINES

2.1 Theoretical Back Ground

Once considering a two dimensional homogeneous anisotropic material, the transient water flow within an unsaturated porous medium is governed by the following equation

$$\frac{\partial \theta}{\partial t} = k_x \frac{\partial^2 h}{\partial x^2} + k_y \frac{\partial^2 h}{\partial y^2} \qquad (1)$$

Where θ is volumetric water content, h is the total head, k_x and k_y are the unsaturated coefficient of permeability in the x- and y- directions, and t is time. To supplement Eq. 1, constitutive equations related to θ, k_x, and k_y to h are required. Iryo, T., (2003) [4], and Knight, M., (2001) [5] concluded that there is considerable evidence to suggest that van Geuchten (VG) [7] and van Genuchten-Mualem (VGM) [8] models are applicable to nonwoven geotextiles. Thus, they are employed to approximate WRC and permeability functions for both the soil and the nonwoven geotextile.

$$S_e = \frac{S - S_{res}}{S_{sat} - S_{res}} == \left[1 + \left(g_a \left|h_p\right|\right)^{g_n}\right]^{g_c} \qquad (2a)$$

$$k_r(S_e) = S_e^{0.5}[1 - (1 - S_e^{-1/g_c})^{-g_c}]^2 \qquad (2b)$$

Where S_e is effective degree of saturation, S is degree of saturation, S_{res} is residual saturation, S_{sat} is the saturation of saturated soil, h_p is matric suction head, k_r is the relative permeability coefficient. g_a [m^{-1}] and g_n are fitting parameters, and according to Mualem hypothesis [9], g_c is assigned as $1/g_n$ -1.

2.2 Materials

The soil used in this investigation is a clean sand which consists of 10% gravel, 87.3% sand, and 2.7% silt. The particle size distribution is presented in the Fig 1 (a). Optimum water content of 5.7 % and maximum dry unit weight, γ_{dmax} of 16.7 kN/m^3. The saturated hydraulic conductivity of the soil is k= 17 m/day. The WRC of the sandy soil was obtained by measuring change of drained water volume during applied matric suction [9], or capillary force using pressure apparatus [6].

The hydraulic properties of the geotextile are as shown in Table 1. The transmissivity of the geonet is 0.004 m^2/sec hence the corresponding saturated permeability of 69120 m/day. The WRC of the sandy soil and the geotextile are presented in Fig 1 (b). The fitting parameters are summarized in Table 1. Iryo, T., (2003) [4] gathered test results of 13 geotextiles and reported the range of VG and VGM model parameters of geotextiles subjected to both wetting and drying cycles. Based on [4], the typical range of g_a and g_n is 10-300 [m^{-1}] and 2-6 [-], respectively.

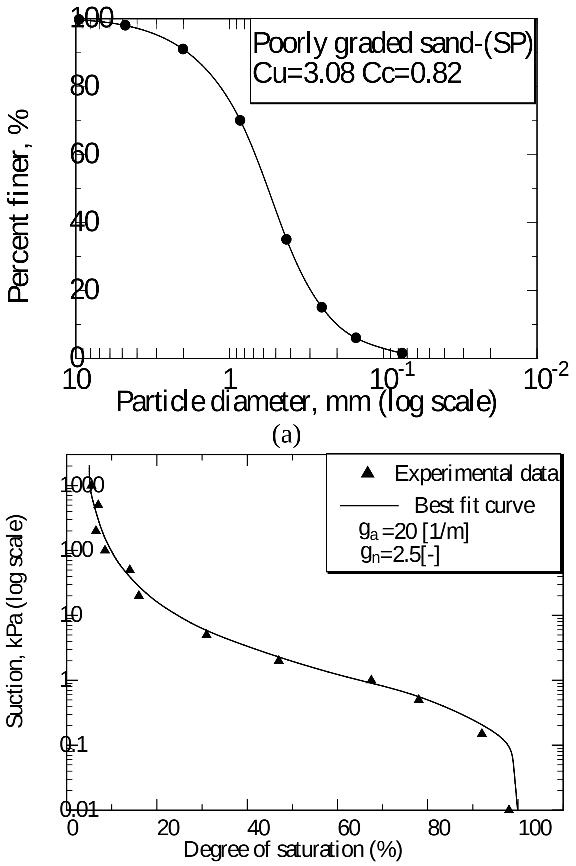

Fig 1. Grain-size distribution (a), and WRC of the soil used in this research (b).

Table 1. van Genuchten parameters of materials

Notations	Unit	Soil	Geotextile	Geonet
g_a	[m^{-1}]	20	20	600
g_n	[-]	1.5	2.5	40
S_{res}	[-]	0.03	0.03	0.00
S_{sat}	[-]	1.00	0.80	1.00
Geotextile: indicative hydraulic properties				
$K_{lateral}$	[m/day]	17	320	69120
K_{long}	[m/day]	17	2000	69120

2.3 Full-scale test experiments

A large scale physical experiments were conducted with the dimensions of the tank are shown in (Fig 2). Two physical experiments were employed: without (case I), and without geocomposite drain installation (case II). After filling sandy soil into the physical model up to height of 1.4m, the upstream water was increased from the initial level to surface of 0.0m, 0.8m. 1.1m, 1.5m, respectively. An acrylic plate was employed to make the wall facing. 5 layers of bearing reinforcements [10] of equal length of 0.7 m [11] were installed in the reinforced zone. Locations of the instruments are illustrated in Fig 2.

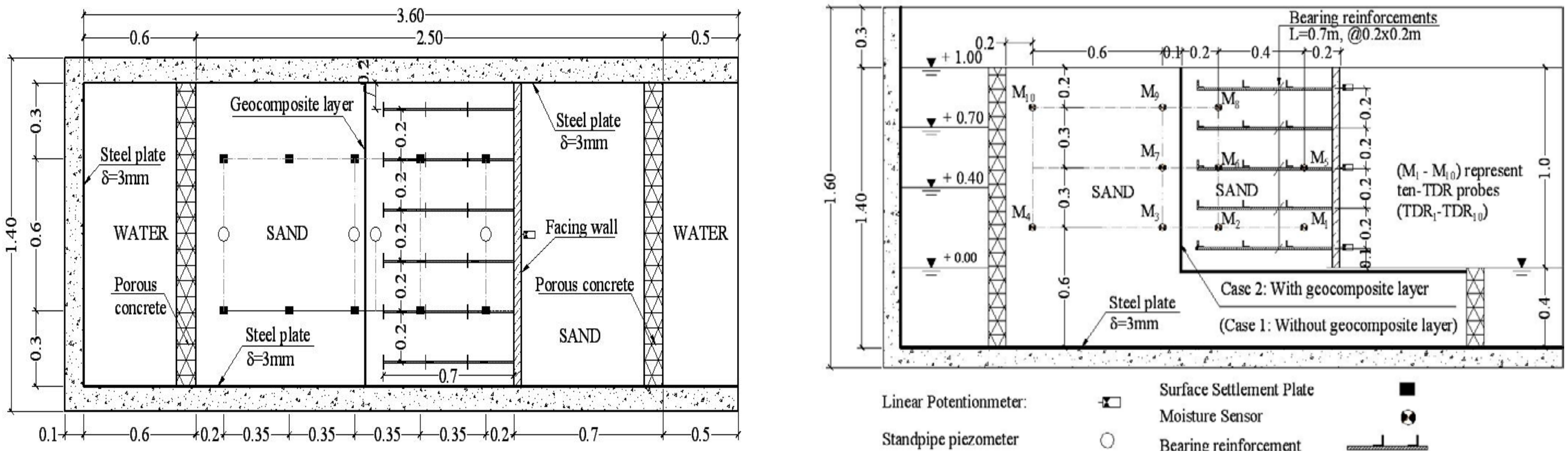

(a) (b)

Fig 2. Sketch of the physical model and location of the instruments (a) Plan view and (b) Side view

Table 2. VG and VGM model parameters assigned to every cases in the numerical experiment

Sandy soil						Geotextile						Geonet						Remarks
S_{res} (-)	S_{sat} (-)	g_n (-)	g_a (m^{-1})	k_x (m/day)	k_y (m/day)	S_{res} (-)	S_{sat} (-)	g_n (-)	g_a (m^{-1})	k_x (m/day)	k_y (m/day)	S_{res} (-)	S_{sat} (-)	g_n (-)	g_a (m^{-1})	k_x (m/day)	k_y (m/day)	
0.03	1.0	1.5	20	17	17	0.03	0.8	2.2 2.5 3.0 4.0	20	320	2000	0	1.0	40	600	6.9E4	6.9E4	Case 1 Case 2 Case 3 Case 4
0.03	1.0	1.5	20	17	17	0.03	0.8	2.5	16 20 40 100	320	2000	0	1.0	40	600	6.9E4	6.9E4	Case 5 Case 6 Case 7 Case 8

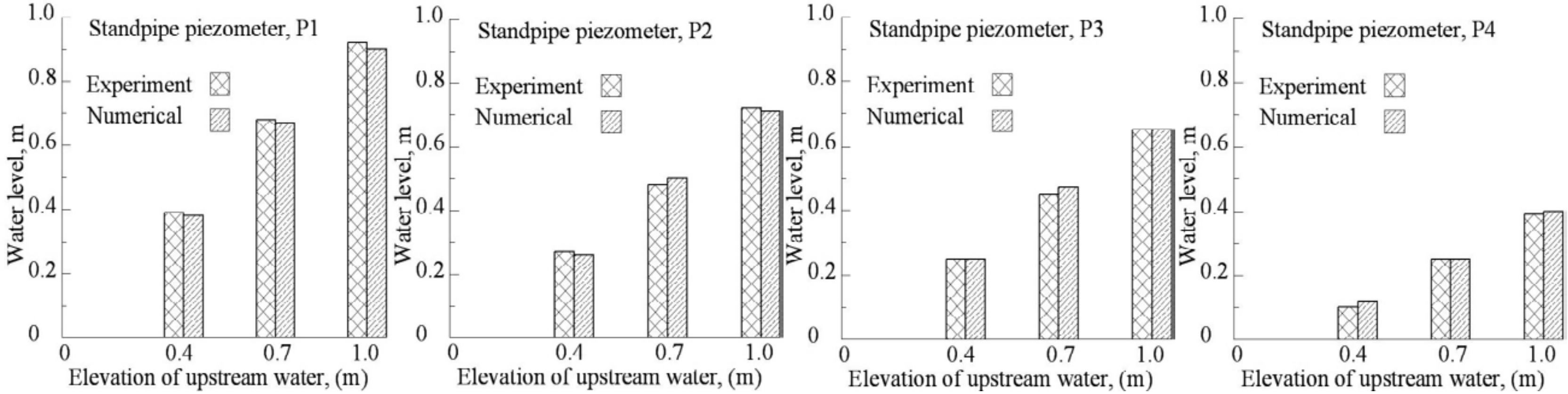

(a)

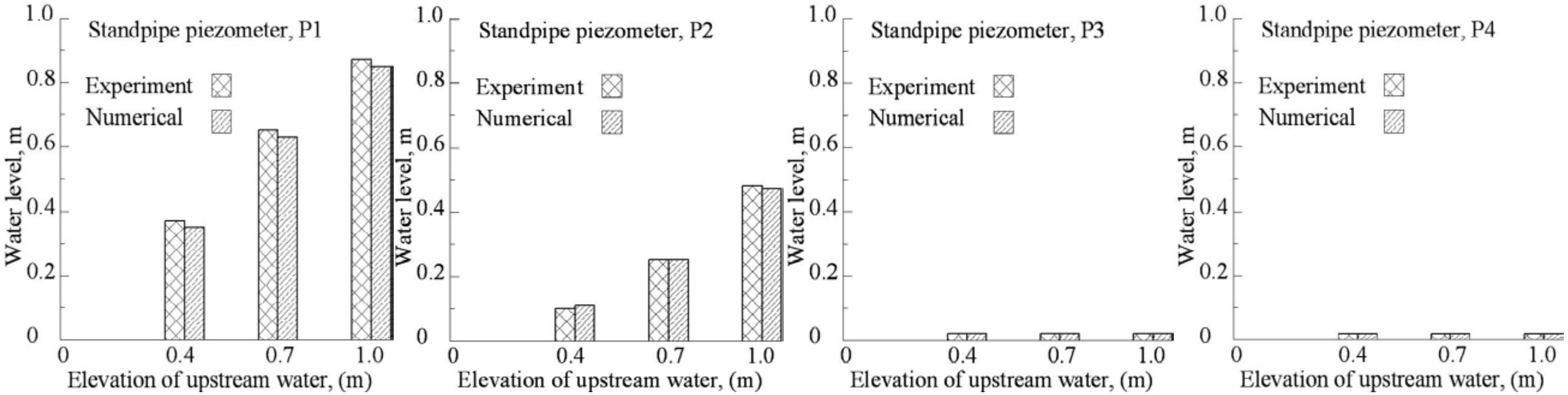

(b)

Fig 3. Phreatic surface for MSE wall (a) Case I and (b) Case II

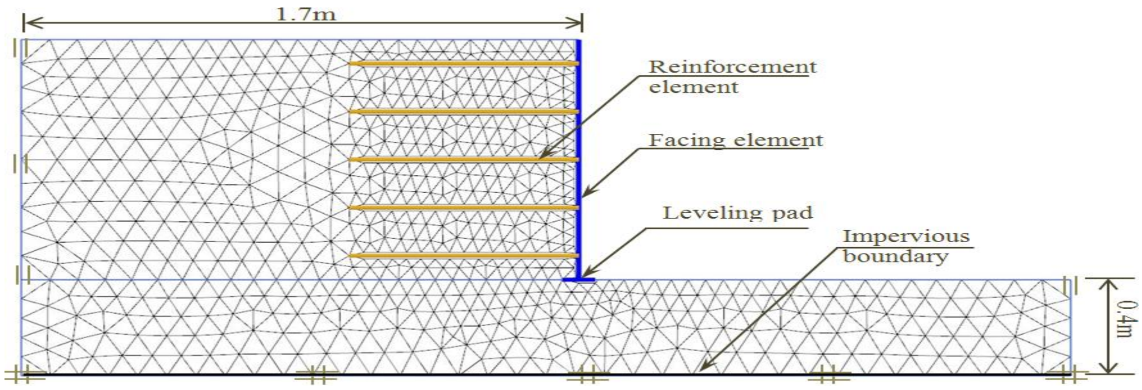

(a)

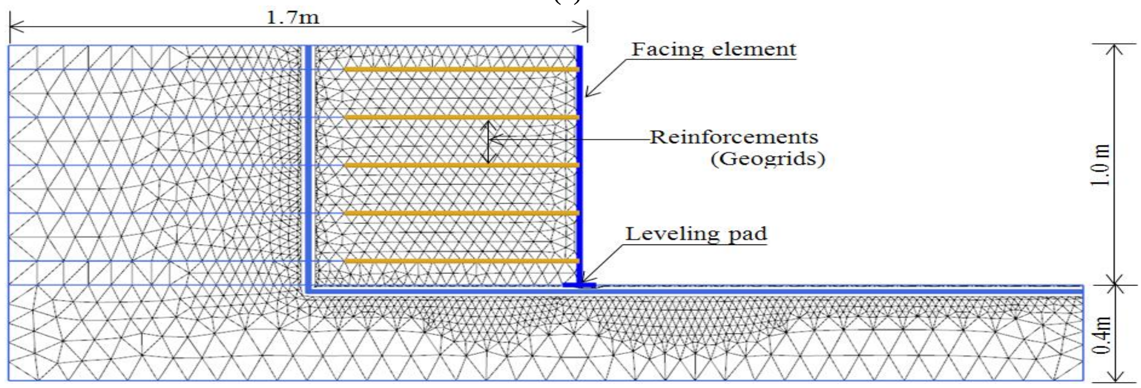

(b)

Fig 4. Mesh discretization of the models (a) without, and (b) with- geocomposite

2.4 Numerical Experiment Outline

The finite element mesh, boundary condition are shown in Fig 4(a) and 4(b) for the MSE wall without and with geocomposite drain installation, respectively. 15-node triangles were assigned to the models. The parameters for the hydraulic constitutive equations VG and VGM for the sandy soil, the geotextile and the geonet assigned to the models are summarized as shown in Table 2. In total, 08 cases of numerical simulation were conducted in this study using Plaxis 2D, 2011.

3. RESULTS AND DISCUSSION

3.1 Flow Through MSE Wall Results

Fig 3a, and 3b show the water level at different upstream water levels for the tests without and with geocomposite installation, respectively. At any height of upstream water level, the water level decreases through the wall face. The significant reduction in water level as well as water table in the protection zone shown in Fig 3a, 3b may result in higher stability of the wall.

3.2 Effect of water retention character of nonwoven geotextile

3.2.1 The van Genuchten parameter g_a

Figure 5 presents the effective saturation profiles along the interface between the soil and the geotextile for various magnitudes of g_a of the geotextile. The effective saturation profiles increases with depth for all g_a values and are found to reach full saturation at a depth of 1.0 m. It is also clearly shown that a greater g_a exhibits a greater degree of saturation along the interfacial section. The saturation profiles at shallow depth are found to be slightly different from each other, but it then notably increase at deeper depth. At the interface between the soil and the geotextile, the capillary barrier will occur if the water flows from a low g_a to high g_a materials [12], and hence the accumulation of water takes place along the interfacial section. This phenomena “capillary barrier” occur until the permeability of the two materials reaches the same value or the magnitude of suction at the interfaces reduces to a critical suction and water breaks through the interface [12].

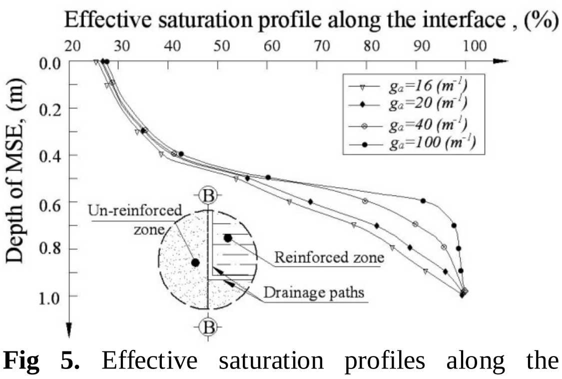

Fig 5. Effective saturation profiles along the interface for various magnitudes of g_a of geotextile.

Fig 6 presents the critical suction at different value of g_a of geotextile. The magnitudes of the critical suction for all cases are quite so low thet water is not able to permeate through the interface at high suction levels. Thus, the saturation profiles at high suction levels are not so different for all cases (Fig. 5). A greater g_a of the geotextile yields a lower magnitude of critical suction, subsequently results in a higher saturation at high saturation levels.

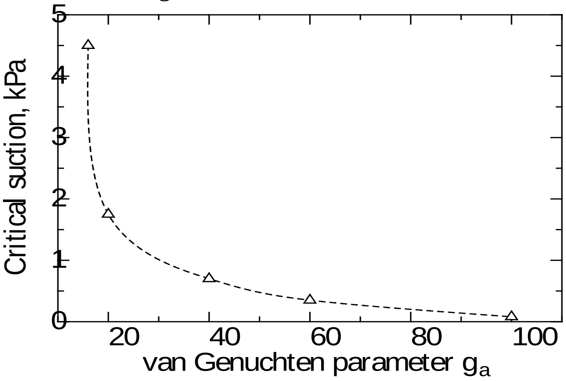

Fig 6. Relationship between critical suction and g_a

3.2.2. The van Genuchten parameter g_n

Figure 7 presents the effective saturation profiles along the soil-geotextile interface for various magnitudes of g_n. It is an evident that the g_n parameter plays a little role on the effective saturation profile along the soil-geotextile interface. The parameter g_n does not affect the pore size of material, hence capillary barrier, resulting in a little difference in the degree of saturation at the interface between soil and geocomposite system.

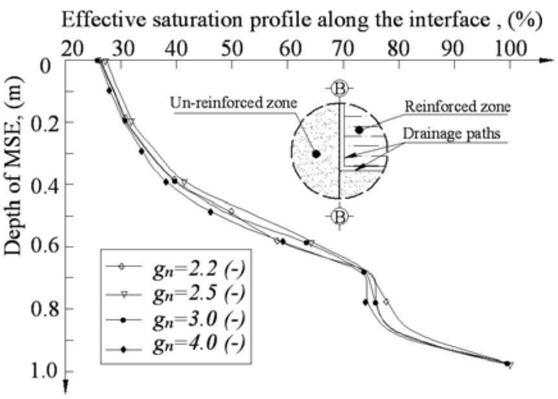

Fig 7. Effective saturation profiles for various magnitudes of g_n of geotextile.

4. CONCLUSION

The experimental results reveal that geocomposite can be employed to prevent water flows into the reinforced zone effectively. Similarly, leading to the following conclusions:

1) The effective saturation profile in the MSE is significantly affected by WRC of geotextile.

2) At the interface between two materials having different pore size, a phenomena known as "capillary barrier" can take place once water flow from a low value of g_a to higher one, this phenomena plays a vital role in the distribution of effective saturation at the soil-geotextile interface. The lower magnitude of suction where the water permeates through the interface results in a greater amount of water accumulation at this interface.

3) Inversely, the parameter g_n does not affect the hence the distribution of effective saturation.

ACKNOWLEDGEMENTS

This work was financially supported by Thailand Research Fund under MRG, the TRF Senior Research Scholar program Grant No. RTA5980005, and Thailand Toray Science Foundation, and the SUT-Ph.D scholarship Program for Asean.

REFERENCES

[1] Koerner, R.M., 2001. "Geosynthetic Reinforced Segmental Retaining Walls". Geotextiles and Geomembranes 19, 359-386.

[2] Shibuya, S.,et al., 2007. "Failure of Reinforced Earth as Attacked by Typhoon No. 23 in 2004". Soils and Foundations 47, 153-160.

[3] Bouazza, A., et al., 2006. "Water Retention of Nonwoven Polyester Geotextiles". Polymer Testing 25, 1038-1043.

[4] Iryo, T., 2003. "On the Hydraulic Behavior of Unsaturated Nonwoven Geotextiles". Geotextiles and Geomembranes 21, 381-404.

[5] Knight, M., Kotha, S., 2001. "Measurement of Geotextile-Water Characteristic Curves Using a Controlled Outflow Capillary Pressure Cell". Geosynthetics International 8, 271-282.

[6] Nahlawi, H., et al., 2007. "Characterisation of Geotextiles Water Retention using a Modified Capillary Pressure Cell". Geotextiles and Geomembranes 25, 186-193.

[7] van-Genuchten, 1980. "A closed-form Equation for Predicting the Hydraulic Conductivity of Unsaturated Soils". Soil science society of America journal 44, 892-898.

[8] Mualem, Y., 1976. "A new Model for Predicting the Hydraulic Conductivity of Unsaturated Porous Media". Water Resour. Res 12, 513-522.

[9] Handoko L, et al. 2013. "Suction controlled triaxial apparatus for saturated-unsaturated soil test". International journal of GEOMATE: geotechnique, construction materials and environment 4(1):466-470.

[10] Horpibulsuk S. 2011. "Performance of an Earth Wall Stabilized with Bearing Reinforcements". Geotextiles and Geomembranes 29(5):514-524.

[11] AASHTO, 2002. "Standard Specifications for Highway and Bridge"..

[12] Ross, B., 1990. "The diversion capacity of capillary barriers". Water Resources Research 26, 2625-2629.

Sixth International Conference on Geotechnique, Construction Materials and Environment, Bangkok, Thailand, Nov. 14-16, 2016, ISBN: 978-4-9905958-6-9 C3051

STABILIZING A STEEP WEATHERED SANDSTONE SLOPE ALONG THE RAILROAD IN SOUTHERN GERMANY

Thomas Hangartner[1] and Christophe Balg[2]
[1]Geobrugg AG, Geohazard Solutions, Switzerland; [2] Geobrugg AG, Geohazard Solutions, Switzerland

ABSTRACT

Due to the fact that the German Railroad reduced the maintenance work on the important railway line Nuremberg – Regensburg, section Deining - Batzhausen they had several cases with blocks laying at the tracks. Therefore they decided to stabilize the 70° steep weathering prone sandstone slope. As a protective measure the flexible slope stabilization system using high-tensile steel wire meshes was selected in combination with nailing. This widely used way to stabilize soil and rock slopes is economical and a good alternative to shotcrete solutions or massive supporting structures. Special concepts have been developed for dimensioning of flexible surface stabilization systems in steeper soil or heavily weathered loosened rock slopes, but also on jointed and layered rock in which the bodies liable to break out are determined by joint and layer planes. Analyzing of the design, explanation of the installation and how the finished installation behaves will be shown. The successful implementation confirmed that flexible slope stabilization systems by the means of high tensile steel wire meshes is well suitable for practical applications. The system proofed to be fast installed, adaptable, aesthetic and economic.

Keywords: RUVOLUM, TECCO, dimensioning, flexible slope stabilization system

INTRODUCTION

The use of flexible slope stabilization systems have proven there suitability around the world, including Europe, Asia, North America and in colder climates, where the stabilizing facings need to be able to flex under the freeze/thaw cycle. Historically, the mesh used for these purposes is produced using mild steel wire with a tensile strength of 400–500 N/mm^2. The development of mesh made from high-tensile steel wire with a tensile strength of at least 1770 N/mm^2, offers new possibilities for the efficient and economical stabilization of slopes (see Figure 1). Sophisticated dimensioning concepts serve to dimension these kinds of slope stabilization systems against superficial instabilities by taking the statics of soil and rock into account [1].

Fig. 1 High-tensile wire mesh for slope stabilization and system spike plate to tension the mesh against the slope surface.

PROJECT

On the important German railway line Nuremberg - Regensburg, section Deining - Batzhausen they had several cases with blocks laying at the tracks afterwards they reduced the maintenance work on this section. Therefore they decided to active stabilize the 70° steep, up to 15 m high and weathering prone sandstone slope. A protective measure had to be selected to stabilize the 8500 m^2 of the exposed cutting against superficial instabilities, tilting as well as sliding of individual blocks and rockfall.

Fig. 2 Location of project in the area of Deining in southern Germany.

Fig. 3 Partly eroded rock slope before the installation works.

Table 1 Parties involved

Client:	German Railway AG, Nuremberg, Germany
Project:	CDM Consult GmbH, Munich, Germany
Nailing and system installation:	SPESA GmbH, Schrobenhausen, Germany
Date of installation:	July 2009 – May 2010 (including winter break)

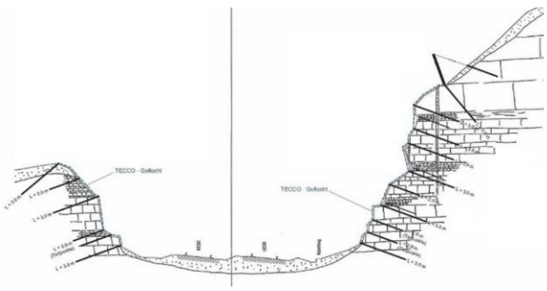

Fig. 4 Typical cross section including protection measure.

PROTECTION MEASURE

The flexible slope stabilization system consists of TECCO G65/3 high-tensile steel wire mesh, system spike plates and soil nails. The mesh is made from 3 mm high tensile wire and uses a zinc-aluminum coating for protection against corrosion. Each diamond of the single twist mesh measures 83 mm x 143 mm. The high tensile steel wire used in the manufacture of the mesh has a tensile strength of 1770 N/mm^2, compared to mild steel which has a tensile strength of 400–500 N/mm^2. As a result TECCO G65/3 mesh has a tensile strength of 150 kN/m, which means substantially higher forces can be absorbed by this mesh in comparison to conventional mild steel wire mesh. Aside from the higher bearing capacity, another advantage of TECCO mesh over conventional mild steel wire mesh is that it has an even load transmission and no weak zones within the mesh. This is achieved by manufacturing TECCO mesh with the same diameter high tensile wire, which forms a unified and homogenous mesh structure [4].

Special diamond-shaped system spike plates which match the load capacity of the mesh serve to fix the mesh to soil or rock nails. By tensioning these nails, and recessing the spike plates into the ground, the mesh is adequately tensioned to ensure it follows the surface contours [4].

With this slope stabilization system the rows of nails are offset to each other by half a horizontal nail distance. This limits the maximum possible break out between the individual nails to a width “a” and a length of “2 x b” (see Figure 5a). The staggered layout is shown in Figure 5b for the project Dongcheon in Korea.

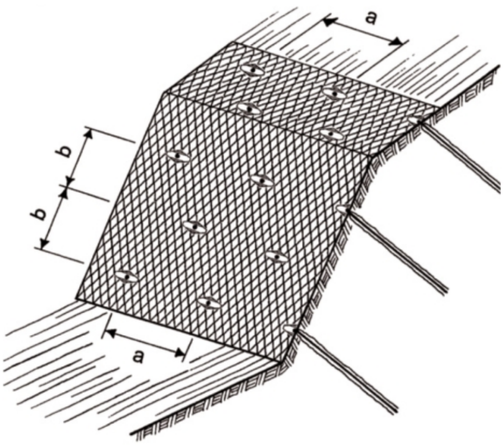

Fig. 5a General profile with nail arrangement [4].

Fig. 5b Staggered pattern of nail installation, project Dongcheon, Korea.

DIMENSIONING

The flexible slope stabilization system was dimensioned against superficial instabilities based on the RUVOLUM concept [2, 3]. The maximum nail spacing and the required nail length can be determined, and by utilizing the high bearing capacity of the mesh, significant cost savings can be realized by reducing the number of nails required. Conventional slope design methods are still required for deeper seated failure mechanisms.

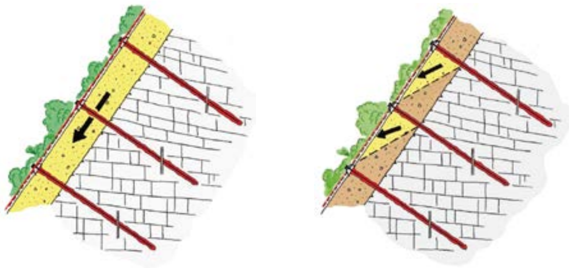

Fig. 6 The dimensioning concept is based on the investigation of superficial slope parallel instabilities (left) and on the investigation of local instabilities between single nails (right) [2, 3, 7].

Table 2 Project information

Height of the slope:	10 - 15 m
Subsoil:	Variable weathered sand- Stone (partly eroded)
Inclination of the slope:	70°
Stabilized area:	8’500 m^2
Nail type:	Gewi ø32 mm

INSTALLATION

Firstly, the slope was cleaned of eroded soil and smaller loose rocks. Due to the fact that there was no access to the top of the slope, the installation company decided to install the nails from scaffolding (see Figure 7). It was very important that the nails could been installed in deep seated spots so that the mesh could been tensioned and kept in contact with the surface. Shotcrete was used at locations where undercutting was occurring, to further secure any blocks from sliding down.

Fig. 7 Scaffold for drilling after cleaning of the slope.

Fig. 8 Beginning of the mesh installation.

Fig. 9 Overview and nail pattern adapted to the local situation.

Fig. 10 Adaptability of the installed mesh.

REVEGETATION/ EROSION PROTECTION

Erosion control mats can be installed underneath the mesh to aid in revegetation. The application of a vegetation layer can be limited by the soil or rock properties, groundwater and climate. The steeper the slope cutting, the more difficult it becomes for vegetation to grow. If revegetation is to be carried out, a species of plant or grass should be selected that is fast growing and suitable for the local conditions [4, 6].

Fig. 11 Condition of the slope in July 2011 one year after successful installation.

CONCLUSION

The TECCO slope stabilization system can be adapted to the site specifics and static conditions in a very flexible manner. The system can be designed and dimensioned against superficial instabilities, which is the first time flexible surface support measures can be properly designed. This approach offers the possibility to arrange the nails in a more economical way due to the capability of TECCO mesh in absorbing and transferring high loads.

When slopes stabilized with flexible high tensile steel wire mesh are combined with erosion control mats, they can regain a natural or vegetated appearance, which aesthetically is normally preferred.

Depending on the country, the price of flexible slope stabilization systems is equal or lower in comparison to reinforced shotcrete solutions including similar fully mortared rock bolts of the same length and diameters.

REFERENCES

[1] Brändlein P. (2004). LGA Nuremberg, Germany, Monitoring and supervision of laboratory testing of the TECCO slope stabilization system, Test report BPI 0400046/1.

[2] Rüegger, R.; Flum, D. (2006). Anforderungen an flexible Böschungsstabilisierungssysteme bei der Anwendung in Boden und Fels. Technische Akademie Esslingen, Beitrag für 4. Kolloquium „Bauen in Boden und Fels".

[3] Rüegger, R.; Flum, D.; Haller, B. (2002). Hochfeste Geflechte aus Stahldraht für die Oberflächensicherung in Kombination mit Vernagelungen und Verankerungen. Technische Akademie Esslingen, Beitrag für 2. Kolloquium „Bauen in Boden und Fels".

[4] Cala , M.; et al. (2012). TECCO® Slope Stabilization System and RUVOLUM® Dimensioning method. AGH University of Science and Technology.

[5] Brisbé York, A.; et al. (2006). RUVOLUM Dimensioning Software 7.0, Spain and Switzerland.

[6] Mrozik, M.; et al. (2006). Stabilization of a 30 m deep cutting along the highway A63 Kaiserslauten – Mainz, Germany, with a flexible slope stabilization system consisting of high tensile steel wire mesh in combination with nailing. Autostrada Polska.

REFLECTION OF TECHNOLOGIES OF NAVIGATION IN SPACE-TIME IN THE STRUCTURE OF ARCHEOLOGICAL OBJECTS

Alina Paranina[1]
[1]Faculty of geography, Herzen State Pedagogical University, Russia

ABSTRACT

The article shows the objective criteria of sacralization of objects of natural and cultural heritage of Eastern Europe and Southern Siberia, based on the performance of informational function in ancient human life-support system (as instruments of navigation in space-time). Transformation of functions of sacral objects from their inception to the beginning of the third millennium, due to the development of geo-cultural space (changes in technology, socio-cultural paradigm and social and economic conditions). The stages of the evolution of navigation technologies, selected by the author on the basis of cultural layering of archaeological objects are reviewed in the article. The carried-out retrospective analysis allows to make the assumption that improvement of technologies of orientation could be a basis of emergence and development of *Homo sapiens* (sapientation): astronomical supervision in horizon observatory develops a system of ecological thinking; supervision over a shadow of the gnomon tool develops abstract thinking (the abstract graphic sign is genetically connected with concrete natural process)

Keywords: Navigation, Adaptation, Modeling, Technology, Evolution.

INTRODUCTION

The navigation concept of information modeling of the world, developed by the author, explains the ancient sacred status of natural and cultural heritage by their important role in addressing the adaptation of the geographical challenges – namely in the development of geographical space-time. Application of methods of cultural geography and paleogeography, paleoastronomy and astroarcheology allows us to prove that these objects were created as orientation tools in space-time and provides the opportunity to "be at the right time in the right place," i.e. performed the informational function in life-support system [1]–[7].

Interdisciplinary studies of natural and cultural heritage of the Eastern Europe and Southern Siberia, conducted by the author in 2009-2015, together with a specialist in the field of archeology, culture, astronomy, showed that: 1. high degree of correlation of the dominant trends of the spatial structure of the ancient sacred objects with calendar azimuths of sunrise / sunset (and other astronomical reference points); 2. coincidence of these areas with the planned figure of the landscape; 3. reflection in the organization of sacred space (in the size of objects and the distances between them) of the system of ancient metrological standards.

The tradition of inheritance underlines the absolute importance of the position in geographic space, *its function in the intergenerational transfer of knowledge* – "comtinuity", and allows us to trace the development of navigation technologies.

OBJECTS AND METHODS OF RESEARCH

For the study were chosen representative archaeological sites (most typical and well studied by standard methods of the natural sciences and the humanities), revered to date: stone labyrinths of the White Sea, revered stones in the North-West Russia, the archaeological complex Divnogorie (Voronezh region), petroglyphs and megalithic complexes Gorny Altai, sacral complex Salbyksky valley (Khakassia), and others [8]–[12].

Field work, cartographic materials, aerial photos, satellite imagery and Google materials, scientific publications for the projects of natural and cultural heritage and the research problem were used to analyze the objects.

The applied methods of field of geographical studies (topographic, geological and geomorphological landscape and geomorphological survey), working with thematic maps and remote sensing data (landscape interpretation, selection and description of lineaments, planetary fracture systems, directions of outline structure of artificial and natural facilities with the construction of diagrams of roses), standard laboratory analytical and statistical methods, the methods of the metrological analysis of archaeological objects and astronomical paleoastronomical calculations (altitude and azimuth position of the sun – with the help of astrocalculator, length and direction of the shadows – using basic trigonometric functions), as well as methods of mathematical, cartographic and conceptual modeling were used.

EVOLUTION OF TECHNOLOGIES

Analysis of Structure of Objects

Stability and continuity of the information function of natural and cultural heritage are proved by numerous examples of the combination of objects of different ages and modern geodetic network: in the North and North-West Russia – "landscape markers and halt points - stone labyrinths - geodetic points"; in Khakassia in "outrigger stele mound (ancient) - mound (later time) -geodesic point" and others. In spatial structure of the studied ancient objects azimuths by which dates of equinoxes and solstices are determined are revealed (Fig. 1-6).

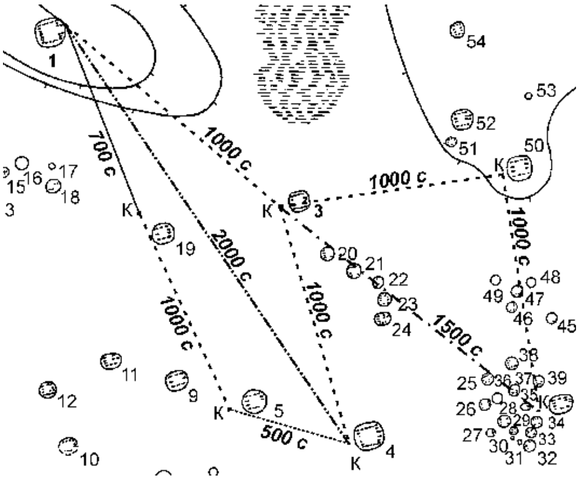

Fig. 1 The plan of a sacral complex in Salbykskaya valleys.

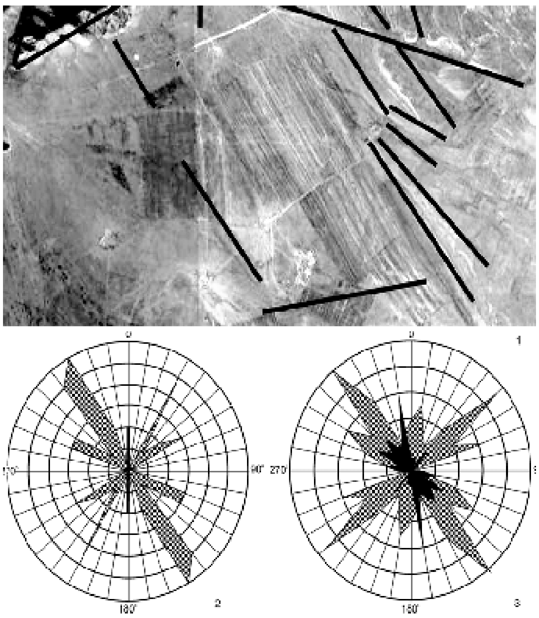

Fig. 2 Comparison of the azimuths measured between barrows and in a surrounding landscape.

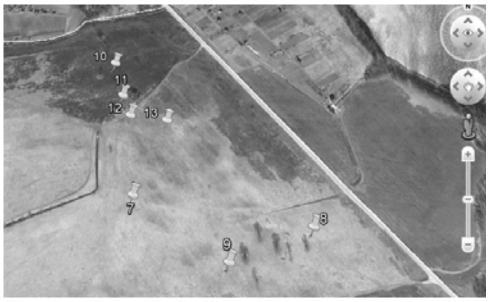

Fig. 3 Megalytic complex of the esteemed stone the St. Paraskev (Leningrad Region, lake Vrevo).

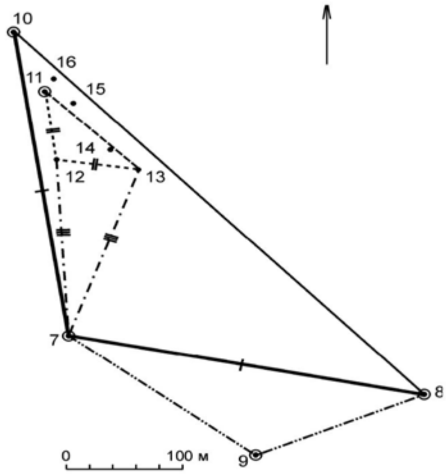

Fig. 4 Plan of a complex St. Paraskev.

Fig. 5 Stone labyrinth- gnomon of the White Sea.

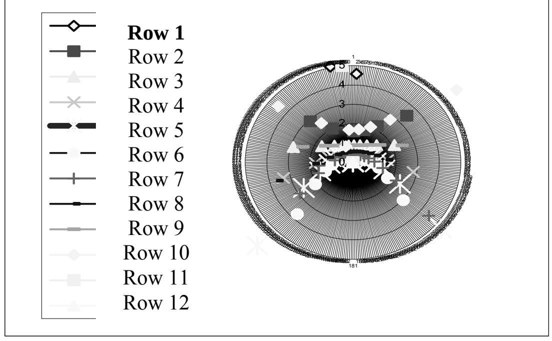

Fig. 6 The schedule of a shadow of a gnomon in a year. Row 1-12 – schedules of every month.

Main Stages of Evolution of Navigation Technologies

Based on the analysis of different age elements of sacral complexes, objectively there are five stages in the development of navigation technology: Landscape and megalithic (direct sight), megalithic (back sight), the historic stage of abstract modeling (development of a rational and creation of irrational symbolic), the current stage of the new navigation technology, communication and modeling.

Landscape stage of development of space-time

Landscape stage of development of space-time, the initial – describes the utilization of geographical space for fixing astronomical directions - space-time benchmarks. Foresight (observation), then check the sunrise / sunset at the solstices and equinoxes (and other astronomical targets) contribute to: 1. open and "rugged" horizon heterogeneity which allows us to record significant azimuths 2. lineaments – linear elements of tectonic structures, topography, linear borders of aquatic and territorial natural complexes. At this stage of development of orientation technology the landscape serves as astronomical instrument, and to keep the life-saving information the energy of natural processes, which indefinitely long maintain the spatial structure, is used.

To fulfill the information function of the landscape, since ancient times, with the economic zoning of the territory they received a special sacred status, the main feature of which is the minimum load in order to maintain the stability of the spatial structure. Thus, *the geographical criterion of sacralization of the landscape is a role in the life support system, which is determined by the need for human resources, information on the procedure of space-time.* This finding is consistent with the ethnographic data on the exclusive role of the revered natural objects in the pre-Christian traditions, dedicated to the Sun and the calendar.

The traditions of minimal impact on sacred landscape in the form of its labeling with stable to the destruction of cells or artificial additions (petroglyphs, petroglyphs on the rocks, the addition of rough stone –“obo”, symbolic gifts in the form of ribbons or trophies fragments) are preserved. Shape and density of man-made additions into the sacred landscape orientation reflect the development of technology and especially the mentality, regional specificities, in particular, the availability of human activities in energy, raw materials and information resources, the demand for navigation information (social order).

Often, natural formations – erosional forms and remnants of weathering, associated with various forms of living beings. The issue of their natural or artificial origin is discussed, but on satellite images are easily determined azimuths of linear "chains" of stone objects, providing the definition of the astronomical seasons boundaries. Obvious possibilities of astronomical use of the natural and natural-artificial sculpture, based on their position in space, are an additional confirmation in the traditions and legends.

Determining the proportion of creative human participation in the formation of animal and anthropomorphic rock sculpture is simple enough: a comparison with neighboring geological and geomorphological complexes of similar genesis shows that the principle of the ancient architects was to "remove the excess." Apparently, this principle developed from the ancient taboo on the number of strokes taken on the stone to the quest for a perfect match to the living prototype (in classical sculpture). The wisdom of ancient technology, reflecting the mentality of "co-creation with nature", limiting the degree of change in the natural substrate, highlights the problems of modern interaction between human and nature as a bold violation of the natural forms of the earth's surface leads to a change, sometimes catastrophic, of water and air flow – those natural processes that remain the major sculptors of the planet.

The later artificially established megalithic sites can be considered as one of the stages of development of this tradition.

The second stage of development of navigation – megalithic

The second stage of development of navigation and information functions of the location of the sacred complex is megalithic, characterized by the use of artificial tools for foresight, fixing the hair lines of main astronomical azimuths and their relationship with the iconic elements of the landscape and visible objects on the horizon by a resistant to destruction and displacement of objects . The requirements of this technology meet the large-megaliths objects placed at a distance of a few hundred meters. Location of the horizon observatory is possible both on high, visually-related points of the relief, and in the valley – decrease, nearing the horizon, which makes landfill compact and relatively independent from the surrounding landscape changes. Exemplary embodiments of this technology can serve megalithical complexes of the Caucasus, the Kola Bay (megaliths city park plateau Sade and Crow stone in Murmansk) and others.

Even if the material of the megalithic complex was not subjected to significant relocations and processing, it should be seen as *artificial, natural and man-made*, because the process of creation of astronomical tools embedded knowledge and human labor. Different size and degree of treatment may indicate the value. One of nearly invisible, but conclusive evidence of artificial stone, or selection criteria, are measures, multiple units of the ancient system of measures – feet, elbows, fathoms. Metrological analysis is needed to define the distance between objects.

In Salbyksky Valley megalithic stage left behind the unique objects ("statuesque", complex "two stones", stone of fertility in the gate of the Grand Salbyksky mound), and the same type outrigger stele located on the west side near the largest burial mounds. Megalithic sites are the oldest in the valley, on the size, shape, quality and extent of the destruction of the stone, they are very different from the material used at a later time to build mounds. Similarly, in other regions – megalithic sites are the most ruined and slightly different from the natural elements of the landscape. So, seids are often perceived as typical "glacial boulders" and to understand "the structure due to function", a comprehensive eco-geographical and astronomical analysis is required, and for the definition of features of "architectural style" – a video, including local and regional variants (e.g., seids of Kola Peninsula, Siberia, North and South America).

At the landscape stage secure fit of astronomical directions was ensured by use of natural rock masses – the most resistant to tectonic movements and shifts under the influence of exogenous geomorphological processes (e.g., slope or cryogenic), at the megalithic stage, the *maximum non-mobility of artificially established monolithic sights was provided by their weight*, as weight determines the dynamics of objects. The gigantic sizes of buildings such as pyramids or temple complex of Baalbek were consistent with this task.

During the first two stages of astronomical observation people could see that horizon observatory after time unavoidably "lose their accuracy," not because of their design or underlying rocks are unstable, but due to the fact that the astronomical azimuths of celestial landmarks climaxes gradually changed, i.e., Space itself is dynamic. On the basis of accumulated knowledge it has become possible to calculate the long-period cycles and switching to more efficient, compact and precise technology, where the temple-observatory - is not just a tool, but it is a fixed point in space, the platform and data warehouse (calendar layout and markings).

The third stage is the backsight technology

Backsight has many embodiments, among which the most famous is path technology of fixation of shadow of the object and a focused beam. It is clear that the transition to monoinstrument – the gnomon of a sundial and the calendar took place gradually, through a series of intermediate options. For example, there are still a lot of megalithic sites, in which the shadow of one object to another object falls at sunrise / sunset (at least – of the Moon) on certain days of the year. In this case, the totality creates the functional integrity of forms – local astronomical and geodetic *network*. Two objects on the line W-E create the most simple form a network, which are linked by shadow twice a year – at the equinox, at sunrise and sunset. This approach revealed the solar calendar function in relief images of labyrinths in Galicia [13].

Observations of the shadow of the subject – the gnomon, not only at the beginning, but also throughout the light of the time of day, gives a person a lot more information – *measuring* horizontal and vertical angles, accurate clock and calendar *binding to the planetary system of coordinates* (latitude), the transition from local astronomical and geodetic network technology to create *regional networks*. The value of switching to navigation technologies of backsight emphasized in all cosmogonic myths, like the creation of the World from Chaos. As a rule, the myth explains the determination of the center of the world – axis, navel, etc., in other words, the center of a regional astronomical and geodetic network, the fixed position of Omphale.

Inclusion of objects into the regional network explains their position on the same latitude of other sacred objects. Thus, Divnogorie and Salbyk are located at the latitude of 51-52º, close to the latitude of Arkaim, Kiev and Stonehenge. This latitude corresponds to one of the boundaries of the seven climates, recorded in written sources of Ancient Babylon. At the latitude of St. Paraskeva there are: stone in the Pskov region, similar in structure and name, Shum-Gora (the largest mound in Europe, presumably – the tomb of Ryurik), Peryn (the ancient sanctuary on Lake Ilmen in the Novgorod neighborhood). The widespread development of local and regional networks provided toponymic marking of territorial navigation systems in space-time by the sun – the principles of a navigational markings developed on the historical geography of the works of V.I. Paranin [1], [2].

The largest number of heritage sites, performing the functions of a sundial-calendar, were revealed for the last 5000 years (labyrinths, stele, idols), perhaps because the older have not survived or have not yet been investigated. The oldest archaeological finds are: Shigir idol – 11,000 years, the sundial of England and Turkey – 10,000 years, and others. The largest amount of solar labyrinth-calendars is concentrated in the Northern Europe. Calculations show that, at the southern orientation of the entrance to the labyrinth, its stone arcs serve as marks of the height of the midday sun, in other cases, the calendar information azimuths fixed entrance and all the spirals.

The biggest and most ancient cluster of stone labyrinths (Stone Age) is located on the island of Bolshoy Zayatsky, Solovetsky archipelago, and individual objects and images – on all continents except Antarctica. Labyrinths were built, as a rule, on the waterways, settlement sites, near freshwater sources. Examples of distance from the coast are not frequent, one of them – the labyrinth of the Bronze Age in Mostishche, 15 km from Divnogorie. Many labyrinth images were found on stone slabs in Dagestan.

An example of embodiment of a backsight technology is just a combination of "stone-tree", where the shadow of a tree falls on a stone at a certain hour. Tradition of honoring of the sacred stone and wood is preserved until recently in the Baltic regions and in Karelia.

The development of navigation is always accompanied by *the process of creating an iconic space-time equivalents and rational life-affirming symbols*. Undoubtedly, the foundation of sign systems is made on the basis of foresight. According to V.B. Frolov, the basis of the primitive graphics in the Old Stone Age was fused astronomical and mathematical knowledge. However, the most productive source of signs should be considered as the shadow of the gnomon, broadcasting navigational information in some regions almost continuously (in the conditions of the polar day). Analysis of the semiotics of light / shadow allows to reconstruct the information model of the world, which is different from the mytho-poetic model of humanities research that sets a measurable quantitative relationship between the natural process (lighting mode) and the spatial structure of cultural objects (layout structures and graphical basis of signs and images).

In general, the progress of technology of navigation of the first three phases expressed in improving the quality, while saving money and space requirements. As a result, *vitally important information about the space-time has been inherited, compressed in form and developed content*.

However, at the beginning of the Iron Age, in the conditions of the artificial urban environment, development of culture takes on a new - humanitarian direction. History tells us that the specific feature of the urban culture and the development of state forms of social order becomes progressive idealism and manipulation of knowledge, including the calendar systems.

Fourth - the historic step of abstract modeling

The historic step of abstract modeling is characterized by advances in navigation infrastructure of geo-cultural space, differentiation of features of tools (magnetic compass, water and hourglass), the development of abstract modeling world with the creation of rational – reflecting real natural processes and irrational characters – reflecting speculative build in the delimitation of the nature of cultural space (even if this limitation – wall laboratories and / or experimental conditions).

Technologies of navigation underlying the lunar-solar calendar, cease to be a priority for scientific and technological direction, falling back to more stable – distant landmarks of the sky of stars. The realization of the principle of the constructive role of the super-system of the universe with respect to the solar system finds its strain – Idealistic expression. There comes a stage of oblivion of achievements and transformation of meanings of the ancient culture based on solar navigation. Created at that time, the objects relate mainly to the cultural heritage category: palaces and religious complexes, but the navigation continues the tradition of binding object to create a space-time coordinates using the gnomon of the "laying" stone.

We know with what bitterness dominant religion eradicated the natural urban culture that has developed as the experience of hundreds of thousands of years: the baptism and enslavement of Rus, the Inquisition – In Western Europe. However, the traditions associated with the life support are very stable. In Christianity, for example, everything that could not be destroyed, was lit and left there under a new – Christian name. In this case, objects that once served as tools to ensure the real nature, according to the order of social life in the new system could save only a formal function - to maintain the tradition of ancestor worship and allow *symbolic treatment to universals of Time* (maintenance of health, prolong life, and the good childbirth – motives of reverence stone, extant). About the former connection to sight and eye, it resembles only water uses from these stone buckets "to improve vision."

Fifth - the current stage of the latest technology

The current stage of the latest technology, characterized in that the ways of orientation, based on the achievements of the space, computer equipment, development of remote sensing data and communication systems develop actively.

In the era of the dictates of the world market and imposed on them by the state, mass consumer culture, the origins of modern culture forgotten objects of natural and cultural heritage of the veneration of objects are transformed into recreational resources (tourism) and other commercial activity (a wide range of health and magical practices).

Today, numerous examples can prove that almost all the heritage sites are focused and related to the calendar. However, the success of astroarchaeological and paleoastronomical studies (e.g., decoding of astronomical features of Stonehenge or the pyramids of Egypt) receives essentially idealistic interpretation – considered in the context of the local activities of the cult character. This line of thought obviously inherits practices and ideological direction, formed at the stage of the merger of church and state. It affects the same lack of scientific methodology, based on the laws of natural diversity, the weak development of methods aimed at identifying cause-and-effect relationship, the traditional art criticism for humanities research focus.

A variety of scientific methods used for navigational objects historic and prehistoric past, involves interdisciplinary cooperation with a view to the mutual enrichment of Sciences and the formation of multifaceted conception of the problem of natural and cultural heritage [1]–[15].

Modern science and engineering technologies enable the broad scientific research of the navigational designation of ancient objects. Geographical information system analysis of primary navigation purpose of sacred objects of nature and culture shows that objects are unique and their technologies are versatile, as technologies reflect the laws of the structure and functioning of the geographic space-time, and record the individual objects unique combination of geography at every point. The collection of iconic qualities of the landscape, representing the real basis of science and practice, become an integral part of the content of sacred geography, semiotics of geographical space and geography culture. Interdisciplinary studies of natural and cultural heritage in the geography will ensure the conservation status of objects, the correct definition of their composition, structure and boundaries, the rational use for tourism and recreation.

CONCLUSION

The spatial structure of the sacred (revered) objects of natural and cultural heritage provides opportunities for instrumental astronomical orientation in space-time. Cultural layering of sacred archaeological sites allows to study forms of inheritance and to identify stages in the development of navigation technologies.

Development of instrumental navigation is connected with development of the abstract thinking and intelligence. The golden age of technology of fore sight can be correlated to appearance of the Homo sapiens and the Stone Age, and broad application of a gnomon – to a metal era (about 7000 years ago).

When dating ancient objects it is necessary to consider speeds of change of rocks and a relief of regions of Earth for the last 2000000 years.

REFERENCES

[1] Paranin VI., Historical Geography of the chronicle of Russia. Petrozavodsk: Karelia, 1990.

[2] Paranin VI., The history of the barbarians, St. Petersburg: RGS, 1998.

[3] Paranina GN., Light in the labyrinth: time, space, information. St. Petersburg: Asterion, 2010.

[4] Paranina GN., “Northern labirinths – gnomon and models of geographical space”. J. Procedia Social and Behavioral Sciences. ELSEVIR, Vol. 19, 2011, pp. 593-601.

[5] Paranina AN., “Northern labyrinth – a key to time, space, information”. J. Natural Resources, Vol. 4, 2013, pp. 349-356.

[6] Paranina AN., “Navigation in space-time as the basis for Information modeling”. J. Archaeological Discovery, Vol. 2, N3, 2014, pp. 83-89.

[7] Paranina AN., “Gnomon as sours of information on planet rhythms”. J. Geomate, Vol. 10, 2016, pp. 1815-1821.

[8] Paranina AN., “Reflection of space-time in ancient cultural heritage of Urals”. Open Access Library Journal. Vol. 3, 2016, e2888.

[9] Paranina AN., Paranin RV., “Navigation in geographical space as a factor of development of civilizations”. in Proc. Int. Conf. on ICAE-2015 (Applied Ecology: Problems, Innovations) 2015, pp. 211-215.

[10] Paranina AN., Paranin RV., “Northern labyrinths as navigation network elements” Activities in Navigation. Marine Navigation and Safety of Sea Transportation. Ed. A. Weintrit. London-New-York-Leiden: CRC Press, 2015, ch. 4.

[11] Marsadolov LS., Paranina GN., “Salbyksky archaeological complex as an object of natural and cultural heritage”. J. Izvestia RGO, T.143, Vol. 2, 2011, pp. 79-90.

[12] Marsadolov LS., Paranina GN., “Megaliths as objects of cultural heritage of the North-West of Russia”. J. Izvestia RGO, T.143. Vol. 6, 2011, pp. 57-65.

[13] http://oestrymnio.blogspot.com.es/2012/12/laberintos-de-mogor-marin.html

[14] Sutriyono E., Hastuti EWD, Susilo BK., “Geochemical assessment of late paleogene synrift source rocks in the South Sumatra basin”. J. Geomate, Vol.11, 2016, pp. 2208-2215.

[15] Zaalishvil V., “Spectral characteristics of seismic waves at strong ground motions”. J. Geomate, Vol. 10, 2016, pp. 1706-1717.

Construction Material

Sixth International Conference on Geotechnique, Construction Materials and Environment, Bangkok, Thailand, Nov. 14-16, 2016, ISBN: 978-4-9905958-6-9 C3051

ACCUMULATIVE DAMAGE OF FIBER SHEET REINFORCEMENT CAUSED BY NEGATIVE THERMAL EXPANSION COEFFICIENT UNDER CYCLIC TEMPERATURE

Hidenori TANAKA[1]
[1] National Institute of Technology, Gunma College, Japan

ABSTRACT

Fiber sheet has been used in retrofitting of concrete structures after The Southern Hyogo Prefecture Earthquake in 1995. It has advantages of light weight, high strength, high rigidity as well as easy to construct. However it has negative thermal expansion coefficient that may cause shear stress between the interface fiber and epoxy resin leading to de-lamination in interfacial area and deterioration of structural strength and durability of the concrete structures. This paper presents experimental studies on interfacial damage of carbon fiber, aramid fiber ,and super maintenance Hozen material using freeze-thaw process test at cyclic low temperature from -10℃ to 3℃, the typical average winter temperature of Hidaka City, Japan. It was found that at 6,000 cycles the plastic strains have been increased in aramid and super maintenance (Hozen material),however the accumulated damages of those materials have been less than that of carbon fibers.

Keywords: Negative thermal expansion coefficient, Freeze-thaw test, Fiber sheet, Damage,Cyclic temperature

1. INTRODUCTION

Concrete is a standard brittle material in civil engineering. Reinforced concrete structures with steel bar resisting tension have been used for infrastructure such as buildings, bridges and tunnels, due to its durability and cost performance. In recent years, special attention has been paid to fiber sheets to resist against earthquake damage and prevent separation failure [1]. The fiber sheet is of light weight (1/5 of steel),high strength (10 times of steel),high rigidity and high durability as well as easy to construct. However, the fibers have a negative thermal coefficient. So, there are some concerned with mechanical interfacial properties between concrete and fiber sheets, or epoxy resin which glued fibers [2] - [4].

We have carried out some experiments with three specimens by a freeze- thaw process test. According to them, there were accumulation of plastic strain and damage for the specimen with carbon fiber sheet by 6,000 cyclic temperature which has been changed from -10 to 3 centigrade. On the other hand, there was little damage for the aramid fiber sheet and the Hozen material that is one of coating methods by polymer cement to reinforce the concrete structures.

2. CYCLIC TEMPERATURE CHANGE TEST

2.1 Specimens

We applied the cyclic temperature change test for 5 specimens using a freeze-thaw process test machine. The basic shape of the specimen is a prism(100 ×100×400 (mm)). All specimens are shown in Table 1.,Carbon and aramid patterns in Figure 1.The admixture of concrete and properties are shown in Table 2 and Table 3, and then the properties of fiber primer and Hozen material are shown in Table 4, Table 5, Table 6 and Table 7 respectively.

Table 1 Specimens

SERIES	TYPE	REMARK
CASE 1	BASE	
CASE 2	PRIMER	t=0.3 (mm)
CASE 3	CARBON FIBER	1 layer (t=0.22 (mm))
CASE 4	ARAMID FIBER	1 layer (t=0.42 (mm))
CASE 5	HOZEN	t=10 (mm)
t:thickness		

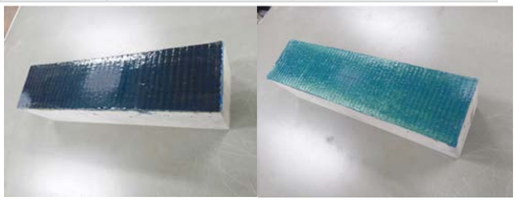

carbon aramid

Fig.1 Specimens of fiber series (CASE 3,CASE4)

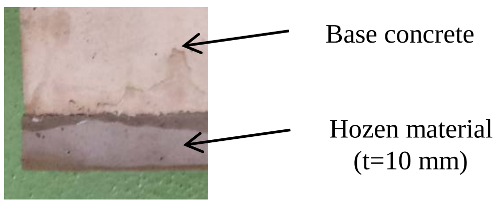

Fig.2 Specimen of Hozen material

Table 2 Admixture of concrete

Gmax	Slump	W/C	Air	s/a
(mm)	(cm)	(%)	(%)	(%)
15	8	55	7	44.5
Unit value (kg/m3)				
Water	Cement	Sand	Gravel	S.P
174	317	761	960	3.17

Table 3 Properties of Concrete

Properties	value
Compressive strength	35 (N/mm2)
Poisson ratio	0.2
Young Modulus	30.2(kN/mm2)

Table 4 Properties of Carbon fiber

Properties	value
Unit weight	308 (g/m3)
Tensile strength	4,657(N/mm2)
Young Modulus	265(kN/mm2)

Table 5 Properties of Aramid fiber

Properties	value
Unit weight	660 (g/m3)
Tensile strength	3,116(N/mm2)
Young Modulus	131(kN/mm2)

Table 6 Properties of primer

Properties	value
Compressive strength	43(N/mm2)
Adhesive strength	3.6(N/mm2)
Young modulus	2.45(kN/mm2)

Table 7 Properties of Hozen material

Properties	value
Bending strength	12.3(N/mm2)
Compressive strength	55.3(N/mm2)
Adhesive strength	2.8(N/mm2)
Young modulus	18.7(kN/mm2)

These fibers and primer are standard materials to repair and retrofit the concrete structures for example ,tunnels, piers and box culverts.

2.2 Freeze-thaw test and principal strain

The strain gauges were respectively set on the center and the corner of the specimens. The corner's gauge could be checked the principal value using by rosettes type which are arranged at 90 degree offsets from each other.

The specimens were settled in the freeze-thaw test machine (refer to Figure 4). And the temperature changes were determined considering the mean of maximum and minimum values (from -10 to 3 centigrade) in Hidaka City where the northernmost concrete pier with carbon fiber was constructed.

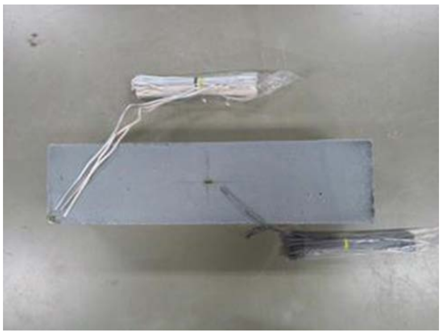

Fig.3 Set on strain gauges for CASE2

Fig.4 Freeze-thaw test machine

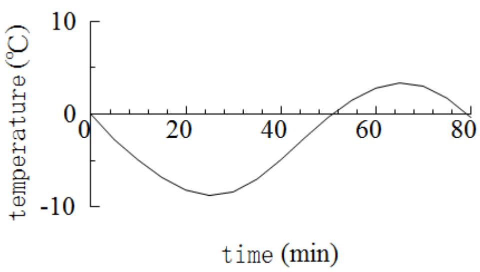

Fig.5 Temperature change

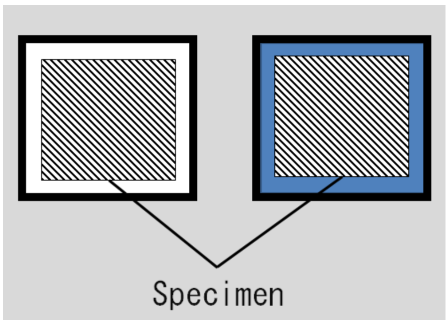

Fig.6 Curing condition

The temperature was changed regularly considering the maximum and minimum range of the machine's

capacity (refer to Figure 5).
In this study, the freeze-thaw test was conducted in air condition .There are generally two ways to set the specimens in air or in water (refer to Figure 6). If we set them in water, we couldn't specify deteriorated factors caused by the different thermal expansion coefficient of fibers or the frost damage by water. Therefore, we carried out the experiments simply in air condition in order to make sure of the affection by the different thermal expansion coefficient of fibers. In addition, it has been known that the diffusional coefficient of concrete in wet has strong nonlinearity around 0 centigrade [5]. But, it is very important and difficult to measure and evaluate the nonlinearity on the surface of concrete. And most of the structures in real environmental condition haven't been exposed in wet at all. So, in this experiments, we focused on the properties of fibers, and then we conducted simple condition.

3. RESULT OF MEASUREMENT

3.1 Relationship between temperature and principal strain for specimens

The relationship between temperature and principal strain of fiber series and Hozen material are shown in Figure 7 , Figure 8 and Figure 9 by 6,000th cycles. The patters of primer and base in Figure 10 and Figure 11 by 2,000th cycles.
Judging from the results of primer and base , they have perfectly glued each other and there were not any damages among them. and then the measurement of 2 specimens were carried out by 2,000th cycles.

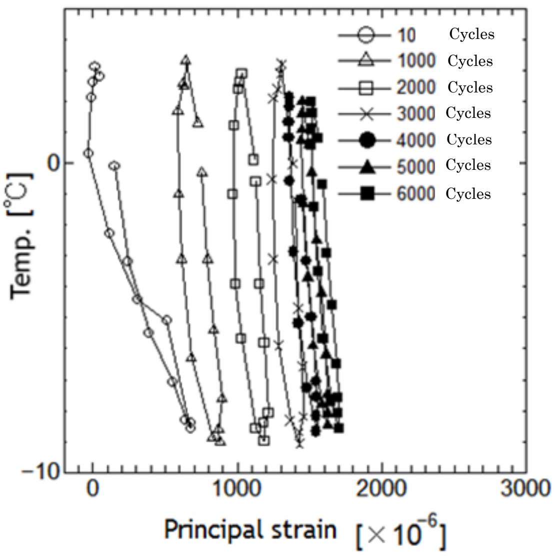

Fig.7 Temperature-strain (CARBON FIBER)

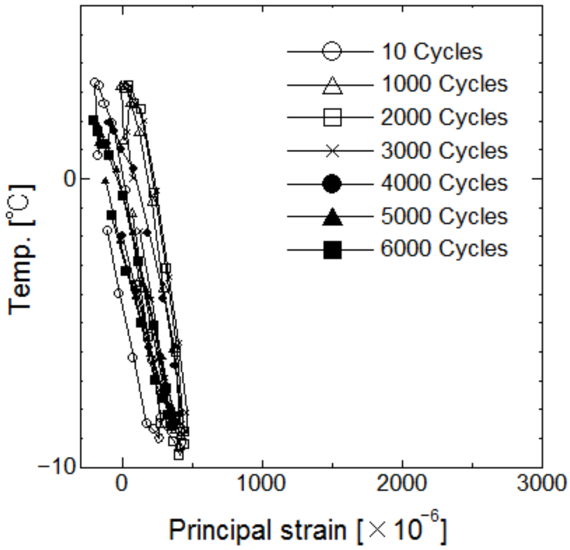

Fig.8 Temperature-strain (ARAMID FIBER)

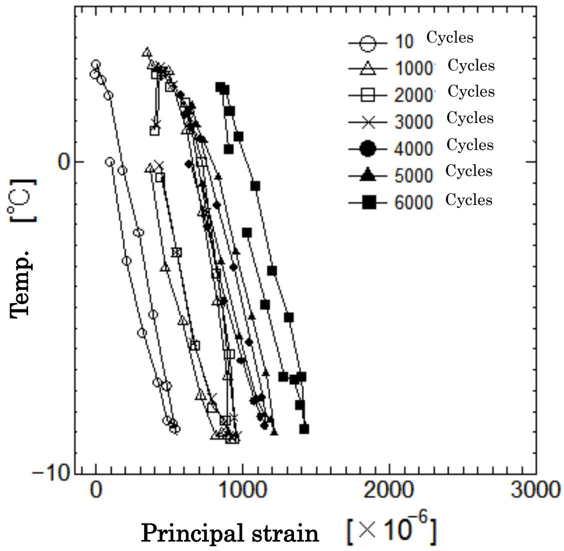

Fig.9 Temperature-strain (HOZEN)

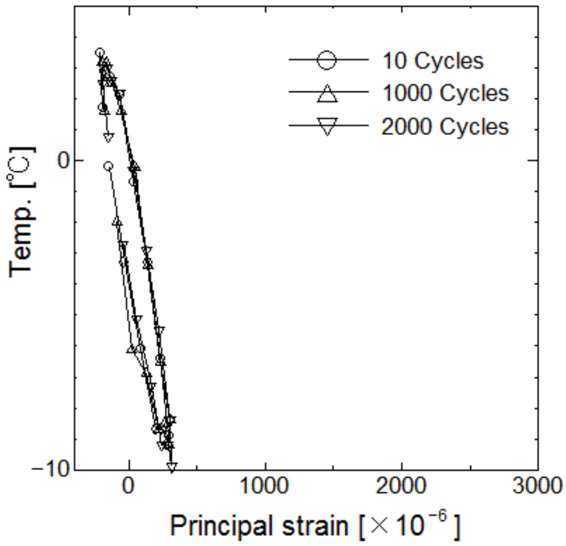

Fig.10 Temperature-strain (PRIMER)

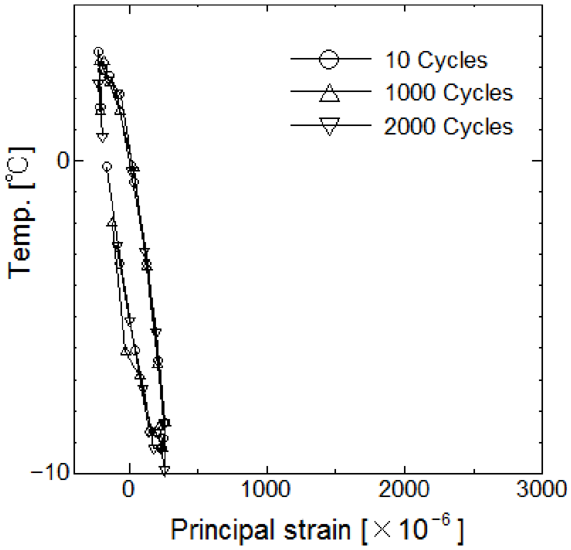

Fig.11 Temperature-strain (BASE)

Table 8 Representative strain of all specimens

SERIES	TYPE	TEMPERATURE	STRAIN（×0.000001）
CASE 1	BASE	−9.5～−8.7 (℃)	258(10), 247(1000), 263(2000)
CASE 2	PRIMER	−9.5～−8.7 (℃)	291(10), 313(1000), 281(2000)
CASE 3	CARBON	−9.5～−8.7 (℃)	691(10), 843(1000), 1181(2000), 1421(3000)
			1551(4000), 1630(5000), 1705(6000)
CASE 4	ARAMID	−9.5～−8.7 (℃)	265(10), 408(1000), 441(2000),458(3000)
			398(4000), 403(5000), 495(6000)
CASE 5	HOZEN	−9.5～−8.7 (℃)	521(10), 882(1000), 928(2000),911(3000)
			1163(4000), 1210(5000), 1431(6000)

Bracket means cyclic numbers

Representative measured strain values are shown in Table 8.

The principal strain of the carbon fibers has been changed due to cyclic numbers. Especially, the plastic strain and the gradient of the loop curves have been increased under cyclic temperature. The inverse of gradient has shown the thermal expansion coefficient of the specimens. And then, this phenomena meant that fibers have split out the epoxy resin. Therefore, we considered that the damage also has been accumulated between epoxy resin and carbon fibers.

On the other hand, the principal strain of the aramid fiber sheet scarcely has been changed due to cyclic numbers. They were without damage under cyclic temperature. In addition ,The specimens of primer and base concrete have exhibited little difference in any cyclic temperature change. This meant primer has perfectly glued the base concrete. The accumulated damage depended on the fibers.

The plastic strain of Hozen material has been increased due to cyclic numbers. But, the gradient of loop curves has hardly been changed.

And then, the principal strains of primer and base have been almost same curves under cyclic temperature. So, primer has glued base concrete perfectly by 2,000th cycles. The accumulative damage have been occurred among fibers and epoxy resin [6] - [8].

4.DURABILITY INDEXES

I proposed durability indexes to focus on the hysteresis curves of carbon , aramid and Hozen material corresponding to cyclic numbers.

4.1 Strain energy

At first, I checked the strain energy that is defined by area of hysteresis curves approximated ellipse (refer to Figure 12).

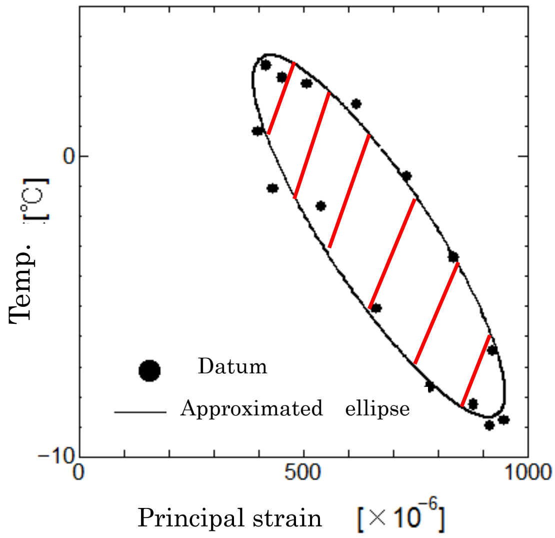

Fig.12 Strain energy by approximated ellipse

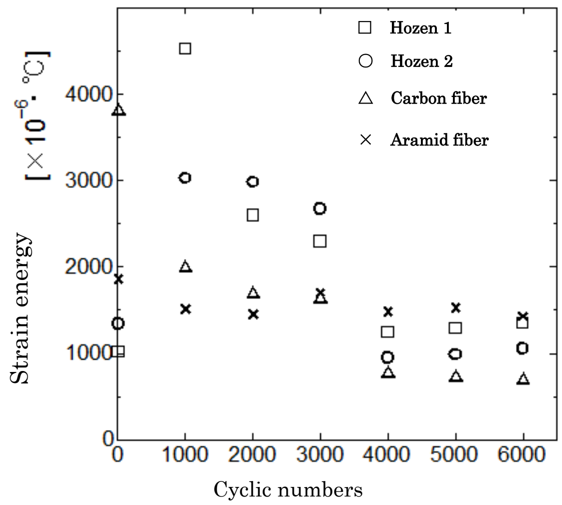

Fig.13 Relation strain energy and cyclic numbers

The values of strain energy about Hozen and carbon fiber have been decreased due to cyclic numbers. This means that the absorbable ability of materials corresponding to deformation have been decreased. From the results, aramid fiber has no influence or small influence by temperature changes.

4.2 Apparent thermal expansion coefficient

I secondly checked apparent thermal expansion coefficient that approximated linear gradient of hysteresis curves (refer to Figure 14).
Generally speaking, there is linear relationship between thermal strain increment and temperature increment using thermal expansion coefficient.

$$\Delta\varepsilon = \alpha\Delta T \qquad (1)$$

Where, $\Delta\varepsilon$ is thermal strain increment, α is thermal expansion coefficient , ΔT is temperature increment.

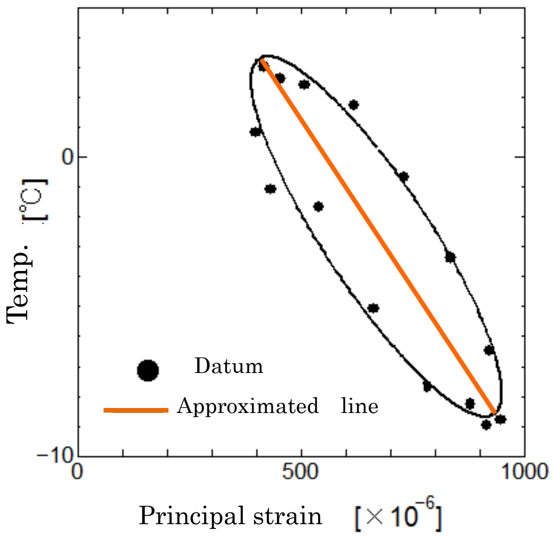

Fig.14 Thermal expansion coefficient by approximated line

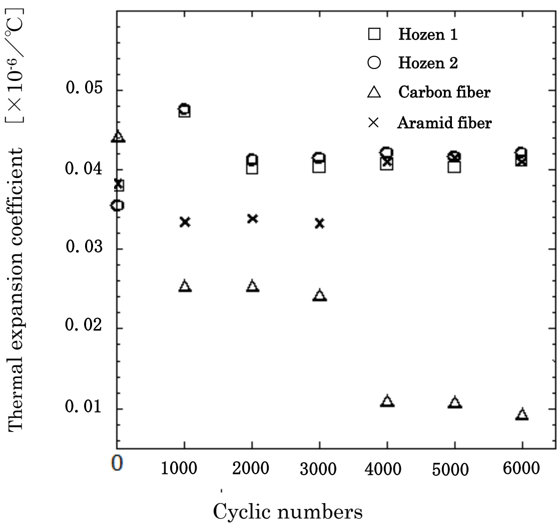

Fig.15 Relation thermal expansion coefficient and cyclic numbers

The thermal expansion coefficients of carbon fiber have been decreased due to cyclic numbers. In this study, Temperature increment ΔT has been constant (-10 to 3 deg.).But The thermal strain increment $\Delta\varepsilon$ has been decreased. This means that the thermal expansion coefficients α have been decreased by the accumulative damage D (D is damage variable). Therefor, The thermal expansion coefficients α have been changed $\alpha(1-D)$ [9] , [10].
From the results of carbon fiber, The damages have been accumulated between fibers and epoxy resin that glued fibers and primer.

5. CONCLUSION

In this study, we introduced the experiments and durability indexes under cyclic temperature changes. The following conclusions have been obtained:
(1) The plastic strain and damage of the carbon fiber have been increased due to cyclic temperature changes by 6,000th . This damage may be occurred because of carbon fibers slipping out of epoxy resin.
(2) The strains of the aramid fiber have only changed from 100th to 1000th .We considered there were not fatal damage under cyclic temperature.
(3) The strains of primer and base concrete have not been changed by 2000th .This means the primer perfectly glued the concrete as a result that the both principal strain have been distributed nearly equal under the cyclic changes.
(4) The strain energy has been decreased under the cyclic temperature change excepting the case of aramid fibers. The damages among the laminated materials have not been evaluated using these values.
(5) The thermal expansion coefficients of carbon fibers have been decreased due to cyclic numbers. These values have been closely correlated with the accumulative damages between fibers and epoxy.
(6) We would like to carry out the analyses and experiments about the carbon , the aramid fibers and Hozen material block to evaluate final fatigue mode under this cyclic temperature change .
(7) We have to consider more complicated natural conditions (high humidity, high temperature change, nonlinearity of diffusional coefficient) in next stage.

6. ACKNOWLEDGMENT

The authors appreciate Nippon Steel Composite Co., Ltd. for providing the carbon and aramid fiber. and Association of Japan Construction Maintenance for providing Hozen material and specimens. In addition, This research was supported by J.S.P.S KAKENHI (No.24560572).

7. REFERENCE

[1] Concrete library 101.”Repaire and Reinforcement guideline of concrete structures with continuous fiber sheet,”,2000,pp.8-19.

[2] Zhishen Wu,Kentaro Iwashita.”Temperature Effect on Bonding and Debonding Behavior between FRP Sheets and Concrete,” J.Soc.Mat,. Sci.,Japan,Vol.54,N0.5,2005,pp.474-480.

[3] Hidenori TANAKA,Yutaka TOI.”Adhesive Failure Analysis of Structural Elements Reinforced with Carbon Fiber Sheets, ” Transaction of the Japan society of Mechanical Engineering, Series A ol.72,No.724,2006,pp.198-204.

[4] Tanaka H,Toi Y.,Maeda,K.,Sakai,T.” Damage and fracture analysis of brittle structural elements reinforced with carbon fiber sheets, ”JOURNAL OF ENVIRONMENT AND ENGINEERING,Vol.3,No.1,2008,pp.111-122.

[5] Uekohara Akihisa,Sugawara Takashi.”Bonding behavior of continuous fiber sheet under freeze-thaw,”Proceedings of the Japan Concrete Institute,Vol.28,No.1,2006,pp.1715-1720.

[6] Makinoshima, F.,Tanaka H.”Influence on Adhesion Characteristic of Concrete with F.R.P Under Cyclical Temperature Change,”the 41st JSCE Kanto Branch Technical presentation,2014, V-13.

[7] Tajima,R.,Tanaka H.”Deformation of Concrete block with Super-hozen ,Fiber sheets under Cyclic Temperature Change, ”the 42nd JSCE Kanto Branch Technical presentation,2015, V-42.

[8] Tanaka H.,Makinoshima F.,”The adhesive Characteristic of Concrete Block with Fiber Sheets Under Cyclic Temperature,” International Conference on the Regeneration and Conservation of Concrete Structures RCCS,2015,I-17.

[9] Lemaitre,J.,Desmorat.R..” Engineering Damage Mechanics,” Springer,2005,pp.10-18.

[10] Tanaka H,Toi Y.”Ultimate Strength and Fatigue Life of Concrete Members Reinforced with Carbon Fiber Sheet Based on Continuum Damage Mechanics,”3rd International Conference on Sustainable Construction Materials & Technologies - SCMT3,2013,pp.99-108.

UTILIZATION OF AGGREGATE QUARRY WASTE IN CONSTRUCTION INDUSTRY

Mary Ann Q. Adajar[1], Euclid de Guzman[2], Ryan Ho[2], Cesar Palma Jr. III[2], and Dennis Sindico[2]
[1]Associate Professor, De La Salle University, Manila, Philippines
[2]Civil Engineer, De La Salle University, Manila, Philippines

ABSTRACT

The use of solid wastes as a new ingredient in construction materials is one possible innovative effort to reduce environmental degradation and to facilitate long term rational and sustainable use of the natural resources. The disposal of the huge amount of wastes from aggregate quarry (WAQ) is one adverse environmental effects of quarrying activities. Finding useful application of this solid waste, specifically as a substitute for fine aggregates in concrete mix, alleviates disposal problems and helps the construction industry to come up with concrete products at lesser cost. This study investigates the structural performance of concrete with WAQ as substitute for fine aggregates in a concrete mix in accordance with ASTM standards. Concrete with WAQ as fine aggregates achieved almost 78% of its target compressive strength at 28th day curing period. The reduced compressive strength is due to the finer and less-angular particles of WAQ in comparison to sand. Empirical model was formulated that can be used to predict the compressive strength of concrete with WAQ as substitute for sand. Using the formulated model, the optimum compressive strength can be achieved at 85% substitution for sand. The flexural strength of concrete with WAQ was in the range of 69% to 72% of the flexural strength of concrete without WAQ. The presence of WAQ in the concrete mixture has no significant effect in its unit weight, however, it affects the workability of the mix due to its cohesive property thus requires higher water-cement ratio. Test results proved that concrete with WAQ as substitute for fine aggregates has strength properties adequate for structural application.

Keywords: Aggregate Quarry Waste, Compressive Strength, Flexural Strength, Unit Weight

INTRODUCTION

Concrete is one of the most used building materials. The boom in construction industry leads to the exploitation of natural resources like river sand and gravel since these are the main source of raw materials for concrete production. The onset of shortage and increasing cost of construction materials has made it important to consider alternative materials that can be used in construction industry. Recycling waste to be potential materials used in construction has become a trend worldwide as this facilitates long term rational and sustainable use of the natural resources and reduces construction cost.

Quarrying activities generate huge amount of solid wastes which are most often dump in open fields. The disposal of aggregate quarry waste is one adverse environmental effect of quarrying activities. Improper management of this waste material can bring serious detrimental effects to the population and the environment. The use of solid wastes as new ingredient in construction materials is one possible innovative effort to reduce environmental degradation and alleviate disposal problems.

Several studies discussed the utilization of solid wastes as an alternative construction material. Recycled aggregates produced from pulsed power technology can be used as concrete component with fly ash as substitute for cement [1]. Waste carpet fiber can suitably be used as fiber reinforcement in concrete [2]. Tungsten mine waste with ground granulated blast-furnace slag is found to be feasible in the development of mortar with acceptable compressive strength [3]. Paper mill sludge, an industrial waste generated by paper mill factories is viable as partial replacement of fine aggregates in manufacturing fresh concrete intended to be used for low cost housing projects [4]. Ceramic waste and quarry dust aggregates have been found as a possible replacement for conventional crushed stone coarse and fine aggregates [5].

This study discusses the structural performance of concrete with waste from aggregate quarry (WAQ) as substitute for fine aggregates in concrete production. Specifically, it determines the compressive and flexural strength of concrete mix when fine aggregates are partially and fully replaced with WAQ in accordance with ACI 211. The study describes the most suitable concrete mix proportion with WAQ as fine aggregates that will yield the highest strength of concrete in compression and flexure. It also investigates the effect of using WAQ in the workability of concrete mix and in the unit weight of hardened concrete.

WASTE FROM AGGREGATE QUARRY

Waste from aggregate quarry is a by-product generated from quarrying activities during the production of aggregates. The solid wastes were collected from a quarrying site at Sapang I, Ternate, Cavite. These are waste products from crushing and washing of mountain rocks to produce coarse and fine aggregates. The residues, which are considered as solid wastes, were produced during the washing of crushed rocks in the siltation pond through the natural process of sedimentation. Moist samples from this source have grayish black color with soft consistency resembling that of fine sand when dry. Previous studies discussed the geotechnical characteristics of WAQ and was proven to be suitable embankment material [6,7]. Prior to experimentation, the solid wastes were dried and sieved to ensure that the grain size conforms to the ASTM requirements for fine aggregates.

EXPERIMENTAL PROGRAM

A series of laboratory tests in accordance to ASTM standard procedures were carried out to determine the structural performance of concrete with WAQ as substitute for fine aggregates. Grain-size analysis, Scanning Electron Microscopy (SEM) test, and Energy Dispersive X-Ray Spectroscopy (EDS) were performed to determine the grain-size distribution, microfabric structure and chemical composition of WAQ, respectively. Its physical and chemical properties were analyzed and compared with that of conventional fine aggregates (sand).

To determine the compressive strength, cylindrical specimens with dimensions of 150mm diameter by 300mm high were subjected to compression test in accordance to ASTM C39. To determine the flexural strength, beam specimens with dimensions of 150mm x 150mm x 500mm were subjected to flexural strength test under a third-point loading condition following the procedure described in ASTM C78. A total of 92 cylindrical specimens and 76 beam specimens were tested.

In this study, WAQ was used as partial and full substitute for sand as fine aggregates in a concrete mix. A typical concrete mix proportion is shown in Table 1. The percentage substitution is done by volume using a specific gravity (Gs) of 2.7 for sand and 2.57 for WAQ [6]. The slump of each mixture was maintained at 2 to 3 inches. The 100B mixture requires greater amount of water to achieve the required slump and to make the mixture workable. A conventional concrete without WAQ, designated as 0B was used as control specimen and base data for comparison of the obtained test results. The target compressive strength of the concrete mix was 28 MPa. Compressive and flexural strengths were measured after 7th, 14th, 21st, and 28th days curing period designated as 7D, 14D, 21D, and 28D curing days, respectively. Prior to testing, the specimens' weight and volume were measured to determine the unit weight of hardened concrete.

Table 1 Concrete mix proportion

	Mix Proportions				
	0B	**25B**	**50B**	**75B**	**100B**
Sand					
Vol. (m^3)	0.028	0.021	0.014	0.007	0.0
kg.	75.60	56.70	37.80	18.90	0.0
WAQ					
Vol. (m^3)	0.0	0.007	0.014	0.021	0.028
kg.	0.0	17.99	35.98	53.97	71.96
Gravel (kg)	109.8	109.8	109.8	109.8	109.8
Water (liter)	15	15	15	15	15 to 18
Cement (bag)	1	1	1	1	1

TEST RESULTS

Grain-Size Analysis

The distribution of grain sizes of WAQ and sand was determined using sieve analysis by mechanical method in accordance with ASTM D422. Fig. 1 illustrates the grain size distribution curve. The grain-size distribution curve shows that WAQ has more percentage of finer particles as compared to sand.

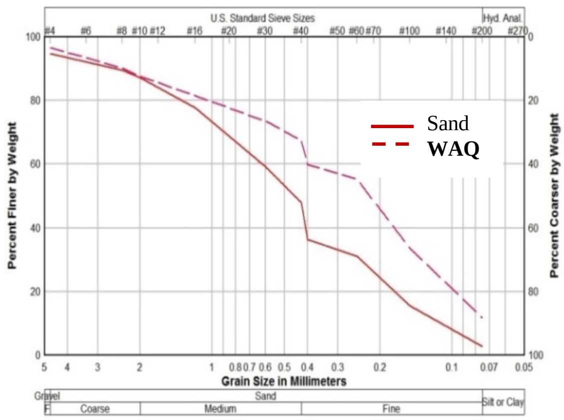

Fig. 1 Grain-size distribution curve of WAQ and sand

The chemical composition of WAQ was obtained from EDS test. Table 2 presents the chemical composition of WAQ in comparison to sand. The data showed that WAQ and sand consisted of the same chemical elements but with different proportions. WAQ has 5.52% more silicon, 5.99% more Iron and 1.11% more calcium as compared to sand. The bonding elements that mix the aggregates together are composed of silicon, calcium, and iron. Silicon is a significant element in cement amounting to 17% to 25% of its chemical composition [8]. Fresh concrete containing WAQ is observed to be more cohesive and less prone to segregation as compared to concrete mix without WAQ. However, water requirement increases for the concrete mix with more WAQ to improve its workability. These observed effects are due to the presence of more silicon content, similar to the effect of mineral admixture like silica fume. The presence of silica fume in concrete increases the degree of flocculation, substantially reduces bleeding by physically blocking the pores in the fresh concrete and results to improved strength properties [9].

Table 2 Chemical composition of WAQ and sand

Element	**WAQ**	**Sand***
	%	%
Magnesium (Mg)	0.59	2.06
Aluminum (Al)	8.15	6.33
Silicon (Si)	24.43	18.91
Potassium (K)	1.00	0.43
Calcium (Ca)	2.77	1.66
Iron (Fe)	6.92	0.93
Sodium (Na)	1.10	3.68
Total Carbon (C) and Oxygen (O)	55.41	34.00

* from Gallardo & Adajar (2006) [4]

Microfabric Structures

The micro-fabric structure of WAQ and sand was obtained using the Scanning Electron Microscope (SEM). As seen in Fig. 2a, WAQ has smaller grain sizes than sand. Its structure consisted of a combination of rounded and sub-angular grains with more silt-size grains while sand is comprised of angular grains of uniform-size particles.

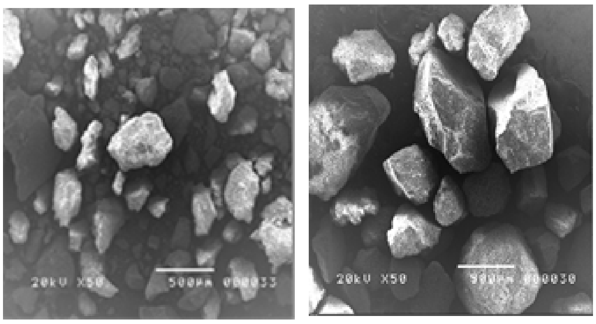

WAQ Sand

Fig. 2a Micrographs at 50X magnification

At higher magnification (Fig. 2b), the micro fabric of WAQ appears to be assemblages of clustered platy particles while sand's grain consisted of flaky particles arranged in some random direction with large inter-assemblage pore spaces depicting loose packing**.**

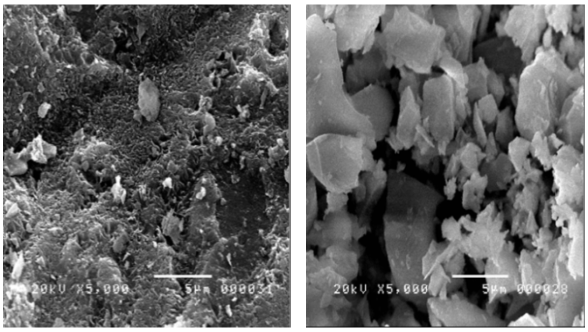

WAQ Sand

Fig. 2b Micrographs at 5000X magnification

Compressive Strength

A tabulated summary of the compressive strength of concrete specimens with different variations of WAQ can be seen in Table 3.

Table 3 Compressive strength of concrete with varying percentage of WAQ

Average Compressive Strength (MPa)					
Curing Day	**0B**	**25B**	**50B**	**75B**	**100B**
7D	21.07	11.68	10.02	17.18	12.62
14D	24.23	14.64	13.13	19.12	14.94
21D	26.28	15.88	14.70	21.51	18.95
28D	28.44	17.28	15.93	22.19	20.61

The control specimen (0B) reached the target compressive strength of 28 MPa at the 28th day curing period. Concrete with WAQ (25B, 50B, 75B, and 100B) have compressive strength lower than 0B. This was observed in all curing periods (7D, 14D, 21D, and 28D). Of the mix with WAQ, the 75B mix achieved the highest compressive strength and attained an almost 78% of the target strength while the 50B mix has the least compressive strength which is almost 56% of the target strength at 28th day curing period.

Figure 3 shows the compressive strength against the curing period of the specimens. It was observed that the increase in compressive strength with respect to curing period of concrete with WAQ follows the same trend as the increase in strength of the control specimen. The compressive strength increase ranges from 7% to 17% per week. The 75B mixture can be considered to have early compressive strength development since the achieved strength at 7th day is almost 61% of the target strength.

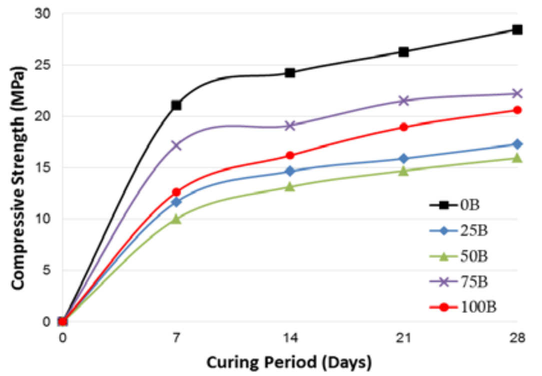

Fig. 3 Compressive strength vs. curing period

Figure 4 shows the relationship between the compressive strength and the WAQ substitution in a concrete mix.

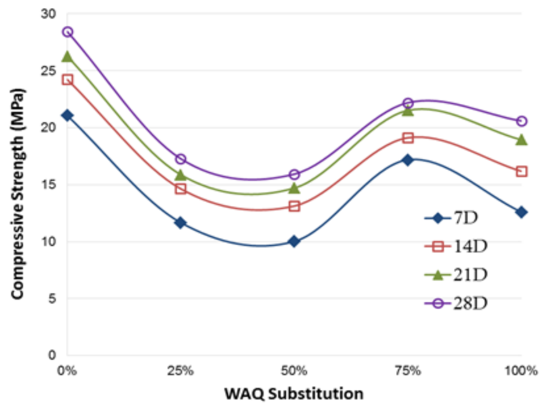

Fig. 4 Compressive strength vs. WAQ Substitution

The addition of WAQ resulted to a decrease in compressive strength. Comparing the compressive strengths with that of 0B mix, the maximum decrease in strength was observed in 50B mix while the minimum decrease was noted in 75B mix. The decrease in compressive strength can be attributed to the finer particles of WAQ in comparison to sand as seen from the grain-size distribution curve (Fig. 1). Moreover, the shape of WAQ particle is rotund and less angular than sand as seen from SEM results (Fig. 2a and Fig. 2b). Finer and less angular particles are factors that can contribute to reduction in particles' frictional resistance, thus can lead to reduction in compressive strength [10]. However, when the percentage of WAQ was more than 50%, it started to gain a slight increase in compressive strength. When WAQ was more predominant in quantity than sand, as in the case of 75B, it contributed positive results which can be attributed to its cohesive property, thus increases the bonding resistance of the particles. From test results, the positive effect of cohesiveness was observed when the quantity of WAQ was more than the quantity of sand. However, at 100B mix, the cohesive property of WAQ produced negative effect in terms of the workability of the concrete mix. More water has to be added in the mix to attain the desired slump and to make the mix more workable, thus resulted to reduction in compressive strength.

Formulation of Empirical Model to Predict the Compressive Strength

The compressive strength for each percentage WAQ substitution was presented in normalized form by dividing the experimental data with the compressive strength of the control specimen. The normalization of data was done to obtain a model that will predict the compressive strength of concrete mix with WAQ substitution at any target compressive strength and at any curing period. Figure 5 shows the normalized graph of the compressive strength against the percentage WAQ substitution. The data points were plotted in a scattered matter and yielded a trend line equation in the form:

$$fc = \left(-7.505x^4 + 11.001x^3 - 2.176x^2 - 1.656x + 1\right) fco \tag{1}$$

where:

fc = the compressive strength of concrete with x% WAQ

fco = the compressive strength of concrete without WAQ (control specimen)

x = WAQ substitution (in decimal form, i.e. 25% is 0.25)

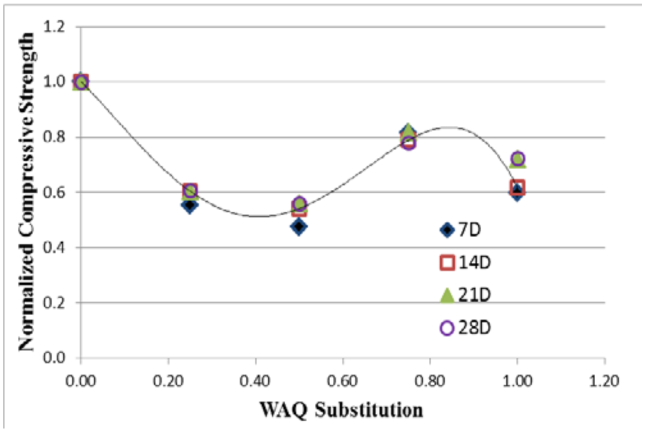

Fig. 5 Normalized Compressive Strength vs. WAQ Substitution

The equation has a coefficient of determination, R^2 = 0.9631. The coefficient of determination, R^2

closed to 1.0 indicates that the model fits the data well. From the equation obtained, the optimum WAQ percent substitution for sand is at 85% in order to produce the highest compressive strength of the concrete mix with WAQ.

Statistical Analysis on Compressive Strength

To verify the predictive capability of the proposed model, the compressive strength (*fc*) calculated using the proposed model was compared with the measured values from experimentation. Statistical analysis using T-test for paired samples was performed to determine if there is a significant difference between the measured values and the predicted values. The paired T-test results for 16 number of observations with a level of significance equals to 0.05 ($\alpha = 0.05$) showed a t_{stat} value (0.466) less than $t_{critical}$ (1.753) and the p-value (0.324) greater than 0.05. It can be stated, at 95% confidence level, that there is no significant difference between the measured compressive strengths and the predicted compressive strengths using the formulated model. The strength of association between measured *fc* and the predicted *fc* was verified using the Pearson's correlation coefficient and the data are presented in a scatter plot as shown in Figure 6. The scatter of data points is nearer to a straight line which means that there is a linear positive correlation between the measured and predicted *fc*. The analysis yielded a Pearson correlation value of 0.97 indicating a very strong association between the two variables (measured and predicted *fc*) [11]. It can be concluded that the proposed model (Eq. 1) can be used to predict the compressive strength of concrete with WAQ as substitute for fine aggregates as a function of the compressive strength of control specimen at any curing period.

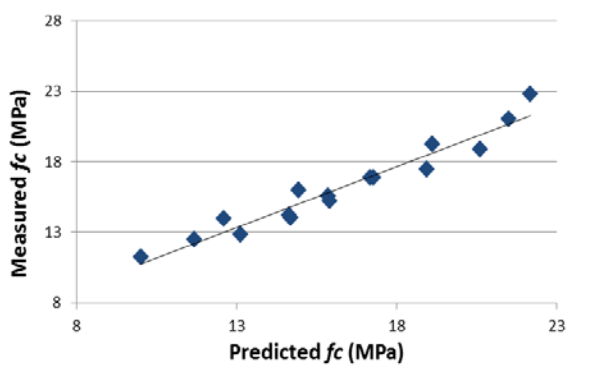

Fig. 6 Correlation of measured *fc* with predicted *fc*

Flexural Strength

The Modulus of Rupture of concrete represents its flexural strength. It is the capacity of concrete to resist failure in bending. The average flexural strength of the specimens is presented in Table 4. It was observed that the flexural strength of concrete with WAQ was in the range of 69% to 72% of the flexural strength of control specimen (0B). The reduced flexural strength can be attributed to the smooth surface texture of WAQ. Smooth texture of aggregate results to weaker bond between the concrete paste and the aggregates, thus leads to lower strength. Furthermore, the flexural strength of concrete with WAQ was found to be 12% to 18% of its compressive strength. This is in agreement with the findings of National Ready Mixed Concrete Association [12] that the flexural strength of conventional concrete is about 10% to 20% of the compressive strength.

Table 4 Flexural Strength of Concrete with Varying Percentage of Banlik

WAQ SUBSTITUTION	FLEXURAL STRENGTH (MPa) AT 28TH DAY
0B	4.25
25B	2.98
50B	3.08
75B	2.94
100B	3.26

Unit Weight of Hardened Concrete with WAQ

The unit weight of hardened concrete is critical to the performance of the structure. Concrete with lower density indicates the presence of more voids. The grading and size distribution has a significant contribution to the unit weight of concrete. It is expected that when the particles are of uniform size, the void spaces between particles are greater. But when a varying range of sizes is used, the void spaces are filled resulting to a larger unit weight. The unit weight of hardened concrete was obtained to determine the effect of WAQ substitution and the results are presented in Table 5. The unit weight of hardened concrete with WAQ was slightly lower than the unit weight of 0B mix. The decrease in unit weight was in the range of 1% to 2% which can be considered as insignificant. This was attested by the result of statistical analysis. Statistical test of One-way ANOVA yielded a *P*- value greater than 0.05. This indicates that the presence of WAQ in the concrete mixture did not produce significant reduction nor increase in its unit weight.

Table 5 Unit Weight of Concrete Cylinders in KN/m^3

Curing Day	0B	25B	50B	75B	100B
7D	23.40	23.13	23.34	23.23	23.16
14D	23.37	22.9	23.09	22.99	22.93
21D	23.28	23.10	23.29	23.18	23.13
28D	23.92	23.34	23.54	23.44	23.37

CONCLUSION

The structural performance of concrete mixed with waste from aggregate quarry (WAQ) as a substitute for sand was investigated. The following conclusions were drawn from the experimental results:

Waste from aggregate quarry contains more silicon, iron, and calcium as compared to sand. These are elements that caused concrete mixture with WAQ to have an increased cohesive property. SEM results showed that WAQ has finer, less-angular particles than sand. The finer particles of WAQ and presence of more Silicon, Iron, and Calcium elements produced positive effect in terms of cohesive property of the concrete.

Concrete with WAQ as fine aggregates achieved an almost 56% to 78% of the compressive strength of concrete without WAQ. Empirical model was formulated that can be used to predict the compressive strength of concrete with WAQ as substitute for sand. Using the formulated model, the highest compressive strength can be achieved at 85% WAQ substitution for sand. The flexural strength of concrete with WAQ was in the range of 69% to 72% of the flexural strength of concrete without WAQ and was found to be 12% to 18% of its compressive strength. The reduced compressive and flexural strengths can be attributed to the finer, less-angular particles and smooth surface texture of WAQ in comparison to sand

The presence of WAQ in the concrete mix has no significant effect on the unit weight of hardened concrete, however, it affects the workability of the mix due to its cohesive property thus requires higher water-cement ratio.

Test results proved that waste from aggregate quarry can be used as substitute for fine aggregates in a concrete mix and produced strength properties adequate for structural application. This study offers an effective waste management solution for WAQ and introduces an alternative material in concrete production thus contributing to a sustainable development.

REFERENCES

[1] Arifi E, Zacoeb A, and Shigeishi M, “Effect of fly ash on the strength of concrete made from recycled aggregate by pulsed power”, Int. J. of GEOMATE, Vol. 7, No. 1 (Sl. No. 13), Japan, Sept. 2014, pp. 1009-1016.

[2] Abdul Awal ASM, Mohammadhosseini H, and Hossain MZ, “Strength, modulus of elasticity and shrinkage behavior of concrete containing waste carpet fiber”, Int. J. of GEOMATE, , Vol. 9, No. 1 (Sl. No. 17), Sept. 2015, pp. 1441-1446.

[3] Yun Wang Choi, et.al, “Utilization of tailings from tungsten mine waste as a substitution material for cement”, Construction and Building Materials, Vol. 23, 2009, pp. 2481–2486.

[4] Gallardo R. and Adajar M, “Structural performance of concrete with paper sludge as fine aggregates partial replacement enhanced with admixtures.” JSPS-DOST Int. Symposium on Environmental Engineering and 5th Regional Symposium on Infrastructure Devt., 2006.

[5] Abdullah, M. et.al. “Concrete with ceramic wastes and quarry dust aggregates.” 5th Annual Conference Management in Construction Researchers Association, 2006, pp. 383 – 388.

[6] Adajar, MQ and Zarco, MH, “An empirical model for predicting hydraulic conductivity of mine tailings”, Int. J. of GEOMATE, Vol. 7, No. 2 (Sl. No. 14), Japan, Dec., 2014, pp. 1054-1061.

[7] Adajar, MQ and Zarco, MH, “Predicting the stress-strain behavior of mine tailing using modified hyperbolic model”, Int. J. of GEOMATE, Vol. 10, Issue 21, Japan, May 2016, pp. 1834-1841.

[8] “Composition of portland cement”, http://theconstructor.org/building/composition-of-portland-cement/5725/, Accessed : May 4, 2016.

[9] Rasol MA, “Effect of silica fume on concrete properties and advantages for Kurdistan Region, Iraq, Int. J. of Scientific & Engineering Research, Volume 6, Issue 1, January 2015, pp. 170 – 173.

[10] Shetty M S, Concrete Technology Theory and Practice, Ram Nagar, New Delhi: S. Chand & Company Ltd., 2005.

[11] Evans JD, Straightforward Statistics for the Behavioral Sciences, Pacific Grove, Calif.: Brooks/Cole Publishing, 1996.

[12] National Ready Mixed Concrete Association, “Concrete in Practice CIP 16 – Flexural Strength Concrete.” , from http://www.nrmca.org . Accessed: Jan. 29, 2015.

Sixth International Conference on Geotechnique, Construction Materials and Environment, Bangkok, Thailand, Nov. 14-16, 2016, ISBN: 978-4-9905958-6-9 C3051

SPENT COFFEE GROUND-FLY ASH GEOPOLYMER: STRENGTH ANALYSIS AS A RECYCLED ROAD SUBGRADE MATERIAL

TA. Kua[1], A. Arulrajah[2], S. Horpibulsuk[3] and YJ. Du[4]
[1,2] Department of Civil and Construction Engineering, Swinburne University of Technology, Melbourne, Australia; [3] Suranaree University of Technology, Nakhon Ratchasima, Thailand; [4] Institute of Geotechnical Engineering, Southeast University, Nanjing, China.

ABSTRACT

Coffee is a staple drink in many countries and cultures. The residue generated from coffee brewing, spent coffee ground (CG), is an organic waste which sees little use apart from occasionally being recycled domestically as an agricultural fertilizer. It is granular and physically similar to sand, hence the potential to be stabilized into a fill material for construction purposes. By combining CG with alkaline-activated Fly Ash (FA), a waste product generated as a result of coal combustion, a geopolymer was formed. An alkaline activator composed of a sodium silicate+ sodium hydroxide (Na_2SiO_3+ NaOH) mix was used to induce geopolymerization. Strength assessment of this geopolymer was done via Unconfined Compressive Strength (UCS) tests. Factors found to affect the strength development of the CG-FA geopolymer are: (1) the ratio of sodium hydroxide and sodium silicate in the activator liquid; (2) the curing time; (3) the replacement ratio of FA in the CG; (4) the alkalinity of the activator liquid used; and (5) the curing temperature. Four-days soaked California Bearing Ratio (CBR) tests conducted on selected mixes meet the requirement for a load-bearing subgrade fill material. This study shows that highly organic CG can be reprocessed to meet strength requirements as a recycled road subgrade material. The resultant product, which constitutes largely of solid waste materials, can potentially be developed into a green industrial fill material and reduce landfill space demand.
Keywords: Spent-coffee-ground; Fly-ash; Geopolymer; Subgrade; Reycling.

INTRODUCTION

Sustainability is a key issue in current researches in construction technology. As a result, reprocessing waste materials into recycled construction materials have become a popular field of research. Wastes including construction and demolition materials [1], [2], crushed glass [3], water treatment sludge [4] and highly organic waste-water biosolids [5] have been treated and laboratory-tested for their suitability as recycled construction materials. Successful implementation of recycled waste materials in the construction industry would diminish the need to harvest raw materials for construction and reduce dependency on landfills for waste disposal.

Spent coffee ground (CG) is the insoluble by-product resulting from the thermal water extraction from ground coffee beans. The global food and beverage industry generates approximately 7.4 million tons of CG each year [6], and this figure is expected to steadily increase due the popularity of the coffee drink [7]. CG is commonly used as a domestic agricultural fertilizer, but otherwise no large scale utilization of this organic waste has been reported. An analysis was recently done on CG [8] to assess its geotechnical properties and it was reported that CG physically resembles sandy soils, but is unsuitable for use as a construction material due to its high organic content of 86-89% and low load bearing strength.

Stabilizing CG for construction uses is a notion that would ideally divert a steadily generated organic waste into the construction industry, thus reducing both landfill space consumption and raw material demand. Chemical stabilization on soft soils conventionally utilizes Portland cement and lime [9]. The treatment results in augmented soil strength and stiffness. However, these additives are purposefully manufactured and are known to leave large carbon footprints [10], hence are contradictory to the idea of sustainability.

An alternative stabilization method by geopolymerization may be used to treat CG to form a green construction material. Geopolymerization is a chemical process which generates cementitious compounds but leaves minimal carbon footprints compared to the production and utilization of Portland cement [11]. Fundementally, the formation of cementitious compounds in geopolymers relies on the co-polymerization of alumina and silica in the base material, or precursor, by highly alkaline solutions. Fly ash (FA) is an aluminosilicate-rich material and a well-established precursor frequently used in geopolymerization [12]. It is a by-product of coal combustion and is easily obtainable due to global reliance on coal-combustion to generate energy [13]. Sodium hydroxide (NaOH) and sodium silicate (Na_2SiO_3) are the typical alkaline activators used in geopolymerization [12], [14].

Melbourne, Australia, is a city known for its deep-rooted coffee culture. On the other hand, a study in 2005 shows that 75% of Australia's energy comes from coal combustion hence 12 million tonnes of FA can be collected annually [15]. This study aims to combine two locally available waste materials, namely CG and FA, to form a green construction material via geopolymerization. Different ratios of NaOH and Na_2SiO_3, NaOH molarities, curing durations, and curing temperature were used to study the factors influencing strength development in this hybrid material. Variations in material strength due to these factors were observed via Unconfined Compressive Strength (UCS) tests, whereas the suitability of the material to be used as a road subgrade fill material was determined by California Bearing Ratio (CBR) tests.

MATERIALS AND METHODS

CG was collected daily from a café in Melbourne, Australia and oven dried at a temperature of 50°C to prevent the charring of organics and subsequent loss of mass at higher temperatures [8]. Due to the relatively low drying temperature and high moisture content in CG, drying typically requires 4 to 5 days. Moisture content was measured according to ASTM D2216-98. Coagulated clumps of CG can be commonly found in the dried material, but can be easily crumbled with abrasion by hand, indicating no chemical bonding. Particle size analysis on dried CG was done according to D442-63.

Commercially available Class F FA was used as the precursor. FA categorized in Class F are low in lime content, hence does not react readily with water and needs alkaline activation to show cementitious properties. Combinations of NaOH and Na_2SiO_3 were used as the alkaline activator. Commercially available reagent grade NaOH with 97% purity and D-grade Na_2SiO_3 composed of 44.1% silicic acid, sodium salt (1.6<Molar Ratio≤2.6) and 55.9% water were used. To prepare each geopolymer specimen, dried CG was manually mixed with the required percentage of FA in a bucket for 5 minutes to ensure material homogeneity. The required percentage of liquid activator was then added to the dry material. This mixture was further mixed for 5 minutes manually. The mixture was then used immediately for compaction to avoid excessive flocculation and hardening.

The UCS tests in this study, summarized in Table 1, consisted of 2 stages. In Stage 1, the ratio of CG:FA was fixed at 70:30 because a 30% binder ratio is known to successfully strengthen waste treatment sludge, another organic material [16]. Three ratios of Na_2SiO_3:NaOH at 90:10, 70:30, and 50:50 were used at varying liquid-to-activator (L/FA) contents. The concentration of NaOH in Stage 1was fixed at 8 mol. Subsequently, optimum liquid contents (OLC) under modified compaction energy was determined according to ASTM D1557-12. After OLC values were obtained, UCS samples were prepared by varying L to incorporate samples from both the dry and wet sides of the OLCs. Two sets of triplicate specimens were produced and cured at 7 and 28 days separately. The curing temperature used at this stage is 50°C, the maximum working temperature for CG as described previously.

Stage 2 fixed the Na_2SiO_3:NaOH ratio at 90:10 and L/FA ratio at 1.8, as 90:10 specimens produced the minimum UCS values among three Na_2SiO_3:NaOH ratios in Stage 1. Also, from the results of Stage 1, these 90:10 specimens achieved maximum UCS at L/FA= 1.8 hence the L/FA ratio used. Remaining controlled variables were tested as follow: 1) The FA content was varied from 10%-30% relative to the dry weight of CG, with NaOH concentration fixed at 8 mol and curing temperature fixed at 50°C; 2) NaOH concentration was varied at 5, 8, 10, 12, and 15 mol, with FA content fixed at 30%; and lastly 3) Curing temperature was varied from 21°C (room temperature), 40°C (summer temperature), to 50°C (maximum workable temperature), with FA content fixed at 30% and NaOH concentration fixed at 8 mol. All specimens in the 2nd stage were cured for a 7-day period. The Na_2SiO_3:NaOH ratio of 90:10 was selected to assess the maximum achievable strength development when NaOH content is at a minimum.

UCS samples were prepared by 1-layer static compression [4],[17] in a 50 mm diameter by 100 mm height split-mould to reach the target dry density previously obtained from the modified Proctor compaction method. The specimens were wrapped and sealed in transparent vinyl wraps to prevent moisture lost, and cured in temperature-regulated ovens. Figure 1 illustrates the apparatus used to produce the UCS specimens and also the wrapped specimens before curing.

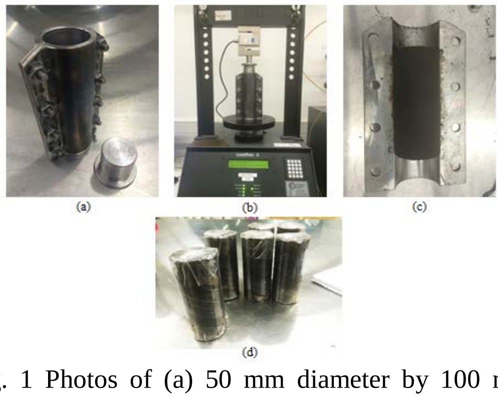

Fig. 1 Photos of (a) 50 mm diameter by 100 mm height split mould used for compaction; (b) apparatus setup during static compaction process; (c)

CG geopolymer specimen after compaction, before extrusion from split mould; and (d) extruded CG geopolymer specimens sealed in vinyl.

CBR tests were done on selected mixes after analyzing the UCS results. The CBR specimens were prepared and tested in accordance with ASTM D1883-07, as the CBR value is one of the key criteria used by the local road authority to assess the suitability of an embankment fill or subgrade materials [18]. These specimens were soaked for 4 days immediately after compaction, to simulate severe flooding of pavements in the open world environment. 3 specimens were prepared for each material combination, with the final assigned CBR taken as the average of the 2 lowest CBR results out of the 3 specimens.

Table 1 UCS Testing Programme Summary

Stage	Modified Variable	FA Replacement % by Dry Weight of CG (%)	Na_2SiO_3:NaOH Ratio (by weight)	L/FA (by weight)	NaOH Molarity (mol)	Curing Temperature (°C)	Curing Time (days)
1	Na_2SiO_3:NaOH Ratio & ActivatorLiquid Content	30	90:10	1.5, 1.8, 2.2, 2.6	8	50	7,28
			70:30	1.2, 1.5, 1.8, 2.1	8	50	7,28
			50:50	1.2, 1.5, 1.8, 2.1	8	50	7,28
2	FA Replacement Ratio	10,15,20,25,30	90:10	1.8	8	50	7
	NaOH Concentration	30	90:10	1.8	5, 8, 10, 12, 15	50	7
	Curing Temperature	30	90:10	1.8	8	21, 40, 50	7

RESULTS AND DISCUSSIONS

Figure 2 shows the particle size distribution curve of dried CG. With particles in the range of 0.075 to 2.36 mm in size, CG resembles poorly-graded sand according to the classification method in ASTM D2487-10, but due to the presence of high organic content it should be identified as an organic clay (OH).

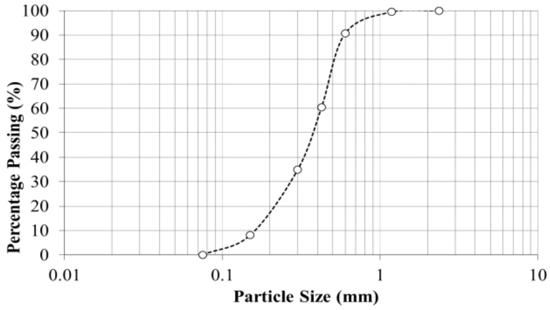

Fig. 2 Particle size distribution of CG.

The compaction curves of 70:30 CG:FA mixes are shown in Fig. 3 and 4. Figure 3 compares the prescribed amount of aqueous Na_2SiO_3:NaOH to the prescribed dry weight of the CG:FA mix. On the other hand, Fig. 4 compares the amount of evaporated water to the dry bulk density of remaining solid, including the solid Na_2SiO_3:NaOH trapped in the mix after evaporation. in the specimen after drying.

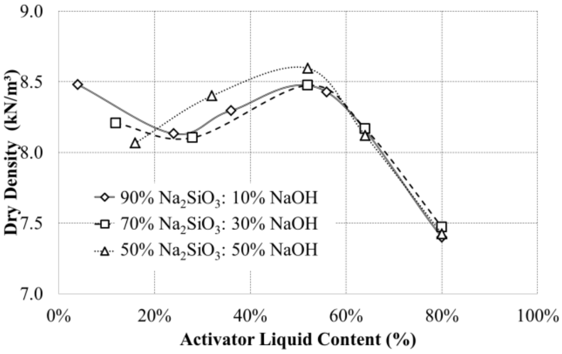

Fig. 3 Dry density vs. liquid alkali activator content for various Na_2SiO_3:NaOH ratios.

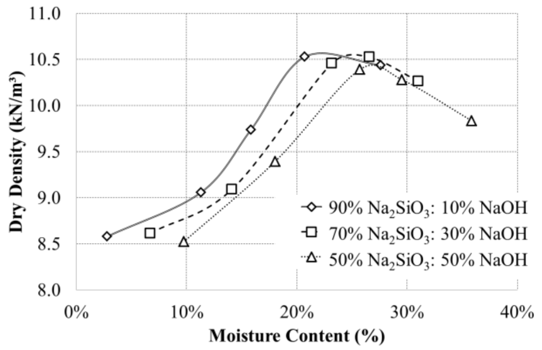

Fig. 4 Dry density vs. moisture content for various Na_2SiO_3:NaOH ratios.

From Fig. 3, it can be observed that the mixes are relatively insensitive to moisture changes below 50% (with variations not exceeding 0.5 kN/m^3), compared to the sharp decrease in dry density as the liquid content is increased after the peak at 52%. The 50:50 Na_2SiO_3:NaOH ratio specimens register the highest maximum dry density (MDD) (8.6 kN/m^3) relative to specimens compacted with the other ratios of Na_2SiO_3:NaOH (8.5kN/m^3). However, ASTM 1557-12 allows a measurement error of approximately ±0.1 kN/m^3 hence making the difference barely significant. This MDD achieved by CG:FA geopolymers is double that of unstabilized CG, which has a reported MDD of 4.4 kN/m^3 [8]. The MDD of these CG:FA geopolymers are similar to that of compacted biosolids, but still are relatively low compared to natural occurring soils. Interestingly, the dry densities in Fig. 3 show sign of increase as the amount of administered liquid approaches 0%, resulting in a sinusoidal curve particularly in the 90:10 Na_2SiO_3:NaOH mix. This occurrence is typically observed in sands [19] where MDD may occur at 0% moisture, but in this case assigning an MDD of 0% to the mixes would be meaningless because the liquid activator is needed for geopolymerization to occur.

On the other hand Fig. 4 shows that all three mixes exhibit a similar dry bulk density of 10.5 kN/m^3. As NaOH increases in the Na_2SiO_3:NaOH ratio used, the amount of moisture corresponding to the MDDs in the curves in Fig. 4 increases. This is attributed to the high water content found in the NaOH.

Strength evaluation of the geopolymers was done by UCS tests. While the OLC was determined to be 52% from Fig. 3, L/FA ratios from both the wet and dry sides of the OLC at smaller intervals were selected to pinpoint the maximum achievable UCS relative to changes in material density. While L/FA= 1.2, 1.5, 1.3, 2.1 were used for the 70:30 and 50:50 Na_2SiO_3:NaOH specimens, a higher L/FA ratio was nominated for 90:10 specimens to offset the hypothesized weaker geopolymer due to the low amount of NaOH present in this mix.

The UCS values of geopolymer specimens in Stage 1, namely with 30% FA cured at 50°C after 7 and 28 days, are illustrated in Fig. 5 and 6, respectively. By analyzing Fig. 5, the maximum 7 days UCS is found at L/FA ratio of 1.8 for Na_2SiO_3:NaOH ratios of 70:30 and 50:50 while it was found at L/FA of 2.3 for the Na_2SiO_3:NaOH ratio of 90:10. While 70:30 and 50:50 samples achieved maximum UCS at OLC, 90:10 samples require liquid contents exceeding its OLC. At L/FA = 1.8 mixes with a 50:50 Na_2SiO_3:NaOH content result in the highest strength at 956.3 kPa. However, maximum 7 days UCS strength was registered by 90:10 specimens at L/FA= 2.2, at 1160.5 kPa. On the other hand, for an extended curing time of 28 days as shown Fig. 6, the maximum UCS for 70:30 occurs at L/FA = 1.8, while 50:50 achieved maximum UCS at L/FA = 1.5. In the case of 90:10, a decrease in gradient starts to develop in the graph beyond L/FA = 1.8, indicating a saturation point. In all, UCS was found to increase when curing time was extended from 7 days to 28 days.

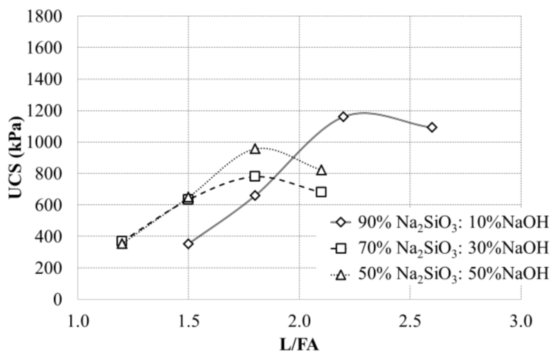

Fig. 5 7 days UCS versus liquid content for various Na_2SiO_3:NaOH ratios.

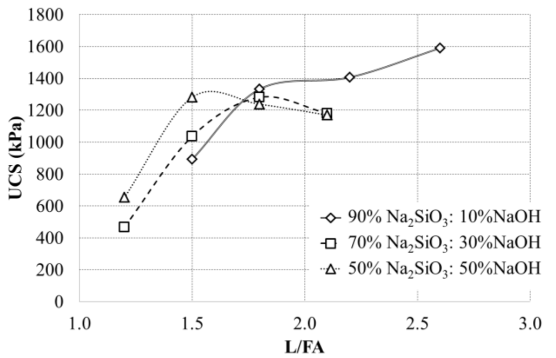

Fig. 6 28 days UCS vs. liquid content for various Na_2SiO_3:NaOH ratios.

As NaOH increases, the rate of precipitation and poly-condensation of FA is accelerated [4], hence the high strength generated by 50:50 specimens at L/FA= 1.8 at 7 days curing. On the other hand, when NaOH is excessively low, FA particlces cannot dissolve efficiently [4], hence the need for higher liquid contents in 90:10 mixes. Consequently, high levels of silicate in a mix would also result in a high rate of geopolymerization [20] via the formation of a different silica-rich sodium aluminosilicate hydrate (NASH) gel hence the high 7-days UCS for 90:10 specimens at L/FA= 2.2. Comparatively, the Department of Highways, Thailand nominates a minimum subgrade UCS of 294.2 kPa [21], whereas subgrade materials used in low-volume-traffic roads in Malaysia are required to have a minimum UCS of 800 kPa [22]. 50:50 specimens at L/FA= 1.8 cured for 7 days meet both benchmarks with the least liquid required.

The 50:50 Na_2SiO_3: NaOH mixture at L/FA = 1.8 was consequently selected to undergo 4-days soaked CBR tests. Seperately, 90:10 and 70:30 CBR specimens were produce at L/FA = 1.8 to obtain comparable results. Figure 7 shows that 50:50 samples achieves the highest CBR strength at 12%. Based on road authority specifications in the state of Victoria, Australia, all specimens pass the minimum acceptance requirement of 2% [18] to function as embankment structural fills or subgrade materials.

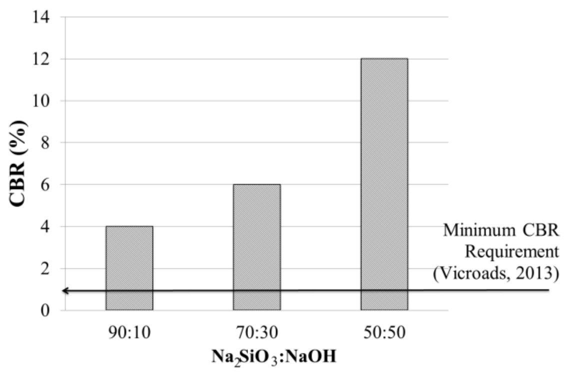

Fig. 7 4 days soaked CBR values various Na_2SiO_2:NaOH ratios.

Subsequently, 90:10 Na_2SiO_3:NaOH with L/FA= 1.8 and 7 days curing was fixed and used to study the effects of various FA contents, NaOH concentrations, and curing temperatures on UCS development. Figure 8 shows that at a curing temperature of 50°C, UCS increases with FA replacement ratio relative to CG, but after 25% the gradient decreases, implying a saturation point. Figure 9 demonstrates that at a fixed FA content of 30% and curing temperature of 50°C, the UCS increases as the molarity of NaOH used increases. Optimally the molarity used should be in the range of 8- 12 mol where small increments in molarity results in larger increase in UCS relative to other parts of the graph. Lastly, Fig. 10 demonstrates that elevated temperature curing at 40°C greatly improves UCS compared to samples cured at 21°C, but increasing the curing temperature from 40°C to 50°C produces only a relatively small increase in UCS.

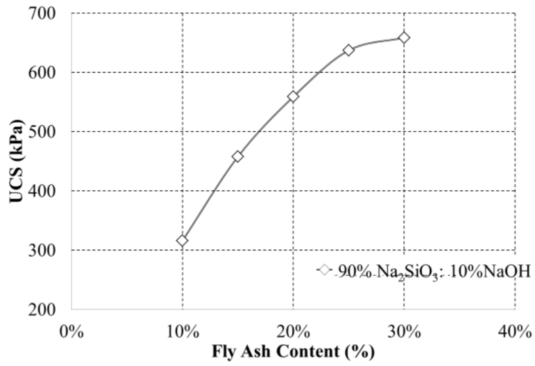

Fig. 8 7 days UCS vs. FA replacement ratio, with 8mol NaOH, and 50°C curing.

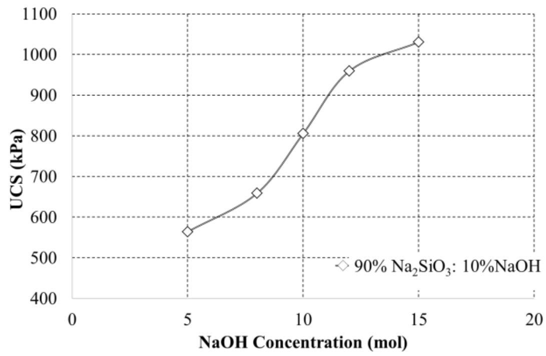

Fig. 9 7 days UCS vs. NaOH molarity, with 30% FA replacement, and 50°C curing.

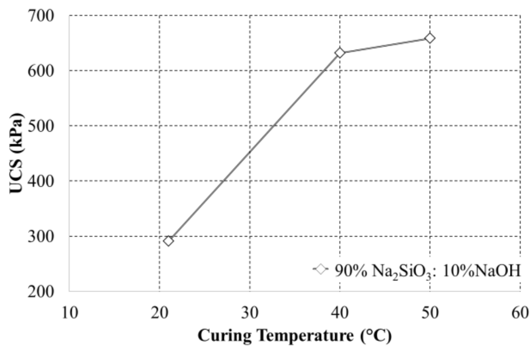

Fig. 10 7 days UCS vs. curing temperature, with 8mol NaOH, and 30% FA replacement.

CONCLUSION

This research indicates that CG can be stabilized via geopolymerization to produce a material with increased compressive strength. Road authority specifications in Victoria, Australia dictate that CBR values for subgrade materials must exceed 2%. This criterion is met by all the mixes studied. Specifically, the mix of 70:30 CG:FA with 50:50 Na_2SiO_3:NaOH and L/FA= 1.8 was found to be an efficient mix when cured at 50°C for 7 days. tests. Factors found to affect the strength development of the CG-FA geopolymer are: (1) the ratio of sodium hydroxide and sodium silicate in the activator liquid; (2) the curing time; (3) the replacement ratio of FA in the CG; (4) the alkalinity of the activator liquid used; and (5) the curing temperature. A recommendation for future works would be to look into the long term durability of this material to produce a green construction material with acceptable design life.

REFERENCES

[1] Arulrajah A, Disfani MM, Horpibulsuk S, Suksiripattanapong C, Prongmanee N. Physical properties and shear strength responses of recycled construction and demolition materials in unbound pavement base/subbase applications. Construction and Building Materials. 2014;58:245-57.

[2] Rahman MA, Imteaz M, Arulrajah A, Disfani MM. Suitability of recycled construction and demolition aggregates as alternative pipe backfilling materials. Journal of Cleaner Production. 2014;66:75-84.

[3] Disfani MM, Arulrajah A, Bo MW, Sivakugan N. Environmental risks of using recycled crushed glass in road applications. Journal of Cleaner Production. 2012;20(1):170-9.

[4] Suksiripattanapong C, Horpibulsuk S, Chanprasert P, Sukmak P, Arulrajah A. Compressive strength development in fly ash geopolymer masonry units manufactured from water treatment sludge. Construction and Building Materials. 2015;82:20-30.

[5] Arulrajah A, Disfani MM, Suthagaran V, Bo MW. Laboratory evaluation of the geotechnical characteristics of wastewater biosolids in road embankments. Journal of Materials in Civil Engineering. 2013;25(11):1682-91.

[6] Kondamudi N, Mohapatra SK, Misra M. Spent Coffee Grounds as a Versatile Source of Green Energy. Journal of Agricultural and Food Chemistry. 2008;56(24):11757-60.

[7] Butt MS, Sultan MT. Coffee and its consumption: benefits and risks. Critical reviews in food science and nutrition. 2011;51(4):363-73.

[8] Arulrajah A, Maghoolpilehrood F, Disfani MM, Horpibulsuk S. Spent coffee grounds as a non-structural embankment fill material: Engineering and environmental considerations. Journal of Cleaner Production. 2014;72:181-6.

[9] Akpokodje EG. The stabilization of some arid zone soils with cement and lime. Quarterly Journal of Engineering Geology. 1985;18(2):173-80.

[10] Horpibulsuk S, Phetchuay C, Chinkulkijniwat A, Cholaphatsorn A. Strength development in silty clay stabilized with calcium carbide residue and fly ash. Soils and Foundations. 2013;53(4):477-86.

[11] Hicks J. Durable "Green" Concrete from Activated Pozzolan Cement. Green Streets and Highways 20102010. p. 408-30.

[12] Sukmak P, Horpibulsuk S, Shen S-L. Strength development in clay–fly ash geopolymer. Construction and Building Materials. 2013;40:566-74.

[13] Malhotra V. Role of FA in reducing greenhouse gas emissions during the manufacturing of Portland cement clinker. 2nd International Conference on Advances in Concrete Technologies in the Middle East Dubai2008.

[14] Phetchuay C, Horpibulsuk S, Suksiripattanapong C, Chinkulkijniwat A, Arulrajah A, Disfani MM. Calcium carbide residue: Alkaline activator for clay–fly ash geopolymer. Construction and Building Materials. 2014;69:285-94.

[15] Morrison AG, P. Nelson, P. Future fly ash availability- Potential consequences of transformation of Australia's energy generation portfolio to 2050. World of Coal Ash (WOCA). Lexington, Kentucky, USA.2005.

[16] Horpibulsuk S, Suksiripattanapong C, Samingthong W, Rachan R, Arulrajah A. Durability against Wetting–Drying Cycles of Water Treatment Sludge–Fly Ash Geopolymer and Water Treatment Sludge–Cement and Silty Clay–Cement Systems. Journal of Materials in Civil Engineering. 2015:04015078.

[17] Sukmak P, Horpibulsuk S, Shen S-L, Chindaprasirt P, Suksiripattanapong C. Factors influencing strength development in clay–fly ash geopolymer. Construction and Building Materials. 2013;47:1125-36.

[18] Vicroads. RC 500.22: Selection and Design of Pavements and Surfacings. Victoria, Australia2013.

[19] Rollings MP, Rollings RS. Geotechnical Materials in Construction: McGraw-Hill; 1996.

[20] Ravikumar D, Neithalath N. Effects of activator characteristics on the reaction product formation in slag binders activated using alkali silicate powder and NaOH. Cement and Concrete Composites. 2012;34(7):809-18.

[21] Teerawattanasuk C, Voottipruex P, Horpibulsuk S. Mix design charts for lightweight cellular cemented Bangkok clay. Applied Clay Science. 2015;104:318-23.

[22] Awg Shahminan DNIA, Rashid ASA, Ridzuan Bunawan A, Yaacob H, Noor NM. Relationship between strength and liquidity index of cement stabilized laterite for subgrade application. International Journal of Soil Science. 2014;9(1):16-21.

Sixth International Conference on Geotechnique, Construction Materials and Environment, Bangkok, Thailand, Nov. 14-16, 2016, ISBN: 978-4-9905958-6-9 C3051

OPTIMIZATION OF COMPRESSIVE STRENGTH OF CONCRETE WITH PIG-HAIR FIBERS AS FIBER REINFORCEMENT AND GREEN MUSSEL SHELLS AS PARTIAL CEMENT SUBSTITUTE

Engr. Jayvee L. Gagan[1] and Dr. Bernardo A. Lejano[2]
[1,2] Civil Engineering Department, Gokongwei College of Engineering
De La Salle University, Philippines

ABSTRACT

The feasibility of different waste materials as substitute to the main components of concrete is attracting attention nowadays. In relation to that, this study focuses on determining the effects of combining two waste materials namely, pig-hair fibers (PHF) as fiber reinforcement and crushed green mussel shells (GMS) as partial cement substitute to the properties of concrete. Response Surface Methodology (RSM) was used to model the relationship between the response and the factors considered. Using central composite design (CCD) to establish the design of experiment, the researchers was able to reduce the required number of experimental runs to 20 from a total of 27 runs for 3 level full factorial experiment that is common for responses with nonlinear behavior. Optimization was conducted to determine the optimum amount of PHF and GMS in concrete that could yield maximum compressive strength while keeping the workability at an acceptable level. As for the results, an increase in compressive strength of concrete was recorded with the incorporation of PHF and GMS to concrete. However, decrease in workability was experienced due to the amount of fiber reinforcement present in the mix. Results of RSM suggested an optimum combination of 0.70% PHF content and 7.81% GMS partial cement substitute at 0.47 w/c ratio to achieve 27.40 MPa and 2.78 MPa compressive and tensile strength respectively with a minimum recommended slump of 25 mm for concrete beams and columns as per ACI. Based on these results, PHF-GMS concrete could be used in structures not requiring compressive strength above 28 MPa and with the use of GMS as a partial cement substitute, it could reduce the overall cement requirement for a project thus incurring savings and most importantly promotes the use of environment friendly materials.

Keywords: Pig-hair Fibers, Green Mussel Shells, Response Surface Methodology, Concrete

INTRODUCTION

Concrete is considered as the second most-consumed substance in the world next to water. As of 2012, a total of 11.5 billion tons of concrete are produced each year and is expected to increase to approximately 18 billion tons a year by 2050 [1]. Based on a study by Rubenstein [2], approximately 5% of the total carbon dioxide emission all over the world is constituted to concrete production. Aside from pollution, another problem on the increasing demand for concrete production is the shortage on locally available raw materials especially in remote areas.

Due to the problems stated above, some researchers [3], [4], [5] today are inclined to study the feasibility of using other materials as substitute to the main components of concrete i.e. cement, sand and gravel. These previous studies were developed to help minimize the negative effects of concrete production on the environment and provide cheaper alternative for the consumers. Addition of natural fiber reinforcement to improve strength and partial cement replacement are examples of application of green concrete technology.

Generally, materials with high lime or silica content could be a potential partial substitute to cement. In relation to this, most sea shells composed of calcium carbonate or limestone that made up almost 95% of its composition. Due to the presence of lime, shells exhibit cementitious characteristics when subjected to refinement. A chemical analysis was conducted by Etuk [3] to determine the chemical composition of powdered shells and based on the results, shells contains large amount of CaO (calcium oxide) and SiO_2 (silica) that are the two main chemical compounds in ordinary Portland cement making it feasible as partial cement substitute. Scallop shell (SS) powder was used as cement additive for grouting, results showed that the unconfined compressive strength of sand piece samples increased by 25% (120 kPa to 150 kPa) upon incorporation of 10% SS powder [4]. Also, a study was conducted on the utilization of Green Mussel Shells (GMS) and results showed that incorporating GMS into concrete as partial cement substitute improves its compressive and tensile strength by 48.28% and 68.06% respectively [5]. These studies illustrated the potential of limestone from sea shells as substitute cementitious material for concrete.

Fiber reinforcement in concrete is used to provide additional durability and improve its overall performance. Polymer based synthetic fibers are the ones that are commonly used in the construction industry as reinforcement. They can be classified as microsynthetic fibers, macrosynthetic fibers or a combination of both. Though it is effective in strengthening concrete, synthetic fibers are more expensive compare to other alternative fiber reinforcement. Studies on natural fibers such as coconut fiber, jute fiber, human hair and etc. as fiber reinforcement to concrete have been conducted by different researchers. Pig Hair Fibers (PHF) are also used as fiber reinforcement to concrete. Study shows that using PHF as fiber reinforcement not only improves the tensile strength of concrete but also its compressive strength [6].

Upon discussing the potential feasibility of the two materials (GMS and PHF) as an alternative component for concrete, it is quite interesting to study these materials when applied simultaneously to concrete. This study could determine whether their combination will yield better results or their interaction can have a negative effect on each other's characteristics. With the use of various statistical analysis techniques, effect of interaction of these two materials on a particular response can be analyzed. Statistical analysis like ANOVA can determine the level of significance of each factor and their interaction to the response. Along with Response Surface Methodology (RSM), it can provide non-linear analysis of results that captures curvature on the response plot. RSM also enables the researcher to determine optimum level of factors to come up with the maximum possible yield and also generate a prediction model for the fresh and hardened properties of concrete based on the proportion of parameters involved.

METHODOLOGY

The systematic plan in Fig. 1 shows the methodology used in conducting the study.

Preparation and Processing of PHF and GMS

As discussed in the introduction, two waste materials were used for this study. PHF and GMS were processed and tested for their physical properties. PHF were collected from the Monterey plant in Cavite, the fibers were washed and dried under the sun for 48 hours to remove impurities accumulated during the dehairing process. The GMS used in this study are called the "Asian Green Mussels", there are the ones commonly found in Philippine shores specifically in the Manila Bay. To extract its lime content, the shells were heated in a pan while continuously stirring for three hours until it became brittle. After heating, the shells were crushed into powdered form. To ensure uniformity in the particle size, crushed shells were sieve with 1 mm diameter opening. These powdered GMS were used as partial cement substitute. PHF content and GMS partial cement replacement are the main parameters for this study.

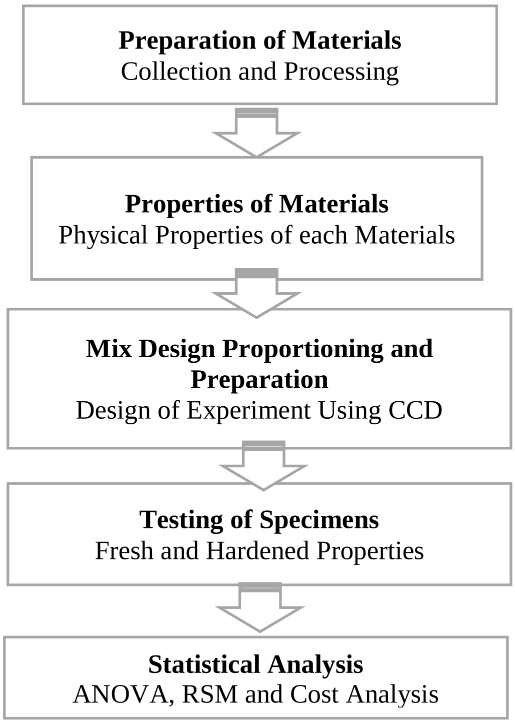

Fig. 1 Systematic plan of the study

Design of Experiment

The authors established proportions based on the best mix design suggested by the previous studies of Talagtag et al. [5] and Lejano et al. [6]. For PHF, 3 levels (0.6%, 0.8% & 1.0%) per volume of concrete of fibers were used. Also, 3 levels (5%, 10% & 15%) of partial cement replacement were used for GMS. These combinations were investigated for different water-cement ratio of (0.4, 0.5 & 0.6). Combination of these parameters is set using central composite design (CCD) as shown in Fig. 2. A total of 10 samples were made for each mix design for compressive and tensile strength test.

Making of Specimen and Testing

Mixing of concrete specimen was based on ASTM C192 [7] or the Standard Method of Making and Curing Test Specimen in the Laboratory. Dry mixing technique was used for the mixing of concrete. This mixing technique prevents accumulation of air pockets in the mixture thus making it more ideal when working with fiber reinforced concrete.

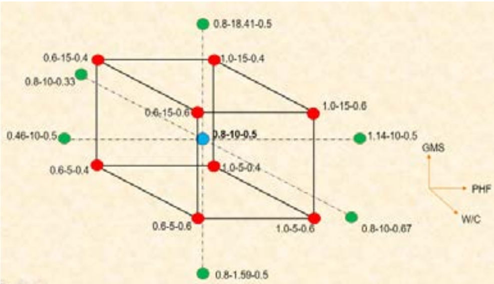

Fig.2 Central composite design of the study

The concrete were then molded into concrete cylinders of 150 mm diameter and 300 mm in height as test specimens. Each specimen was cured for 28 days before being tested using the Universal Testing Machine (UTM) for its compressive and tensile strength.

RESULTS AND DISCUSSION

The results of the 20 mix design tested for workability, compressive and split-tensile strength are shown in Table 1.

Table 1 Experiment results

Mix Design	Slump (mm)	Compressive Strength (MPa)	Tensile Strength (MPa)
0.6-5-0.4	23	32.23	2.73
1.0-5-0.4	18	31.27	3.44
0.6-15-0.4	28	25.81	2.49
1.0-15-0.4	14	23.29	2.25
0.6-5-0.6	35	15.13	1.58
1.0-5-0.6	28	16.19	2.09
0.6-15-0.6	32	14.31	1.62
1.0-15-0.6	27	11.21	1.83
0.46-10-0.5	26	25.41	2.53
1.14-10-0.5	19	20.00	2.51
0.8-1.59-0.5	22	20.14	2.22
0.8-18.41-0.5	23	15.92	2.03
0.8-10-0.33	10	31.21	2.84
0.8-10-0.67	38	13.36	1.24
0.8-10-0.5	26	26.34	2.69
0.8-10-0.5	26	26.03	2.87
0.8-10-0.5	24	25.71	2.78
0.8-10-0.5	29	24.00	2.75
0.8-10-0.5	29	23.96	2.72
0.8-10-0.5	27	23.22	2.58

Note: Mix Design are coded as PHF percentage – GMS cement replacement – water cement ratio.

Workability of Fresh Concrete

Shown in Table 1 are the results of the slump test for each mix. Overall, the workability attained during the experiment ranged from 10 to 38 mm. Based on this result, PHF-GMS concrete would be suitable for foundation application with light reinforcement. Furthermore, with high levels of water cement ratio, reduction of slump due to the increase of fiber content tends to become less compared to samples with lower w/c ratio. With higher water cement ratio, this concrete mixture could be used also for beams and columns. Fig. 3 shows the relation between the w/c ratio and the recorded slump of PHF-GMS concrete mix.

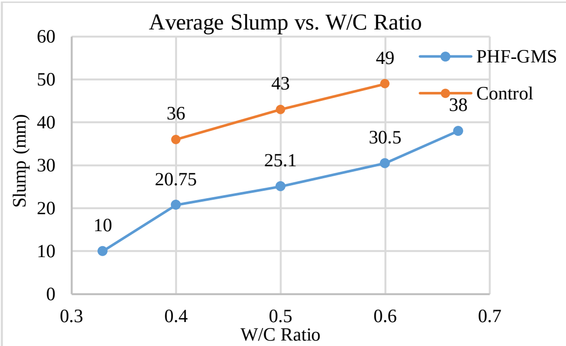

Fig. 3 Average slump for different w/c ratio

Comparing the slump of PHF-GMS concrete to the control specimen, addition of PHF and GMS resulted to a decrease in workability of concrete. These results were expected due to the fact that previous studies conducted on the application of each material also both resulted on a decrease in workability.

Compressive Strength of Concrete

Compressive strength of each mix design was computed using the average of 5 concrete cylinders tested. Like normal concrete, PHF-GMS concrete also experienced an inverse proportional relationship between the w/c ratio and compressive strength as shown in Figure 4. Comparing the results of the PHF-GMS combination to the control specimens, it can be seen that the compressive strength of concrete increased by 21.47% at 0.4 w/c, 32.71% at 0.5 w/c and 5.41% at 0.6 w/c. PHF-GMS concrete with W/C ratio of 0.5 yielded the highest compressive strength gain, this is due of the fact that the optimum content for the two materials (0.8% and 10% respectively) were at the center of the design that is where the 0.5 w/c ratio is also located. However, among the three factors considered in this study, the w/c ratio still had the most effect to the resulting compressive strength as well as the workability of concrete.

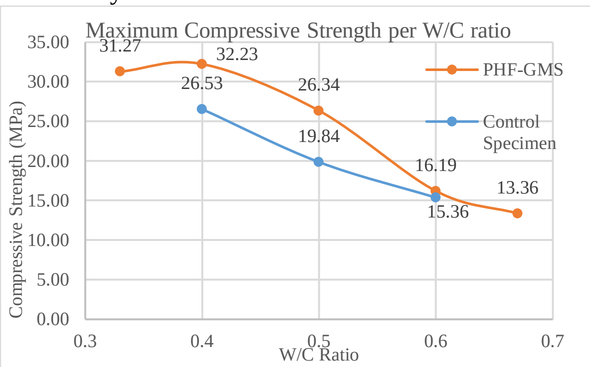

Fig. 4 Maximum compressive strength at different w/c ratio

Aside from the w/c ratio, another factor that showed significant effect to the compressive strength is the GMS content. The graph shown in Figure 5 describes the behavior of the compressive strength with respect to the different amount of GMS as partial cement substitute used in the mixture. Results in Fig. 5 were analyzed using a fixed PHF content of 0.8% per volume of concrete and 0.5 W/C ratio.

It can be seen that higher levels of GMS cement replacement had a negative effect on the strength of concrete. This decrease in strength may be accounted to the unutilized lime-silica reaction of excess lime from higher GMS content to the silica present in Portland-pozzolanic cement used.

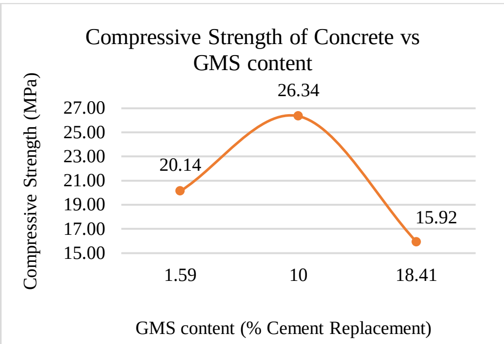

Fig. 5 Compressive strength for varying GMS content

As for the results of the analysis of variance for compressive strength, the 3 factors (PHF content, GMS partial cement substitute and W/C ratio) were all significant to the compressive strength of concrete. Among these factors, w/c ratio has the highest level of significance. This is due to the fact that W/C ratio had the most effect in terms of increasing/decreasing the workability of concrete as it changes. Between the two materials incorporated, PHF content and GMS partial cement substitute, the latter had more significant effect on the compressive strength of concrete. The fact that the cement content of ordinary concrete greatly affects its resulting properties, replacing some parts of it with pure lime from GMS would also have a significant effect on strength of concrete.

After determining significant factors and interaction, results were plotted to generate a response surface that represents the behavior of the compressive strength with respect to the PHF reinforcement content and GMS partial cement substitute. Combination of PHF and GMS are plotted for different water cement ratio as shown in Figures 6 to 8.

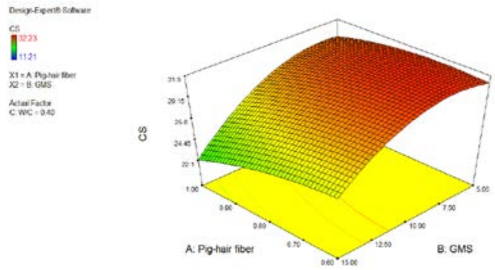

Fig.6 Compressive strength 3D surface for 0.4 w/c

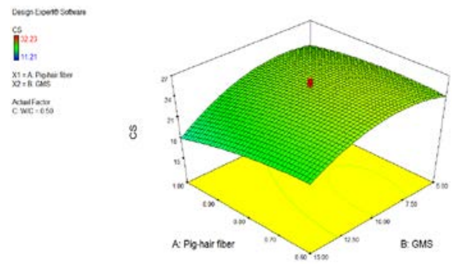

Fig. 7 Compressive strength 3D surface for 0.5 w/c

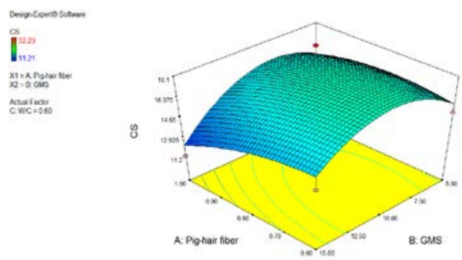

Fig. 8 Compressive strength 3D surface for 0.6 w/c

Based on the 3d response surface plots for compressive strength on different water cement ratio, it was clearly observed that there is a nonlinear behavior of compressive strength with the variation GMS content from 5% to 15% for the 3 W/C ratio level. At W/C ratio of 0.4, the maximum value of compressive strength was located near the minimum amount of GMS content considered which is at 5%. However, as the W/C ratio increases from 0.5 and 0.6 level, a shift on the optimum GMS content near the center of surface was observed. This means that, high w/c ratio promotes better utilization of lime content from GMS that is beneficial in the strength gain of concrete with GMS as partial cement substitute. Substituting type 1P (portland-pozzolan) cement with GMS led to adequate lime-silica reaction between the reactive silica of fly ash and lime extracted from the green mussel shells.

Split Tensile Strength of Concrete

Generally, the tensile strength recorded follows the same behavior as the compressive strength. It can be seen also from the results that an increase in tensile strength of concrete was experienced when increasing the fiber content to 1% compared to specimen containing only a minimum amount of 0.6%. However, maintaining the PHF content of concrete to its optimum percentage as suggested by the previous study had the most positive effect in terms of effectively increasing the tensile strength while keeping the slump of concrete at an acceptable level. This behavior of the tensile strength of concrete to varying PHF content in concrete was illustrated in Fig. 9.

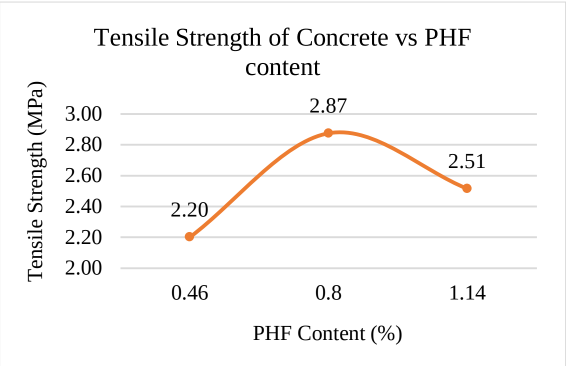

Fig. 9 Tensile strength for varying PHF content

A 2.87 MPa tensile strength was recorded using the optimum condition suggested by previous studies that is about 74% higher compared to the control specimen. It is evident that increasing the fiber content of concrete really increases its tensile strength, however, further increase in PHF content may result to reduced workability and accumulation of air voids that could cause strength reduction in concrete.

Optimization

The regression models in Eqs. (1), (2) and (3) were used in predicting the optimum mix design for the PHF and GMS combination.

$$CS = 32.179 + 24.565A + 0.964B - 8.493C - 0.715AB + 9.000AC + 2.150BC - 17.042A^2 - 0.093B^2 - 83.018C^2 \quad (1)$$

$$TS = -2.299 + 5.808A + 0.101B + 13.118C - 0.156AB + 1.563AC + 0.303BC - 2.750A^2 - 0.0078B^2 - 22.138C^2 \quad (2)$$

$$S = 6.402 - 15.660A - 0.019B + 63.038C \quad (3)$$

where:
CS = Compressive strength of concrete, MPa
TS = Split-Tensile strength of concrete, MPa
S = Slump of concrete, mm
A = Pig-hair fiber content, %
B = Green mussel shell partial cement subs., %
C = Water/cement ratio

The main objective of the optimization was to generate the maximum possible compressive strength while keeping the workability of the mixture at an acceptable level, which for this case, a minimum slump of 25 mm. The optimum mix design was determined using the numerical optimization tool of Design Experts® as shown in Table 2. These results showed that combining PHF and GMS into concrete could yield a maximum compressive strength of 27.394 MPa with an acceptable slump of 25 mm using the optimum combination generated.

Table 2 Optimum mix design

Factors/Response	Optimum Value	Unit
PHF Content	0.70	%
GMS Content	7.81	%
W/C ratio	0.47	
CS	27.40	MPa
Slump	25	mm

Cost Analysis

The cost analysis was focused on determining the economy of the application of the two materials under study. Direct cost such as materials, labor and miscellaneous expenses were considered for PHF and GMS. The fact that both of these materials were considered as wastes, its materials cost could be assumed as zero. However, gathering and processing these materials into concrete component induced labor and operations cost. Table 3 shows the total cost derived for each component material used in the concrete. Also, shown in Table 4 is the cost comparison of ordinary concrete (OC) and PHF-GMS concrete (PGC). Concrete strengths of control specimen at different w/c ratio considered (15.36 MPa, 19.84 MPa and 26.53 MPa) were used as the base strength for OC and PGC.

Table 3 Unit price of materials

Material	Unit Cost	
PHF	4.50	Php / kg
GMS	8.06	Php / kg
Cement	6.00	Php / kg
Gravel	0.71	Php / kg
Sand	0.35	Php/kg

Comparing the results showed that incorporating PHF and GMS reduces the cement content requirement in concrete by the increase in w/c ratio to achieve a particular compressive strength. Savings of about 0.78%, 7.22% and 10.11% were recorded compared to ordinary concrete with 0.6, 0.5 and 0.4 w/c ratio respectively.

Table 4 Cost comparison per strength requirement

CS (MPa)		W/C	GMS	PHF	Cost per cu.m (Php)
15.36	OC	0.60	0	0	2,815.43
MPa	PGC	0.63	9.86	0.68	2,793.43
19.84	OC	0.50	0	0	3,166.70
MPa	PGC	0.58	9.22	0.68	2,938.08
26.53	OC	0.40	0	0	3,693.61
MPa	PGC	0.48	8.3	0.70	3,320.16

CONCLUSION

This study showed that the parameters considered pig-hair fiber reinforcement, GMS partial cement substitute and water cement ratio had a significant individual effect to the resulting properties of concrete. Based on the results, combining pig-hair fibers and GMS into concrete further increased the compressive strength of concrete when compared to the results obtained on the research about application of GMS only by about 13.19% (from 23.27 MPa to 26.34 MPa) at 0.5 w/c ratio. However, reduction in workability was experienced upon the combination of these two materials into concrete. Generally, increasing the amount of PHF on the mixture tends to decrease the workability of the fresh concrete. Adjustment of the overall water content on the mix could be done to address the decrease in workability caused by fiber reinforcement. Compressive strength as high as 32.23 MPa was recorded for PHF-GMS concrete at 0.4 w/c ratio which yielded a slump of only 14 mm thus making it unacceptable for industry application. The maximum compressive strength with above minimum acceptable slump of 26mm was obtained from the 0.8%-10%-0.5 (PHF-GMS-W/C) combination that yielded 26.34 MPa which was 32.74% higher than ordinary concrete strength with the same w/c ratio.

Using the mix design obtained from optimization on actual specimens, PHF-GMS concrete obtained a compressive strength of 26.58 MPa and slump of 26mm. Results suggest that PHF-GMS could be used in structures not requiring above 28 MPa compressive strength or high strength concrete. These includes residential houses, low rise buildings and also concrete pavements. And with the use of GMS as a partial cement substitute, it could reduce the overall cement requirement for a project thus incurring savings and most importantly promotes the use of environment friendly materials.

ACKNOWLEDGMENT

Special thanks to the Department of Science and Technology – Engineering Research and Development for Technology (DOST – ERDT) for providing the financial support for this study.

REFERENCES

[1] Mehta PK and Montiero PJM, "The future challenges in concrete technology", Concrete: Microstructure, Properties and Materials, 3rd ed. 2014, pp 636.

[2] Rubenstein M, "Emissions from the cement industry", The Global Network for Climate Solutions (GNCS Factsheets), The Earth Institute Columbia University, Retrieved from http://www.theGNCS.org, 2012.

[3] Etuk BR, Etuk IF and Asuquo LO, "Feasibility of using sea shells ash as admixture to concrete", J. of Environmental Science and Engineering, Vol. 1, 2012, pp. 121 - 127.

[4] Amarakoon GGNN, Koreeda T and Kawasaki S, "Effect on unconfined compressive strength of sand test pieces cemented with calcium phosphate compound", Int. J. of GEOMATE, Vol. 7, Dec. 2014, pp. 1070 - 1075.

[5] Talagtag R, Sarao III E, Ngo K and Lejano B, "Utilization of perna viridis as partial substitute to cement in concrete mix", Proceedings of the 2014 Seminar Workshop on Utilization of Waste Materials, Philippines, Philippines, Sep. 5, 2014 (In CD).

[6] Lejano B, Templonuevo J, Young CJ and Zotomayor RL, "Properties of fresh and hardened concrete reinforced with hair from sus scrofa domestica", Proceedings of the Seminar Workshop on Utilization of Waste Materials 2013, Philippines, Sep. 5-6, 2013 (In CD).

[7] ASTM International, "ASTM C192, Standard Practice for Making and Curing Test Specimens in the Laboratory", http://www.astm.org, West Conshohocken, PA, 2016.

PULL-OUT STRENGTH OF AN EXPANSION STUD ANCHOR IN CARBON FIBER REINFORCED CONCRETE

Gilford B. Estores[1] and Bernardo A. Lejano[2]
[1]Faculty, Mapua Institute of Technology, Philippines; [2]Faculty, De La Salle University, Philippines

ABSTRACT

Carbon Fiber Reinforced Concrete (CFRC) is considered as an innovative structural material because of its better performance characteristics when compared to conventional concrete. Its common applications where expansion stud anchor connection is possible are in slabs on grade, wall panel, curtain walls, and pre-cast elements. The design of this stud anchor in CFRC is of great interest to many structural engineers, however, no model is available as basis for its design. To develop such model, this study investigated the pull-out strength of an expansion stud anchor embedded in CFRC as influenced by fiber volume content (Vf), fiber length (Lf), compressive strength and tensile strength. Three compression, three tension, and five pull-out CFRC specimens each of different Vf (0.10%, 0.15%, 0.20%, 0.25%, 0.30%) and different Lf (19mm, 30mm, 38mm) were prepared, tested, analyzed, and compared to control concrete specimens at design compressive strength of 21MPa. Tests results show that pull-out strength of an expansion stud anchor in CFRC is maximum at Vf = 0.10% and Lf = 38mm. Among the parameters considered, tensile strength is the most significant contributing factor that could influence the pull-out strength of stud anchor in CFRC. This is further verified numerically by a FEM model with good agreement to the observed tensile strength. Finally, a Response Surface Methodology (RSM) model is proposed to predict the pull-out strength of an expansion stud anchor embedded in CFRC as influenced by the fiber volume content, fiber length, compressive strength, and tensile strength.

Keywords: *Pull-out Strength, Expansion Stud Anchor, Tensile Strength, Fiber Length, Fiber Volume Content*

INTRODUCTION

Synthetic fibers as replacement of steel reinforcement had recently become the focus of many researchers. According to them, these fibers have the potential to be used as reinforcement in concrete to improve certain physical properties. Among the synthetic fibers, carbon has been concluded in many studies to have excellent physical, mechanical and dynamic properties and can be utilized more effectively as reinforcement in concrete material. It is believed that addition of carbon fibers to concrete effectively increases the strength and toughness of concrete. The inclusion of carbon fiber to concrete is termed as CFRC for carbon fiber reinforced concrete. CFRC is proven to have high resistance to corrosion which makes it more durable. It has been successfully applied to many civil engineering projects such as impact resisting structures, precast elements, panels, bridge deck, slabs-on-grade, pavements and curtain walls. It has been claimed by some researchers that chopped carbon fibers, when included within concrete with the appropriate fiber length and volume fraction, can modify the tensile strength, flexural strength, toughness, impact resistance, and fracture energy of the concrete [1]. They recommended that the chopped carbon fibers regardless of its type (PAN or Pitch) should have an average length of not less than the maximum size of the coarse aggregate, preferably at least twice as long as the maximum size of coarse aggregate at minimum of 0.1% fiber volume content to effectively bind coarse aggregate to achieve a significant result for strengthening a concrete structure.

One possible application of CFRC is in the anchorage connection of structural elements. Assuming that the anchor bolts are designed adequately, the pull-out strength of these anchors in concrete is controlled by the failure mode of the base concrete, which could be concrete breakout, concrete splitting, or frictional pull-out. Hence, the behavior of the base concrete where these anchors will be embedded should be carefully considered in design. It is believed that the base concrete will perform better if it is reinforced with fibers. Fiber-reinforced concrete (FRC) has been observed to perform better compared to plain concrete. One study investigated the performance of adhesive anchor bolts in polypropylene fiber reinforced concrete and in steel fiber reinforced concrete [2]. It has been reported that there was a significant increase in pullout load capacity of adhesive anchors both in polypropylene fiber reinforced concrete and in steel fiber reinforced concrete compared to plain concrete. Another study on pullout performance of a single headed anchor in steel fiber reinforced concrete has been investigated [3]. It was found out that the anchor's pullout capacity increased with the addition of steel fibers to concrete.

In this study, CFRC is investigated as base material of expansion anchor connection. As of now, there is no model that can be used as basis for its design. The pull-out strength of an expansion anchor in CFRC is expected to behave differently from usual ordinary concrete. Specifically, this study investigated the pull-out strength of a single expansion stud anchor in CFRC considering the concrete breakout failure mode as influenced by fiber volume content, fiber length, tensile strength and compressive strength. This research will give significant information that is much needed by structural engineers in designing an expansion stud anchor in CFRC which will lead to the solution involving the safety and the economic aspects of its design. Moreover, this study also promotes the application of anchorage in CFRC as well as the utilization of carbon fiber as reinforcement in concrete structures that would result in valuing and increasing awareness of the carbon fiber as innovative construction alternative material. Lastly, the additional benefit of anchorage in CFRC is the ease of drilling for post-installed anchor bolts.

METHODS

Materials

The components of the specimens used in this study were expansion stud anchors and the composite base materials. The composite base material is composed of the carbon fibers (CF) and the concrete matrix. An expansion stud anchor used in this study was a medium-duty anchor with 10 mm diameter with a total length of 90 mm and with yield strength of 640 MPa. The technical data of this anchor such as required torque (T), standard effective embedment depth (h_e), drilling depth (h), drilled hole diameter (D_h), and minimum base thickness (H_{min}) is presented in Table 1.

The fiber type used in this investigation was 0.111 mm thick chopped PAN-based high tensile (HT) strength carbon fibers. According to ACI 544 [4], the length of carbon fibers may vary from 5mm to 50mm, but with the predominance of demand for 19mm or 38mm fiber length. The selected fiber lengths used in this investigation were 19mm, 30mm, and 38mm. The properties of the PAN-based HT carbon fibers used are presented in Table 2.

Table 1 Technical data for expansion stud anchor

Type	T (Nm)	h_e (mm)	h (mm)	D_h (mm)	H_{min} (mm)
	45	60	80	10	120

Table 2 Properties of PAN-based HT carbon fibers

Lf (mm)	F_t (MPa)	E (MPa)	Spec. Gravity	Width (mm)
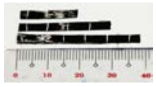	4510	231000	1.8	3.0

Notes: F_t = Tensile Strength of Carbon Fibers
E = Modulus of Elasticity

The concrete matrix was composed of cement (C), water (W), fine aggregates (FA), coarse aggregates (CA), and superplasticizer (SP). A high-early strength and with improved workability Portland cement that meets the ASTM standard specification C595 [5] was used in this study. The water used was clean and of good quality. Crushed coarse aggregates with maximum size of 19mm having a mass density of 1592 kg/m^3 and 1.01% absorption were used. White sand with mass density of 1551 kg/m^3, fineness modulus of 2.4 and having a 3.01% water absorption were used as fine aggregates. A superplasticizer was added to ensure that fresh CFRC mix is workable.

Specimens

The design mix of the composite base materials were based on the compressive strength of 21MPa considering the 25mm to 100mm slump, 2% entrapped air, and water-cement ratio of 0.68. Three compression, three tension, and five pull-out CFRC specimens for each of the different fiber volume contents, Vf (0.10%, 0.15%, 0.20%, 0.25%, 0.30%) and of different fiber lengths, Lf (19mm, 30mm, 38mm) were prepared, tested, and compared to concrete without fiber as the control specimen. The mix proportions of the control and CFRC specimens are given in Table 3.

Table 3 Mix proportions of the specimens

Vf (%)	W (kg/m^3)	C (kg/m^3)	CA (kg/m^3)	FA (kg/m^3)	CF (kg/m^3)	SP (gm/kg of C)
0	182.08	301.47	1054.71	841.07	-	-
0.1	182.08	301.47	1054.71	839.52	1.8	3
0.15	182.08	301.47	1054.71	838.71	2.7	3
0.2	182.08	301.47	1054.71	837.93	3.6	3
0.25	182.08	301.47	1054.71	837.16	4.5	3

0.3	182.08	301.47	1054.71	836.38	5.4	3

Before casting all the specimens, the workability of each mix was checked by measuring its slump as per ASTM C143 [6].

The compressive strength specimens were tested using 100mm x 200mm cylinders as per ASTM C39-05 [7] after 28 days of curing period. The tensile strength specimens using a dumbbell shape with a critical section of 75mm x 50mm, and a gauge length of 300mm were tested after 28 days of curing period. The test set-up for direct tensile strength and its failure mode at the critical section are shown in Fig. 1. The base material specimens in rectangular solid shape measuring 360mm x 360mm x 150mm were made and cured for 28 days. Then, the stud anchors were set in these base materials following the setting instruction recommended by the manufacturer and tested them for pull-out strength in accordance to ASTM E 488-96 [8]. The set-up of pull-out strength test for expansion stud anchors and its concrete breakout failure mode are presented in Fig. 2. The observed pull-out strength of the stud anchor in concrete base material without fiber was compared to ETAG 001 (Guideline for European Approval of Metal Anchors) [9], and ACI 355.2 [10] and NSCP 2010 (National Structural Code of the Philippines) [11] equations for verification. ETAG 001 equation for concrete breakout of a single anchor in non-cracked plain concrete is given by

$$N_{Rk,c}^{0} = 10.1\sqrt{f_{ck,cube}}\,h_{ef}^{\;1.5} \quad (1)$$

The compressive strength using cube specimen was computed using the equation of Kumavat HR and Patel VJ [12],

$$f_{ck,cube} = f'_c / 0.95 \quad (2)$$

While, the NSCP 2010 and ACI 355.2 equation for concrete breakout of a single post-installed anchor in non-cracked plain concrete is given by

$$N_b = 7(1.4)\sqrt{f'_c}\,h_{ef}^{\;1.5} \quad (3)$$

Fig. 1 Tension test set up and failure mode

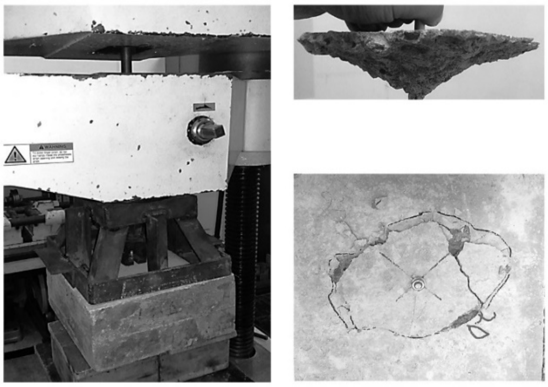

Fig. 2 Pull-out test set up and failure mode

Finite Element Modeling (FEM)

In this study, FEM was applied to simulate, and verify the tensile stress response of the CFRC base material specimens subjected to tensile loading applied into a single expansion stud anchor. Since numerical analysis using FEM may lead to a very large equations and complex solutions, the use of FEM software ABAQUS was used to verify and compare the tensile stress response of CFRC base material specimens subjected to tensile loading applied to a single expansion anchor against the actual tensile stress of the specimens. The base material is modelled as an isotropic 2D elastic material under tensile load induced by an expansion stud anchor as shown in Fig. 3 with assumed Poisson ratio of 0.20.

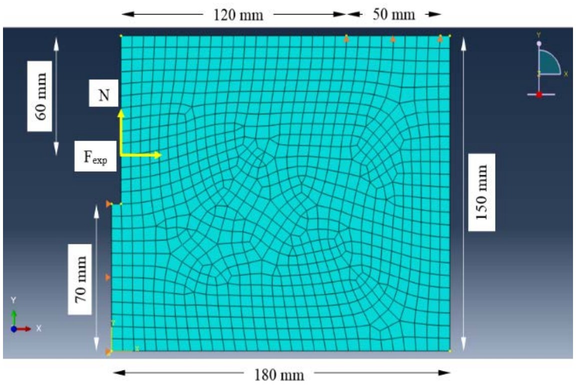

Fig. 3 FEM model

The experimental parameters used in the simulation of tensile stress (FEM_{ft}) are compressive strength (f_c), mass density of base material (w_c), and pull-out strength (N), while normal force through the anchor's sleeve expansion (F_{exp}) was derived using the equation,

$$N = uF_{\exp} \tag{4}$$

where, u is the coefficient of friction and was assumed 0.372. This coefficient is nearly equal to the value cited in CEB (Comite Euro-International du Beton) [13], where u of expansion anchor varies from 0.4 to 0.6. The modulus of elasticity, E_c of the specimens were computed using the equation given by NSCP 2010,

$$E_c = w_c^{1.5} 0.043\sqrt{f'_c} \tag{5}$$

Response Surface Methodology

Response Surface Methodology (RSM) can model linear and non-linear dynamics, and stochastic phenomenon. The data requirement for a given output is low and the errors are assumed to be random. Supposed that Y is the response of interest and x_1, x_2, x_3, x_4 are the predictor variables. The response of interest in this study can be expressed as $Y = f(x_1, x_2, x_3, x_4)$. The function $f(x_1, x_2, x_3, x_4)$ denotes the response surface. The first step in this process is to find an appropriate approximation for the true relationships between the response and the predictor variables [14]. In this study, the response of interest is the pull-out strength of an expansion stud anchor in CFRC, while the predictor variables are the fiber volume content, fiber length, tensile strength and compressive strength at standard h_{ef} = 60mm. First-order and second-order RSM models were considered in developing the proposed model in this study. The fitted model of the first-order and second-order are generally defined as

$$\hat{y} = \hat{\beta}_0 + \sum_{i=1}^{k} \hat{\beta}_i x_i \tag{6}$$

$$\hat{y} = \hat{\beta}_0 + \sum_{i=1}^{k} \hat{\beta}_i x_i + \sum_{i=1}^{k} \hat{\beta}_{ii} x_i^2 + \sum_{i<j}\sum \hat{\beta}_{ij} x_i x_j \tag{7}$$

respectively, where, $\hat{\beta}$ is the least squares estimate of model coefficients. The next step is the evaluation of the adequacy of the fitted model. This is to ensure that the recommended model will give a satisfactory estimate of the true system. The adjusted coefficient of multiple determination or R^2_{adj} was used in this study instead of R^2 because in most cases, it doesn't always increase as the terms are added to the model with k regressors [14]. It is a measure that estimates Pearson's correlation ratio with value from 0 to 1 and is defined as:

$$R^2_{adj} = 1 - \frac{n-1}{n-p}\left(\frac{SS_E}{SS_T}\right) \tag{8}$$

where, SS_E is the sum of squares of the residuals, SS_T is the total sum of squares and p = k+1 degrees of freedom. The fitted model was also subjected to test of significance by F-test at α = 0.05. The best model is the one that has highest R^2_{adj} and has least error.

Error metric was defined to each model and compared. The metric of comparison used aside from R^2_{adj}, is the mean square of error or MSE. The error metric is given as

$$MSE = \frac{\sum\left(y - \hat{y}\right)^2}{n\sigma_y^2} \tag{9}$$

where, y is the observed value, $\hat{y}$ is the predicted value, and σ_y^2 is the variance of the observed value.

RESULTS AND DISCUSSIONS

Slumps of Fresh Concrete

The workability of fresh CFRC mix and plain concrete resulted from the slump tests are presented in Fig. 4. The slump of CFRC mixes range from 75mm down to 47mm, while the control specimen has a slump of 80mm. It reveals that all the mixes have passed the slump requirement from 25mm to 100mm. The addition of superplasticizer to CFRC mixes would have caused this satisfaction in slump. The result indicates that regardless of the fiber length used, the slump tends to decrease consistently with increasing fiber volume content from 0.1% to 0.3%.

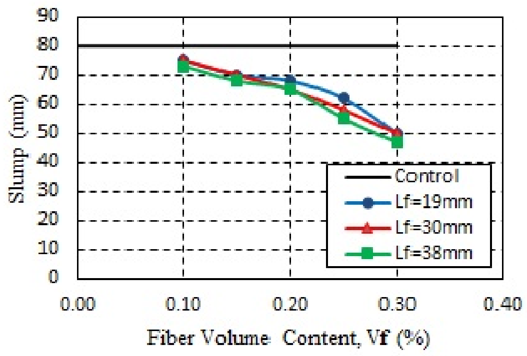

Fig. 4 Effect of Vf to slump of CFRC mix

Pull-out Strength of an Expansion Stud Anchor

Test data on pull-out strength of the expansion stud anchor considering the concrete breakout failure mode of different base material specimens are shown in Fig. 5. The control specimen's pull-out strength was measured 21.53 KN. This result is similar to 21.63 KN computed from Eq. (1). It is also close to 20.46 KN calculated from Eq. (3). Moreover, Fig. 5 shows that in 19mm fiber length case, pull-out strength tends to increase when fiber volume content increases. The pull-out strength measures 21.52 KN initially at 0.1% fiber volume content and increased to 24.33 KN at 0.30% fiber volume by 13.03%.

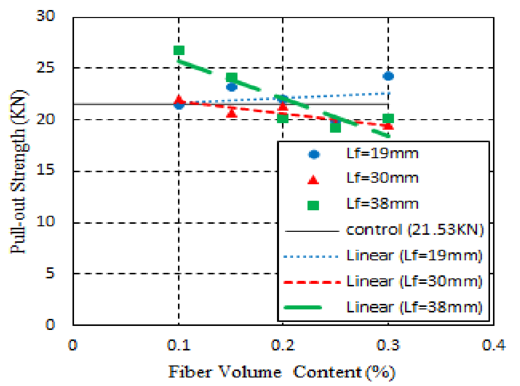

Fig. 5 Influence of fiber volume content to pull-out strength of CFRC

In the case of Lf = 30mm and Lf = 38mm, a negative trend between the pull-out strength and fiber volume content is noticed. Despite this, it is observed that there was a significant increased of pull-out strength with the addtion of Lf = 38mm at Vf = 0.10% and Vf = 0.15% by 24.61% and 11.83% respectively. At Lf = 30mm, however, no significant increased was observed. Among the cases, it has found out that the maximum pull-out strength occurred with the addition of Lf = 38mm at Vf = 0.1% by 24.61% increase compared to control specimen.

On the other hand, Fig. 6 and Fig. 7 consistently shows a positive linear trend with the addition of Lf = 19mm and Lf = 38mm. With 19mm, it is evident that pull-out strength is maximum at f_c = 19.84MPa and at f_t = 1.903MPa. This pull-out measures 24.33 KN and

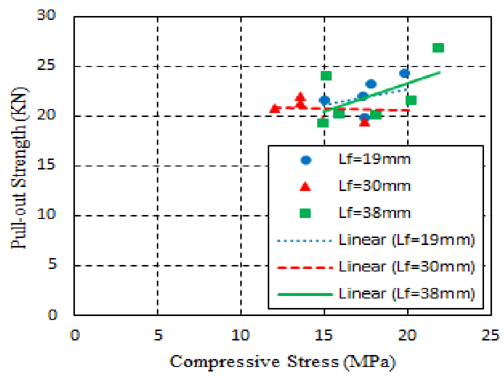

Fig. 6 Influence of compressive stress to pull-out strength of CFRC

is 13.03% more than the pull-out strength of the control specimen at f_c = 20.17MPa and at f_t = 1.683MPa. On the other hand, with 38mm, the pull-out strength is highest at f_c = 21.85 MPa and at f_t = 2.047MPa. This pull-out strength measures 26.82KN and is 24.61% more than the pull-out strength of the control specimen at f_c = 20.17MPa and at f_t = 1.683MPa. It is also evident that compressive stress of CFRC at 19mm and 38mm slightly affect the pull-out strength, but significantly affect by the tensile stress. While, no trend is observed to pull-out strength with the addition of Lf = 30mm both for compressive stress and tensile stress.

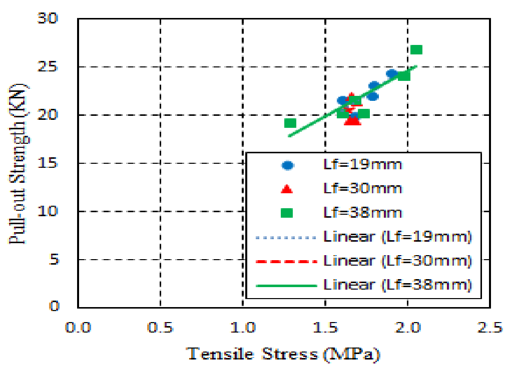

Fig. 7 Influence of tensile stress to pull-out strength of CFRC

FEM of CFRC Tensile Strength

The comparison between the observed tensile strengths and the FEM tensile strengths resulted from the simulation of the tensile strength response of the CFRC base material specimens subjected to tensile loading applied into a single expansion stud anchor using the ABAQUS is presented in Fig. 8. It can be observed that there is a good agreement between the observed tensile stress values and simulated tensile stress values subjected to a tensile loading applied into a single expansion stud anchor embedded in both control and CFRC specimens with R_{adj} of 0.818 and 0.999997 respectively. This result implies only that the tensile strength is the most important influencing factor to predict the pull-out strength of an expansion stud anchor embedded in CFRC. This is similar from finding of a previous study where the pullout load capacity of a headed anchor was dominated by the tensile strength of its composite base material [15].

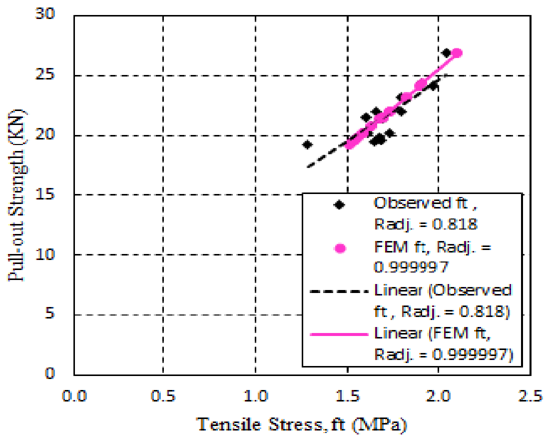

Fig. 8 Comparison of observed f_t and FEM f_t

RSM Model

Table 4 Performance of RSM models

Model	Deg	R_{adj}	MSE	Adequacy
$N=f(f_t)$	1	0.82	0.29	Yes
$N=f(f_c,f_t)$	1	0.81	0.28	Yes
$N=f(Lf,Vf,f_c)$	1	0.60	0.48	Yes
$N=f(Lf,Vf,f_t)$	1	0.85	0.21	Yes
$N=f(Lf,Vf,f_c,f_t)$	1	0.85	0.19	Yes
$N=f(Lf,Vf)$	2	0.76	0.26	Yes

Table 4 shows the performance of each adequate RSM model to predict the pull-out strength of an expansion stud anchor in CFRC as influence by combination of different predictor variables such as Lf, Vf, f_c, and f_t. Each combination was tested for the adequacy of the first-order and second-order RSM models using the R_{adj}, MSE, and F-test at $\alpha = 0.05$. It is noticeable that tensile strength is the most significant lone predictor with R_{adj} of 0.82 and MSE of 0.29. However, it is found out that the pull-out strength of an expansion stud anchor in CFRC is best predicted by RSM model with fiber length, fiber volume content, compressive strength, and tensile strength as its predictor variables which is given by

$$N = 0.038Lf - 8.785Vf + 0.146 f_c + 8.237 f_t + 5.7 \quad (10)$$

CONCLUSION

In general, it is concluded that CFRC increased the pull-out strength of the expansion stud anchor. Test results show that pull-out strength is highest at Vf = 0.10% and Lf = 38mm. Moreover, among the predictors considered, tensile strength turned out as the most significant variable to influence the pull-out strength of an expansion stud anchor in CFRC. This finding is further verified by numerical analysis using the FEM Software, ABAQUS. It is also concluded that pull-out strength of an expansion stud anchor in CFRC is best predicted by RSM model with fiber length, fiber volume content, compressive strength, and tensile strength as its predictor variables.

ACKNOWLEDGEMENTS

The carbon fiber used in this study was UT70-20 TORAYCA, and the expansion stud anchor used in this study was HST M10X90/10 from Hilti. The authors would like to thank DLSU, ERDT, Mapua Institute of Technology, and Alphatec Chemical Corp. for their valuable supports in this study.

REFERENCES

[1] Tezuka M, Awata, M and Shiraki A, “Carbon Fiber-Reinforced Concrete and Method for Preparing the Same”, United States Patent, Patent Number 5685902, 1997.
[2] Coventry K, Richardson A, McIntyre C and Aresh B, “Pullout Performance of Chemical Anchor Bolts in Fibre Concrete”, Fibre Concrete, Prague, 2011.
[3] AlTaan SA, Mohammed AA and Al-Jaffal AA, “Breakout Capacity of Headed Anchors in Steel Fibre Normal and High Strength Concrete”, Asian Journal of Applied Sciences, Vol. 5 (7), 2012, pp. 485-496.
[4] ACI Committee 544, “State-of-the-art Report on Fiber Reinforced Concrete”, 2000, ch. 4.
[5] ASTM C595, “Standard Specification for Blended Hydraulic Cements”, ASTM Standards in Building Codes, Vol. 1 (43), 2006.
[6] ASTM C143, “Standard Test Method for Slump of Hydraulic Cement Concrete”, ASTM Standards in Building Codes, Vol. 1 (43), 2006.
[7] ASTM C39-05, “Standard Test Method for Compressive Strength of Cylindrical Concrete Specimens”, ASTM Standards in Building Codes, Vol. 1 (43), 2006.

[8] ASTM E 488-96, "Standard Test Methods for Strength of Anchors in Concrete and Masonry Elements", ASTM Standards in Building Codes, Vol. 4 (43), 2006.
[9] ETAG 001, "Guideline for European Technical Approval of Metal Anchors for Use in Concrete", Annex C: Design Method for Anchorages, Brussels, Belgium, 1991, pp. 16-21.
[10] ACI Committee 355.2, "Evaluating the Performance of Post-Installed Mechanical Anchors in Concrete (ACI 355.2-00)", Reported by ACI Committee 355, 2000.
[11] NSCP 2010, "National Structural Code of the Philippines 6th Ed.", Anchorage to Concrete, Vol. 1, 2010, pp. 136-144.
[12] Kumavat HR and Patel VJ, "Factors Influencing the Strength Relationship of Concrete Cube and Standard Cylinder", International Journal of Innovative Technology and Exploring Engineering, Vol. 3 (8), 2014, pp. 76-79.
[13] Comite Euro-International du Beton (CEB), "Fastenings to Concrete and Masonry Structures: State of the Art Report", Thomas Telford Services Ltd, London, UK, 1994, pp. 93-94.
[14] Montgomery DC and Runger GC, "Applied Statistics and Probability for Engineers 5th ed. SI. Version", John Wiley and Sons, Inc.. Printed in Asia, 2011, pp. 619-636.
[15] Qian S and Li VC, "Headed Anchor/Engineered Cementitious Composites (ECC) Pullout Behavior", Journal of Advanced Concrete Technology, Vol. 9 (3), 2011, pp. 339-351.

Sixth International Conference on Geotechnique, Construction Materials and Environment, Bangkok, Thailand, Nov. 14-16, 2016, ISBN: 978-4-9905958-6-9 C3051

EVALUATION ON THE EFFECT OF BAMBOO STRIPS REINFORCEMENT TO THE MECHANICAL AND PHYSICAL PROPERTIES OF RICE HULL PARTICLE BOARD

Hermie M. del Pilar[1], Jecelle Elyssa E. Calip [1], Aldwin Christopher A. Loyola[1] and Neil Patrick C. Nase[1]
[1]Department of Civil Engineering, Malayan Colleges Laguna,
Pulo Diezmo Road Cabuyao City, Philippines

ABSTRACT

Adhering on use of sustainable materials and waste management, this study, focused on the effect of bamboo strips reinforcement for rice hull particle board. The evaluation was based on the resulting physical and mechanical properties of the products. Both reinforced and unreinforced boards were made using 70:30, treated polystyrene: rice hull weight ratio with 5mm thickness. The reinforced boards were prepared with variation in orientation at 0^O, 45^O, 90^O weaved bamboo strips. The boards were tested using Water Absorption (WA) and Thickness Swelling (TS) for the physical property, while Modulus of Rupture (MOR), Internal Bonding Strength (IBS) and Impact Resistance (IR) were tested for the Mechanical Property. Each test subjected 12 specimens consisting 3 for each of the 3 orientations of the reinforced boards, while the other 3 was for the unreinforced. Results indicated that the 45^O orientation gave the highest MOR performance at 40.22MPa significantly high, while the 90^O demonstrates highest in IR test at 6.6 N-m, not significantly different with the other boards. The unreinforced board yields 17.35 MPa for MOR but highest in the IBS test at 2.475 MPa, significantly higher with other samples, and an IR of 5.30 N-m. In the WA and TS tests, the unreinforced board yield highest at 8.04% and 1.87% respectively, both not significantly different from the rest. With these results, it was evaluated that reinforcing the particle board with bamboo strips greatly enhances the mechanical and physical properties of the average rice hull particle board.

Keywords: Rice Hull Particle Board, Bamboo Strips Reinforcement, Treated Polystyrene, Mechanical Property, Physical Property

INTRODUCTION

Globally, human population increases and so is the demand for construction materials. There is a need to the sustainability of construction materials that finding alternatives is a must.

Bamboo has proven its worth in construction due to its inherent strength and durability [1]. Tropical countries have adequate supply of bamboo [2] and because it is renewable and can be easily harvested, it is considered as a sustainable construction material. Other characteristics such as being light, flexible, and biodegradable add to bamboo's advantage. It can also be used as a reinforcement material when extracted to appropriate fiber forms for a desired purpose [3]. Bamboo can be a substitute for wood as construction material because their characteristics are comparable if not greater in some respect than wood [2]. This material has double tensile strength than lumber while the compressive strength is estimated to be 1.5 times greater [4]. Also, bamboo has a long line of household products in which bamboo mat is one of them. The bamboo mat can also be used as surface reinforcement for composite boards [5].

Another material being considered as a sustainable substitute for wood and wood-based board products is the rice husk. Rice husk is abundant in tropical countries such as the Philippines [6]. The abundance of rice husk, its low bulk density (90-150kg/m^3), toughness, abrasive property ,resistance to weathering and unique composition are the characteristics why it can be important to the construction industry (Johnson & Bin Yinus, 2009).

In the study of Lagrimas et. al. (2014), the polystyrene to rice hull mix ratio of 70:30 gave the most ideal properties in terms of Modulus of Rapture (MOR), Modulus Of Elasticity (MOE), Water Absorption (WA) and Thickness Swelling (TS) compared to other mix ratios such as 80:20 and 60:40 [7]. However, particleboards made of rice hull demonstrate low mechanical property like the MOR as compared to other particleboards. The common MOR value for a particle board records an average of 16.6 MPa, while only 14.53 MPa for a rice hull particle board [5].

This study aims to evaluate the effect of bamboo reinforcement to the mechanical properties and physical properties of rice hull particleboard using the bamboo strips.

The properties of rice hull particle board reinforced with bamboo strips arranged with different orientations were evaluated. The mechanical properties: modulus of rupture (MOR); internal bond strength (IB); impact strength (IS) and physical properties: density; water absorption (WA) and thickness swelling (TS) were measured. The properties of the reinforced particle board were compared to the unreinforced rice hull particle board. Evaluation of results was done through Analysis of Variance (95% confidence level). The inferential statistic was used to identify if there is a significant difference on the properties of the reinforced and unreinforced rice hull particle boards. This study also helps in identifying the ideal orientation of the bamboo reinforcement for rice hull particleboards.

METHODOLOGY

The proceeding sections discuss how the materials were sourced and prepared, how the particle boards were produced and the manner on how the board specimens were tested.

Materials

The required materials to produce the particle boards are described and prepared as follows.

Rice Hull

Rice hull was collected from Queen Elizabeth Rice Mill Honorville, Macabling Sta Rosa City Laguna with moisture content ranging between 2 to 5 percent. Rice hull were sieved using the sieve number 12 and pan. Only the retained rice hull on the sieve number 12, with a diameter of 1.68 mm, was used.

Binder

Polystyrene wastes were gathered from Armstrong Trading Malitlit Road Bgy. Malitlit, Sta. Rosa Laguna and dissolved in a petroleum naphtha with a weight ratio of 1:2 respectively. The weight ratio was determined through several trials in which the treated polystyrene was liquefied until it reached its optimum paste – like state. Pure polystyrene waste can be melted directly to bind the board particles, but this will not produce good binding effect.

Reinforcements

Bamboo of the type *kawayang tinik* (*Bambusa blumeana*) were purchased from the local bamboo dealer of Bgy. Dita, National Highway Sta. Rosa City. The inner part of the bamboo is processed into thin strips with dimensions of 200 mm x 4 mm x 1 mm. Bamboo strips were weaved into mats with three different orientations namely 0^o, 45^o, and 90^o and these were equally spaced at 12.50 mm. The arranged bamboo strips are then brushed with wood glue to maintain its position and orientation.

(a) 0° (b) 45° (c) 90°

Fig. 1 Different Orientations of Bamboo Strips

Production of Rice Hull Particle Board

Rice hull particle boards were prepared with the use of two roll mill and a hydraulic press found at the Industrial Technology Institute (ITDI) of the Department of Science and Technology (DOST), located at Bicutan, Taguig City, Philippines. The two roll mill was set to a temperature of 130^{o}C and used in mixing the binder and rice hull. The ratio of the mixture was 70:30 binder: rice hull weight ratio. The binder-rice hull mixture was poured constantly in the rotating two roll mill to spread and mixed evenly, and this should be repeated until there is a visual homogenous mixture. The cake like mixture were then placed in a 200 mm x 200 mm x 5 mm to produce the unreinforced particle board by compressing and 200 mm x 200 mm x 2 mm for the production of the reinforced particle board. The molders with mixture will be subject to the hydraulic press with a temperature of 180^{o}C for about 5 minutes and then subjected for another 5 minute cold press.

Three types of reinforced particle boards were made and each contained different orientation of the bamboo strips namely 0^O, 45^O and 90^O. Bamboo strip reinforcement were sandwiched between the two 200 mm x 200 mm x 2 mm size particle board. The composite boards were placed in a 200 mm x 200 mm x 5 mm molder and then it was inserted in the hydraulic press again with the same temperature. Heat press was applied for about 10 minutes and another10 minutes for the cold press.

A total of 8 boards were prepared, 2 for the unreinforced and 6 for the reinforced. There were 3 types of reinforced boards, and each type requires 2 boards, totaling to 6 reinforced boards.

Test Procedures

In each type of board: unreinforced, 0^{O} reinforced, 45^{O} reinforced and 90^{O} reinforced, the following quantity and dimension of test specimens were drawn from 2 boards (total of 8), as shown by the table below.

Table 1: Quantity and Dimension of Test Specimens for each type of board

Type of Test	Dimension (mm)	Quantity
MOR	200mm x 50mm	3
IBS	50mm x 50mm	3
IR	50mm x 10mm	3
WA & TS	50mm x 50mm	3

Modulus of Rupture (MOR)

The three point flexural test was performed based on ASTM D1037-12 to measure the modulus of rupture of the rice hull particleboard. The Shimadzu Universal Testing Machine was used where the test samples were placed longitudinally on two tension rods with measured distances. The third tension rod was lowered slowly and driven to the mid of specimen.

The specimens were subjected to a three point strain and break when the maximum load was attained. Modulus of rupture can be determined using the formula:

$$\text{MOR} = \frac{3\text{PL}}{2\text{bd}^2} \qquad (1)$$

where P is the maximum applied load, L is length of the support, b is the base and d is the depth of the test specimen tested.

Internal Bond Strength (IBS)

In accordance to ASTM D1037, Standard Test Method for Evaluating Properties of Wood-Base Fiber and Particle Panel Materials, test specimens must have a 50 mm by 50 mm base with a height of 5 mm. The test specimens were fastened to the grip fixtures of the machine which induces load to test subject's surface until it reaches failure. Internal bonding strength can be described by the formula:

$$\text{IBS} = \frac{\text{F}}{\text{A}} \qquad (2)$$

where F is the maximum load at failure and A is the cross sectional area of the test specimen.

(A) (B)

Fig.2: (A) MOR test set-up; (B) IBS test set-up

Impact Resistance (IR)

Following ASTM E23, a board size of 10 mm × 50 mm was used as specimen for the Charpy impact test. The sample was set horizontally from the base knocked by a hammer in a swinging pendulum manner. With this test, the impact resistance or the energy absorbed per unit thickness was determined.

Fig. 3: Impact resistance test using the Humburg Pendulum Impact Test

Water Absorption

Based on ASTM D1037-99, the test specimens with dimensions 50 mm x 50 mm were initially weighed. Specimens were then submerged in distilled water for the next 24 hours then removed and re-weighed. Percent water absorption was determined using the formula.

$$\%\ \text{Water absorption} = \frac{\text{Wet Mass} - \text{Dry Mass}}{\text{Dry Mass}} \text{x } 100\% \quad (3)$$

Thickness Swelling

In reference to ASTM D1037-99, the 50 mm x 50 mm specimens used for WA test can also be used to measure the thickness swelling. The initial and final thicknesses were measured to determine the change in thickness. The formula for thickness growth (Gt) is given by:

$$\text{Gt} = \frac{\text{Final Thickness} - \text{Initial Thickness}}{\text{Initial Thickness}} \text{x } 100\% \quad (4)$$

Statistical Tool

The result for each test were statistically analyzed using the Analysis of Variance (ANOVA) with 95% confidence level. The tests for the significant difference between the means of the properties of reinforced particle boards of different orientations (0^O, 45^O and 90^O) were evaluated. Also, t – test analysis was used to determine if there is a significant difference between the mean of unreinforced against mean of the least performing reinforced particle board.

RESULTS AND DISCUSSION

The mean of the physical and mechanical properties of the particle boards are shown in Table 2 below.

Table 2: Mean of Mechanical and Physical Properties of Particle Board

TYPE		ρ kg/m^3	Mechanical Properties			Physical Properties	
			MOR MPa	IBS MPa	IR Nm	WA (%)	TS (%)
Unreinforced		0.925	17.35 (2.44)	2.48 (0.20)	5.30 (0.10)	8.04 (4.53)	1.87 (1.01)
Reinforced	0°	1120	34.60 (1.17)	2.07 (0.22)	5.77 (0.38)	3.94 (4.33)	1.50 (0.02)
Reinforced	45°	1130	40.22 (1.17)	1.59 (0.23)	6.08 (0.38)	2.50 (3.22)	0.74 (0.97)
Reinforced	90°	1120	38.85 (2.10)	1.91 (0.02)	6.60 (0.17)	2.21 (0.99)	0.00 (0.00)

Numbers in parenthesis are the standard deviation

Table 2 shows that the internal bond strength (IBS) of the unreinforced particle board (URPB) has the highest bonding strength when compared to the reinforced particle boards (RPBs). This indicates that the particles' bonding is affected by the reinforcement. This could be explained by the fact that the bamboo strips reinforcement has decreased the contact area of the particles, where the two (2mm) particle boards sandwiched the reinforcement. The MOR and IR however, are much greater for the reinforced than the unreinforced. The results of 45° and 90° orientation of the RPB governed in the MOR and IR respectively. This result also shows that the MOR and IR were affected by the density, the orientation of the reinforcement, and the quantity of bamboo reinforcement.

Figure 4 shows the effect of bamboo strips reinforcement on the MOR of the rice hull particle board.

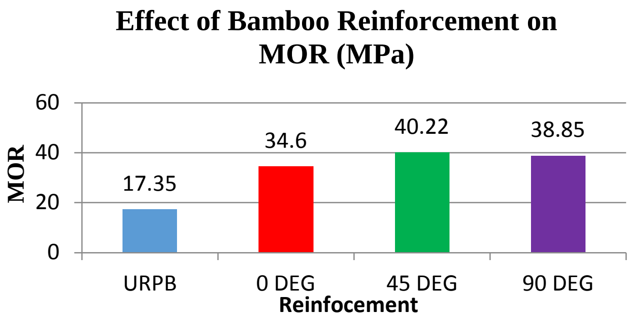

Fig.4: Effect of bamboo strips reinforcement

The physical properties, (WA & TS) of 90^O reinforcement in Table 2 show best results compared to other type of boards, though all exhibit low percentage of absorption and swelling. The least performing in terms of physical properties is the unreinforced board. It is also clear that the water absorption and thickness swelling are correlated as shown in Fig. 5.

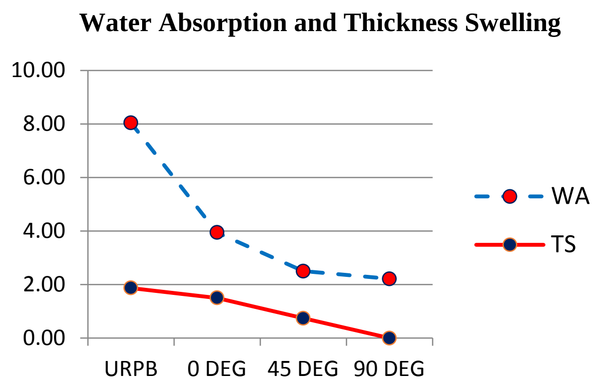

Fig. 5: Water absorption and thickness swelling relation

The table below, Table 3 summarizes the results in determining if there is a significant difference on the properties of the following types of boards using the One Way Analysis of Variance for the 3 reinforced boards, while the statistical t- test was used to compare the least means of reinforced boards against the means of the unreinforced boards.

Table 3: Test for the difference in properties of the particle boards

Comparison between	Mechanical Properties			Physical Properties	
	MOR (MPa)	**IBS (MPa)**	**IR (N-m)**	**WA (%)**	**TS (%)**
3 Types of reinforced Rice Hull Particle Board	**S**	**S**	**NS**	**NS**	**S**
Unreinforced and Reinforced	**S**	**S**	**NS**	**NS**	**NS**

S: Significant; NS: Not Significant

The result shows that the Modulus of Rupture, Internal Bond Strength and Thickness Swelling were significantly different among the 3 types of reinforcements of rice hull particle boards. The impact resistance and water absorption however gives no significant difference on the results of their mean.

In comparing means of the least value of reinforced particle boards against the means of the unreinforced board, the properties which show significant difference are the Modulus of Rupture and the Internal Bond Strength. All other properties show no significant difference.

CONCLUSION

Based on the results on mechanical and physical properties of the reinforced rice hull particle board, the following conclusions were drawn.

1. The 45^{o} orientation is the ideal reinforcement to resist flexural stresses followed by the 90^{O} then 0^{O} and lest for the URPB. The results showed that the difference in means is significant for the different types of reinforcement. Since the least mean for the RPB which is 0^{O} is significantly higher than the mean of the URPB, it can be concluded that the use of bamboo strips reinforcement for the rice hull particle board will really matter to increase the flexural strength of the particle board.

2. The Internal Bond Strength of the reinforced particle boards were significantly different having the 0^{O} as the highest while the 45^{O} is the lowest. Comparing the IBS mean of the RPB with URPB, the latter is significantly higher than the mean of the reinforced boards. This shows that if the quantity of bamboo strips becomes greater, the result for IBS is lower. Therefore the bamboo strips reinforcement does not work for the internal bond strength.

3. The Impact Resistance mean of the reinforced boards are higher than that of the URPB, though there is no significant difference on the types of reinforcement of the rice hull particle boards, as well as the URPB. This shows that the use of bamboo strips reinforcement does not significantly affect the impact resistance of the particle boards, though it may increase the IR value.

4. The use of bamboo strips reinforcement does not affect significantly the water absorption and the thickness swelling, though the reinforcement can increase the water proofing property of the boards. Also, result shows that a 90^{O} orientation for reinforcement is ideal since it has the least WA and TS.

ACKNOWLEDGEMENTS

The authors would like to thank the Industrial Technology Development Institute (ITDI) of the Department of Science and Technology (DOST) in Taguig City and the Malayan Colleges Laguna (MCL) in Cabuyao Laguna, Philippines for allowing the use of their equipment for the testing in research study.

REFERENCES

[1] Syeda, A., & Shrujal, B. (2014). A Case Study on Bamboo as Green Building. *International Journal of Engineering and Advanced Technology*, 78-82.

[2] Bystriakova, N., & Kapos, V. (2006). Bamboo diversity: the need for a Red List review. *Tropical Conservancy* , 12-16.

[3] Van der Lugt, P., van den Dobbelsteen, A. A., & and Janssen, J. J. (2006). An environmental, economic, and practical assessment of bamboo as a building material for supporting structures. *Construction Building Materials* .

[4] Rassiah, K., Ahmad, M., & & Ali, A. (2014). Mechanical Properties of Laminated Bamboo Strips from Gigantochloa Scortechinii/Polyester Composites. *Elseiver Materiald and Design* , 1.

[5] Pandey, C. N., & Sujhata, D. (2011). Crop Residues, the Alternate Raw Materials of Tomorrow for the Preparation of Composite Board. *Indian Plywood Industries Research and Training Institute.*

[6] Coxworth, B. (2015, July 10). *Rice Husk may Find Use in Cheaper, Greener, and Longer-lasting Particleboard:*. http://www.gizmag.com/rice-husk-particleboard/37730/

[7] Lagrimas, J. L., Mailom, M. C., & Matampale, K. A. (2013). Development of Fiberboard with Rice Hull as Base Material on Polystyrene as Resin Binder. 20-28.

STRENGTHENING EFFECT OF A CFRP ROD HAVING RIBS FOR A CANTILEVERED SLAB

Yusuke Kuroda[1], Hiroaki Hasegawa[2], Nobuhiro Hisabe[2] and Isamu Yoshitake[1]
[1]Department of Civil and Environmental Engineering, Yamaguchi University, Japan;
[2] Mitsubishi Plastics Infratec Co., Ltd., Japan

ABSTRACT

The near surface mounted (NSM) method using carbon fiber reinforced polymer (CFRP) rod has been used to strengthen bridge slabs. Bond between concrete and CFRP rod is a concern for strengthening concrete members although the CFRP has superior structural performance. CFRP rods are manufactured by tensioning carbon fibers, and coated with resin. Therefore the CFRP rod has relatively smooth surface and it has little mechanical shear resistance. This study focuses on CFRP rods applied to cantilevered bridge deck slabs. The study examines strengthening effect on reinforced concrete (RC) beams embedding various CFRP rods. To improve the bond performance, CFRP rods coated with an epoxy adhesive incorporating silica sand (sand-coating), and CFRP rods having artificial ribs made with glass fiber reinforced polymers (GFRP) sleeves were used in the experimental investigation. Monotonic and cyclic loading tests were conducted to confirm the flexural behavior of the beam strengthened with the NSM CFRP rods. In addition, finite element (FE) simulation was performed to quantify the bond effect of these CFRP rods.

Keywords: CFRP rod, Cantilevered Slab, Near Surface Mounted (NSM) Method, Bond, Fatigue

INTRODUCTION

Cantilevered reinforced concrete (RC) slabs of highway bridges have been damaged by increase wind and traffic loads in recent year. Development of strengthening method for the upper surface of cantilever slabs has been required. This paper presents the near surface mounted (NSM) method using carbon fiber reinforce polymer (CFRP) rod. The CFRP rod has some advantages such as superior fatigue durability and high chemical resistance. Strengthening method for cantilever slab has been studied previous researches [1]-[7]. The NSM method has already been employed in the world. CFRP materials are categorized to two types which are high-modulus and high-strength. The CFRP rod used in the study is high-modulus type because it has significantly higher Young’s modulus than the modulus of rebar and can decrease stress of reinforcing materials. The most concern of the CFRP rods is low bond characteristic because the rod has no mechanical shear connectors like rebars. Note is that the bond strength of CFRP rod is almost 40 % of the strength of deformed bars. The purpose of this study is to examine the strengthening effect for RC members embedding CFRP rods. In particular, the study focuses on applicability of high modulus CFRP rods for cantilevered slabs subjected to negative bending moment. To improve bond properties, the experimental investigation prepared two kind of CFRP rods; a rod coated with an epoxy adhesive incorporating silica sand (sand-coating); CFRP rods having artificial ribs made with glass fiber reinforced polymers (GFRP) sleeves. Monotonic and cyclic loading tests were conducted to examine the flexural behavior of cantilevered RC beam specimens strengthened with the NSM CFRP rods. In addition, finite element (FE) simulation was performed to quantify the bond effect of the CFRP rods. This paper reports the experimental and numerical investigations.

EXPERIMENTAL PROCEDURE

Materials

Table 1 gives compressive strength and Young’s modulus of concrete and high strength expansive mortar at age of 28 days. Rebars having a nominal diameter of 10 mm and high modulus CFRP rods of moderate tensile strength were used. Young's modulus of HM12 is twice than rebar. The reinforcing material contributes to reduce the stress of rebars. Yield strength of the rebar is 345 MPa. Physical properties of the rebar and the CFRP rod are given in Table 2.

Table 1 Properties of concrete and mortar

	Concrete	Mortar
Compressive strength (MPa)	23.8	43.4
Young’s modulus (GPa)	28.6	26.5

Table 2 Properties of CFRP rod and rebar

	CFRP rod	Rebar
Yielding strength (MPa)	N/A	295
Tensile strength (MPa)	1550	374
Young's modulus (GPa)	418	206

Test specimens

Figure 1 shows a schematic of test specimen. Five slab specimens were prepared to simulate cantilevered bridge deck slabs. The dimensions of slab specimen were 200 mm deep x 250 mm wide x 1,850 mm long as shown in Fig. 1.

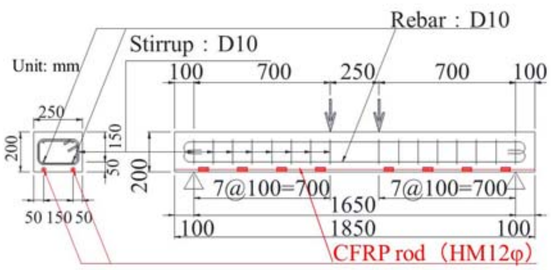

Fig. 1 Detail of test specimen

Rebar and CFRP rods were placed at 150 mm and 187 mm deep, respectively. All test specimens were cured for 2 weeks using wet curing sheets. After that, the surface layer of concrete was removed by using a water-jet (water pressure: 220 MPa, water volume: 15 L/min). CFRP rods were placed on concrete which removed the surface layer. The concrete surface was refilled with high strength mortar. Schematics of CFRP rods used in the test are shown in Fig. 2.

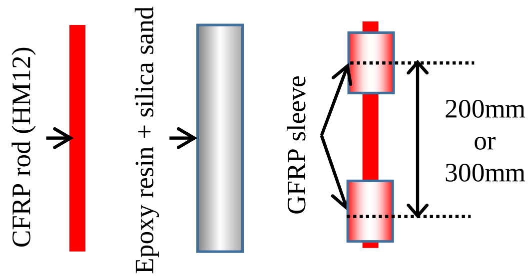

Fig. 2 CFRP rods used in this test

Primary test parameters are reinforcing materials such as CFRP rods (Type N), CFRP rods coated with an epoxy adhesive incorporating silica sand (sand-coating: Type A), and CFRP rods having artificial ribs made with GFRP sleeves (Type B). Two specimens of HM12-GS-300 were prepared and were used for monotonic and cyclic loading tests, respectively. The test specimens are summarized in Table 3.

Table 3 Test specimens

Specimen I.D.	CFRP rod	Test
Control	N/A	M
HM12	Type N	M
HM12-EC	Type A	M
HM12-GS-300	Type B (interval of 300 mm)	M, C
HM12-GS-200	Type B (interval of 200 mm)	M

M: monotonic loading test; C: cyclic loading test

Flexural loading test

Four-points loading test was conducted as shown in Fig.3. Span length and loading span were 1650 mm and 250 mm, respectively. The load of 1.0 mm/min was applied to the slab specimen in the monotonic test.

To examine fatigue durability, cyclic loading test was also conducted by using the slab specimen of HM12-GS-300. The maximum load in the fatigue test was 60 % of the load-carrying capacity, and the cyclic load was applied with 1 Hz up to the 2 million cycles.

Fig. 3 Flexural loading test

RESULTS AND DISCUSSION

Monotonic loading test

Table 4 gives cracking load (*Pcr*), the maximum load (*Pmax*) and failure mode of each specimen. The maximum load of the specimen HM was 1.8 times higher than the *Pmax* of the control specimen. In addition, the maximum loads of HM12-EC, HM12-GS-300, HM12-GS-200 were 2.7, 2.3, 2.8 times higher than the *Pmax* of the control specimen, respectively. The observation confirms that flexural strength of the strengthened beams is higher than the strength of control specimen, high strengthening effect of CFRP rods was confirmed in this test.

Test specimens strengthened with CFRP rods were collapsed due to shear failure while the control specimen indicated flexural failure. It is noteworthy that the NSM of CFRP rods is sufficient for strengthening of flexural member. It should be noted that the NSM strengthening may induce shear fracture of CFRP rod rather than the flexural failure.

Figure 4 shows a typical shear failure. The failure mode of test specimen having GFRP sleeves (HM12-GS-300 and HM12-GS-200) were almost similar, the shear crack generated from edge of GFRP sleeves. In addition, interfacial failure of concrete-mortar layer was observed in the test of strengthened specimens. Figure 5 illustrates a typical failure of CFRP rod. The failure was observed at the edge of GFRP sleeve. The observation confirms that the CFRP rod has relatively low resistance to shear while it has excellent tensile strength.

Fig. 4 Shear failure of test specimen

Fig. 5 Failure of CFRP rod

Table 4 Load bearing capacity

No.	Specimen I.D.	*Pcr* (kN)	*Pmax* (kN)	Failure mode
1	Control	8.7	38.0	Flexural
2	HM12	14.2	68.6	F+S
3	HM12-EC	14.3	101.4	Shear
4	HM12-GS-300	14.8	87.0	Shear
5	HM12-GS-200	13.5	105.6	Shear

Table 5 Maximum deflection and strain of CFRP rod

No.	Specimen I.D.	Deflection (mm)	Strain of CFRP rod
1	Control	31.5	N/A
2	HM12	4.16	1165×10^{-6}
3	HM12-EC	5.36	1516×10^{-6}
4	HM12-GS-300	4.72	1554×10^{-6}
5	HM12-GS-200	6.59	1750×10^{-6}

The maximum deflection and strain of CFRP rod are summarized in Table 5. Also, Figure 6 shows load-deflection responses. The result indicates that the maximum deflections of strengthened specimens were significantly lower than the deflection of control specimen. The observation confirms that the NSM of CFRP rods increases ductility of the flexural member. The deflection of strengthened specimens embedding bond-improved CFRP rods was higher than the deflection of HM12. The result confirms that CFRP rods bonded firmly to concrete up to the shear failure.

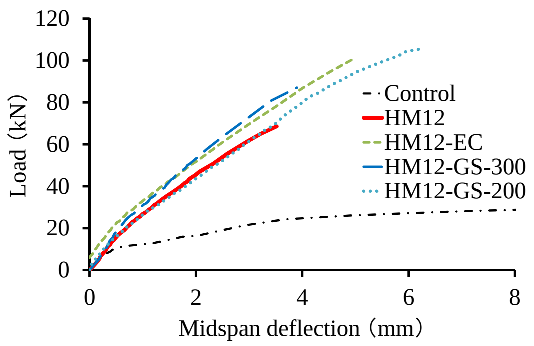

Fig.6 Load-deflection responses

Figure 7 shows load-midspan strain of CFRP rod. Strains of CFRP rods having artificial ribs were higher than the strain of HM12. The result also confirms the improvement of bond performance of CFRP rod having artificial ribs.

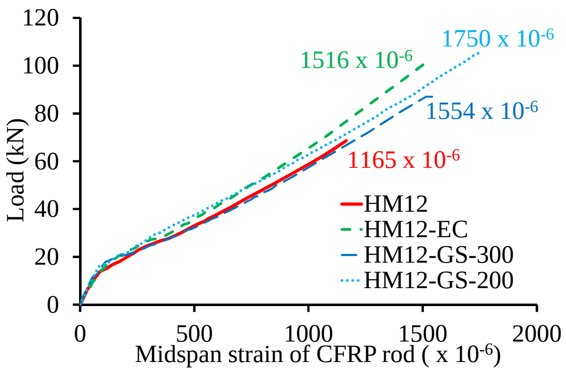

Fig. 7 Load-strain of CFRP rods

Cyclic loading test

A cyclic loading test using HM12-GS-300 was carried out to examine fatigue durability of slab specimen strengthened with bond-improved CFRP rods. Four-points loading system was used as well as the monotonic loading test. The maximum load was designed as 60% of the load-bearing capacity of HM12-GS-300. Herein, the minimum load was 10% of the static strength. At the number of 1, 10, 100, 1000, 10000, and 100000 cycle loadings, the maximum load was provided statically (3 kN/min.) to the slab specimen.

Flexural cracks were firstly initiated near the midspan. The additional bending and shear cracks were observed during the repeated loadings. The shear crack was caused from edge of the GFRP sleeves. It should be noted that the debonding between concrete and mortar layer was not observed in the cyclic loading test. The typical fatigue cracks are presented in Fig. 8.

Fig. 8 Typical fatigue cracks

The repeated loading achieved 2 million cycles. Figure 9 shows the load-midspan deflection response. The deflection increased in accordance with loading cycles.

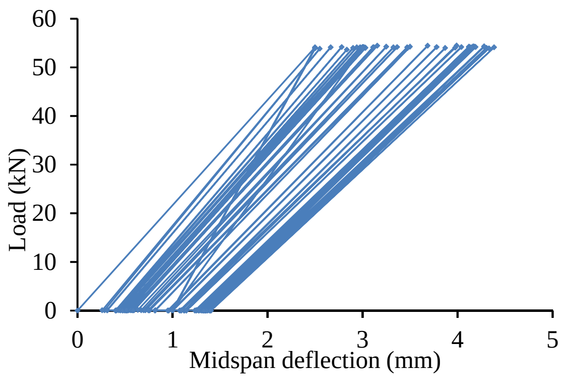

Fig.9 Load-midspan deflection response

Figure 10 shows a transition of flexural rigidity defined as load/deflection. Note is that the flexural rigidity was remarkably decreased by 600,000 loadings and it was stable after the loading cycles of 600,000.

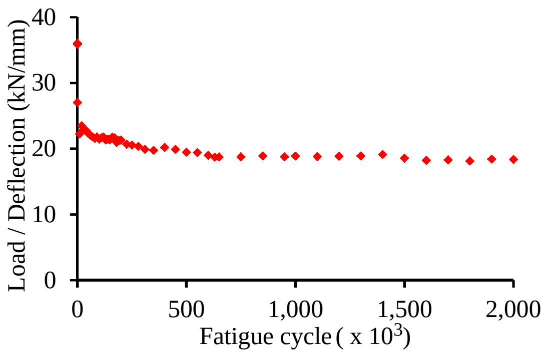

Fig. 10 Transition of flexural rigidity

To examine residual strength of the slab specimen subjected to the cyclic load, a monotonic loading test was conducted after 2 million repeated loadings. The slab was also collapsed by shear failure initiated from the fracture of CFRP rods. The residual loading test indicated the load-bearing capacity strength of 110.4 kN. It is of interest that the residual strength was higher than the static strength (87.0 kN) of the slab.

Figure 11 shows the crack patterns observed in the monotonic loading test and residual loading test. Compared to the monotonic loading test, cracks in the cyclic loading test were distributed uniformly. The crack distribution possibly contributed to deformation of the beam and reduced the stress concentration of the CFRP rod.

Figure 12 shows load-deflection responses of HM12-GS-300. The comparative result confirms that the reduction of flexural rigidity was negligible because the slope of regression line in the residual test is almost equal to the slope in the static test.

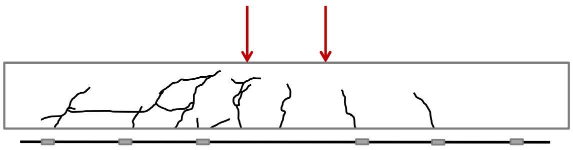

a) Cracks in the monotonic loading test

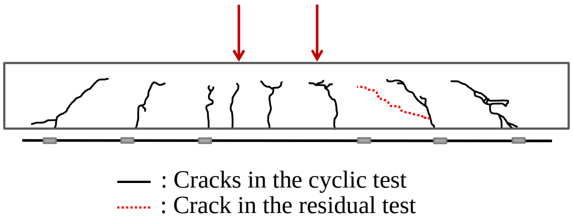

b) Cracks in the residual loading test

Fig. 11 Crack pattern in the residual loading test

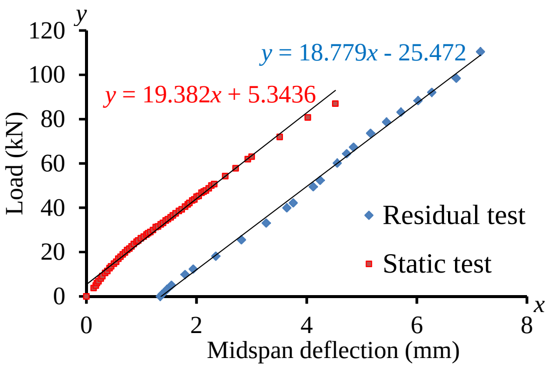

Fig. 12 Load-deflection responses

FE simulation

To examine the bond effect of CFRP rod with GFRP sleeves, finite element (FE) simulation was performed. A beam model embedding CFRP rods with GFRP sleeves (Fig.13) is used in the numerical investigation. The FE simulation uses different bond conditions for the GFRP sleeves (Types I and II). Type I is a full-bond model which the CFRP rod and GFRP sleeves interface is glued firmly to the mortar. On the other hand, Type II is a model that includes unbonded interface except for the blue surface (bond). These models were used to compare the effect of mechanical shear resistance of the GFRP sleeves without chemical bond and/or friction. An FE model of CFRP rods without GFRP sleeves was also used this analysis as control to confirm the effect of sleeves. Bond condition of control was supposed Type I. Young's moduli and Poisson's ratio employed in the FE simulation are given in Table 6.

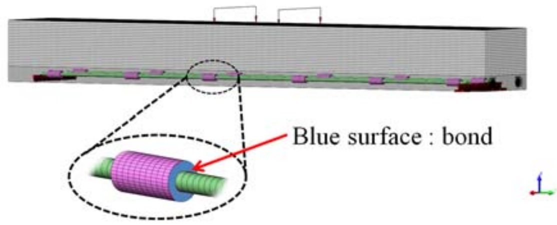

Fig. 13 Analysis model of FE simulation

Table 6 Material properties for FE simulation

	Young's modulus (GPa)	Poisson's ratio
Concrete	28.0	0.20
Mortar	29.5	0.20
HM-CFRP rod	500	0.30
Rebar	200	0.30
GFRP	30.0	0.28

Table 7 Maximum strains (in FE analysis)

	HM12-GS-200	HM12-GS-300
Type I	44.0×10^{-6}	43.9×10^{-6}
Type II	41.3×10^{-6}	39.9×10^{-6}

Table 7 summarizes the maximum strains obtained from the FE analysis. In addition, Figure 14 shows strain distributions of CFRP rod having GFRP sleeves, control (without GFRP sleeves). The applied load in the analysis is 10 kN in order to simulate behavior of uncracked bridge deck slab. The result reveals that the maximum strains obtained by FE analysis are almost equal despite the different bond conditions. In addition, strain observed in the monotonic test (51.2×10^{-6} at 10.3 kN) was compared to the theoretical strain in FE analysis. The comparison implies that the linear FE modeling is appropriate to simulate the strain distribution. This simulation result confirms the bond effect of the mechanical shear connector of the GFRP sleeves (Type II) while strain distribution under unbond condition is different compared to the full-bond condition (Type I) and control.

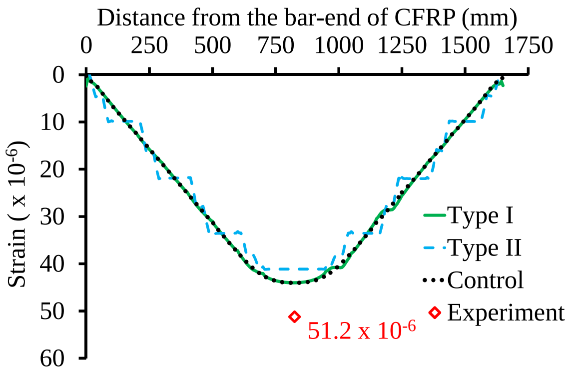

Fig. 14 Strain distribution of CFRP rod

CONCLUSIONS

This paper presents near surface mounted (NSM) technique using carbon fiber reinforce polymer (CFRP) rods for cantilevered RC slabs. Monotonic loading test and cyclic loading test were conducted by using slab specimens strengthened with the CFRP rods. FE analysis was performed to confirm bond performance of CFRP rods having GFRP sleeves. The conclusions of this study are as follows:

(1) The load-bearing capacity of the slab specimen strengthened with CFRP rods was higher than at least 1.8 times to the capacity of the control specimen. Improvement of bond performance of CFRP rods having artificial ribs was confirmed. Shear failures were observed in the test of specimens strengthened CFRP rods.

(2) The fatigue test of slab specimen strengthened with Type B CFRP rod (HM12-GS-300) was achieved 2 million, and high fatigue durability was indicated. Residual test showed the maximum strength of specimen strengthened with HM12-GS-300 (110.4kN) was higher than the static load-bearing capacity of the slab specimen under same condition.

(3) The maximum strains of CFRP rod in the FE simulation were almost equal despite different bond condition of the rod. The simulation confirmed the effectiveness of the mechanical shear connector of the GFRP sleeves (Type II).

Acknowledgements

The authors thank to Mr. Sakaki, a graduate student of Yamaguchi University, for his support in the numerical simulation.

References

[1] Firas A., Arnaud C., Raoul F. and Christian T., “Strengthening of RC members with near-surface mounted CFRP rods”, Composite Structure, Vol.91, 2009, pp.138-147.

[2] Lam L. and Teng J.G., “Strength of RC cantilever slabs bonded with GFRP strips”, Journal of Composites for Construction, Vol.5, No.4, Nov. 2001, pp.221-227.

[3] Moataz B. and Khaled S., “Flexural strengthening of RC beams with prestressed NSM CFRP rods - Experimental and analytical investigation”, Construction and Building Materials, Vol.23, 2009, pp.3292-3300.

[4] Oudah F. and El-Hacha R., “Fatigue behavior of RC beams strengthened with prestressed NSM CFRP rods”, Composite Structures, Vol.94, 2012, pp.1333-1342.

[5] Teng J.G., Cao S.Y. and Lam L., “Behaviour of GFRP-strengthened RC cantilever slabs”, Construction and Building Materials, Vol.15, No.7, 2001, pp.339-349.

[6] Yoshitake I., Kim Y.J., Yumikura K. and Hamada S., “Moving-wheel fatigue for bridge decks strengthened with CFRP strips subject to negative bending”, Journal of Composites for Construction, Vol.14, No.6, 2010, pp.784-790.

[7] Yoshitake I., Kim Y.J., Yumikura K. and Mimura Y., “Composite strips with various anchor systems for retrofitting concrete beams”, International Journal of Concrete Structures and Materials, Vol.5, No.1, June 2011, pp.43-48.

CONSTITUTIVE MODELING OF COAL ASH USING MODIFIED CAM CLAY MODEL

Erica Elice Saloma Uy[1] and Jonathan Rivera Dungca[1]
[1]Civil Engineering, De La Salle University, Philippines

ABSTRACT

Coal ash is a by-product from coal-fired power plants that generates electricity. These waste materials most of the time is kept in storage facilities. Due to the growing demand in electricity generation, storage facilities can no longer accommodate the waste materials. Instead of disposing the waste materials, it can be used as a construction material. A promising civil engineering structure that can use coal ash as a construction material is land reclamation. The structure needs huge volume of materials and this can maximize the usage of coal ash. In the Philippines, most land reclamation projects are conducted at the sea. From this, distilled water was replaced with sea water to have a better evaluation of the strength properties of coal ash. Consolidated drained test was performed having three conditions with respect to sea water exposure. First condition is no exposure, second condition is immediate exposure and third condition is prolonged exposure. Results show that coal ash exposed to seawater, immediate and prolonged, has smaller shear strength. On the other hand, it still has reasonable strength suitable for land reclamation projects. Constitutive modeling using Modified Cam Clay model is incorporated in the study to be able to predict its behavior and failure in terms of mean effective stress, deviator stress and specific volume.

Keywords: Coal Ash, Critical-State, Modified Cam Clay

INTRODUCTION

The Philippine government relies on coal-fired power plant to provide electricity. The country already has 19 power plants, 11 in Luzon, 6 in Visayas and 2 in Mindanao [1]. The Department of Energy recently announced that 23 new power plants will be opened by 2020 [2]. This is to address the increasing demand of electricity of the country. These power plants produce by-products such as fly ash and bottom ash. They are normally stored at impoundments or landfills. There are cases that the capacity of the storage facility is not enough and this leads to problems in proper disposal of the waste materials. This can have a negative impact to the environment and community close to the storage facility. In the Philippines, this incident is possible since coal-fired power plant is one of the main sources of electricity. It provides approximately 40% of the total power generation needed by the country [2]. Furthermore, most power plants operate for 24 hours such as the coal-fired power plant in Calaca, Batangas. The power plant is estimated to discharge at about 62.62 tons of ash per hour [4]. Instead of disposing or storing the by-products it is better to find an alternative use such as a construction material. There are already existing studies that these by-products have a potential in substituting some construction materials for civil engineering structures. A study on its applicability as a sub base material for highway embankments was conducted. Based on the results, it meets the strength requirements for highway embankments [5]. Another study showed its applicability for lightweight concrete production [6]. A promising civil engineering structure that can use the by-product as construction material is land reclamation. This civil engineering structure is normally constructed in areas where there is a shortage in space. This type of structure is usually constructed in the Philippines especially in highly urbanized areas.

It is the objective of this study to determine the performance of the by-product as a construction material. To be specific, bottom ash was tested under Consolidated Drained Triaxial Test. The effect of seawater is considered so distilled water was changed to seawater. Three conditions were simulated in the test, first condition is no exposure, second condition is immediate exposure and third condition is prolonged exposure. Modified Cam Clay model is incorporated to study its behavior with respect to the mean effective stress (p’), deviator stress (q) and specific volume (v).

BOTTOM ASH

The bottom ash samples were obtained from IloIlo Power Plant. From visual inspection, the material had three compositions. Particles with the size of small gravels, sand, and fines were present. For the fines, it is lightweight which makes it easily blown away by air. Its index properties are determined similar to [3] and the results are tabulated in Table 1. For the index properties, bottom ash is classified as silty sand (SM). It has no plasticity since liquid limit and plastic limit is zero. It is noticeable that the sample has sufficient amount of sand particles and followed by fines content. Compared to other studies, the result of the specific gravity is higher than the range of values suggested, 1.899 to 1.903 [7]. Their coal ash was from a different manufacturing plant. This might have contributed to the difference in index properties of the coal ashes.

Table 1. Index properties

Index Property	
Specific gravity(Gs)	2.25
Liquid limit(LL)	0.00%
Plastic limt (PL)	0.00%
Maximum void ratio (e_{max})	0.94
Minimum void ratio (e_{min})	0.85
Maximum dry unit weight(γ_{dmax})	13.94 kN/m^3
Optimum water content (ω_{opt})	15.85%
USCS	SM
%Gravel	0.86
%Sand	50.44
%Fines	48.70

Table 2. Chemical composition of sea water

Compound	Concentration,g/L
NaCl	24.53
MgCl	5.2
NaSO	4.09
CaCl	1.16
KCl	0.695
NaHCO	0.201
KBr	0.101
HBO	0.027
SrCl	0.025
NaF	0.003
Ba(NO	9.94E-05
Mn(NO	3.40E-05
Cu(NO	3.08E-05
Zn(NO	9.60E-06
Pb(NO	6.60E-06
AgNO	4.90E-07

EXPERIMENTAL PROGRAM

Triaxial Compression Phase

Sample Preparation

The sample was prepared by moist tamping. Relative compaction was the controlled parameter to achieve a target initial condition. This was used instead of relative density in order to simulate actual site conditions [8], [9]. The target value is 95% since it was the desired in situ condition. The maximum dry density served as the reference point to achieve the target relative compaction. The amount of distilled water or sea water was based on the value of optimum moisture content.

Three conditions were prepared to check the effect of seawater towards the strength of bottom ash. The first one is the sample with no exposure. For this case, only distilled water was mixed with the bottom ash. The second condition is the immediate exposure to sea water. For this case the sample was still prepared similar to the first condition. It is during the Consolidated Drained Test where the sample was exposed to sea water. For the third condition, prolonged exposure was simulated so sea water was already mixed with the bottom ash prior to the Consolidated Drained Test. The amount of sea water is computed based on the optimum moisture content. The samples for the three conditions were soaked for 16 hours as per ASTM provisions.

Sea water Preparation

Artificial sea water was used in the experiment. It was formulated following ASTM D 1141 – 98, also known as the "Standard Practice for the Preparation of Substitute Ocean Water". A pH value of 8.2 and chlorinity of the sea water was maintained at 19.38. The chemical composition of the sea water is shown in Table 2.

Consolidated Drained Test

Consolidated Drained Test was performed to evaluate the strength of the sample against long-term loading. The test has three phases namely, saturation, consolidation and shearing phase. The saturation phase was first performed to ensure that the sample is fully saturated. The B-value or the ratio of the pore water pressure and confining pressure was constantly monitored. This parameter must have a value greater than 0.95 to ensure a fully saturated sample. The confining pressures (σ_3) used to consolidate the sample are 50 kPa, 100 kPa, and 200 kPa. They are applied incrementally to have a conservative simulation of the stresses. The sample was allowed to consolidate until there are no significant volume changes in the sample. For the shearing phase, a slow rate of 0.05 mm/min was used to ensure the dissipation of pore water pressure is attained. This phase usually lasts for a minimum of 4 hours to a maximum of 7 hours. For the first condition, 3 samples were tested for each confining pressure. For the second condition, 2 samples were tested for each confining pressure. Lastly for the third condition, 1 sample was tested for each confining pressure. From this, a total of 18 samples were tested for this experiment.

RESULTS AND DISCUSSION

Stress-Strain Behavior and Mode of Failure

The stress-strain plots, Fig. 1, presented in this section were based on the sample's critical state or at failure condition. Based on the results, it was observed that all trials for each condition had a similar trend. Therefore, the results presented in this section are based on the last trial.

When no exposure to sea water was tested, it can be seen that at 200 kPa the sample experienced yield at less than 0.1% axial strain. At this point, the sample already exceeded its elastic limit. Following this behavior, the sample reached its plastic state as it is being axially compressed. Strain hardening is more pronounced after the yielding of the soil. This behavior is only visible in this condition. A common trend from all the condition is no defined peak can be seen in the stress-strain plot. Furthermore, the deviator stress and axial strain increases as the confining pressure was increased. The no exposure to sea water condition and prolonged exposure to sea water had almost the same results when it comes to the values the deviator stress experienced. The axial strain for no exposure to sea water had a larger value. For the immediate exposure condition, the deviator stresses are smaller. Based on the stress-strain behavior, prolonged exposure to sea water has minimal impact to the behavior of the bottom ash since it arrived at a similar trend with the first condition.

For its mode of failure, shear failure was observed for all tests as seen in Fig. 3. It is expected when the sample is a brittle sample. Only samples that are sandy can experience this type of failure. From this, the bottom ash used can be classified as a brittle sample. Furthermore, the presence of sufficient amount of sand in its composition contributed to this type of failure.

Critical-State Parameters

The critical state parameters were established based on the critical state model. The slope, M, of the critical state line (CSL) with respect to the deviator stress and mean normal effective stress was first established. This parameter can be obtained from Fig. 3. The area below CSL is the safe zone or the stresses where the sample is still in its elastic state. Based on the results, the second condition had the smallest slope, 1.3531. The third condition has the largest value of 1.4914. The slope has a relation to the effective critical angle of internal friction (φ'_{crit}) as shown [10]:

$$\sin \varphi'_{crit} = \frac{3M}{6+M} \tag{1}$$

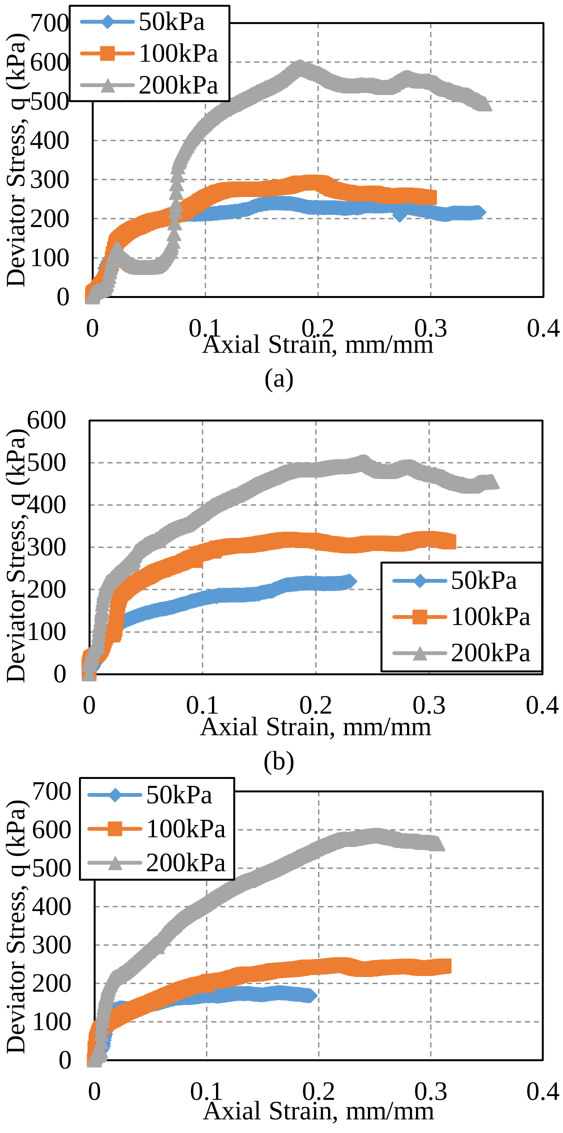

Fig. 1 Stress-strain plot of Bottom Ash a) no exposure b) immediate exposure and c) prolonged exposure.

The resulting values are as follows, 33.51°, 35.26°and 36.67° for the first, second and third condition, respectively. These values are the typical result of silty sand [11].

The equations for isotropic normal compression line (NCL) are also established to determine the critical state line of the bottom ash, Table 3. The equations resemble the equation of the line. From this, the critical state parameters such as slope of NCL (λ), y-intercept of NCL (N_p) and y-intercept of CSL (Γ) can also be established from the equations and are presented in Table 4. These parameters are used to plot create CSL with respect to the deviator stress and the mean normal effective stress. A sample plot is shown in Fig. 4. The points of NCL are from the consolidation phase while the points along CSL are from the shearing phase. The area beyond NCL is the impossible state. The area below NCL is where over-consolidation is encountered. On the other hand, the area below CSL is where expansion happens.

Fig. 2 Mode of failure for bottom ash.

The NCL and CSL for condition 1 and 2 were combined as seen in Fig. 5 and 6. Different behaviors can be observed from the 2 conditions. It is expected that as the confining pressure is increasing the specific volume is also increasing. For the first condition, the specific volume for 50 kPa and 200 kPa are almost similar. On the other hand, for 100 kPa, its specific volume decreased dramatically. The particle rearrangement for this confining pressure is larger compared to 50 kPa and 200 kPa. For the CSL, same observations can be seen for the specific volume. For the mean normal effective stress, 200 kPa had the largest values. For the second condition as seen in Fig. 6, the values of specific volume of NCL for 50 kPa and 100 kPa are almost the same. It can be observed that 50 kPa had slightly higher values. This is also evident for the CSL plot. The exposure to sea water may have affected the results of NCL and CSL of the second condition. The sample were 100 kPa was applied seemed weaker than the other samples for second condition.

Table 3. Isotropic normal compression line equations

σ_3	No Exposure	Immidiate Exposure
50kPa	2.2149 - 0.0954lnp'	1.9657 - 0.0602 lnp'
100kPa	2.8058- 0.2736 lnp'	1.9548 - 0.0684 lnp'
200kPa	2.1871- 0.0845 lnp'	2.4674 - 0.0922lnp'

Table 4. Critical state parameters

	σ_3	λ	N_p	Γ
No Exposure	50kPa	0.0954	2.2149	2.1195
	100kPa	0.2736	2.8058	2.5322
	200kPa	0.0845	2.1871	2.1026
Immediate Exposure	50kPa	0.0602	1.9657	1.9055
	100kPa	0.0684	1.9548	1.8864
	200kPa	0.0922	2.4674	2.3752

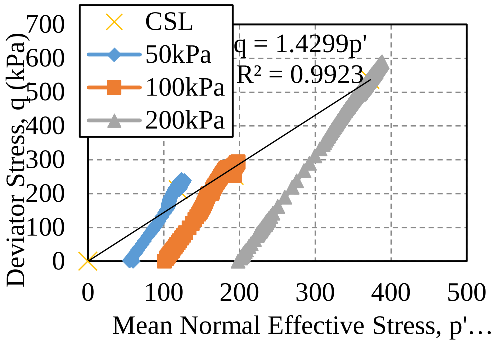

(a)

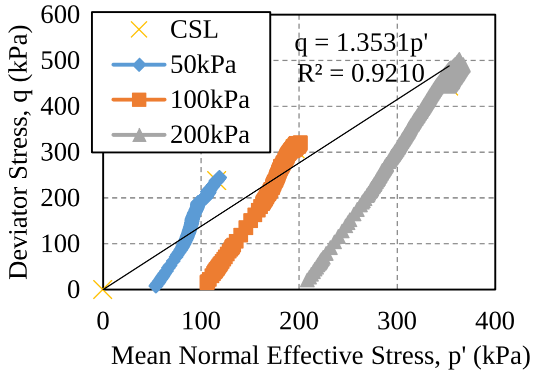

(b)

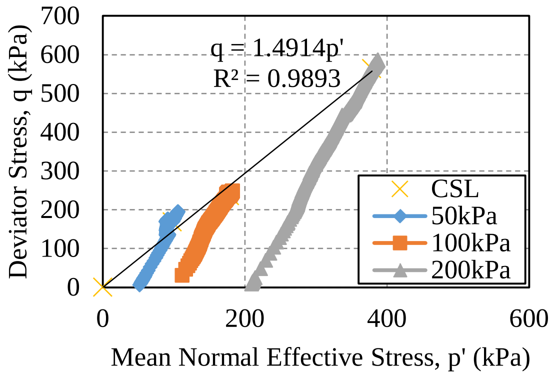

(c)

Fig. 3 Critical state line with respect to the deviator stress and mean normal effective stress a) no exposure b) immediate exposure and c) prolonged exposure.

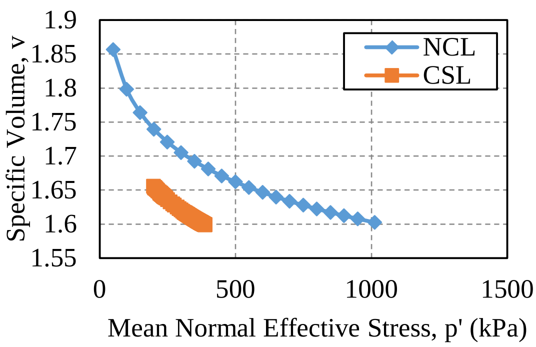

Fig. 4 Critical state line with respect to the deviator stress and mean normal effective stress a) no exposure b) immediate exposure and c) prolonged exposure.

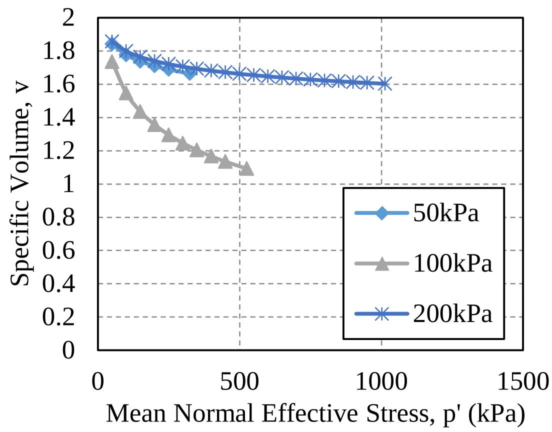

(a)

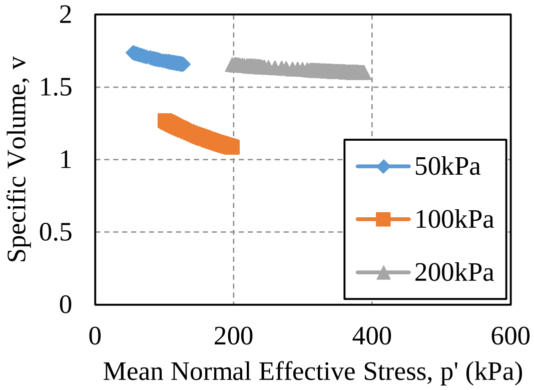

(b)

Fig. 5 Specific volume versus mean normal effective stress plot for no exposure to sea water a) NCL and b) CSL.

Modified Cam Clay Model

Modified cam clay model (MCC) is an elasto-plastic model that characterizes the soil in terms of the mean normal effective stress, deviator stress and specific volume [12]. The model is the result of the enhancements made in the Cam Clay Model. The model has an elliptical yield locus having this equation [10]:

$$\frac{p'}{p'_c} = \frac{M^2}{M^2 + q/p'} \tag{3}$$

where:
p' = mean normal effective stress
q = deviator stress
p'_c = preconsolidation stress
M = slope of CSL from q vs p'

The preconsolidation stress is estimated by using Eq. 3. The q and p' at critical state was used [10]. The largest preconsolidation stress bottom ash can withstand is 1030.02 kPa. This value was obtained from the third condition. The equations presented were used to create the yield locus seen in Fig. 7 for a sample with a confining pressure of 200 kPa. Only the equations with 200 kPa are presented since it can cover all the stresses from 50 kPa and 100 kPa. It can be seen that Eq. 5 had the smallest preconsolidation stress and slope M.

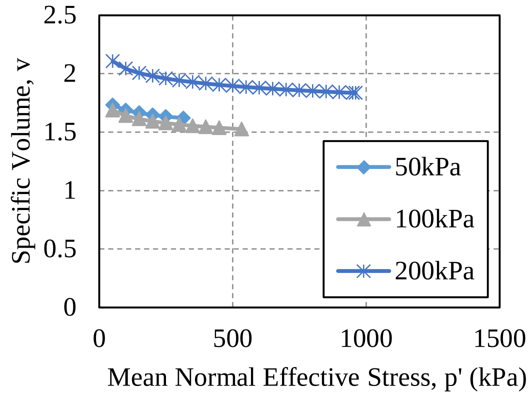

(a)

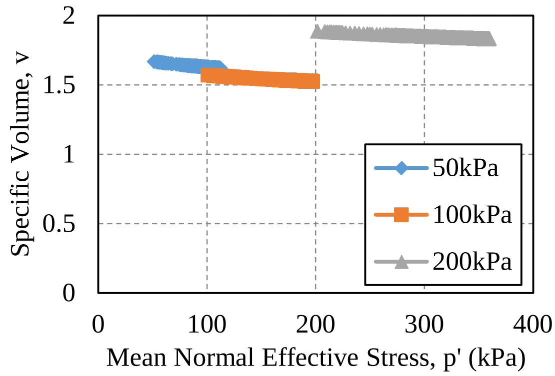

(b)

Fig. 6 Specific volume versus mean normal effective stress plot for immediate exposure to sea water a) NCL and b) CSL.

$$\frac{p'}{1013.16} = \left(\frac{1.4299^2}{1.4299^2 + \left(q^2/p'^2\right)}\right) \tag{4}$$

$$\frac{p'}{960.27} = \left(\frac{1.3531^2}{1.3531^2 + \left(q^2/p'^2\right)}\right) \tag{5}$$

$$\frac{p'}{1030.02} = \left(\frac{1.4914^2}{1.4914^2 + \left(q^2/p'^2\right)}\right) \tag{6}$$

The yield locus presented in Fig. 7 serves as the boundary of the soil with respect to plastic and elastic state. A similar trend was observed for all samples for the plot of yield locus. Points within the yield locus are stresses at the elastic state while points beyond are at its plastic state or failure state.

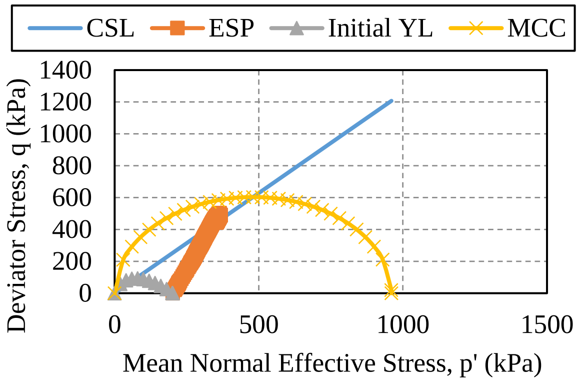

Fig. 7 Stress path with yield locus of bottom ash CD test with 200 kPa confining pressure.

CONCLUSIONS

Bottom ash was tested under Consolidated Drained Triaxial Test. The objective of the study was to investigate on the possibility of using the by-product as a material for reclamation. Exposure to sea water was considered since most reclamation projects are situated at the sea. Three conditions were considered, no exposure, immediate exposure and prolonged exposure. Results show that prolonged exposure to sea water has a minimal difference when compared to the no exposure condition. The values of effective critical angle of internal friction are as follows 33.51°, 35.26°and 36.67°. The value is comparable to a silty soil were its typical values ranges from 26° to 35°. For the Modified Cam Clay Model, the preconsolidation stress was computed and a similar trend was observed. The computed maximum value is 1030.02 kPa. The value is from the prolonged exposure condition. From this, bottom ash is a promising material that can be used in a reclamation project.

REFERENCES

[1] Department of Energy. (2016). List of existing power plants as of December 2015. Retrieved from http://www.doe.gov.ph/power-and-electrification/list-of-existing-power-plants.

[2] Gonzales, I. C. (2015). 23 new power plants to go online by 2020. The Philippine Star. Retrieved from http://www.philstar.com/business/2015/06/15/1465896/23-new-power-plants-go-online-2020.

[3] Dungca, J. R. & Dychango L. F. T. (2016). Strength properties of road base materials blended with waste limestones. International Journal of Geomate. 11(25). 2493-2498

[4] Antonio, O. (2006). Lime-fly ash stabilization of Calaca, Batangas bottom ash. [Graduate Thesis] University of the Philippines, Quezon City, Philippines.

[5] Jao, J. (2012). Strength and permeability characteristics of road base materials blended with fly ash and bottom ash. [Graduate Thesis]. De La Salle University, Manila, Philippines

[6] Ahmaruzzaman, M. (2010). A review on the utilization of fly ash. Progress in Energy and Combustion Science, 36(3), 327-363. Elsevier Ltd. doi:10.1016/j.pecs.2009.11.003

[7] Antonio, O. V. M., & Zarco, M. A. H. (2007). Engineering properties of Calaca Batangas bottom ash, 28(1), 37–56.

[8] Zabielska-Adamska, K. (2006). Shear strength parameters of compacted fly ash–HDPE geomembrane interfaces. Geotextiles andnGeomembranes,n24(2),n91–102. doi:10.1016/j.geotexmem.2005.11.006.

[9] Kim, B., Prezzi, M., & Salgado, R. (2005). Geotechnical properties of fly and bottom ash mixtures for use in highway embankments, 914-924.

[10] Powrie, W. (2004). Soil Mechanics Concepts and Applications Second Edition. London: Spoon Press.

[11] Das, B. & Sobhan, K. (2014). Principles of Geotechnical Engineering Sixth Edition, United States: Chris Carson.

[12] Munda, J., Pradhan, P. K. & Nayak, A. K. (2014). A Review on the performance of Modified Cam Clay Model for fine grained soil. Journal of Civil Engineering and Environmental Technology. 1(5), 65-71.

ASSESSMENT OF CRITICAL-STATE SHEAR STRENGTH PROPERTIES OF COPPER TAILINGS

Erica Elice Saloma Uy[1] and Mary Ann Q. Adajar[1]
[1]Civil Engineering, De La Salle University, Philippines

ABSTRACT

Philippines, with a total of 7,107 islands, have one of the largest mineral resources in the world. The copper and gold deposits are considered to be among the largest in the world (Bureau of East Asian and Pacific Affairs, 2010). Mining minerals generate waste material called mine tailings. Impoundment of mine tailings is normally done to store these waste materials. One of the most common types used in impounding tailings is raised embankments because of its low economic cost. This impoundment uses natural soil, tailings, and waste rocks as the construction material. There are cases that raise embankments experience stability failure which can affect the environment and well-being of the community where it is situated.

It is the interest of this study to assess the possibility of using mine tailings, specifically copper tailings, as a construction material. Index properties were first established following ASTM standards. From this, it was established that the copper tailings has plasticity. Unconsolidated undrained, consolidated undrained and consolidated drained test were conducted to determine the critical shear strength of the copper tailing. The copper tailings were tested having two relative densities namely, 60% and 90%. The effective critical angle of friction was found to have a range of 21°-28°. Since critical-state parameters are considered in the study, Cam clay model can be implemented so that to its behavior and failure mechanism can be predicted.

Keywords: Mine Tailings, Critical-State, Cam Clay

INTRODUCTION

Philippines, with a total of 7,107 islands, have one of the largest mineral resources in the world. According to National Economic Development Authority (NEDA), the country has an estimated USD 840 billion (Php 47 trillion) worth of unexplored gold, copper, nickel, chromite, manganese, silver and iron [1]. The copper and gold deposits of the Philippines are also among the largest in the world. Mining generates waste material called mine tailings. The waste materials are commonly stored by impoundment of the mine tailings. A raised embankment is widely adopted in impounding tailings due to its low economic cost [2]. This storage facility uses natural soil, tailings, and waste rocks as the construction material. There are cases that raise embankments experience stability failure which can affect the environment and well-being of the community where it is situated. One of the well-known disasters in the Philippine mining industry was the Marcopper incident which happened in 1996 [3]. Mine tailing spill occurred because of the leak at the drainage of the storage facility the Tapian Pit. This caused a fracture in the drainage tunnel which resulted to the spill that consists of four million metric tons of waste. Although Philippines is gifted with vast amount of minerals, not all companies follow the framework of responsible mining. One of which is in accordance with the international best practice such as ensuring environmentally responsible mining. Up to this date, there have been 21 tailing dam failures in the Philippines from 1982 up to 2007. Six out of 21 events were classified as major dam failure [3]. These events harmed the communities living near the mining facility. It also polluted the bodies of water destroying the livelihood of the locals. Since mine tailings are valueless and are produced in large volumes, it is normally stored at impoundment of mine tailings. Instead of just storing the waste materials, this study aims to investigate its potential as a construction material. Even though there are already several studies performed in other countries, there is a lack of research in the Philippines regarding the geotechnical characteristics of mine tailings [2].

It is the objective of this study to establish the index properties and critical shear strength of copper mine tailings. Index properties were established following American Society for Testing and Materials (ASTM) standards. Critical state condition is considered to have a better understanding of the mechanical behavior of the copper mine tailings. Unconsolidated undrained (UU), consolidated undrained (CU) and consolidated drained (CD) test were performed using a triaxial apparatus to determine its critical shear strength. Cam clay model is incorporated in the study since critical state condition is applied.

COPPER MINE TAILINGS

Copper mine tailings are obtained from Barrio Maglinao, Municipality of Basay Negros Oriental, Central Visayas. The mining site was operated by Construction and Development Corporation in the Philippines (CDCP) in 1979 and it was closed down in 1983 [4]. The site left negative environmental impacts to the Municipality of Basay especially to the Pagatban River. The mineralization for the Basay Copper Project is copper porphyry. Extensive open mining and limited underground mining was conducted between 1979 and 1983. In order to extract copper, the ore was first crushed and grinded. Forth floatation was performed to remove unwanted rock, gangue, from the copper ore. From this process, a 25% copper concentrate was achieved. Further refinement of the mineral was performed by smelting. The impurities were removed in a form of a slag. The mineral would now be in copper iron sulphide solution or matte. This is followed by conversion from matte to blister copper or partly purified copper having a blistered surface. In preparation for the last stage of extraction, the blister is casted into anodes. Lastly, electrolytic refining is executed by purifying the copper up to 99.99% through electrolysis [4]. The waste generated from extraction, copper mine tailings, were stored in tailing dams. The copper tailings obtained were in a somewhat dry condition and it formed a rock like formation.

EXPERIMENTAL PROGRAM

Preliminary Phase

The index properties of the copper mine tailings were obtained in accordance to ASTM standards. The following are the tests performed: Mechanical Sieve Analysis (ASTM D422), Hydrometer Test (ASTM D422), Atterberg limits [Plastic, Liquid (ASTM D4813) and Shrinkage limit (ASTM D427)], Specific Gravity (ASTM D854), Compaction Test (ASTM D698), Relative Density Test and Unit Weight Determination which includes the Maximum Index Density (ASTM D4253) test and Minimum Index Density Test (ASTM D4254).

Triaxial Compression Phase

Sample Preparation

The reconstituted samples were prepared by moist tamping. The method was applied since it minimizes particle segregation and it is applicable for most types of sands in compacting under a wide range of relative densities. The samples were initially dried to accurately achieve the desired relative density (D_r) of 27%, 60%, and 90% [5]. The mentioned relative densities are used to simulate a loose, medium dense and highly dense reconstituted sample, respectively. The amount of water mixed with the sample was less than its optimum moisture content. This allows the sample to be molded without crumbling. The sample was soaked for 16 hours as per ASTM standards. A cylindrical mold with a diameter of 38 mm and a height of 76 mm was used. This mold was used to ensure that the diameter of the sample was at least 30 mm. The largest particle which was contained within the sample was also maintained to be 1/6 smaller of its diameter. A ratio of the height to diameter between 2 to 2.5 is followed [6].

Unconsolidated Undrained Test

The unconsolidated undrained (UU) test or Quick Test (Q-Test) was performed based on ASTM D 2850. For this set-up, drainage was not permitted all throughout the experiment. Consolidation was not necessary but confining pressures are still applied at a fast rate. The rate of loading used for applying the axial load is dependent on the type of soil tested. For this study, a rate of approximately 1%/min is used since the soil is has plasticity. It was stopped when the sample experiences failure or it reached critical state. For the experiment proper, samples were prepared having an initial relative density of 27%, 60%, and 90%. The confining pressures (σ_3) used are 25 kPa, 50 kPa and 100 kPa [6]. A total of 9 samples were tested for the UU-condition.

Consolidated Undrained Test

The consolidated undrained (CU) test or R-Test (Rapid Test) was performed based on ASTM D 4767 – 02. For this condition, the specimen was allowed to consolidate prior to the shearing phase. There are three phases in this condition namely, saturation, consolidation and shearing phase. For the saturation phase, to ensure that the sample is fully saturated a B-value is computed. It is the ratio of the pore water pressure and confining pressure at the time when the volume change is constant. The B-value must be greater than 0.95 to ensure that the sample is fully saturated. For the consolidation phase, the confining pressure (σ_3) was applied. The drainage was left open until zero pore water pressure is achieved **[8].** For the shearing phase, the rate of loading of 1%/min was applied to simulate rapid loading. It was stopped when failure or critical state condition was experience. For the experiment proper, samples were prepared having an initial relative density 60%, and 90%. The confining pressures used in this condition are 50 kPa, 100 kPa and 200 kPa [9]**.** The 25 kPa confining pressure was not applied in this condition because the range of back pressures used is larger. The sample will not consolidated instead it will saturate. A total of 6 samples were tested for the CU-condition.

Consolidated Drained Test

The consolidated drained (CD) triaxial test or S-Test (Slow Test) was based on the British Standard Methods of test for Soils for Civil Engineering Purposes. The test's purpose was to establish the drained shear strength parameters such as the critical state effective angle of internal friction (φ'_{crit}). For this condition, water was allowed to drain during the shearing phase. This was to simulate and determine the strength of the soil with respect to long-term loading. Similar to the CU test, CD test has three phases. The saturation and consolidation phase are similar with CU test. The rate of loading for the shearing phase must be slow enough to allow the dissipation of excess pore water pressure. A rate of loading of 0.5% axial strain per minute was used since it is applicable for sandy soil [15]. The confining pressure used for the consolidation phase are 50 kPa, 100 kPa and 200 kPa were used.

RESULTS AND DISCUSSION

Index Properties

The index properties of the copper tailings are presented in Table 1. The liquid limit falls under the category of a silty soil since it is in between 30-40%. The plastic limit, when computed, is characterized as a clayey soil based on the range of 25-50% [5]. The specific gravity is within 2.6 to 2.9 which is the range of values for a clayey and silty soil [7]. A grain size distribution curve (GSDC) was established as seen in Fig. 1.

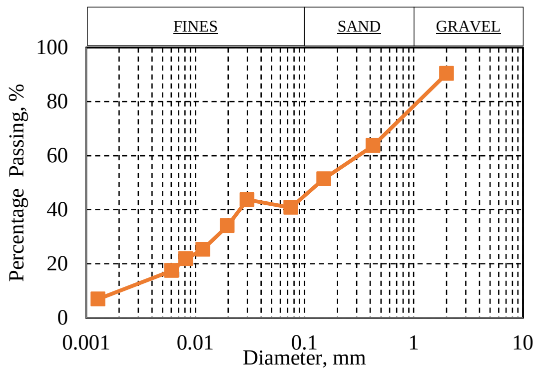

Fig. 1 Grain size distribution curve of copper tailings.

The plot is used to determine the soil gradation of the copper tailings. It contained a flat section at the fines section which is the indication that the sample is gap graded. A gap graded soil usually contains a large percentage of big and small particles with a limited amount of intermediate sizes [12]. When this type of gradation is compacted, it can result to larger voids compared to a well graded soil. The composition of the copper tailings was also determined through the sieving process that was performed in order to create the GSCD. The sample was sieved between #4 and #200 sieve. It resulted to the following composition, 0.15% gravel, 59.04% sand and 40.81% fines.

To properly define the soil classification of the copper tailings, the Unified Soil Classification System (USCS) was used since it can be applied in all types of soil [10]. Also, the system can further classify the soils into coarse-grained and fine-grained soils. From the system, the copper tailings can be classified as silty sand. Another classification system was used to check the suitability of copper tailings as support for roadways. The American Association of State Highway and Transportation Officials (AASHTO) was used since it can classify the material's general subgrade rating for roads. According to AASHTO soil classification system, the soil sample is classified as A-4 with a group index of 0. A group index close to zero indicates it is a good soil for highway subgrade. Its general subgrade rating is fair to poor. For this rating, the copper tailings can have fair to poor drainage and support when used as a subgrade material for embankments [10]. The results of the index properties were compared to some existing researches of copper tailings. The result of the specific gravity was compared to the research Characteristics of Copper Mine Tailings: A Case Study. Their sample was from the Sarcheshmeh Copper Complex Tailings Dam in Iran. Its specific gravity ranges from 2.6 to 2.8 [11]. The copper tailings tested have a larger value, 2.82, and its percentage error is 0.71%. The result of the shrinkage limit was also compared to the research Laboratory Properties of Mine Tailings. Their sample was from Kennecott Mining in Salt Lake County, Utah. Its shrinkage limit is 24.4% [9]. The shrinkage limit of the copper tailings is smaller, 21.58%, and its percentage error is 0.12%. The soil classification of the copper tailing from Kennecott Mining is also silty sand but the fines content is greater. The samples from Kennecott Mining only have 31.3%. Results from other researches may vary since the samples are taken from different areas. The origin of the sample may have an effect to the over-all composition of the sample.

Stress-Strain Behavior and Mode of Failure

The copper tailings were sheared until failure or once critical state is achieved. For the three triaxial tests a common trend was observed from the stress-strain plot. A sample result is presented in Fig. 2. Yield was constantly experienced during the early stages of the shearing phase. Based on the plots it normally happens at less than 5% strain. This behavior shows that the sample had already exceeded its elastic limit and immediately shifted to a purely plastic sample while it is being sheared. It is followed by strain softening for a small amount of time then it shifts to strain hardening all throughout. No peak was observed in the plots which can result to a plastic mode of failure. This was verified during the experiment that the sample had experienced a bulging mode of failure in all tests, Fig. 3. Based on the observed stress-strain behavior and the mode of failure, this indicated that the sample tested is ductile.

Table 1. Index properties

Index Property	Value
Specific gravity(Gs)	2.82
Liquid limit(LL)	32.05%
Plastic limt (PL)	25.81%
Plasticity index(PI)	6.24%
Shrinkage limit(SL)	21.58%
Shrinkage Ratio(R)	1.65
Maximum void ratio (e_{max})	1.441
Minimum void ratio (e_{min})	0.964
Maximum dry unit weight(γ_{dmax})	15.70 kN/m3
Optimum water content (ω_{opt})	19.47%

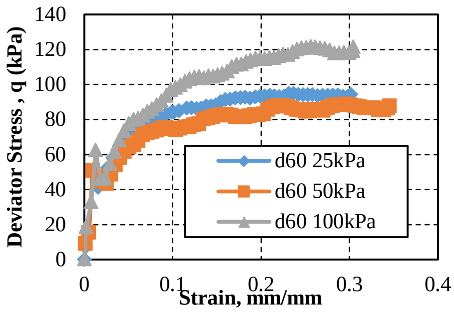

Fig. 2 Stress-strain plot of copper tailings for UU test Dr = 60%

Fig. 3 Stress-strain plot of Copper Tailings

Undrained Shear Strength

Average undrained shear strength (Su_{ave}) was computed from the three confining pressures applied in the UU test. The results are tabulated at Table 2. The average value was obtained since the deviator stress from the Mohr's Circle was not equal. Results of the average undrained shear strength of copper tailings were compared. The sample with 90% relative density had the smallest value of Su_{ave} while the largest has a 60% relative density. When the actual relative density was computed and compared with the target value, an error ranging from 0.66% to 17.7% was observed. Since the samples were reconstituted, difficulties in achieving the same target relative density and soil structure at minimal error can be encountered. It can also be observed that Su_{ave} at 90% relative density decreased. This result is due to the sufficient amount of fines present and a quick test was performed. Copper tailings are composed of 40.81% fines which made it a rather weak sample at this relative density and test [8].

The critical undrained shear strength (Su_{crit}) was obtained from the CU test. Results are tabulated at Table 3. It can be observed that a different trend occurred in this set-up. The samples prepared with a denser composition, D90, had a larger range of values. The void ratio after the consolidation was computed as seen in Table 4. The void ratio is relatively smaller after consolidation when compared to the initial void ratio. A smaller void ratio translates to a higher relative density. This explains the trend experienced in for the Su_{crit}.

The consistency of the sample can be classified based on its undrained shear strength [8]. The Copper tailings' Su_{ave} is classified as a sample with medium consistency. For the Su_{crit} it is classified as a sample with medium to very stiff consistency. A change in consistency can be observed because the consolidation phase of CU test improved the resistance of the sample to compression. A medium to very stiff consistency would have an undrained shear strength ranging from 25 kPa to 200 kPa [8].

Table 2. Average undrained shear strength (Su_{ave})

	Su_{ave} (kPa)		
D_r	D27	D60	D90
CopperTailings	45.39	46.04	32.65

Table 3. Critical undrained shear strength (Su_{crit})

	Su_{crit} (kPa)	
D_r	D60	D90
Copper Tailings	42.42-74.12	78.49-117.75

Critical-Shear Strength

The critical shear strength is measured by determining the critical angle of internal friction from the CU and CD test. The typical values for angle of internal friction for silts range from 26° to 35° [8]. Based on the results as seen in Table 5, only the values at 60% relative density for both CU and CD test are in close agreement. The results are also compared to the shear strength of Copper Tailings from Kennecott Mining which is 34° [9]. Copper tailing's strength is considerably smaller since it has a greater amount of fines content, 40.81%. The samples from Kennecott Mining only have 31.3%. Based on the results of shear strength parameters, Copper tailings has sufficient strength but it is not close to the typical materials used for subgrade, embankment or structural fill. The typical materials used are well-graded sands with greater than 34° angle of internal friction [16].

Table 4. Summary of void ratio (e) for CU test.

D_r (%)	σ_3 (kPa)	e_{target}	e actual Initial	After Saturation	After Consolidation
60	25	1.13	1.09	1.16	1.09
	50	1.13	1.22	1.37	0.94
	100	1.13	1.19	1.59	1.18
90	50	0.98	0.97	0.89	0.99
	100	0.98	0.99	0.78	0.97
	200	0.98	1.03	1.35	1.01

Table 5. Critical angle of interal friction (φ_{crit}).

	Triaxial Test	D_r (%) 60 φ_{crit}	60 φ'_{crit}	90 φ_{crit}	90 φ'_{crit}
Copper Tailings	CU	25°	27°	21°	22°
	CD	-	28°	-	24°

Critical-State Parameters

Critical state parameters are obtained from the CD test based on the concepts from the critical state model [13]. Results are tabulated at Table 6. The isotropic normal compression lines (NCL) of the copper tailings with 90% relative density are presented at Fig. 4.

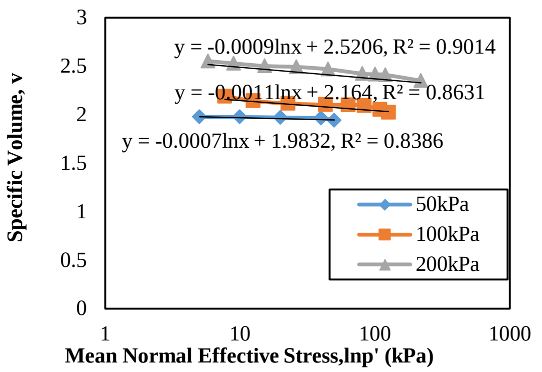

Fig. 4 NCL of copper tailings having D_r = 90% under CD test.

Void ratio (e) can be extracted from Fig. 4 since, specific volume (v) is [13]:

$$v = 1 - e \tag{1}$$

From the computations, the void ratio for 200 kPa NCL has values larger than e_{max}. Exceeding e_{max} can be an indication that the sample had already collapse at that confining pressure. This is also the reason of having a smaller φ_{crit} or φ'_{crit} at 90% relative density. The sample had already a weaker structure prior to the shearing phase. With this, the NCL for 100 kPa is considered as its maximum boundary while NCL for 50 kPa is the minimum boundary. Each data was linearized to determine the slope of NCL or compression index (λ) and y-intercept of the NCL line (Γ). The equations presented in Fig. 4 can be used to predict the specific volume for a certain mean normal effective stress or vice versa. The coefficient of determination for NCL at 100 kPa and 50 kPa is 0.8386 and 0.8631, respectively. Based on these values, the equation has the capability of predicting values at almost 85% accuracy. The slope can be used to compute for the settlement parameter such as compression index (C_c) using equation [14]:

$$\lambda = \frac{C_c}{\ln(10)} = \frac{C_c}{2.3} \tag{2}$$

Values computed, using Eq. 2, were less than the typical values ranging from 0.1 to 0.8 [14]. From this result, Copper tailings can be considered as slightly compressible. The slope of the reloading or unloading line (κ) is zero since this step was not simulated in the experiment. The critical state line (CSL) of deviator stress (q) versus mean normal effective stress (p') has a slope M, Fig 6. It can be observed that sample with 60% relative density has a larger value. This is due to the collapse the sample experienced at 200 kPa for 90% relative density. After establishing the critical state parameters, the specific volume versus p' was redrawn using the formulas from the critical state model, Fig. 5. The area beyond NCL is the impossible state while the area below is where the over-consolidated soil is located. Points along NCL are normally consolidated soil. The area in between NCL and CSL is where compression occurs. The area under CSL is where expansion is encountered.

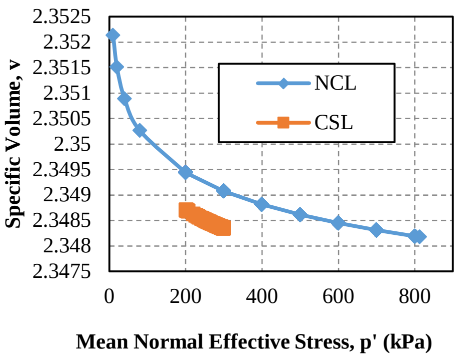

Fig. 5 Specific volume versus mean normal effective stress plot of copper tailings having D_r = 90% under CD test.

Cam Clay Model

The Cam Clay model was proposed by Roscoe and Schofield (1963). It considers the yield behavior of a soil through a yield locus as seen in Fig. 6. The yield locus is defined as the combination of the deviator stress, q, and the mean normal effective stress, p', that caused the yielding of a soil due to a preconsolidation stress, p'_o. The preconsolidation stress is estimated from the deviator stress and mean normal effective stress at critical state [13].

$$\frac{q}{Mp'} + \ln\left(\frac{p'}{p'_c}\right) = 0 \qquad (3)$$

The yield locus serves as the boundary of elastic and plastic state [7]. Elastic state is within the locus while plastic state is beyond it. The model was applied since the sample experienced yield behavior. Furthermore, the model also integrates the critical state parameters together with NCL and CSL in its formulation. The model can be used to predict the possible deviator stress with a desired value of mean normal effective stress or vice versa to assess the behavior of the sample. The yield locus also shows the limiting values for deviator stress and mean normal effective stress.

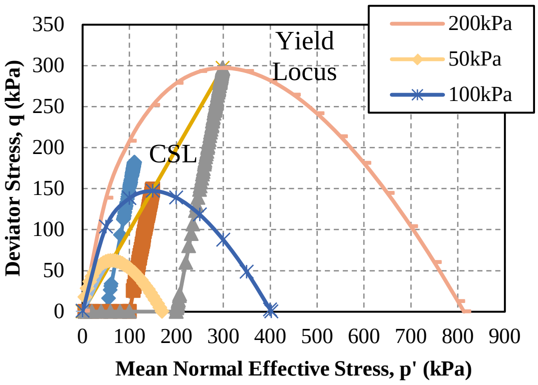

Fig. 6 Stress path with yield locus of copper tailings having D_r = 90% under CD test.

Table 6. Summary of critical-state parameters

	Triaxial Test		D_r (%)	
			60	90
Copper Tailings	CD	λ	0.0002-0.0005	0.0007-0.0011
		Γ	1.7161-2.0176	1.9832-2.1640
		κ	0	0
		M	1.13	0.99

CONCLUSION

It is the interest of this study to assess the possibility of using mine tailings, specifically copper tailings, as a construction material. Index properties and critical shear strength parameters were first established following ASTM standards. From this, it was established that the copper tailings can be classified as silty soil with plasticity and a sufficient amount of fines content. Based on the AASHTO rating it can still be as an embankment material but with proper control. Based on the CU and CD test, the effective critical angle of friction has a range of 21°-28°. The material performs best at 60% relative density at critical state. When the critical state parameters are incorporated to the Cam Clay model, its maximum mean normal effective stress and deviator stress is 812.91 kPa and 297.15 kPa respectively.

The result presented in the research is not enough to completely assess Copper tailings' potential as a construction material. California Bearing Ratio test must be performed to further evaluate its subgrade strength [17]. Furthermore, the Copper tailings' performance as a fine aggregate should be tested [18], [19].

REFERENCES

[1] Senate Economic Planning Office (2005). Retrieved from https://www.senate.gov.ph/publications/PI%20200511%20%20Extracting%20Growth%20from%20Mining.pdf

[2] Adajar, M. A. Q. & Zarco, M. A. H. (2014). An empirical model for predicting hydrauliconductivity of mine tailings. International Journal of Geomate. 7(14). 1054-1061

[3] Wise Uranium Project (2002). Retrieved from http://www.wise-uranium.org/new02.htm

[4] Vigar, A.J., Motton, N.T., & Taylor, I. (2011). Competent person's report on the Basay copperproject, Negros Oriental province, Philippines. Hong Kong: Mining Associates.

[5] Alshible, K., Batiste, S. & Sture, S. (2003). Strain Localization in Sand: Plane Strain versus Triaxial Compression. Journal of Geotechnical and Geoenvironmental Engineering. 129(6).483-494.

[6] Liu, C & Evett, J.B. (2000). Soil Properties: Testing, Measurement, and Evaluation. Upper Saddle River, New Jersey: Prentice-Hall, Inc.

[7] Britto, A.M. & Gunn, M.J. (1987). Critical State Soil Mechanics via Finite Elements. West Sussex, England: Ellis Hordwood Limited.

[8] Das, B. & Sobhan, K. (2014). Principles of Geotechnical Engineering Sixth Edition, United States: Chris Carson.

[9] Qui, Y. & Sego, D. C. (2001). Laboratory Properties of Mine Tailings. Canadian Geotechnical Journal. 38. 183-190.

[10] Coduto, D. P. (1999). Geotechnical Engineering Principles and Practice. Upper Saddle River, New Jersey: Prentice-Hall, Inc.

[11] Shamsai, A., Bateni, S. & Ayatollahi,S. (2007). Geothecnical Characteristics of Copper Mine Tailings: A Case Study. Springer Science+Business Media. 25. 591-602.Marr WA, "Advances and Retreats in Geotechnical Measurements", Judgment and Innovation: The Heritage and Future of the Geotechnical Engineering Profession, 2000, pp. 42-60.

[12] Smith, I., 2006 Smith's Element of Soil Mechanics 8th Edition Blackwell Publishing

[13] Powrie, W. (2004). Soil Mechanics Concepts and Applications Second Edition. London: Spoon Press.

[14] Budhu, M. (2011). Soil Mechanics and Foundations. New York: John Wiley & Sons, Inc.

[15] Bardet, J.P. (1997). Detained description of Triaxial Tests on Coarse-Grained Soils. Chapter 7.7 of Experimental Soils Mechanic. Upper Saddle River, New Jersey: Prentice-Hall.

[16] United States Department of Agriculture. (1994). Slope Stability Reference Guide for National Forests in the United States. Washington, DC. 2.

[17] Prahallada, M. C. and Shanthappa, B. C. (2014). Use of Copper Ore Tailings - as an Excellent Pozzolana in the Preparation of Concrete. International Journal of Advanced Research in Engineering and Applied Sciences. 3(3). ISSN: 2278-6252

[18] Thomas, B. S., Damare, A. and Gupta, R. C. (2013). Strength and durability characteristics of copper tailing concrete. Construction and Building Materials. 48, pp. 894-900.

GEOTECHNICAL PROPERTIES OF LADLE FURNACE SLAG IN ROADWORK APPLICATIONS

Farshid Maghool[1], Arul Arulrajah[2], Suksun Horpibulsuk[3] and Yan-Jun Du[4]
[1,2] Department of Civil and Construction Engineering, Swinburne University of Technology, Australia;
[3] School of Civil Engineering, Suranaree University of Technology, Thailand; [4] Institute of Geotechnical Engineering, Southeast University, China

ABSTRACT

Ladle Furnace Slag (LFS) is an industrial waste from steelmaking process, generated during the final stage in ladle refining furnace. LFS samples were sourced from a steelmaking company in Victoria, Australia. This paper reports on the results of a geotechnical and chemical evaluation on LFS to assess the viability of using this by-product in roadwork constructions. A comprehensive suits of engineering tests was undertaken comprising moisture content, specific gravity, particle size analysis, hydrometer, organic content, flakiness index, Los Angeles (LA) abrasion, hydraulic conductivity, modified compaction, pH, Unconfined Compression Strength (UCS) and California Bearing Ratio (CBR). In addition, the chemical composition of LFS sample was assessed using X-ray Fluorescence analysis (XRF). The engineering properties of LFS were then compared with typical quarry materials. The chemical composition results indicate that LFS contains high amount of calcium. Thus, the effect of 0, 7 and 28 days of curing on the strength of unbound LFS was investigated using UCS test. The specimens with 7 and 28days curing had higher UCS value than uncured samples attributed to high lime content and hydration process. From an engineering perspective, LFS was found to be suitable material to substitute typical quarry material in roadwork applications. The reuse of LFS in roadwork construction will significantly reduce the demand of natural quarry aggregates and will possibly divert huge amount of these waste from landfills and stockpiles. Possible applications of unbound LFS in road pavement are also discussed.

Keywords: Ladle Furnace Slag, Pavement Base, Unconfined Compression Strength, Industrial Waste

INTRODUCTION

Waste materials are universally described as by-products of Commercial, industrial, building and demolition activities that do not have any value [1]. Due to the recent enforcement of more stringent environmental regulations all around the world, recycling and reuse of waste materials has become very critical.

Steel has been known as the one of the world's most recyclable materials. Annually, more than 1400 million tonnes of steel is manufactured worldwide [2]. The steelmaking process generates an industrial by-product termed as slag. In Australia alone, the annual production of steel slag is reported to be around 2.4 million tonnes [3].

In the past decade, noticeable amount of slags was effectively utilized as cementitious and non-cementitious construction materials. More than 60% of the utilized slags in Australia was granulated blast furnace slag, which is really popular among cement and concrete companies [4]. However, there are currently limited studies and reuse options for particular types of slag including LFS.

LFS is formed during the secondary steelmaking process in the ladle refining furnace. In this stage, the molten refined steel is poured out of the furnace and the resulting product on the bottom of the ladle is known as LFS. On average the production of one tonne of steel in steelmaking plants results in 30 to 50 kg of LFS [5].

Limited research on engineering and geotechnical properties of LFS have been conducted up to the present time. Serjun et al. [6] graded LFS as a low quality material due to its fine grain size, adverse leaching potential and expansive behavior. Manso et al. [7] indicated LFS can be a valuable by-product after it has been turned into a dusty product and its expansive characteristics could be reduced in this form.

Manso et al. [8] studied the behavior of soils stabilized with LFS and found similar results of the same soils after mixing with lime. This research also suggested that UCS value was significantly increased in the soils blended with LFS powder while the plasticity index and free swelling behavior of soils can be reduced. Serjun [6] stated that LFS has the potential to be used as a supplementary cementing material in numerous civil and construction applications due to its cementitious hydraulic properties.

The use of industrial wastes as roadwork construction materials will be an optimistic outcome for the waste management hierarchy, provided that the use takes into account the required environmental and engineering considerations [9]. The limited knowledge on the relevant engineering and geotechnical properties of unbound LFS is main obstacle for using these materials in roadwork applications. An extensive suite of engineering and chemical testing were undertaken on LFS to evaluate the feasibility of using these steel slag aggregates as road construction materials.

MATERIALS AND METHODS

Samples for this research were collected from the top of various LFS stockpiles from a steelmaking plant in Victoria, Australia. LFS is well-graded grey material and produced during the secondary steelmaking process in the ladle refining furnace. LFS was poured out from the ladle furnace in a liquid-state and then is cooled down from 1600°C to room temperature [7]. To obtain a representative sample for laboratory testing, LFS samples were properly mixed, split and sieved through a 20mm sieve.

Fig. 1 LFS sample appearance.

Fig. 1 presents the LFS sample appearance after passing through a 20 mm aperture sieve. It is evident from the photo that LFS sample in this study contains some electric arc furnace slag and natural aggregates from the manufacturing site plant. The chemical composition of LFS samples were assessed using X-ray Fluorescence analysis (XRF). The natural moisture content of LFS was also determined using drying oven set at 105°C.

A series of laboratory evaluations was conducted to assess the engineering properties of the LFS comprising particle size distribution [10], hydrometer [11], organic content [12], flakiness index [13], particle density and water absorption [14]-[15], pH [16], modified compaction [17], LA abrasion [18], Hydraulic conductivity [19], CBR [20] and UCS [21], according to relevant established Australian and American standards.

CBR, UCS and hydraulic conductivity samples were prepared and compacted under modified compaction effort at optimum moisture content to reach at least 98% of maximum dry density. Three sets of sample were prepared for each of these tests. The CBR samples were then soaked for 4 days with a surcharge mass of 4.5 kg on top. The swelling of the CBR samples were measured during the 4 days of soaking using a dial gauge supported by a metal tripod. UCS samples were compacted in five layers of predetermined mass in a spilt mold with an internal diameter 100 mm and effective height of 200 mm. To evaluate the effect of curing on mechanical properties of unbound LFS, two extra sets of UCS samples were prepared and cured in a humid chamber with a minimum humidity of 95% and temperature control of 25°C for 7 and 28 days.

Table 1 Chemical composition of LFS.

Chemical compounds	Weight (%)
Fe_2O_3	35.233
CaO	24.899
SiO_2	22.934
MgO	8.633
MnO_2	5.827
Cr_2O_3	0.954
TiO_2	0.498
SO_3	0.498
P_2O_5	0.466
K_2O	0.059
Al_2O_3	non-detected

RESULTS AND DISCUSSION

Chemical composition results of LFS are reported based on 100% normalization of oxide compounds and presented in Table 1.

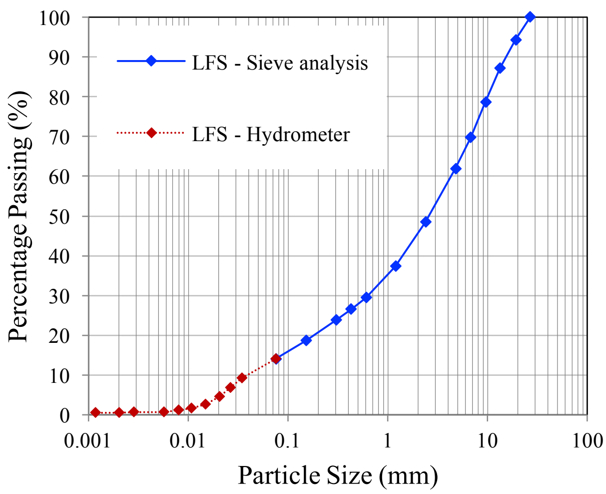

Fig. 2 Particle size distribution plot of LFS.

Table 2 presents the engineering properties of LFS sample. The initial moisture content of sample was measured in a drying oven and found to be less than 2%.

Table 2 Engineering properties of LFS.

Engineering parameters	LFS
Natural moisture content (%)	<2
Clay content (%)	0.5
Silt content (%)	13.5
Sand content (%)	48
Gravel content (%)	38
USCS natation	SM
Organic content (%)	0.5
Particle density: fine (kN/m^3)	3.39
Particle density: coarse (kN/m^3)	3.43
pH	12.2
Flakiness index (%)	30
LA abrasion loss (%)	31
Hydraulic conductivity (m/s)	9.81×10^{-09}
Maximum dry density (Mg/m^3)	2.64
Optimum moisture content (%)	9.2

The organic content value of LFS was found to be very low, possibility due to the high temperatures during the steelmaking process. The both (fine and coarse) apparent densities of LFS were very high, higher than that of typical quarry materials (>2 kN/m^3) and very close to the values previously reported for electric arc furnace slag [23]. The pH values of samples indicate that LFS is alkaline by nature. The flakiness index of LFS was found by separating the flaky particles and was noted to be approximately 30.

Table 3 Strength properties of LFS.

Strength properties	LFS
CBR (%)	156-165
Swell (CBR) (%)	<0.5
UCS_ no curing (MPa)	0.2
UCS_7 days curing (MPa)	0.8
UCS_28 days curing (MPa)	0.9

LFS had a LA abrasion value of 31, which is in the range of the values accepted by state road authority. Hydraulic conductivity of the LFS sample was measured to be 9.81×10^{-09} m/s, which can be labelled as a very low permeable material in accordance with the hydraulic conductivity classification chart presented by Terzaghi et al. [24].

The modified Proctor compaction test results indicated that the LFS had high maximum dry density with relevant optimum moisture content, higher than that of other recycled materials which have been previously used in road applications [23]. The high maximum dry density value can be attributed to very high apparent particle density of the LFS aggregates.

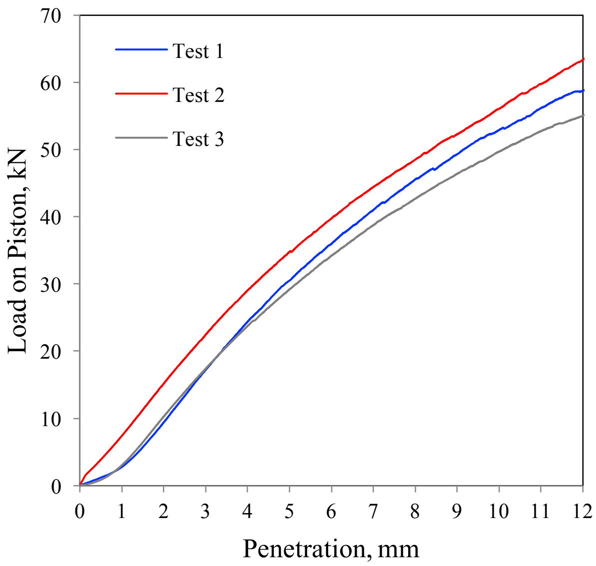

Fig. 3 CBR Load-penetration curve of LFS.

Table 3 present the strength properties of LFS sample. Fig. 3 indicates the load penetration curves obtained from three CBR tests on unbound LFS. The CBR tests were performed after 4 days of soaking condition where the samples believed to be saturated and matric suction is insignificant. The CBR value range of 156% to 165% indicates that the LFS meets the minimum requirement of 80% for typical quarry materials to use in pavement applications [23]. The CBR values for the LFS is higher than of other waste materials such as recycled concrete aggregate, crushed brick and reclaimed asphalt pavement used in road applications [25]. The swell characteristic of the LFS was measured during the soaking condition and it was found to be less than 0.5%.

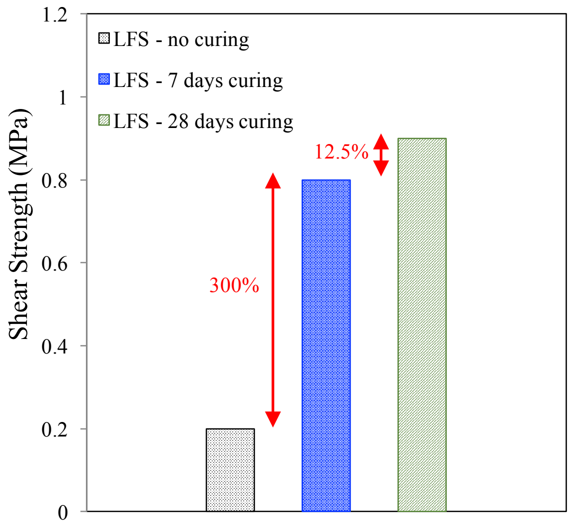

Fig. 4 Development of UCS in LFS with Curing.

The UCS values for unbound LFS with 0, 7 and 28 days of curing were evaluated and the effect of curing time on the UCS value is shown in Fig. 4. Three sets of samples were prepared for each condition and the average UCS value for each condition was individually reported in Table 3. The UCS value of unbound LFS was found to increase considerably with curing time. The significant increase in UCS value was faster and more effective during the first 7 days of curing, which can be attributed to hydration process as chemical bonding develops over time. The curing period was found to play a vital role in the UCS development of unbound LFS samples, which was attributed to the relatively high CaO content of the LFS material.

CONCLUSION

The engineering and geotechnical laboratory evaluation undertaken on LFS to assess the viability of using this by-product in roadwork constructions. The LFS samples were sourced from a steelmaking company in Victoria, Australia. The LFS was classified as silty sand (SM) and particle size distribution plot indicates that the LFS has the potential to be used as pavement materials. LFS was found to be non-plastic with low cohesion and high silt grain size content in the fine fractions.

The durability and LA abrasion loss of LFS aggregates are found to be within the requirements of typical quarry materials used in pavement applications. Natural moisture content and organic content of LFS was found to be very low. Both fine and coarse apparent density of LFS indicate the existence of high quality material and aggregate in LFS sample. The pH value of LFS was measured to be 12.2, which indicates LFS is alkaline by nature.

The LFS was classified as high calcium material due to high lime content, approximately 25% in chemical composition. The modified compaction test indicates that LFS has high maximum dry density value which can be attributed to high apparent particle density. The LFS can be classified as very low permeable material based on hydraulic conductivity test result.

The swelling of the LFS sample was measured during the soaking condition of CBR and it was found to be less than 0.5%. LFS was found to have much high CBR value, higher than of typical quarry materials and other waste materials previously used in base/subbase applications.

The UCS test results indicate that the UCS value of LFS can significantly increase with curing time. The significant increase in UCS can be attributed to high lime content and hydration process as chemical bonding develops over time. The hydration reaction was faster and more effective during the first 7 days of curing.

In term of usage in roadworks application, the engineering properties of LFS were found to be equivalent or even superior to that of typical quarry materials. LFS can be suitable as a construction material for pavement bases/subbase and engineering fills. The reuse of LFS in roadwork applications will significantly reduce the demand of virgin materials and will potentially divert significant quantities of these by-products from landfills and stockpiles.

ACKNOWLEDGEMENTS

The authors would like to thank Harsco Metals & Minerals Asia Pacific (Victoria, Australia) for providing the materials in this study.

REFERENCES

[1]. Arulrajah, A., et al., Spent coffee grounds as a non-structural embankment fill material: engineering and environmental considerations; engineering and environmental considerations. Journal of Cleaner Production, 2014. 72: p. 181-186.

[2]. Brooks, G.A., et al., Developments in the Modelling of Oxygen Steelmaking. Guthrie Symposium Montreal: McGill University, 2011.

[3]. ASA, Membership Annual Survey Results. Wollongong, Australasian (iron & steel) Slag Association Inc., 2014.

[4]. ASA, A Guide to the Use of Slag in Roads. Revision 2. Wollongong, Australasian (iron & steel) Slag Association Inc., 2002.

[5]. Heidrich, C. and A. Woodhead, Benchmarking Report for the Sustainability Victoria Business Partnerships Assessment & Benchmarking Module Wollongong,

Australasian (iron and steel) Slag Association. 2010. p. 22.
[6]. Serjun, V.Z., B. Mirti, and A. Mladenovi, Evaluation of ladle slag as a potential material for building and civil engineering. Materials and technology, 2013. 47(5): p. 543-550.
[7]. Manso, J.M., et al., Ladle Furnace Slag in Construction. Journal of Materials in Civil Engineering, 2005. 17(5): p. 513-518.
[8]. Manso, J.M., et al., The use of ladle furnace slag in soil stabilization. Construction and Building Materials, 2013. 40: p. 126-134.
[9]. EPA, Engineered/structural fill, industrial waste fact sheet, Publication No. 1440. 2012, Environmental Protection Agency of Victoria, Australia.
[10]. AS, Methods for sampling and testing aggregates Method 11: Particle size distribution by sieving, in Australian Standards AS-1141.11. 1996, Standards Australia: NSW, Australia.
[11]. ASTM, Standard test method for particle-size analysis of soils. ASTM Standard D422. 1963, ASTM International: West Conshohocken, PA.
[12]. ASTM, Standard Test Methods for Moisture, Ash, and Organic Matter of Peat and Other Organic Soils. ASTM Standard D2974. 2007, ASTM International: West Conshohocken, PA.
[13]. BS, Method for Determination of Particle Shape; Flakiness Index. British Standard 812-105.1. 2000, British Standard Institution: London, UK.
[14]. AS, Particle density and water absorption of fine aggregate. Australian Standard 1141.5. 2000, Australian Standard: Sydney, Australia.
[15]. AS, Particle density and water absorption of coarse aggregate - Weighing-in-water method. Australian Standard 1141.6.1. 2000, Australian Standard: Sydney, Australia.
[16]. AS, Soil chemical tests—Determination of the pH value of a soil—Electrometric method. Australian Standard 1289.4.3.1. 1997, Australian standard: Sydney, Australia.
[17]. AS, Soil compaction and density tests - Determination of the dry density/moisture content relation of a soil using modified compactive effort. Australian Standard 1289.5.2.1. 2003, Australian Standard: Sydney, Australia.
[18]. ASTM, Standard Test Method for Resistance to Degradation of Small-Size Coarse Aggregate by Abrasion and Impact in the Los Angeles Machine. ASTM Standard C131. 2006, ASTM International: West Conshohocken, PA.
[19]. AS, Soil strength and consolidation tests—Determination of permeability of a soil—Falling head method for a remoulded specimen. Australian Standard 1289.6.7.2. 2001, Australian Standard: Sydney, Australia.
[20]. ASTM, Standard Test Method for CBR (California Bearing Ratio) of Laboratory-Compacted Soils.ASTM-D1883. Annual Book of ASTM Standards, 2007. Vol. 6. 2, ASTM International, West Conshohocken, PA, USA.
[21]. ASTM, Standard Test Method for Unconfined Compressive Strength of Cohesive Soil. ASTM Standard D2166. 2006, ASTM International: West Conshohocken, PA.
[22]. ASTM, Standard Specification for Materials for Soil-Aggregate Subbase, Base, and Surface Courses. ASTM Standard D1241. 2007, ASTM International: West Conshohocken, PA.
[23]. Arulrajah, A., et al., Geotechnical and geoenvironmental properties of recycled construction and demolition materials in pavement subbase applications. Journal of Materials in Civil Engineering, 2013. 25(8): p. 1077-1088.
[24]. Terzaghi, K., R. Peck, and G. Mesri, Soil Mechanics in Engineering Practice. 1996, New York, USA: John Wiley & Sons.
[25]. Arulrajah, A., et al., Physical properties and shear strength responses of recycled construction and demolition materials in unbound pavement base/subbase applications. Construction and Building Materials, 2014. 58: p. 245-257.

TEMPERATURE EFFECTS ON ELASTIC STIFFNESS OF HDPE GEOGRID AND ITS MODELLING

Thitapan Chantachot[1], Warat Kongkitkul[2] and Fumio Tatsuoka[3]
[1,2]Department of Civil Engineering, Faculty of Engineering,
King Mongkut's University of Technology Thonburi, Thailand;
[3]Department of Civil Engineering, Tokyo University of Science, Japan

ABSTRACT

The ambient temperature is one of the important factors that affect the mechanical properties of polymer geosynthetic reinforcement. With an increase in the temperature, the rupture strength and the elastic stiffness decrease. In this study, to understand the temperature effects on the load-strain-time behaviours of a polymer geogrid, a series of tensile loading tests were performed on a high-density polyethylene (HDPE) geogrid at different but constant temperatures, and also under step-increasing temperature conditions. The test results indicated that the elastic stiffness of tested geogrid increases with the load level, while decreases with the ambient temperature. These properties were modelled based on the framework of hypo-elasticity. An existing non-linear three-component (NTC) model, which can simulate the load-strain-time behaviours of many types of polymer geogrid subjected to arbitrary loading histories (e.g., monotonic loading at different rates, creep, load relaxation) under a constant temperature, was modified to account for the dependency of the elastic stiffness on the load level and the temperature, as well as the dependency of the rupture strength on the temperature. The modified model can simulate very well the observed temperature effects on the elasticity of the tested geogrid.

Keywords: Elastic stiffness, Geogrid, Non-linear three-component model, Temperature

INTRODUCTION

A number of different types of polymer geosynthetic reinforcement are used as reinforcements for various geotechnical engineering structures (e.g., slope, embankment, and retaining wall). Typically, constructions of these structures utilising geosynthetic reinforcements are faster and more cost-effective than ordinary conventional methods. In design of a geosynthetic-reinforced soil (GRS) structure, it is required to know the mechanical properties of a given geosynthetic reinforcement, especially the rupture tensile strength. However, the rupture tensile strength is usually determined by an ambient temperature condition that is controlled constant throughout a test (equal to 20 ºC following ASTM D4595 and EN ISO 10319) [1]-[2].

On the other hand, air-temperature cyclically changes both daily and seasonally. This variation of air-temperature affects the ambient temperature of backfill in a GRS structure, and thereafter, the geosynthetic reinforcements arranged inside [3]. From field monitoring of a GRS structure, changes of air-temperature were found to correlate with the geogrid strains arranged inside [3]-[4]. Moreover, effects of temperature rise on the load-strain-time behaviours of geosynthetic reinforcements were also studied in the laboratory. It was found that not only the rupture strength but also the pre-peak stiffness and the elastic stiffness decrease with an increase in the temperature [5]-[8]. Therefore, the study of temperature effects on the load-strain-time behaviours of geosynthetic reinforcements is important.

To simulate the rate-dependent behaviours of geosynthetic reinforcements (i.e., monotonic loading at different but constant strain rates, creep, and load relaxation), an elasto-viscoplastic non-linear three-component (NTC) model was proposed [9]. Subsequently, the NTC model was modified to simulate temperature-accelerated creep tests by taking into account the effects of temperature increase on the rupture tensile strength and stiffness of geosynthetic reinforcement [10]. The simulation results indicated that the NTC model is capable of simulating both rate- and temperature-dependent behaviours. However, in this previous study, the elastic stiffness was treated unaffected by the temperature rise, and validation of the model with experimental data has not been performed.

In view of the above, in this study, a series of tensile loading tests were performed to evaluate effects of temperature and load/temperature history on the elastic stiffness of a HDPE geogrid. Then, the NTC model was modified to realistically simulate the test results by incorporating the dependency of the elastic stiffness on the temperature.

ELASTIC STIFFNESS AS A FUNCTION OF LOAD LEVEL AND TEMPERATURE

To determine the elastic stiffness, k_{eq} , of a geosynthetic reinforcement, small-amplitude unload-reload cyclic loading tests have been performed on many types of geogrid [7]. Then, the following formulations of dependency of k_{eq} on the load level and the temperature was proposed:

$$k_{eq} = k_{eq0}(T)\left(\frac{V}{V_{max}}\right)^{m} \tag{1}$$

$$k_{eq0} = p'\left(A^{f'}\right)^{q'} \tag{2}$$

where: $k_{eq0}(T)$ is the value of k_{eq} when V/V_{max} = 1; V/V_{max} is the load level, defined as ratio of the tensile load, V , to the maximum tensile load at respective ambient temperature, V_{max} ; m , p' and q' are the material constants, depending on types of polymer geosynthetic reinforcement; and $A^{f'}$ is the temperature effect parameter, defined as ratio of the rupture strength at a given temperature to the rupture strength at standard temperature of 20 °C. Note that rupture tensile strength is defined for a strain rate at rupture equal to 0.1 %/min.

TEST MATERIAL AND PROGRAMME

In this study, to determine the elastic stiffness and the temperature effect parameter, a series of special tensile loading tests were performed on a high-density polyethylene (HDPE) geogrid, employing the following two different loading patterns: i) continuous monotonic loading (ML) until the rupture; and ii) sustained (creep) loading (SL) applied during otherwise ML until rupture. A constant load rate of 0.6 kN/m/min was used for ML in both loading patterns i) and ii). In loading pattern ii), ML was first performed until achieving the specified tensile load and then SL was held for three hours, after which another ML was restarted until the rupture. The ambient temperature surrounding the test specimen was controlled constant throughout a test at either 30, 40 or 50 °C by means of a temperature-controlled chamber [7].

TEST RESULTS AND DISCUSSIONS

Temperature Effect Parameter

The relationships between tensile load, V , and tensile strain, ε , obtained from ML tests at different but constant temperatures are shown in Fig. 1. In these tests, any rupture was not observed at the ends of test (denoted by symbol "+"), due to a limited maximum stroke of the tensile loading machine. Therefore, the rupture tensile strengths were defined at the points of maximum curvature along the respective V - ε relations (denoted by symbol "×"). Then, these values were corrected to the values at the same strain rate (0.1 %/min) to eliminate the effects of strain rate on the tensile rupture strength of geosynthetics [7]. The values of corrected rupture strength are summarised in Table 1. It can be seen that with the increasing temperature, the rupture strength decreases.

Figure 2 shows a relationship between the temperature effect parameter, $A^{f'}$, and temperature. The value of $A^{f'}$ is unity at the standard temperature, T_0' , of 20 °C. The procedures to determine the $A^{f'}$ value are explained in details in Kongkitkul *et al.* (2012) [7]. It can be seen that the $A^{f'}$ value decreases from unity at T_0' = 20 °C to a smaller value at a higher temperature. Thus the reduction of rupture tensile strength with the increasing temperature of HDPE geogrid can be described by Eq. (2), which incorporates $A^{f'}$.

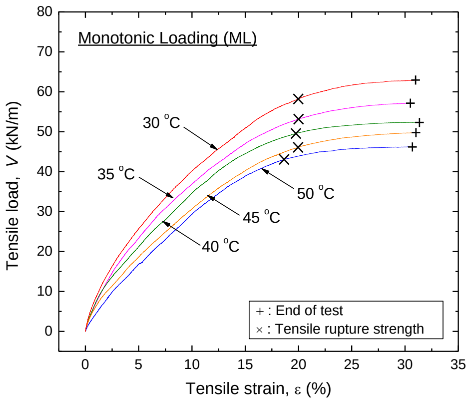

Fig. 1 Tensile load-tensile strain relations from continuous ML tests under different constant temperatures

Table 1 Rupture strength under different constant temperatures

Temperature (°C)	Rupture strength (kN/m)
30	53.2
35	48.1
40	44.9
45	41.8
50	38.9

Note: rupture strength was defined for a strain rate at rupture equal to 0.1 %/min

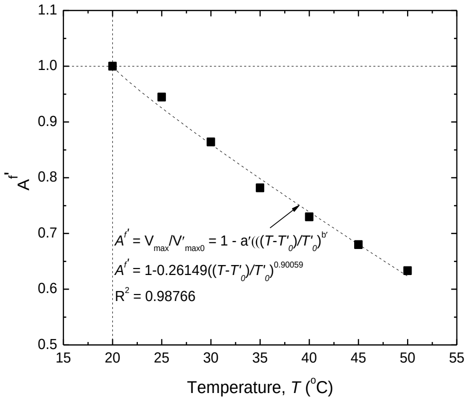

Fig. 2 Temperature effect parameter, $A^{f'}$, as a function of temperature

Elastic Stiffness

Determination of elastic stiffness

Figures 3(a) to 3(c) show the V - ε relations of the HDPE geogrid by SL under different temperatures equal to 30, 40, and 50 °C, respectively. In these figures, SL tests were performed at different tensile load levels, V/V_{max}. The values of V_{max} at respective temperature are shown in Table 1. It can be seen that V - ε relation of the geogrid exhibits a very high stiffness, close to the elastic value when ML was restarted following SL [9]. Therefore, in this study, the elastic stiffness was determined from a linear relation fitted to the initial V - ε curve after the restart of ML following SL, as shown in Fig. 4.

Effects of load level and temperature on elastic stiffness

Figure 5(a) shows the elastic stiffness, k_{eq}, versus load level, V/V_{max}, relations in the full-log plot of HPDE geogrid for different temperatures. The linear lines fitted to the data points for respective temperatures represent Eq. (1). It is readily seen that k_{eq} increases significantly with an increase in the load level, while drastically decreases with an increase in the temperature. These behaviours indicate that the k_{eq} values of HDPE geogrid exhibit a combination of the hypo-elasticity and the degradation by temperature effects.

The behaviours of k_{eq} determined by the method used in the present study are similar to those reported by Kongkitkul *et al.* (2012) [7], in which the k_{eq} values of the same HPDE geogrid were determined by measuring the slope of V - ε relations during small-amplitude cyclic loadings. Equation (1) was used to best fit to the k_{eq} -V/V_{max} data points obtained in this study (Fig. 5(a)). It can be seen that the linear lines fitted to the data points from the present study are consistent very well with the data points from Kongkitkul *et al.* (2012) [7]. In Fig. 5(b), the k_{eq0} values according to Eq. (1) obtained from the fitted relations shown in Fig. 5(a) were plotted against

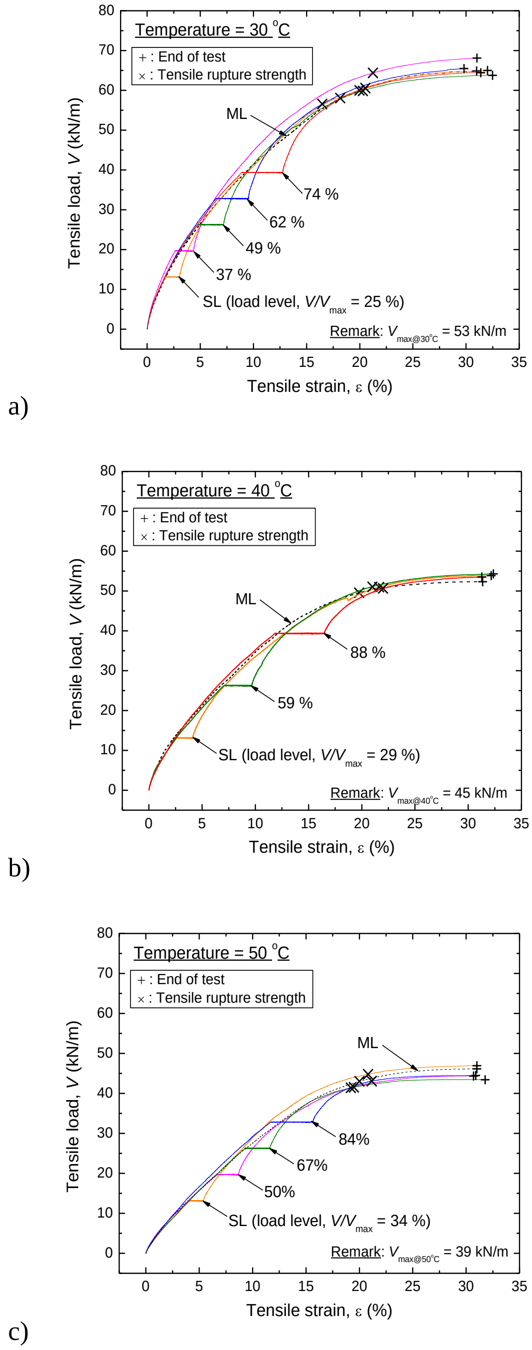

Fig. 3 Tensile load-tensile strain relations from SL tests during otherwise ML under different temperatures of: (a) 30 °C; (b) 40 °C; and (c) 50 °C

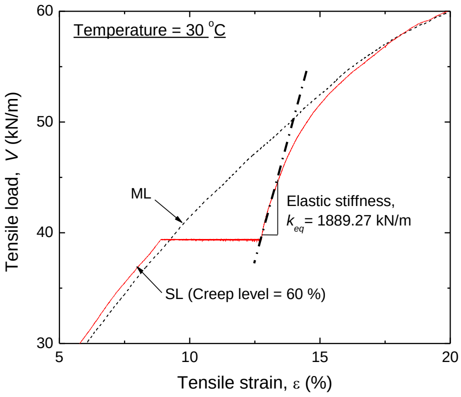

Fig. 4 Determination of elastic stiffness from V - ε relation immediately at the restart of ML following SL

the $A^{f'}$ values for the respective temperatures obtained from Fig. 2. Then, Eq. (2) was fitted to the plotted k_{eq0} and $A^{f'}$ data from the present study. It may be seen that the fitted curve is also in good agreement with the data points from Kongkitkul *et al.* (2012) [7].

MODELLING OF ELASTIC PROPERTIES

Non-linear Three-component Model

For realistic simulation of the load-strain-time behaviours of polymer geosynthetic reinforcements under a constant temperature, an elasto-viscoplastic non-linear three-component (NTC) model was developed [9]. This NTC model consists of elastic, inviscid, and viscous components. In the elastic component, elastic strain rate, $\dot{\varepsilon}^e$, is determined by an hypo-elastic model having the elastic modulus, $k_{eq}(V)$, that is a function of instantaneous tensile load, V:

$$\dot{\varepsilon}^e = \dot{V} / k_{eq}(V) \tag{3}$$

On the other hand, with an increase in the temperature, T, the $k_{eq}(V)$ value at a given load level decreases (Fig. 5(a)). To take into account the coupled effects of load level, $V/V_{\max}$, and temperature, T, on elastic stiffness, $k_{eq}(V,T)$, the NTC model was modified as follows. Figure 6 shows the method to obtain the current elastic stiffness from the current temperature, T, the current tensile load V, and a known rupture strength at T_0' = 20 ºC, $V'_{\max 0}$. By implementing the algorithm shown in Fig. 6 into the modified NTC model, the realistic current elastic stiffness can be easily determined.

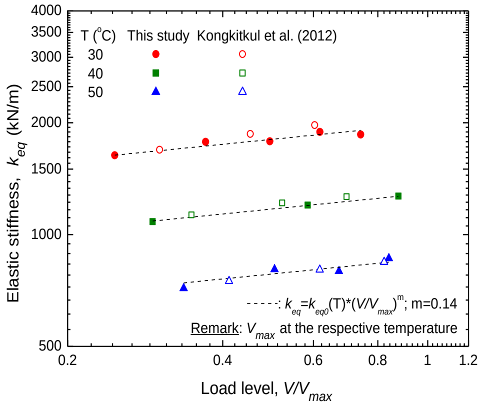

a)

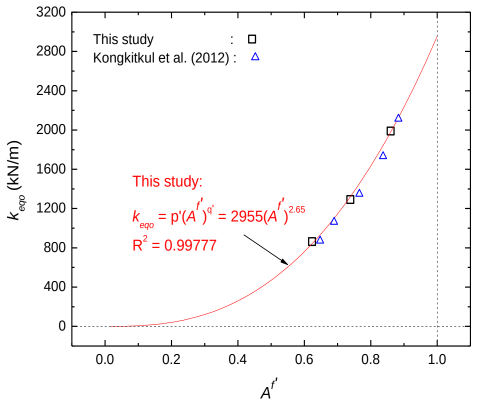

b)

Fig. 5 Elastic stiffness as a function of load level and temperature: (a) k_{eq} - $V/V_{\max}$ relations; and (b) k_{eq0} - $A^{f'}$ relation

Simulation Results

The V - ε relations from continuous ML tests at different constant temperature are presented in Fig. 7(a), while those from tests in which SL was performed during otherwise ML (as those shown in Fig. 7(a)) are presented in Fig. 8 (a). Figures 7(a) and 8(a) compare these experimental results and their simulations. It can be seen that the modified NTC model can simulate very well the measured V - ε relations for various load/temperature histories. The dependency of k_{eq} on the load level and temperature can be seen very well from the tensile load, V, versus the elastic tensile strain, ε^e, relations shown in Figs. 7(b) and 8(b). The tangential slope of V - ε^e relation is equal to the current k_{eq} value. It can be seen from Fig. 7(b) that, at any given V value, the k_{eq} value decreases with an increase in the temperature. On the other hand, at the same temperature, the k_{eq} value increases with an increase in V. This result indicates that the modified NTC model can successfully simulate the coupled effects of load level and temperature on the elastic stiffness.

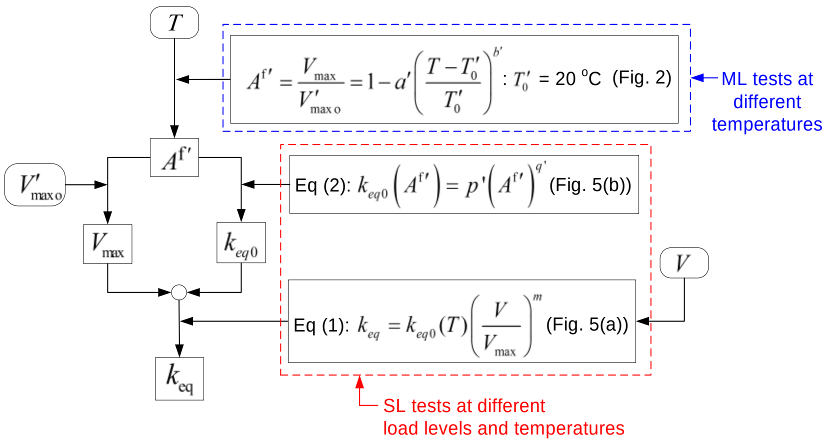

Fig. 6 Diagram to obtain the current elastic stiffness value (modified from Kongkitkul et al., 2012)

The experimental and simulation results described above are obtained under the conditions of constant temperature. To further examine the capability of the modified NTC model, a series of tests in which the temperature was increased during SL from 30 ºC at the start of SL to 50 ºC at the end of SL was performed. Then, the results of these tests and their simulations are presented and compared in Fig. 8(a). Figure 8(b) compares the simulated V - ε^e relation for the SL test in which the temperature was increased from 30 ºC to 50 ºC during otherwise ML with the simulated V - ε^e relations in continuous ML tests during which a SL was performed at an intermediate load level under different constant temperatures of 30, 40, and 50 ºC. It can be readily seen that the V - ε^e states during SL tests under either constant or varying temperature do not move as the tensile loads are kept constant. As a result, the entire V - ε^e relation from the origin to the end of an intermission of ML by SL under the constant temperature condition does not change like obtained by a continuous ML test at a constant temperature. On the other hand, upon the restart of continuous ML at an elevated temperature (i.e., 50 ºC) after a SL test during which the temperature increases from 30 ºC to 50 ºC, the V - ε^e relation starts from a point along the V - ε^e relation from the continuous ML at a constant temperature of 30 ºC while exhibiting a drastic decrease in the slope to the one of the V - ε^e relation from the continuous ML at a constant temperature of 50 ºC, as shown in Fig. 8(c).

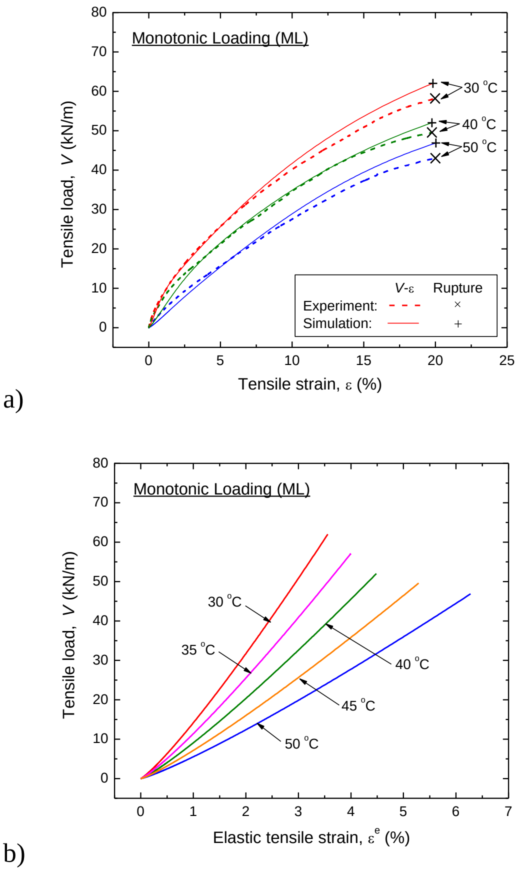

Fig. 7 Behaviours in continuous ML tests under different temperatures: (a) measured and simulated V - ε relations; and (b) simulated V - ε^e relations

CONCLUSIONS

The following conclusions can be derived from the experimental and simulation results that observed in this study:

1. Rupture tensile strength of the tested HDPE geogrid decreases with an increase in the temperature.
2. Elastic stiffness increases with an increase in the load level, while decreases with an increase in the temperature. These trends of behaviour can be expressed by the coupled functional forms proposed in this study.
3. The modified NTC model can well-simulate the variation of elastic stiffness, as a result of the coupled effects between the load level and the temperature

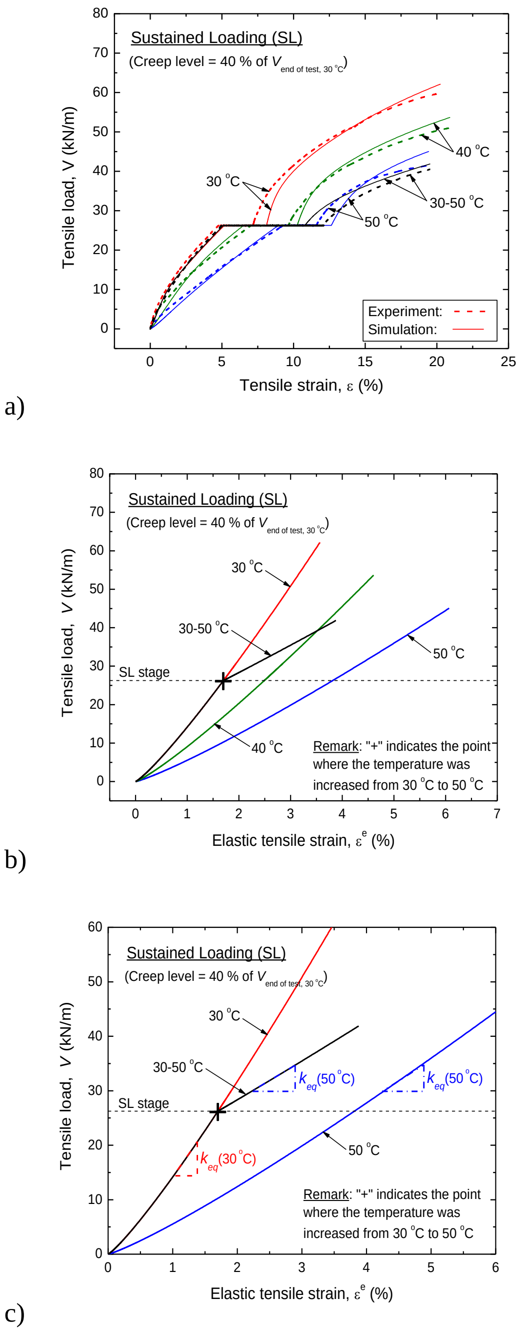

Fig. 8 Behaviours in continuous ML tests with intermediate SL under different temperatures: (a) measured and simulated V - ε relations; (b) simulated V - ε^e relations; and (c) zoom-up of Fig. 8(b)

ACKNOWLEDGEMENTS

The authors are grateful to the National Research Council of Thailand (NRCT), the Commission on Higher Education, the Thailand Research Fund (TRF) and the National Research University (NRU) Project for financial support. Thanks are also extended to Vigor Merger Co., Ltd who provided geogrids for this study.

REFERENCES

[1] ASTM International, "ASTM D4595-Standard Test Method for Tensile Properties of Geotextiles by the Wide-Width Strip Method", 2011.

[2] International Organization for Standardization, "EN ISO 10319-Geosynthetics-Wide-Width Tensile Test", 2008.

[3] Fannin RJ, "Long-term variations of force and strain in a steep geogrid-reinforced soil slope", J. of Geosynthetics International, Vol. 8, Aug. 2001, pp. 81-96.

[4] Tatsuoka F, Tateyama M, Koda M, Kojima K, Yonezawa T, Shindo Y, and Tamai S, "Research and construction of geosynthetic-reinforced soil integral bridges", accepted, 2016.

[5] Zornberg JG, Byler BB, and Knudsen JW, "Creep of geotextiles using Time-Temperature Superposition methods", J. of ASCE, Vol. 130, Nov. 2004, pp. 1158-1168.

[6] Hsieh C, and Tseng YC, "Tensile creep behavior of a PVC coated polyester geogrid at different temperatures, J. of GeoEngineering, Vol. 3, Dec. 2008, pp. 113-119.

[7] Kongkitkul W, Tabsombut W, Jaturapitakkul C, and Tatsuoka F, "Effects of temperature on the rupture strength and elastic stiffness of geogrids", J. of Geosynthetics International, Vol. 19, Apr. 2012, pp. 106-123.

[8] Stępień S, and Szymański A, "Influence of strain rate on tensile strength of woven geotextile in the selected range of temperature", Studia Geotechnica et Mechanica, Vol. 37, Dec. 2015, pp. 57-60.

[9] Hirakawa D, Kongkitkul W, Tatsuoka F, and Uchimura T, "Time-dependent stress-strain behaviour due to viscous properties of geogrid reinforcement", J. of Geosynthetics International, Vol. 10, Dec. 2003, pp. 176-199.

[10] Kongkitkul W and Tatsuoka F, "A theoretical framework to analyse the behaviour of polymer geosynthetic reinforcement in temperature-accelerated creep tests", J. of Geosynthetics International, Vol. 14, Feb. 2007, pp. 23-38.

Sixth International Conference on Geotechnique, Construction Materials and Environment, Bangkok, Thailand, Nov. 14-16, 2016, ISBN: 978-4-9905958-6-9 C3051

EVALUATION OF DIFFERENT FIBER REINFORCED MORTAR AS RETROFITTING MATERIALS FOR RC COLUMNS

Bernardo A. Lejano[1]
[1]Faculty, De La Salle University, Philippines

ABSTRACT

This study is about the use of fiber reinforced mortar (FRM) as a jacketing material for reinforced concrete (RC) columns. Presented in this paper are analyses of the test results of destructive-loading that were conducted to explore the applicability of different jacketing materials as retrofit to RC columns. The jackets used to wrap RC columns were built of mortar mixed with different fibers. The fibers considered were steel fibers and polymer fibers. A simple model based on material properties was used to simulate the axial strength of the columns. The numerical model calculation results as well as the experimental test results were used to assess the performance of the jacketing materials used. The experimental part consisted of testing two sets of column specimens. The first set is wrapped with mortar jackets reinforced with steel fibers and the second set is wrapped with mortar jackets reinforced with polymer fibers with and without fly ash. The efficacy of the different FRM jackets as retrofitting materials was assessed by calculating the effect of confinement. The calculation was accomplished by measuring the maximum load of the retrofitted columns with jackets and then subtracting the load that can be carried by the control specimens, that is, the column with the original cross section. The confining effect was used as the basis in determining the confined compressive strength of concrete and then used to establish a model that can simulate the axial strength of the columns. The results indicate that the FRM jackets are effective as retrofitting material for RC column.

Keywords: Fiber Reinforced Mortar, RC Column, Retrofitting, Confining Effect, Axial Strength, Jacketing

INTRODUCTION

Columns are primarily structural members of a building that should not fail because failure of even one of these columns could result to the collapse of the whole structure. When columns show some sign of weakness, retrofitting is needed. Example to this are aged reinforced concrete (RC) columns, which usually are in need of retrofitting so as to compensate for the lost strength due to various environmental factors. Other reasons why RC columns need rehabilitation are concrete deterioration, unexpected increase in load, or physical damage. Retrofitting may be done by encasing the column with certain material. This retrofitting technique is termed as jacketing. This is the usual solution to fix deteriorated or damaged columns caused by environmental hazards like fire, seismic event, or differential upheaval of the foundation because of expansive clay soil [1].

Jacketing using steel plates is the usual method of retrofitting columns. While it is popular because of its simplicity, efficiency, and effectiveness, it also has its criticisms. Aside from being expensive, another disadvantage is that it may produce larger earthquake forces because it is heavy. Studies [2], [3] have shown that fiber reinforced polymer (FRP) sheet is a good alternative to steel plates. This material is very light, does not corrode and very easy to install. However, it is still very expensive.

As another option steel plates and FRP sheets, jackets made of fiber reinforced mortar (FRM) are investigated in this study. This idea complements other studies [4]-[6] that fiber reinforcement can increase the strength, ductility and toughness of concrete. Even the use of recycled carpet fibers have been used as fiber reinforcement to concrete [7].

The study of Valerio *et al*. [8] recommended Steel Fiber Reinforced Mortar (SFRM) as another option of retrofitting material for RC columns. Their study showed improvement in the load that can be carried by the RC column after it is retrofitted with SFRM. However, they reported that using steel fibers has a down side. Since the fibers were stiff and cannot bend, it is difficult to place and distribute them in the column corners. This resulted to failure of the retrofitted columns initiated by the propagation of cracks at the column corners.

Considering the problem stated above, an alternative to steel fibers was proposed by Oropel *et al*. [9]. Polymer Fiber Reinforced Mortar (PFRM) was used as jacketing material instead of steel fibers because they are more flexible and can be easily placed at the column corners. Moreover, aside from being light, these fibers are resistant to corrosion. Two types of polymer fibers were used, synthetic and cellulose fibers.

This paper focuses on the simulation of the load-carrying capacity of the above-mentioned jacketing materials (SFRM and PFRM). Previous work of the author [10] reported test results on the use of similar retrofitting materials but lacks the model to simulate the behavior of RC columns retrofitted with jackets. This paper attempts to provide a simple model that can predict the axial strength of RC columns retrofitted with FRM jackets once the confinement effect is determined.

CONCEPTS OF RETROFITTING USING FRM

The usual repair of RC column is done by removing the damaged or deteriorated concrete and substituting it with new concrete. To improve its strength, it may be encased with layer (or jacket) of mortar or shotcrete [10]. The effect of the jacket is two-fold, it enlarges the cross-section of the column and it provides confinement to the original core concrete. In this study, the load is applied only to the original section such that the effect of the enlargement of the section may not apply. Hence, only the confinement effect will be emphasized in this study. However, it may not be denied that the section enlargement may have an effect because of the redistribution of stresses.

Confinement Effect

When a material is subjected to axial compression, it would be accompanied by transverse tensile deformation. If this transverse deformation is restrained, it would result to higher axial resistance of the material. This phenomenon is the same for concrete and is termed as the confinement effect. In RC columns, the steel ties or hoops usually provide the partial restrain of the transverse deformation resulting to the confinement of the core concrete. This usually results to an increase in the axial strength of the column. In addition, the hoops avert the concrete expansion and prevent tensile cracking in concrete. Hence, considerable improvement in ductility is usually observed [3].

In retrofitted RC columns, the jackets provide the same confinement effect as mentioned above. To provide adequate confinement the jacket must have enough tensile strength. For this reason, the mortar jacket is reinforced with fibers.

Material Selection

The choice of suitable material is an important factor in deciding the retrofitting technique to be used. The material must match with the RC column and must be easy to install. Prospective clients for retrofitting jobs would usually want something that is economical and that would not drastically impair the use or occupancy of the structure. Reinforced mortar jacket is an ideal material for this job.

To make the mortar jacket suitable as retrofitting material, it must possess the following qualities: low drying shrinkage, fast strength development, and excellent crack resistance. These qualities of mortar may be attained by reinforcing it with fibers. Moreover, shorter fiber reinforcement may be desirable because it can be made into a thinner layer of repair [6]. However, the above mentioned qualities of mortar jacket must be maintained.

One of the materials examined in this study is the Steel Fiber Reinforced Mortar (SFRM) jacket. Mortar was mixed with steel fibers to increase its tensile strength. The steel fibers used in this study have the following properties: unit weight is 19g, length is 50mm and diameter is 0.75mm. Photos of the steel fibers are shown in Fig. 1.

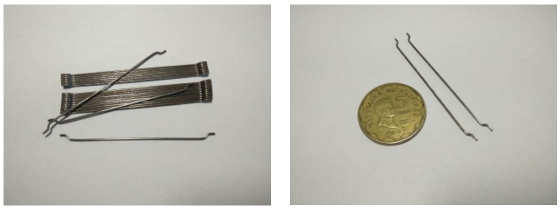

Fig.1 Picture of steel fibers (left) and comparison of a steel fiber with Phil. 5 peso coin (right)

The other material examined in this study is the Polymer Fiber Reinforced Mortar (PFRM). The two polymer fibers used were the synthetic fibers and the cellulose fibers. These fibers were expected to provide the same increase in tensile strength of concrete as steel fibers provided, but more flexible.

The synthetic fibers are especially engineered copolymer fibers designed as substitute to the steel reinforcement in concrete floors on grade and pavements. They are also used as reinforcement in precast concrete products with strength up to 35 MPa. As can be seen in Fig. 2, the size and shape of synthetic fibers suggest that it can be used as substitute for steel fibers. The dosage used is 2.5 kg per cubic meter of mortar [9].

Fig. 2 Pictures of synthetic fibers (left) and cellulose fibers (right)

As shown in Fig. 2, the cellulose fibers appear first as blocks but disperse evenly into concrete as micro fibers after contact with water. Approximately 1500 million crack-fighting micro fibers are produced per kg of concrete on a dosage of 2 bags per cubic meter of concrete. These cellulose fibers have excellent bond with cement resulting to decrease in plastic shrinkage cracking. They also tend to make the concrete denser. The same effects are expected in mortar, hence improving the strength of mortar jacket [9]. In addition, the cellulose fiber is alkali resistant and allows better surface finishing.

EXPERIMENTAL PROGRAM

Several RC column specimens were made and subjected to destructive testing to evaluate their efficacy as retrofitting materials. In this study, 4 cases were studied for the columns with SFRM jacket (referred to as SFRM series). This includes the control specimens (without jacket), and specimens with mortar jackets containing 1%, 2%, and 3% steel fibers by volume. This resulted to 3 control column specimens and 9 column specimens with SFRM jacket. (Refer to Table 1). Sakthivel *et al.* [4] investigated concrete with almost the same steel fiber volume range.

Table 1 Construction details of specimens

	SFRM Series	PFRM Series
Retrofitting material	Mortar w/ Steel Fiber	Mortar w/ Polymer Fiber
Original column size	120x120x300 $Ac=14400mm^2$	180x180x400 $Ac=32400mm^2$
Concrete cover	20 mm	40 mm
Main rebars	4 – 10 mmϕ	4 – 10 mmϕ
Tie diameter	8 mm	8 mm
Tie spacing	160 mm	160 mm
Mortar jacket thickness	20mm	10mm
Different cases (Each case has 3 column specimens)	1) control 2) 1% SFRM 3) 2% SFRM 4) 3% SFRM	1) control 2) mortar 3) Synthetic 4) Cellulous 5) Syn. w/ FA 6) Cel. w/ FA

There were 6 cases that were studied for columns with polymer FRM jackets (referred to as PFRM series). The 1st case is the control specimens without jacket, the 2nd is with mortar jacket, the 3rd is with synthetic FRM jacket, the 4th case is with cellulose FRM jacket, 5th is with synthetic FRM jacket mixed with fly ash (FA), and the 6th case is with cellulose FRM jacket mixed with fly ash. This resulted to 12 column specimens with PFRM jacket, 3 column specimens with mortar jacket, and 3 control specimen (without jacket). (Refer to Table 1)

Shown in Table 1 are the construction details of the RC column specimens. All columns were tied RC columns with square cross-section. The details of the dimension and reinforcement are shown in Fig. 3 and Fig. 4. Although the details shown are for column specimens of PFRM series, the other series were constructed in similar manner with slight variation only in the size of the cross section and the jacket thickness. Furthermore, the ties are the same for all column specimens justifying the assumption that the magnitude of its confinement effect (if there is any) is the same for all column specimens.

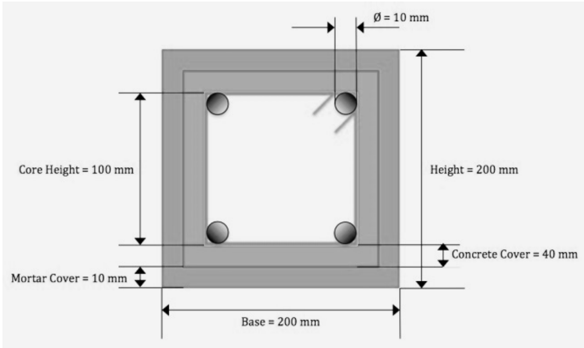

Fig. 3 Typical cross-section of column specimen with PFRM jacket

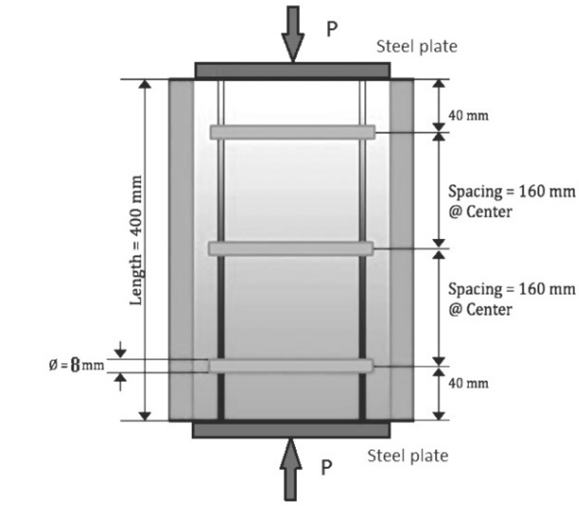

Fig. 4 Typical side-section of column specimens with PFRM jacket

Axial load was applied through steel plates, as shown in Fig. 4, to ensure that the force is applied only to the original cross-section of the column specimen. This is done to simulate the possible actual condition at the ends of the columns. Due to difficulties in application of the mortar at the column ends, the jacket cannot be ensured to be in full contact with the other connected members of the structure at the column ends resulting to ineffective transmission of the axial load through the jacket cross-section.

TEST RESULTS

The results of strength tests of concrete, mortar with fibers, and steel reinforcing bars are tabulated in Table 2. It can be seen that the compressive strength of mortar increased with the addition of fiber. However, the introduction of fly ash in the PFRM series resulted to the decrease in strength. Fly ash was introduced because it was thought to improve the performance of mortar. However, the result was contrary as indicated in the mortar strength test results shown in Table 2. It is not clear why the fly ash did not perform as expected, but it may have something to do with its proportion to the mix. In this study, fly ash was used as 30% replacement to cement.

Table 2 Strength of concrete, mortar, and steel

Material	SFRM series	PFRM series
Concrete, fc'	21.0 MPa	21.5 MPa
Mortar fc' (MPa)	15.2 (0%SF)	18.2 (No Fiber)
	19.2 (1%SF)	23.7 (Synthetic)
	18.6 (2%SF)	21.8 (Cellulose)
	17.6 (3%SF)	20.8 (Syn. w/ FA)
		16.4 (Cel. w/ FA)
Steel, fy	388 MPa	378 MPa

The average maximum recorded axial force (P_{max}) is used as the basis of comparison of these retrofitting materials. It was observed that when the strain reached 0.003, the maximum load was already attained. Tabulated in Table 3 are average maximum loads (P_{max}) for each case investigated.

Table 3 Average maximum load of the columns

Series	Case	P_{max} (kN)	% Increase in P_{max}
SFRM	Control	369.5	0.0
	1% SFRM	401.5	8.7
	2% SFRM	437.9	18.5
	3% SFRM	390.4	5.7
PFRM	Control	697.8	0.0
	Plain Mortar	673.7	-3.5
	Synthetic	894.7	28.2
	Syn. w/ FA	853.2	22.3
	Cellulose	794.3	13.8
	Cel. w/ FA	730.2	4.6

The increase in P_{max} (expressed in %) of each retrofitted column is obtained with respect to the P_{max} of the control specimens of the series. The largest increase in strength is 28.2%. This is for the case of synthetic PFRM jacket. For SFRM series, the maximum increase is 18.5%, which was obtained at 2% steel fiber reinforcement.

It is interesting to note that there is no significant increase in P_{max} when plain mortar jacket was used. This means that enlargement of the section due to mortar jacket did not contribute to the strength increase of the column. Also, it seems that the ties did not provide significant confinement. This was also observed by other research [11] when the tie spacing is medium to large. Furthermore, the introduction of fly ash to the mortar mix did not result to a better jacket.

Shown in Fig.5 are pictures showing the difference in the crack patterns between column with PFRM jacket and column with SFRM jacket, at the final failure. It can be seen that cracks are more scattered in the PFRM series while cracks are concentrated in the corner of the column with SFRM jacket. Since it is difficult to place the steel fibers in the corners of the SFRM jacket, the corners may be considered as zone of weakness.

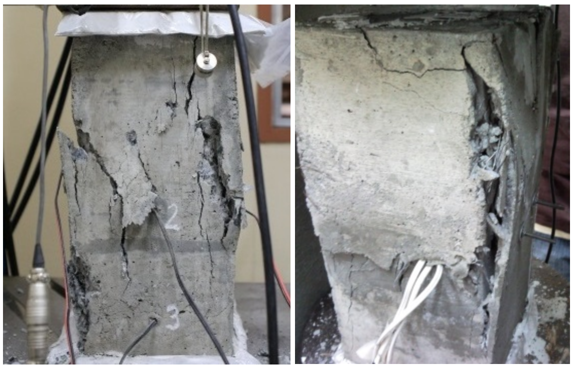

Fig. 5 Comparison of cracks of column with PFRM jacket (left) and with SFRM jacket (right)

ANALYSIS OF DATA

The load that can be carried by control specimens (columns without jacket) may be expressed as Eq. (1). Considering the nominal or maximum loads obtained from tests, the load-carrying efficacy of concrete (represented by α) may be calculated. The results are shown in Table 4. It can be seen that the values obtain for α is very close to the 0.85 value that is commonly used in design formulas.

$$P_{max} = \alpha \ fc' Ac + fy \ As \quad (1)$$

Table 4 Efficacy of concrete, α

Type	P_{max} (kN)	α fc'Ac (kN)	fy As (kN)	α
SFRM	369.5	302.4	121.9	0.82
PFRM	697.8	696.6	118.8	0.83

Simulation Using a Simple Model

To simulate the behavior of columns a simple model is used based on the stress-strain relationships of the materials. Shown in Fig. 6 is the stress-strain curve of concrete and steel. For concrete (shown as solid line in Fig. 4), the exponential stress-strain curve developed by Lejano [12] was used as a constitutive model for concrete. The equation for the ascending branch of the stress-strain curve of this model is shown in Eq. (2). The descending branch is linear from peak stress up to the ultimate strain of 0.003.

$$fc = fc'\left[1-\left(\left(\varepsilon_p-\varepsilon\right)/\varepsilon_p\right)^b\right] \tag{2}$$

Where fc = stress of concrete at strain (ε), fc' = compressive strength of concrete, ε_p = strain at peak stress = 0.0018 + 0.00001 fc', and b = 2 -0.0125 fc'.

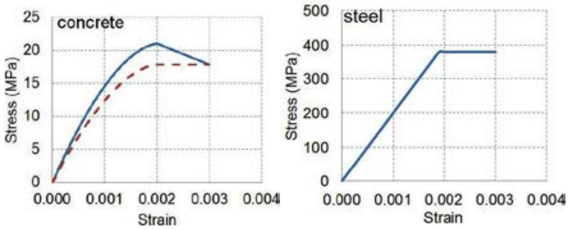

Fig. 6 Stress-strain curve of concrete and steel rebar

For steel, the relationship is simply elastic-plastic model. The steel stress (fs) is linear and proportional to the strain at the ascending branch, and become fully plastic after the yield point, that is, fs=fy.

Using these stress-strain relationships, the axial force (P) at any particular strain of the control column specimens may be calculated by changing Eq. (1) into Eq. (3). Note that α is multiplied to fc up to the peak stress and afterwards the stress is maintained constant, as shown in the dashed curve in the stress-strain curve of concrete in Fig. 6.

$$P = \alpha \ fc \ Ac + fs \ As \tag{3}$$

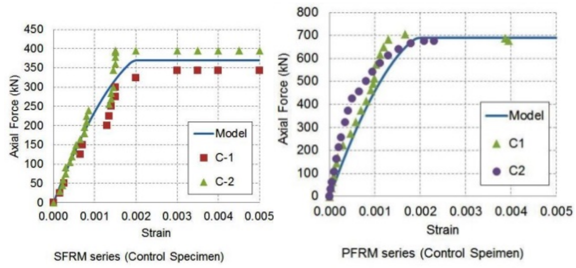

Fig. 7 Comparison of model with test data of control column specimens

The calculation results using this model are compared to the experiment results and are shown in Fig. 7. It can be seen that relatively good agreement is obtained between the calculation and the experiment results. Using this model, the calculated P_{max} are 369.9 kN and 690.0 kN for the control specimens of SFRM series and PFRM series, respectively. These are very close to the test results.

Calculation of Confinement Effect

As indicated by test results, there is no significant increase in axial force because of the enlargement of the section due to the jacket. In fact, if one tries to include the axial force carried by the jacket, the result would be very much greater than the experimentally obtained P_{max}. Hence, the increase in axial force may be concluded to be due to the confinement effect only of the jackets. The axial force due to confinement (which is termed as confinement effect) may be obtained by subtracting the calculated strength of the control column specimen from the experimentally observed P_{max}. This results to Eq. (4), where C_f is the confinement effect.

$$C_f = P_{max} - \left(\alpha \ fc' \ Ac + fy \ As\right) \tag{4}$$

The confinement effect is evaluated for all column specimens. The results are shown in Table 5. By dividing C_f by the force resisted by the concrete, that is, αfc'Ac, then the increase in fc' may be determined. This increase in fc' is denoted as λ and is shown also in Table 5.

Table 5 Confinement Effect and increase in compressive strength of concrete

Case	C_f (kN)	λ = Inc. in fc' (%)
Control	-0.4	-0.2
1% SFRM	31.6	12.8
2% SFRM	68.0	27.4
3% SFRM	20.5	8.3
Control	7.8	1.4
Mortar	-16.3	-2.9
Synthetic	204.8	35.8
Syn. w/ FA	163.3	28.6
Cellulose	104.3	18.3
Cel. w/ FA	40.2	7.0

It can be seen that the FRM provided significant confinement. Among all cases, the synthetic PFRM jacket provided the largest confinement effect. For the SFRM series, the highest increase seems to be obtained in the 2% steel fiber. But when the jacket is made of plain mortar, negligible confinement effect was observed. Furthermore, the incorporation of fly ash resulted to less confinement effect.

Lastly, a model for predicting the load-strain relationship of the column considering the confinement effect is proposed by simply increasing the concrete stress by the factor λ. This is expressed in Eq. (5). The plot of the results of the simulation using the model as compared to the experiment results is shown in Fig. 7. It can be seen that relatively good agreement is obtained. The practical application of this model is in the analysis of RC structure. Columns retrofitted with FRM jacket may be simulated using this model.

$$P = (1+\lambda)\ 0.85\, fc\ Ac + fs\ As \tag{5}$$

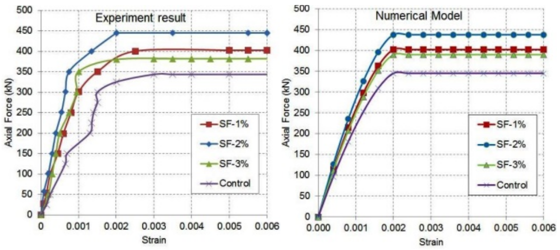

Fig. 7 Comparison of model with test data

CONCLUSION

It had been shown that the FRM jackets were effective as retrofitting material for RC columns. Among all cases investigated, the results indicate that the largest increase in strength is obtained in the column with synthetic FRM jacket. The axial load was increased by as much as 28.2%. The corresponding increase in the confined concrete strength was evaluated as 35.8%. Both occurred for the column with synthetic PFRM jacket. Furthermore, it was shown that the confined concrete strength may be determined through the calculation of the confinement effect by evaluating the contribution of the different materials. A simple model was presented that can simulate the behavior of column as affected by confinement.

ACKNOWLEDGEMENTS

The author acknowledges J.C. Oropel, G.C. Panaligan, J.C. Sy, D.N. Valerio, K.K. Galicia, and J.V. Sia for their vital roles in the conduct of the experimental tests. The author is also grateful to the faculty and staff of the Civil Engineering Department of De La Salle University for their encouragement.

REFERENCES

[1] Daoud OM, “Damage assessment and strengthening of R/C building constructed on expansive soils”, Int. J. of GEOMATE, Vol. 4, No. 2 (Sl. No. 8), June, 2013, pp. 516-521.

[2] Berthet JF, Ferrier E and Hamelin P, “Compressive behavior of concrete externally confined by composite jackets. Part A: Experimental study”, Construction and Building Materials, Vol. 19, Issue 3, 2005, pp. 223–232.

[3] Binici B, “An analytical model for stress–strain behavior of confined concrete”, Engineering Structures, Volume 27, 2005, pp. 1040–1051.

[4] Sakthivel PB, Ravichandran A and Alagumurthi N, “Experimental and predictive mechanical strength of fiber reinforced cementitious matrix”, Int. J. of GEOMATE, Vol. 7, No. 1 (Sl. No. 13), Sept. 2014, pp.993-1002.

[5] Cominoli L, Failla, C and Plizzari GA, “Steel and synthetic fibres for enhancing concrete toughness and shrinkage behavior”, Proc. Int. Conf: Sustainable Construction Materials and Technologies, 2007, pp.231-240.

[6] Sorelli L, Banthia N and Plizzari GA. “Crack growth resistance of thin mortar layers with hybrid fiber reinforcement”, Special Publication 224, Paper N. 12, ACI, 2004, pp. 161-178.

[7] Abdul Awal ASM, Mohammadhosseini H, Hossain MZ, “Strength, modulus of elasticity and shrinkage behavior of concrete containing waste carpet fiber”, Int. J. of GEOMATE, Vol. 9, No. 1 (Sl. No. 17), Sept., 2015, pp. 1441-1446.

[8] Valerio DN, Galicia KK, Sia JV and Lejano B, “Retrofitting of RC columns with steel fiber reinforced mortar”, 15th ASEP International Convention (15AIC), Manila, Philippines, Sep. 28-29, 2011.

[9] Oropel JC, Panaligan GC and Sy JC, “A study on the confinement effects of fiber reinforced mortar (FRM) on RC columns”, Thesis, De La Salle University, 2013.

[10] Lejano B, “Confinement effects of different retrofitting materials on the axial strength of reinforced concrete columns”, 7th HNICEM Conference, Palawan, Phil., Nov. 13-14, 2014.

[11] Demers M and Neale KW, “Confinement of reinforced concrete columns with fibre-reinforced composite sheets - an experimental study”, Can J Civil Eng, Vol 26, 1999, pp. 226–241.

[12] Lejano B, “Modeling the stress-strain relationship of high strength concrete made of local aggregates”, 1st ASEAN Civil Engineering Conference (ACEC), Pattaya, Thailand, March 12-13, 2009.

DEVELOPMENT OF A NEW SOIL-CEMENT BLOCK USING PRODUCED WATER FROM OIL FIELDS: A PRELIMNARY INVESTIGATION

Khalifa S. Al-Jabri[1], A. W. Hago[1], Mahad Baawain[1] and Gyanendra Sthapit[2]
[1]Department of Civil and Architectural Engineering, Sultan Qaboos University, Oman; [2]Habitech Center, School of Engineering and Technology, Asian Institute of Technology, Thailand

ABSTRACT

One of the prime aims of the sustainable development strategies in many countries is to provide safe and secure environment for their inhabitants. This goal can be achieved through the use of environmental friendly building materials, commonly referred to as green building materials and the effective use of waste materials in useful applications such as construction industry. In Oman, saving the environment by finding alternative useful methods for re-using different kind of wastes and seeking ways to reduce the emission of harmful gases, and looking for affordable low-income housing for people are of great concern to the authorities in order to preserve and sustain the environment for the future generations. In order to fulfill such objective, research into the use sustainable materials in the construction industry is encouraged. Therefore, in the same context, this study discusses preliminary results from an ongoing research project between Sultan Qaboos University (SQU) and Petroleum Development Oman (PDO) on the use of produced water from Nimr and Marmoul PDO oil-fields in the development of a new soil-cement block which possesses good strength, good thermal insulation and consume lower quantity of cement than the conventional one. Soil and water samples were brought from Marmoul and Nimr sites. The initial results indicated that both soil and water are suitable for production of compressed blocks with good mechanical properties.

Keywords: Soil Compressed blocks, Produced Water, Oil-fields, Strength

INTRODUCTION

One of the roles of the sustainable development strategies in the developing countries is to provide decent welfare to the community through providing the basic needs to its people such as clean and potable water, housing, clean environment, etc. at affordable and cheap means. Therefore in many developing countries, it is necessary to seek ways to reduce construction costs, especially for low-income housing, as well as adopting easy and effective solutions for their repair and maintenance [1]. This objective can be partially achieved through the use of locally available materials in the construction of low-income housing. Soil is found in abundant quantities all over the world. Its use in the construction industry is significant in applications such as cement mortars, concrete, finishing, cement blocks, and soil compressed blocks and bricks. Compressed earth block (CEB) system is one of the traditional construction materials that exists in many developing countries which have proved to be suitable for a wide range of buildings and which have a great potential in the construction of traditional low-cost dwellings. Adam and Agib [1] reported that soil construction methods are used in 80% of urban buildings and exceeds 90% in rural areas in Sudan. Often a stabilizer material such as cement or lime is added in small quantities in order to improve the mechanical properties and durability of the blocks. These blocks are usually used in non-load bearing construction.

Freshwater is a precious and scarce commodity in all arid regions such as Oman and other Gulf countries. This commodity becomes increasingly more precious in these countries as they witness a rapid development in their urban infrastructure including buildings, hospitals, homes, and roads. Water is needed in road construction where it is used as mixing water for compaction and for dust control. It is also needed as a component in concrete mixtures, primarily for the hydration process of cementitious materials and for curing. Contractors in arid regions, and especially in remote areas of the desert, are sometimes faced with the problem of finding water of acceptable quality for their construction work. However, plenty of non-freshwater is produced in the oil fields during oil exploration. Water produced with oil forms the largest amount of waste in the entire oil production process. An oil field typically produces more than five times the volume of water as oil during its economic life. In Oman, the PDO production of water from oil-fields was nearly 850,000m³/d in 2015. Approximately 9 barrel of water is produced for each barrel of oil. Therefore, PDO is very keen to seek for alternative viable uses of oil produced water (oily water) that can help consuming such large quantity of water. The main objective of this research study is to investigate the potential use of non-fresh water (brackish and production water) from Nimr and Marmoul PDO oil- fields in the development of a new soil-cement block which possesses good strength, good thermal insulation and consume lower quantity of cement than the conventional one.

MATERIALS AND TESTING METHODS

Soil

Two types of soil were provided from PDO oil fields: soil from Marmoul oil-field and that provided from Nimr oil-field. These soils are not contaminated soil. Field and laboratory tests were performed on the two soils to assess their suitability for block manufacturing. Chemical analyses were carried out on the soil samples from Nimr and Marmoul sites to determine heavy metals, anions and organics, whereas tests to determine the physical properties of the soil which include specific gravity, Atterberg limits, shrinkage, and grading.

Produced Water

About 1000L of produced water was brought from each site. For the chemical analysis test of the produced water measurements included certain impurities that could affect soil-cement blocks such as: total alkalinity, sulfate content, chloride content, total dissolved solids and water hardness. Other parameters such as pH and conductivity were also measured. The water quality was compared with the international specifications for producing concrete i.e. ASTM C94 and AASHTO157 as well as the U.S. Environmental Protection Agency (U.S. EPA).

Soil Stabilizer

Ordinary Portland cement (OPC) was used as a stabilizer in the production of Compressed Earth Blocks (CEB).

RESULTS AND DISCUSSION

Analysis of Soil Samples

Chemical analysis of soil

The results obtained from the chemical analysis test indicated that the chloride and fluoride contents in both sites soil samples are similar. The sulphate content in soils samples from Nimr (1000 mg/kg) is relatively higher than soil samples from Marmoul (800 mg/kg). In general, the content of heavy metals in Marmoul soil samples is relatively higher than the soil samples from Nimr. However, the leachability test has to be evaluated for any application of such soils.

Physical properties of soil

Specific gravity for the two soils was carried out in accordance with ASTM D854. Two samples from each soil were selected and tested to determine their specific gravity. The results show that the two soils have almost the same specific gravity of 2.69 in average.

The test results show that Marmoul soil has 29%, 18%, and 11%, liquid limit (LL), plastic limit (PL) and plasticity index (PI), respectively, whereas these values were zero for Nimr soil. The results indicated clearly that Nimr soil contains more sand/silt and has no plasticity. For Marmoul soil, liquid limit LL= 29% and plasticity index PI= 11%. Both values fall within the limits specified by ARS 680 [2] for production of compressed blocks. However, since Nimr soil has no plasticity, its suitability has to be assessed by other tests.

Sieve analysis test was carried out to determine the distribution (grading) of the soil particles for different sizes. To produce a soil-cement block with good properties, the soil should contains 15% gravel, 50% soil, 15% silt, and 20% clay at the most. Since soil contains fine particles i.e. silt and clay, performing sieve analysis test alone is insufficient to classify the soil. Therefore, to classify Marmoul and Nimr soils, three analyses tests were conducted, sieve analysis test, wet sieve analysis test, and hydrometer test for soil particles passing 75µm. The particle distribution curves for the two soils were plotted together with the limits by ARS 680 [2] in Fig. 1. It is clear from the figure that, the two soils have almost the same distribution; both are within limits specified by the code ARS 680 [2] for compressed earth blocks but Nimr soil suits well within those limits.

Also, the results showed that, while the quantity of clay in the two soils are almost the same (2.25% for Marmoul and 2.02% for Nimr), Nimr soil contains more silt than Marmoul soil (18% compared to 11%). The quantity of clay in the soil controls the selection and the amount of the stabilizer. For soils with high clay content, only lime can be used to stabilize the soil. With the low clay content as in Marmoul and Nimr soils, cement can be used as a stabilizer prior to compressing the soil. However, the quantity of the cement stabilizer can be determined by testing a number of mixes with various stabilizer proportions. Soils with higher clay contents compress more than those with lower clay content. In the present case, it is expected that Marmoul soil will require more volume of soil to make the same block than of Nimr soil, due to its higher compressibility.

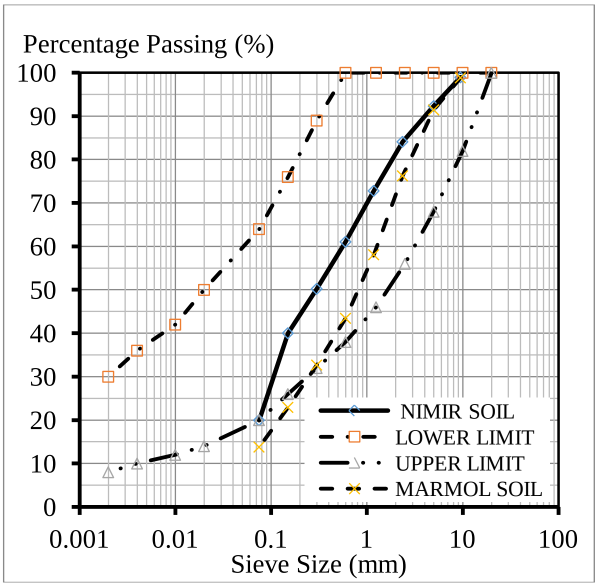

Fig. 1 Particle size distribution for Nimr and Marmoul soils.

The shrinkage test measures the shrinkage of the soil which contains no stabilizer, and the result can be used to give a rough guide for estimating the required amount of cement as a stabilizer. After seven days of casting, Nimr sample did not show any shrinkage in the length. No cracks could be detected on the surface of the specimen. The Marmoul specimen showed one hairy crack on its top surface near the middle of its length. At one end it separated from the mould. The contraction was about 0.5mm.

Analysis Results of Water

Results obtained from the chemical analysis tests demonstrated that the salinity (electrical conductivity) of the produced water samples from Nimr is higher than the ones from Marmoul. This is evident from the higher TDS values (8300 mg/L in Nimr water sample compared to 4780 mg/L in Marmoul water sample). Moreover, the chloride content in Nimr water samples (4378 mg/L as Cl-) is higher compared to Marmoul water samples (2136 mg/L as Cl-). The sulphate (as SO_4) and hardness (as $CaCO_3$) contents in Nimr water sample (333 mg/L and 350 mg/L) are higher compared to Marmoul water sample (120 mg/L and 140 mg/L). However, total alkalinity (as $CaCO_3$) in Nimr water samples (307 mg/L) is lower compared to Marmoul water samples (762 mg/L). The content of heavy metals is relatively low in the water samples from both sites (most are below detection limit except Boron which was in the range of 4 mg/L). Moreover, oil and grease content was found below detection limits in the water samples from both sites (i.e. less than 5 mg/L).

Water quality specifications for producing concrete mixes according ASTM and AASHTO [3]) are shown in Table 1. It can be seen that both water samples from Nimr and Marmoul meet the limits of total solids (<50000 mg/L) and sulphate (<3000 mg/L). However, the chloride content is higher than the specified maximum limits (>500 mg/L). Therefore, further analysis on the production of bricks has to be conducted.

Table 1 Water quality specifications for producing concrete (adopted from Chini et al. [3]).

Chemical Limit mg/L	Specification	
	ASTM C94	AASHTO M157
Sulphate as SO_4	3000	3000
Total Chloride as Cl^-	500	1000
Total solids	50000	50000
Alkalis as Na_2O eqv.	600	600

Production of Soil-Cement Block

Stulz et al. [4] defined compressed earth blocks (CEBs) as “masonry elements, which are small in size with regular and verified characteristics obtained by the static or dynamic compression of earth in a humid state followed by immediate demoulding”. compressed earth block system is one of the traditional construction materials that exists in many developing countries which have proved to be suitable for a wide range of buildings and which have a great potential in the construction of traditional low-cost dwellings.

These blocks are composed of earth materials (soil) with their cohesion is due principally to the clay fraction present in both humid and dry states [5]. The properties and cohesion of the CEBs can be enhanced by the addition of a stabilizer. The quality of these blocks depends on the type of the raw materials used i.e. the soil and the stabilizer, and on the steps and expertise in executing various stages of manufacturing i.e. the preparation of materials, addition and mixing of stabilizers and compaction or compression up to curing stage [5]. In order to produce soil-cement blocks which possess good properties, the most optimum constituent materials should be selected. The best soil suitable for the production of soil compressed blocks should be constituted of 15% gravel, 50% soil, 15% silt, and 20% clay. These properties should be determined before using the block. Also, the quality of the water used in producing the blocks should be analyzed especially if non-freshwater is to be used or the water to be used is of unknown source.

Generally, typical wet compressive strengths of CEBs are within 4 MPa [1].

Three soil stabilization methods are usually used in the production of CEBs. Mechanical stabilization which involves compacting the soil in order to improve its resistance to shearing, compressibility, permeability and porosity. Physical stabilization which concerns with changing soil texture and properties as well as the use of different during methods such as air or moisture curing, and heat treatment. Chemical stabilization is achieved by enhancing the physicochemical properties of the soil by the addition of chemicals. The most two widely used stabilizers in the production of CEBs are cement and lime. In this research cement will be used as the main stabilizer although the use of other materials such as lime or cement kiln dust (CKD) can be investigated.

Adam and Agib [1], and Oyelami and Rooy [5] reported many advantages of compressed earth bricks which are in line with the sustainable development objectives and strategies. In terms of materials efficiency, CEBs use 30% less water compared to what is used in other conventional building material production. They are produced mainly from soil, sustainable resource, which are recyclable, produce very little harmful air emissions, have zero or low toxicity, are durable and readily available [5]. CEBs are energy efficient material; the production of CEBs requires only 1% compared to a similar volume of concrete. About 36 MJ (10 kW h) of energy is required to produce 1m^3 of CEB in comparison with about 3000 MJ (833 kW h) that is required to produce the same volume of concrete. Since the density of CEBs is less than that of concrete, they possess less thermal conductivity than other conventional materials in building construction. Also, compressed earth blocks have much better fire resistance and sound proof than other parent materials. CEB is considered as environmentally friendly material since it reduces the consumption of excessive volumes of cement through the promotion and use of environmentally friendly earth materials that utilizes minimal quantities of cement and consequently decreases significantly CO_2 emission into the atmosphere. Oylemi and Rooy [5] reported that manufacturing of a ton of cement generates around 0.55 tons of CO_2 and the burning of carbon-fuel produces another 0.4 tons of CO_2. Some studies [5] showed that CEB generates about 22kg CO_2/tonne whereas concrete blocks produce, nearly 143kg CO_2/tonne, burnt clay bricks, about 200kg CO_2/tonne and perforated concrete blocks 280 to 375 kg CO_2/ tonne.

In this research, two types of CEB manufacturing machines will be used: a manual and a hydraulic press. These machines are manufactured by the Habitec Center at the Asian Institute of Technology, Thailand. Fig. 2 shows the manual CEB press whereas Fig. 3 shows a block sample produced using the manual press.

Fig. 2 The manual soil-cement block making press.

Fig. 3 Typical soil-cement block.

The manual press produces about 300 bricks per day while the hydraulic brick press can produce 3,000 bricks per day. Water requirement for the production is 2,250 liters per day. In tropical countries, the top layers of the earth (50cm) are not recommended to be used as the top soil contains plants and grasses, which are not good for brick making. The deeper soil that are mostly sandy, are found to be extremely good for the manufacturing of these bricks. Before mixing, the soil lumps must be broken up so that the lumps do not remain. Sand available in Oman could be normally used without any further processing (maybe with slight sieving). Hence, in order to produce good quality bricks, the content of these fine particles in the soil should be in such a proportion that the soil and sand content has optimum water content and clay particles. The bricks are produced by stabilizing with cement, and are air cured for 24 hour followed by water curing for 3 weeks. After 3 weeks the bricks are ready to use for the construction works.

The brick making process is entirely a green process. It doesn't need furnace to process the bricks unlike in the conventional process. The bricks need water as an ingredient as well as for curing. The cement component of the bricks which are predominantly composed of clay and sand is less than 15% to attain strengths comparable or better than conventional bricks. The manufacture of good quality, durable compressed stabilized soil-cement bricks requires the use of soil containing fine gravel and sand for the body of the brick, together with silt or clay to bind the sand particles together. An appropriate type of stabilizer is added to decrease the linear expansion that takes place when water is added to the soil sample. The block is self-interlocking which requires minimum amount of mortar for block alignment and fixing leading to saving in cement used and an improvement in the thermal insulation of the wall by reducing the thermal bridges that are created at the mortar's line.

To study the possibility of using local soil in the production of cement-soil block, two locally available soils in large quantities were used. These soils are mountain soil and dune sand. Before using these soils in the manufacturing of the blocks, their suitability was assessed using the particle determination test which determines the soil particles content. Fig. 4 shows the particle determination test of the mountain soil and dune sand. It can be seen from Fig. 4 that dune sand sample contains one type of soil whereas mountain soil contains 50% soil and 50% clay. Therefore, the two soils cannot be used separately to make good compressed earth block, but they can be mixed together or with other soils to produce blocks that satisfy the requirements.


(a) Mountain soil


(b) Dune sand

Fig. 4 Particle determination test

Four soil mixture proportions were prepared using mountain soil and dune sand as shown in Table 2. Cement was used as stabilizer and kept constant in all mixtures. Three water proportions were used ranging between 0.5 and 1.5. The manual press machine was used in the production of the blocks. Soil, dune sand and cement were mixed together. Then water was added to the mixture providing the necessary moist. The press mold was filled with the mixture and pressed using the pressing arm. After removing the blocks from the mold, they were then moved to the curing area and left for 24 hours in the open air under the shade. After 24 hours, the blocks were moved and stacked under the sun, covered with plastic covers and left to cure until the day of testing. The compressive strength test was carried out on the blocks after 28 days of curing as shown in Fig. 5.

The results presented in Fig. 5 show that the compressive strength of the blocks ranged between 0.87 MPa for Mix-02 and 3 MPa for Mix-04. The maximum strength was achieved for Mix-04 with 4 proportions of mountain soil and 4 proportions of dune sand. Generally these mixtures can be modified in order to obtain better results in the future

Table 2 Mixture proportions for the soil-cement block

Mix no.	Cement	Mountain soil	Dune sand	Water
Mix-01	1	8	0	1.5
Mix-02	1	2	6	0.5
Mix-03	1	3	5	0.75
Mix-04	1	4	4	0.75

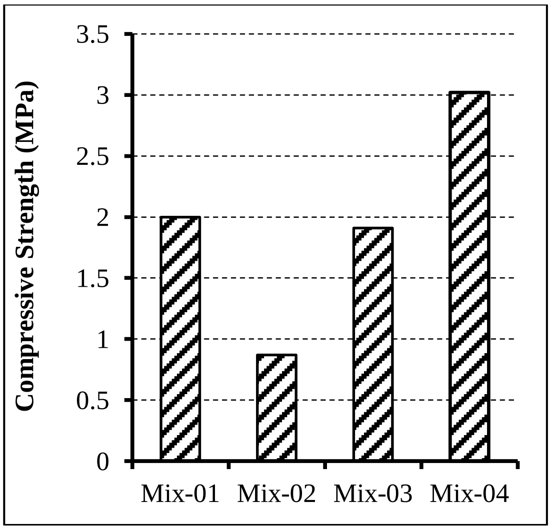

Fig. 5 Average compressive strength of blocks after 28 days of curing.

The compressive strength results was obtained using field compression testing machine which was supplied by the manufacturer of the manual and hydraulic press machines as shown in Fig. 6. The correlation curve between the field testing machine reading and the load cell reading is shown in Fig. 7. It may be seen from this figure that there is an excellent correlation between the two parameters with R^2 value of 0.9987. The compressive strength values were obtained from Fig. 7 by dividing the failure load by the net area of the block.

Fig. 6 Field compression testing machine.

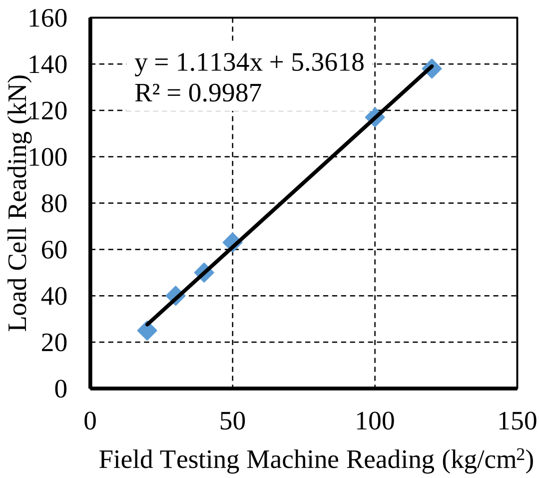

Fig. 7 Correlation between field testing machine and load cell reading

CONCLUSION

This report presented the results of a preliminary investigation on the development a new soil-cement block using produced water from oil-fields. The study reported the results of chemical and physical analyses on produced water and soil samples from Nimr and Marmoul oil-field sites. Chemical analyses measurements were total alkalinity, sulfate content, chloride content, total dissolved solids and water hardness, pH and conductivity, whereas, tests to determine the physical properties of the soil included specific gravity, Atterberg limits, shrinkage, and grading. The study found that the soil and water from Nimr and Marmoul oil-field sites are suitable for production of compressed blocks. Since the percentage of clay in the two soils is small, cement can be used as stabilizer for the two soils. The quantity of the stabilizer has to be determined by studying different mixes containing various cement proportions. The study concluded that it is possible to produce soil-cement blocks with good mechanical properties using local soil in Oman.

ACKNOWLEDGEMENTS

The project's investigators would like to express their gratitude to Petroleum Development Oman (PDO) for providing financial support to the project under contract number: CR/ENG/CIVL/14/09. Also, our sincere gratitude is extended to the Asian Institute of Technology (AIT) for the scientific cooperation in this work.

REFERENCES

[1] Adam E.A. and Agib, A.R.A., Compressed stablised earth block manufacture in Sudan, United Nations Educational, Scientific and Cultural Organization (UNESCO), UN, 2001

[2] ARS 680: Compressed Earth Blocks Standards: A publication by the Center of Development Industry CDI- CRATerre-EAG,1998, ISBN 2-906901-19-9. Contains ARS 680:1996 Code of Practice for the production of compressed earth blocks, African Regional Standards.

[3] Chini A.R., Muszynski L.C., Ellis B.S., Recycling Process Water in Ready-Mixed Concrete Operations, 1999, Final Report, School of Building Construction, University of Florida, Gainesville, USA.

[4] Stulz R., Mukerji K., ILE S.K., für A.T. Appropriate Building Materials: a Catalogue of Potential Solutions, 1993, SKAT, Intermediate Technology Publications, London.

[5] Oyelami C., and Rooy JLV, A review of the use of lateritic soils in the construction/development of sustainable housing in Africa: A Geological Perspective, Journal of African Earth Sciences, Vol. 119, 2016, pp. 1-16.

WASTE PLASTICS AS REINFORCING IN STRUCTURAL COMPOSITE MATERIALS: PROPERTIES AND CHARACTERISTICS

Youssef HALIMI[1,2], Hayat BOUCHOUM[1], Souad ZYADE[2], Mohamed TAHIRI[1]

1: Geoscience Laboratory, Ain Chock's Sciences Faculty, Km8, Rte d'El Jadida BP5366, Maarif, Casablanca , 20100 Morocco

2: Technology High School of Casablanca, Km8, Rte d'El Jadida,

ABSTRACT

The synthetic composite materials have grown spectacularly in the last three decades. Indeed, these lighter and very diverse materials could replace more than 50% of articles and objects made on metals. This is mainly due to their perfect implementation in various possible and adapted forms and the ratio price/optimized performance. The work that we present reports the implementation of composite materials based on marble powder, plastic waste and unsaturated polyester resin with different loads: expanded perlite, Calcium carbonate and kaolin. These multi-phases materials constitute a system characterized upon its: composition, type of reinforcement and texture, type and rate of the used fillers and loads.

Keywords: Eco-Materials, Composite Materials, Plastic Waste Recovery, Expanded Perlite.

INTRODUCTION

Many solid wastes are abandoned in nature. Industrial Plastic wastes are in general somehow dangerous and have long life time (200 -1000 years). Their degradability needs a long-time.

Giving a second life to used plastic is the aim of this study. In this work, we focus on the valorization of marble powder and recycling of plastic waste (bags, bottles, jars, cans ...), while having a purely environmental (recycling and recovery), economic (without energy) and ecological character (own process).

The idea is to use plastic wastes (Synthetic sand) as reinforcement for composite materials based on marble powder, and unsaturated polyester resin with different fillers: expanded perlite, talc, calcium carbonate, and kaolin.

MATERIALS AND METHODS

It is to synthesize a polymer material based on unsaturated polyester resin by polymerization with the catalyst called PMEK (Peroxide Methyl Ethyl Ketone) and a hardener like Cobalt octoate.

The polymer is filled with inorganic materials, for example, marble powder, expanded perlite, calcium carbonate, kaolin, synthetic sand, talc, etc.

Domestic plastic waste such as packaging, cans, yogurt containers, drums and jerricans can be used as reinforcement support if cut to small fibers and be incorporated in composite material. The reinforcement of a composite material is expected to improve the structural or mechanical properties.

The shape of the reinforcement characterizes different types of monolayer. The reinforcement may be long fibers (oriented or random), short fibers, particulate fibers (impregnated or mixed with the paste) or woven fibers.

Then the rheological tests will be performed on the obtained material to determine the nature of the synthesized composite material:

- Resistance to bending and breaking force.
- The water absorption.
- The apparent relative density.
- Resistance to deep abrasion for unglazed tiles.
- The chemical resistance.

RESULTS AND DISCUSSION

1- FAMILY COMPOSITION:

Model of sample's composite materials synthesized:

- Family 1

Matrix	**Insaturated polyster resin**	**25 %**
Reinforcement	**Bags of plastic (Impregnated particulate reinforcement)**	**25 %**
Charge	**Marble powder**	**46 %**
Accelerator	**Octoate of cobalt**	**3 %**
Catalyst	**Methyl ethyl ketone peroxide**	**1 %**

- Family 2

Matrix	**Insaturated polyester resin**	**25 %**
Reinforcement	**Bags of plastics Oriented fibrous reinforcement UD**	**25 %**
Charge	**Marble powder**	**46 %**
Accelerator	**Octoate of cobalt**	**3 %**
Catalyst	**Methyl ethyl ketone peroxide**	**1 %**

- Family 2’

Matrix	**Unsaturated polyester resin**	**25 %**
Reinforcement	**Bags of plastic Oriented fibrous reinforcement UD**	**20 %**
Charge	**Marble powder**	**51 %**
Accelerator	**Octoate of cobalt**	**3 %**
Catalyst	**Methyl ethyl ketone peroxide**	**1 %**

- Family 2’’

Matrix	**Unsaturated polyester resin**	**27 %**
Reinforcement	**Bags of plastic Oriented fibrous reinforcement UD**	**15 %**
Charge	**Marble powder**	**54 %**
Accelerator	**Octoate of cobalt**	**3 %**
Catalyst	**Methyl ethyl ketone peroxide**	**1 %**

- Family 2’’’

Matrix	**Unsaturated polyester resin**	**30 %**
Reinforcement	**Bags of plastic Oriented fibrous reinforcement UD**	**10 %**
Charge	**Marble powder**	**56 %**
Accelerator	**Octoate of cobalt**	**3 %**
Catalyst	**Methyl ethyl ketone peroxide**	**1 %**

- Family 3

Matrix	**Unsaturated polyster resin**	**25 %**
Reinforcement	**Bags of plastics Woven reinforcement**	**25 %**
Charge	**Marble powder**	**46 %**
Accelerator	**Octoate of cobalt**	**3 %**
Catalyst	**Methyl ethyl ketone peroxide**	**1 %**

- Family 4

Matrix	**Unsaturated polyester resin**	**25 %**
Reinforcement	**Bags of plastic Random fibrous reinforcement**	**25 %**
Charge	**Marble powder**	**46 %**
Accelerator	**Octoate of cobalt**	**3 %**
Catalyst	**Methyl ethyl ketone peroxide**	**1 %**

- Family 5

Matrix	**Unsaturated polyester resin**	**25 %**
Reinforcement	**Bags of platic (particulate reinforcement mixed with the paste)**	**25 %**
Charge	**Marble powder**	**46 %**
Accelerator	**Octoate of cobalt**	**3 %**
Catalyst	**Methyl ethyl ketone peroxide**	**1 %**

- Family 6

Matrix	**Unsaturated polyester resin**	**26 %**
Reinforcement	**Glass woven fabrics**	**-**
Charge	**Marble powder**	
Accelerator	**Octoate of cobalt**	**3 %**
Catalyst	**Methyl ethyl ketone peroxide**	**1 %**

- Family 7

Matrix	**Unsaturated polyester resin**	**26 %**
Reinforcement	**Canvas woven fabrics**	**-**
Charge	**Marble powder**	
Accelerator	**Octoate of cobalt**	**3 %**
Catalyst	**Methyl ethyl ketone peroxide**	**1 %**

- Family 8

Matrix	**Unsaturated polyester resin**	**26 %**
Reinforcement	**Glass woven mat**	**-**
Charge	**Marble powder**	**70 %**
Accelerator	**Octoate of cobalt**	**3 %**
Catalyst	**Methyl ethyl ketone peroxide**	**1 %**

- Family 9

Matrix	**Unsaturated polyester resin**	**21 %**
Reinforcement	**Bags of lastic Woven reinforcement**	**25 %**
Charge	**Perlite**	**50 %**
Accelerator	**Octoate of cobalt**	**3 %**
Catalyst	**Methyl ethyl ketone peroxide**	**1 %**

- Family 10

Matrix	**Unsaturated polyester resin**	**25 %**
Reinforcement	**Plastic pots, bottles, cans Cut. UD oriented fiber reinforcement**	**25 %**
Charge	**Marble powder + Kaolin**	**36 % + 10 %**
Accelerator	**Octoate of cobalt**	**3 %**
Catalyst	**Methyl ethyl ketone peroxide**	**1 %**

- Family 11

Matrix	**Unsaturated polyester resin**	**26 %**
Reinforcement	**Plastic pots, bottles, cans Cut. UD oriented fiber reinforcement**	**25 %**
Charge	**Marble powder + Perlite**	**30 % + 15 %**
Accelerator	**Octoate of cobalt**	**3 %**
Catalyst	**Methyl ethyl ketone peroxide**	**1 %**

- Family 12

Matrix	**Unsaturated polyester resin**	**24 %**
Reinforcement	**Plastic pots, bottles, cans Cut. UD oriented fiber reinforcement**	**25 %**
Charge	**Marble powder + synthetic sand**	**37 % + 10 %**
Accelerator	**Octoate of cobalt**	**3 %**
Catalyst	**Methyl ethyl ketone peroxide**	**1 %**

- Family 13

Matrix	**Unsaturated polyester resin**	**25 %**
Reinforcement	**Plastic pots, bottles, cans Cut. UD oriented fiber reinforcement**	**25 %**
Charge	**Marble powder + Calcium Carbonate**	**36 % + 10 %**
Accelerator	**Octoate of cobalt**	**3 %**
Catalyst	**Methyl ethyl ketone peroxide**	**1 %**

- Family 14

Matrix	**Unsaturated polyester resin**	**25 %**
Reinforcement	**Plastic pots, bottles, cans Cut: Woven reinforcement**	**25 %**
Charge	**Marble powder + Kaolin**	**31 % + 15 %**
Accelerator	**Octoate of cobalt**	**3 %**
Catalyst	**Methyl ethyl ketone peroxide**	**1 %**

- Family 15

Matrix	**Unsaturated polyester resin**	**27 %**
Reinforcement	**Plastic pots, bottles, cans Cut: Woven reinforcement**	**25 %**
Charge	**Marble powder**	**44 %**
Accelerator	**Octoate of cobalt**	**3 %**
Catalyst	**Methyl ethyl ketone peroxide**	**1 %**

2- DETERMINATION OF FLEXURAL STRENGTH AND TENSILE STRENGTH:

Table 1: Effect of reinforcement rate

N° Sample	Reinforcement rate	Tensile strength (N)	Stress (MPa)
2	**25 %**	**2380**	**30.64**
2'	**20 %**	**2345**	**30.19**
2''	**15 %**	**2290.1**	**29.5**
2'''	**10 %**	**2275.6**	**29.3**

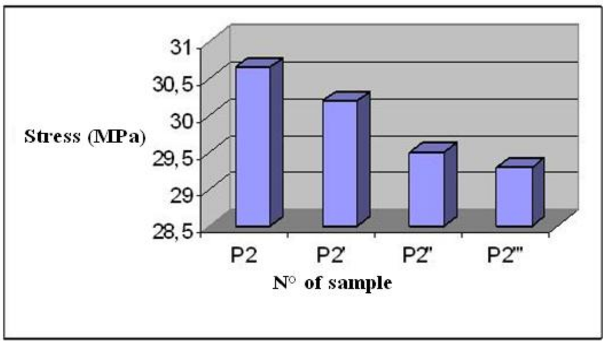

Fig 1. Determination of flexural strength of samples (2, 2', 2", 2"')

The flexural strength increases with increasing the fiber percent. This is due mainly to the adhesion matrix - fiber and the ability to stop the spread of cracks by fibers.

Table 2: Effect of reinforcement architecture

N° sample	Reinforcement architecture	Tensile strength (N)	Stress (MPa)
1	**Particulate reinforcement (Very fine particles): Impregnated**	**2310.5**	**29.75**
2	**Fiber reinforcement (Long fibers): Oriented (Unidirectional)**	**2380**	**30.64**
3	**Mat fabric reinforcement**	**2520**	**32.44**
4	**Fibrous reinforcement (long fibers) : Random**	**2490.9**	**31.93**
5	**Particulate reinforcement (very fine particles) : mixed with paste**	**2360.4**	**30.39**

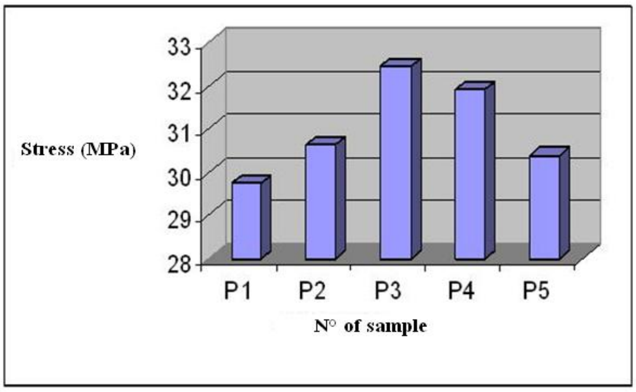

Fig 2. Determination of flexural strength of samples (1, 2, 3, 4, 5)

The mechanical properties of the composites materials are influenced by the fiber architecture.

The fabric texture always has the best strength: Fabrics have surface properties that give them resistance in two dimensions. However the rate of increase of this property is highly dependent on the architecture of fibers introduced in matrix. Thus the mechanical properties of composites depend strongly on the direction.

If the reinforcements are randomly distributed, the obtained material has average performance; while if the fibers are oriented in a specific direction, the produced material has a resistance which depends on the direction of the applied load.

The bending strength in the fiber direction is greater than that perpendicular to the fibers. So it is necessary to provide layers of crossed fibers to ensure interesting properties in different directions. Also, this allows adapting the material to the considered piece by making more fiber in the direction of the principal forces to which the part is subjected.

Table 3: Reinforcement of simples

N° sample	Type of reinforcement	Tensile strength (N)	Stress (MPa)
3	**Plastic bags as tissue**	**2520**	**32.44**
6	**Glass fibers**	**2623.1**	**33.77**
7	**Tissue**	**2500.23**	**32.19**
8	**Mat of glass fibers**	**2583.12**	**33.26**

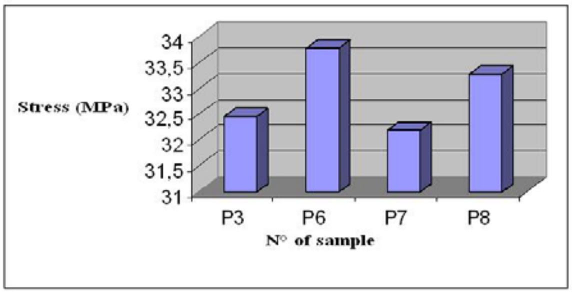

Fig 3. Determination of flexural strength of samples (3, 6, 7, 8)

The used process allows obtaining reinforcement with plastic bags of tissue similar to that obtained by the canvas fabrics. Also, the properties are comparable to other technical fabrics: glass fabric and glass mat.

Table 4: Effect of charge

Type of charges	Rate of charges	Tensile strength (N)	Stress (MPa)
Marble powder + Kaolin	**36 % + 10 %**	**2605.7**	**33.55**
Marble powder + Perlite	**30% + 15 %**	**2420.6**	**31.16**
Marble powder + Synthetic sand	**37 % + 10 %**	**2552.09**	**32.86**
Marble powder + Calcium Carbonate	**36 % + 10 %**	**2615.5**	**33.67**
Marble powder + Kaolin	**31 % + 15 %**	**2755.6**	**35.5**

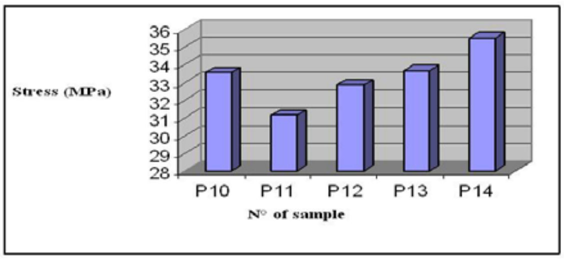

Fig 5. Determination of flexural strength of samples (10, 11, 12, 13, 14)

The addition of an inorganic phase (kaolin, calcium carbonate, perlite, synthetic sand) to the polymer, leads generally to an increase in stress. The material properties are a function of those of each component, but also the proportions in which they operate.

Table 5: Effect of thickness

Thickness (mm)	Tensile strength (N)	Stress (MPa)
10.4	**2380**	**30.64**
20.3	**> 6137.5**	**-**

The bending strength increases with increasing material thickness.

Table 6: Determination of water absorption

Reinforcement architecture	Absorption %
Particulate reinforcement (Very fine particles) : Impregnated	**1.0**
Fibrous reinforcement (long fibers): Oriented (Unidirectional)	**1.4**
Mat woven reinforcement	**1.9**
Fibrous reinforcement (Long fibers) : Random	**1.8**
Particulate reinforcement (Very fine particles) : Mixed with paste	**1.2**

Table 7: Determination of apparent relative density:

Reinforcement architecture	Density
Particulate reinforcement (Very fine particles) : Impregnated	**2**
Fibrous reinforcement (long fibers): Oriented (Unidirectional)	**2.1**
Mat woven reinforcement	**2.05**
Fibrous reinforcement (Long fibers) : Random	**2.03**
Particulate reinforcement (Very fine particles) : Mixed with paste	**1.78**

Composite materials are being increasingly used for reasons of weight gain. These materials allow achieve lower weight structures to those of metallic materials, while keeping rigidity and resistance greater or equal than metallic materials.

Table 8: Determination of resistance to deep abrasion:

Reinforcement architecture	V(cm^3)
Particulate reinforcement (Very fine particles) : Impregnated	**262**
Fibrous reinforcement (long fibers): Oriented (Unidirectional)	**262**
Mat woven reinforcement	**227**
Fibrous reinforcement (Long fibers) : Random	**227**
Particulate reinforcement (Very fine particles) : Mixed with paste	**215**

CONCLUSION

The composite materials with organic matrix, reinforcement in short filaments of used plastic bags (waste) or cut plastic bottles and mineral charges (expanded perlite, marble powder, ...) are a family of environmental friendly materials and the way of sustainable development projects. In fact, these kinds of eco-materials can have various applications in buildings as walls and grounds coating and covering. The physical, mechanical, and chemical properties of these eco-materials compared to their counter family marketed, prove that they can very well meet the customer requirements and conform to standard norms.
Moreover, it should be noted that these materials concern three fundamental aspects:

- Economic: Low cost of energy gains for processing, the use of recycled products (plastics and worn local marble powder) and the ease of the manufacturing process.
- Technical: Mechanical properties comparable to traditional reinforcements based materials (glass fiber), significant reduction in production cycle time, no deformation and withdrawals, low density and chemical stability for different reagents.
- Ecological: allows the reuse and recycling of waste, requires no energy to implement, can be installed throughout the territory in an area near the landfill if necessary

Table 9: Resistance to deep abrasion of materials:

Type of charges	Rate of charges	V(cm^3)
Marble powder + Kaolin	**36 % + 10 %**	**215**
Marble powder + Perlite	**30% + 15 %**	**262**
Marble powder + Synthetic sand	**37 % + 10 %**	**262**
Marble powder + Calcium carbonate	**36 % + 10 %**	**215**

Resistance to deep abrasion of materials is influenced by the fiber architecture and the nature of charges introduced into the matrix, kaolin and calcium carbonate increases the strength compared to the other compositions.

REFERENCES

[1] L. Berreur, B. Maillard, S. Nösperger. L'industrie française des matériaux composites : des enjeux prioritaires pour un développement durable. Etude Digitip. 2001, 129 pages.
(b) Matériaux composites: Comportement mécanique et analyse des structures 3° Ed.

[2] G. Chrétien. Matériaux composites à matrice organiques. Lavoisier, 1986, Partie 1, pp11-52.

[3] G. Chrétien. Matériaux composites à matrice organiques. Lavoisier, 1986, Partie 2, 53-106.
(b) Pratique des Plastiques et Composites, Ouvrage Collectif, Référentiel Dunod. 1999.

[4] G. Chrétien. Matériaux composites à matrice organiques. Lavoisier, 1986, pp495
(b) Durabilité des matériaux composites à matrice organique, Revue des composites et des matériaux avancés. 2002, 12, N° 1. (c) J-A. Manson, L. Carlsson, J-P. Mercier, P-E. Bourban. PPUR. 2004, 18, 234 pages.

[5] N. Bahlouli. Composites. Cours DESS MASI, Université louis Pasteur de Strasbourg, 2002

[6] M.Nardin, Interfaces fibre-matrice dans les matériaux composites. Applications aux fibers végétales, Revue des Composites et des Matériaux Avancés. 2006, 16, 1.

[7] (a) M. Reyne. Technologies des composites, Editions Hermes.1995.
(b) P. Keflouan, F. Boterel, J. Lostec, J-P. Bertotm J-M. Haussonne. J. Phys. 1991, 1, 1723-1750.

[8] C. Bathias. Matériaux composites. Dunod, Collection Technique et Ingénierie. 2005, 432 pages.

[9] Fiche technique de perlite, PERLITE INC. Imm. 4 Saison, Colline 20190 Casablanca

[10] JEAN BOST : Matières plastiques I chimie- applications. Edition TEC et DOC

[11] MAURICE REYNE : Les composites. Edition : que sais-je 1995. pp: 18 ; 19- 21

[12] M.Benhaddou, A Haddout, G. Villotreix, ''Rheological of Polymer Composites PP/FG at high shear rate'',

International Journal of Reinforced Plastics and Composites , Vol.26, N°13, 2007

[13] Caractérisation des matières premières, Laboratoire public d'essais et d'études (LPEE) – Maroc 2002

[14] Norme Marocaine MN ISO 10545-4 : Détermination de la résistance à la flexion et de la force de rupture. Édition : Service de normalisation industrielle marocaine 2000.

[15] Norme Marocaine MN ISO 10545-3 : Détermination de l'absorption d'eau, de la porosité ouverte, de la densité relative apparente et de la masse volumique globale. Édition : Service de normalisation industrielle marocaine 2000.

[16] Norme Marocaine MN ISO 10545-6 : Détermination de la résistance à l'abrasion profonde pour les carreaux non émaillés. Édition : Service de normalisation industrielle marocaine 1995.

[17] Norme Marocaine NM ISO 10545-13 : Détermination de la résistance chimique. Édition : Service de normalisation industrielle marocaine 2000.

MODELLING OF CARBONATION OF REINFORCED CONCRETE STRUCTURES IN INTRAMUROS, MANILA USING ARTIFICIAL NEURAL NETWORK

Richard M. De Jesus[1], Joshua A. M. Collado[2], Jemison L. Go[3], Mike A. Rosanto[4], and John L. Tan[5]
[1]Faculty of Civil Engineering in De La Salle University (Manila), Philippines
[2 - 5]Undergraduate Student of Civil Engineering in De La Salle University (Manila), Philippines

ABSTRACT

Corrosion is a perennial problem in reinforced concrete structures, and is a serious concern due to the deterioration that it causes to reinforced concrete members. Though regarded as having a minor influence to corrosion compared to chloride-induced corrosion, carbonation is becoming a serious threat due to continuous development of cities like Manila. Expectedly, as Manila continues to develop, carbon emission shoots up to alarming proportions, calling out for studies to investigate and mitigate its effect to human health and structures. Artificial Neural Network (ANN) is known for establishing relationships among parameters with unknown dependency towards another variable, similar to the case of carbonation's dependency with age, temperature, relative humidity, and moisture content. Utilizing field-gathered secondary data as training and testing parameter for back propagation algorithm, an ANN model is proposed. Prediction of carbonation depth using ANN Model C421 showed reliable results. Validation of performance of Model C421 was further checked by comparing its prediction with a different set of field-gathered secondary data and results confirmed good agreement between prediction and measured values.

Keywords: Carbonation, Artificial neural network (ANN), Model C421, Reinforced concrete

INTRODUCTION

Recent years had shown Philippines' economy rising fast. As of first quarter of 2016, Philippine economy grew close to 7% and considered to be the highest among 11 Asian countries as reported in [1]. The same news agency, on May 16 2016, reported that Philippines is the top performing country in Southeast Asia based on the report of Oxford Business Group (OBG) [1].

According to the Philippine Statistics Authority (PSA), Philippines' gross domestic product (GDP), for the 1st quarter of 2016, was 6.9 percent. It is recorded to be higher than that of China's 6.7% and Vietnam's 5.7% [2].

The country's economic rise is warmly welcomed by Filipinos. But it calls for the country to also grow accordingly with such economic growth. An indicator that the country is lagging behind with this growth, at some areas, is the failure to anticipate overwhelming increase in motor vehicles and its effects, in the past years. As reported by [3], passenger car sale grew from a little over 20,000 in 2005 to over 63,000 in 2015 while that of commercial vehicles grew from over 10,000 to over 30,000 in the same period.

A quantification of effects of increasing car volume, in terms of carbon dioxide (CO2) emission, was presented in the study of [4]. According to this study, the level of CO2 has reached 90.78 million metric tons in 2013. By the beginning of 2015, CO2 emissions has reached 97.91 million metric tons [5].

With this alarming rate of increasing CO2 levels in Metro Manila, it is not only human health that is at risk, but the health of reinforced concrete (RC) structures as well. CO2 penetration in RC structures, known as carbonation, poses a great threat to the structural health as its risk to corrode reinforcing steel bars (rebar) is high. Structures in urban/cities are most vulnerable to carbonation due to high levels of CO2. And to raise the concern farther, only limited studies were done in the country that investigates the effect of CO2 in RC structures, and how fast it contributes to the deterioration of structures. This deterioration happens within RC members are hard to detect from the outside which makes it threat even more alarming.

THEORETICAL BACKGROUND

Carbonation in Reinforced Concrete

Carbonation is a chemical process that involves the reaction of some chemicals in concrete, specifically the cement hydration elements calcium hydroxide (Ca(OH)2), and calcium-silicate-hydrates (C-S-H), with CO2 from the atmosphere that penetrates into concrete. The chemical reaction produces calcium carbonate ($CaCO_3$) which can potentially lower the passivity of steel bars, hence, contributing to corrosion. This chemical process can be represented by the following chemical equation:

$$CO_2 + Ca(OH)_2 \rightarrow CaCO_3 + H_2O \quad (1)$$

The study of [6] stated that carbonation involves the dissolution of CO_2 with water in the pores of concrete, before reacting with $Ca(OH)_2$, to form carbonic acid ($CaCO_3$). A quantification of how much of CO_2 that penetrates into concrete is attributed to carbonation is explained by [7]. It claimed that only half (50%) of CO_2 reacts with $Ca(OH)_2$. The other half reacts with C-S-H.

The rate of how fast carbonation progresses in concrete is not constant [8]-[9]. This is attributed to continuous hydration of cement particles in concrete and with continuous reaction of CO_2 with $Ca(OH)_2$. With less $Ca(OH)_2$ available, less reaction with CO_2 occurs. The continuous hydration also densifies the microstructure of concrete which lowers the carbonation diffusion rate further.

Several factors were identified to influence carbonation. Major factors were water to cement ratio, degree of hydration, CO_2 concentration of the surrounding air, moisture content, temperature, alkali content, and presence of damaged zones and cracks [10].

This study, however, will only consider age, temperature, relative humidity, and moisture content in modelling carbonation through artificial neural network (ANN) due to availability of data.

Obviously, age is of primary importance in terms of influence to carbonation. With lengthy exposure to CO_2, and extended duration of diffusion of CO_2 in concrete, carbonation depth increases. It is assumed in this study that Fick's law of diffusion which relates carbonation depth with the product of carbonation coefficient and square root of time, is valid.

As temperature increases, the diffusivity of gaseous CO_2 increases [8]. The diffusivity is seen as the rate of CO_2 to react and fully blend with cement hydrating elements. The study further added that the rise in diffusivity can be attributed to increased molecular activity. According to [11], the rise in temperature translates to higher solubility of chemical compounds. This is seen as a process that potentially facilitates the carbonation process faster.

Relative humidity is seen to contribute to carbonation in an opposite manner compared to that of temperature. Higher relative humidity lowers the rate of carbonation according to [8]-[9] due to presence of high moisture in concrete pores. Since diffusivity of CO_2 is lower in water than in air, it is anticipated that CO_2 diffusion in concrete pores lowers with increasing humidity. Moreover, [8]-[9] claimed that thin layer of water covering the pores tend to block the intrusion of CO_2.

Artificial Neural Network

Artificial Neural Network (ANN) is an effective tool for prediction of behavior or phenomenon. Unlike other tools, it requires no assumption as to how independent variables are affected by a single or multiple independent variables. The only basic requirement it requires is sufficient amount of data. ANN can be seen as a black box where input data are being fed to produce an output data [12]. ANN is efficient and effective in modelling systems influenced by multiple variables with unestablished interrelationships especially with incomplete data [12]. Reference [13] described ANN as made up of large number of highly interconnected processing elements called neurons which work in unison to solve a problem.

Before ANN can establish multi-variable interrelationships and come up with a prediction, it needs to learn the system first which can be achieved by feeding input data with set initial conditions. Reference [12] added that ANN requires no functional relationship among variables since the process is data driven implying that it can adopt to the training data and captures the relationship between the input and output variables.

Neural Network Modelling, Data, and Results

Data and its preparation for ANN modelling

A secondary data, based from [14] was utilized for this study for the training of the neural network model. The validation of model was conducted using another secondary data based on the study of [4]. Both studies conducted carbonation test to structures within the same vicinity – Intramuros, Manila.

Normalization of data was performed for these two secondary data. Normalization is to address the wide gap in terms of magnitude between field-measured carbonation data and that of the input variables. The process was done by simply getting the quotient between the data and the maximum value for that particular parameter. This process was implemented to all parameters – age, temperature, relative humidity, moisture content, and carbonation depth. After normalization, all data range from 0 to 1.

Choosing the ANN architecture

A sample ANN architecture is shown in Figure 1. The first 2 brown circles (a.k.a. neurons) are the inputs and could vary from 1 to N depending on the number of variables considered to influence an output (represented by red circle). The two blue circle in between represents the neurons in the hidden layer.

The arrows connecting the neurons have corresponding weights which change as ANN "learns" the relationship between input and output. This sample ANN architecture represents a feed-forward back propagation network which was adopted in this study.

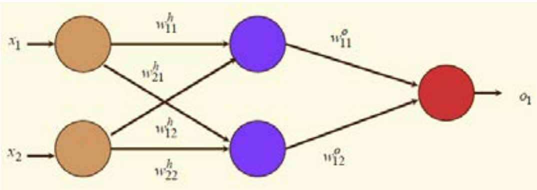

Figure 1. A sample neural network

The neural network architecture adopted in this study considered 4 inputs – age, temperature, relative humidity, and moisture content; while output was set at 1 – carbonation depth. One hidden layer was also considered in this study as more hidden layers tend to make the training and learning with ANN more difficult and complex. The number of neurons in the hidden layer, however, was varied from 1 to 10 based on the recommendation of [15]. Choosing the number of neurons, for the final ANN model, in the hidden layer was based on the following criteria: (1) the training R must be 0.80 or higher; (2) the testing R must be 0.90 or higher; and (3) error must be lower than 5% (or 0.05);

Tansig (or log sigmoid) transfer (or activation) function was adopted in the study with Levenberg-Marquadt (LM) as the training algorithm. The rest of the training parameters used were the default values in MATLAB – the software used to execute ANN process.

Comparison of these 3 criteria for 6 considered ANN architecture was summarized in Table 1. Six ANN architectures, of varying number of neurons in the hidden layer (n =1, 2, 3, 4, 5, & 10), were compared based on the above criteria. Based on all 3 criteria, all architectures met the requirements. Ranking of ANN architectures based on the 3 criteria showed that Model C421 was always in the top three (3). Thus, it was decided that Model C421 will represent the modelling of the carbonation depth using ANN.

Prediction of carbonation depth against measured values is shown on Fig. 2 to 7. These show slight deviation between prediction and measured values showing that ANN closely established the relationship between carbonation depth and the carbonation parameters (age, temperature, relative humidity, and moisture content).

Table 1. Comparison of six ANN architecture

ANN Model	error	training R	testing R
C411	0.034	0.811	0.967
C421	0.011	0.942	0.969
C431	0.010	0.949	0.922
C441	0.015	0.912	0.975
C451	0.014	0.923	0.989
C4101	0.016	0.931	0.959

The measured carbonation depths as presented in Fig. 2 to 7 were taken from field-measured carbonation depth.

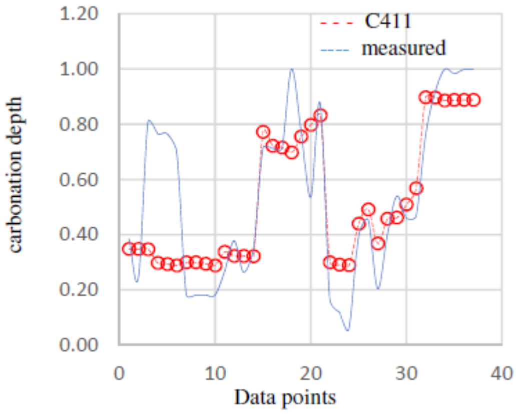

Figure 2. C411 prediction v. actual

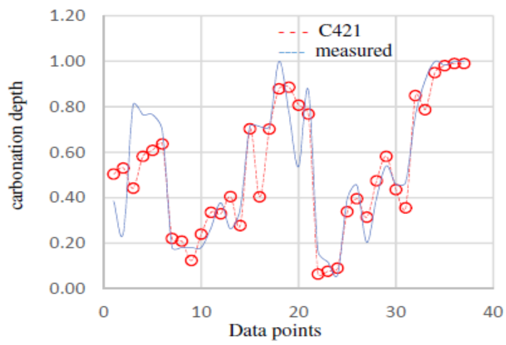

Figure. 3 C421 prediction v. actual

Comparison between measured carbonation depths and the prediction of Model C421, as shown in Fig. 3 showed minimal variation. ANN model C421 is considered to have learned the carbonation behavior via Artificial Neural Network (ANN). How carbonation depth varies with age, temperature, relative humidity, and moisture content is closely predicted by C421 model.

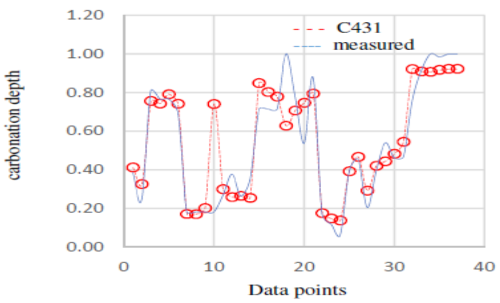

Figure 4. C431 prediction v. actual

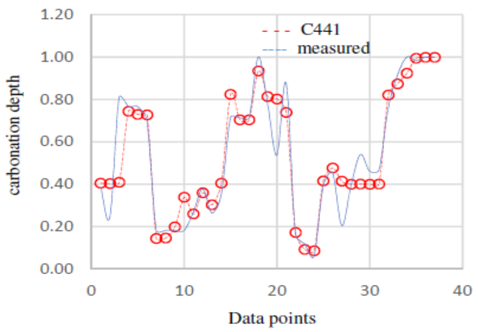

Figure 5. C441 prediction v. actual

Since all models showed close values to measured ones, choosing C421 on the basis of testing R criteria is supported.

Table 2. Initial Biases for C421 Model

Input to hidden	Hidden to ouput
-0.003	0.395
-3.012	

Table 3. Initial Weights for C421 Validation

nodes	Age	Temp	R.H.	m.c.	Depth
1	0.6	0.72	0.078	-1.07	3.30
2	-0.2	-8.97	-1.61	5.00	3.25

Note: nodes refer to hidden nodes, R.H is relative humidity, m.c. is moisture content, and depth is the carbonation depth

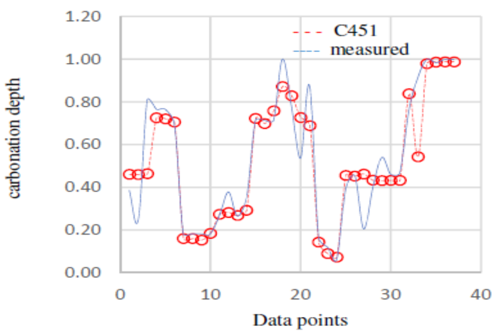

Figure 6. C451 prediction v. actual

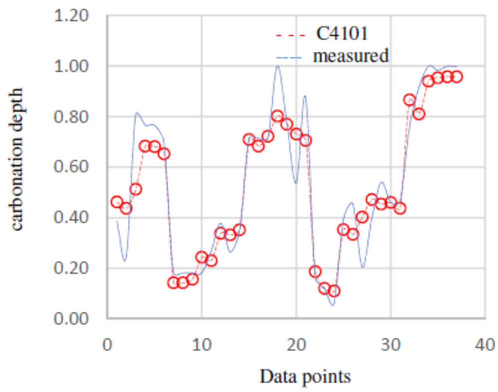

Figure 7. C4101 prediction v. actual

Validation of Model C421

To further evaluate the performance of Model C421, it is tested against the carbonation data gathered from the study of [4]. Raw data from this study were also normalized, similar to the process adopted for [14]. ANN model C421 were adopted and its optimized weights (shown in Table 3) were set as the initial weights for training the network using MATLAB. Its biases, shown in Table 2, were also adopted.

During validation, C421's training R is 0.9831 while its testing R is 1.0. The results of validation can be seen in Fig. 8. This result confirmed that Model C421 approximates the carbonation prediction with high reliability.

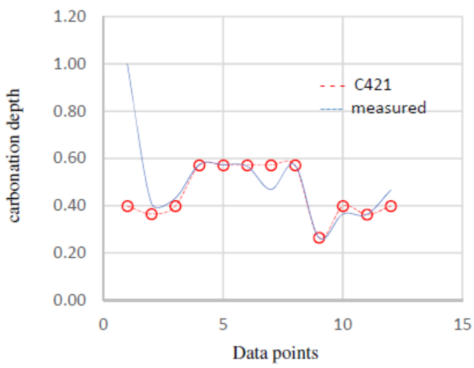

Figure 8. C421 validation

CONCLUSION

The country's remarkable economic growth has been applauded locally and internationally. But some of the environmental effects of a rising economy are treated with less attention. Among these is the alarming increase in CO2 levels in the environment and the potential hazard it poses to reinforced concrete structures due to carbonation.

There are few studies conducted locally to investigate, and analyze the effect of CO2 intrusion in RC structures. This study was among the initial steps to understand the carbonation phenomenon. Here, CO2 intrusion in concrete, through carbonation depth, is related to age, temperature, relative humidity, and moisture content using feed-forward backpropagation artificial neural network.

ANN model C421 were trained using a secondary data and found close prediction values with measured carbonation depth. This was further validated by comparing the prediction values with measured values from another secondary data. Results showed that model C421 were able to validate the reliability and accuracy of the model as depicted by close values between prediction and measured carbonation depths.

ACKNOWLEDGEMENTS

The author would like to thank Engr. Ronaldo S. Gallardo for allowing the use of data from their study in the development (& training) of the ANN model in this paper.

REFERENCES

[1] Jiao, C. (2016, May 16). PH is best economy in Southeast Asia – Oxford Business Group. *CNN Philippines.* Retrieved on June 11, 2016 from http://cnnphilippines.com/business/2016/05/13/ oxford-business-group-economy-philippines-southeast-asia.html

[2] Remitio, R. (2016, May 19). PH is fastest-growing economy in Asia, expands by 6.9% in Q1. *CNN Philippines.* Retrieved on June 11, 2016 from http://cnnphilippines.com/news/2016/ 05/19 /philippines-fastest-growing-economy-asia-gdp-q1.html

[3] Punongbayan, J. C., & Mandrilla, K. (2015, August 15). Carmaggeddon: Why are there so many cars in Metro Manila?. *Rappler.* Retrieved on June 11, 2016 from http://www.rappler.com/ views/imho/102701-carmageddon-metro-manila

[4] Collado, J., Go, J.L., Rosanto, M.A., Tan, J.L., and De Jesus, R.M. (2015). Employing Artificial Neural Network in Assessing Various Factors Affecting Carbonation in old structures. *Thesis.* De La Salle University, Manila.

[5] Philippine Carbon Dioxide Emissions. (2013). Retrieved on June 11, 2016 from https:// ycharts.com/indicators/philippines_carbon_dioxide_emissions.

[6] Burkan Isgor, O., and Razanqapur, A. G. (2004). Finite element modeling of couple heat transfer, moisture transport and carbonation processes in concrete structures. Cement and Concrete Composites, 26(1), 57-73.

[7] Park, D. C. (2008). Carbonation of concrete in relation to CO2 permeability and degradation of coatings. Construction and Building Materials, 22(11), 2260-2268.

[8] Talukdar, S., Banthia, N., & Grace, J. R. (2012). Carbonation in concrete infrastructure in the context of global climate change – Part 1: Experimental results and model development. Cement and Concrete Composites, 34(8), 924-930.

[9] Yoon, I. S., Copuroglu, O., & Park, K. B. (2007). Effect of global climatic change on carbonation progress of concrete. Atmospheric Environment, 41(34), 7274-728.

[10] Houst, Y. F. & Wittman, F. H. (2002). Depth profiles of carbonates formed during natural carbonation. Cement and Concrete Research, 32 (12), 1923-1930.

[11] Kolio, A., Pakkala, T. A., Lahdensivu, J., & Kiviste, M. (2014). Durability demands related to carbonation induced corrosion for Finnish concrete buildings in changing climate. Engineering Structures, 62-63, 42-52.

[12] Oreta, A. W. C. (2004). Simulating size effect on shear strength of RC beams without stirrups using neural networks. Engineering Structures, 26(5), 681-691.

[13] Lu, C., & Liu, R. (2009). Predicting carbonation depth of prestressed concrete under different stress states using artificial neural network. Advances in Artificial Neural Systems,2009,1-8.

[14] Bata, K. J., Beltran, B., Sacaguing, A., & Gallardo, R. (2013). Carbonation profile of old and new reinforced concrete structures in Intramuros, Manila. Thesis. De La Salle University, Manila.

[15] Hect-Nielson, R. (1989). Theory of back propagation neural networks. Proceedings of the International Joint Conference on Neural Networks, 593-611.

INFLUENCE OF 3D NUMERICAL MODEL PARAMETERS IN ANALYSES OF THE SUBSOIL-STRUCTURE INTERACTION

Jana Labudkova [2], Radim Cajka [1]
[1,2] Faculty of Civil Engineering, VSB - Technical University Ostrava, Department of Structures, Ludvika Podeste 1875/17, 708 33 Ostrava – Poruba, Czech Republic

ABSTRACT

For decades attention has been paid to interaction of foundation structures and subsoil and, in turn, to development of interaction models. Complexity of a static solution is given mainly by selection of a computational model, effects of physical-nonlinear behaviour of such structure and co-effects of the upper structure and the foundation structure.). Input data for numerical analysis were observed experimental loading test of steel-fibre reinforced concrete slab. The loading was performed using unique experimental equipment which was constructed in the area Faculty of Civil Engineering, VŠB-TU Ostrava. Homogeneous half-space this takes no account and calculated settlement is strongly dependent on the size of the subsoil model, as parametric study demonstrated. The modulus of deformability changes continuously, depending on the depth, in the inhomogeneous half-space. Values calculated by 3D numerical model were compared with values measured during the loading test of steel-fibre concrete slab.

Keywords: Foundation structure, Soil – structure interaction, Contact stress, 3D FEM element.

INTRODUCTION

Input characteristics of applied material models in subsoil-structure interaction often have lower levels of reliability (especially in the case of the subsoil). This can lead to a lower level of reliability of results of modeling. For this purpose, research and experimental measurements focused on the settlement of loaded foundation soil, deformations of the slabs in interaction with subsoil and dependence of stress in the slabs on the characteristics of the subsoil are still performed. Because calculated subsidence and real subsidence of foundations do not correlate well [9, 10, 17, 18, 20], a site survey is needed and experimental measurements are carried out in order to determine subsidence of foundation soil under structures, deformation of foundation slabs and characteristics of stress in foundation slabs which depend on parameters of subsoil. Using results of such experiments, the methods used for calculation of subsidence are modified and become stricter. In 2010, testing equipment – a stand, was erected in the Faculty of Civil Engineering, VŠB – TU Ostrava [15]. The stand measures deformation and monitors interaction between stress and deformation. In 2014 an experiment was carried out using the stand. Values measured during the loading tests were compared with values calculated by interaction 3D FEM models. The calculations were carried out for several sizes of the subsoil and for different boundary conditions. The values were compared and impacts of 3D numerical model parameters on final deformation and internal forces in the steel-fibre reinforced foundation slab were evaluated. Another experimental loading tests and their results are also described in [2, 3, 6, 7, 8, 11, 19, 21, 22].

EXPERIMENTAL LOADING TEST OF STEEL-FIBRE REINFORCED CONCRETE SLAB

A sample used for the experiment and for monitoring of foundation – subsoil interaction was a steel-fibre reinforced concrete slab. The size of the fibre concrete slab was 2000 x 2000 x 170 mm. The C25/30 concrete was cast there - it was reinforced with scattered reinforcement. The reinforcement consisted of steel fibres, 3D DRAMIX 65/60B6–25 kg.m^{-3}. The slab casting process is shown in Fig. 1.

Fig. 1 Casting of the steel-fibre reinforced concrete slab

The upper layer of subsoil consists of loess loam with F4 consistency. Thickness of that layer is about 5 meters. Poisson coefficient of the subsoil is $\mu = 0.35$, and modulus of deformability is E_{DEF} = 23.7 MPa. From the geologic point of view, foundation soil is not complex.

During the test, the fibre concrete slab was loaded in the middle by the pressure applied by the hydraulic press. Dimensions of the area under load were 200 x 200 mm. The loading was carried out in steps: 50 kN / 30 minutes. The slab failed during the 6th cycle when the loading force was 250 kN. The model of steel-fibre reinforced concrete foundation slab was violated by punching shear. Punching shear of slabs is discussed in detail [1].

Fig. 2 Load test of the steel-fibre concrete slab

3D COMPUTATIONAL MODEL IN ANSYS SYSTEM

A 2D element, SHELL 181, was chosen for the foundation slab which was modelled as a surface with the specified slab thickness. The subsoil was modelled using a 3D element, SOLID 45. The material properties were modelled using the modulus of elasticity E (or the modulus of deformability E_{DEF} in case of soil) and Poisson coefficient μ.

In connection with the creation of a spatial model using 3D elements is particularly problematic correctly to determine the size of the modeled area representing the subsoil, to choose boundary conditions and finite size mesh.

Soil is inhomogeneous and its properties are different from idealised properties of an elastic isotropic and homogeneous substance. In the homogeneous half-space, the modulus of deformability is constant and does not depend on depth (Fig. 3). In the inhomogeneous half-space, the concentration of vertical stress in the foundation axis is different from that in the homogeneous half-space. The modulus of deformability changes continuously, depending on the depth. This means that it is the model of the inhomogeneous half-space which describes the deformation behaviour of the soil better that the homogeneous model. Using of inhomogeneous half-space is also described in papers [12, 13, 14]. Homogeneous half-space and also inhomogeneous half-space were used in numerical analyses.

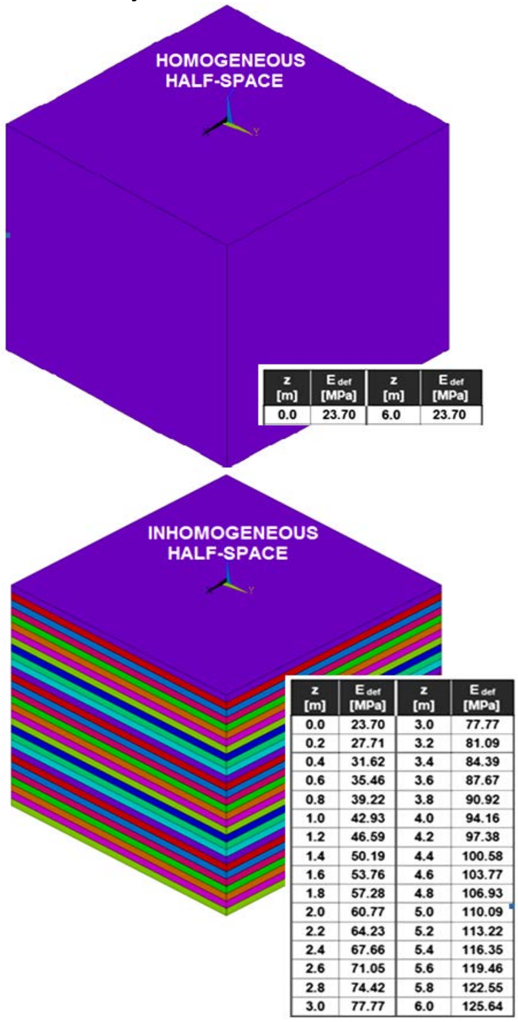

Fig. 3 3D numerical model in ANSYS

Shell 181 is a four-node element with six degrees of freedom in a node. The degrees of freedom represent three dislocations in x, y and z axes and three torsional displacements around x, y and z axes. SOLID 45 is defined by eight nodes where each node is characterised by three degrees of freedom (dislocations of the node in x, y and z axes). Dead weight of soil and dead weight of concrete slab were not considered for the calculation. The slab and subsoil were modelled using the regular finite-element mesh. The sizes of mesh elements were different for the subsoil and for the slab surface where the mesh was denser. The force was specified for each node in the finite-element mesh of the slab. The location and value corresponded to the load applied onto the slab during the experiment. In order to transfer effects of the load, which was applied on the foundation slab, into the subsoil it was essential to create a mutual contact and define a contact surface. The FEM model was solved using the contact elements.

Contact elements mediate the kinematic process of deformation. The contact was created using the contact pair: TARGE170 – CONTA173. Friction between the slab and subsoil was neglected there.

PARAMETRIC STUDY

In connection with the creation of a spatial model using 3D elements is particularly problematic correctly to determine the size of the modeled area representing the subsoil, to choose boundary conditions and finite size mesh. A dependence deformation on these parameters was proved by parametric study. Two aspects were considered when comparing different models. One aspect is dependence of deformation on variable depth of the subsoil, while keeping the same ground plan of the subsoil. The second aspect is dependence of deformation on variable size of ground plan of the subsoil, while keeping the same depth. The comparison was made for three different boundary conditions - see Fig. 4, Fig. 5.

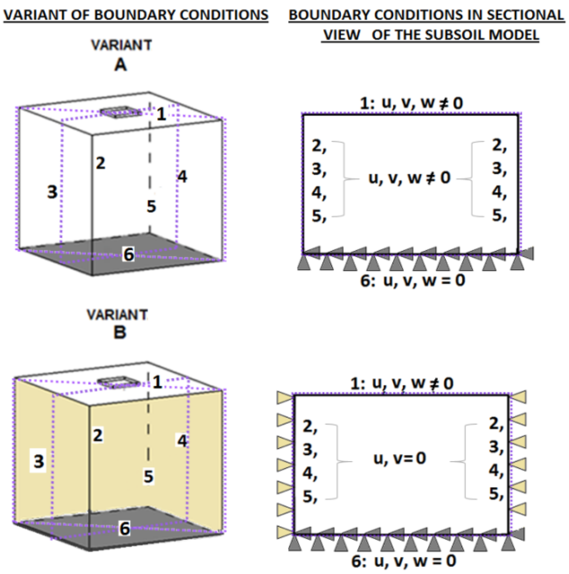

Fig. 4 Variant of boundary condition A, B

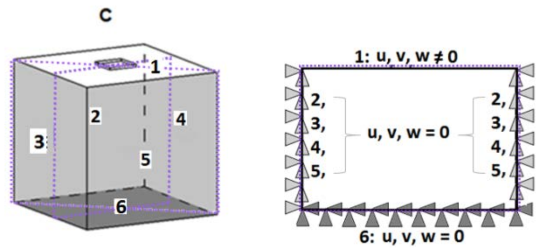

Fig. 5 Variant of boundary condition C

Deformation versus variable depth of the subsoil model

Fig. 6 - Fig. 8 compares the deformations of the slab for the variable depth of the homogeneous half-space (light curve) and inhomogeneous half-space (dark curve) for all variants of the boundary conditions.

The ground plan is 6.0 x 6.0 m and boundary conditions are A:

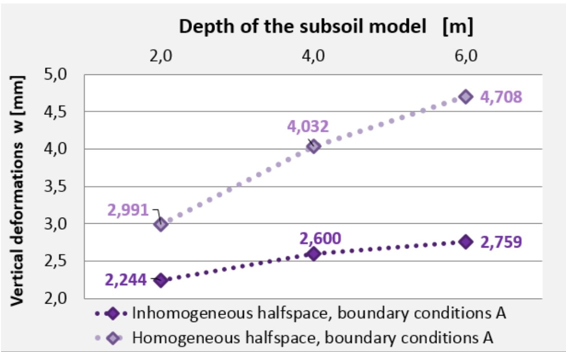

Fig. 6 Deformation versus variable depth of the subsoil model, boundary conditions A

The ground plan is 6.0 x 6.0 m and boundary conditions are B:

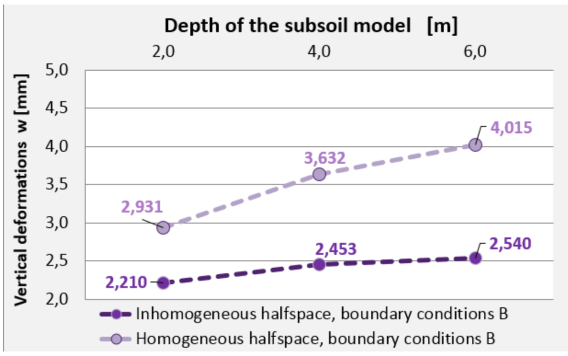

Fig. 7 Deformation versus variable depth of the subsoil model, boundary conditions B

The ground plan is 6.0 x 6.0 m and boundary conditions are C:

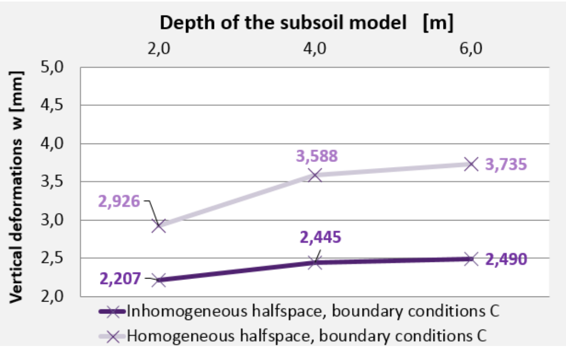

Fig. 8 Deformation versus variable depth of the subsoil model, boundary conditions C

Deformation versus variable ground plan of the subsoil

Fig. 9 - Fig. 11 compares the deformations of the slab for the variable ground plan of the homogeneous half-space (light curve) and inhomogeneous half-space (dark curve) for all variants of the boundary conditions.

The depth is 6.0 m and boundary conditions A:

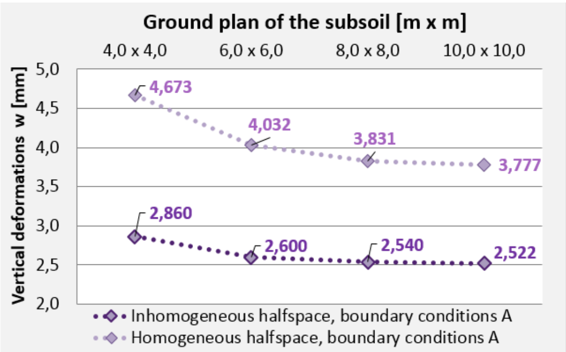

Fig. 9 Deformation versus variable ground plan of the subsoil, boundary conditions A

The depth is 6.0 m and boundary conditions B:

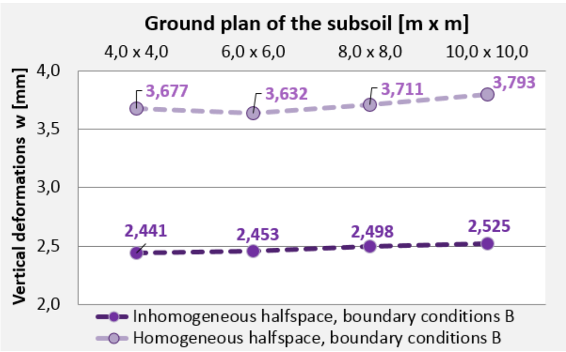

Fig. 10 Deformation versus variable ground plan of the subsoil, boundary conditions B

The depth is 6.0 m and boundary conditions C:

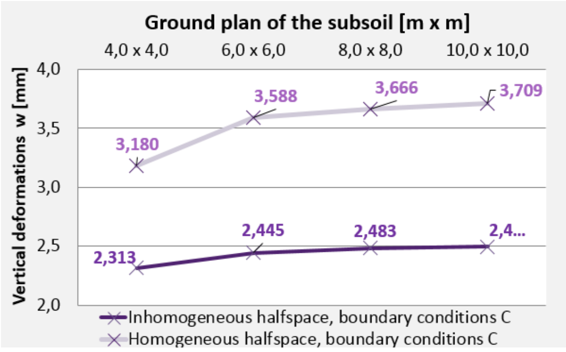

Fig. 11 Deformation versus variable ground plan of the subsoil, boundary conditions C

The deformation in the middle of the steel-fibre reinforced concrete slab measured during the experiment was ca. 2.83 mm.

CONCLUSIONS

It follows from the characteristics deformation vs. variable depth of the subsoil model that the increasing depth results in increases in the vertical deformation. Considering different variants of the boundary conditions, one can compare the growth of vertical deformation once the depth becomes higher (Fig. 12).

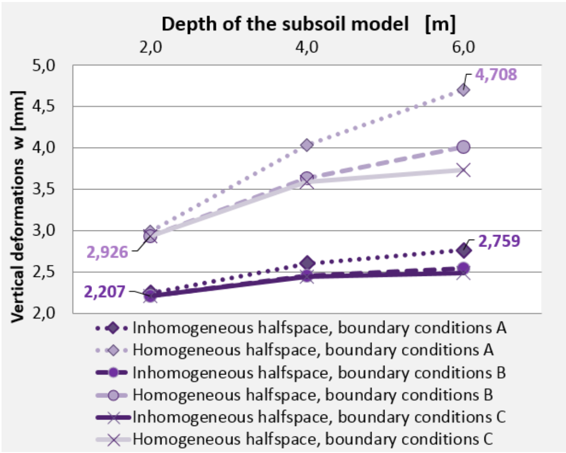

Fig. 12 Deformation versus variable depth of the subsoil model, all boundary conditions

In case of the variant C when all walls except for the upper surface are fixed, the boundary conditions play such an important role that even the increasing depth does not increase the vertical deformation so much as for other variants of boundary conditions. On the other hand, the least influence of boundary condition was for the variant A, when deformation is possible for each wall of the subsoil model in each direction except for the lower base which is fixed. Fig. 12 shows that the higher the depth of the subsoil model is, the bigger the difference is between deformations calculated for the variants of boundary conditions. With the increasing depth of the subsoil model, the selection of boundary conditions is becoming a more important criterion which influences the final vertical deformation.

An important lesson learnt from characteristics describing the deformation versus variable size of subsoil ground plan is that the influence of any boundary condition is becoming weaker with the increasing ground plan of the subsoil. Using the chart in Fig. 13 it can be concluded that the boundary conditions play no role at all, if the ground plan of the subsoil model is big enough.

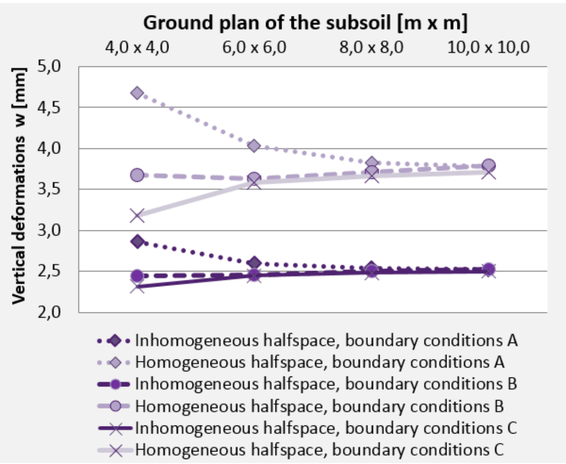

Fig. 13 Deformation versus variable ground plan of the subsoil model, all boundary conditions

Even in that case the boundary conditions influence the characteristics the deformation versus the increasing ground plan of the subsoil model which has been proved by the chart in Fig. 13.

The charts prove the major role played by the size of the model area and by the boundary condition itself. Results were quite scattered for the variants. Charts in Fig. 12 and 13 indicate how the parameters of the area influence considerably the resulting vertical deformation.

From deformations obtained by numerical subsoil model of homogeneous half-space, the conclusion can be drawn that the values of deformation resulting from the 3D model are too scattered. Final deformation measured during the experiment was ca. 2.83 mm. In this set of results in Fig. 12 and Fig 13 the vertical deformation is ranges from 2.926 to 4.708 mm in analyses of homogeneous half-space. This is really great variance in the resulting deformation depending on the size of the subsoil model and its boundary conditions. Fig. 12 and Fig 13 the vertical deformation is ranges from 2.207 to 2.759 mm in analyses of inhomogeneous half-space. This is not so really great variance in the resulting deformation depending on the size of the subsoil model and its boundary conditions as in analyses of homogeneous half-space. This means that the inhomogeneous continuum provides more stable results which are less affected by the choice of the geometry and dimensions of the area representing the subsoil.

ACKNOWLEDGEMENTS

This outcome has been achieved with the financial support of the project GACR No. 16-08937S „State of stress and strain of fiber reinforced composites in interaction with the soil environment“. In this undertaking, theoretical results gained by conceptual development of research, development and innovations for 2016 at the VŠB-Technical University of Ostrava (granted by the Ministry of Education, Youths and Sports of the Czech Republic) were partially exploited.

REFERENCES

[1] R. Halvonik, J., Fillo, “The Maximum Punching Shear Resistance of Flat Slabs, Procedia Engineering”, vol.: 65, 2013, pp 376-381, ISSN 1877 - 7058,

[2] M. Aboutalebi, A. Alani, J. Rizzuto, D. Beckett, “Structural behaviour and deformation patterns in loaded plain concrete ground-supported slabs”. Structural Concrete. 2014, vol. 15, issue. 1, pp. 81-93. ISSN 1464-4177.

[3] T. Clément, A.P. Ramos, M.F. Ruiz, A. Muttoni, “Influence of prestressing on the punching strength of post-tensioned slabs”, Engineering Structure, vol. 72, pp. 56-69 (14 p), ISSN: 0141-0296, 2014

[4] K. Frydrysek, R. Janco, H. Gondek, “Solutions of Beams, Frames and 3D Structures on Elastic Foundation Using FEM”, International Journal of Mechanics, Issue 4, Vol. 7, p. 362-369, 2013.

[5] P. Mynarcik, “The Subsidence Analysis of Experimental Post-tensioned Concrete Slab Model in the Course of the Static Load Test”, Applied Mechanics and Materials, vol. 744 – 746, pp. 1556-1559 (4 p), Trans Tech Publications, Switzerland, 2015.

[6] A. Alani, M. Aboutalebi, “Analysis of the subgrade stiffness effect on the behaviour of ground-supported concrete slabs” Structural

Concrete, Issue 13, Volume 2, pages 102-108, DOI: 10.1002/suco.201100043, 2012.
[7] R. Cajka, R. Fojtik, "Development of Temperature and Stress during Foundation Slab Concreting of National Supercomputer Centre IT4", Procedia Engineering, vol. 65, 2013, pp. 230-235 (6 p), ISSN 1877-7058,
[8] R. Cajka, K. Burkovic, V. Buchta, "Foundation Slab in Interaction with Subsoil", Advanced Materials Research, Vols. 838-841, pp. 375-380, Trans Tech Publications, Switzerland, 2014.
[9] R. Cajka, J. Labudkova, „Influence of parameters of a 3D numerical model on deformation arising in interaction of a foundation structure and subsoil", 1st International Conference on High-Performance Concrete Structures and Materials (COSTMA '13), Budapest, Hungary, 2013.
[10] R. Cajka, P. Mateckova, "Comparison of calculating methods and consequent carrying capacities of pre-stressed precast concrete roof purlin", in proceedings of First International Workshop "Design of Concrete Structures using EN 1992-1-1, Prague, 15 March 2010, ISBN 978-80-01-04581-7, WOS: 000324078100017.
[11] M. Janulikova, R. Cajka, P. Mateckova, V. Buchta, "Laboratory Testing of Asphalt Belts Rheological Properties Exposed to Shear Loads", Transactions of the VŠB - Technical University of Ostrava, Civil Engineering Series, vol. XII, iss. 2, pp. 59–66 (8 p), ISSN (Online) 1804-4824, ISSN (Print) 1213-1962.
[12] K. Zhou , W. W. Chen, L. M. Keer, X. Ai, K. Sawamiphakdi, P. Glaws, Q. J. Wang, "Multiple 3D inhomogeneous inclusions in a half space under contact loading", Mechanics of Materials, Vol. 43, Issue 8, Pages 444–457, 2011.
[13] V. I. Fabrikant, T. S. Sankar, „On contact problems in an inhomogeneous half-space", International Journal of Solids and Structures, Volume 20, Issue 2, Pages 159–166, 1984.
[14] K. Zhou, W. W. Chen, L. M. Keer, X. Ai, K. Sawamiphakdi, P. Glaws, Q. J. Wang, „Multiple 3D inhomogeneous inclusions in a half space under contact loading", Mechanics of Materials, Vol- 43, Issue 8, pp.444–457, 2011.
[15] R. Cajka, V. Krivy, D. Sekanina, "Design and Development of a Testing Device for Experimental Measurements of Foundation Slabs on the Subsoil", Transactions of the VŠB – Technical University of Ostrava, Civil Engineering Series, vol. XI, iss. 1, pp. 1-6, ISSN 1804-4824, ISBN 978-80-248-2332-4.
[16] R. Cajka, "Analytical derivation of friction parameters for FEM calculation of the state of stress in foundation structures on undermined territories", Acta Montanistica Slovaca, vol. 18, iss. 4, pp. 254-261 (8 p), ISSN: 13351788, 2013.
[17] R. Cajka, J. Labudkova, „Dependence of deformation of a plate on the subsoil in relation to the parameters of the 3D model", International Journal of Mechanics, Volume 8, Pages 208-215, 2014, ISSN: 1998-4448.
[18] J. Labudkova, R. Cajka, "Comparsion of Measured Displacement of the Plate in Interaction with the Subsoil and the Results of 3D Numerical Model", Advanced Material Research, vol. 1020, pp. 204-209 (6 p), Trans Tech Publications, Switzerland, ISSN (Online) 1662-8985, ISSN (Print) 1022-6680, 2014.
[19] Cajka, K. Burkovic, V. Buchta, R. Fojtik, "Experimental soil - Concrete plate interaction test and numerical models", Key Engineering Materials, vol. 577-578, pp. 33-36 (4 p), Trans Tech Publications, Switzerland, 2014.
[20] Bin Tian, Rui Li, Yang Zhong, "Integral transform solutions to the bending problems of moderately thick rectangular plates with all edges free resting on elastic foundations", Applied Mathematical Modelling, Vol. 39, Issue 1, 2015, pp. 128–136.
[21] Cajka, R. – Labudkova, J. – Mynarcik, P.: Numerical solution of soil - foundation interaction and comparison of results with experimental measurements, International Journal of GEOMATE, July, 2016, Vol. 11, Issue 23, pp. 2116-2122, Geotec., Const. Mat. & Env., ISSN: 2186-2982(Print), 2186-2990(Online), Japan.
[22] Cajka, R. – Mynarcik, P. – Labudkova, J.: Experimental measurement of soil-foundation interaction, International Journal of GEOMATE, June, 2016, Vol. 10, Issue 22, pp. 2101-2108, Geotec., Const. Mat. & Env., ISSN: 2186-2982(Print), 2186-2990(Online), Japan.

Sixth International Conference on Geotechnique, Construction Materials and Environment, Bangkok, Thailand, Nov. 14-16, 2016, ISBN: 978-4-9905958-6-9 C3051

INVESTIGATION OF POTENTIAL ALKALI-SILICA REACTIVITY OF AGGREGATE SOURCES IN THAILAND

Suvimol Sujjavanich[1], Krit Won-In[2], Thanawat Meesak[1], Watcharagon Wongkamjan[3], Viggo Jensen[4]
[1]Faculty of Engineering, Kasetsart University, Thailand
[2]Faculty of Science, Kasetsart University, Thailand
[3]Faculty of Liberal Arts and Sciences, Roi Et Rajabhat University, Thailand
[4]Norwegian Concrete and Aggregate Laboratory LTD, Norway

ABSTRACT

Since the first local evidence of alkali-silica reaction (ASR) was reported in Thailand in 2011, awareness of ASR was raised and the importance of aggregate performance database was recognized, thus an attempt to set up local aggregate database was initiated. As part of the effort to establish the database, a study of potential ASR reactivities was carried out involving aggregates from several current industrial sources in eastern and central Thailand and the results were presented here. Aggregate samples were randomly collected from various sources and tested by two methods; accelerated mortar-bar test (AMBT) and petrographic examination. The types of aggregate sampled included limestone, greywacke, and rhyolitic tuff. The AMBT expansion results indicated that several aggregate types had larger expansion than the threshold of potentially deleterious ASR behavior as suggested by ASTM C 1260 standard. Furthermore, it was found that samples of same aggregate type, although apparently had mineralogically similar compositions, had different reactivities, particularly when sampled from around geological fault zone compared with that taken from the surrounding area and portions of parent rock were observed to be weathered in this area. Thin section analysis revealed evidence of ASR gel at the aggregates' rim, inside the aggregates and in the matrix. These findings suggest possible future ASR problems in Thailand as well as in neighboring countries where the continuity of geology pattern is observed.

Keywords: Aggregate database, Alkali silica reaction (ASR), Expansion, Petrographic Analysis, Thin Section

INTRODUCTION

The first evidence of alkali-silica reaction (ASR) in Thailand was found in one large infrastructure in 2009 and reported by Sajjavanich in 2011 [1]. The confirmed problematic rocks were black quartzite with traces of pyrite, mica and sericite. Some of these rocks were confirmed as slow late reactive types [2]. Therefore, the awareness of ASR was raised and the importance of aggregate's performance database was recognized as a basis for achieving a better understanding of the reactivity of local materials and the consequent activities to cope the future problems including mitigation, both for research and construction practice. Thus an attempt to set up local aggregate database was initiated. As one part of the ongoing effort to establish the database, a study of potential ASR reactivities was carried out involving aggregates from several current industrial sources in eastern and central Thailand.

Thailand is situated on two adjacent terranes, the Shan-Thai and the Indochina terranes. The Shan-Thai terrane covers the east of part of Myanmar, the west, north, central and southern parts of Thailand with rocks dating back to the Precambrian eon. The Indochina terrane covers the northeastern and eastern parts of Thailand as well as Cambodia and the majority of Laos and Vietnam landmasses with rocks dating back to Paleozoic era. The suture joining the two run down north – south direction giving rise to the Loei-Petchabun mountain ranges that stretches from Thailand's northern border with Laos in Loei province down along the Petchabun fold belt bordering the rim of the Khorat plateau to the east and the central plain to the west. Evidence of ancient volcanic activities can be found along the Petchabun fold belt and igneous rocks such as granite, granodiorite, diorite, monzonite, rhyolitic tuff, andesite, and tuff. The suture runs further down through the eastern region of the country and extends to the upper part of the Gulf of Thailand.

This study investigated aggregates from working industrial mining operation from the central and eastern region of Thailand. These two regions of interest in Thailand have significant differences in landforms. The eastern region is bordered by the Gulf of Thailand to the south and southwest, the southern part of Loei-Petchabun mountain ranges to the northwest and the rim of the Khorat plateau to the north. The area includes undulating coastal plains between the sea and the mountains covering the provinces of Chonburi, Rayong, Chantaburi and Trat. The landform in this region is highly discontinued with evidence of some geologic activities thus rocks with high degree of alteration were not uncommon in these areas. Granite can be found in three separate areas, in Chonburi, Rayong, and Chantaburi, and rhyolite can be found in the extreme east of the region close to the border with Cambodia. High-grade metamorphic rocks with important rock-forming minerals such as quartz, biotite and feldspar can also be found in Chantaburi and Trat provinces. Various sedimentary rocks are found in this region such as quartzite, shale, chert, and limestone found along Chonburi’s coastline. Limestone, shale and greywacke are also found in Chantaburi and Trat provinces. Moreover, because of the suture running through this area and activities of various local faults, the characteristics of rocks found in this area are quite complicated. Some rocks have undergone metamorphism, others have undergone alteration, and the effect can be very localized. History of geological landform and time strongly influence the changes of some of these to low-grade metamorphic rocks [3]. The dominant characteristics of discontinued landform explain the variations of type of rock, which are the sources of industrial aggregates in these areas.

The central region of Thailand consists of fluvial flood plain bordering highlands and mountainous regions to the north and west, flanked by the Loei-Petchabun mountain ranges to the east and extending south to the Gulf of Thailand. The country’s major rivers flow through this region depositing sediment from the highlands. Coastal deposit is found in the lower third of the region. The upper central plain region consists of Uttradit, Sukhothai, Pitsanulok, Pichit, and Kampangpet provinces and northern part of Nakhonsawan province. These provinces lie in the confluence of the major rivers that join together further south in Nakhonsawan province to form Chao Phraya river which forms the border of upper and lower central plains. The lower central plain begins in the southern part of Nakhonsawan province and continues south until the mouth of the Chao Phraya river on the gulf of Thailand. There are isolated rock formations scattered around the region with formations of plutonic rocks such as granite, granodiorite and diorite in the south and southwest of Nakhonsawan and formations of volcanic rocks such as rhyolite, andesite, and dacite in the east of the region as forming part of the Saraburi group of Permian rock formations [4]. In Saraburi area, there are six known formations with mixed carbonate and clastic sequence of outcrops, especially on the most eastern area bordering the western rim of the Khorat plateau [5]. This area is also the source of good quality limestone used in construction industry and cement industry. Gray shale and siltstone with minor or major of sandstone and limestone are found in some formations while others may be characterized by limestone with interbedding with dolomitic limestone, shale, sandstone and tuffaceous sandstone including rhyolite dikes and chert nodules. In addition to the good quality limestone, which typically has been used for construction in the past, it is of interest that the diversity of landform and geological nature indicates various natural rock types in these two areas and these have been utilized as natural resources for construction and other industries. Some of them have been widely reported as potentially reactive aggregates [6]. The variations of these geological parent rocks have strong impact on the local industrial aggregates, which is the main component of concrete, and the chemical deterioration of concrete structure may be a consequence if the potential risk of reactivity of the rock is not properly assessed.

All of the aggregate mines are either privately owned or have been granted long-term government mining concessions and most of them are used for concrete production. Since no concrete deterioration problems as a result of reactive aggregates had previously been reported, it was not uncommon that there was a lack of local information concerning the aggregates except the conventional geology classification. Therefore this paper reports the results of an investigation of the industrial aggregates in term of both geological and chemical durability in engineering aspects. This is expected to provide information and insight into potential risk of chemical deterioration in future concrete structures in Thailand and neighboring countries.

MATERIALS AND METHODS

Materials

Three common rock types used as aggregates in Thailand were selected for this study, namely, rhyolitic tuff (RYSR) from the central region, limestone (LSCB) and greywacke from the eastern region. The greywacke aggregates were from two different sources approximately 100 km apart, one in Chantaburi province (GWCT), and the other in Trat province with two samples taken from this quarry (GRA and REA)

The three rock types were picked because of their differences. While the major mineral compositions of limestone, a non-clastic sedimentary rock, are calcite and aragonite which are only different crystallographic forms of calcium carbonate ($CaCO_3$), on the other hand, greywacke, a clastic sedimentary rock, is a result of sedimentation and lithification of mainly sandstone and other small rock fragments, angular quartz grains, feldspar crystals in a matrix of fine clay, whereas, rhyolite, a felsic volcanic rock is an igneous rock rich in silica.

These three different rock types were investigated in details for microstructure, mineral and chemical compositions as well as expansion in the accelerated mortar bars.

Type I Portland cement, according to ASTM C150-07 [7], with $Na_2O_{equiv.}$ of 0.409 % was used for this study.

Methods

To investigate the potential alkali-silica reactivity of the various aggregate types, samples of aggregates were taken from different sources in many parts of the country and were tested by laboratory methods, namely, petrographic examination and accelerated mortar-bar test (AMBT).

Thin section petrography was carried out using Olympus BX-41 imaging petrographic microscope equipped with plane and cross polarization illumination mode. The petrographic analysis was used to study the microstructure of the aggregates, to identify the constituent minerals and to classify the aggregates. The chemical compositions were analyzed with X-ray Fluorescence spectroscopy (XRF) and X-ray diffraction spectroscopy (XRD).

Accelerated mortar-bar test (AMBT) was used to measure expansion due to alkali silica reactivity of the aggregates and was carried out according to ASTM C 1260 [8] standard testing procedure.

RESULTS AND DISCUSSION

Microstructure Analysis

The XRF results of all the aggregates are shown in Table 1. The investigation showed the major compositions of all studied aggregates. All the greywacke samples even though came from two different sources (GRA and REA from one, GWCT from the other) had very similar composition with amounts of major oxides falling in the same ranges (such as SiO_2 56-58%, Al_2O_3 13-18% and Fe_2O_3 5-7%, CaO 5-7%, MgO 1.9-3.2%). However, the petrographic analysis and XRD analysis were performed on the same specimens and the results showed significant difference, especially the microstructure of GRA and REA observed in thin-section petrographic analysis. GRA aggregates, which were collected from the same mine as REA but from the general areas of mine was coarse-grain greywacke. The microstructure of GRA is shown in Fig. 1 (a) composing of quartz, feldspar, and rock fragments. This was similar to the microstructure of GWCT aggregates that were collected from the other quarry. However, the REA samples, Fig. 1 (b), were collected from the same quarry as GRA but from the shear zone showed fine-grained matrix of subgrained quartz and rock fragments of clay/graphite and high-weathering chlorite, deformed by tectonic forces. The mineralogical compositions were confirmed by XRD analysis. Quantitative XRD analysis showed high content of muscovite and low content of albite found in REA, 31.9% and 7.1% respectively, which was opposite of what was found in GRA where low amount of muscovite and high amount of albite was found, 13.1% and 32.1% respectively. Another striking difference was the difference in granularity of crystals in REA and GRA. REA consisted of small grains of quartz and rock fragments instead of big grains such as those found in GRA. The microstructure of REA consisted of deformation-induced subgrained quartz particles to become

Table 1 Chemical composition of materials used in this study

	SiO_2	Al_2O_3	Fe_2O_3	CaO	MgO	SO_3	Na_2O	K_2O	LOI
GRA	58.22	13.93	6.11	6.96	2.53	0.24	3.08	1.32	6.77
REA	56.48	18.64	5.29	3.21	1.9	0.38	1.15	3.39	8.36
GWCT	57.63	15.33	7.37	5.52	3.19	0.24	2.97	1.41	5.31
RYSR	56.49	17.39	6.51	8.55	3.02	0.04	2.69	4.03	na
LSCB	34.24	7.99	4.53	25.94	2.25	1.92	0.42	2.47	19.34
Cement	18.74	5.22	3.2	65.3	0.82	2.8	0.08	0.5	2.75

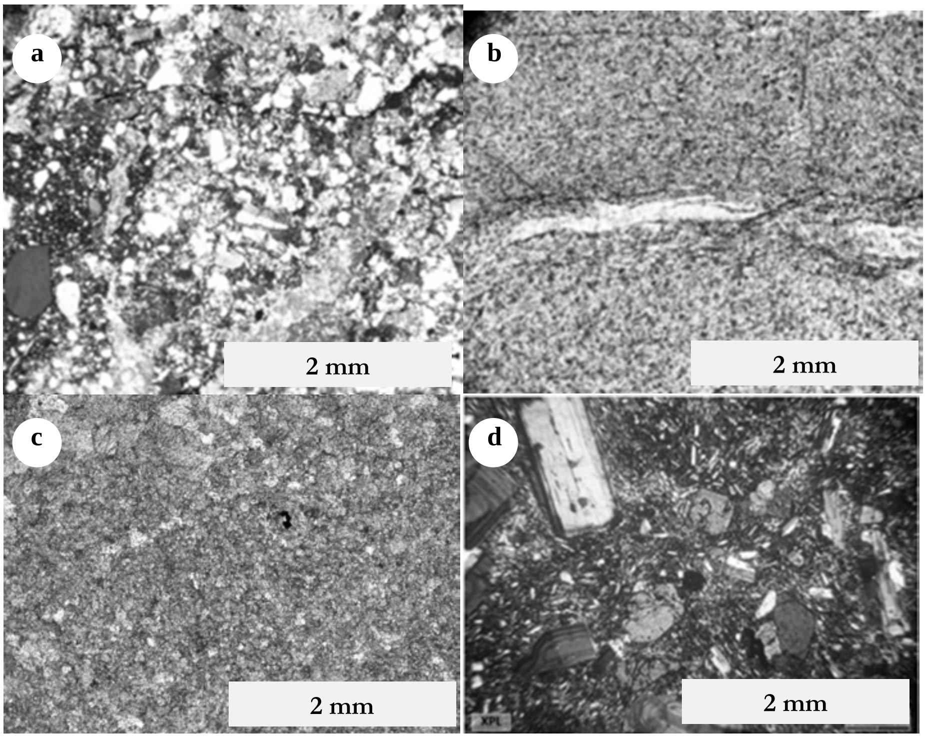

Fig. 1 Thin section microscopy of different aggregates studied (a) greywacke (GRA), (b) greywacke (REA), (c) limestone (LSCB), and (d) rhyolitic tuff (RYSR)

microcrystalline/cryptocrystalline matrix mixed with 30% clay/graphite matrix as shown in Fig. 1 (b). This may explain the highest ASR reactivity in this aggregate group and the proposed classification as “very likely to be alkali-reactive.

Compared to those of greywacke, the chemical compositions of rhyolitic tuff appeared to fall in the same ranges, only a slightly high oxide content of calcium and magnesium and low SO_3 were observed. Slight weathering was observed in hand specimen and from the microstructure analysis. The mineral compositions of the very fine-grained, massive and slightly weathered pale green-gray colored sample was tested using XRD analysis and was found to consist of albite, quartz, calcite, chlorite, K-feldspar and illite. The mineral compositions content from modal analysis indicated subhedral crystals of plagioclase and pyroxene of about 70% and 10% respectively. The anhedral crystals of opaque minerals and calcite were 10% and 5% as well as small amount of olivine, chlorite and epidote of about 1-2% as minor minerals. The average phenocrysts consisted of 0.05-3mm in size and most plagioclase showed zonal texture and lath shape. Some glassy phases were also observed, which, together with microcrystalline and cryptocrystalline quartz present, may account for its reactivity. Other authors also found this rock type to be a reactive aggregate in many countries [2,6].

The non-clastic and stylolitic sedimentary rock, limestone, from the eastern province of Chonburi was slightly high in silica (34.24%) but moderate in CaO (25.94%) with relatively high LOI (19.24%). Because of the high silica content, this aggregate can be classified as siliceous limestone and other authors found this rock type to be reactive [9]. The mineral grain size of the light gray colored sample ranges of 0.1-2 mm, while modal analysis showed major minerals to be calcite, clay, and microcrystalline quartz with some calcite veinlet and quartz veinlet. Opaque minerals, possibly pyrite, were also found in the thin section, which would account for its high LOI. No weathering but fracturing was more commonly observed.

AMBT Results

The results of the AMBT expansion tests of all the studied aggregates, limestone, greywacke and rhyolitic tuff, are shown in Fig. 2. The average expansion of each aggregates were higher than the suggested limit of 0.2% at 14 days exposure to sodium hydroxide solution (except rhyolitic tuff which was slightly less), which indicated that all three rock types were potentially reactive aggregates. The deformation induced subgrained greywacke (REA), showed the highest expansion and rhyolitic tuff the lowest. The comparison between the average expansion of greywacke with different granularity from different location of the same mine (REA and GRA) and the average expansion of similar aggregate type from different mine (GWCT) were also demonstrated in Fig. 2. These agreed well with the petrographic analysis. The effect of deformation-

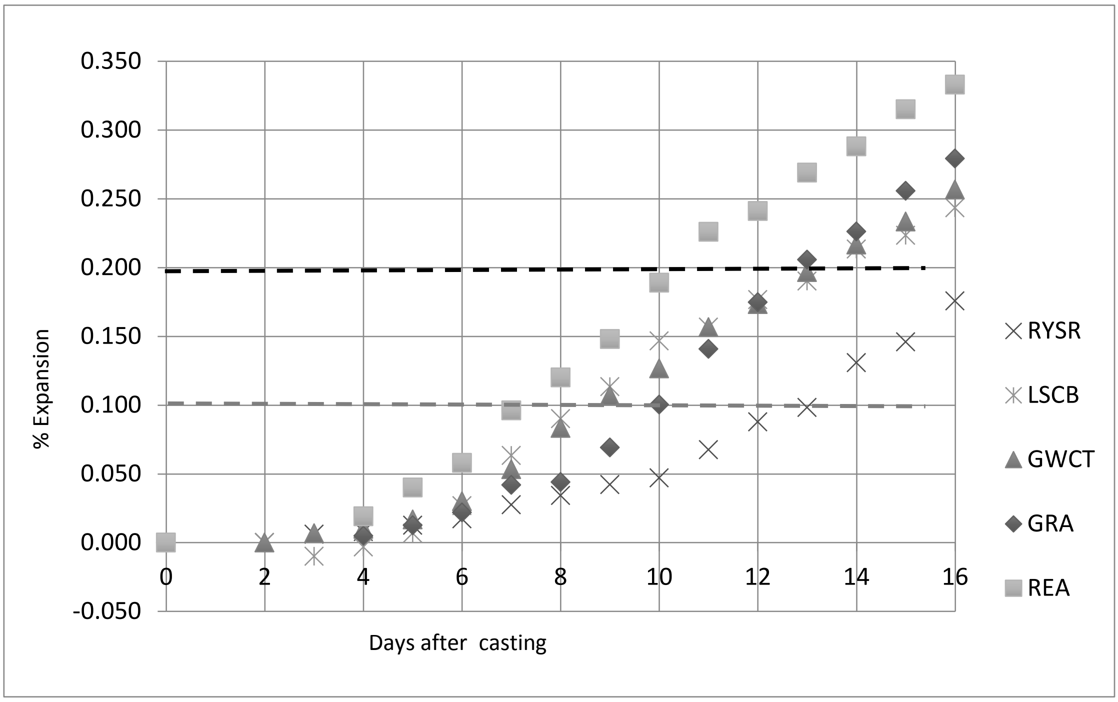

Fig. 2 AMBT results of aggregates. Different granularity of greywacke aggregates affects their average expansions under accelerated conditions

induced subgraining resulted in REA yielded the highest expansion than those of aggregates from typical area (GRA) and from other mine (GWCT). It was clear that mineralogical and the past history of the studied three types of aggregates were strongly influenced the reactivities of these materials, not the chemical compositions.

The expansion results indicated that all studied aggregates, whatever types, had larger expansion than the threshold for potentially deleterious ASR behavior as suggested by ASTM C1260 standard. Furthermore, samples of the same aggregate type, although with mineralogically similar compositions, had different reactivities, particularly when sampled from around geological fault zone compared with that taken from the surrounding area. Portions of parent rocks in this area were observed to be weathered. In addition, thin section analysis of concrete prisms made from REA and GRA from previous study [10] revealed evidence of ASR gel at the aggregates' rim, inside the aggregates and in the matrix. In light of these findings, it suggests possible future ASR problems in Thailand as well as in neighboring countries where the continuity of geology pattern from Thailand or similar are observed.

The ASR Risk In Thailand And South East Asia

The hot and humid weather in Thailand is typical for this region. This may create high risk of ASR in the future if the potentially reactive aggregates from some sources are used, in combination with some specific conditions such as high humidity environment. This is also important for the neighboring countries such as Laos, Myanmar and Cambodia, in which there has been no AAR deterioration reported yet. The similar condition both for geology, materials and climatic condition is of concern for the potential AAR in this region.

CONCLUSIONS

From the study, conclusions as follows are

−Two types of sedimentary rocks, greywacke and limestone from some sources in eastern region of Thailand, as well as an igneous rock, rhyolitic tuff, from the central region, showed the potential reactivity as the root of ASR problem in the future.

−Greywacke from the different sources were almost similar in compositions, but significantly different features have been observed in thin-section analysis. GRA and CTGW were coarse-grained greywacke composed of quartz, feldspar, and rock fragments but REA had different granularity than the other two, with high-weathering chlorite with a matrix of subgrained quartz, rock fragments and clay/graphite, deformed by tectonic forces. The ASR risk is increased significantly from subgraining of the microstructure. The highest expansion of REA agreed well with the microstructure analysis.

−The microstructure investigation of volcanic rock aggregate, rhyolitic tuff showed slight weathering and the expansion result indicated potential reactivity.

−The high silica content found in the limestone sample studied and the expansion higher than the limit suggested potential alkali reactivity.

−All studied samples in this paper revealed the potential alkali reactivity although aggregates types are different.

At present, ASR is not a serious problem in Thailand and only one case is reported. However awareness that ASR might be a possible problem in the near future is important based on the varieties of aggregates from local sources as well as the chemical variation particularly the alkali content of local cement. Therefore, continuing work on database development may be an appropriate use of available resources.

ACKNOWLEDGEMENT

The authors would like to thank Kasetsart University Research and Development Institute (KURDI) and National Research Council of Thailand (NRCT) for their financial support for this study.

REFERENCES

[1] Sujjavanich, S, Suwanvitaya, S, and Rothstein, D (2011): Investigation of ASR in Mass Concrete Structures: A case study. Modern methods and Advances in Structural Engineering and Construction (ISEC-6), Zürich Swizzerland 2011, pp. 1297-1302. Research Publishing Services.

[2] Jensen V, and Danielsen S. W (1992): Alkali-Aggregate Reaction in Southern Norway. The Ninth International Conference on Alkali-Aggregate Reaction in Concrete London, 1992. Vol. 1, pp. 477-484.

[3] Department of Mineral Resources (2001):Geology of Thailand, 5th December 1999 HM the King Golden Jubilee Commemoration Edition, Department of Mineral Resources in 2001

[4] Bunopas, S (1981): Paleogeographic history of western Thailand and adjacent parts of Southeast Asia a plate tectonics interpretation, Ph.D. Thesis, Victoria University of Wellington, New Zealand, Reprinted 1982 as Geological Survey Paper No. 5, Department of Mineral Resources, Ministry of Industry, Thailand, 810

[5] Hinthong, C (1985): Upper Paleozoic system: the central plain and lower Phetchabun ranges. Geological Survey Division, Bangkok, 42 pp.

[6] R.N.Swamy, ed. (2003): The Alkali-Silica Reaction in Concrete: Taylor & Francis e-Library, 2003.

[7] ASTM C1260-01 (2001): Standard Test Method for Potential Alkali Reactivity of Aggregates (Mortar-Bar Method), ASTM International, West Conshohocken, PA, 2001, www.astm.org

[8] ASTM C150-07 (2007); Standard Specification for Portland Cement, ASTM International, West Conshohocken, PA, 2007, www.astm.org.

[9] Y. Monnin, P. Dégrugilliers, D. Bulteel, and E. Garcia-Diaz (2006): Petrography study of two siliceous limestones submitted to alkali-silica reaction. Cement and Concrete Research, vol. 36, no. 8, pp. 1460–1466, Aug. 2006.

[10] Wongkamjan, W, Sujjavanich, S, and Won-In, K (2014): Influence of Recrystallized Silica Aggregates on Alkali-Silica Reactivity. Kasetsart Journal: Natural Science 48(3).

CBR BEHAVIOR OF SOFT MARINE CLAY TREATED WITH CLASS 'F' FLY ASH AND NANO MATERIAL

Prasanna P.Kulkarni [1] and J. N. Mandal[2]

[1] Department of Civil Engineering, Indian Institute of Technology Bombay, Mumbai, India
[2] Faculty, Department of Civil Engineering, Indian Institute of Technology Bombay, Mumbai, India.

ABSTRACT

Soil improvement in expansive soils is an exigent task and it can pose a lot of constructional problems if not tackled in a proper way. Also, the disposal of fly ash, available in abundance in the vicinity of thermal power stations is the biggest global concern today from the environmental perspective. An attempt to improve the soft marine clay soil CBR properties by adopting class 'F' fly ash and organosilane nanomaterial was made in this research by conducting modified CBR tests. Marine clay was treated with Class 'F' fly ash with 0, 5%, 10%, 15% and 20% by dry weight of soil. Each proportion was further treated with nano material diluted in water with four different dilution ratios of (1:150), (1:300), (1:600) and (1:800) by volume. An improvement of 188.88% in the soaked CBR was observed on account of addition of 10% of fly ash to the soil. Further, it was observed that soaked CBR values were drastically improved on treating the soil with nano material. Maximum improvements were observed in soil treated with 10% fly ash and nano material with dilution ratios of (1:150) and (1:300). With 10% flyash and dilution ratio of (1:150) the soaked CBR value was observed to be enhanced by 381.66% and with (1:300) dilution ratio the soaked CBR was enhanced by 478.33%, compared to the neat soil. Also the values of Atterberg's limits were observed to be considerably decreased on account of treating the soil with 10% Fly ash and nano material of dilution ratios (1:150) and (1:300). This research is thus an attempt to stabilize the soil by utilizing the fly ash along with innovative nano-technology which can provide an eco-friendly solution and engender a revolutionary change in pavement infrastructural applications.

Keywords: *Marine Clay, Class 'F' Fly Ash, Nano Material, California Bearing Ratio, Atterberg's Limits*

INTRODUCTION

The overall socio-economic growth of a developing nation highly depends upon the pavement infrastructure of the country. The soil improvement in expansive soils is an exigent task and it can pose a lot of constructional problems like swelling, shrinkage etc. if not treated properly. Therefore stabilization of expansive subgrades becomes mandatory to enhance the life of pavement infrastructures. Many researchers earlier have tried to stabilize the expansive soils by fly ash.

In developing countries like India, the expeditious industrialization has led to more power generation demands. More and more power generation initiates greater production of fly ash. The fly ash production in India is expected to reach by 225 million tons by 2017 [1]. Huge quantity of fly ash lying in the vicinity of thermal power stations needs quicker disposal and utility. If not properly disposed it may cause severe health hazards to the mankind. Therefore the problem of disposal of fly ash needs to be very skillfully dealt with from the environmental perspective. In the recent years utilizing fly ash as an alternative construction material for many important projects has become a trend of the industry and lot of research is being carried out to make the best use of this rich siliceous material to cater various needs in engineering and technology.

Also, there is one such upcoming field of nano sciences which has brought revolutionary changes in the field of science, engineering and technology since last decade. Organo silane compound is one such promising material which works on the concept of nano technology and promises to be very effective in stabilization of soft soils particularly for the road applications**.**

The study aims at optimizing the proportions of Class 'F' fly ash in suitable combinations with nano material and soft soil to unveil the improvements in the engineering parameters which will cater the needs of good subgrade material for pavements.

PRIOR ART

Many earlier researchers have tried to assess the suitability of fly ash in various applications since past two decades. Studies on soil stabilization with fly ash and other cementitious products have been carried out to focus on the effective utilization of fly ash as a suitable material for stabilization of soft soils and subgrades. Pulp mill fly ash and lime has been utilised for improvement in bearing capacity

[2]-[3]. Studies on use of class 'F' fly ash with soil-cement and soil-lime for base layers in highways have been presented as in [4]. The improvements in geotechnical properties of expansive soils by adopting varying percentages of fly ash have been presented as in [5]. Saturated drained triaxial tests were conducted to assess the behaviour of soils with addition of fly ash and calcium chloride considering the curing conditions as in [6]. Randomly oriented polyester fiber inclusions with fly ash and cement additive combinations were studied to bring more ductility to the soil mixes [7]-[8].

In-situ case studies on fly ash stabilized soils also have been undertaken to measure the increase in strength and stiffness of fine subgrade by measuring the CBR and resilient modulus properties [9]. Waste plastic strips have been used in combination with stone dust and fly ash to observe the effect on CBR and secant modulus values as in [10]. Sewage sludge ash has been effectively established as a stabilizing material with lime in improving strength, CBR and plasticity characteristics of soft soil [11]. The influence of fly ash on UCS of soil by placing soil and fly ash layers successively has been presented as in [12].Studies on basic characterization of class 'F' fly ash to be utilized as backfill material in reinforced earth walls have been presented as in [13]. Studies on behavior of cellular reinforced earth walls with fly ash as backfill under strip loading conditions have been discussed as in [14]. Improvement in CBR behavior in soil adopting class 'F' fly ash in varying percentages has been presented as in [15]. Studies on strength and compressibility improvement in marine clay by treating with lime for strong reliable roads and buildings have been presented as in [16]. Stabilization of expansive black cotton soil by dolime fines for utilization in subbases of pavements have been discussed as in [17].

The importance of nano materials grew over the past decade and thereafter few researchers have tried to ascertain the versatility of these very novel materials in various streams of science and technology. Few researchers have presented the importance of nano technology in constructions. Nano-silica was found to be effective in increasing the pozzolanic activities of the high volume fly ash high strength concrete [18]. Strength properties of sewage sludge ash were improved by adding nano silica and nano alumina additives to soft soils in small varying proportions [19]-[21]. Use of nano aluminium has been reported to study the transport through the porous media with the introduction in column studies to measure the leachate concentrations [22]. The physical, mechanical and thermal properties of concrete were improved by addition of nano zinc oxide as in [23]-[24]. Studies on improvement in CBR values on Nigerian soils by treating them with nano material have been presented as in [25]. Studies on improvement in strength characteristics of silty sand samples by adding colloidal nano silica have been discussed as in [26].

Earlier researches report the several applications of nano materials in almost all fields of science and engineering. However it is seen that major work is been done related to cement and concrete industry. However there is very less evidence of work related to the field of geotechnical engineering and pavements and yet there seems to be ample space for research to showcase the advantages of nano materials in soil sciences. This research is thus an attempt to glorify the prospective future of nanotechnology in construction by utilizing fly ash, which will enable in solving the disposal problem to a certain extent.

CHARACTERIZATION OF MATERIALS

Fly ash

Fly ash was procured from a thermal power station near Khopoli, in the Raigad district of Maharashtra. The fly ash is being denoted here as 'FA'. Table 1 represents the physical properties of fly ash.

Table 1 Physical properties of Fly ash and soil

Properties	Values
Specific gravity	2.093
Maximum dry density (gm/cm^3)	1.07
Optimum moisture content (OMC) %	28.5
Coefficient of permeability, k (cm/sec)	1.061 x 10^{-6}
Gravel	--
Sand	26.5%
Silt	70%
Clay	3.5%
D_{10} mm	0.007
D_{30} mm	0.02
D_{60} mm	0.046
Uniformity coefficient (Cu)	6.57
Coefficient of curvature (Cc)	1.24
Group symbol	SM
Liquid Limit (%)	Non Plastic
Plastic Limit (%)	Non Plastic
Soaked CBR (%)	5.6

Chemical analysis of Fly ash was carried out by X-Ray Fluorescence test (XRF). Table 2 depicts the chemical composition of Fly ash. The Fly ash is seen to be very rich in Silica (SiO_2) of about 62.7% and a low Calcium oxide content (CaO) of 0.905%. The Fly ash was classified as Class 'F' Fly ash as per [27].

Table 2 represents the chemical composition of fly ash.

Table 2 Chemical composition of Fly ash

Constituent	(%)
CaO	0.905
Fe_2O_3	5.152
K_2O	0.927
MnO	0.029
P_2O_5	0.188
SO_3	0.015
SrO	0.056
TiO_2	1.642
Al_2O_3	26.986
BaO	0.068
MgO	0.545
SiO_2	62.799
Na_2O	0.110

Fig. 1 represents the electron microscopic image of Fly ash obtained by Field emission Gun Scanning electron Microscope (FEG-SEM).

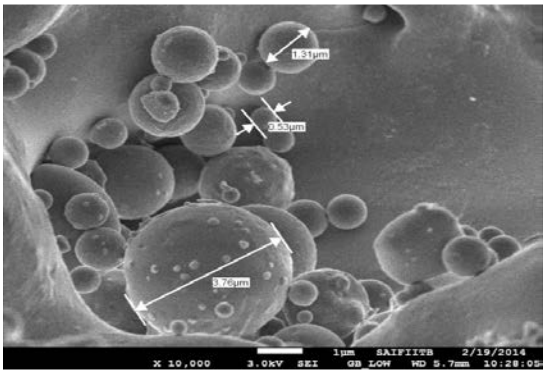

Fig. 1 Scanning electron microscopic image of fly ash obtained by FEG-SEM

Soil

Marine clay soil was obtained from the premises of IIT, Bombay. Table 3 below represents the physical properties of soil.

Table 3 Physical properties of Soil

Properties	Soil
Specific gravity	2.57
Maximum dry density (gms/cm^3)	1.63
Optimum moisture content (OMC) %	22 %
Gravel size	--
Sand size	0.86 %
Silt size	45.14 %
Clay size	54 %
Liquid Limit (%)	78
Plastic limit (%)	40.9
Shrinkage limit (%)	24.6
Plasticity Index	37.1
Group symbol	CH-MH
Coefficient of permeability ‘k’ cm/sec	9.541×10^{-9}
Undrained shear strength (kPa)	8.3
Soaked CBR (%)	1.8

Nano material

Nano material is basically a organo silane compound and was obtained from Zydex Industries, Vadodara, Gujarat, India. The use of commercial name of the material has been avoided to make it more palatable.

The organo silane compound used in the research is a pale yellowish liquid which could be dissolved in water. The compound on reacting with water i.e. hydrolysis forms strong bonds when the nano solution with water is mixed with the soil. The solution coats the soil surfaces by converting water absorbing groups to water repellent surfaces [25]. Since silica has a great affinity towards oxygen, string bonds are formed which create a thin hydrophobic film at the molecular level treated surfaces which makes the soil impermeable thus causing a significant improvement in its geotechnical properties.

Table 4 represents the CHNS analysis of nano material.

Table 4 CHNS Analysis of Nano material

Constituent	Percentage (%)
Carbon	64.173
Hydrogen	9.669
Nitrogen	3.945
Sulphur	Nil

The chemical analysis of the nano material was done by Carbon-Hydrogen-Nitrogen-Sulphur (CHNS) test.

SAMPLE PREPARATION AND METHODOLOGY

Test methodology: Modified proctor compaction and Modified CBR test

Modified proctor densities (simulating the heavy compaction in field) were initially worked out as a prerequisite for conducting the modified CBR tests. Oven dried fly ash was mixed to the soil in increasing proportions by 5%,10%,15% and 20% corresponding to 95%,90%,85% and 80% by dry weight of soil. Further each proportion was treated with nano solution (nano material diluted in water) in four different dilution ratios of (1:150),(1:300), (1:600) and (1:800) by volume. The modified proctor compaction tests were carried out on all variations in accordance as in [28].

Before conducting the CBR tests, the treated soil samples were allowed to interact with nano solution for about 8 hours by covering in a polythene sheet. The moulds were compacted to the respective modified proctor densities and were left to air dry for four days. The unsoaked CBR tests were performed after 4 days of air drying. The moulds were submerged in water for four days. The soaked CBR tests were conducted after four days of submergence in water. The samples tested for modified California bearing ratio were in accordance with [29]. Fig.2 represents the modified CBR set up.

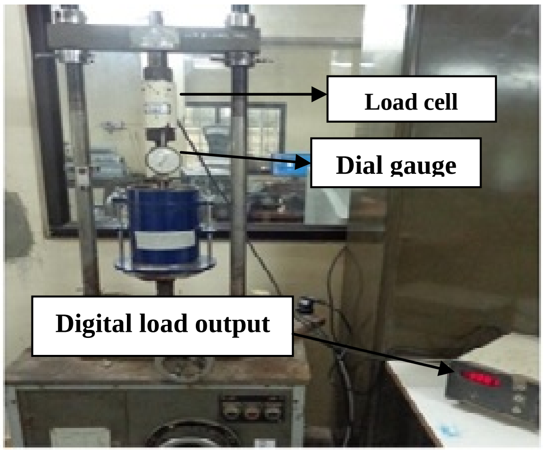

Fig. 2 Modified CBR test set up.

Test methodology: Atterbergs limits

Based on the results and optimization of modified CBR tests the Atterberg's limit tests were carried out on proportions of Marine clay+ 10% fly ash with nano material dilution ratios of (1:150) and (1:300). water) The nano solution treated sample was covered in a polythene sheet and was left to interact with the soil for 8 hours. The liquid limit, plastic limit and shrinkage limit tests were conducted on all the samples in accordance with [30][31].
Table 5 represents the proposed test variations considered in the testing program.

RESULTS AND DISCUSSIONS

Modified California Bearing Ratio (CBR) tests

The Indian Roads Congress specifications for pavement design incorporate only the soaked CBR values of the subgrade material considering the worst conditions of submergence of the soil in water. Therefore, only soaked CBR stress penetration curves are being presented herewith. Figures 3 to 7 represent the Stress penetration curves for soaked CBR samples.

Table 5 Test variations considered in the program

Series no	Sample details
Series I	Marine clay (neat soil)
	Marine clay with (1:150) nano dilution
	Marine clay with (1:300) nano dilution
	Marine clay with (1:600) nano dilution
	Marine clay with (1:800) nano dilution
Series II	95% Marine clay + 5% FA
	95%Marine clay + 5% FA with (1:150) nano dilution
	95%Marine clay + 5% FA with (1:300) nano dilution
	95%Marine clay + 5% FA with (1:600) nano dilution
	95%Marine clay + 5% FA with (1:800) nano dilution
Series III	90% Marine clay + 10% FA
	90%Marine clay + 10% FA with (1:150) nano dilution
	90%Marine clay + 10%FA with (1:300) nano dilution
	90% Marine clay + 10% FA with (1:600) nano dilution
	90% Marine clay + 10% FA with (1:800) nano dilution
Series IV	85% Marine clay + 15% FA
	85% Marine clay + 15% FA with (1:150) nano dilution
	85% Marine clay + 15% FA with (1:300) nano dilution
	85% Marine clay + 15% FA with (1:600) nano dilution
	85% Marine clay + 15% FA with (1:800) nano dilution
Series V	80% Marine clay + 20% FA
	80% Marine clay + 20% FA with (1:150) nano dilution
	80% Marine clay + 20% FA with (1:300) nano dilution
	80%Marine clay +20% FA with (1:600) nano dilution
	80% Marine clay + 20% FA with (1:800) nano dilution

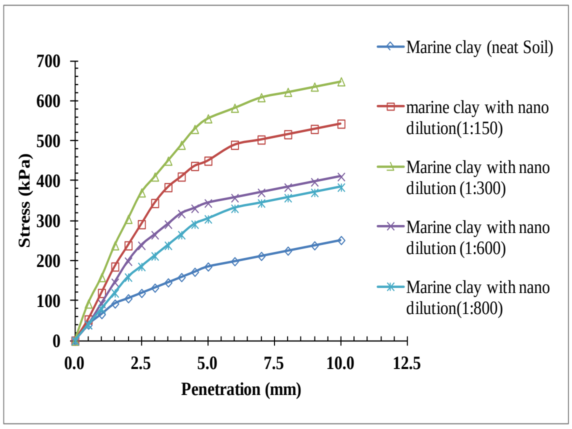

Fig. 3 Stress penetration curves for soaked CBR samples of Series I.

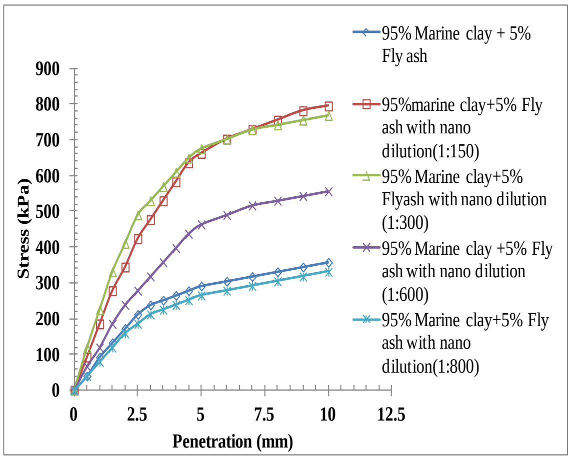

Fig. 4 Stress penetration curves for soaked CBR samples of Series II.

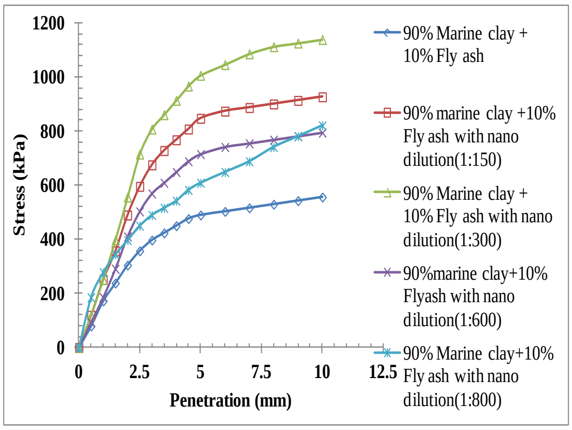

Fig. 5 Stress penetration curves for soaked CBR samples of Series III.

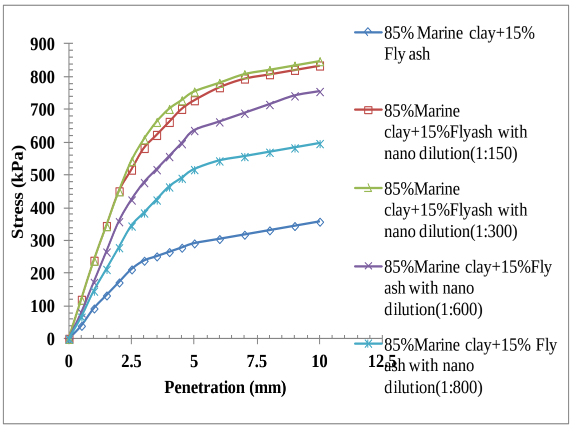

Fig. 6 Stress penetration curves for soaked CBR samples of Series IV.

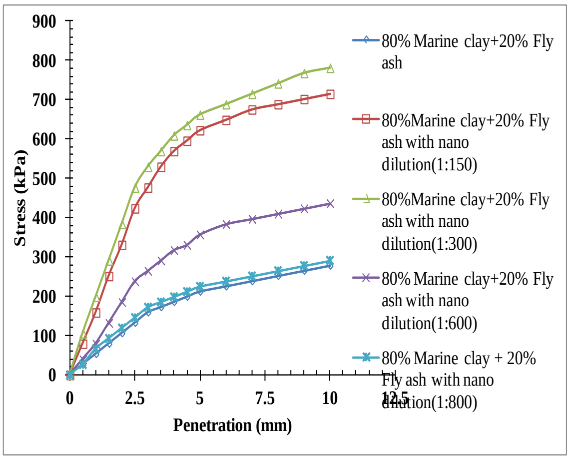

Fig. 7 Stress penetration curves for soaked CBR samples of Series V.

Fig.8 depicts the graphical representation of unsoaked and soaked CBR values considered in the program from test series I to V.

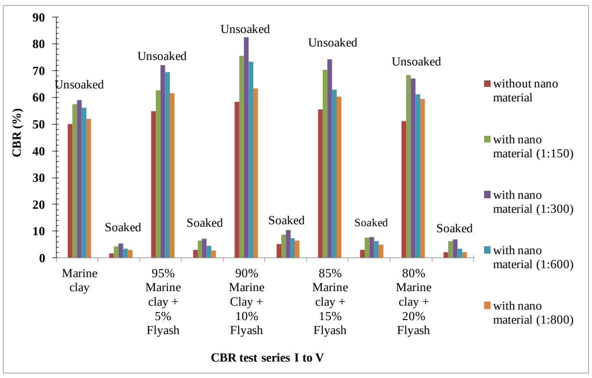

Fig. 8 Graphical representation of unsoaked and soaked CBR samples of Test Series I to V.

Table 6 represents the unsoaked and soaked CBR values of samples of Test Series I to V.

Table 6 Unsoaked and soaked CBR values of test series I to V

Sr. No	Sample details	Un soaked CBR (%)	Soaked CBR (%)
I	Marine clay (neat soil)	50.14	1.8
	Marine clay with (1:150) nano dilution	57.47	4.37
	Marine clay with (1:300) nano dilution	59.01	5.39
	Marine clay with (1:600) nano dilution	56.12	3.47
	Marine clay with (1:800) nano dilution	52.07	2.95
II	95% Marine clay + 5% FA	54.89	3.08
	95% Marine clay + 5% FA with (1:150) nano dilution	62.67	6.42
	95% Marine clay + 5% FA with (1:300) nano dilution	72.12	7.13
	95% Marine clay + 5% FA with (1:600) nano dilution	69.42	4.5
	95% Marine clay + 5% FA with (1:800) nano dilution	61.52	2.7
III	90% Marine clay + 10% FA	58.24	5.2
	90% Marine clay + 10% FA with (1:150) nano dilution	75.59	8.67
	90% Marine clay + 10% FA with (1:300) nano dilution	82.52	10.41
	90% Marine clay + 10% FA with (1:600) nano dilution	73.4	7.32
	90% Marine clay + 10% FA with (1:800) nano dilution	63.25	6.55
IV	85% Marine clay + 15% FA	55.42	3.1
	85% Marine clay + 15% FA with (1:150) nano dilution	70.39	7.52
	85% Marine clay + 15% FA with (1:300) nano dilution	74.24	7.9
	85% Marine clay + 15% FA with (1:600) nano dilution	62.87	6.17
	85% Marine clay + 15% FA with (1:800) nano dilution	60.36	5.0
V	80% Marine clay + 20% FA	51.1	2.12
	80% Marine clay + 20% FA with (1:150) nano dilution	68.27	6.17
	80% Marine clay + 20% FA with (1:300) nano dilution	67.11	6.92
	80%Marine clay +20% FA with (1:600) nano dilution	61.13	3.47
	80% Marine clay + 20% FA with (1:800) nano dilution	59.52	2.18

The soaked CBR values are very lesser as compared to the unsoaked values on account of submergence of soil in water. The CBR values were observed to be increased with the addition of fly ash to the soil. Soaked CBR was observed to be enhanced by 188.88% by adding 10% fly ash as compared to neat soil. Further, both unsoaked and soaked CBR values were observed to be decreased beyond 10% addition of fly ash to the soil. .

On further treating the samples with nano material in four different dilutions of (1:150), (1:300), (1:600) and (1:800) the CBR values were observed to be significantly improved. With 10% fly ash and nano dilution ratio of (1:150) the soaked CBR value was observed to be enhanced by 381.66% and with (1:300) nano dilution ratio the soaked CBR was enhanced by 478.33% as compared to the neat soil. In all the samples of tests series I to V it was observed that the dilution ratio played a vital role in improvement of CBR values.

The significant increase in CBR values is due to the formation of strong bonds when the soils come in contact with organo silane nano material. The stronger long chain bonds are formed on hydrolysis. After breakage of these bonds further affinity of silica towards the oxygen forms stronger bonds which will become parting a good hydrophobicity to the soil surface. Since the Class 'F' fly ash being used in this research is very rich in silica (62.8%), more and more silica becomes available for the interaction with nano material thereby forming more strong bonds within the soil mass.

Atterberg's limit tests

Table 7 summarizes the Atterberg's limit results. LL, PL and SL values were observed to be decreased on treating the soil with 10% fly ash. Further on treating the sample (marine clay + 10% fly ash) with nano material dilution ratio of and (1:300) the LL, PL, SL and PI values significantly decreased by 40.87%, 41%, 37.39% and 49.05% respectively. This indicated a substantial decrease in the plasticity characteristics of soil thereby transforming the highly plastic soil to medium plastic soil as per Indian standard soil classification [32].

Table 7 Atterberg's limits test results

Sample description	LL (%)	PL (%)	SL (%)	PI (%)
Marine clay (neat soil)	78	40.9	24.6	37.1
Marine clay with nano dilution (1:150)	58	30.6	22.7	27.4
Marine clay with nano dilution (1:300)	51	28.7	18.6	22.3
Marine clay + 10% Fly ash	62	31	23.2	31
Marine clay + 10% Fly ash with nano dilution (1:150)	46	28	18.61	18
Marine clay + 10% Fly ash with nano dilution (1:300)	43	24.1	15.4	18.9

The improvement in plasticity of soils can be attributed to the formation of strong bonds. They impart hydrophobicity to the soil and make it more water repelling. The new bonds so formed neutralize the net negative charge on the silt and clay particles [25], thereby reducing the plasticity of soil making it more compatible to be handled on site.

Suitability as a good subgrade material

The soil when treated with fly ash and nano material is seen to improve its CBR properties to a great extent thereby satisfying the subgrade criteria of CBR of 8% for roads having traffic of 450 commercial vehicles per day pertaining to the Indian sub continent as in [33]

CONCLUSIONS

1. Class 'F' Fly ash is found suitable for stabilization of soft soil. Soaked CBR values were found to be increased from 1.8 to 5.2 which was substantially improved by treating the soil with 10% fly ash.
2. Maximum improvements were observed in soil treated with 10% fly ash and nano material with dilution ratios of (1:150) and (1:300).
3. With 10% fly ash and dilution ratio of (1:300) the soaked CBR value was observed to be improved to 10.41 which indicated a good improvement, compared to the unreinforced soil.
4. LL, PL, SL and PI values significantly decrease by 40.87%, 41%, 37.39% and 49.05% respectively on treating the soil with 10% fly ash and nano dilution ratio of (1:300) thus transforming the highly plastic soil to medium plastic soil.
5. Class 'F' fly ash adopted in the study was found to be highly siliceous which helps in formation of stronger long chain bonds, thus imparting good hydrophobicity to the soil and improving the CBR properties.
6. The research is thus an attempt to stabilize the soil together with fly ash and nano material which holds a very promising future for pavement infrastructural applications.

ABBREVIATIONS

The following symbols are used in this paper.
CBR = California Bearing Ratio
FA = Fly ash
LL = Liquid limit
PL = Plastic limit
SL = Shrinkage limit
PI = Plasticity Index

ACKNOWLEDGEMENT

The nano material used in the research was sponsored by Zydex Industries, Vadodara, Gujarat, India. The authors acknowledge the support and cooperation given by Zydex Industries during this research work.

REFERENCES

[1] Kumar,V., Mathur,M.and Sinha,S.S.(2005)," A case study: Manifold increase in |Fly ash Utilization in India", Fly ash Utilization Programme (FAUP), TIFAC, DST, New Delhi.
[2] Zhou,H., Smith,D.W. and Sego, D.C(1999), " Characterisation and use of pulp mill fly ash and lime by-products as road construction amendments", Canadian Journal of Civil Engineering, 27: 581-593.
[3] Kalra, N., Harit, R.C. and Sharma, S.K,(2000), " Effect of fly ash incorporation on soil properties of texturally variant soils", Bioresource Technology 75(2000) 91-93.
[4] Arora, S. and Aydilek, A.H.(2005), " Class F fly ash amended soils as Highway base materials", Journal of materials in Civil Engineering, 2005. 17: 640-649.
[5] Bhuvaneshwari, S., Robinson, R.G. and Gandhi, S.R.(2005), " Stabilization of expansive soils using Fly ash", Fly ash Utilization Programme (FAUP), TIFAC, DST, New Delhi,India.
[6] Consoli, N.C., Prieto, P.D.M., Carraro.,J.A.H, Heineck, K.S,(2001), " behaviour of compacted soil- fly ash- carbide lime mixtures", Journal of Geotechnical and Geo environmental Engineering, 2001.127: 774-782.
[7] Kaniraj,S.R. and Havanagi, V.G (2001)," Behavior of cement stabilized fiber reinforced fly ash –soil mixtures", Journal of Geotechnical and Geo-environmental Engineering, 2001.127 : pp 574-584.

[8] Arvind kumar, Walia, B.S. and Bajaj, A.(2007), "Influence of fly ash, lime and polyester fibers on compaction and strength properties of expansive soils", Journal of Materials in Civil Engineering, 2007.19: 242-248.

[9] Shafique, S. B., Edil, T.B., Benson,C.H. and Senol, A.(2004), " Incorporating a fly ash stabilized layer in to pavement design", Proceedings for the Institution of Civil Engineers, Geotechnical Engineering, 157 Issue GE4.

[10] Dutta, R.K. and Sarda, V.K..(2006), "CBR behavior of Waste plastic strip-reinforced stone dust/ fly ash overlying saturated clay,Turkish Journal of Engineering and Environmental Science, 31(2007), 171-182.

[11] Lin, D. F., Lin, K. L., Hung, M. J. and Luo, H. L.(2007)."Sludge ash / hydrated lime on the geotechnical properties of soft soil" , Journal of Hazardous Materials, Vol. 145(1-2), 25 June 2007, pp. 58-64.

[12] Saha, S. and Pal, S.K.(2013)," Influence of Fly ash on Unconfined compressive strength of soil and fly ash layers placed successively", Electronic Journal of Geotechnical Engineering,Vol.18[2013], Bund.H, pp:1593–1602.

[13] Nadaf, M.B. and Mandal, J. N (2013), " Experimental studies and Analysis for Basic Characterization of Fly ash", Proceedings of 4th Global Engineering, Science and Technology Conference, 27-28 December, 2013, BIAM Foundation, Dhaka, Bangladesh, ISBN: 978-1-922069-43-6.

[14] Ram Rathan lal, B. and Mandal, J. N. (2013)," Study of Cellular reinforced fly ash under triaxial loading conditions", International Journal Of Geotechnical Engineering, 2013; 7(1): pp: 91–104.

[15] Kulkarni,P.P. and Mandal, J.N.(2016)," CBR behaviour of soil treated with Class 'F' Flyash", STM Journal of Geotechnical Engineering, ISSN:2394-1987,Volume 3,Issue 1, pp: 33-43.

[16] Yunus,N.Z.M, Marto,A., Pakir,F.,Kasran,K., Jamal,M.A.K, Jusoh,S.N. and Abdullah,N, " Performance of lime treated marine clay on strength and compressibility characteristics", International Journal of Geomate, June, 2015,Vol.8, No.2 (Sl.No.16), pp. 1232-1238.

[17] Patel,S. and Shahu,J.T, " Engineering properties of Black cotton soil-dolime mix for its use as subbase material in pavements", International Journal of Geomate, March, 2015,Vol.8, No.1 (Sl.No.15), pp. 1159-1166.

[18] Li, Gengying.(2004), " Properties of high volume fly ash concrete incorporating nano-SiO_2," Journal of Cement and Concrete Research, 34(2004) 1043-1049.

[19] Luo, H.L., Lin, D.F. and Kuo, W.T. (2004), "The effects of nano materials on the behaviour of sludge mortar specimens", Water Science and technology, 0273-1223.

[20] Chen ,L and Lin,D.F.(2009), "Applications of sewage sludge ash and nano SiO_2 to manufacture tile as construction material", Construction and Building Materials 23(2009) 3312-3320.

[21] Luo, H.L., Hsiao, D. H., Lin, D. F. and Lin, C. K. (2012). "Cohesive Soil Stabilized Using Sewage Sludge Ash/Cement and Nano Aluminum Oxide," International Journal of Transportation Science and Technology, Vol. 1(1), pp. 83-100.

[22] Doshi, R., Braida, W., Christodoulatos, C., Wazne, M. and Connor, G.(2008), " Nano-aluminium : Transport through sand columns communities", Journal of Environmental research 106(2008) 296-303.

[23] Nazari, A. and Riahi, S. (2011). "The effects of zinc dioxide nano particles on flexural strength of self-compacting concrete , Composites: Part B, Vol. 42, pp. 167-175.

[24] Kawashima, H., Hou, P., Corr, D.J. and Shah, S.P.(2012), " Modification of cement based materials with nanoparticles", Cement and Concrete composites 36(2013) 8-15.

[25] Ugwu, O.O., Arop, J.B., Nwoji, C.U. and Osadebe, N.N.(2013),"Nano technology as a preventive engineering solution to highway infrastructure failures", Journal of Construction Engineering and Management, 2013. 139:987-993.

[26] Moradi, G. and Seyedi, S. (2015), "Effect Of Sampling Method on Strength of Stabilized Silty sands with colloidal Nano Silica", Journal of Civil Engineering Research 2015, 5(6): 129-135.

[27] ASTM C618-08a.2008. Standard specification for coal fly ash and raw or calcined natural pozzolan for use in concrete.

[28] Indian Standard IS 2720 (Part 8)-1983, Methods of test for soils, Part 8: Determination of water content- dry density relation using heavy compaction.

[29] Indian Standard IS 2720(Part16) -1987, Methods of test for soils, Part 16: Laboratory determination of CBR.

[30] Indian Standard IS 2720 (Part5)- 1985, Methods of test for soils, Part 5: Determination of liquid and plastic limit.

[31] Indian Standard IS 2720(Part6)- 1972, Methods of test for soils, Part 6: Determination of Shrinkage factors.

[32] Indian Standard IS 1498 -1970, Classification and identification of soils for general engineering purposes.

[33] IRC:37-2012 (Tentative guidelines for design of flexible pavements).

Environment

USING FLOATING WETLAND TREATMENT SYSTEMS TO REDUCE STORMWATER POLLUTION FROM URBAN DEVELOPMENTS

Peter Schwammberger[1], Chris Walker[2] and Terry Lucke[1]
[1]Stormwater Research Group, University of the Sunshine Coast, Australia
[2]Covey Associates Pty Ltd, Sunshine Coast, Australia

ABSTRACT

Floating treatment wetland (FTW) systems are an innovative stormwater treatment technology currently being trialled in Australia. FTWs provide support for selected plant species to remove pollutants from stormwater discharged into a storage basin. The plant roots provide large surface areas for biofilm growth, which serves to trap suspended particles and enable the biological uptake of nutrients. FTWs can be installed at the start of the construction phase and can therefore start treating construction runoff almost immediately. FTWs have the potential to provide a full range of stormwater runoff treatment (e.g. sediment and nutrient removal) from the construction phase onwards. A 101 m^2 FTWs has been installed within a greenfield development site on the Sunshine Coast, in Australia. The two-year research study investigated the pollution removal performance of the FTW for two different locations, one with low and one with moderate influent pollutant concentrations. This paper presents the research methodology used, and the initial study results of the treatment efficiency of FTWs.

Keywords: urban stormwater runoff, floating treatment wetlands, stormwater pollution, stormwater treatment

INTRODUCTION

Natural floating wetland ecosystems exist in many parts of the world, ranging from large floating marshes covering thousands of hectares in Louisiana [1] to smaller floating mires in the Netherlands [2]. Floating Treatment Wetlands (FTWs) are artificial systems that mimic the water treatment processes that take place in natural floating wetland islands [3]. FTWs are comprised of a floating structure planted with emergent macrophytes where the roots grow into the water column [4]. The roots provide a large surface area (Figure 1) for biofilm attachment. The biofilm adsorbs pollutants [5,6] while physically filtering and trapping suspended solids [7].

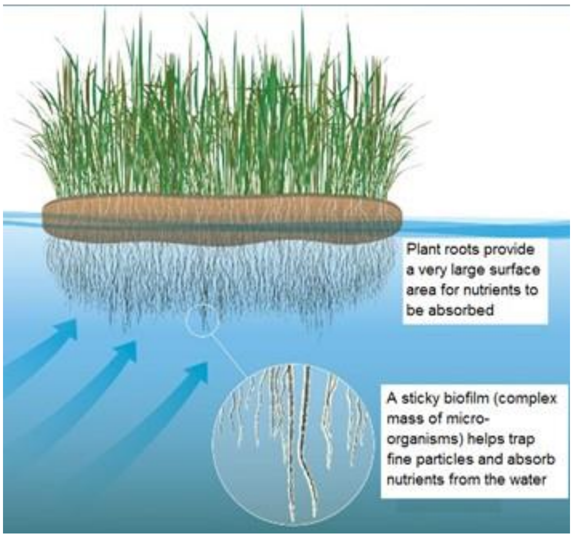

Fig. 1 Figure showing root hairs and vegetation above the floating mat [8].

As FTWs are buoyant, they can be installed in most water bodies without significant earthworks, thereby offering developers an effective, environmentally sustainable and cost-effective water treatment solution [9]. FTWs also offer terrestrial and aquatic habitats for wildlife which allows for greater ecological diversity [3].

Plant growth, establishment and survival in conventional stormwater treatment devices (e.g. constructed wetlands) are often affected by high flow velocities, the duration and depth of inundation, and the frequency of flooding or drought [10]. Consequently, the wetland area may need to be relatively large to buffer against these extreme water level fluctuations. Alternatively, the high flows may be designed to bypass the wetland all together resulting in a significant portion of stormwater runoff being untreated [11].

The buoyancy of FTWs generally enables them to tolerate major fluctuations in water depth. This makes FTWs a reliable stormwater treatment device that protects plant health during extreme rainfall events. Furthermore, the extensive surface area of the root network can provide significantly greater pollution removal rates per unit area compared to constructed wetlands and other stormwater treatment systems.

Several mesocosm studies have been conducted to investigate the treatment efficiency of different plant species planted in FTWs. These studies have shown that FTW are effective at removing pollutants from both wastewater [12-15] and stormwater [7,16,17]. The number of field studies undertaken on FTWs is limited, particularly in the application of FTWs to stormwater treatment [3,18,19]. Smaller-scale field studies in the USA [19] and New Zealand [4] have shown FTWs to be effective in removing a variety of pollutants from stormwater runoff from highways.

To date, no previous studies have been undertaken in an urban residential setting, where there can be higher pollutant loads such as sediment, nutrients, and heavy metals. These urban stormwater pollutants can be readily transported to receiving waters due to an increase in impervious surfaces such as roads, sidewalks, driveways, parking lots and rooftops, as well as more efficient drainage pathways [6]. This paper describes the results of a field study conducted to assess the ability of FTWs to treat urban stormwater runoff from an existing urban development in Southeast Queensland (SEQ), in Australia.

MATERIAL AND METHODS

Study Site

This study was conducted in an existing lake within a development under construction on Bribie Island in Queensland, Australia. The entire development site has an area of 42.3 ha, with construction having commenced in 2014. At the start of the research project in September 2014, stormwater from a 10ha existing residential catchment (external to the new development) discharged through two existing inlets into the study lake (Inlets 1 and 2 in Figure 2).

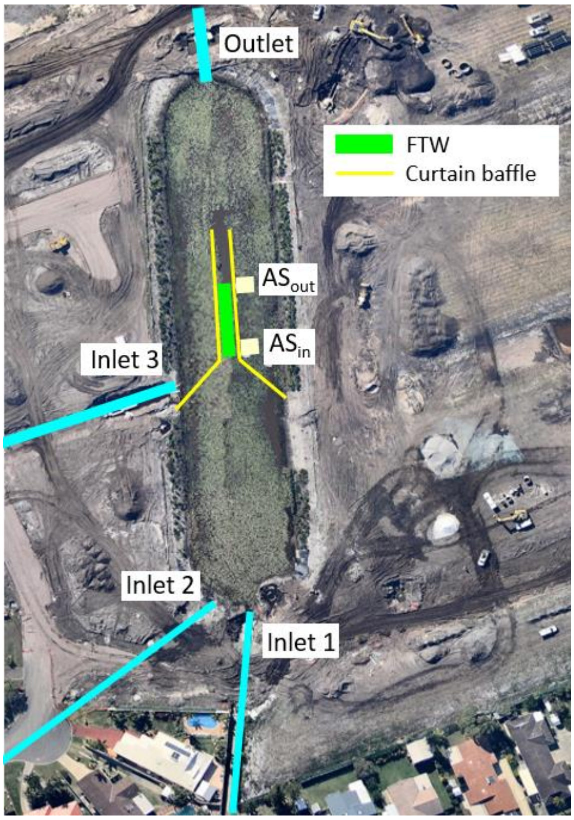

Fig 2 Initial location of the FTW and automatic samplers (AS).

The study involved installing a new FTW in the existing lake shown in Figure 2. The FTW had a total area of 101 m^2 which was equivalent to approximately 1.7% of the development area. The FTW was comprised of 11 FTW modules, each of 9 m^2 in area. The FTWs (www.spel.com.au) used in this study were composed of a 200 mm thick, recycled plastic fibre mat, injected with marine grade foam to provide buoyancy (Figure 3). Each mat had 40 pre-drilled holes to hold the plants. The holes were 100 mm in diameter and 150 mm deep. The mats were covered with coir matting and planted with tube stocks of *Carex appressa* at a density of two plants per hole (Figure 3).

To direct the stormwater inflow into the lake and through the FTWs to limit potential short-circuiting of the FTW (i.e. bypassing flows) experienced in other studies [11,18], impermeable polyvinyl chloride (PVC) curtains were installed along the sides of the FTWs that fanned out towards the lake banks (Figure 2). These ensured all inflows from Inlets 1 and 2 were treated by the FTWs.

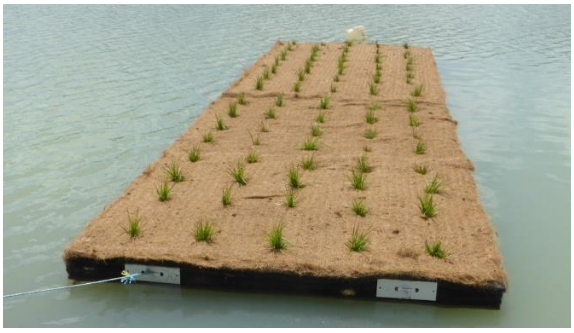

Fig 3 Two of the FTW modules planted with *Carex appressa*.

Water quality analysis results from the first sampling period (from September to February 2015) showed that the influent pollutant concentrations were very low. In late February 2015, the study site was impacted by a tropical cyclone (Marcia - TCM) which caused some minor damage to the FTW. In particular, some of the anchoring cable supports were damaged which caused the FTW to shift its location. Portions of the PVC curtain were also damaged.

As the FTW needed realignment and repair after TCM, it was decided to use this opportunity to relocate the FTW, and to change the baffle configuration to enable the treatment of stormwater inflows from a different part of the catchment which was thought to have potentially higher pollution concentrations. This resulted in relocating the FTW to the new position shown in Figure 4. The new location meant the FTW received stormwater (Inlet 3) from a 5.3 ha existing residential area, as well as stormwater from a new 2.2 ha area of the Bribie Lakes development (Total treatment area = 7.5 ha). As the new 2.2 ha area was under construction, it was expected to have much higher influent pollutant concentrations. Prior to the reconfiguration of the FTW, the discharge from Inlet 3 bypassed the FTW.

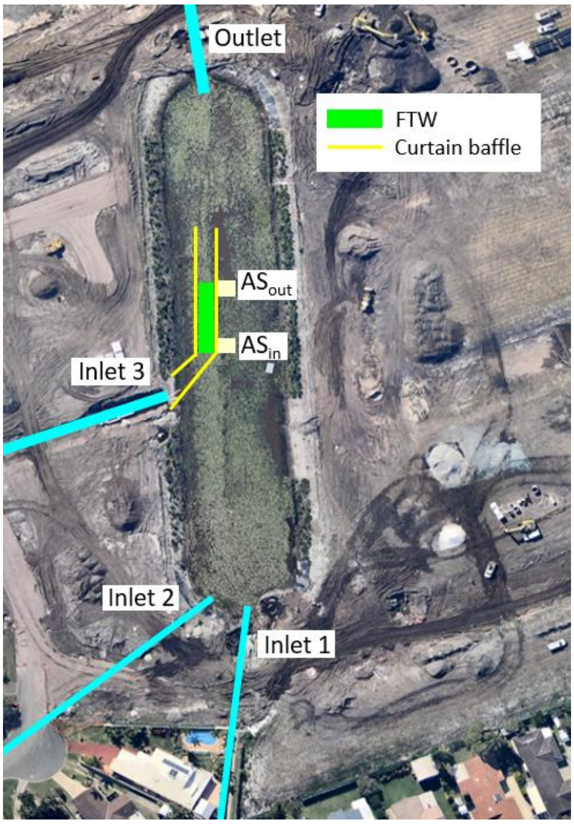

Fig 4 New location of the FTW and automatic samplers (AS) after TCM

Storm Event Sampling and Analysis

In order to standardize the sampling methods and procedures to capture qualifying storm events, a sampling protocol (Table 1) was developed based on the protocol methods prescribed by the United States Environmental Protection Agency's (US EPA) *Stormwater BMP Monitoring Manual* [20] and Auckland Regional Council's *Proprietary Device Evaluation Protocol for Stormwater Quality Treatment Devices* [3,21].

Automatic water samplers (ISCO GLS - www.isco.com) were installed upstream (AS1) and downstream (AS2) of the FTW (Figures 2 and 4) to collect water samples to be analysed for water quality parameters (Table 1) by a NATA (National Association of Testing Authorities) accredited laboratory. The samples were analysed for total suspended solids (TSS), total nitrogen (TN) and total phosphorus (TP) which are the three main stormwater pollutants of concern in Australia. The auto-samplers were triggered by a combination of signals from a rain gauge and flow meter that were installed on site. The auto-samplers were programmed to collect 200 mL flow-weighted aliquots each time a cumulative volume of 15 kL registered at the flowmeter. This was equivalent to the runoff from a rainfall depth of 0.2 mm over the study catchment area. The 200 ml aliquots were composited into a nine litre glass bottle and sent to the laboratory for analysis.

Table 1 Sampling Protocol and Analysis Details

Parameter	Details
Minimum rainfall depth	2mm in 30 min
Rainfall monitoring	Pluviometer
Minimum storm duration	15 min
Minimum antecedent dry period	6 hours
Minimum hydrograph sampling	First 60% of hydrograph
Minimum number of sample aliquots	Minimum 8 influent and 8 effluent subsamples per event
Sampling method	ISCO GLS Auto-samplers, flow-weighted in 15 kL intervals
Sampler location	1.3 m upstream and 3.3 m downstream of FTW
Total Suspended Solids (TSS) & Total Dissolved Solids (TDS)	APHA (2005) 2540 C & D
Total Nitrogen & TKN	APHA (2005) 4500 N
Ammonia N	APHA (2005) 4500 NH3
NOx	APHA (2005) 4500 NO3
Total Phosphorous & Orthophosphate	APHA (2005) 4500 P
Particle Size Distribution (PSD)	Laser Diffraction (Malvern Mastersizer 3000)

The water quality analysis results were used to estimate an Event Mean Concentration (EMC) for each storm event using Equation 1:

$$EMC = \frac{\sum_{i=1}^{n} V_i C_i}{\sum_{i=1}^{n} V_i} \qquad \text{Eq. (1)}$$

where:
V_i = Volume of flow during period i;
C_i = Concentration associated with period i; and
n = total number of aliquots collected during event.

The water quality analysis results were also used to assess the overall system performance by calculating the pollution removal efficiency ratio (ER) using Equation 2:

$$ER = 1 - \frac{Mean\ EMC_{Out}}{Mean\ EMC_{In}} \qquad \text{Eq. (2)}$$

where:
EMC_{in} = Event Mean Concentration at AS1 and
EMC_{out} = Event Mean Concentration at AS2.

RESULTS AND DISCUSSION

Sampling commenced in September 2014 and continued through to February 2015 when the study site was affected by TCM. During this time, five qualifying storm events were captured. As shown in Table 2, results prior to TCM showed low concentrations of TSS, TN and TP. The concentrations ranged from 4 to 10 mg/L for TSS, from 0.41 to 0.91 mg/L for TN, and from 0.005 to 0.078 mg/L for TP. These concentrations were well below the 'typical' Australian average urban pollutant loads expected in SEQ which are 151 mg/L for TSS, 1.82 mg/L for TN and 0.34 mg/L for TP [22].

For events prior to TCM, the average pollutant removal efficiency ratios (ER) for TSS, TN and TP were -5%, 16% and 41%, respectively (Table 2). These were below the minimum pollutant removal ERs recommended for urban developments in SEQ of 80%, 60% and 45%, for TSS, TN and TP respectively [23]. The variation in the results between the individual storm events was substantial and pollution removal ER ranged from between -88% and 80% for TSS, -6% and 47% for TN and between 0% and 59% for TP. However, these results needs to be considered carefully, and within the correct context.

For, example, the 41% ER results for TP removal (Table 2) needs to be considered with care as there was no net removal of TP for three of the five events and these were below detection limits. The high variability of the results was a result of the low pollutant concentrations generated from the existing residential development.

Furthermore, it was thought that the 70 m length of open water in the lake in front of the FTW was probably acting as a type of pre-treatment system for the inflowing stormwater leading to sedimentation, and portions of TSS and particle bound pollutants not reaching the FTW.

Once the location of the FTW was changed after TCM to treat the stormwater from Inlet 3 (Figure 4) water quality sampling results show much higher inlet pollution concentrations (Table 3).

Table 2 Pollution removal efficiency prior to TCM

Parameter	TSS (mg/L)		TN (mg/L)		TP (mg/L)		Peak Flow (L/s)	Inflow Volume (m^3)
Date	In	out	In	out	In	out		
07/09/14	10	14	0.51	0.53	0.005	0.005	54	890.6
23/09/14	5	4	0.41	0.44	0.005	0.005	n/a	n/a
25/09/14	4	4	0.41	0.43	0.005	0.005	34	433.1
07/11/14	10	2	0.65	0.56	0.052	0.038	41	169.9
20/11/14	8	15	0.97	0.52	0.078	0.032	34	367.8
Mean Conc.	7.4	7.8	0.59	0.49	0.029	0.017		
Efficiency Ratio	-5%		16%		41%			

The inlet pollutant concentrations ranged from 11 to 414 mg/L for TSS, from 0.6 to 3.2 mg/L for TN and from 0.03 to 0.28 mg/L for TP. These results are more in-line with the expected pollutant concentration ranges for stormwater runoff from urban developments in SEQ. [22].

The average pollutant removal efficiency ratios for TSS, TN and TP were 80%, 17% and 52%, respectively. Compared to the initial setup where TSS concentrations often increased when passing through the FTW, the results after TCM show much better TSS removal for higher influent concentrations, as well as for higher flow rates (Table 3).

Table 3 Pollution removal efficiency post-TCM

Parameter	TSS (mg/L)		TN (mg/L)		TP (mg/L)		Peak Flow (L/s)	Inflow Volume (m^3)
Date	In	out	In	out	In	out		
28/09/15	323	51	1.00	0.25	0.280	0.1	n/a	n/a
23/10/15	11	4	0.70	0.30	0.030	0.02	100	279.3
07/11/15	414	24	3.20	0.70	0.280	0.03	1,340	511.9
15/11/15	26	16	1.10	0.70	0.050	0.05	2,335	531.0
29/11/15	270	28	2.20	1.30	0.140	0.02	1,160	361.0
30/01/16	50	26	1.10	2.20	0.040	0.04	24	234.8
01/02/16	19	36	0.80	1.60	0.040	0.07	93	281.0
06/02/16	19	24	0.60	0.80	0.050	0.03	126	611.6
13/02/16	37	19	1.40	2.10	0.060	0.04	320	611.4
06/03/16	56	15	1.20	1.10	0.100	0.11	151	148.6
Mean Conc.	122.5	24.3	1.33	1.11	0.107	0.051		
Efficiency ratio	80%		17%		52%			

It is difficult to accurately assess the efficiency of treatment systems when pollution concentrations are close to detection limits, as even a small change in concentration results in a significant change in the average results. The relocation of the FTW after TCM, and the subsequent increase in pollutant loading, resulted in a higher pollutant removal ratio for all pollutants monitored in the study.

The FTW showed a high variability in treatment performance for stormwater runoff with very low pollutant concentrations. However, when the pollutant loads were closer to those typically expected for stormwater in SEQ, the ER was substantially higher. The results of this study demonstrate that the sampling location, and the influent pollutant loads are extremely important. The study showed that these variables can significantly influence the results of performance and efficacy measurements of FTW systems.

To further investigate the stormwater treatment performance of FTWs, a new four-year research study has recently commenced in a new development site on the Sunshine Coast in Queensland, Australia. The new study will be conducted on a 2,100 m^2 FTW treating stormwater runoff from a new 95 ha residential development. The stormwater runoff water quality will be characterised and assessed during both the construction and the operational phases of the development. The ability of FTWs to improve stormwater quality, and to manage urban lake health will be evaluated throughout the four-year study.

The study results will be of significant interest for the developers and local government authorities and could potentially influence stormwater management practices, both in Australia, and internationally.

CONCLUSION

This study initially investigated the pollutant removal performance of a FTW receiving stormwater runoff from a 10 ha residential site. However, stormwater pollutant concentrations from the site were found to be far below typical concentrations for urban stormwater runoff in Australia and this resulted in low pollutant removal performance results for the FTW.

After approximately six months, the FTW was moved to a new location (catchment area = 7.5 ha) with higher influent pollutant concentrations that were more in-line with typically expected values for urban catchments in Australia. The pollutant removal performance of the FTW in the new location increased significantly and the average pollutant removal efficiency ratios were found to be 80%, 17% and 52%, respectively for TSS, TN and TP. These results were much closer to the recommended removal rates in Australia.

The study results demonstrate that sampling location, and influent pollutant loads are extremely important and that these variables can significantly influence the results of performance and efficacy measurements of FTW systems.

The study has demonstrated that FTW are a viable option for urban stormwater treatment that have numerous advantages compared to traditional systems. These include reduced land requirements, resilience to extreme water depth and volume changes, as well as potentially enhancing habitat, recreational, and aesthetic values within the urban landscape. It is anticipated that the study results could significantly influence the stormwater management in Australia and the rest of the world.

REFERENCES

[1] Sasser CE, Gosselink JG, Shaffer GP, "Distribution of nitrogen and phosphorus in a Louisiana freshwater floating marsh", Aquatic Botany, Vol. 41, 1991, pp. 317–331.

[2] van Diggelen R, Molenaar WJ, Kooijman AM, "Vegetation succession in a floating mire in relation to management and hydrology", J. of Vegetation Science, Vol. 7, 1996, pp. 809–820.

[3] Walker C, Nichols P, Reeves K, Lucke T, Nielson M, Sullivan D, "Using Floating Wetlands to Treat Stormwater Runoff from Urban Catchments in Australia", 13th International Conference on Urban Drainage, Sarawak, Malaysia, 2014.

[4] Borne KE, "Floating treatment wetland influences on the fate and removal performance of phosphorus in stormwater retention ponds", Ecolog. Engineering, Vol. 69, 2014, pp. 76-82.

[5] Headley TR, Tanner CC, "Constructed Wetlands with Floating Emergent Macrophytes: An Innovative Stormwater Treatment Technology", Critical Reviews in Environmental Science and Technology Vol. 42 (21), 2012, pp. 2261–2310.

[6] Lynch J, Fox LJ, Owen JS, Sample DJ, "Evaluation of commercial floating treatment wetland technologies for nutrient remediation of stormwater", Ecolog. Engineering, Vol. 75, 2015, pp. 61–69.

[7] Headley TR, Tanner CC, "Floating wetlands for stormwater treatment: Removal of copper, zinc and fine particulates", Auckland Regional Council Technical Report, 2008, New Zealand.

[8] Royal Botanic Gardens Melbourne (RBGM) (2016), Plant Collections, Lake System Wetlands, website, accessed on 15-5-2016 at: https://www.rbg.vic.gov.au/visit-melbourne/attractions/plant-collections/lake-system-wetlands

[9] Hartshorn N, Marimon Z, Xuan Z, Cormier J, Chang NB, Wanielista MP, "Complex interactions among nutrients, chlorophyll-a, and microcystins in three stormwater wet detention basins with floating treatment wetlands", Chemosphere, Vol. 144, 2016, pp. 408–419.

[10] Chang NB, Islam MK, Wanielista MP, "Floating wetland mesocosm assessment of nutrient removal to reduce ecotoxicity in stormwater ponds", Int. J. Environ. Sci. Technol. Vol. 9 (3), 2012, pp. 453–462.

[11] Headley TR, Tanner CC, "Application of floating wetlands for enhanced stormwater treatment: A review", NIWA Client Report, 2006, Auckland Regional Council, New Zealand.

[12] Ash R, Truong P, "The use of Vetiver grass wetlands for sewerage treatment in Australia", 3rd International Conference on Vetiver, 2003, Guangzhou, China.

[13] Ayaz SC, Saygin O, "Hydroponic tertiary treatment", Water Research, Vol. 5, 1996, pp. 1295–1298.

[14] Kyambadde J, Kansiime F, Dalhammar G, "Nitrogen and phosphorus removal in substrate-free pilot constructed wetlands with horizontal surface flow in Uganda" Water, Air, and Soil Pollution, Vol. 165, 2005, pp. 37–59.

[15] van de Moortel AMK, Meers E, De Pauw N, Tack FMG, "Effects of vegetation, season and temperature on the removal of pollutants in experimental floating treatment wetlands", Water, Air and Soil Pollution, Vol. 212, 2010, pp. 281–297.

[16] Kerr-Upal M, Seasons M, Mulamoottil G, "Retrofitting a stormwater management facility with a wetland component" Journal of Environmental Science and Health A, Vol. 35, 2000, pp. 1289–1307.

[17] Revitt DM, Shutes RBE, Llewellyn NR, Worrall P, "Experimental reedbed systems for the treatment of airport runoff", Water Science and Technology, Vol. 36, 1997, pp. 385–390.

[18] Borne KE, Fassman-Beck EA, Winston RJ, Hunt WF, Tanner CC, "Implementation and Maintenance of Floating Treatment Wetlands for Urban Stormwater Management", J. Environ. Eng. Vol. 141, 2015, pp. 4015030.

[19] Winston RJ, Hunt WF, Kennedy SG, Merriman LS, Chandler J, Brown D, "Evaluation of floating treatment wetlands as retrofits to existing stormwater retention ponds", Ecological Engineering, Vol. 54, 2013, pp. 254–265.

[20] Geosyntec Consultants, Wright Water Engineers, "Urban Stormwater BMP Performance Monitoring", United States Environmental Protection Agency, 2009.

[21] Wong G, Ansen J, Fassman E, "GD03 Proprietary Devices Evaluation Protocol (PDEP) for Stormwater Quality Treatment Devices", New Zealand, Auckland Council, 2012.

[22] Malcolm E, "Urban stormwater- Qld BPEM guidelines", Australia, Environmental Protection Agency, 2009.

[23] Queensland Government, "State Planning Policy", Department of State Development, Infrastructure and Planning, 2014, Ch. H.

[24] Knight RL, Clarke RA, Bastian RK, "Surface flow treatment wetlands as a habitat for wildlife and humans", Water Science and Technology, Vol. 44, 2001, pp. 27–37.

[25] Lee JS, Li MH, "The impact of detention basin design on residential property value: case studies using GIS in the hedonic price modelling", Lands. & Urban Planning, Vol. 89, 2009, pp. 7–16.

[26] Rousseau DPL, Lesage E, Story A, Vanrolleghem PA, De Pauw N, "Constructed wetlands for water reclamation", Desalination, Vol. 218, 2008, pp. 181–189.

PROPOSITION OF A DETERIORATION PREDICTION MODEL FOR MAINTENANCE OF RUNWAY PAVEMENT

Hiroto Akimoto[1], Naoaki Suemasa[1], Kazuya Itoho[1], Tsuyoshi Tanaka[1]
[1]Urban and Civil Engineering, Tokyo City University, Tokyo, Japan;

ABSTRACT

Many airports have been built in Japan during the high economic growth period under the policy of "One airport in each prefecture". As a result of this policy, 102 airports are dotted around Japan currently. The number of domestic airline users tends to increase drastically since the air transportation has become more convenient and affordable because of the improvement of long-range flight and the new service of LCC. On the other hand, according as the demand for planes has increased, the increase of the taking-off and landing number greatly influences the deterioration of runway pavement. For that reason, it is essential to provide runways with efficient maintenance to prevent from air accidents. However, a deterioration prediction technique for runways has not yet been established at the moment. Therefore, a simulation model to estimate deterioration degree of runway pavement was proposed in this study. Three elements such as a crack, a rutting and flatness are closely related to the runway deterioration and a deterioration prediction technique was examined focusing on a crack percentage and a rutting in this study. The future progress of deterioration degree was predicted through studying the actual values obtained from the runway pavement in Kumamoto Airport. As a result, a deterioration prediction method was confirmed by using the equation for determining the degree of the asphalt pavement fatigue. In addition, the essential elements intimately related to degradation were able to be extracted through the analysis of data from Kumamoto Airport

Keywords: Run way, Asphalt pavements, Deterioration rate, Crack percentage

INTRODUCTION

It has been more than 50 years since many facilities and buildings were constructed during the rapid economic growth period in Japan. Nowadays, the burden of maintenance for such structures is gradually increasing. Maintenance is regarded as important especially for the airport facilities which scatter in 102 places in the whole of Japan. Fig. 1 shows the change in the number of airline users in Japan [1]. As seen in the figure, the number of airline users and the demand for plane increase. The transportation using planes has increased due to the improvement of long range flight ability and the activation of airport industry by involving new services such as low cost carrier. Accordingly, the number of planes taking off and landing has increased, too. On the other hand, the increase in runway consumption greatly influences the deterioration of pavement. While the number of the check points for maintenance has increased, it has become more difficult for some airports such as Haneda Airport to find enough time to be checked because takeoffs and landings of planes are continuously carried out for 24 hours. It is, therefore, imperative to efficiently perform the maintenance of runway. Since a deterioration prediction method for runway has not been established at present, a degradation prediction model for runway pavement was suggested in this study aiming at improving the efficiency of its maintenance.

A prediction model for cracks on runway was made in the study. The factors such as temperature, running speed and a load of plane were used for constituting the model, which tend to greatly influence the runway crazing. Data was based on the degradation progress degree of the crack percentage of the runway actually measured in Kumamoto Airport. The results from the model were compared with the check data and discussed.

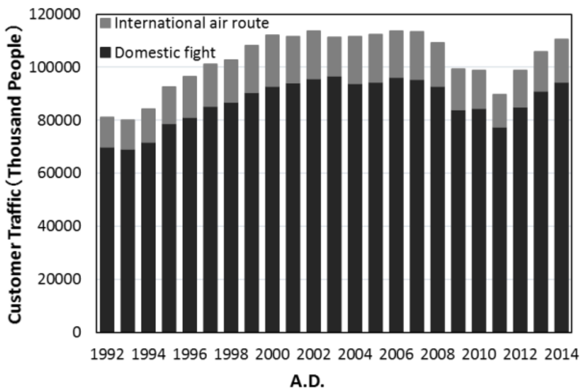

Fig. 1 Change in the number of airline users in Japan

CHANGE OF CRACK PERCENTAGE WITH TIME LAPSE AND CURRENT DEGRADATION STATE IN KUMAMOTO AIRPORT

In the case of runway where heavy planes such as jumbo jets take off and land, a section of the runway with 30m in length and 21m in width is defined as one unit and check and repair of runway are carried out by every unit. Kumamoto Airport adopts this unit system because the length of the runway is 3, 000m and jumbo jets goes into service on the runway. Fig. 2 shows the change of crack percentage measured from 1984 through 2008 at Kumamoto Airport.

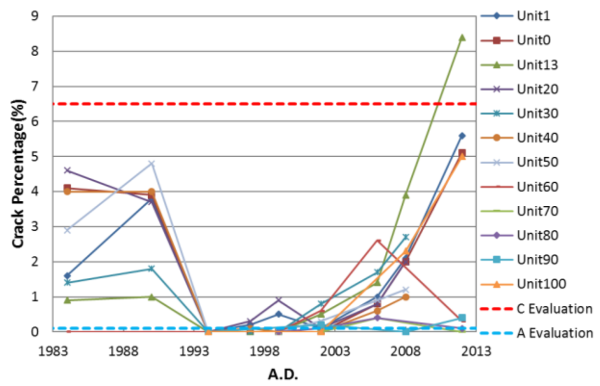

Fig. 2 Relations of year and crack percentage

The red dotted line and the blue dotted line in the figure indicate the damage levels determined by a repair evaluation standard for runway. The red dotted line is the C evaluation level, meaning that prompt repair is required, while the blue dotted line is the A evaluation level, meaning that prompt repair is not yet required. Because repair was given at Kumamoto Airport in the early 1990s, the crack percentage decreased once at the time, however, sudden increase was seen after the year and reached the C evaluation at some units in 2008. Fig. 3 shows the relationship between elapsed month and crack percentage starting from 1994 when repair was performed.

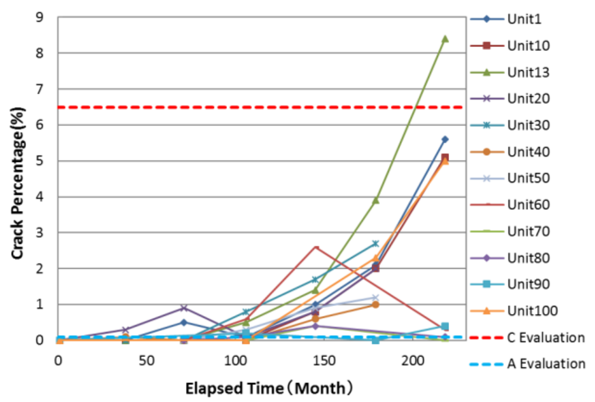

Fig. 3 Relations of elapsed time and crack percentage

It can be confirmed from the elevated crack percentage in the figure that degradation rate has increased with time elapsed. The factor of cracking on asphalt pavements is assumed to be mainly the fatigue by traffic load since the load on runway pavement is extremely greater than that on general road. Especially as for oil asphalt pavement, cracks hardly occur in the initial state, however, once the pavement has become hard after losing oil, cracks tend to occur more easily.

It is thought to be possible to predict the mechanism of runway deterioration by investigating the distribution of crack percentage with time elapsed.

CRAZING DEGRADATION SPEED AND DEGRADATION PREDICTION

The progress degree of deterioration in each unit can be estimated by the slope of the degradation increase from measured values of crack percentage. For Kumamoto Airport, the crack percentage increment after the whole repair performed in 1994 was referred as the measured values. Since the change of the crack percentage with time increased with a wide variety of patterns as shown in Fig. 3, it was difficult to clearly evaluate the vulnerability to cracks by each unit. Therefore, in order to facilitate the comparison of the damage by each unit, it was needed that the progress degree of deterioration which non-linearly increases should be linearized. So, a power function was introduced to linearize the relationship between the progress degree of deterioration and elapsed month, as shown in the following equation. The progress degree of deterioration in crack percentage and the slope of increasing crack percentage were defined as a crack index, Icr, and a crack deterioration speed, vcr, respectively.

$$R^{1/\mu} = I_{cr} \tag{1}$$

$$I_{cr} = v_{cr} \cdot T \tag{2}$$

where R: crack percentage (%), μ: the power number, I_{cr}: the crack index, v_{cr}: the crack deterioration speed, T: the elapsed month after repair. As shown in the equation (2), the crack index "I_{cr}" is defined as the value of the crack percentage, R, raised to the power of μ. I_{cr} should be linearly proportional to the elapsed month after repair, T, and its proportional coefficient is defined as the crack deterioration speed "v_{cr}". From the data of the power best fitted in each unit, the frequency distribution of the power value was made and approximated with the normal distribution curve. Finally, the power number used in the following discussion was chosen from the most frequent value of the curve. The frequency distribution and the normal distribution of power value for the crack percentage are shown in Fig. 4.

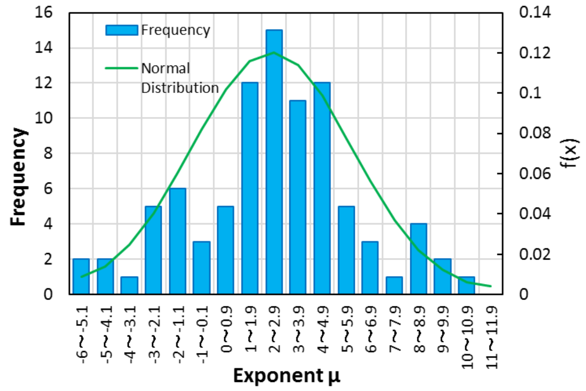

Fig. 4 A frequency distribution and normal distribution of power value in crack percentage

From this result, 2.41 was obtained as its power number. Then, the crack index "I_{cr}" for each unit was calculated using the power function as shown in equation (2), and the crack deterioration speed "v_{cr}" was determined from the slope of crack index I_{cr} to elapsed time. In order to compare among the degradation speeds, five units in order of both higher and lower speeds were extracted as shown in Fig. 5.

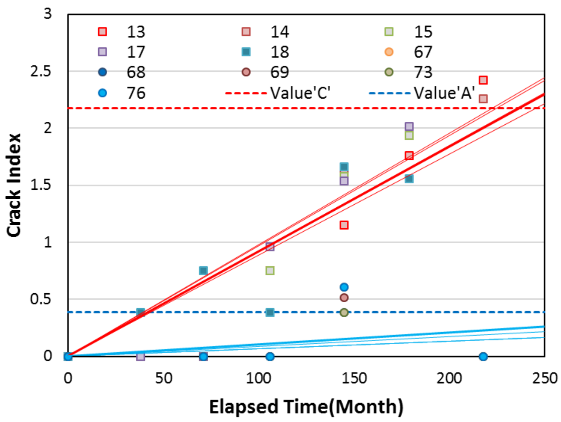

Fig. 5 Five units in order of both higher and lower crack deterioration speeds

It was confirmed that the most crack-prone unit was 13 and the least crack-prone units were 68 and 73 in the runway of Kumamoto Airport. Fig. 6 shows the runway distribution of the crack degradation speed.

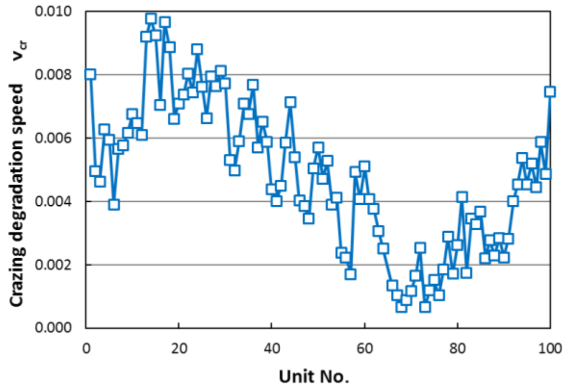

Fig. 6 Runway distribution of crack deterioration speed.

It was cleared from the distribution that the degradation speed was high in the vicinity of the unit 20 and low in the vicinity of the unit 70. Fig. 7 shows the crack indexes of both the most and the least vulnerable units to deterioration.

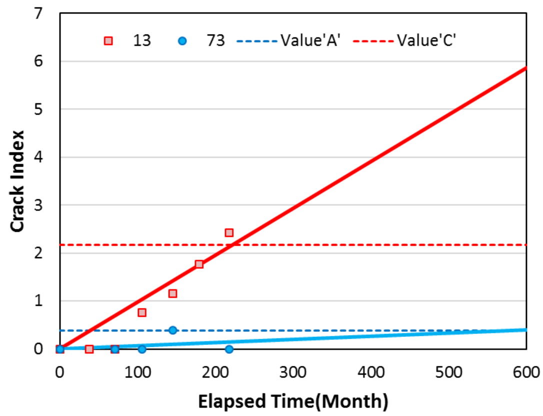

Fig. 7 Crack index in unit 13 and unit 73

Here, the values were evaluated by the cracking level needed to be repaired. The period to reach the level A was 39 months for the unit 13 which was the most vulnerable to deterioration, on the other hand, that of the least vulnerable unit 73 was 585 months. It was revealed that the period of deterioration was remarkably different depending on units. The factor to cause the difference in degradation over time was investigated through the data of Kumamoto Airport.

Although the degradation speed of Kumamoto Airport was able to be determined using the existing maintenance data, it was difficult for a new or repaired runway to derive its degradation speed due to the lack of existing data. Therefore, a method to predict degradation speed was attempted to be established, where degradation speed was obtained by calculating a fatigue coefficient considering pavement fatigue as a cracking factor of the asphalt paving.

METHOD OF CALCULATING A DEFORMATION COEFFICIENT OF ASPHALT MIXTURE

First of all, a fatigue coefficient was calculated based on the data of Kumamoto Airport. The coefficient is defined as the value obtained by dividing the fatigue degree of various kinds of aircrafts by the fatigue degree determined under the condition that the nation's largest aircraft: B777-300 constantly took off and landed on the asphalt pavement 100 times a month at a low speed and a temperature of 20 degrees Celsius. This coefficient is used for the airport pavement design for fatigue cracking [2]. Formulas for calculating the degree of fatigue are shown below.

$$D = \frac{\mathrm{Tv(i)}}{\mathrm{N}_{\mathrm{f(i)}}} \tag{3}$$

$$N_f = \alpha \cdot \left(\frac{1}{\varepsilon}\right)^{\beta} \cdot \left(\frac{1}{E}\right)^{\gamma} \tag{4}$$

where D: the degree of fatigue caused by aircraft, T_v: the traffic volume of aircraft (i) (times), N_f: the number of repetitions of up to destruction (times), ε: the tensile strain generated in asphalt mixture, E: the deformation coefficient of asphalt mixture (MPa), α, β, γ: coefficients. A deformation coefficient changes according to a temperature of pavement and loading time of an aircraft on asphalt pavement. Since the loading time is the time period during which wheels of an aircraft contact with the pavement, it tends to decrease as a speed of the aircraft increased. Fig. 8 shows the change in deformation coefficients due to the pavement temperature when the speed of an aircraft is constant.

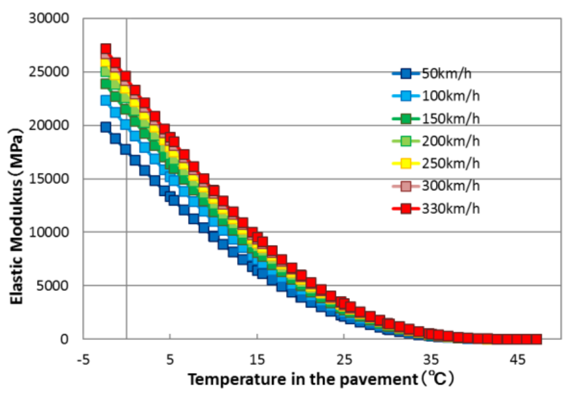

Fig. 8 Change in deformation coefficient due to pavement temperature when the speed of an aircraft was constant.

The lower a temperature becomes, the more frequently cracks tends to occur, because a cracking deformation coefficient becomes greater as a pavement temperature is lower. The asphalt pavement temperature was referred to the 2010 temperature in Mashiki city where Kumamoto Airport [3] was located. Fig. 9 shows a 24-hour change of temperature recorded in Mashiki city.

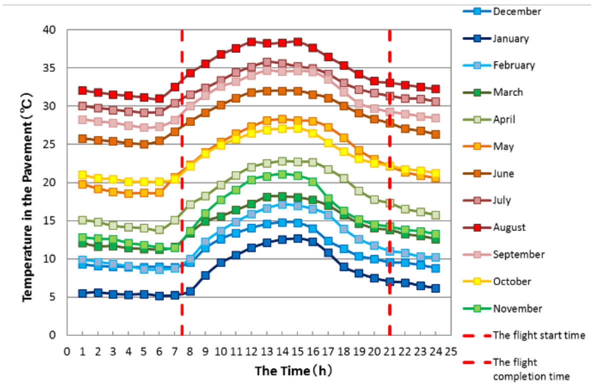

Fig. 9 24-hour temperature change from January to December in Mashiki.

The change of temperature between 7:40 and 21:00 was focused on because it was the time zone for the take-off and landing in Kumamoto Airport. It was cleared that takeoffs and landings around 8 and 21 o'clock in January had a great influence. The aircrafts which mainly takeoff and land on the runway in Kumamoto Airport are as follows: B767-300, B787, B737-800, B737-500, B737-200, A320, DHC8-400, Canadair Regional Jet 200, Embraer 170 and ATR42-600. A deformation coefficient was calculated using a pavement temperature at the take-off and landing time of each aircraft. Fig. 10 shows the change in modification coefficients by loading time when the pavement temperature is constant.

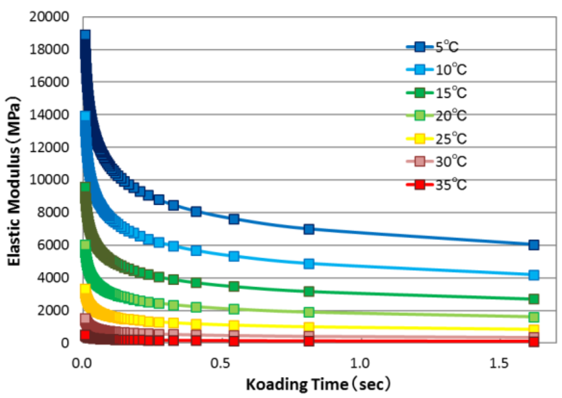

Fig. 10 Change in the modification coefficient by loading time when pavement temperature is constant.

Since a deformation coefficient increases as a speed of aircraft increases, cracking is likely to occur more often. The velocity distribution of the B767-300 is shown in Fig. 11 as an example.

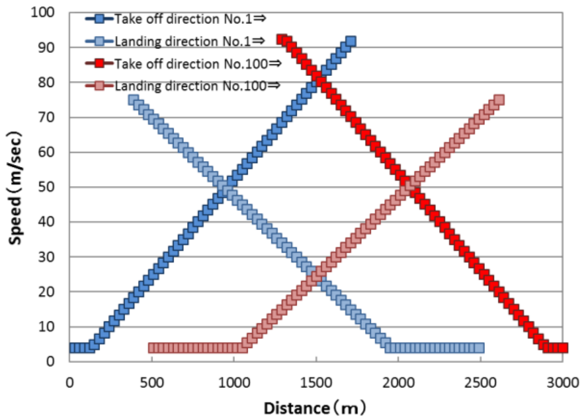

Fig. 11 Velocity distribution of B767-300

As takeoffs and landings were supposed to be performed from both ends of the runway, four velocity distributions were made for a single aircraft. The cracks of runway are significantly affected at the time of take-off at the fastest speed of an aircraft. Consequently, it was confirmed that a temperature of the pavement and a velocity of an aircraft were important factors to determine a deformation coefficient.

METHOD OF CALCULATING A FATIGUE COEFFICIENT

To determine a fatigue coefficient, a tensile strain of asphalt pavements was used in the equation (4). Since a tensile strain hardly changed depending on the size of an aircraft, the variation of strains was converted into the load of the main landing gear and the passing number of wheels. Since each aircraft has different number of main landing gear and therefore the passing number of wheels naturally becomes large in the case of the aircraft with more wheels, the number of repetitions was utilized for the equation as traffic volume. The weights of aircrafts were compared by the load of the main landing gear which supports 90% of the weight of an aircraft. Lift of an aircraft is enhanced according as the running speed increases and accordingly the load of an aircraft applied to the pavement may change [4]. Fig.12 shows the load distribution regarding the lift of the aircraft B767-300.

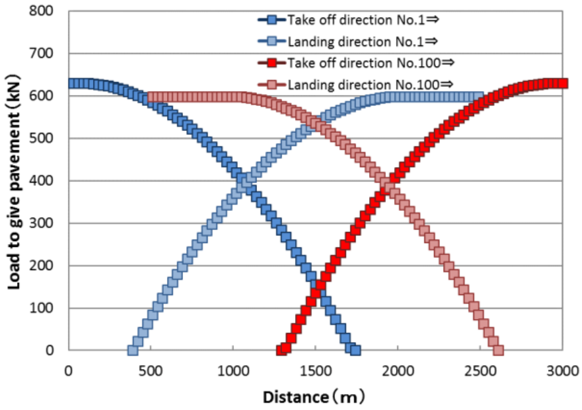

Fig. 12 Load distribution regarding lift of aircraft B767-300

The speeds of take-off and landing were set at 333km / h and 270km / h, respectively. Here, the aircraft was supposed to enter the nearest taxiway once the running speed has reduced to the speed equal to a traveling speed on the taxiway at the time of landing. In Kumamoto Airport, the unit 1 is usually used the most frequently for take-off and landing, however, the unit 100 located in opposition to the unit 1 is also used more frequently during the summer under the influence of the change of wind direction. Assuming these factors greatly affect the crack, an expression of a fatigue coefficient was obtained taking into consideration of these factors. An expression that evaluates a fatigue coefficient is shown below.

$$I_D = \frac{\Sigma D}{D_0} = \sum \left[\left(\frac{F}{F_0}\right)^x \cdot \left(\frac{E}{E_0}\right)^y \cdot \frac{N}{N_0} \cdot \frac{n}{n_0} \cdot k_f \right] \qquad (5)$$

where I_D: the fatigue coefficient, D: the total of fatigue rate of flying aircraft, D_0: fatigue of B777-300 , F: the main landing gear load of flying aircraft (kN), F_0: the main landing gear load of B777-300 during running at 32km / h (kN), E: the deformation coefficient of asphalt mixture (MPa), E_0: the modulus of deformation at the time of the pavement temperature 20 degrees Celsius, N: the traffic volume of a flying aircraft(times), N_0: 2400 times, n: the number of wheel axis of B777-300, n_0: the number of wheel axis of a flying aircraft, k_f: the proportion of take-off and landing direction, x,y : 1.9, 4.3. Fig. 13 shows the distribution of a fatigue coefficient in runway location. Fig. 14 shows the correlation between a fatigue coefficient and crazing degradation speed.

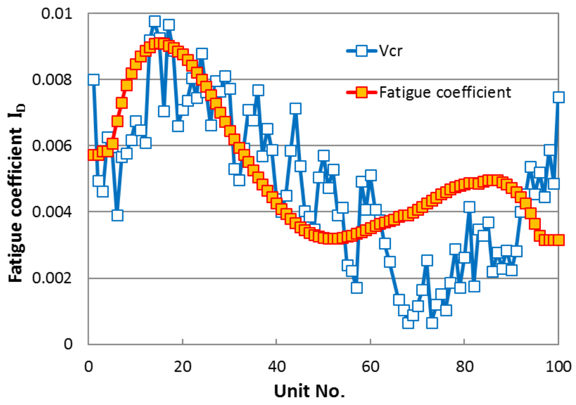

Fig. 13 Comparison between a fatigue coefficient and crazing degradation speed

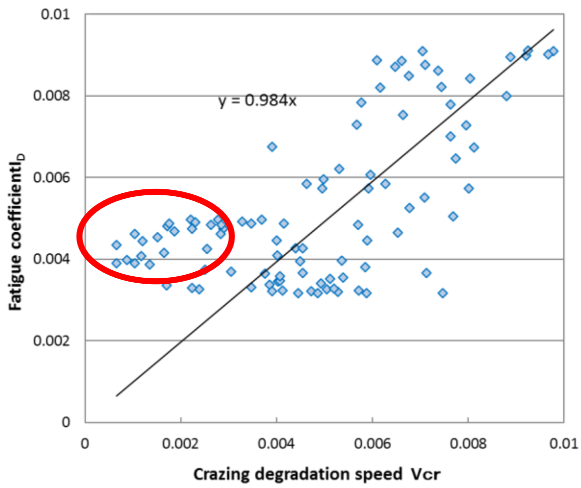

Fig. 14 Correlation between a fatigue coefficient and crazing degradation speed.

The difference between a fatigue coefficient and crazing degradation speed became large at points near the unit 60 as seen in Fig. 13. These diverged plots are assumed to be caused by a mistake of inspection because crack rate reduced with time elapse even though any repair work has not been performed. As shown in Fig. 14, although the measured values in the area surrounded by a red circle has low reliability, the correlation between a fatigue coefficient and crazing degradation speed was confirmed except for a little difference. Moreover, it was found out that it was possible to evaluate crazing degradation speed by the expression of fatigue degree incorporating load of aircraft, a gliding distance, temperature of each airport, wind direction and take-off and landing behaviors.

CONCLUSIONS

This study examined the deterioration prediction of cracking rate in Kumamoto Airport. As a result, the following views were obtained.

1. It is possible to determine cracking rate by fixing non-linear increase of cracking rate to linear form by power number and comparing the obtained slopes. The slope was named crazing degradation speed.
2. From the results, it was confirmed that crazing degradation speed tended to be high in the vicinity of the unit 20 and low in the vicinity of the unit 70 in Kumamoto Airport.
3. It is possible to evaluate crazing degradation speed using an expression of fatigue degree incorporating load of aircraft, a gliding distance, temperature of each airport, wind direction and the take-off and landing behaviors.
4. It was revealed not only that the fatigue coefficient obtained through this study had a high correlation with crazing degradation speed, but also that the cracking rate greatly affected a deformation coefficient and the load in Kumamoto airport.

REFERENCES

[1] Ministry of Land, Statistics information. 2014. December. 12 <http://www.mlit.go.jp/statistics/details/cab_list.html>

[2] Ministry of Land. Japan Civil Aviation Bureau. 2008. Airport pavement design point and design example,2008.ppI10-I13

.

[3] Ministry of Land, The Meteorological Agency. 2014.November.30. <http://www.data .jma. go.jp/obd/stats/etrn>

[4] Formula to calculate the lift of the wing.2014. October, 30 <http://www.cfijapan.com/study/html/to099/html-to035/017b-Lift_CL.htm>

ARTIFICIAL NEURAL NETWORK PERMEABILITY MODELING OF SOIL BLENDED WITH FLY ASH

Joenel G. Galupino[1] and Jonathan R. Dungca[2]
[1,2]Faculty, De La Salle University, Manila, Philippines

ABSTRACT

The determination of the permeability properties of soil is important in designing civil engineering projects where the flow of water through soil is a concern. ASTM D2434 Standard Test Method for Permeability of Granular Soils (Constant Head & Falling Head) is being followed to determine the vertical permeability, while for horizontal permeability, there are none. In this study, tests such as Atterberg limit, relative density tests, and particle size analyses are done to determine the index properties of soil blended with fly ash. Subsequently, microscopic characterizations tests, elemental composition tests and permeability tests are done to determine the chemical and physical properties of the soil mixes. A new permeability set-up was used in determining the horizontal permeability soil mixes. Data were extracted during the experiment and a relationship between the properties of soil and the permeability was established. An artificial neural network model was used to predict the coefficient of permeability when the percentage of fly ash is available.

Keywords: Permeability, artificial neural network, modeling, fly ash, waste utilization

INTRODUCTION

It is very important for engineers to understand the soil underneath because it will affect the way the structures are designed. Without its knowledge, lives would be at stake and it can reveal a lot of information by just analyzing the soil profile of a certain area.

Geotechnical properties of the soil (grain size distribution, Atterberg limits, specific gravity, maximum and minimum index densities, soil classification, permeability, shear strength and compressibility) should be considered by engineers when designing foundation, retaining walls, etc. but these properties change over time and are influenced by physical content, climate and weather.

Permeability generally relates to the propensity of a soil to allow fluid to move through its void spaces [1] and is vital to every project where the flow of water through soil is a concern.

Coal-fired power plants discharge large amounts of fly ash as waste but only half of them are used and the remaining half is trashed to land and sea, its disposal became an environmental concern, there are also local studies in the Philippines that shows the effect of wastes to the environment [2,3,4]. The utilization of fly ash may be a viable alternative for porous backfill material because fly ashes generally consist of silt-sized particles and consequently possess high permeability [5] but tests must be done to determine the permeability [6] of soil-fly ash mixture since there was a lack of information on the horizontal permeability of the said mixes.

METHODOLOGY

Fly ashes generally consist of silt-sized particles and consequently possess high permeability as mentioned by Prashanth (2001) [5].

Shown on Table 1 are the soil mixtures that were checked on the effect of fly ash on soil.

Table 1. Soil Mixtures

Soil Mixture	Fly Ash (%)	Soil (%)
100FA	100	0
75FA25S	75	25
50FA50S	50	50
25FA75S	25	75
100S	0	100

The density of the soil mixtures were determined using ASTM D854 [7], which is the standard for the specific gravity tests. In determining the Liquid Limit, Plastic Limit and the Plasticity Index of the soil mixtures, Atterberg limit tests based on ASTM D4318 was used [8]. Furthermore, the maximum (e_{max}) and minimum (e_{min}) index densities for soil mixtures was discerned using the ASTM D4253 [9] and ASTM D4254 [10], respectively. Then the particle size analyses using ASTM D422 was utilized to determine the percentage of different grain sizes in a soil [11].

Scanning electron microscopy (SEM) with energy dispersive X-ray spectroscopy (SEM/EDX) is the best known of the surface analytical techniques for different materials. The scanning electron microscopy (SEM) was used to evaluate the microscopic characterization of each soil mixture which produces high resolution images of surface topography, while Energy Dispersive X-ray Spectroscopy (EDX is used to determine the chemical composition of the soil and gives information on the elements present in the soil mixture.

The permeability of the different soil mixes were determined by the constant head test method and falling head test method. The direction of the flow weas also considered, thus, vertical and horizontal orientations of permeameter were used. A proposed set-up by Smith (2010) [12] for permeameter was used and modified to determine the horizontal permeability of the soil mixtures, shown on Fig. 1. The equation utilized for the permeability set-up is Eq. 1.

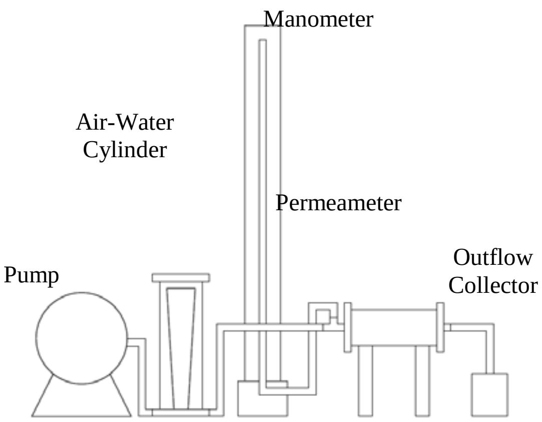

Fig. 1. Horizontal Permeability Set-up

$$\boldsymbol{k = \frac{Ql}{Aht}} \qquad \text{(Eq. 1)}$$

where:

- k = coefficient of permeability, cm/s;
- Q = quantity (volume) of water discharged during test, cm^3;
- l = length between manometer outlets, cm;
- A = cross-sectional area of specimen, cm^2;
- h = head (difference in manometer levels) during test, cm;
- t = time required for quantity Q to be discharged during test, s.

Many numerical modeling techniques have been introduced in the current technological era, and one of them is Artificial Neural Network (ANN). Artificial Neural Network can handle non-linear relationships between variables and incomplete data sets [13]. The proposed Artificial Neural Network Model will be validated by involving a 45-degree line as a guideline that provides insight into the measured variables and as a critical part of the analysis.

RESULTS AND DISCUSSIONS

Index Properties

Using ASTM D854 the specific gravity of each soil blend was determined. The specific gravity of the soil mixtures was reduced by the addition of fly ash [14] since the usual of the specific gravity of fly ash is much lower compared with the soil. Shown on Table 2, we can complement the study of Prabakar (2004) that the addition of fly ash (due to the light weight property of fly ash) reduces the specific gravity of a soil mixture.

Table 2. Summary of Specific Gravity

Soil Mixture	G_s
100FA	2.02
75FA25S	2.11
50FA50S	2.31
25FA75S	2.49
100S	2.58

Fly ash is considered as silt material, it is expected to have a plasticity index less than 1 based on stablished literatures [14], thus, by adding fly ash in the mixture has reduced the plasticity of a soil mixture. Results are shown in Table 3.

Table 3. Summary of Atterberg Limits

Soil Mixture	LL	PL	PI
100FA	66	65	1
75FA25S	64	57	7
50FA50S	61	49	12
25FA75S	59	45	14
100S	52	32	20

It can be noticed from Table 4, the Maximum Void Ratio (e_{max}) ranges from 1.78 to 1.99 because the fine contents of the fly ash contributed to the percentage of voids. 100S has the lowest value while 100FA has the highest, also from Table 4, 100S has the lowest fines content, while 100FA garners the highest. Their fines content and microfabric may have contributed to the minimum and maximum void ratio. These minimum and maximum void ratios together with the target relative density of 90% were used to determine the void ratio to be utilized for the permeability specimens.

To determine the maximum and minimum void ratios of the different soil-fly ash mixes ASTM D4253 and ASTM D4254 were used.

100FA has the greatest percentage of fines compared with other mixtures. Fly ash and soil are considered fines but the classification differ, fly ash is silt and soil is plastic. It can also be noticed that when fly ash is mixed with other soils increases the fines content. The summary of results from the particle size analyses are shown on Table 5.

Table 3. Summary of e_{min} and e_{max}

Soil Mixture	e_{min}	e_{max}
100FA	0.27	1.99
75FA25S	0.37	1.98
50FA50S	0.47	1.94
25FA75S	0.72	1.93
100S	0.84	1.78

Table 5. Summary of Particle Size Analysis Results

Soil Blend	% Passing #200	D_{10}	D_{30}	D_{60}
100F	61.83	0.029	0.03	0.04
75FA25S	50.78	0.019	0.032	0.06
50FA50S	29.79	0.032	0.0375	0.12
25FA75S	25.79	0.015	0.042	0.15
100S	21.84	0.01	0.4	1.2

SEM/EDX Results

In the Energy Dispersive X-ray Spectroscopy (EDX), chemical composition of soil is determined to give information on the element present in the soil, shown in Table 6. Oxygen (O) is very abundant, followed by Silicon (for Silty Sand) and Calcium (for Fly Ash). Silicon and Calcium are predominant in the soil elemental composition. Due to the presence of Oxygen and other dominant elements: Silica (from Silicon), Lime (from Calcium) and Alumina (from Aluminum) are the dominant minerals in the soil sample.

Table 6. Summary of Elemental Composition

Element	Composition (%) for Silty Sand	Composition (%) for Fly Ash
C, Carbon	17.39	5.41
O, Oxygen	46.65	40.64
Al, Aluminum	11.52	5.26
Si, Silicon	15.63	9.1
K, Potassium	1.05	0.78
Ca, Calcium	0.24	21.82
Fe, Iron	5.72	16.34
Cu, Copper	1.8	0.26
S, Sulfur	0	0.39

Most of the soil properties and characteristics like strength, compressibility and permeability are ascribed by its microfabric or microstructure. To evaluate the microfabric of soil, fly ash, the scanning electron microscopy (SEM) was used. Scanning electron microscopy (SEM) with energy dispersive X-ray spectroscopy (SEM/EDX) is the best known of the surface analytical techniques. High resolution images of surface topography of the different soil mixtures were produced using these tests. Pure soil and Fly Ash were initially tested to check their microscopic characteristics, mixed soils were also tested thereafter.

A combination of extremely strandy grains, large angular grains and abundant silt grains formed the micro fabric of 100S. It is well-graded microscopically and the silt grains have a rough surface. A smaller inter-particle voids were created by the smaller particles tend to fill the voids created by the larger particles shown in Figure 1. Looking closer to magnification of 1000x and 5000x, strand-like particles are present, his indicates that these elongated particles also fill the voids, giving small passageways for water to permeate.

While for 100F, it is a combination of larger silt grains and smaller silt grains to form the micro fabric normally 0.002-0.05 mm in size. Compared with silty sand (soil), particles have almost similar size, forming larger inter-particle void that allows water to pass through. On the 1000x and 5000x magnification, the surface of the particle is not smooth, this create passageway/voids for water to pass through.

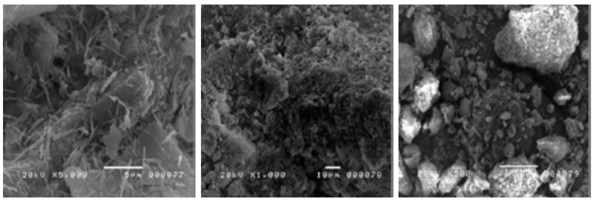

Fig. 1. Microfabric of 100S (5000x, 1000x and 500x Magnification)

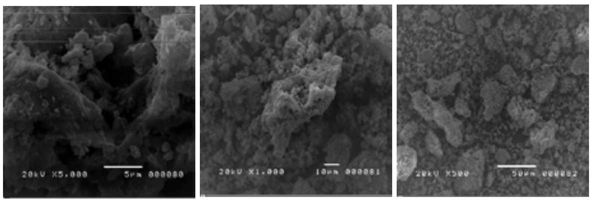

Fig. 2. Microfabric of 100FA (5000x, 1000x and 500x Magnification)

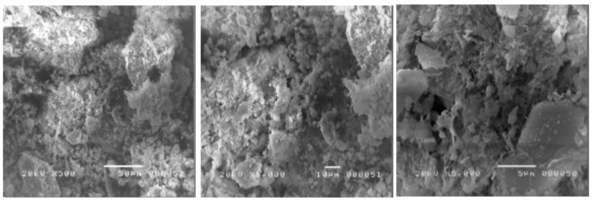

Fig. 3. Microfabric of 50FA50S (5000x, 1000x and 500x Magnification)

A combination of extremely strandy grains, large angular grains and abundant larger silt grains and smaller silt grains formed the micro fabric of 50FA50S. Looking closer to magnification of 1000x and 5000x, strand-like particles are present but noy prevalent compared with the pure soil, the soil particles may contribute to the reduction of permeability but the silt grains of fly ash will counteract to allow water to drain faster.

Permeability

The study of Smith (2010) [15] and was modified to determine the horizontal permeability of the soil mixtures. Shown in Table 7, are the range of permeability values gathered for the vertical oriented constant head permeability test, to determine the effect of fly ash when added to soil, a box and whisker plot is delineated, shown on Figure 4.

A proposed approach in determining the vertical permeability of the various soil mixtures was utilized, it was referred on. The results of the experiment agrees with the study of Prashanth (2001) that fly ashes generally consist of silt-sized particles and consequently possess high permeability since it is prevalent that the permeability is increased when the amount of fly ash is increased. Thus, the amount of fly ash increase the permeability of the soil mixes.

Table 7. Range of permeability values for vertical oriented permeability test

Soil Mixture	Minimum k, cm/s	Maximum k, cm/s
100FA	4.53E-05	5.52E-05
75FA25S	3.40E-05	3.80E-05
50FA50S	2.55E-05	3.16E-05
25FA75S	2.05E-05	2.51E-05
100S	1.47E-05	2.09E-05

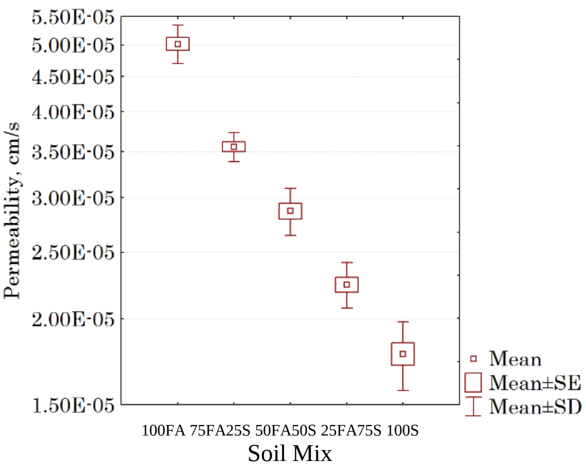

Fig. 4. Effect of fly ash on the vertical permeability when added to soil

In determining how long the contaminated water will penetrate the ground water, the horizontal permeability of soil mixtures shall be considered. Shown in Table 8, are the range of permeability values gathered for the horizontal oriented constant head permeability test. To determine the effect of fly ash in the horizontal permeability when added to soil, a box and whisker plot was drawn and shown on Figure 5. The data garnered in this study agree with the study of Das (2008) [16], that the horizontal permeability values are larger than the vertical permeability values, this is due to the pressure head induced during the permeability test. The specimen is laid in a horizontal position, which experiences no pressure drop within its body, unlike the vertical specimen, which experiences pressure drop, resulting to a slower flow of water.

Table 8. Range of permeability values for horizontal oriented permeability test

Soil Mixture	Minimum k, cm/s	Maximum k, cm/s
100FA	6.02E-05	7.28E-05
75FA25S	4.25E-05	5.02E-05
50FA50S	3.40E-05	4.04E-05
25FA75S	3.04E-05	3.70E-05
100S	2.21E-05	2.70E-05

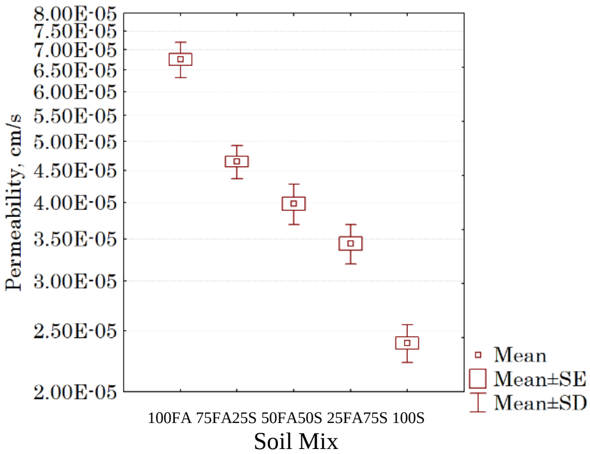

Fig. 5. Effect of fly ash on the horizontal permeability when added to soil

Fly ash is the recommended addition to the soil mixtures since waste materials are aimed to be utilized and the addition of fly ash, which has a combination of larger silt grains and smaller silt grains to form the micro fabric prevalent to the microscopic characterization test for 100F, to soils changes the inter-particle void ratio [14]

Subsequently, silt particles have almost similar size, forming larger inter-particle void, contributing to a much larger inter-particle voids, thus, the permeability of pure fly-ash ranges: (1) vertical oriented $4.51x10^{-05}$ cm/s to $5.35x10^{-05}$ cm/s and (2) horizontal oriented $1.93x10^{-05}$ cm/s to $7.29x10^{-05}$ cm/s.

75FA25S, 50FA50S, 25FA75S, 96S4FA are the mixtures that include fly ash and soil, their microfabric is a combination of extremely strandy grains, large angular grains and abundant larger rough-surfaced silt grains and smaller rough-surfaced silt grains. Evidently shown on Figure 4 and Figure 5, as the amount of fly ash is increased, the drainage also increased. Due to the contribution of fly ash to the inter-particle voids of the soil mixtures, the permeability of mixture of soil and fly-ash ranges: (1) vertical oriented $1.93x10^{-05}$ cm/s to $3.80x10^{-05}$ cm/s and (2) horizontal oriented $2.52x10^{-05}$ cm/s to $5.02x10^{-05}$ cm/s.

To validate the results of the vertical oriented and the horizontal oriented permeability tests, their ratio must be within the given range of Das (2008). The collected usual ratio of horizontal and vertical permeability of soils by Das (2008) is with the range of 1.2-3.3, thus, the data gathered are between 1.3-1.5, thus, ratios are within Das' desired range.

Artificial Neural Network

In the Artificial Neural Network Model, five (5) variables were considered:

1. The percentage of added fly ash in the soil
2. Specific gravity
3. Liquid Limit
4. Maximum Void Ratio
5. Minimum Void Ratio

The data garnered were divided into three (3) groups: 70% for training the neural network, 15% for validation and 15% for testing. In the hidden layer, tan-sigmoid transformation function was utilized, while in the output layer a linear transformation function was used. The feed-forward backpropagation technique was used to generate the best model for estimating the permeability of the soil mixtures. Also, fastest backpropagation algorithm and highly recommended Levenberg-Marquardt network training function was also employed. The authors utilized Matlab for the ANN Algorithm.

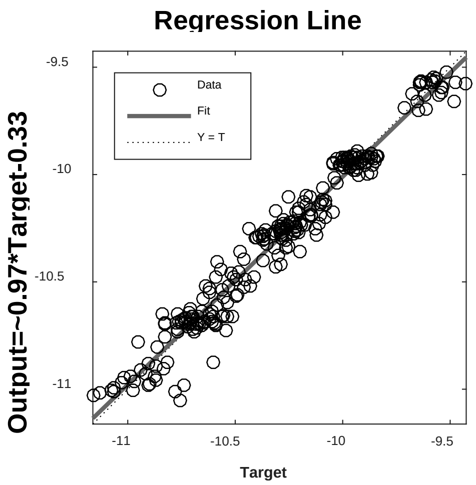

Fig 6. Regression Line for ANN Structure 5-9-2

By determining the number of neurons in the input and output layers, number of hidden layers and the number of neurons in each hidden layer, the best Artificial Neural Network model for the soil mixtures can be garnered. Thus, after numerous trial the ANN structure 5-9-2 (5 input, 9-nodes and 2 output) was determined to be the best model to estimate the permeability of the soil mixtures. The model was able to give an acceptable values of R: 0.98414, 0.97570, and 0.96843 for validation, training and testing, respectively. Figure 6, represents the regression line for ANN 5-9-2. Also, the 45deg line shows a validation and an agreement between the experimental (actual) and the predicted parameters. Subsequently, Figure 7 shows the performance curve of the ANN model, the mean squared error is 0.0061175 and occurred at epoch 25.

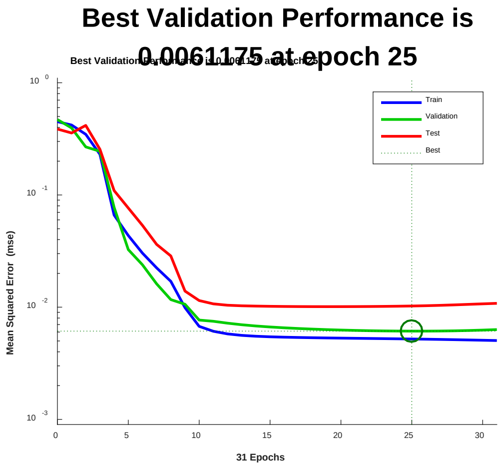

Fig. 7. Best validation performance of the model

There are many studies that provided a numerical approach in determining the permeability when the amount of fly ash is available [17]. The permeability coefficient was further compared with a regression model. The said regression model gave an R^2 value of 0.9335 which is lower compared to calculated R^2 value of the ANN method for validation 0.9685, 0.9520, and 0.9379 for validation, training and testing, respectively.

CONCLUSION AND RECOMMENDATIONS

The addition of fly ash to soils changes the inter-particle void ratio [5], it increases the permeability, thus, the microscopic characteristics of the soil mixtures may contribute to the increase in permeability. Based on the tests, fly ash is a combination of larger silt grains and smaller silt grains to form the micro fabric. Silt particles have almost similar size, forming larger inter-particle void, contributing to a much larger inter-particle voids.

ANN Structure 5-9-2 is the best architecture since it has the highest correlation coefficient, R^2, and the said model has a good predicting ability compared with previous studies. To improve the results, extensive manipulation of parameters should also be considered. Sensitivity analyses may be conducted to further validate the model and the results.

Furthermore, it is recommended for the purpose of ground improvement engineering, testing the shear strength and the compressibility of the soil mixtures should be determined and relate them to the permeability.

REFERENCES

[1] Liu, C., & Evett, J. B. (2000). Soil Properties: Testing, Measurement and Evaluation. (E. Francis, Ed.) Charlotte, North Carolina, USA: Prentice Hall.

[2] Caplano, J. (2001, December 30). Closed landfills contaminating groundwater, World Bank warns. (Philippine Star) Retrieved November 2013, from Philippine Star: http://www.philstar.com/nation/145333/closed-landfills-contaminating-groundwater-world-bank-warnsAnnnn B, “Unpublished work but accepted”, accepted, Year.

[3] World Bank. (2012, October 24). Philippines: Toward Greener Waste Management. Retrieved November 2013, from World Bank: http://www.worldbank.org/en/news/press-release/2012/10/24/philippines-toward-greener-waste-management

[4] Adajar, M. A., & Zarco, M. (2014, September). An empirical model for predicting hydraulic conductivity of mine tailings. International journal of GEOMATE: geotechnique, construction materials and environment. 7, 1054-1061.

[5] Prashanth, J., Sivapullaiah, P., & Sridharan, A. (2001). Pozzolanic fly ash as a hydraulic barrier in landfills. Engineering Geology, 60, 245-252.

[6] Baxter, D. Y. (2000, April 14). Mechanical behavior of soil-bentonite cut-off wall. Virginia Polytechnic Institute and Stat University, Department of Civil Engineering. Blacksburg, Va.

[7] American Society for Testing and Materials. (n.d.). Standard Test Methods for Specific Gravity of Soil Solids by Water Pycnometer. ASTM D854. ASTM D854.

[8] American Society for Testing and Materials. (n.d.). Standard Test Methods for Liquid Limit, Plastic Limit, and Plasticity Index of Soils. ASTM D4318.

[9] American Society for Testing and Materials. (n.d.). Standard Test Methods for Maximum Index Density and Unit Weight of Soils Using a Vibratory Table. ASTM D4253.

[10] American Society for Testing and Materials. (n.d.). Standard Test Methods for Minimum Index Density and Unit Weight of Soils and Calculation of Relative Density. ASTM D4254

[11] American Society for Testing and Materials. (n.d.). Standard Test Method for Particle-Size Analysis of Soils. ASTM D422.

[12] Smith, C. B. (2010). Horizontal Permeameter. Magna Cum Laude Honors Research Project, University of Florida, Department of Civil and Coastal Engineering, Gainesville, Florida.

[13] Oreta, A., & Ongpeng, J. (2011), “Modeling the confined compressive strength of hybrid circular concrete columns using neural networks”, Computers and Concrete, 8(5), 597-616.

[14] Prabakar, J., Dendorkar, N., & Morchhale, R. (2004). Influence of fly ash on strength behavior of typical soils. Construction and Building Materials, 18, 263-267.

[15] Smith, C. B. (2010). Horizontal Permeameter. Magna Cum Laude Honors Research Project, University of Florida, Department of Civil and Coastal Engineering, Gainesville, Florida.

[16] Das, B. M. (2008). Advanced soil mechanics. New York: Taylor & Francis.

[17] Galupino, J., Dungca, J. (2015). Permeability characteristics of soil-fly ash mix. ARPN Journal of Engineering and Applied Sciences, 15, 6440-6447.

ITERATIVE ALGORITHM TO CONSTRUCT AN EXACT FINITE ELEMENT MODEL FOR AXIALLY LOADED PILE IN ELASTO-PLASTIC SOIL

Chinapat Buachart and Chayanon Hansapinyo
Department of Civil Engineering, Faculty of Engineering, Chiang Mai University

ABSTRACT

An iterative algorithm to construct a displacement based finite element method for analyzing axially loaded pile embedded in finite depth of elasto-plastic soil is presented. The investigation herein is conducted on the condition of shape function by which exact solutions may be reproduced at the nodal points regarding to a few number of elements. The examined shape functions which satisfy the homogeneous governing equations in elastic and plastic soil through bisection iterative algorithm are introduced to obtain the so-called exact element stiffness matrix via total potential energy principle. Numerical examples of elastostatic pile embedded in elasto-plastic Winkler foundation illustrate the accuracy of proposed element compare with conventional finite element shape functions. Axial force and displacement solutions show very good agreement with data from the available literature i.e. the exact nodal displacement solution is obtained correspond to any point load level even with a single element mesh employed.

Keywords: Axially loaded pile, Displacement method, Finite element, Iterative algorithm, Soil-pile interaction

INTRODUCTION

In this study, the displacement of axially loaded pile embedded in elasto-plastic soil is solved via proposed finite element procedure. The nodal exact shape function concept suggested in [1]–[4] are used to construct the tangent stiffness matrix and equivalent nodal force incorporate with Newton-Rapshon algorithm to solve nonlinear algebraic equations. An internal point which is separate elastic and plastic portion soil around embedded pile then determined via simple iterative bisection procedure.

Example of elasto-static pile embedded in elasto-plastic soil subjected to quasi-static point load on top soil level is analyzed. The results from proposed element are compared with analytical solution from [5] and conventional simplex bar element to verify the accuracy of proposed pile element.

MATHEMATICAL FORMULATION

Problem Definition

The analysis considers a single circular pile [4], with diameter d (cross section A = $0.25\pi d^2$ and perimeter $U = \pi d$), embedded into soil deposit (Fig. 1). The pile has a total length L and is subjected to an axial force P_0 at the pile head which is flush with the ground surface. The soil medium is assumed to be elastio-plastic, isotropic and homogeneous, with elastic properties described by equivalent spring coefficient k_s. Once the soil displacement goes beyond the yielding displacement w_*, the shear resistance will keep constant as long as the displacement increases. The soil bearing capacity at pile's end is presented by coefficient k_b. The pile is assumed to behave as an elastic column with Young's modulus E. The Poisson's ratio of the pile material is neglected. Figure 1(a) shows the elastic and plastic zone occurred in soil due to the axial displacement w_0 at top pile head is greater than yielding displacement w_*. Suppose that yielding displacement occurred at depth z_0 from pile head. Hence, the length of an elastic portion in Fig. 1 is denoted by ℓ, the magnitude of axial displacement in elastic portion is less than or equal to yielding displacement.

Governing Differential Equations

Consider one-dimensional element in Fig. 2. Assuming that soil surrounding pile element is in elastic condition for whole length. The total potential energy of this soil-pile element subjected to the axial forces P_1 and P_2 is defined as the sum of internal potential energy (strain energy) and the external potential energy due to external load as follow [4]:

$$\Pi = \frac{1}{2}\left[EA\int_0^L \left(\frac{dw}{dz}\right)^2 dz + k_s U \int_0^L w^2 dz \right] - P_1 w_1 - P_2 w_2 \tag{1}$$

where $w(z)$ is the vertical pile displacement at depth z. The first and second terms in Eq. (1) represent the strain energy in pile and surrounding soil, respectively.

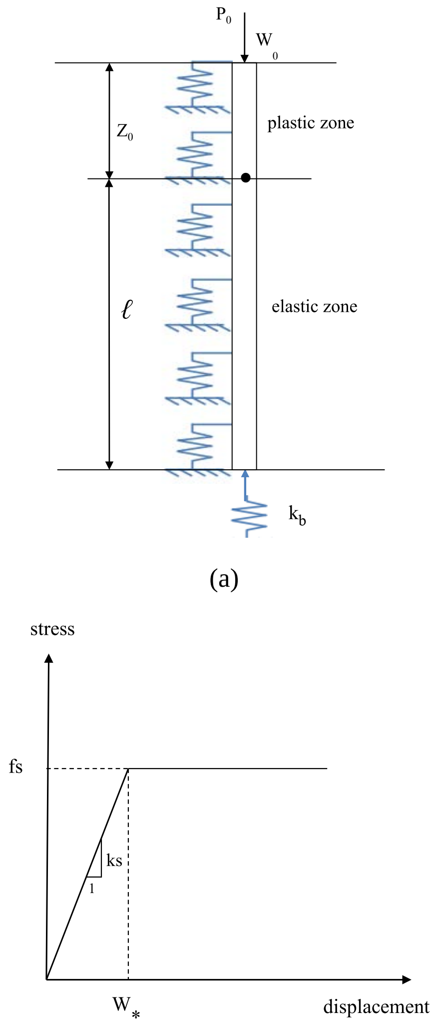

Fig. 1 Axially loaded pile and soil model [4]

The first variation of Eq. (1) leads to

$$\delta\Pi = EA\int_0^L \left(\frac{d\delta w}{dz}\right)\left(\frac{dw}{dz}\right)dz + k_s U\int_0^L (\delta w)w\,dz - P_1\delta w_1 - P_2\delta w_2 \tag{2}$$

Applying the appropriate Gauss-Green theorem to Eq. (2) and setting $\delta\Pi = 0$, gives the differential equation for equilibrium

$$\frac{d^2w}{dz^2} - \alpha^2 w = 0 \quad \text{for} \quad 0 < z < L \tag{3}$$

where $\alpha^2 = k_s U / EA$ is the characteristic parameter of pile surrounding by elastic soil region.

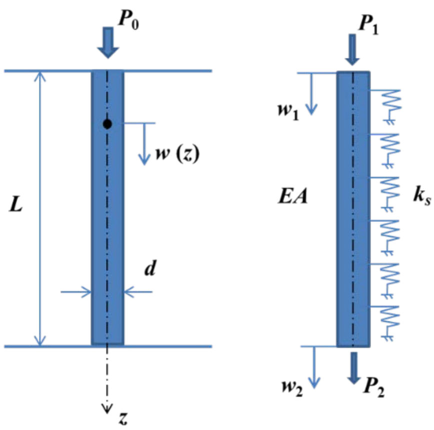

Fig. 2 Axially loaded pile element [4]

A set of natural boundary conditions are as follows

$$P_1 = -EA\left.\frac{dw}{dz}\right|_{z=0} \quad \text{and} \quad P_2 = EA\left.\frac{dw}{dz}\right|_{z=L} \tag{4}$$

Plastic soil conditions

Suppose that ended load at top soil level reach some limit, the soil portion at level $0 < z < z_0$ is in plastic condition. Consider the plastic soil portion, upper portion in Fig. 1, displacement w in second term of equilibrium equation (3) have to be replaced by yielding displacement w_* as follow

$$\frac{d^2w}{dz^2} - \frac{f_s}{EA} = 0 \quad \text{for} \quad 0 < z < z_0 \tag{5}$$

In which $f_s = k_s U w_*$ is the maximum shearing force occurred in soil surrounding pile element. Shearing force in soil surrounding pile element is linearly dependent on pile displacement until they reach some limit of yielding displacement magnitude w_*.

The nodal exact finite element solutions of Eqs. (3) and (5) for a given value of plastic soil depth z_0 can be found in [4]. In present work, the proposed finite element procedure to solve Eqs. (3) and (5) for a given load P_0 (Fig. 1) will be explained in next section. Then, the results from proposed nodal exact element and conventional linear element will be compared with available analytical solution in [5].

Newton-Raphson Iteration

Due to elasto-plastic behavior of shear force in soil surrounding pile element, finite element discretization of Eqs. (3) and (5) leads to the steady steady-state set of non-linear algebraic equations given by the residual equation as follows [6]–[9]:

$$\mathbf{r}^{(k)} = \mathbf{f} - \mathbf{F}\left(\mathbf{w}^{(k)}\right) \tag{6}$$

In which internal force $\mathbf{F}$ is a non-linear function (bilinear function in this case) of nodal displacement $\mathbf{w}$ at iteration number k. The external nodal load $\mathbf{f}$ is presented in term of specified vector. A solution of residual $\mathbf{r} = \mathbf{0}$ is obtained by solving an algebraic equation:

$$\mathbf{K}_T^{(k)} \Delta\mathbf{w}^{(k)} = \mathbf{r}^{(k)} \tag{7}$$

where $\mathbf{K}_T^{(k)} = \partial\mathbf{F}/\partial\mathbf{w}^{(k)}$ is so-called tangential stiffness matrix, used to obtain the incremental nodal solution $\Delta\mathbf{w}$. Then update the nodal solution:

$$\mathbf{w}^{(k+1)} = \mathbf{w}^{(k)} + \Delta\mathbf{w}^{(k)} \tag{8}$$

An iteration is repeated until the magnitude of incremental nodal solution $\Delta\mathbf{w}$ and residual $\mathbf{r}$ close to zeros.

Element Internal Force

Nodal internal force $\mathbf{F}$ in Eq. (6) can be derived from first variation of strain energy term in Eq. (2). In conventional linear finite element, the trial solution $w(z)$ and variation $\delta w(z)$ are approximated via linear shape functions $N_a(z)$, a = 1 or 2, which results in non-exact nodal solution $\mathbf{w}$. To produce the nodal exact solution of unknown $\mathbf{w}$, the trial solution $w(z)$ and variation $\delta w(z)$ are approximated via the set of shape function $N_a(z)$ which satisfy homogeneous solutions of governing equations (3) and (5) as discussed in previous work [4]. Hence, nodal internal force of conventional and proposed two nodes element can be expressed as follow.

Plastic soil conditions

Consider the upper part of soil (plastic zone) in Fig. 1(a). The displacement of soil surrounding pile element is in plastic condition, *.i.e.* $w(z) \geq w_*$. The internal force of proposed element can be expressed as follow:

$$\mathbf{F} = \frac{EA}{z_0}\begin{bmatrix} 1 & -1 \\ -1 & 1 \end{bmatrix}\begin{Bmatrix} w_1 \\ w_* \end{Bmatrix} + \frac{f_s z_0}{2}\begin{Bmatrix} 1 \\ 1 \end{Bmatrix} \tag{9}$$

Note that the internal force Eq. (9) is derived from linear shape function as shown in appendix

Elastic soil conditions

Now consider the lower part of soil (elastic zone) in Fig. 1(a). The displacement of soil surrounding pile element still be in elastic condition, *.i.e.* $w(z) \leq w_*$. Hence, trial solution of pile in elastic soil condition was in hyperbolic functions as described in [4]. The internal force of proposed element can be expressed as follow:

$$\mathbf{F} = \alpha EA\begin{bmatrix} \coth\beta & -\operatorname{csch}\beta \\ -\operatorname{csch}\beta & \coth\beta \end{bmatrix}\begin{Bmatrix} w_* \\ w_2 \end{Bmatrix} \tag{10}$$

In which non-dimensional parameter $\beta = \alpha\,\ell$.

Conventional linear element

To compare the accuracy and efficiency of proposed element, the internal force of conventional linear finite element has to be recalled. An expression of internal force vector for conventional linear finite element in elasto-plastic soil condition is shown in Eq. (11).

$$\begin{aligned}\mathbf{F} &= \frac{EA}{L}\begin{bmatrix} 1 & -1 \\ -1 & 1 \end{bmatrix}\begin{Bmatrix} w_1 \\ w_2 \end{Bmatrix} \\ &+ \frac{\alpha^2 EA}{6L^2}\begin{bmatrix} 2\ell^3 & \ell^2\left(L+2z_0\right) \\ \ell^2\left(L+2z_0\right) & 2\left(L^3 - z_0^3\right) \end{bmatrix}\begin{Bmatrix} w_1 \\ w_2 \end{Bmatrix} \\ &+ \frac{f_s}{2L}\begin{Bmatrix} z_0\left(L+\ell\right) \\ z_0^2 \end{Bmatrix}\end{aligned} \tag{11}$$

Then the procedure to construct tangent stiffness matrix used to determine incremental displacement following Eq. (7) will be explained.

Tangential Stiffness Matrix

Tangential stiffness matrix in Eq. (7) will be constructed from matrices of internal force in Eqs. (9) and (10). First, nodal internal forces from Eq. (9) and (10) are assembled to form three members vector, following degree of freedom w_1, w_2 and w_*. Then degree of freedom corresponding to yielding displacement w_* will be *condensed* out via static condensation technique [7]. Hence, tangential stiffness matrix is *reduced stiffness* represents a set of two equations with two unknowns corresponding to ended displacements, w_1 and w_2.

Estimation of plastic zone

Construction of the internal force term in Eqs. (9)–(11) require the estimated length of plastic zone (z_0) at present iteration. Let assume that the yielding of soil surrounding pile element occurs in upper zone of pile element in Fig. 2, *i.e.* $w_1 > w_2$ and $w_2 <$

$w_* < w_1$. Imply the continuity of internal axial force via finite element equilibrium equation at $z = z_0$ (*ghost* node). Hence, relation between yielding displacement at given position z_0 and specified value of nodal solutions (w_1 and w_2) for proposed nodal exact element is:

$$w_* = \frac{w_1 \sinh\beta + w_2 \alpha z_0}{\left[1 + \frac{(\alpha z_0)^2}{2}\right]\sinh\beta + \alpha z_0 \cosh\beta} \tag{12}$$

Equation (12) is numerically solved via *bisection* method to obtain the length of plastic zone, namely z_0. Then the tangential stiffness matrix $\mathbf{K}_T$ can be obtained from procedure described in previous section. Note that if the continuity of force from natural boundary conditions, Eq. (7) were used to derive the relation between nodal displacements and length of plastic zone instead of finite element equilibrium equation. Then the result is similar with Eq. (12), except that the square term $(\alpha z_0)^2$ in denominator of Eq. (12) will be disappeared.

Besides, in the case of conventional linear finite element, the value of plastic length z_0 can be estimated directly from linear interpolation, *i.e.*

$$z_0 = \left(\frac{w_1 - w_*}{w_1 - w_2}\right) L \tag{13}$$

For a given value of point load at pile head, *i.e.* force P_0 in Fig. 1(a), iteration processes in Eqs. (7) and (8) are repeated until equilibrium conditions satisfied.

NUMERICAL EXAMPLES

In this section, numerical example is presented to illustrate the effectiveness of nodal exact finite element proposed in previous section. Results from proposed element then compare with conventional linear finite element. Accuracy of proposed element is verified using analytical solutions available in [5].

A bored pile was installed in the medium silt clay and the end bearing layer is sandstone. The pile length is 45 m, and the diameter d = 1 m. The elastic modulus of pile shaft $E = 2.2 \times 10^7$ kPa. From soil tests, the values of equivalent soil elastic coefficient k_s = 12000 kPa/m, the yielding displacement of soil w_* = 2.6 mm, and end bearing stiffness k_b = 684000 kPa/m [4]. The value $k_b A$ is added into the last diagonal member of stiffness matrix.

The numerical test was performed using one proposed nodal exact element and one conventional linear element. The magnitude of point load at pile head P_0 is gradually increased. The results from proposed and conventional elements are shown in Table 1. Finite element solutions of proposed element are identical to the exact analytical solutions in [5]. Additionally, the conventional linear element behaves stiffer than proposed element. Pile head displacements of conventional linear element are less than results from proposed element and analytical solution [5].

Table 1 Calculated plastic depth and settlement of pile head at any values of load P_0.

P_0(kN)	Present (Exact)		Linear FEM	
	z_0 (m)	w_0 (mm)	z_0 (m)	w_0 (mm)
2086	0	2.60	-	2.21
2951	9	3.91	9.64	3.24
3796	18	5.64	23.60	4.96
4593	27	7.71	33.49	7.29
5291	36	9.95	40.37	9.82
5807	45	11.98	45	11.98

For comparison, the load and settlement in Table are also plotted in Fig. 1. The load-settlement relations curves show nonlinear behavior when the load at pile head is gradually increased.

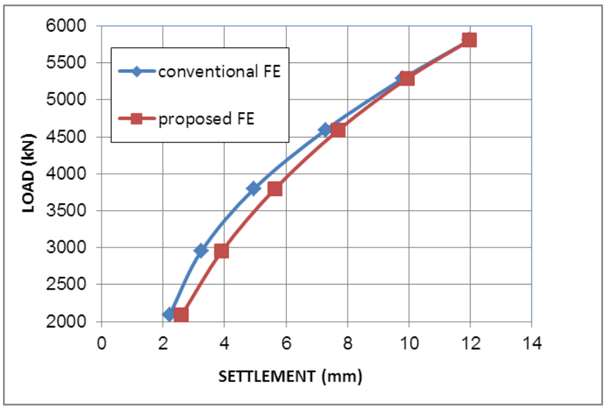

Fig. 1 Load-settlement curves of proposed versus conventional finite elements.

CONCLUSION

The finite element model for pile embedded in elasto-plastic soil subjected to axial load is proposed. The nonlinear algebraic equation has been solved via Newton-Raphson iteration. Tangential stiffness is constructed through static condensation technique and bisection search method. Numerical example for static load pile embedded in elasto-plastic soil was tested by gradually increase load on pile head until shear force in surrounding soil reach ultimate soil capacity. Results obtain from proposed element were compared with analytical solution and conventional linear finite element solution. Numerical test indicates that an exact finite element solution can be obtained even with minimum number of element used. Linear conventional finite element behaved stiffer than the proposed nodal exact finite element.

REFERENCES

[1] Tong P, "Exact solutions of certain problems by finite element method", AIAA J., Vol. 7, 1969, pp. 178-180.

[2] Kanok-Nukulchai W, Dayawansa PH, and Karasudhi P, "An exact finite element model for deep beams", Int. J. of Struc, Vol. 1, Jan. 1981, pp. 1-7.

[3] Ma H, "Exact solutions of axial vibration problems of elastic bars", Int. J. Numer. Meth. Eng., Vol. 75, 2008, pp. 241-252.

[4] Buachart C, Hansapinyo C, and Sommanawat W, "An exact displacement based finite element model for axially loaded pile", Int. J. of GEOMATE, Sept., Vol. 11(25), 2016, pp. 2474-2479.

[5] Chou YC and Hsiung YM, "A normalized equation of axially loaded piles in elasto-plastic soil", J. Geo Eng., Vol. 4(1), 2009, pp. 1-7.

[6] Bathe KJ, Finite Element Procedures. Prentice Hall, 1996, ch. 6.

[7] Cook RD, Malkus DS, Plesha ME, and Witt RJ, Concept and Applications of Finite Element Analysis. Wiley & Sons, 2002, ch. 6 and 17.

[8] Simo JC and Hughes TJR, Computational Inelasticity. New York: Springer, 1998, ch. 1.

[9] Zienkiewicz OC and Taylor RL, The Finite Element Method. Vol. I. Oxford: Butterworth-Heinemann, 2000, ch. 20.

[10] Chapra SC, Applied Numerical Methods with Matlab for Engineers and Scientists. McGraw-Hill, 2005, ch. 5.

APPENDIX

A.1 Exact Solution of Pile Static Load Test [5]

Assume that displacement at pile head in Fig. 1(a) is greater than or equals to yielding displacement w_*. Prescribe the boundary conditions (4) into the solution of governing Eqs. (3) and (5), obtain the solution of load at pile head as follows:

$$P_0 = \alpha E A w_* \left[\tanh\left(\alpha\ell + \gamma\right) + \alpha z_0 \right] \tag{14}$$

where the variable γ is the characteristic value of the end bearing stiffness of soil (k_b) at pile tip:

$$\tanh\left(\gamma\right) = \frac{k_b}{\alpha E} \tag{15}$$

The ratio of displacement at the pile head w_0 with respect to yielding displacement is therefore

$$\frac{w_0}{w_*} = 1 + \alpha z_0 \tanh\left(\alpha\ell + \gamma\right) + \frac{\left(\alpha z_0\right)^2}{2} \tag{16}$$

In addition, ratios of pile tip displacement w_t with respect to yielding displacement:

$$\frac{w_t}{w_*} = \frac{\cosh\left(\gamma\right)}{\cosh\left(\alpha\ell + \gamma\right)} \tag{17}$$

On deriving Eqs. (14)–(17), soil under pile tip is assumed to be in an elastic condition. Detail derivation of Eqs. (14)–(17) are described in reference [5].

A.2 Shape Function of Nodal Exact Element [4]

In reference [4], shape functions of proposed pile element were derived from homogeneous solutions of Eqs. (3) and (5). There are expressed in the following forms:

Plastic soil conditions ($0 \le z \le z_0$)

$$N_1\left(z\right) = \frac{\left(z_0 - z\right)}{z_0},\ N_2\left(z\right) = \frac{z}{z_0} \tag{18}$$

Elastic soil conditions ($z_0 \le z \le L$)

$$N_1\left(z\right) = \frac{\sinh\left[\alpha\left(L - z\right)\right]}{\sinh \alpha\ell}$$

(19)

$$N_2\left(z\right) = \frac{\sinh\left[\alpha\left(z - z_0\right)\right]}{\sinh \alpha\ell} \tag{20}$$

where $L = z_0 + \ell$ is total length of pile element (Fig. 1(a)). Either elastic or plastic soil portions, subscripts "1" and "2" always refer to upper and lower nodes, respectively.

Sixth International Conference on Geotechnique, Construction Materials and Environment, Bangkok, Thailand, Nov. 14-16, 2016, ISBN: 978-4-9905958-6-9 C3051

ARTIFICIAL SLUDGE BASED ON COMPOSITIONAL INFORMATION OF A NATURAL SEA SLUDGE

Hirosuke Hirano[1†], Takeshi Toyama[2], Nobuyuki Nishimiya[2], Davin H. E. Setiamarga [1,3], Shugo Morita[1], Yuto Uragaki[1], and Kyoichi Okamoto[2]

[1] National Institute of Technology, Wakayama College, Japan
[2] College of Science and Engineering, Nihon University, Japan
[3] Graduate School of Science, The University of Tokyo, Japan
†: Corresponding author

ABSTRACT

The chemical and physical properties of sludge collected from different aquatic areas differ from one another. Such differences have made the universal standardization of early settings difficult. Usage of artificial sludge with stable characteristics has been thus proposed in the present study. First, values of organic matter, sulfide content, and the inorganic content were measured for the sea sludge collected from Funabashi Port in Japan. Using the obtained chemical and physical properties as reference, we then produced artificial sludge by mixing dry yeast made from yeast cultured in liquid sodium sulfide nonahydrate solutions (3.5-4.0%) and zeolite for inorganic material. In the present study, we understood that we couldn't obtain the desired organic content for the artificial sludge, simply by adding the yeast with the amount similar to the organic content percentage we aimed. We thus calibrated the amount of yeast by measuring the actual organic content of several artificial sludge samples by thermo-gravimetry analysis. We found out that we need only to write a calibration curve of three measurements (zeolite-dry yeast w/w% = 0%, mid-point, and 83.3%) in order to obtain the information about the right amount of dry yeast addition to produce an artificial sludge with desired percentage of organic material. Finally, we mixed 31.4% of dry yeast (zeolite and other inorganic materials = 68.6%), in order to obtain an artificial sludge with 23.6% organic content. This percentage is similar to the organic content of the sludge collected from Funabashi Port.

Keywords: Artificial sludge, Zeolite, Dry yeast, Water area

1. INTRODUCTION

Sludge easily accumulates in closed water system, such as lakes, ponds, and bays. This problem occurs because such systems lack the ability of extensive water circulation. The accumulation of sludge might then cause problems because the anaerobic condition of the sludge might then cause decompositions by microorganisms. In order to solve this problem, it has conducted a study of cleaning sludge in closed water area by using aerobic microorganisms and micro bubbles [1]. In such studies, it is important to collect fresh sludge from water area every time, because the organic content of the sludge makes storage difficult. However, collecting fresh samples every time makes universal standardization of early settings difficult, because of differences in weather and environmental conditions such as temperature and humidity.

In order to overcome the difficulties of setting initial values, we propose the usage of artificial sludge with stable characteristics for such studies. An artificial sludge, with its early values set, will not be affected by even the subtle differences of environmental and weather changes, thus making standardization possible. However, producing an artificial sludge with characteristics mimicking those of the natural one is not easy, since many factors must be calculated in during the production process.

Here, we report our result of producing an artificial sludge useful for research requiring sludge with its early values constant. Moreover, we also achieved our aim of constantly reproducing the artificial sludge, with stable standard values and easy to reproduce.

2. ANALYSES OF NATURAL SLUDGE PROPERTIES

In order to produce an artificial sludge useful for studying the environment, we need the artificial sludge to mimic the characteristic and properties of the natural one. However, since natural sludge samples taken from different locations and times would show different starting values, it has needed to choose one sample to use as the point of reference. For this purpose, we decided to use the natural samples taken from Funabashi Port in Chiba, Northeast Japan, as the reference of the present study. This is because Funabashi Port is located close to our campus hence allowing multiple sampling trips easy and practical, and since it has been using the samples from the location in other studies (e.g. [2]).

Thus, in order to understand the natural properties of the sludge, in first studied material of natural sludge it has collected from Funabashi port in Chiba, northeast Japan.

2.1 Organic contents

We conducted thermo-gravimetry (TG) analysis in order to check the value of organic content. At temperatures above 100ºC, moisture content of the sampled material will boil away, while above 600ºC, the organic content of the material will completely evaporate, leaving only the inorganic part. Accordingly, in order to allow us to measure the pure value of the organic content, TG analyses were conducted between the values of 100ºC and 600ºC. The result of TG analyses on the natural sludge sample collected from Funabashi Port showed that the organic content is 23.6% (Fig. 1, solid line). For comparison, we also measured natural sludge samples collected from other the Hidaka-port in Wakayama in southwest Japan, where is located about >350 km in Funabashi port in southwest Japan. The Hidaka-port sludge has a 7.3% organic content (Fig. 1, dashed line).

2.2 Inorganic contents

In order to check the property of inorganic matter, we conducted energy dispersive X-ray spectrometry (EDX) on the samples. From EDX analyses, we found out that this sample has the mineral content of: silicon (Si), aluminum (Al), iron (Fe) and sulfur (S) (Table 1). X‐ray diffraction (XRD) analysis also showed that the Si content were silicon dioxide (SiO_2) and kyanite (Al_2SiO_5) (Fig. 2).

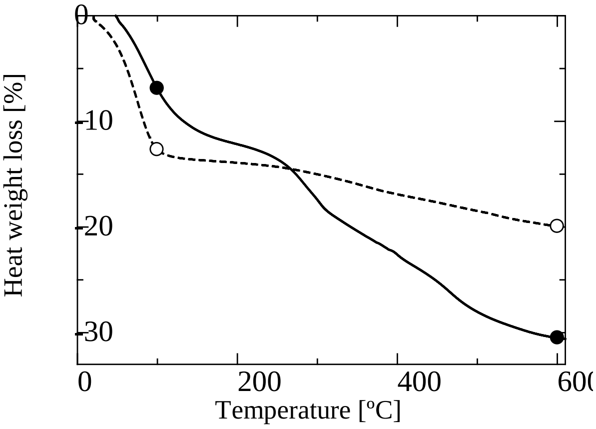

Fig. 1: Values of organic contents by TG
○: in Hidaka port, ●: in Funabashi port

2.3 Sulfide

We then used gas detector tube to check the value of hydrogen sulfide (H_2S). And about the value of H_2S by gas detector tube, it was tried like these conditions about sample water; by mixing 1 g of sludge and 100 cm3 of water. As a result, value was 0.016 g/1g, so concentration of S in sludge was 1.5% by molecular weight.

3. ARTIFICIAL SLUDGE PRODUCTION

3.1 Preliminary artificial sludge production

In order to obtain the data about the amount of materials needed to produce the final artificial sludge, we conducted a preliminary experiment of mixing materials to synthesize an artificial sludge. In this experiment, it has mixed dry yeast and aqueous solution of sodium sulfide nonahydrate ($Na_2S{\cdot}9H_2O$), which was 3.5 to 4.0 mass%, that ratio was 1 g of dry yeast to10 cm^3 of $Na_2S{\cdot}9H_2O$. After discarding the supernatant, we collected the "dry yeast mud", and mixed it with SiO_2 three times the amount of the yeast mud. It was measured this trial artificial sludge by TG and compared the value with Funabashi's sludge, but we were unable to mimic the organic content of the natural sludge, and thought that this was caused because the inorganic content (sulfur compounds, etc.) in the yeast mud was added to the total inorganic content of the preliminary artificial sludge, causing a decrease in the percentage of the organic content.

Table 1 Conditions of inorganic matter in sludge

Funabashi	Si [%]		Al [%]		Fe [%]		S [%]	
1st	46.41	47.9	20.02	20.6	19.20	21.3	14.37	10.3
2nd	46.47		19.70		22.19		11.64	
3rd	50.98		21.09		18.19		9.74	
4th	46.17		21.19		24.69		7.95	
5th	49.26		20.88		22.12		7.74	

Hidaka	Si [%]		Al [%]		Fe [%]		S [%]	
1st	65.84	65.7	23.69	23.5	7.01	7.4	3.47	3.4
2nd	68.54		23.04		6.40		2.02	
3rd	67.95		22.60		6.30		3.16	
4th	62.65		24.27		8.69		4.39	
5th	63.42		23.92		8.68		3.97	

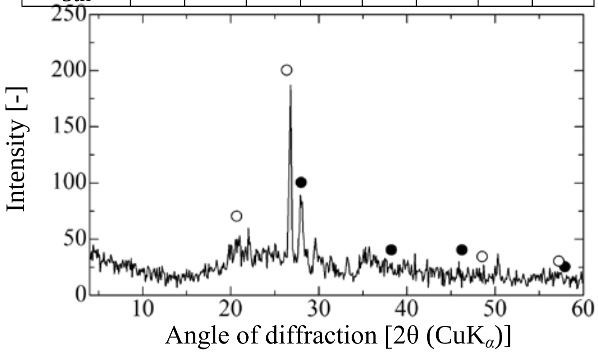

Fig. 2 Components in a typical sludge detected by XRD
○: SiO_2, ●: Al_2SiO_5

We tried varying compositions of organic contents (= yeast mud; 0%, 25%, 50%, 75%, and 100% of yeast mud, of the total SiO_2 yeast mud mix). The results are plotted on the calibration curves shown as Fig. 3 and Fig. 4. However, we still could not mimic the value of the organic content of Funabashi Port sludge when it has followed the values shown in the figures.

We then switched to use average of the values in the first order and quadratic, and were successful in obtaining an artificial sludge with the organic content of 23.8%, which was within 1.0% error. In second trial, it was successful to make 23.6% of organic matter in artificial sludge. Although reasons why we were able to reproduce the value of organic matter in artificial sludge by averaging the first order and quadratic values was still unknown, it was able to set the value of organic content in artificial sludge by any numerical values, if we use the average values of the callibration curve mentioned above.

We also found an interesting characteristic of the calibration curves in Fig. 5: calibration curves by approximation formula of first order and quadratic must intersect at 83.3%. It is unknown about this reason too. However, this information helps in drawing an easier calibration curve: rather than writing the intersection points at several standard points, it is able to use the calibration curves 0% and 83.3%, and the middle point.

3.2 Zeolite addition

After success on finding the right amount of organic matter addition as explained in the previous section, it was tried to use artificial sludge to reproduce previous studies about sea sludge, and see if the results of such studies were reproduced, when using artificial sludge. We chose trying to reproduce previous experiments about cesium ion (Cs^+) decontamination [3], and set the experimental conditions to be similar with that. For the study, it was added cesium nitrate ($CsNO_3$; 1000 ppm) to preliminary artificial sludge (dry yeast and SiO_2; totaling to 10 g). We prepare 5 samples of the mix, and then further added 20cm^3 of hydrogen peroxide solution (H_2O_2) with 5 types of concentrations, between from 0% to 34.5%.

In the present study, no decontamination effect was observable in artificial sludge like what we expected (Fig. 6: white dots = expected result, black dots = obtained result). This suggested that the artificial sludge could not adsorb Cs^+, and it was difficult to show the effect of decontamination reproducively as in the previous study [3], by the

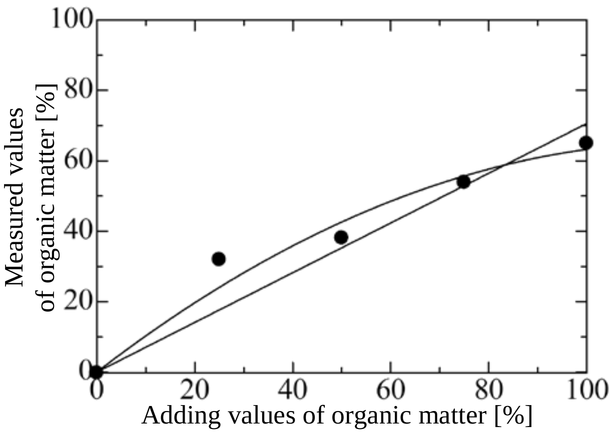

Fig. 3 Calibration curve in trial (1)

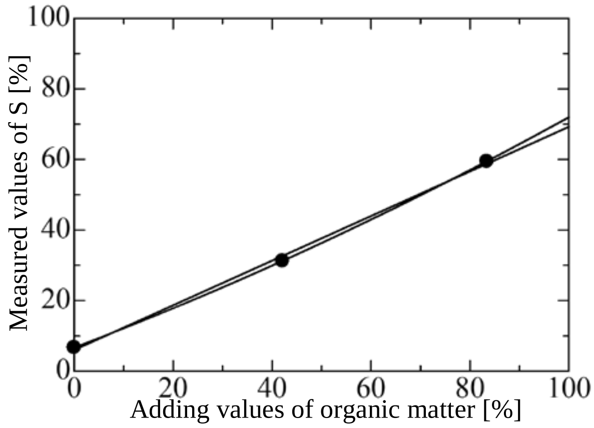

Fig. 5 Calibration curve in artificial sludge

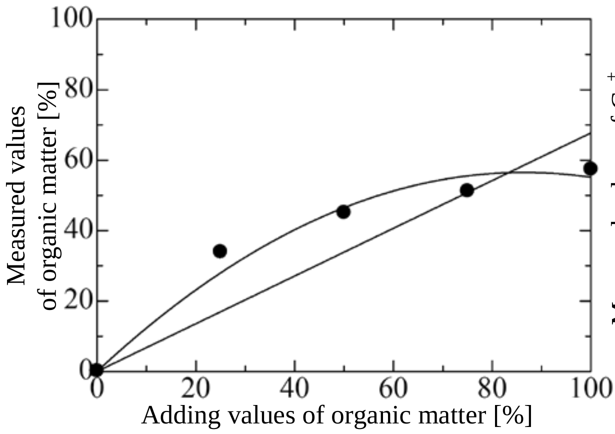

Fig. 4 Calibration curve in trial (2)

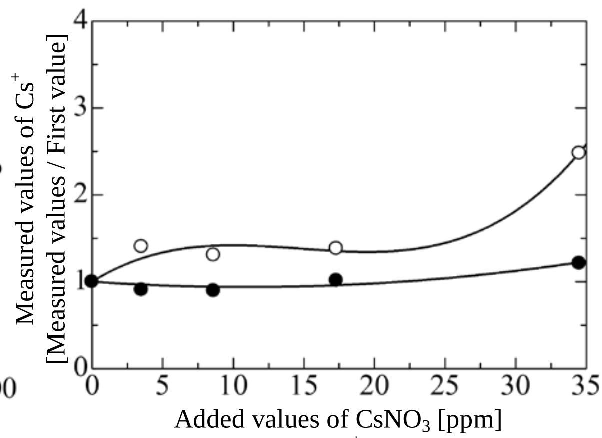

Fig. 6 Results of Cs^+ decontamination
○: Funabashi's sludge, ●: Artificial sludge by SiO_2

lack of as the sludge, or in other words, the absence of adsorbed Cs^+ in the first place.

Previous studies have shown that in sludge, the organic content has Cs^+ adsorption ability (e.g. [4] and [5]). However, our study here also suggests that besides the organic content, the inorganic content has a Cs^+ adsorption ability (Table 2) by [6], which was lacking in preliminary sludge.

Based on the result of XRD analysis, we added zeolite (vermiculite, kind of silicate mineral) to preliminary artificial sludge for the inorganic material, in order to add the Cs^+ adsorption ability of artificial sludge. Another reason of choosing zeolite as one of the inorganic content ingredients was because previous studies have shown that zeolite has the ability of Cs^+ adsorption (e.g. [6]), similar to the inorganic matter in natural sludge, which is also a Si compound (e.g. kyanite).

3.3 Final result

After succeeded in deciding the best composition of materials for artificial sludge through various trials and analyses, we synthesized final artificial sludge, and then analyzed its characteristics and values. We plot the results in another calibration curves as shown in Fig. 5. According to the new calibration curves, it was found that in order to reproduce Funabashi sludge, we found to need the addition of 28.8% organic materials to the total mixture. To test the accuracy of recipe based on new calibration curves, and made additional artificial sludge with various amount of organic material additions (27.1% and 27.7%). The resulting organic contents based on TG analyses were 23.2% and 22.6%, respectively. These values theoretically are less than 1% of error, when compared to the expected values (22.6% and 23.0%, respectively).

Table 2 Adsorption ability of zeolite

	First value of Cs^+ [ppm]	Captured [ppm/g]
Nothing to add	640.7	-
Zeolite (Large)	632.4	8.2
Sea sand	637.3	3.4
SiO_2	641.2	-0.5
Inorganic matter by sludge	621.4	19.3

		Values of Cs^+ (Before) [ppm]	Values of Cs^+ (After) [ppm]	Captured values by inorganic matter [ppm/g]
Inorganic matter in sludge（1 g）		640.5	588.9	51.6
Zeolite（1 g）	Large	647.5	617.7	29.8
	Small		607.8	39.6
	Powder		536.4	111.1
	Avarage	-	-	60.2

4. CONCLUDING REMARKS

4.1 An artificial sludge as a model system for environmental studies

In previous studies, we have analyzed the characteristics of sludge such as cesium adsorption [4] and [6], and cesium decontamination by [3]. We used the obtained data from such analyses as references when making artificial sludge.

In the present study, in order to obtain preliminary data to produce an artificial sludge with the characteristics mimicking those of the natural one, we initially studied material of natural sludge collected from Funabashi port. We also produced different preliminary artificial sludge, by trying various amount of compositions and materials. These preliminary data have allowed us to find the best composition and materials to utilize in order to produce artificial sludge.

We used dry yeast in order to recreate the organic content of artificial sludge, because it has similar ability of Cs^+ adsorption as the organic matter collected from the supernatant of a sludge suspension liquid (Fig. 3). Moreover, that will be like mud when added water. Also, a natural sludge obtains its organic content from biological sources such as carcasses of living organisms. Using dry yeast as the organic content source will mimic this condition. Dry yeast is also easy to obtain, making artificial sludge production easy.

We used SiO_2 and zeolite in artificial sludge for the inorganic material, basing on the result of XRD analysis. Moreover, previous studies have shown that zeolite has the ability of Cs^+ adsorption (e.g. [5]), similar to the inorganic matter in natural sludge, which is also a Si compound (e.g. kyanite).

EDX analyses showed that the organic content of a natural sludge also contain sulfur. In order to mimic such condition, it was added $Na_2S{\cdot}9H_2O$ to dry yeast. The amount of the added $Na_2S{\cdot}9H_2O$ was found to be 3.5 to 4.0 mass% in aqueous solution of $Na_2S{\cdot}9H_2O$ for the dry yeast culture (Fig. 7).

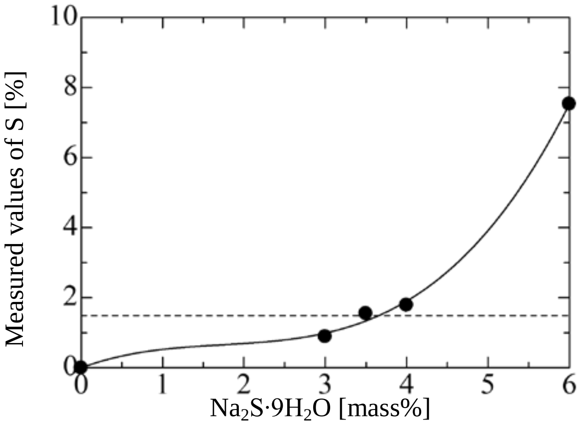

Fig. 7 The best value of adding $Na_2S{\cdot}9H_2O$

4.2 Future prospects

In the present study, we had tried to use artificial sludge for experiment of Cs^+ decontamination. Thus, we can safely say that artificial sludge can be beneficial for future experiments about Cs^+ decontamination.

About results with H_2O_2 addition to artificial sludge containing $CsNO_3$, Cs^+ was leached out by the H_2O_2 into the liquid phase. This has caused the measured values to differ from result by Fig. 6. But when we compared this result and a previous study using the natural sludge, our artificial sludge did not reproduce the study. By the way, natural sludge samples collected from Funabashi Port and Hidaka Port, showed similar values, suggesting that the decontamination ability of these natural sludge samples taken from two different areas could be similar [5].

Future studies would also include trying to reproduce the characteristics of the natural sludge taken from various locations with a variability of differing characteristics, conditions, and setting values. Such studies will allow for further testing of the robustness of our result reported here.

5. REFERENCES

[1] Hirano H, Nishimiya N, Kojima Y, Toyama T, Umegaki T, Hotta K, Okamoto K, "Purification experiments on sludge by micro–bubble and microorganisms activator – using detergent including enzyme as microorganisms activator –", Proceedings of the 23rd Ocean Engineering Symposium, 2012.

[2] Hirano H, Nishimiya N, Kojima Y, Toyama T, Umegaki T, Okamoto K, "Investigation of radioactive cesium decontamination from sea sludge using microbial activity", The International Symposium on Inorganic and Environmental Materials 2013, 2013.

[3] Hirano H, Toyama T, Nishimiya N, Okamoto K, "Removal of Cesium from Sea Sludge through Decomposition of Organic Matter with Aqueous Hydrogen Peroxide", International Journal of GEOMATE, Vol. 8, No. 1, 2015, pp. 1203-1206

[4] Uragaki Y, Morita S, Hirano H, "Ability of adsorbed cesium by organic matter from sea sludge, by Name of Presenter", 50th Annual Conference of Japan Society on Water Environment, 2016, pp. 622

[5] Nakao A, "Cesium Adsorption and Fixation on Soils", TREND IN THE SCIENCE, Vol. 17, No. 10, 2012, pp. 10_40-10_45

[6] Morita S, Uragaki Y, Hirano H, "Comparison of adsorbed ability for cesium, by inorganic matter and sea sludge", 50th Annual Conference of Japan Society on Water Environment, 2016, pp. 621

[7] Hirano H, Toyama T, Nishimiya N, "Preparation of prototype artificial sludge based on compositional information of sea sludge", 48th Annual Conference of Japan Society on Water Environment, 2014, pp. 298

Hirano H, Uragaki Y, Morita S, "Preparation of prototype artificial sludge based on compositional information of sea sludge Part 2: Improvement idea about contents", 50th Annual Conference of Japan Society on Water Environment, 2016, pp. 190

COLONIZATION AND MORPHOLOGICAL CHANGES OF A SEDGE RESTRICTING REGENERATION AFTER WIND DAMAGE IN A NATURAL FOREST IN KISO DISTRICT, CENTRAL JAPAN

Teruo Arase, Tetsuo Okano and Tetsuoh Shirota
Faculty of Agriculture, Shinshu University, Japan

ABSTRACT

Many old trees were blown down by typhoons in 1959 and 1961 in a natural coniferous forest deep in the mountains of Kiso District, Central Japan, and dense dwarf bamboo subsequently delayed the growth of tree seedlings. Forest engineers have tried to suppress dwarf bamboo to promote the regeneration of arboreal vegetation. However, after suppression of dwarf bamboo, an unknown grass unexpectedly colonized the area and replaced them. Afterward, almost no tree seedlings could be observed in the newly formed community, which seemed to worsen the extent of regeneration. It has been identified that the grass as *Carex oxyandra*, a native sedge species indigenous to Kiso District. Commonly, *Carex oxyandra* grows as short as about 10 cm like lawn grass, but it seems to have exceedingly enlarged the size in the community. Thus, investigation on the morphological variation of this sedge in Miure Experimental Forest within the Kiso National Forest was carried out. Leaf blade length, basal tiller length, and number of leaves per tiller were measured in upper and lower stands on three slopes in 2009. Results revealed that leaf blade length and basal tiller length in lower stands were approximately twice as large as those in upper stands on each slope, whereas the number of leaves per tiller was almost the same (8.8-9.4 leaves). Consequently, tussocks of this sedge became large in lower stands on a slope, which made the community overcrowded and damp, restricting tree regeneration.

Keywords: Natural Forest, Regeneration, Dwarf Bamboo, Carex oxyandra, Cilonization

INTRODUCTION

After weather damage in natural forests far from human habitats, natural regeneration of trees is expected, instead of requiring artificial introduction of vegetation by revegetation. If vegetation damage occurs in a natural forest where germination and establishment of tree seedlings is difficult for a long period, technology promoting the growth of spontaneous seedlings is needed.

Recently, revegetation technologies have been developed and applied especially to cut slopes and landslide slopes adjacent to human habitats. This involves construction of foundations for retaining the soil and introducing vegetation. It is important to monitor succession of vegetation after its introduction, since plants will grow or decline, and the species composition is altered by surrounding species year after year. As an example, it was reported that the process of vegetational succession on landslide slopes on Mikura-jima Island, where native tree and herb species were initially planted using simple terracing [1], [2]. In contrast, regeneration technology in natural forests has scarcely been studied in Japan.

In a natural coniferous forest deep in the mountains of Kiso District, Central Japan (Fig. 1), large Japanese cypress (*Chamaecyparis obtusa*) trees aged up to about 300 years are known by a famous timber brand, 'Kiso-Hinoki'. The trees have been selectively cut for use as high-quality timber, and the trees have naturally regenerated for several hundreds of years. However, many old trees including Japanese cypress were blown down by typhoons in 1959 and 1961. Subsequently, dwarf bamboo (*Sasa* sp.), the dominant species on the forest floor, remained dense on the land surface [3], [4].

Forest engineers and researchers have tried to promote the regeneration of arboreal vegetation. They deduced that the seedlings had not successfully established, and suggested that the dwarf bamboo should be suppressed. The growth of Japanese cypress seedlings requires a very limited environment: it demands a shaded habitat with a relative luminous intensity from 2 to 5%, and moderately humid soil. However, the relative luminous intensity reaches only 1 to 2% under a dense community of dwarf bamboo. In addition, the cool pluvial climate in this district (an average annual temperature of 7°C and an annual precipitation of 3500 mm at the meteorological station, which is at an elevation of 1300 m [4]) has caused formation of a wet podzol layer in the soil, which is too humid and nutritionally poor for the seedlings. Thus, after the wind damage from the typhoons, the dense community of dwarf bamboo prevented the growth of tree seedlings in this district,

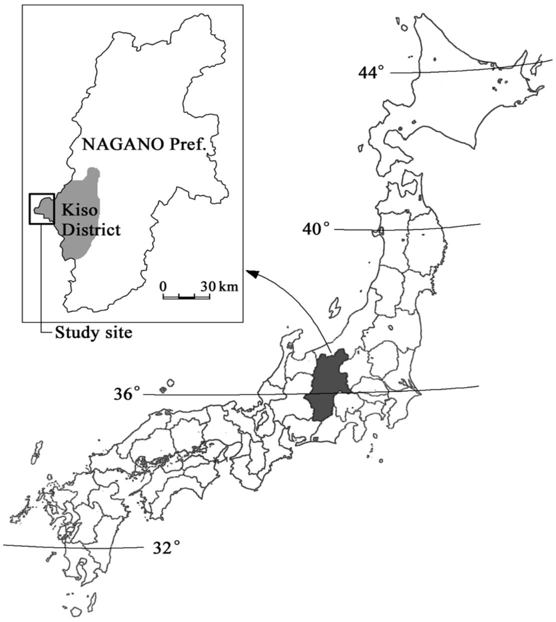

Fig. 1 Location of study site

Fig. 2 A case of colonizing *Carex oxyandra* (at forest compartment No. 2630) after withering of dwarf bamboo

especially in the higher elevation areas [3], [4].

In 1966, the Miure Experimental Forest of the Nagano Regional Forest Office was established to find a suitable regeneration method for forests in the wet podzolic zone, which appears in the peneplain area (at an elevation of about 1200 to 1500 m) on the southwest slope of Mt. Ontake in the Kiso District [4]. Many forest compartments (divided sections for forest managements or experiments) were established to examine various methods of regeneration involving the suppression of dwarf bamboo. In successful forest compartments, dwarf bamboo was suppressed by herbicide for several years, and the seeds of Japanese cypress germinated during this period and grew in moderate shade under the community of regenerating young dwarf bamboo.

However, in 2006, an unexpected phenomenon was observed in higher-elevation areas: an unknown grass began to colonize and replace the withered dwarf bamboo (Fig. 2). Afterward, few tree seedlings could be observed in the newly formed community, which seemed to reduce regeneration further.

Forest engineers at first suspected that the grass might be an invasive foreign species, but it has been identified as *Carex oxyandra*, a native sedge species indigenous to Kiso District. Commonly, *Carex oxyandra* grows as tussocks as short as about 10 cm like lawn grass, but it seems to have exceedingly enlarged the size in the community. *Carex oxyandra* is reported to remain at the forest floor as a low-preference foliage by sika deer [5], and to colonize bare ground after mining as a pioneer plant [6], but cases of colonizing in a forest or grassland where vegetation has already developed were previously unknown.

In the present study, the investigation of the morphological variation of *Carex oxyandra* in the Miure Experimental Forest within Kiso National Forest was carried out to identify the replacement dwarf bamboo by this sedge.

METHODS

The study site was located in Miure Experimental Forest, in the center of the mountain in Kiso District, at an elevation from 1400 to 1500 m.

In October 2009, we observed communities of *Carex oxyandra* on three slopes (forest compartments No. 2626, 2627 and 2630), and selected both upper and middle stands on each slope. Leaf blade length, basal tiller length (reddish-purple part near the base) and number of leaf blades per tiller were measured for five individuals per strand. The environmental conditions were as follows:

(a) Stands in No. 2626 were located at an elevation from 1400 to 1420 m, with a slope direction of 0° and an inclination of 27°. Dwarf bamboo were withered (dry culms remained), and the community of the sedge was observed on bare ground.

(b) Stands in No. 2627 were located at an elevation from 1500 to 1520 m, with a slope direction of 260° and an inclination of 30°. Communities were observed where dwarf bamboo dominated and where sedge dominated.

(c) Stands in No. 2627 were located at an elevation from 1480 to 1500 m, with a slope direction of 220° and an inclination of 20°. Dwarf bamboo was rarely observed, and the sedge constituted the largest community.

In each stand, arboreal vegetation (comprised of Japanese cypress and some broad-leaved deciduous trees) was sparse, and plants with sizes common for *Carex oxyandra* were observed in the area near the ridge above the upper stand. The difference in elevation between upper and middle stands on each slope was approximately 10 m.

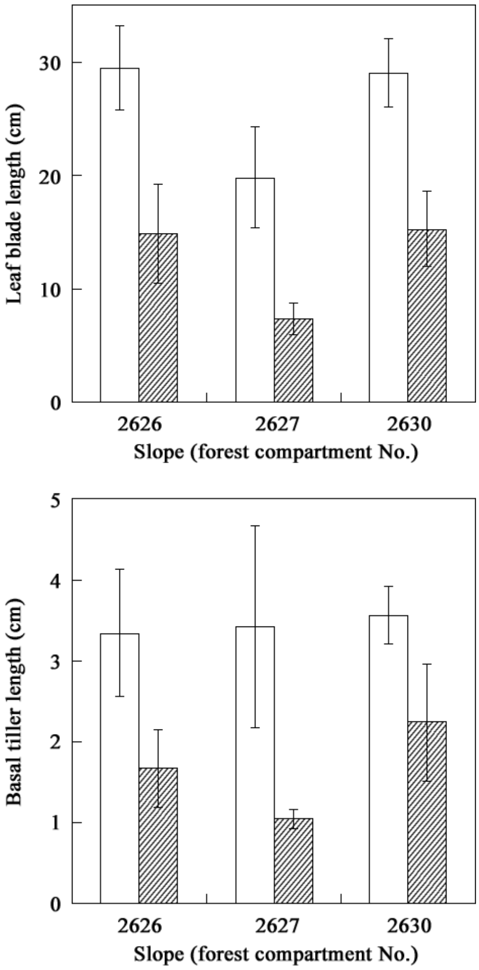

Fig. 3 The leaf blade length and basal tiller length of *Carex oxyandra* in each stand. Solid columns (left) and hatched columns (right) show the middle stand and the upper stand on the slope, respectively. The bar on the top of each column indicates ±1 SD.

RESULTS

Fig. 3 shows the leaf blade length and basal tiller length in each stand. The average leaf blade length was 7 to 15 cm in upper stands, whereas it was 20 to 30 cm in middle stands. The maximum length was 36.0 cm (in the middle stand of No. 2626 slope). Analysis of variance detected a significant difference based on location on a slope (F-test, $p<0.01$). A significant difference based on specific slope was also detected (F-test, $p<0.05$), since the lengths were smaller on No. 2627 slope than the others.

Average basal tiller length was 1.0 to 2.2 cm in upper stands, whereas it was 3.3 to 3.6 cm in middle stands (Fig. 4). The maximum length was 5.2 cm (in the middle stand of No. 2627 slope). Analysis of variance detected a significant difference based on location on a slope (F-test, $p<0.01$). However, no significant differences based on specific slopes were detected (F-test).

Fig. 4 Herbarium specimens of *Carex oxyandra* collected on the slope No. 2630 (left: middle stand; right: upper stand). The black scales in the figure are 16 cm.

In contrast, the number of leaf blades per tiller proved relatively stable among stands; the average was 8.2 to 9.0 in upper stands, and 8.8 to 9.4 in middle stands. No significant differences were detected based on either location on a slope or on specific slopes (F-test). In Fig. 4, we present images of actual samples of the sedge on the same slope (No. 2630) that were obviously different from each other: the number of leaves per tiller did not seem to differ, but the leaf blade length and basal tiller length in the middle stand were twice as large as in the upper stand.

DISCUSSION

At the study site, the native sedge *Carex oxyandra* proved to change the above-ground morphology drastically. Between communities close to each other on the same slope, leaf blade length and basal tiller length in middle stands were twice as large as in upper stands (Figs. 3 and 4). In addition, the number of leaf blades per tiller was relatively stable independent of the location on a slope, meaning the sedge community was dense in the middle stands.

For *Carex oxyandra*, the upper and middle stands in each slope were not considered to be genetically remote, since the distance between them was relatively close. The morphological changes in this sedge were presumably the result of adaptation to growth environments, such as soil moisture and air temperature. For example, water stress and high temperature are reported to influence leaf morphology in some grasses [7] and trees [8]. If excessive soil moisture favors large tillers and leaf blades of *Carex oxyandra*, the above-ground environment would also become wetter, which impedes the establishment of Japanese cypress

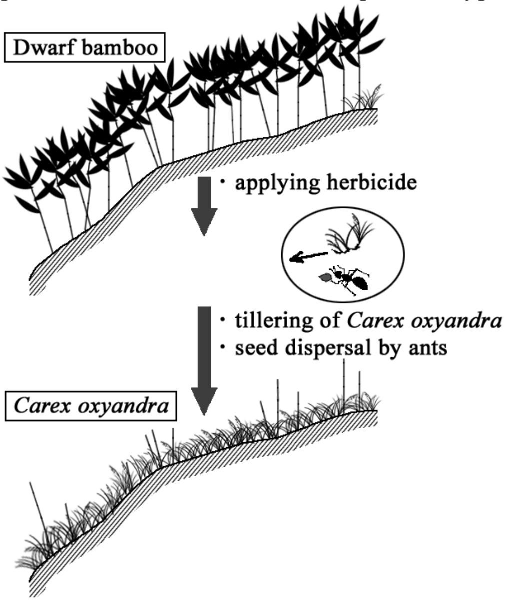

Fig. 5 Schematic depiction of the presumed process of *Carex oxyandra* colonization after withering of dwarf bamboo

seedlings. Therefore, a method to suppress this sedge is needed for the regeneration of Japanese cypress at the study site.

Finally, we try to explain why *Carex oxyandra* replaced dwarf bamboo. There are two means of expansion, vegetative reproduction (clonal growth) and seed dispersal. From the viewpoint of vegetative reproduction, tillering from the base is one means, since this sedge produces many tillers.
However, the sedge is able to expand only incrementally outward merely by clonal growth. From the other viewpoint of seed dispersal, it has been reported that *Carex oxyandra* seeds are dispersed by ants: an elaiosome is attached to the seed surface, and ants take the seeds to their nest and bite off only the elaiosome [9]. Consequently, we suggest a process for colonizing by *Carex oxyandra* in Fig. 5. How long the dominance of the sedge lasts or whether dwarf bamboo can recover in the sedge-dominated community are worth investigating in terms of the regeneration of the forest.

REFERENCES

[1] Arase, T. and Okano, T., "Influence of fertilization on native plants and exotic pasture grasses on the fascined landslide slopes in Mikura-jima Island, Japan", International Journal of GEOMATE, Vol. 8 (2) 2015, pp. 1316-1322

[2] Okano, T. and Arase, T., "Vegetation recovery process on landslide steep slope after *Alnus sieboldiana* and *Miscanthus condensatus* planting with simple terracing work in Mikura-jima Island, Japan", International Journal of GEOMATE, Vol. 10 (3) 2016, pp. 1884-1890

[3] Akai, T. and Asada, S., "Studies on Natural Regeneration (I) The reproduction of *Chamaecyparis* at wet podozolic zone in Kiso District", Bulletin of the Kyoto University Forests, Vol. 39, 1967, pp. 35-63. (in Japanese with English Résumé)

[4] Akai, T., "Studies on Natural Regeneration (II) The regeneration of *Chamaecyparios obtusa* at Miure Experimental Forest in Kiso District", Bulletin of the Kyoto University Forests, Vol. 44, 1972, pp. 68-87. (in Japanese with English Résumé)

[5] Yoshikawa, M., Imafuku, H. and Hoshino, Y., "Distribution of forest floor vegetation after the disappearing of dwarf bamboo in the senjugahara area, Oku-Nikko", Journal of the Japanese society of Revegetation Technology, Vol. 39, 2014, pp. 368-373 (in Japanese with English abstruct)

[6] Tsujimura, A., "The ecology of *Carex oxyandra* II. The behavior of seedling and tillers", Ecological Research, Vol. 2 (3), 1987, pp. 279-288.

[7] Yoshikawa, K. and Wang, L.H., "Effects of water stress on leaf developments of several tree species", Journal of the Japanese Society of Revegetation Technology, Vol 16 (4), 1991, pp. 18-30 (in Japanese with English summary)

[8] Sasaki, O., "Effect of high water temperature on the morphology of crown roots and leaf in rice plants", Japanese Journal of Crop Science, Vol. 61 (3), 1992, pp. 388-393 (in Japanese with English abstruct)

[9] Tanaka, K., Yamawo, A. and Yano, O., "Seed dispersal by Ants in *Carex oxyandra* var. *oxyandra* (Cyperaceae) from Japan", The Journal of Japanese Botany, Vol. 90(2), 2015, pp.129-133

METHODS OF SUPPRESSING COLONIZING SEDGE TO HELP TO ESTABLISH TREE SEEDLINGS IN A NATURAL FOREST IN KISO DISTRICT, CENTRAL JAPAN

Teruo Arase, Tetsuo Okano and Tetsuoh Shirota
Faculty of Agriculture, Shinshu University, Japan

ABSTRACT

Dense bamboo grasses have delayed the growth of tree seedlings after the wind damage in a natural coniferous forest in deep mountains of Kiso District, Central Japan. After suppression treatment of the bamboo grass, a native sedge *Carex oxyandra* replaced them and made the growth of tree seedlings worse. The technique to suppress colonized *Carex oxyandra* is unknown, since this sedge has not ever been a harmful weed to be controlled. Thus, we established first experimental plots for suppressing *Carex oxyandra* by a herbicide, glyphosate potassium salt solution (Roundup Max load) by normal levels of dilution (control without herbicide, diluted to ×25, ×50 and ×100 volume with water) in May 2010. Next experimental plots with above-normal levels (diluted to ×100, ×200, ×400, ×800, ×1600 and ×3200) were established in June 2011. Coverage percentage, plant height of *Carex oxyandra* and tree seedlings were measured in each plot in autumn up to 2015. As a result, coverage and plant height of *Carex oxyandra* decreased obviously after a half year in all dilution levels, and the suppressing effect continued during 2 years in the lower dilution from ×25 to ×400. However, withered leaves formed a carpet-like thick mat, which remained several years and was suspected to restrict the germination and growth of tree seedlings. Consequently, the herbicide proved out effective to the sedge for 2 years, but some additional treatment is needed to secure the foundation space for tree seedlings within the mat of withered leaves.

Keywords: Carex oxyandra, herbicide, Japanese cypress, seedling, natural forest

INTRODUCTION

In a natural coniferous forest deep in the mountains of Kiso District, central Japan, many old trees including Japanese cypress (*Chamaecyparis obtusa*, known as the famous timber brand 'Kiso-Hinoki') were blown down by typhoons in 1959 and 1961. Subsequently, dwarf bamboo (*Sasa* sp.), the dominant species in the forest floor, remained dense on the land surface. In addition, the wet podzolic soil formed by the cool pluvial climate in this district (an average annual temperature of 7°C and an annual precipitation of 3500 mm at the closest meteorological station at an elevation of 1300 m) was too humid and nutritionally poor for seedling establishment. Thus, after the wind damage due to the typhoons, the regeneration of trees in this district, especially in the higher-elevation areas, was prevented [1], [2].

In forestry of afforested land, suppressing forest-floor vegetation (dwarf bamboo or other shrubs in Japan) is important [3]. Weeds influence planted trees by interception of light and capture of nutrients and water [3]. In dwarf bamboo, suppression of the community is reported to enhance the species diversity of forest floor vegetation and the density of regenerated trees [4]. If the dwarf bamboo community falls under snow cover, it acts as a sliding surface and induces gliding of the snow cover and avalanches [5]. On the other hand, the dwarf bamboo community plays a significant role in retention of basic cations in the surface soil and prevention of soil acidification [6].

There are several methods for suppressing dwarf bamboo, such as weeding, application of herbicide, and grazing by herbivorous livestock [7]. Application of herbicide, i.e., chemical control, has been preferred because its effects last a long time.
Forest engineers and researchers have suppressed dwarf bamboo by herbicide application since 1967 in Miure Experimental Forest in the Kiso District to promote regeneration of the forest. However, unexpected colonization by *Carex oxyandra*, a native sedge indigenous to this area, was found after the withering of dwarf bamboo following herbicide treatment in higher-elevation areas in 2006. Afterward, almost no tree seedlings could be observed in the newly formed community, which seemed to indicate even poorer regeneration [8].

It has been reported that exposure to light improves germination of Japanese cypress seeds, with a typical germination percentage from 10 to 40%, which varies according to area and year [9]. However, the growth of seedlings requires a shaded habitat with a relative luminous intensity from 2 to 5% (germination is suspected to be impaired at a relative luminous intensity over 10%) [1], [2]. Japanese cypress seeds are reported to lose germination ability after 1 year in field conditions [9], and some seeds suffer predation by animals [10]. Therefore, the seeds must germinate rapidly in the absence of covering vegetation, and then the seedlings need to be shaded by recovered vegetation. The effect of herbicide suppressing dwarf bamboo is estimated to last about 3 years based on remote sensing [7], which is reasonable for the regeneration of Japanese cypress trees: seeds can germinate in a bright environment and then the seedlings can grow while shaded by recovered dwarf bamboo.

However, no method is yet known to suppress *Carex oxyandra*, because harmful colonizing by this sedge is uncommon. Considering the cost and labor for forest management, it is reasonable to employ a method similar to that of suppressing dwarf bamboo as a first approach.

In the present study, we examined the effect of herbicide at various dilution levels on suppressing the community of *Carex oxyandra* in the Miure Experimental Forest within the Kiso National Forest. The influence of suppressing the sedge on the establishment of Japanese cypress seedlings is also discussed.

Fig. 1 Suppression of *Carex oxyandra* community by herbicide. Top: inside (left) and outside the zone of herbicide application (right). Bottom: carpetlike thick mat of withered leaves. Both photographed in fall 2010, half a year after herbicide application.

METHODS

Study Site

The study site was located in forest compartment No. 2630 in the Miure Experimental Forest, the deepest area in the Kiso District, at an elevation of 1500 m. At the site, most of the dwarf bamboo had already withered or disappeared, and the sedge formed a large-scale community on an almost level land surface (slightly inclined to the north).

Experiment 1: Herbicide at Normal Levels of Dilution

In May 2010, we applied a generally circulated herbicide, glyphosate potassium salt solution (brand name: Roundup Max load), to the sedge community at four levels of dilution (control without herbicide, and herbicide diluted with water to ×25, ×50 and ×100 by volume).

For each of the four treatments, an application zone of 15 m^2 (3 m ×5 m) involving three fixed-survey 1-m^2 plots (1 m × 1 m) were designed, and two blocks were established. The experimental design was a randomized block method with one-way layout (4 dilution levels ×2 blocks = 8 application zones).

After application of herbicide, seeds of Japanese cypress were sown that had been harvested from surrounding trees in 2009. Sowing density was 6,000 seeds per zone (i.e., 400 seeds per m^2).

Coverage percentage and height of *Carex oxyandra* were measured yearly in fall (from mid-October to early November), from 2010 to 2015. In measuring the plant height, we measured 5 plants per plot randomly (or all plants if the number of surviving plants was less than 5) and averaged the values. We also observed and measured the thickness of the carpet-like mat of withered leaves that formed after the application of herbicide (Fig. 1). On the same day, the number of seedlings and height of each Japanese cypress seedling were measured.

Experiment 2: Herbicide at Above-normal Levels of Dilution

In June 2011, we applied the same herbicide to the sedge community at six more dilute levels (diluted with water at ×100, ×200, ×400, ×800, ×1600 and ×3200 by volume).

For each of the six levels, an application zone of 4 m^2 (2 m ×2 m) was established. Only one plot was established for each level, because we intended this experiment as a preliminary one to determine whether above-normal levels of dilution (i.e. lower concentrations of herbicide) would be effective. The plots were established in a community of *Carex oxyandra* near the experimental zones treated at normal dilution levels; the elevation, inclination and landform were similar to them.

Coverage percentage and height of *Carex oxyandra* were measured yearly in fall (from mid-October to early November), from 2010 to 2015.

RESULTS

Experiment 1: Herbicide at Normal Levels of Dilution

Changes in *Carex oxyandra* growth after treatment are shown in Fig. 2. In fall 2010, the coverage percentage of the sedge decreased to less than 5%, and plant height also decreased by over 10 cm at dilution levels of ×25, ×50 and ×100. The differences from the control in coverage percentage and plant height were significant in fall 2010 and 2011 (Dunnett's test, $p<0.05$). However, after 2012, the sedge recovered and the differences from control

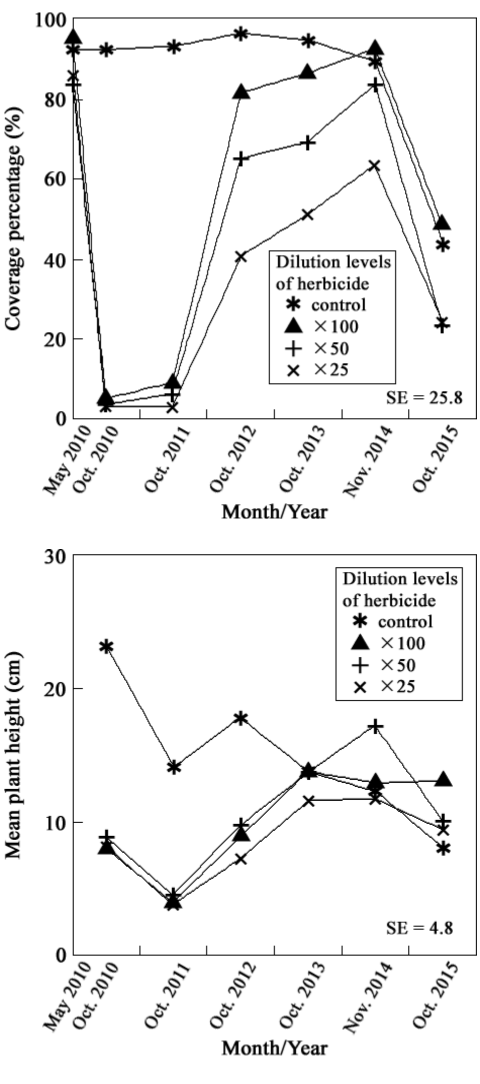

Fig. 2 Changes in *Carex oxyandra* growth after applying herbicide at normal levels of dilution

became more obscure year by year, and in 2015 reached 60 to 90% of control coverage, and the height of plants reached 11 to 17 cm. However, the extent of sedge coverage had unexpectedly declined on a massive scale in all plots, involving even the control, in 2015.

Table 1 demonstrates the growth of Japanese cypress seedlings in the experimental plots. In control plots, no seedlings were observed till 2015. In other plots, the lower the concentration of herbicide, the more germinated seedlings were found in fall 2010 (from 7.4 to 22.2 individuals per m^2). However, in 2011, the number of seedlings decreased markedly in each plot (to 1.5 to 3.2 individuals per m^2). In 2012, the number of seedlings also decreased (to 1.0 to 1.9 individuals per m^2), whereas the plants generally increased by approximately 2 cm in height. A gradual decrease in number of individuals and plant height occurred subsequently. Finally, in 2015, seedlings survived only in the plot treated at an herbicide dilution level of ×100 (0.4 individuals per m^2), in which some seedlings elongated by over 10 cm in height.

The thickness of the mat of withered *Carex oxyandra* leaves was 1.5-2.5 cm in each stand in fall 2010 (Fig. 1), half a year after herbicide application

Table 1 Mean number of Japanese cypress seedlings per m^2 after applying herbicide at normal levels of dilution to a *Carex oxyandra* community. Sowing density of Japanese cypress seeds was 400 seeds per m^2.

Levels	Year	Ranks of plant height (cm)						Total
		0-	2-	4-	6-	8-	10-	
control	2010							0.0
	2011							0.0
	2012							0.0
	2013							0.0
	2014							0.0
	2015							0.0
×100	2010	8.0	13.8	0.3				22.2
	2011		2.2	0.8	0.3			3.2
	2012	0.2	0.3	0.3	0.2	0.2	0.2	1.3
	2013		0.2					0.2
	2014			0.2	0.2	0.3		0.7
	2015			0.2				0.2
×50	2010	5.3	7.8					13.2
	2011		1.2	0.7	0.2	0.2		3.2
	2012		0.7	0.2	0.8	0.2		1.8
	2013			0.3			0.2	0.5
	2014				0.2			0.2
	2015							0.0
×25	2010	2.0	5.2	0.2				7.3
	2011	0.5	0.8	0.2				1.5
	2012		0.3	0.5	0.2			1.2
	2013			0.2				0.2
	2014							0.0
	2015							0.0

at dilutions of ×25, ×50 and ×100. The thickness decreased to 0.5-1.0 cm in 2011, 0.3-1.0 cm in 2012, and 0-0.5 cm in 2013. In 2014, the mat seemed to have decomposed and had disappeared from all stands.

Experiment 2:
Herbicide at Above-normal Levels of Dilution

Changes in *Carex oxyandra* growth after herbicide treatment are shown in Fig. 3. In fall 2011, the coverage percentage of the sedge drastically decreased to less than 5% even in the plot at the highest dilution of ×3200. The coverage percentage slightly increased in 2012 in the plot treated at lower levels of concentration, and obviously recovered in general in 2013 (25 to 90%) and 2014 (50 to 90%). However, the coverage percentage suddenly decreased in 2015 (to 1 to 50%) due to unknown causes. The coverage percentage was significantly and negatively correlated with the level of dilution of herbicide in 2012 (Spearman's rank correlation, r_s =-0.83, p<0.05), but no significant correlation was detected in 2013.

In contrast, plant height showed a complicated fluctuating pattern. During 2011 and 2012, it slightly increased or leveled off in the plots treated at ×100, ×200 and ×400, but decreased or leveled off in the plots at ×800, ×1600 and ×3200. The plant height increased in all plots during 2012 and 2013, but showed diverse changes in 2014. In 2015, the plant height had also unexpectedly declined on a massive scale in most plots. Plant height was significantly and negatively correlated with the level of dilution of herbicide in 2013 (Spearman's rank correlation, r_s =-0.93, p<0.05), but no significant correlation was detected in 2014.

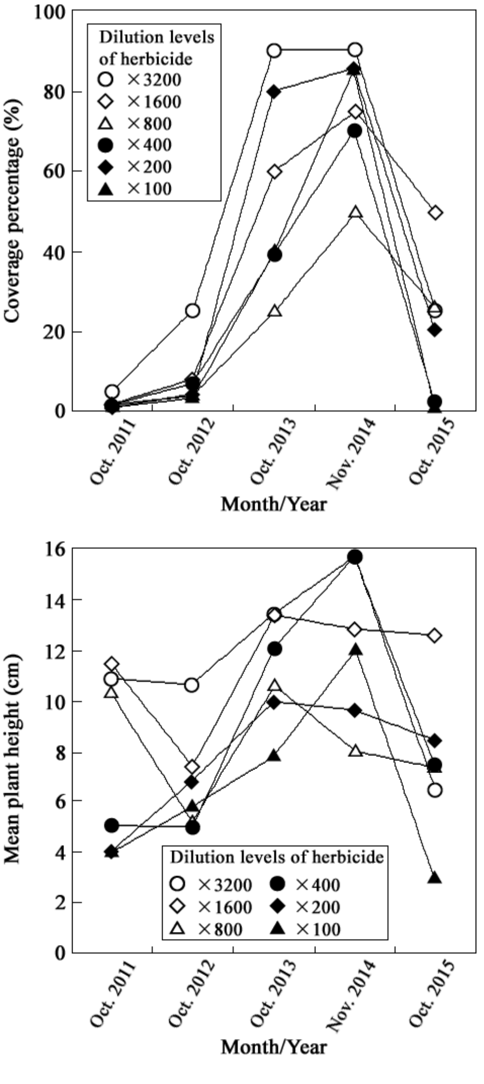

Fig. 3 Changes in *Carex oxyandra* growth after applying herbicide at above-normal levels of dilution

DISCUSSION

Suppression of *Carex oxyandra*

In experiment 1, herbicide diluted to normal levels suppressed communities of *Carex oxyandra* in fall 2010 and 2011, i.e., for 2 years after treatment. After 3 years, the sedge steadily recovered and recolonized the area (Fig. 2).

Also in experiment 2, herbicide diluted to above-normal levels suppressed communities of the sedge in fall 2011 and for the whole of 2012, i.e., for 2 years after treatment. After 3 years, the sedge steadily recovered and recolonized the area (Fig. 3).

In both experiments 1 and 2, the plant height was significantly decreased by the herbicide for a limited period. However, the plant height seemed to fluctuate, which is probably attributable to the averaging process used in the study: if some slightly damaged large plant survived among small plants that regenerated after withering, the average plant height would be a middle value between them.

In a similar case of herbicide application to sedge in a natural field, it has been reported that *Carex kobomugi*, an invasive foreign species in coastal dunes, was reduced but not eliminated after repeated herbicide (Roundup) application [11]. In comparison, *Carex oxyandra* was suppressed for approximately two years by herbicide treatment, so careful choice of herbicide and examination of its effectiveness are needed according to the target plant species.

However, the reason for the sudden decrease in *Carex oxyandra* in 2015, which simultaneously occurred in both experiments 1 and 2, was not explainable in the present study. It might have been caused by some extraordinary meteorological event, such as an extremely heavy snow or a long period of when snow remained that is unusual in this area, because this sedge is an evergreen species. It might also have been caused by the innate life span of the community: some sedge species have been reported to decline spontaneously after forming dominant communities, without any treatment to suppress them [12]. Monitoring *Carex oxyandra* communities is also desirable, since it not known whether the community is transient or more permanent.

Establishment of Japanese Cypress Seedlings

Seedlings of Japanese cypress were not successfully established after herbicide treatment of *Carex oxyandra* communities. At the early stage of establishment, neither germination of seeds nor survival for half a year past germination were satisfactory. Half a year after sowing 400 seeds per m^2, at most 22.2 individuals per m^2 (5.6%) could be counted in fall 2010 (Table 1). This percentage is inferior to the commonly expected germination percentage (from 10 to 40%) of Japanese cypress seeds [9].

One of the causes of inferior establishment is considered to be the thick mat of withered sedge leaves, which occupied the soil surface for about 3 years in the present study. Removing such a thick obstacle that interferes with root elongation into the soil is critical. Japanese cypress seeds are viable for a short period [9], so they cannot survive until the mat decomposes. It is probable that more seeds had germinated initially, but most died and had disappeared before our survey, which also shows the severity of the growth environment. A gradual decrease in the number of individuals and elongation in height after 2011 indicates a phenomenon like self-thinning, which could be caused by an inferior environment in the area of the withered sedge, rather than by competition among Japanese cypress seedlings. Therefore, withering of a *Carex oxyandra* community is insufficient to promote the establishment of seedlings.

Considering the inferior early growth of the tree seedlings, some additional treatment is needed to improve the growth environment. The most characteristic *Carex oxyandra* community after herbicide treatment is a thick, carpet-like mat of withered leaves. It has been reported that soil disturbance plays an important role in increasing the survival rate of viable seeds of Japanese cypress [10], and soil scarification to remove dwarf bamboo is effective in promoting regeneration of a forest (though the effect depends on the physiochemical features of the soil) [13].

CONCLUSIONS

In the present study, the effect of herbicide was examined at various dilution levels on suppressing the community of *Carex oxyandra* in the Miure Experimental Forest within the Kiso National Forest. Coverage and plant height of *Carex oxyandra* decreased obviously after a half year in all dilution levels, and the suppressing effect continued during 2 years in the lower dilution from ×25 to ×400. However, the influence of suppressing the sedge on the establishment of Japanese cypress seedlings is also confirmed: withered leaves formed a carpet-like thick mat, which remained several years and was suspected to restrict the germination and growth of tree seedlings.

Our results suggest this method to promote the establishment of trees if an established community of *Carex oxyandra* can be suppressed:

(a) Scratching treatment (to breaking up mats) should be done after the community of *Carex oxyandra* has been suppressed. Based on our observations, a small cutting tool like a hand dredge or sickle is sufficient to break up or remove the mat. Though the mat is thick just after withering (maximum thickness was 2.5 cm in the present study), it is not so hard as to be difficult to break, unlike dwarf bamboo.

(b) If the establishment of tree seedlings is not sufficient, herbicide should be reapplied to prevent the sedge from recolonizing.

REFERENCES

[1] Akai, T. and Asada, S., "Studies on Natural Regeneration (I) The reproduction of *Chamaecyparis* at wet podozolic zone in Kiso District", Bulletin of the Kyoto University Forests, Vol. 39, 1967, pp. 35-63. (in Japanese with English Résumé)

[2] Akai, T., "Studies on Natural Regeneration (II) the regeneration of *Chamaecyparis obtusa* at Miure Experimental Forest in Kiso District", Bulletin of the Kyoto University Forests, Vol. 44, 1972, pp. 68-87. (in Japanese with English Résumé)

[3] Suzaki, T., "Study on herbicidal use in silviculture", Bulletin of the Kyushu University Forest, 42, 1968, pp. 99-233 (in Japanese with English Résumé)

[4] Hasegawa, M., "Effect of different regeneration methods on species composition and sapling density of regenerated forests within clear-cut areas in a heavy snow region", Japanese Journal of Forest Environment, Vol. 47 (1), 2005, pp. 9-20 (in Japanese with English summary)

[5] Aiura, H., "Erosive phenomenon in heavy snow mountainous regions in Japan", Journal of Forest Research, Vol. 7 (2), 2002, pp. 57-66 (in Japanese with English summary)

[6] Takamatsu, T., Kohno, T., Ishida, K., Sase, H., Yoshida, T. and Morishita, T., "Role of the dwarf bamboo (Sasa) community in retaining basic cations in soil and preventing soil

acidification in mountainous areas of Japan", Plant and Soil, Vol. 192, 1997, pp. 167-179

[7] Morisawa, T., Sugita, H., Hashimoto, R. and Akai, T., "Natural regeneration of *Chamaecyparis obtusa* for 36 years by Strip logging in relation to dwarf bamboo elimination, examined by aerial photographs in Kiso", Journal of the Japanese Forestry Society, Vol. 92, 2010, pp. 22-28 (in Japanese with English summary)

[8] Arase, T., Okano, T. and Shirota, T., "Colonization and morphological changes of a sedge restricting the regeneration after wind damage In a natural forest in Kiso District, central Japan", Sixth International Conference on Geotechnique, Construction Materials and Environment, Bangkok, Thailand, Nov. 2016 (under submission)

[9] Nakayama, K., Seed germination of useful plants. Tokyo: Uchida Rokakuho Publishing Co. Ltd., 1966, pp.282-285 (in Japanese)

[10] Yamamoto, S. and Tsutsumi, T., "The population dynamics of naturally regenerated hinoki seedlings in artificial hinoki stands (III) Dynamics of the seed population on the forest floor", Journal of the Japanese Forestry Society, vol. 66 (12), 1984, pp. 483-490 (in Japanese with English summary)

[11] Wootton, L.S., Halsey, S.D., Bevaart, K., McGough, A., Ondreicka, J. and Patel, P., "When invasive species have benefits as well as costs: managing *Carex kobomugi* (Asiatic sand sedge) in New Jersey's coastal dunes", Biological Invasions, Vol. 7, 2005, pp. 1017-1027

[12] Arase, T. and Uchida, T., "Growth and persistency of five terrestrial sedge species on a cutting slope", Journal of the Japanese Society of Revegetation Technology, Vol. 35 (1), 2009, pp. 119-122 (in Japanese)

[13] Yamada, K., "Growth of secondary forests on serpentine soil after different soil disturbance intensity", Journal of the Japanese Forestry Society, Vol. 81 (4), 1999, pp. 291-297 (in Japanese with English summary)

DYNAMICS OF EXOTIC GRASS COVER PLANTS ON SLOPES

Taizo Uchida[1], Jun Tanaka[2], Kentaro Kondo[3], Daisuke Hayasaka[4], Yuki Tomoguchi[3], Teruo Arase[5] and Tetsuo Okano[5]

[1]Faculty of Engineering, Kyushu Sangyo University, Japan; [2]Conservation Engineers Co., Ltd., Japan; [3]Graduate School of Engineering, Kyushu Sangyo University, Japan; [4]Faculty of Agriculture, Kindai University, Japan; [5]Faculty of Agriculture, Shinshu University, Japan

ABSTRACT

Alien species in the family Poaceae play an important role as cover plants for erosion control on slopes, particularly in Japan. However, concerns have arisen regarding the adverse effects of these species on the local ecosystem and biodiversity. This study examined the succession and seed propagation of alien Poaceae that are used for erosion control on the cut slopes of Sakurajima volcano in southeastern Japan. Although the alien species used as cover plants were dominant for 2-3 years following their introduction to the slopes, they were displaced entirely by native species after 6 years, which is considerably faster than ordinary succession on other volcanoes. In addition, heading (flowering) of alien species were rarely observed. It is considered that the observed results were caused by the oligotrophic conditions that resulted from the bioengineering techniques that were employed on Sakurajima.

Keywords: Alien, Cover plant, Cut slope, Erosion control, Poaceae, Seed propagation, Succession, Volcano

INTRODUCTION

There are numerous active volcanoes around the world. The slopes of many of these volcanoes are typically bare or sparsely vegetated due to volcanic ejecta, such as pumice, scoria, ash, and volcanic gas, causing soil erosion and debris/mud flows. Consequently, volcano slopes are intentionally covered with plants for erosion control. In Japan, numerous alien species in the family Poaceae have been used for this purpose, including *Agrostis stolonifera*, *Cynodon dactylon*, *Dactylis glomerata*, *Eragrostis curvula*, *Festuca arundinacea*, *Festuca rubra*, *Lolium multiflorum*, *Lolium perenne*, *Paspalum notatum*, *Phleum pretense* and P*oa pratensis*. These species, which are indigenous to Europe, South Africa and South America, are well suited to growing in Japan where they typically grow at much faster rates than the native species.

However, concerns have arisen regarding the negative effects that these alien plant species have on the ecosystems and biological diversity present in the areas that they invade. Although numerous studies have been conducted on plant succession on volcanoes, e.g. [3], [5], [6], [8], [13], [15]-[17], [24]-[31], [33], [36], [37], only a few have examined the succession of alien species used as cover plants for erosion control on volcanoes [14], [18], [20], [21], [34]. It is therefore important to further clarify the succession of alien plant species on volcanoes for preventing soil erosion and debris/mud flows, and conserving ecosystem integrity and biological diversity.

Kondo et al. [14] reported that within six years after being introduced, all of the alien species in the family Poaceae that were used for erosion control on Sakurajima volcano were completely displaced by native plant species. Although they suggested that the potential of these alien plants to disperse had decreased in this area, the risk of seed dispersal by these species in this six-year period has not yet been assessed. We therefore reinvestigated the succession of alien plant species in the family Poaceae that are used as cover plants for erosion control on Sakurajima and examined the seed-propagation ability of these species.

METHODS

Study Site

The archipelago of Japan, which is located on the Pacific Ring of Fire, has as many as 110 active volcanoes [11]. Of these, Sakurajima in Kagoshima Prefecture in southwestern Japan, which is where this study was performed, is one of the most active. Sakurajima is located in the warm temperature zone where the mean annual temperature and annual precipitation over the last decade (2006-2015) have ranged from 18.2 to 19.3°C and 1,530 to 3,664 mm, respectively. Volcanic activity accompanied by ash fall, soil erosion and debris/mud flows continue to this day.

In this study, the 85 cut slopes that resulted from the construction of check dams were surveyed on the eastern side of Sakurajima; these sites included some of the same sites investigated by Kondo et al. [14]. The slopes, which were created during 2005-2014, were located at an altitude of 366 to 655 m above sea level and their angles of inclination ranged from 25 to 82°. Volcanic gas appeared to have no effect on the vegetation on the cut slopes, but ash-fall was constantly observed on the slopes.

Alien species belonging to Poaceae, such as *A. stolonifera*, *C. dactylon*, *D. glomerata*, *E. curvula*, *F. arundinacea* and *F. rubra*, have been introduced for erosion control on the cut slopes in this area using a bioengineering technique known as the slurry application method, which is an aerial seeding method. While the method typically calls for the repeated application of additional fertilizer [12], [18], [22], no additional fertilizer has been applied to the slopes of Sakurajima.

Vegetation Surveys

Surveys of the vegetation on the cut slopes were conducted in October 2015. Three survey quadrats (1 × 1 or 2 × 2 m) were randomly placed on each cut slope. The species composition of the plants in each quadrat was recorded and scored using the Braun-Blanquet cover-abundance scale [2]. All of the recorded plant species were categorized as native or alien, and as ferns, herbaceous plants or woody plants based on published literature [1], [10], [19], [23]. In addition, heading (flowering) of *Miscanthus sinensis* (native) and *F. rubra* (alien) was also observed at this time, and the number of scapes in each quadrat was also enumerated.

The number of years that had passed since the bioengineering techniques were implemented (NYPSB) was obtained from the Kagoshima District Forest Office, Kyushu Regional Forest Office, Forestry Agency. The Braun-Blanquet cover-abundance scale (r, +, I, II, III, IV, and V) was transformed as follows: r and + were taken as 0.1%; I as 5.0%; II as 17.5%; III as 37.5%; IV as 62.5%, and V as 87.5%. The cut slopes were classified into vegetation types based on their species composition by a two-way indicator species analysis, TWINSPAN, using the PC-ORD statistical software package (ver. 4.0 for Windows, MjM Software Design, OR).

RESULTS

Vegetation Type

The vegetation on the 85 cut slopes was classified into four types (α, β, γ and δ) using TWINSPAN (Fig. 1); types α, β, γ and δ were found on 10, 40, 7 and 28 slopes, respectively. *M. sinensis*, *D. glomerata*, *F. rubra*, *Polygonum cuspidatum*, *Rhaphiolepis indica* and *C. dactylon* were used as indicator species.

Type α plants were dominated by the alien species *C. dactylon* and *F. rubra*, which had been used as cover plants for erosion control and reached 82.17% in coverage (Table 1). Type β plants were dominated by the alien species *F. rubra* and *D. glomerata*, which are also used for erosion control. However, the extent of coverage by these alien species was lower (62.18%), while that of native species was higher than it was for Type α plants. For Type γ plants, coverage of alien and native species was generally similar; for example, coverage for *F. rubra* and *M. sinensis* was 10.26% and 17.38%, which was the highest coverage for the alien and native species of this type, respectively. Conversely, Type δ vegetation was characterized as having almost no alien species (coverage <0.01%; frequency was 2/28 slopes) and native species, mainly *M. sinensis* (53.51%), were dominant.

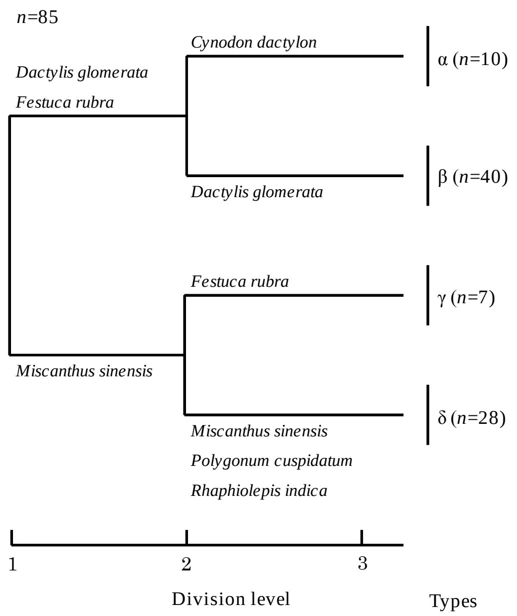

Fig. 1 Classification of vegetation on cut slopes by TWINSPAN, using species composition (coverage data, %). Cut levels of 0, 20, 40, 60, and 80 were employed in the analysis.

The NYPSB for each type is shown in Table 1. In terms of succession, the findings show that the vegetation communities on cut slopes would likely progress through types α, β, γ and finally δ after the bioengineering technique had been implemented.

Relationship between NYPSB and Component Species

The relationship between NYPSB and component species is shown in Fig. 2. At two years after the bioengineering technique had been implemented, most of the species on the cut slopes

Table 1 Plant coverage for each vegetation type classified by TWINSPAN.

Species	Vegetation types α (*n*=10)	β (*n*=40)	γ (*n*=7)	δ (*n*=28)
<Alien species>				
Cynodon dactylon #, †	63.17	2.92	0.96	0.01>
Festuca rubra #, †	19.00	30.09	10.26	0.01>
Dactylis glomerata #, †	3.77	32.09		
Trifolium repens #	0.51	2.07	0.24	
Phalacroloma annuum #		0.01>		
<Native species>				
Miscanthus sinensis #		1.54	17.38	53.51
Polygonum cuspidatum #	0.01>	0.01	0.02	2.65
Alnus firma ω		0.01>	0.01	1.23
Eurya japonica ω			0.01>	1.33
Artemisia indica #		0.05	0.01>	0.06
Lespedeza cuneata #	0.01>		0.01>	
Pinus thunbergii ω				0.39
Rhododendron obtusum ω				0.06
Rhaphiolepis indica ω				1.05
Albizia julibrissin ω				0.01>
Boehmeria spicata #				0.01>
Dennstaedtia hirsuta θ				0.01>
Indigofera pseudotinctoria ω				0.01>
Ligustrum japonicum ω				0.01>
Frequency ‡	10/10	40/40	7/7	2/28
NYPSB (Min.-Max.)	1.8 (1-2)	2.0 (1-4)	3.4 (3-5)	6.6 (4-10)

#, herbaceous plant (excluding fern); †, species (Poaceae) used as cover plants for erosion control; ω, woody plant; θ, fern and ‡, number of slopes which had alien species/total number of slopes. See Fig. 1.

were alien species. Of these, almost all (98.4%) were species that had been used as cover plants for erosion control (i.e., *C. dactylon*, *F. rubra* and *D. glomerata*). However, the coverage of these species decreased markedly after the third year, before disappearing completely by the sixth year after implementation of the bioengineering technique. Native species were observed from the first year, and *M. sinensis* and woody plants were observed from the third year onwards; these species became dominant after the fourth year, particularly *M. sinensis* (83.7%).

Seed Propagation

Scapes of *M. sinensis* were observed three years after implementing the bioengineering technique (Fig. 3). Scape numbers increased gradually thereafter, reaching 22.0 m^{-2} by the tenth year.

Festuca rubra scapes were observed in the first year after implementation of the bioengineering technique, but they were not observed by the fourth year; specifically, the number of *F. rubra* scapes was 0.1 m^{-2} in the first year, 1.8 m^{-2} in the second year, and 0.2 m^{-2} in the third year, which are significantly low compared to those for *M. sinensis* at the experimental sites, and general *F. rubra*.

DISCUSSION

It is considered that implementation of the bioengineering technique would result in the composition of the plant communities on the cut slopes of Sakurajima progressing gradually from communities dominated by alien Poaceae, which have been used extensively as cover plants for erosion control, to communities dominated by native species (Fig. 1 and Table 1). In this study, native species became dominant after the fourth year and alien species disappeared entirely by the sixth year (Fig. 2). As also reported by Kondo et al. [14], the rate of alien plant succession on Sakurajima was markedly higher than succession on other active volcanoes where alien species have remained established for more than 10 years (10-33 years) after implementation of the bioengineering technique [18], [20], [34]. In addition, scapes of alien species such as *F. rubra*, which have been used extensively as cover plants, were rarely observed on Sakurajima (Fig. 3).

It is therefore considered that alien species used for erosion control on Sakurajima have little effect on ecosystem integrity and biological diversity when compared to other active volcanoes [18], [20], [34]; however, we cannot state with certainty that these alien species will not disperse to other areas, and further investigation is needed. Meanwhile, although alien species disappeared rapidly on the slopes of Sakurajima, their coverage was initially relatively high after implementation of the bioengineering technique (Fig. 2). It is therefore considered that these plants played an important role in erosion control on Sakurajima. Indeed, none of the slopes examined in this study showed any evidence of erosion.

By the way, why did all of the alien species in the family Poaceae rapidly disappear on the cut slopes of Sakurajima? Since the nutrient (fertilizer) demand of alien species in the family Poaceae is typically very high [4], [7], [9], [32], [35], the alien plants on Sakurajima would initially have flourished due to the eutrophic conditions that would have accompanied the implementation of the bioengineering technique. Conversely, the

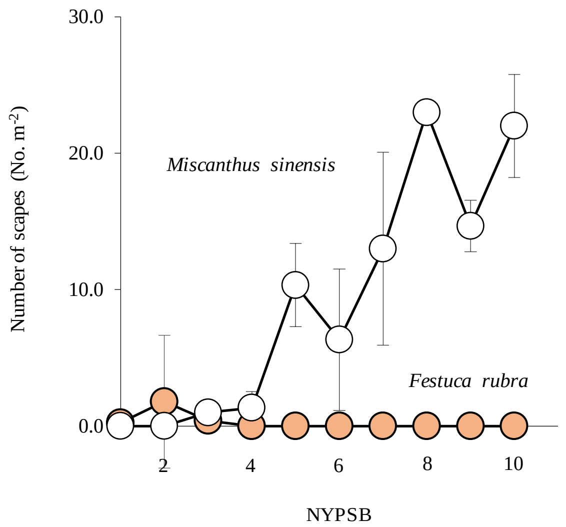

Fig. 3 Changes in the number of scapes after implementation of the bioengineering technique.
Error bars indicate the standard deviation.

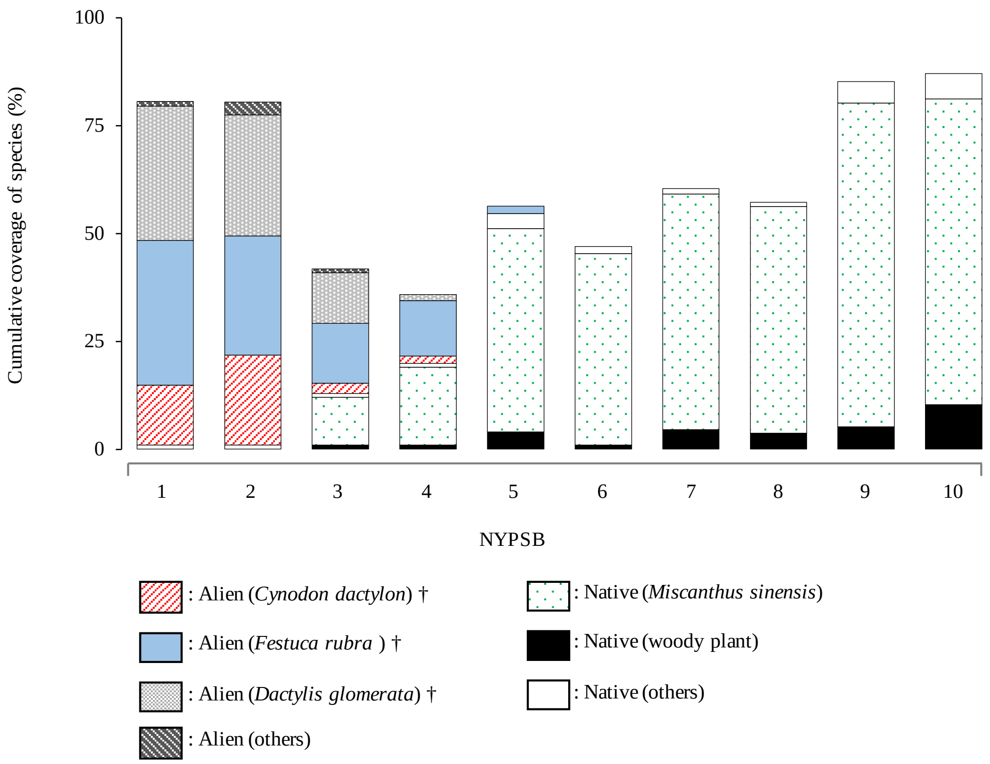

Fig. 2 Relationship between NYPSB and component species on the cut slopes of Sakurajima.
†, species (Poaceae) used as cover plants for erosion control.

subsequent decrease observed in alien plant coverage may have occurred rapidly due to the establishment of oligotrophic conditions resulting from no more fertilizer being applied to the slopes. These findings would be supported by reports of alien species at other active volcanoes being present more than ten years after being introduced, where fertilization schemes including the use of a thick cultivation base, additional fertilizer at a later date and arbuscular mycorrhizal fungi, were employed [18], [20], [34]. Incidentally, of *C. dactylon*, *F. rubra* and *D. glomerata* which have been used as cover plants for erosion control, *C. dactylon* is warm-season grass, and the rest belong to cool-season grass. It seems therefore that the difference between the two is not directly related with the above succession of alien species on the cut slopes of Sakurajima (see Table 1 and Fig. 2).

It is not clear why heading (flowering) of *F. rubra* were rarely observed on the slopes of Sakurajima, but we consider that volcanic ejecta such as ash might have some influence seed propagation of alien species in the family Poaceae in a negative way.

The high germination rate and rapid growth of alien plants in Japan mean that using alien species as cover plants is indispensable for erosion-control efforts in Japan. In addition, sales of these species are already well established and they can be obtained more easily and cost more effectively than indigenous Japanese species. However, as the concerns have increased in recent years regarding the adverse impacts of alien species on ecosystems and biological diversity, accumulating knowledge on the invasiveness of alien species as cover plants is important for developing future erosion control measures. Thus we consider that findings of this study on the succession of alien plants used for erosion control on the slopes of Sakurajima would be very meaningful.

CONCLUSIONS

Our study provides information on the succession of alien Poaceae, which have been used as cover plants for erosion control on the cut slopes of Sakurajima volcano. Although alien plants used for erosion control were dominant for the first couple of years from implementation of the bioengineering technique, native species were dominant thereafter and alien species completely vanished by the sixth year, which corresponded well with previous report by Kondo et al. [14]; this trend of succession on the slopes of Sakurajima would have been caused by fertilizer management (i.e. low fertilizer application) employed on Sakurajima. In contrast, the difference between grass types (warm- or cool-season grass) of alien species used for erosion control would not likely have an effect on their succession on the slopes of Sakurajima. It was also clarified that heading (flowering) of alien species, *F. rubra*, which have been used as cover plants for erosion control were hardly formed after implementing the bioengineer technique on the cut slopes of Sakurajima.

REFERENCES

[1] Baba T, 1999. Identifying woody species by their leaf appearances. Shinano Mainichi Shinbunsha, Nagano. 396 pp. In Japanese

[2] Braun-Blanquet J, 1964. Pflanzensoziologie. Grundzüge der Vegetationskunde, 3rd ed. Springer-Verlag, Vienna. 865 pp.

[3] Dimopoulos P, Raus T, Mucina L & Tsiripidis I, 2010. Vegetation patterns and primary succession on sea-born volcanic islands (Santorini archipelago, Aegean Sea, Greece). Phytocoenologia 40, 1-14.

[4] Ehara K, 1971. Research of feed crop and grassland. Yokendo, Tokyo. 402 pp. In Japanese

[5] Elias RB & Dias E, 2004. Primary succession on lava domes on Terceira (Azores). Journal of Vegetation Science 15, 331-338.

[6] Garcia-Romero A, Alanis-Anaya RM & Munoz-Jimenez J, 2015. Environmental factors that affect primary plant succession trajectories on lahars (Popocatepetl Volcano, Mexico). Journal of Mountain Science 12, 1254-1266.

[7] Harada I, 1977. Nutrition of pasture and fertilization. Yokendo, Tokyo. 272 pp. In Japanese

[8] Haruki M & Tsuyuzaki S, 2001. Woody plant establishment during the early stages of volcanic succession on Mount Usu, northern Japan. Ecological Research 16, 451-457.

[9] Hoshiko T, 1999. A study on the invasions of woody-plants and seed dispersal form on man-made expressway slopes. J. Jpn. Soc. Reveget. Tech. 25, 102-114. In Japanese

[10] Iwatsuki K, 1992. Ferns and fern allies of Japan. Heibonsha, Tokyo. 311 pp. In Japanese

[11] Japan Meteorological Agency, 2016. http://www.jma.go.jp/jma/index.html. In Japanese

[12] Kagoshima District Forest Office & Forestry and Civil Engineering Consultant, 2006. Report on project for preserving Sakurajima district. 246 pp. In Japanese

[13] Kamijo T, Kitayama K, Sugawara A, Urushimichi S & Sasai K, 2002. Primary succession of the warm-temperate broad-leaved forest on a volcanic island, Miyake-jima, Japan. Folia Geobotanica 37, 71-91.

[14] Kondo K, Uchida T, Hayasaka D, Tanaka J, Sato A & Arase T, 2016. Vegetation succession on cut slopes covered with exotic grasses for erosion control, Mt. Sakurajima. International Journal of GEOMATE 11, 2136-2142.

[15] Korznikov KA, 2015. Vegetation cover of the young mud fields of Maguntan Mud Volcano (Sakhalin Island). Moscow University Biological Sciences Bulletin 70, 99-103.

[16] Korznikov KA, 2015. Vegetation cover at the Maguntan mud volcano (Sakhalin Island , Russia): species composition and spatial distribution. Phytocoenologia 45, 125-134.

[17] Marler TE & del Moral R, 2013. Primary succession in Mount Pinatubo. Habitat availa-bility and ordination analysis. Communicative & Integrative Biology 6, e25924 (online).

[18] Miyasihita S & Yamada M, 2010. Succession of vegetation on the southern slope of Mount Usu after aerial seeding work. Forest Consultant 122, 8-14. In Japanese

[19] Miyawaki A, Okuda S & Fujiwra R, 1994. Handbook of Japanese vegetation. Shibundo, Tokyo. 646 pp. In Japanese

[20] Nakano Y & Futami T, 2004. Observation on plant succession at the past cut slope landscaping sites in Miyakejima Island. J. Jpn. Soc. Reveget. Tech. 30, 383-388. In Japanese

[21] Ogawa Y, Akema T & Daimaru H, 2011. A field survey of revegetation plants and field observation of overland flow on slopes overlain by pyroclastic-flow deposits, Unzen volcano, Japan. Journal of the Japan Society of Erosion Control Engineering 63, 78-82. In Japanese

[22] Ogawa Y, Shimizu A, Shimizu T, Daimaru H & Miyabuchi I, 2002. Surface runoff and sediment discharge for three years on a slope revegetated by aerial seeding work at Unzen Volcano. J. Jpn. Soc. Reveget. Tech. 28, 255-258. In Japanese

[23] Shimizu T, 2003. Naturalized plants of Japan. Heibonsha, Tokyo. 337 pp. In Japanese

[24] Tagawa H, 1964. A study of the volcanic vegetation in Sakurajima, south-west Japan. I. Dynamics of vegetation. Mem. Fac. Sci. Kyushu Univ. Ser. E (Biol.) 3, 165-228.

[25] Tsuyuzaki S, 1987. Origin of plants recovering on the volcano Usu, northern Japan, since the eruptions of 1977 and 1978. Vegetatio 73, 53-58.

[26] Tsuyuzaki S, 1997. Wetland development in early stages of volcanic succession. Journal of Vegetation Science 8, 353-360.

[27] Tsuyuzaki S, 2009. Causes of plant community divergence in the early stages of volcanic succession. Journal of Vegetation Science 20, 959-969

[28] Tsuyuzaki S & del Moral R, 1995. Species attributes in early primary succession on volcanoes. Journal of Vegetation Science 6, 517-522.

[29] Tsuyuzaki S & Hase A, 2005. Plant community dynamics on the volcano Mount Koma, northern Japan, after the 1996 eruption. Folia Geobotanica 40, 319-330.

[30] Tsuyuzaki S, Titus JH & del Moral R, 1997. Seedling establishment patterns on the Pumice Plain, Mount St. Helens, Washington. Journal of Vegetation Science 8, 727-734.

[31] Voronkova NM, Verkholat VP & Kholina AB, 2011. Specific features of plants at early stages of the colonization of loose volcanic matter. Biology Bulletin 38, 237-241.

[32] Watanabe K, Katsura I, Sekimura S & Kumano S, 1968. The effects of fertilization and cutting on the growth of grasses in mixed sward and the chemical properties of soil. Bull. Tohoku Agric. Res. Cent. 36, 97-111. In Japanese

[33] Watanabe M, Takaoka S, Morishima W, Sakagami N, Collado M & Oguchi T, 2011. Vegetation succession and land recovery process based on soil properties in the upper Mt. Pinatubo, the Philippines. Journal of Geography 120, 631-645. In Japanese

[34] Yamamoto K, Marumoto T, Okabe H, Ichimura M, Niimi Y, Ozaki A, Ohkubo T, Ueki T, Sekiyama S & Tatewaki S, 2006. Soil fertility and vegetation after 10 years from the dry aerial seeding work in Mizanashigawa area, Mt. Unzen-Fugen. J. Jpn. Soc. Reveget. Tech. 32, 195-198. In Japanese

[35] Yoshida H & Kikuchi T, 1993. Research of the variation on spraying thick cultivation method: the transition of 17 years after application. J. Jpn. Soc. Reveget. Tech. 18, 219-226. In Japanese

[36] Yoshii Y, 1932. Revegetation of Volcano Komagatake after the great eruption in 1929. Botanical Magazine 46, 208-215

[37] Yoshioka K, 1966. Development and recovery of vegetation since the 1929 eruption of Mt. Komagatake, Hokkaido. 1. Akaikawa pumice flow. Ecological Review 16, 271-292.

NEW DATA ON AFRICAN-EURASIAN LIMIT AND SPATIAL DISTRIBUTION OF THE CURRENT DEFORMATION THROUGH ACTIVE STRUCTURES IN THE CENTRAL MEDITERRANEAN AND THE SURROUNDING AREAS

Adnène KASSEBI [1,2] and Fouad ZARGOUNI [1]
[1] Faculty of Sciences of Tunis, University of Tunis El Manar, Tunisia; [2] National Center for Mapping and Remote Sensing, Tunis, Tunisia

ABSTRACT

The Mediterranean region is constituted by a complex mosaic of plates and microplates, which move relative to each other. Although there is general agreement to consider that the subduction and closure of the Tethyan Ocean and the interaction between European and African dishes were the main drive mechanism controlling the evolution of basins orogenic extension and arches in the western and central Mediterranean.

We aim in this work, introduce new insights into the evolution of time and space scattered relics of the external areas of the maghrébide belt in the central Mediterranean, and its tectonic behavior as part of the current border of the Africa-Europe course.

The integration of digital data (in a Geological Spatial Database) to seismic processing and spatio-temporal data analyzes performed, allows the identification of new data on seismic risks and Hazards associated with zones of tectonic surface and deep. Trading volumes in our project are directly related to geometric, topographic and geological characteristics of the study area and the characteristics of lineaments that integrates data mining methods and different geoprocessing made.

We define segment boundaries internal offshore zones, and characteristics of tectonic structures responsible for their arrangement, and we finally found those who are still working. The flush results are: (i) the kinematic active deformations in the Mediterranean area; (Ii) the spatial distribution of the current deformation through active structures in the central Mediterranean (Sicilian-Tunisian Strait and surrounding lands); (Iii) the sliding velocities of seismic recurrence and associated risks.

Keywords: Central Mediterranean, Seismic processing, Active fault, Spatio-temporal data, Earthquakes

1. INTRODUCTION

Earthquakes in the Mediterranean, recorded in recent years strong Ambrasseys, 1962; Rothe, 1969; McKenzie, 1972, 1978; Udias et al., 1976; Cagnetti et al., 1976; Hatzfeld, 1978; Bonjer and Fuchs, 1979; Mayer-Rosa and Pavoni, 1977; Ben Ayed, 1986; Zargouni and Abbès, 1987; Zenati, 1990; Boutib and Zargouni, 1997; Dlala, 2002 ; Kacem, 2004; Kassebi, 2007, Kassebi et al., 2013, Kassebi and Zargouni, 2013, 2014 and many neotectonic studies in the Mediterranean area clearly show that very different deformation mechanisms can coexist in areas very close to one than another. But the different types of distortion to be the expression of the same phenomenon; in this case, the N-S convergence of European and African plates acting for the past 70 Ma (Pitman and Talwani, 1972, Dewey et al, 1973. Le Pichon et al, 1977. Tapponnier, 1977 ; Savostin et al. 1986). This convergence, which is stronger in the eastern part of the Mediterranean (McKenzie, 1972) is absorbed by the deformations that are distributed in the regions of variable size: near the Aegean and Tyrrhenian subduction zone and continental collision zones Western Mediterranean.

The distribution of focal mechanisms of earthquakes such as the various types of deformities found in the Mediterranean area suggest that the distribution of deformation zones (that is to say, affected by a single type of deformation zones) does not follow a simple rule and that only the interpretation of geological and geophysical data may lead to a coherent seismotectonic a complex domain model. To define the distribution and spatial variation of various types of deformation as well as the evolution of the stress field from the Pliocene. The example we have considered is the Tyrrhenian Arc and Tellian extension in northern Tunisia which seems to correspond to a transition from subduction to crash diets.

2. GEOGRAPHICAL SETTING OF THE STUDY AREA

The central Mediterranean and specifically the Sicilian-Tunisian Strait composed by shoals located between Sicily and Tunisia, also called Sicilian-Tunisian threshold is a sea separating the two shoals or basins of the Mediterranean Sea: 1^{st}, consisting of the Algerian-Provencal basin and the Tyrrhenian sea forms the western Mediterranean; the 2nd consisting of the Ionian Sea and the Levantine basin forms the eastern Mediterranean. The first covers an area of about 0.85 million square kilometers while the second covers about 1.65 million square kilometers. Both sets shallows form abyssal plains with a depth of 2000 to 5000 m and consist of an ocean floor.

This stretch of sea is bordered to the northwest by Sardinia, to the south by the Pelagie Islands (including the island of Lampedusa) and southeast of the islands of Malta which, together with Sicily, Malta channel ; the latter channel is sometimes geopolitically integrated as part of the broader Sicily Channel to designate the whole area south of Sicily in Italian territorial waters.

In its narrowest part, between Cap Feto near Mazara del Vallo and near Cap Bon-El Haouaria, the canal is 145 km wide.

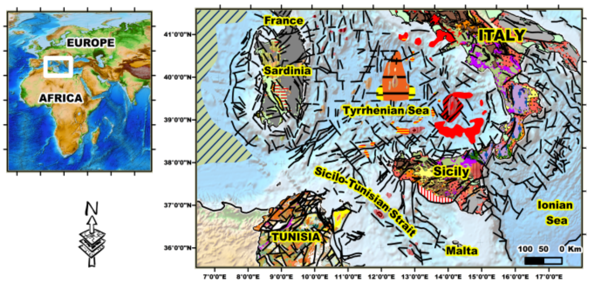

Fig. 1 Geographical and geological map of the study area.

3. GEOLOGICAL HISTORY

The central Mediterranean Sea separated from the Messinian evaporites the eastern and the western Mediterranean basins (Fig. 1). The Sicilian-Tunisian threshold is of major interest for the study of sea level changes, exchange of seawater, sediment and transits the importance of the carbonate production during the pre-evaporite history of these areas. This threshold zone is formed by the Pelagian platform, extending the Mesozoic and Cenozoic of southern Sicily, Tunisia and Tripolitania, extending northward Saharan craton. It is now almost completely submerged in shallow (Winnock & Bea 1979 Pedley & Grasso 1992). This bedrock was deeply sawed Pliocene by a network of faults N120 in response to crustal thinning axis maximum in the area of Pantelleria (Reuther 1987) WNW-ESE, equated to an area of bulge pre-rift age upper Miocene, largely collapsed in the Plio-Quaternary. Thus, the few witnesses to the Messinian sedimentation they are only limited to areas of outcrop horst now emerged, that of the Maltese Islands on the one hand, on the island of Lampedusa other (Fig. 1).

North Africa is bound by an Alpine orogeny kind resulting from the subduction and closure of the Tethyan Ocean and the interaction between the European and African dishes. Sicily lies on part of the complex convergent boundary where the African Plate is subducting beneath the Eurasian Plate. This subduction zone is responsible for the formation of the stratovolcano Mount Etna and considerable seismic activity. Most damaging earthquakes however, occur on the Siculo-Calabrian rift zone. This zone of extensional faulting runs for about 370 kilometres (230 mi), forming three main segments through Calabria, along the east coast of Sicily and immediately offshore, and finally forming the southeastern margin of the Hyblean Plateau. Faults in the Calabrian segment were responsible for the 1783 Calabrian earthquakes sequence (Catalano et al. 2008).

In Tunisia, as in the rest of the Maghreb, recent strains are related to the collision (Bousquet, 1977; Ben Ayed and Viguier, 1981). The examination of extensional tectonic compressive and the Alps Tunisia and its foreland shows that these tectonic are not any. In particular, the compression and distension present a orthogonal directions extension and shortening. Indeed, the arrangement of deformations and quaternary neogene Tunisia, shows that in general, the maximum principal stress which is either $\sigma1$, $\sigma2$ either, keeps almost the same direction.

Tectonics first located only in the Far North of Tunisia and is associated with the episode of establishment of groundwater is contemporaneous strike-slip extensional tectonics central Tunisia ahead of the front of tablecloths. Over time, the compression zone has migrated to the South; it will reach the central Tunisia during the lower Tortonian.

4. GEOMETRIC AND STRUCTURAL ANALYSIS

4.1. Structural analysis

The presence of three key unconformities is important to note and is the key to unravelling the presence and location of traps. (Messinian, Intra-Tortonian and Pyrenean)

- The Pyrenean (Oligocene) Unconformity is present and marks a change in structural style in the deeper section. In well w1, this is found just above the Bou Dabbous Formation.
- Understanding the biostratigraphy is at times more important that the lithostratigraphy as names change across the border and from well to

well.

- The "w2" sandstones and the "w3" Carbonate (Fig. 2) are most likely time equivalent units encapsulated in the Mahmoud Shale. Just different depositional environments.
- The Nummulites Fichteli (marks the top of Bou Dabous) whereas the Nummulites Vascus (marks the top of the Soaur / Base of Fortuna and end of the Pyrenan phase).

An alternative interpretation: "w2" and "w3" are not Formations (Fig. 2). These events are stratigraphic units (i.e. w2 sands and w3 limestones) representing different depositional settings during the Mahmoud Formation. The key is the biostratigraphy.

It is then overprinted at times by long N-S lineaments representing the extensional phase.

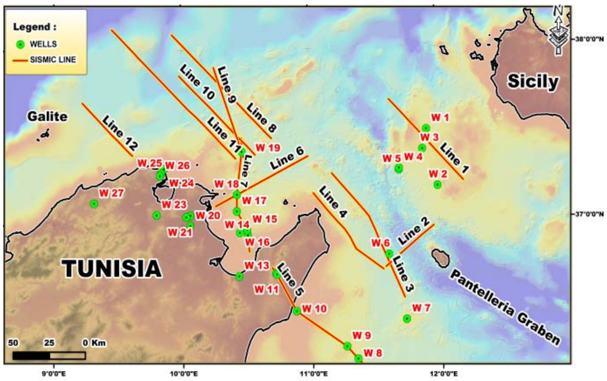

Fig. 2 Regional cross sections

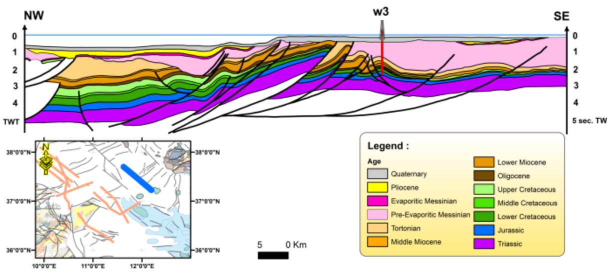

Fig. 3 Regional cross section NO. 1 Casero, 2004

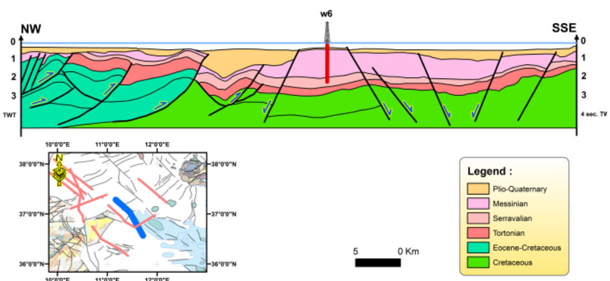

Fig. 4 Regional cross section NO. 2

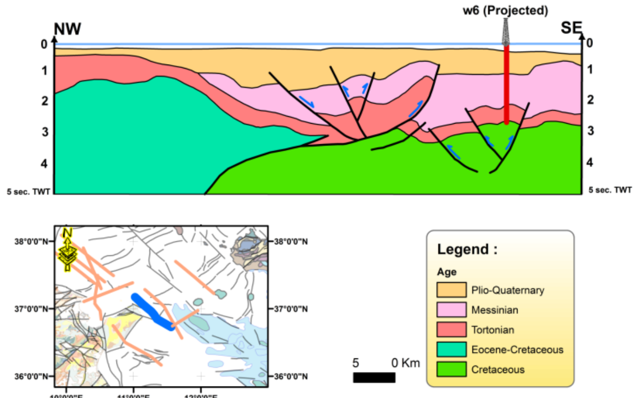

Fig. 5 Regional cross section NO. 3

1. Two main structural trends are observed in Sicilian-Tunisian threshold as extended from the South and North of the permit:

- NW-SE Normal Faulting (possibly Messinian Time);
- SW-NE Thrust Faulting (possibly Pre-Pyrenean Time);

2. There is a third overprint of the NNW-SSE reidel shears as seen on the 3D;

3. Several trap styles (both shallow and deep) could be assumed;

This structural style above in the shallow and deep can be seen in the shallow and deep throughout the Sicilian-Tunisian threshold.

It is then overprinted at times by long N-S lineaments representing the extensional phase.

4.2. Geodynamic analysis

A special comment must be devoted to the evolutionary model of the western Mediterranean region given by Dewey et al. (1989), since it is the last proposed in literature and in addition, it presents the most detailed reconstruction of the African-Eurasian kinematics during the time that we considered.

This model suggests, among other things, that the migration of the Calabrian Arc (to the Southeast), and the consequent opening of the Tyrrhenian basin, occurred in the context of African-Eurasian convergence led just against it (SE-NW). No clear explanation is given dynamics of this very special phenomenon. Only a vague reference is made mechanisms back-arc or rolling back.

The final note of Dewey and colleagues about the evolutionary models in this area is a direct relationship cannot always be provided between the relative movement of blocks of imprisonment and main trends deformations inter dish. They attribute this mismatch to the complex kinematics of micro-plate in the central Mediterranean area. We believe, instead, that this problem is due to the fact that the post-Tortonian kinematics of Africa-Eurasia assumed by Dewey et al. (1989) is not reliable. This hypothesis is also suggested by a strange detour into the path of movement of Africa proposed by Dewey et al., the drastic change of the drifting trend of this dish, from NE to NW. Such rapid movement of large deflection of continental blocks does not seem very likely the physical point of view and, in addition, it is supported by any clear change in pattern of deformation in the areas around the African-Eurasian system and in the Mediterranean region in particular.

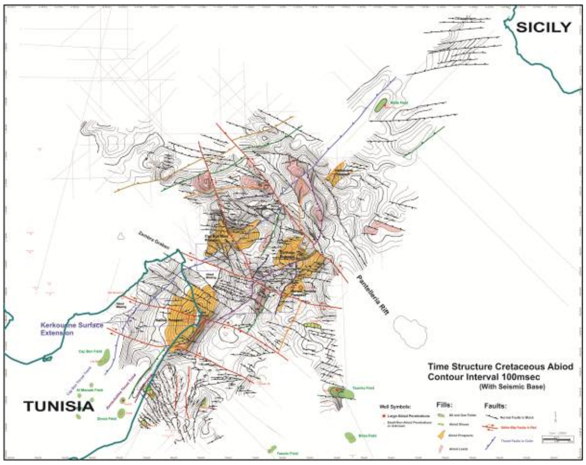

Fig. 6 Time Structure Cretaceous Abiod Contour Interval 100msec.

4.3. Discussion

4.3.1. Limits of the Internal Zones

From the observations described in the sections above, we propose a new structural map for the offshore domain (Fig. 6). With the deep coring, basement samplings and dense seismic reflection data in order to support our hypotheses, we attempt to relate the lithology offshore to the one onshore from the changes of geometry, morphology, bathymetry, roughness and seismic structures reported.

The contact between Internal and External Zones is clearly mapped at east of Bizerte, along the east–west accident delimitating the southern end of the Kechabta bassin deep-sea fan (Fig. 6). Elsewhere, we have used several geomorphic markers and changes in the roughness of the bathymetry or seismic facies, together with geological evidence onland, in order to propose a connection of offshore domains either to the Internal Zone or External Zones. However, several limitations and doubts about the basement nature remain, that are discussed hereafter.

4.3.2. Reactivation of structures

The seismicity from the last three decades shows great changes from east (Pantelleria Rift zone) to west (Tunis gulf zone). The Pantelleria Rift area is by far the most active. Nowadays, the major active faults depict compressional focal mechanisms, and these are a potential hazard for the coastal cities of Tunisia and Sicily. Only the SW–NE striking structures seem active in the present-day stress field, whereas NW–SE structures are apparently not. These latter ones were probably active under a different stress field. Some authors suggest the presence of active strike-slip faults along the Sicilian-Tunisian strait.

However, according to the recent focal mechanisms and seismicity distribution, it appears that these faults have no clear activity today. They may have played an important role in the past (at least before the Quaternary, but probably before the beginning of the compressive stage of the margin, during the Miocene), and some of them favourably oriented could be reactivated as thrust faults in the present-day stress field. This could be the case of the border faults of the horst Pantelleria (Fig. 4). Conversely, the series of north-verging thrusts offshore Tunis Gulf is probably neoformed Plio-Quaternary structures, and corresponds to the beginning of the margin inversion. The Cap Bon area is slightly seismogenic, with small earthquakes that appear spread offshore, according to the INM catalogue of earthquakes from 1971 to present. Most large earthquakes occurred inland, and are associated to Tellian folds and thrusts, some other examples of more limited active features are found offshore.

5. SEISMIC DEFORMATION

Literature review of work on the seismicity of the central Mediterranean seismic analysis shows more or less variable and sometimes contradictory, the authors suggest a quiet seismicity in Tunisia as reliable sources shows destructive earthquakes of registration in Part north-eastern, central and in offshore Tunisia (Fig. 7).

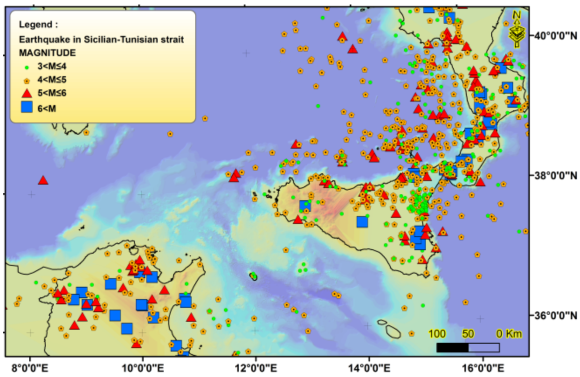

Fig. 7 Seismicity map of Sicilian-Tunisian Strait

Comparing total and seismic deformation along the Northern Africa to Sicily sections, we find an interesting relation between geometry and amount of deformation due to seismicity. Within sections affected by pure thrust motion we find a higher seismic deformation (26% for the Algeria section and 10% for the Tunisia to Sicily section) with respect to the sections where the strike-slip motion prevails, characterized instead by very small percentages of seismic deformation (<1%) (Pondrelli, 1999).

For all sections, however, the seismicity accounts for low percentages of total expected deformation normal to the boundary: 31% in the Calabria section, 30% in the Central to Southern Apennine section, 3% in the Friuli section and 10% in the Eastern Adriatic section. Only in the Sicily Strait section do we find a high value of strain accommodated by seismicity that here accounts for 79% of total strike slip deformation (Pondrelli, 1999).

It is clear that these values are generally low, but comparable values have also been found in this area (Jackson and McKenzie, 1988; Pondrelli et al., 1995; Ward, 1998). We assume that these small percentages are due to the fact that 100 years are not representative of the seismic recurrence cycle of these zones, as already suggested by Ward (1998). However, more and more studies are showing that aseismic deformation is effectively high and often related to silent events (or slow earthquakes) (Amoruso et al., 1998; Hirose et al., 1998; Linde et al., 1996, 1998).

6. DISCUSSION

Analysis of seismic values recorded by local sources (Institute of Meteorology (Tunisia) and Parametric Catalogue of Italian Earthquakes: CPTI11 (Italy)) are consistent with the African-Eurasian boundary identified in this work, indicating a close relationship with plate tectonics associated with the movement of the African continent converge NE-SW in the area of the Sicilian-Tunisian Strait. The study of the geometry of the seismic deformation calculated on a larger scale inferred from seismicity is a fairly continuous sketch of the deformation pattern.

Only along the Alps the high seismicity, representative of the regional stress is insufficient to derive a clear tectonic model (Pondrelli 1999). The heterogeneity of the deformation of this zone has been confirmed by studies of more small events that demonstrated the co-existence of contemporaneous compression and extensional stress regime (Frepoli and Amato, 1997).

Going North of Tunisia to the island of Sicily, we see the different characteristics of typical transpressive limits that have been shown where a simple compression limit is expected from global models.

In the central Apennines and southern and eastern Adriatic, the geometry of the seismic deformation shows that the two areas are directly involved in the development of peri-Tyrrhenian area where the slab is removed and the opening of the Tyrrhenian basin product migration to the East (Malinverno and Ryan, 1986) and the likely rotation of the plate Adria (Anderson and Jackson, 1987). The consequent NE-SW prevailing strain pattern overprints the NNW-SSE Africa Eurasia plate convergence (Pondrelli, 1999).

7. CONCLUSIONS

The summation moment tensor has been applied in the western Mediterranean from data representing 100 years of intermediate to strong earthquakes (3 <M). Percentages ranging from 3 to 31% of strain received by seismic activity have been found. Only the section of the Sicilian-Tunisian Strait made the strike slip seismic deformation account for 79% (Pondrelli 1999).

We still do not know if the seismic deformation can reach such high values, and we must remember that 100 years may not be representative of the seismicity recurrence characteristic of the central Mediterranean. In all cases, the amount of seismic deformation is lower than expected, but the deformation pattern obtained has some interesting features that the movement of the overall plate and geodetic measurements do not disclose, as transpressional model along Africa North to Sicily area or the influence of the evolution of the peri-Tyrrhenian area on this deformation periadriatic sections.

The northwest side of the Sicilian-Tunisian channel in the central Mediterranean has been shaped by the emergence of two independent tectonic processes that overlap each other, the accretionary prism Maghrebides-Apennines and the rift Canal Sicilian-Tunisian .

Since at least the Pliocene, these two processes have acted simultaneously, each being associated with subduction Apennines and the African Rift. Linked to the movement of the accretionary prism, containing nearly orthogonal normal faults related rifts and vice versa (Pondrelli, 1999). Analog modeling supports kinematics inferred from regional structural data. alkaline magmatism associated with the fracture is more pronounced in the foreland of the prism, where the extension is more concentrated.

This particular parameter confirms the independence of geodynamic processes that can interact in the same area at the same time suggesting that the plate boundaries are passive features that meet the velocity fields in the far field of the lithosphere (Pondrelli, 1999).

A general agreement has estimated that the Tyrrhenian subduction of the Arc and the South Aegean Volcanic Arc was the main drive motor of evolution and expansion of orogenic arcs of the western and central Mediterranean.

Although the study area is part of a broad zone of deformation reactivated under compression stress field current, the study area should suffer the highest rates of deformation related to the subduction in the southern Italy presented by the recent earthquakes of considerable magnitude located in the Sicilian-Tunisian Strait and the Ionian sea and volcanic activity of Mount Etna on the island of Sicily.

8. REFERENCES

[1] AMBRASSEYS N. N. (1962) - The seismicity of Tunis. Anali di geofisica, vol. Xl, n°2-3, Roma.

[2] ANDERSON, H. and J. JACKSON (1987): Active tectonics in the Adriatic region, Geophys. J. R. Astron. Soc., 91, 937-983.

[3] AMORUSO, A., L. CRESCENTINI and R. SCARPA (1998): Slow earthquakes and seismicity in Central Italy, AGU abstract volume, F606.

[4] BEN AMARA R., KASSEBI A. et BOUKADI N., 2013. Apport de la sismique réflexion et de la télédétection à l'identification du risque sismique dans la plaine de Mornag (Tunisie nord-orientale). Congrès International ICNHG2013 : 1ère édition, intitulé : « Congrès International sur les Risques Naturels et Géomatiques ». Hammamet, Tunisie, 17–20 Mai 2013.

[5] BEN AYED, N., Viguier, C. 1981. Interprétation structural de la Tunisie Atlasique. Comptes Rendus Académie des Sciences Paris.292, II, 1445-1448.

[6] BEN AYED N., 1986. Evolution tectonique de l'avant-pays de la chaîne alpine de Tunisie du début du Mésozoïque à l'actuel. Thèse d'Etat, Univ. de Paris, Sud- centre d'Orsay.

[7] BOUSQUET, J.C., 1977. Contribution fi l'étude de la tectonique récente en Méditerranée Occidentale: Les données de la néotectonique dans l'arc de Gibraltar et dans l'arc Tyrrhénien. In: B. Biju-Duval and L. Montadert (Editors), Structural History of the Mediterranean Basins. Technip, Paris, pp.194 214.

[8] BONJER, K. P. and FUCHS, K., 1979. Real-time monitoring of seismic activity and earthquake mechanisms in the Rhinegraben area as a basis for prediction, Proceedings ESA-Council of Europe Seminar on Earthquake Prediction, Strasbourg-ESA SP-149.

[9] BOUTIB L. et ZARGOUNI F., 1997. Évolution géométrique des mégastructures anticlinales et découpage en lanières tectoniques de l'Atlas centro-méridional de Tunisie. 14ème Coll. Bassins Sédimentaires. Marocains, p. 142.

[10] CAGNETTI, V., PASQUALE, V., and POLINARI, S. (1976) Focal mechanisms of earthquakes in Italy and adjacent regions, CNENRT/AMB, Roma. 76(4), 41 pp.

[11] CATALANO, S., DE GUIDI G., MONACO C., TORTORICI G. and TORTORICI L. (2008). "Active faulting and seismicity along the Siculo–Calabrian Rift Zone (Southern Italy)".Tectonophysics (Elsevier) 453 (1-4): 177–192. Bibcode: 2008 Tect p.453. 177C.

[12] DEWEY, J.F., PITMAN, W.C., RYAN, W.B.F. and BONNIN, J., 1973. Plate tectonics and the evolution of the Alpine system. Geological Society of America Bulletin, 84: 3137-3180.

[13] DEWEY, J.F., HELMAN, M.L., TURCO, E., HUTTON, D.H.W. and KNOTT, S.D., 1989. Kinematics of the western Mediterranean. In: M.P. Coward, D. Dietrich & R.G. Park (Editors), Alpine Tectonics, Geological Society, London, Special Publications 45, pp. 265-283.

[14] DLALA M., 2002. Les manifestations tectono-sédimentaires d'âge Campanien-Maastrichtien en Tunisie : implication sur l'évolution géodynamique de la marge Nord-Africaine. C.R Geoscience, 334, pp. 135-140.

[15] FREPOLI, A. and A. AMATO (1997): Contemporaneous extension and compression in the Northern Apennines from earthquake fault-plane solutions, Geophys. J. Int., 129, 368-388.

[16] MALINVERNO, A. and W.B.F. RYAN (1986): Extension in the Tyrrhenian Sea and shortening in the Apennines as result of arc migration driven by sinking of the lithosphere, Tectonics, 5, 227-245.

[17] HATZFELD, D., 1978. Etude sismotectonique de la zone de collision lbero-Maghrebien. Thèse Doct., Univ. Grenoble. 281 pp.

[18] HIROSE, I., I. KAWASAKI, Y. OKADA, T. SAGIYA and Y. TAMURA (1998): An M 6 class interplate silent earthquake of December 9, 1989, as revealed by borehole observations of the crutal movement in the South Kanto District, Central Japan, AGU abstract volume, F601.

[19] KACEM J., 2004. Etude sismotectonique et évaluation de l'Aléa sismique régional du Nord–Est de la Tunisie : apport de la géophysique dans l'identification des sources sismogéniques. Thèse Es Sciences Géologique, Univ. Tunis II, Fac. Sc. Tunis, 389 p.

[20] KASSEBI, A. 2007. Signification géodynamique des pointements calcaires au Sud de la ville de Tunis. Thèse de 3ème Cycle, Faculté des Sciences de Tunis, 95 P.

[21] KASSEBI A., ABROUD Gh., SLAIMI S. et GHANMI M.. Conception et Mise en place d'une Base de Données Spatiale 3D multi-échelles de la Tunisie (BD TOPO 3D). Congrès

International Géotunis : 9ème édition, intitulé : « Gis and Geospace Applications ». Hammamet, Tunisie, 01–05 Avril 2015.

[22] KASSEBI A. et ZARGOUNI F., 2013. Contribution of geological mapping and new technologies to the identification of a major, pre–existing and active fault over the Capital of Tunisia. International Conference on Geotechnique, Construction Materials and Environment – GEOMATE 2013: 3th edition. Nagoya, Japan, 13–15 November 2013.

[23] LE PICHON, X., SIBUET, J.C., and FRANCHETEAU, J., 1977. The fit of the continents around the North Atlantic ocean, Tectonophysics,v. 38, p. 169-209.

[24] LINDE, A.T., M.T. GLADWIN, M.J.S. JOHNSTON, R.L. GwYTHER and R.G. BILHAM (1996): A slow earthquake sequence on the San Andreas fault, Nature, 383, 65-68.

[25] LINDE, A.T., I.S. SACKS, M.T. GLADWIN, M.J.S. JOHNSTON and P.G. SILVER (1998): Slow earthquakes at plate boundaries — a connection with large earthquakes? AGU abstract volume, F600.

[26] MCKENZIE, D., 1972. Active tectonics of the Mediterranean region, Geophys. J. R. astr. SOC., 30, 109-185.

[27] MCKENZIE, D., 1978. Active tectonics of the Alpine-Himalayan belt; the Aegean Sea and surrounding regions, Geophys. J. R. astr. SOC., 55, 217-254.

[28] MANTOVANI, E., D. ALBARELLO, C. TAMBURELLI and M. VITI (1995): Tectonic interpretation of large scale geodetic measurements (VLBI, SRL) in the Central Mediterranean region: constraints and uncertainties, Ann. Geofis., 38 (1), 67-84.

[29] MAYER-ROSA, D. and PAVONI, N. (1977): Fault plane solutions of earthquakes in Switzerland from 1971 to 1976. Publ. Inst. Geophys. Pol. Acad. Sc., A-5 (116), 321-326, 1977.

[30] JACKSON, J. and D.P. McKenzie (1988): The relationship between plate motions and seismic moment tensors, and the rates of active deformation in the Mediterranean and Middle East, Geophys. J. Int., 93, 45-73.

[31] PEDLEY, H. M., and M. GRASSO (1992), Miocene syntectonic sedimentation along the western margins of the Hyblean-Malta Platform: A guide to plate margin processes in the central Mediterranean, J. Geodyn., 15, 19 – 37.

[32] PITMAN, W.W., III, and M. TALWANI, 1972. Sea floor spreading in the North Atlantic, Geol. Soc. Amer. Bull., 83, 619-646.

[33] PONDRELLI, S., 1999. Pattern of seismic deformation in the Western Mediterranean. ANNALI DI GEOFISICA, VOL. 42, N. 1, pp. 57-70.

[34] PONDRELLI, S., A. MORELLI and E. BosCifi (1995): Seismic deformation in the Mediterranean area estimated by moment tensor summation, Geophys. J. Int., 122, 938-952.

[35] REUTHER, C.D., 1987. Extensional tectonic within Central Mediterranean segment of the Afro-European zone of convergence, Mem. Soc. Geol. It., 38, 69–80

[36] SAVOSTIN. L.A., SIBUET, J.C., ZONENSHAIN. L.P., LE PICHON, X. and ROULET, M.J., 1986. Kinematic evolution of Tethys belt from the Atlantic Ocean to the Pamirs since the Triassic. Tectonophysics, 123 : l-35.

[37] ROTHE J. P. (1969) - Mission d'information seismolorque, Moyen-Orient et Afrique du nord. UNESCO, n° de serie: 1759/BMS. 336p. 24 fig., 50 tabl., Paris.

[38] Rovida A., Camassi R., Gasperini P. and Stucchi M. (eds.), 2011. CATALOGO PARAMETRICO DEI TERREMOTI ITALIANI: CPTI11, the 2011 version of the Parametric Catalogue of Italian Earthquakes. Istituto Nazionale di Geofisica e Vulcanologia, Milano, Bologna. 30 p.

[39] TAPPONNIER, P., 1997. Evolution tectonique du système alpin en Méditerranée: poinçonnement et écrasement rigide—plastique, Bull. Soc. Ge´ol. Fr., XIX, 437–460.

[40] UDIAS A., LOBEZ-ARROYO A. and MEZCUA. J. (1976). - Seismotectonic of the Azores-Alboran Region, Tectonophysics, 31, p. 259-289.

[41] WARD, S.N. (1998): On the consistency of earthquake moment release and space geodetic strain rates: Europe, Geophys. J. Int., 135, 1011-1018.

[42] WESTAWAY, R. (1992): Seismic moment summation for historical earthquakes in Italy: tectonic implications, J. Geophys. Res., 97, 15437-15464.

[43] WINNOCK, E. and BEA, F., 1979. La mer pélagienne. Structure de la mer pélagienne. Géologie méditerranéenne VI-I : 35-49.

[44] ZARGOUNI F. and ABBES C., 1987. Zonation structurale de la Tunisie. Rev. Sci. Terre, édition I.N.R.S.T., Tunisie, V-3. pp. 63-69.

[45] ZENATI H. (1990) - Etablissement d’un catalogue des séismes historiques de la Tunisie: évolution des données recueillies pour la période 365-1950. Tome I, Soc. Tun. Elec. Gaz (rapport inedit).

Sixth International Conference on Geotechnique, Construction Materials and Environment, Bangkok, Thailand, Nov. 14-16, 2016, ISBN: 978-4-9905958-6-9 C3051

REMOVAL OF ORGANIC MATTER IN WASTEWATERS OF A MILK FACTORY AND A HOSPITAL USING A CUBIC LATTICE BASED ROTATING BIOLOGICAL CONTACTOR IN VIETNAM

Tatsuhide Hamasaki[1], Phan Do Hung[2] and Hiroshi Tsuno[3]
[1,3]Faculty of Human Environment, Osaka Sangyo University, Japan;
[2]Institute of Environmental Technology, Vietnamese Academy of Science and Technology, Vietnam

ABSTRACT: Pilot tests of a cubic-lattice-based rotating biological contactor were implemented to remove organic matter from wastewater from a milk factory and a hospital in Vietnam. In the milk factory wastewater, the biochemical oxygen demand (BOD) removal ratio was stable between 60% and 90% (average 75%) using this method, with a BOD surface load of 0.002–0.020 kg•m^{-2}•day^{-1}. The average nutrient ratio of the raw wastewater was 0.13 of total nitrogen and 0.015 of total phosphorus compared with 1.0 of BOD. The BOD of treated water was less than 50 mg•L^{-1}, achieving category B of the industrial wastewater standard of Vietnam (QCVN 40:2011). For the hospital wastewater, the BOD removal ratio was stable between 60% and 90% (average 78%), with a BOD surface load of 0.005–0.022 kg•m^{-2}•day^{-1}. The average nutrient ratio of the raw wastewater was 0.25 of total nitrogen and 0.018 of total phosphorus compared with 1.0 of BOD. The BOD of treated water was less than 50 mg•L^{-1}, satisfying category B of the medical wastewater standard of Vietnam (QCVN 28:2010/BTNMT). The electric power consumption was 0.73 KWh•m^{-3} of wastewater. The sludge conversion ratio from BOD was 0.51 kg TSS•kg BOD^{-1} based on the excess sludge and suspended solids in raw wastewater and treated water.
Keywords: Organic Matter, Rotating Biological Contactor, Wastewater, Vietnam

1. INTRODUCTION

A rotating biological contactor comprises a number of disc-shaped rotating contactors. Approximately 40% of the contactor surface is dipped into wastewater in a reactor [1]. The contactors are rotated by an electric motor through their axes (Fig.1). Microorganisms adhere on the surface of the contactor, forming a film known as a biofilm. The biofilm decomposes organic matter in wastewater by taking up oxygen when the biofilm emerges from the wastewater.

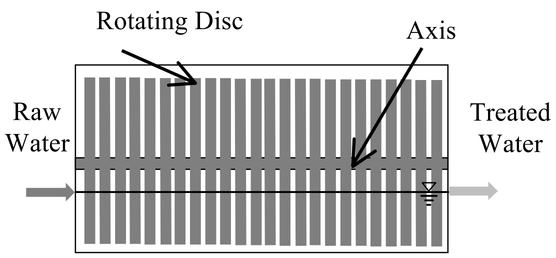

Fig.1 Schematic of the rotating biological contactor

The rotating biological contactor disk used for this research is illustrated in Fig.2. The disk comprises a cubic lattice made from polypropylene to ensure a larger surface area. The manufacturer is Sekisui Aqua Systems Co., Ltd [2].

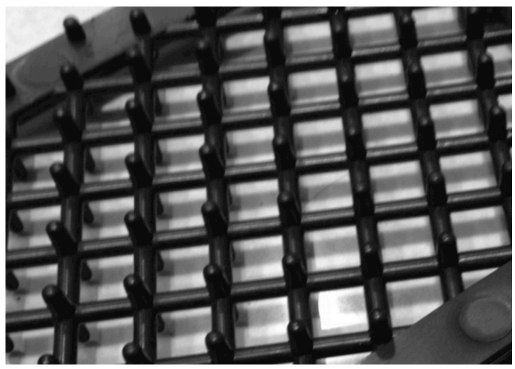

Fig.2 Disk of the rotating biological contactor

This wastewater treatment process does not use a blower for aeration to supply oxygen to wastewater, and thus does not consume more energy compared with the activated sludge process.

This process is widely used for industrial wastewater treatment in Japan and Europe [3][4][5][6][7], and has been researched and developed for mainly wastewater treatment of small and medium sized factories, and in developed countries so far. The manufacturer has experiences for industrial wastewater treatment using this process, mainly in Japan. However, they are not yet used in Vietnam and other Asian countries, and nor are they used for sewage treatment, even in Japan.

The manufacturer recently starts manufacturing apparatus of the process in China for promoting sales.

This research had two aims: to apply this process to industrial wastewater to remove organic matter in Vietnam, and to use the process for sewage treatment to remove organic matter. The sites of the pilot tests of the research were a milk factory and a hospital in Hanoi city.

The main industry of Vietnam is agriculture, mainly rice cropping, with an active livestock industry in mountainous areas and a substantial fishing industry on the coast. In recent years, the Vietnamese diet has become increasingly westernized, so the consumption of milk and milk products has gradually increased and the amount of milk and milk products in Vietnam has risen.

However, many factories have not conducted appropriate wastewater treatment, and the water quality of public waters such as rivers and lakes has deteriorated. Both factories and public facilities such as hospitals have not treated wastewater properly.

Industrial wastewater standards have been established by law (called QCVN 40:2011), as have medical wastewater standards (called QCVN 28:2010/BTNMT). The values for biochemical oxygen demand (BOD) and chemical oxygen demand (COD) of both standards are listed in Tables 1 and 2. BOD analysis uses the five-day method, based on the Vietnamese standard, as for the Japan Industrial Standard and USEPA methods. COD analysis uses potassium dichromate as an oxidizing agent, based on the Vietnamese standard, which is the same as the USEPA method.

In the Vietnamese standards, category A means that the treated water outlet is located in public water that is a water source for domestic and industrial use; category B means that the treated water outlet is not located in public water that is a water source for domestic and industrial use.

Table 1 BOD and COD of QCVN 40:2011

Items	Unit	Category A	Category B
BOD	$mg \cdot L^{-1}$	30	50
COD	$mg \cdot L^{-1}$	75	150

Table 2 BOD and COD of QCVN 28:2010/BTNMT

Items	Unit	Category A	Category B
BOD	$mg \cdot L^{-1}$	30	50
COD	$mg \cdot L^{-1}$	50	100

2. OBJECTS AND METHODS

Objects of the research are to remove organic matter such as BOD and COD under each standard continuously and confirm sludge production of this process.

Two pilot tests used the same test plant, the specifications of which are listed in Table 3.

To confirm the removal capability of organic matter in terms of BOD and COD, inlet samples were obtained between the flow control unit and the reactor, and outlet samples were taken between the reactor and the equalizing tank. BOD removal was calculated using Eq. (1). COD removal was calculated using Eq. (2) [1].

Table 3 Specifications of the test plant

Component	Flow Control Unit – Reactor with Disks – Equalizing Tank – Sedimentation Tank
Reactor Volume	1.78 m^3
Diameter of Disk	1.2 m
Total Surface Area of Disks	420 m^2
Electric Power	1.5 KW
Design Drainage Discharge	30 $m^3 \cdot day^{-1}$

$$\boldsymbol{BOD\ Removal}\ (\%) = \frac{\boldsymbol{BOD_{Inlet} - BOD_{Outlet}}}{\boldsymbol{BOD_{Inlet}}} \times \mathbf{100} \quad (1)$$

$$\boldsymbol{COD\ Removal}(\%) = \frac{\boldsymbol{COD_{Inlet} - COD_{Outlet}}}{\boldsymbol{COD_{Inlet}}} \times \mathbf{100} \quad (2)$$

The BOD surface load was calculated using Eq. (3) [1].

$$\boldsymbol{L_{Surface}} = \frac{\boldsymbol{L_f \times Q}}{\boldsymbol{A}} \quad (3)$$

$L_{Surface}$: BOD surface load (kg $BOD \cdot m^{-2} \cdot day^{-1}$)
L_f: BOD inlet ($mg \cdot L^{-1}$)
Q: Inlet flow ($m^3 \cdot day^{-1}$)
A: Total surface area of disks (m^2)

The hydraulic detention time (HDT) was calculated using Eq. (4) [1].

$$\boldsymbol{HDT(hours)} = \frac{\boldsymbol{Reactor\ Volume\ (m^3)}}{\boldsymbol{Q(m^3 \cdot day^{-1})}} \times \mathbf{24} \quad (4)$$

Equation (5) was used to calculate the hydraulic loading rate [8].

$$\boldsymbol{Hydraulic\ loding\ rate(m^3 \cdot m^{-2} \cdot day^{-1})} = \frac{\boldsymbol{Q(m^3 \cdot day^{-1})}}{\textbf{Total Surface Area of Discs}\boldsymbol{(m^2)}} \quad (5)$$

In addition, the total nitrogen (TN) and total phosphorus (TP) levels of the samples were analyzed to assess the relations of these parameters with BOD, based on Vietnamese standards.

2.1 Milk Factory

The milk factory is located in Hanoi city. The designed drainage discharge of the factory is 300 $m^3 \cdot day^{-1}$; however, it was operated at 100 to 250 $m^3 \cdot day^{-1}$ during the pilot test. The factory has a wastewater treatment plant that uses a trickling filter process and an activated sludge process.

The pilot test plant was installed in front of the existing wastewater treatment plant. Water samples in the form of raw water for the pilot test were obtained at the equalizing tank of the existing wastewater treatment plant, as shown in Fig.3.

The pilot test at the milk factory ran from July 2013 to January 2014. During this time, samples were taken at the inlet and outlet on 28 occasions. The inlet BOD was 40–320 $mg \cdot L^{-1}$, inlet COD was 140–640 $mg \cdot L^{-1}$, inlet TN was 1.0–46 $mg \cdot L^{-1}$, and inlet TP was 0.2–3.3 $mg \cdot L^{-1}$. The average ratio of BOD, TN, and TP was 100 BOD: 13 TN: 1.5 TP. The average inlet flow was 29 $m^3 \cdot day^{-1}$, so the average HDT was approximately 1.5 hours and the hydraulic loading rate was 0.07 $m^3 \cdot m^{-2} \cdot day^{-1}$.

Figure 4 shows rotating disks with biofilm in the reactor at the milk factory.

Fig.3 The pilot test plant at the milk factory

Fig.4 Rotating disks with biofilm at the milk factory

2.2 Hospital

The hospital is located in Hanoi city. The hospital has approximately 800 beds and an average drainage discharge of 400 $m^3 \cdot day^{-1}$. The hospital has a wastewater treatment plant that uses an anaerobic treatment process and a trickling filter process. The wastewater is mainly from the linen room.

The pilot test plant was installed in front of the existing wastewater treatment plant. During the pilot test, raw water samples were obtained at the equalizing tank of the existing wastewater treatment plant, as shown in Fig.5.

The pilot test at the hospital was conducted from July to December 2014. During this period, samples were taken at the inlet and outlet on thirteen occasions. The inlet BOD was 51–270 $mg \cdot L^{-1}$, inlet COD was 91–300 $mg \cdot L^{-1}$, inlet TN was 21–44 $mg \cdot L^{-1}$, and inlet TP was 1.1–3.5 $mg \cdot L^{-1}$. The average ratio of BOD, TN, and TP was 100 BOD:25 TN:1.8 TP. The average inlet flow was 31 $m^3 \cdot day^{-1}$, so the average HDT was approximately 1.4 hours and the hydraulic loading rate was 0.07 $m^3 \cdot m^{-2} \cdot day^{-1}$.

For the hospital, the production of the sludge generated in the reactor was calculated.

Figure 6 shows rotating disks with biofilm in the reactor at the hospital.

Fig.5 The pilot test plant at the hospital

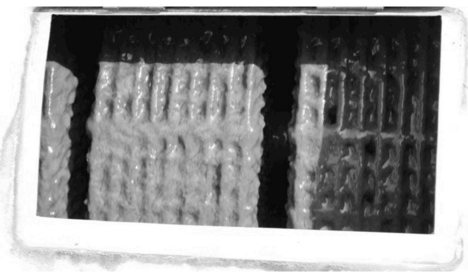

Fig.6 Rotating disks with biofilm at the hospital

3. **RESULTS AND DISCUSSION**

3.1 Milk Factory

Figure 7 shows the BOD of the inlet and the outlet, and the BOD surface load for the milk factory. The average BOD surface load was 0.009 kg BOD•m^{-2}•day^{-1}. At the beginning of the test, BOD removal was lower, but it gradually increased with time. The average value of BOD removal was 75%. The BOD outlet value was less than 50 mg•L^{-1}, falling into category B of the industrial wastewater standards of Vietnam, except at the beginning of the test, and the BOD of half of the samples was less than 30 mg•L^{-1}, satisfying category A of the Vietnamese standard.

Figure 8 shows the relation between BOD removal and BOD surface load. These results indicate that more than 60% of BOD could be removed irrespective of the BOD surface load, which was less than 0.020 kg BOD•m^{-2}•day^{-1} in almost all cases.

Figure 9 shows the COD measurements for the inlet and outlet of the milk factory. Similarly to the BOD results, COD removal was lower at the beginning of the pilot test; however, COD removal gradually rose, and the average COD removal was 72%. According to the industrial wastewater standards of Vietnam, 64% of the outlet COD values were less than 75 mg•L^{-1}, falling into category B.

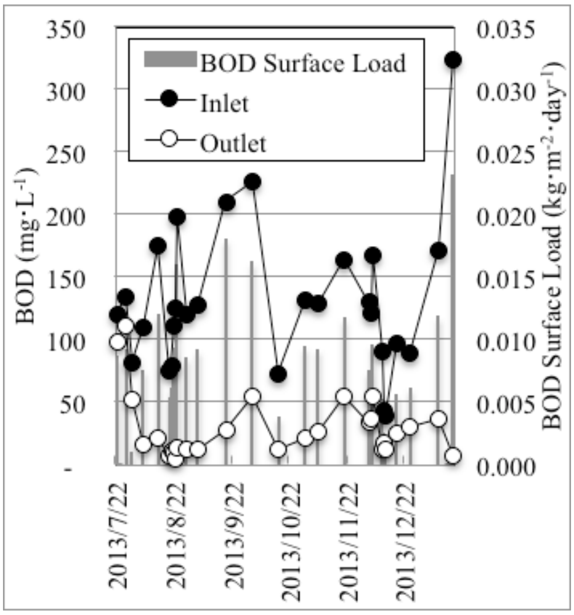

Fig.7 BOD and BOD surface load of the milk factory

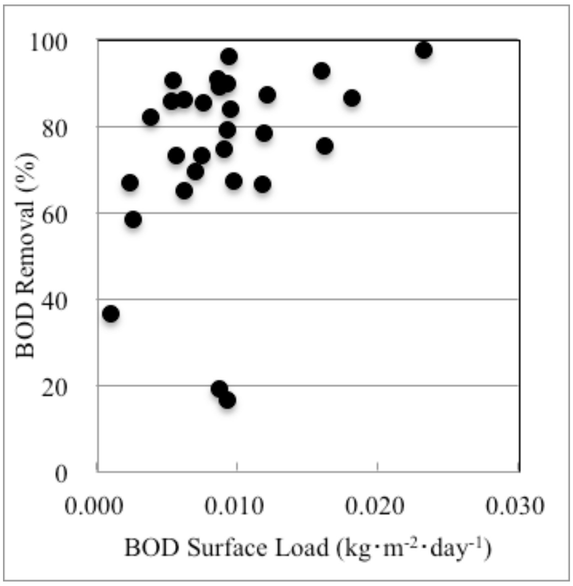

Fig.8 Relation between BOD removal and BOD surface load for the milk factory

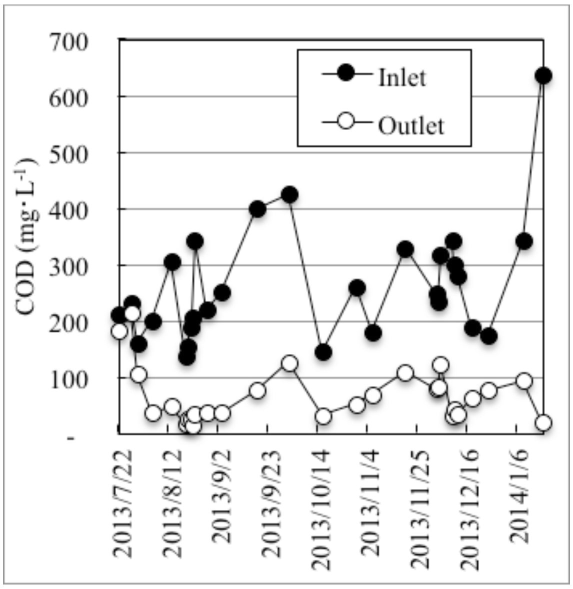

Fig 9. COD of the milk factory

3.2 Hospital

Figure 10 shows the inlet and outlet BOD and BOD surface load of the hospital. The average BOD surface load was 0.010 kg BOD•m^{-2}•day^{-1}. The BOD of the inlet gradually increased from 51 mg•L^{-1} to 270 mg•L^{-1}; however, the outlet BOD was always less than 50 mg•L^{-1}, falling into category B of the medical wastewater standards of Vietnam. Approximately 60% of the outlet BOD measurements were less than 30 mg•L^{-1}, satisfying category A of the Vietnamese standard.

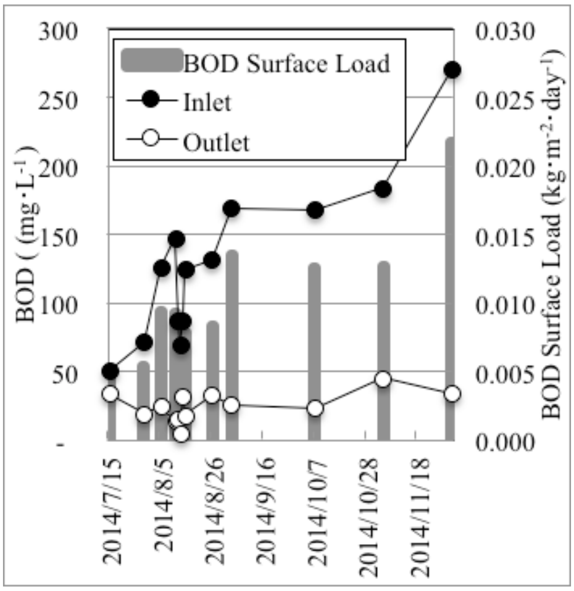

Fig.10 BOD and BOD surface load of the hospital

Figure 11 shows the relation between BOD removal and BOD surface load. The graph indicates that more than 60% of BOD could be removed in most cases, irrespective of the BOD surface load, which was less than 0.015 kg BOD•m^{-2}•day^{-1}.

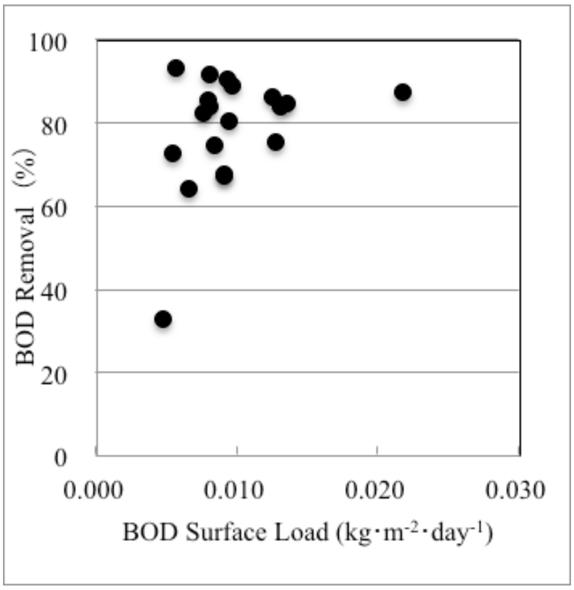

Fig.11 Relation between BOD removal and BOD surface load for the hospital

Figure 12 shows the inlet and outlet COD measurements for the hospital. Similarly to the BOD results, the inlet COD values gradually increased from 91 mg•L^{-1} to 300 mg•L^{-1}. However, the outlet COD was always less than 100 mg•L^{-1}, falling into category B of the medical wastewater standards of Vietnam. Approximately 70% of the outlet COD values were less than 50 mg•L^{-1}, satisfying category A of the Vietnamese standard.

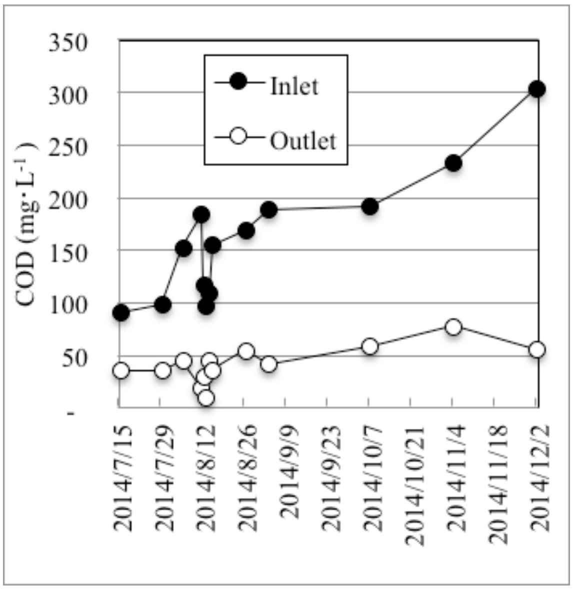

Fig.12 COD of the hospital

For the calculation of the sludge production in the reactor, samples from the inlet and outlet and samples after the sedimentation tank were obtained to measure BOD and TSS in January 2015. The BOD and TSS results are provided in Table 4. The sludge in the sedimentation tank of the pilot test plant was produced at a rate of 0.63 m^3•day^{-1}.

The amount of sludge generated was 1.17 kg•day^{-1} and the removed BOD volume was 2.3 kg•day^{-1}, so the sludge conversion rate was 0.51 kg TSS•kg BOD^{-1}.

Table 4 BOD and TSS values for sludge production

Items	Unit	Inlet	Outlet	After Sed. Tank
BOD	mg•L^{-1}	92	28	-
TSS	mg•L^{-1}	41	36	2,140

During the period of the pilot test, the pilot test plant treated 6,140 m^3 of water and consumed 4,500 KWh of electric power, representing an electric power consumption of 0.73 KWh• m^{-3} of wastewater.

4. CONCLUSION

According to [2], the design criteria for rotating biological contactors are a hydraulic loading rate of 0.08–0.16 m^3•m^{-2}•day^{-1}, a surface load of 0.0098–0.0172 kg BOD•m^{-2}•day^{-1}, HDT of 0.7–1.5 hours, and BOD in the effluent of 15–30 mg•L^{-1}. For the milk factory, the hydraulic loading rate was 0.07 m^3•m^{-2}•day^{-1}, the average surface load was 0.009 kg BOD•m^{-2}•day^{-1}, HDT was 1.5 hours, and the average BOD in the effluent was 30 mg•L^{-1}. For the hospital, the hydraulic loading rate was 0.07

$m^3 \cdot m^{-2} \cdot day^{-1}$, the average surface load was 0.010 kg $BOD \cdot m^{-2} \cdot day^{-1}$, HDT was 1.4 hours, and the average BOD in the effluent was 25 $mg \cdot L^{-1}$. Thus, both pilot tests almost fulfill the design criteria.

According to [3], the required sludge conversion rate for rotating biological contactors is 0.75–1.0 kg $TSS \cdot kg\ BOD^{-1}$; however, the sludge conversion rate of the pilot test at the hospital was 0.51 kg $TSS \cdot kg\ BOD^{-1}$.

From this pilot testing, the rotating biological contactor formed of a cubic lattice can be applied for the removal of organic matter from industrial wastewater and sewage water in Vietnam. In addition, there were no mechanical troubles during the pilot test.

5. ACKNOWLEDGEMENTS

This research had been supported by Sekisui Aqua Systems Co., Ltd and Osaka prefectural government, and funded by the ministry of the environment in Japan.

6. REFERENCES

[1] "Technology and Regulation for Pollution Control", Water Quality Series, Japan Environmental Management Association for Industry, 2016 (In Japanese).

[2] Web Site of Sekisui Aqua Systems Co., Ltd http://www.sekisuia.co.jp/english/plant/product/esrotae/index.html

[3] Web Site of Japan Protect of Environment Co.,Ltd (In Japanese) http://www.jpex-net.co.jp/products/index.html

[4] Arasuna, M., Advanced Wastewater Treatment Now -Ideal Development of Rotating Biological Contactor for Wastewater from Small and Medium Sized Factories-, Journal of Global Environment, Vol.31 、 No.4 、 p.146-147 、 2000 (In Japanese)

[5] Fukuda, F., Improvement of Biofilm Methods of Resource Recycling Type Wastewater Treatment Technology -Review of Rotating Biological Contactor-, Journal of Chemical Apparatus, Vol.43, No.8, pp.29-35, 2001 (In Japanese)

[6] Nishidome, K., etc., Wastewater Treatment using Rotating Biological Contactor, Journal of Water and Waste, Vol.43, No.2, pp.125-140, 2001 (In Japanese)

[7] Winkler G., etc., Mass Flow Balances of Triclosan in Small Rural Wastewater Treatment Plants and the Impact of Biomass Parameters on the Removal, English Life Science, Vol.7, No.1, pp.42-51, 2007

[8] Marcos von Sperling, Activated Sludge and Aerobic Biofilm Reactors. Biological Wastewater Treatment Series, IWA, Vo1.5, 2007, pp.287-293.

GREEN INNOVATION OF CALCIUM SULFATE OR GYPSUM PREPARATION FROM DUCK EGGSHELL VIA PYROLYSIS

Nuchnapa Tangboriboon[1]* and Wanitcha Unjan[2]
[1*, 2] Materials Engineering Department, Faculty of Engineering, Kasetsart University, Bangkok 10900, Thailand

ABSTRACT

Calcium sulfate dihydrate is an important material for construction i.e. wall, roof, and decorative parts. It can be made from calcium carbonate from duck eggshell react to sulfuric acid at room temperature (25ºC). Calcium sulfate dihydrate was dried in an oven at 110ºC and calcined at 700°, 800°, and 900°C for 2 hr. It can change the microstructure from calcium sulfate hemihydrate or plaster of Paris ($CaSO_4.0.5H_2O$) to anhydrite or anhydrous calcium sulfate. The best condition to obtain the calcium sulfate or gypsum is calcined at 900°C for 2 hr. The best anhydrous calcium sulfate or anhydrite calcined at 900°C for 2 hr has true density, color, specific surface area, avg. pore diameter, and avg. particle size equal to 2.95 g/cm^3, white powder, 3.57 m^2/g, 96.98 Å, and 3.983 µm, respectively. In addition, characteristics, microstructures, phase transformation, and physical properties of raw materials and calcium sulfate compounds are reported here by using XRF, SEM, XRD, pycnometer method, and BET.

Keywords: Calcium sulfate, Duck eggshell, Pyrolysis, Anhydrite, Construction.

INTRODUCTION

Calcium sulfate is a ceramic material useful for many kinds of industrial applications i.e. a binder for building material, bone graft materials, periodontal disease treatment, endodontic lesions, alveolar bone loss, maxillary sinus augmentation, filler for plastic, rubber, coating, construction materials, desiccant, coagulant, and catalysts [1-3]. Calcium sulfate compounds in terms of γ-or β-anhydrite namely anhydrous calcium sulfate, calcium sulfate hemihydrate or plaster of Paris, and gypsum are the most abundant sulfate mineral found in the nature [4]. Natural gypsum or calcium sulfate dihydrate is a monoclinic-prismatic mineral with a layered crystal lattice containing the water. When the calcium sulfate dihydrate heated, it can be converted to the metastable hemihydrate and anhydrite type III. Anhydrite type III can be transformed to anhydrite type II with the most densely packed ion lattice and does not react very readily with water at high temperature [5]. Therefore, phase transformation, crystal structure, morphology, and growth rate of calcium sulfate depend on temperature, pressure, dissolved electrolytes or organics, and other minerals [4]. Furthermore, there are many types calcium sulfate i.e. calcium sulfate dihydrate or gypsum, subhydrate calcium sulfate ($CaSO_4.0.81H_2O$), α- and β-hemihydrate calcium sulfate ($CaSO_4.1/2\ H_2O$), calcium sulfate anhydrite I, II, and III [6-12]. The synonyms, characteristics (color, odor, and density values), crystal structures, chemical solubility performances, physical-optical-mechanical properties (translucence, refractive index, hardness, etc.) and their applications are some differences. The calcium sulfate compounds can be prepared from a variety of processes i.e. dissolved in aqueous sulfuric acid, flue gas desulfurization (FGD), reverse micro-emulsion, chemical precipitation, ion exchange, adsorption, reverse osmosis and electro-chemical methods, etc. [13-21].

Eggshell is a calcium carbonate source obtained by consuming and industries as food, drug, cosmetics, filler in other industries, etc. The by-product eggshell represents about 11% of the total weight approximately 60 g of an egg [22-24]. The main composition of eggshells is calcium carbonate ($CaCO_3$) known as calcite more than 94 wt% and the other oxides including organic compounds 6 wt% [22-24]. Eggshell is potential to be used as a useful waste in a variety of applications [22-27].

The objective in this research, the raw duck eggshell was used as a calcium carbonate to react with sulfuric acid under calcination temperature in order to obtain the calcium sulfate compounds i.e. calcium sulfate dihydrate or gypsum, hemihydrate or plaster of Paris, and anhydrite. The characteristics, micro- structures, phase transformation, and physical properties of samples were reported here by using XRF, SEM, XRD, pycnometer method, and BET.

EXPERIMENTAL

Materials and Methods

Duck eggshell was collected from the cafeteria at Kasetsart University, Thailand**.** The duck eggshells were cleaned with tap water, dried in the air for 2 days, and ground with high speed mill for 120 min. ***Hydrosulfuric acid (H_2SO_4)*** is high purity 98% and was purchased from Arsom Co., Ltd., Thailand. Hydrosulphuric acid is colorless, odorless, melting temperature at 104°C and 1.0 atm.

Instruments

Muffle furnace (Nebertherm, Ceramotherm with thermocouple type K, NiCr-Ni) was used to calcine samples with a heating rate of 10°C/min. The precipitate calcium sulfate powder prepared from the reaction between duck eggshell and concentrated sulfuric acid at room temperature was calcined at temperature 700°, 800°, and 900°C for 2 hr with a heating rate of 10ºC/min. ***High speed mill*** model RM 1105 with speed 500 rpm was supplied by Compound Clay Co., Ltd., Thailand. The rapid mill is a porcelain pot containing the amount of 2/3 porcelain ball mills of the porcelain pot volume. The rapid mill was used for grinding the duck eggshell to be fine powder for the calcium sulfate preparation. ***X-ray diffraction (XRD)*** was taken and analyzed using a Bruker AXS analyzer (D8 Discover) with VANTEC-1 Detector. Samples were analyzed using a double-crystal wide-angle goniometry. Scans were measured from 5°- 80° 2θ at a scan speed of 5° 2θ/min in 0.05° or 0.03° 2θ increments using CuK_α radiation (λ = 0.15406 nm). Peak positions were consistent with those of the International Center for Diffraction Data Standard (JCPDS) patterns to identify crystalline phases. ***Scanning Electron Microscope (SEM)*** was taken and characterized using SEM, JEOL-5200. The samples of raw material and calcium sulfate compound were mounted on a stub using carbon paste and were sputter-coated to ~0.1 µm of gold to improve conductivity. The acceleration voltages of 11 and 13 kV with magnifications of 1000 and 5000 times were used.

Calcium Sulfate Powder Preparation ($CaSO_4$. $2H_2O$, $CaSO_4.0.5H_2O$, and $CaSO_4$)

The duck eggshell ground for 120 min acted as calcium carbonate source ($CaCO_3$) to react with sulfuric acid at room temperature (25ºC) as equations (1), (2), (3) and (4):

$$2CaCO_3+2H_2SO_4 \longrightarrow 2CaSO_4.2H_2O+2CO_2 \quad (1)$$

Gypsum or calcium dihydrate

$$2CaO+2H_2SO_4 \longrightarrow 2CaSO_4.2H_2O \quad (2)$$

$$2CaSO_4.2H_2O \xrightarrow[\Delta]{} CaSO_4.0.5H_2O+1.5H_2O \quad (3)$$

Calcium hemihydrate

$$CaSO_4.0.5\ H_2O \xrightarrow[\Delta]{} CaSO_4+0.5H_2O \quad (4)$$

When the $CaCO_3$ reacts to H_2SO_4, the precipitated calcium sulfate or calcium sulfate dihydrate powder was filtered, rinsed with tap water 2-3 times, and dried in the oven at 110°C for 24 hr. Calcium sulfate dihydrate can transform to calcium sulfate hemihydrate according to the equation (3). After that, the dried calcium sulfate hemihydrate powder was calcined at 700°, 800°, and 900°C for 2 hr. Calcium sulfate hemihydrate converted to anhydrite or anhydrous calcium sulfate according to the equation (4). The obtained calcined powder was measured the physical properties and characterized by SEM, XRD, particle size distribution, BET, and pycnometer measure ment.

RESULTS AND DISCUSSION

Characteristics of Raw Material and Calcium Sulfate Powder

The chemical composition comparison of duck eggshell and calcined duck eggshell was measured by XRF as data tabulated in Table 1. The main raw duck eggshell composed of calcium carbonate ($CaCO_3$) 98.101 wt% and other oxide compounds 1.899 wt%. While the calcined duck eggshell composed of calcium oxide (CaO) 97.805 wt% and the other oxide compounds such as MgO, Na_2O, K_2O, SiO_2, etc. 2.195 wt%. However, both of raw duck eggshell and calcined duck eggshell can react to sulfuric acid at room temperature (25ºC) according to the equations (1) and (2) to obtain calcium sulfate dihydrate or gypsum. When calcium sulfate dihydrate was heated, it can be transformed to calcium hemi hydrate or plaster of Paris and anhydrite according to equations (3) and (4), respectively.

Physical Properties and Microstructures of Calcium Sulfate Powder

The physical properties (average particle size, true density, specific surface area, and average pore diameter) of raw duck eggshell and anhydrous calcium sulfate calcined at 800º and 900ºC for 2 hr were measured and reported as data tabulated in Table 2. The particle size distribution at d_{90}, d_{50}, d_{10}, and d_{avg} of raw duck eggshell is 90.02, 15.75, 1.55, and 34.35 µm, respectively. The true density, specific surface area, and average pore diameter of the raw duck eggshell are 2.25 g/cm^3, 7.79 m^2/g, and 196.90 Å, respectively. While the particle size distribution at d_{90}, d_{50}, d_{10}, and d_{avg} of calcium sulfate calcined at 900°C for 2 hr is equal to 7.39, 3.13, 1.08, and 3.99 µm, respectively. Furthermore, the true density, specific surface area, and average pore diameter of calcium sulfate calcined at 900°C for 2 hr for 2 hr are 2.95 g/cm^3, 3.57 m^2/g, and 96.98

Å, respectively. The porosity of calcium sulfate calcined at 900°C for 2 hr is in the range of meso-porous structure (20Å-500Å). The physical properties of the raw duck eggshell i.e. particle size and shape, specific surface area, true density, solubility, etc., are important factors of calcium sulfate formation and its applications [6, 29-31].

Raw duck eggshells		Calcined duck eggshells	
Compounds	Weight (%)	Compounds	Weight (%)
Na_2O	0.204	Na_2O	0.161
MgO	0.286	MgO	0.656
Al_2O_3	0.035	SiO_2	0.255
SiO_2	0.073	P_2O_5	0.775
P_2O_5	0.443	SO_3	0.215
SO_3	0.764	Cl	0.053
Cl	0.035	K_2O	0.059
K_2O	0.038	CaO	97.805
$CaCO_3$	98.101	SrO	0.019
CuO	0.009		
SrO	0.013		

Table 1 Chemical composition of raw materials measured by XRF

Samples	Avg. particle size (μm)	True density (g/cm^3)	Specific surface area (m^2/g)	Avg. pore diameter (Å)
Raw duck eggshell	34.35	2.25	7.79	196.90
$CaSO_4$ calcined at 800ºC	5.560	2.87	N/A	N/A
$CaSO_4$ calcined at 900ºC	3.983	2.95	3.57	96.98

Table 2 Physical properties of samples

The XRD peak patterns of raw duck eggshell before firing and dried calcium sulfate compounds obtained from raw duck eggshell react to sulfuric acid calcined at 700°, 800°, and 900°C, for 2 hr, as shown in Fig. 1. The XRD peak pattern of raw duck eggshell shows the crystalline phase formation of rhombohedral or calcite consistent with the JCPDS file no. 01-086-2339 at the (hkl): (104) 29.364°, (012) 23.058°, and (113) 39.424° while the XRD peak pattern of calcined raw duck eggshell shows the crystalline phase formation of lime or calcia consistent with the JCPDS file no. 00-037-1497 at the (hkl): (200) 37.347°, (220) 53.856°, and (111) 32.204°. The main XRD peak pattern of the dried precipitated calcium sulfate powder before firing shows the rhombohedral structure of calcium sulfate hemihydrate consistent with JCPDS file no. 01-070-0909 at the (hkl): (020) 25.432º, (104) 29.364º, (012) 31.366º, (022) 38.648º, (212) 40.820º, and (032) 48.696º. Then, the dried precipitated samples, calcium sulfate hemihydrate powder calcined at 700° and 800°C for 2 hr, show the same XRD peak patterns of metastable phase of anhydrous calcium sulfate in hexagonal phase formation consistent with the JCPDS file nos. 01-089-1458 and 01-070-0909 at the (hkl): (100) 14.665°, (200) 29.577°, (102) 32.011° and (020) 25.432°, (012) 31.366°, and (212) 40.820°, respectively, mixed with small amount of the calcium hydroxide or portlandite ($Ca(OH)_2$) belong to orthorhombic consistent with the JCPDS file no. 00-004-0733 at the (hkl): (101) 34.089°, (102) 47.124°, and (110) 50.795°. Furthermore, the dried precipitated calcium sulfate dihydrate sample calcined at 900°C for 2 hr, shows the stable crystalline phase formation of hexagonal namely anhydrite structure ($CaSO_4$) consistent with the JCPDS file no.01-089-1458 at the (hkl): (020) 25.432°, (012) 31.366°, and (022) 38.648°, respectively, consistent with the anhydrite crystal structure obtained by Zhao, Wu et al [3]. Therefore, the obtained XRD phase transformation of calcium sulfate dihydrate suggests it can transform to calcium sulfate hemihydrate or plaster of Paris ($CaSO_4.0.5H_2O$) or anhydrite crystal structures depending on firing temperature and firing time consistent with the calcium sulfates equations (1)-(4) of dehydration-rehydration.

The SEM micrographs of duck eggshell powder, calcium sulfate hemihydrate powder before firing, and dried precipitated calcium sulfate hemihydrate powder calcined at 700°, 800°, and 900°C with the magnifications of 1000 and 5000 times as shown in Fig. 2. The SEM micrographs of ground raw duck eggshell powder show the particulate agglomeration and non-uniform size as shown in Figures 2a and 2a-1. The SEM micrographs of the precipitated calcium sulfate hemihydrate powder dried at 110ºC without firing show uniform needle shape crystal structure consistent with the results obtained by Freyer, D et al. [4], Licong, D. et al. [13], and Azimi G. et al. [32]. The SEM microstructures show particles agglomeration and microstructure changing from the needle shape to plate- or disk-like shape due to phase transformation at the firing temperature 700°C as shown in Figures 2c and 2c-1 consistent with the SEM results obtained by Gartner, E.M. [33]. Then, the microstructures changed to more plate-like due to crystallization as a metastable phase at firing temperature 800°C as shown in Figures 2d and 2d-1. Furthermore, the microstructures changed and crystallized completely to form the small rod-like in shape belonging to stable anhydrite at calcination temperature 900°C as shown in Figures 2e and 2e-1 consistent with the SEM results obtained by Azimi G. et al. [32].

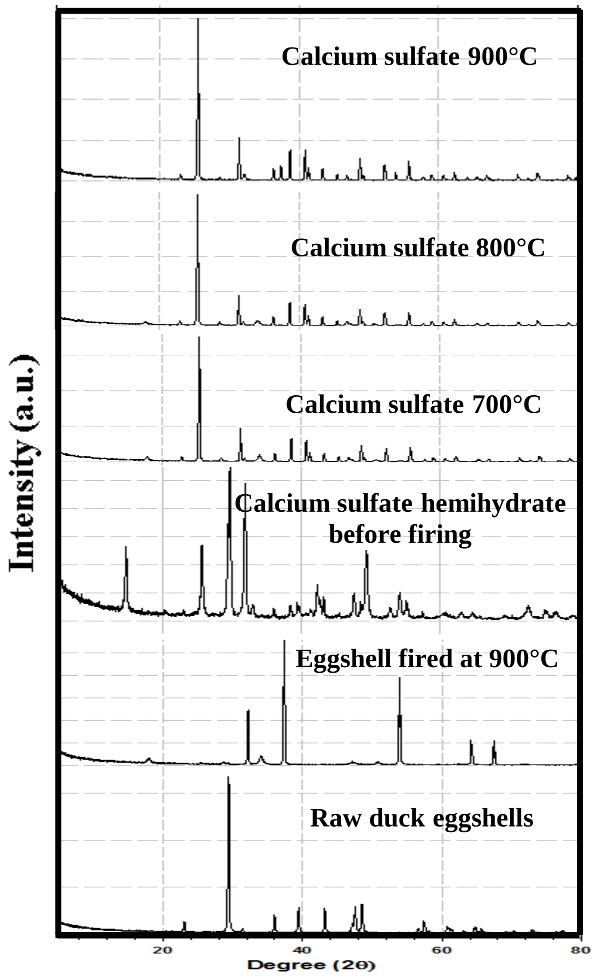

Fig.1 XRD peak patterns of raw duck eggshell before calcination and dried calcium sulfate hemihydrate powder calcined at 700°, 800°, and 900°C, for 2 hr, respectively.

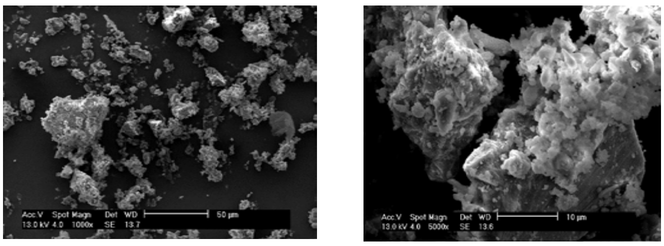

a) a-1)

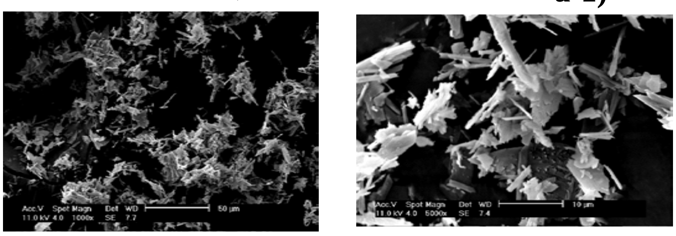

b) b-1)

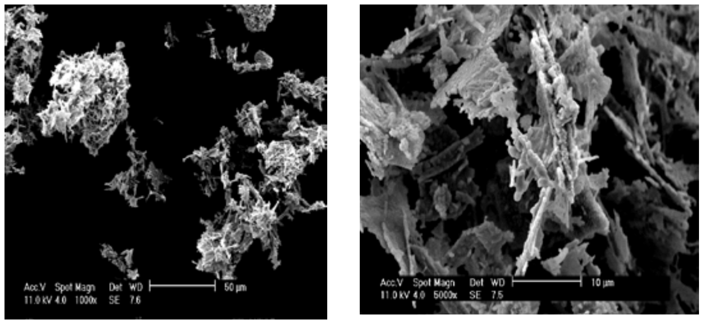

c) c-1)

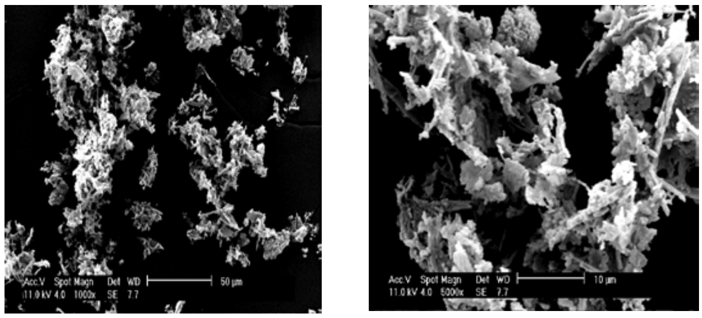

d) d-1)

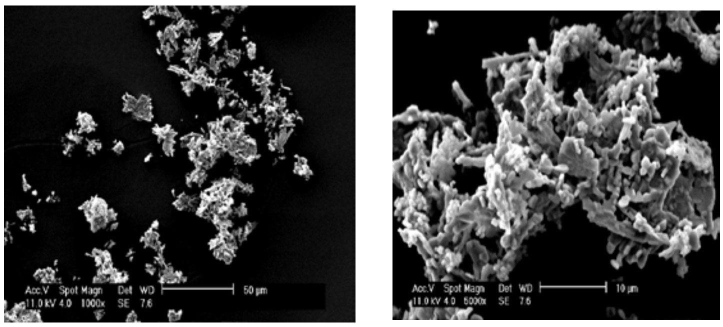

e) e-1)

Fig. 2 SEM micrographs of samples with the magnifications of 1000 and 5000 times: a) and a-1) raw duck eggshell powder; b) and b-1) calcium sulfate hemihydrate ($CaSO_4.0.5H_2O$) powder before firing; c) and c-1) calcium sulfate hemihydrate powder calcined at 700°C; d) and d-1) calcium sulfate hemihydrate powder calcined at 800°C; and e) and e-1) calcium sulfate hemihydrate powder calcined at 900°C.

CONCLUSIONS

Duck eggshell is a potential starting material for use as a calcium carbonate ($CaCO_3$) source to react with sulfuric acid in order to prepare the calcium sulfate dihydrate or gypsum, calcium sulfate hemihydrate or plaster of Paris, and stable anhydrite in terms of $CaSO_4.xH_2O$ (x = 0.0-2.0) by thermal process. Calcium sulfate can form hydration and dehydration process due to water adsorption-desorption ability within the layer microstructure. Calcium sulfates have a potential candidate functioned as a binder, filler, adsorbent, catalyst, and coagulant in a variety of buildings, ceramics, petroleum and petrochemical, dental and mechanical industries. Calcium sulfate dihydrate or gypsum is one of important materials suitable for building and mold making, etc., whereas anhydrite or anhydrous calcium sulfate is suitable for function as a filler in various industries such as paint, plastic, rubber, coating, cement, etc. [34-36]. There are many advantages of chemical precipitation method used in this study for calcium sulfate compounds preparation i.e. easily and convenient forming, low price, and high purity calcium sulfate including waste eggshell reduction. The obtained calcium sulfate dihydrate or gypsum can form at room temperature. When the calcium sulfate dihydrate was dried at 110ºC and calcined at 700°, 800°, and 900°C for 2 hr effect to the microstructure changing. The microstructure of calcium sulfate dihydrate can transform to calcium sulfate hemihydrate or plaster of Paris and then transform to anhydrite or anhydrous calcium sulfate ($CaSO_4$) type III, type II, and type I. The XRD phase formation of calcium sulfates will change from rhombohedral (gypsum) to hexagonal (anhydrite) crystal structure. The SEM micrograph will change from needle-like shape (hemihydrate or plaster of Paris) to plate- or disk-like, and finally to rod-like shape (anhydrite). The suitable condition to receive the completely anhydrous calcium sulfate is firing at 900°C for 2 hr. The true density, color, odor, specific surface area, average pore diameter, and average particle size of anhydrous calcium sulfate calcined at 900ºC for 2 hr are equal to 2.95 g/cm^3, white powder, odorless, $3.57 m^2/g$, 96.98 Å, and 3.983 µm, respectively.

ACKNOWLEDGEMENTS

The authors sincerely thank the Petroleum and Petrochemical College, and the Scientific and Technological Research Equipment Center, at Chulalongkorn University, Thailand; the Department of Materials Engineering, at Kasetsart University for the use of analytical instruments. We have to thank the Energy and Environmental Engineering Center, Faculty of Engineering, Kasetsart University for eggshell classification. This work is grant supported from Agricultural Research Development Agency (Public Organization) or ARDA of Ministry of Agricultural and Cooperatives, the Thailand Research Fund, encoded PRP5605010080. In addition, we also would like to acknowledge the financial supports from the Conductive and Electroactive Polymers Research Unit of Chulalongkorn University, the Thailand Research Fund (TRF), and the Royal Thai Government.

REFERENCES

[1] Greish, Y.E. Phase evolution during the low temperature formation of stoichiometric hydroxyapatite-gypsum composites, Ceram. Int., Vol. 37, 2011, pp. 715-723.

[2] Orsini, G., Rieei, J., Scarano, A., Pecora, G., Lezzi, G., and Biomed, J., Bone-defect healing with calcium-sulfate particles and cement: an experimental study in rabbit, Mater. Res. B: Appl. Biomater., Vol. 68/2B, 2004, pp. 199-208.

[3] Zhao, W., Yang, H., and Huo, C. Surface nano crystallization modification of anhydrite, Colloids Surf. A: Physicochem. Eng. Aspects, Vol. 393, 2012, pp. 128-132.

[4] Freyer, D. and Voigt, W. Crystaalization and Phase Stability of $CaSO_4$ and $CaSO_4$-Based Salts, Monatshefte für Chemie, Vol.134, 2003, pp. 693-719.

[5] Reisdorf, K. and Abriel, W., System $CaS0_4$ - H_20 über die Na-Polyhalit $Na_2Ca_5(S0_4)_6(H_20)_3$, Neues Jb. Miner. Abh. Vol.157, 1987 S, pp.35-46.

[6] Çetin, E., Eroğlu, İ, and Özkar, S. Kinetics of gypsum formation and growth during the dissolution of colemanite in sulfuric acid, J. Cryst. Growth, Vol. 231, 2001, pp. 559-567.

[7] Hand R. J. Calcium Sulphate hydrates: a re-view, British Ceramic Trans., Vol. 96, 1997, pp. 116-120.

[8] Deer, W. A., Howie, R. A., and Zussman, J. in: An Introduction to the rock-forming mineral, 2nd ed., Longman, London, 1992, pp. 627.

[9] Packter, A., The precipitation of calcium sulphate dihydrate from aqueous solution. Induction periods, crystal numbers and final size, J. Cryst. Growth, Vol. 21/2, 1974, pp. 191-194.

[10] Klepetsanis, P. G., Dalas, E. and Koutsoukos, P.G., Role of temperature in the spontaneous precipitation of calcium sulfate dihydrate, Langmuir, Vol. 15/4, 1999, pp.1534-1540.

[11] Boisvert, J. P., Domenech, M., Foissy, A., Persello, J., and Mutin, J. C., Hydration of calcium sulfate hemihydrate ($CaSO_4$ center dot $1/2H_2O$) into gypsum ($CaSO_4$ center dot $2H_2O$). The influence of the sodium poly (acrylate)/surface interaction and molecular weight, J. Cryst. Growth, Vol. 220/4, 2000, pp. 579- 591.

[12] Kontrec, J., Kralj, D., and Brečević, L. Trans formation of anhydrous calcium sulphate into calcium sulphate dehydrate in aqueous

solutions, J. Cryst. Growth, Vol. 240, 2002, pp. 203-211.
[13] Licong, D., Yifei, Z., Fangfang, C., Shaotao, C., Shaowei, Y., Yan, L., and Yi, Z., Reactive Crystallization of Calcium Sulfate Dihydrate from Acidic Wastewater and Lime, J. Chem. Eng., Vol. 21/11, 2013, pp.1303-1312.
[14] Baltpurvins, K. A. Burns, R. C., Lawrance, G. A., Heavy metals in wastewater: modeling the hydroxide precipitation of copper II from wastewater using lime as the precipitant, Waste Manage., Vol. 16/8, 1996, pp.717-725.
[15] Baltpurvins, K. A., Burns, R. C., Lawrance, G. A., Stuart, A. D., Effect of electrolyte composition on zinc hydroxide precipitation by lime, Water. Res., Vol.31/5, 1997, pp. 973-980.
[16] Dabrowski, A., Hubicki, Z., Podkoscielny, P., and Robens, E., Selective removal of the heavy metal ions from waters and industrial wastewaters by ion-exchange method, Chemosphere, Vol.56/2, 2004, pp. 91-106.
[17] Wingenfelder, U., Hasnsen, C., Furrer, G, Schulin, R., Removal of heavy metals from mine water by natural zeolites, Environ. Sci. Technol., Vol. 39/12, 2005, pp. 4606-4613.
[18] Dipalma, L., Ferrantelli, P., Merli, C., Petrucci, E., Treatment of the solution extracted from metal contaminated soils by reverse osmosis and chemical precipitation, Ann. Chim. (Rome), Vol. 93/12, 2003, pp. 1005-1011.
[19] Lai, C. L. and Lin, K. S., Sludge conditioning characteristics of copper chemical mechanical polishing wastewaters treated by electrocoagulation, J. Hazard. Mater., Vol. 136/2, 2006, pp. 183-187.
[20] Böke, H., Akkurt, S., Özdemir, S., Göktürk, H., and Caner Saltik, E. N., Quantification of $CaCO_3$-$CaSO_3.0.5H_2O$-$CaSO_4.2H_2O$ mixtures by FTIR analysis and its ANN model, Mater. Lett., Vol. 58, 2004, pp. 723-726.
[21] Kong, B., Yu, J., Savino, K., Zhu, Y., and Guan, B., Synthesis of α-calcium sulfate hemihydrate submicron-rods in water/n-hexanol/CTAB reverse microemulsion, Colloids Surf. A: Physicochem. Eng. Aspects, Vol. 409, 2012, pp. 88-93.
[22] Tsai, W. T., Yang, J. M., Lai, C. W., Cheng, Y. H., Lin, C. C., and Yeh, C. W., Characterization and adsorption properties of eggshells and eggshell membrane, Bioresour. Technol., Vol. 97, 2006, pp. 488-491.
[23] Nys, Y., Gautron, J., Garcia-Ruiz, J.M., Hincke, M.T., Avian eggshell mineralization: biochemical and functional characterization of matrix proteins, C. R. Palevol, Vol. 3, 2004, pp. 549-562.
[24] Murakami, F. S. and Rodrigues, P.O., Physico-chemical study of $CaCO_3$ from egg shells, Ciénc. Technol. Aliment., Campinas, Vol. 27/3, 2007, pp. 658-662.
[25] Tangboriboon,N., Kunaruraksapong, R., Sirivat, A., Meso-porosity and phase transformation of bird eggshells via pyrolysis**,** J. Ceram. Process. Res., Vol. 13/4, 2012, pp. 413-419.
[26] Tangboriboon,N., Khongnakhon,T., Kittikul,S., Kunanuraksapong,R., and Sirivat, A., An innovative $CaSiO_3$ dielectric material from eggshells by sol-gel process, J. Sol-Gel Sci. Technol., Vol. 58/1, 2011, pp. 33-41.
[27] Tangboriboon,N., Phudkrachang,P., Kunanuruk sapong,R., and Sirivat,A., REMOVING EXTRACTABLE PROTEINS IN NATURAL RUBBER LATEX BY CALCIUM CHLORIDE FROM CHICKEN EGGSHELLS, RUBBER CHEM. TECHNOL., Vol. 84/4, 2011, pp. 543-564.
[28] Manual of Gas Sorption System," QUANTACHROME INSTRUMENTS, Auto sorb-1, Quantachrome Coorporation, Version 1.19.
[29] Ferreira, J. M. F., Role of the Clogging Effect in the Slip Casting Process, J Eur. Ceram. Soc., Vol. 18, 1998, pp. 1161-1169.
[30] Guan, B., Ye, Q., Wu, Z., Lou, W., and Yang, L., Analysis of the relationship between particle size distribution of α-calcium sulfate hemihydrate and compressive strength of set plaster-Using grey model, Powder Technol., Vol. 200, 2010, pp. 136-143.
[31] Singh, N. B. and Middendorf, B., Calcium sulphate hemihydrate hydration leading to gypsum crystallization, Prog. Cryst. Growth Charact. Mater., Vol. 53, 2007, pp. 57-77.
[32] Azimi, G. and Papangelakis, V. G., Mechanism and kinetics of gypsum-anhydrite transfor mation in aqueous electrolyte solutions, Hydrometallurgy, Vol. 108, 2011, pp. 122-129.
[33] Gartner, E. M., Cohesion and expansion in polycrystalline solids formed by hydration reactions – The case of gypsum plasters, Cem. Concr. Res., Vol. 39, 2009, pp. 289-295.
[34] Singh, M. and Garg, M., Making of anhydrite cement from waste gypsum, Cem. Concr. Res., Vol. 30, 2000, pp. 571-577.
[35] Muraiu, M., Ferreira, A.D.S., Duquesne, E., Bonnaud, L., and Dubois, P., Polylactide (PLA) and highly filled PLA-calcium sulfate composites with improved impact properties, Macromol.Symp., Vol. 272, 2008, pp. 1-12.
[36] Gardette,M., Thérias, S., Gardette, J. I., Muraiu, M., and Dubois, P., Photooxidation of polylactide/calcium sulfate composites, Polym. Degrad. Stab., Vol. 96, 2011, pp. 616-623.

VELOCITY STRUCTURE AND EARTHQUAKE RELOCATIONS AT CENTRAL PENINSULAR MALAYSIA REGION

Abdul Halim Abdul Latiff[1] and Amin Esmail Khalil[2]

[1]Faculty of Geoscience and Petroleum Engineering, Universiti Teknologi PETRONAS, Malaysia
[2]School of Physics, Universiti Sains Malaysia, Malaysia

ABSTRACT

In between 2007 to 2009, there are several earthquake occurrences in Bukit Tinggi and Janda Baik, which are located 50 km from Malaysia capital, Kuala Lumpur. However, the absent of subsurface structural information and crustal velocity data for central peninsular Malaysia region had prevent further analysis on the potential seismic hazard in the area. Thus, this study was carried out in determining the new velocity structure of central Peninsular Malaysia region, while relocate the hypocenter of the local earthquake. Initially, a data conditioning procedure was carried out for both weak and strong motion data from various sources. Then, P-wave and S-wave arrivals were picked on the waveform recorded, before we derived a 1-D velocity model through simultaneous inversion process. The process involved also produced a new hypocenter location based on the new 1-D velocity structure, correcting the original earthquake location. The outcome from the data analysis was used to understand the subsurface images and tectonics system of the central peninsular Malaysia region while overcome the uncertainty surrounding the earthquakes occurrences in the area. In addition, the study also contributes to updating current geological and geophysical map as well as tectonic regime of Peninsular Malaysia while the 1-D velocity model will be used as an initial reference model for further analysis in 3-D tomography inversion.

Keywords: Earthquake, 1-D Model, Peninsular Malaysia

INTRODUCTION

Although Peninsular Malaysia lies on the stable Sundaland and generally safe from major earthquake disaster (5.0 M_w and above), the small scale tremors that occurred in Bukit Tinggi, Pahang in between 2007 to 2009, might give a cause of concern [1]. Up till today, there is no proof that these seismic activities are stable and will not strike again in the near future. It was deduced that the short-time frame but frequent small scale tremors could have occurred due to re-activation of paleo-faults lines that pass through the Peninsular Malaysia, such as Bukit Tinggi and Kuala Lumpur fault lines (Fig. 1). However, due to the limitation of Peninsular Malaysia seismological data analysis and its associate information, previous research unable to confirm the current state of fault line movements.

Without proper study and research work on subsurface imaging, these small earthquakes which release an equivalent 15,000 tons of TnT energy, might re-occur in the future with a larger amount of energy and strength. The existing magnetic and gravity image data of Peninsular Malaysia subsurface might able to reveal the basinal structures of these zones, but were less accurate compare to available seismic methodology which is very expensive. In recent years, there are various theory relating the present day Peninsular Malaysia structure to the collision of Sibumasu Terrane and Sukhothai Arc [2]. This geological model of Peninsular Malaysia, in term of crustal thickness is directly correlated to the magnitude and depth of localized earthquakes [3]. With this in mind, there is an urgency to develop the local velocity structure before further analysis can be carried out.

Fig. 1 The seismotectonic of Peninsular Malaysia, showing the Bukit Tinggi and Kuala Lumpur fault lines.

The Bukit Tinggi and Kuala Lumpur fault lines are the two paleo-fault lines that are said to be in the process of re-adjustment in order to accommodate the build-up tectonic pressures originating from Indo–Eurasian plates movements [4]. Generally, the resultant faults re-activation can be proven through a comprehensive 3-D velocity tomography with magnetic, gravity and geological data correlation. In the last ten years, seismologist discovered that the reliable subsurface information can also be obtained by correlating two or more seismometers data, which will produce a result as if there had been a real earthquake or seismic activity at the other seismometers [5]. This technique, called seismic interferometry is being developed further by incorporating ambient noise signal to produce the tomography update [6].

However, before we carry out the 3-D velocity tomography of the area studied a 1-D priori velocity model need to be established. While there are a number of global velocity model available and been used extensively such as IASP91 (Fig. 2) and AK135 models, the local crustal models are often been ignored. This local information is essential in processing the earthquake data, developing crustal structure and locating the fault lines. Therefore, a few local velocity model determination techniques being experimented, among them are inversion of arrival times and receiver function method.

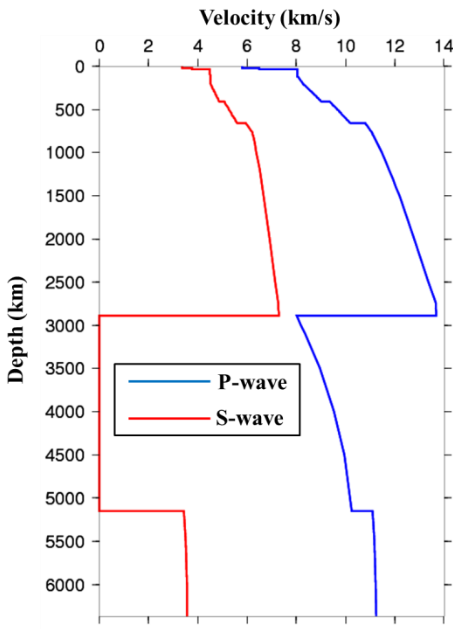

Fig. 2 IASP91 model that was constructed as a reference and parametrizes velocity model.

The inversion of arrival times works by inverting the well-located hypocenters data to improve the local structure as well as the existing hypocenters. In this procedure, which commonly implemented using VELEST software [7], the calculation of a minimum 1-D model requires multiple iterations with selected control parameters, in order to achieve a unique solution. On the other hand, the receiver function method is a phase conversion technique, which requires P and S-waves arrivals from the teleseismic data. The receiver information then can be derived by deconvolving the horizontal component from vertical component, thus reveal the structure for crustal and upper mantle [8].

DATA DESCRIPTION

Data used for travel time inversion was obtained from Malaysia Seismological Network (MSN), which is being operated by Malaysia Meteorological Department (MMD), a government agency under Ministry of Science, Technology and Innovation (MOSTI). At the moment, there are 44 seismology stations being used within Peninsular Malaysia, Sabah and Sarawak, where 17 of them are the weak motion stations. However, a number of stations were only installed after the earthquake occurrences in Bukit Tinggi. In order to enhance the recorded seismological data in the affected area, three of the stations were installed in Bukit Tinggi, Goh Tong Jaya and Janda Baik (Fig 3).

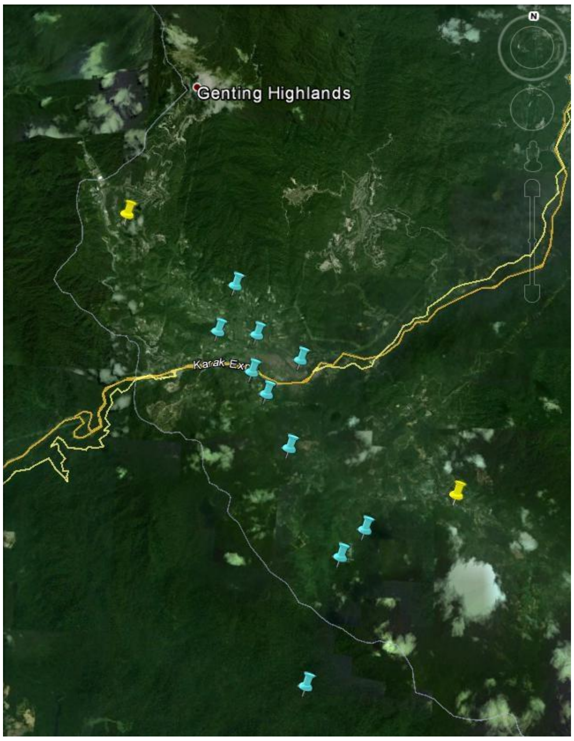

Fig. 3 The location of ten earthquake in Bukit Tinggi (blue pins), and the nearest seismology stations (yellow pins).

Table 1 The list of earthquake occurrences within Peninsular Malaysia in between 2007 and 2013.

No.	Date	Time (UTC)	Latitude	Longitude	Magnitude	Depth	Earthquake Location
1	2013-08-20	00:26:27	5.4160	101.3600	4.10	1.60	Tasik Temenggor
2	2009-12-04	01:41:45	3.3726	101.8038	1.95	5.04	Bukit Tinggi
3	2009-11-30	06:29:48	2.7310	102.0670	3.50	14.67	Kuala Pilah
4	2009-11-30	01:12:30	2.7382	102.1432	3.04	4.00	Kuala Pilah
5	2009-11-29	16:15:05	2.7363	102.1169	3.30	1.75	Kuala Pilah
6	2009-11-29	06:26:51	2.7398	102.0910	3.10	3.00	Kuala Pilah
7	2009-10-08	04:05:55	3.2700	101.8270	0.98	10.00	Bukit Tinggi
8	2009-10-07	22:20:59	3.3438	101.8135	0.31	1.89	Bukit Tinggi
9	2009-10-07	22:09:45	3.3030	101.8340	3.16	10.00	Bukit Tinggi
10	2009-10-07	21:51:11	3.3538	101.8218	4.23	3.00	Bukit Tinggi
11	2009-10-07	21:26:05	3.3890	101.9020	1.02	10.00	Bukit Tinggi
12	2009-10-07	21:21:26	3.3495	101.8094	1.66	1.94	Bukit Tinggi
13	2009-04-29	13:53:54	4.1500	100.7290	2.76	22.55	Manjung
14	2009-03-27	01:46:25	3.8621	102.5194	3.24	50.00	Jerantut
15	2008-05-25	01:36:22	3.3600	101.7500	2.60	Shallow	Bukit Tinggi
16	2008-03-15	00:50:57	3.3300	101.7100	3.30	Shallow	Bukit Tinggi
17	2008-03-14	23:35:34	3.3000	101.8600	2.50	Shallow	Bukit Tinggi
18	2008-03-14	23:16:18	3.3300	101.7400	2.90	Shallow	Bukit Tinggi
19	2008-01-14	15:45:00	3.4200	101.8000	3.40	Shallow	Bukit Tinggi
20	2008-01-13	10:18:00	3.3300	101.8300	2.40	Shallow	Bukit Tinggi
21	2008-01-13	02:24:00	3.3100	101.8300	2.50	Shallow	Bukit Tinggi
22	2008-01-10	15:38:00	3.3900	101.7300	3.00	3.00	Bukit Tinggi
23	2007-12-31	09:19:00	3.3200	101.8100	2.60	Shallow	Bukit Tinggi
24	2007-12-12	10:01:00	3.4700	101.7600	3.20	Shallow	Bukit Tinggi
25	2007-12-09	12:55:00	3.3300	101.8200	3.50	4.90	Bukit Tinggi
26	2007-12-06	15:23:00	3.3600	101.8100	2.70	Shallow	Bukit Tinggi
27	2007-12-04	19:57:00	3.3700	101.8000	3.30	Shallow	Bukit Tinggi
28	2007-12-04	10:12:00	3.3600	101.8100	3.00	Shallow	Bukit Tinggi
29	2007-11-30	12:42:00	3.3100	101.8400	3.20	6.70	Bukit Tinggi
30	2007-11-30	02:42:00	3.3400	101.8000	2.80	Shallow	Bukit Tinggi
31	2007-11-30	02:13:00	3.3600	101.8000	3.50	2.30	Bukit Tinggi

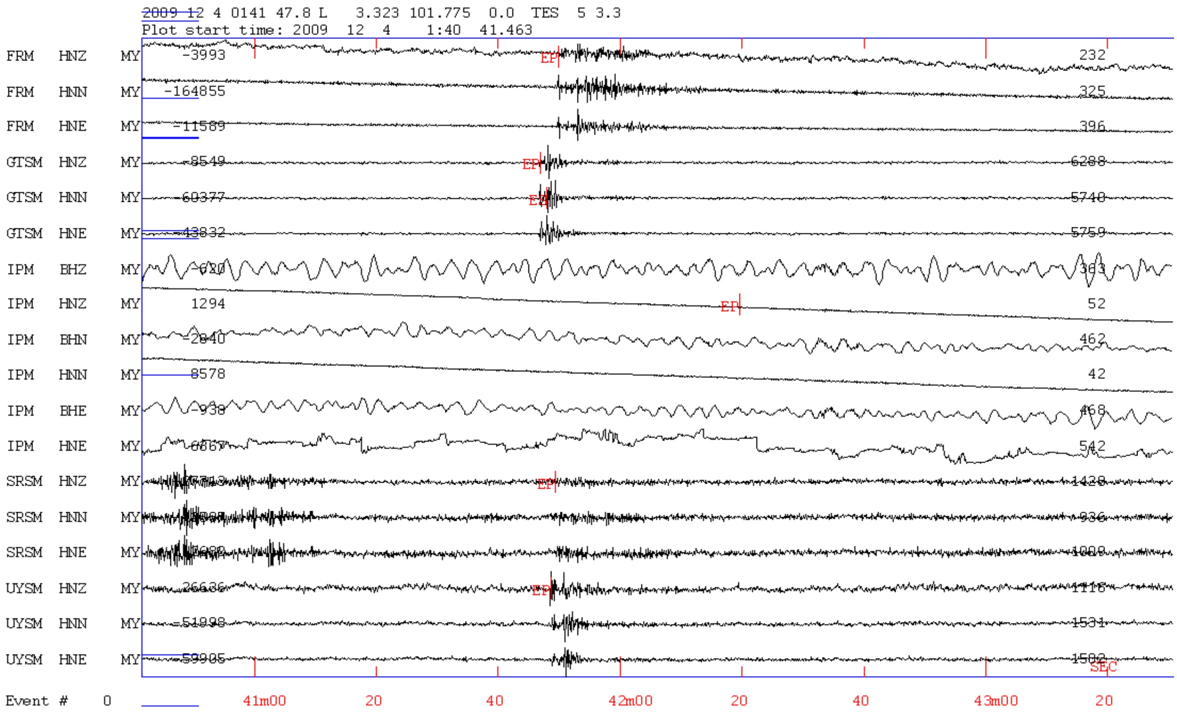

Fig. 4 The waveforms for earthquake on 4th December 2009 which was recorded by stations in Peninsular Malaysia.

For this study, we incorporate waveform time series and arrival times from local earthquakes in Peninsular Malaysia in between November 2007 to August 2013 (Table 1). In the analysis conducted, we manually picked the time arrivals for both the P and S phases in all 31 earthquakes. After several rounds of phase picking and analysis, it was decided to discard 14 of the events due to poor data condition as the main phase information has been masked with ambient noise signal. In this initial observation, it was found that the poor waveform data is due to unavailability of weak motion data (not installed at that moment) which should be able to detect weak earthquakes below 4.0 M_w. Further analysis then eliminate another 8 earthquakes that were not located in the central Peninsular Malaysia, as our objective is to look into velocity structure in central peninsular Malaysia region.

METHODOLOGY

To obtain the minimum local 1-D velocity model, several steps beforehand are needed. Once the data was acquired and reformatted, waveform conditioning and processing such as filtering and phase picking were conducted, by using the SEISAN software [9]. In the phase picking, only the clear P or S arrivals will be chosen, while the ambiguous arrivals will be flag off. Throughout the process, several earthquakes were discarded due to data insufficiency. All the events in the list are local earthquake, thus it is natural that the station close to the event recorded clear phase arrival compare to the one further away from the event (Fig. 4). Although the phase can also be read as P_g and S_g, we picked them as P and S-wave respectively. With regards to the area under study, the identification of the minimum 1-D model has been carried out based on 34 P-observations and 14 S-observations. All S-phases were picked on the horizontal component stations which explain the smaller number of picks.

In next step, the crustal model was determined by simultaneously inverting the priori waves' arrival, initial 1-D models of both V_p and V_s, as well as station coordinates (Fig. 5). In the 1-D minimum model, the velocity of a given layer is considered as the best average lateral velocity that belongs to that layer. Since the precision of routine earthquake location is strictly linked to the accuracy velocity model being used, we had chosen IASP91 velocity model as the initial velocity model for this region. In addition, as our target velocity model of crustal area is in central Peninsular Malaysia region, we decided to discard other seismic events that located in other Peninsular Malaysia region, such as in Manjung and Temenggor, in the simultaneous inversion procedure. Eventually, there are only nine events that were used in determining 1-D velocity model of this region. The simultaneous inversion approaches provide three outputs; updated hypocentral parameters, crustal model and station corrections. In addition, it should be note that a single iteration of simultaneous inversion is not sufficient, as the model produced is not minimum.

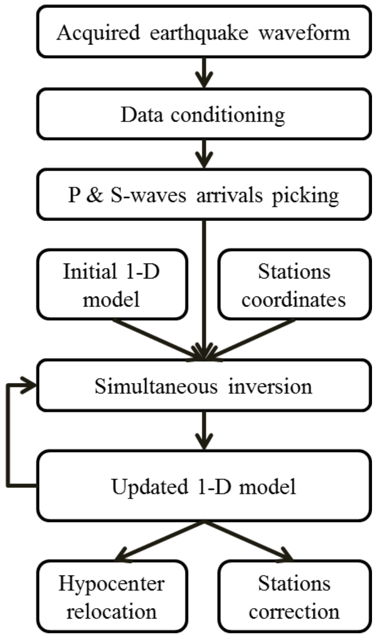

Fig. 5 The workflow used in determining the updated 1-D model of central Peninsular Malaysia

DATA INVERSION

The inversion was run until the earthquake locations, station delays and velocity values did not vary significantly in the subsequent iterations. From the resultant P-wave velocity model obtained (Fig. 6) it shows a significant velocity reduction of 4.5% at the Moho boundary of 31 km depth. By assuming the crustal depth is constant for both models, the updated 1-D model indicate that central Peninsular Malaysia region contain a slightly different material compare to regional velocity of the world. Meanwhile, the S-wave velocity (Fig. 7) shows a slightly faster velocity at the Moho depth, compare to the input model. These findings again reinforce our belief that the central Peninsular Malaysia was made up from slightly different granitic block compare to surrounding region. Another importance from this study was described by the earthquake relocations (Table 2). From the outcome of simultaneous inversion, there are slight differences in the origin time of the earthquake, its longitude and latitude as well as the depth of the seismic events. Although the changes are minimal, the new hypocenter parameters can be used for future determination of 3-D velocity tomography analysis in the region.

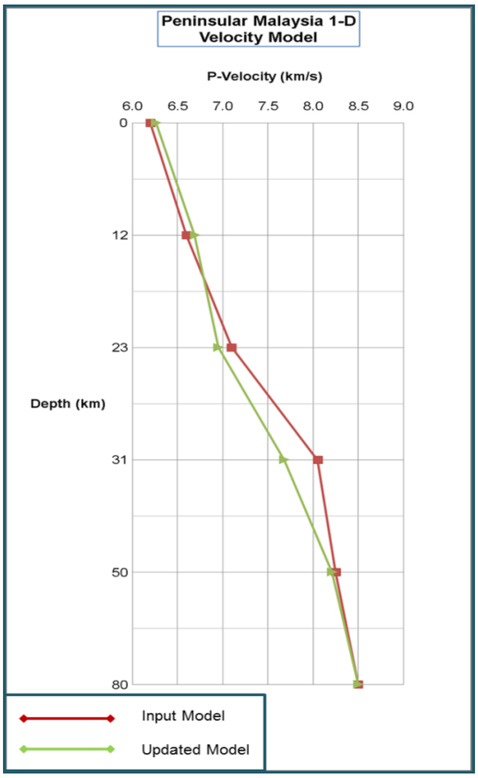

Fig. 6 1-D V_P model for Peninsular Malaysia before and after iterations.

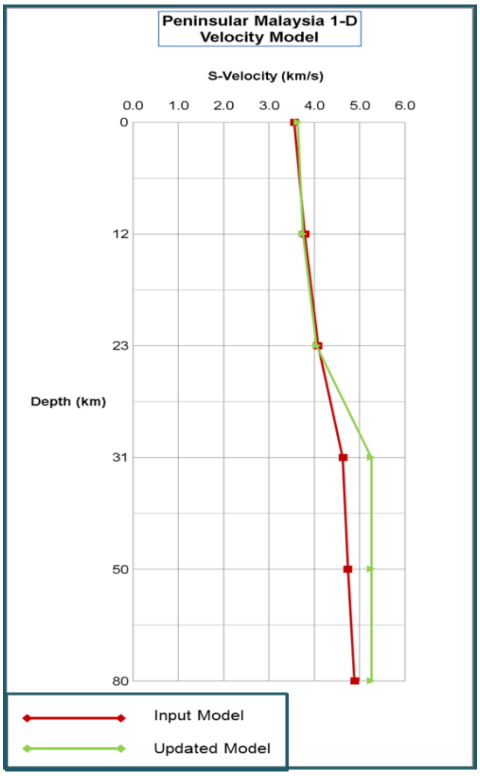

Fig. 7 1-D V_S model for Peninsular Malaysia before and after iterations.

Table 2 The hypocenter relocation parameter of 9 earthquakes in Peninsular Malaysia.

Date	Time	Time Differences	Latitude Differences	Longitude Differences	Depth Differences
4th December 2009	0141	4.9	-0.029	-0.128	0.4
8th October 2009	0405	2.8	0.024	-0.011	0.5
4th December 2007	1011	-0.1	0	0.004	2.5
7th October 2009	2149	2.8	0.021	-0.013	0.7
7th October 2009	2121	3.5	-0.042	0.002	-2.3
12th December 2007	1001	-0.6	-0.003	-0.016	0
9th December 2007	1255	0.1	0.003	0.014	4.3
30th November 2007	1242	-0.5	0.001	-0.011	0.1
30th November 2007	0213	-0.2	0.001	0.007	1.3

CONCLUSIONS

Although the results shown are encouraging, caution must be exercised when interpreting the 1-D velocity model as no other geological and geophysical models prove otherwise. The updated 1-D velocity models has shown that the Peninsular Malaysia has a slightly different subsurface characteristic compare to other continental velocity structure. The application of simultaneous inversion techniques to a small scale region, where the seismic networks are fully operational can improve the quality of the 1-D model, hypocenter parameter relocations and enhance station correction. It is suggested that the 1-D model produced is to be used as the initial 3-D velocity tomography model process.

ACKNOWLEDGEMENTS

We are grateful to Universiti Teknologi PETRONAS for the opportunity to conduct this research, Malaysia Meteorological Department for the earthquake waveforms and to Ministry of Higher Education, Malaysia for the financial grant support.

REFERENCES

[1] Malaysian Meteorological Department (MMD), 2008.http://www.kjc.gov.my/english/service/seismology/seismoevent.html.

[2] Metcalfe, I., (2013). Tectonic evolution of the Malay Peninsula, *Journal of Asian Earth Sciences 76, pp.193-pp213.*

[3] Hagen, M., (2016). Induced earthquakes correlations with earth's crustal thickness, *International Journal of GEOMATE, Vol. 11, Issue 23, pp.2228 - pp.2234.*

[4] Shuib, M.K. (2009). The recent Bukit Tinggi earthquakes and their relationship to major

geological structures, *Bulletin of the Geological Society of Malaysia 55, pp. 67 – 72.*

[5] Wapenaar, K., Draganov, D., Snieder, R., Campman, X., and Verdel, A., (2010). Tutorial on seismic interferometry: Part 1 — Basic principles and applications, Geophysics, Vol. 75, No.5, pp.. 195 - 209.

[6] Nicolson, H., Curtis, A., Baptie, B., Galetti, E., (2012). Seismic interferometry and ambient noise tomography in the British Isles, Proceedings of the Geologists' Association, Vol. 123, pp. 74–86.

[7] Kissling, E., Elssworth, W.L., Eberhart-Phillips, D., Kradolfer, U., (1994). Initial reference models in seismic tomography, Journal of Geophysical Research, Vol. 99, No. B10, pp 19635 – 19646.

[8] Ammon, C. J. (1991). The isolation of receiver effects from teleseismic P waveforms. Bull. Seism. Soc. Am. Vol. 81, pp. 2504–2510.

[9] Ottemoller, V. and Havskov, (2014). Seisan Eearthquake Analysis Software for Windows, Solaris, Linux and Macosx.

Sixth International Conference on Geotechnique, Construction Materials and Environment, Bangkok, Thailand, Nov. 14-16, 2016, ISBN: 978-4-9905958-6-9 C3051

VEGETATIVE INFLUENCE ON ROUGHNESS LEVELS FOR PAVEMENTS FOUNDED ON ALLUVIAL EXPANSIVE SOIL DEPOSITS

Md Yeasin Ahmed[1], Robert Evans[1] and Monzur Imteaz[1]
[1]Department of Civil and Construction Engineering, Faculty of Science Engineering and Technology, Swinburne University of Technology, Melbourne, Australia

ABSTRACT

Expansive soils shrink and swell when subjected to variations in moisture content, which often result from seasonal climatic changes and the presence of nearby vegetation. These variations in moisture can create non-uniform ground movements that may lead to structural distress and increased roughness levels in road pavements. Although the drying effect of roadside vegetation has always been expected to exacerbate moisture variation and associated roughness levels in areas of expansive soil deposits, no studies have yet quantified this influence on roughness levels. In order to evaluate the relationship between roadside vegetation and pavement roughness levels, vegetation data was collected and analyzed against historical road roughness data for 109 sections (each 100 m in length) for a rural highway in Victoria, Australia. Compilation of the vegetation database consisted of collecting information such as; number and location of roadside trees, size of canopy area, tree height, and a density rating for any grass present in the unsealed shoulder. The road roughness data set comprised of six biannual sets of international road roughness indices. This paper describes the development of the roadside vegetation database and includes procedures for extracting accurate information from satellite and street view imagery. It also presents the relationship finding between the presence of vegetation and increased roughness levels for a rural highway pavement in Victoria, Australia, founded on expansive soils.

Keywords: Expansive Soils, Road Roughness, Roadside Vegetation, Pavement Deterioration

INTRODUCTION

Expansive soils are common throughout Australia with six out of the eight capital cities and surrounding areas affected by such geological conditions [1], [2]. Expansive soils are defined as those that shrink and swell when subjected to variations in moisture. Factors that affect this behavior is the particle size distribution, type and quantity of clay present, and everything else that controls ground moisture variation such as climate, site drainage (topography) and the presence of vegetation. This shrink-swell action creates many problems for light structures such as road pavements [3]. The presence of an expansive soil subgrade can increase roughness levels (loss of surface shape) and longitudinal cracks in the pavement structure. Longitudinal cracking usually develops due to rapid (seasonal) desiccation and shrinkage of the soil beneath the edge of the pavement [4], while road roughness can be attributed to non-uniform volume change beneath the pavement. Gilgai phenomenon is often responsible for such non-uniform volume changes [5]-[7].

Gilgai is an Aboriginal (Australian) word that means “small waterhole”, which represents the water that collects in the depressions of undulating ground. The general physical features of soils exhibiting Gilgai formation was first discussed by Aitchison [8], but is best described in the Australian Handbook of Soils [9]. In short, expansive soils are primarily responsible for the formation of Gilgai terrain as it is the deep shrinkage cracks that allow moisture to penetrate deep in the ground and promote deep seated swelling, which initiates the formation of the mounds.

In Victoria (Australia), approximately 50 per cent of its land area is covered by moderately to highly expansive soils [10], [11]. Moreover, a considerable amount of these soils have the potential to develop Gilgai characteristics. This presents a significant problem to the maintenance of the State’s road network. Furthermore, as a significant amount of Victoria’s highway network incorporates the use of trees and vegetation into the road reserve to improve the overall experience of the road user, these roadside trees can exacerbate the development of Gilgai and associated roughness. Current literature suggests that trees can influence ground moisture conditions up to 10 m below the ground and horizontally up to 1.5 to 2 times the height of the tree [11]. However, no studies have ever quantified the relationship between the presence of roadside trees and roughness levels.

SITE DESCRIPTION

To evaluate the effect of roadside vegetation on road roughness levels, the Borung Highway in Victoria (Australia) was selected as: (i) it is located in a highly expansive (alluvial) geological area, (ii) Gilgai formation is common, (iii) climatic conditions promote significant shrink-swell behaviour, (iv) a good distribution of varying roadside vegetation exists, and (v) availability of quality historical road roughness data. The section of Borung Highway used in this study is located between the townships of Litchfield and Dimboola (approx. 80 kms in length), which is shown in Fig. 1. In this figure, the yellow and orange zones represent the presence of alluvial expansive soils, whereas the pink zones indicate residual expansive soils. The degree of expansive potential of the soil is indicated by the depth of color. The Borung Highway is a two-lane flexible rural highway that comprises of a thin sprayed seal wearing course. In total, 109 sections (each 100 m in length) were evaluated in this study.

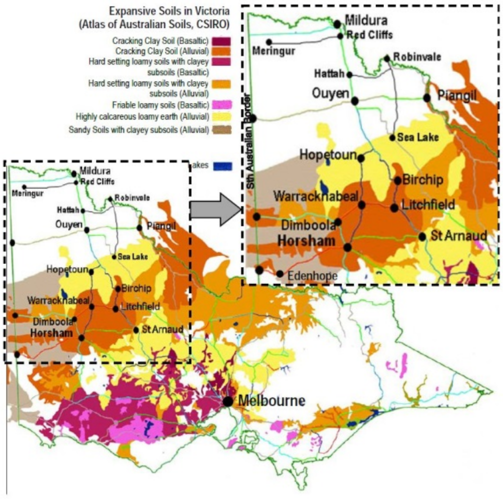

Fig. 1 Expansive soil map of Victoria (Australia) vs location of test site [12]

DATA COLLECTION AND METHODOLOGY

Data for this study was collected in two parts. This included pavement roughness data and roadside tree and vegetation data. The road roughness data was provided by Vicroads (State Road Authority of Victoria, Australia), whereas the roadside tree data was mostly collected using satellite imagery.

Pavement Roughness Data Collection

Vicroads typically conduct detailed road surveys once every two years across the State of Victoria, which consists of measuring the longitudinal road profiles and calculating the International Roughness Index (IRI) at 100 m intervals. For the Borung Highway, consecutive road roughness data was available from 1995 to 2009. From the 80 km of Borung Highway selected, more than 150 sections (each 100 m in length) were identified as containing high levels of roughness. These sections were located and referenced through the State Road Referencing System (SRRS). This allowed roughness progression rates (pre-maintenance and post-maintenance) to be accurately calculated for each 100 m section, of which 109 sections were identified as potential test sections for this study. Pre-maintenance roughness progression rates refer to the change in roughness (IRI) per year before maintenance. Pre-maintenance sections were easily identified through observation as any sudden drop in IRI values clearly indicated maintenance intervention.

Tree Data Collection

In order to evaluate the relationship between pavement roughness and the presence of roadside vegetation, a roadside tree database was developed. This database included information such as (i) number of trees on each side of the pavement, (ii) location of individual trees along the pavement measured in SRRS chainages, (iii) offset distances between the trees and centre-line of pavement, (iv) canopy area of each tree, (v) height of each tree, and (vi) density of grass present in the shoulder. To achieve this, each tree was identified and was given its own unique identification number. All of this data was collected using satellite and street view imagery (Google Earth Pro). A schematic diagram showing some of the variables measured for the roadside tree database is presented in Fig. 2.

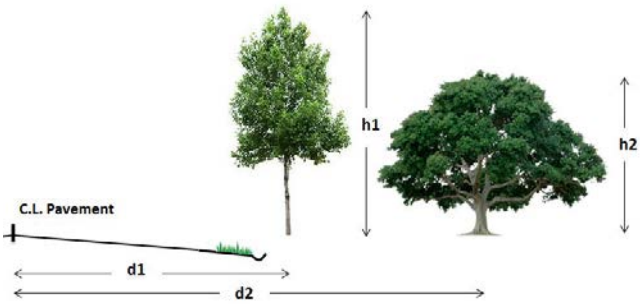

Fig. 2 Elevation view of roadside trees with variables measured

Number of trees

From satellite imagery (Google Earth Pro), the number of trees present in the road reserve can easily be counted. Mature trees, young trees (including bushes) and even trees with no canopy were all counted and input into the database. For large groups of trees, street view imagery was also used to help identify individual trees.

Offset distance between tree and pavement

The distance between each tree and centre-line of the pavement was measured using Google Earth Pro. An example of this using the "Ruler" function is shown in Fig. 3. In this figure, the tree is identified as DTLR104783 as it is located on left side at a chainage of 104783 and has an offset distance of 17.6 m from the centre-line of the pavement.

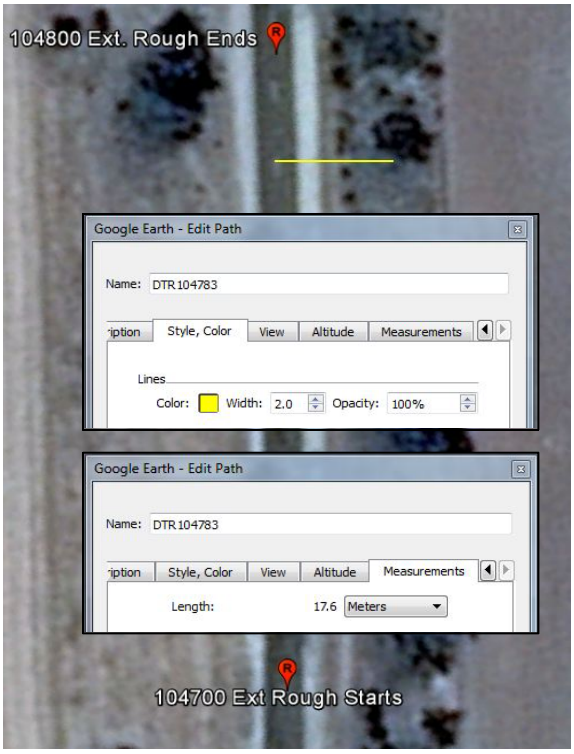

Fig. 3 Example measurement of offset distance between tree and pavement using Google Earth Pro

Canopy area

Similar to measuring distance, the canopy area can be estimated in Google Earth Pro. The outline and fill option should be used for accuracy. Proper care should also be taken while drawing the polygon to not include any tree shadows, as this may result in over- estimating the area. Fig. 4 shows an example of a polygon, which measures the tree canopy area as 47.1 m^2.

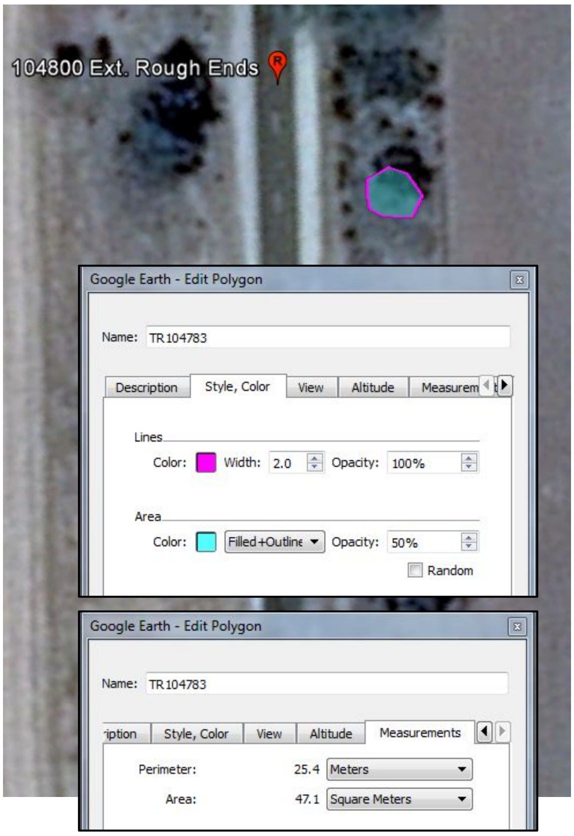

Fig. 4 Example measurement of tree canopy area using a polygon in Google Earth Pro

Tree height

To measure tree height, both satellite and street view type images in Google Earth Pro need to be used. First, satellite imagery is used to position a small polygon near the base of the tree (using 3D Polygon tab). A narrow or slender polygon is preferable as it is easier to position (see Fig. 5a). The sides of the polygon then need to be extended to the ground using the scale, and the height of the polygon adjusted. The style and color of the polygon can be modified for better visibility depending on the image. Street view is then used to adjust or fine-tune the height (if required) of the polygon to match the height of the tree (see Fig. 5b). The accuracy of this approach may depend on the initial positioning of the polygon and visual adjustment of the height. The closer the position of the polygon to the base of the tree, the greater the level of accuracy will be achieved. In Fig. 5, the height of the tree was measured as 9 m.

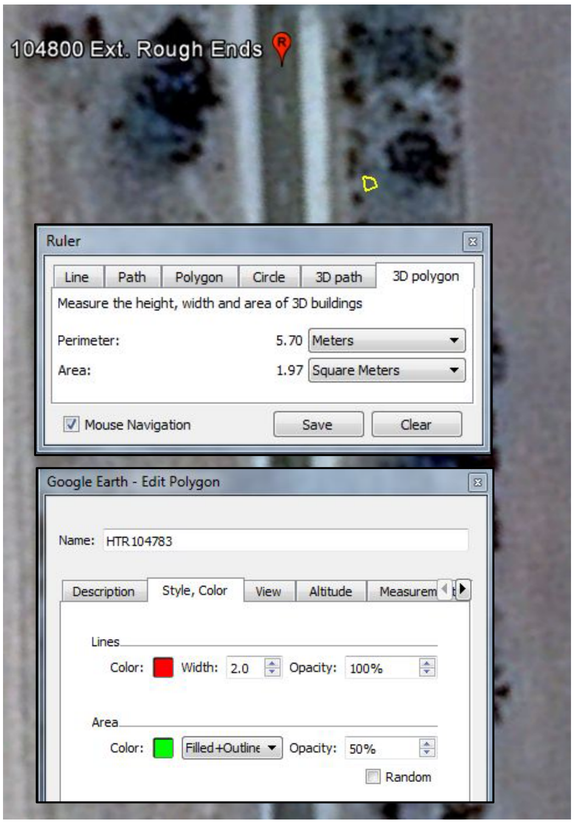

(a)

(b)

Fig. 5 Example measurement of tree height using 3D polygon tab in Google Earth Pro: (a) Satellite image, and (b) Street view image

Shoulder vegetation

To assess the effect of any grass present in the road shoulder on road roughness, a rating system (using values between 0 and 5) was employed. A zero rating indicated no grass present, while a value of 5 referred to a shoulder fully occupied with grass. It was decided to use this rating system to approximate the density of vegetation (grass) in the shoulder and convert into a metric scale. The rating of the shoulder vegetation was performed through street view of Google Earth. An example of a street view image with varying degrees of shoulder vegetation density is shown in Fig. 6. Here, the density rating for grass present in each unsealed shoulder was 2 and 1 for the left and right shoulders. This is because grass (moderate) has started to encroach into the left shoulder, while nearly no grass was present in the right shoulder.

Fig. 6 Example density ratings of grass present in each shoulder of the pavement using Google Earth Pro

DATA ANALYSIS AND RESULTS

As the primary objective of this study was to evaluate and quantify the effect of roadside trees on the development of road roughness, all measured tree parameters were statistically evaluated as independent variables and pavement roughness (in terms of IRI) was set as the dependent variable.

Statistically, no correlation against the presence of roadside trees (i.e. quantity, height, or location with respect to the pavement) could be established against individual pavement roughness levels, which were based on single road surveys. This is most likely due to the fact that road pavements naturally deteriorate over time due to a number of different factors, and the age of the pavement was not considered in this initial analysis. Therefore, to remove the age (or time factor) of the pavement from the analysis, we evaluated the roadside tree and vegetation variables against roughness progression rates (RPR) instead.

The roughness progression rates were calculated for pre-maintenance and post maintenance events, and were based on change in IRI per year. Pre-maintenance roughness progression data consisted of any change in roughness (per year) before any noticeable effects from maintenance or rehabilitation. While post maintenance roughness progression data consisted of any changes after a significant maintenance event.

The results of the statistical analysis using roughness progression rates (instead of individual roughness levels) yielded much better correlations, which is presented in Table 1. The independent variables evaluated were (i) Number of Trees (NoT), (ii) Average Distance between Trees and Pavement (AvDTrPv), (iii) Average Canopy Area (ACA), (iv) Average Tree Height (ATH), and Average Grass Density (AGD) rating. In this study, trees were considered up to a AvDTrPv distance of 39.4 m, and the average tree height ranged from 4 to 16.7 m. In addition, the statistical analysis was performed in three modes. First, only the roadside tree population on the “near” side adjacent to the surveyed lane was considered for the analysis. Then, only roadside trees on the “far” side were evaluated. Finally, all roadside trees (both sides) were taken into consideration and evaluated with the lane roughness progression rates.

Table 1 List of independent roadside vegetation variables and associated correlations with overall lane roughness progression rates.

Independent Variables		Significance p	Pearson r
Near Side Trees	NoT	0.222	0.118
	AvDTrPv	0.227	0.117
	ACA	0.101	0.158
	ATH	0.175	0.131
	AGD	0.142	0.141
Far Side Trees	NoT	0.392	0.083
	AvDTrPv	0.835	0.02
	ACA	0.634	0.046
	ATH	0.513	0.063
	AGD	0.625	0.047
All Trees	NoT	0.111	0.154
	AvDTrPv	0.015	0.233
	ACA	0.198	0.124
	ATH	0.02	0.223
	AGD	0.17	0.132

Results showed that when we considered trees on only one side of the pavement; the correlation was not significant for any of the independent variables as all p values exceeded 0.05. The correlation results when considering the nearside trees only (although not significant) was much better than the correlation results when only the far side trees were considered. The reason for this is simply due to the near side trees being much closer to the surveyed pavement lane. Fig. 7 defines the nearside and far side trees with respect to the surveyed lane. From the results in Table 1, it is clear that the further the tree is from the pavement, the less influence it has on the RPR. Furthermore, when trees are located on both sides of the pavement the drying influence zones may merge. This may result in greater moisture loss in the merged zone and create greater associated shrinkage and roughness progression. This fact was supported by the correlation results as when we considered the roadside trees on both sides of the pavement together the significance of the correlations improved yet again. The best correlation developed in this study was recorded between RPR and the average distance between tree and pavement (AvDTrPv) with a p value of 0.015. This was closely followed by the correlation between RPR and the average tree height (ATH) with a p value of 0.02. The Pearson coefficient of both of these correlations was measured at 0.233 and 0.223 respective, which indicated a small to medium effect [13].

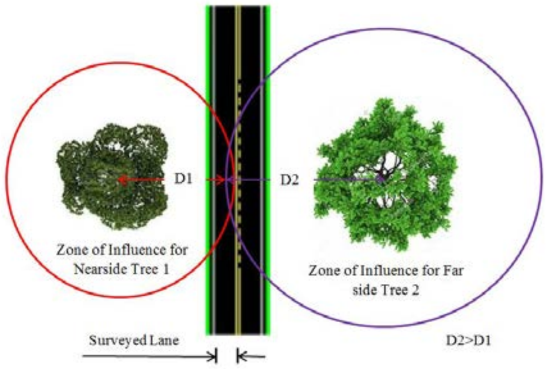

Fig. 7. Definition and influence of nearside and far side trees relevant to surveyed lane

Between RPR and AvDTrPv, a negative relationship exists, which means the RPR decreases when the AvDTrPv increases. Thus, the further the roadside tree is from the pavement, the less effect it has on road roughness. The equation for predicting RPRs with respect to the average distance between the roadside trees and pavement is shown in Eq. (1).

$$\boldsymbol{RPR_{Lane} = 0.241 - 0.006AvDTrP} \quad (1)$$

Between RPR and ATH, a negative relationship was also found to exist. This suggests that the greater the height of the tree, the lower the roughness progression. This finding seems unusual at first as it is commonly believed that the bigger the tree, the more widespread the root system, and thus the greater the influence of moisture variation. However, this finding implies that the small the tree, the greater the influence. This could be due to smaller trees being younger trees, which have greater growth rates and thus require more moisture. The equation for predicting RPRs with respect to the average tree height is shown in Eq. (2).

$$\boldsymbol{RPR_{Lane} = 0.219 - 0.012ATH} \quad (2)$$

When both of these independent variables were evaluated together, the significance improved marginally as the Pearson coefficient increased to 0.302 and thus became a medium effect on the RPR. The equation for predicting RPRs with respect to a combination of AvDTrPv and ATH is shown in Eq. (3).

$$\boldsymbol{RPR_{Lane} = 0.321 - 0.005AvDTrPv - 0.01ATH} \quad (3)$$

CONCLUSIONS

This study revealed that the presence of roadside trees do have some salient effect on the development of roughness for flexible pavements located in areas of alluvial expansive soils. Although no relationship between the studied tree parameters and individual roughness levels could be established, weak to medium correlations were verified when based on roughness progression rates. The best correlations were found between roughness progression rates and (i) the relative distance between the tree and pavement, and (ii) the height of the tree. Surprisingly, no correlation was able to be established between roughness progression and the quantity of trees present in the road reserve or the canopy area.

As road roughness was measured using the International Roughness Index (IRI) in this paper, it is planned to further examine the effect of these physical tree parameters on other roughness indices, such as those derived through the Butterworth Filter or Power Spectral Density (PSD). By evaluating roughness progression within the individual wavebands, it is anticipated that a better prediction model to quantify the effect of roadside vegetation can be determined.

ACKNOWLEDGEMENTS

The authors acknowledge the support offered by Vicroads in providing the raw longitudinal road profile measurements, which was used to calculate the roughness indices.

REFERENCES

[1] Delaney M, Li J, and Fityus S, "Field monitoring of expansive soil behavior in the Newcastle-hunter region," Journal of Australian Geomechanics, Vol. 40, 2005, pp. 3-14.

[2] Fityus S, Smith D, and Allman M, "Expansive soil test site near Newcastle," Journal of Geotechnical and Geoenvironmental Engineering, Vol. 130, 2004, pp. 686-695.

[3] Krohn JP, Slosson JE, "Assessment of expansive soils in the United States," Expansive Soils, 1980, 99.596-608.

[4] Luo R, and Prozzi JA, "Development of longitudinal cracks on pavement over shrinking expansive subgrade," Road Materials and Pavement Design, Vol. 11, 2010, pp. 807-832.

[5] Evans RP, Arulrajah A, and Horpibulsuk S, "Detecting gilgai relief beneath sealed flexible pavements using road profile and road roughness measurements," Indian Geotechnical Journal, Vol. 45, 2015, pp. 431-440.

[6] Lytton RL, Boggess RL, and Spotts J, "Characteristics of expansive clay roughness of pavements," Transportation Research Record, 1976.

[7] Velasco MO, and Lytton RL, "Pavement roughness on expansive clays," Transportation Research Record, 1981.

[8] Aitchison G. "The mechanics of gilgai formation", in Proc. of Conference on Soil Science, 1953, pp. 1-3.

[9] Hallsworth E, "A handbook of Australian soils," Adelaide, Rellim Publications, 1968.

[10] Holland J, and Richards J, "Road pavement on expansive clays," Australian Road Research, Vol. 12, 1982.

[11] Richards B, Peter P, and Emerson W, "The effect of vegetation on the swelling and shrinking of soils in Australia," Geotechnique, Vol. 33, 1983, pp. 127-139.

[12] Evans R, "Synchronisation of road profile data and the assessment of road roughness using waveband analysis," PhD Thesis, Department of Civil and Construction Engineering, Swinburne University of Technology, Melbourne, Australia, 2013.

[13] Field A, "Discovering statistics using SPSS," Sage Publications, 2009.

Sixth International Conference on Geotechnique, Construction Materials and Environment, Bangkok, Thailand, Nov. 14-16, 2016, ISBN: 978-4-9905958-6-9 C3051

INFLUENCE OF WEATHERING OF BOTTOM ASH ON THE LEACHING BEHAVIOR OF CESIUM

Yasumasa Tojo[1], Saori Iwamoto[1], Mikako Ishii[1], Toshihiko Matsuto[1] and Takayuki Matsuo[1]
[1]Graduate school of Engineering, Hokkaido University, Japan

ABSTRACT

After nuclear accident in 2011, incineration residue contaminated by radioactive cesium had been produced. Government decided in 2011 that incineration residue with less than 8000 Bq/kg of radioactivity could be disposed of into conventional MSW landfill. Since radioactivity of bottom ash was reported to be low compared with fly ash, it had been disposed of MSW landfill based on the government regulation. However, long-term leaching behavior of cesium contained in bottom ash when being disposed of into landfill was not known. Thus, in this study, phase transformation and leaching of cesium from incineration bottom ash were investigated by conducting accelerating weathering experiment. Four kinds of weathering condition were set; namely, blank (under nitrogen gas condition), wetting and drying, freezing and thawing, and exposure to carbon dioxide gas. Leaching of cesium under blank condition didn't change. On the other hand, drastic decrease of leaching of cesium was identified under carbon dioxide exposure. From XRD analysis, formation of calcite was identified. It was deemed that newly formed calcite inhibited the leaching of Cs by covering reactive surface of bottom ash. In both wetting-drying and freezing-thawing condition, leaching of Cs increased initially. But it decreased after several weeks then it became lower than blank finally. This decrease of leaching also seems to be caused by formation of calcite. Besides, in order to confirm the assumption in which the restrain of cesium leaching occurred by calcite formation, SEM-EDS analysis was performed. By the analysis, calcite formation on the surface was clearly identified.

Keywords: Incineration Bottom Ash, Cesium, Leaching, Carbonation

INTRODUCTION

After the accident of Fukushima-Daiichi nuclear power plant in 2011, municipal solid waste incinerators in east Japan generated ashes containing radioactive cesium (Cs) in high concentration. Government decided that the waste of 8000 Bq/kg or less could be disposed of into MSW landfill as before [1]. Radioactivity of fly ash was very high and special measure is necessary for its disposal. On the other hand, radioactivity of bottom ashes was low and many of them satisfied the government's criteria so that its disposal to MSW landfill has been carried out. National Institute for Environmental Studies was conducted sequential extraction test for various kinds of waste that were contaminated by radioactive cesium. And they reported that water-soluble form of cesium in bottom ash is only about 3% and approximately 80% of cesium existed as residual form (i.e. the last fraction of extraction tests) [2]. Their results indicated that possibility of cesium leaching was low even if the bottom ash was disposed of into ordinary MSW landfill sites. However, it is well known that the incineration residue is unstable substance and its mineral phases are changed by various environmental factors. Especially, leaching behavior of inorganic elements changes by weathering along with elapsed time. Therefore, it is not certain that Cs keeps being stably captured in the ash for long-term after disposal into MSW landfill. Thus, in this study, the effect of weathering of the bottom ash on the leaching behavior of Cs was investigated in order to confirm their long-term stability in landfill.

MATERIALS AND METHODS

Materials

In general, the total cesium content (stable cesium and radioactive cesium) in the incineration bottom ashes discharged from a real incinerator is very small, and moreover the content of radioactive cesium is also very small. For instance, total cesium content, which is comprised of mainly stable-cesium, is reported to be less than several mg/kg [3]. As for the content of radioactive cesium, it is estimated to be several ng/kg, if radioactivity of the incineration ash is assumed to be several thousands Bq/kg. These values imply that chemical analysis of cesium contained in the incineration residue is quite difficult, especially radioactive cesium. So, in this study, artificially created ash, of which stable cesium content was made quite high, was used. The ash was created by adding cesium carbonate (Cs_2CO_3) to RDF (Refuse-Derived Fuel) and combusting it by pilot-scale stoker incinerator of which capacity was 3 tons/day [4]. After combustion, the bottom ash was cooled under ambient temperature. Since, the furnace allows collecting fly ash and bottom ash separately, the bottom ash doesn't contain fly ash.

After creation, 20 kg of the bottom ash was taken to the laboratory. Immediately, the ash was pulverized to less than 0.5 mm by jaw crusher (Retsch, BB-50) to obtain uniform sample. At first, the metal content was measured by aqua-regia digestion and the atomic absorption spectrometry in order to elucidate characteristics of this artificially created bottom ash. Moreover, to determine the amount of soluble cesium, the serial batch leaching test was executed [5]. In the serial batch test, leaching test in L/S (liquid to solid ratio) =10 was repeated five times. Fig. 1 shows the content of Cs, K, Na, and Ca.

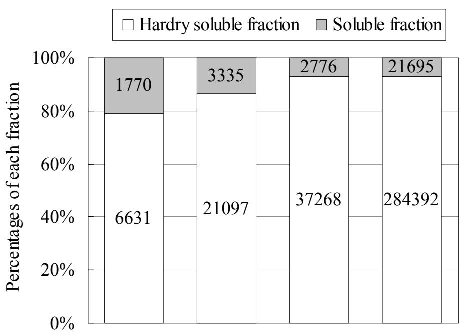

Fig. 1 Content of hardly soluble and soluble fraction on Cs, K, Na, and Ca in artificially created bottom ash. Number in the bar shows each content (unit: mg/kg-ash).

In the figure, content of each element is indicated by distinguishing the soluble fraction and hardly soluble fraction. Although metal content and the amount of soluble fraction were almost the same with that of general incineration ashes, soluble fraction of Cs was 20% and it was higher than the one that had been detected in actual furnaces. Because hardly soluble Cs occupied the majority of the content in the ash actually generated from the incinerator in East Japan, existence of soluble Cs is undesirable in the examination of a long-term behavior of Cs. Therefore, the ash used for the weathering acceleration experiment was washed in L/S=10 beforehand. Amount of soluble Cs becomes to about 1% in total content after the pretreatment. And it was not below the detection limit. Thus, it was regarded as suitable to pursue the change in the leaching amount.

Methods of Weathering Acceleration

The Four different conditions (Blank, Drying and wetting, Freezing-thawing, and CO_2 gas exposure) were established for the weathering experiment.

Blank: 10g of pretreated ash samples was put into the 50mL screw bottle. To prevent any reaction and so as not to cause weathering, N_2 gas was purged into the head space. After capping, it was left sitting at the room temperature. To prevent any reaction as much as possible, the N_2 purge was done once a week. This system was created for the comparison with another three series.

Drying and wetting: 10g of the pretreated sample was filled in the small crucible and then the crucible was fixed in a steel tray that spread the glass bead. Distilled water was added to the sample to become saturated water content and it was left sitting for 30 minutes. Then, it was heated in the dryer for 1.5 hours at 100˚C. This process was repeated three times a day and it was continued for eight weeks. This series was made in order to accelerate physical weathering (i.e. physical collapse of the particle structure of the ash) by repetition of drying and wetting.

Freezing and thawing: 10g of the pretreated sample was filled in the small crucible. After adding distilled water to the sample to make its saturated water content, the crucible was capped and it was cooled in the freezer for 1.5 hours. After that, the frozen sample was heated with the crucible for one hour at 40˚C in the dryer, and melted. This process was repeated three times a day and it was continued for eight weeks. This series was made in order to accelerate physical weathering (i.e. physical collapse of the particle structure of the ash) according to the expansion and shrinkage of pore water by the freezing and melting.

The CO_2 exposure: 10g of pretreated sample was spread in the steel tray and then distilled water was added to make its water content at field capacity. The tray with sample was put into the air-tight desiccator and CO_2 gas was filled in it. To keep the humidity in the desiccator, steel tray filled with distilled water was placed inside. The moisture content was monitored everyday and readjusted to the field capacity. Besides, CO_2 gas was always kept injected into the inside. This series was made in order to accelerate chemical weathering (i.e. chemical transformation by contacting with CO_2). This is because the major weathering reaction occurring in the incineration ash is reported to be the carbonation [6].

Eight pieces of sample were made for one weathering series. The weathering acceleration was done at the same time by above-mentioned each four methods. One piece was collected every week, and the sample was subjected to the analysis.

Leaching Test Procedure

2g of weathered sample was put into Erlenmeyer flask and 20mL of distilled water was added (L/S=10). The flask was shaken for six hours by using the desk-top shaker. It was reported that there are two types of Cs leaching from soil (i.e. Cs absorbed with soil colloid and free ion state). Thus, in this study, the leaching liquids were filtered through two stages. At first, it was filtered by 1μm glass-fiber filter and then a part of the filtrate was used for the analysis. After that, remainder filtrate was filtered by 0.1μm membrane. Both liquids were analyzed by frame atomic absorption spectrometry (AAS: Hitachi Z-8200). Analyzed elements were Cs, K, Na, and Ca.

Identification of Minerals

The Samples after two weeks of weathering were subjected to the Powder X-ray Diffraction (XRD) analysis in order to investigate changes of major minerals contained in the ash. Before analysis, samples were dried at 80°C and then they were milled. X-ray diffractometer (Rint-2000, Rigaku) with Cu-Kα radiation was used. Scan range was 5-80° with scan speed 4° per minute.

Microscopic Analysis of Weathered Ash

In the weathering experiment, obvious inhibition of Cs leaching was confirmed in the sample of CO_2 exposure condition. Thus, by using weathered sample of the CO_2 exposure and blank, thin sections were prepared. Thin sections were observed by Scanning Electron Microscope - Energy Dispersive X-ray Spectroscope (SEM-EDS: JEOL JSM-6360LA) and elemental distribution was investigated. Besides, to analyze formation of newly formed minerals in weathered ash samples, Polarizing microscopes （OLYMPUS CX31-P） was used.

RESULTS AND DISCUSSION

Change of Leaching Behavior of Cs by Weathering

The leaching amount of Cs from the ash exposed to each weathering condition is shown in Fig. 2. Though the direct result obtained by AAS is the concentration of the leaching liquid, the leaching

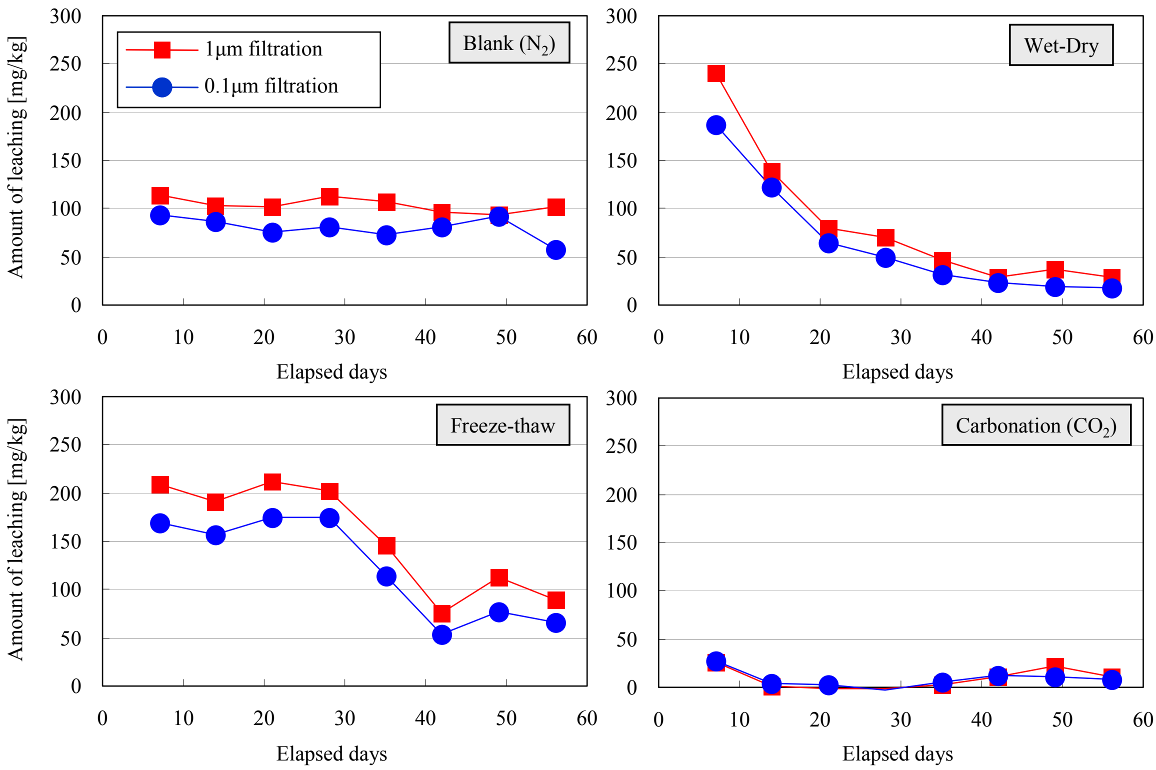

Fig. 2 The amount of Cs that leached out from the weathered bottom ash at each elapsed day

amount, which is converted from the concentration by using L/S ratio, is indicated. Each panel shows the result of the sample that was exposed to each weathering condition. In addition, the results of two filtration stages are shown by separate line. As indicated in the figure, the leaching amount obtained by both filtration stages didn't differ much. Concentration of the filtrate obtained by 1um filter is slightly high. This implies that Cs leached out in this study was mainly ionic form.

Leaching amount of Cs from blank sample (i.e. N_2 exposure) didn't change and it kept almost constant value similar to the initial for through entire experimental period. On the other hand, leaching of Cs from sample exposed to CO_2 circumstance drastically decreased within a week as indicated in the lower right panel. It reached to below the detection limit at two weeks. This rapid decrease is thought to be caused by the formation of calcite at the surface and it may inhibit the Cs leaching by covering the ash particle. The result obtained from both drying-wetting and freezing-thawing conditions shows slight increase of Cs leaching in the first week. The increase of leaching amount was almost 2.5 times to the result of blank. This increase is thought to be caused by collapse of the ash particle structure, which captures Cs to the inside of it, by the physical action due to the thermic effect or the expansion/contraction of pore space. For example, Saffarzadeh [7] reported that Cs is captured in glassy-amorphous phase or some alminosilicates. Thus, if these structures are affected by weathering, leaching of Cs seems to be possible. However, subsequently, the leaching of Cs from both weathering conditions showed the decreasing trend. Especially, Cs leaching from the ash subjected to the drying-wetting condition became lower than it of the blank. This means that the soluble Cs contained in the ash was transformed to the hardly soluble Cs. The conceivable reason of this trend is the carbonation similar to the CO_2 exposure condition. In both weathering conditions, the ash is exposed to the atmosphere. As for the wetting-drying condition, the ash is exposed to the atmosphere during drying. In the freezing-thawing, the situation is the same.

Change of Mineral Phases by Weathering

Minerals identified in XRD analyses which were conducted for each sample after two weeks are indicated in Table 1. The values in the table are the peak height of these minerals. Moreover, the X-ray diffraction charts of each sample are also shown in Fig. 3. In the figure, main peak of calcite is enclosed by the rectangle of dashed line. The peak height of calcite in weathered sample except for the blank increased in common. Especially, the height of the CO_2 exposed sample became five times higher than the blank. From these results, carbonation is deemed to be occurred in the weathered sample and calcite formed. This calcite formation might affect the leaching of Cs.

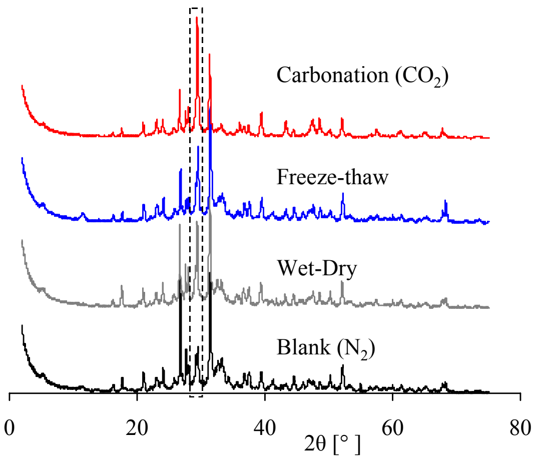

Fig. 3 Powder XRD diffractogram on the each weathered bottom ash samples (after two weeks). Rectangle drawn by dashed line encloses main peak of calcite.

Table 1 Change of main peak height of minerals identified each bottom ash samples.

Mineral	Blank	Wet-dry	Freeze-thaw	CO_2 Exposure
Gehlenite	1327	1575	1290	1503
Quartz	1381	1198	579	965
Lime	193	206	181	196
Calcite	438	851	784	1903
Hematite	235	201	185	121

Microscopic Analysis on the mechanism of the leaching inhibition of Cs

Since calcite formation in weathered ash could be confirmed from the result of XRD, microscopic analyses were performed to verify the existence of calcite and its location. At first, some ash particles were observed at a low magnification by using polarizing microscope. Images observed by the transmissive light mode on the blank and the CO_2 exposed sample are shown in Fig. 4. Some ash particles exposed to CO_2 can be seen in panel (b). It seems that the perimeter of the particles shines in yellow. When the observed object emits various colors depending on the rotation angle in the polarizing microscope analysis, the object is considered to be some crystal. This is because mineral in general is composed of some crystal structure and it has polarization property. Therefore, the image of these particles shows that some sort of mineral formed in the sample exposed to CO_2.

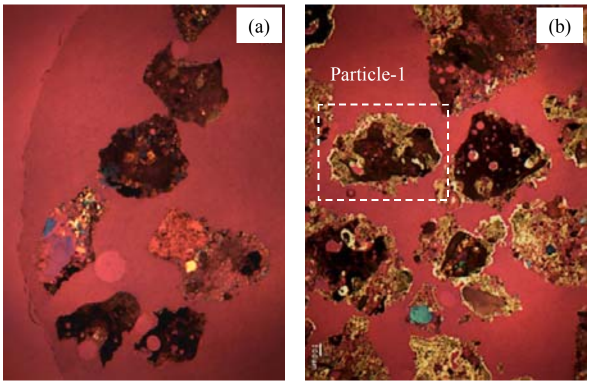

Fig. 4 Observed image of weathered ash particles by polarizing microscope; (a) blank, (b)CO_2 exposure.

Next, a particle (Partilce-1) shown in Fig. 4 (b) (enclosed by rectangle) was focused and observed with much higher magnification. As indicated in Fig. 5, obvious luminescence at the perimeter of the particle can be confirmed.

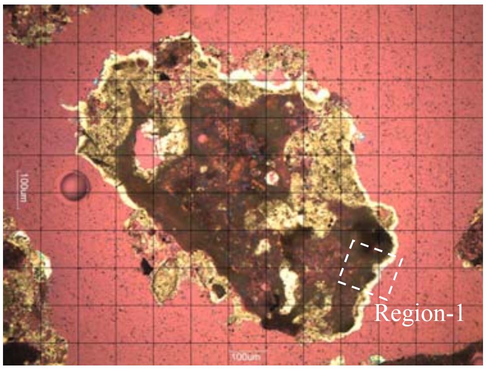

Fig. 5 Magnified image of a particle-1 in Fig. 4.

In order to identify the kind of the substance formed at the perimeter of the particle, a region (Region-1) which is enclosed by rectangle in Fig. 5 was observed by SEM. Figure 6 shows the backscattered electron image of the Region-1. The edge of the particle is located at slightly right side of the center. In this image, existence of some sort of substance at the edge of the particle is obvious and it is seen as pale gray color. This substance seems to be formed as if it surrounds the particle.

Moreover, EDS analysis was performed in this region in order to know the element distribution. Element mapping image of calcium and silicon is indicated in Fig. 7. Much Ca is distributed at the peripheral region of the particle. The location where Ca is abundant coincides with the gray color part in Fig. 6. Furthermore, this region corresponds to the perimeter which shines in yellow in the image of polarizing microscope. On the other hand, as for the distribution of Si, its intensity is high at the inside of the particle. And Si is not much distributed at the peripheral region. This implies that some sort of calcium mineral surrounded the particle comprised of silicon.

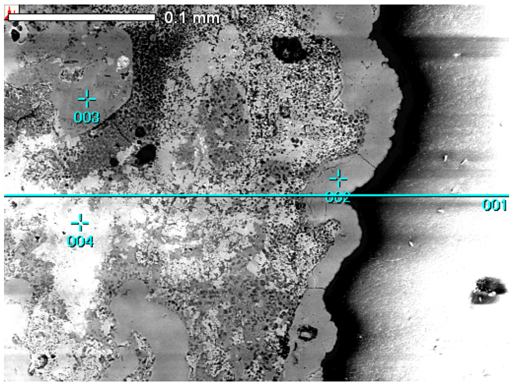

Fig. 6 Magnified image (backscattered electron image) of a region-1 in Fig. 4 and EDS analyzing line and points.

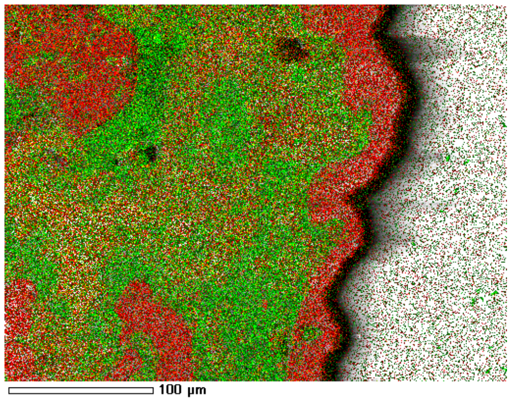

Fig. 7 EDS mapping image (red: calcium, green silicon)

The result of EDS line analysis on line001 in Fig. 6 is shown in Fig. 8. Peak intensities of calcium and silicon along with the distance are indicated. Peak intensity of Si is higher than Ca until 2mm of distance from left side. However, when the distance exceeds 2mm, their intensities become reverse. The point of reversal corresponds to the gray color part in the BEI (Fig. 6). And also it corresponds to the area where the Ca is abundant in the element mapping image (Fig. 7). Results of EDS point analysis are shown in Table. 2. When focusing on Ca, it was 9.5% at the point 004 that is the inside of the particle. However, at the point 002 that locates at the perimeter, percentage of Ca increased to 26.5%. From all of the results mentioned above, it can be concluded that some sort of calcium mineral formed at the perimeter of the ash particle which is exposed to the CO_2 as the weathering acceleration.

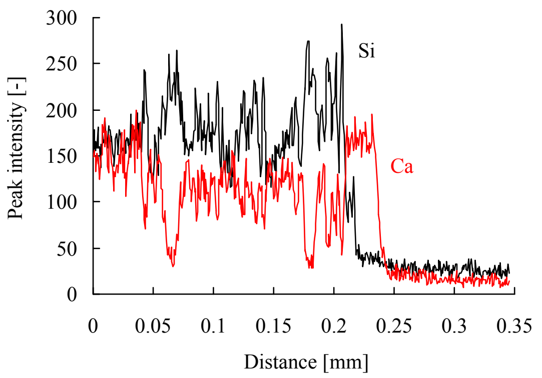

Fig. 8 Result of EDS line analysis on line001 in Fig. 6.

Table 2 Result of elemental analysis by Energy Dispersive X-ray Spectroscopy (EDS) on points indicated in Fig. 6.

Point	002	003	004
C	23.7	19.9	19.4
O	42.5	48.9	36.1
Al	1.1	1.1	8.2
Si	2.3	2.7	15.8
Ca	26.5	25.2	9.5
Other	3.9	2.3	11.0
Total	100	100	100

Numbers in the table indicate percentage of each element (%).

It is difficult to determine concretely that the formed mineral is calcite from the element ratio identified by EDS. However, as mentioned earlier, the peak of calcite was increased in XRD analysis. Besides, the trend of Cs leaching inhibition is most remarkable in the ash subjected to CO_2 exposure. Based on these facts, the possibility of calcite formation at the surface of the ash particle is quite high. And it will work to restrict Cs leaching from the incineration ash disposed of into MSW landfill.

CONCLUSION

In this study, to confirm long-term stability of Cs contained in incineration ash disposed of into MSW landfill, leaching of Cs from ash and phase transformation were investigated by conducting accelerating weathering experiment. Drastic decrease of the Cs leaching was identified under carbon dioxide exposure. From XRD analysis, formation of calcite was identified. By microscopic analysis by using SEM-EDS and polarizing microscope, newly formed mineral that is comprised of Ca mainly was identified at the perimeter (i.e. surface) of the ash particle. Thus, it deemed that newly formed mineral is calcite and it inhibited the leaching of Cs by covering surface of bottom ash. Incineration bottom ash is highly alkaline material and carbonation promptly occurs after disposal. Since the pH of the ash landfill is reported to be kept high for long-term, Cs in bottom ash will be kept stably by calcite for a long term.

ACKNOWLEDGEMENTS

This research was supported by an Environment Research and Technology Development Fund of the Ministry of the Environment, Japan. Besides, many of microscopic analyses conducted in this work were assisted by Hokkaido University Microstructure Characterization Platform's facility allocated in Nanotechnology Platform Program of the Ministry of Education, Culture, Sports, Science and Technology (MEXT), Japan.

REFERENCES

[1] Japan Ministry of Environment, "Management of off-site Waste Contaminated with Radioactive Materials due to the Accident at Fukushima Nuclear Power Stations", 2012, http://www.env.go.jp/en/focus/docs/files/20121128-58.pdf.

[2] Japan National Institute for Environmental Studies, "Proper treatment of wastes contaminated by radioactive substances, 2012, http://www.nies.go.jp/shinsai/techrepo_publicver_e_121128.pdf, 2012.

[3] Landsberger S, Buchholz B. A, Kaminski M, Plewa M, "Trace elements in municipal solid waste incinerator fly ash", Journal of Radioanalytical and Nuclear Chemistry, Vol. 167(2), 1993. pp 331-340.

[4] Iguchi T, Kawano T, Fujihira H, "Combustion Behavior of Cesium in MSW Incineration Process", Proceedings of the 1st IWWG-ARB Symposium, 18-21 March, 2013.

[5] Sakanakura H, Osako M, Kida A, "Effect of exposure test conditions on leaching behavior of inorganic contaminants from recycled materials for roadbeds", Waste Management, Vol.29 (5), 2009, pp.1658-1665.

[6] Meima J.A, Comans R.N.J, "The leaching of trace elements from municipal solid waste incinerator bottom ash at different stages of weathering", Applied Geochemistry, Vol.14, 1999, pp.159-171.

[7] Saffarzadeh A, Shimaoka T, Kakuta Y, Kawano T, "Cesium distribution and phases in proxy experiments on the incineration of radioactively contaminated waste from the Fukushima area, Journal of Environmental Radioactivity, Vol.136, 2014, pp.76-84.

THERMOELECTRIC POWER (TEP) MEASURMENT OF GEL GROWN BARIUM OXALATE CRYSTAL

Paresh Vasantlal Dalal[1]

[1]Physics Research Lab, Shri V. S. Naik Arts, Commerce and Science College, Raver-425508, India

ABSTRACT: An attempt is made in the present work to characterize gel grown barium oxalate crystals by Thermo Electric Power (TEP) measurement. Different parameters such as Fermi energy and mode of scattering were calculated. To calculate Fermi energy and scattering parameter of a material, a graph of Seebeck coefficient(S), versus reciprocal of temperature difference (1/ΔT) is plotted. The slope of the graph is -27.50 mV and intercept is 0.181 mV/K, and hence Fermi energy, E_F = 0.028 eV. Scattering parameter has calculated 0.4. The experimental value obtained for A = 2.10 is in well agreement to conclude that the conduction of heat in the material may be due to the lattice or phonons and can be associated with lattice or phonon scattering.

Keywords: Barium oxalate, Thermo Electric Power (TEP), Fermi energy, Mode of scattering

1. INTRODUCTION

Thermoelectric power (TEP) has attracted many researchers for its applications in designing a portable refrigerator [1], and power generations. Narrow gap Bi_2Te_3 semiconductors and its alloys, are found to be the most efficient thermo-electric materials [2]–[5], as its Figure of merits (Z = S2/kρ, where S is Seebeck coefficient, k is thermal conductivity and ρ is resistivity) have high Seebeck coefficient and therefore they have high demand in electronics field. Many insulators have shown the characteristics of exhibiting large TEP. Insulators have extremely high resistance; therefore conduction can take place by several mechanisms such as thermal or Schottky emission, tunneling, Poole-Frenkel effect, field emission, space charge limited conduction etc.[6]. Measurement of thermoelectric power has distinctive advantages over other methods because measured thermoelectric voltage is directly related to the carrier concentration [7]. Many researchers have reported thermoelectric power measurement of semiconducting materials [8]-[9], and some on organic materials [10]-[17]. However, there are no such studies are reported on oxalate material.

Looking at the importance of the thermoelectric power (TEP), author of this paper has therefore carried out a systematic investigation of gel grown barium oxalate crystals. Different parameters such as Fermi energy and mode of scattering were also calculated.

2. EXPERIMENTAL

Thermo electric power of barium oxalate single crystal was measured on an instrument assembled in the Physics Research Lab, Shri V. S. Naik Arts, Commerce and Science College, Raver. (Maharashtra). A single crystal of barium oxalate was placed in the instrument at a proper position and made all equipment ready for working. One end of the crystal was heated with the heating device upto certain fixed temperature. The temperature difference occurred between two ends and corresponding developed e.m.f. were recorded.

3. OBSERVATIONS AND RESULTS

Employing electrical heating device to one end of a crystal produces a temperature gradient, (ΔT) between two ends of a material and give rise to an e.m.f. This developed e.m.f. is known as thermo e.m.f (ΔE), which is directly proportional to ΔT. The temperature difference, ΔT between two ends of a crystal is ranging within a limit of 9 to 12K.Thus, Seebeck coefficients 'S' at different temperatures were calculated by using the equation:

$$S= (\Delta E/\Delta T)$$

The variation of thermo electric power, or Seebeck coefficient 'S' with respect to absolute temperature is shown in **Fig. 1.**

To calculate Fermi energy and scattering parameter of a material, a graph of Seebeck coefficient(S), versus reciprocal of temperature difference (1/ΔT) is plotted and shown in **Fig. 2**.

The slope of the graph is -27.50 mV

And intercept is 0.181 mV/K

So the Fermi energy,

E_F = (slope X charge on an electron)

= $27.50 \times 1.6 \times 10^{-19}$ joules

= 27.50 meV

= 0.028 eV

Constant A = $\frac{(\text{intercept})}{K_B}$ meV/K

Where K_B is Boltzmann constant

$$\text{Constant A} = \frac{(0.181X10-3)eV/K}{(8.617X10-5)\ \ eV/K}$$

A = 2.10

Scattering parameter

$\boldsymbol{\alpha_s}$ = (5/2) – 2.10

= 0.4

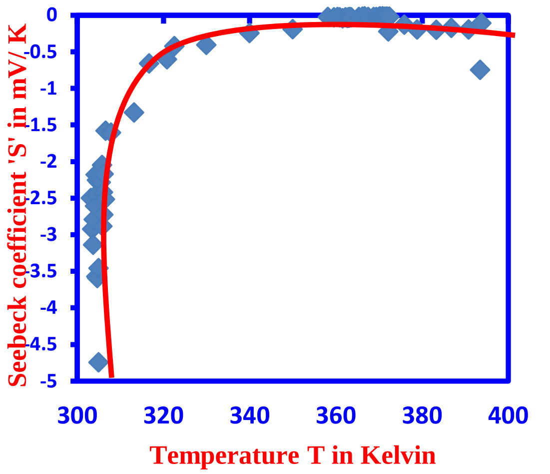

Fig. 1: Plot of Seebeck coefficient (S) versus Temperature(T)

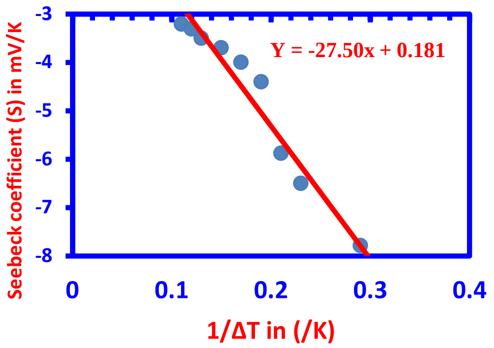

Fig.2: Plot of Seebeck coefficient 'S' versus Reciprocal of Temperature

3.1 Discussion

The value of Fermi energy E_F is obtained from the slope of a graph and the constant A obtained from the intercept on Y-axis. The value of constant 'A' gives valuable information regarding the mode of scattering occurred in the material during the conduction of heat.

The experimental value obtained for A, 2.10 is in well agreement to conclude that the conduction of heat in the material may be due to the lattice or phonons and can be associated with lattice or phonon scattering [6] (**Table 1)**.

Table 1 Values of A and their corresponding Mode of scattering

Scattering mode	Constant A
Ionized impurity	4
Piezoelectric (ionic lattice)	3
Grain boundary	-
Lattice or phonons	2
Vibrations at	1
Constant frequency	0.5
Ionic lattice	2.5
Degenerate system	-

4. CONCLUSION

In the present study, gel grown barium oxalate single crystal was characterized by Thermo electric power (TEP) measurement. From the above studies, following points are observed:

1. Calculated Fermi energy E_F = 0.028 eV
2. Calculated Scattering parameter α_s = 0.4
3. It is concluded that the conduction of heat in the material may be due to lattice or phonon
4. And, can be associated with lattice or phonon scattering.

5. ACKNOWLEDGEMENTS

The author is thankful to the University grants Commission, New Delhi for providing financial assistance under Minor Research Project Scheme.

6. REFERENCES

[1] Mahan G. D., "Good Thermo electrics", Solid State Physics, Vol. 51, 1998, pp. 81-157.

[2] Heikes R. R., and Ure R. W., "Thermoelectricity: Science and Engineering" (Interscience,New York), 1961, pp. 576.

[3] Rosi F. D., "Thermoelectricity and thermoelectric power generation", Solid-State Electron., Vol.11, 1968, pp. 833-848.

[4] Wood C., "Materials for thermoelectric energy conversion", Rep. Prog. Phys., Vol. 51, 1988, pp.459-539.

[5] Goldsmid H. J., and Douglas R. W., "The use of semiconductors in thermoelectric refrigeration", Brit. J. Appl. Phys., Vol. 5, 1954, pp. 386.

[6] Goswami A., "Thin film Fundamentals", New Delhi: New Age International (P) Limited, 1996, pp.314.

[7] Brixner L. H., "X-ray study and thermoelectric properties of the $W_xTa_{1-x}Se_2$", J. Electrochem Soc, Vol.110, 1963, pp. 289.

[8] Calliat T., Fileurial J. P., and Borshchevsky A., "Preparation and thermoelectric properties of semiconducting Zn_4Sb_3", J. Phys Chem Solid, Vol. 58(7), 1997, pp. 1119.

[9] Static V., Pierre A. C., Etsall T. H., and Mikula R. J., "Preparation of tungsten sulfides by sol-gel processing", J Non-Cryst Solids, Vo. 220, 1997, pp. 58.

[10] Wei, Q.S.; Mukaida, M.; Kirihara, K.; Naitoh, Y.; Ishida, T., "Thermoelectric power enhancement of PEDOT:PSS in high-humidity conditions". Appl. Phys. Express, Vol. 7, 2014, 031601.

[11] Wei, Q.; Mukaida, M.; Kirihara, K.; Ishida, T., "Experimental studies on the anisotropic thermoelectric properties of conducting polymer films", ACS Macro Lett., Vol. 3, 2014, pp. 948–952.

[12] Chang, K.-C.; Jeng, M.-S.; Yang, C.-C.; Chou, Y.-W.; Wu, S.-K.; Thomas, M.; Peng, Y.-C., "The thermoelectric performance of poly(3,4-ethylenedioxythiophene)/poly(4styrenesulfonate) thin films", J. Electron. Mater., Vol. 38, 2009, pp. 1182–1188.

[13] Zhang, B.; Sun, J.; Katz, H.E.; Fang, F.; Opila, R.L. "Promising thermoelectric properties of commercial PEDOT:PSS materials and their Bi2Te3 powder composites", ACS Appl. Mater. Interfaces, Vol. 2, 2010, pp. 3170–3178.

[14] Kim, G. H.; Shao, L.; Zhang, K.; Pipe, K.P.,"Engineered doping of organic semiconductors for enhanced thermoelectric efficiency", Nat. Mater. Vol. 12, 2013, pp. 719–723.

[15] Park H., Lee S. H., Kim F. S., Choi H. H., Cheong I. W., "Enhanced thermoelectric properties of PEDOT:PSS nano films by a chemical dedoping process", J. Mater. Chem. A, Vol.2, 2014, pp. 6532-6539.

[16] McGrail, B.T.; Sehirlioglu, A.; Pentzer, E. "Polymer composites for thermoelectric applications", Angew. Chem. Int. Ed., Vol. 54, 2015, pp. 1710–1723.

[17] Yoshida, A.; Toshima, N., "Gold nanoparticle and gold nanorod embedded PEDOT:PSS thin films as organic thermoelectric materials", J. Electron. Mater. Vol. 43, 2014, pp. 1492–1497.

Sixth International Conference on Geotechnique, Construction Materials and Environment, Bangkok, Thailand, Nov. 14-16, 2016, ISBN: 978-4-9905958-6-9 C3051

IMPACT ON AIR QUALITY BY INCREASE IN AIR POLLUTANT EMISSIONS FROM THERMAL POWER PLANTS

Akira Kondo[1], Hikari Shimadera[1] and Mai Chinzaka[1]

[1]Osaka University, Japan

ABSTRACT: The amount of thermal power generation has increased significantly in Japan since the Great East Japan Earthquake in 2011, resulting in increase in emissions of air pollutants. This research evaluated the impact of the emission increase on air quality in Kinki region, Japan by using the Community Multiscale Air Quality model (CMAQ) driven by the Weather Research and Forecasting model (WRF). Three cases of CMAQ simulations were conducted with emission data considering thermal power generation for the year 2010 and 2012, and without power plant emissions, using the meteorological field fixed to 2010.The simulation for the year 2010 well agreed with observations. The emission increase caused higher air pollutant concentrations around power plants, and the contribution of power plant emissions was up to 15 % of NO2 concentration in 2012.

Keywords: Thermal Power Plant, Air Quality Model, Meteorological Model, Nitrogen Dioxide, Sulfur Dioxide

1. INTRODUCTION

The amount of thermal power generation has significantly increased in Japan since the accident of Fukushima Daiichi nuclear power station due to the Great East Japan Earthquake in 2011. The ratio of nuclear power generation to the total power generation in the major 10 companies in Japan was 29% in 2010. In 2012 after the Great East Japan Earthquake, it decreased in 2%. The ratio of thermal power generation rapidly increased from 62% to 89%. As the power generation in the Kinki district of Japan depended heavily on nuclear power generation, the ratio of thermal power generation increased from 46% to 80%[1]. It resulted in the increase in emissions of air pollutants. It is important to assess air quality by the increased air pollutants in the view of the environmental conservation.

In this study, the simulations of air quality by the increased air pollutants from thermal power generation after the Great East Japan Earthquake were carried out in the Kinki district by using air quality model.

2. CALCULATION CONDITIONS

2.1 Outline of Model

The air quality was simulated by Community Multiscale Air Quality system (CMAQ5.02), which was developed by United States Environmental Protection Agency. The meteorological data was provided from the simulation by Weather Research Forecasting model (WRF3.51), which was developed by National Center for Atmospheric Research. The configuration of WRF and CMAQ used in this study is shown in Table 1.

Table 1 WRF/CMAQ configurations

Parameter	Setting
WRF	
Version	ARW 3.5.1
Initial and boundary	NCEP FNL, MSM-GPV, RTG-SST-HR
Land use	USGS 24-category data
Horizontal grid number	98×88 (D1), 108×120 (D2), 92×92(D3)
Vertical grid number	30（surface-100 hPa layer）
Explicit moisture	WSM-6
Cumulus	Kain-Fritsch
PBL	YSU scheme
Surface layer	Noah land-surface model
Radiation	RRTM and Dudhia
Parameter	**Setting**
CMAQ	
Version	5.0.2
Horizontal grid number	76×76 (D1), 92×104 (D2), 76×76(D3)
Initial and boundary	Made from MOZART-4
Baseline emission	INTEX-B, JATOP(vehiecle), OPRF(ship), EAGrid2010-JAPAN
Horizontal/vertical advection	WRF-based scheme
Horizontal/vertical diffusion	Multiscale/ACM2
Photolysis calculation	CCTM in-line calculation
Gas phase chemistry	CB05
Aerosol	AERO 6

Three simulations were carried out against varying emissions from power generation; use of the emissions in 2010 (2010case); use of the emissions in 2012 (2012case) and not considering the emissions from power generation (base).

The boundary conditions of CMAQ were set to the calculations by Model for Ozone and Related Chemical Tracers version 4 (MOZART-4).

2.2 Calculation Period and domain

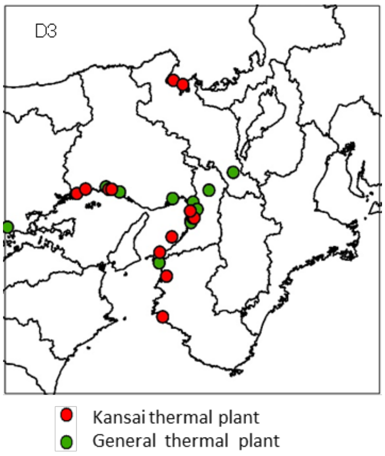

Fig. 1 Location of thermal power plants in D3

Meteorology simulations were conducted by using WRF from April 2010 to March 2011 with an initial spin-up period of 22-31 March 2010. The calculation domains include domain 1 (D1) covering a wide area of Northeast Asia, domain 2 (D2) covering almost the entire area of Japan and domain 3(D3) covering the Kinki district. The horizontal resolutions and the number of grid cells are 64 km and 76 × 76 for D1, 16 km and 92 × 104 for D2, and 4 km and 76 × 76 for D3, respectively. The vertical layers consist of 30 sigma-pressure coordinated layers from the surface to 100 hPa with the middle height of the first layer being approximately 28 m. Figure 1 shows the domain 3 and the location of the thermal power plants.

2.3 Emissions from thermal power stations

The emissions of NOx, SO_2, PM_{10}, $PM_{2.5}$, NH_3 from thermal power stations shown in Figure 1 were estimated. The emissions of NOx, SO_2 from the thermal power stations in the Kansai Electric Power Co. were given from the electric power generation performance in 2014[2]. The emissions of PM_{10}, $PM_{2.5}$, NH_3 were estimated from the emission database of EAGrid2010-JAPAN [3] in 2010 and fuel consumption in 2010 and 2012. The ratio of oil consumption, LNG consumption and coal consumption in 2010 and 2012 is 4.19, 1.56, and 1.15, respectively. The emissions from the thermal power stations in other companies were predicted from the electric power generation ratio in the Kansai Electric Power Co. and other companies. The hourly variation of the emissions each month were considered from the hourly variation of the electric power generation in 2012[4].

Figure 2 shows the emissions of NOx and SO_2 each power stations in 2010 and 2011. In the Kainan oil power station, the emissions extremely increased in 2012, because the Kainan oil power station was the peak load electricity source. On the other hand, the emissions in the Kobe coal power station in 2012 were almost same as 2010, because the Kobe coal power station was used as the base load electricity source.

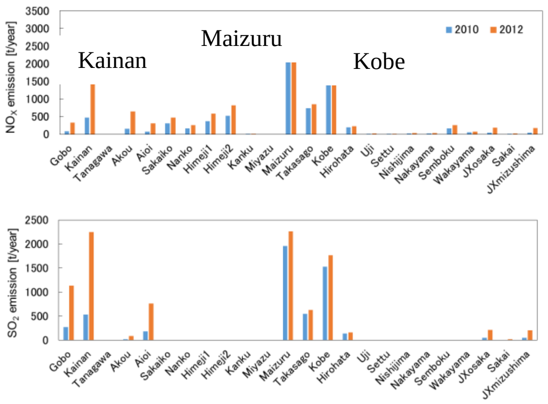

Fig.2 NO_X and SO_2 emissions from thermal plant in 2010 and 2012

3. RESULTS

3.1 Comparison between simulations and observations

The simulations in WRF and CMAQ and the observations were compared by several statistical indexes, which were correlation confident (R), Mean Absolute Error (MAE), Mean Bias Error (MBE) and Index of Agreement (IA). Table 2 shows the statistical indexes of mean daily temperature, specific humidity and wind speed on April, July, October and January in 2010 Japan fiscal year at several monitoring stations in Osaka prefecture simulated by WRF. The criteria of the statistical indexes, which were MBE $\leqq \pm 0.5^{o}$C, MAE$\leqq 2^{o}$C, IA $\geqq 0.8$ for temperature, MBE$\leqq \pm 1$ g/ kg, MAE$\leqq 2$ g/kg, IA$\geqq 0.6$ for mixing ratio and MBE $\leqq \pm 0.5$ m/s, RMSE$\leqq 2$ m/s, IA$\geqq 0.6$ for wind speed, was proposed by Emery[5]. Except for MBE of temperature on January, temperature, mixing ratio and wind speed satisfied the criteria. Figure 3 shows the mean daily variations of temperature, mixing ratio and wind speed in 2010 Japan fiscal year at several monitoring stations in Osaka prefecture. The simulations well captured the observations. Table 3 shows the statistical indexes of mean daily NO_2, SO_2 $PM_{2.5}$ and O_3 in 2010 Japan fiscal year at several monitoring stations in Osaka prefecture simulated by CMAQ. Figure 4 shows the mean daily variations of NO_2, SO_2 $PM_{2.5}$ and O_3 concentration in 2010 Japan fiscal year at several monitoring stations in Osaka prefecture. The simulations well captured the observations.

Table 2 Statistical indexes of temperature, mixing ratio and wind speed in Osaka prefecture

Statistic	Apr.	Jul.	Oct.	Jan.
Temperature (2010JFY)				
number	720	744	744	744
Obs.ave	13.56	27.91	19.91	4.36
Sim.ave	13.15	28.33	20.37	3.29
R	0.96	0.89	0.95	0.90
MBE	--0.42	0.42	0.47	-1.07
MAE	0.94	1.00	0.84	1.25
IA	0.97	0.93	0.97	0.90
Mixing ratio (2010JFY)				
number	720	744	744	744
Obs.ave	5.66	16.42	9.30	2.73
Sim.ave	5.73	16.39	9.65	2.97
R	0.95	0.65	0.93	0.81
MBE	0.08	-0.03	0.36	0.24
MAE	0.53	0.86	0.71	0.35
IA	0.97	0.81	0.96	0.86
Wind Speed (2010JFY)				
number	720	743	744	744
Obs.ave	2.63	2.54	2.11	3.08
Sim.ave	2.76	2.82	2.56	2.72
R	0.69	0.68	0.65	0.70
MBE	0.12	0.28	0.45	-0.35
MAE	1.28	1.26	1.09	1.48
IA	0.82	0.81	0.77	0.82

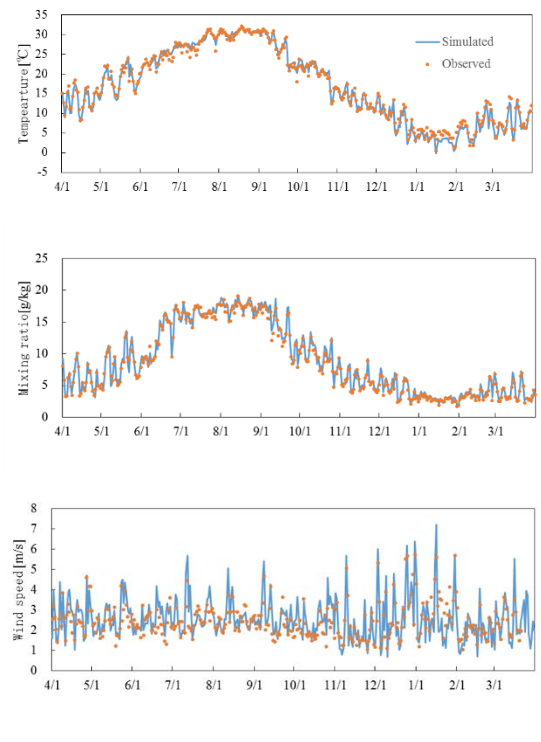

Fig.3 mean daily variations of temperature, mixing ratio and wind speed in 2010 Japan fiscal year

Table 3 Statistical indexes of NO_2, SO_2 $PM_{2.5}$ and O_3 concentration in Osaka prefecture

Statistic	NO_2	SO_2	$PM_{2.5}$	O_3
number	358	363	358	360
Obs.ave	22.03	4.77	19.21	49.82
Sim.ave	21.80	3.05	14.27	49.17
R	0.85	0.65	0.88	0.84
MBE	-0.23	-1.72	-4.95	-0.66
MAE	4.04	2.00	5.70	7.79
IA	0.91	0.69	0.89	0.90

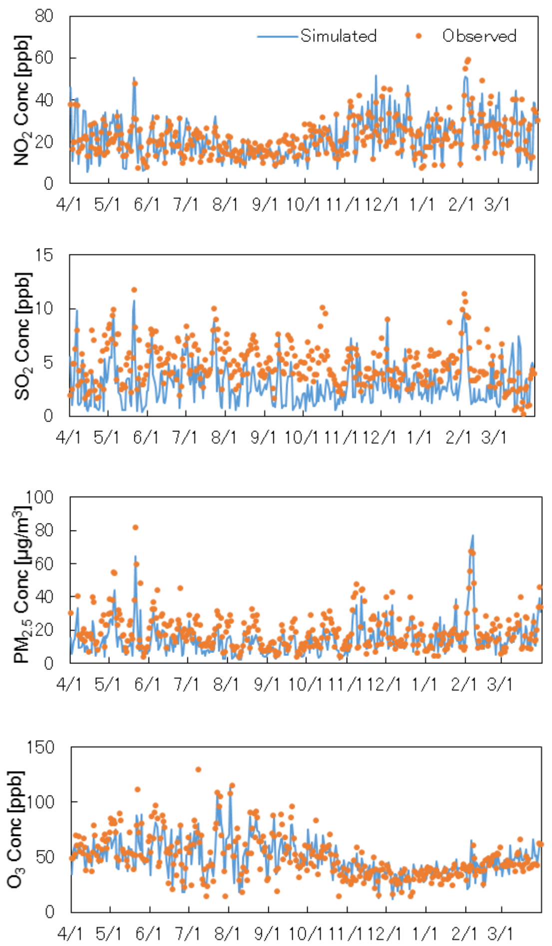

Fig.4 mean daily variations of NO_2, SO_2 $PM_{2.5}$ and O_3 concentration in 2010 Japan fiscal year

3.2 Contribution to Air Quality by emissions from thermal power stations

The detail analysis was performed at the neighborhood of Kainan thermal power station and the Kobe thermal power station in which the pollutant emissions extremely increased in 2012 Figure 5 shows the NO_2 concentration in 2012, the contribution to NO_2 concentration by the emissions from thermal power station in 2010 (2010-base) and the contribution to NO_2 concentration by the increment emissions from thermal power station in 2012 (2012-2010) at the Kainan and Kobe. The mean NO_2 concentration, the mean contribution NO_2 concentration and the mean contribution rate was 6.2ppb, 0.8ppb and 13.4% at the Kainan and 11.6ppm, 0.2ppb and 2.0% at the Kobe, respectively. NO_2 concentration in the maximum contribution by the emission from the thermal power station was 24.1ppb at the Kainan on 6 December and 20.5ppm at the Kobe on 13 March, respectively. The contribution NO_2 concentration and the contribution rate on the above day was 3.7ppb and 15.3% at the Kainan and 1.1ppb and 5.1% at the Kobe, respectively.

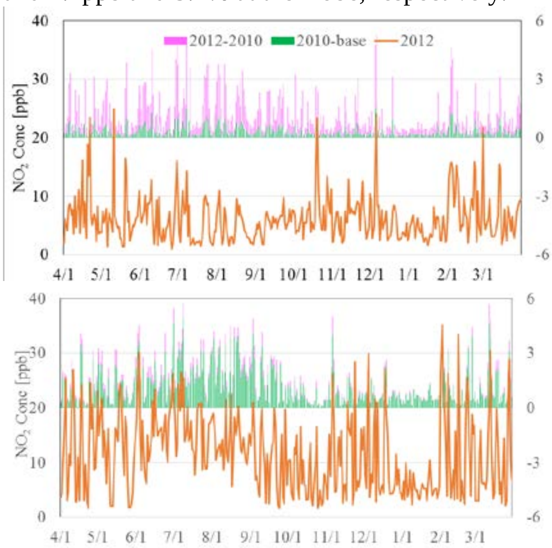

Fig.5 Time series of NO_2 concentration and the contribution to NO_2 from thermal power station at Kainan (top) and Kobe (bottom).

Figure 6 shows the distribution of NO_2 concentration in D3 and D1, and the distribution of the incremental NO_2 concentration at 7 JST of 1 July, when the contribution to NO_2 concentration by the increment emissions from thermal power station at Kainan was maximum by the simulation. The transboundary pollution of NO_2 didn't occurred in the simulation in D3. In the coast areas and the industry areas, the high NO_2 concentration occurred in the simulation in D1, because the main emissions of NO_2 was from factory, vehicles and vessels. The remarkable increase of NO_2 concentration occurred at the Kainan and at the Maizuru faced to Japan Sea. The increase of NO_2 concentration at the Kobe was small compared at the Kainan. The spread of NO_2 concentration from the power stations was limited.

Figure 7 shows the SO_2 concentration in 2012, the contribution to SO_2 concentration by the emissions from thermal power station in 2010 (2010-base) and the contribution to SO_2

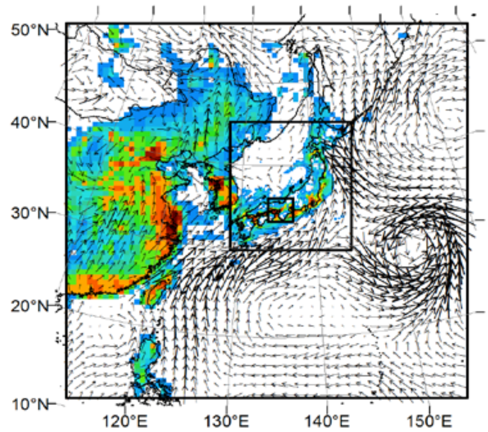

concentration by the increment emissions from thermal power station in 2012 (2012-2010) at the Kainan and Kobe. The mean SO_2 concentration,

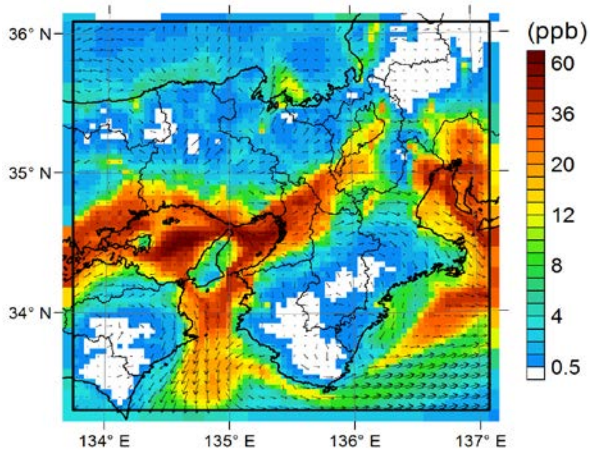

the mean contribution SO_2 concentration and the mean contribution rate was 3.3ppb, 0.9ppb and 26.0% at

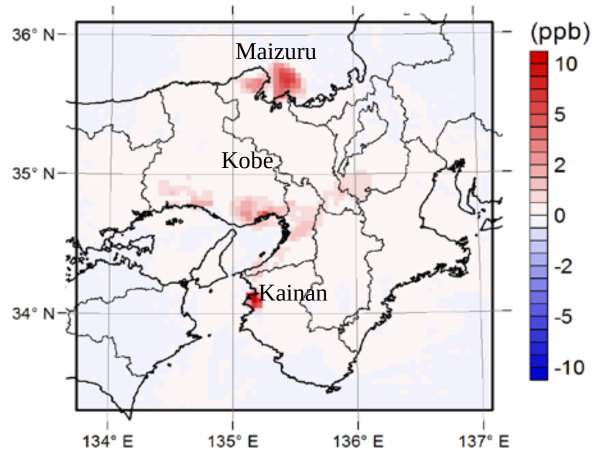

Fig.6 Distribution of NO_2 concentration in D3 (Top) and D1 (Middle), and the distribution of the incremental NO_2 concentration (Bottom) at 7 JST of 1 July

the Kainan and 4.0ppm, 0.2ppb and 3.7% at the Kobe, respectively. SO_2 concentration in the maximum contribution by the emission from the thermal power station was 13.3ppb at the Kainan on 6 December and 12.0ppm at the Kobe on 5 May, respectively. The contribution SO_2 concentration and the contribution rate on the above day was 4.2ppb and 32.0% at the Kainan and 0.6ppb and 5.4% at the Kobe, respectively.

Figure 8 shows the distribution of SO_2 concentration in D3 and D1, and the distribution of the incremental SO_2 concentration at 7 JST of 5 May, when the contribution to SO_2 concentration by the increment emissions from thermal power station at Kainan was maximum by the simulation. The transboundary pollution of SO_2 didn't occurred in the simulation in D3. In the coast areas and the industrial areas, the high SO_2 concentration occurred in the simulation in D1, because the main emissions of SO_2 was from factory and vessels. The remarkable increase of SO_2 concentration occurred at the Kainan. The increase of SO_2 concentration at the almost thermal power stations occurred. SO_2 concentration diffused in the wide area.

The contribution rate of NO_2 and SO_2 concentration by the emission from the thermal power station was almost same for the mean concentration and for the maximum concentration. These results suggested that the difference of the contribution concentration occurred from the difference of the meteorological conditions. SO_2 concentration relatively diffused in the wide area compared with NO_2 concentration, because NO_2 was more reactive chemicals in the atmosphere.

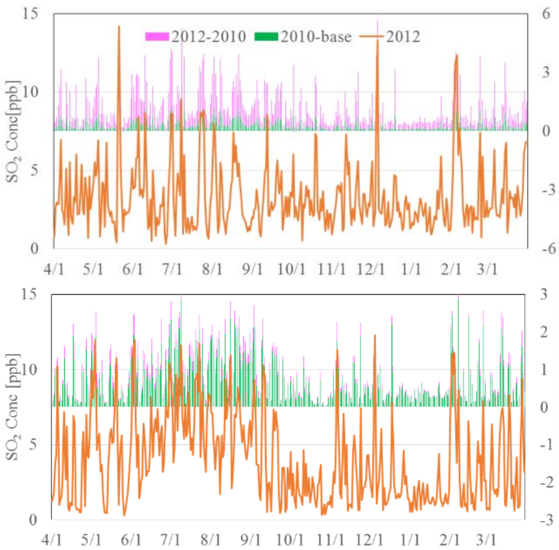

Fig.7 Time series of SO_2 concentration and the contribution to SO_2 from thermal power station at Kainan (top) and Kobe (bottom).

Figure 9 shows the O_3 concentration in 2012, the contribution to O_3 concentration by the emissions from thermal power station in 2010 (2010-base) and the contribution to O_3 concentration by the increment emissions from thermal power station in 2012 (2012-2010) at the Kainan and Kobe. The maximum O_3 concentration and the mean contribution O_3 concentration was 53ppb and -0.9ppb at the Kainan and 99ppm and -0.08ppb at the Kobe, respectively. The contribution O_3 concentration by the emission from the thermal

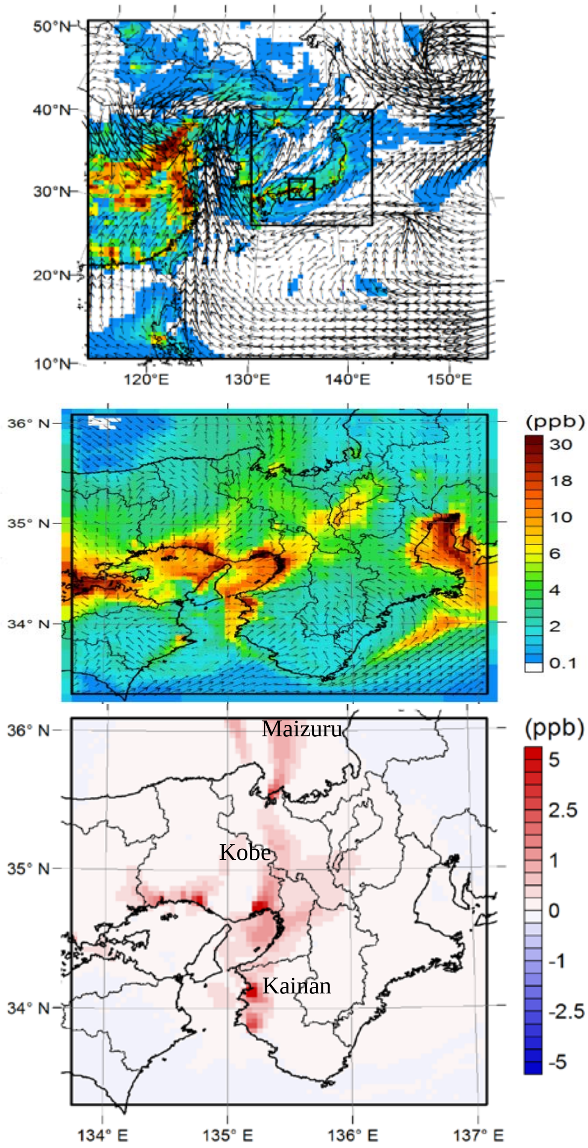

Fig.8 Distribution of SO_2 concentration in D3 (Top) and D1 (Middle), and the distribution of the incremental SO_2 concentration (Bottom) at 7 JST of 5 May

power station became negative because of NO titration.

Figure 10 shows the distribution of O_3 concentration in D3 and D1, and the distribution of the incremental O_3 concentration at 18 JST of 2 August, when O_3 concentration became maximum at Kainan by the simulation. O_3 concentration in the simulation in D1 became high in inland that was apart from urban area with much air pollution emissions. Due to the increment of emissions from thermal power stations, O_3 concentration increased in the wide area of D1 except for the neighborhood of the thermal power stations because of NO titration.

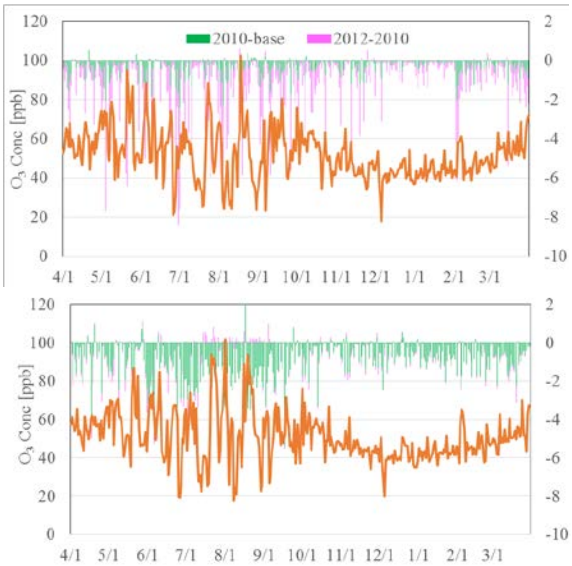

Fig.9 Time series of O_3 concentration and the contribution to O_3 from thermal power station at Kainan (top) and Kobe (bottom).

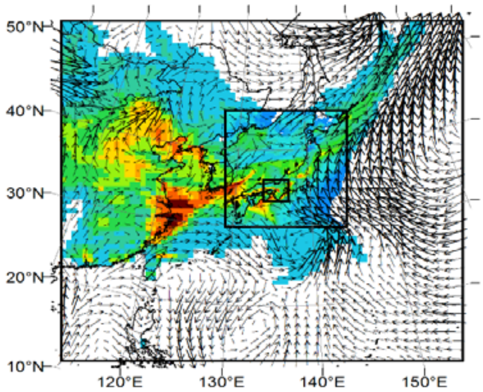

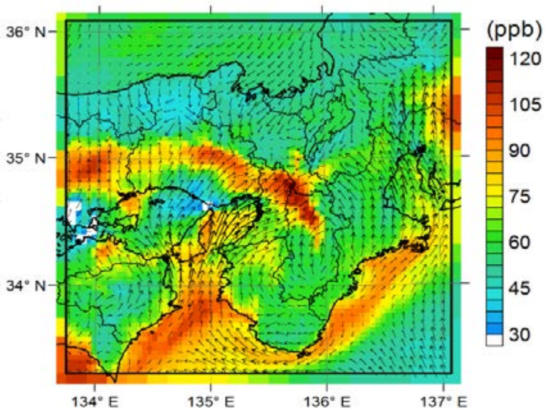

4. CONCLUSION

The simulations of air quality by the increased air pollutants from thermal power generation after

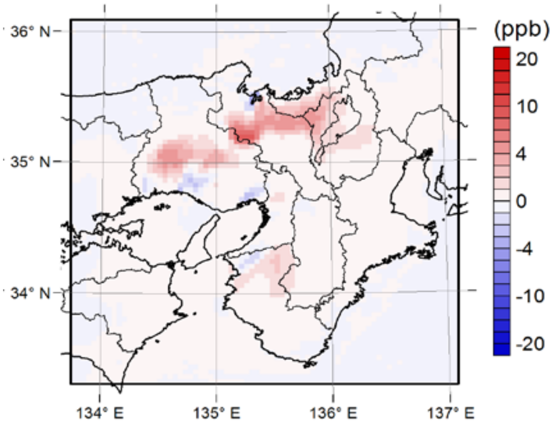

Fig.10 Distribution of O_3 concentration in D3 (Top) and D1 (Middle), and the distribution of the incremental O_3 concentration (Bottom) at 18 JST of 2 August

the Great East Japan Earthqu ake were carried out in the Kinki district by using WRF/CMAQ. The emissions of NOx and SO_2 from the thermal power stations after the Great East Japan Earthquake heavily increased. The simulations showed that (1) the remarkable increment of air pollution concentration of NO_2 and SO_2 was limited in the neighborhood of the thermal power stations, (2) the increment of O_3 concentration was widely spread but O_3 concentration in the neighborhood of the thermal power stations decreased because of NO titration.

4. REFERENCES

[1] URL:http://www.fepc.or.jp/library/pamphlet/zumenshu/

[2] URL:http://www.kepco.co.jp/sustainability/kankyou/report/data/karyoku01.html

[3] Fukui T., Kokuryo K., and et. al., Updating EAGrid2000-Japan emissions inventory based on the recent emission trends, Japan Society for Atmospheric Environment, 49, 2014, pp.117-125 (in Japanease).

[4] URL:http://www.kepco.co.jp/energy_supply/supply/denkiyoho/download.html.

[5] Emery C., Tai E. and Yarwood G.: Enhanced meteorological modeling and performance evaluation for two Texas ozone episodes. Prepared for The Texas Natural Resource Conservation Commission 12118 Park 35 Circle Austin, Texas 78753, 2001.

OCEAN DECONTAMINATION: HIGH ABILITY REMOVAL METHOD TO RADIOACTIVE CESIUM FROM OCEAN SLUDGE BY USING MICRO BUBBLES AND ACTIVATING MICROORGANISMS

Kyoichi OKAMOTO[1], Takeshi TOYAMA[2] and Tomoe KOMORIYA[3]

[1]Department of Oceanic Architecture and Engineering, CST, Nihon University, Japan;
[2]Department of Materials and Applied Chemistry, CST, Nihon University, Japan
[2]Department of Sustainable Engineering, CIT, Nihon University, Japan

ABSTRACT

The Fukushima nuclear accident of March 11, 2011, soil and water had been contaminated by radioactive cesium. Moreover, radioactive cesium was found in the ocean sludge in Tokyo Bay flowing from rivers. Cesium which is adsorbed to the sludge cannot be easily removed. One of the authors developed decomposition and purification system, a circulation-type system by micro bubbles, that is, by creating aerobic state, aerobic bacteria are activated resulting to decomposition and purification of ocean sludge. Based on the hypothesis that radioactive cesium is adsorbed on the surface of the sludge deposition. It is considered that cesium can be eluted after decomposing the deposited sludge. Once the cesium is eluted in the water, it can fix to a mineral such as zeolite. Eluting and fixing cesium adsorbed on sludge takes so much time. In this case, the concept of removing the left sludge by flocculation method and then followed by coagulating sedimentation method is studied. In this study, our objects is to show the effectivity and efficiency of using flocculation and coagulating sedimentation in removing radioactive cesium. As the results, we pointed out this method is very good.

Keywords: Ocean Decontamination, Radioactive Cesium, Micro Bubbles, Microorganism Activator, Coagulant

INTRODUCTION

The Fukushima nuclear accident of March 11, 2011, soil and water had been contaminated by radioactive cesium. Moreover, radioactive cesium was found in the ocean sludge in Tokyo Bay flowing from rivers. Cesium which is adsorbed to the sludge cannot be easily removed.[1] One of the authors developed decomposition and purification system, a circulation-type system by micro bubbles, that is, by creating aerobic state, aerobic bacteria are activated resulting to decomposition and purification of ocean sludge. [2]

Based on the hypothesis that radioactive cesium is adsorbed on the surface of the sludge deposition, it is considered that radioactive can be eluted after decomposing the deposited sludge. Once the cesium is eluted in the water, it can fix to a mineral such as zeolite. [3] But eluting and fixing cesium adsorbed on sludge takes so much time. In this case, the concept of removing the left sludge by flocculation method and then followed by coagulating sedimentation method is studied.

In this study, our object is to show the effectivity and efficiency of using flocculation and coagulating sedimentation in removing radioactive cesium.

DECOMPOSITION SYSTEM WITH CIRCULATION TYPE

It is very important to reduce sedimentary sludge in the ocean. Plans to reduce the sludge are usually dreading or sand covering. Dredging is a simple way and aims to cut off the sludge. But after cutting off, treating the dredged sludge takes much more time and, of course, cost. Sand covering, in general, gives a big

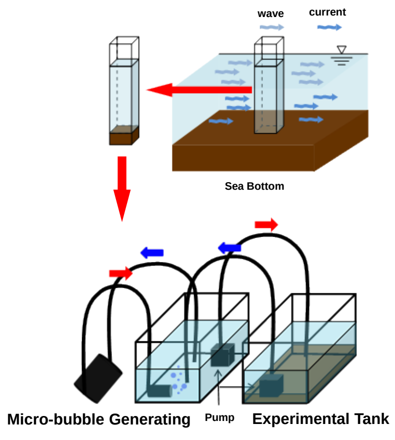

Fig. 1 Purification System of Circulation Type.

load to living organisms and the ecological system.

So that, a more efficient way is needed to reduce the sludge while not imparting environmental load in the local sea area. Here, attention was paid to micro-bubble technology for application to the purification of the sludge. The important point in this technique is to activate the bacteria existing in the area by micro-bubbles. Micro-bubbles (that is MB) can change conditions into an aerobic state. [4], [5] If the bubbling stops, the situation changes into anaerobic state, according to recent research. So, we selected a method for decomposing the sludge by microorganisms.

One of the authors had developed the decomposition system for ocean sludge with circulation type by micro-bubbles, shown in Fig.1, which decompose and purification sludge by activating the aerobic bacteria, after creating an aerobic state by micro-bubbles. [3]

MECHANISM ON REMOVING CESIUM

In general, ocean sludge has a negative charge. When cesium with a positive charge flows from river, sludge was adsorbed cesium, shown in Fig. 2. So that, sludge adsorbed cesium cannot eliminate by usual way.

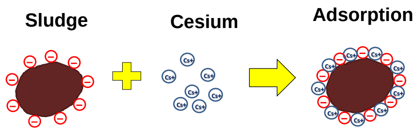

Fig. 2 Mechanism on Adsorption of Cesium.

Here, we have a way by using of the decomposition system for ocean sludge with circulation type. After decomposition of the sludge adsorbed cesium by our system, cesium is eluted into water, shown in Fig. 3. That is our hypothesis.

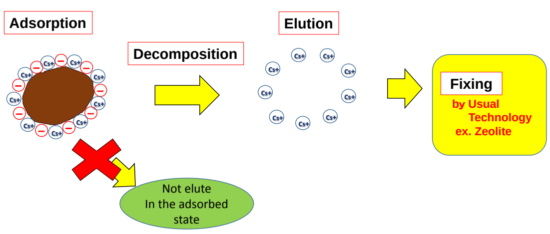

Fig. 3 Mechanism on Fixing of Cesium after Elution.

But, it takes much time to elute and fix all of cesium adsorbed on sludge. Now, we have new idea which is to use flocculation method against to the rest of decomposed sludge, and then make the precipitation of cesium and sludge, shown in Fig. 4.

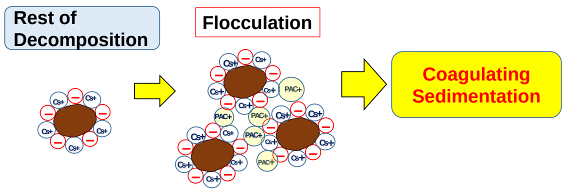

Fig. 4 Mechanism on Coagulating Sedimentation by PAC, to the left of Decomposition Sludge with Cesium.

REMOVAL EXPERIMENTS FOR CESIUM

Experimental System

The experimental devices consist of two parts, shown in Fig. 5. The water circulates through two tanks. In one tank (Width40xLength28x Hight28cm), micro-bubbles are generated. The micro-bubbles have micro-size diameter and high solubility. This means the water with high concentration of dissolved oxygen circulates through these tanks. The other part is the experimental tank (W60xL29xH35cm). We used sea-water 30(litter) and sludge 1(kg). Here, a micro-bubble generator is based on [4], [5] and the flow rate is 900 (litter/hour). The flow rate of water pumps connected each tanks are 300 (litter/hour). A cooler for water tank was set at side of the tank for generating microbubbles, for the purpose of setting water temperature 30 degree centigrade.

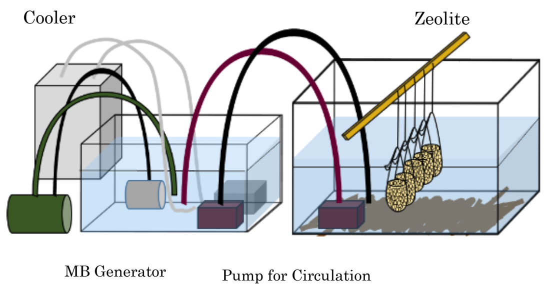

Fig. 5 Experimental System for Removal of Cesium.

Experimental Procedure

We had caught the sludge and the sea water at Funabashi Port in Chiba Prefecture in JAPAN, as shown in Fig.4 and 5. Here, we had picked up the sludge under 10cm from seabed before sampling as experimental procedure, because we have to cut the initial value of cesium in the sludge, from [3].

We used the cesium chloride before 24 hours of starting time and the concentration of cesium ion is 100 (ppm).

After setting the decomposition system with circulation type by micro-bubbles, experiment starts at the same time of generating micro-bubble device and also the zeolites were set in the tank. The zeolite is the composed type and the pore size is 4A type that is 0.4[nm]. Diameter of cesium is generally 0.338[nm], so that this diameter is much closer.

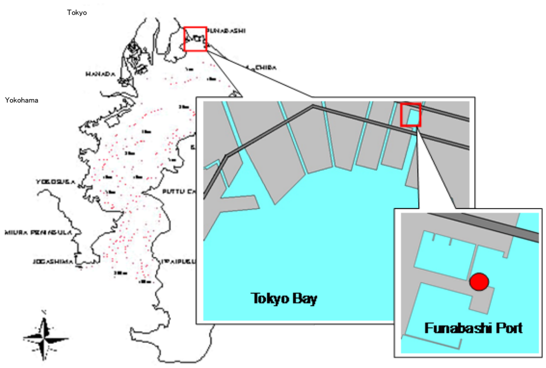

Fig. 6 Catching Point of Sludge and Sea Water at Funabashi Port in Tokyo Bay.

After 6 hours later, the microorganism activator was put in the experimental tank. Main staff of the activator is Kelp and including nutrients and some enzyme. Our used activator is reported to show effective results in purification for grease trap.

Dissolved oxygen (DO), water temperature and pH are measured by using of multi-parameter water quality meter. Ammonium nitrogen (NH_4-N), total nitrogen (T-N) are measured by using of digital-water-analyzer by digital “Packtest”, by water filtered after sampling in experimental tank.

Procedure for Liquid Measurements

Measurements for liquid phase did each 6 hours until 12 hours, and then every 12 hours to120 hours, shown in Fig.7.

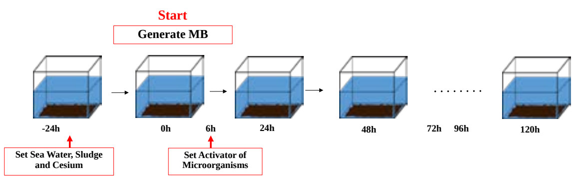

Fig. 7 Experimental Procedure for Liquid Measurements.

Procedure for Solid Measurements

As procedure of solid phase, experimental tanks are prepared for each measurement time; 0, 24, 48, 72, 96, 120. When the objective tank after worked system is stopped the system, coagulant was put and mixing. After this, water quality and cesium are measured. After filtration and dry, cesium in solid was analyzed by the energy dispersion type X-ray analysis device (EDX). Here, our used coagulant is PAC (Poly Aluminum Chloride) and the solution concentration is 10%. [6]

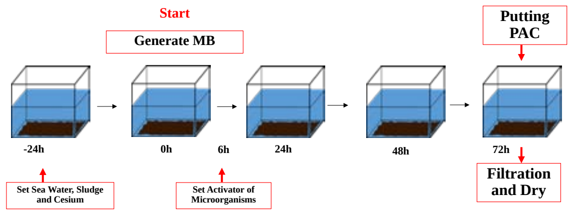

Fig. 8 Experimental Procedure of for Solid Measurements (For Example: 72hours Case).

Experimental Conditions

Experimental conditions are the concentration of PAC according to the putting time, shown in Table 1. The another cases are PAC concentration is 500 ppm at 0, 24 hours, 25 ppm at 96 hours and 10 ppm at 120 hours.

Table 1 Experimental Conditions

at 48h	at 60h	at 72h
PAC (ppm)	PAC (ppm)	PAC (ppm)
600	200	100
400	100	75
200	75	50

RESULTS AND CONSIDERATION

Results on Water Quality

Water Temperature, pH, DO (Dissolved Oxygen) and H_2S (Hydrogen Sulfide)

As the results of environmental conditions; water temperature, pH and DO, water temperature was almost 30 centigrade degrees because of using water cooler. pH showed the values of 7.5 to 8.7. DO is saturation state by the values of 7.5 to 8.0. These results are almost same as ordinary results. [3]

H_2S decreased rapidly by 24 hours by the supply of O_2 of microbubble device and then became zero at 48 hours. This is also the same as ordinary results. [3]

DIN (Total Inorganic Nitrogen), T-N (Total Nitrogen) and Cesium in Water

DIN and T-N as purification items decreased well by the denitrification. T-N is reduced to 82%. This is also the same as ordinary results. [7], [8]

Cesium in liquid was analyzed by the iron chromatography, and the initial value for cesium is 50.06 (ppm) but the value by 12 hours is not detective, so that reduction rate of cesium was 100%.

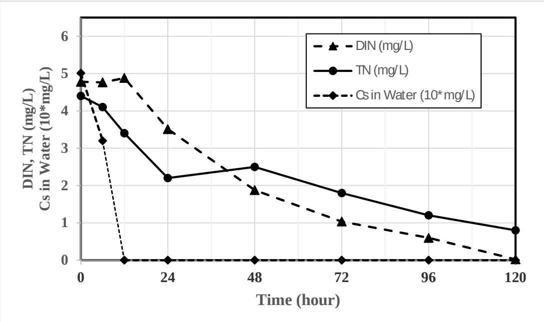

Fig. 9 Changes on DIN, TN and Cesium in Water.

Most Suitable Concentration of PAC

We are going to find the most suitable concentration of coagulant (PAC) depended on the working time, by putting the coagulant with concentration according to experimental condition.

By focusing on the T-N as the index of Table 2, the relationship of minimum concentration of PAC and working time of the system was shown in Fig.10. Here, the results of T-N were N.D. in case of 0, 24, 96 and 120 hours.

When it's the concentration of PAC of the upper part of a solid line in Fig.10, cesium of solid phase indicates the maximum purification performance and coagulating sedimentation is executed. Therefore, most suitable working time of the system is 48 to 60 hours, so that the reducing working time can be supposed and expected.

Table 2 Experimental Results.

at 48h		at 60h		at 72h	
PAC (ppm)	TN/TN0	PAC (ppm)	TN/TN0	PAC (ppm)	TN/TN0
600	ND	200	ND	100	ND
400	ND	100	ND	75	ND
200	0.24	75	0.22	50	0.20

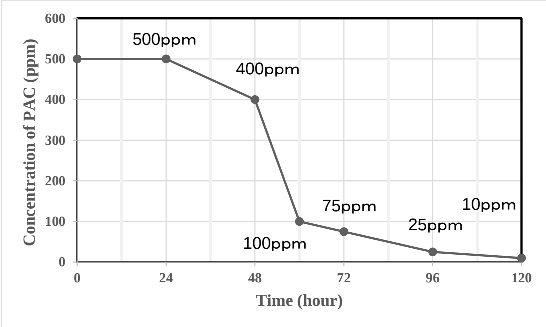

Fig. 10 Suitable Concentration of PAC According to Working Time in Experimental System.

ADDITIONAL EXPERIMENT

We get the relationship of most suitable concentration of PAC according to working time of the system. But we need the changes of cesium before and after working system.

Now we executed the additional experiments for the purpose of getting of the amount of cesium before and after working system. The experiments are made in cases of 48 hours and 72 hours, and as comparative target is the case of 0 hour.

Water Quality

The results for water quality are shown Fig. 11. DIN and T-N are very good decrease by the denitrification. This is also the same as our ordinary results.

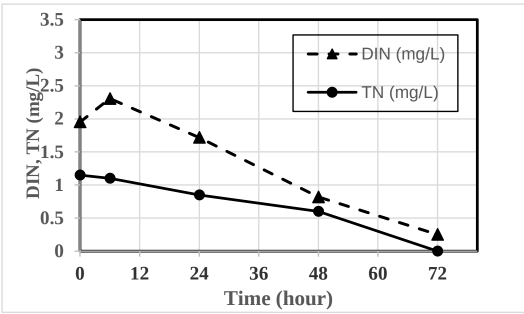

Fig. 11 Changes on DIN, TN in Additional Experiment.

Cesium in Water

Cesium in liquid was analyzed by atomic absorption spectrometry, and the value for cesium is not zero at 48 hours and 72 hours, shown in Fig.12. This is caused by weak circulation of experiment, and this analytical way is very good precision. But this is not big problem. We can understand the eluting cesium from sludge and have another way; adsorption cloth and other for cesium adsorption and fixing.

The difference is small in the cesium amount before and after investment of PAC, in case of at 48 and 72 hours.

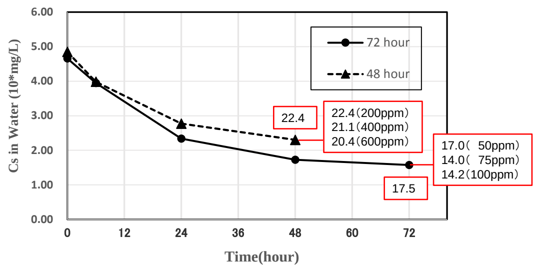

Fig. 12 Changes on Cesium in Water before and after investment of PAC.

About Safety to all Ecosystem by this System

Coagulant used in this experimental system is PAC (Poly Aluminum Chloride) and the solution concentration is 10%. [6] This is basically safe according to appropriate usage. It's supposed PAC is certainly the substance which isn't diffused around the environment. It seems it is no problem as far as clear layer at the top of liquid is discharged, because coagulant power is strong. Toxicity to short-necked clam and laver (Medial Tolerance Limit) is 10000(ppm)/48(hour) from safety data sheets (SDS). [9] Even if PAC we added doesn't have an influence on the environment. PAC hydrolyzes with passage in time and changes into a stable aluminum hydroxide.

CONCLUSION

We carried out the removing cesium in solid phase for experimental system which is to use flocculation method against to the rest of decomposition sludge, after the elution and fixing cesium by setting zeolite in the decomposition system with circulation type by micro-bubble and activating microorganisms.

(1) From the results by measurements for water qualification, T-N decreases maximum 82.0%. Cesium in water was fixed 100% and became zero by 12 hours of the experiment.
(2) We pointed out the relationship of most suitable concentration of PAC according to working time in experimental system. It assumed this concentration of PAC shows the maximum purification efficiency in water and is very good.
(3) It seemed the most suitable time for working the experimental system is 48 to 60 hours, so that the working time of system can be reduced.

We also executed the additional experiments for the purpose of getting of the amount of cesium before and after working system, in case of 48 hours and 72 hours, and 0 hour as comparative target. As the results are

(4) Cesium in water after stopping of the system and investment of PAC in case of 48 and 72 hours, is almost the same as the quality before investment of PAC.

ACKNOWLEDGEMENTS

The authors would like to express sincere thanks for executing the experiments to Takahiro ARAKAWA and Taiyo KOKATSU, Students of Nihon University, in Japan.

This work was supported by KAKENHI (Grant-in-Aid for Scientific Research (C-26420831)).

REFERENCES

[1] Tokyo News Paper: Radioactivity pollution in the Tokyo Bay, "A nuclear power plant, far convergence", March 10, 2015. http://www.tokyo- np.co.jp/feature/ tohokujisin/ archive/fouryears/150310_1.html
[2] Okamoto K, Hotta K, Toyama T and Kohno H, "Purification System of Ocean Sludge by Activating Microorganisms", International Journal of GEOMATE (Geotec, Const. Mat. & Env.), Vol.6, No.1, pp.791-795, March, 2014.
[3] Okamoto K and Toyama T: Ocean Decontamination: Removal of Radioactive Cesium from Ocean Sludge by Using Micro bubbles and Activating Microorganisms, The Japan Society of Naval Architects and Ocean Engineers, May, 2014.
[4] Imai T, Shioshige K, Ukita M, Sekine M, Higuchi T, Fukagawa K and Fujisato T, "Development of Device for Dissolving High Concentration Gas for Purification at bottom layer around enclosed water area like Dam Lake", Proc. 39th Forum on Environmental Engineering of Civil Engineering Society, pp.10-12, 2002.

[5] Matsuo K, Maeda K, Ohnari H, Tsunami Y and Ohnari H, “Water Purification of a Dam Lake Using Micro Bubble Technology”, Progress in Multiphase Flow Research I, pp.279-286, 2006.

[6] Okamoto K and Hotta K, “Purification System of Ocean Sludge by Using Coagulants and Activating Microorganisms”, International Journal of GEOMATE (Geotec, Const. Mat. & Env.), Vol.4, No.2, pp.574-579, June, 2013.

[7] Sone T, Yamashita K and Okamoto K, “Identification of Microorganism in Purification Process for Ocean Sludge by using Purification System with Circulation Type”, Japan Association for Coastal Zone Studies, July 2014.

[8] Okamoto K and Toyama T, ”Ocean Decontamination: High Efficiency Removal Method of Radioactive Cesium from Ocean Sludge by Using Microbubbles and Activating Microorganisms”, The Japan Society of Naval Architects and Ocean Engineers, May, 2016.

[9] Poly Aluminum Chloride (PAC), UPC-0100, Safety Data Sheets (SDS), January, 2014 (in Japanese).

Sixth International Conference on Geotechnique, Construction Materials and Environment, Bangkok, Thailand, Nov. 14-16, 2016, ISBN: 978-4-9905958-6-9 C3051

EFFECT OF ADDITION OF BACTERIA ON THE REMOVAL OF RADIOACTIVE CESIUM FROM OCEAN SLUDGE IN A CIRCULATION TYPE PURIFICATION SYSTEM

Tomoe KOMORIYA[1], Kyoichi OKAMOTO[2] and Takashi TOYAMA[2]
[1]CIT, Nihon University, JAPAN; [2]CST, Nihon University, JAPAN

ABSTRACT

Following the Fukushima nuclear accident of March 11, 2011, soil and water were contaminated by radioactive cesium. Moreover, radioactive cesium was found in the ocean sludge in Tokyo Bay, carried by rivers flowing into the bay. The cesium adsorbed in the sludge cannot easily be removed. The objective of this study was to investigate the effect of the addition of bacteria to the micro-bubble circulation system on the efficient removal of radioactive cesium from ocean sludge. One of the authors has developed an ocean sludge decomposition system employing circulation of micro-bubbles. Model sludge was prepared using seawater, sea sludge, and cesium chloride. Bacteria were added to the system after 24 h. Dried tangle extract was added as a nutrient at 24 h and 36 h. The decomposition experiment was carried out for 120 h. The circulation of micro-bubbles created an aerobic state that activated aerobic bacteria, facilitating decomposition and purification of the sludge. Thus, decomposition of the deposited sludge using our system renders the elution of the radioactive cesium possible. If the cesium is eluted in the water, we can fix it using existing technology such as zeolites. We identified and isolated the most useful bacteria for sludge decomposition. Effects on purification seem to be greatest when additional bacteria are added directly to the process. The methodology proposed is expected to facilitate decomposition of sludge and removal of radioactive cesium from the environment.

Keywords: Decontamination, Radioactive Cesium, Ocean Sludge, Micro-bubble, Bacteria

INTRODUCTION

The 2011 accident at the Fukushima Daiichi nuclear power station has resulted in radioactive cesium contamination of soil and water. Radioactive cesium has been detected in the sludge in Tokyo Bay [1], carried by rivers flowing into the bay.

It has been reported that cesium easily adsorbs to the microscopic particles that constitute soil [1], [2]. Most cesium adsorbed by soil is difficult to remove by external factors, and remains present over long timescales. Moreover, closed water areas such as river and bay systems make it difficult to decompose piling organic sludge. Therefore, radioactive cesium is predicted to be deposited in the sediment of the seabed over time, expanding contamination into the ocean. It is important to decontaminate this sediment.

One of the authors developed a decomposition system for ocean sludge that employs the circulation of micro-bubbles. These create aerobic conditions that activate aerobic bacteria, facilitating decomposition and purification of the sludge [3]. Accordingly, it is considered that radioactive cesium can be eluted, after decomposition of the deposited sludge by our system. If the cesium can be eluted in water, it can then be fixed using existing technology such as zeolites [4]. We would thus be able to decontaminate the sediment**.**

To remove radioactive cesium effectively, we carried out isolation and identification of bacteria to break down sludge in the micro-bubble circulation system, and investigated the effect of the addition of microorganisms to the decomposition system on the efficient removal of radioactive cesium from ocean sludge.

MATERIALS AND METHODS

Isolation and Identification of Bacteria to Break Down Sludge in the Micro-Bubble Circulation System

The micro-bubble circulation system consists of two parts, shown in Fig. 1 (without zeolite). The water circulates through two tanks. In one tank (length 40 × width 28 × height 28 cm), micro-bubbles are generated. The micro-bubbles have micro-size diameter and high solubility. This means that water with a high concentration of dissolved oxygen (DO) circulates through these tanks. The experimental tank is 60 × 29 × 35 cm. We used 30 L of seawater and 1 kg of sludge. The micro-bubble generator was based on [6] and the flow rate was

900 L/h. The flow rate of the water pumps connected to each tank was 300 L/h. A cooler for the tank that generates the micro-bubbles was set at 30 °C.

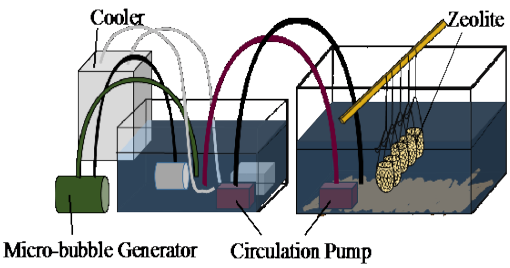

Fig. 1 Circulation purification system

We took samples of sludge and seawater at Funabashi Port in Chiba Prefecture in Japan. We removed the first 10 cm of sludge from the seabed before samples were taken.

After setting up the micro-bubble circulation decomposition system, the experiment started as the generation of micro-bubbles began. After 0, 36, 72, 108, and 120 h, we sampled the sludge in the experimental device.

Samples were diluted in distilled water and 10 μL of each sample was plated on standard agar plates (Nissui Pharmaceutical Co., Ltd., Japan) and cultured at 30 °C for 3–5 days. Thereafter, a bacterial colony was picked for isolation. The isolated bacteria were identified by 16S rRNA gene sequence analysis.

Experiments on Decomposition of Deposited Sludge for Cesium Removal

The system shown in Fig. 1 was used to experimentally remove cesium from ocean sludge. Model sludge containing cesium chloride was poured into the system. One kg of sea-sludge and 30 L of seawater and cesium chloride was mixed and stirred for 24 h. The final concentration of cesium was approximately 100 ppm.

Zeolites were placed in the tank (Fig. 2), micro-bubbles were generated, and the experiment began. The micro-bubble generator again used a flow rate of 900 L/h. The flow rate of the water pumps connected to each tank was 2400 L/h. The cooler was set at 30 °C.

Fig. 2 Zeolites set in experiment tank

After 24 h, isolated bacteria (15 × 10^8 cell/mL) and an activator [7] were added. An extract of kelp was added to the experimental tank after 24 and 60 h. After 0, 12, 48, 60, 72, 96, and 120 h, DO, water temperature, and pH were measured by a multi-parameter water quality meter. A digital pack test (Kyoritsu Chemical-Check Lab. Corp., Japan) was used to measure ammonium ions (as ammonium nitrogen, NH_4-N), nitrite ions (as nitrite nitrogen, NO_2-N), nitrate ions (as nitrate nitrogen, NO_3-N), total nitrogen (T-N), and hydrogen sulfide (H_2S). The seawater was then filtered. We checked the shape of the sea sludge and the effect of cesium removal with SEM-EDX, after 0 and 120 h. Experimental conditions, including the amount of kelp used, are shown in Table 1.

Table 1 Experimental conditions

	Additive amount of bacteria	Activator	Extract of kelp
Case 1	1.5 × 10^8 cell	–	500 ppm
Case 2	1.5 × 10^8 cell	–	–
Case 3	–	100 ppm	–

RESULTS AND DISCUSSION

Isolation and Identification of Bacteria

Water was sampled from the experimental device after 0, 24, 72, and 120 h. Fifty-three strains of bacteria were isolated from these samples and identified by 16S rRNA gene sequence analysis. Six species of bacteria were identified from samples at 0, 36 and 72 h: *Bacillus cereus*, *B. clausii*, *B. licheniformis*, *B. thuringiensis*, *B. subtilis*, and *Alcaligenes fecalis*.

B. clausii is alkaliphilic and produces high-alkaline proteases. *B. licheniformis* is commonly known to cause food poisoning and food spoilage. *B. subtilis* is non-pathogenic. It can contaminate food, however seldom results in food poisoning. *B. cereus* produces two types of toxins and is known to cause food poisoning. *B. thuringiensis* is a close relative of *B. cereus*. It produces insecticidal protein. Thus, *Bacillus* species are almost ubiquitous in nature, however, epidemiologically they are unsuitable to use for sludge decomposition.

Alcaligenes fecalis is commonly found in the environment in soil and in wastewater disposal apparatus. *A. fecalis* has heterotrophic nitrification and aerobic denitrification functions [8]. Thus, we assumed that *A. fecalis* would be useful for decomposition of deposited sludge. We carried out experiments of decomposition of the deposited sludge using our system (Fig. 1) with micro-bubbles and *A. fecalis*.

Experiments of Decomposition of Deposited Sludge for Cesium Removal

Results of water temperature, pH, DO and H_2S in varying environmental conditions

Figures 3–5 show the water temperature, pH, and DO respectively, resulting from the environmental conditions of cases 1–3 (Table 1). Water temperature is almost constant at about 30 °C after 6 h, as a result of using a cooler for the experimental water tank. The pH of case 1 is constant at about 9.5, and that of cases 2 and 3 is constant at about 7.5 to 8.0: the pH of case 1 was higher than cases 2 and 3. The initial concentrations of DO are 1.9 mg/L, 5.3 mg/L and 5.6 mg/L in cases 1, 2, and 3 respectively. The DO of all cases is saturated at about 7.5 to 8.3 mg/L after 6 h, because the concentration of oxygen saturation is 8.11 mg/L-pure water.

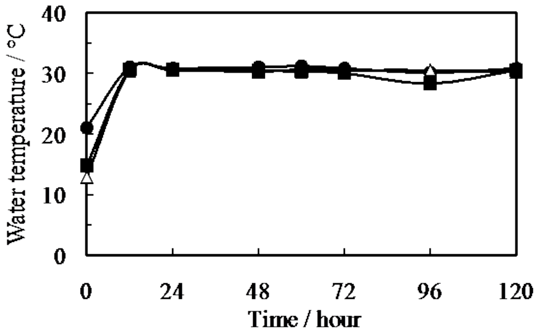

Fig. 3 Change in water temperature over time in case 1 (●), case 2 (Δ), and case 3 (■).

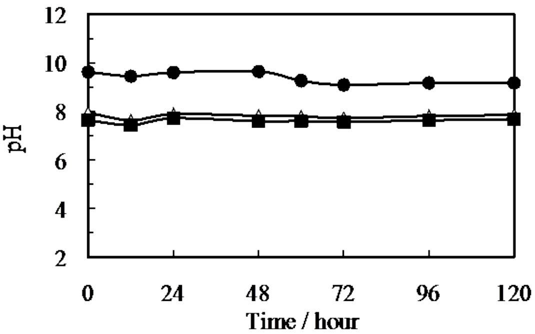

Fig. 4 Change in water pH over time in case 1 (●), case 2 (Δ), and case 3 (■).

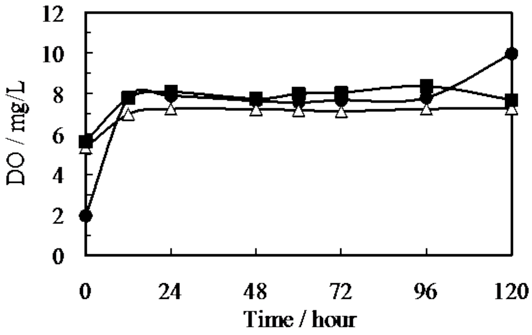

Fig. 5 Change in DO concentration over time in case 1 (●), case 2 (Δ), and case 3 (■).

H_2S concentration is shown in Fig. 6. In all cases, H_2S decreases up to 24 h, before the addition of *A. fecalis* to the experimental tank. *A. fecalis* is not inhibited by H_2S.

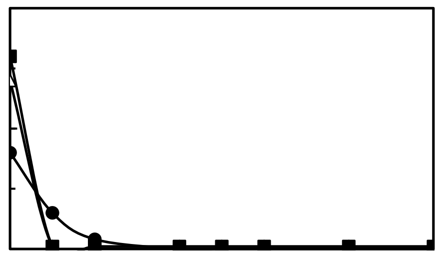

Fig. 6 Change in H_2S concentration over time in case 1 (●), case 2 (Δ), and case 3 (■).

Results of NH_4-N, NO_2-N, NO_3-N and T-N

Figure 7 shows the change in NH_4-N (ammonium nitrogen) concentration in the experimental tank over time. In all three cases (Table 1), initial concentrations of NH_4-N are approximately 2.0 mg/L. In case 1, NH_4-N decreases; at 24 h it is no longer detected. The effect of *A. fecalis* on NH_4-N concentration could not be ascertained, because *A. fecalis* was added at 24 h. In case 2, NH_4-N decreases up to 48 h and then remains constant at 0.2 mg/L. In case 3, NH_4-N decreases up to 24 h and then remains constant at 0.2 mg/L.

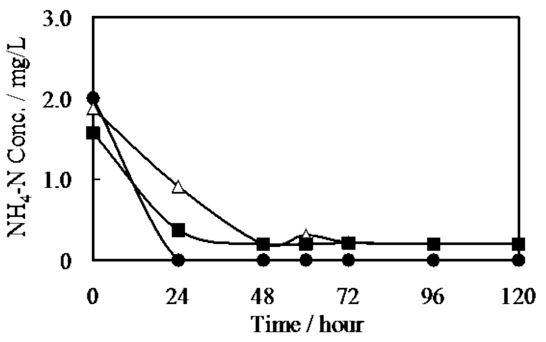

Fig. 7 Change in NH_4-N concentration over time in case 1 (●), case 2 (Δ), and case 3 (■).

Figure 8 shows the change in NO_2-N (nitrite nitrogen) concentration in the experimental tank over time. In case 1, initial concentrations of NO_2-N are approximately 0.30 mg/L. Subsequently NO_2-N decreases up to 72 h, after which it is constant at 0.80 mg/L. In case 2, initial concentrations of NO_2-N are approximately 0.20 mg/L. NO_2-N increases to 0.4 mg/L at 24 h before decreasing up to 96 h, and then remains constant at 0.08 mg/L. In case 3, initial concentrations of NO_2-N are approximately 0.15 mg/L. Following this, NO_2-N increases to 0.25 mg/L at 24 h, then decreases up to 72 h after which it remains constant at 0.01 mg/L.

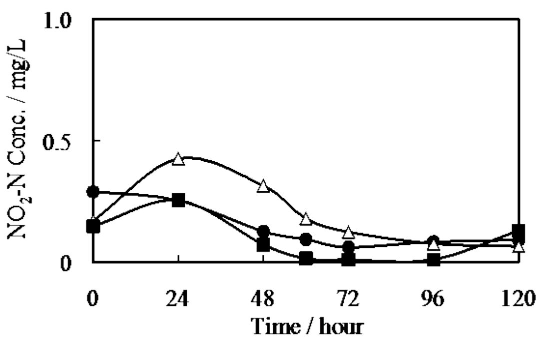

Fig. 8 Change in NO_2-N concentration over time in case 1 (●), case 2 (Δ), and case 3 (■).

Figure 9 shows the change in NO_3-N (nitrate nitrogen) concentration in the experimental tank over time. In case 1, initial concentrations of NO_3-N are approximately 4.3 mg/L. Subsequently NO_3-N decreases up to 96 h, after which it remains constant at 0.9 mg/L. In case 2, initial concentrations are approximately 2.0 mg/L. Following this, NO_3-N increases to 6.4 mg/L at 24 h, then decreases to 3.0 mg/L at 60 h before continuing to gradually decrease to 1.5 mg/L at 120 h. In case 3, initial concentrations are approximately 2.0 mg/L. NO_3-N increases to 3.9 mg/L at 24 h, then decreases to 0.2 mg/L at 96 h. NO_2-N and NO_3-N showed similar trends.

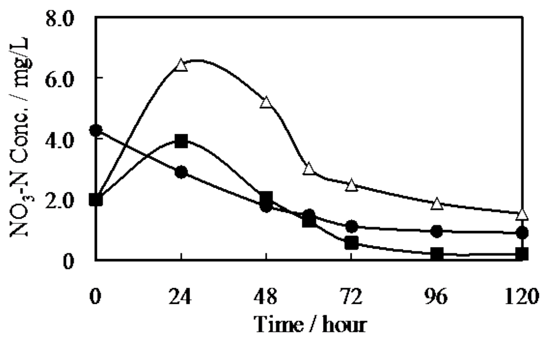

Fig. 9 Change in NO_3-N concentration over time in case 1 (●), case 2 (Δ), and case 3 (■).

In the initial 24 h, NH_4-N concentration decreased, and NO_2-N and NO_3-N concentrations increased. It is assumed that the metabolism of the bacteria switched from denitrification to nitrification because the experimental tank water changed from anaerobic to aerobic conditions (Fig. 5). Therefore we suppose that the nitrogen source shifts with $NH_4^+ \rightarrow NO_2^- \rightarrow NO_3^-$ and that this trend of NO_3-N concentration was similar to NO_2-N.

Dissolved inorganic nitrogen (DIN; NH_4-N + NO_2-N + NO_3-N) shows 85 % and 90 % decreases in cases 1 and 3 respectively (Fig. 10).

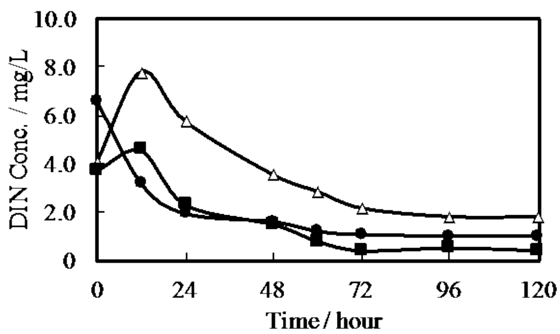

Fig. 10 Change in DIN concentration over time in case 1 (●), case 2 (Δ), and case 3 (■).

The effect of the addition of *A. fecalis* on T-N (total nitrogen, and inorganic and organic nitrogen) concentration was investigated. After adding *A. fecalis* to the water, T-N decreased and was eventually no longer detected (Fig. 11).

Observation of sludge shape

The shape of the sea sludge was observed using SEM at 0 and 120 h in case 1. Fig. 12 shows the SEM photomicrographs at 0 (a), and 120 (b) h. At 120 h after exposure to micro-bubbles and bacteria, the sludge particles had become smaller.

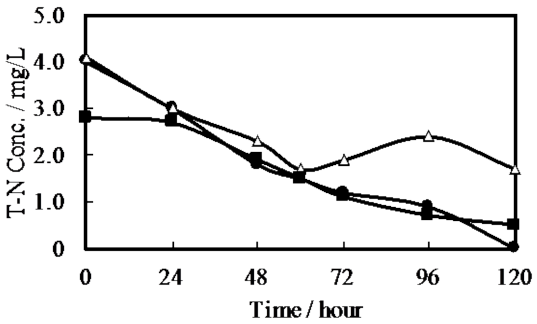

Fig. 11 Change in T-N concentration over time in case 1 (●), case 2 (Δ), and case 3 (■).

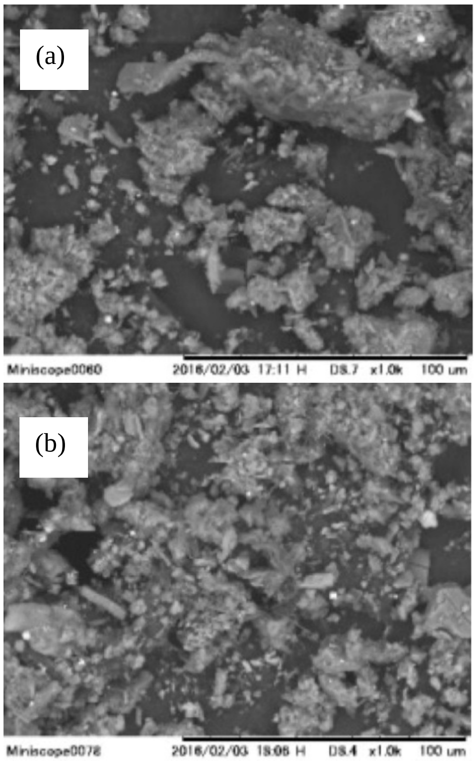

Fig. 12 SEM photomicrographs of sludge (a) before experiment and (b) after 120 h in case 1.

Results of cesium concentration

We measured cesium and silica in the sludge using energy dispersive X-ray analysis (EDX). The weight ratios of cesium to silica (Cs/Si) in dry sludge are shown in Fig. 13. The cesium decontamination ratio was calculated from the ratios of cesium content at 0, 24, 72, and 120 h as measured by EDX, using standard values for silica after measuring the weight of the dried sludge. The decontamination ratio obtained in case 1 was about 50 %.

It has been reported that cesium concentration in water decreased abruptly after the beginning of similar experiments [9]. Therefore, eluted cesium from the sludge was adsorbed to zeolite, after the sludge was decomposed by micro-bubbles and *A. fecalis*.

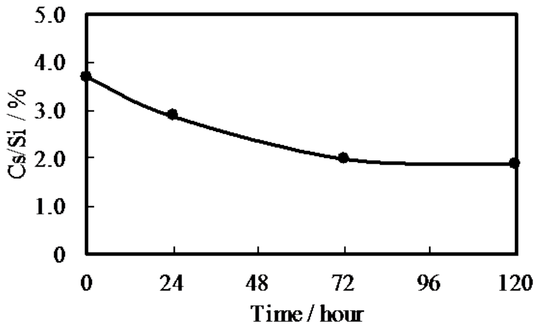

Fig. 13 Change in Cs/Si over time in case 1.

CONCLUSION

We carried out elution and fixing of cesium by micro-bubble and bacteria circulation decomposition system for ocean sludge. From water quality measurements, it can be concluded that after adding *A. fecalis*, T-N decreases and then is no longer detected. *A. fecalis* has a remarkable ability to treat samples through denitrification.

The sea-sludge particles decrease in size through treatment with micro-bubbles and bacteria for 120 h. We predict from the results shown here that the system proposed would greatly facilitate cesium removal from ocean sludge.

ACKNOWLEDGEMENTS

The authors would like to express sincere thanks to Takaaki Sone, Hiroki Kazama and So Miyamoto, students of Nihon University, in Japan, for executing the experiments.

This work was supported by KAKENHI C-26420831 (Grant-in-Aid for Scientific Research).

REFERENCES

[1] Soemori A, Shozugawa K, Nogawa N, Higaki S, Matsuo M, “A change in the concentrations of radioactive cesium in Tokyo-bay’s sediments released by the Fukushima Dai-ichi Nuclear Power Station accident”, Bunseki Kagaku, Vol. 62(12), 2013, pp. 1079–1086.

[2] He Q, Walling D E, “Interpreting particle size effects in the adsorption of ^{137}Cs and unsupported ^{210}Pb by mineral soils and sediments”, J. Environ. Radioactivity, Vol. 30(2), 1996, pp. 117–137.

[3] Okamoto K, Hotta K, Toyama T, Kohno H, “Purification system of ocean sludge by activating microorganisms”, Int. J. of GEOMATE, Vol. 6(1), 2014, pp. 791–795.

[4] Okamoto K, Toyama T, "Decontamination of radioactive cesium from ocean sludge by micro-bubble and microorganisms", Int. J. of GEOMATE, Vol. 9(1), 2015, pp. 1390–1394.

[5] Tsukada H, Takeda A, Hisamatsu S, Inaba J, "Concentration and specific activity of fallout ^{137}Cs in extracted and particle-size fractions of cultivated soils", J. Environ. Radioactivity, Vol. 99(6), 2008, pp. 875–881.

[6] Matsuo K, Maeda K, Ohnari H, Tsunami Y, Ohnari H, "Water purification of a dam lake using micro bubble technology", Progress in Multiphase Flow Research, Vol. 1, 2006, pp. 279–286.

[7] Okamoto K, Hotta K, "Purification experiments on sedimentary sludge by microorganism activator", In Proc. of Pacific Congress on Marine Science and Technology (PACON), 2008.

[8] Inamori Y, Wu X-L, Kimochi Y, "Characteristics of N_2O production by *Alcaligenes faecalis* under aerobic conditions", Journal of Japan Society on Water Environment, Vol. 22, 1999, pp. 904–909.

[9] Okamoto K, Toyama T, "Ocean decontamination: Removal efficiency of radioactive cesium from ocean sludge by using micro bubbles and activating microorganisms", Int. J. of GEOMATE, Vol. 10(21), 2016, pp. 1924–1928.

A STUDY ON GROUND IMPROVEMENT TECNIQUE WITH IN-SITU MICROOGANISMS ISOLATED FROM JAPAN

Rusutsu Ito[1], Toshiro Hata[1]
[1]Graduate School of Engineering, Toyama Prefecture University, Japan

ABSTRACT

Damage by a liquefaction phenomenon was a problem in recent years, and the Great East Japan Earthquake occurred on March 11, 2011 in Japan, and liquefaction damage occurred frequently. There is also more adoption of Paris agreement in COP21 of the end of last year, and correspondence to a global warming problem is also desired reduction in greenhouse effect gas amount of emission in the construction field. Therefore considered ground improvement technology is necessary for the environment in Japan an earthquake-ridden country. So we considered for practical use ground improvement techniques based microorganism. That is watched as new liquefaction countermeasure technology for reduction in cost and the point of view by which material and construction waste are reduction. In that ground improvement techniques, it is difficult to using specific microbes. So we aimed at Microbial carbonate precipitation using in-situ microorganism as the method to solve this problem. We made solidify sand using isolated microorganisms in japan and *Bacillus pasteurii* the solidification ability becomes clear. We measured to urease activity values of each microorganism. And we making of the test pieces, undrained cyclic triaxial test and acid decomposition for using $CaCO_3$(0.5mol/L). And we compared results. We understood two things from examination results. 1) The difference occurs to liquefaction strength by urease activity value. 2) The improvement effect of the liquefaction strength was admitted in Microbial carbonate precipitation using in-situ microorganisms in the spots selected by this research.

Keywords: Microbial carbonate precipitation, Urease activity, Undrained cyclic triaxial test, Liquefaction

INTRODUCTION

The Great East Japan Earthquake occurred on March 11, 2011. Many earthquakes also occur to others in Japan which is an earthquake-ridden country. The liquefaction phenomenon which occurs with those earthquakes in recent years is a problem, and it's said that they need liquefaction countermeasure technology which corresponds to various cases. Correspondence to a global warming problem is also desired reduction in greenhouse effect gas amount of emission in the construction field. So reduction in greenhouse effect gas amount of emission was expected more than conventional technology by this research. And the calcium carbonate way which is the soil stabilization technology for which the microorganism solidification watched as new liquefaction countermeasure technology was used was considered for practical use.

BACKGROUND

To use the microorganism with the higher urase activated value (U/L), when doing microorganism solidification by a calcium carbonate way in the past, the case for which the microorganism from which unlined clothing was separated already (alien species) is used is seen much. But we can think the use of a foreign microorganism is difficult from influence to a local ecosystem when making a practical use of. We aimed at utilization of a in situ microorganism as the method to settle this problem by this research.

The soil stabilization technology for which microorganism solidification was used was made a practical use of with a final goal in Japanese whole and Abashiri city, Hokkaido was selected as a Japanese northern end by this research. Imizu city, Toyama was selected as the spot where the dangerous degree of the liquefaction is higher than Toyama-ken liquefaction map and isolation of a urase activated positive microorganism where each spot lives in the ground and the liquefaction strength improvement effect were inspected. We write down the point that isolated a microbe in figure -1. We also inspected about *Bacillus pasteurii* it's said that the solidified effect is clear where at the same time and considered the validity of the suggestion technology for which a in situ microorganism is used through comparison of a result.

MATERIALS AND METHODS

By the calcium carbonate method which we paid my attention to in this study, we produce hydrolysis of the urea by the metabolism of the microbe and let you precipitate calcium carbonate all over the gap of the sand. We write down a chemical reaction formula in expression (1),(2). In hydrolysis in expression (1), an enzyme activity level of the microbe becomes important.

$$CO(NH_2)_2+2H_2O \rightarrow 2NH_4^{+}+CO_3^{2-} \quad (1)$$

$$Ca^{2+}+CO_3^{2-} \rightarrow CaCO_3 \downarrow \quad (2)$$

We carried out an examination about four kinds of the Toyoura sand which saturated in pure water, the Toyoura sand which we solidified by an isolated microbe from all over the soil in Abashiri city, Hokkaido, the Toyoura sand which we solidified by an isolated microbe from all over the soil in Imizu city, Toyama, solidification ability solidified using *Bacillus pasteurii* which became clear in this study. We write down in list of examination cases table -1, composition of the solidified liquid table -2, an enzyme activity level of the microorganisms which measured it using LCR meter in composition of the solidification solution, table -3. We performed repetition Undrained cyclic triaxial test (DA=5%) of the soil with the test specimen which we made and found the repetition stress amplitude ratio of each test specimen, the repetition loading number of times. Furthermore, we demanded R_{L20} and compared the improvement effect of the liquefaction strength. In addition, we performed acid decomposition using HCl (0.5 mol/L) about the test specimen after the examination. We considered liquefaction strength and a $CaCO_3$ separation rate, the relations of the enzyme activity level.

Table 1 List of examination cases

	CASE A	CASE B	CASE C
Bacterial strain	Microbe of the Abashiri city, Hokkaido origin	Microbe of the Imizu city, Toyama origin	*Bacillus pasteurii*
Sand class	Toyoura sand		
Relative density	Dr=50%		
Test specimen height	100mm		
Test specimen diameter	50mm		
The passing solidified liquid number of times	Three times		
Passing water interval	72 hours		

Table 2 Composition of the solidified liquid

Reagent name	Weight
Nutrient Broth	0.3g
NH_4Cl	1.0g
$NaHCO_3$	0.21g
$CO(NH_2)_2$	1.80g
$CaCl_2$	3.33g
Pure water	100ml

Fig. 1 Point that isolated a microbe

Table 3 An enzyme activity level of the microorganisms

	Microbe of the Abashiri city, Hokkaido origin	Microbe of the Imizu city, Toyama origin	*Bacillus pasteurii*
Enzyme activity level(U/L)	28	74	654

RESULTS

(1) Comparison of liquefaction properties

We write down the stress distortion relations that the loading number of times compared about a case becoming equal repeatedly of test specimen and CASE A,B,C which saturated only Toyoura sand in pure water in figure -2. Because a tendency that axis distortions gradually increase together and liquefy CASE A,B,C from a figure is recognized, we am guessed when a solidification effect by the $CaCO_3$ separation promotion derived from a microbe is provided. Then, we write down the repetition loading number of times in DA=5% in each examination CASE and the relations of the shear stress ratio in figure -3. It followed that we could expect a liquefaction strength improvement effect most about CASE C using *Bacillus pasteurii* where the effectiveness became clear than a study of the past from a figure. In CASE A,B, an improvement effect of the liquefaction strength was accepted equally, but less than CASE C it followed. It is thought that an enzyme activity level of the microbe which we used for CASE A,B as a cause is low.

(2) Comparison of the $CaCO_3$ separation rate

We write down the value of the $CaCO_3$ precipitation rate for the sand weight of each test specimen which we got from acid decomposition in table -4. It was intended to clarify the influence that the difference in microbe class gave for crystal separation. But it was revealed that a $CaCO_3$ separation rate did not have a big difference by a microbe class as we showed it in table -4. Influence by the solidification situation (including the unevenness in crystal size and the test specimen of calcium carbonate) is thought about than the above.

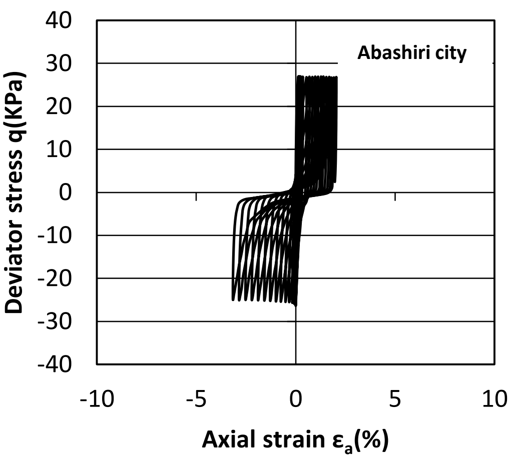

CASE A

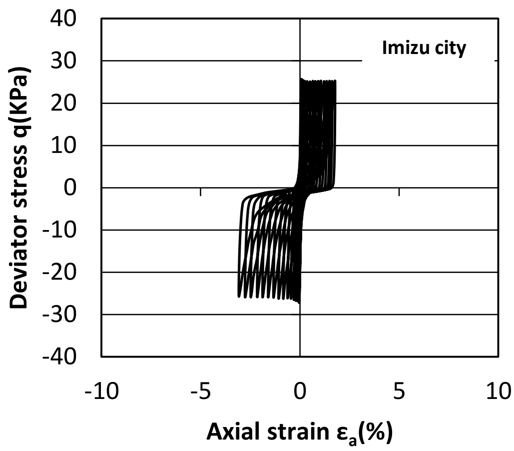

CASE B

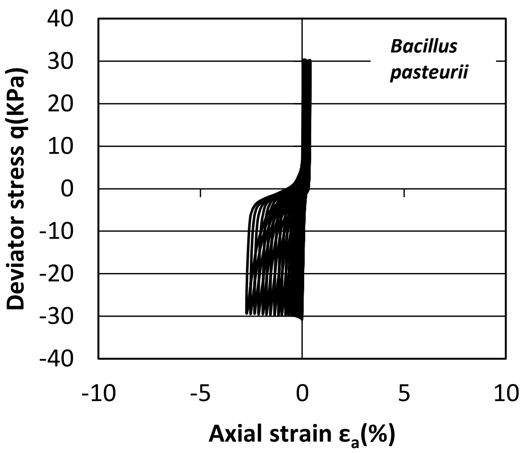

CASE C

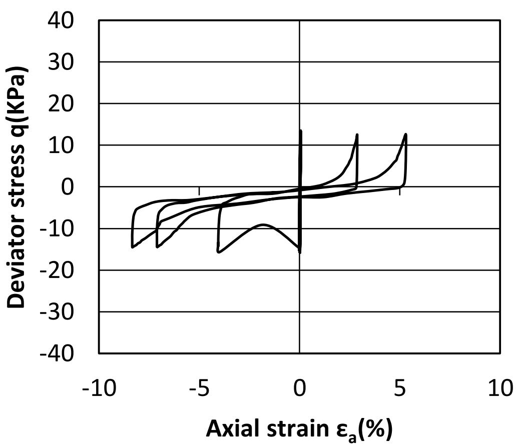

Toyoura sand

Fig. 2 The stress distortion relations that the loading number of times

DISCUSSION

From this test result, an improvement effect of the liquefaction strength due to the isolated microbe became clear from all over the soil in Abashiri city, Hokkaido and Imizu city, Toyama. The improvement of the liquefaction strength due to the original position microbe is guessed regardless of a point when at the same level. About both points the value of R_{L20} less than *B.pasteurii* it followed. We paid my attention to a $CaCO_3$ separation rate as a cause, but the value of the acidolysis became at the same level. Based upon the foregoing, it is guessed that an enzyme activity level of the microbe to use for microbe solidification affects the separation place of $CaCO_3$ in the test specimen. Furthermore, it is different in a trend after having injected it in a test specimen, and the possibility that a difference and the deflection of the movement place affect the $CaCO_3$ separation place is thought about by a microbe class. Based on the above-mentioned situation, we perform similar examination using the microbe varying in the enzyme activity level, and it is thought that it is necessary to make an enzyme activity level and relations of the liquefaction strength clear more.

CONCLUSIONS

We understood two things from examination results.

1) The difference occurs to liquefaction strength by urease activity value.

2) The improvement effect of the liquefaction strength was admitted in Microbial $CaCO_3$ precipitation using in-situ microorganisms in the spots selected by this research.

In addition, we divide a test specimen into the upper part, the central part, the lower part and perform acid decomposition about each plans pushing forward further examination about the infusion methods to get a homogeneous solidification effect.

REFERENCES

[1] Mastromei, G., Marvasi, M., and Perito, B.: Studies on bacterial calcium carbonate precipitation for stone conservation, BGCE, pp.103-105, Delft, 2008.

[2] Whiffin, V.S., Van Paassen, A.L. and Harkes, M.P.: Microbial Carbonate Precipitation as a Soil Improvement Technique, Geomicrobiology Journal, 24, pp.417-423,2007.

Table 4 Value of the $CaCO_3$ separation rate for the sand weight

	CASE A	CASE B	*CASE C*
$CaCO_3$ separation rate(%)	2.044	2.236	2.038

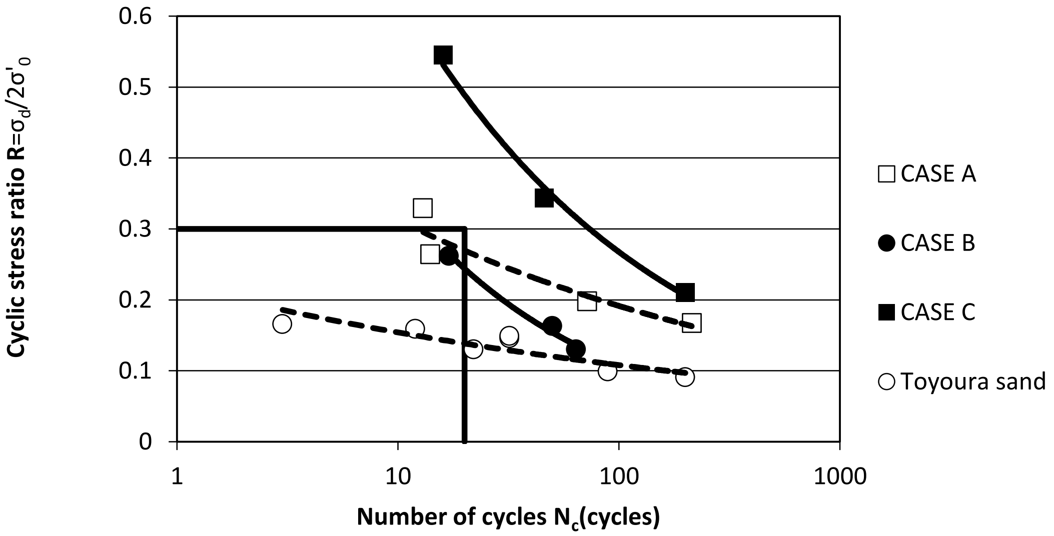

Fig. 3 Repetition loading number of times in DA=5%

Sixth International Conference on Geotechnique, Construction Materials and Environment, Bangkok, Thailand, Nov. 14-16, 2016, ISBN: 978-4-9905958-6-9 C3051

A STUDY OF RESTRAINT TECHNIQUES FOR CEMENT TREATED SOIL'S DETERIORATION BY MICROBIAL FUNCTIONS

Kazuki Mihara[1], Toshiro Hata[2]
[1,2] Department of Environmental Engineering, Toyama Prefectural University, Japan

ABSTRACT

Cement treated soil is used as a countermeasure for poor ground. But, cement treated soil deteriorate by calcium leaching because of exposing seawater. This study considered a technology of reducing deterioration of cement treated soil by using urease-producing bacteria. Authors tested seawater exposure tests using 2 types of the urease-producing bacteriums of *Sporosarcina aquimarina* isolated from the sea off the coast of Korea and *Bacillius pasteurii* isolated from land. The purpose of this tests are checking effect of reducing deterioration of cement treated soil by the urease-producing bacteria. At the same time, we performed tests to confirm the growth of the bacteria in cement treated soil. We tested seawater exposure tests 2 types of conditions of temperature 20℃ is used for exposure tests, and 30℃ is a temperature that is suitable for the growth of bacteria, the purpose of this tests are checking relation temperature and deterioration speed. The main outcomes are as follows:
1) 2 types of the urease-producing bacteria have an effect of reducing deterioration 2) 2 types of condition of temperature have relation to deterioration speed.

Keywords: cement treated soil, reducing deterioration, seawater exposure test, Micro Carbonate Precipitation

INTRODUCTION

In Japan, an alluvial bed develops in coastal zone, there are poor grounds. Therefore, Ground improvement is necessary to build the structure. Today, cement treated soil is used as a countermeasure for poor ground. But, cement treated soil is deteriorate by the exposure of seawater. Cement treated soil exposures to seawater, deteriorate by calcium leaching because of exposing seawater [1]-[3]. Therefore it is necessary to examine long-term stability. This study considered a technology of reducing deterioration of cement treated soil by using urease-producing bacteria. Urea is hydrolyzed by urease, generates ammonia, carbonate ion, and hydrogen ion. This carbonate ion reacts with leaching calcium to form $CaCO_3$ in cement treated soil. Eq. (1) is hydrolyzing urea by urase-producing bacterium. Eq. (2) is formation of $CaCO_3$'s precipitation mechanisms [4].

$$CO(NH_2)_2 + 2H_2O \rightarrow 2NH_3 + CO_3^{2-} + 2H^+ \tag{1}$$

$$Ca^{2+} + CO_3^{2-} \rightarrow CaCO_3 \downarrow \tag{2}$$

MATERIAL AND METHOD

In this study, authors examed seawater exposure test of cement treated soil. Authors tested seawater exposure tests using 2 types of the urease-producing bacteria of *Sporosarcina aquimarina* isolated from the sea off the coast of Korea and *Bacillius pasteurii* isolated from land. Table.1 shows Both bacteria's characteristics [5]. Authors made test pieces by combination to show in Table.2(case C's liquid medium include *B.pasteurii,* Case D's liquid mediums include *S.aquimarina*), and tested it according to a test flow to show in Fig.1. This test pieces were cured in the air for 28 days under 20℃. Test pieces were sealed the side and the base like Fig.2, only the top surface of test pieces exposure seawater.

Table 1 Characteristics of bacteria

	B.pasteurii	*S.aquimarina*
isolate source	land	coast
salinity tolerance (NaCl %)	10	13
optimum pH	9	6.5～7
anaerobiosis	+	+

Table 2 combination table

Case	A	B	C	D
pure water (%)	21.05	20.99	14.43	
blast-furnace slag cement type B (%)	6.58	6.56		
potter's clay (%)	6.58	6.56		
silica sand (%)	65.79	65.57		
Urea (%)	0.00	0.33		
liquid medium (%)	0.00	0	6.56	6.56

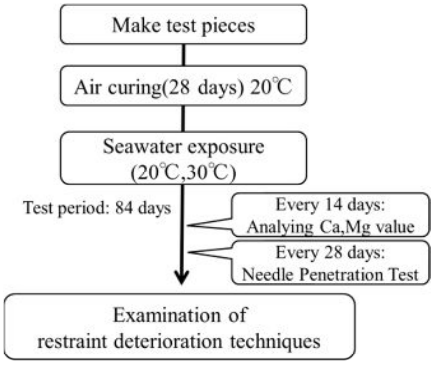

Fig.1 Test flow

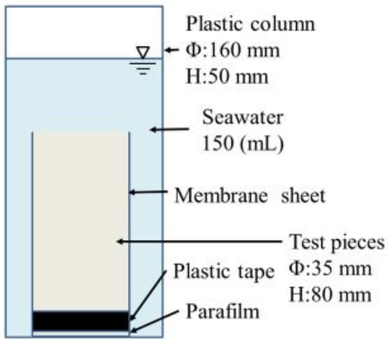

Fig. 2 seawater exposure test setup

Table 3 Seawater's composition table

Including elements	Cl, N, C, Na, Ca, Sr, Mg, K, B, S,Br
Ca^{2+} concentration (ppm)	125
Mg^{2+} concentration (ppm)	830
pH	8.32

Seawater used artificial seawater of commercially available. Table.3 shows Seawater's composition table. Test period is 84 days, seawater was sampled every 14day, changing water and testing needle penetration test every 28 days.

In needle penetration test, authors pricks the top surface and bottom surface with a needle, measure 2 types of penetration value. 2 types of penetration values difference assumed deterioration depth. Sampled water was analyzed Ca ion and Mg ion by Atomic Analyzer.

Authors tested seawater exposure tests 2 types of conditions of temperature 20℃ is used for exposure tests, and 30℃ is a temperature that is suitable for the growth of bacteria, the purpose of this tests are checking relation temperature and deterioration speed.

Therefore, in case D, authors measured urease activity when finished air curing 28days for confirming the growth of bacteria under high alkali condition in cement created soil. Put part of test pieces in NH4-YE mediums (ATCC medium: 1376), grow for a week, measured urease activity.

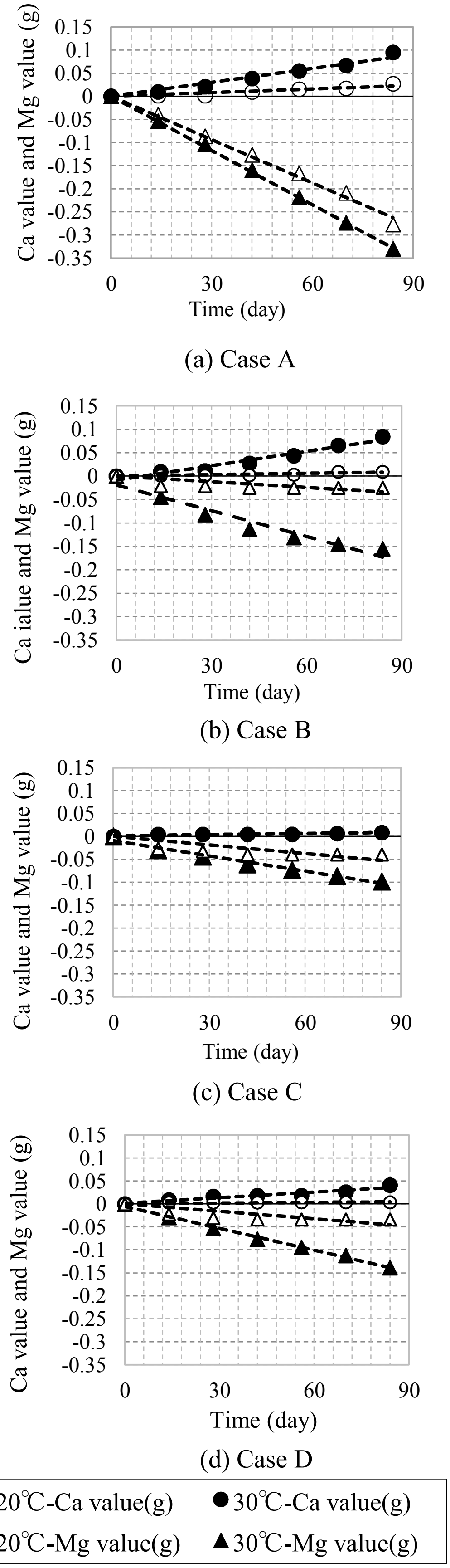

Fig.3 Ca value and Mg value

RESULTS AND DISCUSSIONS

Ca leaching and Mg absorption

Fig.3 shows Analyzing results of Ca value and Mg value. This figure shows that it is leaching from test pieces when plots are increasing, and it is absorption from test pieces when plots are degreasing. In case A to D, Ca's plots are increasing, so Ca is leaching from test pieces, Mg's plots are decreasing, so Mg is absorption to test pieces. Moreover, 30 ℃ of temperature condition's Ca leaching and Mg absorption is more than 20 ℃ of temperature condition. From those trends, it is thought that temperature condition has relation to deterioration. Therefore, in case C and D of including urease-producing bacteria, Ca leaching and Mg absorption value restrain in compared with case A and B that case without urease-producing bacteria.

Deterioration depth

Fig.4 shows deterioration depth of case A~D. in case A~D, 30 ℃ of temperature condition's deterioration depth is more than 20℃ of temperature condition. From those trends, it is also thought that temperature condition has relation to deterioration.

Therefore, in case C and D of including urease-producing bacteria, deterioration depth restrain in compared with case A and B that case without urease-producing bacteria. The factor affecting is $CaCO_3$ precipitated in test pieces' gap.

Especially, in both temperature conditions, case C is effective most in those cases.

Growth of bacteria in cement treated soil

Table.4 shows urease activity of case D. Urease activity of after air curing is 22.02 (U/L). Urease activity of after air curing decreased a one-fifth of urease activity of liquid mediums before add to test pieces, authors could be confirmed growth of bacteria.

Table 4 Urease activity of case D (including *S.aquimarina*)

	Before add to test pieces	After air curing 28days
Urease activity(U/L)	110.08	22.02

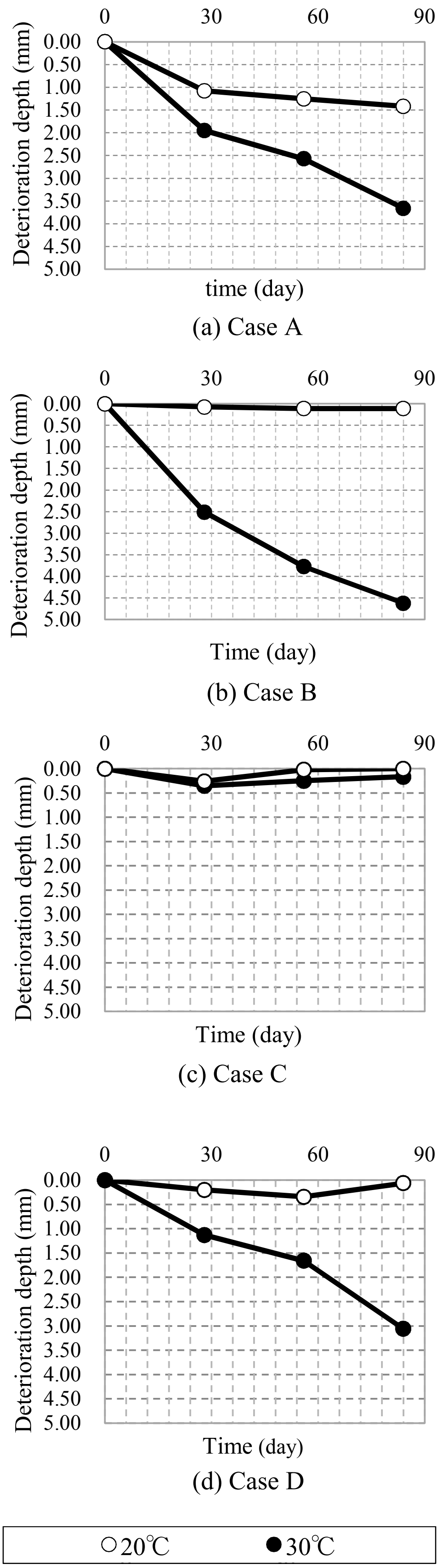

Fig.4 Deterioration value

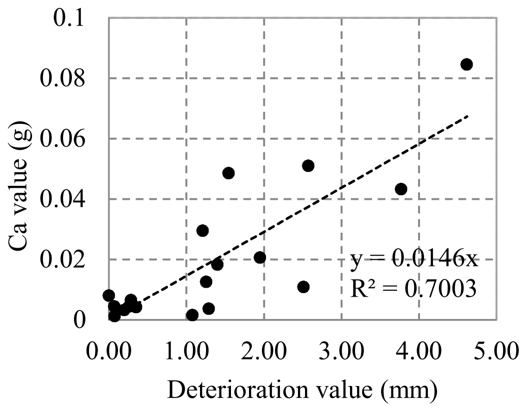

Fig.5 Relationship between Ca value and deterioration.

Relation to Ca leaching value and deterioration depth

Fig.5 shows a relationship between Ca leaching value and deterioration. As shown in Figs.5, there are scattering, deterioration value increases with increase in calcium leaching value. Ca leaching value related to deterioration value. From this, authors thought to be able to estimate deterioration value by analyzing calcium leaching value in non-destruction.

CONCLUSIONS

In this study, Authors considered a technology of reducing deterioration of cement treated soil by using urease-producing bacteria. Authors tested seawater exposure tests using 2 types of the urease-producing bacteria of *S.aquimarina* and *B.pasteurii*. At the same time, we performed tests to confirm the growth of the bacteria in cement treated soil. We tested seawater exposure tests 2 types of conditions of temperature 20℃ is used for exposure tests, and 30℃ is a temperature that is suitable for the growth of bacteria. In addition, in case D, authors measured urease activity when finished air curing 28days for confirming the growth of bacteria under high alkali condition in cement created soil.

The main outcomes are as follows:
1) 2 types of the urease-producing bacteria have an effect of reducing deterioration. Especially, case C is effective most in those cases, *B.pasteurii* can be expected restraint techniques for cement treated soil's deterioration.
2) 2 types of condition of temperature have relation to deterioration speed. Deterioration speed becomes higher with temperature condition become higher.
3) Urease-producing bacteria growth under high alkali condition in cement treated soil, urease-producing bacteria may show restraint deterioration effects for a long term.
4) Analyzing calcium leaching value can estimate deterioration value in non-destruction.

ACKNOWLEDGEMENTS

I would like to show my greatest appreciation to Tomomi Takamatsu who offered continuing support and constant encouragement. I would also like to thank Takumi Nagai and Kenta Teranishi whose meticulous comments were an enormous help to me. Finally, I would like to express my gratitude to Grants-in-Aid for Scientific Research foundation-(B) No.26289154 for their financial support.

REFERENCES

[1] Hara S, Suestugu D, Hayashi S, "Calcium Leaching Mechanism of Lime Treated Soil Immersed in Seawater", J. of the Society of Materials Science, Japan, Vol. 61, No.1, Jan. 2012, pp. 11-14.
[2] Nakamura T, Kitazume M, "Laboratory Tests on Durability of Cement Treated Soils", TECHNICAL NOTE OF THE PORT AND AIRPORT RESEARCH INSTITUTE, No.1128, Jun. 2006.
[3] Hara H, Suetsugu D, Hayashi S, Matsuda H, "DETERIORATION MECHANISM OF CEMENT-TREATED SOIL UNDER SEAWATER", J of JSCE division C: Geotechnics, vol.69, No.4, Apr. 2013, pp. 469-479.
[4] Qabany, A.A, Soga, K., Santamaria, J.C., "Factors Affecting Efficiency of Microbially Induced Calcite Precipitation", Journal of Geotechnical and Geoenvironmental Engineering, Vol.138, No.8, 2012, pp. 992-1001.
[5] Hata T, Yokoyama T, and Abe H, "Investigation of a soil improvement technique for coastal regions on the basis of calcium carbonate precipitation by using the urea hydrolysis rate" J of Geotechnical engineering, Vol.8, No.4, Jan, 2013, pp. 505-514.

Sixth International Conference on Geotechnique, Construction Materials and Environment, Bangkok, Thailand, Nov. 14-16, 2016, ISBN: 978-4-9905958-6-9 C3051

REMOVING FLUORIDE FROM A HOT SPRING USING AN ELECTROLYSIS SYSTEM

Yuki Imai, Shiori Yanagawa, Misa Konishi, and Tomonori Kawakami

Faculty of Engineering, Toyama Prefectural University, Japan

ABSTRACT

A high concentration of fluoride in the wastewater from hot springs is an environmental issue in Japan, since some of the wastewater exceeds the national minimum effluent standards of 8 mg/l. However, an effective treatment for fluoride removal has not yet been developed. Accordingly, the temporal effluent standards of 15mg/l - 50 mg/l have, so far, been applied to the wastewater from hot springs.

In this study, an electrolysis system consisting of an anode bath and a cathode bath separated by a diaphragm made of a clay panel was tested for the removal of fluoride. In an electrolysis system, fluoride is removed by co-precipitation with magnesium hydroxide formed in a cathode bath under a high pH condition.

As a pretreatment of wastewater, 100 mg/l of magnesium was added to water from Gero hot spring, Gifu, Japan, to enhance the formation of the precipitation of magnesium hydroxide, since water from Gero hot spring contains less than 1 mg/l of magnesium. Water from Gero hot spring to which 100 mg/l of magnesium had been added was treated by an electrolysis system with a flow rate of 10 l/day and a current of 120 mA. The electrolysis system reduced the fluoride concentration from 16.6 mg/l to 6.4 mg/l, which meets the national minimum effluent standards of 8 mg/l.

Keywords: Gero hot spring, co-precipitation, sequential flow reactor, national minimum effluent standard

INTRODUCTION

UNICEF has designated Japan as one of the countries with endemic fluorosis due to excess fluoride in drinking water [1]. The health problem has been remedied by using alternative water sources that are free of fluoride. However, high concentrations of fluoride in the wastewater remain an environmental issue in Japan, since some wastewaters exceed the national minimum effluent standards of 8 mg/l [2]. Since no effective treatment for the removal of fluoride has been developed, temporal effluent standards have been applied to the wastewater of some industries. The operation of hotels with hot springs, very popular with Japanese people for vacations, is one such industry, since the wastewater discharged by the hotels sometimes contains a high concentration of fluoride originating from the hot spring. Different temporal effluent standards for fluoride concentration are applied to hotels with hot springs depending on the amount of the effluent and the type of hot spring. Hotels that have an effluent of more than 50 m^3/day have a temporal effluent standard of 15 mg/l. For the other hotels, different standards, such as 30 mg/l or 50 mg/l, are applied based on the type of hot spring, i.e., pumped out or gushed out naturally, respectively. The possibility of stiffening temporal effluent standards has been discussed by the Japanese Ministry of Environment every three years; however, as decided at the council held in 2015, no changes will be made in the regulation due to the lack of appropriate technologies for effectively removing fluoride [3]. There are some techniques to remove fluoride from drinking water such as reverse osmosis [4], electrodialysis and nanofiltration [5-6], however, these are the techniques just separate fluoride into the solution with higher fluoride concentration and the solution with lower concentration. These techniques are not suitable for wastewater treatment.

To remove fluoride from industrial wastewater, the primary treatment has generally been to add calcium to produce insoluble CaF_2, followed by coagulation. According to the solubility product of CaF_2 (3.9×10^{-11} mol^3/l^3), 8.8mg/l of calcium is sufficient to obtain 8 mg/l of fluoride theoretically; however, in the actual cases, an 8-mg/l concentration of fluoride cannot be achieved even by adding 300 mg/l of excess calcium. As a result, secondary treatments, such as ion exchange or the addition of aluminum, are introduced to meet the regulation [7-9].

Gero hot spring is located 35°48'N and 137°14'E in Gifu Prefecture, Japan. It is widely regarded as one of the three best hot springs in Japan [10]. More than 40 hotels offer rooms and hot spring baths. Hot water is pumped out to deliver to the hotels. Temporary effluent standards of 30 mg/l and 15 mg/l are applied to small and large hotels, respectively. The fluoride concentration, which is officially reported to be 16.5 mg/l [11], exceeds regulations for large hotels. However, the above-mentioned treatments to remove fluoride are quite prohibitive for the hotel business due to the high cost compared to their business scale.

In the current study, a new electrolysis system was examined as a cost-effective system for removing fluoride from wastewater from hotels with hot springs to the level of the national minimum effluent standard of 8 mg/l. We focused on the water of Gero hot spring as a model.

MATERIALS AND METHODS

Gero hot spring

Raw hot spring water from Gero was used for fluoride removal. The objective of the current research is the removal of fluoride from wastewater; however, raw hot spring water was used for the experiments, since it has the highest concentration of fluoride without dilution. Fluoride removal was examined in a laboratory using a batch reactor and a sequential flow reactor.

Batch reactor

Electrolysis using a batch reactor was performed to remove fluoride. The batch reactor shown in Fig. 1 consisted of two electrolysis baths separated by a membrane filter into a cathode bath and an anode bath. Each bath had a volume of 300 ml. In an electrolysis system, fluoride is removed by co-precipitation with magnesium hydroxide formed in the cathode bath under a high pH condition. Magnesium was added to the water from Gero hot spring to enhance the formation of magnesium hydroxide, since the magnesium concentration of water from Gero hot spring, less than 1 mg/l, is too low for the formation of magnesium hydroxide. The magnesium concentration was adjusted to 50 mg/l with magnesium chloride. A constant current power supply, adjusted to 80 mA, was used for the electrolysis. Electrolysis was performed for 1 hour.

Since it was found that alkalinity (HCO_3^-) interfered with the formation of magnesium hydroxide by forming magnesium carbonate, alkalinity was removed before electrolysis.

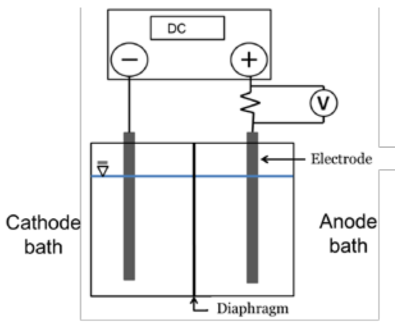

Fig. 1 Schematic flow of the batch reactor

Alkalinity was removed from the solution by adding sulfuric acid in accordance with the following equation:

$$HCO_3^- + H^+ \rightarrow CO_2 + H_2O.$$

CO_2 formed and dissolved in the solution was removed by aeration.

Using the solution mentioned above, the first of a two-series electrolysis was performed. After the first electrolysis, part of fluoride was co-precipitated with magnesium hydroxide in the cathode bath. At the same time, part of the fluoride was transferred to the anode bath by the Coulomb force. Since one- and two-sided treatments are both required for wastewater treatment, a second electrolysis was performed to treat the solution in the anode bath. The solution taken out of the anode bath was mixed with the same amount of the raw hot spring water to which magnesium had been added. The second electrolysis was performed with this solution. The addition of sulfuric acid was not needed because the solution taken out of the anode bath was sufficiently acidic to remove alkalinity.

Sequential flow reactor

As a sequential flow reactor, a reactor with an anode bath and a cathode bath separated by a clay panel was used (Fig. 2). The volume of each bath was 420 ml. An aeration bath was installed at the inlet of the cathode, where alkalinity was removed by the acid solution formed in the anode bath. Water from Gero hot spring to which magnesium had been added in advance was introduced to the anode and aeration baths. The total flow rate was set at 10 l/day, which is equivalent to a retention time of 2 hours. In the experiments, the flow ratio of Gero hot spring water into the aeration bath (b) to the anode bath (a) was varied with 4 ratios, i.e., b:a=0:10, 5:5, 8:2, and 9.4:0.6. The Mg concentration was adjusted to 100 mg/L. One hundred twenty mA was applied for electrolysis with a constant current power supply.

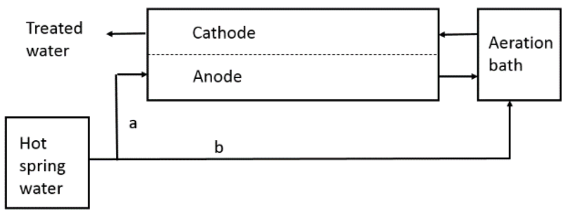

Fig. 2 Schematic diagram of the sequential flow reactor

Table 1 Water quality of Gero hot spring. The concentration for 2013 is from the official record

Date Y/M/D	pH	EC mS/m	Na mg/l	NH_4 mg/l	K mg/l	Mg mg/l	Ca mg/l	F mg/l	Cl mg/l	NO_3 mg/l	SO_4 mg/l	Alkalinity meq/l
2015/ 9/11	8.9	35	107.2	0	1.0	0.1	0.6	17.7	75	0	10.8	1.66
2013/11/ 5	9.5	52.2	108.9	0	1.2	0	1.9	16.5	75	0.1	10.9	1.65

Analyses

Major ions were measured by an ion chromatography after samples were filtered by a membrane filter with a pore size of 0.45 µm. The pH was measured by a glass electrode method. Titration to the endpoint of pH=4.8 by sulfuric acid was used to measure alkalinity.

RESULTS AND DISCUSSION

Gero hot spring

The quality of water from Gero hot spring sampled on September 11, 2015, is shown in Table 1, together with the official record sampled on November 5, 2013. The official record is the analytical concentrations of chemical components registered in Gifu Prefecture based on Japan's Hot Spring Law.

The concentrations of the major ions, including alkalinity, of our analysis were quite similar to those of the official record, with the exceptions of calcium and fluoride. The concentration of fluoride fluctuated in the other samples between 15.8 mg/L and 18 mg/L. In the sample from September 11, 2015, the fluoride concentration was as high as 17.7 mg/L, which is approximately twice the national minimum effluent standard of 8 mg/L. The Mg was contained slightly, the pH was 8.9, and the alkalinity was 1.66 meq/L.

Batch reactor

Table 2 shows the fluoride removed by electrolysis from the hot spring water with alkalinity. The pH decreased in the anode bath while it increased in the cathode bath. The fluoride concentration decreased in the cathode bath; however, it increased in the anode bath, indicating that fluoride was transferred from the cathode bath to the anode bath by the Coulomb force. Accordingly, the decrease in the fluoride concentration was very small when the averaged concentration of both baths (14.7 mg/l) after electrolysis is compared with the initial concentration (16.9 mg/l). Even when the average magnesium concentration decreased from 45.9 mg/l to 19.7 mg/l and white precipitation appeared in the cathode bath, there could be little co-precipitation of fluoride with magnesium hydroxide, due to the formation of magnesium carbonate.

The fluoride removed from the hot spring water without alkalinity by the first electrolysis is shown in Table 3. Due to the addition of sulfuric acid to remove alkalinity, the pH value of the initial solution was low. The fluoride concentration decreased in the

Table 2 Fluoride removed by electrolysis with alkalinity

	pH	F (mg/L)	Mg (mg/L)
Initial	8.83	16.9	45.9
Anode	2.43	22.3	37.7
Cathode	11.1	7.0	1.7
Average		14.7	19.7

Table 3 Fluoride removed by the first electrolysis without alkalinity

	pH	F (mg/L)	Mg (mg/L)
Initial	3.9	15.8	47,1
Anode	2.3	19.6	28.7
Cathode	11.6	5.2	0.0
Average		12.4	14.4

Table 4 Fluoride removed by the second electrolysis without alkalinity

	pH	F (mg/L)	Mg (mg/L)
Initial	2.8	17.2	49.2
Anode	2.3	19.4	42.3
Cathode	11.0	8.3	0.4
Average		13.9	21.4

cathode bath but increased in the anode bath, indicating that fluoride was transferred in the same manner as with alkalinity. However, some amount of fluoride was found to have been removed by precipitation during electrolysis, since the average concentrations of fluoride in both baths after treatment were well below that of the initial solution. When the average concentrations of the anode and cathode baths are compared, electrolysis without alkalinity was showed to more effectively remove fluoride than electrolysis with alkalinity.

The result of the second electrolysis is shown in Table 4. After treatment, the fluoride concentration in the cathode bath decreased to 8.3 mg/l. The fluoride concentration in the anode bath was 19.4 mg/l, which was similar to the concentration of fluoride in the anode bath with the first electrolysis. This indicates that the fluoride concentration could be decreased to approximately 8 mg/l when batch electrolysis is repeated.

Sequential flow reactor

According to the experimental results of the batch reactor showing that repeated batch electrolysis could remove fluoride, a sequential flow reactor was tested for removing fluoride.

The effect of the flow ratio on the removal of fluoride is shown in Fig. 3. In the figure, the flow ratios of b:a=0:10, 5:5, 8:2, and 9.4:0.6 are

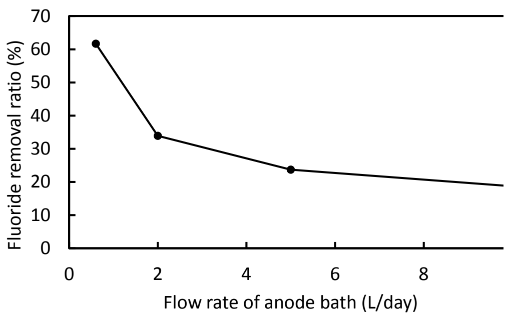

Fig. 3 Effect of the flow ratio on the removal of fluoride

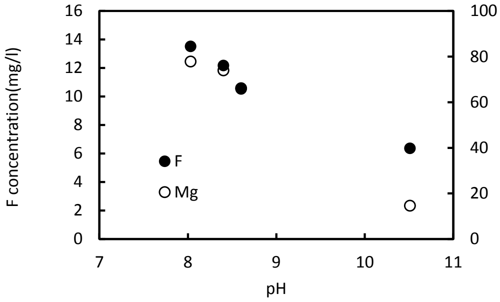

Fig. 4 Relationship between pH and fluoride concentration and the relationship between pH and magnesium in the cathode bath

expressed in flow rates of the anode bath of 10, 5, 2, and 0.6 l/day, respectively.

A lower flow ratio resulted in higher fluoride removal. In the case of the ratio of 9.4:0.6, the fluoride removal rate was 62%, and the fluoride concentration after treatment was 6.4 mg/l; as a result, the national minimum effluent standard of 8 mg/l was achieved. The relationship between pH and fluoride concentration and the relationship between pH and magnesium in the cathode bath are shown in Fig. 4.

When pH was higher, the fluoride removal rate increased and the magnesium concentration decreased. The change in pH, the concentration of fluoride, and the magnesium concentration in the hot spring water, the anode bath, the aeration bath, and the cathode bath are shown in Figures 5, 6, and 7, respectively, at flow ratios of b:a=0:10 and 9.4:0.6.

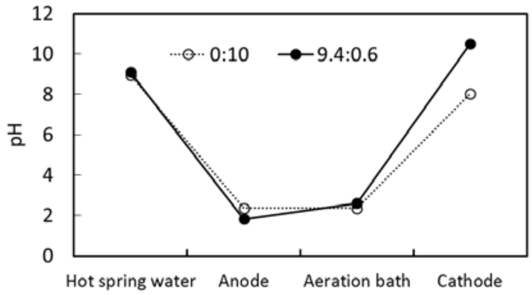

Fig. 5 Change in the pH along the flow

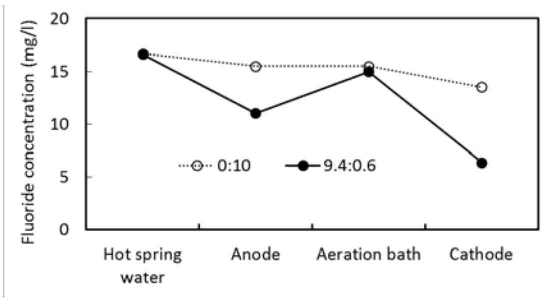

Fig. 6 Change in the fluoride concentration along the flow

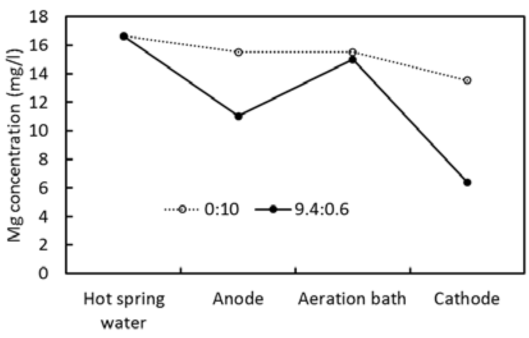

Fig. 7 Change in the Mg concentration along the

flow.

When the flow ratio was 0:10, the fluoride concentration in the treated water slightly decreased from that in the hot spring water. When compared with the batch reactor, the pH was as low as 8.0 in the cathode bath, and the concentration of dissolved magnesium was high. The reason is that the pH did not recover in the cathode bath after the pH in the mixing bath decreased to 2.35. Therefore, magnesium hydroxide did not form well, and co-precipitation with fluoride did not take place. When the flow ratio was 9.4:0.6, acidic solution with a pH value of 1.8 was formed in the anode bath. However, due to smaller volume of the acid solution that flowed into the aeration bath, a higher pH value of 2.60 was obtained in the aeration bath. As a result, pH increased to 10.5 at the outlet of the cathode bath, and the fluoride concentration decreased to less than the standard concentration of 8 mg/l. The concentration of dissolved magnesium decreased to 14.6 mg/l, as well. The difference in the pH values of 2.60 and 2.35 in the aeration bath between cases with flow ratios of 9.4:0.6 and 0:10, respectively, seems not to be significant. However, this is because pH is expressed in a logarithmic scale. When pH values are converted into hydrogen ion concentrations, a pH of 2.35 is equivalent to 4.5 mmol/l of H^+, while a pH of 2.60 is equivalent to 2.5 mmol/l of H^+. The difference in the concentrations of H^+ as 2.0 mmol/l was large enough to cause a difference in the OH^- concentration in the cathode bath of 0.3 mmol/l, which was calculated from the difference between pH=8.0 and pH=10.5.

Cost and maintenance

We proved that with this electrolysis system, it is possible to remove fluoride from hot spring wastewater. In the proposed electrolysis system, the devices can be made inexpensively, since the diaphragm of the electrolysis baths is made of a clay panel that would be robust against fouling, as well. Electric consumption for the electrolysis was approximately 1 W, excluding consumption by the water pumps, indicating that 24 Wh would be required for the treatment of 10 L of Gero hot spring water in one day. Supposing that 1 kWh=17 Japanese yen, the treatment of 10 L would require only 0.4 Japanese yen.

It could be possible to reuse magnesium by lowering the pH to dissolve the precipitation. The recovery ratio of magnesium as precipitation was as high as 85%, indicating that most of the magnesium added to the solution might be reused. When the hot spring water contains magnesium naturally, it is not necessary to add magnesium; however, the precipitation that does not need to be reused, in this case, will generate sludge. Nevertheless, the amount of sludge would be much less than that when a Ca-adding method is used, since excess Ca should be added to the solution. In spite of this, reducing electricity, magnesium usage, and sludge would be challenges for the future.

CONCLUSION

The electrolysis system for treating Gero hot spring water to remove fluoride was tested in a laboratory. The sequential flow reactor could remove fluoride to a level of 6.4 mg/l, which meets the national minimum effluent standards of 8 mg/l. It would be a cost-effective method for removing fluoride from wastewater.

ACKNOWLEDGEMENTS

This research was partly supported by JSPS KAKENHI Grant Number 15H05120 and Center of Community (COC) program by MEXT.

REFERENCES

[1] Qian, J., A. K. Susheela, A. Mudgal and G. Keast G. F1luoride in water: An overview, Waterfront: A UNICEF Publication on Water, Environment, Sanitation and Hygiene, 1999, 13, 11-13

[2] http://www.env.go.jp/water/onsen-haisui/conf/11.html

[3] Japan’s Ministry of the Environment, http://www.env.go.jp/water/onsen-haisui/conf/12.html

[4] Peter Sehn, Fluoride removal with extra low energy reverse osmosis membranes: three years of large scale field experience in Finland, Desalination, Vol. 223, Issues 1–3, 73-84, 2008

[5] Zakia Amor, Suad Malki, Mohamed Taky, Bernard Bariou, nabil Mameri, Azzeddine Elmidaoui, Optimization of fluoride removal from brackish water by electrodialysis, Desalination,120, 263-271, 1998

[6] Simons, R., Trace element removal from ash dam waters by nanofiltration and diffusion dialysis, Desalination, Vol. 89, Issue 3, 325-341, 1993

[7] Yuji Wada, The high class treatment of fluoride-containing wastewater, Kagaku To Kogyo 76(11), 557-564, 2002

[8] Paripurnanda Loganathan, Saravanamuthu Vigneswaran, Jaya Kandasamy,Ravi Naidu, Defluoridation of drinking water using adsorption processes, Journal of Hazardous

Materials, 248-249, 1-19, 2013
[9] Sachin V. Jadhav, Eugenio Bringas, Ganapati D. Yadav, Virendra K. Rathod, Inmaculada Ortiz, Kumudini V. Marathe, Arsenic and fluoride contaminated groundwaters: A review of current technologies for contaminants removal, Journal of Environmental Management, Vol. 162, 1, 306-325, 2015
[10] Japan National Tourism Organization, JAPAN: The Official Guide, http://www.jnto.go.jp/eng/location/regional/gifu/gero.html
[11] Gifu public health inspection center, Analytical report of hot spring, Gero hot spring (No.125), 2013

GENETIC DIVERSITY AND GENETIC STRUCTURE OF AN ENDANGERED SPECIES, *ERIOCAULON NUDICUSPE*, GROWING IN ARTIFICAL DISTURBING HABITATS

Michiko Masuda[1], Tadamasa Fukagawa[2] and Fumitake Nishimura[3]
[1,2] Department of Civil Engineering, Nagoya Institute of Technology, Japan; [3]Department of Environment Engineering, Kyoto University, Japan

ABSTRACT

Eriocaulon nudicuspe (Eriocauloaceae) is an endangered species in Japan. Habitats of the species are lost by city development. So many conservation areas are established in Aichi Prefecture, and protection activities are done by many natural protecting groups, and the extinction rate in recent years is being decelerated. But many protecting groups often transplanted from some other places, and genetic disturbance was a problem. We sampled 12 populations of the species from nature reserved areas, and studied them for allelic variation at 17 enzyme loci. There was no significant correlation between the real distance of conserved areas and genetic distances, suggesting that the gene disturbances occurred in these areas especially in frequently managed areas. On the other hand, the degree of the genetic differentiation at strictly conserved area where conservation management is done only once a year was high and there was no evidence about genetic disturbances. There was a possibility peculiar genetic disappearance of each habitat for genetic disturbance, and the necessity with which a guideline of protection activity is made was indicated.

Keywords: Genetic disturbance, Genetic distance, Conservation management, Nature reserved area, Endangered species

INTRODUCTION

Ueda (1989) defined Tokai hilly land element, 14 species plants, a lot of local endemic, semi-endemic and relict taxa growing in small wetlands in the Central Japan [1]. The habitats of the elements have been destructed by the urban growth, and all species are defined endangered species. Tomita (2004) reported the distribution change of *Eriocaulon nudicuspe* for 25 years, almost 50% areas are disappeared [2]. So Aichi Prefecture supported the conservation activities of the species.

For the conservation, the moderate disturbance is very important, so many nature protecting groups keep being active for decades [3][4]. The extinction rate of the endangered species is less than 5 % for the activities, and another population was appeared. Everyone easily collects seeds of the species and grows up by sowing. Sometimes people can easily move seeds of the species attaching the sole.

But there is another problems occurred in the disturbance. Some researchers pointed out the genetic disturbance affect serious damage of the endangered species [5][6]. The conservation activities sometimes transplant the endangered species from one habitat to another habitat. This manipulation causes hybrid breakdown, dilution and outbreeding depression [7]-[9].

Tsumura and Suyama (2015) published the book “The guideline for transplanting of trees seedling” where the genetic boundaries were shown in maps. But there is no herbaceous plants guideline about transplantation because of the difficulties of the samplings. Then we investigated the genetic structure and genetic diversity of *Eriocaulon nudicuspe* and analyzed the effect of the conservation activities with 3 questions, 1) Is there a relationship between the location and genetic distance? 2) Is there a relationship between the conservation activities and genetic diversity? 3) Is there a relationship between population size and genetic diversity? It was paid attention to the three points and analyzed.

MATERIALS AND METHODS

The Study Site

The study was carried out on the wetland at Aichi Pref. and Shizuoka Pref. (Table 1). 36 habitats of the species reported in the previous research [2], but growing could be confirmed only in 17 habitats in 2007. The investigation was done at 12 populations that can secure the enough number of individuals. Fig.1 shows the locations of 12 populations that were investigated. The capital letter of each location exhibits same river systems.

Table 1 The characters of study site, location

Study site	location North	East
A1	34° 44' 45"	137° 27' 09"
A2	34° 42' 10"	137° 24' 58"
A3	34° 38' 38"	137° 16' 30"
B1	34° 55' 04"	137° 46' 20"
B2	34° 49' 38"	137° 45' 54"
B3	34° 48' 56"	137° 45' 56"
C1	34° 56' 06"	136° 56' 14"
C2	34° 55' 11"	136° 53' 00"
C3	34° 54' 00"	136° 52' 15"
C4	34° 52' 07"	136° 53' 53"
C5	34° 50' 09"	136° 53' 10"
D1	35° 08' 56"	137° 04' 57"
D2	35° 06' 10"	137° 00' 05"
E1	35° 14' 43"	137° 03' 08"
E2	35° 14' 08"	137° 02' 35"
F1	35° 06' 01"	137° 14' 23"
F2	35° 07' 52"	137° 09' 30"

The same capital indicates the same water system

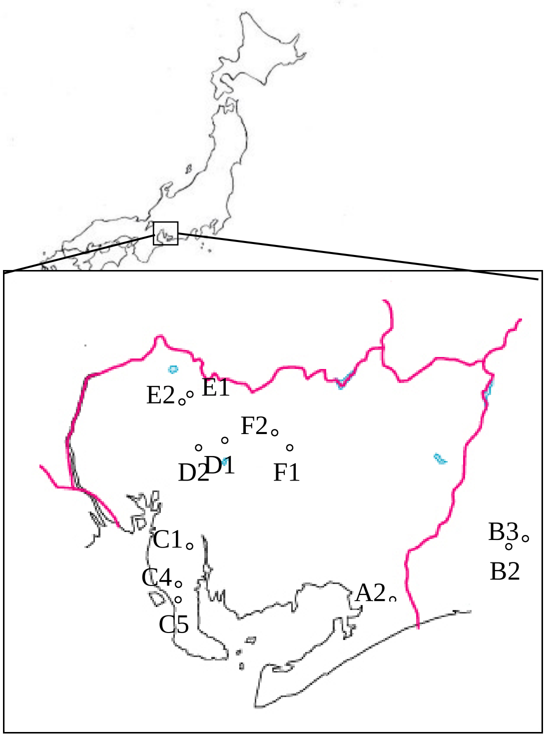

Fig. 1. Distribution of the population examined.

The Study Plant

Eriocaulon nudicuspe Maxim. (Fig. 2) is an annual plant distributed in circum-Ise Bay area, the center of Japan [1]. However its population has been decreasing and Red Data Book of Japanese vascular plants listed the species a 'vulnerable' level species [10][11]. This species is distributed in acid marsh with low nutrient, wetland around paddy fields and edge of reservoirs around Ise-Bay area. The seeds of the species emerge in spring and bloom late summer to early autumn. An individual has 1-10 inflorescence and produces 0-12 seeds per inflorescence.

Fig. 2 The flowers of *E. nudicuspe*.

Electrophoresis

Fresh leaves were collected from 30 individuals per population at June in 2007. Leaves were kept on ice during 2 hours transportation to the laboratory. The following enzyme systems were examined: aconitase (ACO), sikimate dehydrogenase (SKDH), iso-citrate dehydrogenase (IDH), malate dehydrogenase (MDH), acid phosphate (ACP), phospho-glucose isomerase (PGI), phospho-glucomutase (PGM) and menadione reductase (MR). Leaves were used to resolve the following 17 putative loci: aco-1, aco-2, skdh, idh, mdh-1, mdh-2, mdh-3, acp-1, acp-2, acp-3, acp-4, acp-5, pgi-1, pgi-2, pgh-3, pgm and mr. Samples were ground in a cold extraction buffer described by Odrzykoski and Gottlieb [12]. The enzymes were resolved on 10.8% starch gel. System 5 of Soltis et al. [13] were used. Staining procedures followed previous works [13]-[15].

The Statistical analysis

For each population the number of alleles per locus (*A*), proportion of polymorphic loci (*P*), and gene diversity (*h*) were calculated. We used all loci data in the calculation of *A*, and regarded a locus as polymorphic if the frequency of its most frequent alleles is under 0.95. In addition, total gene diversity [16] was calculated for species level. The population genetic structure was analyzed by initially calculating Nei's G_{ST} value [16]. Values for genetic identities (*I*) and standard genetic distance (*D*) were computed for each pairwise comparison of all populations. The neighbor joining method [17] based on *D* was used for constructing a phenogram for *E. nudicuspe*.

RESULTS

The Study Site

The number of individuals and the frequency of conservation activities were shown in Table 2. The number of individuals ranged from 20 to 50000. C5 and F2 wetland are left, and few persons hardly enters. C4 and F1 are managed severely, and protection activity is permitted only once a year. And in the other area conservation activity is performed, and reaping and organic matter removal are conducted periodically.

Table 2. The number of individuals of each population in 2007, Geographical Features, and frequency of conservation activities within a year

Study site	No. of individuals	Geograhical Features	Freq. of act.
A1	1000	silt, clay, gravel	4
A2	1000	Terrace sediment	10
A3	200	Terrace sediment	4
B1	50000	silt, clay, gravel	12
B2	1500	silt, clay, gravel	4
B3	30000	silt, clay, gravel	4
C1	1430	silt, clay, gravel	1
C2	20	mud marsh	1
C3	800	silt, clay, gravel	4
C4	5190	silt, clay, gravel	1
C5	3000	silt, clay, gravel	0
D1	7200	kaoline, gravel	12
D2	4000	granite	12
E1	1000	silt, clay, gravel	1
E2	5000	silt, clay, gravel	1
F1	7000	silt, clay, gravel	1
F2	5200	silt, clay, gravel	0

Genetic Diversity

Seventeen loci were scored: aco-1, aco-2, skdh, idh, mdh-1, mdh-2, mdh-3, acp-1, acp-2, acp-3, acp-4, acp-5, pgi-1, pgi-2, pgh-3, pgm and mr, fifteen loci were polymorphic. In all population aco-1 and mr were monomorphic. Allele frequencies at the polymorphic loci are listed in Appendix.

Table 3 summarizes the resultant values of *A*, *P* and *h* for each population.

And total gene diversity (H_T) of the species was 0.293. The levels of genetic diversity in *E. nudicuspe* was almost same that of other endangered species, for example, *Aster kantoensis* growing in the river bed were 0.36(*P*), 1.53 (*A*) and 0.142 (*h*) [18]. And other endangered species showed, *P* (0.199 to 0.65), *A* (1.44 to 2.01) and *h* (0.037 to 0.43) [19]-[22]. But the index of river wetland endangered species, *Penthorum chinense*, is higher than that of *E. nudicuspe* [23], these were 2.42 (*A*), 0.75(*P*) and 0.308 (*h*).

Table 3. Mean number of polymorphic loci (*A*), proportion of polymorphic loci (*P*), and gene diversity within a population *(h)* at 17 loci for examined populations of *E. nudicuspe*

Population	*P*	*A*	*h*
A2	0.647	2.059	0.156
B2	0.765	2.118	0.165
B3	0.706	1.941	0.129
C1	0.800	2.400	0.350
C4	0.818	2.636	0.473
C5	0.765	1.941	0.141
D1	0.294	1.471	0.078
D2	0.588	1.941	0.194
E1	0.412	1.529	0.078
E2	0.588	1.765	0.116
F1	0.706	2.059	0.157
F2	0.471	1.529	0.079

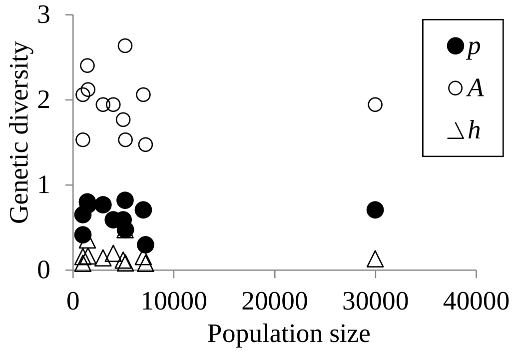

Fig. 3. The relationships between population size and genetic diversity indexes *p*, *A* and *h*

Fig. 3 showed the relationships between population size and genetic diversity. There are no significant relationships between the population size and genetic diversity.

Fig. 4 showed the genetic distance among population. The genetic distance between the nearest populations were small, but the longest distant population. Especially B2, B3 are the edge of the distribution of the species, but they close to the center of the distribution. It is suggested that gene flow occurred constantly among the populations.

The result of total population genetic structure G_{ST} was 0.236. The value of G_{ST} suggested that middle level differentiation occurred. It is always observed isolated populations (no differentiation: 0-0.05, low level differentiation: 0.05-0.15, middle level: 0.15-0.25, high level: 0.25-).

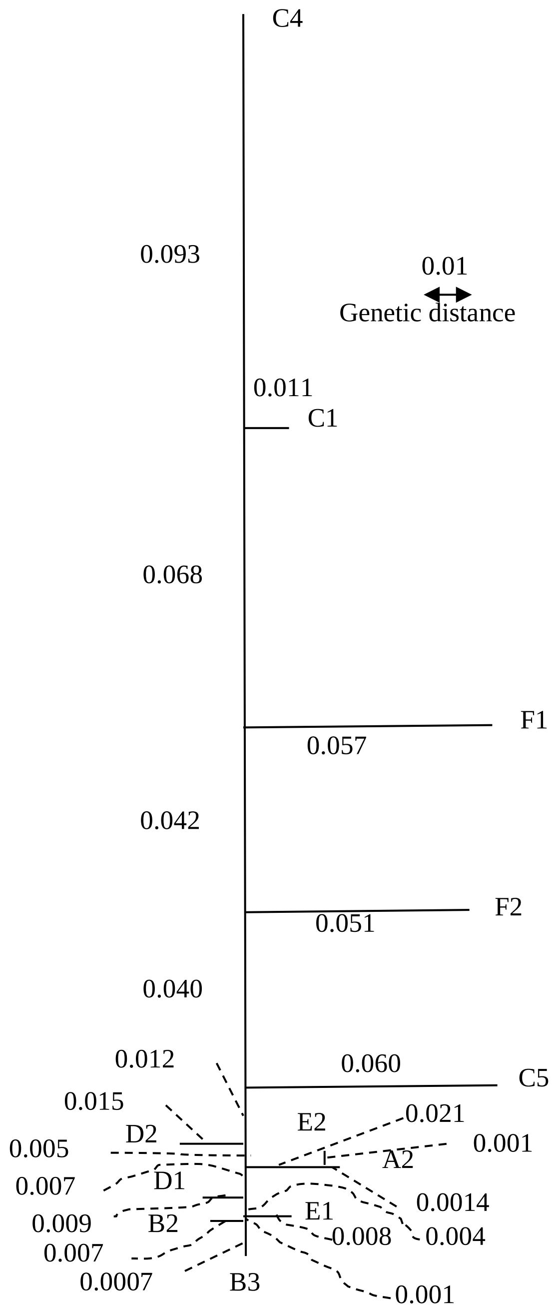

Fig. 4. Phenogram using the neighbor joining method based on Nei's (1987) standard genetic distance.

DISCUSSION

No significant correlation existed between any of the genetic diversity parameters and the actual size of populations, which indicates that the effective population size is independent of the actual population size. Several factors are known to reduce the effective size of population [24]: (1) fluctuation in population size, (2) variation in fecundity among individuals, (3) overlapping generations, (4) geographic dispersion of populations, and (5) unequal numbers of males and females. Factors 2-5 are not plausible as cause of the observed lack of correlation between the genetic diversity and actual population sizes. Fluctuation in population size represented by genetic drift severely reduces the effective population size of population, which is the harmonic mean of the actual number of individuals in the last t generations [24]. For an endangered species like *E. nudicuspe* nursing by many conservation groups, the bottleneck effect is a primary factor acting to reduce the effective size of populations. The species rapidly establishes new populations by conservation activities. Thus even large population with N > 5000 are likely to have a high probability of being of recent origin and remain influenced by the bottleneck effects.

Because *E. nudicuspe* only occurs in the wetlands along the river system, its distribution is disjunct, and as a result, inter-river gene flow is expected to be less than intra-river gene flow. Sometimes wild animals occur the gene flow, but many constructions, road, buildings and railways, prevent long distant movements. *E. nudicuspe* is mainly pollinated by small sap chafers with limited flight ability (personal obs.) and its seeds have no specialized mechanism for long distance dispersal, inter river gene flow is considered feasible due to their geographical proximity.

But the hierarchical analysis of the population gene structure of the species showed the relationships among the river system nor real distance system. Especially B2 and B3 are placed the east end of the distribution, near to E or D population that are placed the center of the distribution. D1, D2 and A2 populations are well managed by three conservation groups. The members of the groups sometimes visit another conservation area, so we guess that the people make the gene flow among the different river system. On the other hand, among strictly conserved area, C1, C4, C5 F1 and F2, the gene flow aren't almost observed. Genetic distance is over 0.07 among the populations. It was suggested that high Gst was dependent on the isolated 4 populations. The conservation activities cause unexpected gene flow.

Generally each population is exposed to natural selective pressure each area and adapts itself to it. Therefore, if an artificial gene flow occurred, human disappears an adaptive gene of to each habitat. Sometimes annual fluctuation of environment selects adaptive genes, another gene disappear the adaptive gene by their reproductive ability when the selective event did not occur. It is suggested that the artificial gene flow decrease the gene diversity of endangered species. It is suggested that we must not occur artificial gene disturbance in order to conserve endangered species. The conserved area should be protected strictly. There were some populations with gene disturbance about *E. nudicuspe* observed. Among these populations we cannot recover from gene disturbance. We make a proposal that in order to avoid the inbreeding depression high level gene flow management among the populations. That cause the uniformity of gene diversity, but there is low inbreeding depression expected, so among populations the individual has high fecundity.

CONCLUSION

We get three main conclutions.

1) There is no relationship between the real distance and genetic distance.
2) There is a relationship between the conservation activities and genetic structure.
3) There is no relationship between population size and genetic diversity.

Based on the conclusions, two proposals about the conservation activities

1) The conservation activities should be strictly managed, because of unexpected genetic disturbances.
2) We should make the networks among the habitats where the genetic disturbance occurred, the networks cause high level gene flow and avoid the inbreeding depression, because the recovering from genetic disturbance is very difficult.

ACKNOWLEDGEMENTS

We wish to thank the members of Shimada wetland conservation association for research support and permission to work in the wetland. We also thank the members of our laboratory for their assistance in the field works.

REFERENCES

[1] Ueda K, “Phytogeography of Tokai Hilly Land Element I. Definition”, Acta Phytotax. Geobot. Vol. 40, 1989, pp190-202.

[2] Tomita K, “The restoration *Eriocaulon nudicuspe* distribution using a hearing method”, the bachelor’s thesis of Nagoya University, Mar. 2004.

[3] Leakey R and Lewin R, Phylsiological Plant Ecology, 3rd ed. New York: Springer, 1995.

[4] Ono T, “Geological, geographical and ecological approach to the “Kinjo-hill”-changes of landscape since the Edo period-“, Kinjo Gakuin Univ. Bulletin, Nature Sci. Vol. 9(2), 2013, pp10-21.

[5] Naito Y et al., “Density-dependent selfing and its effects on seed performance in a tropical canopy tree species, Shorea acuminate (Dipterocarpaceae)“, For. Ecol. Manage. Vol. 256, 2008, pp375-383.

[6] Naito Y et al., “Selfing and inbreeding depression in seeds and seedlings of Neobalanocarpus heimii (Dipterocarpaceae)”, J. of Plant Res. Vol. 118, 2005, pp423-430.

[7] Lynch M, “ The genetic interpretation of Inbreeding depression and outbreeding depression”, Evolution Vol. 45, 1991, pp622-629.

[8] Templeton AR, “Coadaptation and outbreeding depression”, Conservation Biology, Soule ME Ed. Sinauer, Massachusetts, 1986, pp105-116.

[9] Price MV et al., “Pollen dispersal and optimal outcrossing in Delphinium nelsoni“, Nature Vol. 277, 1979, pp294-297.

[10] Endangered Plant Survey Group, The Red Data Book of Japanese Vascular Plants. Tokyo: Nature Conservation Society of Japan, 1989. (in Japanese)

[11] Kato T & Ota H, Endangered Wild life of Japan. Osaka: Hoikusha Publishing Co., 1993. (in Japanese)

[12] Odrzykoski IJ & Gottlieb LD, “Duplications of gene coding 6-phosphofluconate dehydrogenase in Carkia (Onagraceae) and their phylogenetic implications” Systematic Botany, Vol. 9, 1984, pp479-486.

[13] Soltis DE et al., “Starch gel electrophoresis of ferns: a compilation of grinding buffers, gel and electrode buffer and staining schedules”, Amer. J. of Bot. Vol. 73. Jan. 1983, pp9-27.

[14] Wendel JF & Weeden NF, “The effect of serpentine on the population structure of Silene dioica (Caryophyllaceae)”, Evolution, Vol. 46, 1989, pp1537-1548.

[15] Chepliak WM & Pitel JA, Techniques for starch electrophoresis of enzymes from forest tree species. Information report PI-X-42. Penthawana: Penthawana National Forestry Institute, Canadian Forestry Service, 1984.

[16] Nei M, Molecular evolutionary genetics. New York: Columbia University Press, 1987.

[17] Saitou N & Nei M, “The neighbor joining method: a new method for reconstructing

phylogenetic trees", Molecular Biology and Evolution, Vol. 4, 1987, pp106-425.
[18] Maki M et al., "Genetic diversity and hierarchical population structure of a rare autotetraploid plant, Aster kantoensis (Asteraceae)", American J. of Botany, Vol. 83, Mar. 1996, pp296-303.
[19] Soltis DE & Soltis PS, "Genetic consequences of autotetraploidy in Tolmiea (Saxifragaceae), Evolution, Vol. 43, 1989, pp586-589.
[20] Ness BD et al., "Autotetraploidy in Heuchera micrantha (Sazifragaceae)", American J. of Botany, Vol. 76, 1989, pp614-626.
[21] Wolf PG et al. "Chloroplast-DNA and electrophoretic variation in diploid an autotetraploid Heuchera grossularifolia", American J. of Botany, Vol. 77, 1990, pp232-244.
[22] Shore JS, " Tetrasomic inheritance and isozyme variation in Turnera ulmifolia vars. elegance Urb. and intermedia Urb. (Turnraceae)", Heredity, Vol. 66, 1991, pp305-312.
[23] Masuda M and Nishimura F, "Genetic diversity of restored endangered species, *Penthorum chinsense* in the riverbed", Int. J. of GEOMATE, Vol. 10, 2016, pp1810-1814.
[24] Hartl, DL & Clark AG, Principles of population genetics, 2d ed, Sunderland, MA, 1989, Sinauer.

Appendix Allel frequencies at 15 loci of 12 examined populations of *Eriocaulon nudicuspe.*

		population											
locus	allele	A2	B2	B3	C1	C4	C5	D1	D2	E1	E2	F1	F2
aco-1	N	19	22	28	30	28	28	14	19	30	30	30	30
	a	1.000	1.000	1.000	1.000	1.000	1.000	1.000	1.000	1.000	1.000	1.000	1.000
	b	0.000	0.000	0.000	0.000	0.000	0.000	0.000	0.000	0.000	0.000	0.000	0.000
aco-2	N	19	22	28	-	-	28	14	19	30	30	30	30
	a	0.921	0.932	0.911	-	-	1.000	0.929	0.947	0.983	0.933	0.967	0.950
	b	0.079	0.068	0.089	-	-	0.000	0.071	0.053	0.017	0.067	0.033	0.050
skdh	N	19	22	28	-	-	28	14	19	30	30	30	30
	a	0.947	0.932	0.929	-	-	1.000	1.000	0.921	1.000	0.950	1.000	0.967
	b	0.053	0.068	0.071	-	-	0.000	0.000	0.079	0.000	0.050	0.000	0.033
idh	N	19	22	28	-	-	28	14	19	30	30	30	30
	a	0.026	0.000	0.000	-	-	0.946	0.000	0.132	0.000	0.000	0.017	0.000
	b	0.974	0.955	0.839	-	-	0.054	1.000	0.868	0.950	0.917	0.933	1.000
	c	0.000	0.045	0.161	-	-	0.000	0.000	0.000	0.050	0.083	0.050	0.000
mdh-1	N	19	22	28	30	28	28	14	19	30	30	30	30
	a	0.526	0.909	0.839	0.733	0.143	0.946	1.000	0.763	1.000	1.000	0.133	0.950
	b	0.474	0.091	0.161	0.267	0.482	0.054	0.000	0.237	0.000	0.000	0.867	0.050
	c	0.000	0.000	0.000	0.000	0.375	0.000	0.000	0.000	0.000	0.000	0.000	0.000
mdh-2	N	19	22	28	29	25	28	14	19	30	30	30	30
	a	1.000	0.864	0.804	0.690	0.600	1.000	1.000	0.763	0.967	0.950	1.000	0.950
	b	0.000	0.136	0.196	0.310	0.400	0.000	0.000	0.237	0.033	0.050	0.000	0.050
mdh-3	N	19	22	28	-	-	28	14	19	30	30	30	30
	a	1.000	0.977	0.982	-	-	0.911	1.000	1.000	1.000	1.000	1.000	1.000
	b	0.000	0.023	0..018	-	-	0.089	0.000	0.000	0.000	0.000	0.000	0.000
acp-1	N	46	49	28	-	-	28	12	49	30	30	30	30
	a	0.957	0.980	0.893	-	-	0.839	1.000	1.000	1.000	0.983	0.917	1.000
	b	0.043	0.020	0.107	-	-	0.161	0.000	0.000	0.000	0.017	0.083	0.000
acp-2	N	38	49	28	26	28	28	17	49	30	30	30	30
	a	0.947	0.959	1.000	0.288	0.173	0.821	1.000	1.000	1.000	1.000	0.950	1.000
	b	0.053	0.041	0.000	0.346	0.500	0.179	0.000	0.000	0.000	0.000	0.050	0.000
	c	0.000	0.000	0.000	0.308	0.288	0.000	0.000	0.000	0.000	0.000	0.000	0.000
	d	0.000	0.000	0.000	0.058	0.038	0.000	0.000	0.000	0.000	0.000	0.000	0.000
acp-3	N	43	44	28	28	28	28	17	47	30	30	30	30
	a	0.154	0.000	0.052	0.444	0.411	0.036	0.265	0.021	0.000	0.000	0.367	0.467
	b	0.231	0.193	0.328	0.556	0.589	0.339	0.176	0.149	0.000	0.100	0.633	0.450
	c	0.286	0.409	0.121	0.000	0.000	0.464	0.118	0.447	0.433	0.400	0.000	0.083
	d	0.176	0.227	0.628	0.000	0.000	0.161	0.206	0.266	0.400	0.217	0.000	0.000
	e	0.154	0.170	0.172	0.000	0.000	0.000	0.235	0.117	0.167	0.283	0.000	0.000
acp-4	N	46	49	28	-	11	28	17	49	30	30	30	28
	a	0.239	0.153	0.339	-	0.318	0.036	0.029	0.643	0.283	0.283	0.167	0.071
	b	0.457	0.837	0.661	-	0.455	0.964	0.971	0.357	0.717	0.717	0.75	0.929
	c	0.000	0.01	0.000	-	0.227	0.000	0.000	0.000	0.000	0.000	0.083	0.000

acp-5	N	26	26	27	19	-	28	16	30	30	30	30	30
	a	1.000	1.000	1.000	0.500	-	1.000	1.000	1.000	1.000	1.000	0.783	1.000
	b	0.000	0.000	0.000	0.500	-	0.000	0.000	0.000	0.000	0.000	0.217	0.000
pgi-1	N	19	49	17	29	30	28	12	15	30	29	30	30
	a	0.000	0.112	0.152	0.534	0.283	0.054	0.000	0.092	0.017	0.000	0.067	0.967
	b	0.921	0.755	0.783	0.414	0.433	0.786	1.000	0.618	0.983	0.966	0.267	0.033
	c	0.079	0.133	0.065	0.052	0.283	0.161	0.000	0.289	0.000	0.034	0.667	0.000
pgi-2	N	19	22	28	28	0	0	12	49	30	30	30	30
	a	1.000	1.000	1.000	0.117	0.071	1.000	1.000	1.000	1.000	1.000	0.629	1.000
	b	0.000	0.000	0.000	0.300	0.286	0.000	0.000	0.000	0.000	0.000	0.371	0.000
	c	0.000	0.000	0.000	0.350	0.411	0.000	0.000	0.000	0.000	0.000	0.000	0.000
	d	0.000	0.000	0.000	0.150	0.214	0.000	0.000	0.000	0.000	0.000	0.000	0.000
	e	0.000	0.000	0.000	0.083	0.018	0.000	0.000	0.000	0.000	0.000	0.000	0.000
pgi-3	N	19	48	28	-	-	28	11	49	23	21	29	30
	a	0.053	0.000	0.000	-	-	0.036	0.000	0.000	0.000	0.000	0.241	0.000
	b	0.026	0.063	0.000	-	-	0.304	0.255	0.255	0.017	0.033	0.172	0.867
	c	0.737	0.531	0.964	-	-	0.500	0.510	0.510	0.800	0.850	0.276	0.133
	d	0.184	0.000	0.036	-	-	0.161	0.235	0.235	0.183	0.117	0.310	0.000
pgm	N	35	49	28	30	28	28	0,	34	30	30	30	30
	a	0.348	0.061	0.000	0.150	0.536	0.679	0.000	0.000	0.000	0.000	0.000	0.000
	b	0.485	0.776	0.893	0.850	0.464	0.286	0.542	0.468	1.000	1.000	0.017	1.000
	c	0.167	0.143	0.107	0.000	0.000	0.036	0.458	0.456	0.000	0.000	0.850	0.000
	d	0.061	0.020	0.000	0.000	0.000	0.000	0.000	0.076	0.000	0.000	0.133	0.000
mr	N	19	22	28	30	30	28	12	49	30	30	30	30
	a	1.000	1.000	1.000	1.000	1.000	1.000	1.000	1.000	1.000	1.000	1.000	1.000
	b	0.000	0.000	0.000	0.000	0.000	0.000	0.000	0.000	0.000	0.000	0.000	0.000

N; No. of examination, –; non signal

THE ANALYSIS OF FLOODING CONDITION USING BY GIS DATA IN THE THAILAND IN 2011

Masanobu Taniguchi[1], Hiroyuki Ii[1], Yuji Hara[1] and Danai Thaitakoo[2]
[1] Faculty of System Engineering, Wakayama University, Japan;
[2]Faculty of Architecture, Chulalongkorn University, Thailand;

ABSTRACT

The purpose of this study is to clarify the cause of the flooding in Thailand that occurred in 2011. The Thailand flooding in 2011 is analyzed by survey and GIS data. The flow condition in flooding was estimated by altitude because water flows along to geographical features. The gradient is change at the lower site from Nakhon Sawan, and the gradient at upper site from Nakhon Sawan is flat, and therefore it is estimated that the flooding is occurred at Nakhon Sawan. The road is build higher than the other ground, so the road is shut the flooding water. Therefore it is estimated that the flooded water could not flow out, there is the water between 3 months. The rain runoff was analyzed by precipitation and GIS data. As a result, it was estimated that the rain runoff is bigger than 1.7 times of the river flow.

Keywords: Flood, Thailand, Precipitation, Runoff, GIS

INTRODUCTION

The flood was continued 3 months in 2011 in Kingdom of Thailand. The total precipitation in the flood time is not particular big from 1985 to 2015. As clear the cause of the floods, the river flow pass of Chao Phraya River Basin is estimated. The water pass is very complex by construction of agricultural water. The flood extends to a fairly wide range. The grasp of the flood area is very difficult, so it is difficult to identify the study area. However it is need to clear the cause of flooding. The study purpose is clarify to cause of the flooding.

STUDY METHOD AND THE STUDY AREA

Fig.1 shows study area information. The data of flooding area was created using by locate of flooding point in Japanese Government Report[1][2]. The flood area data is roughly, it might contain an error of several kilometers. The data is compared with altitude and the location data provide the distance and slope. The average annual precipitation is 1653mm/year, the annual precipitation in 2011 is 2240mm/year. The population of Thailand is 67 million people. The area of Chao Phraya River Basin is 160,400km^2.

The usual flow rate in fine day is 718m^3/sec. The Chao Phraya River has 2 rivers, Nan, Ping, Chao Phraya and Tha Chin. The Ping River and Nan River meet in Nahon Sawan. The red triangle is the place of flooding area in 2011. The aqua color line is canal, the distribution of canal is between the Chao Phraya River and the The Chin River.

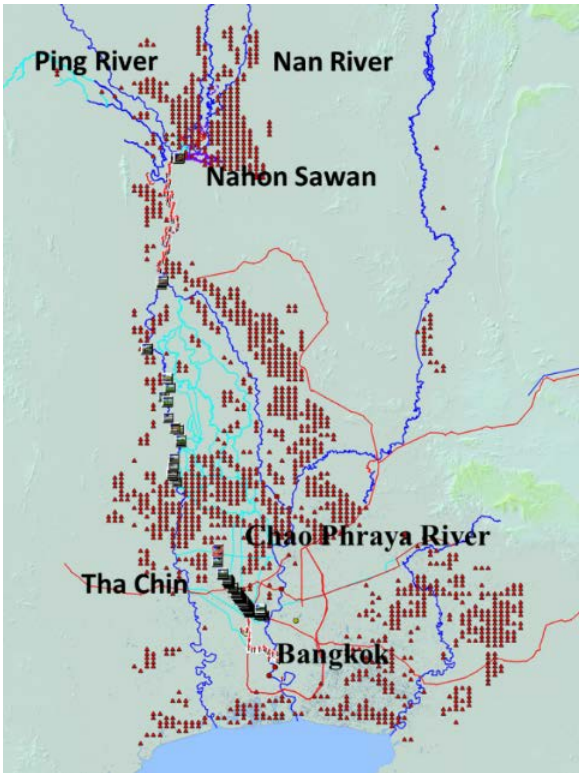

Fig. 1 Study area information

The river, canal, and road data were created by tracing the river while looking at the map of Google Earth. The local conditions was confirmed by GPS photograph at fine day. Moreover the other place that we not checked place was using by the Google Street View[3]. The amount of rain runoff was calculated by the monthly precipitation data and area that was created by author's GIS software using space shuttle altitude data. The precipitation data is opening to public by Japan Meteorological Agency. The altitude data is published by Shuttle Radar Topography Mission[6].

CHARACTERISTICS OF RAINFALL

Fig. 2 shows Time series of monthly precipitation. The maximum of precipitation is 600mm, the minimum is 300mm. The precipitation in 2011 is 600mm, the value is not particularly high[5].

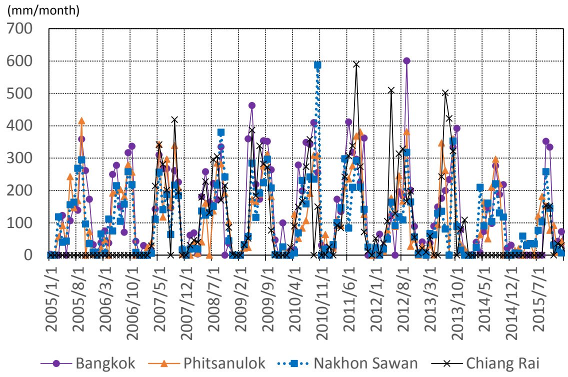

Fig. 2 Time series of monthly precipitation

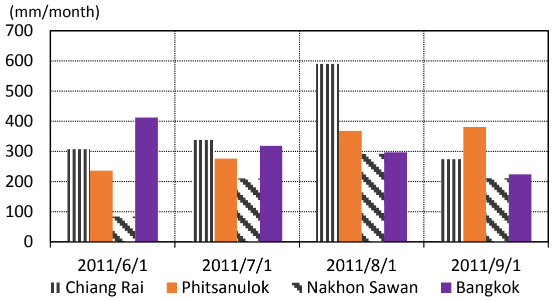

Fig. 3 Monthly precipitation of each observing station

Fig.3 shows monthly precipitation of each observing station[2]. The precipitation in June is a little, the precipitation in August in Chang Rai is about 2 times compared with the other place. It is estimated that the precipitation of Chang Rai is important for the analysis of flooding, because Chang Rai becomes water source of two big river[1]. However the observing station of Chang Rai has no data some years. Moreover daily precipitation data was not able to get.

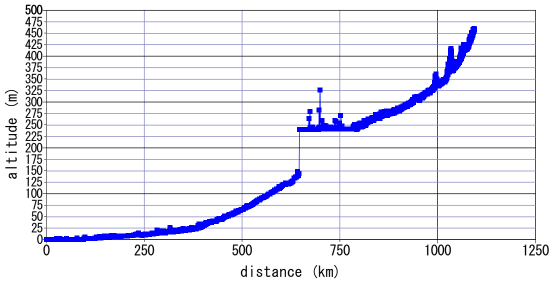

Fig. 4 The altitude from Upper stream to Bangkok

Fig.4 shows the altitude from Upper stream to Bangkok. The altitude of 600km distance from sea is about 120m, the gradient of 600km distance from sea is 0.0002. The gradient from 600km distance from sea to Nakhon Sawan is 0.0003. The height difference from Nakhon Sawan to Bangkok is m per 250km. The gradient is calculated as 0.00012.

NAHON SAWAN

Fig. 5 shows the map of around the Nakhon Sawan. The area is the confluence of Ping River and Nan River. The purple color is Wetlands. The red color line is old water pass that separated from the current river. The area is very flat, and all of upper basin water is collected at this place. There is the raised bed river around the Nakhon Sawan as shown by altitude data. The flooding is occurred at 30m altitude, it is estimated that the water could not flow to downstream.

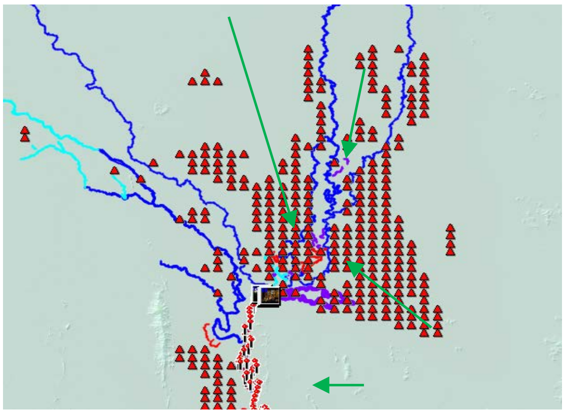

Estimated flooding direction

Fig. 5 The map of around the Nakhon Sawan

Fig. 6 The picture at Nakhon Sawan

Fig. 6 shows the picture at Nakhon Sawan. The red line shows water level of the flood in 2011. The height is about 1.5m. The city is surrounded by the rivers, so it is estimated that the water could not flow out.

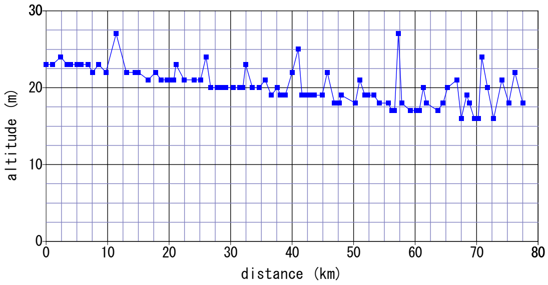

Fig. 7 The altitude from Nakhon Sawan to Chai Nat

Fig.7 shows the altitude from Nakhon Sawan to Chai Nat. The height difference from Nakhon Sawan to Chai Nat is 5m per 75km. The gradient is calculated as 0.0006. The gradient changes big at Nakhon Sawan before and after.

UPPER STREAM OF CHAO PHRAYA DAM

Fig.8 shows the map of around the Chao Phraya Dam. There is the dam across the Chao Phraya River. The river breadth is about 245m. The dam can flows max 3300m^3/sec. The dam has 16 channel of 12.5m breadth. And there is a diversion weir of agricultural water upper stream of the Chao Phraya Dam. The estimated flooding direction is from river to ground. It is estimated that the water flows over the bank of the river at the flooding point, because the river altitude is higher than the lower land point.

Fig.9 shows the overview of breadth of the Chao Phraya River. As the gradient is a very little in whole, the river breadth is important for the river flow. The gradient is same or a little change between some hundred kilometers. It is estimate that the

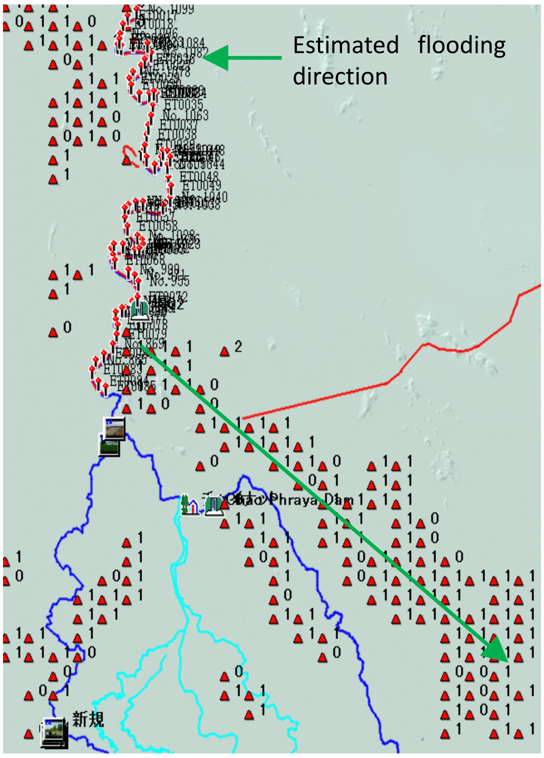

Fig. 8 The map of around the Chao Phraya Dam

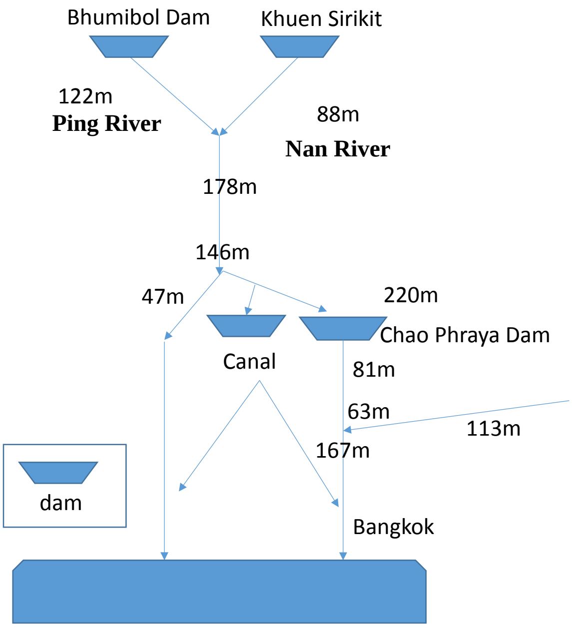

Fig. 9 The overview of the Chao Phraya River breadth

breadth is almost decide the flow rate. The some breadth is narrow at the main stream in the Chao Phraya River. Moreover it is estimated that the Chao Phraya Dam has stopped the flow of water. And it is thought that the water level at the upper dam became higher at least a little.

INFULUENCE OF DAMS

Table 1 shows the volume of dam. The total of volume is 24 billion m^3. Bhumibol Dam is biggest in the Chao Phraya River Basin. Khuen Sirikit is 9.5 illion m^3.

Table.1 The volume of dam

Dam Name	Volume(m^3)
Bhumibol Dam	13,500,000,000
Khuen Sirikit	9,500,000,000
Other	1,700,000,000
Total	24,700,000,000

ANALISYS OF RAIN RUNOFF

Fig. 10 shows the precipitation of between four months. The area is calculated by Thiessen Law, and to calculate the amount of rain runoff is need the area. The amount of rain runoff is calculated by multiplied by the amount of rainfall in the area. The area is divided by the river basin, and the data of the river basin is created by the altitude data. The flood is occurred in July, and the flood is continued between 3months, the amount of the precipitation is summed from June to September. The precipitation of the period tends to bigger in a year. The

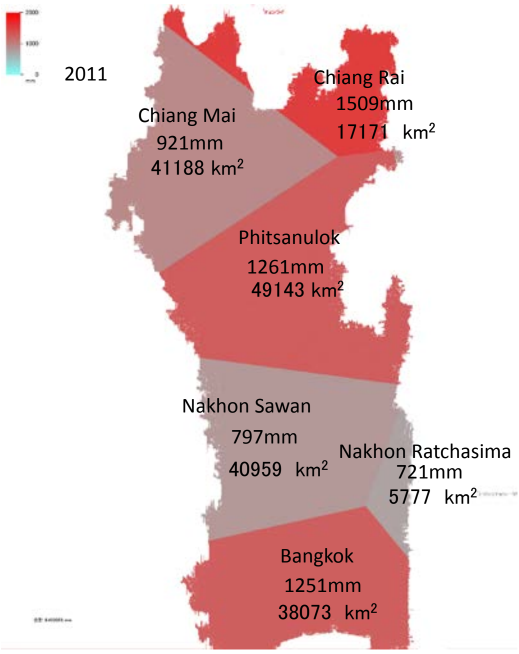

Fig. 10 The precipitation of four months

precipitation in Phitsanulok and in Chang Rai is over than 1000 mm, and moreover the area is large. So the amount of rain runoff is biggest in the Chao Phraya Baisn. Phitsanulok is located in middle stream of the Chao Phraya River, the Chao Phraya River meet at Nakhon Sawan, all of the basin's water corrected in the Nakhon Sawan. It is need to calculated the amount of rain runoff.

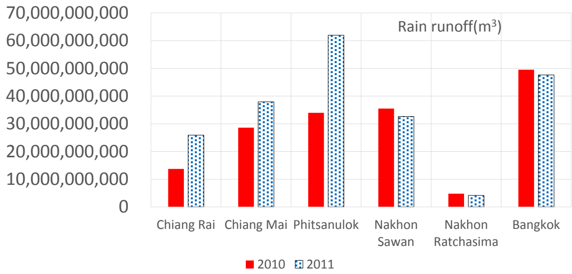

Fig. 10 The amount of rain runoff of four months

Fig. 10 shows the amount of rain runoff of four months. The amount of rain runoff was compared with in 2010 and in 2011. The monthly precipitation changes very little by a month. The anount of rain runoff in 2011 ara increase over 10 billion m3 compared with 2010 in Chang Rai and in Phitsanulok. In particular, In Phitsanulok, the amount of rain runoff increase 25billion m3 compared with in 2010. In fact, the lowerstream of Phitsanulok at Nakhon Sawan was flooding, the city was big damaged.

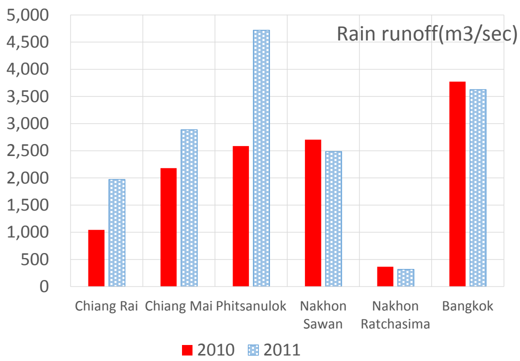

Fig. 11 The amount of rain runoff per second

Fig. 11 shows the amount of rain runoff per second. The rain runoff was compared with the river flow rate. The actual flow rate is unknown. To collect the daily precipitation data is difficult. The daily rain runoff data was calculated by the monthly precipitation data between 4 months and the basin area. The Chao Phraya Dam is possible to flow $3300m^3/sec$. The amount of rain runoff at upper the Chao Phraya Dam is 5800 m3/sec, the rain runoff is 1.7 times from the Chao Phraya Dam flow.

IMPACT OF THE ROAD

Fig. 12 shows the overview of the road. The flooding area is devided at National load No.1 and No.346 located near Bangkok shown in Fig.1. The road is higher than the other ground. Therefore it is estimated that the water is difficult to flow over the road. It is estimated that the flooded water could not flow out, there is the water between 3months.

Fig. 12 The overview of the road

CONCLUSION

The study purpose is clarify to cause of the flooding. The Thailand flooding in 2011 is analyzed by survey and GIS data. The data of information of water control was collected as location data. The gradient changes big at Nakhon Sawan before and after, at the lower Nakhon Sawan, and the gradient is a very little, and therefore it is estimated that the flooding is occurred. And it is thought that the water level at the upper Chao Phraya dam became higher at least a little. The road is higher than the other ground. Therefore it is estimated that the water is difficult to flow over the road. It is estimated that the flooded water could not flow out, there is the water between 3 months.

REFERENCES

[1] Land, Infrastructure and Transportation Ministry, http://www.mlit.go.jp/river/kokusai/disaster/thailand/thailand_flood_111111.pdf.

[2] Japan Meteorological Agency , http://www.data. jma.go.jp/gmd/cpd/monitor/

[3] Google Map, http://www.google.co.jp

[4] Masanobu Taniguchi, and Hiroyuki Ii ,” Distribution characteristics of the Annual nitrogen load in Yamato River Basin in 2011”, International Journal of GEOMATE, June, 2016, Vol. 10, Issue 22, pp. 2043-2049 , Japan

[5] Kazuyuki Mizumura, Hydrosphere hydrology, 1998.

[6] Shuttle Radar Topography Mission, http:// e4ftl01.cr.usgs.gov/SRTM/SRTMGL3.003/2000.02.11/

UTILIZATION OF TOFU LIQUID WASTE GENERATED FROM ANAEROBIC PROCESSING IN COMPOST PREPARATION

M. Faisal
Department of Chemical Engineering, Syiah Kuala University, Banda Aceh, Indonesia

ABSTRACT

This study aims to identify the ability of tofu liquid waste generated from anaerobic processing to act as a microorganism source to help expedite compost decomposition. In this research, composting was performed on 2 kg of rice husks to which tofu liquid waste was added in various volumes (500–2000 mL) and 1 kg of cow manure. This research used a nonfactorial completely randomized design with five treatments and four repetitions, which made a total of 20 unit trials. Changes in pH, humidity (rH), C composition, N, C/N ratio, and number of colonies were analyzed to observe the compost quality. The data collected were then analyzed using SPSS 16. The research findings showed that increasing the volume of tofu liquid waste has a significant impact on composting temperature, and all compost outputs were within proper compost criteria. Increasing tofu waste volume can improve the population of microorganisms, which accelerated the decomposition process of organic matter. The highest number of bacterial colonies, 73 colony forming units, was found on 1500-mL treatment. At this condition the values obtained were 17.94%, 0.9%, and 20.1 for C, N, and C/N ratio, respectively.

Keywords: Compost, Tofu Waste, C/N Ratio, Bacteria Colonies

INTRODUCTION

Tofu is a traditional oriental food and is typically processed by grinding and boiling of soybeans. The tofu industry is one of the industries that use a large amount of water in its processes. The water used in the process produces a large amount of tofu waste. Without a good handling process, tofu waste containing a high proportion of organic compounds may cause various adverse impacts, such as water pollution, various diseases, bad smell, increased mosquito population, and degrading the aesthetics of the environment. Liquid waste disposed to a water body without prior processing may also kill the biotic community in the water, including microorganisms, which have important roles in managing biological balance in the water. Small tofu processing industries usually dispose of their waste into the sewage system and do not go through appropriate processing [1],[2]. Some researchers have utilized liquid waste from the tofu industry as sources of methane and hydrogen gas [3],[4] by biological degradation (anaerobic process). After going through an anaerobic process, tofu liquid waste still contains mixed cultures of bacteria and organic matter. In previous research, Faisal et al. [4] used a thermophilic stirred anaerobic (TSA) reactor to process tofu liquid waste. The chemical oxygen demand value of the waste generated by the TSA process was in the order of 1900–2000 mg/L. This high organic matter could not be discharged to the environment, Thus, further processing was required (for example, aerobic, membrane) for proper waste quality that meets effluent regulations. One of the methods to utilize the waste is making it into a microorganisms' source in the composting process.

Composting technology adoption is one of the alternatives that can reduce the amount of waste production [5]. Composting is one of the methods that have proven to be efficient and effective in waste processing, from both economic and environmental points of view [6]. Many studies on composting using various types of microorganisms have been done with relatively effective results [7],[8]. The success of compost production is determined by the ability of decomposer microorganisms to decompose organic matter. Mancebo and Hettiaratchi [9] conducted an intensive study on assessment of the composting dynamics of different organic residues (i.e., food wastes, dewatered sludge, sawdust, and herbal). The aerobic composting process is a cost-effective technique for the treatment and sanitization of biodegradable solid wastes fractions [10-13]. Composting can also effectively improve soil condition and farm product quality [14]. Nowadays, different types of microorganisms are added to accelerate the composting process, one of which is EM4, which contains a mixed culture of microorganisms.

The objective of this research was to identify the ability of tofu liquid waste produced from the TSA process to act as a microorganisms' source to help accelerate the decomposition process of composting. It was expected that the mixed-cultures bacteria contained in the tofu waste could accelerate the decomposition process of the compost.

RESEARCH METHOD

The materials used to make compost in this research consisted of rice husks, manure (the matured type), and tofu liquid waste produced from TSA reactor processing. The characteristic of tofu waste has been described previously [2].

Trial Design

This research used a nonfactorial completely randomized design with five treatments and four repetitions, which made a total of 20 trial units.

Types of treatment: P0: 2 kg rice husks + 1 kg manure; P1: 2 kg rice husks + 1 kg manure + 500 mL tofu liquid waste; P2: 2 kg rice husks + 1 kg manure + 1000 mL tofu liquid waste; P3: 2 kg rice husks + 1 kg manure + 1500 mL tofu liquid waste; P4: 2 kg rice husks + 1 kg manure + 2000 mL tofu liquid waste.

Data analysis was conducted using SPSS 16, where if the analysis of variance showed a significant difference, it would be followed by the Smallest Real Difference Test at the 5% level.

Experimental

Preparation of compost

The materials used to make the compost were rice husks and manure, at a ratio of 2:1. One (1) kg of trash-free dry rice husks was mixed with 2 kg of manure. The manure used in the process was matured manure that had characteristics of low temperature, less strong smell, and dry. All bacteria (tofu waste) were fed into the composter (with a capacity of 30 L and equipped with a temperature indicator). The temperature, pH, and relative humidity (rH) of the composting were observed on a daily basis for 60 days. The observation was limited to the C/N ratio, C organic, total N, and the number of decomposer microorganism colonies. The analyses followed the procedure given in Standard Methods for the Examination of Water and Wastewater. Determination of total nitrogen was done based on the total Kjeldahl nitrogen content and carbon was measured by gravimetric analysis.

RESULTS AND DISCUSSION

Temperature Changes

Temperature is one of the key indicators in compost making. Heat is generated by microorganisms' activity when decomposing organic matter. Temperature can also be used to find out how well the composting process is and to what extent decomposition has taken place. The results of analysis of variance using SPSS 16 showed that the tofu waste volume treatment had a significant impact ($P = 0.001 < 0.05$) on the compost. The observation results revealed that the average composting temperature during each treatment showed irregular temperature fluctuation and this was almost the same in each treatment.

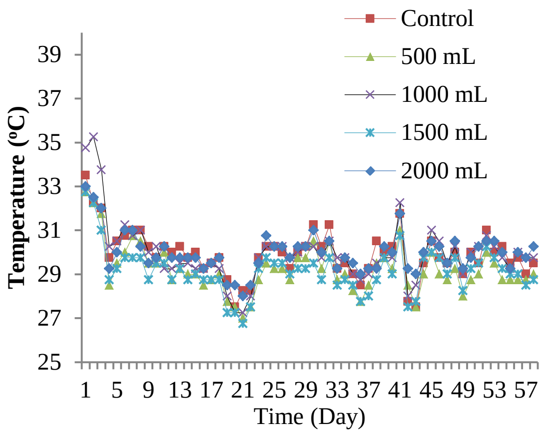

Fig. 1 Temperature as a function of time.

Figure 1 shows that the highest composting temperature of 34.75 °C occurred with the 1000-mL treatment during the first week of the composting period. In contrast, the lowest temperature of 26.75 °C occurred on the 1500-mL treatment during week 21. The observation results also revealed that adding tofu waste in various volumes caused significant temperature increases during the composting period.

The maximum temperature of the composting process involving thermophilic microorganisms is 45–59 °C, where at that point the composting process will be better [15]. In this study, the initial highest composting temperature was only 34.75 °C, which indicated that all treatment variations did not reach the required temperature for thermophilic microorganisms to grow and develop. In other words, mesophilic microorganisms played a role in this composting process. This was presumably caused by the high humidity of the pile, which prevented maximum heat production. This caused the compost to be unable to reach the optimum temperature required for thermophilic microorganisms to grow, resulting in a slow composting process. The compost temperature declined after the first week as microorganisms' activity to decompose organic matter reduced. The temperature decline could also mean that the compost had matured and mineralization process of nutrients had taken place.

Compost Characteristics (C/N Ratio, Organic C, and Total N)

On day 60, chemical analysis to find out compost quality was carried out. The compost testing consisted of C, N, and C/N ratio analyses. The results of laboratory analysis of the matured compost's chemical contents are shown in Table 1. Tables 2 and 3 show the standard compost criteria according to the Indonesian National Standard (SNI) and Regulation of the Minister of Agriculture No. 2/Pert/HK.060/2/2006, respectively [16].

Table 1 Compost's chemical contents.

Treatment	C organic (%)	N total (%)	Ratio C/N	Tempe-rature (°C)	rH (%)	pH
Control	20.52	1.09	18.73	29.9	0	7
500 mL	19.03	0.94	20.42	28.7	12.4	6.7
1000 mL	18.48	0.87	21.09	29.9	20.2	6.5
1500 mL	17.94	0.9	20.1	29.1	44	5.6
2000 mL	17.51	0.7	25.08	29.9	53. 6	5.3

Table 2 Compost characteristics according to the Indonesian National Standard (SNI-19-7030-2004).

Limit	C organic (%)	N total (%)	Ratio C/N	Tempe-rature (°C)	rH (%)	pH
Min.	9.8	0.4	10	–	–	6.8
Max.	32	–	20	30	50	7.49

Table 3 Compost characteristics according to the Regulation of the Minister of Agriculture No. 2/Pert/HK.060/2/2006.

Contents	C organic (%)	N total (%)	Ratio C/N	Tempe-rature (°C)	rH (%)	pH
Solid	≥12	0.4	10 ± 25	–	13 ± 20	4 ± 8

The C/N ratio is a comparison between carbon and nitrogen. The C/N ratio is widely used as an indicator of compost maturity [17]. The C/N ratio is used to identify the presence of microorganisms in an area because nitrogen is absorbed by plants and dead microorganisms leave carbon sediment.

A low C/N ratio of between 4 and 10:1 generally comes from the sea. Plants with wood vessels on land will provide sediment (organic matter pile) with C/N ratio <20 [18]. According to Setyorini et al.[19], the C/N ratio of good compost is 10–20, depending on the raw materials and humidity level.

Based on Table 1, the C/N characteristics of compost according to the SNI on the control treatment and the 1500-mL treatment with C/N ratio value were 18.73 and 20.1, respectively. Table 1 also shows that the C/N ratio from the highest compost treatments, i.e., in volume 2000 mL, was an average of 25.08 and the content of the N element was 0.7%, which was also the lowest of all treatments. We assume that the 2000 mL compost treatment requires longer decomposition to reach the level where the C/N ratio is <20.

As shown in Table 3, however, all treatments to the tofu waste compost with various volumes met the criteria of good solid compost. The analysis results also showed that organic C and total N contents on all treatments met the criteria of good compost for agriculture.

The high C/N ratio found in the 2000 mL volume treatment was presumably due to too much tofu waste being added to the compost, causing low temperature and a slow decomposition process. In contrast, the low C/N ratio in the control treatment was due to temperature rise, causing rapid microorganism effectiveness. The higher the temperature, the lower the C/N value will be [20]. The decline in C/N ratio was due to the increased microorganisms' activity during the organic matter break down process. The pile containing too little nitrogen would not produce heat for a rapid break down of matter, causing the C/N value to stay high.

Acidity (pH) and Humidity (rH)

1.Acidity (pH)

The results of data analysis using SPSS showed that the influence of tofu waste volume on compost pH was significant, where $P < 0.05$, thus H0 was rejected, which means that the average acidity (pH) of each volume treatment applied to the tofu waste was different. The pH change in the composting process varies vastly [21] depending on the types of composting materials and the microorganisms in it.

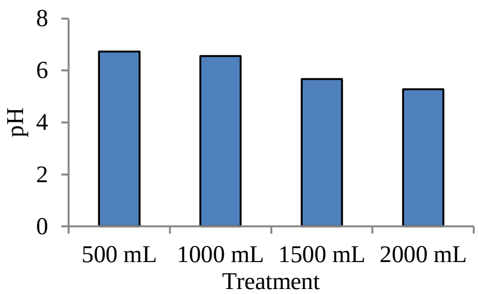

Fig. 2 Influence of waste volume on pH of compost.

Figure 2 shows the influence of waste volume on pH of compost. Compost acidity criteria are: very acidic <4.5, acidic 4.5–5.5, semi-acidic 5.6–6.5, neutral 6.6–7.5, semi-alkali 7.6–8.5, alkali >8.5. In Figure 2, the 1500 mL and 1000 mL volumes were included in semi-acidic, the 500 mL and control were included in the neutral criteria. Matured compost usually has a pH very close to neutral. The pH of optimum composting ranged between 5.5 and 8.0. The pH of the 2000-mL treatment was included in acidic criteria as the activity of the microorganisms was to decompose organic matter and to produce simple organic acids. This signified that the composting process on that particular treatment was still continuing.

The composting process of organic matter can occur in a large pH range. The composting alone would cause changes to the organic matter and the pH. Although the pH of several treatments involving tofu waste was still in the acidic category, according to the standards in Table 3, all of the treatments with tofu waste met the criteria of compost used in agriculture, as the pH of the compost was higher than 4 and close to neutral.

2.Humidity (rH)

Humidity plays an important role in the metabolism process of microbes and indirectly influences oxygen supply. Microorganisms can utilize organic matter if the organic matter is dissolved in water. Sufficient humidity is required during the composting process [22]. High levels of humidity are harmful for efficient composting development because of decreasing the air void volume available for oxygen movement [22].

The results of data analysis showed that the influence of tofu waste volume on compost rH was significant, where the value of $P < 0.05$, so that H0 was rejected. In other words, the average humidity (rH) of each tofu waste volume treatment was indeed different.

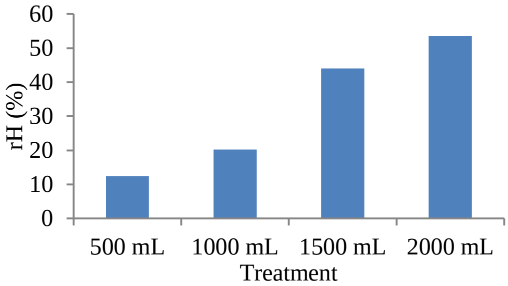

Fig. 3 Influence of waste volume on rH of compost.

Figure 3 shows the influence of tofu waste on compost rH. It can be seen that the smaller the volume of tofu waste in the composting process, the lower the humidity. Figure 3 also shows that the 500-mL treatment had humidity below the standard matured compost. The 1000-mL, 1500-mL, and 2000-mL treatments met the criteria of proper compost, as indicated in Table 3.

Number of Bacteria Colonies

Figure 4 shows the influence of various tofu waste volumes on the number of bacteria colonies in the compost. Analysis of variance showed that treatment of adding tofu waste did not have a significant influence ($P = 0.744 > 0.05$) on the number of microorganisms, especially bacteria. In other words, the number of bacteria colonies in each treatment was the same or no different from one another.

The maximum number of bacteria colonies was mostly found in the 1500-mL treatment. This was related to the value of C/N for that particular treatment. In the 1500-mL treatment, the bacteria had sufficient energy sources.

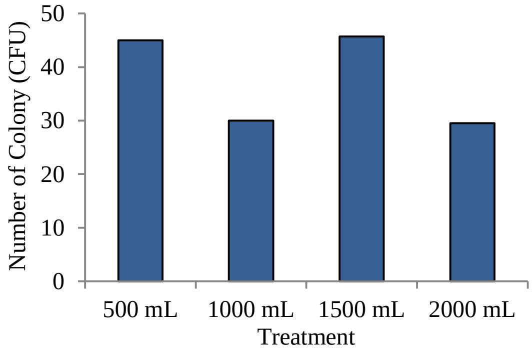

Fig. 4 the influence of various tofu waste volumes on the number of bacteria colonies.

Although there was a difference between the analysis of variance and the number of bacteria colonies in each treatment, adding tofu waste in the composting process gave significant results. This is consistent with Hindersah's study [20], which found that adding tofu waste and bioactivator (cow manure) can increase the quality of compost microbiology. It is explained further that tofu waste can increase the total population of bacteria, fungi, Azotobacter sp. and phosphate-solubilizing bacteria. The basic components required as nutrients for microorganisms are carbon, nitrogen, and water. Microorganisms will use C compounds as an energy source to breed and use N to synthesize protein. During the composting process, many fungi and bacteria are responsible for the degradation of complex polymeric substrates, such as pectin, lignin, cellulose, and hemicellulose [8]. Li et al. [23] reported that, in general, the most efficient lignocellulose degraders are fungi due to the fact that their mycelial structure has a competitive advantage over bacteria.

The species of bacteria found in the compost on each treatment remain unknown. It was assumed that the decomposer bacteria that played a role in decomposing the organic material in the tofu waste compost were the lactate acidic bacteria (Lactobacillus sp.). Bacteria of this type are commonly found in composting material. Bacteria Lactobacillus sp. were able to reduce dangerous microorganisms and to decompose organic matter rapidly.

CONCLUSIONS

Microorganisms found in tofu waste generated using a TSA reactor can be used as decomposers in the making of rice husk compost. Increasing tofu waste volume can increase the population of microorganisms, which accelerates the organic material degradation process. All treatments of tofu waste compost involving various volumes meet the criteria of good solid compost. The analysis results also showed that organic C and total N contents in all treatments meet the criteria of good compost for agriculture. The highest number of bacteria colonies was mostly found in the 1500-mL treatment. Further research with various compost quality analyses (e.g., P, K, trace elements) will support this preliminary study.

ACKNOWLEDGEMENTS

This work was supported by the Ministry of Research, Technology, and Higher Education of Indonesia with a research grant for International Research Collaboration and Scientific Publication. The authors also thank Ms. Afriyani, who helped in the data analysis of this study.

REFERENCES

[1] Faisal M, Machdar I, Mulana F, Daimon H, “Potential renewable energy from tofu processing waste in Banda aceh city, Indonesia. Asian J. Chem.”, Vol. 26, No.18, Oct. 2015, pp. 6601-6604.

[2] Faisal M, Mulana F, Gani A, Daimon H, “Physical and chemical properties of wastewater discharged from tofu industries in Banda Aceh city, Indonesia”, Res. J Pharm. Bio. Chem. Sci., Vol. 6, No. 4, Jul. 2015, pp. 1053-1058.

[3] Lay CH, Sen B, Huang SC, Chen CC, Lin CY, “Sustainable bioenergy production from tofu-processing wastewater by anaerobic hydrogen fermentation for onsite energy recovery”, Renew. Energ., Vol. 58, Oct. 2013, pp 60-67.

[4] Faisal M, Gani A, Mulana F, Daimon H, “Treatment and utilization of industrial tofu waste in Indonesia”, Asian J. Chem, Vol. 28, No.3, Feb. 2016, pp. 501-507.

[5] Mohee R, Boojhawon A, Sewhoo B, Rungasamy S, Somaroo GD, Mudhoo A, “Assessing the potential of coal ash and bagasse ash as inorganic amendments during composting of municipal solid wastes”, J. Envi. Mana., Vol. 159, Aug. 2015, pp. 209-217.

[6] López R, Giráldez I, Palma A, Díaz MJ, “Assessment of compost maturity by using an electronic nose”, Waste Mana., Vol. 48, Feb. 2016, pp.174-180.

[7] Chen Y, Zhou W, Li Y, Zhang J, Zeng G, Huang A, Huang J, “Nitrite reductase genes as functional markers to investigate diversity of denitrifying bacteria during agricultural waste composting” Environ. Biotechnol., Vol. 98, May 2014, pp. 4233-4243.

[8] Ventorino V, Parillo R, Testa A, Viscardi S, Espresso F, Pepe O,”Chestnut green waste composting for sustainable forest management: Microbiota dynamics and impact on plant disease control”, J. Environ. Manage., Vol. 166, Jan 2016, pp.168-177.

[9] Mancebo U, Hettiaratchi JPA, “Rapid assessment of methanotrophic capacity of compost-based materials considering the effects of air-filled porosity, water content and dissolved organic carbon”, Bioresour. Technol. Vol.177, Feb. 2015, pp.125-133.

[10] Komilis D, Evangelou A, Voudrias E, “Monitoring and optimizing the cocomposting of dewatered sludge: a mixture experimental design approach”, J. Environ. Manage. 92 (9), Sep. 2011, pp. 2241-2249.

[11] Lopez R, Burgos P, Madrid F, Camuna I,” Source separate collection of recyclables reduces chromium and nickel content in municipal solid waste compost. CLEAN - Soil, Air. Water, Vol. 43, No.3, Mar 2015, pp. 427-433.

[12] Wong JWC, Fung SO, Selvam A, “Coal fly ash and lime addition enhances the rate and efficiency of decomposition of food waste during composting, ”Bioresour. Technol., Vol. 100, Jul. 2009, pp. 3321-3324.

[13] Zhou Y, Selvam A, Wong JW, “Evaluation of humic substances during co composting of food waste, sawdust and Chinese medicinal herbal residues”. Bioresour. Technol., Vol.30, No.168, Sep. 2014, pp. 229-234.

[14] Mandal A, Patra AK, Singh D, Swarup A, Masto RE, “Effect of long-term application of manure and fertilizer on biological and biochemical activities in soil during crop development stages”, Bioresour. Technol. Vol. 98 , Dec. 2007, pp. 3585–3592.

[15] Tom LR, “Municipal solid waste composting: biological processing”, Center for the Environment, Cornell Waste Management Institute, 1993, pp. 1-6

[16] National Standardization Agency, Compost Spesification from domestic organic wastes, Indonesian National Standard 19-7030-2004.

[17] Bernal MP, Paredes C, Sanchew-Monedero MA, Cegarra J, “Maturity and stability parameters of composts prepared with a wide range of organic wastes”, Bioresour. Technol., Vol. 63, Jan. 1998, pp.91–99.

[18] Raj D, Antil RS, “Evaluation of maturity and stability parameters of composts prepared from agro-industrial wastes”, Bioresour. Technol., Vol 102, No.3, Feb. 2011, pp.2868-2873.

[19] Setyorini DR, Saraswati, Anwar EK, “Compost”, Research Center for Agricultural Technology, DI Yogyakarta, 2003.

[20] Hindersah R, Hernanto Y, Joy B, Mulyani, O, “Utilization of tofu waste in composting of household waste for increasing quality of compost microbiology", Agrinimal, 2011, pp. 15-21.

[21] Juárez MFD, Prähauser B, Walter A, Insam, H ,Franke-Whittle IH, “Co-composting of biowaste and wood ash, influence on a microbially driven-process”, Waste Manage., Vol. 46, Dec. 2015, pp. 155-164.

[22] Ahn H, Richard T, Glanville T, “Optimum moisture levels for biodegradation of mortality composting envelope materials”, Waste Manage. 28, Dec. 2008, pp, 1411-1416.

[23] Li H, Xu X, Chen H, Zhang Y, Xu J, Wang J, Lu X, “Molecular analyses of the functional microbial community in composting by PCR-DGGE targeting the genes of the b-glucosidase”, Bioresour. Technol., Vol. 134, Apr. 2013, pp. 51-58.

Sixth International Conference on Geotechnique, Construction Materials and Environment, Bangkok, Thailand, Nov. 14-16, 2016, ISBN: 978-4-9905958-6-9 C3051

COMPARATIVE ANALYSIS OF NEW GROUND MATERIAL AND EMBANKMENT CONSTRUCTION METHODS IN CONSIDERATION OF RECYCLING BY LCA

Hideyuki Ito[1], Koichi Yamanaka[2], Hideo Noguchi[3], Takahiro Fujii[4] and Kunio Minegishi[5]
[1,2,4,5] College of Science and Technology, Nihon University, Japan;
[3] Tsuchiura City Hall, Japan

ABSTRACT

The cutting and embankment construction method, which is a conventional embankment construction method, would possibly cause grand subsidence or landside at a location of a soft ground or with the risk of landside. From these points of view, the construction method employing a new ground material such as EPS (Expanded Polystyrene) is effective for construction at such a location with soft ground or the landslide risk because of its light weight and workability. However, such new materials have not much construction examples, expect a few existing researches such as Ito et al. (2014) conducing comparative analysis in terms of environmental load and cost in view of life cycle assessment (LCA). Thus, the accumulation of researches on the new materials is still not enough. The purpose of this research is to extract what to be improved and solved in new ground materials by analyzing various environmental loads and life cycle costs, which arise from the life cycle in case of various embankment construction methods in consideration of whether they have used new ground materials and recycle of waste materials. As a result, the research demonstrated a possibility of reducing the environmental loads or life cycle costs by employing recycling in the various embankment constructions methods.

Keywords: Life Cycle Assessment, Lightweight Geomaterial Mixed with Expanded Polystyrol Beads, Expanded Polystyrol Construction Method, Foamed Waste Glass Construction Method, Life Cycle Cost

INTRODUCTION

Among the various embankment construction methods, the conventional cut and fill method can cause ground subsidence and landslides on soft ground and in landslide-prone areas. To deal with this issue, a construction method has been developed, using a new lightweight and workable composite geomaterial mixed with expanded polystyrene (EPS), which is believed to be effective for construction on soft ground and landslide-prone areas.

Using Life Cycle Assessment (LCA) and Life Cycle Cost (LCC), Ito et al. [1] have analyzed the environmental load and costs of embankment construction using the cut-and-fill and newly developed EPS construction methods. The results show potential for reducing the environmental load by recycling embankment materials. Ochiai et al. [2] have summarized the added value and physical properties of various mixed geomaterials and have classified the constituent materials. They also used LCA to analyze embankment materials composed of recycled tires, with respect to the manufacturing process for the materials alone. Inazumi et al. [3] also assessed the recycling of construction sludge generated from embankment works. Onizuka et al. [4] have described the engineering characteristics of foamed waste glass material and provided useful examples of its applications.

There have been a number of conventional studies examining the new geomaterials, but few have provided examples of their use in construction work or performed LCA analyses. Conventional comparative analyses of environmental load and costs from the LCA perspective include those performed by Ito et al. [1] and Ochiai et al. [2], who introduced the possibility of using waste in mixed geomaterials, but there has been an insufficient number of studies on the use of new geomaterials containing recycled embankment materials.

These present researches aim to identify areas for improvement and the problems associated with the use of new geomaterials. Thus, in this research, we estimated CO2 and air pollutant emissions generated by SOx and NOx, by comparatively analyzing the LCCs of four construction methods throughout the life cycle of the materials, from raw materials collection to construction, and from usage to disposal. For our analyses, we assumed an earth filling design for a mountainous area with the possibility of land slide. We analyzed four methods in the construction of embankments in mountainous areas, including the conventional cut-and-fill method, the expanded polystyrol construction method using the new EPS geomaterial, the lightweight embankment construction method with EPS beads, and the foamed waste glass construction method using embankment material with recycled waste.

METHOD AND SYSTEM DETAILS

In this research, Mineoka area located in the southern part of Chiba prefecture was selected as a case research area as well as previous research [1] because landside control works are conducted in mountainous roads (Fig.1). For comparative LCA analysis, we assumed conventional method, lightweight geomaterial mixed with expanded polystyrol beads and expanded polystyrol construction method and the foamed waste glass construction method using embankment material with recycled waste for constructing mountainous roads.

Based on an embankment design for a mountainous area with the possibility of land slide, we focused on the weight savings and recycled embankment materials in our analyses of the conventional cut-and-fill method, the EPS method with new geomaterials, the lightweight embankment construction method with EPS beads, and the foamed waste glass construction method using recycled waste glass as embankment material.

In the EPS method, EPS blocks are stacked as embankment materials and are integrated by dedicated clamps. When stacked, these ultra-lightweight embankments are characterized by their compressive resistance, durability, and independent stack design.

In the lightweight embankment construction method with EPS beads, lighter earth is used, comprising EPS mixed with earth and sand. This method is effective for use in earth fills on soft ground and in landslide-prone areas due to its capability of reducing the applied load on the ground more effectively than ordinary earth and sand.

Foamed waste glass is a porous embankment material manufactured by pulverizing, burning, and foaming recycled waste glass. The specific gravity and degree of water absorption can be controlled during manufacturing according to the requirements of specific applications. Hence, foamed waste glass is used in a wide range of applications including civil engineering, greening of slopes and rooftops, agriculture, water purification, and heat insulation. This material is lightweight, water permeable, water retentive, fire resistant, and a good thermal insulator.

Also, we set a functional unit that provides a logical basis for comparing the environmental performance of alternatives for applying LCA to these 4 construction methods. We defined the target road condition (2 lanes, 7m wide and 1m long) as a functional unit as shown in the Fig.2. In addition, we hypothesized that the inclined angle of the mountain and road slope is 35 degree respectively (Table 1).

Fig. 1 Location of case research area.

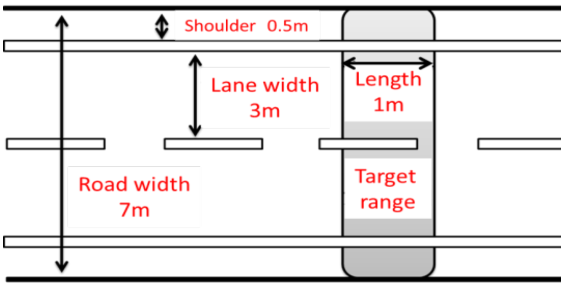

Fig. 2 Functional unit.

Table 1 Set condition of each construction method.

Construction method	Cut-and-fill	EPS construction method	Lightweight embankment construction method	Foamed waste glass construction method
	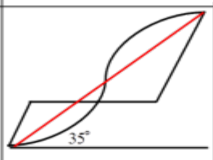	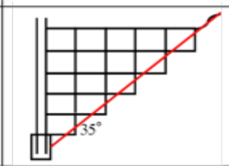	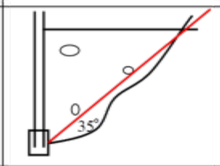	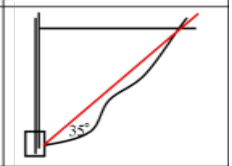
Fill	12.375m³	17.5m³	17.5m³	17.5m³
Cut	26.25m³	—	—	—
Weight per unit volume	14kN/m³	0.4kN/m³	7kN/m³	4kN/m³

SYSTEM BOUNDARY AND RECYCLING METHODS

The system boundaries of the conventional cut-and-fill method, the expanded polystyrol construction method using the new EPS geomaterial, the lightweight embankment construction method with EPS beads were set up same condition of previous research [1].

To consider the recycling impacts, we performed four embankment tasks and assumed that the road would be reconstructed every 100 years after its initial construction for 400 years. For the EPS and waste glass cases, as used in system boundaries of lightweight soil mixed with EPS beads, we calculated the CO2, air pollution, and LCCs for all life cycles with and without recycled materials. As recycling methods for most embankment materials are still in the research and development phases, we based our analyses on a method used in the industry for recycling embankment materials, as identified by results from a questionnaire and interviews with 10 business operators. Table 2 shows the recycle conditions of each construction method.

The system boundary of the foamed waste glass construction method using embankment material with recycled waste is shown in Fig.3. Foamed waste glasses are produced by recycled glass in the plant, and then they are leveled and compacted. At the waste phase, used embankment materials will be recycled. We assumed that the method used recycled embankment material of foamed waste glass materials collected after the roads had been demolished. We established distances based on the location of factories, etc. located around the Mineoka mountain district in Chiba Prefecture, where embankment work is often conducted.

To calculate the total amount of air pollutants and CO2 emitted by each method, we set the CO2, SOx and NOx unit (Table 3) and cost unit for each material (Table 4). These units were developed based on data from sources such as the LCA guidelines for building [5], IDEA (Inventory Database for Environmental analysis) [6], the LCA database developed by the Life Cycle Assessment Society of Japan [7], the database of the Express Highway Research Foundation of Japan [8] and the

Table 2 Recycle conditions.

Construction method	Recycle method (first time)	Recycle method (after second time)
Cut-and-fill	Raw materials are used for cut-and-fill first	Banking material used for cut-and-fill are recycled by mixing cement
EPS construction method	Expanded polystyrene is not able to recycle, so the recycle is not considered	
Lightweight embankment construction method	Mixed breaking foamed styrol used once, soil and cement are used for lightweight embankment construction method	After removing beads from dismantled banking material, foamed styrol is recycled
Foamed waste glass construction method	Raw materials of glass are used for foamed waste glass construction method first	Dismantled banking material is recycled.

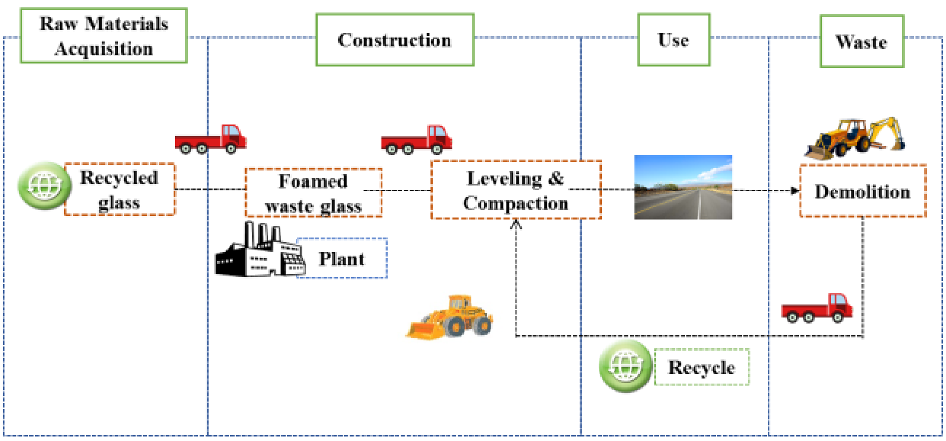

Fig. 3 System boundary of foamed waste glass construction method.

database of JEMAI-LCA PRO [9]." The cost unit for each material was estimated using the Input-Output Table of Japan's Ministry of Internal Affairs and Communications [10].

Table 3 CO2, SOx and NOx unit.

Life-cycle	Materials	CO_2 (kg-CO2)	SOx (g-SOx)	NOx (g-NOx)
Raw Materials Acquisition	Soil, Sand (kg)	0.0020	0.0034	0.0106
	Limestone (kg)	0.0047	0.0009	0.0015
	Foamed EPS (kg)	1.3123	0.2555	1.1651
	Aluminum (kg)	9.218	76.8	30
	Zinc (kg)	1.443	5.92	1.327
	Porous lightweight foam material	0.176	0.268	0.082
Construction	Leveling (m^2)	20.900	28.919	48.173
	Compaction (m^2)	12.100	16.742	27.890
Transport	20t Truck (Diesel) (km)	1.180	1.450	3.640
	15t Truck (Diesel) (km)	0.962	1.180	2.970
	10t Truck (Diesel) (km)	0.742	0.910	2.229
	4t Truck (Diesel) (km)	0.472	0.560	1.450
	2t Truck (Diesel) (km)	0.323	0.400	1.000
Waste	Dismantlement and recycle (kg)	0.00196	0.00341	0.01060
	EPS (kg)	2.64	0.544	1.22
	Metal (kg)	0.366	0.325	0.591
Energy	Diesel (L)	0.069	2.999	0.005
	Electricity (Thermal power plant) (kwh)	0.425	0.170	0.130

Table 4 Cost unit for each material.

Materials	Unit	Cost
Soil, Sand	JPY/kg	2.000
Polystyrene	JPY/kg	209.862
Limestone	JPY/kg	0.633
Aluminum	JPY/kg	76.539
Zinc	JPY/kg	186.132
Additive agent	JPY/m^3	1000.000
Diesel	JPY/L	78.000
Electricity	JPY/kwh	16.198
Leveling & Compaction	JPY/m^2	934.271

RESULTS

Estimated amount of air pollutants and CO2 emissions of each construction method is shown in Fig. 4. The CO2 emission amount results, from larger to smaller, are as follows: the EPS method, the lightweight embankment construction method with EPS beads (without recycle and with recycle), the foamed waste glass construction method (without recycle and with recycle), and the cut-and-fill method. The EPS method results were due to the high amount of CO2 emitted by the manufacturing and burning of EPS during its raw material collection and construction stages. In the lightweight embankment construction method with EPS beads, most CO2 is emitted during construction and disposal. This is due to the heavy equipment used in the work. With respect to recycled materials, the CO2 generated during raw material collection is reduced. The CO2 emitted by the foamed waste glass construction method occurs mostly in the construction stage; hence, CO2 reduction is achieved by using recycled materials rather than by collecting raw materials.

SOx emissions by the four construction methods, from largest to smallest, are in the following order: foamed waste glass construction method, foamed waste glass construction method without recycle, foamed waste glass construction method with recycle, lightweight embankment construction method with EPS beads without recycle, lightweight embankment construction method with EPS beads with recycle, cut-and-fill method, and the EPS method. Large emission impacts were observed in the raw materials acquisition and construction stages in the foamed waste glass construction method, in the construction stage alone in the lightweight embankment construction method with EPS beads and in the cut-and-fill method, and in the raw materials collection and disposal stages in the EPS method. SOx emission during raw materials collection was reduced using recycled embankment materials in the lightweight embankment construction method with EPS beads and in the foamed waste glass construction method.

The amounts of NOx emissions, from larger to smaller, are as follows : the lightweight embankment construction method with EPS beads (without recycle and with recycle), the foamed waste glass construction method (without recycle and with recycle), the EPS method, and the cut-and-fill method. Emissions during the construction stage had the greatest impact in the lightweight embankment construction method with EPS beads, the foamed waste glass construction method, and the cut-and-fill method. In the EPS method, in contrast, emissions during the raw materials collection and disposal stages had greater impact. However, NOx emissions during raw materials collection was reduced, as with Sox, by using recycled embankment materials in the lightweight embankment construction method with EPS beads and in the foamed waste glass construction method.

Fig. 5 shows estimated total LCCs of each construction method. LCCs, from higher to lower, are in the following order: the lightweight embankment construction method with EPS beads, the EPS method, the foamed waste glass construction method, and the cut-and-fill method. The raw materials collection and disposal stages were more costly in the lightweight embankment construction method with EPS beads and in the cut-and-fill method. In the EPS and foamed waste glass construction methods, more than 90% of the costs occurred during the raw materials collection stage. However, in the lightweight embankment

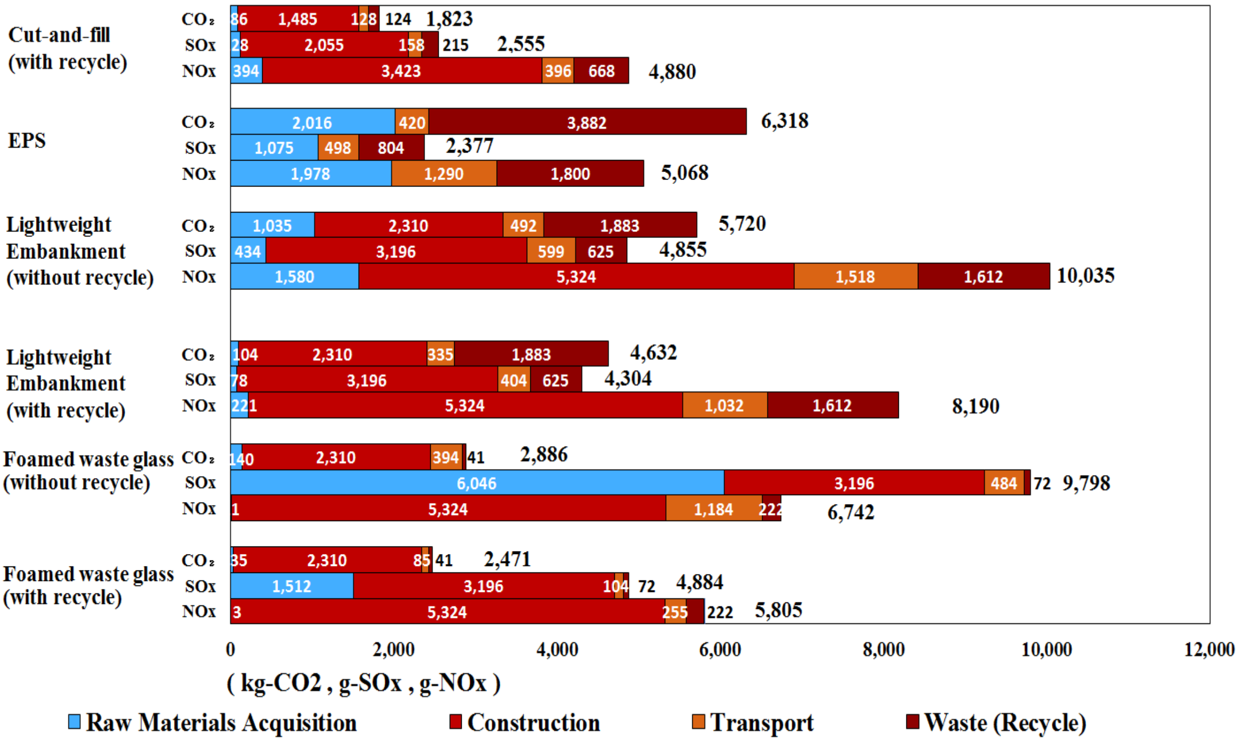

Fig. 4 Estimated amount of air pollutants and CO2 emissions of each construction method.

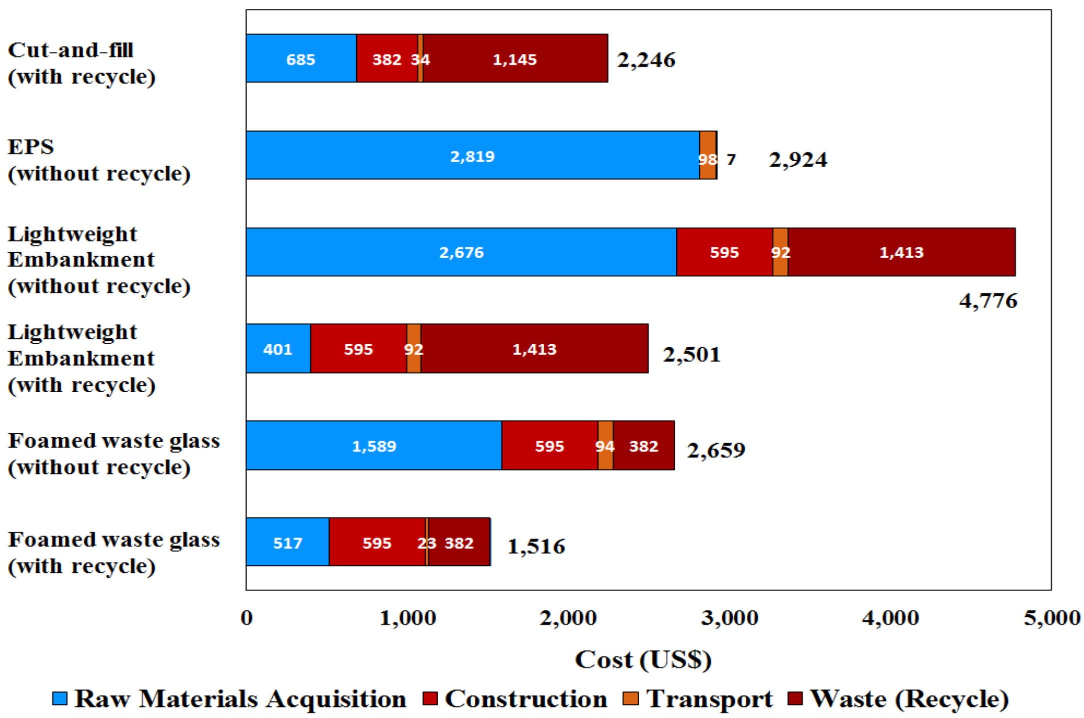

Fig. 5 Estimated total life-cycle cost of each construction method.

construction method with EPS beads and in the foamed waste glass construction method, the cost of raw materials collection was reduced by recycling embankment materials.

DISCUSSION

In this research, it was shown that all construction methods need to recycle or reuse for lower negative impacts because to produce new materials was bigger adverse impacts than recycling or reusing materials.

As the evaluation results of CO2, air pollutants and LCC, conventional cut and fill method was lower impacts to environment and reasonable life cycle cost than other methods. Regarding the lightweight embankment construction method, it was bigger impacts on environment and cost in spite of "with recycle" because CO2 and air pollutants at the construction phase including manufacturing process were greatly influenced in particular. Thus, it was pointed out that it is necessary to improve the lower impact techniques to produce and recycle EPS beads.

EPS method was the biggest CO2 emission than other methods. We need to develop new technics to recycle or reuse EPS after dismantlement because EPS blocks were just dumped now due to no recycle and reuse method. On the other hand, Foamed waste glass construction method with recycle was around second lowest impacts than other methods.

This research just only focused on CO2 emissions, air pollutants and cost. Thus, we should select appropriate construction method based on not only those results but also those environmental performance and regional characteristics on construction site.

CONCLUSION

In the present research, the potential for reducing environmental load and LCCs using recycled materials in various embankment construction methods has been proved.

For further research, estimated LCCs must include external costs and considerations such as health impacts must also be included in life cycle impact assessments. In addition, it is necessary to perform comprehensive evaluation that included the perspective of safety degree for a fair comparison through life cycle impact assessment.

REFERENCES

[1] H. Ito, K. Yamanaka, S. Nehashi, A. Fukuda and K. Minegishi, "Comparative Analysis of Three Embankment Methods for Road Construction by Life Cycle Assessment and Cost", International Journal of GEOMATE, March 2015, Vol.8, No.2, pp. 1278-1282.

[2] H. Ochiai, K. Omine, "Evaluation of environmental impact and development of mixed composite materials with new additional value." The Foundation engineering & equipment, Vol. 32, Aug. 2004, pp.9-11.

[3] S. Inazumi, H. Otsu, T. Isoda, Y. Shigematsu "Evaluation of social environmental efficiency". on recycling of construction sludges as ground materials" Journal of geological engineering, Vol.68. 2012, pp.163-174.

[4] K. Onitsuka, M.Yokoo, Y. Hara, S. Yoshitake, "Engineering Properties of Foaming Waste-glass Material and an Example of its Utilization", Journal of Soils & Foundations, Vol.47(4), 1999, pp.19-22.

[5] Architectural Institute of Japan, "LCA guideline for building", 2006.

[6] Advanced Industrial Science and Technology, "IDEA (Inventory Database for Environmental analysis)", 2010.

[7] Life Cycle Assessment Society of Japan, "LCA database", 2003.

[8] Express Highway Research Foundation of Japan, "Proposal of Estimation Method of CO_2 emissions on Road Projects", 2004.

[9] Japan Environmental Management Association for Industry, "JEMAI-LCA PRO", 2000.

[10] Ministry of Internal Affairs and Communications, "Input-Output Tables of Japan", 2005.

TSUNAMI IMPACT ANALYSIS TO GEOLOGICAL LANDSCAPE IN PERAK COAST, MALAYSIA

Sukhveender Singh Sukhdev Singh[1] and Abdul Halim Abdul Latiff[2]
[1,2]Faculty of Geosciences and Petroleum Engineering, Universiti Teknologi PETRONAS, Malaysia

ABSTRACT

On the 26th December 2004, the world had witnessed one of the strongest ever seaquake measured at 9.1 M_w caused a highly catastrophic tsunami event, taking over more than 300,000 lives. The mega-earthquake was believed due the rupture of a segment within the 1200 km fault line which lies off the coast of Sumatra, raising the seafloor to over 8 meters in height, and produced the tsunami wave that was travelling at a speed of nearly 800 km/h. In this study, the presence of coastal vegetation and geological landscape were analyzed to reduce the tsunami impact, as well as determining the potential escape route in the event of the tsunami. In addition, a tsunami computer simulation was performed along the Malacca Straits with reference to the earthquake source located at Andaman Sea. The findings from this simulation were integrated with coastal profiling of Perak region to produce a possible geological impact scenario and the potential evacuation plan, in the event of future stronger earthquake. The resultant outcomes shall be shared with local government for a better tsunami disaster management procedure in Malaysia.

Keywords: Tsunami; Coastal Vegetation; West Malaysia Coastline

INTRODUCTION

The Sumatra-Andaman earthquake that occurred on the 26th December 2004 with the magnitude of 9.1 produced a tsunami that affected the coastlines adjacent to the Indian Ocean, killed more than 300,000 individuals, and brought about loss of property and vocation [1]. In definition, tsunami is a gigantic wave that contains long wavelength and period which generated by the sudden, rough and impulsive undersea aggravations. Based on the statistic, a total of 10 major tsunamis have taken place around the world in between the year of 2004 to 2013, which has taken lots of lives with damages costing up to hundreds of billion dollars [2]. Malaysia was one of the 13 countries in the Indian Ocean that were flooded by the 26th December 2004 mega-thrust earthquake. It was recorded that the total of 68 lives were taken when the tsunami hit Malaysia, where the highest number of casualties was in Penang (52 deaths), Kedah (12 deaths), Perak (3 deaths), and Selangor (1 death) [3].

Previously, various studies and researches were carried out with respect to the potential tsunami in the west coast of Peninsular Malaysia, especially in the Penang coastline where the beach was badly hit by the tsunami. To complement those studies, this paper will be focusing mainly in the coasts of Perak due to the lack of study and research was previously conducted in this area.

BACKGROUND STUDY

The study area chosen for this research work is in Pasir Panjang beach, Segari, along the coast of Perak, about 28 km north of Lumut. The Pasir Panjang coastline is 8 km in length, 20 m in width, and almost in straight line with no particular barriers blocking the giant waves from reach the beach (Fig. 1). The open and straight nature of the beach made it highly vulnerable to the potential tsunami impact. Our general observation found that, there is a slight elevation just by the coast of the beach with oil palm trees were located few meters away from the shoreline. This vegetation can be acted as the potential natural barriers to the tsunami with further studies being carried out to prove this. There are also a few buildings such as Segari Turtle Care and Baitul-Hilal complex, which were constructed as a tourist attraction zone.

Due to the lack of coastal study conducted in this region, we took the initiative to look into the potential tsunami impact on the coastal vegetation and geological landscape in Segari, west coast of Peninsular Malaysia, by determining the tsunami wave height run-up and its corresponding inundation distance. The run-up which represents the vertical limit of the tsunami wave can be determined by conducting a computer simulation of the flooded coastal area. The detailed study on the tsunami inundation will determine how far tsunami can travel onshore which might affect the coastal vegetation and geological landscape of the study area.

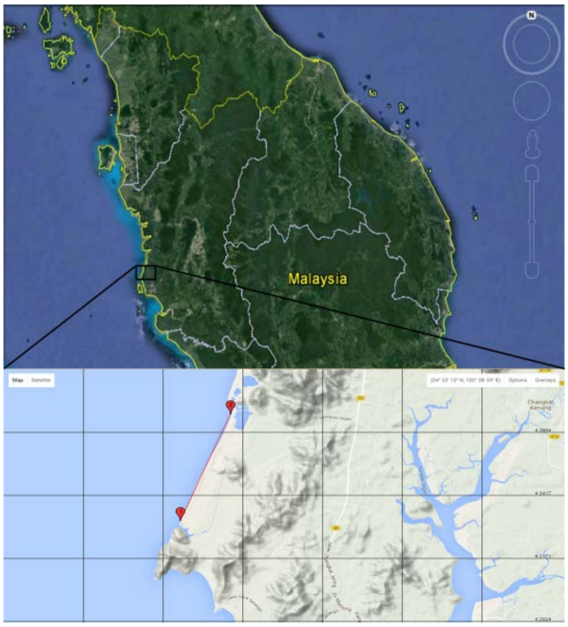

Fig. 1 Location map of Pasir Panjang beach in Perak coastline (indicate by the two pins).

METHODOLOGY

At the beginning of the study, a couple of fieldworks were conducted to scrutinize few important aspects related to the potential tsunami impact such as:

- Geological landscape and topography (e.g. beach profile, ground elevation).
- Presence of coastal vegetation as natural barriers.
- Potential escape route.

All these aspects were observed and studied in order to reduce the potential tsunami impact that might occur in this coastal area.

The information obtained then was used as an input to tsunami computer simulation that conducted in the latter stage. The simulation method used to model the tsunami wave propagation that originated from Andaman-Sumatra, is based on the Shallow Water Equation (SWE). There are a number of controls parameters that require close attention, with the source and bathymetry data are the main parameters that being experimented. Within the controls, there are a few parameters requiring input in each of the domain.

The source of tsunami wave generation can be initiated by using either one of the two available options; Gaussian hump in the initial tsunami generation, or incorporating the Okada model to generate the tsunami source [4]. Parameters such the coordinate origin and the nature of the earthquake that producing tsunami wave, were experimented in order to initiate the Gaussian hump. Throughout the simulation period, the dip, rake and focal depth of the earthquake are also being manipulated, to enhance our understanding in potential catastrophic tsunami. The resultant simulation model in term of wave height than was analyzed and integrated with the collected coastal data information.

COASTAL ANALYSIS

From the fieldwork conducted at the Pasir Panjang beach, a beach profile map was developed. The method used is the manual traversing along the shoreline and record all the surface information. It was observed that the water depth away from the shoreline gradually become deeper with a gentle slope, while the elevation of the beach is increasing significantly inland (Fig. 2). Higher ground availability in tsunami prone area is highly crucial in reducing the number of casualties in the event of tsunami.

Another observation that could be noted was the size of the sand grains. It was found that the fine grain sands filled the south-west part of the Pasir Panjang beach. Traversing towards the north-east side of the beach, the sand is getting coarser with a mix of fine sand and eventually was just filled with the coarse grained sand at the north of Pasir Panjang beach.

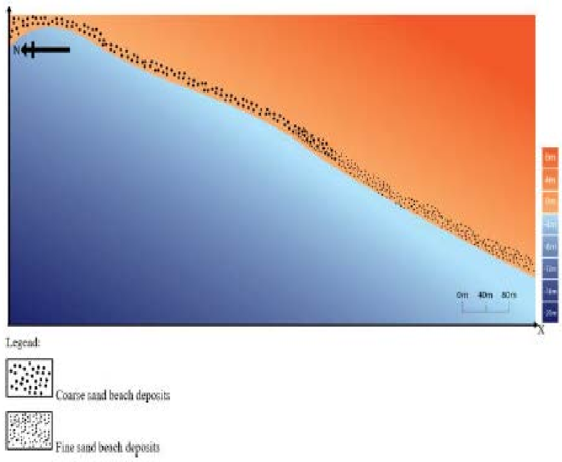

Fig. 2 Coastal map of the Pasir Panjang beach area where mix of fine and coarse sand can be observed.

BATHYMETRY ANALYSIS

Before the tsunami simulation work can be carried out, the bathymetry data which was obtained from National Oceanic and Atmospheric Administration (NOAA) need to be analyzed (Fig. 3). Since the tsunami wave originated from Andaman Sea and propagated into the Strait of Malacca, both bathymetry data were acquired from NOAA as well as from Malaysian authorities. This bathymetry map then was used as a reference to produce the tsunami wave simulation in determining the wave run-up and inundation distance at the Perak coastal region.

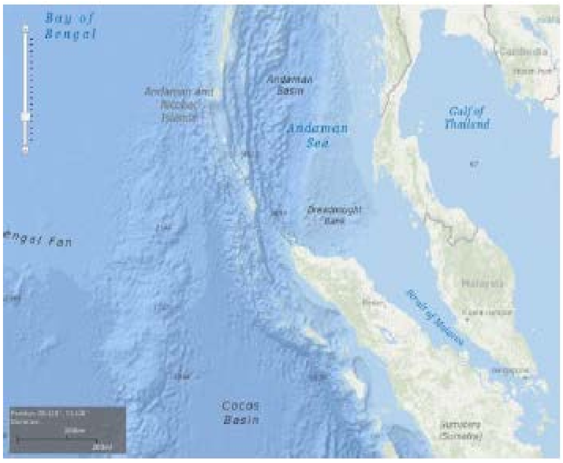

Fig. 3 Bathymetry map of the Andaman Sea and Strait of Malacca with reference to the earthquake and tsunami source in the Sumatra-Andaman subduction zone.

TSUNAMI SIMULATION

Before embarking into tsunami simulation using Shallow Water Equation (SWE) method, a simplified tsunami simulation was first carried out by using interactive tsunami simulation program that available online [5]. The program known as Tsunami Mapper, use the flood fill algorithm with the combination of elevation data provided in the google map. By using Andaman subduction zone as the point source (based on the 26th December 2004 mega-earthquake,) we set the maximum wave height of 50 meters and the wave energy propagation across the Indian Ocean of more than 1000 km.

The resultant tsunami wave could be seen spreading and propagating into the Strait of Malacca where it will directly hits the west coast of Peninsular Malaysia (Fig. 4). Tsunami wave was also predicted to reach the shore of Perak, specifically in Pasir Panjang beach, where it is an open coast and might impact the local reside at the area. However, it should be noted that the simulation provided by this program is highly inaccurate as several factors was not taken into account; the earthquake characteristics such as magnitude, focal depth and orientation, the bathymetry of the affected area and the wave energy at the shoreline. Thus, a better and comprehensive program and algorithm is required to carry out further simulation in order to determine the accurate wave run–up and inundation distance at the coastal area.

To overcome the shortcoming shown in Tsunami Mapper program, a simulation was carried out by using TUNA-M2 software [6]. The software which contains all the missing components that were not available in the previous program, provide an accurate tsunami wave's direction and propagation towards the study area. As the shallow water equation has pointed out, the wave amplitude indicates a significant decrease as the wave approaching the shoreline (Fig. 5). However, a higher precision wave simulation was not achievable due to the difficulties of obtaining the suitable bathymetry format that suit the computer program.

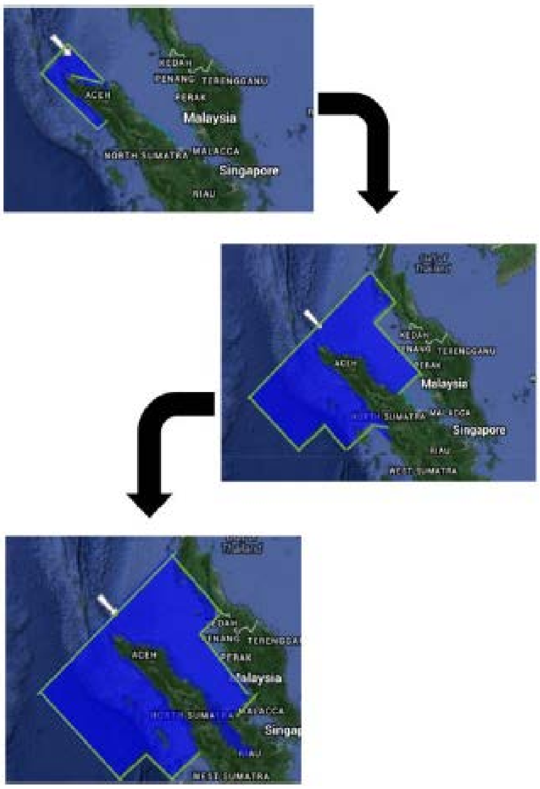

Fig. 4 The potential tsunami wave propagation from the Sumatra-Andaman subduction zone towards the Strait of Malacca, by using the Tsunami Mapper program.

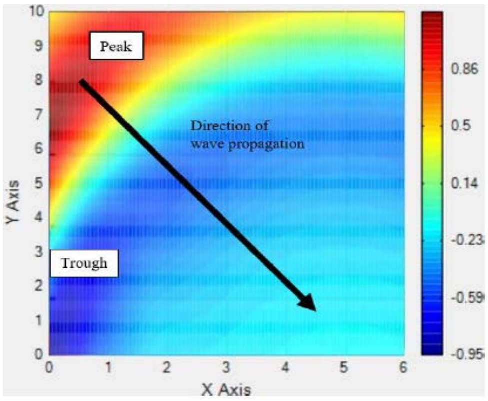

Fig. 5 Tsunami wave propagation model of the Pasir Panjang beach area.

TSUNAMI IMPACT ANALYSIS

In general, the impact of the tsunami wave is more severe if the shoreline topography lack of significant vegetation and elevation that can act as a natural barrier. To understand this impact, a cross section map of the seafloor (Fig. 6) was made based on the beach profile map generated in Fig. 2. This cross section map aids in the assumption on determining the wave run up and inundation in order to determine the potential impact tsunami wave has on the coastal vegetation and geological landscape of the study area.

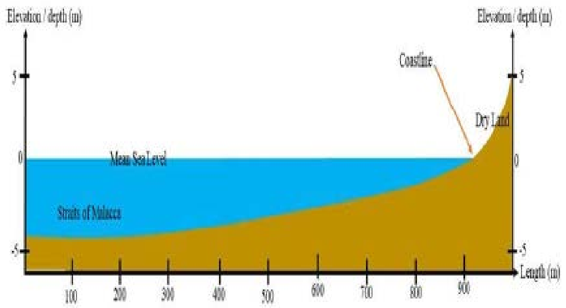

Fig. 6 Cross section of the Pasir Panjang beach bathymetry and coastline.

Based on the 26th December 2004 earthquake characteristics, the simulation indicates that wave height along Pasir Panjang beach able to reach 2.5 meters along the shoreline (Fig. 7). We used this information to estimate the wave's inundation distance. Since there is ground elevation by the coastal area, the simulated inundation distance indicates that the water could flood up to 55 meters from the shoreline (Fig. 8).

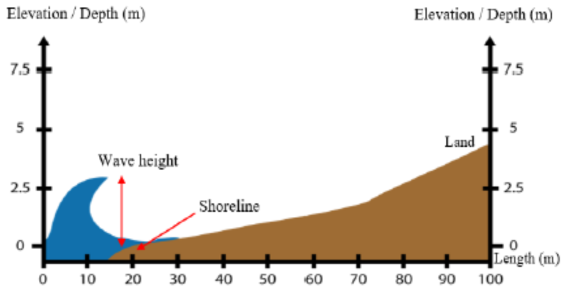

Fig. 7 The maximum wave height at the Pasir Panjang beach based on 26th December 2004 earthquake and tsunami characteristics.

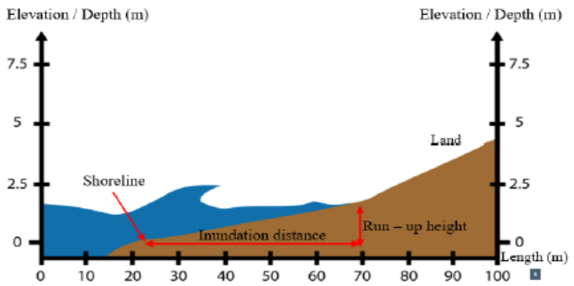

Fig. 8 The maximum inundation distance at the Pasir Panjang beach based on December 26, 2004 earthquake and tsunami characteristics.

Nevertheless, data observation along the Pasir Panjang beach indicates the previous 2004 tsunami event had not produced the predicted wave run-up and inundation distance simulation. To this extent, we modify the earthquake's fault orientation, from Northwest-Southeast to North-South orientation [7]. By changing the fault orientation, the tsunami impact from the Sumatra-Andaman earthquake is more severe as the Perak coastal line is now facing directly the tsunami wave propagation. The maximum wave height simulated was able to reach 6 meters tall (Fig. 9).

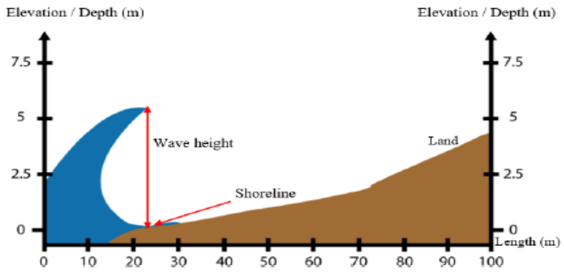

Fig. 9 The projected maximum wave height at the Pasir Panjang beach based on the modified earthquake parameter.

In the previous simulation, it was found that, the simulated inundation distance along the Strait of Malacca is generally around 15 to 20 times longer than the recorded wave height [7]. Due to the shallow bathymetry and gentle coastal gradient, this assumption is valid for the west coast of Peninsular Malaysia and Strait of Malacca. It can be calculated that the corresponding tsunami wave's inundation distance will be around 90 meters (Fig. 10). However, it should be noted that several factors such as wave velocity and gravity were not taken in consideration in producing this model, thus making this inundation model to be slightly inaccurate. Nonetheless, this model outcome shall be used as a reference or guidance to aid tsunami education and awareness among the Pasir Panjang's coastal community.

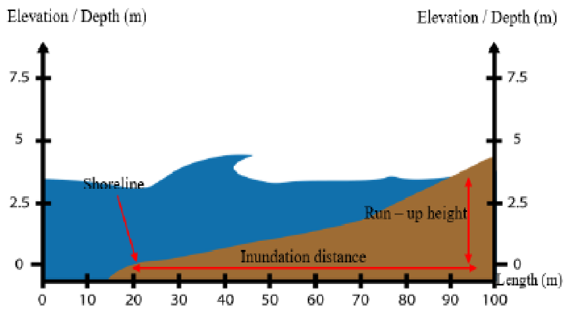

Fig. 10 The projected maximum inundation distance at the Pasir Panjang beach based on modified earthquake parameter.

EVACUATION ROUTE RECOMMENDATION

The chalets, turtle sanctuary and other buildings just close by the beach will be affected if a bigger tsunami wave hit the study area. However, the coastal elevation of around 1-1.5 meters might reduce the strength and impact of the incoming wave. A few oil palm plantations will also be affected in this event but will help in as a “natural barrier” to prevent the tsunami wave from further travelling inland. In this particular case, it would be wise to evacuate the people around this tourist and recreation area earlier and head to the nearest tallest building that is located right behind the Segari Turtle Sanctuary (Fig. 11). It should be note that there are only a single lane and narrow road into and out from the Pasir Panjang beach area. Thus in the event of a massive tsunami wave during a festive season, the road will become highly congested, preventing an efficient evacuation process. Therefore, it is also recommended the local authority to widen the road and built an alternative road lead to and out from this popular tourist spot.

Fig. 11 Potential evacuation route in the event of tsunami in Pasir Panjang beach area. Safe zone indicate the high-rise building that can be used as the shelter.

CONCLUSION

In a nutshell, the general idea of the tsunami impact towards Perak coastal area, particularly in Pasir Panjang beach has been presented from this study. It is clear that Pasir Panjang beach in the west coast of Peninsular Malaysia, is an area that highly vulnerable to tsunami as it is located along the Strait of Malacca and without any coastal protection near to its shoreline. From the analysis of both the previous 2004 tsunami event and the possible maximum scenario tsunami event which has different earthquake fault orientation (Table 1), it can be deduced that an emergency evacuation route should be determined. In addition, the locals should be briefed regularly about tsunami evacuation process in order to prepare for any possibilities, even though a tsunami of this magnitude may not occurred for the nearest time. It also suggested that a wave breaker should be built near to the coastline to minimize the casualty in the event of tsunami.

Table 1: Comparison of 2004 tsunami simulation to maximum scenario tsunami simulation.

Parameter	2004 Tsunami	Maximum Scenario
Magnitude	9.0	9.0
Focal Depth	30 km	30 km
Fault Orientation	NW-SE	N-S
Wave Height	~2.5 m	~5.5 m
Run-up Height	~3.5 m	~6.5 m
Inundation Distance	35 – 45 m	80-90 m

ACKNOWLEDGEMENT

We would like to thank Universiti Teknologi PETRONAS for funding this research project.

REFERENCES

[1] Colbourne, F. W. (2005). Tsunami Impact on the West Coast of Penang Island, Malaysia. Emporia State University.
[2] National Oceanic and Atmospheric Administration. Retrieved October 13, 2015 (http://www.tsunami.noaa.gov/tsunami_story)
[3] Penang Office for Human Development (2005). Retrieved December 18, 2015 (http://www.pohd.org/media/Files/pgreport)
[4] Okada, Y., (1985). Surface Deformation due to Shear and Tensile Faults in a Half-Space, Bulletin of the Seismological Society of America, Vol. 75, No. 4, pp. 1135-1154.
[5] Tsunami Mapper. Retrieve June 9, 2016 (http://tsunami-maps.com).
[6] Koh, H. L., & Teh, S. Y., (2010). TUNA User Manual.
[7] Koh, H. L., Teh, S. Y., Majid, T., Lau, T. L., & Ahmad, F. (2011). Earthquake and Tsunami Research in USM: The Role of Disaster Research Nexus.

THE EXPERIMENTAL DESIGN AND CARBON FOOTPRINT ASSESSMENT OF NON-GLAZED FLOOR TILES

Karin Kandananond
Faculty of Industrial Technology, Valaya Alongkorn Rajabhat University, Thailand

ABSTRACT

Carbon emission from the manufacturing sector is a critical issue which is concerned by the environmental authorities since the violation of the carbon emission cap might lead to the sanction by one of Thailand's largest trade partner, European Union (EU). As a result, it is important for the manufacturers to be able to assess their own products' carbon footprint. In this study, the selected case study is a ceramic factory which manufactures non-glazed floor files. The scope of evaluation covers Business-to-Customer (B2C) transaction while the life cycle of a product includes four stages, i.e., resource extraction, manufacturing, distribution, use and waste disposal. The study results indicate that the highest contribution to the carbon emission is from the extraction of ceramic clay while the manufacturing stage has the second highest effect on the emission. The distribution of products, use and disposal are the life cycle stages which have small effects on the emission. Another objective of this research is to conduct an empirical study which leads to the capability to quantify the effect of different factors on the manufacturing of floor tiles. According to the experimental study, three factors, i.e., chalk clay, ball clay and feldspar, are considered as the process inputs while the response variables are percent absorption and hardness. Elaborately, 2^3 full factorial design was deployed to study the find the relationship between inputs and outputs. The results has two folds. The first fold is useful for the manufacturers who would like to understand how much their product has emitted the greenhouse gas to the atmosphere and it might lead to the minimization of their emission. Moreover, the relation between the tile characteristic and factors affecting the manufacturing is known so the manufacturer is able to efficiently optimize the manufacturing process in order to achieve the highest quality products.

Keywords: Business-to-Customer, Carbon footprint, Design of experiment, Life cycle, Non-glazed floor tile.

INTRODUCTION

Greenhouse gas (GHG) emission is the critical issue which is on the spotlight of the world community since it is one of the possible causes of the world's climate change. There are initiations from developed countries to address the issue and also the resolution to reduce the emission. European Union (EU) is among the very first group of nations which create the awareness by issuing the carbon credit and carbon footprint schemes. On the other hand, President Barack Obama of the United States has declared in 2015 that the US will decrease the emission for one-third by reducing the emission from power generation which is based on coal-burning power plants. For the emerging economies like Southeast Asian countries, Thailand is one of the leading nations which is aware of the carbon footprint issue since it has the official organization body (Thailand Greenhouse Gas Management Organization or TGO) which is responsible for managing the GHG emission in Thailand. As a result, the manufacturers in Thailand have the guidelines for calculating the carbon footprint of their products and the assessment will lead to the awareness of the average emission per functional unit to the atmosphere.

Among many industries, ceramic manufacturing is among the industries which are responsible for the emission of a large amount of GHG in Thailand. According to the report by the European ceramic industry association, the emission due to the ceramic production will be reduced if all the kilns used in the industry are improved to fire products efficiently [1]. In 1998, the National Pollutant Inventory unit of the Queensland department of environment issued the emission report for bricks, ceramics, clay and product manufacturing [2]. Quinteiro, Araujo, Dias, Oliveira and Arroja [3] conducted a study to compute the GHG emission of different ceramic earthernware pieces. Similary, Quinterio, Almeda, Dias, Araujo and Arroja [4] had extended their research in 2012 to cover other ceramic products, i.e., brick, roof tile, wall, floor tile and sanitary ware. Peng, Zhao, Jiao, Zheng and Zeng [5] have calculated the CO_2 emission and also suggest the options to reduce the emission in a ceramic tile manufacturer. For construction purpose, Sazedj, Morais and Jalali had compared the CO_2 emission from two types of materials, bricks and concrete block [6]. Bribian, Capilla and Uson [7] also studied the energy demand and CO_2 emission among different construction materials which are ceramic, steel, PVC, wood, mortar, cement, aluminium and lime. The gas release during firing of clay to produce bricks was studied by Toledo, Santos, Faria, Carrio, Auler and Vargas [8]. In this study, the experiment was conducted to examine the amount of emission at the different temperatures.

According to the literature, the emission from the production of different ceramic products is studied while the focus is on the construction materials. However, the emission from small manufacturers seems to be ignored even it also contributes a large portion on the emission since, in Thailand, most ceramic manufacturers are small and medium enterprises. The awareness regarding the emission is important to both manufactures and consumers. The selected case study for the emission assessment in this research is the emission from the whole life cycle of a ceramic product, non-glazed floor tiles manufactured in a small factory. Elaborately, the emission from each stage of the life cycle is profoundly analyzed and calculated. Moreover, the study also points out the hotspot which is highly contributed to the major emission. Last but not least, the recommendation for the reduction in the emission is also addressed and discussed.

MANUFACUTRING PROCESS

According to the study, the instructions by Thailand greenhouse gas management organization (TGO) are carefully followed while the evaluation is based on the transaction of B2C (businesss-to-customer). A product chosen as a case study in this research is a non-glazed floor tile as shown in Fig. 1. The weight of a floor tile (functional unit) is 0.225 kg. The main ingredient of the floor tile is the clay excavated from the area of Lampang province (Fig. 2 and 3). Other ingredients are Feldspar (20% of the floor tile weight = 0.045 kg) and Kaolin (20% of the floor tile weight = 0.045 kg). The production facility is located in Prathumthani province. The kiln used for firing tiles is illustrated in Fig. 4 and the source of fuel for this kiln is liquefied petroleum gas (LPG). Another important aspect for the life cycle analysis is the clarification of manufacturing process. For producing floor tiles, the manufacturing process consists of the following steps, forming and finishing, biscuit firing and glost firing and it is concluded in a flow chart (Fig. 5).

Fig. 1 Sample of floor tiles.

Fig. 2 Excavation site.

Fig. 3 Excavation.

Fig. 4 Kiln fuelled by LPG.

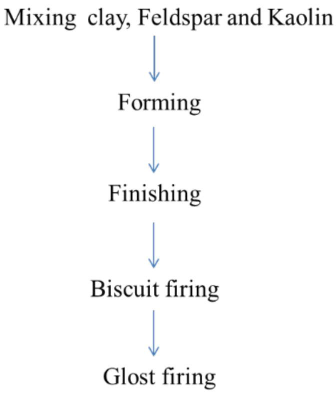

Fig. 5 Manufacturing process.

LIFE CYCLE ANALYSIS

The life cycle analysis of non-glazed floor tile is differentiated into five stages, resource extraction, manufacturing, distribution, use and waste disposal.

Resource Extraction

The main ingredient of the floor tile in this research is the clay excavated from a paddy rice field which is located in Lampang province. Other two ingredients are Feldspar and Kaolin and their emission analysis is shown in Table 1 which illustrates the quantity in weight per unit and emission for each ingredient.

Table 1 GHG emission of raw materials extraction

Raw Materials	Quantity (kg)	EF ($kgCO_2$ eq/kg)	Emitted GHG ($kgCO_2$ eq)
Clay	0.135	-	-
Feldspar	0.045	0.8635	0.03886
Kaolin	0.045	0.2167	0.0097515
Total			0.0486115

Another important source of emission which cannot be ignored is the emission due to the transportation of raw materials to the factory. After the excavation, the clay is shipped to the factory which is located in Prathumthani province by a ten-wheeled truck with the maximum load of 16 ton. The distance between the factory and the source of clay is 568 km. On the other hand, other ingredients (Feldspar and Kaolin) are transported from a supplier in Bangkok by a four-wheeled truck with the maximum load of 75% of 7 ton. The supplier's warehouse is 65 km from the factory. The computation is separated into two parts, delivery and return. In Table 2, the load of the transportation is illustrated in the form of tkm unit. The GHG emission of the transportation of raw materials for the delivery trip is shown in Table 3.

Table 2 Load of raw material (delivery)

Raw Material	Quantity (kg)	Distance (km)	Load (tkm)
Clay	0.135	568	0.07668
Feldspar	0.045	65	0.002925
Kaolin	0.045	65	0.002925

Table 3 GHG emission of the transportation of raw materials (delivery)

Raw Material	Mean of Transportation	EF ($kgCO_2$ eq/tkm)	Emitted GHG ($kgCO_2$ eq)
Clay	Ten-wheeled Truck (max load: 16 ton, 100% Loading)	0.0451	0.003458268
Feldspar	Four-wheeled Truck (max load: 7 ton, 75% Loading)	0.239	0.000699075
Kaolin	Four-wheeled Truck (max load: 7 ton, 75% Loading)	0.239	0.000699075
Total			0.004856418

Besides the delivery of raw materials, the emission from the return trip of the trucks has to be included in the calculation as shown in Table 4 and 5. For the return trip, the maximum load of the mean of transportation must be included in the calculation as recommended by TGO. For example, the load of clay is equal to 0.135*568/(1000*16) = 0.0047925 tkm.

Table 4 Load of raw material (return)

Raw Material	Quantity (kg)	Distance (km)	Load (tkm)
Clay	0.135	568	0.0047925
Feldspar	0.045	65	0.000417857
Kaolin	0.045	65	0.000417857

Table 5 GHG emission of the transportation of raw materials (return)

Raw Material	Mean of Transportation	EF ($kgCO_2$ eq/tkm)	Emitted GHG ($kgCO_2$ eq)
Clay	Ten-wheeled Truck (max load: 16 ton, 0% Loading)	0.5711	0.002736996
Feldspar	Four-wheeled Truck (max load: 7 ton, 0% Loading)	0.3324	0.000138895
Kaolin	Four-wheeled Truck (max load: 7 ton, 0% Loading)	0.3324	0.000138895
Total			0.003014786

The total emission of the raw materials regarding the delivery and return trip is concluded in the following Table 6 and 7.

Table 6 GHG emission of the transportation of raw materials

Raw Material	Emitted GHG ($kgCO_2$ eq)		
	Extraction	Transport Delivery	Transport Return
Clay	-	0.003458268	0.002736996
Feldspar	0.03886	0.000699075	0.000138895
Kaolin	0.0097515	0.000699075	0.000138895

Table 7 Total GHG emission of the transportation of raw materials

Raw Material	Total Emission ($kgCO_2$)
Clay	0.006195264
Feldspar	0.03969797
Kaolin	0.01058947
Total	0.056482704

Manufacturing

The manufacturing process basically depends on firing floor tiles and it is expected to be the main source of GHG emission. The fuel used in the kiln is liquefied Propane gas (LPG). The emission due to LPG is divided into two substages, acquisition and use. The emission factors for acquisition and use are 0.4116 and 0.4122 $kgCO_2$ eq/kg respectively. The LPG use is for two processes, biscuit firing and glost firing. The total emission due to the manufacturing is shown in Table 8.

Table 8 GHG emission of the manufacturing (LPG use)

Resouces	Process	Quantity (kg)	EF ($kgCO_2$ eq/kg)	Emitted GHG ($kgCO_2$ eq)
LPG	Biscuit Firing	0.2	0.4116 + 0.4122	0.16476
LPG	Glost Firing	0.3	0.4116 + 0.4122	0.24714
Total				0.4119

Distribution

Since the distribution stage solely relies on the transportation, the computation of GHG emission is similar to the shipment of raw materials to the factory. After the manufacturing stage, floor tiles as the finished product are shipped to the Chatuchak Sunday market which is 75 km away from the factory. For the delivery trip, the emitted GHG is calculated as shown in Table 9 and 10 respectively.

Table 9 Weight and distance per unit of floor tile (delivery)

Product	Weight (kg)	Distance (km)	Load (tkm)
Floor tile	0.225 (1Piece)	75	0.016875

Table 10 GHG emission due to the delivery per unit of floor tile

Product	Mean of Transportation	EF ($kgCO_2$ eq/tkm)	Emitted GHG ($kgCO_2$ eq)
Floor tile	Four-wheeled Truck (max load: 7 ton, 100% Loading)	0.1402	0.002365875

On the other hand, the return trip for a truck has emitted the amount of GHG gas as shown in the following Table 11 and 12 while the total emission is depicted in Table 13.

Table 11 Weight and distance per unit of floor tile (return)

Product	Weight (kg)	Distance (km)	Load (tkm)
Floor tile	0.225 (1Piece)	75	0.0024107143

Table 12 GHG emission due to the return trip per unit of floor tile

Product	Mean of Transportation	EF ($kgCO_2$ eq/tkm)	Emitted GHG ($kgCO_2$ eq)
Floor tile	Four-wheeled Truck (max load: 7 ton, 100% Loading)	0.3111	0.0007499732

Table 13 Total GHG emission regarding the transportation

Product	Emitted GHG ($kgCO_2$ eq)		Total Emission ($kgCO_2$ eq)
	Transport Delivery	Transport Return	
Floor tile	0.002365875	0.0007499732	0.0031158482

Use

Approximately, floor tiles are cleaned monthly to remove dust, mud and fungi. Water spray is used to clean the surface of floor tiles. The amount of emission regarding the use is shown in Table 14.

Table 14 GHG emission due to the use

Resource	Quantity (kg)	EF ($kgCO_2$ eq/unit)	Emitted GHG ($kgCO_2$ eq)
Water	0.2	0.0003	0.0006

Waste Disposal

Since this type of floor tiles is non-glazed and no additional color is applied to the tiles (earth tone), the recycling rate is almost 100 percent. Therefore, there is no GHG emission in this stage.

Overall emission

Due to the life cycle analysis, the total emission of each stage is shown in Fig. 6 and 7 consecutively. Most of the emissions fall into the category of resource extraction and manufacturing process. The implication is that the large portion of contribution on the emission is caused by the raw material supplier and manufacturer. Since the manufacturing process depends on the firing by using LPG, the acquisition and use of fossil fuels is the main source of emission in this case.

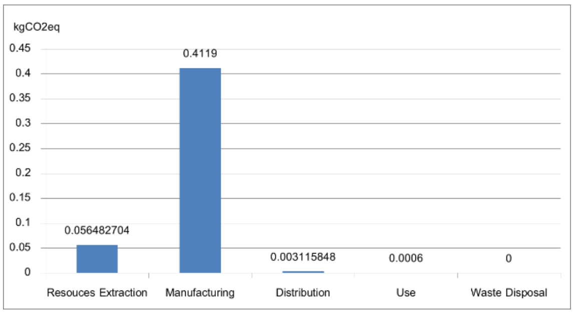

Fig. 6 Elaborated GHG emission by each category.

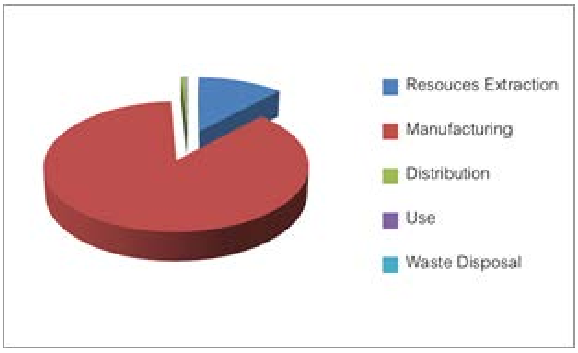

Fig. 7 Overall GHG emission by category.

The transportation of raw material to the manufacturer and the shipment of finished goods to the market also rely on the fossil fuel. Therefore, if there is a reduction in the use of fossil fuel, it will significantly decrease the GHG emission to the atmosphere. On the other hand, if the alternative source of energy besides fossil fuel with low GHG emission is explored and used, it will lead to the reduction in the carbon footprint of the whole process as well.

DESIGN OF EXPERIMENT

The 2^k factorial design of experiment is deployed to study the effect of three factors' ingredients, ball clay (A), Kaolin (B), Feldspar (C) on two crucial characteristics of tiles, namely, rate of water absorption and hardness. Table 15 illustrating input factors and their levels are shown as follows:

Table 15 Total GHG emission regarding the transportation

Factor	High (1)	Low (-1)
Ball Clay(A)	10%	30%
Kaolin (B)	5%	20%
Feldspar (C)	10%	20%

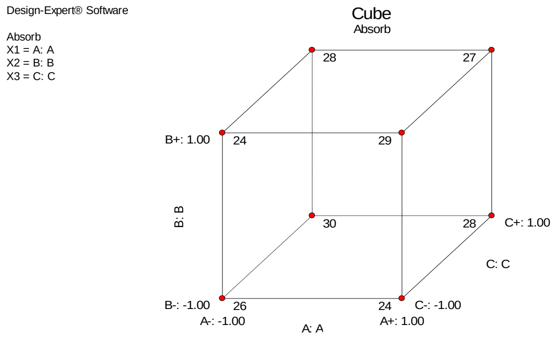

Fig. 8 Cube plot for rate of absorption rate.

If the interested characteristic is the rate of water absorption, the statistical analysis indicates that there is a three factor interaction (ABC) among all three factors (ingredients), Ball Clay (A), Kaolin (B) and Feldspar (C). According to the cube plot in Fig. 8 , floor tile will have the low water absorption rate when the percentage ingredients of each factor are set at the following levels:

-A (low), B (high), C (low) and

-A (high), B (low), C (low).

For the hardness, the result obviously shows that there is an interaction between Kaolin (B) and Feldspar (C). The important finding is the percentage of Kaolin is high (20%), it will result in the reduction of the hardness of the floor tile no matter the Feldspar component is set at the low or high level.

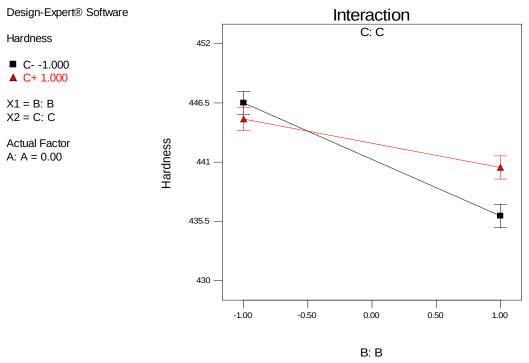

Fig. 7 Interaction plot for rate of water absorption.

CONCLUSION

This objective of this research has two folds, the life cycle analysis and the conduction of experimental analysis which leads to the desired characteristic of floor tiles. For the life cycle analysis, the manufacturing fraction seems to mostly contribute on the greenhouse gas emission. Therefore, the process improvement should focus on the reduction of emission from the activities of the manufacturing process. According to the experimental analysis of the desired characteristic, the result shows that there are interactions among two and three factors which affects the rate of water absorption and hardness of floor tiles.

REFERENCES

[1] European ceramic industry association, “National Pollutant, “Emissions estimation technique manual for bricks, ceramics, & clay” 1998.

[2] European integrated pollution prevention and control Bureau, “Ceramic Manufacturing Industry”, 2007.

[3] Quinteiro P, Araújo B, Oliveira B, Dias AC, Arroja L, “The carbon footprint and energy consumption of a commercially produced earthenware ceramic piece”, Journal of the European Ceramic Society, Vol. 32(10), 2012, pp. 2087–2094.

[4] Quinteiro A, Almeida M, Dias AC, Araújo A, Arroja L, “The Carbon footprint of ceramic products”, EcoProduction, Vol. 1, 2014, pp. 113-150.

[5] Peng A, Zhao Y, Jiao L, Zheng W, Zeng L, “ CO_2 emission calculation and reduction options in ceramic tile manufacture-the Foshan case”, Energy Procedia, Vol. 16, 2012, pp. 467-476.

[6] Sazedj S, Morais AJ, Jalali S, “Comparison of embodied energy and carbon dioxide emissions of brick and concrete based on functional units. Congresso Internacional, Luso-Brasileiro de Materials de Contrucao Sustentaveis, Vol. 1, 2014, pp. 81–88.

[7] Bribian IZ, Capilla AV, Uson AA, “Life Cycle Assessment of Building Materials: Comparative Analysis of Energy and Environmental Impacts and Evaluation of the Eco-Efficiency Improvement Potential”, Building and Environment, 2011.

[8] Toledo R, Dos Santos DR, Faria Jr. RT, Carrio JG, Auler LT, Vargas H, “Gas Release During Clay Firing and Evolution of Ceramic Properties”, Applied Clay Science, Vol. 27, 2004, pp. 151–157.

DAMAGE QUANTIFICATION OF BEAMS USING FREQUENCY SIGNATURE

Bryan Josef T. Medrano[1] and Lessandro Estelito O. Garciano, D. Eng[2]
[1]Graduate student, De la Salle University - Manila, Philippines; [2] Associate Professor, De la Salle University - Manila, Philippines

ABSTRACT

A rapid method for determining the damage severity sustained by a beam proved to be challenging due to either limited studies conducted on the subject or alternative methods require highly sophisticated and costly equipment to perform. In this research, the unique frequency signature emitted by a beam when excited by an external force was utilized in order to determine the changes in the properties of the beam. Experiments were performed using a roving accelerometer hammer impact test on a beam with a grounded configuration to test the changes occurring as the controlled damage sustained by the beam increases. The acceleration response of the beam obtained from the experiment is then processed using software incorporating Kalman Filter and structural dynamics. Results show that the dominant frequency obtained in both the Fast Fourier Transform and Power Spectral Density of the acceleration response of the beam decreases as the damage incurred by the beam increases. The results also show that regardless of the position of the accelerometer, dominant frequencies tend to converge to a value depending on the damage sustained in the beam.

Damping ratio of the beam also decreased as the damage sustained by the beam increased. Inversely, the increase in damage of the beam corresponds to an increase in the dissipation rate of the beam. The study was able to achieve its goal of quantifying damage in a beam through the use of frequency signature by identifying the changes in its dominant frequencies and the damping ratio and dissipation rate.

Keywords: Damage Quantification, Impact Hammer Test, Frequency Signature, Damping Ratio

INTRODUCTION

In a modern community, engineering structures play a vital role and therefore they are usually designed to have long life spans. Human lives and property may be affected or disrupted by the failure or unsatisfactory performance of these structures and is therefore necessary to ensure the safety and reliability of structural members.

Structures are prone to damage due to loading from continuous use or due to stress caused by external loads such as earthquakes. With this, structural damage detection is a vital factor in maintaining the integrity of the structure and reduces the likelihood of structural failures which can have grave consequences [1]. At present, the use of non-destructive examination is being used by engineers in determining the damages of a structure without the need to demolish the structural element of the building being analyzed [2].

The method of detecting damage in a structure should also consider the quickness of identifying the problem in the structure. Vital structures including hospital, bridges and fire stations require rapid identification of damage in the structure in order to prevent secondary damage [3]. A recent study shows that there are five levels of damage detection to be considered in monitoring the condition of a structure. These are mainly the identification of existing damage, localization of damage, identification of damage type, quantification of damage severity and prediction of the remaining life service of the structure [2].

Several studies have been made in order to determine the damage sustained by beams. A study using the Artificial Neural Networks that makes use of global and local vibration-based analysis data as input were conducted to determine the location and quantified depth of damage in beam like structures were done in previous years [4]. Another recent study on the other hand, makes use of guided waves and Bayesian statistical framework for the characterization of the damage in beams [5]. Other studies conducted made use of modal power flow generated by structural elements subjected to vibrations in determining the crack length and depth [6], [7]. The most recent studies made for damage identification made use of the acoustic emission techniques which make use of state-of-the-art equipment to determine the location and severity of the damage [8], [9].

This research therefore aims to provide a means of detecting the level of damage severity a structural element has sustained. With this method, damage can be quantified and the damages incurred by the structure can be prioritized according to the degree of severity. The need for the prioritizing the damage sustained by the beams would be useful to further understand the situation and be able to quickly remediate the problem and avoid serious damage.

The repairs necessary for the structure can be determined based on the output of the study.

Damage severity is one of the five key levels in damage detection of a structure [2]. Damage severity is a necessary procedure when conducting damage detection in a structural element of a building. However, the lack of a quick and convenient method for determining the severity of a structural damage is currently not present. On the other hand, methods for determining the damage severity of the structure require serious amounts of data to provide accurate results. There is a need to study a method for determining and quantifying the severity of damage in a structural element of a building.

As seen in several stated literatures, the main focus of other studies is on damage identification and localization. Damage quantification alone was not dwelled in most literature. On the other hand, damage quantification that is determined along with the other levels of damage quantification requires state-of-the art machinery or tools to determine the unknown parameter.

Damage severity detection is crucial in determining the status of a structure. It should be determined along with the other levels of damage detection such as existence detection, localization of damage, damage type identification and prediction of remaining service life [2]. Fewer studies have been conducted to determine the severity of the damages as compared to studies which determine the location and existence of damage. This gives all the more reason to conduct the study. Also, most important structures are found in urbanized and densely populated areas, the study is vital to ensure the safety of both the structure and the people occupying it.

CONCEPTUAL FRAMEWORK

Structural elements gave off a frequency signature when the element experienced an external load. These frequency signatures were captured through the use of a sensor to gather data and store on to a laptop. Each beam gave off a unique frequency signature due to the minute differences caused by the imperfections found in the beams. Given that the structural element was set at a constant properties and imperfections are set to a minimum, the frequency signature produced was also presumed to be at a constant.

In order to test and determine the degree of severity that a structure has sustained, the frequency of the beam was tested at different depth of damage. The cracks or fractures of the beam was represented by a chipped off portion and these damages are varying in depth to record the change in frequency signature. The recorded frequency signatures of the damaged and undamaged beam were then compiled and were then used in the Kalman filter program. The data is then analyzed to obtain the final output in terms of a frequency of the fast Fourier transform and power spectral density as well as the damping ratio of the element.

THEORETICAL FRAMEWORK

The study aims to identify the changes to the dynamic properties of the box beam using the different theories and techniques presented in previous researches and published material. The approach to the study involves the use of three theories, i.e., Kalman Filter, direct integration method and the approximation of the damping ratio.

Kalman Filter

The Kalman Filter is an optimal solution to filtering problems which have systems and observation models that are both linear and have Gaussian probability density functions. With the following assumption considered, the equations taken from the optimal Bayesian equations would be reduced to the following.

$$\boldsymbol{x}_k = f\boldsymbol{x}_{k-1} + \boldsymbol{w}_k \qquad \text{Eq. 1}$$

$$\boldsymbol{z}_k = h\boldsymbol{x}_k + \boldsymbol{v}_k \qquad \text{Eq. 2}$$

And Kk is the Kalman gain given as

$$K_k = f_{k+1/k} P_{n/n-1} h_k^T \left(h_k P_{n/n-1} h_k^T + R_k \right)^{-1}, \qquad \text{Eq. 3}$$

And Pk is the Variance-covariance matrix which is given as

$$P_k = P_{n/n-1} - f_{k/k+1} K_k h_k P_{n/n-1} \qquad \text{Eq. 4}$$

Equation of motion for a discretized beam

Considering a finite element beam model wherein the properties are distributed to each element, a motion of equation can be setup for each element present in the beam. Figure 1 shows a typical beam with an n-th number of elements. Each element is considered for analysis and that the motion of the entire beam can be determined with respect to the movement of each element. Similar to a single oscillating object, the elements of the beam have properties such as mass, damping coefficient, stiffness and external force acting on the element which are independent from one element to the other and values such as acceleration, velocity and displacement which are the basis for the motion of the beam.

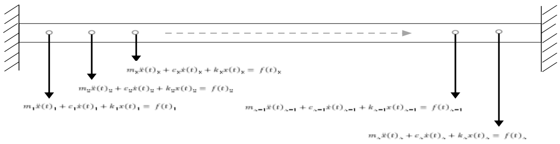

Fig. 1 Typical Beam with n number of elements

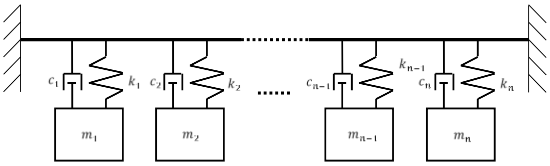

Fig. 2 Free Body Diagram of a beam with an n-th number of elements

State of the system equation and Observation equation

As one of the methods for direct integration of second order derivatives, Newmark's Constant Average Acceleration method make use of the fact that the acceleration of a given time interval is equal to a constant value. The algorithm numerically updates the response acceleration, velocity and displacement of an object from t_i to t_{i+1}. Following the previous stated assumption and isolating $\ddot{x}_i$, the equation of motion becomes

$$\ddot{x}_i = \frac{f_i - c\left(\dot{x}_{i-1} + \frac{\Delta t}{2}\ddot{x}_{i-1}\right) - k\left(x_{i-1} + \Delta t\dot{x}_{i-1} + \frac{\Delta t^2}{4}\ddot{x}_{i-1}\right)}{\left(m + \frac{\Delta t}{2}c + \frac{\Delta t^2}{4}k\right)} \qquad \text{Eq. 5}$$

Using the truncated Taylor's series expansion, the following equation that would complement the previous equation and complete the algorithm are

$$\dot{x}_i = \dot{x}_{i-1} + \frac{\Delta t}{2}\left(\ddot{x}_{i-1} + \ddot{x}_i\right) \qquad \text{Eq. 6}$$

$$x_i = x_{i-1} + \Delta t\dot{x}_{i-1} + \frac{\Delta t^2}{4}\left(\ddot{x}_{i-1} + \ddot{x}_i\right) \qquad \text{Eq. 7}$$

Incorporating previous equations and the new equation becomes the state equation of the Kalman filter updates the acceleration based on the numerical integration of the equation of motion and would be used to compared the measured acceleration obtain from the experimental portion of the study.

$$x_k = (\ddot{x}_t) = \begin{bmatrix} A_1 & 0 & \cdots & 0 & 0 \\ 0 & A_2 & \cdots & 0 & 0 \\ \vdots & \vdots & \ddots & \vdots & \vdots \\ 0 & 0 & \cdots & A_{n-1} & 0 \\ 0 & 0 & \cdots & 0 & A_n \end{bmatrix} \begin{bmatrix} \ddot{x}_{t-1_1} \\ \ddot{x}_{t-1_2} \\ \vdots \\ \ddot{x}_{t-1_{n-1}} \\ \ddot{x}_{t-1_n} \end{bmatrix} + \begin{bmatrix} B_1 & 0 & \cdots & 0 & 0 \\ 0 & B_2 & \cdots & 0 & 0 \\ \vdots & \vdots & \ddots & \vdots & \vdots \\ 0 & 0 & \cdots & B_{n-1} & 0 \\ 0 & 0 & \cdots & 0 & B_n \end{bmatrix} \begin{bmatrix} \dot{x}_{t-1_1} \\ \dot{x}_{t-1_2} \\ \vdots \\ \dot{x}_{t-1_{n-1}} \\ \dot{x}_{t-1_n} \end{bmatrix} + \begin{bmatrix} C_1 & 0 & \cdots & 0 & 0 \\ 0 & C_2 & \cdots & 0 & 0 \\ \vdots & \vdots & \ddots & \vdots & \vdots \\ 0 & 0 & \cdots & C_{n-1} & 0 \\ 0 & 0 & \cdots & 0 & C_n \end{bmatrix} \begin{bmatrix} x_{t-1_1} \\ x_{t-1_2} \\ \vdots \\ x_{t-1_{n-1}} \\ x_{t-1_n} \end{bmatrix} + \begin{bmatrix} D_1 & 0 & \cdots & 0 & 0 \\ 0 & D_2 & \cdots & 0 & 0 \\ \vdots & \vdots & \ddots & \vdots & \vdots \\ 0 & 0 & \cdots & D_{n-1} & 0 \\ 0 & 0 & \cdots & 0 & D_n \end{bmatrix} \begin{bmatrix} f_n(t)_1 \\ f_n(t)_2 \\ \vdots \\ f_n(t)_{n-1} \\ f_n(t)_n \end{bmatrix} + w_k \qquad \text{Eq. 8}$$

Wherein

$$A_n = \frac{\left(-\frac{\Delta t}{2}c - \frac{\Delta t^2}{4}k_n\right)}{\left(m_n + \frac{\Delta t}{2}c + \frac{\Delta t^2}{4}k_n\right)};\ B_n = \frac{(-c - k_n\Delta t)}{\left(m_n + \frac{\Delta t}{2}c + \frac{\Delta t^2}{4}k_n\right)};$$

$$C_n = \frac{-k_n}{\left(m_n + \frac{\Delta t}{2}c + \frac{\Delta t^2}{4}k_n\right)};\ D_n = 1/M_n \qquad \text{Eq. 9}$$

Considering the latter of the two equations, the observation equation is based on the independent variable that has been measured in the experimental portion of the study. Given that the input actuators or the accelerometers each measures only the acceleration response of the material being tested, the observation equation would be a vector matrix and an identity matrix defined as

$$z_k = (\ddot{x}_{meas}) = \begin{bmatrix} 1 & 0 & \cdots & 0 & 0 \\ 0 & 1 & \cdots & 0 & 0 \\ \vdots & \vdots & \ddots & \vdots & \vdots \\ 0 & 0 & \cdots & 1 & 0 \\ 0 & 0 & \cdots & 0 & 1 \end{bmatrix} \begin{bmatrix} \ddot{x}_{meas_1} \\ \ddot{x}_{meas_2} \\ \vdots \\ \ddot{x}_{meas_{n-1}} \\ \ddot{x}_{meas_n} \end{bmatrix} + v_k \qquad \text{Eq. 10}$$

Measuring Damping Ratio

In evaluating the damping ratio of a free vibrating structure, the logarithmic decrement method can be used. The logarithmic decrement method is used to measure damping in time domain. In this method, the free vibration displacement amplitude history of a system to an impulse is measured and recorded. Logarithmic decrement is the natural logarithmic value of the ratio of two adjacent peak values of displacement in free decay vibration. Given that the damping ratio is small and with the exponential in the ratio x_1/x_2 can be expanded in series retaining only the first two terms, since $\omega_d \cong \omega_n$ this leads to

$$\varepsilon \cong \frac{x_1 - x_2}{2\pi x_2} \qquad \text{Eq. 11}$$

For cases where the difference between two amplitude peaks are very small, it is more convenient to choose two non-consecutive peaks and the equation would be

$$\varepsilon \cong \frac{x_i - x_{i+m}}{2\pi m x_{i+m}} \quad \text{Eq. 12}$$

RESEARCH METHODOLOGY

Pre-experimentation phase

As the initial step to the study, the research was required to design the appropriate beam in order to produce result which will represent beams in its true scale and purpose in a structure.

The following were considered in the design of the beam element which would represent the structural element of a building and would provide the necessary data needed for the study.

The beam element was made of a rectangular aluminum box beam, specifically the material was a 6061 T6 3x3" Aluminum Square Tube.

As for the length of the beams, the original piece used for the test were 3 pieces of standard length which amounts to a total length of 21 ft. per piece or approximately equal to 6.4m per piece. The each material was cut into 3 equal part wherein the 2m of the beam was considered as the effective length of the beam. The remaining portions of the beam was buried inside the wooden box frame to dissipate vibration that would reflect back. Figure 3 illustrates the dimensions of the beam from the front view.

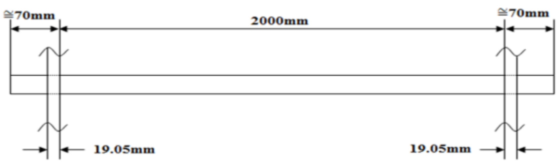

Fig. 3 Box beam dimensions

The beams were classified in to two cases, wherein there will be one undamaged and five damaged beam. The damaged beam were the representation of the deterioration or cracks developed by the beam with each case having a different degree of damage that was predetermined in order to consider only the quantification of damage. The damage ranges from 1 to 4 percent of the total length of the beam. Its design also had a constant depth of damage equal to 50 percent of the total height of the beam. Figure 4 shows the dimensions of the damage.

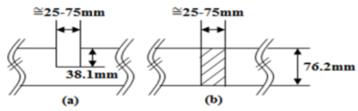

Fig. 4 Dimensions of damage (a) Elevation (b) top

All damages on the beam trial were located on the first quarter mark which was equal to 0.5m from origin.

The beams were supported on box filled with sand in order to make use of the boundary effects when vibrations passed through the beam.

Once the pieces were sawed, it is then nailed and wood glue is placed on its corners to avoid breaking from the weight of both the beam and the sand. A hole with the exact size of the beam was then punctured and filled with sand up to the bottom portion of the hole.

The input actuator with negligible mass that was used for recording and measuring the response of the beam was a triaxial accelerometer as seen in Fig. 5.

Fig. 5 Triaxial Accelerometer

The hammer that was for all trial in the experiments was an ordinary rubberized hammer typically used for basic construction and carpentry

Experimentation proper

With all beams cut according to specification, the beam ends were covered using packaging tape to reduce the amount of unnecessary matter such as sand from entering the beam.

Proceeding to the next step of the experiment, five accelerometer were used for the undamaged beam and six accelerometers for all damaged beams.

Given that the setup is ready and the triaxial accelerometers' capabilities were tested, the vibration test could now proceed. The vibration test used for the experiments was the impact hammer test. The design of the experiment incorporated the use of a rubberized hammer that was dropped at the center of the beam which provided the maximum movement possible for the beam to produce.

In Summary, Fig. 7 shows the complete experimental setup

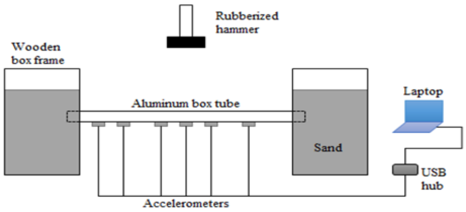

Fig. 7 Complete experimental setup

Post-experimentation phase

Using the obtained acceleration data from the experiments, the Kalman filter processed this data for the observed stated and has been incorporated by the use of the observation equation as defined in previous sections of the study which will be expounded depending on the case being studied.

DATA PRESENTATION AND ANALYSIS

Sensors were based on the predetermined location set to each sensor; FL2, FL1, L, M, R & FR corresponds to Far Left 2, Far Left 1, Left, Middle, Right and Far Right respectively. From the acceleration data, the time domain of the acceleration is transformed to a frequency domain using the fast Fourier transform and the Welch power spectral density analysis.

With regards to the Fast Fourier Frequency, the estimate acceleration response of the beam which was taken from the Kalman filter code was subjected to the process of determining the magnitude of the Fast Fourier Frequency. Based from Fast Fourier Frequency of all test trials, all frequency exhibit a dominant frequency in the higher frequencies levels. In each case, dominant frequencies of all trial fall on a specific frequency level. The sample data was then subjected to an increase in the sampling rate to reduce the amount of spectral leakage when a signal is being filtered or processed. To further eliminate the possible spectral leakage in the Fourier analysis, a process called Hanning windowing.

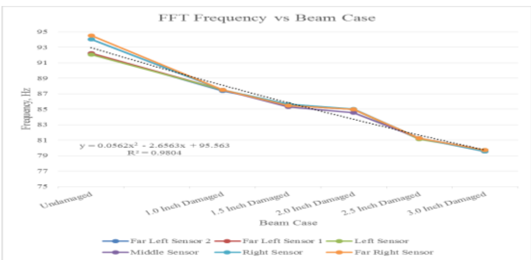

Fig. 8 Resampled FFT Frequency vs beam case

The trend indicates that as the damage sustained by the beam or any structural element increase, the frequency produced by the said beam or element decreases accordingly. Also, it could be pointed out that the drop in frequency is consistent regardless of the position of the accelerometer whether it is position nearest to the sensor or it is place nearest to the point of impact or even positioned at the father point from the damage. Table 1 established the percent difference between the frequencies recorded by each sensors and the mean frequency of each beam case.

Table 1 Percent differences of FFT frequencies in beam cases

Sensor/Beam Case	0”	1”	1.5”	2”	2.5”	3”
FL2	0.00 %	0.18 %	0.18 %	0.00 %	0.00 %	0.20 %
FL1	0.17 %	0.18 %	0.00 %	0.00 %	0.19 %	0.00 %
L	1.98 %	0.18 %	0.37 %	0.55 %	0.00 %	0.20 %
M	1.98 %	0.18 %	0.00 %	0.05 %	0.00 %	0.20 %
R	2.48 %	0.18 %	0.18 %	0.00 %	0.00 %	0.00 %
FR	1.05 %	0.15 %	0.12 %	0.08 %	0.03 %	0.10 %

Using the same acceleration estimate obtained from the impact hammer test which has been refined by the Kalman filter, the PSD or the Power Spectral Density of the beams response was established. Similar to the FFT, a decline in the peak frequency was also determined in the PSD and position of the sensors were also negligible.

Considering the damping ratio as a parameter to quantify and determine the damage severity of a structural element, the results of the analysis show that the damping ratio of the beam decreases as the as the damaged found in the beam increases is an indication that the damage inflicted on the beam was detected using the damping ratio as the parameter. The severity of the damage was identified due to the fact that a continuous decrease in the damping ratio was observed in all sensors. Although sensors further away from the actual damage are less reliable due to inconsistent decrease in damping ratio was observed, sensors that are nearer the damage could be noted to be more reliable and consistent.

Dissipation time however, increases as the damaged sustained by the beam decreases. The gradual increase in dissipation time go hand in hand with the gradual decrease in damping ratio due to the loss in the ability to remove the external force from the beam. Results show that the sensor furthest from the actual damage tend to have more sporadic data and is therefore less reliable as compared to the result shown by the sensors near the cut.

In order to justify the completion of the study's objectives a summary of all results is tabulated to show that the damaged was quantified and that several methods can be used to determine the damage severity levels of a beam or any other structural element being analyzed. Table 5.15 collected all the information from all previous results of the study.

Table 2 Summary of Results

Beam Case	Damage w/L	FFT, Hz	PSD, Hz	Damping Ratio	Dissipation Rate
0”	0.00%	93.19	94.585	0.2884	0.1451
1”	1.27%	87.47 (6.14%)	87.318 (7.68%)	0.1915 (33.60%)	0.1702 (17.30%)
1.5”	1.91%	85.52 (8.23%)	85.144 (9.98%)	0.1911 (33.74%)	0.1778 (22.54%)
2”	2.54%	84.93 (8.86%)	84.778 (10.37%)	0.1531 (46.91%)	0.1982 (36.60%)
2.5”	3.18%	81.22 (12.84%)	80.931 (14.44%)	0.1110 (61.51%)	0.2442 (68.30%)
3”	3.81%	79.61 (14.57%)	79.237 (16.23%)	0.0981 (65.98%)	0.2769 (90.83%)
R-Value		0.9804	0.9761	0.9023	0.9629

CONCLUSION

The study was able to establish a link between the current condition of the beam to the unique frequency signature it emits using experimental modal analysis such as the impact hammer test and the use of filtering techniques such as the Kalman filter. Moreover, the damage severity of the structural element, which in the study is a beam element, was determined using the parameters such as the dominant frequency of the frequency signature, damping ratio and duration of damping. Based from all the data gathered and analyzed from the study, the following observations and conclusion were identified:

For determining the severity of the damage sustained by the beam, sensor placement may be negligible as seen in several analysis wherein position of the sensor did not affect the results of the study. This could prove useful in monitoring the condition of structural elements which are not easily accessible for placement of measuring devices. This however may not be the case for all parameters such as the damping ratio wherein position was key to having an improved results.

Properties and parameter which include the damping ratio, dissipation rate and dominant frequencies found in both the fast Fourier transform and the power spectral density remain constant in a structural elements until its condition deteriorates through damage. Besides the dissipation rate, these parameters decrease depending on the damage sustained by the said element. Larger decrease indicate a severer damage whereas smaller changes can be caused by smaller damages.as for the dissipation rate, damage is directly proportional to the dissipation of energy in a structural element. By evaluating any of these parameters, the damage was quantified to determine its overall condition.

REFERENCES

[1] Wang, S, Ren, Q & Qiao, P, “Structural Damage Detection Using Local Damage Factor”, Journal of Vibration and Control, Vol. 12, Sept. 2006, pp. 955-973.

[2] Yan, Y, Cheng, L, Wu, Z & Yam, L, “Development in Vibration-based Structural Damage Detection Technique”, Mechanical Systems and Signal Processing, Vol. 21, 2007, pp. 2198–2211.

[3] Yoshida, I & Sato, T, “Health Monitoring Algorithm by the Monte Carlo Filter Based on Non-Gaussian Noise”, Journal of Natural Disaster Science, Vol. 24, 2002, pp. 101-107.

[4] Sahin, M & Shenoi, R, “Quantification and Localisation of Damage in Beam-like Structures by Using Artificial Neural Networks with Experimental Validation”, Engineering Structures, Vol. 25, 2003, pp. 1785–1802.

[5] Ng, C, Veidt, M & Lam, H, “Probabilistic Damage Characterisation in Beams Using Guided Waves”, Procedia Engineering, Vol. 14, 2011, pp. 490–497.

[6] Zhu, X, Li, T, Zhao, Y & Yan, J, “Vibrational Power Flow Analysis of Thin Cylindrical Shell with a Circumferential Surface Crack”, Journal of Sound and Vibration, Vol. 302, 2007, pp. 332–349.

[7] Huh, Y, Chung, T, Lee, J & Kim, J, “Damage Identification in Plates Using Vibratory Power Estimated from Measured Accelerations”, Journal of Sound and Vibration, Vol. 336, 2015, pp. 106-131.

[8] Aldahdooh, M, Muhamad Bunnori, N & Megat Johari, M, “Damage Evaluation of Reinforced Concrete Beams with Varying Thickness Using the Acoustic Emission Technique”, Construction and Building Materials, Vol. 44, 2013, pp. 812–821.

[9] Nor, N, Ibrahim, A & Bunnori, N, “Diagnostic of Fatigue Damage Severity on Reinforced Concrete Beam Using Acoustic Emission Technique”, Engineering Failure Analysis, 2014, pp. 1-9.

Sixth International Conference on Geotechnique, Construction Materials and Environment, Bangkok, Thailand, Nov. 14-16, 2016, ISBN: 978-4-9905958-6-9 C3051

STUDY DOWNTOWN STVANGER TO THE PEDESTRIAN SPACE

Tetsuya YANOBE[1], Kazunari TANAKA[2] and Shin YOSHIKAWA[3]
[1] Engineering, Osaka Institute of Technology, Japan; [2,3] Osaka Institute of Technology, Japan

ABSTRACT

The pedestrian space is substantial in downtown Stavanger. On the other hand, there are many big slopes in the downtown of Stavanger. investigate the characteristic of the building and topography in the target space. The authors make the characteristic of the city area using GIS. In this study, The authors clarified the influence of the pedestrian by watching the relationship between an element and the topography.

Keywords: Stavanger, Waterfront, Pedestrian, Slope

1. INTRODUCTION

Norway is located in the Scandinavia peninsula west coast in northern Europe. The shipbuilding industry and the shipping trade prospered in Norway. On the other hand, the shipbuilding industry suddenly declined after the 1970s. Thus it becomes the big problem in the city structure that waterfront and a city area divide. After the 1980s, the city reproduction project that used shipbuilding industry ruins started. "A fjord city strategy" was devised in 2000. As a result, divided city area and waterfront were unified. And the location of functions such as shopping, eating and drinking, the residence and the culture was promoted in a shore part.

The pedestrian space is substantial in downtown of Stavanger. On the other hand, there are many big slopes in the downtown of Stavanger. The authors clarify the actual situation of the substantial pedestrian space in a shore part and the city area. The intention of this research was to clarify the actual situation of the pedestrian space paging attention to the shape of building and topography. Finally, a purpose of my study is to catch an opportunity leading to the growth to find out leading for regional by clarifying the actual situation of the boundary of spaces in the downtown Stavanger.

Fig. 1 Stavanger

2. CASE STUDY AREA STAVANGER

Stavanger is a Norwegian city and is the capital of the Rogaland region. The area is about 71 km^2. The population is about 130,000 people. The history of the town dates back to the Middle Ages, and old buildings and new buildings exist together. Stavanger is blessed with rich nature represented by the fjord, and a pattern of the green tract of land and a waterside. The characteristic city is mixed.

In the downtown, a shopping area, a natural scene district, bay area exist around a big pond. Particularly, in the shopping area, the center does well in composite facilities having a library and a movie theater. An open terrace characterizes many restaurants. On the other hand, many place having intense slant, which greatly affect the pedestrian.

Fig. 2 Case study area

3.A PURPOSE AND METHOD OF RESEARCH

In down town Stavanger, pedestrian space is substantial. However, there are many big slopes in the downtown of Stavanger. It is necessary to cancel level differences between slope and store of the front part of store in the slope, in front of various wall surface forms and stores space exists. It is thought that a lot of slopes influence pedestrian and a getting out boundary of spaces in front of the store. I clarify the actual situation of the boundary of space, which paid its attention to the slope. As a summary, I clarify the actual situation of the borderland by the influence of the slope.

For the method of the study, the authors investigate the shape of the building in the target space and overflow of the store. The authors make the characteristic of the city area using GIS. Because there are many slopes in target area, The authors calculate the road incline of the slope and clarify a relationship between the shape of building and the incline of the slope. As a result, the authors grasp relationship between the characteristic of boundary of space and incline of the slope.

4. BOUNDARY OF SPACES

The boundary of space is ambiguous space. According to the previous study and the documents, there are a Pilotis, an Arcade, an Atrium and a Buffering space. My study looks for an existing boundary of space between public space and private space. I define the public space in the site or the private space outside the site as a boundary of space.

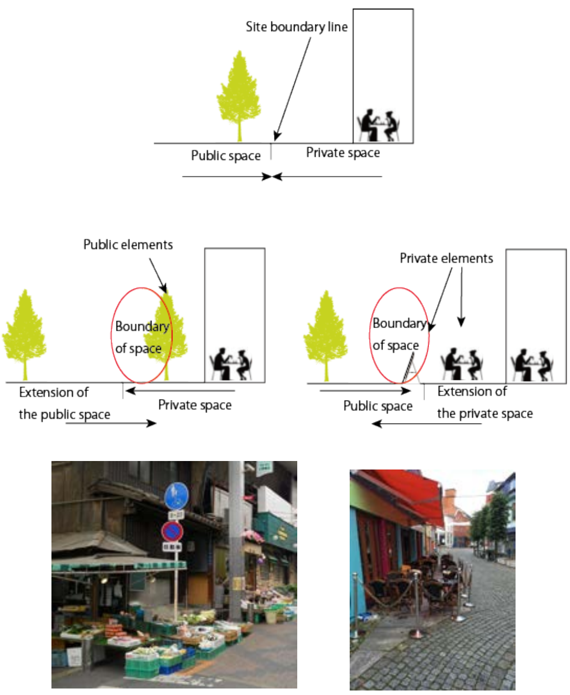

Japan Norway

Fig.3 In lecture to extension of boundary space

5. THE CHARACTER OF BUILDING

The target area of this study is a downtown of the Stavanger. A lot of shops exist in the downtown of the Stavanger. In addition, the coast is full of tourists because there are hotels, and many open cafés. This space to my study is a doorway in the downtown. The authors show a doorway to intend for at a red point (Fig.4). The method was to collect data was three ways: observation, photo and note. The authors photographed from No. 1 to No.150. And The authors clarified from 151 to 389 by observation. The authors finally summarized findings from No.1 to No.389 in a note. The authors show below a method of listing (Tab.1).

Fig.4 Target area

Tab.1 The method of listing

No.	The type in front of the shop	The type of building	elements
1	IS type	Apparel	
2	IS type	Others	Billboard
3	Pocket type	Apparel	Billboard

6. THE ROAD INCLINE OF THE SLOPE

For the method of the road incline of the slope, Firstly, The authors understand the spot where height changes by Google Earth. And, the authors find the distance of each change point by Google Earth and calculate the road incline of the slope. The authors show a calculating formula in Fig.5.

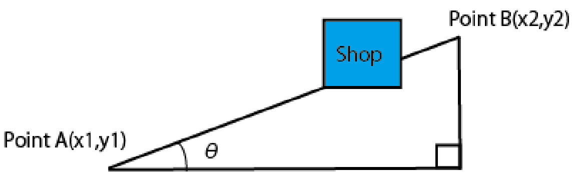

$$\theta = tan^{-1}\frac{(y_2 - y_1)}{(x_2 - x_1)}$$

Fig.5 The calculate of incline

7. THE TYPE OF BUILDING AND ELEMENTS

The authors investigated the shape of the building, the type of the store and the kind of the element for from September 2015 to October 2015. And the authors paid my attention to the road incline.

The authors show the shape of building, the type of the shop and the kind of the element in the map (Fig.6.7.8). The authors made clear that a pocket type, stairs type, a restaurant, an apparel shop and a general store occupied most in the building of the downtown. And the authors clarified many products are exhibited in the south side of the downtown. The authors understood the change of the building shape every street. It is thought that eaves type and the stairs-shaped street come under other influences. The authors paid my attention to the road incline.

Fig.6 The shape of building

Fig.7 The type of shop

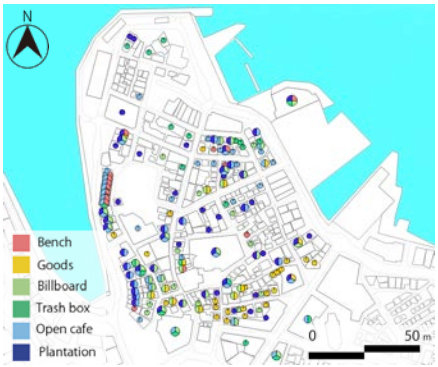

Fig.8 The kind of element

8. RELATIONSHIP BETWEEN A BUILDING SHAPE AND THE ROAD INCLINE

The authors hypothesized that the shape of the building might change by the slant of the slope. The authors calculated the road incline of the slope by each building unit and grasped the relationship with the building shape. The target street is 6 streets which roads incline has a big and a small street in total.

As a result, there is much roof type of buildings at the road incline less than 4% more than 0%. On the other hand, the authors clarified that stairs type of buildings was strong at the incline less than 8% more than 4%. Stairs type is more likely to be installed in the doorway as the shape that a pedestrian is easy to go in and out of the building when a road incline is big. On the other hand, it is thought that there are many eaves types that set up open cafe and planting when a road incline is small.

As a result of having paid its attention to a road incline, I clarified the relationship between the shape of the building doorway and the outdoor space element.

Fig.9 The target street

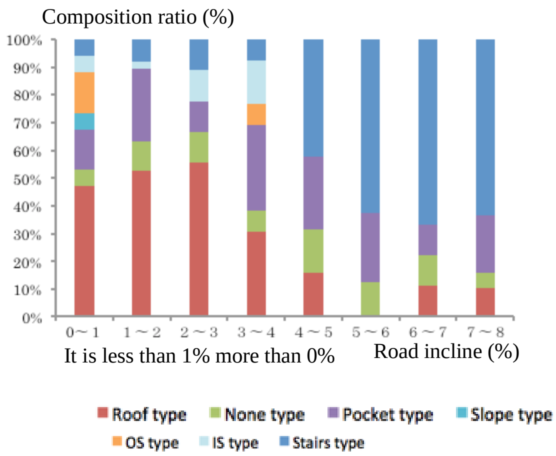

Fig.10 The result of analysis

9.ANALYSIS AND DISCUSSION OF RESULTS

I clarified that the type that accounted for most of the target area was roof type and a pocket type and stairs type. Moreover, I made clear that a billboard, planting, an open cafe, a goods accounted for most as for the existing element in a boundary of space. I clarified relationship between the element in the borderland and the shape in front of the building. A lot of planting and open cafes existed in the roof-shaped building. The variety of elements existed in the pocket-shaped building. Thus, I thought that the pocket-shaped building had high borderland degree.

By these investigations and analyses, I was able to get knowledge about a connection of the public space and private space in Stavanger. Depending on a shape and the slant in front of the building, it is necessary for the people of the store to place the elements such as products in front of a shop to use this knowledge in practice. I strongly suggest it to the owner of the building.

10. CONCLUSION

As a result of having arranged the type of the shop and the data of the shape of the building, The authors clarified the kind of the element and the relations of the position. The authors understood the influence of the pedestrian by watching the relationship between an element and the topography. The authors suggest the space that is easy to walk in sidewalk for a pedestrian by considering the relationship between the characteristic of the sidewalk and a shape of the building.

I think when the boundary of space changes by time of the day. Thus, I will find new technique to make a boundary of space in future by paying its attention to a change at time, and analyzing a boundary of space. In future, the authors will suggest the space that is easy to come and go to the building for a walker by considering the relationship of the characteristic of the sidewalk and a shape of the building in the downtown of Stavanger.

ANNEX

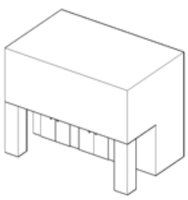

passage type

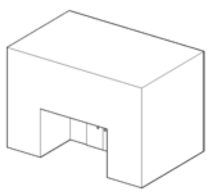

pocket type

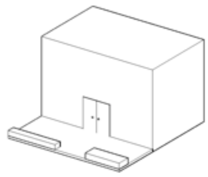

outside open space type

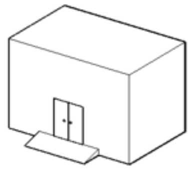

slope type

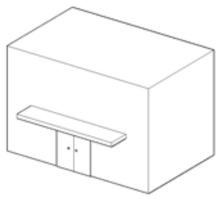

roof type

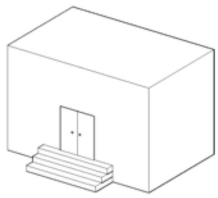

stairs type

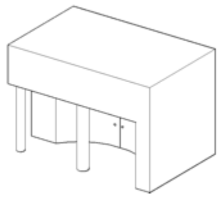

outside open space type

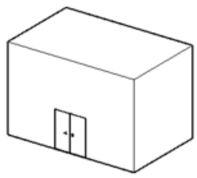

none type

・The method of pedestrian behavior listing

A purpose of the investigations is to clarify whether a pedestrian pays his/her attention to what kind of building, element. This table is a listing example of the observation result.

No.(person)	Gender	No.(buildig)	No.(Element)	No.(Behavior)
1	M			
2	W			
3	M			

REFERENCES

[1] Hori Masahiro : Sustainable urban development in North Europe three countries Private urban development promotion mechanism
Urban Study Vol.55 2012

[2] Ashihara Yoshinobu: Aesthetics of the cityscape

[3] Space study subcommittee : Space education celebration for a building, city planning Inoueshoin

ON THE RELATIONSHIP BETWEEN THE SPATIAL ELEMENTS AND PERCEPTUAL SPACE OF CHILDREN

Takumi SAKAI[1], Kazunari TANAKA[2] and Shin YOSHIKAWA[3]
[1] Engineering, Osaka Institute of Technology, Japan; [2,3] Osaka Institute of Technology, Japan

ABSTRACT: It is realized the Comprehensive Support System for Children and Child-rearing at many cities in Japan. On the other hand, this idea is that guardian is a subject that the child cares. It is important that the relationship of the environment for the child and city planning. The authors understand the cognitive space of children by the questionnaire survey. And the authors analyzed the relationship between the shape of town and reality space by Geographic Information System. The authors measure the distance between objects by network distance.

Keywords: Cognitive Map, Cognitive Space, Distortion

1. INTRODUCTION

Our country makes the towns that established an important point for the childcare support as declining birthrate measures. However, there are few places where children play in city space. The current city planning does not become the child-based measures. Thus, it is necessary to plan a city after having grasped the relationship between a children and the town.

In this study, the authors analyze a relationship between the cognitive space of the children and reality space. In previous of study, the authors analyzed the element that gave a distortion on a map by grasping a difference of the cognitive space and reality space as a distortion. As a result, the authors understood the distortion of the cognitive space is distance and an angle [1]. The authors pay attention to a school road and a road incline as a kind of distortion elements. The authors analyze image amplification and the spatial perception of the target space.

Fig.1 Amusement place of children

2. A PURPOSE AND METHOD OF RESEARCH

A purpose of this research is to grasp space and a factor to feel that a child is attractive by analyzing relationship between the cognitive space of the children and reality space. The authors grasp a distortion of the cognitive space from a psychology side and physical aspect. To do that, it is necessary to externalize cognitive space. There are three method of externalization (1:Map Drawing Method, 2:Multi Dimensional Scaling, 3:Cognitive Distance Estimation method) [2]-[4]. It is necessary to consider the characteristic of research participants and research conditions. The map drawing method is suitable for the case for children than the cognitive distance estimate method to require abstract work [5]. In this study, the authors acquire the cognitive map by conducting a questionnaire survey (1:Map Drawing Method). In the research method, the questionaries' survey to confirm the cognitive space of the children is performed. The authors calculate the amplification of the space image as a standard of the distance in a school road. The authors measure the distance using network distance. It is considered that the information of the height direction and analyze the cognitive space.

3. THE TARGET AREA

The target area of this research is an elementary school and outskirts area in Osaka (Fig.2). The precinct range is north-south 800m, east-west 1,600m. There are many slopes in the precinct range. The pedestrian moves to the height direction in addition to a plane. So, it is important that the authors understand the distortion of the height direction.

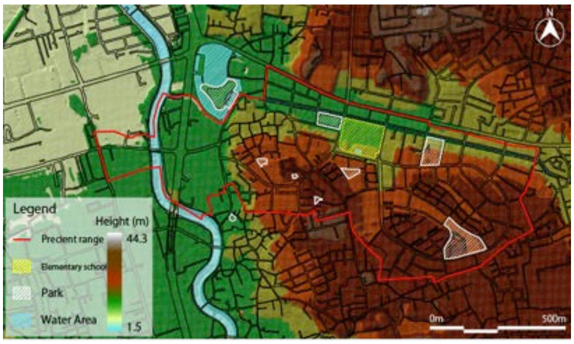

Fig.2 Precinct range

4. THE QUESTIONAIES'S SURVEY

The authors investigated cognitive map survey from September 2014 to October 2014. The subject is a 5th grader and a 6th grader (83students) [6],[7]. The authors order subjects that can write the town where you lived in (Fig.3). When a subject surpassed a range of the distribution paper, the authors performed addition of the paper.

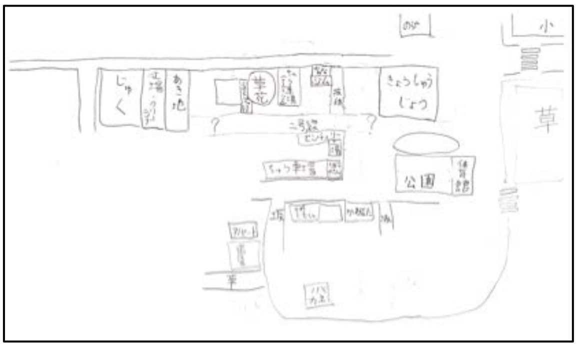

Fig.3 Cognitive map

5. THE IMAGE AMPLIFICATION

The range to use well of the cognitive map of the children is drawn (school road, home etc.). Many elements are drawn on the imminent space.

Therefore, The authors calculate amplification of the space by comparing the distance of the road with the reality space and the cognitive map. Not only the distance of the road but also the element in the space is considered. The amplification that the authors calculated assumes it the amplification of the image of the space. There are not a scale and a direction on a cognitive map. Therefore, it is necessary to arrange the standard line to compare it with the reality space on a cognitive map. In this study, the authors assume the school road as a kind of the standard line (Fig.4).

As a result, the authors grasped that the space around the home and the school extend (Fig.5). So, the authors clarified that many children can write the place that usually lives well. On the other hands, the subject did not write the road that passed without thinking about anything.

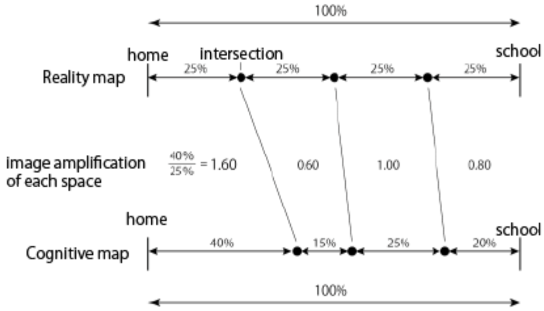

Fig.4 The method of calculation

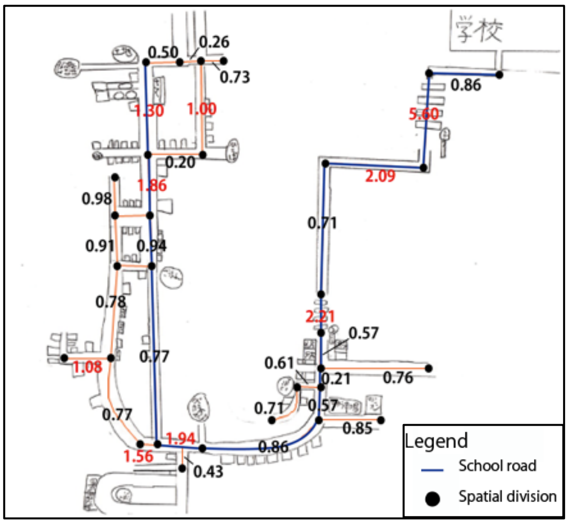

Fig.5 The calculation results

6. THE POSITION OF SPACE

The authors measure the distance between each space and home or schools to clarify the relationship between an image amplification of the space and the position. The distance measurement is not distance in a straight line between two points (Euclidean distance). The authors use network distance. So, the authors can perform analysis in consideration of the everyday life of the children. In this study, the authors classify space as the outside of the school road and inside of the school road. And the authors classify the home side (A) and the school side (G) in outside the school road. On the other hands, the authors classify in front of the home side (B), in front of the school side (F), home side is based on network distance (C), center area (D), school side is based on network distance (E) in inside the school road.

Because the cognitive map is described into a halftone plate form, it is necessary to make a standard to judge the inside and outside. If distance of home and a school and the each space did not exceed the shortest course distance of the school road, the authors assumed it with the inside school (Fig.6).

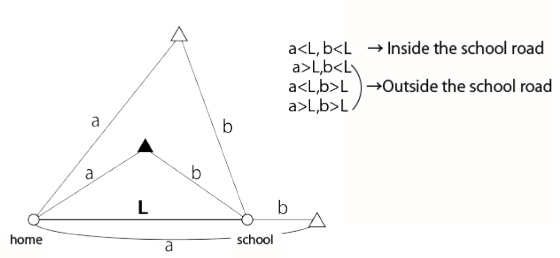

L: The shortest course distance of the school road
a: The shortest course distance from the home
b: The shortest course distance from the school

Fig.6 The judgment of inside and outside

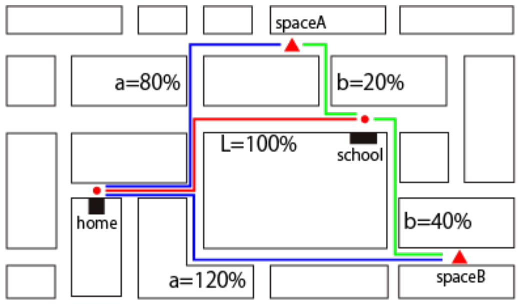

spaceA:
The position of inside school road is 20% away from the school (GroupE)
spaceB:
The position of outside school road is 40% away from the school (GroupG)

Fig.7 The calculation e.g. of the space distance

7. THE RELATIONSHIP BETWEEN IMAGE AMPLIFICATION AND POSITION

The authors grasped relationship between a position of each space and the amplification of the image (Fig.8). The home position and an elementary school are written in acquired 83 maps. Therefore, the author used the samples by the 20 maps that these lead to on a road. And the authors indicated the average and the median, the number of the space that spread and the number of the space that reduced (Tab.1). A difference occurred to the mean and the median. Because the cognitive map has the map that subject extremely describe. So, the authors use the median to clarify the characteristic of each space.

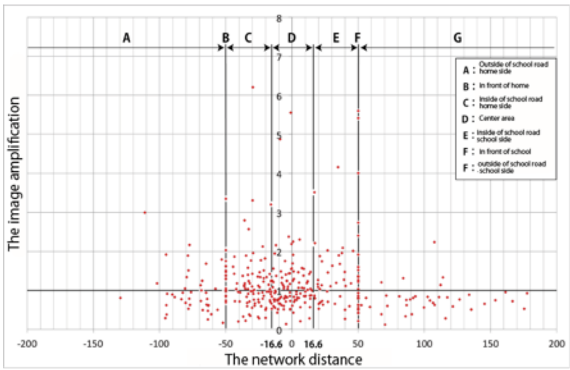

Fig.8 The result of analysis

Tab.1 Classification result

	Average	Median	More than 1	Less than 1
A	0.964	0.816	14	26
B	1.341	1.292	13	7
C	1.160	1.031	40	37
D	1.128	0.961	52	62
E	1.321	1.130	24	15
F	1.473	0.936	13	15
G	0.769	0.753	5	33

As a result, the space that spread is approximately 2 times than the space that reduced. Because the median doubles 1.29, the authors can grasp what children greatly image in cognitive space. However, there is the median becomes the value that is almost 1.000. So, the authors clarified existence of the child who greatly had the image of the school and the child who had small (P-value < 0.01).

The medians of the home side and the school side are less than 1.000 in outside of school road. The authors understand a cognitive map image tends to be reduced. Therefore, Image distance becomes small in the outside of the school road. The authors can grasp a thing that is not important.

The median of the home side and the central space are the values that are almost 1.000. And there are not the differences between reduction space and extended space. However, there are differences between reduction space and extended space in the school side. Thus, the authors clarified existence of elements that children is easy to recognize.

8. THE DISTORTION OF THE HEIGHT

The children wrote the height information such as the slope on a cognitive map. The authors thought this information affects the distortion of the cognitive space. Thus, the authors investigated cognitive map survey about the distortion of the height on March 2016 (Fig.9). The subject is 10 people in 50s from the teens (1241points data). As a result, the authors classified the relationship between height of road incline and distortion of the height on cognitive space (Fig.10).

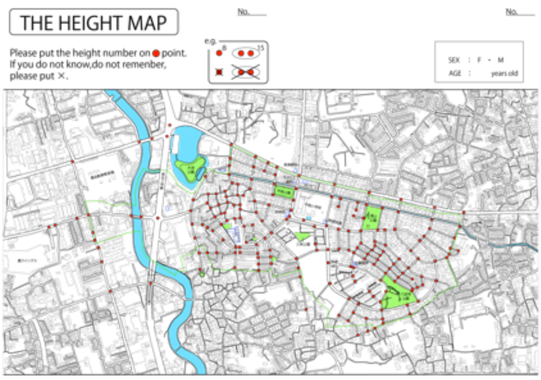

Fig.9 The questionnaire

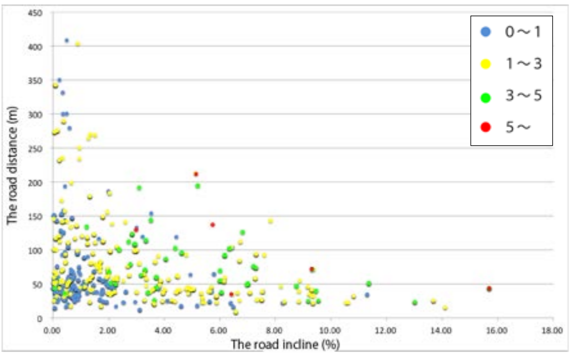

Fig.10 The cognitive difference (distance, incline)

9. CONCLUSION

In this study, the authors caught a distortion of the space as image of the children. The authors clarified the space that is important to children by calculating image amplification. And the authors understood the characteristic of children's cognitive space by clarifying the relationship between the amplification and position.

In addition, the authors classified that the distortion of the height affected a road incline and distance by investigating the distortion of the height.

We, urban designers plan the parks using the formal form. However, children plays everywhere we do not image normaly, like a part of road, a river, big trees in cities and so on (Fig.11). They are not prepare by urban designers. There were also the special places for children. [8] In the study of Umekawa [9], the children do not choose the place to play by its size.

As a result of this study, it is clear that the cognition sizes of the spaces by children is different where they are. We, the designers have the possibilities to design new place for children in real space.

In the future, the authors will analyze the relationship between the spaces that shows frequent use and the position of the drawing element.

Fig.11 The children play on the road

10. REFERENCES

[1] Sakai T, Tanaka K, Yoshikawa S "The study of distortion on children's cognitive map"JSCE-KC Ⅳ-４ 2015
[2] Lynch K, "The Image of the City", MIT Press
[3] Masui Y, Imada H, "Methods and methodological issues in the externalization of the cognitive maps", 42(2), pp.65-81, humanities review 1992
[4] Okamoto K, "A Review of Cognitive Distance Studies", Vol.34 No.5, pp.429-448, Japanese Journal of human geography 1982
[5] Wakabayashi Y, "The spatial analysis of cognitive map", pp.1-318, Tijin Shobo, 1999
[6] Murata K " The map of children' world-Secret base・Children's route・The space that a haunted house forms", pp.1-176, ReimeiShobo, 1988
[7] J. Piaget "A condition and learning of the development", pp.1-219, Seishin Shobo, 1979
[8] Kaneda H, Nakagawa T, Biwa Y, Tanaka K, Yoshikawa S, "The pedestrian space that paid its attention to the viewpoint of the children", JSCE-KC Ⅳ-47 2013
[9] Umekawa K, Yokoyama H, Miyagishi Y "A study on the playgrounds for the children and the space cognition in the city", AIJ-Kinki Branch, pp.365-368, 2009

CHARACTERISTICS OF COLLAPSE TIME OF EARTHQUAKE SOURCE ROCK AS ONE PARAMETER TO PREDICTION THE EARTHQUAKE IN YOGYAKARTA REGION

Hita Pandita[1)], Sukartono[2)] and Agustinus Isjudarto[3)]
Department of Geology, Sekolah Tinggi Teknologi Nasional, Yogyakarta, e-mail: hita@indo.net.id
Department of Geology, Sekolah Tinggi Teknologi Nasional, Yogyakarta, e-mail: kartono_skt@yahoo.co.id
Department of Mining Engineering, Sekolah Tinggi Teknologi Nasional, Yogyakarta, e-mail: is_darto@yahoo.com

Abstract

Indonesia is a country with high potential to get an earthquake, one of them is Yogyakarta and surrounding areas. Although earthquake attack in Yogyakarta area have been several times, efforts to reduce the number of victims is dificult to do. It’s cause the absence of parameters that can be used to estimate the arrival time of the earthquake. One of the parameters that may be used is predicted when a fault will move on, using an earthquake if get an increase of pressure constantly. This study aimed to find out when a rock will collapse if it get a varied pressures, so it can get a collapse rock time formula. If the formula is known, it can be modeled to the load received a fracture for understand when the fracture will move on. The research method used is a field investigation, and rocks compressive strength test. By using the test six variations of loading finally made it known pattern of the outbreak of the rock. Formulation successfully arranged by using four models of the curve, namely: linear, logarithmic, exponential and quadratic functions (power). Three types of rocks have been tested, and the results show the most likely around earthquake source rocks around Opak fault is a diorite rock, since the collapse of this rock closest to the timeframe of seismicity induced by Opak fault.

Keywords: Prediction, Earthquake, Strength test, Time, Opak fault

INTRODUCTION

Yogyakarta is an area with high potential earthquake. A number of large magnitude earthquake hit the region like in 1867 and 2006 [1]. Damage and casualties from those earthquake is very large. The large number of souls who drift and loss of property caused by the lack of accurate predictions about when an earthquake will occur.

According from many geologist, most of the earthquake is cause by sudden release of strain energy that has built up over a period of time [2]. The pressure on the earth's crust in the earthquake areas are generally caused by the collision between two or more plates or continents and oceans. Based on the theory of occurrence of the earthquake, then the expected arrival of an earthquake in a region can be estimated from the time exceeding of the durability of rocks in the earth's crust. So understanding the durability of the rocks in the earth's crust will be able to help improve the accuracy of prediction of the earthquake in the region.

This study aimed to find out when a rock will collapse if it get a varied pressures, so it can get a collapse rock time formula. If the formula is understand, it can be modeled to the load received a fracture for understand when the fracture will move on. The research object is rocks which predicted as earthquake source around Opak Fault in Yogyakarta area. The choice of Opak Fault becaused many great earthquake occurred around this fault [1].

METHOD

The method used in this research is the field survey, stratigraphic analysis and compressive strength test. Field survey carried out in the Southern Mountain to determine the thickness of sedimentary rocks and understanding of earthquake source rock. The field investigation also taken rock samples were estimated as earthquake source rocks. Laboratory investigations carried out in the form of uniaxial compressive strength test of the earthquake source rocks.

REGIONAL GEOLOGY

The research areas included in border between the Southern Mountains of East Java Zone and Yogyakarta Depression (van Bemmelen, 1949) [3]. The boundary between these two physiographic zones by some researchers suspected a Northeast-

Southwest Fault known as the Opak Fault Depression Yogyakarta is a lowland filled by deposition of volcanic activity of Merapi. Southern Mountains of East Java is a high land stretches from the eastern part of Yogyakarta to the southeastern tip of the island of Java.

Regional stratigraphy research area has been reviewed by several researchers such as Rahardjo, et al (1995) [4], Surono, et al. (1992) [5] and van Bemmelen (1949) [3]. The thickness of sedimentary rocks in the Southern Alps is estimated at more than 5,000 m (Pandita & Sukartono, 2014) [6], the bedrock is estimated to (Rahardjo, et al, 1995) [4]. be Cretaceous metamorphic complex. Unconformity at top of the bedrock deposited limestone from Wungkal Formation at Eocene. Series of volcanic deposits began to appear at Kebo-Butak Formation begins at Olgosen (Surono, 2008) [7]. Then sequentially formed Semilir Formation and Nglanggran Formation the Early Miocene to Middle Miocene. In the early Late Miocene volcanic series is gradualy being replaced by a series of carbonate rocks, beginning by Sambipitu Formation and ending by Kepek Formation (Pandita, et al, 2014) [6].

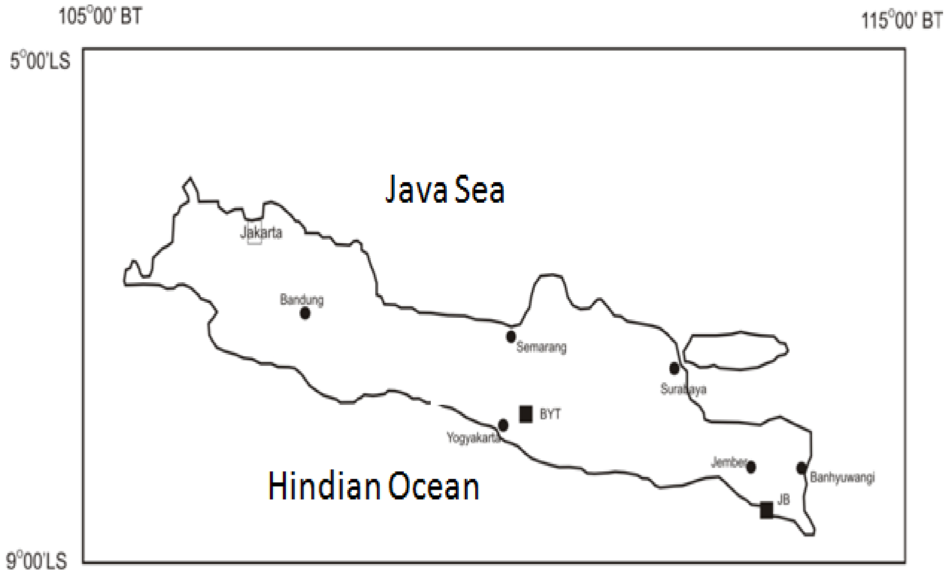

Fig1. Samples location BYT=Bayat, dan JB = Jember

RESULT

Material And Location

Sampling locations for compressive strength test selected based on the type of rock to be tested. Sampling in the form of surface samples from some rocks that are suspected as earthquake source rocks. Pandita, et al. (2014) [6] and Prasetyadi (2007) [8] based on stratigraphic studies predict that the bedrock of the Southern Mountains are metamorphic complex. Santosa (2014) [9] is based on the gravity study estimated bedrock Southern Mountains is characterized like diorite rocks. Sribudiyani, et al. (2003) [10] and Smyth, et al (2007) [11] estimates that the bedrock of East Java is the continental crust.

Based on the study of the researchers mentioned above, then there are three possible earthquake source rocks around Opak fault, namely the continental crust rocks (granite), metamorphic complex and diorite. According to these, there were three locations selected for sampling. Two locations of the Bayat region, namely in the Pendul hill (BYT14) and Jokotuo (BYT10), whereas one location area Rajegwesi, Jember (Figure 1). At BYT10 of samples taken in the form of marble rocks of the complex metamorf Bayat. At BYT14 samples taken form of diorite rock. Location Rajegwesi an analog samples of the continental crust in the form of dacite rock.

Uniaxial Test

Three rocks prepared for uniaxial test, with each rock type was prepared in six different loading. Samples were prepared in the size of 5x5x5 cm appropriate standard test ISO 2825: 2008 [12]. Tests carried out at the Laboratory of Materials and Construction Engineering at the Faculty of Civil Engineering UII Yogyakarta. Condition of the sample in a dry state. Compressive strength testing is done with six different loading speeds, namely: 1 kN/s, 2 kN/s, 3 kN/s, 4 kN/s, 5 kN/s and 6 kN/s. Full results of the compressive strength test can be seen in Table 1.

Rock Sample	Wide (cm^2)	v (KN/s)	t (second)	σca (Mpa)
Diorit	19.78	1	416.41	77553.08
	26.46	2	116.19	86545.73
	28.05	3	90.3	58823.53
	24.96	4	110.25	66426.28
	23.04	5	107	65190.97
	27.03	6	37.14	73251.94
Marble	26.5	1	810.06	92150.94
	29.16	2	271.67	62825.79
	27.03	3	110.53	45024.05
	28.08	4	63.85	76210.83
	28.08	5	79.69	87500.00
	28.62	6	36.54	99510.83
Dacite	27.04	1	2009	176516.27
	26.5	2	218	104905.66
	25	3	92	72000.00
	26.5	4	87	135471.70
	26.5	5	71	131698.11
	30.24	6	59	161210.32

Table 1. Result of uniaxial test from three rocks

Analysis

Data processing was performed using Excel 2007 program to get formula using Power curve (quadratic function). Power curve (quadratic function) is the best results were obtained through a series of processing from the other curves (Figure 2). The curve shows the X-axis as speed of loading in kN/sec, the Y axis is the collapse time of the rocks in a seconds.

Based on the power curve (quadratic function) obtained formula the relationship between speed of loading with the collapse time of the rock. The formula are (Fig. 2):

Marble: $y = 793.3x^{-1.65}$ 1)
Dacite: $y = 1266.x^{-1.90}$ 2)
Diorite: $y = 342.9.x^{-1.02}$ 3)

Because x represents the magnitude of loading, whereas the compressive strength test loading has notation v, then a notation "x" changed to "v". Likewise with "y" which is the time, and in a general sense the notation is "t", so the notation "y" replaced with "". Thus the formula can be changed to:

Marble: $t = 793.3v^{-1.65}$ 4)
Dacite: $t = 1266.v^{-1.90}$ 5)
Diorite: $t = 342.9.v^{-1.02}$ 6)

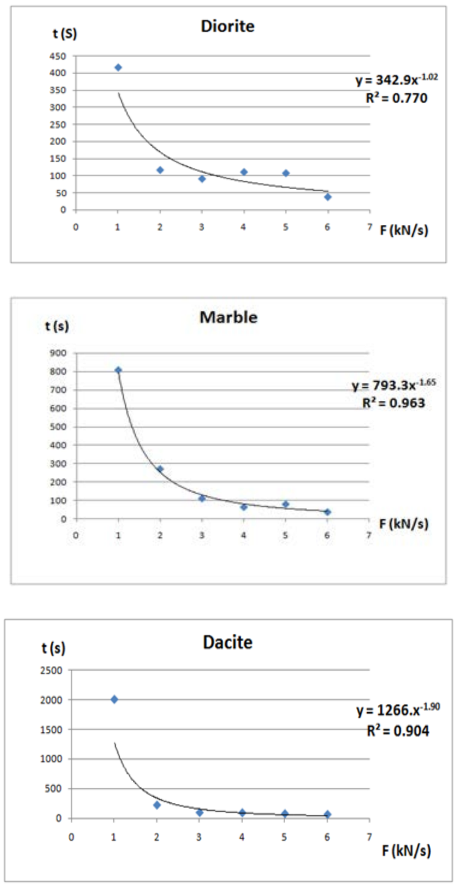

Figure 2. Quadratic function curve relationship between variations in the speed of load with the collapse times of three rocks results from processing using Excel program.

DISCUSSION

Force of Collision

Until now there has been no study that calculates the magnitude of the force or load that occurs as a result of plate collision in the southern island of Java. To get these formulations then were calculated theoretically based on the general character of the type and speed of plate. Calculation of two types, namely the imposition of macro and micro load. The macro loading according to its natural condition based on area of collision in the plane of Opak fault. Imposition of a micro is simulation if the size of the collision area corresponding scale of laboratory test. For the calculation required data of the volume of plate, speed of plate movement and density.

On a macro scale counting the length of the plate is calculated from the collision point to the spreading point, based on a calculation from the Google Earth obtained 2790.97 km. Width has calculated from the collision area with the Opak fault, ie 21.35 km. The thickness is calculated based on the average thickness of the oceanic plates, which is 5 km. The final result of the volume can be seen in Table 2..

Scale	Macro	Micro
Volume (km^3)	297980.1944	0.000007
Density (g/cm^3)	3.3	3.3
Weight (gr)	9.8×10^{17}	2,302,555,025
Speed (cm/year)	6	6
Speed (cm/sec)	2.22×10^{-7}	2.22×10^{-7}
Load (kN/sec)	1870.9	4.38×10^{-5}

Table 2. The results of the theoretical calculation of geometry and its burden on the Indo-Australian plate movement against geometry of Opak fault

Calculation of macro-scale load can be calculated by knowing the average speed of the Indo-Australian by 6 cm / yr (Whittaker et al., 2007) [13] or 1.9 x10-7 cm/sec. By using an average density oceanic plates 3.3 gr/cm^3. It can be seen from the plate macro load of 1870.9 kN/sec.

Because in this study did not test the sample size variable, then the load on a macro scale can not be used to calculate the time of rupture of rocks. In this connection it is necessary to micro-scale modeling or calculation in accordance with a surface area in the laboratory tests. On a micro scale modeling of some value on a macro scale still, the only difference being the volume due to changes in the loading area. The final result obtained at the micro scale imposition of 4.38×10^{-5} kN/sec (Table 2).

Earthquake Prediction

Formulas of the collpase time of each rock will use to calculate the earthquake prediction. Calculations performed by a micro scale load, this is due to micro-scale approach the area on a scale laboratory tests. Value of v is taken from the amount of pressure that occurs in kN/sec, while t is the time of earthquake prediction searched in seconds.

The result of calculation shows that dacite rock takes more than 7,800 years to get an earthquake, marble rocks need 400 years and diorite rocks need 173 years (Table 3). The study on the history of seismicity around Opak fault, there are two major earthquakes that in 1867 and 2006. This represents an interval of 139 years between the first quake toward the second quake. Based on that show diorite rocks closest to the earthquake time interval. So there is a great possibility the earthquake source rock is diorite rocks.

Rocks	Load (kN/sec)	Prediction Time (t)	
		second	Year
Marble	4.38×10^{-5}	1.2×10^{10}	400.78
Dacite	4.38×10^{-5}	2.42×10^{11}	7861.72
Diorite	4.38×10^{-5}	5.33×10^{9}	173.24

Table 3. Calculation time prediction of an earthquake on Opak fault of the three types of seismic source rocks.

Seeing the time difference between simulation on rock diorite with intervals of earthquake that occurred on Opak fault, it is likely due to several things:

1) Opak Fault is already a weak field, so it does not require loading large when compared with the condition before the fracture.
2) The possibility of an earthquake source rocks have lower resistance values of diorite.
3) There are many assumptions in this study like the volume of the Indo-Australian plate, the density of which is taken from the average value oceanic plate, thus affecting the value of the load.

CONCLUSION

This research is still an early stage in an effort to prediction of earthquake in the future in the Yogyakarta area. However, this study has shown the possibility of the arrival of an earthquake can be expected from collapse time of the earthquake source rocks. This research still needs to be improved, with a variety of other rock samples and also variations in loading time, so that the preparation of the formula becomes more accurate.

ACKNOWLEDGEMENT

This study was established with funds from the Ministry of Research and Higher Education, in the form of competitive grants during 2014 and 2015, with the contract number SPDIPA-023.04.2.189971 / 2014 to 2014 and SPDIPA-023.04.1.673453 / 2015 for funding in 2015. Thanks are expressed to the paleontology laboratory assistants who assist in data collection in the field.

REFERENCES

[1] Thant, M., Kawase, H., Pramumijoyo, S., Hendrayana, H., & Adi, A. D., "Focal Mechnisms of Subduction Zone Earthquakes Along The Java Trench: Preliminary Study For The PSHA For Yogyakarta Region, Indonesia", The 14th World Conference on Earthquake Engineering October 12-17, Beijing, China. 2008,

[2] Kearay, P., Klepeis, K.A., & Vine, F., *Global Tectonics*, 3rd ed., Wiley-Blackwell, A John Wiley & Sons, Ltd, 2009, pp 92-94.

[3] Van Bemmelen, *The Geology of Indonesia*. The Hague, Martinus Nijhoff, vol. IA. 1949, p. 546-658

[4] Rahardjo, W., Sukandarrumidi, & Rosidi, H.M.D., *Geological Map of Yogyakarta Sheet, Jawa*, Geological Research And Development Centre, Bandung, 1995.

[5] Surono, Toha B., Sudarno I., & Wiryosujono, S., *Geological Map of Surakarta and Giritontro Jawa*, GRDC Bandung, 1992.

[6] Pandita, H. & Sukartono, "*Karakteristik Nilai Kuat Tekan Batuan Sumber Gempa Sebagai Salah Satu Parameter Penentuan Terjadinya Gempa Bumi di Wilayah Yogyakarta"*, Research Report, STTNAS, 2014, pp. 53.

[7] Surono, "Litostratigrafi dan Sedimentasi Formasi Kebo dan Formasi Butak di Pegunungan Baturagung, Jawa Tengah Bagian Selatan", Jurnal Geologi Indonesia, Vol. 3 No. 4 Desember 2008: 183-193

[8] Prasetyadi, C., "Evolusi Tektonik Paleogen Jawa Bagian Timur", Doctoral Thesis, Unpublished, ITB, 2007.

[9] Santosa, A., "Determination of Ancient Volcanic Eruption Centre Based on Gravity Methods in Gunungkidul Area Yogyakarta", Proc. International Symposium of Geoheritage, UPN, 2014. pp

[10] Sribudiyani, Muchsin,N., Ryacudu, R., Kunto, T., Astono, P., Prasetya, I., Sapiie, B., Asikin, S., Harsolumakso, A.H., & Yulianto, I., "The Collision of the East Java Microplate and Its Implication for Hydrocarbon Occurences in East Java Basin", Proc. Ann. Conv. IPA 29th, Jakarta, 2003, pp 1-12

[11] Smyth, H.R., Hamilton, P.J., Hall, R., & Kinny, P.D., "The deep crust beneath island arcs: Inherited zircons reveal a Gondwana continental fragment beneath East Java, Indonesia", Earth and Planetary Science Letters, Science Direct, Elsevier, 2007, pp 269-282.

[12] SNI, *Cara Uji Kuat Tekan Batu Uniaksial*, Badan Standardisasi Nasional, 2008.

[13] Whittaker, J.M., Muller, R.D., Sdrolias, M., & Heine, C., "Sunda-Java trench kinematics, slab window formation and overriding plate deformation since the Cretaceous", Earth and Planetary Science Letter, 255, Science Direct, Elsevier, 2007, pp 445-457.

MATHEMATICAL MODELING OF FOREST FIRES INITIATION, SPREAD AND IMPACT ON ENVIRONMENT

Valeriy Perminov[1], Alexander Goudov[2]
[1]Department of Ecology and Basic Safety, Tomsk Polytechnic University, Russia
[2]Mathematical Faculty, Kemerovo State University, Russia

ABSTRACT

A mathematical model of surface and crown forest fires spread and impact is considered. A three dimensional multiphase, physic based model is used. The boundary-value problem is solved numerically by finite volume method. This model has been applied to describe the process of initiation and spread of surfaces forest fires and their transfer into crown of forest fires. The results of numerical solutions present the distribution of the main functions of the process (the velocity field, the temperature of gas and solid phase, the concentration of the oxygen, gas product of pyrolysis and inert components, etc.) over time. Scenarios modeled within this study represent a possible approach to the preliminary assessment of risk and should be verified by more detailed CFD modeling.

Keywords: Crown Fire, Surface Fire, Mathematical Modeling, Finite Volume Method

INTRODUCTION

One of the objectives of these studies is the improvement of knowledge on the fundamental physical mechanisms that control forest fires initiation and spread. A great deal of work has been done on the theoretical problem of how forest fire initiation. In forest there are two steps for crown forest fire initiation: spread of fire from crow to crown and crown fires are initiated by convective and radiative heat transfer from surface fires. However, convection is the main heat transfer mechanism. Firstly, crown forest fire initiation has been studied and modeled by Van Wagner [1]. There are three simple crown properties: crown base height, bulk density and moisture content of forest fuel in this theory. Also crown fire initiation have been studied and modeled in detail (eg: Alexander [2], Van Wagner [3], Xanthopoulos, [4], Rothermel [5,6], Van Wagner, [7], Cruz [8], Albini [9], Scott, J. H. and Reinhardt, E. D. [10]. The discussion of the problem of modeling forest fires is provided by a group of co-workers at Tomsk University (Grishin [11], Grishin and Perminov [12]. The general mathematical model of forest fires was obtained by Grishin [11] based on an analysis of known and original experimental data [11,13], and using concepts and methods from reactive media mechanics. The physical two-phase models used in [14-15] may be considered as a continuation and extension of the formulation proposed by Grishin and Perminov [12]. However, the investigation of crown fires has been limited mainly to cases studied of forest fires initiation in two dimensional settings and did not take into account space properties of these phenomena.

PHYSICAL AND MATHEMATICAL MODEL

It is assumed that the forest during a forest fire can be modeled as 1) a multi-phase, multistoried, spatially heterogeneous medium; 2) in the fire zone the forest is a porous-dispersed, two-temperature, single-velocity, reactive medium; 3) the forest canopy is supposed to be non-deformed medium (trunks, large branches, small twigs and needles), affects only the magnitude of the force of resistance in the equation of conservation of momentum in the gas phase, i.e., the medium is assumed to be quasi-solid (almost non-deformable during wind gusts); 4) let there be a so-called “ventilated” forest massif, in which the volume of fractions of condensed forest fuel phases, consisting of dry organic matter, water in liquid state, solid pyrolysis products, and ash, can be neglected compared to the volume fraction of gas phase (components of air and gaseous pyrolysis products); 5) the flow has a developed turbulent nature and molecular transfer is neglected; 6) gaseous phase density doesn’t depend on the pressure because of the low velocities of the flow in comparison with the velocity of the sound. Let the coordinate reference point x_1, x_2 , x_3= 0 be situated at the center of the domain of surface forest fire source at the height of the roughness level, axis $0x_1$ directed parallel to the Earth’s surface to the right in the direction of the unperturbed wind speed, axis $0x_2$ directed perpendicular to $0x_1$ and axis $0x_3$ directed upward (Figure 1).

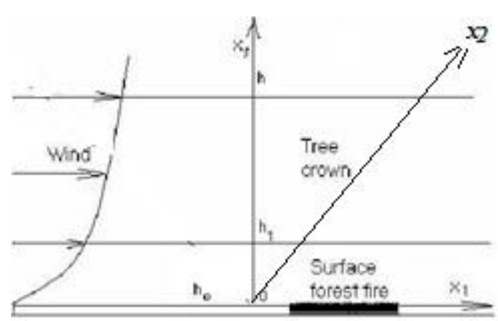

Fig. 1. Schematic of a forest fire domain.

Using the results of [11-12] and known experimental data [13] we have the following sufficiently general equations, which define the state of the medium in the forest fire zone, written using tensor notation.

$$\frac{\partial \rho}{\partial t}+\frac{\partial}{\partial x_j}(\rho v_j)=\dot{m}\,,\;\; j=1,2,3,\;\; i=1,2,3; \qquad (1)$$

$$\rho\frac{dv_i}{dt}=-\frac{\partial P}{\partial x_i}+\frac{\partial}{\partial x_j}(-\rho\overline{v_i'v_j'})-\rho s c_d v_i\,|\vec{v}\,|- \qquad (2)$$

$$-\rho g_i-\dot{m}v_i;$$

$$\rho c_p\frac{dT}{dt}=\frac{\partial}{\partial x_j}(-\rho c_p\overline{v_j' T'})+q_5R_5-\alpha_v(T-T_s)+ \qquad (3)$$

$$+k_g(cU_R-4\sigma T^4)$$

$$\rho\frac{dc_\alpha}{dt}=\frac{\partial}{\partial x_j}(-\rho\overline{v_j' c_\alpha'})+R_{5\alpha}-\dot{m}c_\alpha\;,\;\alpha=\overline{1,3}; \qquad (4)$$

$$\frac{\partial}{\partial x_j}\left(\frac{c}{3k}\frac{\partial U_R}{\partial x_j}\right)-kcU_R+4k_S\sigma T_S^4+ \qquad (5)$$

$$+4k_g\sigma T^4=0,\,k=k_g+k_S\,,$$

$$\sum_{i=1}^{4}\rho_i c_{pi}\varphi_i\frac{\partial T_S}{\partial t}=k_s(cU_R-4\sigma T_S^4)+ \qquad (6)$$

$$+q_3R_3-q_2R_2+\alpha_V(T-T_S);$$

$$\rho_1\frac{\partial \varphi_1}{\partial t}=-R_1,\rho_2\frac{\partial \varphi_2}{\partial t}=-R_2,$$

$$\rho_3\frac{\partial \varphi_3}{\partial t}=\alpha_C R_1-\frac{M_C}{M_1}R_3,\rho_4\frac{\partial \varphi_4}{\partial t}=0; \qquad (7)$$

$$\sum_{\alpha=1}^{3}c_\alpha=1,\;p_e=\rho RT\sum_{\alpha=1}^{3}\frac{c_\alpha}{M_\alpha},\vec{v}=(v_1,v_2,v_3).$$

The system of equations (1)–(7) must be solved taking into account the initial and boundary conditions:

$$t=0: v_1=0, v_2=0, v_3=0, T=T_e, c_\alpha=c_{\alpha e}, \qquad (8)$$
$$T_s=T_{se},\varphi_i=\varphi_{ie};$$

$$x_1=-x_{1e}: v_1=V_e, v_2=0, v_3=0, T=T_e, c_\alpha=c_{\alpha e}, \qquad (9)$$
$$-\frac{c}{3k}\frac{\partial U_R}{\partial x_1}+\frac{c}{2}U_R=0,$$

$$x_1=x_{1e}:\frac{\partial v_1}{\partial x_1}=0,\;\frac{\partial v_2}{\partial x_1}=0,\frac{\partial v_3}{\partial x_1}=0,\;\frac{\partial c_\alpha}{\partial x_1}=0, \qquad (10)$$
$$\frac{\partial T}{\partial x_1}=0,\frac{c}{3k}\frac{\partial U_R}{\partial x_1}+\frac{c}{2}U_R=0\,;$$

$$x_2=x_{20}:\frac{\partial v_1}{\partial x_2}=0,\;\frac{\partial v_2}{\partial x_2}=0,\;\frac{\partial v_3}{\partial x_2}=0,\frac{\partial c_\alpha}{\partial x_2}=0, \qquad (11)$$
$$\frac{\partial T}{\partial x_2}=0,-\frac{c}{3k}\frac{\partial U_R}{\partial x_2}+\frac{c}{2}U_R=0\,;$$

$$x_2=x_{2e}:\frac{\partial v_1}{\partial x_2}=0,\;\frac{\partial v_2}{\partial x_2}=0,\frac{\partial v_3}{\partial x_2}=0,\frac{\partial c_\alpha}{\partial x_2}=0, \qquad (12)$$
$$\frac{\partial T}{\partial x_2}=0,\frac{c}{3k}\frac{\partial U_R}{\partial x_2}+\frac{c}{2}U_R=0\,.$$

$$x_3=0: v_1=0,\;v_2=0,\frac{\partial c_\alpha}{\partial x_3}=0,-\frac{c}{3k}\frac{\partial U_R}{\partial x_3}+\frac{c}{2}U_R=0\,, \qquad (13)$$
$$v_3=v_{30}, T=T_g\,,\;|x_1|\le\Delta,|x_2|\le\Delta$$
$$v_3=0,\;\;T=T_e\,,\;|x_1|>\Delta,|x_2|>\Delta;$$

$$x_3=x_{3e}:\frac{\partial v_1}{\partial x_3}=0,\;\frac{\partial v_2}{\partial x_3}=0,\frac{\partial v_3}{\partial x_3}=0,\frac{\partial c_\alpha}{\partial x_3}=0, \qquad (14)$$
$$\frac{\partial T}{\partial x_3}=0,\frac{c}{3k}\frac{\partial U_R}{\partial x_3}+\frac{c}{2}U_R=0\,.$$

Here and above $\frac{\mathrm{d}}{\mathrm{d}t}$ is the symbol of the total (substantial) derivative: $\frac{d}{dt}=\frac{\partial}{\partial t}+v_1\frac{\partial}{\partial x_1}+v_2\frac{\partial}{\partial x_2}+v_3\frac{\partial}{\partial x_3}$, α_V is the coefficient of phase exchange; ρ - density of gas – dispersed phase, t is time; v_i - the velocity components; T, T_S, - temperatures of gas and solid phases, U_R - density of radiation energy, k - coefficient of radiation attenuation, P - pressure; c_p – constant pressure specific heat of the gas phase, c_{pi}, ρ_i, φ_i – specific heat, density and volume of fraction of condensed phase (1 – dry organic substance, 2 – moisture, 3 – condensed pyrolysis products, 4 – mineral part of forest fuel), R_i – the mass rates of chemical reactions, q_i – thermal effects of chemical reactions; k_g , k_S - radiation absorption coefficients for gas and condensed phases; T_e - the ambient temperature; c_α - mass concentrations of α - component of gas - dispersed medium, index α=1,2,3, where 1 corresponds to the density of oxygen, 2 - to carbon monoxide CO, 3 - to carbon dioxide and inert components of air; R – universal gas constant; M_α , M_C, and M molecular mass of α -components of the gas phase, carbon and air mixture; g is the gravity acceleration; c_d is an empirical coefficient of the resistance of the vegetation, s is the specific surface of the forest fuel in the given forest stratum. To define source terms which characterize inflow (outflow of mass) in a volume unit of the gas-dispersed phase, the following formulae were used for the rate of formulation of the gas-dispersed mixture $\dot{m}$, outflow of oxygen R_{51} and changing carbon monoxide R_{52}.

$$\dot{m}=(1-\alpha_c)R_1+R_2+\frac{M_c}{M_1}R_3\,,$$

$$R_{51}=-R_5-\frac{M_1}{2M_2}{}'R_{52}=\nu_g(1-\alpha_c)R_1-R_5,R_{53}=0,$$

$$R_1=k_1\rho_1\varphi_1\exp(-\frac{E_1}{RT_S}),R_2=k_2\rho_2\varphi_2T^{-0.5}\exp(-\frac{E_2}{RT_S}),$$

$$R_3=k_3\rho\varphi_3S_\sigma c_1\exp(-\frac{E_3}{RT_S}),$$

$$R_5 = k_5 M_2 \left(\frac{c_1 M}{M_1}\right)^{0.5} \left(\frac{c_2 M}{M_2}\right) T^{-2.25} \exp(-\frac{E_5}{RT}).$$

The initial values for volume of fractions of condensed phases are determined using the expressions:

$$\varphi_{1e} = \frac{d(1-\nu_z)}{\rho_1}, \varphi_{2e} = \frac{Wd}{\rho_2}, \varphi_{3e} = \frac{\alpha_c \varphi_{1e} \rho_1}{\rho_3}.$$

where d -bulk density of forest combustible materials, ν_z – coefficient of ashes of forest fuel, W – forest fuel moisture content. It is supposed that the optical properties of a medium are independent of radiation wavelength (the assumption that the medium is "grey"), and the so-called diffusion approximation for radiation flux density were used for a mathematical description of radiation transport during forest fires. To close the system (1)–(7), the components of the tensor of turbulent stresses, and the turbulent heat and mass fluxes are determined using the local-equilibrium model of turbulence (Grishin, [1 processes of transfer within the entire region of the forest massif, which includes the space between the underlying surface and the base of the forest canopy, the forest canopy and the space above it, while the appropriate components of the data base are used to calculate the specific properties of the various forest strata and the near-ground layer of atmosphere. This approach substantially simplifies the technology of solving problems of predicting the state of the medium in the fire zone numerically. The thermodynamic, thermophysical and structural characteristics correspond to the forest fuels in the canopy of a different (for example pine [10,12]) type of forest.

NUMERICAL SOLUTION AND REZULTS

The boundary-value problem (1)–(7) we solve numerically using the method of splitting according to physical processes [12]. In the first stage, the hydrodynamic pattern of flow and distribution of scalar functions was calculated. The system of ordinary differential equations of chemical kinetics obtained as a result of splitting [12] was then integrated. A discrete analog was obtained by means of the control volume method using the SIMPLE like algorithm [12,16]. The accuracy of the program was checked by the method of inserted analytical solutions. The time step was selected automatically. Fields of temperature, velocity, component mass fractions, and volume fractions of phases were obtained numerically. Figure 2 illustrate the time dependence of dimensionless temperatures of gas (1) and condensed phases (2), Figure 3. – mass concentrations of gas components (1- oxygen, 2- gas products of pyrolysis), and Figure.4 - relative volume fractions of solid phases (1), moisture (2) and coke (3) at crown base of the forest (V_e=5m/s). At the moment of ignition, the gas combustible products of pyrolysis burn away, and the concentration of oxygen is rapidly reduced. The temperatures of both phases reach a maximum value at the point of ignition. The ignition processes are of a gas - phase nature, i.e. initially heating of solid and gaseous phases occurs, moisture is evaporated. Then decomposition process into condensed and volatile pyrolysis products starts, the latter being ignited in the forest canopy.

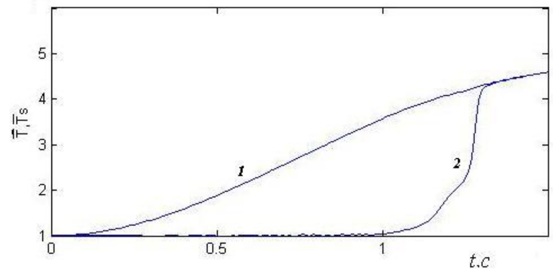

Fig. 2 Temperature of gas (1 - $\bar{T}$) and solid phase (2 - $\bar{T}_S$); $\bar{T}=T/T_e$, $\bar{T}_S=T_S/T_e$, T_e=300K.

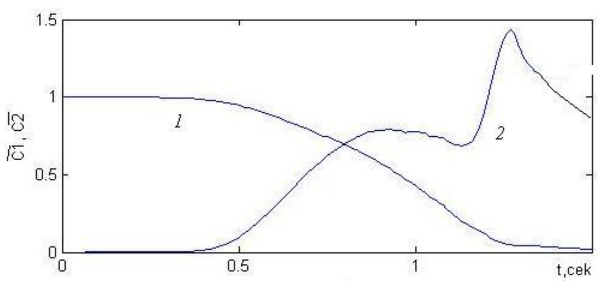

Fig. 3 Concentration of oxygen (1- $\bar{c}_1$) and gas products of pyrolysis (2- $\bar{c}_2$); $\bar{c}_\alpha = c_\alpha / c_{1e}, c_{1e} = 0.23$.

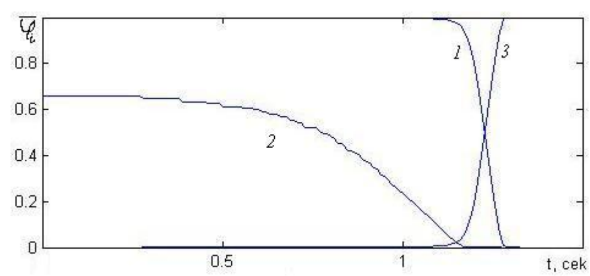

Fig. 4 Volume fractions of solid phase:

$1-\bar{\varphi}_1 = \varphi_1/\varphi_{1e}, 2-\bar{\varphi}_2 = \varphi_2/\varphi_{2e}, 3-\bar{\varphi}_3 = \varphi_3/\varphi_{3e}$.

The vector field of velocities and isotherms of gas phase (Fig. 5): 1-6 correspond to the isotherms $\bar{T}$ = 1.1, 1.5, 1.7, 2, 3 and 4. In the vicinity of the source of heat and mass release, heated air masses and products of pyrolysis and combustion float up. The wind field in the forest canopy interacts with the gas-jet obstacle that forms from the surface forest fire source and from the ignited forest canopy base. Recirculating flow forms beyond the zone of heat and mass release, while on the windward side the movement of the air flowing past the ignition region accelerates. Under the influence of the wind the tilt angle of the flame is increased. As a result, this part of the forest canopy, which is shifted in the direction of the wind from the center of the surface forest fire source, is subjected to a more intensive warming up. The isotherms of the gas and condensed phases are deformed in the direction of the wind.

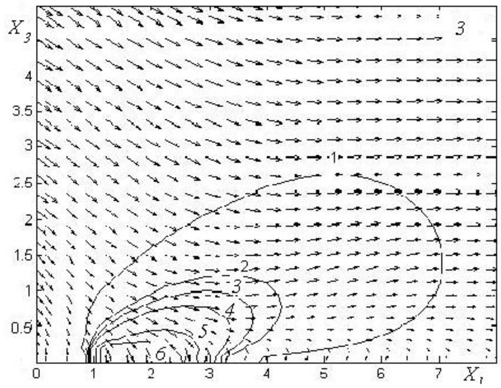

Fig. 5. The vector field of velocities and isotherms of gas phase; (t=4 sec.).

Figure 6 presents isolines of oxygen for different instants of time (t=2, 3, 4 sec.): 1-5 correspond to the isolines $\bar{c}_1$ = 0.9, 0.8, 0.7, 0.5 and 0.1. Figure 7 presents isolines of gas products of pyrolysis: 1-4 correspond to the isolines $\bar{c}_2$ = 0.02, 0.05, 0.1 and 0.5.

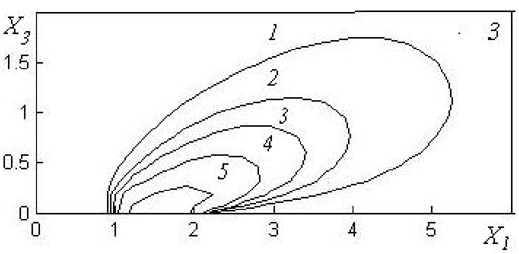

Fig. 6 Isolines of oxygen (t= 4 sec.).

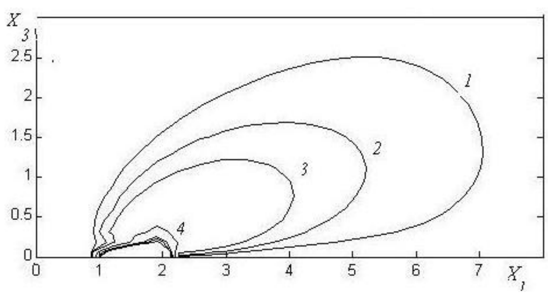

Fig. 7. Isolines of gas products of pyrolysis (t=4 sec.).

At $V_e \neq 0$ the forest fire source ignites the forest crown and burn away in the forest canopy. Forest fire begins to spread in the forest canopy. The distribution of temperature, concentrations of gas products of pyrolysis and oxygen in the forest fire front are presented in the Figure 8. It is seen that the combustion wave looks like as a soliton.

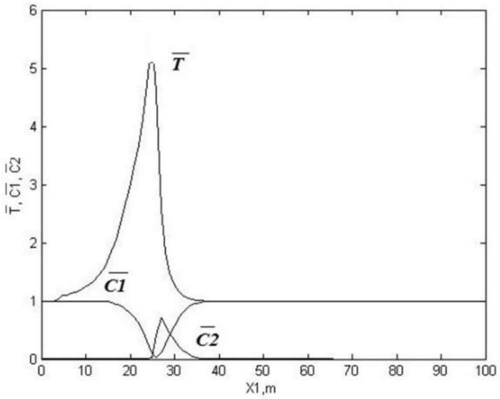

Fig. 8 The distribution of gas temperature, concentrations of gas products of pyrolysis and oxygen.

The oxygen concentration drops to near zero in front of a fire. It is consumed in the combustion of the pyrolysis products, the concentration of which is reached their maximum before the maximum of temperature. Figures 9 - 10 present the distribution of temperature $\bar{T}\,(\bar{T} = T/T_e, T_e = 300K)$ (1- 1.5, 2 - 2., 3 – 2.6, 4 – 3, 5 – 3.5, 6 – 4.) for gas phase, concentrations of oxygen $\bar{c}_1$ (1 – 0.1, 2 – 0.5, 3 – 0.6, 4 – 0.7, 5 – 0.8, 6 – 0.9) and volatile combustible products of pyrolysis $\bar{c}_2$ (1 – 1., 2- 0.1, 3 – 0.05, 4 – 0.01) ($\bar{c}_\alpha = c_\alpha / c_{1e}, c_{1e} = 0.23$) at different instants of time for wind velocity V_e= 5 m/s (Fig.9) and V_e= 10 m/s (Fig.10). The distribution of isotherms of combustion temperature shows the moving of forest fire front with time. Figure 10 shows that with the increase of wind speed up to 10 m/s increases the rate of fire spread to 5 m/sec. Ignition of forest due to spotting is one of the most difficult aspects to understand the behavior of fires. The phenomenon of spotting fires comprises three sequential mechanisms: generation, transport and ignition of recipient fuel.

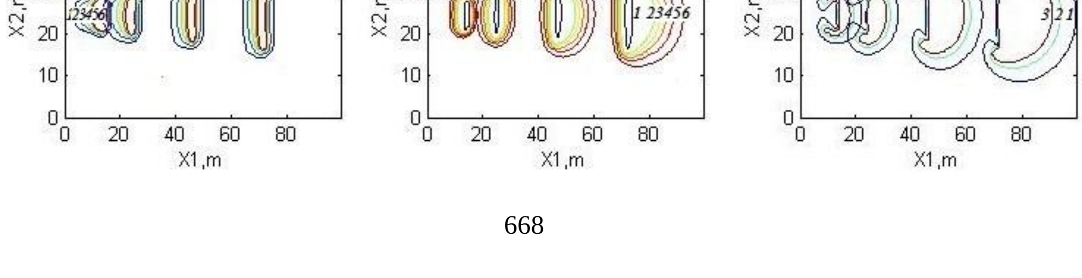

Fig. 9 The distribution of *a*) temperature for gas phase, *b)* concentration of oxygen and c) volatile combustible products of pyrolysis; V_e= 5 m/s, at different instants of time: I - t=3 sec., II - t=6 sec, III - t=12 sec., IV - t= 20 sec.

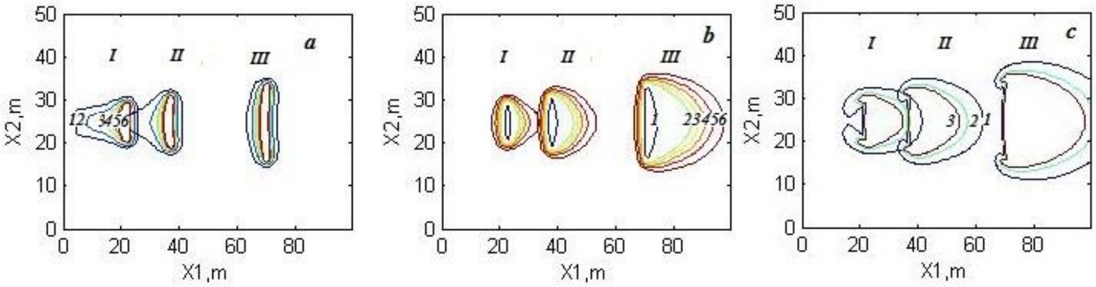

Fig. 10The distribution of *a*) temperature for gas phase, *b)* concentrations of oxygen and c) volatile combustible products of pyrolysis; V_e= 10 m/s, at different instants of time: I - t=3 sec., II - t=6 sec, III - t=12 sec., IV - t= 20 sec.

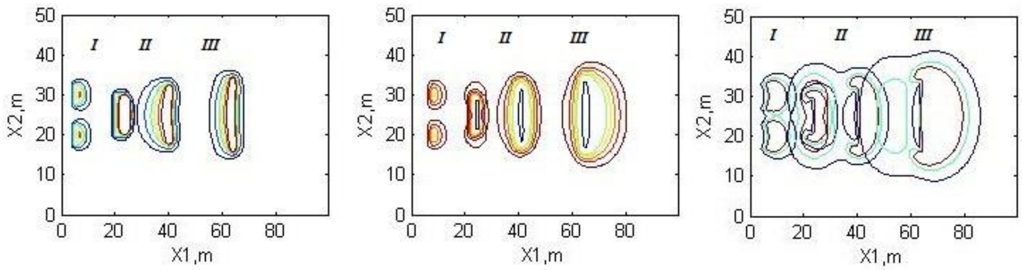

Fig. 11. The distribution of temperature, concentrations of oxygen and volatile combustible products of pyrolysis.

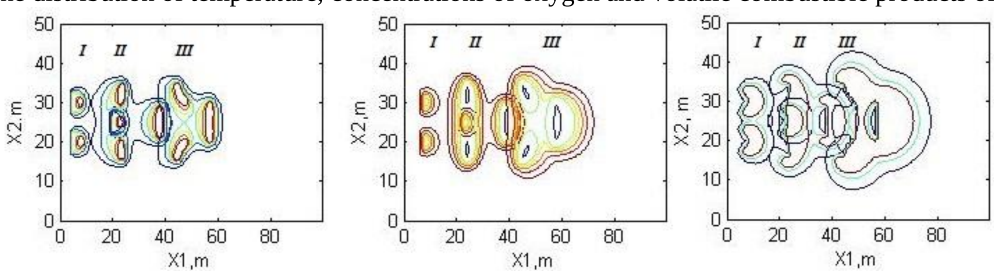

Fig. 12. The distribution of temperature, concentrations of oxygen and volatile combustible products of pyrolysis.

The present mathematical model and results of calculation are used to illustrate picture of the formation of large fires by combining small combustion sources arising from the transfer of firebrands. In order to understand these mechanisms, many calculation experiments have been performed. In the Figures 11 - 12 the process of formation large forest fire front as a result of integration of various sources of combustion is showed. The distributions of temperature for gas phase(a), concentrations of oxygen (b) and volatile combustible products of pyrolysis (c) at different times (I - t=3 sec., II - t=6 sec, III - t=12 sec.) for *Ve=* 5 m/s are presented. There are present the same values of isotherms and isolines of concentration for and as well as in the Figures 11-12. If the sources of ignition from the burning particles are arranged in a triangle, the processes of formation of the forest fire front are shown in Figures 11-12.

In the second case (Figure 12), the right ignition source in the x_2 direction was 2 times less than in the first case (Figure 11).

CONCLUSION

Results of calculation give an opportunity to describe the different conditions of the forest fire spread taking account different weather conditions and state of forest combustible materials, which allows applying the given model for prediction and preventing fires. It overestimates the rate of crown forest fire spread that depends on crown properties: bulk density, moisture content of forest fuel, wind velocity and etc. The model proposed here gives a detailed picture of the change in the temperature and component concentration fields with time, and determine as well as the influence of different conditions on the crown forest fire spreading for the different cases of inhomogeneous of distribution of sources of forest fires initiation.

ACKNOWLEDGEMENTS

This research was financially supported by the Russian Foundation for Basic Research in 2016 (the project № 16-41-700022 p_a) and on the state task № 2014/64, the state project "Scientific researches organization".

REFERENCES

[1] Van Wagner CE, "Conditions for the start and spread of crown fire", Canadian Journal of Forest Research, vol. 7, 1977, pp. 23-34.

[2] Alexander ME, "Crown fire thresholds in exotic pine plantations of Australasia", PhD thesis, Department of Forestry, Australian National University, Australia, 1998.

[3] Van Wagner CE, "Prediction of crown fire behavior in conifer stands", Proc. '10th conference on fire and forest meteorology. Ottawa, Ontario. (Eds D. C. MacIver, H. Auld and R. Whitewood), 1989, pp. 207-212.

[4] Xanthopoulos G., "Development of a wildland crown fire initiation model", PhD thesis, University of Montana, USA, 1990.

[5] Rothermel RC, "Crown fire analysis and interpretation", Proc. International conference on fire and forest meteorology. Missoula, Montana, USA, 1991.

[6] Rothermel RC, "Predicting behavior of the 1988 Yellowstone Fires: projections versus reality", Int. Journal of Wildland Fire, vol. 1, 1991, pp. 1-10.

[7] Van Wagner CE, "Prediction of crown fire behavior in two stands of jack pine", Canadian Journal of Forest Research, vol. 23, 1999, pp. 445-449.

[8] Cruz MG, "Predicting crown fire behavior to support forest fire management decision-making", Proc. IV International conference on forest fire research, Luso-Coimbra, Portugal. (Ed. D. X. Viegas), 11 [CD-ROM]. (Millpress), 2002.

[9] Albini FA, "Modeling ignition and burning rate of large woody natural fuels", Int. Journal of Wildland fire, vol. 5, 1995, pp. 81-91.

[10] Scott JH, "Assessing crown fire potential by linking models of surface and crown fire behavior", USDA Forest Service, Rocky Mountain Forest and Range Experiment Station. Fort Collins: RMRS-RP-29, (Colorado, USA), 2001.

[11] A.M. Grishin, Mathematical Modeling Forest Fire and New Methods Fighting Them, Publishing House of Tomsk University, Tomsk, Russia, 1997.

[12] Grishin AM, Perminov VA, "Mathematical modeling of the ignition of tree crowns", Combustion, Explosion, and Shock Waves, vol. 34, 1998, pp. 378-386.

[13] Konev EV, The physical foundation of vegetative materials combustion, Nauka, Novosibirsk, Russia, 1977.

[14] Morvan D, Dupuy JL, "Modeling of fire spread through a forest fuel bed using a multiphase formulation", Combustion and Flame, vol. 127, 2001, pp. 1981-1994.

[15] Morvan D, Dupuy JL, "Modeling the propagation of wildfire through a Mediterranean shrub using a multiphase formulation", Combustion and Flame, vol. 138, 2004, pp. 199-210.

[16] Patankar SV, Numerical Heat Transfer and Fluid Flow, Hemisphere Publishing Corporation, New York, 1981.

Sixth International Conference on Geotechnique, Construction Materials and Environment, Bangkok, Thailand, Nov. 14-16, 2016, ISBN: 978-4-9905958-6-9 C3051

UNIT WEIGHT AND COMPRESSIVE STRENGTH OF CELLULAR LIGHTWEIGHT RECYCLED GLASS-FLY ASH GEOPOLYMER

Cherdsak Suksiripattanapong[1], Rutchakit Maythathirut[2], Sermsak Tiyusangthong[3], Suksun Horpibulsuk[4] and Arul Arulrajah[5]

[1,3]School of Civil Engineering, Faculty of Engineering and Architecture, Rajamangala University of Technology Isan, Thailand
[2,4]School of Civil Engineering, and Center of Excellence in Innovation for Sustainable Infrastructure Development, Suranaree University of Technology, Thailand
[5]Faculty of Science, Engineering and Technology, Swinburne University of Technology, Australia

ABSTRACT

This paper investigates unit weight and compressive strength of cellular lightweight recycled glass-fly ash geopolymer. The Recycled Glass (RG) was collected from Gaew Grung Thai Co., Ltd. in Thailand and Fly Ash (FA) was obtained from the Mae Moh power plant of the Electricity Generating Authority of Thailand. The influential factors studied are liquid alkaline activator content (L), NaOH concentration and air content (A_c). Test results show that unit weight of cellular lightweight RG-FA geopolymer decreases significantly as the A_c increases and regardless of L and NaOH concentration. The 7-day compressive strength of cellular lightweight RG-FA geopolymer increases with increasing NaOH concentration. However, the excessive of L and A_c results in the reduction of 7-day compressive strength of RG-FA geopolymer. The maximum 7-day compressive strength of RG-FA geopolymer is found at L/FA ratio of 0.6, Na_2SiO_3:NaOH ratio of 70:30 and NaOH concentration of 7 M, which is 20, 14, 5 and 2.5 MPa for air content of 0, 1, 3 and 5%, respectively.

Keywords: Cellular Lightweight, Recycled Glass, Geopolymer, Fly Ash

INTRODUCTION

Massive amounts of waste glass are produced worldwide every year. In Australia, approximately 1.0 million tonnes of Recycled Glass (RG) is destined for landfill annually [1]. In the UK, households throw away over 29.1 million tonnes of waste annually [2]. RG is the by-product of crushing mixed color bottles and other glass products collected from Gaew Grung Thai Co., Ltd. in Thailand. RG is mainly composed of sand and silt particles with a small percentage. RG has recently been used in construction materials such as concrete [2,3], roads [4-7], footpaths [8] and masonry unit [1].

Fly Ash (FA) derived from coal-fired electricity generation provides the greatest opportunity for commercial utilization of this technology due to the plentiful worldwide raw material supply [9]. Palomo et al [10] found that the different FA activated with 8-12 M NaOH cured at 85^{o}C for 24 hours produced a material with compressive strength of 35-40 MPa and about 90 MPa if sodium silicate (Na_2SiO_3) is added to the NaOH solution. Xie & Yunping [11] reported that the hardening process of FA activated with Na_2SiO_3 is mainly attributed to the gel-like reaction products that bind FA particles together. FA is extensively used as a precursor for geopolymers in Thailand [12]

Suksiripattanapong et al. [13] investigated strength development in water treatment sludge-FA geopolymer. The optimum ingredient providing maximum unit weight and strength is NaOH/Na_2SiO_3 ratio of 80:20 and L/FA ratio of 1.3, irrespective of heat condition and curing time. The optimum heat temperature and duration for the optimum ingredient are 75^{o}C and 72 hours, respectively. The durability against wet-dry of sludge-FA geoplymer is better than that of clay-cement [14].

Recently, Arulrajah et al. [8] investigated strength and microstructure evaluation of RG-FA geopolymer as low-carbon masonry units. The Na_2SiO_3/NaOH ratio of 70/30 with L/FA ratio of 0.625 were most efficient combination to provide the required unconfined compression strengths for manufacturing masonry. The maximum strength of RG-FA geopolymer was about 17 MPa.

This research investigates unit weight and compressive strength of cellular lightweight RG-FA geopolymer. The influential factors studied are liquid alkaline activator content (L), NaOH concentration and air content (A_c). This research enables RG traditionally destined for landfill to be used in a sustainable manner in cellular lightweight masonry unit.

MATERIALS AND METHODS

Materials

Recycled glass (RG) was collected from Gaew Grung Thai Co., Ltd. in Thailand. Figure 1 indicates the particle size of RG determined by laser particle size analysis, indicating that an average grain size, D_{50}, of RG is 0.592 mm and a specific gravity is 2.62. Table 1 shows the chemical compositions of RG. It is composed of high SiO_2 content of 85.64% and the CaO content is 10.63%.

FA was obtained from the Mae Moh power plant of the Electricity Generating Authority of Thailand (EGAT) in the northern region of Thailand. Table 1 summarizes the chemical composition of FA using X-ray fluorescence (XRF). Total amount of the major components (SiO_2, Al_2O_3 and Fe_2O_3) are 77.15% while the CaO content is 16.09%. Figure 1 shows the grain size distribution curve of FA, which was tested by laser particle size analysis. It is shown that the RG particles are larger than the FA ones. The average grain size of FA is 17.37 micron. The specific gravity of FA is 2.31. The morphology of the RG and the FA is shown in Figure 2. The FA particles are fine and spherical whereas the RG particles are irregular in shape. The liquid alkaline activator is a mixture of Na_2SiO_3, which consists of 9% Na_2O and 30% SiO_2 by weight, and NaOH with various concentrations of 1, 3, 5 and 7 molars.

Air foam agent, Sika Poro 40 from Sika (Thailand) Company limited, was used in this study. Sika Poro 40 is a blend of anionic surfactants and foam stabilizers. It is a liquid air entraining agent used in various types of mortar, concrete and cementitious material. The air foam was prepared by mixing the foaming agent with water at a ratio of 1:50 by weight.

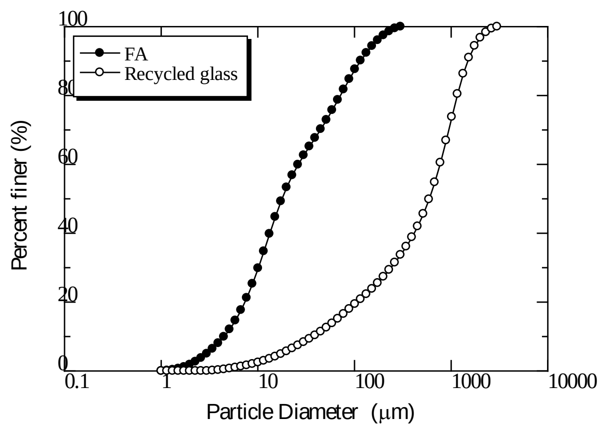

Fig. 1 Grain size distribution of RG and FA.

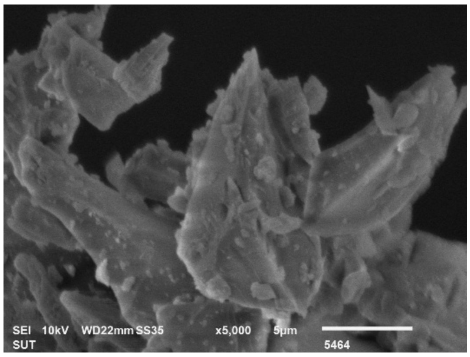

RG

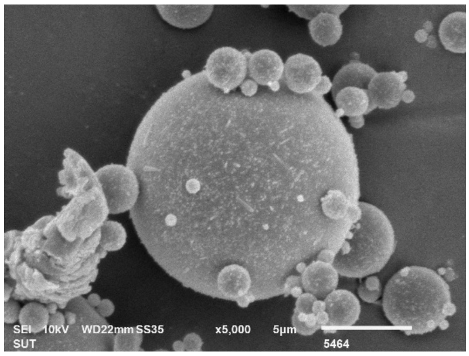

FA

Fig. 2 Scanning electron microscopy (SEM) images of RG and FA.

Table 1 Chemical composition of recycled glass and fly ash.

Chemical composition (%)	Recycled glass	Fly ash
SiO_2	85.64	43.10
Al_2O_3	N.D.	18.95
Fe_2O_3	0.58	15.10
CaO	10.63	16.09
MgO	2.81	N.D.
SO_3	N.D.	3.66
Na_2O	N.D.	0.73
K_2O	0.16	1.76
LOI	0.18	0.61

Remark: N.D. = not detected

Sample Preparation

The cellular lightweight RG-FA geopolymer sample is a combination of RG, FA, liquid alkaline activator (Na_2SiO_3 and NaOH) and air content (A_c). The RG/FA ratio was fixed at 50:50. The Na_2SiO_3/NaOH ratio was 70:30. The FA and L were mixed for 5 minutes in a mixer to ensure homogeneity of the mixture. The input L contents in the cellular lightweight RG-FA vary from 0.6 to 0.8 times FA. The mixer was stopped and then mixed with RG for additional 5 minutes. The air form was added into the RG-FA-L mixture and mixed for 5 minutes. The A_c values were 1, 3 and 5% by total weight of FA. The uniform cellular lightweight RG-FA geopolymer was transferred to containers of 50x50x50 mm. The samples were dismantled, wrapped within vinyl sheet and subsequently cured at room temperature (27-30°C). Unit weight and strengths of cellular lightweight RG-FA geopolymer samples were measured after 7 days of curing in accordance with ASTM C138 and ASTM C69-09, respectively.

UNIT WEIGHT AND COMPRESSIVE STRENGTH OF CELLULAR LIGHTWEIGHT RECYCLED GLASS-FLY ASH

Figure 3 shows the relationships between 7-day unit weight versus concentration of NaOH of cellular lightweight RG-FA geopolymer at different air content for Na_2SiO_3/NaOH ratio of 70:30. The amount of liquid alkaline activator is 0.6FA, 0.7FA, and 0.8FA. The air content (Ac) values varied between 1 and 5% by weight of fly ash. The test result shows that the unit weight of cellular lightweight RG-FA geopolymer decreases as air content and L increases. The unit weight of cellular lightweight RG-FA geopolymer increases as concentration of NaOH increases. It is because the density of the NaOH solution increases with the increase in concentration of NaOH.

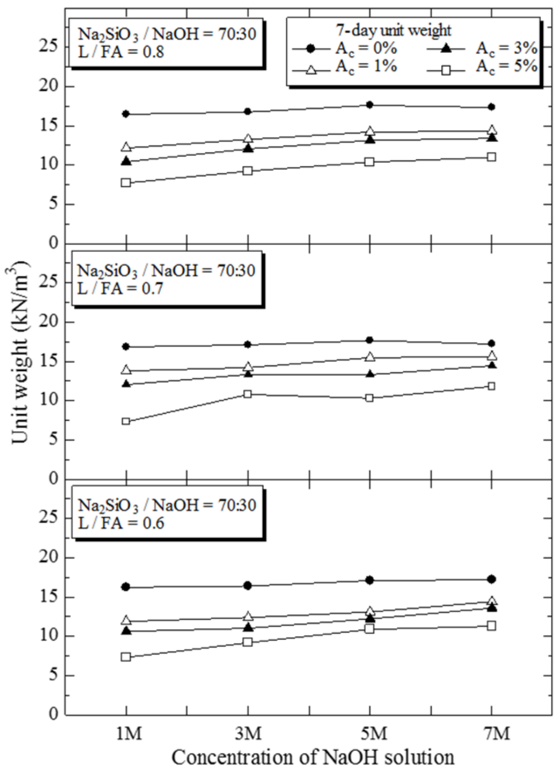

Fig. 3 Relationship between unit weight and NaOH concentration of cellular lightweight RG-FA geopolymer at different air content.

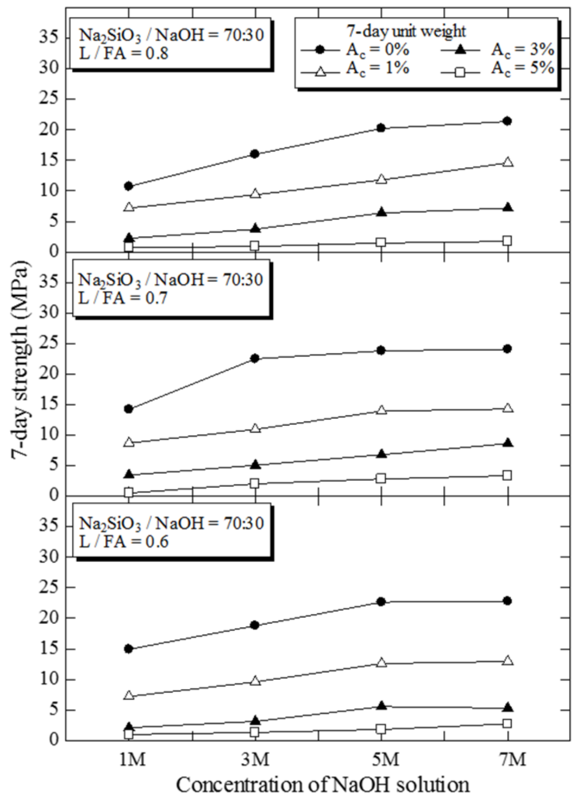

Fig. 4 Relationship between compressive strength and NaOH concentration of cellular lightweight RG-FA geopolymer at different air content.

Figure 4 shows the relationship between 7-day compressive strength and NaOH concentration of cellular lightweight RG-FA geopolymer at different A_c. The amount of L was 0.6FA, 0.7FA and 0.8FA at Na_2SiO_3/NaOH ratio of 70:30 and A_c of 0, 1, 3 and 5%. The test result shows that the 7-day compressive strength of cellular lightweight RG-FA geopolymer varies with the L content for all A_c. The 7-day compressive strength of cellular lightweight RG-FA geopolymer decreases with increasing L. It is because the excessive liquid alkaline activator results in the bleeding in sample [15]. The maximum compressive strength of cellular lightweight RG-FA geopolymer is at L = 0.7FA for all A_c. Compressive strengths of cellular lightweight RG-FA geopolymer on L = 0.6FA and L = 0.8FA are similar.

CONCLUSION

The unit weight and compressive strength of cellular lightweight Recycled Glass-Fly Ash (RG-FA) geopolymer are evaluated in this study. The conclusions can be drawn as follows.

1. The unit weight of cellular lightweight RG-

FA geopolymer increases as NaOH concentration increases. It is because the density of the NaOH solution increases with the increase in NaOH concentration.

2. The 7-day compressive strength of cellular lightweight RG-FA geopolymer decreases with increasing L. It is because the excessive liquid alkaline activator results in the bleeding in sample

3. The maximum compressive strength of cellular lightweight RG-FA geopolymer is at L = 0.7FA for all air contents. Compressive strengths of cellular lightweight RG-FA geopolymer at L = 0.6FA and L = 0.8FA are similar.

ACKNOWLEDGEMENTS

This work was financially supported by the Thailand Research Fund under the TRF Senior Research Scholar program Grant No. RTA5680002. The financial support from the Office of Higher Education Commission under NRU project of Thailand, as well as Suranaree University of Technology are also very much appreciated. The first author acknowledges the financial support from the Rajamangala University of Technology Isan.

REFERENCES

[1] Arulrajah A., Kua TA., Horpibulsuk S., Phetchuay C., Suksiripattanapong C., Du Y.J. “Strength and microstructure evaluation of recycled glass-fly ash geopolymer as low-carbon masonry units”, Construction and Building Materials, 2016, Vol.114, pp.400-406.

[2] Al-Sibahy A., Edwards R. “Mechanical and thermal properties of novel lightweight concrete mixtures containing recycled glass and metakaolin”, Construction and Building Materials, 2012, Vol.31, pp.157-167.

[3] Ali E.E., Al-Tersawy S.H. “Recycled glass as a partial replacement for fine aggregate in self compacting concrete”, Construction and Building Materials, 2012, Vol.35, pp.785-791.

[4] Arulrajah A., Ali M., Disfani M., Horpibulsuk S. Recycled-glass blends in pavement base/subbase applications: laboratory and field evaluation, J. Mater. Civ. Eng. 26 (7) (2013)

[5] Grubb D., Gallagher P., Wartman J., Liu Y., Carnivale M. Laboratory evaluation of crushed glass-dredged material blends, J. Geotech. Geoenviron. Eng. 132 (5) (2006) pp.562–576.

[6] Ooi P., Li M., Sagario M., Song Y. Shear strength characteristics of recycled glass, Transp. Res. Rec.: J. Transp. Res. Board 2059 (2008) 52–62.

[7] Imteaz M.A., Ali M.Y., Arulrajah A., Possible environmental impacts of recycled glass used as a pavement base material, Waste Manage. Res. 30 (9) (2012) 917–921.

[8] Arulrajah A., Ali M., Disfani M., Piratheepan J., Bo M. Geotechnical performance of recycled glass-waste rock blends in footpath bases, J. Mater. Civ. Eng. 25 (5) (2012) 653–661.

[9] Davidovits J., Buzzi L., Rocher R., Gimeno D., Marini C.. & Tocco S., “Geopolymeric cenment based on low cost geologic material”, results from the European Researh project GEOCIS-TEM. In: Davidovits et al., editors., Proceedings of the second international conference gropolymere Vol. 99, 1999, pp.83-96.

[10] Palomo A., Grutzek M.W. & Blanco M.T., “Alkali-activated fly ashes. A cement for the future”, Cement and Concrete Research Vol.29, 1999, pp.1323-1329.

[11] Xie Z. & Yunping X., “Hardening mechanisms of an alkaline-activated class F fly ash”, Cement and Concrete Research Vol.31, 2001, pp.1245-1249.

[12] Chindaprasirt C., Chareerat T. & Sirivivatnanon V., “Workability and strength of coarse high calcium fly ash geopolymer” Cement and Concrete Composites, Vol.29, 2007, pp.224-229.

[13] Suksiripattanapong C., Horpibulsuk S., Chanprasert P., Sukmak P. & Arulrajah A., “Compressive strength development in fly ash geopolymer masonsy units manufactured from water treatment sludge”, Construction and Building Materials, 2015, Vol.82, pp.20-30.

[14] Horpibulsuk S., Suksiripattanapong C., Samingthong W., Rachan R. & Arulrajah A., “Durability against wet-dry cycles of water treatment sludge-fly ash geopolymer”, Journal of Materials in Civil Engineeing (2015)

[15] Posi, P., Teerachanwit, C., Tanutong, C., Limkamoltip, S., Lertnimoolchai, S., Sata, V., Chindaprasirt, P. “Lightweight geopolymer concrete containing aggregate from recycle lightweight block.” Materials and Design Vol.52, 2013, pp.580–586.

Sixth International Conference on Geotechnique, Construction Materials and Environment, Bangkok, Thailand, Nov. 14-16, 2016, ISBN: 978-4-9905958-6-9 C3051

FINITE ELEMENT SIMULATION OF EMBANKMENTS UTILIZING SMALL-SCALE CENTRIFUGAL DIMENSIONS

Ali Sobhanmanesh[1,2], Ramli Nazir[3], Tan Choy Soon[1] and Deprizon Syamsunur[1]
[1] Department of Civil Engineering, Faculty of Engineering, Technology and Built Environment, UCSI University, 56000, Kuala Lumpur, Malaysia;
[2] Process System Engineering Center, Faculty of Engineering, Technology and Built Environment, UCSI University, 56000, Kuala Lumpur, Malaysia
[3] Department of Geotechnics & Transportation, Faculty of Civil Engineering, University Teknologi Malaysia (UTM), Malaysia

ABSTRACT

Four different cases of unreinforced and reinforced embankment models constructed on soft and stiff grounds were studied. Small-scale physical modelling by means of centrifuge tests and numerical modelling by means of finite element simulations were performed. As the small-scale model was rotated in different acceleration fields during the centrifuge test, the dimensions of the centrifugal model were different from the original states of the prototype in different stages of the test. This paper focused on developing a finite element simulation based on the dimensions of a centrifugal model in different incremental acceleration fields applied during the stages of the test. Comparing the results of finite element simulations with the measurements of the centrifuge tests showed a good agreement between the two methods, which verified the reasonableness of the finite element models in analysis of embankments based on small-scale centrifugal dimensions. Moreover, The results showed the different deformation behaviour for embankments on soft and stiff grounds and indicated the significant effect of the geosyntheic reinforcement on increasing the stability of the embankment on soft ground.

Keywords: Finite Element Simulation, Centrifuge Test, Reinforced Embankment, geosynthetics

INTRODUCTION

The behaviour of geosynthetically-reinforced structures has been studied through observation of full-scale physical models by many researchers. However, The cost of construction and monitoring the full-scale embankment model is quite high and is a time consuming procedure with some limitations. Hence, an alternative method such as scaled-down modelling can be used. Although a small-scale model is relatively economical, in terms of finance and time, it is not reliable in predicting the actual prototype behavior due to the differences in stress levels surrounding the model and prototype respectively. For this reason the centrifugal modeling technique has become increasingly used as it has ability to reproduce the same stress levels in a small-scale dimension model as those present in a full-scale prototype. Centrifuge modeling also has some limitations, e.g. the prototype is under earth's gravity field where the radius of the earth is infinite compared to the prototype size. Thus the earth's gravitational field will act parallel and be uniform in direction at all points in the prototype. However in the centrifuge, since it has finite radius compared to the model size, the artificial gravitational field is radial, which is non-linear and non-uniform.

There are two methods of the staged-construction of a model in the centrifuge test: 1) constructing the model in flight using raining technique 2) applying incremental acceleration fields in different stages of construction on a pre-constructed model with constant dimensions. The first method results in more accurate results but needs more advanced fully equipped apparatus. However, due to the limitations, second method is also used commonly in many centrifuge tests.

A number of these centrifuge tests have been modelled by numerical approaches. In numerical simulation of centrifugal models, most of researchers have only utilized the full-scale prototype dimensions. [1]-[11]. It should be mentioned that using the second method, a centrifugal model has same dimensions and same stress levels only at the final stage (final acceleration field) of the test compare to the prototype, i.e. the centrifugal model has different dimensions and stress level in different acceleration fields before reaching the final stage. Therefore, a numerical simulation, which can consider these differences in dimensions and stress levels in varying acceleration fields of the centrifuge test, is very important and can consequence in more accurate results. Nevertheless, such simulations are rare and limited so far.

Therefore, the focus of this paper is to conduct a realistic numerical simulation of centrifugal models utilizing small-scale centrifugal model dimensions to consider exact procedure of a centrifuge test utilizing abovementioned factors, i.e. different dimensions and stress levels in different applying acceleration fields of the test. Comparing the results of theses numerical simulations with measurements of centrifugal models validates this numerical modelling technique.

EMBANKMENT MODEL CASES

In this research, four embankment models with different foundation soil and reinforcement condition were considered in both centrifugal and numerical modelling. Details of these cases are shown in Table 1. A plan view and cross section of embankment model used in both centrifuge and numerical modeling is shown in Fig. 1. The scaled-down embankment model has a height of 5 cm, a crest width of 14 cm and slope of 1V to 1H, underlain by 7 cm foundation soil. Due to inherent symmetry about the centerline, only one half of the model was considered.

Table 1 Details of four embankment cases

Case	Foundation	Fill material	Reinforcement
I	Kaolin	Claye sand	-
II	Kaolin	Claye sand	Textile
III	Sand	Claye sand	-
IV	Sand	Claye sand	Textile

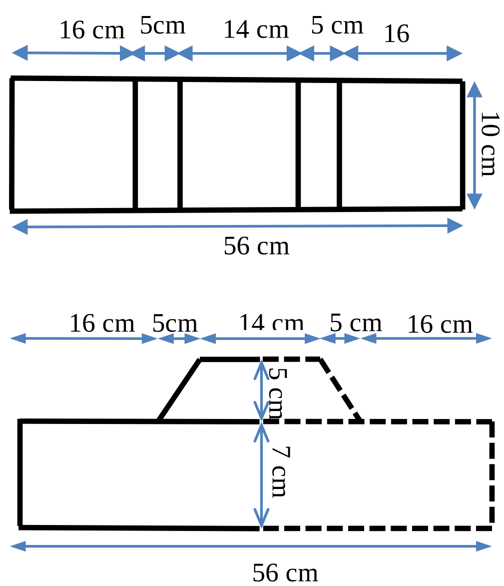

Fig. 1 Plan view and cross-section of embankment model

CENTRIFUGE TEST

Different centrifuge tests were conducted using a mini centrifuge apparatus of Universiti Kebangsaan Malaysia (UKM). It is a beam-type centrifuge, designed to allow centrifuge testing of soil package up to 6 kg with a maximum rotational speed of 500 rpm and can accelerate up to 140 g at an effective radius of 0.5 m [12].

Because of limitations and technical difficulties of UKM mini-centrifuge apparatus in constructing a shaped embankment in flight, the centrifuge model was constructed before the test running and incremental accelerations was applied to simulate staged-construction of centrifugal modeling. In this method, the acceleration increased slowly to reach the predefined level. The rotation was maintained in this specific acceleration level for a certain time, and then the acceleration increased to reach the next level. Details of centrifuge test processes are depicted in Table 2.

Table 2 Centrifuge test procedures

ω (rpm)	Gravity (g) $g = (1.18\times10^{-3})\times r^{*}\times(\omega)^{2}$	Maintained Time (minute)
130	10	5
184	20	5
225	30	5
260	40	15
291	50	30

FINITE ELEMENT MODELING

In this research, numerical modeling by means of finite element simulations were conducted using PLAXIS software, which is a powerful program in simulating and analyzing the geotechnical problems. Properties of materials used in the finite element analysis are shown in Table 3. These results are adopted from laboratory tests. The undarined shear strength (Su) of kaolin considered as 8 kPa, which was defined by a mini-vane shear test.

Table 3 Properties of materials in FE modeling

Parameters	ClayeySand	Sand	Kaolin
Material Model	MC	MC	MC
Behavior	Drained	Drained	Undrained
Unit weight (kN/m^3)	18	19	16
Permeability $K_x = K_y$ (m/day)	0.5	1	3×10^{-4}
Young's Modulus (kN/m^2)	6000	10000	1000
Poison's ratio ν	0.3	0.3	0.35
Cohesion(kN/m^2)	5	1	8
Friction angle φ	30	31	0

The standard fixities were used to define the boundary conditions, i.e. full fixity (rough rigid boundary) was assumed along the bottom of the model and the vertical boundaries of the model were fixed in the horizontal direction (smooth rigid boundary). Geogrid reinforcement was modeled as line elements with two translational degrees of freedom in each node (ux, uy). The only material property of the geogrids in 2-D simulation is an elastic normal (axial) stiffness EA determined from the curve of the elongation of the geogrids plotted against the applied force and is the ratio of the axial force per unit width to the axial strain. The interface elements are considered to model the interaction between reinforcement and soil. The roughness of the interaction is modeled by choosing a suitable value for the strength reduction factor in the interface (R_{inter}). Based on the direct shear tests carried on the interface of the soil and textile, the interfaces ratio between geotextile and soil was calculated as 0.95 for this study.

Simulation Procedure

Construction stages by means of plastic analysis and post-construction stages by means of consolidation analysis were utilized as PLAXIS allows for undrained, drained and consolidation analyses of two-dimensional plane strain or axisymmetric problems. The elastic perfectly plastic materials with consideration of Mohr–Coulomb failure criterion were utilized to model the behavior of the embankment and foundation materials for all cases; the reinforcement element was modeled as linear-elastic material model. Fig. 2 shows the generated mesh and the considered plate at centerline of the embankment to simulate the interaction between soil and side-wall of strong box.

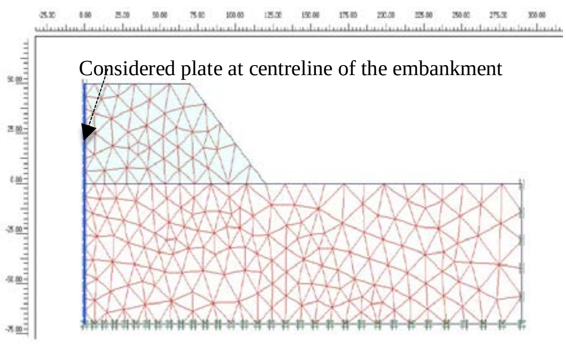

Fig. 2 generated mesh and boundary fixities

To consider varying dimensions of model due to the different acceleration fields of centrifugal tests, the FE modelling was performed based on the small-scale centrifugal model dimensions but under the accelerations more than earth gravitational acceleration (g).

In PLAXIS, the earth gravitational acceleration (g) can be simulated by considering the multiplier (Σ*Mweight)* equal to 1. Therefore, the process of varying incremental centrifugal accelerations was simulated in PLAXIS by considering different multiplier of Σ*Mweight* more than 1 related to different acceleration fields of centrifuge test (5 g, 10 g, 20 g, 30 g, 40 g, and 50 g) and also correspond to time period of rotation in that acceleration level as shown in Fig.3. Increasing the acceleration up to five levels of 10 g, 20 g, 30 g, 40 g, and 50 g simulated a five-staged construction of the embankment in centrifuge test. The five level accelerations corresponded to the construction heights of 0.5 m, 1 m, 1.5 m, 2 m, and 2.5 m, respectively, according to the law of similarity. After each staged construction, a rest period was considered in the centrifuge model that is almost equal to the 10 hours for thickness of 0.5 m, 1.0 day for thickness of 1 m, 3 day for thickness of 1.5 m, 16.5 days for thickness of 2.0 m, and 52 days for thickness of 2.5 m.

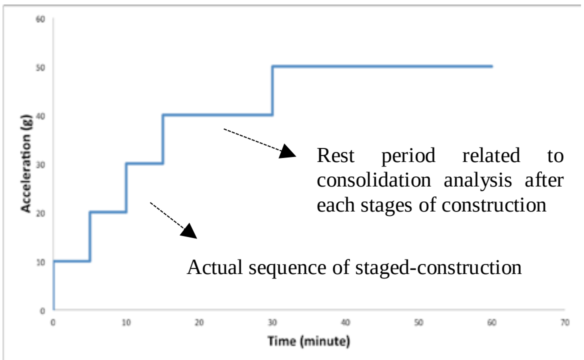

Fig. 3 Sequence staged-construction of model with varying acceleration fields

RESULTS AND DISCUSSION

The results of centrifuge tests and FE analyses for all cases are described in the following. A side-by side comparison between the FE results and centrifuge measurements are also depicted at the last section. Deformed mesh and shading of vertical displacements for different cases are shown in Figs. 4, 5 and 6. It is clear that vertical and horizontal displacements occurred at the embankment fill, beneath the fill and at toe of the embankment. For cases constructed on soft ground i.e. cases I & II (refer to Table 1), slight heave and uplift occurred at the embankment toe and ground surface beyond the toe due to the undrained behaviour of subsoil layers. The extreme total displacements occurred at topside of the fill slope at embankment crest. The maximum displacement of case II at topside of fill slope of embankment computed as 3.1 mm, which reduced about 24.4% compare to the displacements of the unreinforced model (4.1 mm for case I). The uplift of the embankment toe was also decreased significantly compare to case I. This shows the effect of the geotextile reinforcement on increasing the stability and reducing the deformations of the embankment constructed on soft ground.

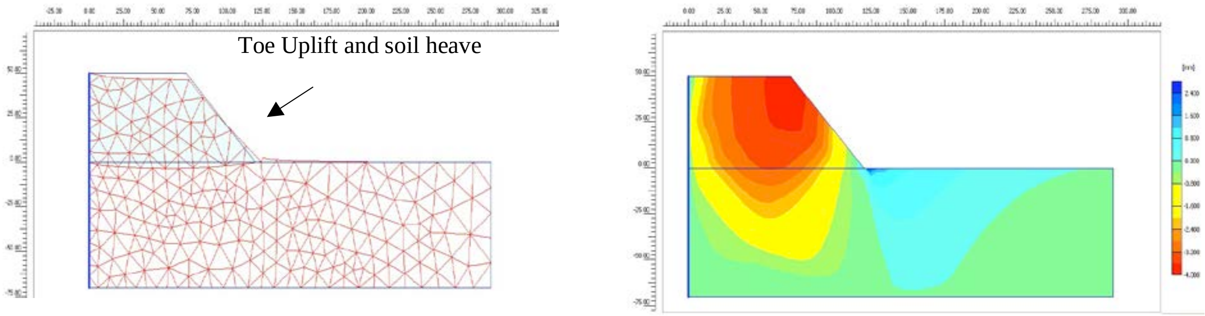

Fig. 4 (a) Deformed mesh (b) vertical displacements (case I)

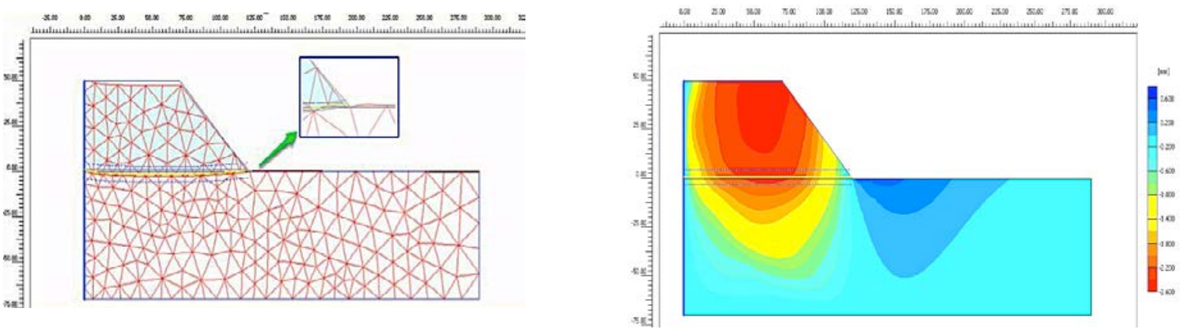

Fig. 5 Deformed mesh (b) vertical displacements (Case II)

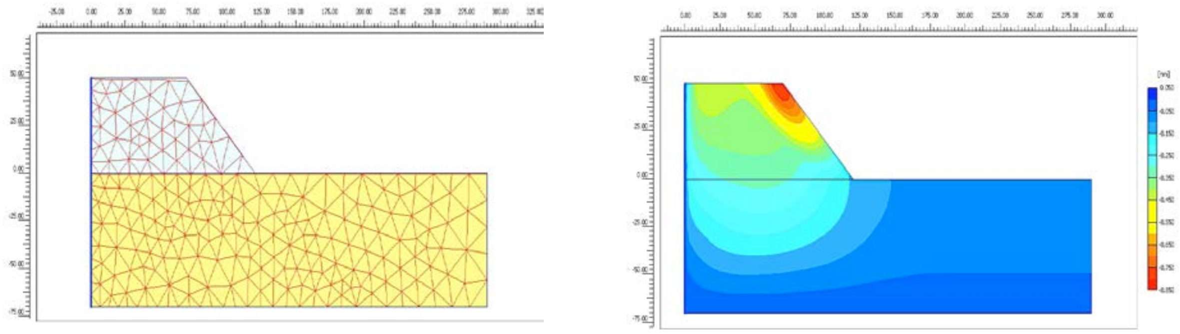

Fig. 6 Deformed mesh (b) vertical displacements (Case III)

For cases constructed on stiff ground (cases III & IV), there was not any considerable difference in deformations and displacements of unreinforced and reinforced models. It indicated that the geosynthetic reinforcement have small influence on deformation behaviour of embankments on stiff ground because of small induced vertical displacements and lateral movements.

Comparison Between the Results of the Finite Element and Centrifuge Modelling

A side-by-side comparisons between the deformation patterns resulted from the measurements of centrifuge tests and analysis of finite element simulations for four different cases are shown in Fig. 7. It is clear that the deformation patterns of the centrifugal model test and finite element simulation are almost similar for all cases, which validates the simulation of centrifugal model tests, using finite element simulation, based on small-scale modelling procedure.

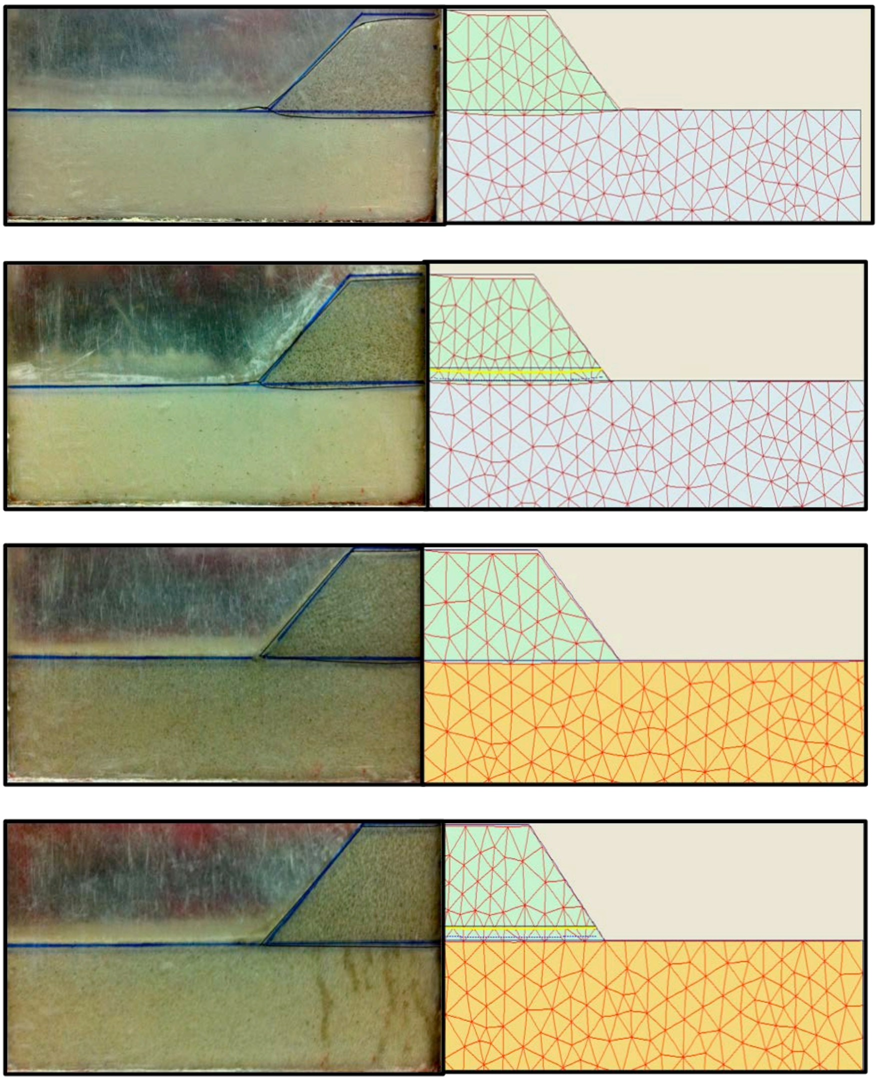

Fig. 7 Side-by side comparison of the deformation patterns resulted from centrifuge and FE models a) Case I, b) Case II, c) Case III, d) case IV

A comparison between resulted vertical displacements of the centrifuge test and FE analysis for all cases are shown in Fig. 8. Moreover, the maximum vertical displacement obtained from centrifuge test and FE analysis is presented in Table 4. The coincidence of the lines correspond to centrifuge tests and FE analysis for each case in Fig. 8 and results of Table 4 indicates a good agreement between displacements obtained from these two methods of modelling.

CONCLUSIONS AND SUMMARY

Small-scale physical modeling and numerical analysis of different embankment cases have been carried out using centrifugal test and finite element simulations. Important affective factors have been studied to provide a better understanding and deeper insight of the embankment behavior under different conditions. In reinforced embankments, the tension mobilized in the reinforcement can be very effective in improving the short-term stability of the embankment. The tension in the reinforcement is sensitive to the magnitude and distribution of shear strength of clay foundation. Basal reinforcement of the embankment using geotextile resulted in reduction of the displacements up to 25% and leads to construction of higher fill embankment or steeper slope. Under a relatively small deformation, however, the influence of interfaces behavior of geosynthetic reinforcement and soil on the system performance is expected to be less important as observed in cases on stiff ground (Cases III and IV).

Finite element simulations are successful in predicting the overall behavior of unreinforced and reinforced embankments. The results of FE simulation using full-scale prototype dimensions can have some differences with centrifuge measurements. However, FE simulations using small-scale centrifuge dimensions and actual conditions of test with considering affective parameters (e.g. varying gravitational acceleration level, side-wall friction and small boundary condition), minimizes the differences between FE predictions and centrifugal measurements. It is shown a good agreement between results of these two methods, which validates the finite element simulation.

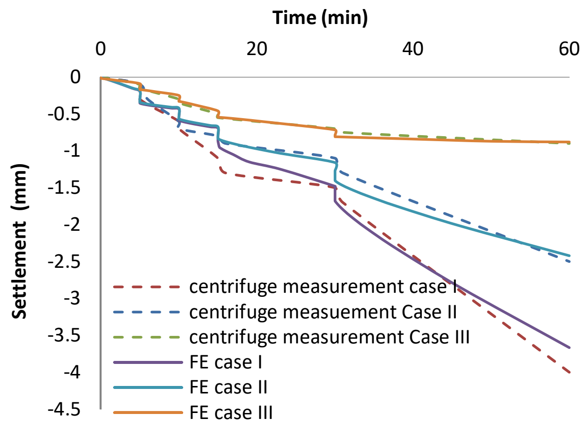

Fig. 8 vertical displacement of different cases from centrifuge test and FE analysis

Table 4 Maximum settlements resulted from centrifuge test and FE analysis

Cases	Centrifuge Test	FE analysis
Case I	4 mm	4.10 mm
Case II	3 mm	3.10 mm
Case III	1 mm	1.0 mm
Case IV	1 mm	1.0 mm

The effect of side friction between soil and sidewall on deformation behavior can be significant on the deformation pattern and behavior of models. Efforts should be made in the centrifuge work to minimize the effects of side friction by using some materials like silicon grease to reduce the friction.

ACKNOWLEDGMENT

The first author would like to thank the faculty of Science and Technology, Universiti Kebangsaan Malaysia (UKM) for providing centrifugal facilities.

REFERENCES

[1] Ding, J. H. and Bao, C. G., “Centrifugal model test and finite element analysis of geosynthetic-reinforced embankments on soft ground and dredger fill”, China Civil Eng Journal, 1999.

[2] Sharma, J. and Bolton, M. D., “Centrifugal and numerical modelling of reinforced embankments on soft clay installed with wick drains”, Geotextiles and Geomembranes, 19 (1), 2001, pp. 23–44.

[3] Hu, H. R., Chen, S. L. and Shen, Z. L., “Centrifugal & numerical modeling of geosynthetic reinforced embankments on soft clay”, Rock and Soil Mechanics, 24 (3), 2003, pp. 389–394.

[4] Wang, H. and Huang, X, “Centrifuge Model Test and Numerical Analysis of Embankment Widening on Soft Ground”, ASCE. In: Eighth International Conference on Applications of Advanced Technologies in Transportation Engineering (AATTE), 2004, Beijing, pp. 548–553.

[5] Jiang, X., Qiu, Y. J. and Wei, Y. X., “Engineering behavior of subgrade embankments on sloped weak ground based on strength reduction FEM”, Chinese Journal of Geotechnical Engineering, 29 (4), 2007, pp. 618–625.

[6] Chen, J.-F. and Yu, S.-B., “Centrifugal and Numerical Modeling of a Reinforced Lime-Stabilized Soil Embankment on Soft Clay with Wick Drains”, International Journal of Geomechanics, 11 (3), 2011, pp. 167–173.

[7] Zhang, J., Zheng, J. and Huang, X., “Centrifuge Model Test and Numerical Analysis of Geosynthetic-Reinforced Embankments for a Road Widening”, Road Pavement and Material Characterization, Modeling, and Maintenance, ASCE, (213), 2011, pp. 204–210.

[8] Chen, J.-F. and Yu, S.-B., “Centrifugal and Numerical Modeling of a Reinforced Lime-Stabilized Soil Embankment on Soft Clay with Wick Drains”, International Journal of Geomechanics, 11 (3), 2011, pp. 167–173.

[9] Li, B., Yu, W., Gong, B. and Cheng, Z., “Centrifugal and numerical modeling of high and steep geosynthetic-reinforced slopes”. In Proc. Geo-Congress 2013, ASCE, 2013, pp. 482–488.

[10] Mohamed, S. B., Yang, K. H. and Hung, W.Y., “Finite element analyses of two-tier geosynthetic-reinforced soil walls: Comparison involving centrifuge tests and limit equilibrium results”, Computers and Geotechnics, 61, Elsevier Ltd, 2014, pp. 67–84.

[11] Zhang, J., Cen, G., Zhou, C. and Ouyang, Y., “Centrifuge Model Test and Numerical Analysis of Properties of a Soft Foundation with an Upper Crust”, The Electronic Journal of Geotechnical Engineering (EJGE), (19) 2014, pp. 17195–17208.

[12] Sobhanmanesh, A., Ramli, N. and Gofar, N., “3D Numerical Analysis of centrifuge tests on embankments on soft and stiff ground”, Advanced Materials Research”, (831), 2014, pp. 314-320.

BEHAVIOR OF ACCIDENTAL CASES OF TBM SEGMENTAL LINING

Mostafa Zaki[1], Ahmed Hassan[2], and Mostafa Asaad[3]
[1,2] Faculty of Engineering, Minia University, Egypt; [3] NAT, Egypt

ABSTRACT

This research aims to study the behavior of segmental lining at accidental cases. To achieve this goal, first a short study is performed to develop an appropriate model for simulating segmental lining components. Then a comprehensive study is introduced for the effect of parameters which may lead to excavation failure. Investigation includes deformation and plastic zones generation, around tunnel segments and connecting bolts for different cases during construction. Consequently better understanding is possible for the interaction between different segmental lining components and the annular grout. It is concluded that installation of bolts is very important during the construction of lining and should be carefully handled. If more than one bolt isn't installed during the construction of the ring, ring failure may happen. Excessive grout concentrated at some rings has destructive effect on the ring and may lead to collapse of ring. Consequently this situation should be totally avoided during the construction of TBM segmental lining.

Keywords: Tunnels excavation; lining components; safety limits; accidental cases

INTRODUCTION

Mechanized tunnelling has speedily spread worldwide for tunnels excavation due to high safety degree and high speed rate of work. If an accidental case happens during construction, the consequences for time, cost, and human losses are significantly high. To reduce this risk, the interaction between lining components with grout and surrounding soil should be comprehensively understood. The aim of studying the nonlinear behavior of TBM segmental lining is to predict its behavior in accidental cases. Generally the structural design model should yield criteria related to failure cases, against which the tunnel should be designed safely [6].

This paper focuses on studying the behavior of segmental lining to avoid any possible failure of the lining. Furthermore if the previous goal wouldn't be possible in some cases, at least it will be possible to reduce the time of the delay consumed to investigate the reasons of failure and to overcome them. Firstly a suggested technique is developed to simulate the TBM segmental lining. In this technique the important components of TBM segmental lining (segments, joints, and bolts) are simulated by their own properties. Two possible accidental cases for failure are studied in this study. First case focuses on studying the effect of not installing some or all bolts on the stability of the ring during construction. The second case is concerned with effect of excessive grout concentrated in certain segments on the stability of the model.

SOIL MODELLING

During the construction of lining and before the hardening of the grout, there is no direct interaction between the lining and the soil. This case is considered critical during tunnel construction as most failure cases happen during it. Hence, it is reasonable to model soil confinement by series of springs. Simulation of soil as springs will help to more focus on the local behavior of the lining during construction.

Stiffness of Springs

The springs' stiffness was calculated using linear load deformation relationship according to Duddeck and Erdman [1], [2], [7] and [8].

$$E_c = \frac{E(1-\nu)}{(1+\nu)(1-2\nu)} \quad (1)$$

$$C_r = \frac{E_C}{R} \quad (2)$$

$$K = C_r \, A \quad (3)$$

Where:
E, ν = Young's Modulus and Poisson's ratio of soil,
R = equivalent tunnel radius,

A = area of soil to be represented by the equivalent radial spring. This is distance between adjacent radial springs multiplied by unit length.

Spring constants is determined based on tributary projections on the X and Y axis of each joint [12]. It worth mentioning that ground behavior in tangential direction is generally ignored in beam spring model method. Although this leads to frictionless sliding of the lining against the ground, it has a negligible effect on member forces [3].

FEM MODEL

A three-dimensional FEM model was used to perform the analyses. The FEM software package Midas GTS [9] was used in this research. Fig. 1 shows segmental lining simulation. Segments joints simulation is shown in Fig. 2. Since the purpose of this paper is to study the local behavior of segmental lining, 3-D simulation will be used. Consequently it will be possible to accurately simulate and study the behavior of each component of TBM segmental lining. In this approach, all elements of segmental lining are modelled with solid elements

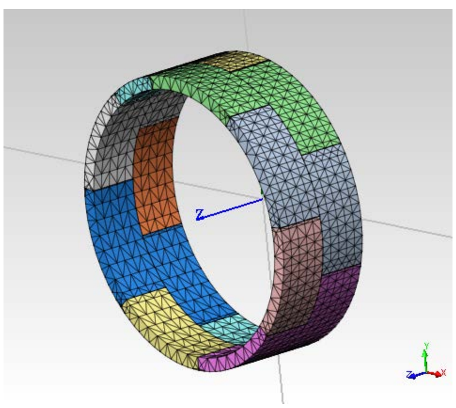

Fig. 1 Numerical simulation of segmental lining.

Model Parameters

Data for the model considered in this research is taken from the accident of Cairo metro Line 3 Phase 1, at tunnel section between Bab El-Sharia and El-Giesh stations [10]. Fig. 3 shows the zone of failure in red in the clouded area. diameter is 8.0 m eight segments of thickness 0.4 m and length 1.5 m were used. The used bolts 300 m length and 28 mm diameter. Model parameters are shown in Table 1.

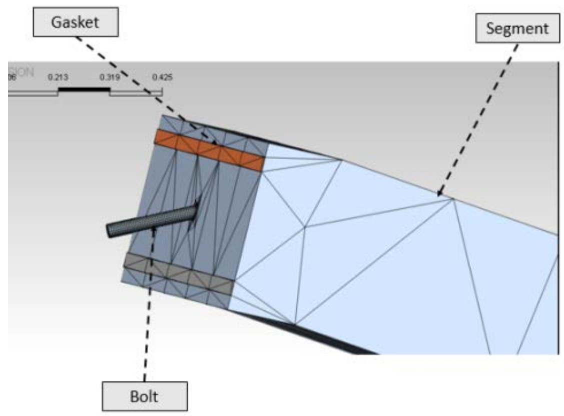

Fig. 2 Simulation of segments joints.

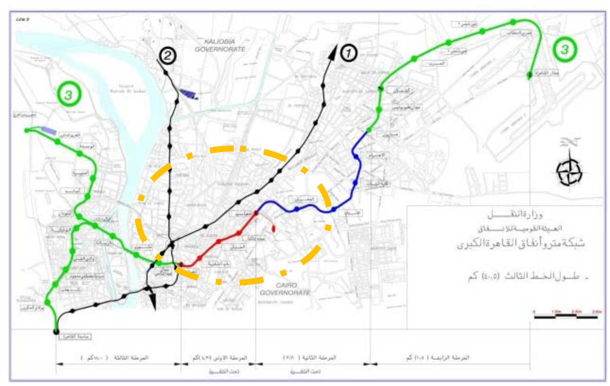

Fig. 3 Map showing the route of Cairo Metro Line 3.

Table 1 Parameters of different materials used in the analysis

Parameter	Segments (Concrete)	Grout	Bolts
Initial Tangent Elastic Modulus (E) MPa	30000	100 to 2000	210000
Poisson's Ratio (ν)	0.2	0.4	0.3
Density kg/m^3	2600	-	8030
Unconfined Compressive Strength(fcu) MPa	60	-	-
Initial Yield Stress (σy) MPa	48	-	350
Tensile failure stress MPa	4	-	800
Type of Selected Element	Solid Element	Solid Elem	Solid Elem
Model Behavior	Drucker Prager	Mohr Coulomb	Von Mises

NORMAL CONSTRUCTION CASE

The first considered case is for normal construction condition, where no accidental cases occurred during construction. This model is used to check the value of deflection and to check any local plastic points occurred in the model in ordinary cases. Three load cases are considered in this category. In the first case, lining and grout layer are activated but the modules of elasticity of the grout is very small. This situation doesn't allow direct contact between the lining and the soil. In the second case, only the load of the grout and the own weight of lining and grout are activated. The soil load is not applied because there is still a gap between the lining and the soil. The gap is filled with grout but in this case the grout is too week to transfer the loads. In the third case the modulus of elasticity of the grout is increased to its maximum value in Table 1 which is the final value after hardening. In the same time the connecting bolts are removed from the ring. This case aims to study the possibility of removing the connecting bolts after hardening of the grout around the ring.

Analysis of Results

As shown in fig. (4-7), the deflection at crown of tunnel after construction of ring 2 is 21mm after ring construction, where the bolts are installed. No plastic zones generated around the segments except a very local plastic zones generated around bolts. Due to the high tensile forces in bolts, bolts got deformed and plastic zones generated on the bolts. The settlement slightly increases if bolts removed after hardening of grout, the increase is very small. Whereas, no plastic concentration occurs after removing bolts. As a conclusion, after the hardening of grout there is no need for bolts and can be safely removed from the ring.

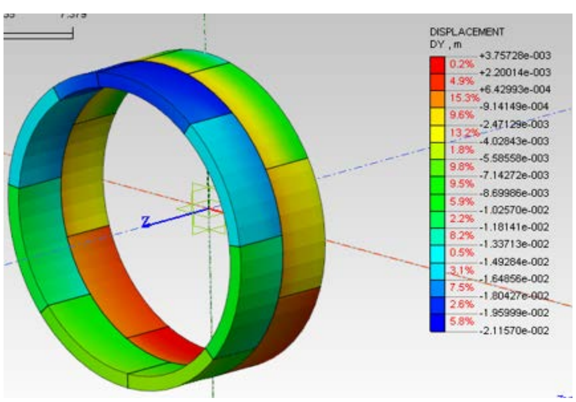

Fig. 4 Vertical deformation after construction of ring.

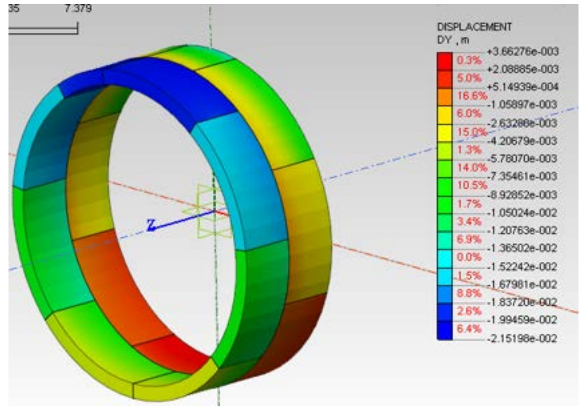

Fig. 5 Vertical deformation after hardening of grout and removing bolts.

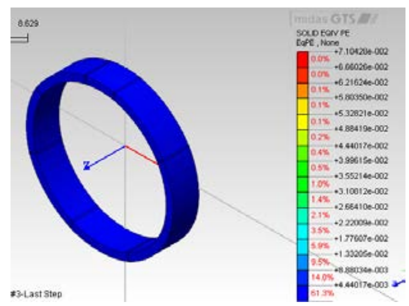

Fig. 6 Distribution of plastic zones after hardening of grout and removing bolts.

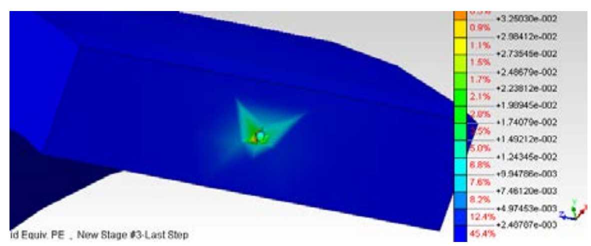

Fig. 7 Plastic zones in the area of segment around connecting bolt.

EFFECT OF BOLTS–A PARAMETRIC STUDY

During the erection of rings, sometimes TBM machine crew does not erect some or all bolts between the segments. This could happen by mistake or intentionally to reduce the consuming time or cost. Erection of bolts has great effect on the stability of rings during construction of rings until the hardening of the surrounding grout layer. In this section, the effect of not installing some or all bolts during construction of the ring is investigated and examine to which extent this case could lead to collapse of the ring.

The same load cases used in the previous section are applied (The normal construction case). Number of bolts in the ring are 8 bolts, one bolt for each joint as shown in Fig. 8. In each analysis a number of bolts are not activated.

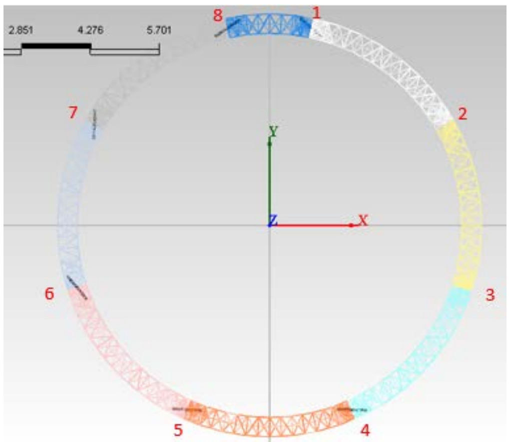

Fig. 8 Numbering and orientation of bolts/joints.

Analysis Results

As shown in Fig. 9, longitudinal bolts have great effect in the stability of the segmental lining during construction. Even if one bolt only is not activated, the value of crown deflection increases by percentage of 39% of the normal case. Fig. 10 shows plastic zones at Bolt No. 8 when only one bolt is not installed.

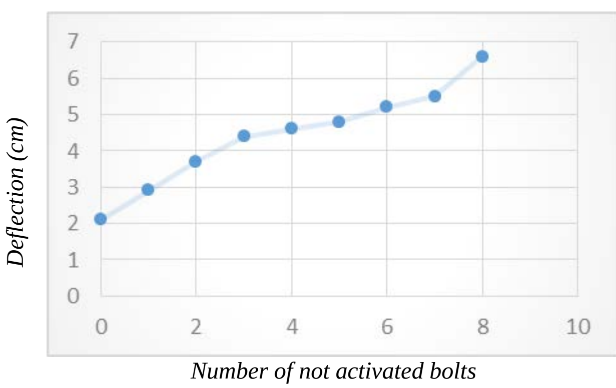

Fig. 9 Value of crown deformation versus the number of not activated bolts.

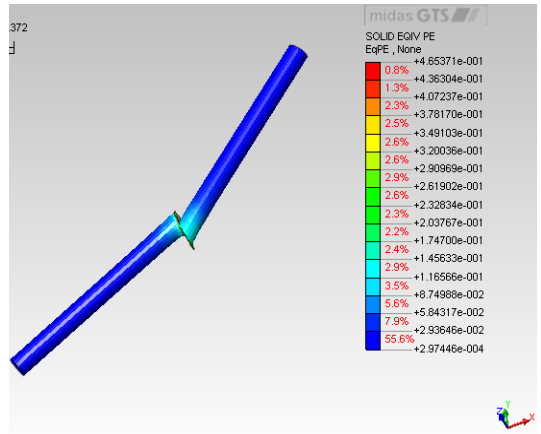

Fig. 10 Distribution of plastic zones at bolt No. 8 for not activating 1 bolt.

EFFECT OF EXCESSIVE GROUT ON RING STABILITY

Grouting are used to fill the annular void between the segmental lining and surrounding ground. The interaction between machine, lining and the grout is very important. Attention should be paid to avoid excessive grout which causes destructive effect on lining. Excessive grout could be generated from two possible ways:

After grouting the lining, grouting volume will settle, opining a gap on the upper part of cross section. In this case more grouting is required to fill this gap, this grouting called secondary grouting. Secondary grouting is usually undertaken within 20m of the last ring built. It may cause destructive effect if its value overestimated, which makes it concentrated by large value in certain segments [11].

The other possible source of excessive grout comes from the fact that grout pushed into the annular void between lining and ground through nozzle. If some nozzles got clogged the grout around lining will be redistributed and will be concentrated around certain segments.

Two cases will be studied as follows:

1- Uniform excessive grout around the whole ring.
2- Excessive grout in some segments.

The study will consider increase in grout by value start from 10% of original value to 100% of the original value.

Analysis of Results

As shown in Fig. 12, the main damage effect on ring from excessive grout will happened in case of some segments only have excessive grout. As long as the excessive grout value increases the deflection will increase until the failure case.

From the distribution of plastic zones shown in Fig. (13-15), it is clear that in all accidental cases any failure or plasticity zones generated first in bolts at the joint between segments until failure. This leads to the following suggestions:

1- Using nonlinear criteria for modeling concrete segmental lining have small importance, since most of expected failure will occur at joints.

2- It is better to use two bolts between each two segments to face any unexpected accidental cases, and reduce the risk of accidental cases on segments.

Effect of excessive grout in certain segments is very destructive and one of major reasons which may cause failure.The required grout pressure value should be carefully calculated and grout injection process should be carefully performed under careful supervision to prevent any excessive pressure generated on segments.

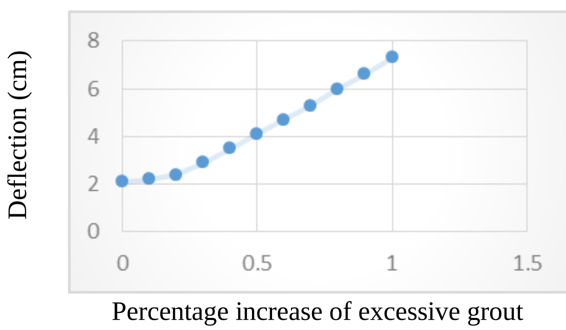

Fig. 12 Value of crown deformation versus the value of excessive grout.

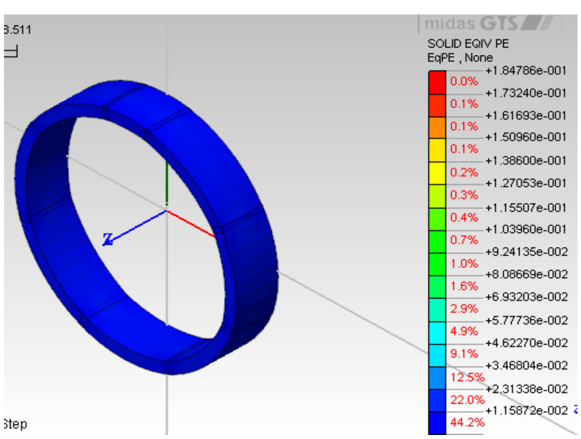

Fig. 13 Distribution of plastic zones at segments for uniform excessive grout at all segments by 100%

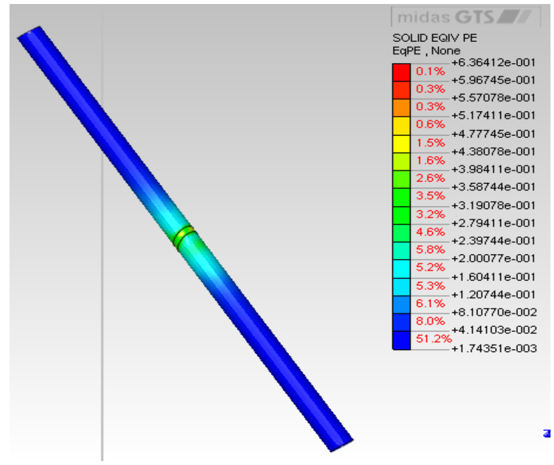

Fig. 14 Distribution of plastic zones at bolts for uniform excessive grout at all segments by 100%

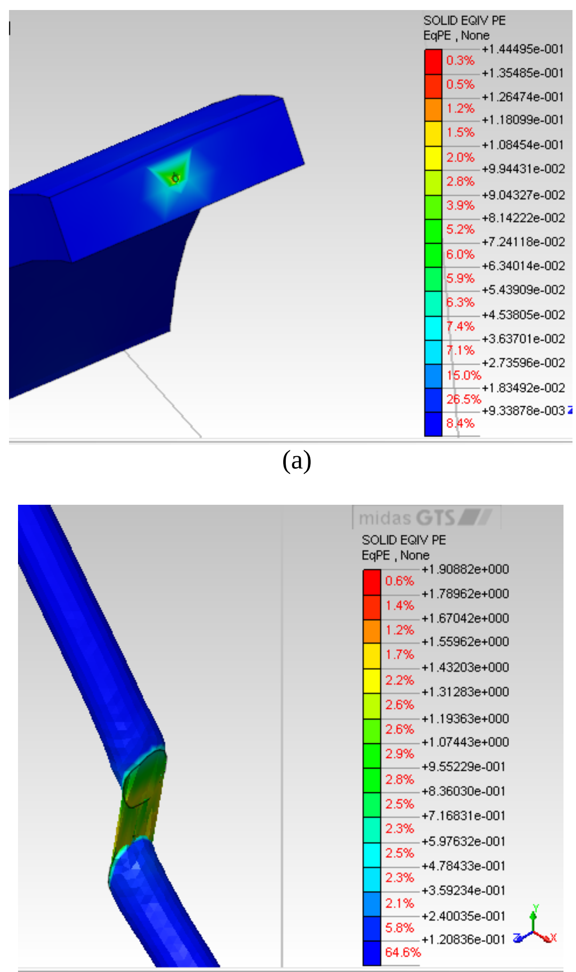

(a)

(b)

Fig. 15 Distribution of plastic zones for excessive grout by 100% value at one segment:

(a) At the edges of segments, (b) At bolt.

CONCLUSIONS

Several cases have been investigated to study the behavior of TBM segmental lining at accidental cases during construction. From these cases the following conclusions may be drawn:

- After ring construction, where the bolts installed, no plastic zones generated around the segments except very local plastic zones generated around bolts.
- In normal cases and due to the tensile forces in bolts, bolts got deformed and plastic zones generated on them.
- The settlement slightly increases if bolts removed after hardening of grout, the increase is very small, whereas, no plastic concentration occurs after removing bolts.
- After the hardening of grout there is no need for bolts and it can be safely removed from ring.
- Installation of bolts is very important during the construction of lining and should be carefully handled.
- If more than one bolt isn't installed during construction of the ring, this could lead to ring failure.
- Excessive grout concentrated at some rings has destructive effect on the ring. This situation could lead to collapse of ring. Consequently this situation should be avoided during construction of TBM segmental lining.
- Uniform excessive grout around the whole ring have small effect on the stability of ring. Especially in cases where the value of excessive grout is small. Noting that, the case of uniform excessive grout is rarely happened and normally the excessive grout concentrated in certain segments.
- From the distribution of plastic zones shown earlier, it is notable that in all accidental cases, any failure or plasticity zones generated first in bolts at the joint between segments. Consequently it is better to use two bolts between each successive segments to minimize any unexpected accidental cases.

REFERENCES

[1] Duddeck H., Erdmann J., "Structural design models for tunnels", Scribd wbsite 2012, Universitat Braunschweig, Germany, 1982.

[2] Gruebl F., "Segmental ring design (New challenges with high tunnel diameters)", World Tunnel Congress 2012, Bangkok, Thailand, Tunnelling and Underground Space for a Global Society, 20 / 23 May 2012.

[3] Güray A., "Evaluation of structural analysis methods used for the design of TBM segmental linings", Post Graduate Ms. Thesis, The Graduate School of Natural and Applied Sciences of Middle East Technical University, Turkey, 2010.

[4] Hinchberger S.D., Ahn T., Lo K.Y., "Investigation of segmental concrete tunnel liner joint stiffness", World Tunnel Congress and 36th General Assembly, Vancouver, Canada, ITA-AITES, 17 and 19 May, 2010.

[5] ITA WG2 on General Approaches to the Design of Tunnels, "Guidelines for the design of shield tunnel lining", International Tunnelling Association, Working Group No. 2, Research, 2000.

[6] ITA WG2 on General Approaches to the Design of Tunnels, "Guidelines for the design of tunnels second report", International Tunnelling Association, Working Group No. 2, Research, 1988.

[7] JSCE, "Japanese standard for shield tunnelling, Japan Society of Civil Engineers", The fourth edition, Tokyo, 2000, English translation 2007.

[8] Mahajan R., "3 Dimensional Structural Modelling of Segmental Tunnel Lining", Australian Tunnelling Society (ATS) Journal, October 2010.

[9] MIDAS, MIDAS GTS NX V3.0.0 (4), MIDAS GTS Manual, MIDAS Information Technology Co., Ltd, Gyeonggido, Korea.

[10] NAT, National Authority for Tunnels. Greater Cairo Metro Line III, Project Documents, Cairo, Egypt, 2009.

[11] Toan N. D., "TBM and lining, essential interfaces", Post Graduate Ms. Thesis, Politecnico Di Torino, 2006.

[12] U.S Department of transportation – Federal Highway administration (U.S.A), "Technical manual for design and construction of road tunnels", Civil Elements, Publication No. FHWA-NHI-, December 2009, Pp. 10-34.

EFFECT OF THICKNESS ACOUSTIC PANELS UTILIZING COCONUT COIR

D.Salinah[1], M.T.Fadzlita[1] , G.Habibah[1] , L.Janice Ayog[1], A.Adriana[1] and A.Hassanel[1]
[1]Faculty of Engineering, University Malaysia Sabah, Malaysia

ABSTRACT

This research was carried out to study the effect of thickness acoustic panels of coconut coir to its acoustic properties. The acoustic panels were tested for its acoustical properties to determine its acoustical performance and characteristics. The coconut coir was tested with thickness of 10 mm, 20 mm, 30 mm and 40 mm with a constant area of 6 m^2. Two types of test were conducted toward the specimens, which are, the stimulation test using the WinFLAG^{TM} and the reverberation room experimental test. The stimulation is used to predict the result of the sound absorption coefficient in the reverberation room. All specimens were tested at the acoustic laboratory of Faculty of Engineering University Malaysia Sabah accordance to ISO 354 (1985) standard for noise absorption coefficients at frequencies of 125 Hz, 250 Hz, 500 Hz, 1000 Hz, 2000 Hz and 4000 Hz. The result shows that coconut coir has better sound absorbing quality than fiberglass for low frequency at 500 Hz and below. Hence, coconut coir has high potential to be applied as sound absorbing material.

Keywords: Acoustic; Thickness; Coconut coir; Sound absorption coefficient.

INTRODUCTION

Sound absorption panels are panels design and used for the purpose of absorbing sound as noise control. Generally, noise control is critical aspect in any structural and civil engineering designs. Acoustical appliances which in this case sound absorbing acoustic panel, synthetic fiber-based material such as rock wool and fiberglass are widely used as sound absorbent in acoustic panels. The problem with these acoustic panel material are its health hazard issues if exposed in long period. For fiberglass and other synthetic-fiber based materials, there are growing concerns related to health and safety issues due to the potential health hazards these materials possess. The shredding of these materials can be detrimental to the health when exposed to the eyes or lungs for instance when their fibers are inhaled, since they can lay down in the lung alveoli. In addition, they can cause skin irritation [1].

This give opportunity for alternative materials from organic fibers to be developed as a replacement materials for producing sound absorbing panels. Thus, many research have been carried out to discovered potential usage of new materials for sound absorption panel. Many researches focused on use of natural fiber due to its advantages in sense of cost, abundant and no risk in health and safety [2]-[8].

Natural fibers such as oil palm fiber, coconut coir, wood husk and paddy husk have a common characteristic that is crucial for acoustical appliances which is, they all have porous surface. This characteristic, enable them to be used in acoustical appliances such as acoustic panels where they could absorb and insulate sound that propagates at them[9]. Previous researches discovered that coconut coir fibers have a good potential as sound absorbing panel as it have a good sound absorbing properties for a wide frequency range [10]-[12].

Many previous researches have been made in the studies of the effect of material thickness to the quality of absorption of the material. Everest [13] states that, for the lower frequencies it is logical to expect greater sound absorption from thicker materials. Meanwhile, higher frequency has inverse effect of declining absorption coefficient with increasing thickness of materials.

Thus, it is a fact that this research will bring benefit to various people. It is a necessity to fully utilize the natural fibers to replace the used of synthetic fiber glass that are non- environmental and health friendly. Furthermore, there is a lack of a comprehensive, validate and easily accessible database on effect of thickness on coconut coir fiber panel to its acoustic performance and charactericticsas related to its structural applications. Therefore, the aim of this research is to study the potential use of coconut coir fiber as sound absorption panel and the effect of thickness on sound absorption coefficient of acoustic panel was also studied.

EXPERIMENTAL DETAILS

Materials

Two types of sample were tested to determine their sound absorption coefficient which is glass fiber and coconut coir fiber. Readily made glass fiber of 1 m^2 size each, obtained from Acoustic Laboratory, Faculty of Engineering. Coconut coir fiber of 1 m^2 size each is obtained from coconut coir manufacturing company with different thickness. The coconut coir fiber mat sample was ordered from a local coconut coir manufacturer that produces the fiber for furniture appliances. The coconut coir mats dimension is approximately 1 m in length and 1 m in width. In this research, the effect of thickness to the sound absorption coefficient were studied. The coconut coir was tested with thickness of 10 mm, 20 mm, 30 mm and 40 mm with a constant area of 6 m^2. The total weight of the specimen is approximately 10.5 kg and the density is approximately 108.03 kg/m^3. In this research, the type of fiberglass used is Woven fiberglass Type T, which is used for commercialized thermal and sound insulation material. The fiberglass was tested to determine its sound absorption coefficient which then compared with coconut coir fiber.

Fig. 1 Coconut coir test specimen.

Fig. 2 Woven Fiberglass mat Type T.

Test Conditions

Test was conducted by reverberation room method and simulation using WinFLAG^{TM}. In this research, coconut coir fiber will be used as sound absorbing material. The area of the test specimen is approximately 6m^2 which covers 20% of the total area of the reverberation room floor. The areas of the test specimen were constant for every test. The only parameters that were manipulated are the thickness of the test specimen. Series of random noise with different frequencies were used in the test. The absorption of the reverberation room is measured as outlined in both before and after placing a specimen of material to be tested in the room. The increase in absorption is divided by the area of the test specimen to obtain the dimensionless sound absorption coefficient. Sound absorption coefficients for the panels to be tested were determined by reverberation room method accordance to ASTM C423-02a (Standard Test Method for Sound Absorption Coefficients by the Reverberation Room Method) and ISO 354. The overall internal working dimensions of the room were 7150 mm length, 4100 mm width, and 5150 mm height. The working volume of the room, V is approximately 151 m^3. Measurement, analyzing and calculation of reverberation time and value of sound absorption coefficient were done using dBBATI32 software developed by dB STELL. In this research, WinFLAG^{TM} was used to simulate and calculates sound absorption coefficient of porous absorber. The result of this simulation was then compared to the result obtained from reverberation room method.

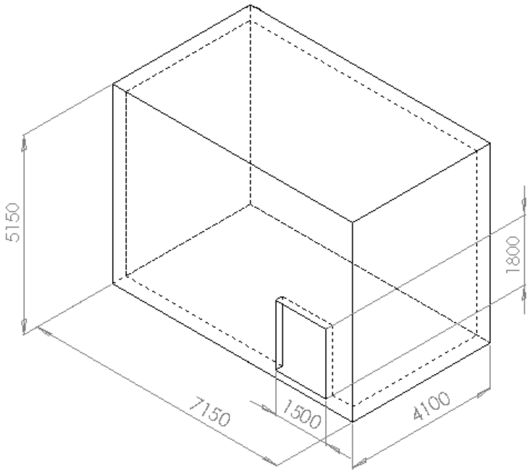

Fig. 3 Schematic and dimension of the reverberation room without test specimen.

Fig. 4 Reverberation room with 20 mm thickness 6 m^2 area of coconut coir fiber.

Fig. 5 Reverberation room with 20 mm thickness 6 m^2 area of fiberglass

RESULT AND DISCUSSION

The result consisted of stimulation data and experimental data. The stimulation data were obtained through the use of WinFLAG^{TM}. Table 1 and 2 show the stimulation (S) and experimental (E) test result obtained for coconut coir panel and fiberglass.

Comparison of Sound Absorption Characteristic between Fiberglass and Coconut Coir Fiber

Table 1 Stimulation and experimental results for Fiberglass and coconut coir fiber panel sample

f (Hz)	Sound Absorption Coefficient, α	
	Fiberglass	
	Stimulation	Experimental
125	0.04	0.06
250	0.19	0.11
500	0.51	0.56
1000	0.68	0.82
2000	0.75	0.77
4000	0.84	0.61
	Coconut Coir Fiber	
	Stimulation	Experimental
125	0.08	0.10
250	0.26	0.15
500	0.53	0.42
1000	0.67	0.72
2000	0.71	0.66
4000	0.78	0.51

Table 2 Stimulation and experimental results for coconut coir fiber panel sample - Different Thickness

f (Hz)	Sound Absorption Coefficient, α			
	10 mm		20 mm	
	S	E	S	E
125	0.04	0.05	0.06	0.10
250	0.12	0.10	0.26	0.15
500	0.28	0.34	0.53	0.42
1000	0.44	0.65	0.67	0.72
2000	0.53	0.68	0.71	0.66
4000	0.62	0.52	0.78	0.51
	30 mm		40 mm	
	S	E	S	E
125	0.13	0.16	0.19	0.27
250	0.41	0.28	0.57	0.41
500	0.73	0.58	0.87	0.69
1000	0.78	0.75	0.85	0.81
2000	0.80	0.63	0.86	0.62
4000	0.85	0.49	0.90	0.51

Table 1 shows that at low frequency range from 0 to 500Hz, sound absorption coefficient value for both material increases linearly. The pattern indicates that for low frequency of 125 Hz, 250 Hz, and 500 Hz, coconut coir fiber have better sound absorption coefficient than fiberglass. For higher frequency of 1000 Hz, sound absorption coefficient, α for fiberglass increase to 0.68 which is higher than coconut coir fiber with sound absorption coefficient, α of 0.67. Fiberglass reaches it maximum sound absorption coefficient, α at 4000 Hz with value of 0.84 and coconut coir fiber with maximum of 0.78 at 4000 Hz.

Clearly that for low frequency of 250 Hz and below, sound absorption coefficient, α for coconut coir fiber is higher than fiberglass, but for higher frequency of 500 Hz until 4000 Hz, fiberglass have higher sound absorption coefficient, α than coconut coir fiber. From the relation of $\lambda = C/f$ where f is frequency, λ is wavelength, and C is speed of sound which is 3.00×10^8 m/s it can be deduce that low frequency have longer wavelength. With longer wavelength, the sound wave can easily travels inside the larger pores of coconut coir fiber rather than fiberglass that have smaller pores. The sound wave of low frequency can travel into coconut coir fiber and vibrates with the fibers surface more easily to compare with fiberglass thus converting the sound energy into heat energy. As results, it gives coconut coir fiber a higher sound absorption coefficient, α for low frequency [13].

For higher frequencies, it has smaller wavelength according previous relation. With much more smaller wavelength, the sound wave can travels into small fiberglass pores and convert sound energy to heat energy thru vibration more effectively. Coconut coir fiber has larger pores, thus it unable to absorb effectively sound wave with smaller wavelength because it has more gap in interstices of fiber making collision of sound wave with coconut coir surface much less to compare with much tightly packed structure of fiberglass [14].

Effect Of Coconut Coir Thickness To Sound Absorption Characteristics Of Coconut Coir Acoustic Panel

The effect of coconut coir fiber thickness was studied to observed the behavior of sound absorption characteristic of coconut coir when different thickness is use. Test is conduct by reverberation room method and simulation using WinFLAG™. Four tests were conducted with coconut coir having different thickness of 10 mm, 20 mm, 30 mm, and 40 mm. All four test specimens have constant area of 6 m^2. This test was also done to studied the optimum thickness that gives the best sound absorption quality for every frequency band

Based on table 2, all four test specimens have almost the similar pattern where sound absorption coefficient, α for all test specimens increases with increasing frequency. Maximum sound absorption coefficient, α for coconut coir with 10 mm thickness is at 4000 Hz with value of 0.62. Coconut coir with other thickness also reaches its maximum sound absorption coefficient, α at 4000 Hz with value of 0.78 for 20 mm, 0.85 for 30 mm and 0.9 for 40 mm. Also, at all frequency coconut coir with larger thickness have larger sound absorption coefficient, α. At low frequency, 125 Hz, all four test specimens have very low sound absorption coefficient, α with value below 0.2. Hence from this simulation it can be concluded that larger thickness gives larger sound absorption coefficient, α thus higher sound absorption quality.

It can be observed that sound absorption coefficient, α increase from 125 Hz and keep increasing until maximum point at 1000 Hz for 20 mm, 30 mm, and 40 mm but 2000 Hz for 10 mm. For frequency above 1000 Hz, sound absorption coefficient, α for all four test specimens started to decrease to average value of 0.5. For 10 mm coconut coir thickness, minimum sound absorption coefficient, α is 0.05 and maximum sound absorption coefficient, α is 0.68. For 20 mm coconut coir thickness, minimum sound absorption coefficient, α is 0.1 and maximum sound absorption coefficient, α is 0.72 which is higher than 10 mm coconut coir thickness. For coconut coir with 30 mm thickness, minimum sound absorption coefficient, α is 0.16 and maximum sound absorption coefficient, α is 0.75, higher than 10 mm and 20 mm coconut coir thickness. For coconut coir with 40 mm thickness, minimum sound absorption coefficient, α is 0.27 and maximum sound absorption coefficient, α is 0.81 which is the highest value to compared with other thickness.

For 10 mm coconut coir thickness, sound absorption coefficient, α at 2000 Hz and 4000 Hz decrease to 0.68 and 0.52 respectively. Meanwhile, for 20 mm thickness, sound absorption coefficient, α at 2000 Hz and 4000 Hz also decrease to 0.66 and 0.51 respectively. For 30 mm coconut coir thickness, sound absorption coefficient, α also decrease at same point to 0.63 and 0.49. Meanwhile, for 40 mm thickness, sound absorption coefficient, α at 2000 Hz and 4000 Hz decrease to 0.62 and 0.51 respectively.

This shows that for low frequency band ranging from 100 Hz to 1000 Hz, thicker coconut coir gives higher sound absorption coefficient, α means, better sound absorption quality. For higher frequency above 1000 Hz, sound absorption coefficient, α decrease with increasing thickness. Hence, for high frequency application, thicker coconut coir is not recommended. This theory is supported by previous research by Everest [13] stated that it is logical to expect greater sound absorption from thicker materials, but this logic holds primarily for the lower frequencies.

CONCLUSION

Experimental result shows that coconut coir has better sound absorbing quality than fiberglass for low frequency at 500 Hz and below. Therefore, coconut coir has high potential to be applied as sound absorbing material. By using coconut coir as substituting the use of other commercial porous sound absorbing material, cost can be reduce as coconut coir fiber is easier to obtain, cheaper and easier to process. Moreover, coconut coir fiber is safe and not hazardous to humans compare to fiberglass or other synthetic fibers. Meanwhile, sound absorption coefficient increases with increasing of thickness. However, it holds only for low frequency range. The effect of test specimen area to sound absorption characteristics of coconut coir acoustic panel is also studied in this research. Result shows that lower area of test specimen gives better sound absorption. This is due to the diffraction effect of sound energy around the perimeters of the sound absorbing materials and to the additional absorption provided by the exposed panel edges. It can be concluded that coconut coir show high potential to be applied as sound absorbing material. This natural fiber can be used to replace synthetic fiber and mineral wool in the context of acoustics environment and control.

ACKNOWLEDGEMENTS

The author of this paper would like to express their gratitude and sincere appreciation to University Malaysia Sabah for providing the financial support.

REFERENCES

[1] Asdrubali, F. 2006. Survey on the Acoustical Properties of New Sustainable Materials for Noise Control. Proceedings of Euronoise 2006. 30 May - 1 June, 2006. Tampere, Finland,. pp. 1- 10.

[2] Yang, H. S., Kim, D. J. and Kim, H. J. 2003. Rice straw-wood particle composite for sound absorbing wooden construction materials. Bioresource Technology 86(2): pp.117-121.

[3] Hong, Z., Bo, L. Guangsu, H. and Jia, H. 2007. A novel composite sound absorber with recycled rubber particles. Journal of Sound and Vibration 304(1): pp.400-406.

[4] John, M. J., Indira, K. N., Geethamma, V. G., Shaji, J. and Thomas, S. Coir and Hemp FiberReinforced Polymer Composites. In Fakirov, S. and Bhattacharyya D. (Eds.) 2007. Handbooks of Engineering Biopolymers: Homopolymers, Blends and Composites, pp. 285-309. Munich: Hanser Gardner Publications, Inc.

[5] Joshi, S. V., Drzal L. T., Mohanty, A. K. and Arora, S. 2003. Are natural fiber composites environmentally superior to glass fiber reinforced composites?. Composites Part A: Applied Science and Manufacturing 35(3): pp. 371-376.

[6] Satyanarayana, K. G., Kulkarni, A. G. and Rohatgi, P. K. 1981. Structure and properties of coir fibres. Sadhana 4(4): pp.419-436.

[7] Sivapragasam, A. 2008. Coconuts in Malaysia – current developments and potential for revitalization. Shah Alam: MARDI

[8] Wambua, P., Ivens, J. and Verpoest, I. 2003. Natural fibres: can they replace glass in fibre reinforced plastics?. Composite Science and Technology 63(9): pp.1259-1264.

[9] Clemons, Craig M., Caulfield, Daniel F. 2005. Natural Fibers: Functional Fillers for Plastics. Weinheim: Wiley-VCH, 2005: pp.195-206.

[10]Fouladi, M. H., Ayub, Md. and Nor, M. J. M. 2011. Analysis of Coir Fiber Acoustical Characteristics. Applied Acoustics 72 (1): pp.35-42.

[11]Mahzan, S., Zaidi, A. M. A., Arsat, N., Hatta, M. N. M., Ghazali, M. I. and Mohideen, S. R. 2010. Study on sound absorption properties of coconut coir fiber reinforced composite with added recycle rubber. International Journal of Integrated Engineering (Issue on Mechanical, Materials and Manufarcturing Engineering 2(1): pp.29-34.

[12]Ayub, Md., Nor, M. J. M., Amin. N., Zulkifli. R. and Ismail, A. R. 2009. A Preliminary Study of Effect of Air Gap on Sound Absorption of Natural Coir Fiber, Proceeding of the Regional Engineering Postgraduate 2009.

[13]Everest,F,A. 2001. Master Handbook of Acoustic. New York: McGraw-Hill.

[14]Bucur,V. 2006. Acoustic of Wood. Berlin: Springer Publications.

GEOMATE 2017

Seventh International Conference on

Geotechnique, Construction Materials & Environment

21-23 November 2017, Mie, Japan

Invitation to participate

- The "International Journal of GEOMATE" is a Scientific Journal of the GEOMATE International Society that encompasses a broad area in Geotechnique, Construction Materials and Environment.
- The key objective of this journal is to promote interdisciplinary research from various regions of the globe.
- The editorial board of the journal is comprised of extensively qualified researchers, academicians, scientists from Japan and other countries of the world.
- It is peer-reviewed Journal that is published quarterly till 2015 and now monthly. All articles published in this journal are available on line.
- Contributors may download the manuscript preparation template for submitting paper or contact to the Editors-in-Chief

  [editor@geomatejournal.com].